Frontiers in Earth Sciences

Gilles Ramstein
Amaëlle Landais
Nathaelle Bouttes
Pierre Sepulchre
Aline Govin *Editors*

Paleoclimatology

Springer

Frontiers in Earth Sciences

More information about this series at http://www.springer.com/series/7066

Gilles Ramstein • Amaëlle Landais •
Nathaelle Bouttes • Pierre Sepulchre •
Aline Govin
Editors

Paleoclimatology

Springer

Editors
Gilles Ramstein
LSCE/IPSL, CEA-CNRS-UVSQ
Université Paris-Saclay
Gif-sur-Yvette, Ariège, France

Amaëlle Landais
LSCE/IPSL, CEA-CNRS-UVSQ
Université Paris-Saclay
Gif-sur-Yvette, Ariège, France

Nathaelle Bouttes
LSCE/IPSL, CEA-CNRS-UVSQ
Université Paris-Saclay
Gif-sur-Yvette, Ariège, France

Pierre Sepulchre
LSCE/IPSL, CEA-CNRS-UVSQ
Université Paris-Saclay
Gif-sur-Yvette, Ariège, France

Aline Govin
LSCE/IPSL, CEA-CNRS-UVSQ
Université Paris-Saclay
Gif-sur-Yvette, Ariège, France

ISSN 1863-4621 ISSN 1863-463X (electronic)
Frontiers in Earth Sciences
ISBN 978-3-030-24981-6 ISBN 978-3-030-24982-3 (eBook)
https://doi.org/10.1007/978-3-030-24982-3

Translated from the original French by Mary Minnock

This Springer imprint is published by the registered company Springer Nature Switzerland AG
The registered company address is: Gewerbestrasse 11, 6330 Cham, Switzerland

Foreword

A brief history of paleoclimates

Climate is undeniably a topical issue of utmost importance. It has been the focus of attention for several decades now, during which the study of ancient climates (paleoclimatology) has progressed and gained a solid reputation. Currently, this work has become fundamental to our understanding of how the climate system functions and to validate the models used to establish future projections. Thanks to the study of past climates, a database documenting a much greater diversity of climate changes than during recent centuries, has been created. This diversity makes it possible to test climate models in situations that are vastly different from those we have known over the last 150 years and, in some cases, for climates that are closer to those that await us in the future if we apply the conclusions of the Intergovernmental Panel for Climate Change.

The Earth's climate changes have always changed over time and will continue to change in the future. While we are all aware of the weather phenomena that condition our daily lives, few of us are aware of what climate really is. Climatology is the science that explores the great variability in meteorological conditions over time and space, throughout history. This word comes from the Greek word *klima* meaning inclination, in this case referring to that of the rays of the Sun. Since the dawn of our civilization, therefore, we have linked the variations in climate and in the energy received from the Sun in a relationship of cause and effect. For a long time, the term 'climate' was reserved to describe the characteristics of air temperature and precipitation particular to different parts of the globe. This description was based on meteorological measurements and their averages conducted over a few decades. It is only recently understood that climate also varies over much longer time scales and therefore concerns more than just the atmosphere. At present, specialists studying climate and its variations analyze all of the fluid and solid envelopes of the Earth. Along with the atmosphere, we associate the hydrosphere and the cryosphere which, together, represent the systems where water exists in solid (snow, glaciers, and ice sheets) and liquid form (rivers, lakes, and seas), the continents where plate tectonics and volcanic activity occur, and finally at the surface, the whole living world (biosphere) that influences nature, the properties of soil cover, and the biogeochemical cycles.

Climatology has evolved from being a descriptive discipline to become a multidisciplinary science involving five complex systems and their various interactions. It is therefore not surprising that the resulting climate studies vary on scales ranging from the season to millions of years. Although it is only in the last few decades that this science has exploded, the first discovery and study of climate change beyond the annual and decadal scales date back to the eighteenth century. It was at this time that the presence of erratic boulders in the mountainous landscape became associated for the first time with the massive extension of glaciers. In 1744, the Grenoble geographer Pierre Martel (1706–1767) reported that the inhabitants of the Chamonix Valley in the Alps attributed the dispersion of *roches moutonnées* to the glaciers themselves, which would have extended much further in the past. This was a revolutionary idea, because until then, most scientists still referred to the myth of the Biblical Flood to explain landscape structures. This was the case of Horace Benedicte de Chaussure (1740–1799) from Geneva, the French paleontologist, Georges Cuvier (1769–1832) and the Scottish geologist,

Charles Lyell (1797–1875), who continued to assume that these boulders were carried by the strength of strongly flowing waters. However, the location and nature of these boulders and other moraines led some scientists to admit that ice transport would provide a better explanation for the various observations. The Scottish naturalist, James Hutton (1726–1797), was the first to subscribe to this idea. Others followed his lead and detected the imprint of climatic changes in the fluctuations of the extent of the glaciers. These pioneers were the Swiss engineer, Ignace Venetz (1788–1859); the German forestry engineer, Albrecht Reinhart Benhardi (1797–1849); the Swiss geologist, Jean de Charpentier (1786–1855); and the German botanist, Karl Friedrich Schimper (1803–1867), who introduced the notion of ice ages. But it was the Danish-Norwegian geologist, Jens Esmark (1763–1839), who, in pursuing his analysis of glacier transport, proposed in 1824, for the first time, the notion that climate changes could be the cause and that these could have been instigated by variations of Earth's orbit.

It was the work of these pioneers that led the Swiss geologist, Louis Agassiz (1801–1873) to make the address to the Swiss Society of Natural Sciences of Neufchatel in 1837 entitled 'Upon glaciers, moraines and erratic blocks'. It was also at the beginning of the nineteenth century that the Frenchman Joseph Adhémar (1797–1862), not content with studying the polar ice caps, attempted to explain in his book, *Révolutions de la Mer, Déluges Périodiques* (1842), the pattern of ice ages stemming from the precession of the equinoxes. The astronomical theory of the paleoclimates was born and would be continued, thanks to the development of celestial mechanics, by the Frenchmen, Jean le Rond d'Alembert (1717–1783), Jean-Baptiste Joseph Delambre (1749–1822), Pierre-Simon Laplace (1749–1827), Louis Benjamin Francoeur (1773–1849), and Urban Le Verrier (1811–1877). In parallel, other advances were made with the first calculations of the long-term variations in the energy received from the Sun, variations due to the astronomical characteristics of the eccentricity of the Earth's orbit, the precession of the equinoxes, and the obliquity of the ecliptic. This was demonstrated by the work of John Frederick William Herschel (1792–1871), L.W. Meech (1821–1912), and Chr. Wiener (1826–1896), supported by the work of the mathematicians André-Marie Legendre (1751–1833) and Simon-Denis Poisson (1781–1840).

This sets the stage for James Croll (1821–1890) to develop a theory of ice ages based on the combined effect of the three astronomical parameters, a theory according to which winter in the northern hemisphere played a determining role. This theory was much appreciated by the naturalist, Charles Robert Darwin (1809–1882), and was taken up by the Scottish geologist brothers, Archibald (1835–1924) and James (1839–1914) Geikie, who introduced the notion of the interglacial. It is also the basis for the classification of alpine glaciations by Albrecht Penck (1858–1945) and Edward Brückner (1862–1927) and American glaciations by Thomas Chowder Chamberlin (1843–1928). However, geologists became increasingly dissatisfied with Croll's theory and many critics of it emerged. Many refuted the astronomical theory and preferred explanations that related to the Earth alone. The Scottish geologist, Charles Lyell (1797–1875), claimed that the geographical distribution of land and seas explained the alternation of hot and cold climates, while others turned to variations in the concentration of certain gases in the atmosphere. Hence, the French physicist, Joseph Fourier (1786–1830), expounded on the first notion of the theory of the greenhouse effect. He was followed by the Irish chemist, John Tyndall (1820–1893), to whom we owe the first experiments on the absorption of infrared radiation and the hypothesis of the fundamental role played by water vapor in the greenhouse effect. Later, the Italian, Luigi de Marchi (1857–1937) and the Swedish chemist, Svante Arrhenius (1859–1927) proposed, along with other scientists of their time, that the ice ages were caused by decreases in atmospheric carbon dioxide concentration. In 1895, Arrhenius suggested, in an article published by the Stockholm Physics Society, that a 40% reduction or increase in CO2 concentration in the atmosphere could lead to feedback processes that would explain glacial advances or retreats.

A revival of the astronomical theory became, however, possible with advances in the calculation of astronomical elements by the American astronomer John Nelson Stockwell (1822–1920) and the Serbian astronomer Vojislava Protich Miskovitch (1892–1976) and of

solar irradiation (1904) by the German mathematician, Ludwig Pilgrim (1879–1935). It was Joseph John Murphy (1827–1894), however, who, as early as 1869, proposed that cool summers of the northern hemisphere had instigated the ice ages. This original idea was taken up in 1921 by the German paleoclimatologist Rudolf Spitaler (1859–1946), but was popularized by the Serbian geophysicist engineer, Milutin Milankovich (1879–1958), mainly through his books *Mathematical Theory of Thermal Phenomena Produced by Solar Radiation* (1920) and *Kanon der Erdbestrahlung und seine Anwendung auf des Eizeitenproblem* (1941). Milankovitch was a contemporary of the German geophysicist Alfred Wegener (1880–1930) with whom he became acquainted through the Russsian-born climatologist Wladimir Köppen (1846–1940), Wegener's father-in-law (Thiede, 2017). The modern era of astronomical theory was born, even if there remained much criticism related to the lack of reliable paleoclimatic data and of a reliable timescale, both by geologists and meteorologists. It was not until the 1950s and 1960s that new techniques made it possible to date, measure, and interpret the climate records contained in marine sediments, in ice and on land. In 1955, the American, Cesare Emiliani (1922–1995), proposed a stratigraphy, which still applies today, based on the succession of minima and maxima of the oxygen-18 / oxygen-16 isotopic ratio measured in the foraminiferal shells found in sediments taken from the deep ocean. The interpretation of this isotopic ratio in terms of salinity was made by Jean-Claude Duplessy (1970), and in terms of temperature and volume of ice (1973) by Nicholas Shackleton (1937–2006) and Niels Opdyke (1933–2019). Mathematical tools made it possible to establish transfer functions to quantitatively interpret information collected in the oceans in 1974 by the American paleoceanographers John Imbrie (1925–2016) and Nilva Kipp (1925–1989),) and in tree rings (Harold Fritts, 1968). Efforts by the CLIMAP group (1976) resulted in the first seasonal climate chart of the Last Glacial Maximum and the pivotal article by James Hays, John Imbrie, and Nicholas Shackleton (1976). The arrival of big computers allowed the first climate simulations to be conducted using general circulation models (Fred Nelson Alyea, 1972), and further astronomical calculations led to the establishment of a high-precision time scale reference, as well as the determination of the daily and seasonal irradiation essential for climate modeling (André Berger, 1973 and Berger and Loutre, 1991).These calculations of the astronomical parameters were based on the 1974 and 1988 developments of the orbital elements by the French astronomers Pierre Bretagnon (1942–2002) and Jacques Laskar, respectively. These are valid over a few million years. The Laskar solution was extended over a few tens of millions of years by Laskar et al. (2011) and over the whole Mesozoic with the American paleobiologist Paul Olsen and colleagues (2019).

This evolution and the recent advances in paleoclimatology show the difficulties involved in tackling the study of the climate system. Overcoming these difficulties requires high-quality books to improve understanding and to update the range of disciplines involved. It is with this perspective in mind that this book was written. Written originally in French, it unquestionably fills a gap in the field of graduate and postgraduate third-level education that goes far beyond its description. It provides an overview of the state of knowledge on a number of key topics by outlining the information necessary to understand and appreciate the complexity of the disciplines discussed, making it a reference book on the subject. The first of the two volumes is devoted to the methods used to reconstruct ancient climates, the second to the behavior of the climate system in the past. Many of the thirty-one chapters are written by researchers from the *Laboratoire des Sciences du Climat et de l'Environnement* and associated research laboratories each focusing on his or her area of expertise, which ensures a reliable document founded on solid experience.

Understanding the evolving climate of the Earth and its many variations is not just an academic challenge. It is also fundamental in order to better understand the future climate and its possible impacts on the society of tomorrow. Jean-Claude Duplessy and Gilles Ramstein have achieved this huge feat by bringing together fifty or so of the most highly reputed researchers in the field.

The book they have written is a whole, providing both the necessary bases on the reconstruction techniques of ancient climates, their chronological framework, and the functioning of the climate system in the past based on observations and models. This book will allow all those who want to know more, to explore this science, which, although difficult, is hugely exciting. It will also give them the essential information to establish an objective idea of the climate and its past and future variations.

You may find most of the references and pioneering studies mentioned in this preface in BERGER A. 2012. A brief history of the astronomical theories of paleoclimates. In: "Climate change at the eve of the second decade of the century. Inferences from paleoclimates and regional aspects". Proceedings of Milankovitch 130th Anniversary Symposium, A. Berger, F. Mesinger, D. Sijacki (eds). 107–129. Springer-Verlag/Wien.DOI 10.1007/978-3-7091-0973-1.

André Berger
Emeritus Professor at the Catholic University of Louvain
Louvain la Neuve, Belgium

Introduction

For a long time, geology books devoted only a few lines to the history of past climates of our planet, mostly to establish the deposition framework for the sediments that geologists found on the continents, the only area of enquiry available to them. Scientists soon realized that the copious coal deposits of England, Belgium, Northern France, Germany, and Poland resulted from the fossilization of abundant vegetation facilitated by a warm and humid equatorial climate that reigned over Western Europe, some 350 million years ago (an illustrated insert in Chap. 2 volume I provides a diagram of continental drift since 540 Ma). Fifty million years later, the sediments of these same regions, red sandstone, poor in fossils and associated with evaporites testify to the replacement of forests by desert areas, dotted with occasional highly saline lakes, similar to what we currently find in Saharan Africa. Humidity gave way to intense aridity and we had no idea why. It was not until the discovery of plate tectonics that we realized that Europe had slowly drifted toward the tropics. This transformation of the face of the Earth due to tectonics is illustrated through 16 maps in Chap. 2 volume I.

The discovery of glaciations was a revelation for the geologists of the nineteenth century. A major polemic broke out at the Swiss Society of Natural Sciences in Neuchâtel when, in 1837, its president Louis Agassiz presented his explanation, incredible at the time, for the presence of gigantic boulders that dot the Jura mountains. He daringly claimed that these erratic boulders were not the remnants of the Biblical Flood, but rather enormous rocks transported over long distances by gigantic glaciers which used to cover the high latitudes of our hemisphere.

The controversy died down quickly, when European and American geologists discovered traces of glaciers all over the Northern Hemisphere, just as Agassiz imagined. In Europe, as in North America, mapping of the terminal moraines left behind by glaciers when they melted showed proof of the presence of gigantic ice caps in a past that seemed distant. especially since there was no idea how to date them.

As the idea of the Biblical Flood fell out of favor, a new theory, based on astronomical phenomena, soon appeared. Scientists like Joseph Adhémar and James Croll realized that there were small, quasi-periodic variations over time in the movement of the Earth around the Sun and suggested that associated mechanisms could periodically cause glacial advances and retreats. Finally, it was Milutin Milankovitch, a professor in Belgrade, who would lay the foundations for a complete mathematical theory of glaciations, the legitimacy of which was proven when paleoceanographers found the frequencies of orbital parameters reflected in the isotopic analysis of marine cores. We now know that the last one of these glacial periods culminated only 20,000 years ago and was preceded by many others.

The great contribution by Milankovitch was to plant a new idea within the scientific community: Ancient climates are not only of immense curiosity to geologists; they obey the same physical laws as those governing the current climate.

This intellectual revolution has had far-reaching consequences and has profoundly altered the approach to the study of ancient climates making paleoclimatology a science with many links to geology, geochemistry, oceanography, glaciology as well as the approach to the physical and dynamic dimensions of the climate. The first part of this book describes the

physical, chemical, and biological phenomena that govern the functioning of the climate system and shows how it is possible to reconstruct the variations in the past at all timescales.

This is the work of paleoclimatologists. As soon as the means became available to them in the second half of the twentieth century, they undertook to track down all traces of climate change so as to establish a planetary vision. This led them to develop new methods of sampling continental sediments, marine sediments in the context of major oceanographic campaigns, and ice cores by carrying out large-scale drilling campaigns of mountain glaciers and the ice sheets of Greenland and of Antarctica. The level of resources that needs to be mobilized is such that the drilling campaigns of polar ice and of marine sediments from all the world's oceans could only be carried out in an international cooperative framework which makes it possible to coordinate the efforts of the various teams.

This scientific investment has produced an abundant harvest of samples containing records of past climates. On the continents, lake sediments; peat bogs; concretions in caves; and fossil tree rings have provided many indicators of environmental conditions, especially of the behavior of vegetation and the atmosphere. In the ocean, samples have been taken from all of the large basins and cores are able to trace the history of the last tens of millions of years. Finally, the large drillings in the ice sheets have provided information not only on polar temperatures, but also on the composition of the atmosphere (dust and the concentrations of greenhouse gases, such as carbon dioxide and methane).

Unfortunately, nature has no paleothermometer or paleopluviometer, and therefore, there is no direct indicator of the changes in temperature or precipitation: Everything has had to be built from scratch, not only to reconstruct the climates, but also to date them. Extracting a reconstruction of the evolution of the climate from these samples has necessitated considerable developments using the most innovative methods from the fields of geochemistry, biology, and physics. Firstly, it was essential to establish a timeframe to know which period was covered by each sample. Many methods were developed, and they are the subject of the second part of this book. Radioactive decay, which is governed by strict physical laws, plays a vital role. It has made it possible to obtain timescales converted into calendar years, and it has provided clarification on stratigraphic geology. Other more stratigraphic approaches have been implemented: identification of characteristic events that need to be dated elsewhere; counting of annual layers; or modeling of ice flow. It has thus been possible to establish a chronological framework, and paleoclimatologists are now trying to make it common to all data via an on-going effort to make multiple correlations between the various recordings. Few climatologists rely on one indicator. The confidence that they have in reconstructing a climate change at a given time is obtained by intersecting reconstructions from independent indicators but also by confronting them with results from models. Methods of reconstructing the evolution of the different components of the climate system from geological indicators then had to be developed. These are extremely varied, and their description constitutes the main and third part of volume I. Many use the latest developments in paleomagnetism, geochemistry, and statistical methods to empirically link the distribution of fossil plants and animals with environmental parameters, primarily air and water temperature. Reconstructions achieved in this way have now reached a level of reliability such that, for certain periods, not only qualitative variations (in terms of hot/cold, dry/wet) can be obtained, but even quantitative ones with the associated uncertainties also quantified. This is the level of climate reconstruction necessary to allow comparison with climate models.

The use of climate models also gained momentum during the second half of the twentieth century. First established to simulate atmospheric circulation, they have progressed by integrating more and more efficiently the physics, processes, and parameterization of the radiative budget and the hydrological cycle, in particular, by incorporating satellite data. However, the atmosphere only represents the rapid component of the climate system.

The late 1990s dramatically demonstrated the need to link atmospheric models to global patterns of the ocean and vegetation to reconstruct climate change. Indeed, teams from the GISS in the USA and from Météo-France bolstered by their atmospheric models that had

succeeded in reconstructing the current climate, independently tried to use the disruption of the radiative budget calculated by Milankovitch to simulate the last entry into glaciation 115,000 years ago. In both cases, it was a total fiasco. The changes induced by the variation of the orbital parameters in these models were far too small to generate perennial snow. The components and feedbacks related to the ocean and terrestrial vegetation needed to be included. Developing a model that couples all three of these components is what modelers have been striving to achieve over the last 20 years, and these are the models that now contribute to the international IPCC effort.

Today, the so-called Earth system models that incorporate aspects from the atmosphere–ocean–terrestrial and marine biosphere, chemistry, and ice caps are used to explore the climate of the future and the climates of the past. Spatially, they are increasingly precise, they involve a very large number of processes and are run on the largest computers in the world. But, the flip side of this complexity is that they can only explore a limited number of trajectories because of the considerable computing time they require. Also, from the beginning, climate modelers armed themselves with a whole range of models. From behemoths like the 'general circulation models' to conceptual models, with models of intermediate complexity in-between. From this toolbox, depending on the questions raised by the paleoclimatic data, they choose the most appropriate tool or they develop it if it does not exist. With the simplest models, they can explore the possible parameter variations and, by comparing them with the data, try to establish the most plausible scenario. All of these modeling strategies are described in detail in volume II, which constitutes the last and fourth part of this book.

This investigative approach at each step of the research work, dating, reconstruction, modeling, and the back and forth between these stages allows us to develop and refine the scenarios to understand the evolution of the past climates of the Earth. We are certain that this approach also allows us, by improving our understanding of the phenomena that govern the climate of our planet and through continuous improvement of the models, to better predict future climate change. This comparison between models and data, which makes it possible to validate numerical simulations of the more or less distant past, is an essential step toward the development of climate projections for the centuries to come, which will, in any case, involve an unprecedented transition.

Acknowledgement

This book would never have been possible without the very efficient help of Guigone Camus and Sarah Amram. We are grateful to Mary Minnock for the translation of each chapter. We also thank the LSCE for its financial support and Nabil Khelifi for his support from the origin to the end. Last but not least, thank you to all our colleagues—more than 50—who patiently contributed to this book.

Preface

Before taking this journey together into the Earth's paleoclimates, it is important to know what we will be facing. This exploration will bring us into the heart of the 'Earth system': a tangle of interwoven components with very different characteristics and response times, a system in constant interaction.

The first volume is dedicated (Chaps. 1 and 2) to an introduction to climate of the Earth. Chapters 3–9 focus on different time measurement and datation technics. The most important part of this first volume deals with the reconstructions of different climatic parameters from the three major reservoirs (ocean, continent, cryosphere, Chaps. 10–21). The second volume is devoted to modeling the Earth system to better understand and simulate its evolution (Chaps. 1–9). Last but not least, the final chapter (Chap. 10) describes the future climate of the Earth projection from next century to millennia.

The first part of this book (Chaps. 1 and 2) will equip the reader with a 'climate kit' before delving into the study of paleoclimates. This quick overview shows the great diversity in the systems involved. From the microphysics of the clouds that can be seen evolving over our heads by the minute to the huge ice caps that take nearly 100,000 years to reach their peak, the spatiotemporal differences are dizzying (Chap. 1). Yet, it is the same 'Earth system' that, throughout the ages, undergoes various disturbances that we will address. Chapter 2 takes us on a journey through the geological history of our planet. The distribution of continents, oceans, and reliefs changes how energy and heat are transported at the Earth's surface by the ocean and the atmosphere.

The study of paleoclimates requires an understanding of two indispensable concepts in order to describe the past climates of the Earth.

The first is the concept of time. Measuring time is fundamental to our research, and an understanding of the diversity of temporalities particular to paleoclimatic records is essential. The second part (Chaps. 3 to 9) of this book is devoted to the question of the measurement of time. Different techniques may be implemented depending on the timescales considered in Chap. 3. Thus, although carbon-14 (Chap. 4) provides us with reliable measurements going back to 30,000–40,000 years ago, other radioactive disequilibria (Chaps. 5 and 6) need to be used to access longer timescales. But it is not only the radioactivity-based methods that inform us of the age of sediments; the use of magnetism (Chap. 7) is also a valuable way of placing events occurring on the geological timescale into the context of climate. On shorter timescales, the use of tree rings is also a valuable method (Chap. 8). Ice core dating techniques will also be outlined (Chap. 9). This gamut of different methods shows how researchers have succeeded in developing 'paleo-chronometers' which are essential to locate climate archives within a temporal context, but also to establish the connections of cause and effect between the different components of the Earth system during periods of climatic changes.

The second concept is that of climate reconstruction. Indeed, in the same way that there is no single chronometer that allows us to go back in time, there is not one paleothermometer, pluviometer, or anemometer. Just as it was necessary to invent paleo-chronometers based on physical or biological grounds in order to attribute an age and an estimate of its uncertainty to archives, the relevant climatic indicators had to be invented to quantify the variations in temperature, hydrological cycle, and deepwater current. The third part of this book (Chaps. 10

–21) is devoted to the slow and complex work of reconstruction by applying this whole range of indicators. Thus, we can reconstruct the climate of the major components of the climate system: the atmosphere, the ocean, the cryosphere, and the biosphere. But we can also take advantage of the specificities of temperate or tropical lakes, of caves and their concretions (speleothems), of tree rings and even, more recently, of harvesting dates (Chap. 17). How can paleo-winds or, to put it in more scientific jargon, the variations in atmospheric dynamics be reconstructed? Based on the isotopic composition of precipitation (Chap. 10) or of the loess (Chap. 13), not only can the evolution of the surface and deep ocean be reconstructed, but also the geometry and dynamics of large water masses (Chap. 21). For land surfaces, palynology and dendroclimatology enable us to retrace the evolution of vegetation and climate, respectively (Chaps. 12 and 16). Finally, the cores taken from the ice caps of both hemispheres make it possible to reconstruct the polar climate (Chap. 11).

In addition to these two main concepts, we also need to understand how fluctuations in the hydrology of the tropics have caused variations in lakes (Chaps. 18 and 19) and glaciers (Chap. 20); these factors also tell a part of the climate story. Other markers, such as speleothems (Chap. 14) or lake ostracods (Chap. 15) reveal changes in climate in more temperate areas.

Thus, a description of the global climate emerges from the local or regional climate reconstructions. Through coupling these reconstructions with dating, our knowledge of climate evolution progresses constantly. Nevertheless, this image is both fragmentary, because of the strong geographic and temporal disparity of our knowledge, and unclear, because of the uncertainties in the reconstructions that the paleoclimatologist tries to reduce. There is still a long way to go in terms of developing new indicators and improving those widely used in order to complete and refine this description.

The second volume of this book (Chaps. 22–30) focuses on the major processes and mechanisms explaining the evolution of past climate from geological to historical timescales, whereas last Chap. 31 examines future climate projections. First of all, we address, in the very long term, the interactions between tectonics and climate over the timescale of tens to hundreds of millions of years (Chap. 22). Then, we deal with the biogeochemical cycles that govern the concentrations of greenhouse gases in the atmosphere over the last million years (Chap. 23). And finally, we consider the interactions with ice caps (Chap. 24).

We will continue our journey simulating the climate evolution through time from the formation of the Earth (4.6 billion years ago) up to the future climates at scales from a few tens of thousands to a hundred of years. On this journey, it becomes obvious that the dominant processes, those that drive climate change, vary according to timescales: solar power, which increases by about 7% every billion years places its stamp on very long-term evolution, whereas at the scale of tens of millions of years, it is tectonics that sculpt the face of the Earth, from the high mountain ranges to the bathymetry of the ocean floor. Finally, 'the underlying rhythm of Milankovitch,' with a much faster tempo of a few tens of thousands of years can produce, if the circumstances permit, the glacial–interglacial cycles described in the preceding parts. On top of this interconnection of timescales, a broad range of processes and components of the climate system is superimposed. Through these chapters, we would like to highlight the need to model a complex system where different constituents interact at different timescales (Chap. 25). With the development of these models, the scope of investigation is vast. Indeed, ranging from recent Holocene climates (Chap. 30) to geological climates (Chaps. 26 and 27), how they evolve is underpinned by very different processes: from plate tectonics (Chap. 22) to orbital parameters (Chap. 28). The complexity of the system can also be seen in the abrupt reorganizations of the ocean–atmosphere system (Chap. 29). The capacity acquired in recent decades to replicate past climate changes using a hierarchy of models, and to compare these results with different types of data, has demonstrated the relevance of this approach coupling model simulations with data acquisition.

Nevertheless, the field of investigation of the Earth's past climates remains an important area of research with many questions being raised about the causes of climate reorganizations throughout the Earth's history. Even though several chapters clearly show recent breakthroughs in our understanding of past climate changes, and the sensitivity of our models to climate data has undeniably increased the extent to which we can rely on their outputs, we can legitimately question what they contribute to future climate. Chapter 10 addresses these issues. Will the ice caps, which have existed on Earth for only a short time relative to geological time, withstand human disturbance? And can this disturbance, apart from its own duration, have an impact on the rhythm of glacial–interglacial cycles?

At the end of these two volumes, you will have obtained the relevant perspective to project into the Earth's climates of the future. Indeed, by absorbing the most up-to-date knowledge of paleoclimatology in this book, you will be provided with the necessary objectivity to critically assess present and future climate changes. It will also give you the scientific bases to allow you to exercise your critical judgment on the environmental and climatic issues that will be fundamental in the years to come. Indeed, in the context of the Anthropocene, a period where man's influence has grown to become the major factor in climate change, the accumulated knowledge of the climate history of our planet gathered here is precious.

Gif-sur-Yvette, France

Gilles Ramstein
Amaëlle Landais
Nathaelle Bouttes
Pierre Sepulchre
Aline Govin

Contents

Volume 1

About the Editors

Gilles Ramstein is a director of research at Laboratoire des Sciences du Climat et de l'Environnement (LSCE, France). His initial degree is in physics and since 1992 he has specialized in climate modeling.

He has been responsible for many French and European research projects on the Pleistocene, Cenozoic, and Precambrian eras. He has also been the advisor of many Ph.D. students who have explored and expanded the frontiers of paleoclimate modeling.

As a climate modeler, he studies very different climate contexts from 'Snowball Earth' episodes (717–635 Ma) to more recent, and occasionally future, climate situations.

The main research topics he focuses on are

• **Geological time from the Precambrian to the Cenozoic**:

– Investigation of relationships between tectonics, the carbon cycle, and the climate with an emphasis on the impact on the climate and the atmospheric CO_2 cycle of major tectonic events such as plate movements, shrinkage of epicontinental seas, mountain range uplift, and the opening/closing of seaways.

– Leading international collaborations on projects on monsoon evolutions and the dispersal of human ancestors during the Neogene periods.

• **From the Pleistocene to future climate**: In this framework, his major interests are interactions between orbital forcing factors, CO_2 and climate. More specifically, his focus is on the response of the cryosphere, an important component of the climate system during these periods, with an emphasis on the development of the Greenland ice sheet at the Pliocene/Pleistocene boundary and abrupt climate changes driven by ice sheet variations.

He has also published several books and co-edited the French version of 'Paleoclimatologie' (CNRS Edition) and contributed to an online masters program devoted to educating journalists on climate change (Understanding the interactions between climate, environment and society ACCES).

Amaëlle Landais is a research director at Laboratoire des Sciences du Climat et de l'Environnement (LSCE, France). Her initial degree is in physics and chemistry and, since her Ph.D. in 2001, she has specialized in the study of ice cores.

She has been responsible for several French and European research projects on ice cores working on data acquisition both in the laboratory and in the field, interacting extensively with modelers. She has been the supervisor of ten Ph.D. students and is deeply committed to supporting and training students in laboratory work.

Her main research interests are the reconstruction of climate variability over the Quaternary and the links between climate and biogeochemical cycles. To improve our understanding of these areas, she develops geochemical tracers in ice cores (mainly isotopes), performs process studies using laboratory and field experiments, and analyzes shallow and deep ice cores from polar regions (Greenland and Antarctica). Through numerous collaborations and improvement of ice core dating methods, she tries to establish connections with other paleoclimatic archives of the Quaternary.

Nathaelle Bouttes is a research scientist at the Laboratoire des sciences du climat et de l'environnement (LSCE/IPSL). Following the completion of her Ph.D. in 2010 on the glacial carbon cycle, she went to the University of Reading (UK) for a five-year postdoc on recent and future sea-level changes. She then spent a year at Bordeaux (France) with a Marie–Curie Fellowship on interglacials carbon cycle before joining the LSCE in 2016. Since then, she has specialized in understanding glacial–interglacial carbon cycle changes using numerical models and model–data comparison.

She is mostly using and developing coupled carbon-climate models to understand past changes of the carbon cycle, in particular the evolution of the atmospheric CO_2. She has been focusing on the period covered by ice core records, i.e., the last 800,000 years. She uses model–data comparison by directly simulating proxy data such as $\delta^{13}C$ to evaluate possible mechanisms for the orbital and millennial changes. She has been involved in several projects covering this topic as well as teaching and supervising Ph.D. students.

Pierre Sepulchre is a CNRS research scientist at the Laboratoire des sciences du climat et de l'environnement (LSCE/IPSL). He completed a Ph.D. on the Miocene climate of Africa in 2007, then went to UC Santa Cruz (USA) for a two-year postdoctoral position working on the links between the uplift of the Andes and atmospheric and oceanic dynamics. His lifelong research project at CNRS is to evaluate the links between tectonics, climate, and evolution at the geological timescales, focusing on the last 100 million years. Through the supervision of Ph.D. students and his collaboration with geologists and evolutionary biologists, he also worked at evaluating paleoaltimetry methods with the use of an isotope-enabled atmospheric general circulation model, as well as linking continental surface deformation, climate, and biodiversity in Africa and Indonesia. In recent years, he led the implementation and validation of a fast version of the IPSL Earth system model that allows running long climate integrations dedicated to paleoclimate studies.

Aline Govin is, since 2015, a research associate at the Laboratoire des Sciences du Climat et de l'Environnement (LSCE, Gif sur Yvette, France). She studied Earth Sciences at the Ecole Normale Supérieure of Paris (France) and obtained in 2008 a Ph.D. thesis in paleoclimatology jointly issued by the University of Versailles Saint Quentin en Yvelines (France) and the University of Bergen (Norway). Before joining the LSCE, she worked for five years as a postdoctoral fellow at the Center for Marine Environmental Sciences (MARUM, University of Bremen) in Germany.

Her research activities focus on the reconstruction of paleoclimatic and paleoceanographic changes by applying various types of geochemical and sedimentological tracers on marine sediment cores. She has mostly worked on the Earth's climatic changes of the last 150,000 years and is an expert of the last interglacial climate, which is an excellent case study to investigate the response of the Earth's climate to past warming conditions that could be encountered in the coming decades. Her research interests include the past variability of the deep North Atlantic circulation, the responses, and drivers of tropical monsoon systems (e.g., South American Monsoon), the development and calibration of paleo-tracers, the development of robust chronologies across archives, and the quantification of related uncertainties, as well as the comparison of paleo-reconstructions to climate model simulations of past climates.

She has authored around 30 scientific publications and has been involved in many French, German, and other international (e.g., Brazilian) projects.

The Climate System: Its Functioning and History

1

Sylvie Joussaume and Jean-Claude Duplessy

Climate plays an important role for mankind. It determines the conditions in which societies can develop as well as the resources available to them such as water and biological inputs (agriculture, forests, livestock). However, climate is a complex system. It is the result of interactions not only between the atmosphere, the oceans, landmasses and ice but also the biosphere: the living world. It varies depending on the timescale, and different mechanisms may come into play at different scales. The aim of this book is to show how a multi-disciplinary scientific community can now reconstruct, with increasing accuracy, the major features of past climates and discover how they are regulated by the geological evolution, geochemistry, physics and biology of our living planet, Earth.

Human living conditions are dependent on climate, but human beings, in turn, influence the climate system. They change the atmospheric concentration of greenhouse gases and aerosols, as well as the vegetation through deforestation and agriculture. For this reason, it is of major importance to society to understand how climate works and how man may be altering its course. This is a complex scientific problem because of the large number of feedbacks likely to occur and the study of past climates contributes to a better understanding of them by analyzing major climate changes provoked by natural causes.

Climate Change

Definition of Climate

Climate is defined by the statistics of the physical characteristics of the atmosphere. It differs from meteorology by focusing on statistics over several decades, by calculating the average state of the atmosphere and its variability from this average. In practice, climate is defined by the average conditions over a thirty-year period. Although this working definition makes sense while the weather is relatively stable, it becomes more difficult to apply during a period of rapid change. This was the case in the twentieth century during which two phases of rapid increase in the average temperature of our planet were detected by weather stations in the WMO network, one from 1910 to 1940 and the other from 1975 onwards (Fig. 1.1d). The period 1961–1990 is often taken as a reference.

Climate Changes in the Past

Climate is essentially variable, regardless of the time scales under consideration. Over past two millennia, historical chronicles and earliest instrumental measurements dating back to the seventeenth century have shown the existence of a very cold period in Europe from the sixteenth to the nineteenth century (the Little Ice Age), preceded by the Medieval Warm Period and another warm period during Roman times.

Geological data also show large upheavals in climate. Of course, this is over much longer periods than thirty years, but geologists strive to define a stratigraphic framework and precise geochronology to put these events into context within the history of our planet (Fig. 1.1). For example, about seven hundred and fifty million years ago, the Earth went through an intense glaciation phase; glaciers flowed down to sea level on every continent, even in low latitudes, to such an extent that our planet could be described as a snowball. Conversely, during the Mesozoic Era (25–65 million years), the conditions were hot, even at high latitudes. During the Cenozoic Era (from 65 million years), the glaciers grew slowly, first on the Antarctic continent and then on Greenland. For the past three million years or so, the Earth has experienced a succession of ice ages, marked by glaciers advancing over land at high and middle latitudes of

S. Joussaume (✉) · J.-C. Duplessy
Laboratoire des Sciences du Climat et de l'Environnement, LSCE/IPSL, CEA-CNRS-UVSQ, Université Paris-Saclay, 91191 Gif-sur-Yvette, France
e-mail: sylvie.joussaume@lsce.ipsl.fr

G. Ramstein et al. (eds.), *Paleoclimatology*, Frontiers in Earth Sciences,
https://doi.org/10.1007/978-3-030-24982-3_1

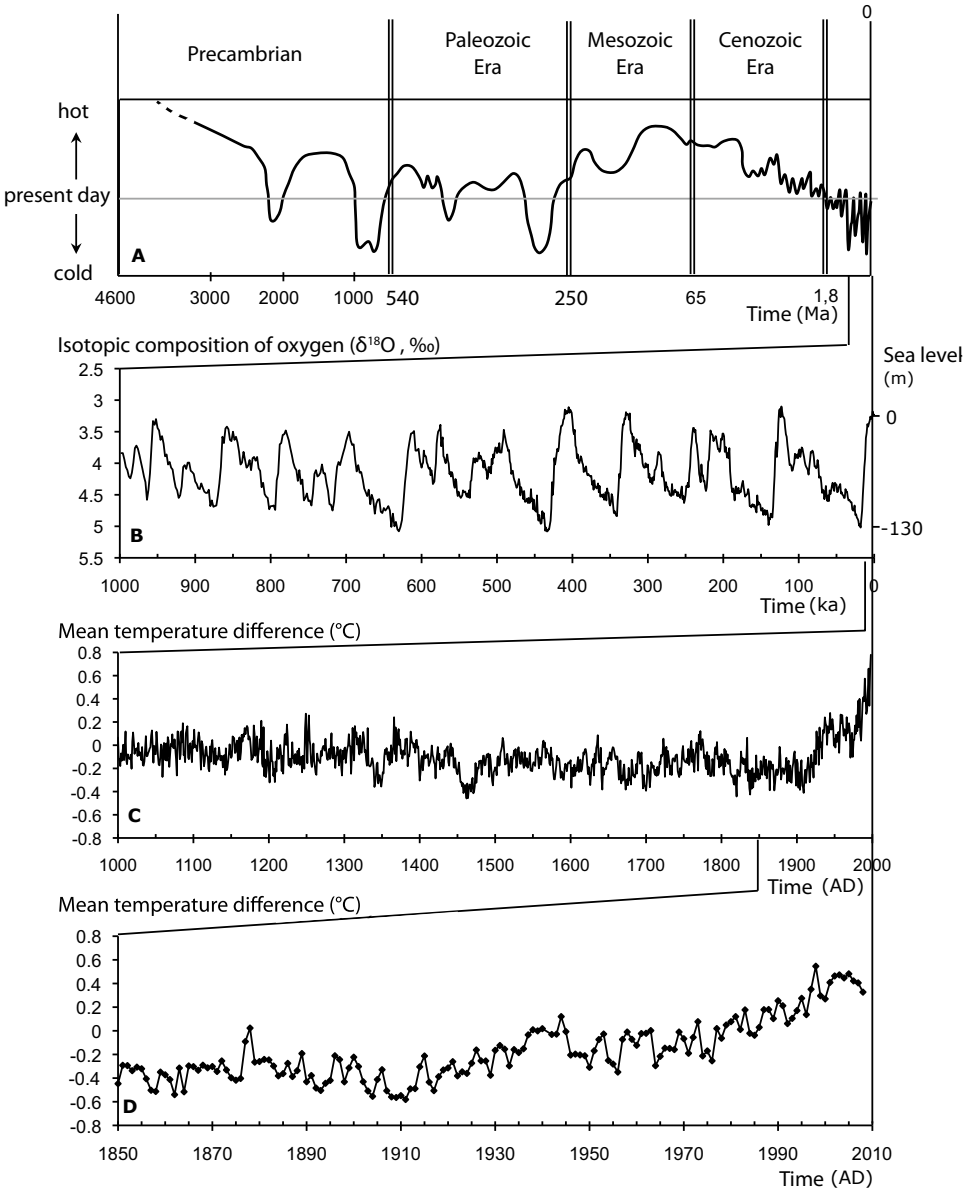

Fig. 1.1 **a** Variations in the climate of Earth over the past 4 billion years, estimated from geological data. **b** Changes in mean climate estimated from variations in the volume of glaciers and ice sheets present on the surface of continents for the last million years. **c** Variations in the average air temperature in the northern hemisphere from the year 1000 reconstructed from paleoclimate data, including historical data and the study of tree rings. **d** Variations in the average surface air temperature calculated from the global meteorological network data for the period 1860–2010. Note that the number of stations has varied during this period and was sparse throughout the late nineteenth century

the northern hemisphere, separated by interglacial periods when the ice caps receded and remained confined to the Antarctic and Greenland.

We have been in an interglacial period, called the Holocene, for the past 11,000 years. The various aspects of the evolution of climate will be expanded upon later in this book.

The last million years is the best understood geological period, because climate can be reconstructed from detailed information provided by polar ice and marine and continental sediments. Over this period, a succession of oscillations between glacial and interglacial periods marks intervals which are the result of small changes in the Earth's orbit around the Sun. The glacial periods last almost ten times longer than the interglacial periods but they are interspersed with rapid warmings which follow the outbreaks of cold in the North Atlantic and neighboring landmasses. All these major climate shifts do not occur as a result of chance and it is the work of climatologists and paleoclimatologists to understand them by analyzing climate mechanisms and the causes of their variability.

Climate Mechanisms

The Sun is the major driver of climate. Received solar energy plays a key role in establishing climate conditions on the surface of our planet. But these depend critically on the composition of the atmosphere and energy exchanges between the surface of the planet and the atmosphere that surrounds it. The Earth radiation balance compares, for each point on the Earth's surface, the energy received from the Sun and that which is emitted back into space. Significant geographical differences drive wind and ocean currents which redistribute energy, influenced by the shape of the ocean basins and the relief of the land.

The Radiation Balance of the Earth

The Greenhouse Effect

A disk with a surface area of 1 m^2, located equidistant between the Earth and the Sun and intercepting solar radiation at a perpendicular angle, would receive an energy flow of 1368 W at the top of the Atmosphere (TOA). However, the Earth is a sphere whose surface area is four times greater than that of a disk with the same diameter. This is why, on average and over the course of a year, the solar flux intercepted by a unit area is four times lower. It corresponds to a power of 340 W/m^2 TOA with a known accuracy of roughly 1 W/m^2 (Fig. 1.2). Yet all this energy is not accessible to the Earth/atmosphere. A portion, about 36%, returns back to space after being reflected by the clouds, the suspended aerosols in the air, the Earth's surface and by the air molecules themselves. So, the real amount of energy absorbed amounts to 161 W/m^2. It is offset by an infrared flux emitted by the Earth and its atmosphere to space. In fact, the Earth behaves as a 'black body': it emits energy whose intensity is proportional to the fourth power of its absolute temperature (287 K), in accordance with Stefan's law. This radiation is almost entirely concentrated in the infrared range between 4 and 100 μm (microns), with a maximum intensity centered around 12 μm. Solar radiation also behaves like a 'black body' but at temperatures of around 6000 K, and covers a range of wavelengths from ultraviolet to near infrared, from 0.2 to 4 μm, and has a maximum intensity in the visible wavelengths of around 0.6 μm.

In the absence of any greenhouse effect, i.e. if the atmosphere were perfectly transparent to infrared radiation emitted by the Earth, the temperature in equilibrium with an average absorbed flow of 161 W/m^2, would be only −19 °C. In reality, water vapor, liquid water in clouds, carbon dioxide and other trace elements present in the air absorb a large portion of infrared radiation emitted by the surface, limiting the loss of energy towards space. Acting as 'black bodies', all these constituents re-emit infrared energy in all directions including towards the ground. This additional contribution means that the average surface temperature of the Earth is 14 °C, not −19 °C. This greenhouse effect is a natural phenomenon due in large part to the presence of water vapor, which contributes about 55% of the total greenhouse effect, to other greenhouse gases (carbon dioxide, methane, nitrous oxide) which account for 28%, with the remainder caused by clouds. Throughout the geological history of the Earth, the composition of the atmosphere has changed significantly and changes in the greenhouse effect have greatly contributed to past climate variations (see

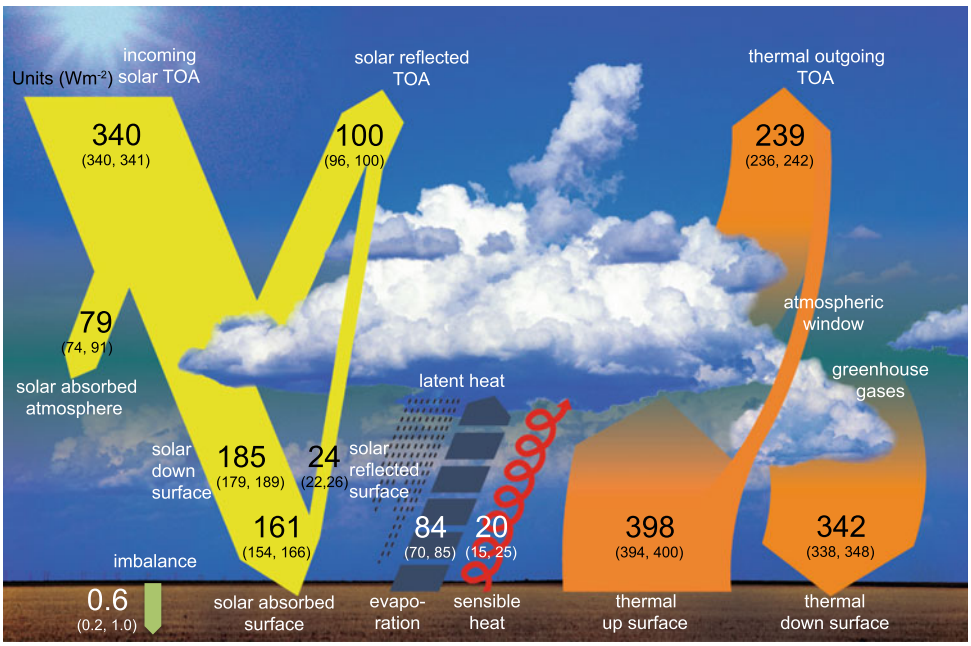

Fig. 1.2 Radiation balance of the Earth. The solar radiation incident at ground level is fully offset by infrared radiation emitted towards space (*Source* IPCC 2013)

Chap. 2, Volume 1 as well was Chaps. 22, 26 and 27, Volume 2). Since the beginning of the industrial era (about 1850), human activities have significantly increased the concentration of greenhouse gases already naturally present in the air and have introduced new ones, such as chlorofluorocarbons (CFCs) which are active agents of the greenhouse effect.

The Water Cycle

As solar radiation passes through the different layers of the atmosphere, part of it is absorbed by ozone in the stratosphere and by water vapor in the troposphere. About half of the incident energy reaches the surface of Earth, where it is partially compensated for by the loss of infrared radiation to the atmosphere. An energy surplus of 104 W/m^2 (Fig. 1.2) remains available at the surface. This energy warms up the surrounding air and causes evaporation of water from the surface of oceans and land, feeding into the water cycle on our planet. The water vapor is then transported by winds until it condenses as precipitation, releasing into the atmosphere the energy acquired at the surface during evaporation. Thus, the cycle of evaporation and precipitation of water takes energy from the surface of the oceans and land and redistributes it in the atmosphere. This transfer of latent heat cools the surface and warms up the atmosphere, thus lessening the differences in temperature between the upper and lower layers of the atmosphere, as well as between the equator and the poles. The water cycle thus plays a fundamental role in the redistribution of energy between the surface and the atmosphere.

Evaporation and condensation continuously renew the store of water vapor in the atmosphere. However, the amount of water vapor in the air at any given moment remains quite low. If it were completely condensed, the liquid layer thus formed would cover the Earth's surface in a layer 2.5 cm thick. Yet, on average, the water cycle involves the evaporation and the precipitation of water which would correspond to a layer of about 80 cm per year. The recycling time of water in the atmosphere is therefore very fast and the water vapor is completely renewed in ten days. The water, most of which evaporates from the oceans (86%), returns there either by precipitation or through the flow of rivers and streams after runoff from land. Globally, on average, evaporation and rainfall balance each other exactly, thereby maintaining a constant concentration of water vapor in air, as long as the average temperature of the air remains constant.

Sun-Related Variability

Variations in energy emitted by the Sun and the variations in the solar energy received by the Earth will affect the climate. In the first case, the solar activity cycles and the evolution of the Sun since the formation of the solar system modify the amount of energy it emits. In the second case, the slow variations of the movement of the Earth around the Sun influence the seasonal and geographical distribution of energy received in a given place on our planet.

Solar Cycles

In the mid-nineteenth century, the German astronomer, H. Schwabe, discovered spots on the Sun's surface that appear and disappear over an eleven-year cycle. When solar activity is more intense, marked by a greater number of spots, the Sun emits more energy. Since the 1980s, satellite measurements allow the estimation of variations in intensity of solar energy. These are around 0.1%, which corresponds to a very small perturbation (0.24 W/m^2) in the radiation balance of the Earth. Solar activity directly reflects changes in the Sun's magnetic field. The spots reappear in larger numbers when the magnetic field intensifies. Solar flares then become stronger; they eject a larger number of particles toward outer space and thus reinforce the solar wind. These electrically charged particles, mainly electrons and protons, reach the Earth's atmosphere where they cause magnetic storms—strong disturbances in the magnetic field—as well as magnificent auroras in the polar regions.

The influence of solar activity on climate has been debated for many years. In the second half of the seventeenth century, documented observations indicate an almost total disappearance of spots for a period of several decades, during the Little Ice Age (Fig. 1.3). At the end of the nineteenth century, the German astronomer H. Spörer and his English colleague W. Maunder linked these two phenomena, thus starting a controversy that persists today. The nature of the connection between the minimum solar activity (called the Maunder minimum) and a decrease in the intensity of solar radiation sufficient to induce a marked cooling that coincided with that time, still needs to be explained.

As the direct disruption in the solar radiation balance is too small to explain the phenomenon, it is believed that solar activity may affect climate through circulation in the upper atmosphere. Nevertheless, the link between variations in solar activity and the Earth's climate remains a subject of research and a source of controversy given the absence of a recognized physical mechanism. The relative role of external forcing (solar radiation) and internal/geological forcing (volcanism) in explaining the Little Ice Age still needs to be assessed.

The Sun exhibits variations over longer periods. These can be seen not only in the number of sunspots, but also in variations in solar diameter. This varies with a periodicity of 900 days, but this oscillation is influenced by solar activity. It is minimal when the activity is at its maximum. Like sunspots, solar diameter measurements started in the

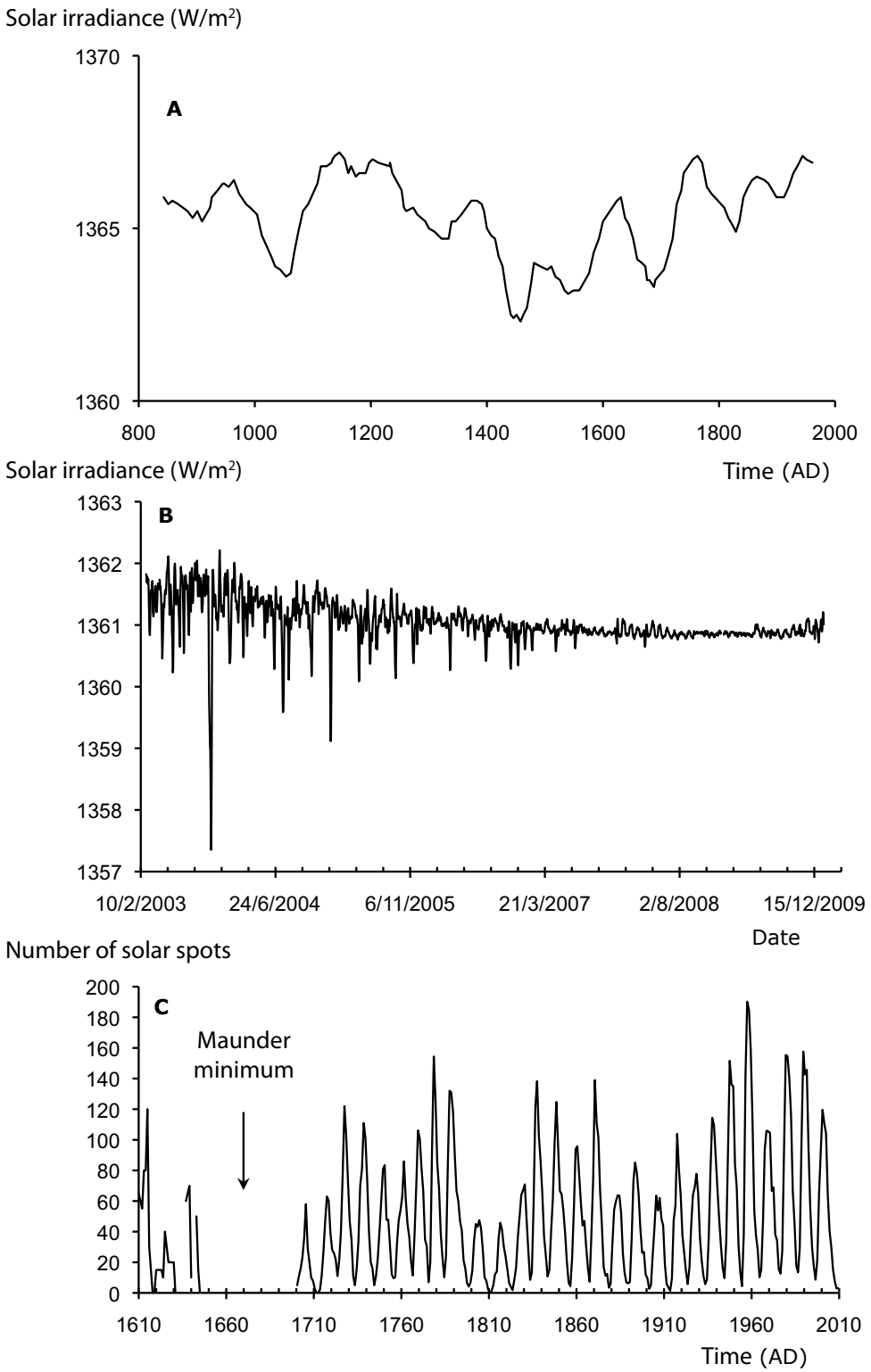

Fig. 1.3 **a** Variations in solar energy reconstructed from changes in the beryllium content of polar ice and from the modeling of stellar activity. It should be noted that the mean values calculated using stellar-activity modeling are higher, by about 5 W/m^2, compared with values measured using satellites. **b** Variations in energy emitted by the Sun, NASA satellite measurements. **c** Changes in the number of sunspots observed by astronomers since 1610

seventeenth century. They led to the discovery of a cycle of 80–90 years, called the Gleisberg cycle, which modulates the Schwabe cycle.

Solar wind plays only a minor role in the flow of charged particles received by the Earth. Most comes from galactic cosmic rays, which consists of electrons, protons, α particles (ionized helium nuclei) and heavier ions in very small quantities. It is isotropic and comes from everywhere in space. In periods of high solar activity, intense solar wind, through the magnetic field it creates, acts as a shield repelling the galactic cosmic radiation falling to Earth. This phenomenon inspired a geochemical method for determining variations in solar activity. Indeed, galactic cosmic rays, through spallation reaction on the atoms in the upper atmosphere, are responsible for the production of several cosmonucleides, the most well-known of which is Carbon-14. Less Carbon-14 is produced during intense solar activity. Measurements by geochemists on well-dated tree rings showed pseudo-periodic variations in the production of this cosmonucleide. This is attributed to fluctuations in solar activity, with periods of about 150–300 years (Suess cycles) and 2300 years (Hallstattzeit cycles). The existence of these cycles has been confirmed by the measurement of other cosmonucleides, such as beryllium-10, in polar ice. These are trapped in ice in Greenland, whose location in time can be determined simply by visually counting the annual layers or, for earlier periods, through more complex methods described in Chap. 9. The paleoclimatologists are now investigating if these periodicities can be reflected in geological records.

Long-Term Variations in the Movement of the Earth Around the Sun

The movement of the Earth around the Sun varies over time under the influence of the gravitational attraction of other planets (see Chap. 28, Volume 2). The orbit traveled by the Earth over a full year is almost exactly an ellipse with an eccentricity (the parameter which defines the degree of flattening of the ellipse with respect to a circle) that can vary over time. With periodicities close to 100,000 and to 400,000 years, the orbit goes from a circle with an eccentricity of zero to a slightly flattened ellipse with a maximum eccentricity of 6%.

The tilt in the axis of the Earth relative to the ecliptic plane is known as its obliquity and it influences the amount of sunshine received at different latitudes in different seasons. It is the reason for phenomena such as the polar night in winter and the midnight sun in summer at the highest latitudes. For this reason, the climate at high latitudes is especially sensitive to variations in the obliquity. With a periodicity of around 41,000 years, the obliquity angle oscillates between 22° and 25°, the current value being close to 23° 26′.

Because of the elliptical nature of the Earth's orbit, the distance between the Earth and the Sun varies at different times of the year. Currently, in the northern hemisphere, this distance is at its minimum in winter and at its maximum in summer, and the opposite is true for the southern hemisphere. In fact, the amount of solar radiation intercepted by the Earth decreases as the distance increases. This causes milder winters and cooler summers in the northern hemisphere, while the seasonal contrasts are accentuated in the southern hemisphere (although this impact is minor compared with the seasonal variations in high latitudes caused by obliquity).

Over the millennia, the position of the solstices and equinoxes slowly moves along the ellipse resulting in a variation in the solar energy received during each season. This movement of precession of the equinoxes is caused by a combination of two rotational movements. The first is the rotation of the Earth around an axis running through the poles which is perpendicular to the elliptic plane. A gradual shift in the orientation of the axis of rotation is caused by the attraction of the Sun and the Moon and traces out a circle over the North Pole in a cycle of approximately 26,000 years. The second is the elliptical orbit of the Earth around the sun which is superimposed on the first. The combination of these two movements results in a periodicity of the precession of the equinoxes of about 22,000 years. More specifically, the Earth's distance from the Sun fluctuates, not only due to the precession movement of the equinoxes, but also due to variations in the eccentricity of its orbit which varies according to a set of cyclical changes occurring over two proximate periods, one of 19,000 years and the other 23,000 years. Thus, approximately 10,000 years ago, the Earth reached its closest point to the Sun at the time of the summer solstice and not at the boreal winter solstice as it does today. At that time, the northern hemisphere received more solar energy in summer than it does today and obviously less in winter.

All of these modifications in the orbital parameters affect sunshine levels (still referred to as the insolation) at the different bands of latitude on Earth, and particularly the intensity of the seasonal cycle. Already, in 1924, the Serbian mathematician, Milutin Milankovitch, proposed that these slow variations of the movement of the Earth around the Sun could explain the glacial cycles. Indeed, as these slow variations induce a decrease in solar energy received in the summer at 60° N, snow, which has fallen in the winter, does not melt completely. Furthermore, it strongly reflects solar radiation, facilitating the snow to persist. Gradually, the snow accumulates and turns into an ice cap. This hypothesis has been debated for many years and was strongly opposed until the 1970s, when the cycles predicted by this theory were clearly confirmed by paleoclimate records in marine sediments and later in polar ice. We will see more precisely in Chap. 28 of

Volume 2 the state of our knowledge about the Milankovitch theory, or the 'astronomical theory' of paleoclimates.

The Sun's Evolution

Since the formation of the solar system, the Sun, like all stars of the same type, slowly consumes its hydrogen to produce helium, and the amount of heat it emits varies very slowly over long time scales. The standard stellar evolution models estimate that four billion years ago the luminosity of the Sun was 25–30% lower than it is today, and that it has increased more or less linearly over time. This model seems in accordance with observations made by astronomers of young stars. With the same Earth's atmosphere as today four billion years ago, the average temperature of the Earth would be below 0 °C, oceans would be frozen, and life would be impossible. Geological observations, however, indicate the presence of water in the liquid state and the first traces of life 3.5 billion years ago. This is the 'Pale Young Sun paradox' which is solved by assuming that the atmosphere had a very different chemical composition from that of today. Indeed, the elimination of carbon dioxide by the young Earth, and the low rates of weathering given the absence of continental crust, meant that the atmosphere during these ancient periods acquired an exceptionally high level of CO_2 and hence was responsible for a strong greenhouse effect, further enhanced by the presence of methane produced by bacteria. This will be discussed in detail in the chapter on the Precambrian (Chap. 26, Volume 2).

Reconstruction of the History of Atmospheric Composition

Although the Sun is the source of energy for the Earth, the energy made available depends essentially on the composition of the atmosphere: greenhouse gases and particles. Reconstructing the past history of the composition of the atmosphere is therefore an important element in understanding climate dynamics.

Again, the last hundreds of thousands of years constitute the best documented period because of the fossil air bubbles contained in the polar ice caps. The snow falling on the polar caps forms a porous firn, within which air circulates freely. Under the weight of accumulated snow, the pores gradually compact and the firn turns into ice that traps tiny air bubbles within it. This air keeps its original chemical composition, which allows the reconstitution of variations in the composition of the atmosphere over time, as long as we can find well-preserved ancient ice. The oldest ice is found in Antarctica, where a continuous recording of the greenhouse gas content (CO_2, CH_4) over the last 800,000 years has been established. These records show that the levels of carbon dioxide have not remained constant; they were high in warm periods, around 280 ppmv (280 cm^3 of CO_2 per m^3 of air) and only 200 ppmv during cold periods. Similarly, methane ranged from $\sim$700 ppbv (mm^3 per m^3 of air) in warm periods to less than 400 ppbv during cold ones, with a high temporal variability (Fig. 1.4).

Polar ice is the only direct recording of the composition of the atmosphere. As ice in the ice caps flows very slowly and is continuously renewed throughout geological time, it is impossible to reconstruct a record of carbon dioxide levels before a million years ago. For earlier periods, it is therefore necessary to use indirect empirical methods which have a much lower level of precision. These indirect "proxies" to reconstruct atmospheric CO_2 may be derived from stomata, boron isotope or alkenone (Chap. 27, Volume 2). For example, botanists observed that the stomata—pores through which leaves absorb carbon dioxide from the air—are smaller and fewer when carbon dioxide is high. This plant characteristic has been used as a means of establishing CO_2 levels for the past. However, the results were not clear-cut. For one, the fossil species being studied must be the same as the current species on which the empirical relationship between the levels of carbon dioxide and the number or diameter of the stomata is being established. Moreover, the relationship, which can only be determined in the current conditions, also depends on the availability of water to the plant, so it is not clear whether changes observed in fossil stomata are due to variations in CO_2 or in moisture.

As the CO_2 content of the air is governed by the partial pressure of this gas in the surface waters of the ocean, geochemists have tried to use carbon-13, a tracer of the oceanic phase of the carbon cycle, as a tool to reconstruct changes in atmospheric CO_2. One of the proposed markers is the $^{13}C/^{12}C$ ratio in foraminifera, microscopic animals in the form of plankton living in the surface waters of the oceans. These animals secrete a calcareous shell whose size is a few tenths of a millimeter and which are found in abundance in marine sediments. The $^{13}C/^{12}C$ ratio of planktonic foraminifera therefore depends on the isotopic composition of dissolved CO_2 in the surface waters, and indirectly on that of the atmosphere.

This isotopic approach can be compared against the independent records provided by the polar ice cores, so that the method can be evaluated over the last few hundred thousand years. The correlation is only proximate due to the complexity of the oceanic carbon cycle which depends in particular on the temperature of the sea water, on the primary production of the ocean, on the decomposition of organic matter and on the circulation of the bodies of water. Biologists came up with another method when they noticed that the fractionation of carbon isotopes during the absorption of carbon dioxide by seaweed depends on the dissolved carbon dioxide content and therefore the partial pressure of CO_2 in the seawater. This led them to the hypothesis that variations

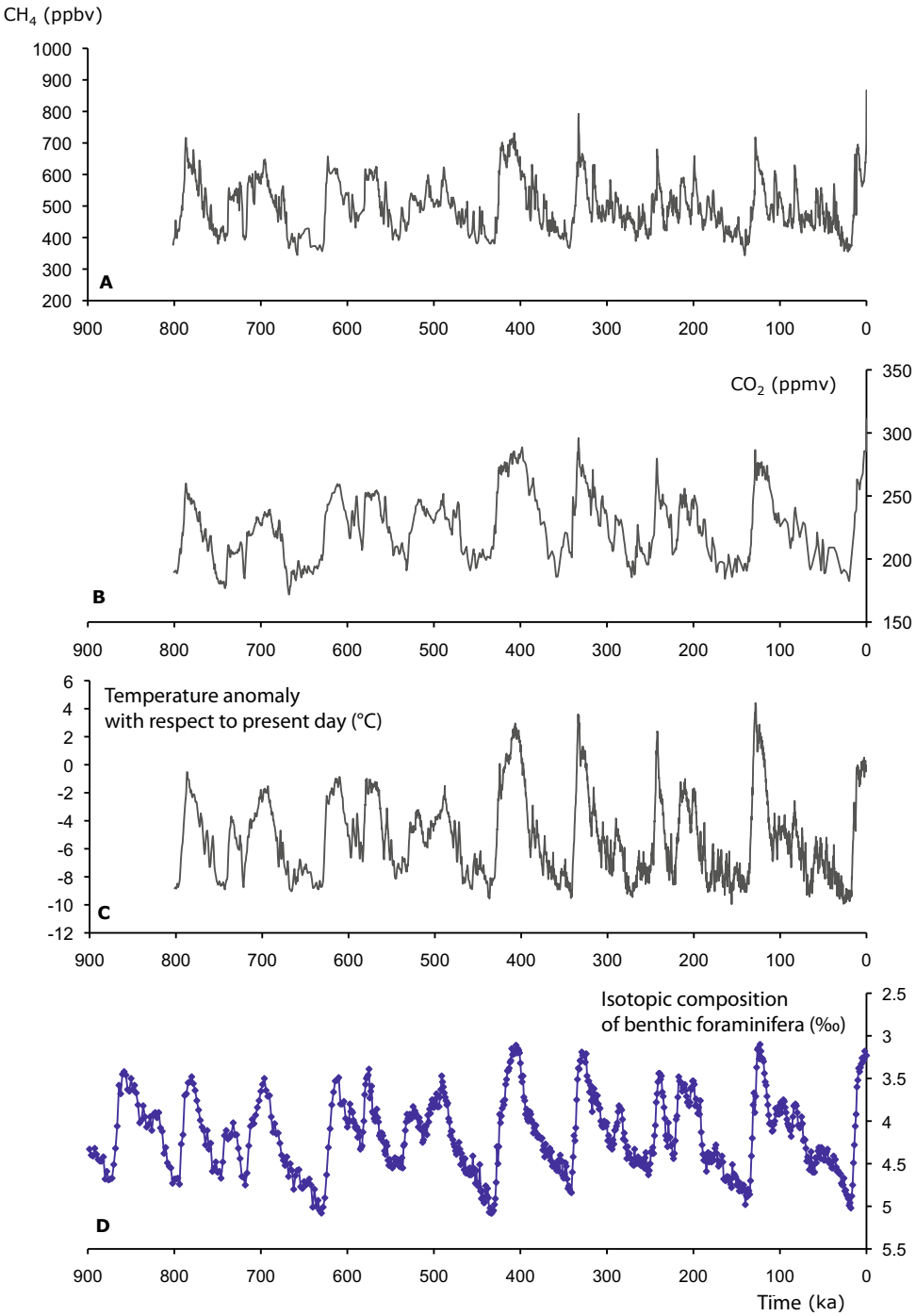

Fig. 1.4 **a** Variations in atmospheric methane concentrations inferred from variations in methane concentration in the air bubbles trapped in the ice cores drilled at Dome C (EPICA). **b** Variations in atmospheric carbon dioxide concentrations inferred from variations in carbon dioxide concentration in the air bubbles trapped in the ice cores drilled at Dome C (EPICA). **c** Air temperature variations in Antarctica inferred from changes in the isotopic composition of the ice cores drilled at Dome C (EPICA). **d** Changes in mean climate of the Earth estimated from variations in the isotopic composition of oxygen in benthic foraminifera, a proxy for variations in the volume of glaciers and ice caps on land surfaces over the last million years

in the $^{13}C/^{12}C$ ratio in specific compounds formed during photosynthesis, such as in alkenones found in marine cores, would reflect changes in the CO_2 composition of the surface waters of the ocean and of the air. However, the relationship obtained depends on the ratio of surface to volume of cells performing photosynthesis, which introduces a new uncertainty in the reconstructions. Finally, it is clear that even isotopic methods, which use accurately measurable geochemical parameters, produce only rough estimates of the carbon dioxide composition of the air and its variations.

At long time scales ($>10^6$ years), the changes in the levels of CO_2 in the atmosphere are determined by the relative extent of degassing by volcanoes and mid-ocean ridges on the one hand, and the consumption of CO_2 by chemical erosion of silicates on the other. This means that the key role is played by plate tectonics. Thus, a gradual reduction of

CO_2 in the air may be due to either a lower degassing rate or an increase in erosion of the surface of the continents. The latter depends on a complex set of parameters, themselves related to climate, such as air temperature, precipitation, continental runoff and vegetation. Geochemists therefore try to reconstruct the changing partial pressure of atmospheric CO_2 using models; CO_2 emissions are estimated using geological data on the speed of movement of the plates; consumption of the gas is taken into account in simplified models by coupling the carbon cycle to climate and by considering the geographical context resulting from plate tectonics. For example, the breaking-up of the arid supercontinent Rodinia, into a multitude of small humid continental masses, 800–700 million years ago, led to the creation of basaltic regions, easily erodible chemically. This resulted in a significant drop in carbon dioxide levels in the air which may explain the great glaciations of the period.

Airborne dust also plays an important role in the radiation balance of the atmosphere, mainly by intercepting solar radiation and thereby reducing the amount of energy reaching ground level. Dust levels have varied considerably in the past, as is evidenced in polar ice. Falling snow brings down atmospheric dust with it which then remains trapped in the ice. The more the air is charged with dust, the more of it the snow absorbs. In this way, strong atmospheric dust levels during the glacial periods of the Quaternary have been demonstrated. The dust came from continental erosion which was then transported by winds. They gave rise to huge accumulations of very fine particles. These created the loess present in China, and in smaller quantities, in Western Europe (Chap. 13, Volume 1).

The Atmosphere

The Main Features of Atmospheric Circulation

The net balance between the radiation received from the Sun and that emitted into space does not have a uniform distribution. The net energy flux varies, depending on the latitude, geographic regions and season. Solar radiation decreases significantly between the equator and the poles, but there is little difference in emitted infrared radiation. The result is a surplus of energy in the tropics and a deficit in the north and south latitudes above 40°. Heated at the equator, cooled at the poles, the atmosphere and the ocean are activated and carry the excess energy from tropical regions to the deficient higher latitudes. According to currently available measurements, the two fluids of the planet contribute with relatively similar amplitude to this transport (Fig. 1.5).

A strong circulation in the atmosphere traveling from the equator to the poles is established in order to ensure the transport of energy necessary for the thermal balance of the planet. The warmer air, and therefore lighter, rises above the equator, before diverging and heading at high altitudes towards the poles. Above the polar regions, on the contrary, cold, dense air descends toward the surface, and travels toward the equator, which forms a large loop between the equator and poles. This mechanism, described in 1735 by the English scientist George Hadley, would happen if the Earth was turning very slowly. In reality, this large convection cell remains confined between the equator and the subtropical regions, where it forms the so-called 'Hadley' circulation. Associated with the Hadley circulation, low-pressure belts

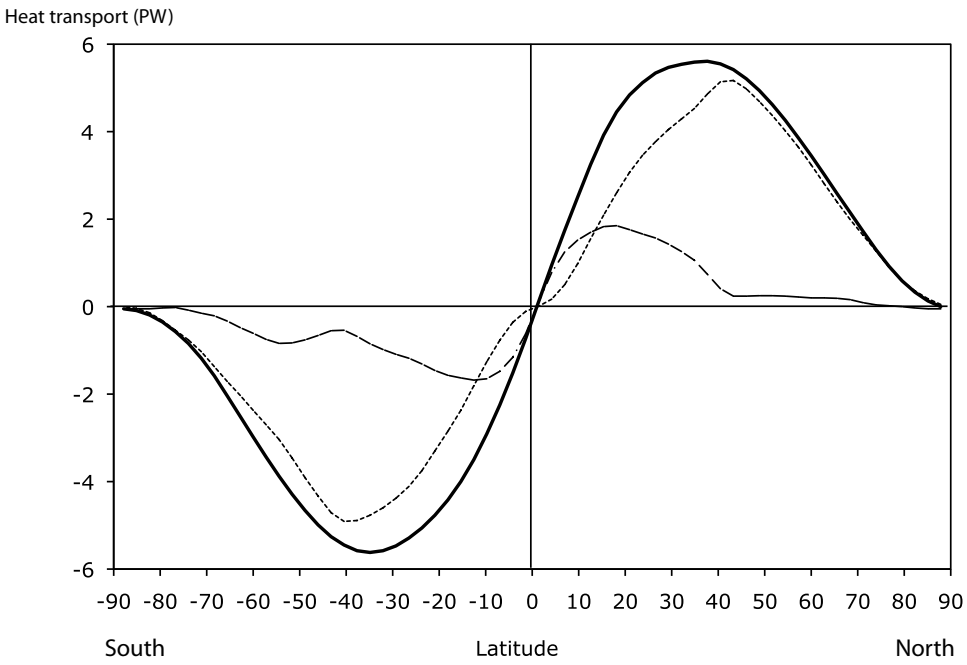

Fig. 1.5 Average transport of energy by the atmosphere (thin dotted) and ocean (dashed), and total transport (solid line). Positive transport towards the north and negative towards the south is recorded

predominate in the equatorial regions, while high pressures belts predominate in subtropical regions. A convergence of winds towards the equator, the trade winds, is thus observed in the tropics at sea level. The trade winds are dry at the start of their journey, since they are powered by the descending branch of the Hadley cell. Like the Harmattan over Africa, they maintain desert conditions on tropical continents. Over the ocean, there is high evaporation of surface waters heated by solar radiation and the trade winds pick up this vapor and carry it towards the low latitudes.

At the equator, with its ascending branch of warm moist air, low-altitude convergence is manifested by strong convective activity and heavy rainfall. These allow the development of a lush, tropical rainforest on land, while over the great ocean basins, convective activity is focused along a narrow longitudinal strip of one hundred kilometers wide: the intertropical convergence zone. It is in this area that storms and rain are concentrated: the 'doldrums', dreaded by sailing vessels in the past, and now by solo sailors.

Beyond 30° latitude, the flow of air, deflected eastward by the Coriolis force, reaches such speeds that it becomes unstable and breaks into eddies and meanders. Large meanders in this western circulation appear as vast oscillations, usually between three and six of them, which encircle the Earth. Depressions and anticyclones succeed each other in the middle latitudes between 30 and 60° north and south, creating very variable weather conditions. This is the cause of the 'temperate' climate prevailing in Western Europe. By mixing the hot subtropical air and cold polar air, these vortices take over the transfer of the excess energy from the tropics to the poles from the Hadley circulation. However, this circulation is affected by the contrast between land and oceans, and by the presence of mountains, both favoring the anchoring of global planetary waves whose intensity and position change over time. These waves impact on the geographical distribution of climate and cause, for example, a warmer climate on the west coasts than on the east coasts of the continents of the northern hemisphere. The contrast between the climate of Canada and that of France is a striking example.

There have been very significant changes in the intensity and location of the winds in the past, particularly during glacial-interglacial oscillations. They are evidenced by the presence, more or less marked, of pollen or desert dust transported to the ocean, sometimes very far from the coast, where they contribute to marine sedimentation. In the marine environment, when the wind blows parallel to the coast, it causes upwelling of deep cold water. Variations in their intensity, reflecting that of the wind, result in variations in the temperature of surface water that paleo-oceanographers have managed to reconstruct (see Chap. 21).

For recent periods, historical records provide information, sometimes subtle, on the variability of the winds and storms. For example, during the Little Ice Age, variations in the position of the winds were detected in the Pacific Ocean by analyzing the travelling time of galleons transporting goods between Manila (Philippines) and Acapulco (Mexico). The General Archive of the Indies held in Seville relates that the journey could take between less than three months and more than four months. The routes were always the same: departing from Manila, the galleons went east, allowing themselves to be carried by the stable westerly winds. For the return, they headed west, catching the northeast trade winds, and the duration of the journey was determined, in the end, by the location of the opposing winds (from the southwest) that they encountered as they approached Manila. Historians were thus able to show the existence of a period of about forty years in the middle of the seventeenth century when the headwinds were very common due to a northward shift of the large depressions. Changes in the strength and direction of winds are therefore an important manifestation of past climate changes.

Water Vapor, Clouds and Rainfall

Water in the atmosphere, in the form of vapor in the air, or as a liquid or ice in clouds, plays an important role in climate dynamics. Firstly, the amount of water vapor contained in the air is a function of increasing temperature as defined by the Clausius-Clapeyron relationship that links the saturation level of water vapor in air to temperature. When air temperature increases, its water vapor content increases. Furthermore, water vapor is the most important greenhouse gas in the atmosphere. Any increase in its concentration in the air in turn induces further warming of the atmosphere, engaging a positive feedback mechanism which amplifies the original disturbance.

When the water vapor content exceeds the threshold of saturation, water vapor condenses, causing cloud formation. Clouds have a particularly complex role, because of two opposite effects. On the one hand, they reflect part of the solar radiation, which has the effect of cooling the surface of the Earth. On the other hand, they have a greenhouse effect that causes it to heat up. These two effects are not completely balanced. On average, with current climate conditions, the reflectivity effect is more important that the greenhouse effect, and so, overall, clouds cool the Earth. But in the case of climate change, will clouds play a moderating or amplifying role? Low-level clouds and clouds in the upper layers of the troposphere are very different. Low-level clouds are usually thicker, and reflect solar radiation, but being near the surface, they have little impact on the greenhouse effect. Conversely, high altitude clouds like cirrus, are much thinner and are very cold. They let solar radiation pass through, but they contribute strongly to an increase in the greenhouse

effect. It is not clear if global warming will be accompanied by more low-level clouds with a moderating effect, or high-level clouds with an amplifying effect. The answer is complicated further by the fact that it depends on changes in the general circulation in the atmosphere.

Through coalescence, micro-droplets of water grow and turn into rain, snow or ice, depending on the temperature. How precipitations are distributed reflects the main features of the general circulation of the atmosphere: ascendance and heavy rains at the equator, subsidence associated with a lack of rainfall in the sub-tropics, rainfall in the mid-latitudes linked to the passage of depressions. On average, excess in the evaporation rate over the oceans is offset by a surplus of rain over land. This transfer of water from oceans to land is particularly apparent during the seasonal phenomenon of the 'monsoon', well known in South East Asia but also in Africa. In summer, when the land warms up, low-pressure heat expands and causes a convergence of ocean winds towards the mainland. Charged with humidity, the winds rise and discharge a large amount of rain over land.

Reconstructing Changes in Precipitation

There are many signs to be found on the surface of our planet of how precipitation has changed over a given area. The accumulation of ice in the polar ice caps is directly dependent on the supply of snow. Glaciologists have shown that snowfall was half as abundant during glacial periods as it is today. At lower latitudes, fluctuations in rainfall are recorded in lake sediments. Deposits left above the current water level are evidence of phases of intense rain, particularly in the beginning of the interglacial periods. The levels of the lakes drop when rains abate. For example, an aerial view of Lake Chad shows tracks of the various shorelines that record the regression of the lake over past millennia. About 6000–8000 years ago, it occupied an area of 340,000 km^2 (equivalent to more than 2/3 of the area of France). By 2000, it was reduced to 1500 km^2, or less than 1% of its maximum size.

Lakes are not the only records of rainfall fluctuations on land. In limestone terrain, variations in the growth of concretions in caves are another indicator of fluctuations in the supply of groundwater by rain. Dating using geochronological methods (see Chap. 14) can detect slowdowns or arrested growth during dry periods, followed by recovery when the groundwater supply resumes in wet periods.

Monsoons are a prime example of intense rainfall affecting large areas, both in Africa and Asia. Rain falls during the summer months when the overheated land masses are the source of low pressures towards which the humidity-charged oceanic air masses converge. The intensity of the monsoons has fluctuated considerably during the Quaternary. This has resulted in enormous variations in the volume of water flowing in the major rivers which are fed by the rains, such as the Niger and the Nile in Africa, or the great rivers that drain the Himalayas and discharge into the Bay of Bengal. Variations in freshwater inputs to the ocean have been so significant that they have resulted in large fluctuations in salinity in areas close to the mouths of these rivers. Paleoceanographers are able to reconstruct these changes through isotopic and micropaleontological analysis of marine sediments deposited near the river mouth (Fig. 1.6, Chap. 21, Volume 1).

Land surfaces contain many other traces of major changes in the hydrological cycle in the past. During periods of great aridity, dry winds have facilitated the creation of dunes which became established when the rains returned. The vegetation growing in different regions is as much determined by air temperature as it is by precipitation and water availability. This is what causes the variation in the thickness and density of the annual rings of trees. Pollens found in lake sediments, peat bogs and in marine sediments close to the coast are used by geologists to reconstruct the major vegetation types that developed throughout the various geological periods allowing them to infer the temperature and humidity conditions that then prevailed (Chap. 12, Volume 1).

Modes of Variability of the Atmosphere

Atmospheric circulation is very variable. Over short timescales, variability is dominated by the duration of depressions, usually a few days. Over longer time scales, the circulation shows variability patterns over periods of up to several years. In Europe, the variability is dominated by fluctuations in the system caused by low-pressure from Iceland and high pressure from the Azores. This dipole oscillates between a 'positive' phase which is marked by a strengthening of the low and high pressures, stronger westerly winds bringing rain, and high temperatures in northern Europe, and the 'negative' phase where pressures and westerly winds subside, moving the rainy zone to the south of Europe (Fig. 1.7). The 'North Atlantic Oscillation' (often designated by the acronym NAO) occurs at all time scales and explains about a third of the variability in weather conditions in Western Europe, especially in winter. Positive and negative phases tend to predominate for ten years or more, which makes the NAO particularly interesting in the study of the climate of Europe. This mode seems to be caused by the atmosphere alone, and yet it has an influence over ocean circulation. The mechanisms that allow atmospheric circulation to present an oscillation over such a long period are still not fully understood.

Did the North Atlantic Oscillation exist in the past? Measurements of atmospheric pressure, in particular ones

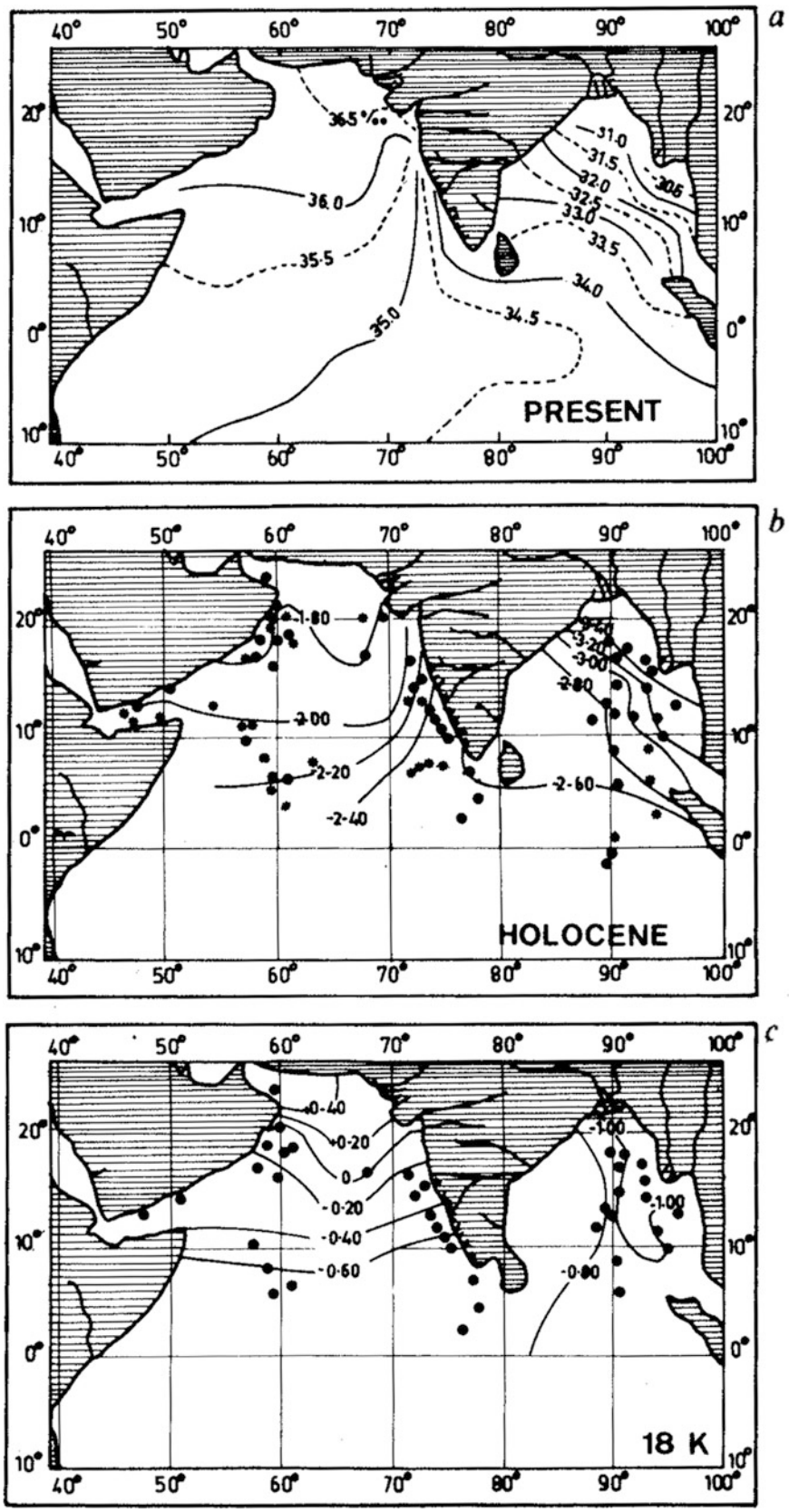
a
PRESENT
36.5 ‰
36.0
35.5
35.0
34.5
34.0
33.5
33.0
32.5
32.0
31.5
31.0
30.5
b
HOLOCENE
-1.80
-2.00
-2.20
-2.40
-2.60
-2.80
-3.00
-3.20
-3.40
c
18 K
+0.40
+0.20
0
-0.20
-0.40
-0.60
-0.80
-1.00
-1.00
40° 50° 60° 70° 80° 90° 100°
20° 10° 0° 10°

◀ **Fig. 1.6** Impact of variations in the intensity of the monsoon between the last glacial maximum and current times on the hydrology of the North Indian Ocean. **a** The current salinity of the Bay of Bengal where the rivers draining the Himalayas flow is much lower than that of the Arabian Sea where evaporation is dominant. **b** The isotopic composition of oxygen in planktonic foraminifera in recent marine sediments is a good record of these changes because there is little variation in the temperature of the northern Indian Ocean. **c** The isotopic composition of oxygen in planktonic foraminifera in marine sediments deposited during the last glacial maximum dated by ^{14}C at around 18,000 years BP shows a considerable decrease in the flow of rivers into the Bay of Bengal and thus in the intensity of monsoon rains

carried out in Reykjavik and Gibraltar, allow scientists to reconstruct past trends as far back as 1850. Comparison between winter air temperatures measured in weather stations shows that during the positive phase of the NAO, temperatures are higher than average in Western Europe and the southeast of Northern America, but below average in Greenland, the Labrador Sea, in northwestern Africa and the Eastern Mediterranean. The opposite is true in the negative phase of NAO.

These teleconnections between different sites are used by paleoclimatologists to reconstruct changes in the NAO in the pre-instrumental period. Tree rings provide a good record of climate conditions, especially of periods of extreme heat or drought (Chap. 16, Volume 1). Recordings obtained from trees of North America and Europe show alternating phases, some positive, some negative, since the beginning of the eighteenth century, with short periodic elements (8 and 2.1 years) but also multi-decadal ones (70 and 24 years).

Snowfall and ice accumulation in the western part of Greenland are abnormally low during the positive NAO

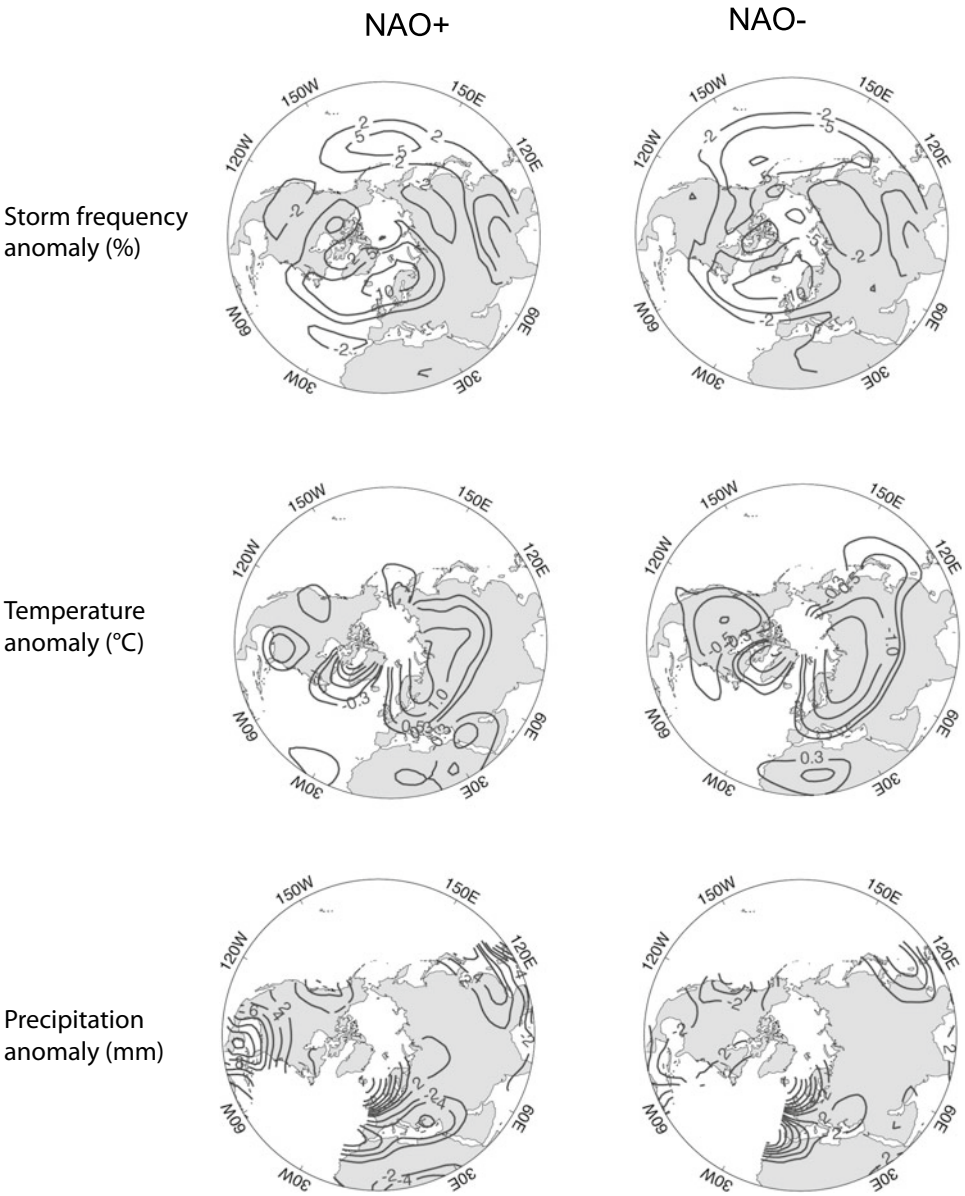

Fig. 1.7 The positive and negative phases of the NAO and their impacts on the distribution of temperature, precipitation and winds

phase, and this has allowed the reconstruction of the NAO and its intensity over the last 350 years with, again, the detection of multi-year and multi decadal intervals. Teleconnections associated with the NAO are also recorded in marine sediments. Over the last ten thousand years, there has been a tendency towards cooling of the surface waters of the eastern North Atlantic Ocean while there has been a contrasting warming of the subtropical western Atlantic and the eastern Mediterranean. This trend is seen as a sign of a continued weakening of the NAO during the Holocene.

However, on these time scales, it becomes difficult to distinguish between a change in the NAO expressed over several millennia and a long-term climate trend, driven by the slow fluctuations in orbital parameters. Indeed, cyclic variations in the precession (with a cycle of 21,000 years) were responsible for an increase in the winter incident solar radiation in the tropics 10,000 years ago, followed by its progressive decrease accompanied by a drop in the difference in atmospheric pressure between the tropics and the high northern latitudes during the Holocene. This is an example of the changes in insolation changes predicted by astronomical theory.

The Oceans

Main Characteristics of the Oceans

The oceans cover two thirds of the surface of the planet. With an average depth of 3900 m, they have a very high thermal inertia, much greater than that of the atmosphere. A layer 3 m deep of ocean surface waters has the same heat capacity as the 10 km troposphere. This feature explains why coastal regions have a much less contrasted climate than regions in the interior of large landmasses. It also plays an important role in determining the response time of the atmosphere-ocean system to a disturbance in the radiation balance.

The atmosphere and the oceans exchange momentum through the friction exerted by winds at the air-sea interface. They are thus responsible for the great marine currents, well-known to ocean-going sailors. The atmosphere and the oceans also exchange energy and water. Energy exchanges, through solar radiation, the infrared flow, turbulent eddies at the surface, and sensitive and latent heat, impact on the temperature of surface waters of the ocean. Water exchanges, through evaporation and precipitation, have an impact on salinity: evaporation increases the salinity of seawater while rain, conversely, decreases salinity. These interactions, which create variations in the temperature and salinity of seawater, ultimately determine its density. Density is indeed inversely proportional to temperature and directly proportional to salinity. Density differences are then the cause of the movement of large, deep-water masses in the world's oceans.

These physical interactions, shown schematically in Fig. 1.8, are supplemented by exchanges of matter, such as, for example, of carbon dioxide or sulfur compounds, which interact with the biogeochemical cycles of the different elements. In this way, physics, chemistry and biology are very closely linked in the ocean.

Oceanic Circulation

In the tropics, winds cause large ocean anticyclonic circulation, called 'vortices' or 'gyres', turning in a clockwise direction in the northern hemisphere and counterclockwise in the southern hemisphere. However, there is a marked asymmetry between the eastern and western sides of the ocean basins. For example, to the east of the North Atlantic, the Canary Current spans a much wider area and has a much lower intensity than the current on the western side, the Gulf Stream, which is very intense and is only a little more than 100 km wide. This strengthening of currents along the western edges of ocean basins is not specific to the Atlantic

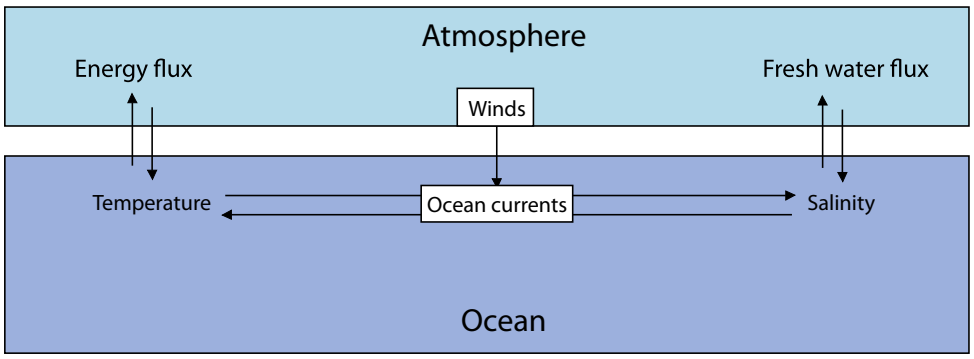

Fig. 1.8 Interactions between the atmosphere and the oceans: winds drive the surface currents that transport temperature and salt in the oceans. The exchange of energy and water between the atmosphere and oceans condition the temperature and surface ocean salinity that change the density of the water, thereby causing ocean currents

Ocean. It is also observed in the warm current of Kuro-Shivo in the North Pacific and in the Agulhas Current which runs along the South African coast in the southern hemisphere. This phenomenon is a complex result of the increasing strength of the Coriolis force with distance from the equator.

Differences in density also lead to large movements of the oceanic water masses. The densest waters are in the polar regions where sea ice forms. Already dense because of their low temperature, the waters receive a further load from two salt inputs: one coming from the flow of currents from the subtropics, where evaporation is intense and the other from salt released during sea ice formation. These dense waters tend to drop due to gravity below the warmer and less salty waters, then to spread out at the bottom of the ocean where the temperature, around 0–2 °C, varies little from the poles to the equator. These dense water masses are the starting point of the great global circulation loop of the ocean, called thermohaline, since denser waters tend to sink below less dense waters and the density of water masses is dependent only on temperature and salinity. This mechanism plays an important role in ocean circulation, as it contributes over 75% to the formation of all the masses of deep waters of the world ocean. Paradoxically, this process of downwelling deep water occurs only in a very small fraction of the surface of the oceans: in the Labrador Sea, the Norwegian and Greenland Seas and in some regions of North Atlantic as well as at the edge of the Antarctic continent, particularly in the Weddell Sea. In overall, the combination of the thermohaline circulation and the circulation caused by winds makes up the ocean meridional overturning circulation.

Downwelling waters in the North Atlantic descend to a depth of 2000–3000 m up to latitude of around 60° south, where water masses undergo a slow movement of ascent to the surface. Carried by the Antarctic Circumpolar Current that runs from west to east around the southern polar continent, the deep waters from the North Atlantic then spread out in the South Pacific and the Indian Ocean. The return part of this great circulation loop occurs through warm currents near the surface. They pass between the Indonesian islands, cross the Indian Ocean, circumnavigate Africa by the Agulhas Current, and then up towards the North Atlantic with the Gulf Stream and the North Atlantic Drift. But, while the return by the warm currents takes a few decades or even up to a hundred years, it takes several hundred to a thousand years from the time the cold waters sink in the North Atlantic to their arrival in the center of the Pacific, showing the slowness of this gigantic mixing achieved by the deep circulation.

Reconstructing Ocean Circulation in the Past

Paleoceanography reconstructs past ocean circulation by analyzing sediments that have settled in more or less regular layers on the ocean floor, the uppermost layers corresponding to the most recent deposits. This discipline has flourished thanks to several scientific and technical developments. One of these developments is in the methods of coring and drilling which allow cores to be brought to the laboratories which have relatively undisturbed sediments reliably recording the conditions in the ocean at the time the sediment was deposited. Furthermore, in-depth analysis of fauna (foraminifera) and flora (diatoms, coccoliths) fossils that lived in the illuminated area or in the water column permit the reconstruction of the temperatures of surface waters (see Chap. 21). Finally, new geochemical methods based on the analysis of stable and radioactive isotopes of elements present in marine sediments have provided dating methods, stratigraphic markers and tracers of large marine currents (see Chaps. 4, 6 and 7, Volume 1).

It is now possible to draw up temperature maps of surface waters of the ocean at critical times of the history of climate on Earth, such as during the Last Glacial Maximum with a ^{14}C age close to 18,000 years (in other words, a calendar age of about 20,000 years, Chap. 2) or during interglacial periods of the Quaternary. Paleoceanography also allows the reconstruction of the movements of fronts separating surface water masses with very different characteristics: a descent of polar waters in lower latitudes, driving out temperate waters, is accompanied by a strong cooling also felt by adjacent coastal areas. Conversely, their retreat is accompanied immediately by a significant warming.

Marine sediments also contain markers for the conditions that prevailed at depths, at the water-sediment interface. The most important of these are benthic foraminifera, microscopic animals with a calcareous shell whose isotopic composition is a particular reflection of the temperature and dissolved carbon dioxide content of the deep waters of the ocean. Measurements by oceanographers show that at a certain depth in the ocean, the physical and chemical characteristics of the waters are almost constant over a distance of several dozen kilometers. By taking sediment cores at different depths in an ocean basin, it is possible to reconstruct the features of large deep water masses, to deduce the main features of their circulation within a given period and to track their variations over time. Paleoceanography therefore allows the reconstruction of the main features of changes in the ocean in three dimensions.

El Niño, Interplay Between the Atmosphere and the Oceans

Interactions between the atmosphere and the oceans can lead to climate variability modes. El Niño is a perfect example. Every two to ten years, an abnormal situation occurs in the Pacific, manifested by the appearance of unusually warm waters along the coast of Peru and major disruptions in the tropical rainfall pattern.

In 'normal' periods, the water temperature is around 28–29 °C in the western tropical Pacific, while it does not exceed 20–25 °C in the east. This strong asymmetry in temperature between the east and west maintains the atmospheric circulation which, in turn, maintains the temperature gradient. The warmer waters provide the heat and humidity necessary for the development of strong convective activity over the western Pacific, which develops the air ascendance associated with the Hadley circulation, while the air descends over the cold waters of the eastern Pacific. This asymmetry between the eastern and western Pacific is associated with a circulation called Walker. In turn, the trade winds at the surface, which blow from east to west, maintain the east-west temperature gradient.

In the eastern Pacific, they cause a surface current deflected by the rotation of the Earth to the right in the northern hemisphere and to the left in the southern hemisphere, which drives out the surface water on both sides of the equator, and causes an upwelling of cold water to compensate. The trade winds also propel surface waters towards the west, where the accumulation of water inhibits the upwelling process; heated by the Sun, these waters reach the highest ocean temperatures, thereby favoring intense convective activity. This situation is called *La Niña* when the differences between east-west are particularly strong.

During an *El Niño* event, the circulation of both the ocean and the atmosphere change simultaneously following a series of mutual actions and reactions in which it is impossible to distinguish which of the ocean or the atmosphere triggers the phenomenon. In particular, the water of the central Pacific is warmed to 28–29 °C, which has the effect of moving the high convective activity towards the east. A decrease in the strength of the trade winds in the western Pacific follows, and possibly even a reversal of their direction. With weaker trade winds, the surface current weakens and the warm waters of the western Pacific flow back towards the east, a backlash that warms the central Pacific and interrupts the upwelling of cold waters at the coasts of South America. But *El Niño* starts a series of waves in the ocean that eventually pans out and restores the so-called 'normal' situation.

Because of their well-recorded and varied consequences, the existence of variations in the intensity and frequency of *El Niño* events in the past are known. In the Andes, the arrival of the warm waters on the Pacific coast brought heavy, sometimes catastrophic, rainfall that caused floods or even huge landslides that geologists are able to date. Prehistoric sites also bear traces of these events, and archaeologists have established that certain Andean civilizations developed during periods when El Niño events were rare or weak and regressed with the return of torrential rains. However, the most precise way to reconstruct the sequence of these events is by analyzing the geochemistry of the corals abundant in the waters of the equatorial Pacific Ocean and located at the heart of the phenomenon. For example, Tarawa Atoll located near the International Date Line (180° meridian) usually has a dry, almost desertic climate. When an *El Niño* event occurs, the warm waters reach it, atmospheric convection becomes intense locally and heavy rains fall on the entire atoll and the coral reef that surrounds it. Corals, animals with a calcareous skeleton with recognizable annual bands, record these rainy passages. Analysis of them has allowed the number of *El Niños* in the last century to be counted and to show that their frequency has changed over the last hundred years. Conversely, near Australia, which is usually in a region of warmer water, *El Niño* events are characterized by decreased rains and cooling, which were reliably recorded by the coral reefs of New Guinea or Fiji. These recordings show that *El Niño* events have also existed during periods of glacial climate, and confirm that their frequency and intensity have varied in the past, the twentieth century being a period during which they were particularly strong (Fig. 1.9).

The Terrestrial and Marine Biosphere

The biosphere, defined as all living organisms, also intervenes in the operation of the climate system. Some theories even propose that, throughout geological time, the biosphere has contributed to the regulation of climate in order to create conditions compatible with life.

The Geographical Distribution of the Biosphere

On land, the biosphere is mainly made up of vegetation which is distributed according to the critical climate characteristics which are sunshine, temperature and precipitation. Rainforests can only develop if temperature and humidity conditions are favorable for the twelve months of the year. They are replaced by a dry forest or savannah if the soil water content decreases over several months. The savannah itself becomes increasingly sparse as aridity increases eventually becoming a desert. North of the tropics, seasonal

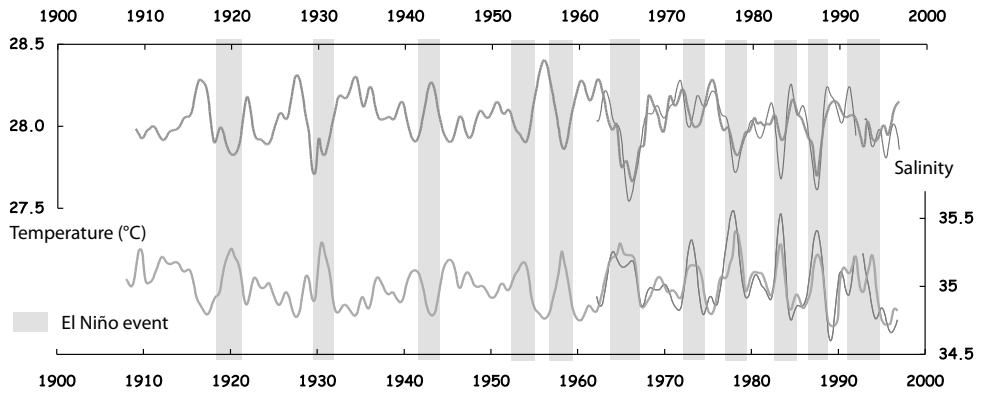

Fig. 1.9 Changes in the temperature and salinity of surface waters in the archipelago of Fiji (Western Pacific) reconstructed from changes in the isotopic composition of coral living in coastal areas. The period 1960–1995 for which instrumental measurements are available was used as a calibration period (Courtesy of Dr. Anne Juillet LSCE)

changes in temperature and humidity dominate the climate. Vegetation takes the form of deciduous forests in humid temperate regions, of drought-resistant flora in the Mediterranean area or prairie grass in dry areas with strong seasonal contrasts. Even further north is the area of the boreal forest (taiga), consisting of birch and conifers, and finally the tundra, where trees cannot grow. The mapping of current vegetation is therefore closely linked to major climate zones.

In the oceans, the marine biosphere depends on the temperature and salinity, but also on the amount of light and nutrients available to enable the production of phytoplankton which forms the basis of the ocean food chain. However, the areas where the production of phytoplankton is abundant are very limited. Apart from some coastal fringes of tropical regions, the Southern Ocean and the North Atlantic are the only areas capable of producing enough nutrients to continuously feed a wide range of living matter. Most of the ocean areas consist of essentially sterile water, hence the bright blue color of tropical waters.

The Role of the Biosphere

On land, vegetation alters the exchanges of energy, water and momentum. Vegetation permits greater solar energy absorption than bare soil. Indeed, the albedo (reflection power) of vegetation cover is 10–15% compared to 35% for bare soil. Trees also enhance the evaporation from the surface, through transpiration by the foliage and through pumping water from the soil by the root system. Finally, a tree creates an obstacle at the surface and increases turbulence close to the ground, hindering the wind more efficiently than bare soil. Based on numerical simulations, these physical effects of vegetation seem to have reinforced the intensification of monsoon rains during the mid-Holocene, 6000 years ago.

During the 1980s, the discovery of past variations in carbon dioxide and methane in air trapped in Antarctic ice has directed the spotlight onto the role of the biosphere, hitherto neglected. Indeed, these changes that show disruption of biogeochemical cycles cannot be explained solely by the physical exchanges between the atmosphere and oceans. The biosphere must be taken into account. The land-based biosphere absorbs carbon dioxide by photosynthesis, but emits it by respiration during the life of the plant and also later, during its decomposition in the soil through the action of bacteria. On average, as long as the climate remains constant, the absorption and emission of carbon dioxide by the land-based biosphere balances out and biological activity recycles atmospheric carbon.

In the oceans, phytoplankton also absorbs carbon dioxide through photosynthesis. This carbon is then reused to form the tissues of other living organisms in the food chain as well as organic waste of all kinds. In this way, phytoplankton is responsible for a rapid recycling of carbon in the surface waters of the oceans: the absorption carried out during photosynthesis is offset by the constant emission of carbon dioxide caused by the respiration of algae, zooplankton and fish, as well as by the oxidation of waste. A fraction of this carbon, about 10%, is subtracted from this recycling. Fecal pellets, dead tissue and other waste sink as a result of their weight and take some of the carbon absorbed at the surface of the oceans with them to the ocean floor. Most of this 'marine snow' dissolves or decomposes through the action of bacteria before reaching the bottom of the ocean, releasing carbon organic matter which is added to the dissolved carbon in the deep ocean waters. A tiny fraction of this 'marine snow', around 1% of the carbon taken from the surface, is

deposited in the ocean abysses, forming sediment in which carbon is trapped for millions of years.

Biosphere of the Past and Paleoclimates

For a long time, geologists have known that the land-based and marine biospheres varied greatly in the past in response to the slow process of evolution (on the scale of millions of years, Chap. 27, Volume 2) but also to changes in the global climate and in the general circulation of the atmosphere and oceans, particularly at the pace dictated by the astronomical paleoclimate theory (Chaps. 28, 30, Volume 2).

During their reproduction cycle, most plants produce tiny grains with a shape and decoration characteristic of their species. These are the pollen (the male fertile element of the flower) and spores (vegetative structure for propagation or reproducing) which have a very hard outer shell. They are transported by wind or streams and stored well if they land in a low-oxygen environment. They have been found in lake sediments and bogs, where they provide a reasonably accurate picture of the vegetation once covering the vicinity of the lake or bog. In this way, it has been discovered that, twenty thousand years ago, the vegetation of France was that of a polar steppe, at the peak of the last glaciation.

Land sediments contain other fossils which also provide information on the local climate: diatoms, mollusks, ostracods (tiny crustaceans with a calcareous shell) living in freshwater, larger remains of plants (stem and leaf), charcoal remains from large natural fires, fossil remains of larger animals, such as bones of mammals found in archaeological sites.

The link between the climate and plant fossils is so close that statistical methods have been developed to quantify this link, based on current observations. The resulting relationships, called 'transfer functions' are used to estimate past climate conditions if the same plant associations are found in ancient sediments as those known today (see Chap. 12, Volume 1).

Leaving aside the abundant fossils present in coastal areas and in coral reefs, the marine biosphere leaves many traces of its diversity in marine sediments: fish otoliths and teeth, aragonitic shells of pteropods (marine snails), calcareous shells of planktonic and benthic foraminifera, coccoliths (calcareous sheets secreted by microscopic algae, called coccolithophorids and living in warm or temperate waters), siliceous skeletons of marine diatoms (algae living in cold waters rich in silica) and radiolarians (microscopic animals living in deep water). The relationship between the temperature of the sea water and abundance of various species of foraminifera fossils and diatoms is close, which helps to establish transfer functions to estimate marine paleotemperatures with an accuracy close to 1–2 °C (Chap. 21, Volume 1).

It is important to be aware that transfer functions are only valid insofar as the species discovered in ancient sediments, both land and marine, are the same species as those that are present today. Even if only a rough estimate of the conditions that prevailed in the geological past is required, it is important to remember that species evolve and are likely to adapt to very different environments over millions of years. Thus, in the Jurassic era, 150–200 million years ago, well-developed coral reefs in warm waters harbored a variety of mollusks such as *Pholadomya*, *Tridacna* and *Astarte*. Their distant descendants can be found today in very different environments: *Pholadomya* buried in the mud in warm coastal waters, in a reef environment for *Tridacna* and in polar waters for *Astarte*. This shows how the reconstruction of paleoenvironments requires a cautious approach and the comparison of the various clues found in fossils.

The Cryosphere

Water in the form of ice or snow is the cryosphere. Glaciers and ice caps cover approximately 11% of the surface of the Earth. Spread out over the oceans, the water they contain would increase the sea level by about 77 m. Sea ice, which is formed by freezing seawater, covers approximately 7% of the oceans, but is only a few meters thick. As it floats, its melting does not cause the sea level to rise. On land, snow cover varies greatly with seasons.

The Role of the Cryosphere

The main property of the cryosphere is its albedo. It can reach 80–90% for fresh snow and barely drops below 50% when surface ice melts or when the snow covers trees. This property introduces the second major positive feedback loop of the climate system. Where snow or ice melts out, the ground absorbs a larger fraction of the incident solar energy. Containing more energy, it heats up, thus facilitating the melting of the remaining snow and ice. The process thus becomes amplified. In the Milankovitch theory of ice ages (see Chap. 28, Volume 2), the decrease in incoming solar radiation, due to the slow variations of the orbit of the Earth around the Sun, triggers the formation of ice caps thanks to this positive feedback. Indeed, following the decrease of sunshine, snow accumulated in the winter does not melt completely, in turn less energy is absorbed and the snow starts accumulating until ice caps are formed. As we shall see later (Chap. 25, Volume 2) the mechanism is actually more complex, and involves feedback from the ocean and boreal biosphere in response to changes in insolation, even if this positive feedback does constitute the factor triggering the start of an ice age.

However, the role of the cryosphere is not limited to its impact on the surface albedo. On the oceans, sea ice cuts off the ocean from the atmosphere, and blocks the air-sea exchanges of water, salt and other chemicals. When it is forming, sea ice eliminates salt which makes the surrounding sea water denser causing it to sink to depths, thus feeding the ocean thermohaline circulation. Conversely, when it melts in summer, the salinity of surface water decreases abruptly. On land, glaciers are not static. They flow under their own weight at a speed of up to several hundred meters per year. When they reach the coast, the ice breaks into icebergs that are propelled by winds and currents, and melt when they arrive in warmer water, causing a drop in salinity of surface waters of the ocean. Such changes are likely to bring about important feedbacks, such as stopping deep-water formation and the thermohaline circulation (see Chap. 29, Volume 2).

A climate change favoring the flow of glaciers could promote the destabilization of ice sheets, such as the one covering West Antarctica. Indeed, it rests on a base that would normally be covered by the sea, and the ice sheet is in contact with the ocean on all sides. Such a mass of ice is unstable. Because of this instability, gigantic floating ice platforms, several hundred meters thick, surround the entire part of the ice sheet in contact with the ocean.

The sheets covering the Ross and Ronne Seas, each with a surface area similar to that of France, calve huge icebergs, tens of kilometers in length, into the Weddell Sea. Without any rocky terrain, they are in direct contact with the ice cap and their speed often reaches several meters per day. What helps to safeguard the West Antarctic ice sheet is the presence of several islands around it. These anchor points slow down the ice flow. Ice therefore progresses slowly until that last barrier which, once crossed, leaves the field open to the calving of icebergs resulting from the fragmentation of the ice platform. The future of the West Antarctic ice cap in response to ongoing climate change is a real concern for the centuries to come.

The Cryosphere in the Past and Paleoclimates

The variability in the cryosphere is considerable, no matter what time scale is considered. Over the span of a season, snow cover and sea ice show the biggest variations. Measurements taken since the mid-twentieth century show that the area of sea ice each year goes from 15 million km^2 in early spring to just 6 million km^2 at the end of the summer. However, since 1980, a clear decrease in this range has been observed and it has reduced to nearly 3 million km^2 in 2012 summer. A similar trend in the retreat of mountain glaciers is observed during the twentieth century, whether in the Alps, or in the mountains of Africa or South America.

On a geological scale, the variability of the cryosphere is even greater. It is seen in the geological traces left by glaciers recording their passage and their broadest expansion (moraines, boulders streaked by friction marks as they were transported by the glacier over the surface bedrock on which it rested, vast continental shields like Canada eroded away). Geological observations have thus led us to believe that some 750 million years ago, all continents were covered with glaciers, and that the oceans were probably covered with perennial sea ice at the same time.

About 450 million years ago, during the Ordovician, a gigantic ice cap covered the Sahara where even today one can see striated rocks, glacial valleys, remains of moraines and channels that collected the water from the melting ice in summer and brought it to North Africa. Flying over western Mauritania, one can recognize the sandy bed of a great river that came into being beside an ice cap and traced out many meanders before flowing further north, to the seas bordering the glaciated African continent. These rivers were covered by icebergs that melted slowly and released stones they carried. They can be found today in exposed terrains, in Morocco, Galicia and even in the Armorican massif, south of Caen.

About two hundred million years ago, a long, globally warm era commenced (Jurassic and Cretaceous), during which time glaciers appear to have been rare, if they had not completely disappeared. The wide variety of flora and fauna reflects a variety of environmental conditions, from temperate in Japan, Siberia and Australia to very hot in America, Africa and Eurasia. There are no known tracks of large glaciers, even on the Antarctic continent, although, of course, as the continent is now covered with a thick ice cap it is only accessible to geological observations at its periphery.

The glaciations of the Quaternary are the culmination of a long process of cooling of the Earth that began more than thirty million years ago, firstly with the development of an ice sheet on Antarctica, and then on Greenland. For the last million years, glacial-interglacial oscillations have dominated the climate of our planet. While today it is the Southern hemisphere which is the most glaciated with Antarctica containing about 28 million km^3 of ice for only 1 million km^3 of ice in Greenland, it was the Northern hemisphere that was the most glaciated at the height of the last glaciation 20,000 years ago, with 50 million km^3 of ice over Canada (Laurentide Ice Sheet, 4 km thick) and northern Europe.

Throughout the last ice age, the Laurentide Ice Sheet extended beyond the American continent to reach the Atlantic continental shelf and the Labrador Sea. This cap could become unstable, suddenly releasing huge numbers of icebergs which invaded the entire North Atlantic where they melted. The sudden appearance of these armadas of icebergs, designated as ‘Heinrich events’ caused a significant decrease

in the salinity of the water at high latitudes, preventing downwelling of dense water in winter, thus stopping the thermohaline circulation and the transport of warm water by the Gulf Stream and North Atlantic Drift. The result was a freezing of Europe and a disruption of the climate over almost the entire planet. The behavior of the ocean-atmosphere-cryosphere interactions during glacial climate periods is complex. In addition to the Heinrich events that occurred during the last glaciation at intervals of eight to ten thousand years, the paleoclimate record inferred from the isotopic analysis of Greenland ice indicates a sudden warming (>10 °C) between Heinrich events, over periods of less than a few centuries that end with a slower cooling leading to a return to glacial conditions. These are the Dansgaard-Oeschger events which occur every two to three thousand years and which are not explained by any one unanimously accepted theory (instability of the European ice sheets, internal oscillation in ocean circulation, amplification of a weak solar forcing). The climate of the ice ages appears to have been much more variable than the climate we have known for the past 10,000 years, but the conditions for stability of the climate system remain a research topic that is far from fully understood (Chap. 29, Volume 2).

The Lithosphere: Over Large Timescales

The surface of the Earth, which makes up the lithosphere, also intervenes over long time scales of the order of a million years or more. Plate tectonics determine the position of the continents, the relief, the shape of the ocean basins, as well as the level of carbon dioxide emitted by volcanoes (Chap. 2, Volume 1 and Chap. 22, Volume 2). For example, the glaciation of the Sahara during the Ordovician is linked with the movement of the African plate, which had a polar location at that time. Pioneer studies suggested that the Antarctic ice cap was triggered 34 million years ago, when the American and Australian continents had sufficiently drifted from the Antarctic to allow the establishment of the circumpolar current that isolated Antarctica from the mid-latitudes. More recently, it has been shown that the long trend decrease of atmospheric CO_2 was pivotal in the triggering of Antarctica ice sheet. The uplift of the Himalayas, through its impact on the weathering and erosion of surface rocks, has likely contributed to increased consumption of atmospheric carbon dioxide and to the global cooling observed since the Eocene. The uplift of Tibetan Plateau as well as the Paratethys shrinkage amplified the Asian monsoon. The major tectonic phenomena therefore have a major impact on global climate on a geological scale (Chap. 2 Volume 1 and Chaps. 22, 26 and 27, Volume 2).

The lithosphere also interacts with the atmosphere through volcanism. During violent volcanic eruptions, large amounts of dust and gas are ejected into the atmosphere, up to several tens of kilometers in altitude. The emitted sulfur dioxide combines with the water vapor present in the stratosphere to form micro droplets of sulfuric acid, which is very effective in reflecting solar rays and causes a significant cooling of the surface of the Earth, of around 0.5–1 °C on average. In addition, these very small droplets can remain in the stratosphere for several years before falling into the troposphere where they are eliminated by rain. For example, the most intense volcanic eruption of the last two centuries, that of the Indonesian volcano Tambora in 1815, projected about 150 km^3 of debris and gases into the atmosphere and was followed by two exceptionally cold years. The year 1816 was even deemed to Canada and New England to have been 'the year with no summer'. Recently, after the eruption of the Philippine volcano Pinatubo in June 1991, one of the largest of this century, the weather stations recorded a significant lowering of temperature for several months.

Although the influence of volcanic eruptions on climate is limited mostly to a cooling for a relatively short time, rarely exceeding a few years, geologists think that unusually intense eruptions, called trapps, could have contributed to large-scale disruptions in climate and mass extinctions through their emissions. For example, it is estimated that the fissure eruptions that continued for several hundred thousand years to form the gigantic Deccan plateau, could have been of sufficient magnitude severally increased the carbon dioxide content of the air and to warm it by 3–4 °C until the weathering of rocks consumed the excess. Further in the past, 250 million years ago, huge fissure eruptions in Siberia are often cited as one of the factors responsible for global warming that marked the end of the Permian (Chap. 27, Volume 2).

The Climate System

Atmosphere, oceans, cryosphere, biosphere, and the lithosphere, all contribute to climate changes through a complex set of actions and reactions, both physicochemical and biological (Fig. 1.10). The atmosphere and the ocean, the two fluids that transport the excess energy received in the tropics to the poles, are central in climate dynamics, and this is true for all periods of time ranging from a few years to millennia. Strongly coupled with the mechanical effect of wind on the surface of the sea and through the exchange of heat and water, together they can cause fluctuations in natural climate phenomena, the scale of which can be glimpsed in *El Niño* for example. Their interactions can be strongly modified by changes in the land surface (vegetation, snow, ice). By their impact on the albedo and the water cycle, these changes modulate the exchange of heat and water between the two hemispheres, and between the oceans and land. Finally, past

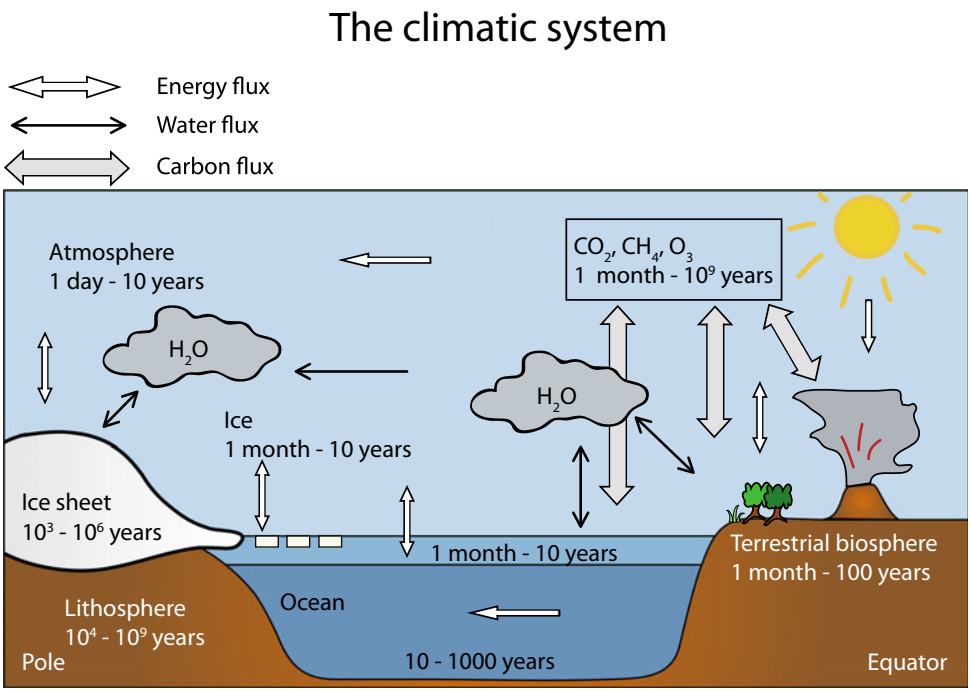

Fig. 1.10 The climate system and the exchanges of energy, water and carbon that affect it

climates provide many examples of fundamental reorganizations of the climate system.

For periods extending beyond a few thousand years, changes in insolation due to slow changes in the Earth's orbit around the Sun, the formation of ice sheets, the sinking of bedrock and changes in the composition of air also become drivers of climate change. Drivers which are however themselves dependent on other components of the climate system: the atmosphere, oceans and biosphere, through the underlying energy, water and carbon cycles. The formation of ice sheets is in effect controlled by the temperature of the air and by the accumulation or melting of snow. The concentration of carbon dioxide depends on the gas exchanges between the atmosphere and oceans, themselves governed by winds and temperature; it also varies with the activity of marine phytoplankton, itself strongly controlled by ocean circulation. As a result, these interconnections can transform the slow variations of the movement of the Earth around the Sun into spectacular glaciations. Over millions of years, plate tectonics become dominant, changing not only the geography of the Earth's surface, but also the composition of the atmosphere.

For a long time, scientists believed that climate changes of very large amplitude were phenomena that occurred slowly relative to the scale of human life, governed mainly by phenomena occurring over large time scales, such as the evolution of the Sun measurable over hundreds of millions of years, plate tectonics, the effects of which are felt gradually over millions of years, or the astronomical forcing with cycles of a few dozen millennia. The recent discovery of large iceberg armadas (Heinrich events), which can tip the climate into a glacial state in only a few decades shows that this is not the case. As soon as the calving of icebergs stops, the climate warms suddenly, a new rapid change that Neanderthals and Cro-Magnon witnessed. And between two Heinrich events, Dansgaard-Oeschger events are another manifestation of quick, abrupt climate change. All these observations show that the climate system as a whole is unstable due to multiple feedbacks that can result from the slightest disturbance.

We are not immune today to a brutal, unexpected change in climate, since human activity has reached a level that significantly disrupts the radiation balance of the atmosphere. The role of paleoclimatology is to document climate variability at all time scales and to help to highlight the mechanisms that come into play so as to understand the resulting changes. As such, paleoclimate information is analyzed in the Intergovernmental Panel on Climate Change assessment reports to outlines our understanding of climate change and mechanisms as well as to evaluate climate models. For example, the 5th Assessment Report reported how the current atmospheric concentration of carbon dioxide is unprecedented in the past 800,000 years, and how the rate of sea level rise since the mid-nineteenth century has been larger than the mean rate for the previous two millennia. It also informed on high sea levels during the last interglacial climate and proved the capability of models to reproduce past warm and cold climates.

Find out more

References to studies mentioned in this chapter presenting the climate system will be detailed and reported in the various chapters of this book. We indicate below some general literature which readers may want to consult to deepen their knowledge of the behavior and history of the climate system.

References

Berger, A. (1978). Long-term variations of daily insolation and quaternary climatic changes. *Journal of the Atmospheric Sciences, 35*, 2362–2367.

Berger, A. (1992). *Le Climat de la Terre, un passé pour quel avenir* (479 p). Bruxelles: De Boeck Université.

Broecker, W. S., & Peng, T. H. (1982). *Tracers in the sea* (690 p). Palisades, N.Y.: Eldigio Press.

Crowley, T. J., & North, G. R. (1991). *Paleoclimatology* (349 p). Oxford: Oxford University Press.

Duplessy, J. C., & Morel, P. (1990). *Gros Temps sur la planète* (296 p). Paris: Éditions Odile Jacob.

Holland, W. R., Joussaume, S., & David, F. (1999). Modeling the Earth's climate and its variability. In *École des Houches* (565 p). Amsterdam: Elsevier.

Hurrell, J. W. (2003). *The North Atlantic oscillation: Climatic significance and environmental impact* (279 p). Washington, D.C.: American Geophysical Union.

IPCC (Ed.). *Climate change (2013): The physical science basis; Contribution of Working Group I to the fifth assessment report of the Intergovernmental Panel on Climate Change*. Cambridge, United Kingdom and New-York, USA: Cambridge University Press.

Johnson, G. C., Mecking, S., Sloyan, B. M., & Wijffels, S. E. (2007). Recent bottom water warming in the Pacific Ocean. *Journal of Climate, 20,* 5365–5375.

Joussaume, S. (2000). *Climat, d'hier à demain* (143 p). Paris: CNRS éditions.

Mélières, M. A., & Maréchal, C. (2015). *Climate change: Past, present and future* (416 p). Hoboken: Wiley.

Neelin, D. (2011). *Climate change and climate modeling* (282 p). New York: Cambridge University Press.

Philander, G. S. (1989). *El Niño, La Niña, and the southern oscillation* (293 p). London: Academic Press.

Rohling, E. J. (2017). *The oceans: A deep history*. Princeton: Princeton University Press.

Ruddiman, W. F. (1997). *Tectonic uplift and climate change*. New York and London: Plenum Press.

Schneider, S., & Londer, R. (1984). *The co-evolution of climate and life* (563 p). San Francisco: Sierra Club Books.

Steffen, W. Sanderson, R.A., Tyson, P. D., Jäger, J., Matson, P. A., Moore III, B., Oldfield, F., Richardson, K., Schellnhuber, H. J., Turner, B. L., Wasson, R. J. (2005). *Global change and the earth system*, *IGBP Series* (336 p). Berlin: Springer.

Tomczak, M., & Godfrey, J. S. (2005). *Regional oceanography: An introduction*. PDF version available at: http://www.cmima.csic.es/mirror/mattom/regoc/pdfversion.html.

Wang, B. (2006). *The Asian monsoon*. Springer-Praxis books in *Environmental Sciences* (779 p).

The Changing Face of the Earth Throughout the Ages

2

Frédéric Fluteau and Pierre Sepulchre

The face of the Earth has changed dramatically over the last 4.5 billion years. The growth and emergence of the continental crust transformed a largely ocean-covered planet in its early days into a planet with land masses. Under the action of mantle dynamics, the first continental crusts merged with island arcs to constitute the first continents at the end of the Archean and the Paleoproterozoic (see Fig. 2.1 for a chart of geological time). These continents gathered to form the first documented supercontinent (Bleeker 2003) around 1.5 Ga, before breaking up and then coalescing again. Each phase has profoundly changed the Earth's surface. Vast mountain ranges got uplifted and ocean basins formed, then disappeared, through erosion or later geological events for the former, by posterious closure linked to tectonics for the latter. The climatic upheavals that have marked the Earth's history are strongly linked to these paleogeographic events through direct or indirect coupling between the different solid, liquid and gaseous envelopes that are depicted in volume 2. Here we provide an overview of the major geological stages of the early Earth before detailing the paleogeographic changes of the modern Earth in terms of continental distribution and paleotopography.

Paleogeographic Reconstructions

Paleogeographic reconstruction requires to quantify the changes in location of the continents, as well as their coastlines and topography, through the geological ages. Here we describe the techniques and tools used to retrieve such information, as well as the uncertainties inherent in each method.

Continental Drift

In 1915, the German meteorologist, Alfred Wegener, laid the foundations for continental drift in a book entitled *Die Entstehung der Kontinente und Ozeane* (The Origin of Continents and Oceans). This theory is based on several arguments, in particular on the complementarity of the continents bordering the Atlantic Ocean and the continuity of the terrain and their deformations. But Wegener was not the first to make these observations. A Dutch cartographer, Abraham Ortelius, observed this complementarity of the Old and New Worlds in his atlas *Theatrum Orbis Terrarum* published in 1570 and questioned the cause of this rupture and this expansion towards the west in his book *Thesaurus Geographicus* published in 1596 (Romm 1994). Two hundreds and fifty years later, the French geographer, Antonio Snider-Pellegrini, published "The Creation and its Unveiled Mysteries" (1858) in which he drew the position of the continents after the closure of the Atlantic Ocean. However, the theories of Wegener were not limited to the complementarity of the continents bordering the Atlantic Ocean and geological continuity, he also postulated on the basis of the paleontological continuity of flora (*Glossopteris*) and fauna (*Mesosaurus*, *Lystrosaurus*, *Cynognathus*), and paleoclimatic continuity. Glacial sediments from the Carboniferous era were discovered at the end of the nineteenth century in Africa, India and Australia. Wegener showed that by closing the Atlantic and Indian oceans, all these outcrops would form a coherent cluster close to what was the South Pole at the time. All these arguments supported the idea of a supercontinent, the Pangea. This revolutionary theory of the continental drift was strongly rejected by the Earth sciences community who preferred to believe in their fixity, and who criticized Wegener for the absence of mechanisms

F. Fluteau (✉)
Université de Paris, Institut de physique du globe de Paris, CNRS, 75005 Paris, France
e-mail: fluteau@ipgp.fr

P. Sepulchre
Laboratoire des Sciences du Climat et de l'Environnement, LSCE/IPSL, CEA-CNRS-UVSQ, Université Paris-Saclay, 91191 Gif-sur-Yvette, France

G. Ramstein et al. (eds.), *Paleoclimatology*, Frontiers in Earth Sciences,
https://doi.org/10.1007/978-3-030-24982-3_2

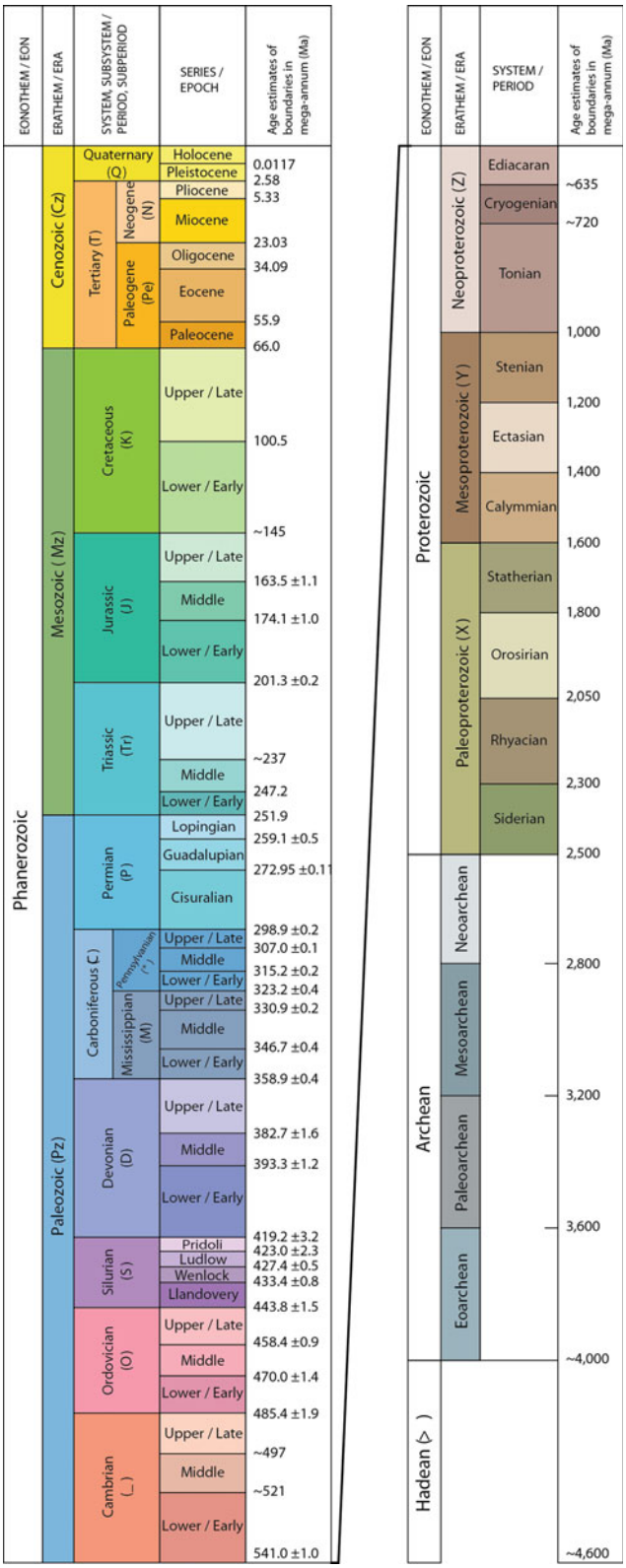

Fig. 2.1 Divisions of the geological time approved by the U.S. Geological Survey Geologic Names Committee (2018)

demonstrating his theory. The paleontologists of the early twentieth century clung to the concept of fixed geography, and invented the theory of "continental bridges," land ties that would have linked the continents, to explain the migration of fauna and flora. Nevertheless, some geologists believed in continental drift and supported it, such as Alexander Du Toit and Emile Argand. A decisive argument in favor of Wegener's theory was established by Arthur Holmes. He was the first to establish the basics of thermal convection of the Earth's mantle (Holmes 1929). But here again, this argument did not receive the expected positive response from the Earth science community, and it was not until the 1960s that Holmes was seen as a pioneer of plate tectonics.

From the 1940s, exploration of the ocean floor would revolutionize Earth sciences. The mapping of the morphology of the ocean floor, and the discovery of the Atlantic Ridge under the initiative of Bruce Heezen and Marie Tharp (Heezen 1962; Heezen and Tharp 1965), led Harry Hess[1] to propose a theory of the expansion of the ocean floor (Hess 1962). Half a century after Wegener, Earth sciences were experiencing a revolution, following the discovery of magnetic anomalies (Chap. 7). An American oceanographic campaign mapped the magnetic field around the Juan de Fuca Ridge, off the North American coast, in the eastern Pacific Ocean. By subtracting the ambient magnetic field from the magnetic data, alternately positive and negative anomalies were found (Raff and Mason 1961). Based on these observations, both Morley, and Vine and Matthews (Vine and Matthews 1963), proposed the theory of the renewal and expansion of the ocean floor in 1963.

These marine magnetic anomalies result from the acquisition of a thermoremanent magnetization by the iron and titanium oxide particles in the oceanic crust subjected to the Earth's magnetic field, after the oceanic crust (basaltic lava), emitted at the ocean ridges at a temperature of about 1100 °C, begins to cool. When basalt reaches the Curie point (the magnetic particle-dependent temperature, about 570 °C for the ferromagnetic magnetite crystals contained in the basalt), the direction of the field is fossilized by the magnetic carriers of the oceanic crust. Above the Curie point, the material is paramagnetic, and each magnetic carrier behaves like a small compass that follows the direction of the magnetic field without storing it. As soon as the temperature of the rock passes below the Curie temperature, the magnetic carriers aligned along the lines of force of the Earth's magnetic field are permanently frozen in this direction. The Earth's magnetic field can also be recorded in sedimentary rocks if they contain magnetic particles (Chap. 7).

Sea floor spreading is the cornerstone of plate tectonics, but to complete this theory, temporal constraints needed to be integrated, enabling the understanding of the pace at which ocean ridges opened. During this same period, the geophysicists Cox and Doell, and the geochemist Dalrymple established the first timetable of magnetic reversals for the last 4 million years (Chap. 7), using a new technique of isotopic dating with the potassium and argon elements (Cox et al. 1964) (Chap. 5). By comparing the magnetization polarity and the age of basalt samples taken at sea, it is clear that the age of the oceanic crust increases with distance from the line of the ridge. From the 1960s onwards, the DSDP (Deep-Sea Drilling Project) and ODP (Ocean Drilling Program) scientific missions were launched with the aim of drilling for sediment deposits on this oceanic crust. These sedimentary cores allow the sequences of magnetic polarities fixed by period to be established, thanks to the fossil content, and thus, to also date the marine magnetic anomalies. The speed of opening of the ocean ridges can then be determined. In 1968, Heirtzler and his group quantified the speed of opening of the South Atlantic Ocean by analyzing a marine magnetic sequence dating back to the Pliocene (3.35 Ma). In the following years, the kinematic parameters of all the oceans were determined one after another, and the evolution of the different ocean basins could then be traced. These parameters reflect the movements of one lithospheric plate relative to another one that is arbitrarily fixed. These movements being defined on a quasi-spherical surface, they can be expressed by an angle of rotation about an axis passing through the center of the Earth and defined by the longitude and latitude of its pole.

Moving on from the oceans to the land, in the early 1950s, some scientists studied the natural remanent magnetization of rocks. At all points of the globe, the magnetic field is defined by a vector collinear to the field lines. The magnetic field of the Earth originates from convective movements within the outer core, which consists of liquid iron (about 90 wt%), nickel (about 4 wt%), along with some lighter elements, such as silicon, sulfur and oxygen. The movements within the conductive core induce electric currents which, in turn, generate a magnetic field. The Earth's magnetic field functions like a self-excited dynamo. To compensate for the energy losses associated with the electrical resistivity within the Earth's core, energy input obtained from the conversion of ohmic dissipation into heat, from the gravitational energy and from the release of latent heat during the crystallization of the inner core ensures the thermal equilibrium of the milieu and permits the functioning of the geodynamo, as well as its continuity over geological time.

[1]When B. Heezen presented their findings to Princeton in 1957, Harry Hess stood up and said: "Young man, you have shaken the foundations of geology!" (Yount 2009).

It is therefore important to check the time at which the geodynamo was set up. To do this, it is necessary to find very old rocks that would have registered and retained a primary magnetization. Samples taken from the Matachewan Dikes dated at 2.5 Ga or basalts from the Fortescue Basin of the Pilbara Craton (Australia) dated at 2.7 Ga yielded a primary remanent magnetization which suggests the presence of a dipolar magnetic field at the end of the Archean (Tarduno et al. 2014). Knowing this, it is technically possible to measure the direction of magnetization from this time onwards. But what about rocks older than this? Archean formations are highly likely to have undergone a complex geological history, and, in particular, one or more episodes of metamorphism erasing the primary magnetic signal in favor of a more recent secondary magnetization. To overcome this problem, a technique based on the measurement of the magnetization carried by an isolated mineral (single feldspar, quartz phenocrysts) was developed to show the presence of a magnetic field as far back as 3.5 Ga. Finally, zircons dated between 3.3 and 4.2 Ga discovered in the Jack Hills metaconglomerate showed a magnetic signal carried by magnetite and considered to be primary. The paleointensity of the magnetic field (not its direction) was measured and it varies between 12 and 100% of the value of the current field at the equator possibly suggesting the presence of a terrestrial magnetic field as far back as the Hadean era (Tarduno et al. 2015).

The geomagnetic field **H** at any point on the surface of the globe can be defined by two angles, the declination D (angle between the magnetic north and the geographic north (counted positive east of true north)) and the inclination I (the angle between the horizontal plane and the direction of the field**H** (counted positive if downward)). At the first order, the present-day magnetic field can be represented by the field produced by a magnetic dipole inclined to the Earth's axis of rotation by 11.5° and slightly off-centered by about 500 km from the center of the Earth. Differences between the current magnetic field and this theoretical field exist locally, as evidenced by the contribution of non-dipolar terms (quadrupole, octupole). In the even stronger hypothesis of a perfectly dipolar, axial and centered magnetic field, a simple mathematical relation connects the magnetic inclination measured at a point of the Earth's surface to the latitude of this point. In other words, knowing the inclination of the magnetization vector fossilized by the magnetic minerals at a site at different times in the past allows us to calculate the successive paleolatitudes of this site by assuming that the geomagnetic pole has always coincided with the geographical pole, itself supposed fixed. Conversely, from a set of samples distributed over a continental land mass, we can calculate the position of the magnetic pole associated with the continent or geological mass under consideration, always assuming the axial and centered dipole magnetic field: this is therefore a "virtual" geomagnetic pole (VGP), since the reference is a continental land mass whose past position is not known.

The successive positions of the VGP over time track the path of the apparent drift of the magnetic poles, with the continent being studied fixed at its current position. The first apparent polar wander path (APWP) over a period of 600 Ma was established in 1954 by Creer and his research group, based on magnetic measurements of samples taken from geological formations in Great Britain (Creer et al. 1954). The virtual magnetic poles constituting the APWP approximate, supposing a geocentric axial dipole, the successive paleopositions of the rotation axis with respect to the continent from which the paleomagnetic pole was determined (Fig. 2.2). In the 1950s and 1960s, the existence of a central axial dipole was challenged, calling into question the importance of the APWP. In 1964, however, Irving was able to verify by means of climate indicators the hypothesis of a central axial dipole. Indeed, the climate of the Earth is, first and foremost, a function of insolation. The result is that the distribution of climate indicators (e.g. evaporites for subtropical zones, coral reefs for tropical areas, glacial sediments at high latitudes), tends to be symmetrical on either side of the equator.

To check if the distribution of the paleoclimate indicators discovered within geological formations changed over time, Irving replaced the continents (and the sites of the paleoclimatic indicators) in their paleopositions, using the virtual magnetic poles, and applied the hypothesis of a geocentric

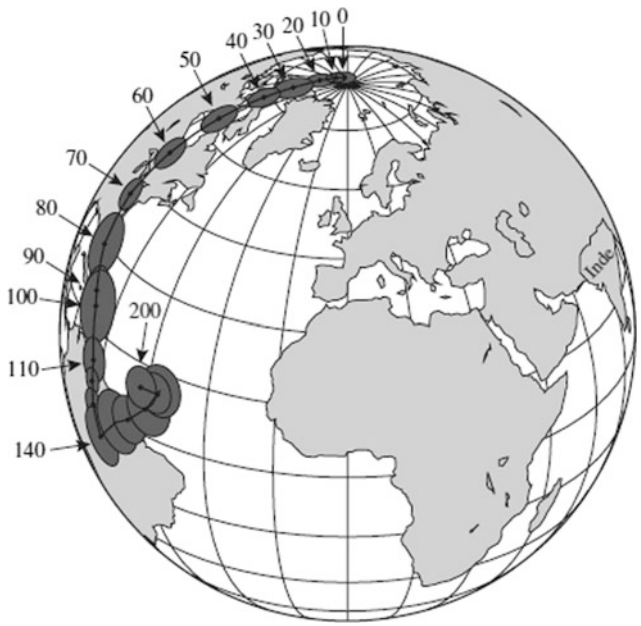

Fig. 2.2 The apparent polar wander of the magnetic poles of India (according to data from Besse and Courtillot 1991). The age of the magnetic pole (in Ma) is indicated. The ellipses represent the uncertainty (95%) on the magnetic pole position at a given age

axial dipole. Thus reconstructed, the latitudinal distribution of the paleoclimate indicators is statistically identical to their present distribution, thus supporting the hypothesis of the axial centered dipole. Other studies carried out in the 1960s made it possible to validate this hypothesis, first for the Plio-Pleistocene and then gradually as far back as the Precambrian. In 1968, Le Pichon proposed a model of movement of rigid land masses relative to each other, thereby reconstructing seafloor spreading for all the Cenozoic (Le Pichon 1968).

The trajectories of the APWP make it possible to place the continents in their original position with respect to the axis of rotation of the Earth, in other words, in terms of paleolatitude and orientation. However, paleomagnetism is not enough, since it does not specify the paleolongitude of the continents because of the spherical symmetry of the magnetic field (assuming an axial and centered dipole magnetic field). Kinematic parameters of the oceans are used to pin down the position of a continent relative to another. However, this method can only be used when the ocean separating two continents is bordered by passive margins and especially when these kinematic parameters are known (available for the last 170 million years only). If one of these oceanic margins is active, the positioning of one plate relative to another is nevertheless possible by traveling across one or more other intermediate continents separated by passive margins. Nevertheless, there are cases where the deformation of the continental land masses by tectonics (in a collision zone, for example), the presence of active margins, or the age of reconstruction prevent the use of this method combining paleomagnetism and ocean kinematics. In these cases, paleogeographic reconstructions depend on paleomagnetism and the APWP.

These trajectories of the apparent polar wander are not all of equivalent quality. To overcome this disadvantage, Besse and Courtillot (1991, 2002) and Torsvik et al. (2012) proposed calculating artificial trajectories of APWP where the poles of all the plates of a certain age are integrated into a single referential (i.e. transferred from one lithospheric plate to another using the kinematic parameters of the oceans). This method is applicable to the last 320 million years (despite the absence of kinematic data for the oceans beyond 170 Ma since all the continents were then combined into a supercontinent, the Pangea). Before 320 million years, for all continents and regardless of the period for those land masses surrounded by active margins, reconstructions rely solely on the trajectories of APWP, although geological and/or paleontology arguments may provide constraints on the relative position of the masses. Of course, there is an overall increase in uncertainties with age.

The now well-known movements of large lithospheric masses are part of the classical theory of plate tectonics. However, the whole Earth can also tilt relative to the axis of rotation in response to the heterogeneities of masses in the mantle, modifying the tensor inertia of our planet (the maximum axis of inertia is aligned with the axis of rotation of the Earth). In the paleomagnetic reference system, the APWP is thus caused by the movement of the plate due to plate tectonics and to the overall movement of the continents.

In 1972, Morgan proposed using hot spots associated with convective plumes from the D″ transition zone as a definitive frame of reference. Deep mantle convective plumes are assumed to be fixed because of the sufficiently slow movements in the lower mantle. The movements of some lithospheric plates can thus be positioned within the "hot spots" reference frame. Unlike magnetic poles, paleolatitude and paleolongitude are constrained (by a frame of reference associated with the mantle), but this method can only be used for the last 130 million years. Before this time, the traces of hot spots on the ocean floor cannot be traced, erased by the subduction zones, while the few remaining traces are not constraining enough.

The differences in latitude and in rotation of the continents between the paleomagnetic and hotspot reference frames make it possible to isolate the movement of the global drift of the crust-mantle couple with respect to the axis of rotation or the true polar wander from the perspective of a continent. The amplitude of the global drift generally does not exceed 1° per million years over the last 130 million years (Besse and Courtillot 2002). Nevertheless, there are some rapid events (occurring over a few million years) during which a global drift of about 10° of all the continental masses has been observed, for example in the Paleocene (Moreau et al. 2007). Even with a lack of data in the hot spot reference, it is possible to isolate the true polar wander by determining common drifts in APWP of different continents. Events of great amplitude have also been suggested, for example a 90° movement between the Lower and Middle Cambrian (Kirschvink et al. 1997) or during the Ediacaran (Robert et al. 2017). These events result in a continental drift rate of the order of 10° per Ma, therefore much higher than the maximum continental drift rate caused by plate tectonics of about 2° per Ma (Seton et al. 2012) but perfectly compatible with the theoretical maximum speed of the true polar wander of about 10° per Ma, taking into account a viscoelastic Earth (Greff-Lefftz and Besse 2014; Robert et al. 2017).

The Paleomagnetic Tool, Tests and Uncertainties

To understand the difficulty of obtaining robust paleogeographic reconstructions, it is important to look at the paleomagnetic tool used (Chap. 7). The direction of the magnetic field is measured in a laboratory using a magnetometer, an

instrument capable of detecting natural remanent magnetizations of less than 10^{-12} A/m, on cylindrical samples of approximately 10 cm^3 taken from sedimentary or volcanic formations and as perfectly oriented in space as possible. This orientation in space of the sample collected in the field is essential in order to determine the direction of the magnetization vector (represented by inclination and declination) and then to calculate the position (longitude and latitude) of the virtual magnetic pole associated with it. To obtain a reliable virtual magnetic pole, several criteria must be met. First of all, one needs to have a sufficient number of samples. The number of samples collected is usually eight per site, and the number of sampling sites within a geological formation is at least six sites. As in the processing of the signal, increasing the number of sites and samples per site improves the signal-to-noise ratio (thus reducing the sources of errors). The uncertainty on the virtual magnetic pole is of the order of a few degrees (1° = 111 km) in the best case, which still represents a few hundred kilometers. The displacement of continent of less than several hundred kilometers is therefore difficult to detect, which, taking into account the average speed of plate drift ($\sim$4 cm/year), represents a time span of about ten million years. The dating of the sampled geological formations must also meet a standard of robustness in order to produce a reliable virtual magnetic pole. The primary character of the magnetization of the ferromagnetic carriers must be verified. The magnetization signal must be synchronous or recorded in the millions of years (<5 Ma) after diagenesis (in the case of sedimentary formations). This is to ensure that the magnetization age is essentially the same as the "stratigraphic" age of the formation. When these two ages differ, a subsequent re-magnetization has occurred (in response, for example, to the burial at several kilometers deep, which has the effect of imprinting a new magnetic signal in the sample masking partially or wholly the primary magnetization).

Tests have been developed to evaluate the quality of the measured primary natural remnant magnetization (NRM). The first is the reversal test. On average, the magnetic field experiences several reversals per million years (there are, nevertheless, periods of several tens of millions of years during which no reversal is observed, Chap. 7). Over a time period of less than a few million years (<5 Ma), the calculated virtual magnetic pole must be statistically identical, regardless of the polarity of the magnetic field. This test increases the confidence in the primary character of the NRM and ensures that the secular variation of the magnetic field resulting from the movements of molten iron in the outer core has indeed been averaged. The secular variation of the magnetic field gives rise to a rapid drift of the magnetic pole which can move the virtual pole by more than 10° from its mean position. Thus, the direction provided by a single lava flow cooled in less than one year does not correspond to the average direction of the dipole. A second test consists of checking the reliability of the magnetic pole determined from sampling sites for which the dip in the geological layers differs. Indeed, the geological formations can be subjected to deformations. To calculate the virtual magnetic pole, the paleo-horizontality of the sampled sedimentary formation that prevailed at the moment of the acquisition of the magnetic signal must be restored. Taking into account the tectonic (tilt) correction for each sampling site must have the effect of clustering the set of magnetic directions obtained for each site. If this structural correction does not have the desired effect on the data, this means that the magnetization was acquired during or after deformation.

However, these tests are not sufficient to certify the robustness of the data that can be affected by various biases. Regional tectonics in areas of active collisions such as in the Alps or by rifting in Afar could lead to horizontal block rotation that is well recorded by paleomagnetism. These regional tectonics can mask the large drifts of plates or larger masses. A second bias is related to the geometry of the magnetic field. The calculation of a virtual magnetic pole is based on the assumption of a geocentric axial dipole. In the case of samples collected from sedimentary formations, the magnetic measurements are carried out on cylinders of approximately 10 cm^3. Given the low accumulation rate of sediments and the effects of diagenesis (such as compaction), a cylinder of 10 cm^3 may represent a time period of several thousand years, and the measured magnetic direction is in some sense an "average" direction of this time period. For a sampling site, the magnetic direction is the average of the magnetic directions of the samples taken from a unit of a sedimentary formation. It is therefore possible that the time interval associated with the mean magnetic direction represents several thousand years, or even more. The variations of the magnetic field are thus smoothed, and the magnetic direction measured is indeed that produced by a geocentric axial dipole field in the study area under consideration.

In the case of volcanic series, the thermoremanent magnetization (TRM) is acquired during the cooling of the lava flow. It thus represents a (quasi-) instantaneous photography of the Earth's magnetic field. To overcome the effect of the secular variation, the average direction of a large number of sites must be measured, so as to tend towards the direction which would be obtained with an axial geocentric dipole. However, the presence of a persistent quadrupole term in the paleomagnetic data has been identified as a possible source of errors. The presence of quadrupole terms of about a few percent (the level generally observed) implies an error of a few degrees in latitude at the equator. This does not therefore significantly affect the virtual magnetic pole which is calculated assuming the axial geocentric dipole hypothesis. There is also a possibility that the magnetic field could include an octupole component affecting Asia during the Tertiary and Pangea during the Permian. If we

consider an octupole term equal to 10% (resp. 20%) of the dipolar component, the maximum error committed is ~7° (resp. 13°) in the mid-latitudes. Finally, a last source of error is related to the preservation of the magnetic signal in the sedimentary series. Indeed, during diagenesis, the magnetic carriers can undergo a decrease in the inclination of the magnetic carriers. The inclination measured is therefore less than the actual inclination of the magnetic field that prevailed at the time this detrital remanent magnetization was acquired. This inclination flattening can be a source of error in paleoreconstructions (Cogné et al. 2013).

The Topography of the Earth

Mountain ranges and high plateaus play an important role in atmospheric circulation. The uplift of the Himalayas and the Tibetan plateau is undoubtedly the most characteristic example of the relationship between topography and the evolution of atmospheric circulation and climate. The hypsometric curve of the Earth reveals that today, reliefs higher than 2 km represent about 10% of the land area. Still, this curve reflects the orogenic context of the Earth that has prevailed since the beginning of the Cenozoic only, and one expects that this curve evolved through time.

The great areas of high-altitude terrain (~>2 km) typically developed during the formation phases of a supercontinent (for example, in the Carboniferous, during the formation of the supercontinent Pangea), while periods of break-up of the supercontinents (the Mesozoic for example) are characterized by more modest reliefs (although low reliefs of less than 2 km in general, can form in case of continental rifting). In the oceans, seafloor reliefs are mostly dominated by ocean ridges and some high oceanic plateaus rising above the abyssal plains.

The altitude of the continents, plains, collision mountain ranges (Himalayas, Alps) and the zones of the East African Dome result first of all from the (quasi-) isostatic equilibrium of the lithospheric column marked by density heterogeneities on the underlying asthenosphere. The bathymetry of the ocean floor is controlled by the cooling and by the progressive thickening of the oceanic lithosphere formed at the dorsal ridges in isostatic equilibrium on the asthenosphere.

However this scheme does not apply everywhere, suggesting other mechanisms. Some reliefs are not at isostatic equilibrium, as is the case, for example, of volcanic islands that develop on an oceanic crust (like Hawaii) or continental crusts previously subjected to the weight of an ice cap (like the Scandinavian region). The charge brings about a flexure whose wavelength is related to the elastic rheology of the crust. After the rapid melting of an ice cap, the deformation gradually fades over time with a rate depending on the viscosity of the underlying mantle.

Topography can also be controlled by dynamic processes[2] related to movement of matter and heat transfer within the viscous mantle. Upward or downward movements of mantle matter or dipping of a lithospheric plate into the mantle create mass anomalies that can induce long-wave crustal deformations. This is known as dynamic topography (Husson 2006) as opposed to isostatic topography. The uplift of the southern African plateau and the Colorado plateau during the Cenozoic is explained by movements of mass anomalies in the mantle. Dynamic topography also helps to explain the history of the Western Interior Seaway that connected the Arctic Ocean to the Gulf of Mexico across the North American continent during the Cretaceous, but also the flooding followed by the exondation of part of Australia at the same time, or the flooding of the Sunda shelf in Indonesia during the Pleistocene (Sarr et al. 2019).

Restoring the past topography of the Earth is undoubtedly the most difficult part of paleogeographic reconstructions. It involves determining the spatial expanse of the terrain, its age and altitude. The reliefs bring about deformations and/or structural and petrological markers which, when fixed in time, are used by geologists to constrain the tectonic event. These markers are not always easy to detect because more recent events often mask earlier events. A phase of continental accretion caused the India-Asia collision in Southeast Asia during the Triassic period, but this orogeny remains uncertain, partly because this collision erased part of the previous geological history. Determining the paleoaltitude of mountains is therefore crucial in order to model pre-Quaternary paleoclimates. Several methods (flora, sediment, oxygen isotopes, cosmogenic isotopes) have been developed, but only the most commonly used will be depicted here. It is very important to differentiate between absolute methods, which makes it possible to estimate the paleoaltitude of a relief at a given time and methods estimating the vertical velocity of the rocks in these mountains. The relative methods reflect a balance between the vertical movements linked to a geodynamic event (a collision for example) and those due to erosion which denudes the surface, favoring the rise of deep-set rocks by isostatic readjustment.

To measure an altitude or to estimate a paleoaltitude, a reference level is essential. The surface of the oceans provides this reference, but this fluctuates over geological time. However, the amplitudes in these variations are less than the uncertainty obtained on paleoelevations, regardless of the methods used. Nonetheless, eustatic variations are crucial when examining the regions between the continental shelf (> −200 m) and the vast lowland plains (<200 m).

[2]Although dynamic, collision mountain ranges and intracontinental rifting are essentially isostatic equilibrium processes.

The Evidence from Flora

The assemblage of plant fossils has been used as a marker for paleoelevation for almost half a century. This method is based on the relationship between the vegetation type and the average temperature at a given location. It is broken down into several variants. The first method relies on finding an assemblage of modern plant taxa equivalent to that of the fossil site (or at least sharing the highest possible number of taxa with it), but it assumes that there was no adaptation by these taxa to climatic variations in the past (Su et al. 2019). This method is particularly well adapted to the last 10 million years. A second method is based on the physiognomy of the leaves of plants (size, shape, thickness, type of leaf margin), synonymous with the adaptation of the plant to a given climatic context. A relationship between the physiognomy of current plant leaves and the mean annual temperature has been established. This method assumes, however, that the response of the leaf physiognomy to the climate has been constant over time. This tool is calibrated on dicots and does not take into account all biogeographic provinces (e.g., Australia) or all taxa (such as conifers). Moreover, it is only applicable as far back as the Upper Cretaceous, since flowering plants only appeared during the Cretaceous. However, the main advantage of this approach is that it avoids any systematic recognition of taxa because only the morphological characteristics count (which implies optimal fossilization conditions). To determine altitude, it is necessary to know the average temperature at sea level of a site of the same age. The difference in temperature between these two sites divided by the vertical gradient of the temperature indicates the paleo-altitude. However, the temperature lapse rate varies from 4 to 10 °C/km. This depends on the latitude, the humidity of the air mass, the continentality of the site and the topography itself. The choice of this parameter is therefore decisive. Uncertainty remains high (Peppe et al. 2010), around 700–1000 m for paleo-altitudes estimated at 3–4 km.

To overcome the problem of the vertical gradient, a method based on the preservation of moist static energy h in the atmosphere has been developed (Forest et al. 1995). The parameter h is the sum of a thermodynamic parameter, the enthalpy H of humidity and the potential energy gZ and has the advantage of a distribution that is relatively zonal, especially in the mid-latitudes of the northern hemisphere. This method requires an atmospheric circulation where horizontal movements predominate over vertical movements, to ensure the conservation of moist static energy. The humid enthalpy H was calibrated on current leaf indices (similar to the mean temperature in the previous method). To determine the paleo-altitude of a site, its humid enthalpy H and the humid enthalpy H_0 of a contemporary reference site located at sea level must be known. The uncertainty on paleoaltitude is only slightly lower than for the preceding method.

The plant-based methods are also subject to uncertainties because of the impact of vegetation on the climate that are ignored. The vegetation cover affects the radiative balance of the Earth through its albedo and the water balance through evapotranspiration (e.g. Otto-Bliesner and Upchurch 1997), thereby could introduce a bias and cause paleo-altitudes to be mis-estimated.

The Evidence from Erosion Sediment

By restoring the mass of deposited sediments in a basin to the original relief, it is possible to calculate paleo-altitudes. This presumes that the geometry of the sediment source is known and that this has not changed over time, that there are no sediment losses due to subduction or to incorporation during more recent orogenic events and finally it assumes that the relief has always been in isostatic equilibrium. These considerations considerably limit the use of this method to a few endorheic basins that do not have subduction zones (intracontinental), such as the Tien Shan range in Asia during the Miocene. Its application to older orogeny is complex.

Stable Isotope Paleoaltimetry

Water oxygen is made of different stable isotopes (^{16}O, ^{17}O, ^{18}O, e.g. Chaps. 11, 14, 15, 16, 21). The ratio of heavy to light isotopes, when compared to a global reference value (namely the Vienna standard mean ocean water, VSMOW), is noted $\delta^{18}O$. It can be measured in various surface waters (ice, ocean, lakes, rivers), carbonates from pedogenic or lacustrine sediments, or biogenic archives. At the global scale, is has been observed that $\delta^{18}O$ in rainfall decreases from low to high latitudes, and from coastal to inland areas. On continents, $\delta^{18}O$ measured directly in precipitation or in rivers along different elevation transects also has been shown to scale with altitude, with $\delta^{18}O$ decreasing as elevation increases. These observations have been explained by the Rayleigh-type distillation process that occurs theoretically in a cooling air parcel ascending along a mountain range: As air rises and cools, water vapor condenses then precipitates. During these steps, heavy isotopes are more favorably removed from the air parcel, progressively depleting water vapour along the way. Ultimately, rainfall is more and more depleted in heavy isotopes with elevation, i.e. $\delta^{18}O$ decreases (Fig. 2.3). This theoretical framework, together with regional measurements of $\delta^{18}O$ have led to determine

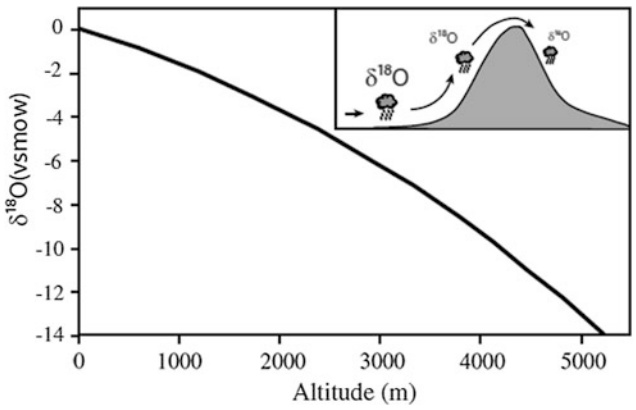

Fig. 2.3 Evolution of the isotopic ratio of oxygen ($\delta^{18}O$) as a function of altitude

"isotopic lapse rates", i.e. expected change in $\delta^{18}O$ as a function of elevation (Mulch 2016). These lapse rates depend on many parameters, including initial relative humidity and temperature of the air parcel.

The relation between $\delta^{18}O$ and elevation has been used to estimate paleoelevations since the late 90s (e.g. Chamberlain 1999; Quade et al. 2007; Rowley and Garzione 2007; Mulch 2016). Oxygen isotopic ratios can be measured in lacustrine or soil carbonates, and used to infer the paleo-rainfall $\delta^{18}O$ using a relationship involving the temperature of carbonate formation (Kim and O'Neil 1997) and assuming thermodynamical equilibrium between the water and calcite. Reconstructing rainfall $\delta^{18}O$ of dated records thus allowed to infer past elevations and numerous studies have been carried out to reconstruct uplift history of mountain ranges worldwide, including the Andes, the north American cordillera and the Tibetan Plateau.

Still, several processes can cause bias in the results. The isotopic fractionation depends not only on temperature but also on physical processes that alter the simple model of air parcel ascent and depletion. Large-scale climate conditions (e.g. greenhouse climate) and dynamics can modify moisture advection and can also lead to mixing of air masses with different origins and isotopic signatures. Moreover, changes in atmospheric dynamics related to the peculiar conditions of the warm climates of the Paleogene have been shown to alter the isotopic lapse rates. Such potential biases have been highlighted for the reconstruction of the altitudes of the Tibetan plateau (e.g. Botsyun et al. 2016, 2019; Li and Garzione 2017) and the Andes (Poulsen et al. 2010), with either extensive datasets of river $\delta^{18}O$ measurements or the use of isotope-enabled general circulation models. Lastly, the isotopic anomaly recorded in pedogenic carbonates is not from rainwater, but from runoff waters. In the case of the Himalayas, for example, measurements of $\delta^{18}O$ carried out on various modern rivers can differ significantly from meteoric waters. The $\delta^{18}O$ of the pedogenic carbonates is more a reflection of the averaged $\delta^{18}O$ of the drainage basin than of the meteoric waters. For lake carbonates, $\delta^{18}O$ is affected by evaporation on the surface of the lake. Depending on the data location, these biases can add up to a significant uncertainty, close to that observed with the plant-based methods (see Mulch 2016 for a review).

As for the estimates of ocean paleo-temperatures (Chap. 21), the clumped isotope (Δ_{47}) measurement (Eiler 2007; Bonifacie et al. 2017) appears to be the next promising tool in paleoaltimetry. The propensity to form molecules containing bonds between heavy isotopes of carbon (^{13}C) and of oxygen (^{18}O) in a carbonate (mainly in the form of $^{13}C^{18}O^{16}O$) is more probable, the lower the temperature is at the formation of the pedogenic carbonate (Chap. 21). There is therefore a relationship between this quantity and the formation temperature, which makes it possible to work back to paleo-altitudes by establishing the vertical temperature lapse rate (which still may have varied in the past) (Quade et al. 2007). Moreover, the measurements independent of the formation temperature through Δ_{47} and of the $\delta^{18}O$ isotopic ratio of these carbonates, make it possible to trace back to the $\delta^{18}O$ of the water and thus to isolate the effect of altitude from parasitic influences, such as climate, season, or latitude. Burial does not appear to affect the measurement of Δ_{47} in general, an advantage in the case of orogeny. This method makes it possible to obtain paleo-altitudes with a lower uncertainty than other methods. This isotopic tool was used to constrain the evolution of paleo-altitudes and the speed of uplift of the Altiplano, a high plateau in the Andes in South America, during the Miocene (Garzione et al. 2014).

Eustatic Variations and Ocean Gateways

Ocean circulation plays an important role in the climate system by transporting heat from low to high latitudes, particularly through surface currents. However, this transport depends on the distribution of the continents and the shape of the ocean basins. At present, deep waters are formed mainly in the North Atlantic Ocean, specifically in the Norwegian Sea and the Labrador Sea. Therefore, the configuration of deep ocean circulation must have been different in the past. At the end of the Cretaceous, the North Atlantic Ocean was not yet open and exchanges between the central Atlantic Ocean and the Arctic Ocean were very limited. Deep water formation could therefore be transferred to the Pacific Ocean, based on numerical models simulating the large-scale circulation of the ocean and atmosphere (e.g. Otto-Bliesner et al. 2002).

Changes in geographical configuration through continental drift, or more radically, through the opening or closing of ocean basins, are therefore likely to cause profound changes in ocean circulation. Either shallow or deep, ocean gateways play a crucial role in water masses circulation and associated heat and salt fluxes (Ferreira et al. 2018). During the Cenozoic, the position of the continents has not drastically changed but some ocean gateways have been opened or closed thereby impacting ocean circulation. The Tasman seaway opened during the Late Eocene, the Drake passage during the Late Eocene/Oligocene, the Fram Strait during the Oligocene. Conversely the East Tethys seaway closed during the Early/Middle Miocene, the Central American Seaway during the Late Miocene, the Indonesian throughflow during the Late Miocene/Pliocene. The timeline of these opening/closures are therefore crucial for paleoclimate reconstruction purposes, and can be constrained through the use of paleoceanographic markers and sea level records.

Sea level changes profoundly change the face of the Earth. Periods of high sea level, such as during the Cenomanian ($\sim$95 Ma) studied by Eduard Suess at the end of the nineteenth century, caused the flooding of large continental areas. Vast shelf seas, generally shallow (<200 m), covering up to 30% of the land area, were thus observed during the Phanerozoic period. In some cases the combination of a high sea level and a flexure of the lithosphere can result in the formation of shelf seas several hundred meters deep. In other cases, flooding or drying is controlled by dynamic topography.

The dynamics of these epicontinental seas are still not well understood because there is no analog of such large shallow water basins today. These epicontinental seas would have favored climates with little thermal contrast due to the high calorific capacity of the water and their thermal inertia. Conversely, periods with low sea levels would have favored more contrasted climates. Analysis of the sedimentary facies makes it possible to locate the coastlines. These have changed with eustatic variations (change of sea level), but also with continental uplift and subsidence, the flexure of the lithosphere in response to the build up of ice sheet or its melting or variations in the sedimentary fluxes. Changes in coastlines inferred from the sedimentary facies do not therefore constitute a direct marker of sea level.

In 1977, Peter Vail and his team, geologists with the American oil company Exxon, produced a curve of sea level changes. Vail showed that the geometry and position of the sedimentary units deposited on the continental shelves and in the basins had varied according to sea level, the subsidence of the area of deposition, the sedimentary flow and the carbonate production. The geometry and position of the sedimentary units are the main influencers of variations in sea level, as subsidence, deposition and carbonate production are considered to be less variable. The determination of sedimentary facies from core samples taken by drilling and the location of seismic reflectors on the continental margins and adjacent basins make it possible to reconstruct the arrangement of sedimentary deposits and to infer eustatic variations. Several curves have since been produced (Haq et al. 1987; Haq and Schutter 2008). The curves obtained (Fig. 2.4) show nested eustatic cycles. The largest eustatic variations, about 200 m, with a timescale of tens of million years, are related to life cycle of supercontinents (Wilson cycle), plate reorganization, dynamic topography and crustal production variations. Secondly, significant variations (several tens of meters) but with a lower timescale (from $\sim$2 to $\sim$10 Ma) are likely due to regional tectonic forcing. Thirdly, the sea level fluctuations on the timescale of 0.5 to $\sim$2 Ma are not well understood, it could be related to the climate changes or ice volume variations. Even more rapid variations on the timescale of tens to hundred years are clearly related to glacioeustatism whereas postglacial rebound acts on timescale of thousands to hundreds of thousands of years.

However, this interpretation of the high frequency variability found on an eustatic graph at the scale of geological time has been called into question. Moreover, the covering of coasts observed in sedimentary systems may not necessarily translate into eustatic variations.

A different method from that of Haq et al. (1987) was proposed by Miller et al. (2005). It determines eustatic variations using an inverse model by calculating the effects of the sediment load, compaction and the oceanic load necessary to simulate the deformation of a basin (subsidence or uplift) located on a passive margin. The variations in sea level obtained by this method do not exceed 100 m, which is half that proposed by Haq et al. (1987) for the Phanerozoic. Moreover, the eustatic variations obtained by these two methods may be out of phase with each other. Unlike the curve by Haq et al. (1987), which is based on numerous records, Miller's sea level variation curve is based on a small number of sites on the eastern margin of North America. The deformation undergone by this basin caused by internal dynamic processes originating in the mantle is not corrected. This basin may have recorded a "dynamic" topography with long wavelength radiation (as opposed to the topography linked to isostasy of a lithospheric column) partially skewing the eustatic signal. Debates still exist regarding the exact evolution of sea-level throughout the Phanerozoic, as a more recent study, based on a full geodynamical model, provided a large range of sea-level fluctuations for the last 500 Ma (Vérard et al. 2015) (Fig. 2.4).

To understand these discrepancies, one must analyze the mechanisms of sea level change. Variations in the position of coastlines can come from several different sources: variation in the volume of water (the content) or variation in the

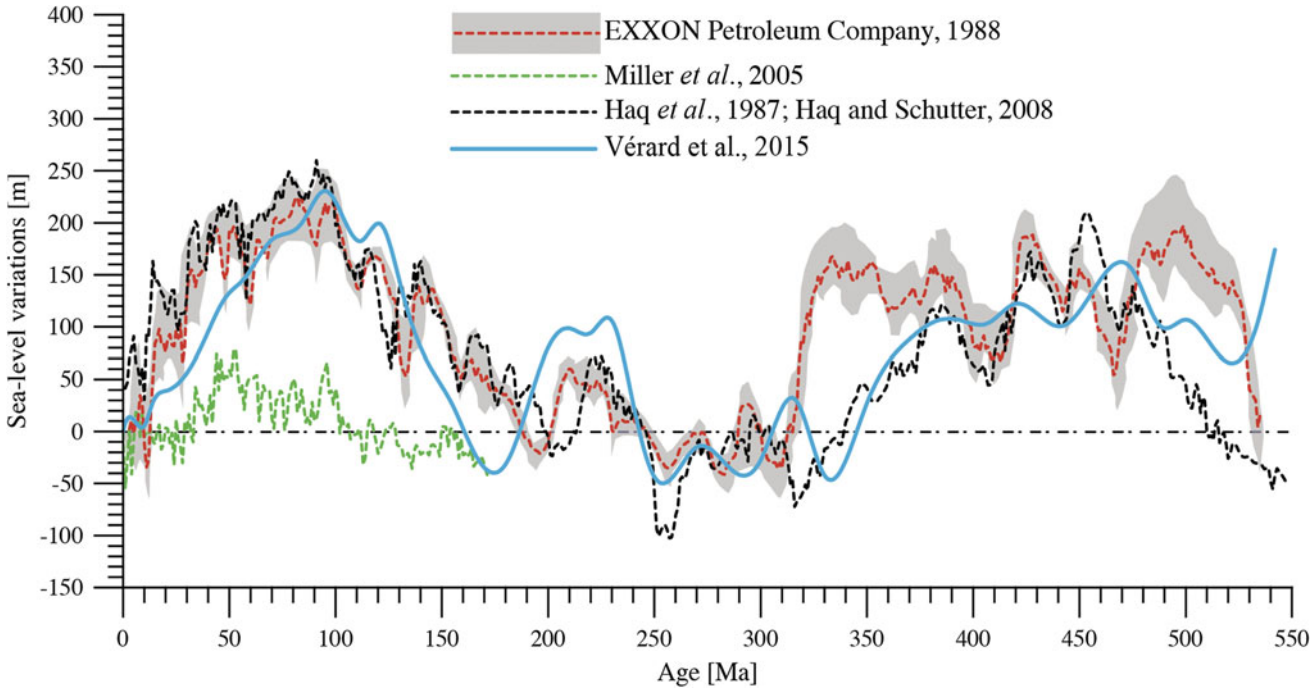

Fig. 2.4 Variations in sea level throughout the last 550 million-years, according to various reconstructions. Red curve is from the EXXON company, retrieved in Vérard et al. (2015); black curve is from Haq et al. (1987) and Haq and Schutter (2008); green curve is from Miller et al. (2005), blue curve is from Vérard et al. (2015). The figure is modified from Vérard et al. (2015)

capacity of ocean basins (the container). Changing the volume of water in the ocean involves a process of contraction or thermal expansion, capture or release of this water by another reservoir (e.g., ice caps), subducted down with hydrated minerals in the mantle or released through degassing at oceanic ridges. Although the volume of water present in the atmosphere in vapor and liquid form ($\sim$13,000 km^3) is fundamental to the functioning of the climate system, it is negligible compared to the volume of water contained in the ocean basins ($\sim$1347 million km^3). Variations in water volumes in ocean basins on a time scale of between 1 and 100 ka is due to the formation or melting of ice caps. The quantity of water held in the form of ice can lead to eustatic variations of more than 100 m. At the geological time scale, the presence of ice at the poles is an episodic phenomenon, because it implies the presence of a continent in a near-polar position and climate conditions allowing the formation of permanent snow cover. For example, glaciation covered the southern part of the Gondwana continent (which corresponds to the southern part of South America, the southern part of Africa, the southern part of the Arabian Peninsula, parts of India and Australia and the whole of Antarctica, these areas having been united at one time) for about 70 million years (335–265 Ma), marked by alternating phases of growth and melting of the ice cap. The Gondwana ice sheet at its climax may have sequestered a volume of water of approximately 200 m (compared with 70 m for the Antarctic cap of today). Finally, water storage in lakes, rivers ($\sim$0.26 million km^3) and in underground reservoirs ($\sim$9 million km^3) makes a very marginal contribution.

The most frequently cited mechanism to explain sea level changes over the scale of geological time is oceanic crustal production rates and extruded oceanic plateaus. In the 1980s, the oceanic production rate was estimated for the last 180 Ma. For the lower Cretaceous it was estimated to be twice as high as today, while a drop of about 50% over the last 50 million years was found. However these estimates have been called into question following new estimates of accretion rates and normalized fluxes which suggested variations in the fluxes with an amplitude of 30% or less around the present value (Cogné and Humler 2006). Such estimates could challenge the role of the ridges in sea level variations. The Wilson cycles, i.e. the construction followed by the fragmentation of a supercontinent, have been identified as a possible mechanism to explain the first-order eustatic variations. Indeed, fragmentation periods produce young oceanic crust. The volume occupied by the ridges at the expense of the old crust lost by subduction reduces the total volume of the oceans and raises their level, and conversely during the period of supercontinent construction, the total volume of the ridges decreases and the level of the oceans drops. In other words, the average age of the oceans reflects the first-order eustatic variations. It is thus a major challenge to develop plate motion models than can provide

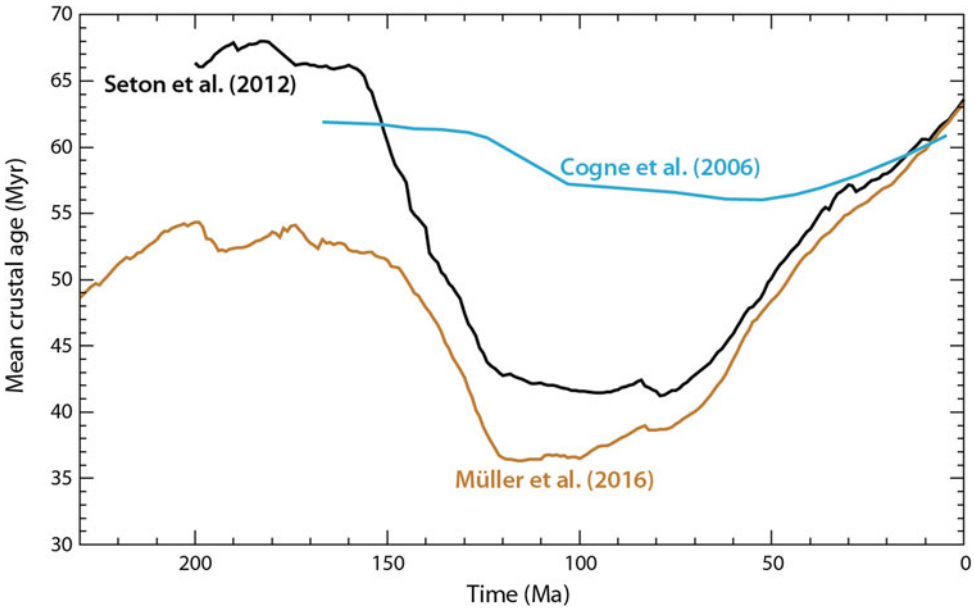

Fig. 2.5 Mean crustal age through time according to different models. Retrieved and modified from Müller et al. (2016)

estimates of the seafloor age evolution through time. Müller et al. (2016) have provided a synthesis of the different model results since the pioneering works of Cogné et al. (2006), that shows how including new assumptions can make the chronology of seafloor evolution change. Figure 2.5 depicts some of them.

An Overview of the Changing Face of Earth Through the Ages

To reconstruct the paleogeography of the past, the locations of the large plates as defined by Morgan in 1968 and a number of smaller continental masses need to be known. This is a difficult task for the periods prior to 1.1 Ga (1100 Ma) due to the smaller number of paleomagnetic data available. The position of the paleoshorelines depends on the available lithological information. Using available data, we sketch the portrait of the Earth since the Archean. The main features of paleogeographic evolution are shown in the atlas (Fig. 2.6).

Currently, the oldest observable geological units in a rocky outcrop are more than 3 billion year-old, but they are rare and do not allow to estimate the area of land present at that time. However, the dating of a large number of zircons, an ubiquitous mineral in many rocks (igneous, metamorphic and sedimentary), has allowed to retrace the main periods of continental crust production. Zircons older than 4 Ga discovered in Archean geological formations testify to the existence of a continental crust, even ephemeral, a few hundred million years after the formation of the Earth. Around 3.5 Ga, the first stable continental land masses appeared. Analysis of the oldest cratons reveals that these were formed by the amalgamation of modest-sized scraps of continental crust, island arcs, accretion prisms and oceanic volcanic plateaus. The first major peak of continental crust production dates back to 2.7 Ga, initiated by an avalanche in the mantle leading to the formation of a large number of mantle plumes. This 2.7 Ga event resulted in an increase in the number of cratons, that is to say, a permanent continental crust, and thus a sharp increase in the continental surface (Hawkesworth et al. 2017). However, the existence of a supercontinent at this period remains unlikely (Bleeker 2003).

Reconstructing the paleogeography of the Archean is very uncertain because paleomagnetic data are not sufficient to constrain the position of all cratons in space and time. However their geological histories can provide additional information. The outlined scenarios are based on the similarity between the geological series preserved on each craton (similarity in the lithological sequences, synchronism of metamorphic and magma events affecting the cratons, continuity of magmatic intrusions). However, this combination does not always produce a unique scenario. For the period between 2.7 and 1.8 Ga, Bleeker (2003) counts no fewer than 35 pieces of this paleogeographical puzzle. Internal heating twice as strong at this time is conducive to an organization of the plates more fragmented than today, and makes a vast and unique supercontinent unlikely. However, it is not impossible that groupings of small cratons occurred during the Late Archean. Indeed, the presence of numerous dykes dated between 2.4 and 2.1 Ga could testify for the dislocation of these ephemeral land masses.

The following period was marked by the formation of the first supercontinent, Columbia (also referred to as “Nuna”), through the assembly of small cratons causing numerous

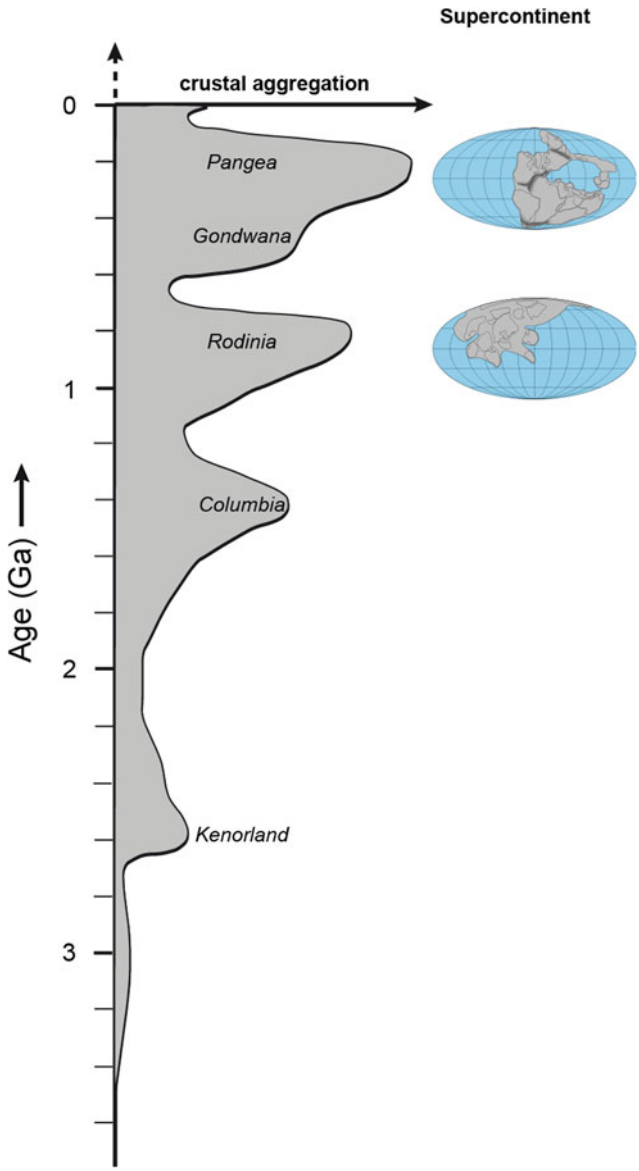

Fig. 2.6 Crustal aggregation states (supercratons and supercontinents) through time [adapted from Bleeker (2003)]. Position of the major continents and land masses in the past [according to Li et al. (2008) for the Neoproterozoic, McElhinny et al. (2003) for the Paleozoic, Atlas Tethys and Peritethys, as well as reconstructions by the author for various studies on the Mesozoic, Fluteau et al. (2001, 2006)]. AFR = Africa; NAM = North America; SAM = South America; AMZ = Amazonia; ANT = Antarctic; ARA = Arabia; AUS = Australia; BAL = Baltic; NCH = Northern China; SCH = Southern China; EAN = Eastern Antarctic; IND = Indochina; INDIA = India; IRA = Iran; KAL = Kalahari; KAZ = Kazakhstan; LHA = Lhasa; LAU = Laurussia; MAD = Madagascar; NUB = Nubia; QAN = Qantiang; RDP = Rio de Plata; SFCG = Sao Francisco-Congo; SIB = Siberia, WAF = West Africa, WAN = West Antarctica. The thick lines represent the assumed location of the ridges (divergent lithospheric plates); the thick black lines with triangles represent the assumed location of the subduction zones (convergent lithospheric plates). The shaded areas indicate the active orogenic zones for the period being studied. The names of the main orogenies are indicated in italics. For the Cretaceous, the main shelf seas are represented in white (in a simplified way)

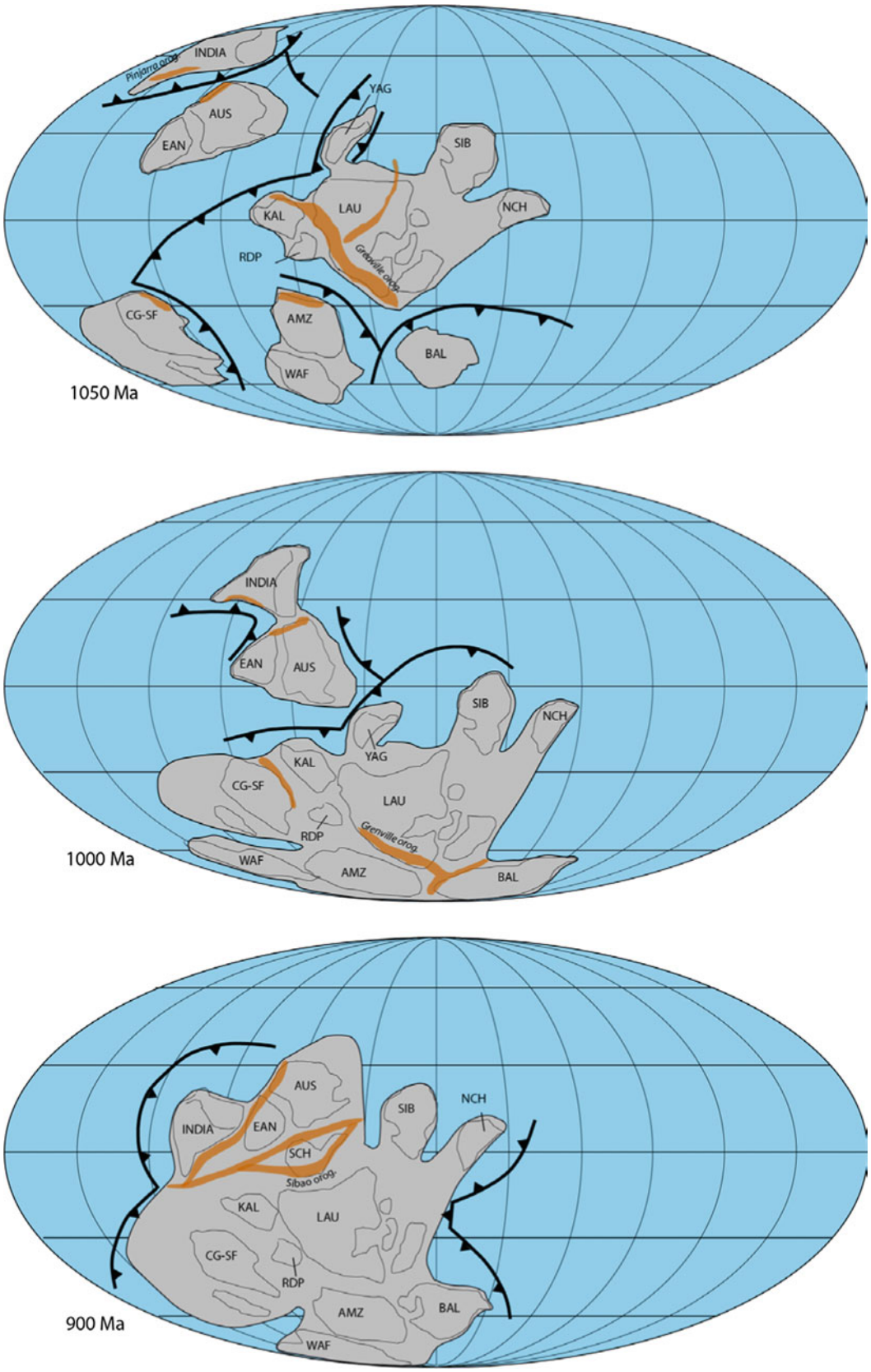

Fig. 2.6 (continued)

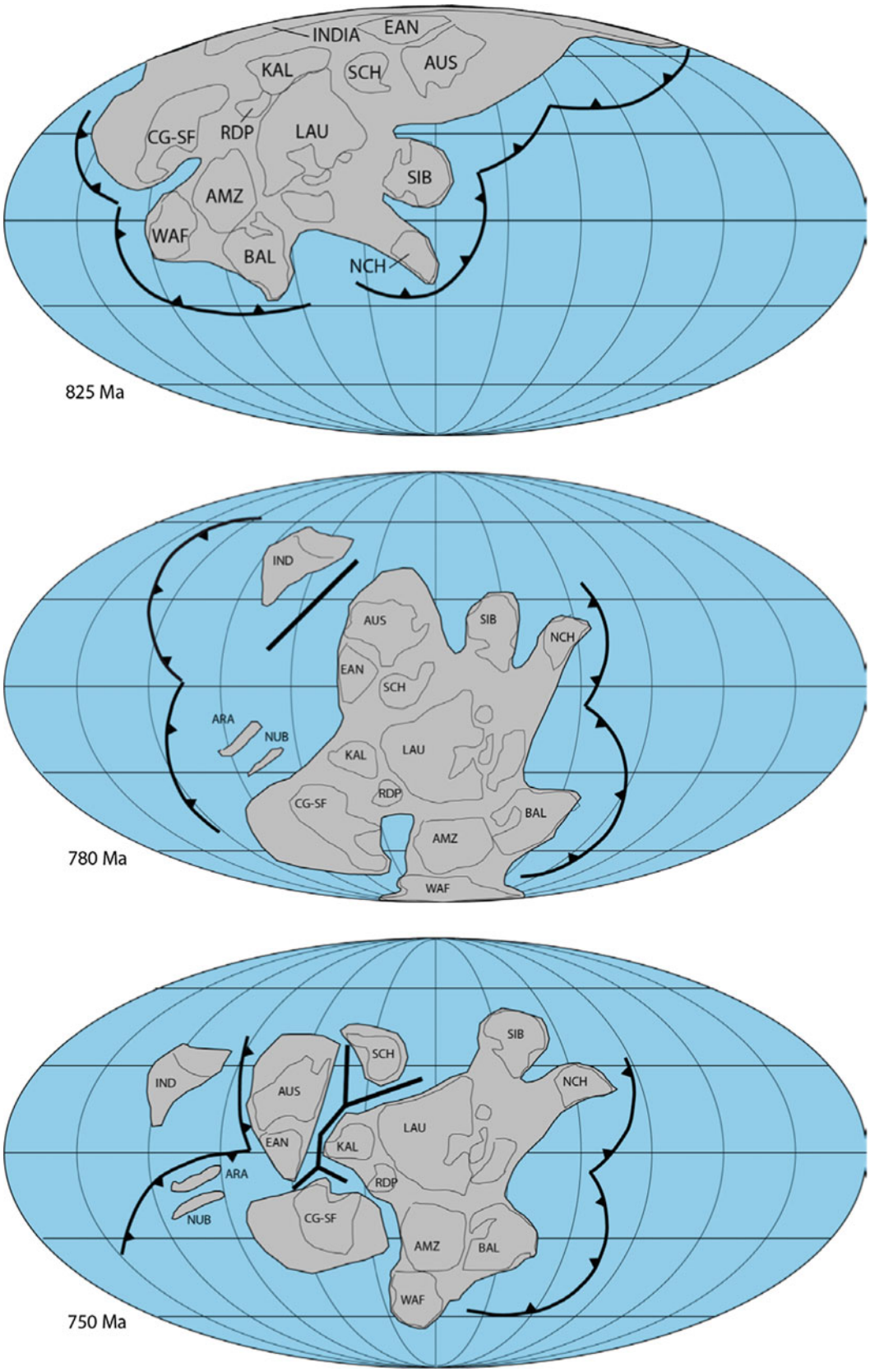

Fig. 2.6 (continued)

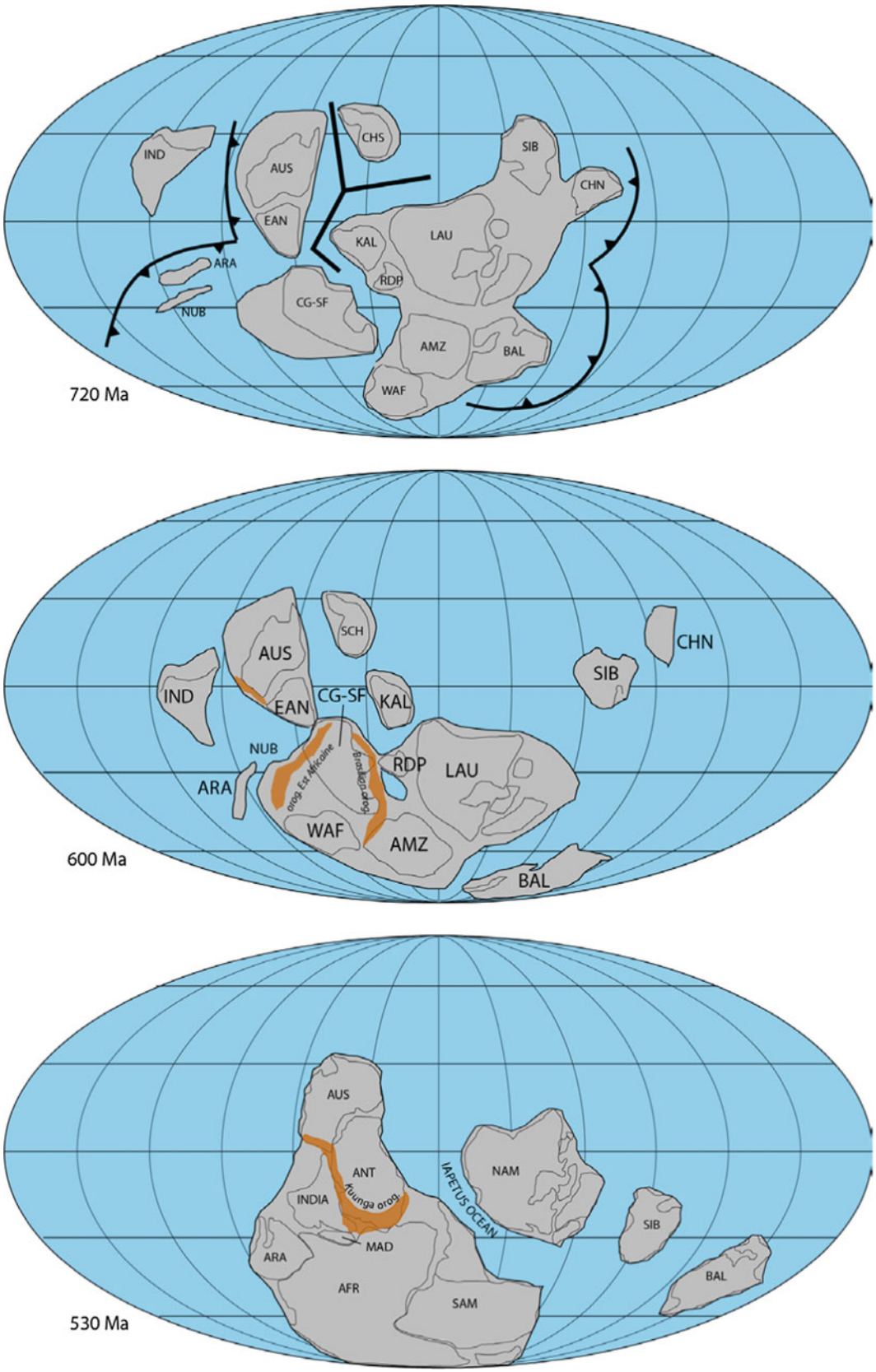

Fig. 2.6 (continued)

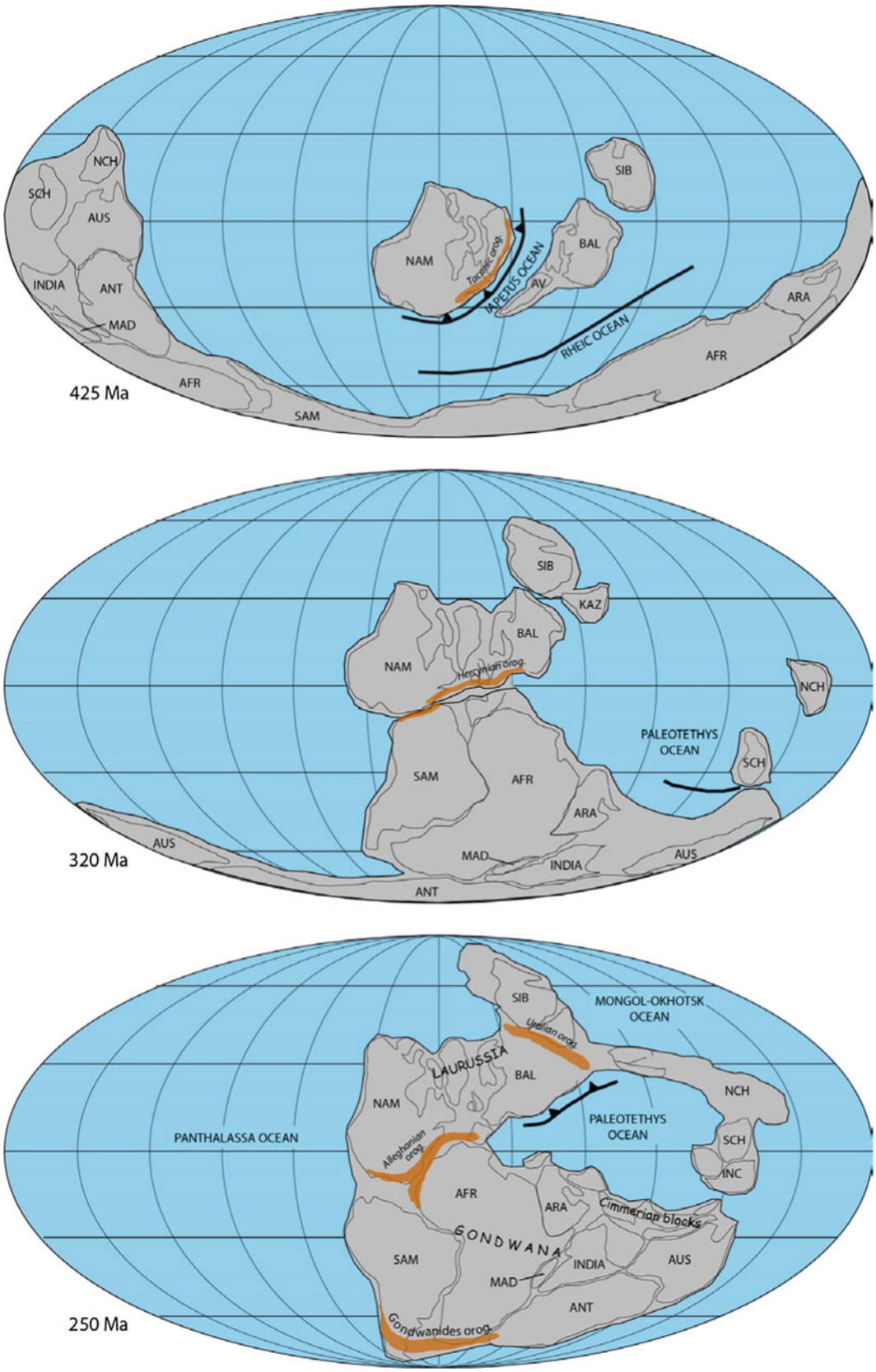

Fig. 2.6 (continued)

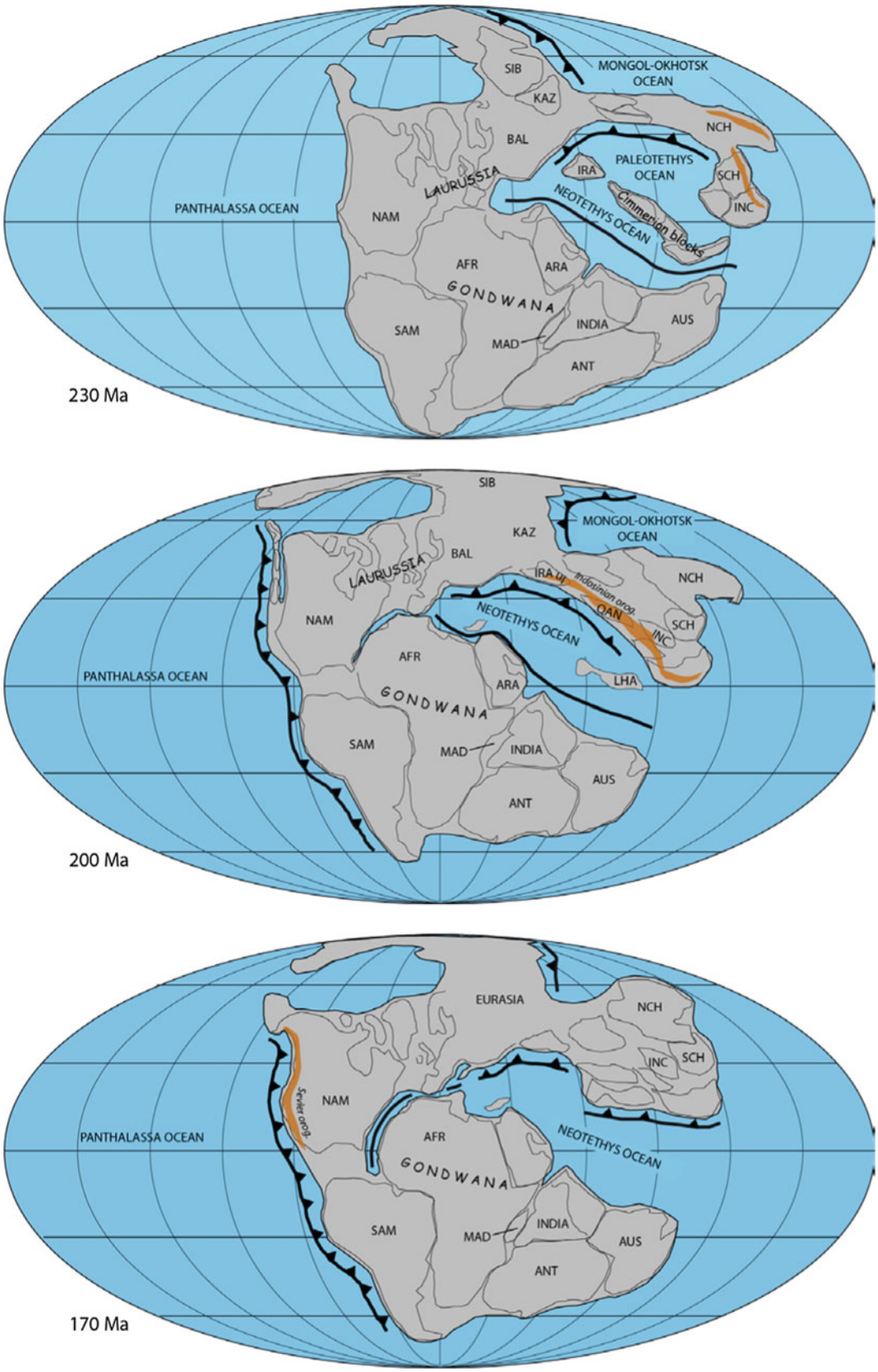

Fig. 2.6 (continued)

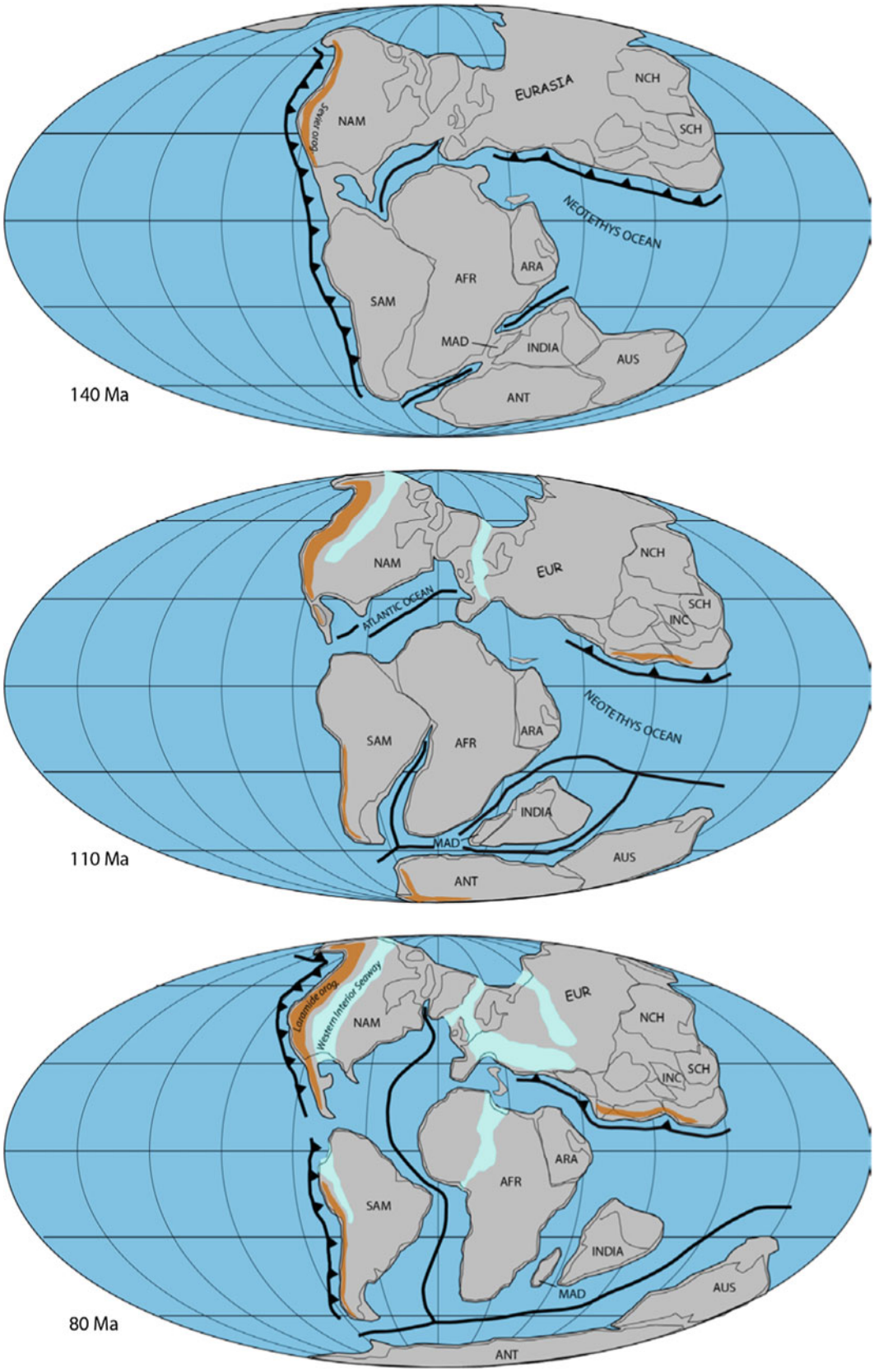

Fig. 2.6 (continued)

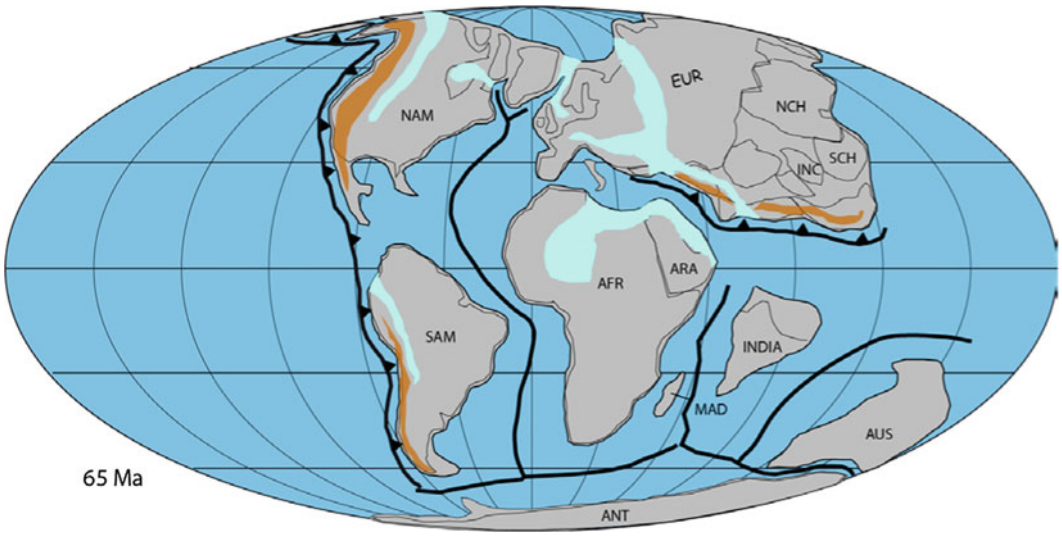

Fig. 2.6 (continued)

orogenies (Rogers and Santosh 2002; Zhao et al. 2002) and the structuring of several large cratons (Laurentia, Baltica, Greenland, Siberia, Western Australia, India, Amazonia-West Africa, Congo-Sao Francisco) (Meert and Santosh 2017). The Laurentia craton is the result of the assembly of several terranes (Superior, Rae, Slave, Hearne, Nain) between 1.95 and 1.8 Ga, and incorporated Wyoming province by 1.7 Ga. The collisions of Volgo-Uralia with Sarmatia by 2 Ga and with Fennoscandia by 1.7 Ga lead to the formation of Baltica. Between 1.8 and 1.3 Ga, the Columbia supercontinent experienced a period of continuous accretion along the active margins (subduction zones). These magmatic accretionary belts significantly increased the emerged land surface. A reconstruction of the Columbia supercontinent is made possible through paleomagnetic data of some cratons at 1.5–1.4 Ga interval (Meert and Santosh 2017). The development of continental rifts towards 1.5 Ga marked the beginning of the fragmentation of the supercontinent Columbia which lasted about 300 million years. However, very quickly, a new assemblage commenced. The southern coast of Laurentia (which corresponds to the current east coast of the North American continent) collided with the Amazon mass (a constituent block of South America), and shortly after, the north Laurentian coast collided with Australia, East Antarctica and the South China. The unification of all existing cratons at that time ended around 950 Ma and the new supercontinent Rodinia was formed. These various collisions between continents brought about the existence of several large mountain ranges, whose geological signature is found in metamorphic belts. This is the case in North America, where the Grenville orogeny was dated to 1 Ga, and in South China with the Sibao orogeny. However, there is still no consensus on the history of the Rodinia supercontinent. The number of continents that constituted Rodinia, the age of its formation or of its dislocation, and even its very existence for some, remain open questions. The reason for the lack of consensus is that the number and quality of the geological, geochronological and paleomagnetic data does not lead to one single solution. For a much more in-depth analysis of the paleomagnetic data and the consequences in terms of configurations, the reader is referred to the work of Li et al. (2008).

After having drifted north, the supercontinent Rodinia broke apart around 780–750 Ma. The dispersion of the continents resulted in the opening up of ocean basins oriented approximately north-south. Due to the spherical symmetry of the geocentric dipole magnetic field, the width of these ocean basins is poorly constrained. At the end of the Neoproterozoic, around 600 Ma, a new supercontinent, Pannotia, could have formed. Made up of Laurentia and Gondwana domains, the existence of this short-lived supercontinent could only be linked to the uncertainties that impaired the age of break-up of Laurentia, Amazonia and Baltica and the timing of Gondwana assembly (Li et al. 2008; Oriolo et al. 2017). This is why the possibility of the Pannotia supercontinent has not been retained in the reconstructions presented in this book.

The period from the late Precambrian to the early Paleozoic is marked by the gradual amalgamation of Gondwana from a mosaic of continents separated by oceans. These oceans constricted and closed, continents collided, causing orogenesis. These mountains have long disappeared, but the present-day continents still bear relicts of them, such as metamorphic belts of high pressure, magmatism and/or deformations. These events, that have been dated by isotopic methods, have been extensively discussed in Cawood and Buchan (2007).

The Nubie craton (NUB) and several small blocs were amalgamated between 750 and 600 Ma. This event was the first phase of the East African orogeny dated to between 750 and 600 Ma. A little further east, the convergence of the Congo-Sao Francisco (CG-SF) and Amazon (AMZ) cratons led to the closure of the Adamastor ocean, and their collision around 650 Ma caused the Brazilian orogeny. This assembly of cratons formed part of the future Gondwana continent. At the end of Precambrian, around 550 Ma, Laurentia and Amazonia separated, marking the opening of the Iapetus ocean, while the cratons of Australia, Antarctica, West Antarctica and India assembled to form another part of the future Gondwana continent. This event is reflected in the Kuunga and Pinjarra orogens. The closure of the ocean separating the Kalahari and Congo-Sao Francisco cratons leads to their collision shortly after 520 Ma, instigating the Damara/Zambezi orogeny. This event occurred approximately synchronously with the final amalgamation of the Gondwana continent around 530 Ma. This final stage in the construction of the Gondwana continent brought about a new orogenic phase in Eastern and Southern Africa (which was superimposed on the older one dated at 600 Ma). In the final step in the construction of Gondwana, the passive margin that bordered the western part of this continent became an active margin (the oceanic crust was subducted under the Gondwana continent) over nearly 18,000 km, as evidenced by the ages of magma activity between 550 and 500 Ma. This active margin is linked with the Ross-Delamerian orogeny in Australia and Antarctica, the Saldanian orogeny in Southern Africa and Pampean orogeny in South America. The final assembly of Gondwana and the establishment of an active margin mark the end of the orogens along the sutures of the Gondwana mosaic. It is clear that the height of the reliefs remains very hypothetical, but the intensity of the collisions and geological evidence suggest that the reliefs were high.

The Gondwana continent would continue to exist for nearly 400 million years until it ended during the Cretaceous. At the beginning of the Ordovician (∼480 Ma), the Avallon plate, originally located close to the South Pole (its remnants can be found in northeastern North America and Western Europe), separated from Gondwana, causing the birth of a new ocean, the Rheic Ocean (Nance et al. 2012). The Avallon plate migrated towards the north and collided with Baltica at the end of the Ordovician around 440 Ma. At the end of the Silurian (∼420 Ma), the collision between Laurentia and Avalonia + Baltica completed the disappearance by subduction of the Iapetus Ocean and leads to the Taconic orogeny in Laurentia. A new continent, Laurussia, was formed. This collision brought about the Caledonian/Acadian orogeny, which affected Scandinavia, Greenland, Western Europe and the northeast part of North America. The Rheic Ocean was gradually subducted underneath Laurussia, inexorably bringing Laurussia and Gondwana closer together. The closure of this ocean continued until the Devonian (∼360 Ma), after which period a generalized collision occurred along the suture between Gondwana and Laurussia (Matte 1986). On the Laurussia side, this resulted in the Alleghanian orogeny in North America and the Hercynian (or Variscan) orogeny in Europe. The Alleghanian orogeny affected the eastern margin of the North American continent (Canada and the United States) and extended south through the state of Texas in the United States to Mexico with the Ouachita orogeny. The Hercynian orogeny can also be observed on the Gondwana side through the Mauritanide orogeny in West Africa (Villeneuve 2008). The dating of deformation and metamorphism associated with this collision ranges from 340 to 270 Ma. The Hercynian orogeny affected much of western and central Europe. This event is dated to between 340 and 290 Ma. At the end of the Carboniferous, these reliefs could have been as high as those of the Himalayas at the present time (Matte 1986). The amalgamation of Gondwana with Laurussia would go on to form the Pangea supercontinent, which would exist until 170 Ma. This supercontinent reached its maximum size with the accretion of the Siberian-Kazakhstan plate in response to the closure of the Uralian ocean at the northeastern margin of Pangea during the Permian, giving rise to the uplift of the Urals. The active margin on the south of Gondwana experienced a new orogenic cycle that occurred between the late Carboniferous (∼310 Ma) and the Upper Triassic (∼220 Ma). The Gondwanide orogeny affected Australia, southern Africa and southern regions of South America, already deformed by the Ross-Delamerian, Saldanian and Pampean orogenies during the Cambrian.

The Lower Permian marked the beginning of the separation of an assemblage of plates, called the Cimmerian plate, from the northeastern margin of Gondwana, leading to the opening of a new ocean, Neotethys (also known as Meso Tethys) (Metcalfe 2002). The Cimmerian plate (southern China, Indochina, Lhasa, Qiangtang and others) drifted northward, closing the Paleo Tethys Ocean by subduction under the northeastern margin of Pangea (the eastern part of Laurussia and Kazakhstan) and under Tarim and North China, while to the south the Neotethys Ocean continued to open. This string of plates could have, for a while, isolated the Paleo Tethys Ocean from the Panthalassa Ocean.

The configuration of the Pangea is full of uncertainties (this debate is not shown in the maps of Fig. 2.6). The Pangea reconstruction is well constrained by geological and geophysical data for the Late Triassic-Early Jurassic at the beginning of continental breakup. This is not the case for the pre-Late Triassic. Bullard et al. (1965) used to rotate the two APWPs in a common frame permit to restore the paleopositions of two landmasses during these periods. Doing that, it

results in a large continental overlap between Gondwana and Laurussia in excess of 1000 km. To solve this discrepancy, a large disconnecting dextral fault operated during the Permian and Triassic periods was proposed (Irving 1977), resulting in a relative movement of Laurussia to the north and of Gondwana to the south. Based on paleomagnetic data, the total dislocation length of this detachment could have been several thousand kilometers, but could be much less if observations in the field of the cumulated dislocations of the known disconnecting faults in operation at that time are considered. Moreover, the non-dipolarity of the magnetic field (strong influence from an octupolar field) during this period but more likely the lack of fidelity in the magnetic field recorded in the red sandstones caused by inclination shoaling may be "distorting" the paleomagnetic data (Domeier et al. 2012).

At the beginning of the Jurassic, around 200 Ma, the Pangea supercontinent broke into two vast continents, Laurasia (Laurussia + Siberia + other smaller plates) to the north and Gondwana to the south. This separation marked the beginning of the opening of the central Atlantic Ocean. The opening directed the drift of North America northwestwards. This initiated the subduction of the Farallon and Kula plates (northeast region of the Pacific Ocean) under the western margin of North America, resulting in the accretion of small heterogeneous blocks and island arcs to the North-American continent during the Jurassic. As this margin deformed, this was the Sevier orogeny which lasted until the Lower Cretaceous.

Further east, the Paleo-Tethys Ocean became totally subducted around 200 Ma and the Cimmerian plates collided with the North China and Tarim plates. This continental mosaic was separated from the southern margin of Siberia by the Mongol-Okhotsk Ocean. Triangular in shape, this ocean closed like a scissors during the Jurassic and at the end of this period (~150 Ma), the small continent formed by the mosaic of small plates collided with the southern margin of Siberia. The Eurasian continent was formed. The multiple collisions between the small plates more than likely caused deformation, but probably did not create any significant reliefs. The opening of the central Atlantic Ocean continued. The Panthalassa, Neotethys and Central Atlantic oceans all become connected in the subtropical zone of the northern hemisphere.

The Middle Jurassic (~170 Ma) marked the beginning of the break-up of Gondwana. Madagascar, India, Australia and Antarctica separated from the Africa-South America duo. During the Lower Cretaceous (~130 Ma), South America and Africa started to split and the South Atlantic Ocean opened between Patagonia and Southern Africa. This event could mark the beginning of the deformation of the western central Andes margin in South America (Torsvik et al. 2009). The complete separation of the two continents and the connection with the central Atlantic Ocean only occurred at the end of the Lower Cretaceous period, about 30 million years later. At the beginning of the Lower Cretaceous (~110 Ma), India began its drift northwards. The Neo-Tethys Ocean was subducted under the southern margin of Eurasia, while in the south of India, the Indian ocean opened (McKenzie and Sclater 1971). Jagoutz et al. (2015) concluded that the exceptional rate of convergence exceeding 140 mm yr^{-1} is due to the existence of a double northward dipping subduction zones between the Indian and Eurasian plates during the Cretaceous. Around 90 Ma, Madagascar and India separated, the Carlsberg ridge is formed and marked the beginning of the opening of the northwestern part of the Indian Ocean.

The Cretaceous is characterized by a high sea level which led to the formation of vast shelf seas starting at the Albian (~100 Ma) to the Maastrichtian (~65 Ma). The flooding of the continents reached its maximum at the beginning of the Upper Cretaceous, around 95 Ma, when a large part of Europe was inundated. At the height of the marine incursion, a shallow sea developed over North Africa across the current Sahara Desert, temporarily linking the Neo-Tethyan Ocean to the South Atlantic Ocean. In North America, during the Upper Cretaceous, a sea passage, the Western Interior Seaway, was established between the Arctic Ocean and the Gulf of Mexico, while a new orogenic phase affected the margin of this continent (Laramide orogeny). A sea passage formed in western Siberia linking the Arctic Ocean and the Neo-Tethyan Ocean, and only disappeared during the Eocene.

The beginning of the Cenozoic is marked in the northern hemisphere by the opening of the third and last part of the Atlantic Ocean, the northern part. North America and Eurasia separated. However the Arctic Ocean remains almost isolated from the rest of the oceans during the Early Cenozoic favouring the deposits of black shales due to poorly oxygenated water (Jakobsson et al. 2007) until the deepening of the Fram Strait during the Late Eocene, ~36 Myr (Poirier and Hillaire-Marcel 2011). In the southern hemisphere, Australia and Antarctica are definitively separated during the Eocene. The Antarctic migrated to its polar position. The circum-Antarctic basin was formed. In the western part of North America, subduction geometry evolved, deformation progressed eastward, the Rocky Mountains lifted up, while some more coastal reliefs were lowered due to a change in the pattern of constraints in this region. In South America, the uplift of the Andean Cordillera appears to have accelerated towards the end of the Cenozoic. India collided with Asia at the beginning of the Cenozoic (~50 Ma). India's drift to the north continued after the collision at a rate of 5–6 cm/year. Part of the crustal thickening is accommodated by the play of large right-lateral deformations reactivating old sutures between the plaques

constituting the Asian mosaic, and by the uplift of the Himalayas and other chains farther north. These great disconnecting systems laterally eject plaques such as South China and Indochina (Tapponnier et al. 2001). This deformation of the southern margin of Asia is in fact generalized throughout the southern margin of Eurasia, in response to the Africa-Europe overlap resulting in the Alpine orogeny. This deformation contributed to the establishment of sea basins, sometimes deep, in Eurasia. These basins were connected to each other and extended from Western Europe to the foot of the Tibetan zone (during the process of uplifting) to form a vast epicontinental sea, the Paratethys, connected to the Atlantic Ocean and to the Tethys. The intense deformation of the southern margin of Eurasia during the Miocene gradually isolated the Paratethys from the rest of the oceans. Supplied only by runoff waters and subjected to the deformation of the substratum, this sea was gradually reabsorbed. Today, the Caspian Sea and the Black Sea are the only descendants of the Paratethys.

The Arabia-Eurasia collision during the Early Miocene lead to the closure of the Neo-Tethys sea and the uplift of the Zagros collisional wedge (Pirouz et al. 2017). In the Middle Miocene, the northern part of the Arabian Peninsula became exposed, marking the birth of the Mediterranean Sea. This would dry up almost completely at the end of the Miocene (the Messinian crisis) for a few hundred thousand years, due to an upheaval in the Betic zone (Gibraltar region) combined with a slight decrease in sea level. During the late Miocene, the northward drift of Australia initiated the closure of the Indonesian seaway, while the closure of the Central American Seaway linked to a tectonic uprising permanently isolated the Atlantic and Pacific waters.

Box: Focus on the uplift of the Tibetan Plateau.

Since 50 Ma, the average convergence speed between India and Asia has remained around 5 cm per year. The Himalayan range occurred due to the deformation of the northern edge of the Indian sub-continent when it was subducted under the Asian continent. To the south of the Tsangpo suture is the Himalayan domain: on Indian crust with remnants of the Tethyan sedimentary cover and accretion prism associated with subduction of the Tethyan Ocean before collision. North of the suture, the Tibetan plateau has sedimentary layers from the Asian paleomargin. These are two very different realms with different Cenozoic geological histories, although related to the same event. During the millions of years after the collision, a proto-Himalayan chain must have developed on the remains of the Andean chain associated with the subduction of the Tethys, but the extent of this is not known. The Tibetan plateau was still a low-lying area.

Two contrasting opinions have been proposed to explain the uplift of the Tibetan plateau: a "soft Tibet" model and a "staggered model". The "soft Tibet" model considers the uplift to be the result of an isostatic rebound caused by the "sinking" of the crustal root of a thickened Tibetan proto-plateau. The plateau reached its stable altitude of about 5000 m, and began to creep, as evidenced by the normal faults that line the southern plateau. The other theory (Tapponnier et al. 2001) considers, on the contrary, that the uplift took place in successive stages. Part of the India-Asia collision is absorbed by the lateral extrusion of landmasses (South China, Indochina), which caused old sutures inherited from the accretion of small landmasses during the Paleozoic and Mesozoic to protrude, profoundly modifying the paleogeography of South-East Asia (resulting in the closure of the Indonesian passage). These large strike-slip faults, separating the landmasses, connect with small perpendicular faults parallel to each other. The associated reliefs isolate small endorheic sedimentary basins which gradually fill up with the output from the dismantling of the chain "like a bathtub". The uplift of the Tibetan plateau would have occurred in successive stages since 50 Ma. The southern part of the Tibetan plateau rose during the Eocene, the central part during the Oligocene-Miocene and the northeastern part is currently uplifting.

Conclusion

The Earth moved from being entirely composed of an oceanic crust to the emergence of the first shreds of continental crust during the Archean, then to its episodic growth, mainly during the Precambrian. The paleogeography of this period is uncertain, given the small number of paleomagnetic data available, but it seems that the first consolidation of landmasses into a supercontinent (followed by a break-up phase) dates back to that time. It is only from the end of the Precambrian that we have global paleogeographic reconstructions, but there are no unique and definitive solutions for much of the Paleozoic, as uncertainties remain on the arrangement of some continents and the dimensions of the oceans. Paleogeographic reconstructions become more reliable at the end of the Paleozoic, and data from ocean kinematics makes it possible to constrain the relative positions of some continents relative to others. The distribution of the continents, either as they grouped together or dispersed, represents an important climate forcing through direct and

undirect effects, while a second trigger of long-term climate change is mountain uplift. In that respect, the last 60 million-years have been crucial, since most of present-day mountain ranges have uplifted during this time interval. The Himalayan orogeny and the uplift of the Tibetan plateau are certainly the two most studied geological events over the past three decades in terms of impact on climate, but other mountain ranges such as the Andes, the Rockies and the east African dome very likely have played important roles on the Cenozoic climate change. Some clues on this point are provided in Volume 2, Chap. 22. Still, the paleoelevations of the reliefs remain shrouded in uncertainty, and efforts both on the modeling and the paleoelevation indicator sides will need to be pursued to improve our understanding of paleogeography evolution of Earth through time, and ultimately better quantify its impact on long-term climate changes.

References

Besse, J., & Courtillot, V. (1991). Revised and synthetic apparent polar wander path of the African, Eurasian, North American and India plates, and true polar wander since 200 Ma. *Journal of Geophysical Research: Solid Earth*, *95*, 4029– 4050.

Besse, J., & Courtillot, V. (2002). Apparent and true polar wander and the geometry of the geomagnetic field over the last 200 Myr. *Journal of Geophysical Research: Solid Earth, 107*, EPM 6-1–EPM 6-31.

Bleeker, W. (2003). The Late Archean record: A puzzle in ca. 35 pieces. *Lithos, 71,* 99–134.

Bonifacie, M., Calmels, D., Eiler, J. M., Horita, J., Chaduteau, C., Vasconcelos, C., et al. (2017). Calibration of the dolomite clumped isotope thermometer from 25 to 350 °C, and implications for a universal calibration for all (Ca, Mg, Fe) CO_3 carbonates. *Geochimica et Cosmochimica Acta, 200*(1), 255–279.

Botsyun, S., Sepulchre, P., Donnadieu, Y., Risi, C., Licht, A., & Caves Rugenstein, J. K. (2019). Revised paleoaltimetry data show low Tibetan Plateau elevation during the Eocene. *Science, 363*. http://doi.org/10.1126/science.aaq1436.

Botsyun, S., Sepulchre, P., Risi, C., & Donnadieu, Y. (2016). Impacts of Tibetan Plateau uplift on atmospheric dynamics and associated precipitation $\delta^{18}O$. *Climate of the Past, 12,* 1401–1420.

Bullard, E. C., Everett, J. E., & Smith, A. G. (1965). The fit of the continents around the Atlantic. *Philosophical Transactions of the Royal Society London, 258A*, 41–51.

Cawood, P. A., & Buchan, C. (2007). Linking accretionary orogenesis with supercontinent assembly. *Earth-Science Reviews, 3–4,* 217–256.

Chamberlain, C. P., Poage, M. A., Craw, D., & Reynolds, R. C. (1999). Topographic development of the Southern Alps recorded by isotopic composition of authigenic clay minerals, South Island, New Zealand. *Chemical Geology, 155*, 279–94.

Cogné, J.-P., Besse, J., Chen, Y., & Hankard, F. (2013). A new Late Cretaceous to present APWP for Asia and its implications for paleomagnetic shallow inclinations in Central Asia and Cenozoic Eurasian plate deformation. *Geophysical Journal International, 192,* 1000–1024.

Cogné, J. P., & Humler, E. (2006). Trends and rhythms in global seafloor generation rate. *Geochemistry, Geophysics, Geosystems, 7,* Q03011. https://doi.org/10.1029/2005GC001148.

Cogné, J. P., Humler, E., & Courtillot, V. (2006). Mean age of oceanic crust drives eustatic sealevel change since Pangea breakup. *Earth and Planetary Science Letters, 245*, 115–122.

Cox, A., Doell, R. R., & Dalrymple, G. B. (1964). Reversals of the earth's magnetic field. *Science, 144,* 1537–1543.

Creer, K. M., Irving, E., & Runcorn, S. K. (1954). The direction of the geomagnetic field in remote epochs in Great Britain. *Journal of Geomagnetism and Geoelectricity, 6,* 163–168.

Domeier, M., van der Voo, R., & Torsvik. T. H. (2012). Paleomagnetism and Pangea: The road to reconciliation. *Tectonophysics, 514–517*, 14–43.

Eiler, J. M. (2007). "Clumped-isotope" geochemistry—The study of naturally-occurring, multiply-substituted isotopologues. *Earth and Planetary Science Letters, 262,* 309–327.

Ferreira, D., Cessi, P., Coxall, H. K., de Boer, A., Dijkstra, H. A., Drijfhout, S. S., et al. (2018). Atlantic-Pacific asymmetry in deep water formation. *Annual Review of Earth and Planetary Sciences, 46,* 327–352.

Fluteau, F., Besse, J., Broutin, J., & Ramstein, G. (2001). The Late Permian climate. What can be inferred from climate modelling concerning Pangea scenarios and Hercynian range altitude? *Palaeogeography, Palaeoclimatology, Palaeoecology, 167*, 39–71.

Fluteau, F., Ramstein, G., Besse, J., Guiraud, R., & Masse, J. P. (2006). The impacts of the paleogeography and sea level changes on the mid cretaceous climate. *Palaeogeography, Palaeoclimatology, Palaeoecology, 247*, 357–381.

Forest, C. E., Molnar, P., & Emanuel, K. A. (1995). Palaeoaltimetry from energy conservation principles. *Nature, 374,* 347–350.

Garzione, C. N., Auerbach, D. J., Jin-Sook Smith, J., Rosario, J. J., Passey, B. H., Jordan, T. E., et al. (2014). Clumped isotope evidence for diachronous surface cooling of the Altiplano and pulsed surface uplift of the Central Andes. *Earth and Planetary Science Letters, 393,* 173–181.

Greff-Lefftz, M., & Besse, J. (2014). Sensitivity experiments on true polar wander. *Geochemistry, Geophysics, Geosystems, 15,* 4599–4616.

Haq, B. U., Hardenbol, J. A. N., & Vail, P. R. (1987). Chronology of fluctuating sea levels since the Triassic (250 million years ago to present). *Science, 235*, 1156–1166.

Haq, B. U., & Schutter, S. R. (2008). A chronology of paleozoic sea-level changes. *Science, 322*(5898), 64–68. https://doi.org/10.1126/science.1161648.

Hawkesworth, C. J., Cawood, P. A., Dhuime, B., & Kemp, T. I. S. (2017). Earth's continental lithosphere through time. *Annual Review of Earth and Planetary Sciences, 45,* 169–198.

Heezen, B. C. (1962). The deep-sea floor. In S. I. Runcorn (Ed.), *Continental drift* (pp. 235–288). New York: Academic Press.

Heezen, B. C., & Tharp, M. (1965). Tectonic fabric of the Atlantic and Indian Oceans and continental drift. In P. M. S. Blackett, E. Bullard, & S. K. Runcorn (Eds.), *A Symposium on Continental Drift*, *Philosophical Transactions of the Royal Society A*, 1033, 90. https://doi.org/10.1098/rsta.1965.0024.

Heirtzler, J. R., Dickson, G. O., Herron, E. M., Pitman, W. C., & Pichon, X. L. (1968). Marine magnetic anomalies, geomagnetic field reversals, and motions of the ocean floor and continents. *Journal Geophysical Research, 73,* 2119–2136.

Hess, H. H. (1962). History of ocean basins. In A. E. J. Engle, H. L. James, & B. L. Leonard (Eds.), *Petrologic studies: A volume in honor of A. F. Buddington* (pp. 599–620). New York: Geological Society of America.

Holmes, A. (1929). A review of the continental drift hypothesis. *Mining Magazine* 1–15.

Husson, L. (2006). Dynamic topography above retreating subduction zones. *Geology, 34*(9), 741–744.
Irving, E. (1964). *Paleomagnetism and its application to geological and geophysical problems*. Hoboken: Wiley.
Irving, E. (1977). Drift of the major continental blocks since the Devonian. *Nature, 270*, 304–309.
Jagoutz, O., Royden, L., Holt, A. F., & Becker, T. W. (2015). Anomalously fast convergence of India and Eurasia caused by double subduction. *Nature Geoscience, 8*, 475–479.
Jakobsson, M., Backman, J., Rudels, B., Nycander, J., Frank, M., Mayer, L., et al. (2007). The early Miocene onset of a ventilated circulation regime in the Arctic Ocean. *Nature, 447*, 986–990.
Kim, S. T., & O'Neil, J. R. (1997). Equilibrium and nonequilibrium oxygen isotope effects in synthetic carbonates. *Geochimica et Cosmochimica Acta, 61*, 3461–3475.
Kirschvink, J. L., Ripperdan, R. L., & Evans, D. A. (1997). Evidence for a large-scale reorganization of early cambrian continental masses by inertial interchange true polar wander. *Science, 277* (5325), 541–545.
Le Pichon, X. (1968). Sea-floor spreading and continental drift. *Journal Geophysical Research, 73,* 3661–3697.
Li, L., & Garzione, C. (2017). Spatial distribution and controlling factors of stable isotopes in meteoric waters on the Tibetan Plateau: Implications for paleoelevation reconstructions. *Earth and Planetary Science Letters, 460,* 302–314.
Li, Z. X., Bogdanova, S. V., Collins, A. S., Davidson, A., De Waele, B., Ernst, R. E., et al. (2008). Assembly, configuration, and break-up history of Rodinia: A synthesis. *Precambrian Research, 160*, 179–210.
Matte, P. (1986). Tectonics and plate tectonics model for the Variscan Belt of Europe. *Tectonophysics, 126,* 329–374.
McElhinny, M. W., Powell, C. M., & Pisarevsky, S. A. (2003). Paleozoic Terranes of Eastern Australia and the drift history of Gondwana. *Tectonophysics, 362*, 41–65.
McKenzie, D., & Sclater, J. G. (1971). The evolution of the Indian Ocean since the Late Cretaceous. *Geophysical Journal International, 24,* 437–528.
Meert, J. G., & Santosh, M. (2017). The Columbia supercontinent revisited. *Gondwana Research, 50,* 67–83.
Metcalfe, I. (2002). Permian tectonic framework and palaeogeography of SE Asia. *Journal of Asian Earth Sciences, 20,* 551–566.
Miller, K. G., Kominz, M. A., Browning, J. V., Wright, J. D., Mountain, G. S., Katz, M. E., et al. (2005). The Phanerozoic record of global sea-level change. *Science, 310,* 1293–1298.
Moreau, M.-G., Besse, J., Fluteau, F., & Greff-Lefftz, M. (2007). A new global Paleocene-Eocene apparent polar wandering path loop by "stacking" magnetostratigraphies: Correlations with high latitude climatic data. *Earth and Planetary Science Letters, 260,* 152–165.
Morgan, W. J. (1968). Rises, trenches, great faults and crustal blocks. *Journal Geophysical Research, 73*(308), 1959–1982.
Morgan, W. J. (1972). Deep mantle convection plumes and plate motions. *AAPG Bulletin, 56,* 203–213.
Mulch, A. (2016). Stable isotope paleoaltimetry and the evolution of landscapes and life. *Earth and Planetary Science Letters, 433*, 180–191. https://doi.org/10.1016/j.epsl.2015.10.034.
Müller, R. D., Seton, M., Zahirovic, S., Williams, S. E., Matthews, K. J., Wright, N. M., et al. (2016). Ocean basin evolution and global-scale plate reorganization events since Pangea breakup. *Annual Review of Earth and Planetary Sciences, 44*(1), 107–138.
Nance, R. D., Gutierrez-Alonso, G., Duncan Keppie, J., Linnemann, U., Brendan Murphy, J., Quesada, C., et al. (2012). A brief history of the Rheic Ocean. *Geosciences Frontiers, 3*(2), 125–135.
Oriolo, S., Oyhantçabal, P., Wemmer, K., & Siegesmund, S. (2017). Contemporaneous assembly of Western Gondwana and final Rodinia break-up: Implications for the supercontinent cycle. *Geoscience Frontiers, 8,* 1431–1445.
Otto-Bliesner, B. L., & Upchurch, G. R. Jr. (1997). Vegetation-induced warming of high-latitude regions during the Late Cretaceous period. *Nature, 385*, 804–807.
Otto-Bliesner, B. L., Brady, E. C., & Shields, C. (2002). Late Cretaceous Ocean: Coupled simulations with the National Center for Atmospheric Research climate system model. *Journal of Geophysical Research: Atmospheres, 107*(D2), ACL 11-1–ACL 11-14.
Peppe, D. J., Royer, D. L., Wilf, P., & Kowalski, E. A. (2010). Quantification of large uncertainties in fossil leaf paleoaltimetry. *Tectonics, 29*(3). https://doi.org/10.1029/2009TC002549.
Pirouz, M., Avouac, J. P., Hassanzadeh, J., Kirschvink, J. L., & Bahroudi, A. (2017). Early Neogene foreland of the Zagros, implications for the initial closure of the Neo-Tethys and kinematics of crustal shortening. *Earth and Planetary Science Letters, 477,* 168–182.
Poirier, A., & Hillaire-Marcel, C. (2011). Improved Os-isotope stratigraphy of the Arctic Ocean. *Geophysical Research Letters, 38*, L14607.
Poulsen, C. J., Ehlers, T. A., & Insel, N. (2010). Onset of convective rainfall during gradual Late Miocene rise of the Central Andes. *Science, 328,* 490–493.
Quade, J., Garzione, C., & Eiler, J. (2007). Paleoelevation reconstruction using pedogenic carbonates. *Reviews in Mineralogy and Geochemistry, 66*, 53–87.
Raff, A. D., & Mason, R. G. (1961). Magnetic survey off the west coast of North America, 40° n. latitude to 52° n. latitude. *GSA Bulletin, 72,* 1267–1270.
Robert, B., Besse, J., Blein, O., Greff-Lefftz, M., Baudin, T., Lopes, F., et al. (2017). Constraints on the Ediacaran inertial interchange true polar wander hypothesis: A new paleomagnetic study in Morocco (West African Craton). *Precambrian Research, 295,* 90–116.
Rogers, J. J. W., & Santosh, M. (2002). Configuration of Columbia, a Mesoproterozoic supercontinent. *Gondwana Research, 5,* 5–22.
Romm, J. (1994). A new forerunner for continental drift. *Nature 367*, 407.
Rowley, D. B., & Garzione, C. N. (2007). Stable isotope-based paleoaltimetry. *Annual Review of Earth and Planetary Sciences, 35,* 463–508.
Sarr, A. C., Husson, L., Sepulchre, P., Pastier, A. M., Pedoja, K., Elliot, M., et al. (2019). Subsiding Sundaland. *Geology, 47*(2), 119–122. https://doi.org/10.1130/G45629.1.
Seton, M., Müller, R. D., Zahirovic, S., Gaina, C., Torsvik, T., Shephard, G., et al. (2012). Global continental and ocean basin reconstructions since 200 Ma. *Earth Science Reviews, 113,* 212–270.
Su, T., Farnsworth, A., Spicer, R. A., Huang, J., Wu, F.-X., Liu, J., et al. (2019). No high Tibetan Plateau until the Neogene. *Science Advances, 5*(3), eaav2189. https://doi.org/10.1126/sciadv.aav2189.
Tapponnier, P., Zhiqin, X., Roger, F., Meyer, B., Arnaud, N., Wittlinger, G., & Jingsui, Y. (2001). Oblique, stepwise rise and growth of the Tibet Plateau. *Science, 294*, 1671–1677.

Tarduno, J. A., Blackman, E. G., & Mamajek, E. E. (2014). Detecting the oldest geodynamo and attendant shielding from the solar wind: Implications for habitability. *Physics of the Earth and Planetary Interiors, 233,* 68–87.

Tarduno, J. A., Cottrell, R. D., Davis, W. J., Nimmo, F., & Bono, R. K. (2015). A Hadean to Paleoarchean geodynamo recorded by single zircon crystals. *Science, 349,* 521–524.

Torsvik, T. H., Rousse, S., Smethurst, M. A., (2009). A new scheme for the opening of the South Atlantic Ocean and the dissection of an Aptian salt basin. *Geophysical Journal International, 183(1)*, 29–34.

Torsvik, T. H., Van der Voo, R., Preeden, U., Mac Niocaill, C., Steinberger, B., Doubrovine, P. V., et al. (2012). Phanerozoic polar wander, palaeogeography and dynamics. *Earth Science Reviews, 114,* 325–368.

U.S. Geological Survey Geologic Names Committee. (2018). Divisions of geologic time—Major chronostratigraphic and geochronologic units. U.S. Geological Survey Fact Sheet 2018–3054, 2 p. https://doi.org/10.3133/fs20183054.

Vail, P. R. (1977). Seismic stratigraphy and global changes of sea level. *Bulletin American Association of Petroleum Geologists Memoir, 26,* 49–212.

Vérard, C., Hochard, C., Baumgartner, P. O., Stampfli, G. M., & Liu, M. (2015). 3D palaeogeographic reconstructions of the Phanerozoic versus sea-level and Sr-ratio variations. *Journal of Palaeogeography, 4*(1), 64–84.

Villeneuve, M. (2008). Review of the orogenic belts on the western side of the West African craton: The Bassarides, Rokelides and Mauritanides. In N. Ennih & J.-P. Liégeois (Eds.), *The boundaries of the West African Craton* (Vol. 297, pp. 169–201). Geological Society, London, Special Publications.

Vine, F. J., & Matthews, D. H. (1963). Magnetic anomalies over oceanic ridges. *Nature, 199,* 947.

Yount, L. (2009). *Alfred Wegener: Creator of the continental drift theory*. New York: Infobase Publishing.

Zhao, G., Cawood, P. A., Wilde, S. A., & Sun, M. (2002). Review of global 2.1-1.8 Ga orogens: Implications for a pre-Rodinia supercontinent. *Earth-Science Reviews*, *59*, 125–162.

Introduction to Geochronology

3

Hervé Guillou

Accurate knowledge of climate variations in the past is an essential preamble to any realistic modeling of future climate, and requires an understanding of the mechanisms that govern the natural dynamics of the climate, and especially of its rapid changes. One of the current major concerns for this research is the quantification of the phase shift in climate between different regions of the globe. This requires having reliable, precise and comprehensive chrono-stratigraphic tools in order to temporally locate and to synchronize the various archives.

Establishing a common time frame for all climate archives remains a major challenge. Research on long time scales emphasizes the climate system's response to external forcing, but the study of rapid and abrupt changes in climate allows the internal variability of the climate system and the interactions between its various components to be investigated. The last glacial period was characterized by a succession of very rapid changes in the climate in the North Atlantic, which resulted in massive reorganization of the climate system on a global scale and was manifested in particular by the massive discharge of icebergs into the ocean, known as Heinrich events. These events mainly occurred during glacial periods but some occurred as soon as ice sheets developed on land in the northern hemisphere at the end of the last interglacial, and also at the beginning of the Holocene, even though interglacial periods seem to have been much more stable. In order to understand and model the mechanisms involved, it is important to know the precise chronology of all these events.

Another purpose of geochronological studies is to enable the comparison of climate records on a common and absolute time scale. It is only through this approach that the phase shifts between the hemispheres or between low and high latitudes can be understood and explained. By harmonizing the time scales for different types of records, both from the land and ocean, isotopic stratigraphy plays an essential role in providing a better understanding of the chronology and dynamics of the mechanisms responsible for climate variations.

Variations in climate are caused by many factors with characteristic durations ranging from hundreds of millions of years for the evolution of the Sun to a few years for internal reorganization of the climate system. In addition, records of climate signals that can potentially be dated are represented in very different substrates (sediments, ice, coral, cave concretions known as speleothems). The choice of the best adapted geochronological tools to date them will depend on the nature of the records, their age, the time span of the phenomena to be dated and the desired level of accuracy.

The dating methods most commonly used in paleoclimatology are: dendrochronology, ^{14}C, the Uranium/Thorium relationship, Potassium-Argon ($^{40}K/^{40}Ar$) and its variant $^{40}Ar/^{39}Ar$ (isotopic methods), and magnetic stratigraphy (indirect method of dating). Often, in order to provide an accurate geo-chronological framework, two or more of these methods need to be compared.

In the following chapters, we will present the absolute dating methods implemented to provide a time scale independent of astronomical parameters and to refine the stratigraphic scales commonly used in paleoclimatology and in paleo-oceanography, very often based on variations in the $^{18}O/^{16}O$ relationship in ice and benthic foraminifera related to the orbital signal. The principles of the methods mentioned above, their field of application, their implementation in the laboratory, their accuracy and limitations will also be presented. The scope of each method will be illustrated with a concrete example.

Geochronology plays an essential role for both geologists and paleoclimatologists. For geologists, it has allowed traditional stratigraphy to be linked to a time scale covering the full history of the Earth and to estimate the time constants of the great geological phenomena (plate tectonics, uplift of mountains, renewal of ocean basins, long-term

H. Guillou (✉)
Laboratoire des Sciences du Climat et de l'Environnement, LSCE/IPSL, CEA-CNRS-UVSQ, Université Paris-Saclay, 91190 Gif-sur-Yvette, France
e-mail: herve.guillou@lsce.ipsl.fr

G. Ramstein et al. (eds.), *Paleoclimatology*, Frontiers in Earth Sciences,
https://doi.org/10.1007/978-3-030-24982-3_3

global climate changes). The latest version of the chronostratigraphic scale is available on the website of the International Commission on Stratigraphy: http://www.stratigraphy.org/.

For paleoclimatologists, geochronology has provided a time scale entirely independent of astronomical parameters. This has allowed the Milankovitch theory to be validated, a work that has been a focus of attention of geochemists over the last forty years. Currently, a major experimental effort is underway to try to improve the dating accuracy and to detect the phase shifts that accompany the response of various components of climate system to the insolation forcing.

Carbon-14

4

Martine Paterne, Élisabeth Michel,
and Christine Hatté et Jean-Claude Dutay

Seventy years after its discovery by W.B.F. Libby and collaborators (Arnold and Libby 1949; Libby 1952), the radiocarbon (^{14}C) method of dating is still of great interest in many scientific fields in biology, earth science, climate, environment and archeology. Libby received the Nobel Prize in Chemistry in 1960 and the chairman of the Nobel Committee highlighted the importance of this discovery in these terms: "*Seldom has a single discovery in chemistry had such an impact on the thinking of so many fields of human endeavor. Seldom has a single discovery generated such wide public interest*". The history of the ^{14}C method is an excellent example of the fruitful exchanges among different scientific fields and of the complementarity between scientific advances and technological innovations. Since its discovery, more than a hundred and fifty laboratories in the world are now dedicated to ^{14}C dating. In the 1980s, new technologies, notably the accelerator mass spectrometry, allowed the use of samples of increasingly reduced sizes and a better precision of the ^{14}C ages. Now, the physical and chemical processes involved in biological and environmental changes may be analyzed at the molecular scale.

The method and techniques of ^{14}C dating have been the subject of several web and journal publications to which readers may refer (Libby 1981; Taylor 1987; Taylor et al. 1992; Currie 2004).

Principles of the Radiocarbon Method

Discovery of the Method

Kamen (1963) reported the history of the ^{14}C discovery and Libby's meeting with ^{14}C in 1939 at Berkeley. He attributed the *physical* prediction of the existence of this isotope to the physicist Kurie (Kamen 1963), who studied neutron-induced disintegration of light elements such as nitrogen (^{14}N). During these experiments, Kurie observed infrequent and *abnormal* long thin traces in a cloud chamber filled with air. He attributed them to the emission of protons following the reaction ^{14}N (n, ^{1}H) ^{14}C although other reactions such as ^{14}N (n, ^{2}H) ^{12}C and ^{14}N (n, ^{3}H) ^{12}C could also have been possible. In 1936, Burcham and Goldhaber demonstrated that no α-particles were emitted in the slow neutron disintegration of ^{14}N and only the reaction $^{14}N(n, ^{1}H)^{14}C$ was possible with proton emission and formation of ^{14}C noted $^{14}N(n, p)^{14}C$ (Kamen 1963).

The evidence of the *chemical* existence of ^{14}C is due to Ruben, a chemist and Libby's student, and to Kamen, a radiochemist of the Lawrence Livermore Radiation Laboratory at Berkeley. They investigated the assimilation processes of CO_2 during photosynthesis by incubating plant species with the radioactive isotope ^{11}C, which was produced in the Livermore cyclotron (Ruben et al. 1949). Labeled intermediate solutions were deposited on a blotting paper, and, once dried, the paper was protected by a plastic film and wrapped inside a screen-wall counter. The use of ^{11}C in biology was however very difficult due to long separation phases of various photosynthetic pigments by ultracentrifugation and a half-life of 21 min. Furthermore, it was not very competitive with the ^{13}C labeling of plants. At the request of Lawrence, who invented the cyclotron and received the Nobel Prize in Physics in 1939, the existence or not of long-lived radioactive isotopes was systematically sought for each element of the first column of the periodic table (H, C, N, O), and thus the search for the *chemical* existence of ^{14}C (Kamen 1963). Kamen submitted a graphite target to a deuteron beam in the cyclotron overnight. After burning the graphite, Ruben precipitated the CO_2 into a carbonate. This precipitate was furnished to their colleague in the chemistry department, W.F. Libby, who developed proportional counters to measure the radioactivity of elements such as neodymium, samarium, rubidium and lutetium, to determine their period (Libby 1934). The detection

M. Paterne (✉) · É. Michel · C. H. et Jean-Claude Dutay
Laboratoire des Sciences du Climat et de l'Environnement, LSCE/IPSL, CEA-CNRS-UVSQ, Université Paris-Saclay, 91190 Gif-sur-Yvette, France
e-mail: martine.paterne@lsce.ipsl.fr

G. Ramstein et al. (eds.), *Paleoclimatology*, Frontiers in Earth Sciences,
https://doi.org/10.1007/978-3-030-24982-3_4

of a weak activity was the first proof of the existence of artificially created ^{14}C; its half-life was estimated to be between 10^3 years and 10^5 years (Kamen 1963).

This research was interrupted in the early 1940s as Libby joined Harold Urey's team in Chicago to develop techniques of isotopic enrichment of uranium for nuclear weapons in the frame of the Manhattan Project. He would later use these enrichment techniques in natural samples for ^{14}C studies. While the ^{14}C was artificially created, the existence of a natural production of ^{14}C still needed to be proven and thus the existence of slow neutrons in the Earth's atmosphere in order to assess the feasibility of ^{14}C dating.

The method of ^{14}C dating is linked to the discovery of cosmic radiations, later termed cosmic rays, by Victor Hess in 1912 by using electroscopes aboard a balloon (Libby 1964; Rossi 1952). This discovery was the beginning of numerous studies, which investigated the composition, intensity, origin, and effect of the cosmic rays on the Earth's atmosphere. Cosmic rays caused nuclear reactions in the atmosphere, which were suspected by Grosse (Libby 1981). These reactions were first evidenced by Blau in 1932, who pioneered the technique of photographic plates covered by thick nuclear emulsions to separate the α-particles from proton tracks. Such plates were exposed in the Austrian Alps revealing disintegration stars in the emulsion (Rossi 1952). Rumbaugh and Locher determined the nature of this radiation by sending photographic plates into the stratosphere to an altitude of about 20 km in the gondola of a balloon (Rossi 1952). Some plates were covered with different materials about 1 cm thick and the others were free of materials. The control plates showed no traces, while those covered by paraffin, for example, showed four times more traces than those covered by lead or carbon. Due to the absence of traces on the control plates, the traces could be only protons and not α particles, and these protons could have been emitted only from the different materials during collision of atoms with neutrons. Korff and colleagues then performed new experiments using proportional counters aboard balloon, some filled with boron trifluoride (boron is a neutron absorber and emits a α particle upon collision with a neutron), and others filled with a mixture of hydrogen, methane and carbon monoxide (sensitive to fast neutrons) (Rossi 1952; Simpson 2000). These counters permitted precise measurement of the density of the neutrons and their energy spectrum. These authors have thus shown that the density of slow neutrons reached a maximum at an altitude between 12 and 16 km, and then decreased towards the sea level. When entering the atmosphere, the protons, which compose about 90% of the cosmic rays, collide with atoms and molecules (mainly nitrogen and oxygen). The products of their disintegration are protons and neutrons, which collide with other atoms while neutrons lose some energy on each collision. This explains the increase in neutron density at around 16 km and the decrease towards the sea-level.

During collisions, the neutrons slow down, and Korff suggested that these secondary slow neutrons were captured by nitrogen nuclei to form the cosmogenic isotope ^{14}C following the reaction ^{14}N (n, p) ^{14}C (Korff 1951). When receiving the Nobel Prize in 1960, Libby (1964) indicated that the idea of the ^{14}C dating method was inspired by Korff's results. Later, Simpson (2000) showed that the density of neutrons varied with the latitude, as a function of the lines of the Earth's magnetic field that deflect the (electrically charged) particles of cosmic rays. The average production of ^{14}C is in the range of 2.25 ± 0.1 atoms of $^{14}C/cm^2/s$. It varies from one to six between the equator and the poles, and at the poles, it can vary by a factor of almost four depending on solar activity. Of minor importance, other reactions on ^{16}O, ^{17}O, ^{13}C, contribute also to the formation of atmospheric ^{14}C.

Principle of the ^{14}C Dating Method

Libby postulated in 1946 (Arnold and Libby 1949) that the production of ^{14}C atoms and their decay as ^{14}N by emitting a β particle would be in equilibrium at steady-state conditions (Fig. 4.1). As the cosmic rays continuously bombard the Earth and as the Earth age is much higher than the estimated period of 10^3–10^5 years, the distribution of ^{14}C would be in equilibrium within all the reservoirs of exchangeable carbon (atmosphere, ocean, biosphere). Estimating the production of neutrons per cm^2 and per second based on the distribution of neutrons observed by Korff (1951) and the amount of exchangeable carbon between the reservoirs, Libby wrote that the specific activity of exchangeable carbon could be easily calculated taking into account the balance between production and decay:

$$\frac{d^{14}C}{dt} = Q - \lambda^{14}C = 0$$

where Q is the production of a ^{14}C atom per second and λ, the decay constant, is equal to $\ln(2)/T_{1/2}$, where $T_{1/2}$ is the half-life (half of the radioactive atoms have decayed).

$$\frac{d\left(\frac{^{14}C}{^{12}C}\right)}{dt} = 0 = \frac{1}{(^{12}C)^2}\left[^{12}C\frac{d^{14}C}{dt} - ^{14}C\frac{d^{12}C}{dt}\right] = \frac{^{12}C}{(^{12}C)^2}\left[Q - \lambda^{14}C\right]$$

because

$$^{14}C\frac{d^{12}C}{dt} = 0$$

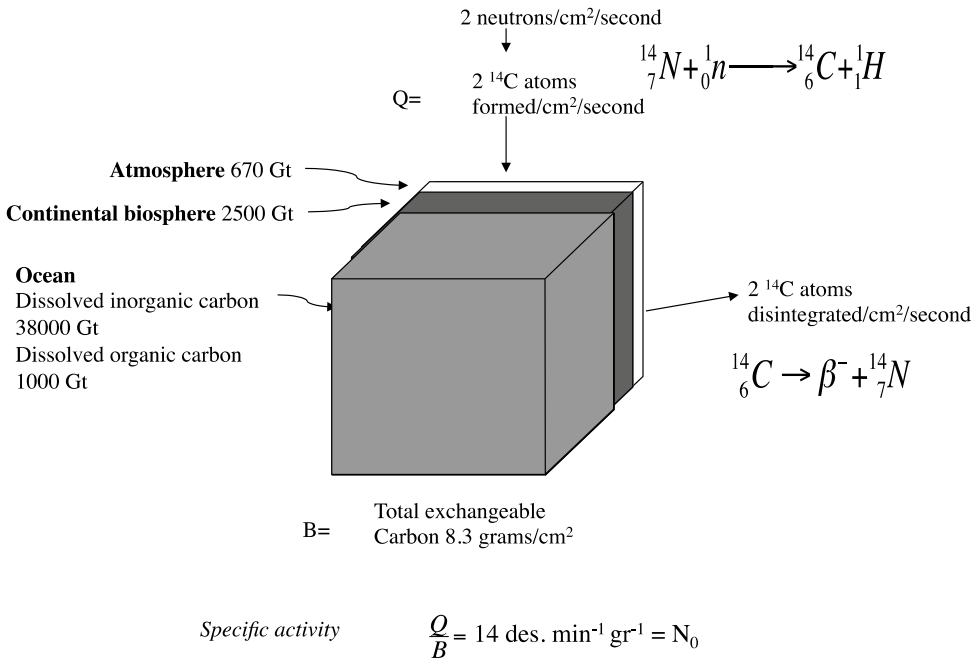

Fig. 4.1 Diagram of the ^{14}C formation and mixing in the different terrestrial reservoirs (Libby 1964)

The carbon stocks are expressed in Gt (Gigatons) and the number of neutrons per cm^2 per second corresponds to pre-1950 estimates (modified according to 10):

$$\lambda \frac{^{14}C}{^{12}\{C\}} = \frac{Q}{^{12}C}$$

The predicted activity should have been between 1 and 10 decays per minute per gram of carbon, given the uncertainties, in all living matter. ^{14}C activities of 10.5 disintegrations per minute per gram were measured from isotopically enriched samples of biomethane in 1947, in good agreement with the prediction. Libby and collaborators measured then the specific activities of natural tree samples from different continents by reducing background counting with lead and iron shielding. They found worldwide homogeneous ^{14}C activities at around 12.5 disintegrations/min/g of carbon[1] (Libby 1981). A precise measurement of the ^{14}C half-life, and the specific activity of samples of known ages were further undertaken to validate the ^{14}C dating method.

Estimation of the Half-Life and the First ^{14}C Dating

The half-life of ^{14}C was determined through many experiments (Engelkemeir et al. 1949; Olsson et al. 1962). One of them consisted of measuring, by mass spectrometry, the isotopic ratio ^{14}C/^{12}C of highly enriched barium carbonates [$BaCO_3$] (up to 6%) produced by submitting to neutrons beams, solutions of ammonium nitrate in a cyclotron (Engelkemeir et al. 1949). Proportional counters were then filled with the CO_2 released by $BaCO_3$ hydrolysis. By measuring the number of disintegrations per minute and per gram of carbon (dN/dt) and knowing the number of atoms of ^{14}C (N) in the samples, the half-life was estimated at 5720 ± 47 years. Averaging all the published estimates, Libby estimated the half-life at 5568 years. Redeterminations have led to a value of 5730 ± 40 years (Godwin 1962). The latter value has recently been debated (Chiu et al. 2007).

Libby and collaborators then undertook the dating of samples of known ages, mostly from the tombs of the Egyptian kingdoms, and published them as the Curve of Knowns (Libby 1964).

Principle of the Method

Carbon-14 is formed in the upper atmosphere, where it is rapidly oxidized to form $^{14}CO_2$ molecules. All living matter contains carbon, and, thus a very small proportion of ^{14}C. The ^{14}C abundance is of some 1.2×10^{-10}% (or 1.2×10^{-12} g of ^{14}C per g of carbon), while those of the isotopes ^{13}C and ^{12}C are respectively 1.108% and 98.892%. The ^{14}C exchanges between the living material and their environment cease at the death of the animals or plants. The time (t) since the death can be measured by comparing the residual specific activity in dead organisms to that of the atmosphere.

[1]The specific activity is now determined at 13.56 ± 0.07 disintegrations/min/g of carbon.

The radiocarbon age (t) is calculated using the radioactive exponential decay:

$$\frac{^{14}C}{^{12}C} = \left(\frac{^{14}C}{^{12}C}\right)_0 e^{-\lambda t}$$

where $(^{14}C/^{12}C)_0$ is the atmospheric ratio and $\lambda = \ln(2)/T_{1/2}$ the decay constant. By convention, the Libby's half-life at 5568 years is used to calculate the ^{14}C ages. The mean lifetime of the ^{14}C atoms before decay is $T_{1/2}/\ln(2)$.

The calculation of age becomes:

$$t = \frac{1}{\lambda}\ln\left(\frac{\frac{^{14}C}{^{12}C}}{\left(\frac{^{14}C}{^{12}C}\right)_0}\right)$$

The ^{14}C dating method is based on the hypothesis of a constant radioactive equilibrium between the ^{14}C formation and its disintegration in ^{14}N. If we look at Libby's diagram (Fig. 4.1), we may observe that this is true if the production of ^{14}C, the size of the various reservoirs of carbon (atmosphere, oceans, land and marine biosphere) and their carbon content remain constant over time, as well as the fluxes between the various reservoirs. In addition, the physico-chemical integrity of the dated fossils must have been preserved after the death of organisms. For example, no isotopic exchange or secondary crystallization should have occurred. Finally, the samples should have not moved from their burying sites to date precisely any events.

Validity of the Assumptions and Definition of a Reference Standard for the Atmosphere

The first offsets between the ^{14}C and known ages appeared very quickly, notably with the major contribution of dendrochronology, a counting method of the annual tree-ring growth. In 1955, Suess demonstrated (Taylor 1987; Damon et al. 1978) that the ^{14}C content in the atmosphere varied in the last hundred years and decreased from 1890 AD to 1950 AD (Fig. 4.2). He suggested that the decrease was the result of the CO_2 release into the atmosphere from the domestic and industrial combustion of ^{14}C-depleted fossil fuels (coal, oil). These annual emissions, approximately 150Gt of C as CO_2 until 1950 AD, were responsible for a ^{14}C aging of the atmosphere of about 160 years between 1890 AD and 1950 AD, the so-called '*Suess effect*'. In 1957, Rafter and Fergusson observed a rapid atmospheric ^{14}C increase that they attributed to the ^{14}C production during the aerial atomic bomb tests. These peaked between 1960 and 1961 and doubled the ^{14}C concentration in atmospheric CO_2. This atmospheric ^{14}C spike led later to life-size experiments to monitor carbon exchanges between the various earth reservoirs.

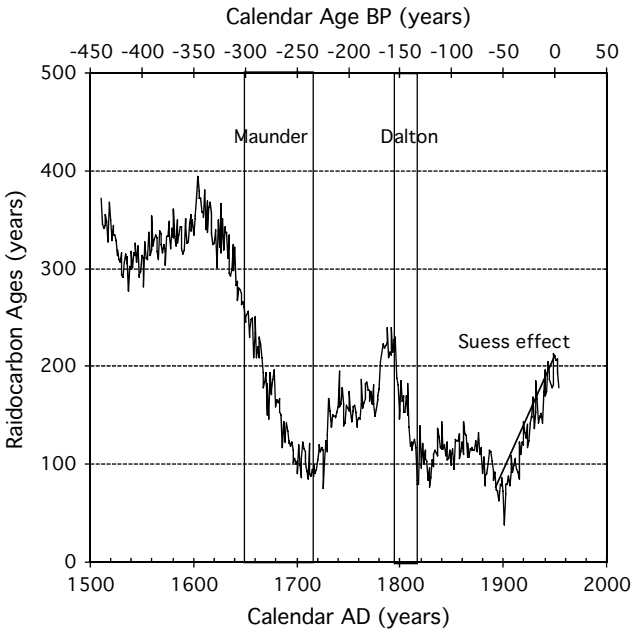

Fig. 4.2 Variations of the ^{14}C ages as a function of calendar ages in tree-rings. The time interval of the '*Suess effect*', the Maunder and Dalton minima of solar magnetic activity are shown. The last two coincide with a rapid decrease of the atmospheric ^{14}C ages due to lower filtering of cosmic protons by the solar magnetic field. The 'Suess effect' corresponds to the increase of the ^{14}C ages due to the dilution of atmospheric $^{14}CO_2$ by the industrial and domestic emissions of CO_2 into the atmosphere from the ^{14}C-free fossil fuels

Besides the anthropogenic changes of ^{14}C, the natural variations of ^{14}C in the different carbon reservoirs were then identified by comparing the ^{14}C and dendrochronological ages over the past millennia (Damon et al. 1978; Stuiver et al. 1991). They are attributed to changes in ^{14}C production in the upper atmosphere and to variations in the natural carbon cycle linked to the size of the carbon reservoirs, their composition and the carbon exchange fluxes.

De Vries observed rapid fluctuations (wiggles) in the atmospheric ^{14}C from tree-ring analyses (Damon et al. 1978; Stuiver et al. 1991). He attributed these fluctuations to changes in climate and solar activity, as both the Little Ice Age (about 1560 AD to 1830 AD) and the Maunder and Dalton minima, two time intervals of few sunspots, occurred over this time.

The charged particles released from the Sun, known as the solar wind, create a magnetic field in the interplanetary space. These eruptions are a manifestation of the magnetic activity of the Sun, with a minimum dipolar magnetic field corresponding to the maximum equatorial activity, and their intensity is reversed every 11 years. The solar magnetic field varies with a cycle of 22 years, reversing its polarity every 11 years at every change of solar activity. The particles of the galactic cosmic rays are deflected by the solar wind. The higher the solar magnetic activity, the fewer particles

penetrate into the upper atmosphere. As a result, the ^{14}C production decreases as the solar activity increases, and vice versa. Similarly, the cosmic ray intensity in the upper atmosphere is modulated by the changes in the Earth's magnetic field, which acts as a shield against the electrically-charged cosmic protons. The greater the intensity of the geomagnetic field, the fewer the number of cosmic protons arriving in the upper atmosphere, and therefore the production of ^{14}C is lower in the atmosphere (Damon et al. 1978; Stuiver et al. 1991). Changes in the Earth's magnetic field could explain about 50% of the ^{14}C variation in the atmosphere between the last glacial and the Holocene, and the ^{14}C aging of the atmosphere during the last glacial related to a high magnetic field intensity (Lal and Charles 2007).

The dendrochronological record of the atmospheric ^{14}C content over the last 10,000 years has, in turn, given the opportunity to evaluate the changes of solar activity beyond the first observations in the seventeenth century. Spectral analyses of the atmospheric ^{14}C emphasize long cycles of 88 years, 208 years and 2050 years attributed to changes in solar activity (Damon and Peristykh 2000). During the last 70 years, the solar activity was at an exceptionally high level and many other periods of high activity, although shorter, occurred in the past, such as, for example, at the beginning of the Holocene. In addition, some authors have thought that the unusual solar activity may have contributed, in a small part, to the recent climate change observed in the late twentieth century (Muscheler et al. 2005).

Climate changes modify the size of the carbon reservoirs and the CO_2 fluxes between them and therefore the atmospheric $^{14}CO_2$ as noted by de Vries (Stuiver et al. 1991). Libby (1952) had already estimated the impact of climate changes on the ^{14}C ages. He assumed that the sea level lowering ($\sim$100 m) and the temperature decrease during the last ice age reduced the oceanic carbon inventory, resulting in an increase of the specific activity of ^{14}C (Fig. 4.1). Assuming that the ^{14}C activity in the reservoir exchange changed by 10%, Libby calculated that the glacial ^{14}C ages would be too young by some 800 years. We know now that the ^{14}C ages are too young by about 2000 years with respect to 'true' ages during the last glacial maximum (Reimer et al. 2013). The ocean circulation and the carbon cycle were deeply modified during the last ice age that modulated the concentration of atmospheric CO_2. Between the last glacial maximum and the Holocene, the atmospheric CO_2 concentration increased from 190 to 280 ppm as recorded in the Antarctic ice cores.

The growing evidence of the atmospheric ^{14}C variations through time led to two consequences: the establishment of a standard, i.e. a reference value of ^{14}C for the atmosphere (N_0), and the calibration process which precisely quantifies the difference between the true or 'absolute' ages and the ^{14}C ages.

As requested by Arnold in 1956, the National Bureau of Standards (Washington) prepared a standard (NBS-I) of 450 kg of oxalic acid (HOOC-COOH), an organic compound extracted from a French crop of sugar beet in 1955 (Arnold and Libby 1949). It provided the reference activity of year zero, from which the ^{14}C age of a sample is calculated. The reference activity was taken at 95% that of NBS-I to account for the Suess and nuclear bomb effects and the reference year has been set arbitrarily at 1950. Since that time, other standards were prepared (NBS-II, sucrose). The ^{14}C ages are expressed in years BP (Before Present, present being equal to 1950 AD). In archeology, the terms Anno Domini (AD) and Before Christ (BC) are used. Lately appears the term Common Era (CE) which is equivalent to AD and BCE to BC.

Before measuring the ^{14}C activity in a sample and calculating its ^{14}C age, the fractionation of the stable isotopes of carbon must be considered. Craig in 1953 demonstrated that the $^{13}C/^{12}C$ ratios ($\delta^{13}C$) vary in contemporary materials as a function of the reservoir's $\delta^{13}C$ in which they form. The amount of enrichment/depletion of ^{14}C due to biological and physicochemical fractionation processes is approximately two times that measured by $\delta^{13}C$ in the same sample. The $\delta^{13}C$ value, expressed in ‰ compared to the standard PDB (Pee Dee Belemnite), is about −6.5‰ for the pre-industrial atmospheric CO_2. It varies between −2‰ and +3‰ in the carbonates of seashells and between −20 and +3‰ for those of lake shells. The $\delta^{13}C$ values of plants vary between −27 and −14‰ due to photosynthesis processes. Processes of assimilation of atmospheric CO_2 by plants are carried out mainly according to two cycles of transformation of organic compounds, called the Calvin cycle and the Hatch and Slack cycle, or also as C3 and C4, the second with a lower isotope discrimination than the first. As a result of the great variability of the $\delta^{13}C$ values, the ^{14}C activities have been normalized to a common reference of $\delta^{13}C$ set at −25‰ (see below). The complete procedure for calculation of age is explained in Box 1.

Box 1

As in most definition of isotopes, the ^{14}C content is expressed by a δ in ‰, which defines the difference between a sample and a standard, which may be the NBS-I standard, the $\delta^{13}C$ of which is equal to −19‰ relative to the PDB (Broecker and Olson 1959; Olsson

and Osadebe 1974; Stuiver and Polach 1977; Stenström et al. 2011).

The $\delta^{14}C$ may be written as follows:

$$\delta^{14}C = \left(\frac{A_s}{A_{Ox}} - 1\right) \times 1000 \quad (4.1)$$

With A_s and A_{Ox}, the respective activities of the sample and of the standard NBS-I of oxalic acid.

$$A_{ON} = 0.95 \times A_{Ox}\left[1 - \frac{2 \times (19 + \delta^{13}C_{Ox})}{1000}\right] \quad (4.2)$$

The ^{14}C activity in the atmosphere in 1950 (A_{ON}) is equal to 95% of the NBS-I standard activity, corrected for $\delta^{13}C$ (Eq. 4.2). The isotopic fractionation of $\delta^{13}C$, which affects the abundance of the mass 14, is noted by the number 2. It indicates that the fractionation between the mass 14 and mass 12 is double that between the masses 13 and 12. The negative sign assigned to fractionation $\delta^{13}C$ means that the ^{14}C activity measured in organisms with a negative $\delta^{13}C$, that is to say with less affinity for the mass 13 than the PDB standard, must increase to compensate for the loss caused in ^{14}C by fractionation (Broecker and Olson 1959; Olsson and Osadebe 1974; Stuiver and Polach 1977; Stenström et al. 2011).

$d^{14}C$ is defined as:

$$d^{14}C = \left(\frac{A_s}{A_{ON}} - 1\right) \times 1000 \quad (4.3)$$

To take into account the variability in the fractionation of isotopic $\delta^{13}C$ measured in the samples, $\delta^{14}C$ is normalized to a common value, $\delta^{13}C$, set at −25‰ versus PDB, regardless of the sample type (carbonate, dissolved inorganic carbon or organic matter). This value was obtained by averaging the measurements of the isotopic ratio $\delta^{13}C$ of several pieces of wood with an age less than 1890 AD (Broecker and Olson 1959; Olsson and Osadebe 1974).

We define:

$$D^{14}C(‰) = \left(\frac{A_{SN}}{A_{ON}} - 1\right) \times 1000 \quad (4.4)$$

with

$$A_{SN} = A_S\left(1 - \frac{2 \times (25 + \delta^{13}C_S)}{1000}\right) \quad (4.5)$$

$$D^{14}C(‰) = d^{14}C - 2(\delta^{13}C_S + 25)\left(1 + \frac{d^{14}C}{1000}\right) \quad (4.6)$$

The calculation of the ^{14}C age is then:

$$t(years) = \frac{1}{\lambda} \times \ln\left(\frac{1}{1 + D^{14}C/1000}\right)$$

In the case of precise measurements of activity performed in oceanography or to calibrate the ^{14}C ages, it is necessary to consider the ^{14}C decay between the age of the sample (x) and its measurement (y) using the period T of 5730 years. Equations 4.1 and 4.6 then become:

$$\delta^{14}_n C = \left(\frac{A_{SN}e^{\lambda(x-y)}}{A_{OxN}e^{\lambda(y-1950)}} - 1\right) \times 1000$$

since the ^{14}C activity of the sample decreases at the same rate as the standard

$$\delta^{14}_n C = \left(\frac{A_{SN}e^{\lambda(1950-x)}}{A_{OxN}} - 1\right) \times 1000$$

and

$$\Delta^{14}C(‰) = \delta^{14}C - 2(\delta^{13}C_S + 25)\left(1 + \frac{\delta^{14}C}{1000}\right)$$

As the activity of a sample in 1950 is the same than that of the standard, then $\Delta^{14}C$ is zero in 1950 AD.

Now, the activity of a sample is expressed as fraction modern (F) that represents the $^{14}C/^{12}C$ ratio in a sample such that:

$$F^{14}C = \frac{A_{SN}}{A_{ON}}$$

In oceanography, the 14C concentration is expressed as $\Delta^{14}C$ or Δ in ‰:

$$\Delta^{14}C = \left(\frac{A_{SN}}{A_{ABS}} - 1\right) \times 1000(\text{without age correction})$$

$$\Delta = \left(\frac{A_{SN}e^{\lambda(y-x)}}{A_{ABS}} - 1\right) \times 1000(\text{with age correction})$$

with AABS is the absolute age, y the year of measurement, x the year of growth, and $\lambda = \ln(2)/5730$. The notation Δ is often written as $\Delta^{14}C$-age corrected.

Calibration of the ^{14}C Ages

It is now well-established that the ^{14}C ages are not equal to the absolute ages because (i) the ^{14}C ages are calculated with the 5568 year half-life, (ii) the ^{14}C concentration in the atmosphere varies as a function of time due to changes in the production rate by cosmic rays which are modulated by the solar and earth magnetic fields and (iii) of the changes in the carbon cycle. The ^{14}C calibration consists of the precise measurement of the difference between an absolute (calendar) age and a ^{14}C age. An international group of scientists led by Stuiver and Reimer joins efforts to iterate the calibration datasets. The last product is the IntCal13 calibration, which extends over the past 50,000 years (Reimer et al. 2013).

Methods and Results

The calibration procedure consists in measuring the ^{14}C age of a sample while the absolute ages are determined by three methods with the best possible accuracy. The first is based either on the counting of annual tree-ring growth (dendrochronology) or on the counting of the annual laminae (varves) deposited in marine or lake sediments. The second consists in the precise U-Th dating of carbonates (warm water corals or speleothems) by mass spectrometry (Chap. 6). The third consists in synchronizing the variations of climate proxies in marine sediments and in speleothems, the last two being dated by the U-Th method.

In the eighties, the ^{14}C and U-Th dating benefitted from new techniques in mass spectrometry coupled to an accelerator or by thermal ionization (TIMS), respectively—which allowed their precision to be greatly improved and the size of samples to be reduced by a factor of 1000 (from one gram to a few milligrams). Bard had first proposed to extend the calibration from 10,000 to 22,000 cal BP through paired ^{14}C and Th-U dating of corals from the Barbados islands (Fig. 4.3) (Bard et al. 1990; Reimer et al. 2013). The calibration record IntCal13 is based on the ^{14}C dating of the terrestrial and marine samples referenced onto an 'absolute' timescale. It extends up to 13,900 cal BP by means of dendrochronology and up to ~50,000 cal BP from terrestrial plant species deposited in the varved sediments of Lake Suigetsu. It is completed by U-Th-dated samples and has corrected ^{14}C ages (see below) of the Hulu speleothem and of Atlantic and Pacific corals. Finally, corrected ^{14}C ages of foraminifera in the varved and unvarved sediments from the Cariaco basin linked to the Hulu speleothem by coeval climatic fluctuations are also included. The marine calibration record similarly covers the past 50,000 cal BP and it is based on the dating of corals from the Atlantic and Pacific oceans and of planktonic foraminifera in the Cariaco sediments in the Caribbean Sea (Fig. 4.4). The sea surface ^{14}C is not in equilibrium with that of the atmosphere. The comparison of the atmospheric and marine ^{14}C dating at a same calendar age between 0 and 13,900 cal BP allowed the atmosphere-ocean ^{14}C difference (the marine reservoir age-see below) to be quantified and the marine calibration to be anchored to the atmospheric record by subtracting the reservoir age to the marine ^{14}C ages. In IntCal13, the variability of the reservoir ages during the glacial period were taken into account by augmenting the value by 200 years prior to 13,900 cal BP. Similarly, the ^{14}C in speleothems is not equal to that of the atmosphere, and the difference (dead carbon fraction—see below) is measured between the time interval 0–13,900 cal BP and then considered constant prior to 13,900 cal BP.

As initiated with IntCal04, the mathematical approach that defines the envelope of IntCal13 takes into account both uncertainties on ^{14}C dating and those associated with the absolute ages. In addition, it also takes into account the diversity of records and the representativeness of atmospheric ^{14}C by assigning different statistical weights to them before returning the most likely fit between measured ^{14}C activity and absolute age. The IntCal13 error envelope represents the best fit between the included datasets and it is much smoother than those of the previous calibration records. It does not take into account the scattering of the ^{14}C ages in the different datasets, which do not permit 'real ^{14}C variations' to be discriminated from measurement noise. Those real variations are likely to be attributable to the complex history of each carbon reservoir in either the terrestrial (atmospheric) or marine environments over the past 50,000 cal year due to climate and oceanic circulation fluctuations, and to production changes through the variations of the Earth and solar magnetic field.

Examples of Precise Calibration of ^{14}C Ages

The Dating of the Eruption of Santorini

During the eruption of Santorini in Cyclades in the Aegean Sea, huge amounts of volcanic ash were emitted into the atmosphere and spread eastward and southward, covering much of the Middle East. The ash bed is a useful chronological marker for the whole region, allowing the chronology of human connections to be refined throughout the eastern basin of the Mediterranean Sea during the second millennium BC. Archaeologists, for example, linked the apogee of the Minoan civilization to that of the New Kingdom in Egypt in the sixteenth century BC, on the basis of the elegance of the decorations of objects found in the ash layer in Santorini. The date of this eruption could not be defined to within 60 years, despite hundreds of ^{14}C dating of charcoals found

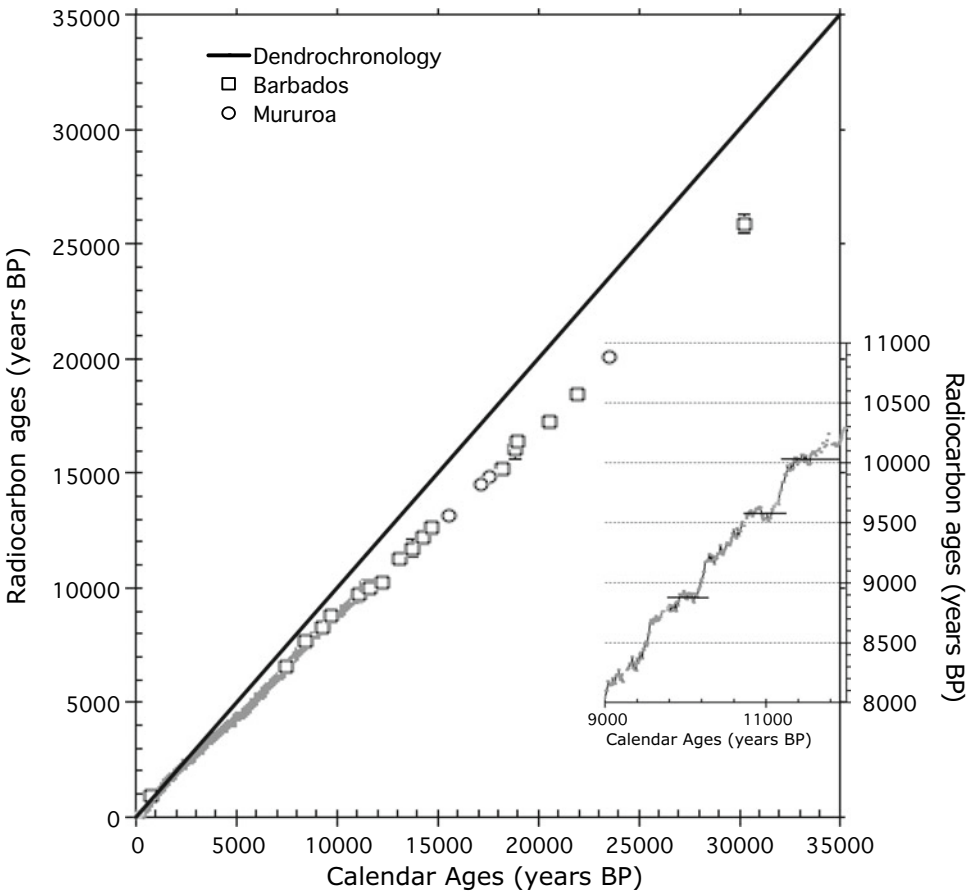

Fig. 4.3 Variations between ^{14}C and calendar ages (Reimer et al. 2013). The calendar ages are based on tree ring counting back to 11,950 cal BP and on the U-Th dating of corals from Barbados and Tahiti (in Reimer et al. 2013). The ^{14}C age plateau are shown in the inset between 9000 cal BP and 12,000 cal BP

in the ash-bed (Friedrich et al. 2006). The discovery of an olive branch with leaves buried in the ash bed enabled a very precise dating of the eruption. Friedrich et al. (2006) dated the annual tree-rings of a piece of branch (Fig. 4.5). The variation (wiggle) of the ^{14}C ages in the tree-ring matched precisely that of the calibration record, the number of calendar years being equal to that of the tree-rings.

The calendar age of the eruption of Santorini was thus estimated to be between 1627 and 1600 BC, with a confidence level of 95%. The apogee of the Minoan civilization would then be earlier than that of the New Kingdom, and would be contemporary to the time when foreign kings—Hyksos—occupied the country (Friedrich et al. 2006).

The Bipolar Seesaw or the North-South Heat Transfer

Rapid fluctuations of climate, referred to as Heinrich events, Younger Dryas, and Dansgard-Oeschger events, punctuated the last glacial period and the deglaciation.

They were attributed to variations in the thermohaline oceanic circulation (see Chap. 21). The mechanisms of these rapid fluctuations were clarified by the analysis of the ^{14}C variations in the varved deposits in the Cariaco Basin (Hughen et al. 1998; Reimer et al. 2013). The atmospheric $^{14}CO_2$ concentration is very sensitive to the rate of formation of deep water, because the CO_2 in the atmosphere is transferred to the deeper layers of the ocean via the oceanic circulation. This rate also regulates the heat transfer to the northern high latitudes. During the cold event of the Younger Dryas, which lasted approximately 1200 calendar years, the atmospheric $\Delta^{14}C$ increased (younger ^{14}C ages) during the first 200 years and then decreased during the following 1000 years (Fig. 4.6a). The increase of $\Delta^{14}C$ is in agreement with a reduction in the deepwater formation in the northern North Atlantic, contributing to a cold climate, but how may the further $\Delta^{14}C$ decrease be explained when the climate is still cold in the northern latitudes?

Glaciologists have shown that the abrupt cooling observed in the northern hemisphere was accompanied by a warming in Antarctica, and vice versa (Blunier et al. 1998). Comparing these two results, Broecker (1998) proposed a seesaw pattern of the north-south heat transfer via the ocean or the "thermal bipolar seesaw" (Fig. 4.6b): a reduction in deep water formation in the North Atlantic Ocean led to the installation of a cold climate in the northern hemisphere and an increase in the atmospheric ^{14}C. Deep waters further form in the Southern Ocean contributing to the atmospheric $\Delta^{14}C$ decrease.

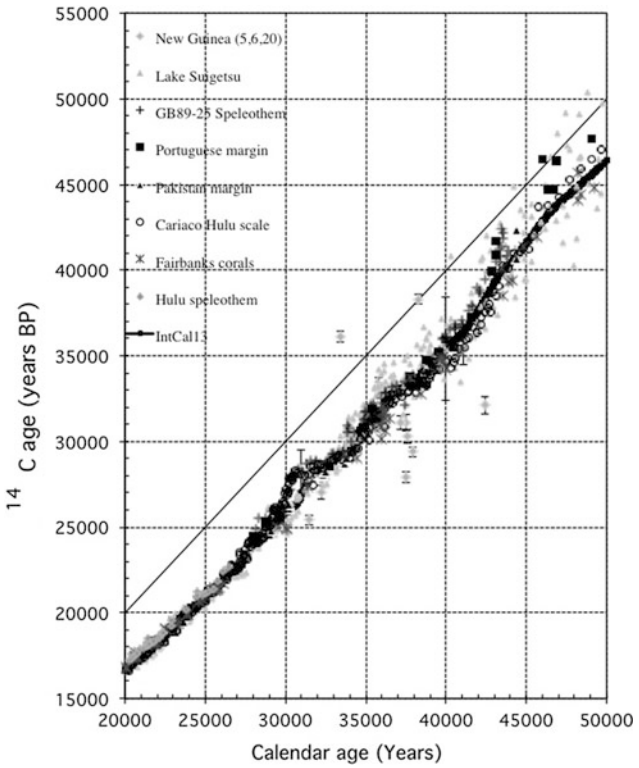

Fig. 4.4 Variations between ^{14}C and calendar ages between 20,000 and 50,000 cal BP from the calibration record IntCal 13 (Reimer et al. 2013). The straight line represents the 1:1 relation

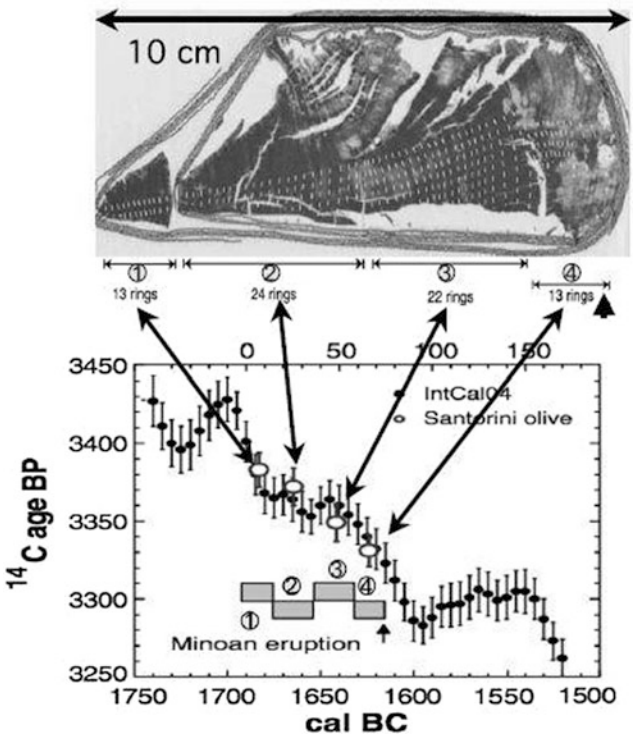

Fig. 4.5 ^{14}C and calendar ages of the Santorini eruption (modified from Friedrich et al. 2006). Four groups of rings counted (grey rectangles) from an olive branch of an approximately ten centimeters length were dated. The total number of rings equals the number of calendar years. The ^{14}C ages match the ^{14}C variations of the calibration record (Reimer et al. 2013). The calendar age of the eruption range between 1621 and 1605 BC at the 1σ confidence level (68.2%) and between 1627 and 1600 BC at the 2σ confidence level (95.4%)

Apparent Ages

Oceanic Environments: The Reservoir Ages

Carbon exists in several forms: carbon monoxide CO and carbon dioxide CO_2, methane CH_4, many complex organic molecules (cellulose, etc.). The dominant forms are the bicarbonate and carbonate ions (CO_3^{2-}, HCO_3^-, H_2CO_3) dissolved in water, and calcium, barium and magnesium carbonates ($CaCO_3$, $BaCO_3$, $MgCO_3$). Most of the Earth's living species directly assimilate the $^{14}CO_2$ from the atmosphere. In the ocean, the organisms incorporate ^{14}C, which is not in equilibrium with the atmospheric $^{14}CO_2$. The benthic foraminifera are calcareous organisms living on the surface of marine sediments. When collected alive at a water-depth of 2000 m in the North Atlantic and Pacific oceans, they will have ^{14}C ages of about 600 years and 1400 years, respectively (before the nuclear bomb tests). These ^{14}C ages are apparent ages that include the age of the organism and that of the water body in which the organisms formed their tests from the dissolved ions according to:

$$CO_2 + H_2O \leftrightarrow H_2CO_3 \leftrightarrow H^+ + HCO_3^-$$
$$HCO_3^- \leftrightarrow H^+ + CO_3^{2-}$$
$$(Ca^{2+} + 2HCO_3^- \rightarrow CaCO_3 + H_2O + CO_2).$$

The ^{14}C aging of deep waters is the result of the conveyor (thermohaline) circulation. In the modern ocean, wind-driven warm saline surface waters from the North Atlantic low latitudes flow poleward where they cool and sink to form the North Atlantic Deep Water (NADW). NADW flows at depth to the Indian and Pacific Oceans where it mixes and upwells then flowing back to the North Atlantic. All the deep waters flow to the Southern Ocean where they upwell and downwell to form a return flow to the north through the intermediate waters and the Antarctic bottom waters. Once isolated from the atmosphere, the dissolved $^{14}CO_2$ in the intermediate and deep waters starts to decrease. Although in contact with the atmosphere, the sea surface ^{14}C is not equal to the atmospheric ^{14}C, because of the mixing between the sea surface and the underlying sub-surface waters. The difference between the apparent ^{14}C ages of living organisms in the ocean and the atmospheric ^{14}C ages for the same absolute age is termed the reservoir age R. The sea surface values of R as well as those of the intermediate or deep waters differ in each one of the ocean basins and regionally within the basins.

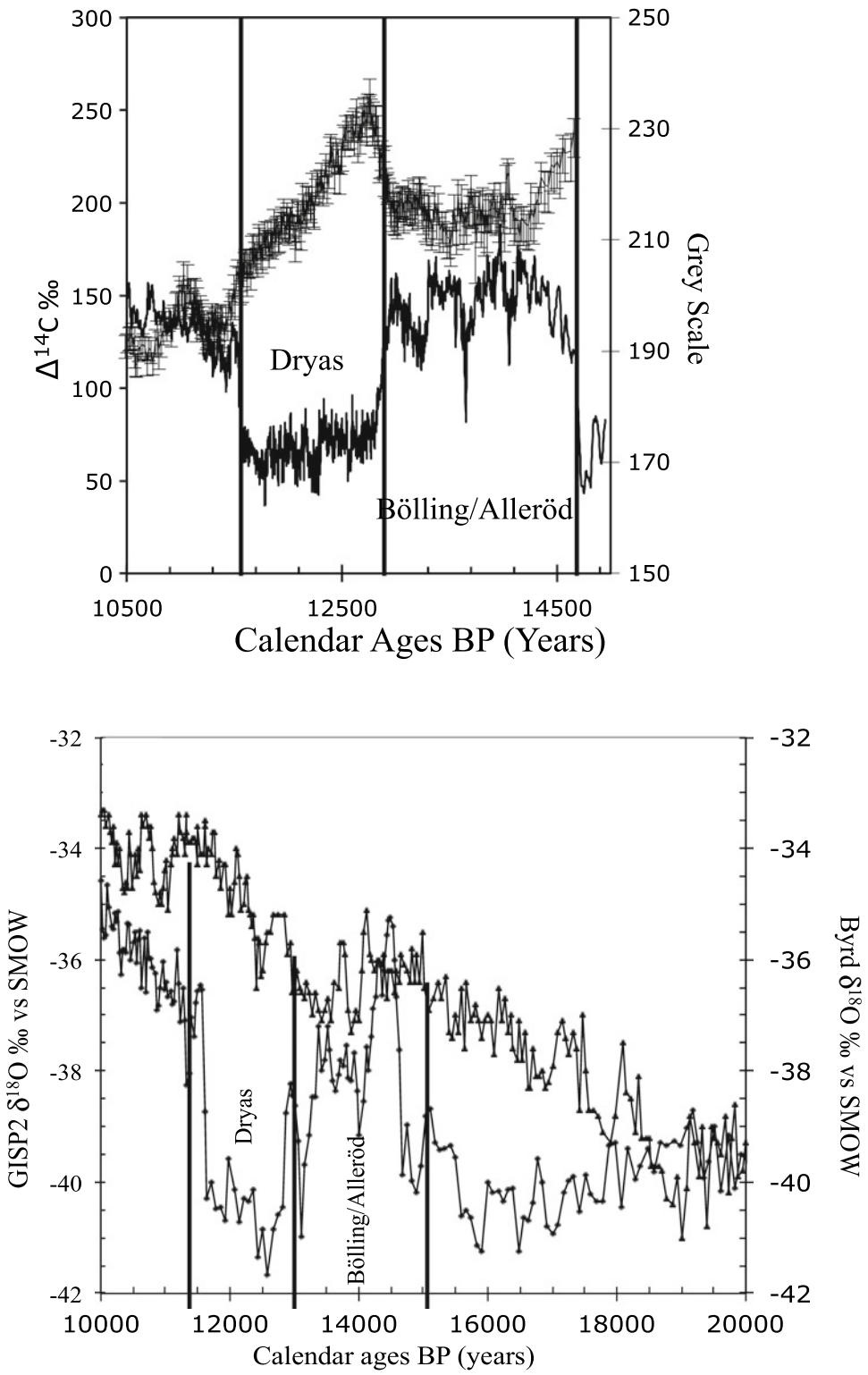

Fig. 4.6 **a** Variations in the atmospheric ^{14}C content ($\Delta^{14}C$ in ‰) (triangle) and grey scale (line) in marine varved sediments from the Cariaco Basin as a function of calendar ages by varve counting (Hughen et al. 1998; Reimer et al. 2013). **b** Variations of $\delta^{18}O$ trapped in CO_2 air bubbles in the Greenland ice core GISP2 sites in Greenland (line) and in the Byrd ice core in Antarctica (diamond) as a function of synchronized time from analyses of CH_4 concentrations in the two sites (Blunier et al. 1998)

The modern values of R are quantified by the ^{14}C dating of carbonates (mollusk shells, corals) of known ages from the historic collections of museums (Bard 1988; Siani et al. 2000; Tisnérat-Laborde et al. 2010) and, for older ages than those of these collections, by subtracting the ^{14}C age of a marine organism from that of the atmospheric calibration record at the same absolute age (Reimer et al. 2013). The mean value of R is about 300–400 years in the subtropical sea surface, and it may be some 1100 years around the Antarctic continent. Values of approximately 700 years were

measured in oceanic regions close to upwelling of intermediate and deep waters in the North Indian and Pacific Oceans. ΔR is the local departure from the global mean value of R. The latter is calculated from the modeled global sea surface ^{14}C age, using a global box-diffusion carbon model, which accounts for the^{14}C production and carbon cycle (Reimer et al. 2013).

In the past, the oceanic circulation changed as the reservoir ages did. Changes of the differences between the marine and atmospheric ^{14}C ages may be estimated by dating the charcoals and foraminifera from widespread volcanic ash layers in both marine sediments and on land (Bard et al. 1994; Siani et al. 2001; Austin et al. 2011; Thornalley et al. 2011; Siani et al. 2013; Sikes and Guilderson 2016), as well as by dating paired charcoals and mollusk shells found in the same deposits (Bondevik et al. 2006; Ascough et al. 2009). These studies demonstrated that sea surface R changed during the first step of the deglaciation from the modern value of 400 to 2000 years in the North Atlantic (Bard et al. 1994; Bondevik et al. 2006; Austin et al. 2011; Thornalley et al. 2011) and to 800 years in the Mediterranean Sea (Siani et al. 2013). In the South Pacific, the subtropical R augmented from ~300 to ~700 years (Sikes and Guilderson 2016), while those of the sub Antarctic surface waters increased from ~800 to 1400 years and to 3200 years (Siani et al. 2013; Sikes and Guilderson 2016).

Past increases in the sea ice extent at high latitudes during the glacial periods prevents the atmosphere-ocean $^{14}CO_2$ exchanges contributing to the increase of the sea surface R. In the IntCal13 calibration record, the modern value of R was subtracted to the ^{14}C ages of the marine samples to be compared to the atmospheric ^{14}C ages. To account for changes in the oceanic circulation, the modern value of R was augmented by 200 years from ~14,000 cal BP and then considered as constant down to 50,000 cal BP (Reimer et al. 2013).

Continental Environments: The Hard Water and Dead Carbon Effects

Modern lake vegetation and calcium carbonates in lakes in calcareous regions exhibit older ^{14}C ages than those of the atmosphere. The dissolved inorganic carbon $^{14}CO_2$ in lakes, used during photosynthetic processes and during the precipitation of calcium carbonates originates from the dissolution of ^{14}C-free carbonates of geological age (dead carbon) and from the mineralization of old organic matter enclosed in lake sediments. Impact of the later on the apparent ^{14}C ages of lacustrine plants is much higher in lake surrounded by peats and in artificial lakes implemented by soils flooding. The resulting aging of ^{14}C ages is called '*hard water*' effect. In addition, water stratification in lakes or the presence of an ice cover in high altitude and polar lakes tend to prevent the atmospheric $^{14}CO_2$ input to the lake waters, that tends to increase the ^{14}C age in lake waters relatively to that of the atmosphere.

The speleothems are composed of calcium carbonates, formed by the dissolution of ^{14}C-free geological carbonates by slightly acidified waters by CO_2 from the atmosphere and from the degradation of the soil organic matter. In Fig. 4.7 the procedure to estimate the fraction of dead carbon (DCF) in a Bahamas speleothem, located in the western North Atlantic, is shown (Beck et al. 2001). To an U-Th age corresponds an atmospheric ^{14}C age in the calibration record. The DCF is calculated by subtracting the ^{14}C age of the speleothem to that of the contemporaneous atmosphere. In this example, the ^{14}C ages of the speleothem are older than those of the atmosphere at an average of about 1450 years between 11,000 cal. BP and 15,000 cal. BP, which corresponds to a DCF of 16%. This aging is not constant as a function of time and varies between 1000 years and 2000 years. These variations appear to be closely correlated to the climatic fluctuations recorded either in the Greenland ice-core GISP2 or in the marine varved sediments of the Cariaco Basin. About 30% of the variability of the DCF in this speleothem may be explained by such fluctuations by the way of changes of the local temperature and rainfall patterns.

The ^{14}C Exchanges in the Carbon Reservoirs

Radiocarbon is commonly used to test numerical simulations of the oceanic circulation in Ocean General Circulation Models (O-GCM) (Toggweiler et al. 1989; Key et al. 2004). The systematic measurements of the ^{14}C content of the dissolved inorganic carbon (DIC) in the different world ocean basins started with the international oceanographic campaigns GEOSECS (1972-1978), followed by WOCE (World Ocean Experiment, 1990–2002), and others (Broecker et al. 1995; Key et al. 1996). In addition to ^{14}C analyses, the physicochemical properties of the worldwide basin water masses were measured along depth profiles. Both the natural and anthropogenic components of the ^{14}C concentration in the oceans offer the opportunity to validate the general ocean circulation simulated by numerical models (Toggweiler et al. 1989; Key et al. 2004). The natural component tests the circulation of deep waters, while the anthropogenic component, resulting from the thermonuclear tests in the 1960s, allows the analysis of physical processes with time constants of a few decades, such as the formation of deep and intermediate waters and the ventilation of the thermocline (transition zone between the cold intermediate and deep waters and the warm surface waters). Because of radioactive decay, the ^{14}C content of an ocean water mass decreases during the oceanic transport, once the water mass is isolated from exchanges with the atmosphere.

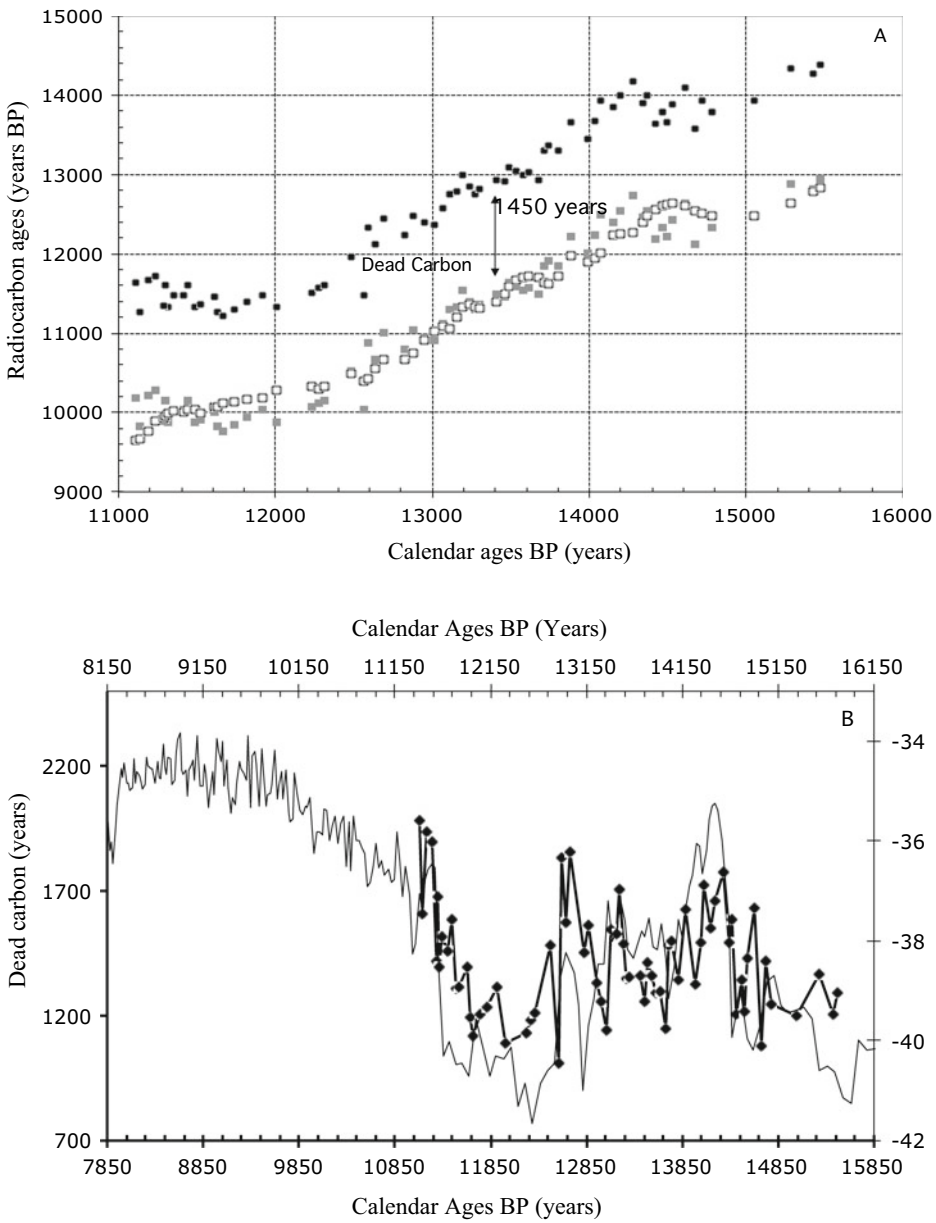

Fig. 4.7 Variations of the ^{14}C ages as a function of U-Th calendar ages from a Bahamas speleothem (Beck et al. 2001, Reimer et al. 2013). **a** The black squares represent the ^{14}C ages from the speleothem and the white squares to the ^{14}C ages of the speleothem adjusted onto the atmospheric calibration record (grey squares). The mean dead carbon age is 1450 years. **b** Comparison of the variations of dead carbon (bold line) (Paterne, unpublished) and of GISP 2 δ ^{18}O (Blunier et al. 1998)

The ^{14}C provides independent and additional constraints for ocean circulation models validation beside conventional tracers of the water masses (temperature, salinity), by allowing estimates of the time constants of the ocean ventilation.

Examples of Simulation of Modern Oceanic Circulation

Figure 4.8 represents the ^{14}C distribution simulated with the NEMO global ocean circulation model. The simulation is evaluated using the GEOSECS data (Broecker et al. 1995; Key et al. 1996). The model reproduces a realistic structure of the ventilation of the deep ocean producing concentrations similar to observations. In particular, the ventilation signature of the deep ocean associated with the Antarctic deepwater formation coming from the Southern Ocean (Antarctic Bottom Water AABW) is reproduced, characterized by high values of $\Delta^{14}C$ at the ocean floor.

The eastern Pacific is characterized by a thick water mass between 2000 m and 3500 m of almost homogeneous ^{14}C-depleted values at around −200 and −240‰. These deep waters correspond to the oldest deep waters of the world ocean with ^{14}C ages of 1790 years and 2200 years respectively.

The temporal changes of the sea surface ^{14}C may be measured from the annual growth bands of recent corals over

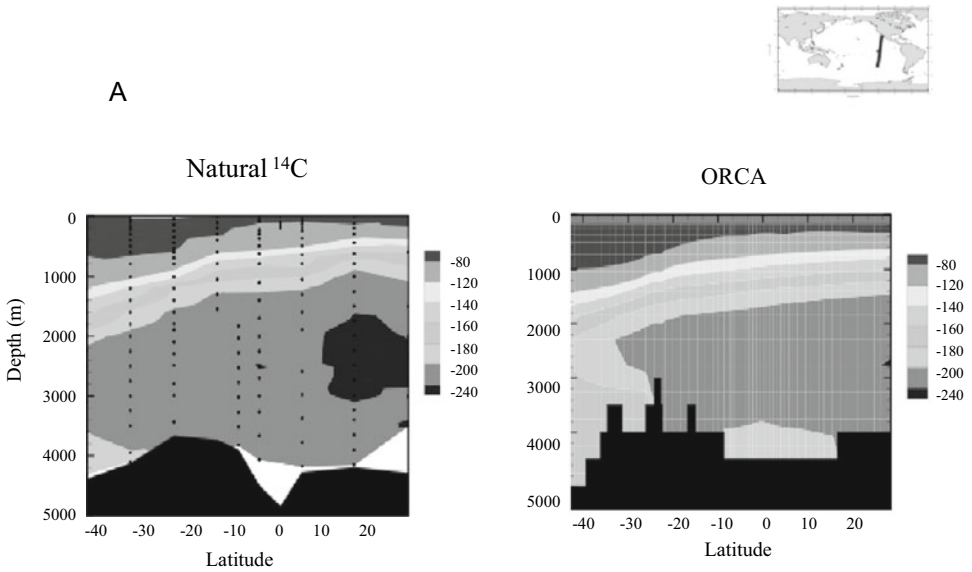

Fig. 4.8 Observed and simulated ^{14}C concentration (in ‰) in the eastern Pacific Ocean. The negative value indicates an aging of the water bodies compared with the age of the atmosphere. A decrease of 10‰ is equivalent to an aging of about 80 years. A mass of nearly homogeneous water between −200 and −240‰ occupies the eastern Pacific Ocean from depths between 2000 and 3500 m. At about 40 °S, the presence of a more recent water mass, between −180 and −200‰ at 4000 m depth, formed on the edge of the Antarctic continent should be noted. It corresponds to the Antarctic Bottom Water (AABW)

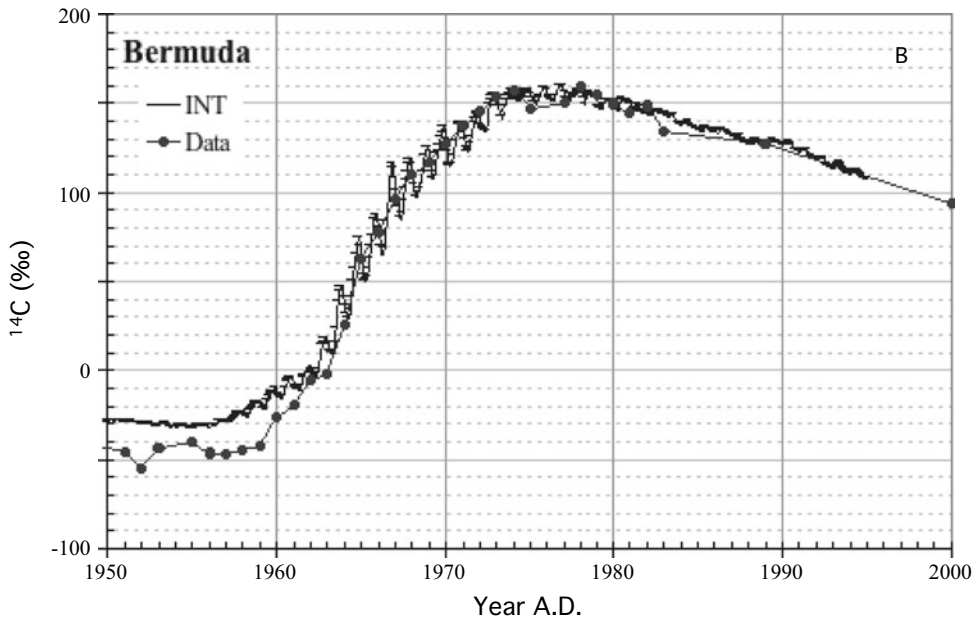

Fig. 4.9 Variations in Δ^{14}C in ‰ (circles) in a banded coral collected near Bermuda (Druffel 1989), in the subtropical surface waters of the North Atlantic between 1950 and 1990. Δ^{14}C increased rapidly between 1960 AD and 1965 AD due to the ^{14}C input into the atmosphere during the aerial nuclear bomb tests. Results of the interannual OPA simulation (INT) (8.1) are represented. This simulation highlights the importance of the winds in the atmosphere-ocean exchanges in the subtropical North Atlantic (Tisnérat, Dutay, personal communication)

several decades. These data provide additional validation of general circulation models, which, in turn, allow a better identification of the causes and mechanisms of the temporal variability of ^{14}C. Figure 4.9 represents the ORCA/IPSL model simulation of ^{14}C data measured in one coral from Bermuda shore (Druffel 1989).

Both the ^{14}C coral data and the modeled ^{14}C at the sea surface show coeval changes, indicating that the model

correctly reproduced the transfer of the tracer at the air-sea interface, as well as its penetration below the sea surface into the ocean.

Oceanic Paleocirculation

In the meantime, from the systematic ^{14}C measurements in the world ocean layers, the idea quickly emerged to recover past changes in ocean circulation from ^{14}C analyses of marine biocarbonates. The ^{14}C concentration of large volume samples such as corals and mollusks shells were first measured by radioactive decay measurements (Stuiver et al. 1986; Druffel 1989). This could be achieved for small volume samples with the new AMS ^{14}C technique. The planktonic and poorly abundant benthic foraminifera contemporaneously deposited in deep-sea sediment cores from different water-depths could henceforth be easily dated allowing the paleo-ventilation of the paleocean layers to be recovered to the limit of the ^{14}C dating (theoretically 10 times the half-life). Meantime the changes of the Earth's orbital parameters, and thus changes of the insolation, the atmospheric and oceanic circulation changes modulate the Earth's climate. Considerable efforts, compiled in (Zhao et al. 2018), have been made to measure the ^{14}C differences in the deep to surface ocean water masses in the past from benthic-planktonic foraminifera. Benthic corals have provided additional estimates of the deep $\Delta^{14}C$ as a function of calendar ages as they can be dated by both the U-Th and ^{14}C methods (Adkins et al. 1998; Goldstein et al. 2001; Robinson et al. 2005; Burke and Robinson 2012; Chen et al. 2015). Opposite results in the estimates of the paleo-ventilation of the ocean during the deglaciation emerged when using either the ^{14}C dating of paired benthic-planktonic foraminifera or paired ^{14}C/U-Th dating of benthic corals (Adkins et al. 1998; Goldstein et al. 2001; Robinson et al. 2005; Burke and Robinson 2012; Chen et al. 2015) or the paired atmospheric-marine ^{14}C dating from ash-layers (Sikes et al. 2000; Ikehara et al. 2011; Siani et al. 2013; Ezat et al. 2017). Values of $\Delta^{14}C$ are obtained from the absolute (calendar) age and the ^{14}C age (see Box 1). Thus the conflicting results are very likely related to the estimated $\Delta^{14}C$ from paired benthic-planktonic foraminifera due to (i) an incorrect estimate of the sea surface reservoir age subtracted to marine ^{14}C ages (in order to be referenced to calendar ages), (ii) the use of different atmospheric ^{14}C calibration records, notably the much smoother variations of ^{14}C in IntCal13 than those estimated in previous records (Reimer et al. 2013), (iii) the use of ^{14}C values of foraminifera picked in deep-sea sediment cores with a low sedimentation rate (see below: the bioturbation effects), and (iv) few planktonic foraminifera spend their entire life at the sea surface, and their ^{14}C content represents that of the upper ten to hundreds of meters of the water column in which they lived. More constraints on the changes of the sea surface reservoir ages allowing robust calculation of $\Delta^{14}C$ from benthic foraminifera and more ^{14}C analyses from deep sea corals will be very useful for model simulations of the oceanic circulation during the last glacial maximum and the deglaciation using three-dimensional models (Tagliabue et al. 2009). In the study by Zhao et al., (2018), the box model resolution, which should at least take into account the changing geometry of water masses in the last 25 kyr (Michel et al. 1995), is a limitation to estimate regional changes in paleoventilation.

Mineralization of Organic Matter in Soil

The contribution of soils and their role as sinks and sources in the global carbon cycle remain misunderstood until now. The stock of soil organic matter is defined as a balance between the input of organic matter through vegetation and the loss through microbial decomposition. The balance can be disrupted by changes in agricultural practices and climate variations. For instance, a temperature increase may clearly increase the activity of soil microorganisms and the subsequent soil organic matter mineralization. No consensus has however been reached on the relative importance of the various climatic factors that affect soil organic matter dynamics, such as temperature, aridity, land use. To better evaluate the effect of these disturbances on the global carbon cycle, it is essential not only to characterize soil carbon stocks but also soil carbon dynamics. To do so, ^{14}C is a powerful tool as it can be considered as a clock that registers the carbon residence time in the soil organic mixture (Scharpenseel and Shiffmann 1971; Balesdent and Guillet 1982).

Conceptual views of soil organic carbon dynamics have greatly evolved with time. Carbon sequestration was considered to be related to the chemical structure of the components (lignin having a longer mean residence time than sugar), to the accessibility of organic matter in aggregates (the higher the pore, the more labile the organic matter), to the affinity between organic matter and mineral surface (the stronger the bond, the more refractory the components) (Six et al. 2002). The conceptual view is still developing (Kleber et al. 2007) and ^{14}C brings powerful elements. ^{14}C measurement is thus done on bulk organic matter, on density fractions, on granulometric fractions, on molecular fractions and on molecules according to the process or to the turnover to be characterized.

Isotopic methods, such as dating by carbon-14, natural (percentage of plants in C3 and in C4) and artificial carbon-13 labeling are very powerful tools in so far as they make it possible to estimate the residence time of natural

organic matter in the soil. Instrumented monitoring of the ^{13}C content in experimental soil plots can be used to estimate the mean residence time from a few years to some decades. Many studies have been conducted since the beginning of the ^{14}C method (Balesdent and Guillet 1982; Gaudinsky et al. 2000). At first, they were carried out by radioactive counting measurements (a few grams of carbon), and then by mass spectrometry coupled to an accelerator (AMS), which did not allow the targeted molecular level to be reached, because a few milligrams of carbon were still required. Nevertheless, their scope was large, and they identified kinetic pools among the various elements of the soil's organic matter, in other words, compartments that can be defined by a specific carbon residence time. It has been shown that the residence time of different carbon compartments in soil can range from one to several decades or even to a few thousand years for the stable fraction.

Using the contamination of plant species by ^{14}C nuclear explosions in 1960 AD, Gaudinsky et al. (2000) modeled over time the ^{14}C activity of the different compartments of the soil receiving a constant organic input every year, according to their residence time (Fig. 4.10). The pool with a residence time of 10 years reached a maximum activity of ^{14}C in 1972, eight years after that recorded in the atmosphere. The one with a 50-year residence time recorded a maximum activity in 1985. Using the results of this modeling to interpret the measurements conducted on the separate fractions from the same soil, the residence time of the different fractions can be estimated. These, along with the relative weights of the different fractions, can then be used to characterize the dynamics of carbon of the soil and to assess carbon stocks over time.

It is important to keep in mind that whatever the fraction and since soil is the result of balance between input and output, the dated sample is always a mixture of components of different ^{14}C ages. The resulting ^{14}C is only a mean age of all components of different ^{14}C age. Likewise, it is important to remind that soil is alive and any molecule is recycled. It might reach the soil as vegetal sugar and as a source of energy for microbial life be bio-assimilated and metabolized into a microbial lipid. It will however keep the same ^{14}C signature of the original vegetal sugar. That's why a microorganism molecule can give its old ^{14}C age even if the microorganism is still alive. We definitively characterize the mean age of carbon and not the mean age of the molecule we analyzed.

Treatment of Samples and Calculations of ^{14}C Ages

Radiocarbon dating is based on either decay-counting from gas (CO_2, C_2H_2, C_6H_6) in proportional or liquid scintillation counters or atom-counting of ^{14}C, ^{13}C and ^{12}C from graphite targets by mass spectrometry (Accelerator mass spectrometry: AMS). The greatest advantage of the AMS technique is the very small sample size required, nowadays as small as a few tens of micrograms. At the end of the seventies, the

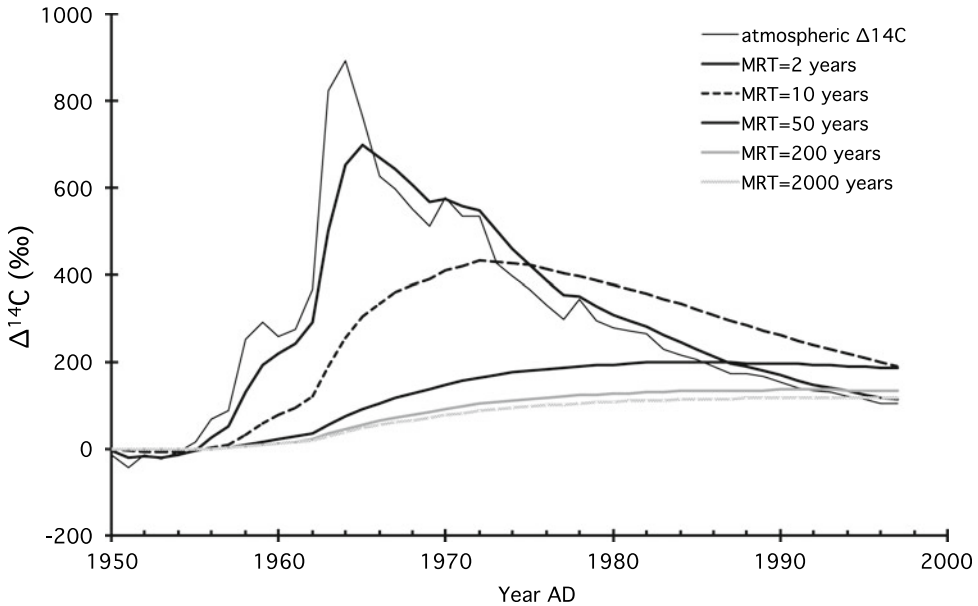

Fig. 4.10 ^{14}C activity in a soil with a constant annual supply of carbon over time, expressed as $\Delta^{14}C$ in ‰ (Gaudinsky et al. 2000). The thin black line represents the atmospheric ^{14}C activity in the northern hemisphere; the bold line represents that of the soil fractions with different mean residence time (MRT). We note that the peak of bomb detonations is clearly reflected in the more recent fractions (<10 years), while the effect is diluted in the fractions with MRT of a few decades. It is virtually nonexistent in older fractions

extracted ions from the graphite by a Cesium gun, were accelerated to a voltage difference of 2 MeV while the acceleration voltage is nowadays reduced at 0.5 MeV. The reader is referred to various publications and web descriptions on the equipment and measurement methods (Taylor et al. 1992).

Physical-Chemical Treatment

The samples are first cleaned by physicochemical treatments to eliminate contaminants. Vegetation samples collected in soils may include old carbonates and living rootlets, and the ^{14}C ages would thus increase or decrease respectively. After a visual examination, the organic remains (seeds, coal, plants) undergo the classic Acid-Alkali-Acid chemical treatment (noted AAA). The aim is to eliminate contaminants from bacterial decomposition of organic matter since the burial of the sample. Finally, CO_2 is obtained by burning the sample into an evacuated quartz sealed tube filled with copper oxide at about 800 °C. Carbonate samples (foraminifera, pteropods, corals, speleothems, earthworm granules) are examined under the microscope to check their homogeneity. Corals and mollusk shells are pre-cleaned by sand blasting to eliminate secondary calcite precipitation, which may lower the ^{14}C ages. All the carbonates are leached in a weak acid to remove surface contaminants before hydrolysis in a vacuum device. For AMS ^{14}C measurement, the obtained CO_2 is converted into graphite by metal catalysis (Tisnérat-Laborde et al. 2001; Hatté et al. 2003).

Determination of a ^{14}C Age

The ^{14}C age is obtained by comparing the activity of a sample to that of a standard reference, representative of the atmospheric ^{14}C content in 1950 (NBS-I; NBS-II; sucrose) regardless of the dating techniques. Chemicals as well as vacuum lines and counting devices are contaminated by modern $^{14}CO_2$ which has a $^{14}C/^{12}C$ ratio of 1.2×10^{-12} in 1950 AD. The effect of such a contamination on the ^{14}C ages of a 1 mg carbon sample may be estimated using a simple mixing equation. A ^{14}C age of 40,000 years ($^{14}C/C = 6.88 \times 10^{-15}$) would be lowered by 4300 years to 7200 years, due to a modern contamination of 5 µg to 10 µg, respectively. This emphasizes the importance of a careful cleaning of the sample. The same amounts of ^{14}C-free contaminants will have little effect: about 40 years and 80 years respectively regardless of the ^{14}C age of the sample.

The first ^{14}C dating of cave paintings revealed an age of about 31,000 years BP that deeply modified our understanding of how human art evolved (Valladas et al. 1992; Cuzange et al. 2007). Clearly, such old ages cannot be due to a contamination by the carbonates precipitate on cave walls, as was frequently hypothesized. To increase the ^{14}C age of a painting of 1 mg carbon and 15,000 years old, for example, to an age of about 33,000 years would require some 900 µg of ^{14}C-free contaminants, which is almost the entire sample and this would have been seen through visual examination.

The *internal* contamination of samples, due to the cleaning treatments, is carefully assessed by measuring the ^{14}C activity of an old (^{14}C-free) sample (blank), cleaned in a similar manner to samples of unknown ages. During a ^{14}C-AMS run of measurements, standard references, blank samples and the samples to date are inserted. The "blank" or "background" activity is subtracted from the activity of the sample of unknown age. The smaller the sample, the greater the effect of the *internal* contamination on the ^{14}C age. This contamination varies depending on the nature of the samples. Even if the blank activity is very low, its variability determines the accuracy of the ^{14}C age and the ^{14}C age limit. Consider two samples of carbonate and charcoal, with a $^{14}C/C$ activity of 6.88×10^{-15} (an age of 40,000 years BP) and an absolute error of 5%. The blank variability accounts for 25% and the subtracted blank value for the carbonate and charcoal is 5×10^{-16} and 19×10^{-16}, respectively. If the blank variability increases by a factor of 2, the ^{14}C age uncertainties will increase by 100 years for the carbonate and by 700 years for the charcoal, respectively. The precision of a ^{14}C age older than 30,000 years BP may be appreciably affected by a few thousand years when the blank activity is not well-estimated.

Some Examples of Post-depositional Disturbances of the ^{14}C Ages

The validity of the ^{14}C dating of climatic, archaeological or geological events depends, in many cases, of mechanical or biological disturbances of sedimentary deposits that may occur after the death and the burial of organisms. In archaeological sites, stratigraphic inversions of ^{14}C ages may be due to soils disturbances linked either to successive occupations by human and animals, or to wind and water effects, or both. The increasingly small size of ^{14}C-dated samples, which tend to migrate through the sedimentary deposits, favors such ^{14}C age inversions.

Archaeological sites contain numerous ^{14}C datable remains, such as mollusk shells, charcoals and bones. Researchers give priority to the ^{14}C dating of charcoals, because the ^{14}C dating of marine shells requires a correction of the reservoir ages to be compared with those of bone and vegetation samples. In a seaside Peruvian site, paired marine mollusk shells and charcoals were associated in several sediment layers to allow the sea surface reservoirs ages

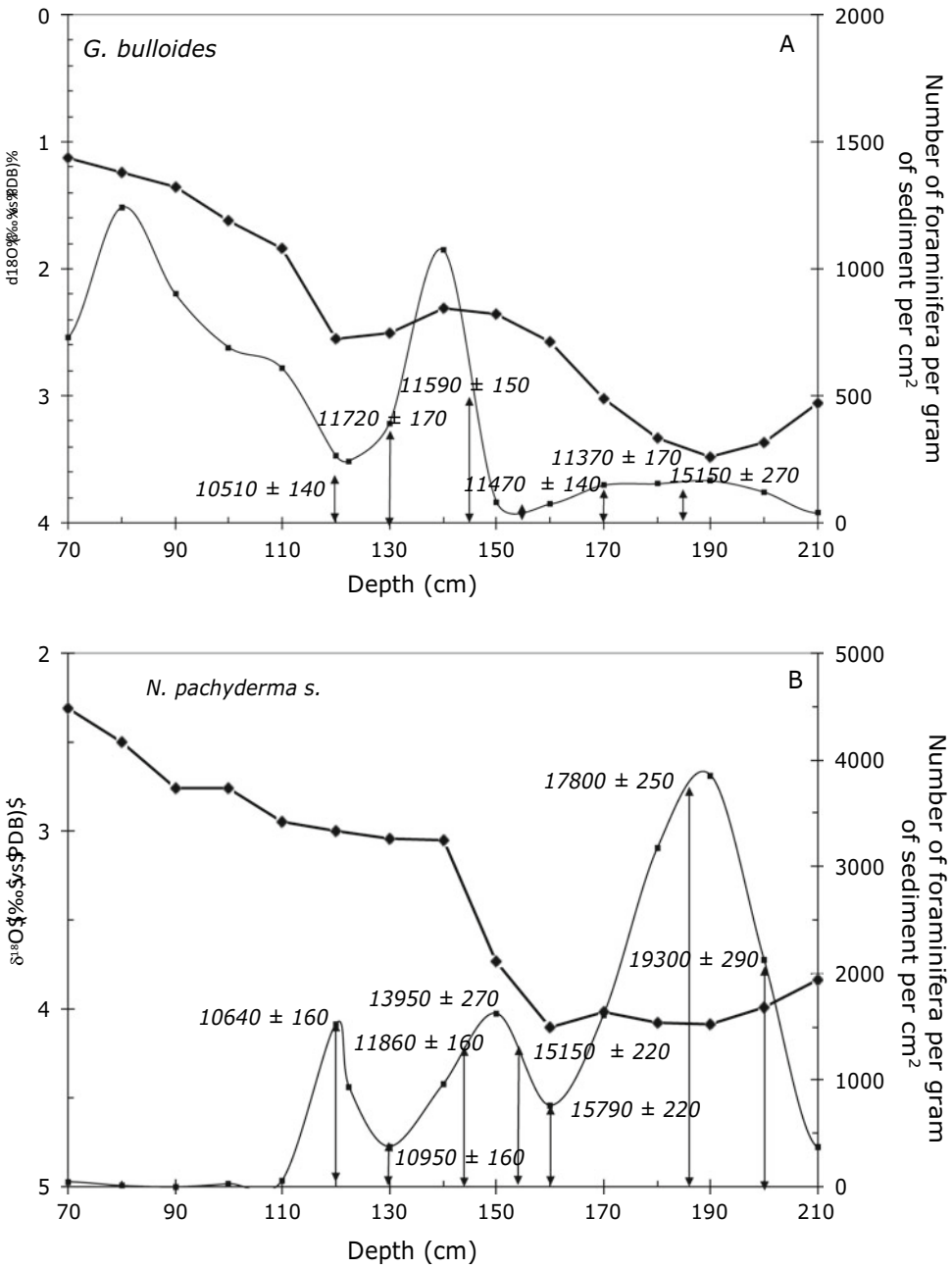

Fig. 4.11 Variations in the $\delta^{18}O$ (bold line and diamonds) and in the number of foraminifera per cm^2 and per gram of sediment (thin line): **a** for the subpolar planktonic foraminifera *Globigerina bulloides*; **b** for the polar planktonic foraminifera *Neogloboquadrina pachyderma sinistral* as a function of depth in a North Atlantic deep-sea sediment core. The ^{14}C ages at 1 sigma (in BP years) at the different depths (arrows) are shown (modified from Bard et al. 1987)

(R) during the Holocene (Kennett et al. 2002) to be quantified. While the modern value of R varies from 540 years to 970 years depending of the intensity of the Peruvian upwelling (the rise to the surface of ^{14}C-depleted intermediate and deep waters), it was slightly lower at 430 years between 5000 and 5300 cal BP and much lower at only 30 years between 5600 and 5900 cal BP. The much lower value of R is very unlikely, as charcoals and associated mollusk shells would have the same ^{14}C ages. This may be due to two phenomena: the charcoals originate from the burning of old trees at the time of burial (living over some hundred years) or the small charcoals migrated downwards in the archaeological layers. Only statistical analyses of the ^{14}C ages of charcoals and shells would enable a conclusion to be reached. This Peruvian study clearly emphasizes that charcoals are not always the best candidates in radiocarbon dating.

A second example is related to the ^{14}C dating of two species of planktonic foraminifera during the deglaciation in a North Atlantic deep-sea sediment core (Bard et al. 1987). The species are characteristic of the cold polar waters (*Neogloboquadrina pachyderma sinistral*) and of the warmer subpolar waters (*Globigerina bulloides*). It can be seen from Fig. 4.11 that the ^{14}C ages of *G. bulloides* are constant

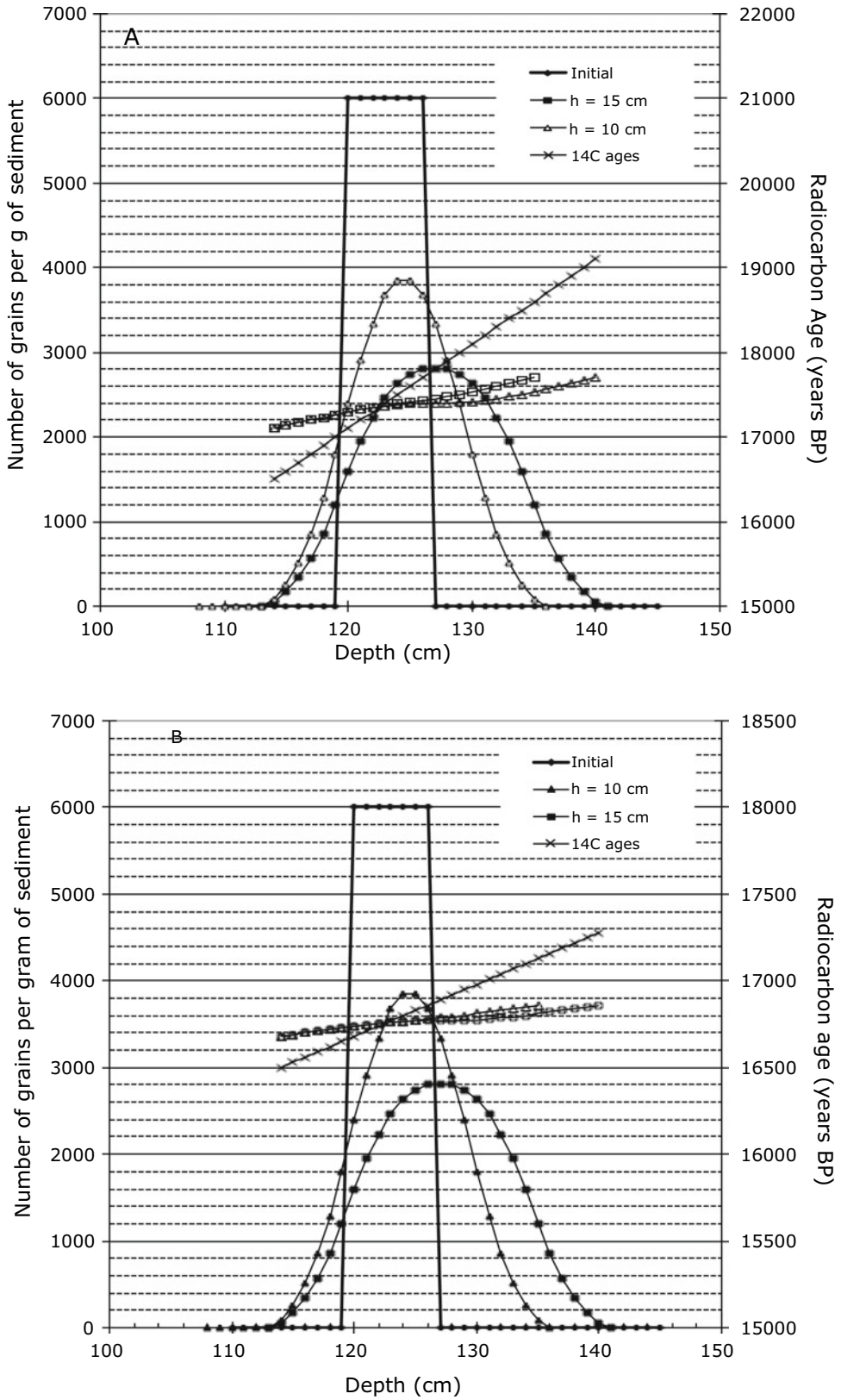

Fig. 4.12 Bioturbation effects on ^{14}C age of an event, observed in a deep sea sediment core with sedimentation rates of 10 cm/1000 years (**a**) and 30 cm/1000 years (**b**) using bioturbation depth (h) of 10 cm (black triangles) and 15 cm (black squares). The initial ^{14}C ages are plotted by crosses, and the resulting deviations from a bioturbation depth of 10 cm (white triangles) and 15 cm (white squares). Note the change of the ^{14}C age scales in **a** and **b**

between 170 cm and 140 cm, while those of *N. pachyderma* decreased. Moreover, the latter are much older than the subpolar species. The abundance of these species varies along core depth and peaks of abundance spreads over several tens of cm. The ^{14}C age distribution of the two species is due to bioturbation, a mixing process of sediment grains by benthic organisms, which move up and down through the sedimentary deposits. Applying a simple mixing filter of a constant thickness (h) over time, we can observe that the estimated abundance is lower than at the time of deposition. The abundance peak is no longer at its initial position in the sediment, and its position depends of the mixing depth (h) (Fig. 4.12). In the examples, the bioturbation effects on ^{14}C ages led to lower the ^{14}C age with respect to the 'real' ^{14}C age at the onset of the event. The effect is 900 and 1400 years depending on the *h* value with a sedimentation rate of 10 cm per 1000 years. A much higher sedimentation rate of 30 cm per 1000 years tends to lower the bioturbation effects as the ^{14}C ages decrease by 270 years and 420 years, with *h* equal to 10 cm and 15 cm respectively. The ^{14}C age of the end of the event increased by 600 years using a sedimentation rate of 10 cm per 1000 years. The higher the sedimentation rates, the lower the impact of bioturbation on the ^{14}C ages.

Accurate marine ^{14}C ages are obtained from the ^{14}C dating of foraminifera picked at the depth of maximum abundance in deep-sea cores with a high sedimentation rate. The example on Fig. 4.11 also emphasizes that the selected species must be in adequacy with the climatic period to be dated. The variability in the compiled deep and surface $\Delta^{14}C$ values in Zhao et al. (2018) may be partly explained by bioturbation and inadequately dated species.

References

Adkins, J. F., Cheng, H., Boyle, E. A., Druffel, E. R., & Edwards, R. L. (1998). Deep-sea coral evidence for rapid change in ventilation of the deep North Atlantic 15,400 years ago. *Science, 280,* 725–728.

Arnold, J. R., & Libby, W. F. (1949). Age determinations by radiocarbon content: Checks with samples of known Age. *Science, 110,* 678–680.

Ascough, P. L., Cook, G. T., & Dugmore, A. J. (2009). North Atlantic marine ^{14}C reservoir effects: Implications for late-Holocene chronological studies Quaternary. *Geochronology, 4,* 171–180.

Austin, W. E. N., Telford, R. J., Ninnemann, U. S., Brown, L., Wilson, L. J., Small, D. P., & Bryant, C. L. (2011). North Atlantic reservoir ages linked to high Younger Dryas atmospheric radiocarbon concentrations. *Global and Planetary Change, 79*, 226–233.

Balesdent, J., & Guillet, B. (1982). Les datations par le ^{14}C des matières organiques des sols. *Science du sol, 2,* 93–112.

Bard, E. (1988). Correction of accelerator mass spectrometry ^{14}C ages measured in planktonic foraminifera: Paleoceanographic implications. *Paleoceanography, 3,* 635–645.

Bard, E., Arnold, M., Duprat, J., Moyes, J., & Duplessy, J. C. (1987). Reconstruction of the last deglaciation: Deconvolved records of $\delta^{18}O$ profiles, micropaleontological variations and accelerator mass spectrometric ^{14}C dating. *Climate Dynamics, 1,* 101–112.

Bard, E., Arnold, M., Mangerud, J., Paterne, M., Labeyrie, L., Duprat, J., et al. (1994). The North Atlantic atmosphere-sea surface ^{14}C gradient during the Younger Dryas climatic event. *Earth and Planetary Science Letters, 126,* 275–287.

Bard, E., Hamelin, B., Fairbanks, R. G., & Zindler, A. (1990). Calibration of the ^{14}C timescale over the past 30,000 years using mass spectrometric U-Th ages from Barbados corals. *Nature, 345,* 405–410.

Beck, J. W., Richards, D. A., Edwards, R. L., Bernard, W., Silverman, B. W., Smart, P. L., et al. (2001). Extremely large variations of atmospheric C-14 concentration during the last glacial period. *Science, 292,* 2453–2458.

Blunier, T., Chappellaz, J., Schwander, J., Dällenbach, A., Stauffer, B., Stocker, T., et al. (1998). Asynchrony of Antarctic and Greenland climate change during the last glacial period. *Nature, 394,* 739–743.

Bondevik, S., Mangerud, J., Birks, H. H., Gulliksen, S., & Reimer, P. (2006). Changes in North Atlantic radiocarbon reservoir ages during the Allerød and Younger Dryas. *Science, 312,* 1514–1517.

Broecker, W. B. F. (1998). Paleocean Circulation During the Last Deglaciation: A Bipolar Seesaw. *Paleoceanography, 13,* 119–121.

Broecker, W. S., & Olson, E. A. (1959). Lamont radiocarbon measurements VI. *American Journal of Science. Radiocarbon Supplement, 1,* 111–132.

Broecker, W. S., Sutherland, S., Smethie, W., Peng, T. S., & Ostlund, G. (1995). Oceanic radiocarbon: Separation of the natural and bomb component. *Global Biogeochemical Cycles, 9,* 263–288.

Burke, A., & Robinson, L. F. (2012). The Southern Ocean's role in carbon exchange during the last deglaciation. *Science, 335,* 557–561.

Chen, T., Robinson, L. F., Burke, A., Southon, J., Spooner, P., Morris, P. J., et al. (2015). Synchronous centennial abrupt events in the ocean and atmosphere during the last deglaciation. *Science, 349* (6255), 1537–1541.

Chiu, T. C., Fairbanks, R. G., Cao, L., & Mortlock, R. A. (2007). Analysis of the atmospheric C-14 record spanning the past 50 000 years derived from high-precision Th-230/U-234/U-238, Pa-231/U-235 and C-14 dates on fossil corals. *Quaternary Science Review, 26,* 18–36.

Currie, L. A. (2004). The remarkable metrological history of radiocarbon dating. *Journal of Research of the National Institute of Standards and Technology, 109,* 185–217.

Cuzange, M. T., Delque-Kolic, E., Goslar, T., Grootes, P. M., Higham, T., Kaltnecker, E., et al. (2007). Radiocarbon intercomparison program for the chauvet cave. *Radiocarbon, 49,* 339–347.

Damon, P. E., Lerman, J. C., & Long, A. (1978). Temporal fluctuations of atmospheric ^{14}C: Causal factors and implications. *The Annual Review of Earth and Planetary Sciences, 6,* 457–494.

Damon, P. E., & Peristykh, A. N. (2000). Radiocarbon calibration and application to geophysics, solar physics, and astrophysics. *Radiocarbon, 42,* 137–150.

Druffel, E. R. M. (1989). Decade time scale variability of ventilation in the North Atlantic: High-precision measurements of bomb radiocarbon in banded corals. *Journal of Geophysical Research, 94,* 3271–3285.

Engelkemeir, A., Hamill, W. H., Inghram, M. G., & Libby, W. F. (1949). The half-life of radiocarbon (^{14}C). *The Physical Review, 75,* 1825–1833.

Ezat, M. M., Rasmussen, T. L., Thornalley, D. J. R., Olsen, J., Skinner, L. C., Hönisch, B., et al. (2017). Ventilation history of Nordic Seas over-flows during the last (de)glacial period revealed by species-specific benthic foraminiferal ^{14}C dates. *Paleoceanography, 32,* 172–181.

Friedrich, W. L., Kromer, B., Friedrich, M., Heinemeier, J., Pfeiffer, T., & Talamo, S. (2006). Santorini eruption radiocarbon dated to 1627–1600 BC. *Science, 312,* 548.

Gaudinsky, J. B., Trumbore, S., Davidson, E. A., & Zheng, S. (2000). Soil carbon cycling in a temperate forest: Radiocarbon-based estimates of residence times, sequestration rates and partitioning of fluxes. *Biogeochemistry, 51,* 33–69.

Godwin, H. (1962). Half-life of radiocarbon. *Nature, 195,* 984.

Goldstein, S. J., Lea, D. W., Chakraborty, S., Kashgarian, M., & Murrell, M. T. (2001). Uranium-series and radiocarbon geochronology of deep-sea corals: Implications for Southern Ocean ventilation rates and the oceanic carbon cycle. *Earth and Planetary Science Letters, 193,* 167–182.

Hatté, C., Poupeau, J. J., Tannau, J. F., & Paterne, M. (2003). Development of an automated system for preparation of organic samples. *Radiocarbon, 45*(3), 421–430.

Hughen, K. A., Overpeck, J. T., Lehman, S. J., Kashgarian, M., Southon, J., Peterson, L. C., et al. (1998). Deglacial changes in ocean circulation from an extended radiocarbon calibration. *Nature, 391,* 65–68.

Ikehara, K., Danhara, T., Yamashita, T., Tanahashi, M., Morita, S., & Ohkushia, K. (2011). Paleoceanographic control on a large marine reservoir effect offshore of Tokai, south of Japan, NW Pacific, during the last glacial maximum-deglaciation. *Quaternary International, 246,* 213–221.

Kamen, M. D. (1963). Early history of carbon-14. *Science, 140,* 584–590.

Kennett, D. J., Ingramm, L. B., Southon, J. R., & Wise, K. (2002). Differences in ^{14}C age between stratigraphically associated charcoal and marine shell from the archaic period site of kilometer 4, Southern Peru: Old wood or old water? *Radiocarbon, 44,* 53–58.

Key, R. M., Kozyr, A., Sabine, C. L., Lee, K., Wanninkhof, R., Bullister, J. L., Feely, R. A., Millero, F. J., Mordy, C., & Peng, T.H. (2004). A global ocean carbon climatology: Results from Global Data Analysis Project (GLODAP). *Global Biogeochemical Cycles, 18,* GB4031. https://doi.org/10.1029/2004gb002247.

Key, R. M., Quay, P. D., Jones, G. A., McNichol, A. P., von Reden, K. F., & Schneider, R. J. (1996). WOCE AMS radiocarbon I: Pacific ocean results; P6, P16 & P17. *Radiocarbon, 38,* 425–518.

Kleber, M., Sollins, P., & Sutton, R. (2007). A conceptual model of organo-mineral interactions in soils: self-assembly of organic molecular fragments into zonal structures on mineral surfaces. *Biogeochemistry, 85,* 9–24.

Korff, S. A. (1951). Cosmic-ray neutrons. *American Journal of Physics, 19,* 226–229.

Lal, D., & Charles, C. (2007). Deconvolution of the atmospheric radiocarbon record in the last 50,000 years. *Earth and Planetary Science Letters, 258,* 550–560.

Libby, W. F. (1934). Radioactivity of neodymium and samarium. *Physical Review, 45,* 196–204.

Libby, W. F. (1952). *Radiocarbon dating* (Vol. 37, 124 p.). Chicago, IL: The University of Chicago Press.

Libby, W. F. (1964). *Radiocarbon dating*. Nobel Lecture 12 December 1960. Nobel Lectures, Chemistry 1942–1962, Amsterdam: Elsevier Publishing Company.

Libby, W. F. (1981). In R.Berger & L. M. Libby (Eds.), *Radiocarbon and tritium* (Vol. I, 300 p.). Ocean Way Santa Monica, CA: 129 Geo Science Analytical Inc., 90402.

Michel, E., Labeyrie, L. D., Duplessy, J.-C., Gorfti, N., Labracherie, M., & Turon, J.-L. (1995). Could deep Subantarctic convection feed the world deep basins during the Last Glacial Maximum? *Paleoceanography, 10,* 927–942.

Muscheler, R., Joos, F., Müller, S. A., & Snowball, I. (2005). Climate: How unusual is today's solar activity? *Nature, 436,* E3–E4.

Olsson, I., Kaplen, I., Turnbull, A. H., & Prosser, N. J. D. (1962). Determination of the half-life of ^{14}C with a proportional counter. *Arkiv för fysik, 14,* 237–255.

Olsson, I., & Osadebe, F. (1974). Carbon isotope variations and fractionation corrections in ^{14}C dating. *Boreas, 3,* 139–146.

Reimer, P. J., Bard, E., Bayliss, A., Beck, J. W., Blackwell, P. G., Bronk Ramsey, C., et al. (2013). IntCal13 and Marine13 radiocarbon age calibration curves 0–50,000 years cal BP. *Radiocarbon, 55,* 1869–1887.

Robinson, L. F., Adkins, J. F., Keigwin, L. D., Southon, J., Fernandez, D. P., Wang, S., et al. (2005). Radiocarbon variability in the western North Atlantic during the last deglaciation. *Science, 310,* 1469–1473.

Rossi, B. (1952). *High Energy Particles* (p. 268). Englewood cliffs, NJ: Prentice Hall Physics series Inc.

Ruben, S., Kamen, M. D., & Hassid, W. (1949). Photosynthesis with radioactive carbon: II. Chemical properties of the intermediates. *Journal of the American Chemical Society, 62,* 3443–3450.

Scharpenseel, H. W., & Shiffmann, H. (1971). Radiocarbon dating of soils, a review. *Zeitschrift für Planzenernähring, Düngung, Bodenkunde, 140,* 159–174.

Siani, G., Michel, E., De Pol-Holz, R., Tim DeVries, T., Lamy, F., Carel, M., et al. (2013). Carbon isotope records reveal precise timing of enhanced Southern Ocean upwelling during the last deglaciation. *Nature Communications, 4,* 2758. https://doi.org/10.1038/ncomms3758.

Siani, G., Paterne, M., Arnold, M., Bard, E., Métivier, B., Tisnerat, N., et al. (2000). Radiocarbon reservoir ages in the Mediterranean Sea and Black Sea. *Radiocarbon, 42*(2), 271–280.

Siani, G., Paterne, M., Michel, E., Sulpizio, R., Sbrana, A., Arnold, M., & Haddad, G. (2001). Mediterranean Sea surface radiocarbon reservoir age changes since the last glacial maximum. *Science, 294,* 1917–1920.

Sikes, E. L., & Guilderson, T. P. (2016). Southwest Pacific Ocean surface reservoir ages since the last glaciation: Circulation insights from multiple-core studies. *Paleoceanography, 31,* 298–310.

Sikes, E. L., Samson, C. R., Guilderson, T. P., & Howard, W. R. (2000). Old radiocarbon ages in the southwest Pacific Ocean during last glacial period and deglaciation. *Nature, 405,* 555–559.

Simpson, J. A. (2000). The cosmic ray nucleonic component: The invention and scientific uses of the neutron monitor. *Space Science Reviews, 93,* 11–32.

Six, J., Conant, R. T., Paul, A., & Paustian, K. (2002). Stabilization mechanisms of soil organic matter: Implications for C-saturation of soils. *Plant and Soil, 241,* 155–176.

Stenström, K. E., Skog, G., Georgiadou, E., Genberg, J., & Johansson, A. (2011). A guide to radiocarbon units and calculations. International Report LUNFD6 (NFFR-3111), Lund University, 1–17.

Stuiver, M., Braziunas, T. F., Becker, B., & Kromer, B. (1991). Climatic, Solar, Oceanic and Geomagnetic Influences on Late-Glacial and Holocene Atmospheric $^{14}C/^{12}C$ Change. *Quatemary Research, 35,* 1–24.

Stuiver, M., Pearson, G. W., & Braziunas, T. (1986). Radiocarbon age calibration of marine samples back to 9000 cal yr bp. *Radiocarbon, 28,* 980–1021.

Stuiver, M., & Polach, H. A. (1977). Reporting of ^{14}C. *Radiocarbon, 19,* 355–363.

Tagliabue, A., Bopp, L., Roche, D. M., Bouttes, N., Dutay, J.-C., Alkama, R., et al. (2009). Quantifying the roles of ocean circulation and biogeochemistry in governing ocean carbon-13 and atmospheric carbon dioxide at the last glacial maximum. *Climate of the Past, 5,* 695–706.

Taylor, R. E. (1987). *Radiocarbon dating: An archeological perspective* (212 p.). London: Academic Press Inc. Ltd.

Taylor, R. E., Long, A., & Kra, R. S. (1992). *Radiocarbon after four decades. An interdisciplinary perspective* (596 p.). New York: Springer.

Thornalley, D. J. R., McCave, N., & Elderfield, H. (2011). Tephra in deglacial ocean sediments south of Iceland: Stratigraphy, geochemistry and oceanic reservoir ages. *Journal of Quaternary Science, 26,* 190–198.

Tisnérat-Laborde, N., Paterne, M., Métivier, B., Arnold, M., Yiou, P., Blamart, D., et al. (2010). Variability of the northeast Atlantic sea surface $\Delta^{14}C$ and marine reservoir age and the North Atlantic Oscillation (NAO). *Quaternary Science Reviews, 29,* 2633–2646.

Tisnérat-Laborde, N., Poupeau, J. J., Tannau, J. F., & Paterne, M. (2001). Development of a semi-automated system for routine preparation of carbonate sample. *Radiocarbon, 43,* 299–304.

Toggweiler, J. R., Dixon, K., & Bryan, K. (1989). Simulations of radiocarbon in a coarse-resolution world ocean model. 1. Steady state prebomb distributions. *Journal of Geophysical Research, 94*, 8217–8242.

Valladas, H., Cachier, H., Maurice, P., De Quirost, F. B., Clottes, J., Valdes, V. C., et al. (1992). Direct radiocarbon dates for prehistoric paintings at the Altamira, El Castillo and Niaux caves. *Nature, 357,* 68–70.

Zhao, N., Marchal, O., Keigwin, L., Amrhein, D., & Gebbie, G. (2018). A synthesis of deglacial deep-sea radiocarbon records and their (in) consistency with modern ocean ventilation. *Paleoceanography and Paleoclimatology, 33,* 128–151.

The $^{40}K/^{40}Ar$ and $^{40}Ar/^{39}Ar$ Methods

5

Hervé Guillou, Sébastien Nomade, and Vincent Scao

The $^{40}K/^{40}Ar$ method and its variant, $^{40}Ar/^{39}Ar$, are based on the natural radioactive decay of ^{40}K, one of the isotopes of potassium, in ^{40}Ar, one of the isotopes of argon. ^{40}K decreases in $^{40}Ar^{*}$ (the * symbol indicates that this is a radiogenic isotope) with a period of 1.25×10^{9} years, according to the law of radioactive decay $N = N_0\ e^{-\lambda t}$. In other words, if we consider a closed system, containing at an initial time (t_0) N_0 atoms of ^{40}K, then $N_0/2$ atoms of ^{40}K will remain in the system after 1.25×10^{9} years. This gives us an indication of the geochronological application. If, in a geological sample, both the number of parent atoms remaining (^{40}K) and the number of daughter atoms formed ($^{40}Ar^{*}$) can be measured, then it is possible to calculate the age of formation of this sample. The relatively high abundance of the isotope ^{40}K (K is the seventh most abundant element on Earth), combined with a low decay rate, makes the $^{40}K/^{40}Ar$ method and its variant $^{40}Ar/^{39}Ar$ two of the most widely used geochronological tools in Earth Sciences. They are applicable to various geological materials and cover a wide range of ages, given the long period of ^{40}K.

Already in 1921, Aston, using a mass spectrograph, proved the existence of two isotopes of potassium (^{39}K and ^{41}K). In 1935, Klemperer, and also Neuman and Walker, experimentally demonstrated the natural radioactive decay of ^{40}K to ^{40}Ca and $^{40}Ar^{*}$. In 1948, Aldrich and Nier confirmed the radiogenic origin of argon $^{40}Ar^{*}$. They experimentally determined the $^{40}Ar/^{36}Ar$ ratio of several potassic minerals and compared it to that of the atmosphere, assuming it to be constant and equal to 298.56 (this updated value, determined by Lee et al. (2006), replaces the previous one of 295.5 established by Steiger and Jäger (1977)). As the ratios obtained were superior to that of the atmosphere, the source of argon $^{40}Ar^{*}$ by radioactive decay of ^{40}K was demonstrated. In parallel, understanding of the decay constant of ^{40}K became more accurate. Aldrich and Nier could therefore see the potential of the $^{40}K/^{40}Ar$ pair for the dating of rocks.

The K-Ar clock is based on the principles of radioactive decay and the accumulation of a daughter isotope. However, studies subsequent to Aldrich and Nier's work showed that there were many causes of disturbance in the K/Ar clock. Among these are the inability of certain rocks or minerals to retain all of the radiogenic argon-40 ($^{40}Ar^{*}$), or the presence of 'excess argon' in some samples. Consequently, for a K-Ar age to be accepted as correct, the following must be true:

1. when starting the clock (at time zero t_0), the $^{40}Ar/^{36}Ar$ ratio in the sample is the same as that of the atmosphere (298.56), in other words that $^{40}Ar^{*} = 0$;
2. and between t_0 and the moment the sample is dated, it behaves as a closed system with regard to ^{40}K and ^{40}Ar.

The conventional K/Ar method does not allow verification of these two major assumptions. To remedy this, the $^{40}Ar/^{39}Ar$ variant was developed by Wänke and König (1959) and Merrihue (1965), which showed that the $^{40}K/^{40}Ar$ ages can be obtained by irradiating samples of rocks or minerals. When a sample is subjected to a neutron flux in a reactor, some ^{39}K becomes ^{39}Ar. The measurement of the ^{39}Ar content by a counting method calculates the number of parent atoms (^{40}K) remaining in the sample, since we know the relative abundances of different isotopes of potassium (see below). Using the same counting method, the number of ^{40}Ar isotopes present in the sample can also be measured. However, this approach is unsatisfactory because it does not allow for necessary corrections related to the process of irradiation to be made, as we shall see later, and the precision achieved on the different concentrations of argon isotopes is insufficient. The crucial work for the $^{40}Ar/^{39}Ar$ method was carried out by Merrihue in 1965. He showed that the argon ^{39}Ar generated in a nuclear reactor from the ^{39}K of a sample can be measured precisely by mass spectrometry. This ^{39}Ar, derived from the ^{39}K, is annotated as $^{39}Ar_K$. In addition, the other isotopes of argon, ^{40}Ar and

H. Guillou (✉) · S. Nomade · V. Scao
Laboratoire des Sciences du Climat et de l'Environnement, LSCE/IPSL, CEA-CNRS-UVSQ, Université Paris-Saclay, 91190 Gif-sur-Yvette, France
e-mail: herve.guillou@lsce.ipsl.fr

G. Ramstein et al. (eds.), *Paleoclimatology*, Frontiers in Earth Sciences,
https://doi.org/10.1007/978-3-030-24982-3_5

^{36}Ar (essential for the atmospheric correction and $^{40}Ar^{*}$ content calculation) can be measured in the same way. Thus, in a single measurement, one can calculate the proportions of ^{40}K and $^{40}Ar^{*}$ present in a sample, and from this, calculate its age. In their 1966 article, Merrihue and Turner established the fundamentals in terms of approach and concepts for the $^{40}Ar/^{39}Ar$ method. In particular, they showed that the relative proportions of radioactive parents and radiogenic daughters can be calculated accurately from a measurement by mass spectrometry.

In addition, since isotopic ratios can be measured more precisely than the concentrations of K and Ar, this method improves the accuracy of the ages and can be used for dating smaller samples than the $^{40}K/^{40}Ar$ method does. This same work laid the groundwork for the application of isochrones and age spectra (concepts that will be discussed below) to the $^{40}Ar/^{39}Ar$ method.

The $^{40}K/^{40}Ar$ and $^{40}Ar/^{39}Ar$ methods became very popular in geology as they are applicable to different terrestrial geological materials, such as terrestrial magmatic rocks (volcanic, plutonic, metamorphic) and extraterrestrial (meteorites, moon samples) ones. For some measurements, the $^{40}K/^{40}Ar$ method is also well suited to the dating of clay minerals. The range of application of these isotopic age dating methods has an upper limit of 3 billion years and a lower limit of 10,000 years.

These two methods were used to date major events in the history of the Earth (fauna and flora of the Mesozoic and Cenozoic, mass extinctions, origin and evolution of hominids, major volcanic eruptions, genesis and evolution of the large mountain chains, etc.). They were, and still are, used to establish and calibrate the geological time scale, including the time scale of the reversals of Earth's magnetic field, very useful tie-points in paleoclimatology.

In the following, we present the main principles and areas of application of these two methods. For further details, the reader may refer to the works of Dalrymple and Lanphere (1969) and McDougall and Harrison (1988).

Principles of the K-Ar Method

Diagram of Radioactive Decay in ^{40}K

The principle of the $^{40}K/^{40}Ar$ method is based on the natural radioactive decay of ^{40}K in ^{40}Ar (Fig. 5.1). The decay of ^{40}K is complex. At 88.8%, the ^{40}K decays to ^{40}Ca by emitting β^{-}. At 11.2% it decays to $^{40}Ar^{*}$, either by emitting β^{+} (0.01%), or by direct electronic capture (0.16%) or by electron capture followed by a γ emission (11%). This last mechanism is the most common. An electron from the atom is captured, resulting in the formation of a neutron at the expense of a proton. The ^{40}Ar atom thus produced is in an excited state. It then returns quickly to its ground state by emitting gamma radiation.

The Age Equation

As with the other isotopic clocks, the fundamental law of radioactive decay applies:

$$N = N_0 e^{-\lambda t} \tag{5.1}$$

N: number of radioactive parent atoms (^{40}K) at time t, N_0: number of radioactive parent atoms at t_0, λ: decay constant.

From Eq. (5.1), we can calculate the number of daughter atoms (D^{*} = ^{40}K + ^{40}Ca) formed over time t:

$$N_o = N e^{\lambda t}$$

$$D^{*} = N_o - N = N e^{\lambda t} - N = N\left(e^{\lambda t} - 1\right) \tag{5.2}$$

The constants and isotopic abundances required for the age calculation are listed in Table 5.1.

The age equation is established from Eq. (5.2):

$$^{40}Ar^{*} = \frac{\lambda_\epsilon}{\lambda} {}^{40}K\left(e^{\lambda t} - 1\right) \tag{5.3}$$

where $^{40}Ar^{*}$ is the isotope of argon produced from the in situ decay of ^{40}K, λ the total radioactive decay constant of ^{40}K equal to $\lambda_\varepsilon + \lambda_\beta$. The ratio of proportionality $\frac{\lambda_\epsilon}{\lambda}$ corresponds to the fraction of the decay leading to the formation of $^{40}Ar^{*}$ (and not of $^{40}Ca^{*}$).

From Eq. (5.3) we get:

$$t = \frac{1}{\lambda} \ln\left(\frac{^{40}Ar^{*}}{^{40}K} \frac{\lambda}{\lambda_\epsilon} + 1\right) \tag{5.4}$$

with t expressed in years.

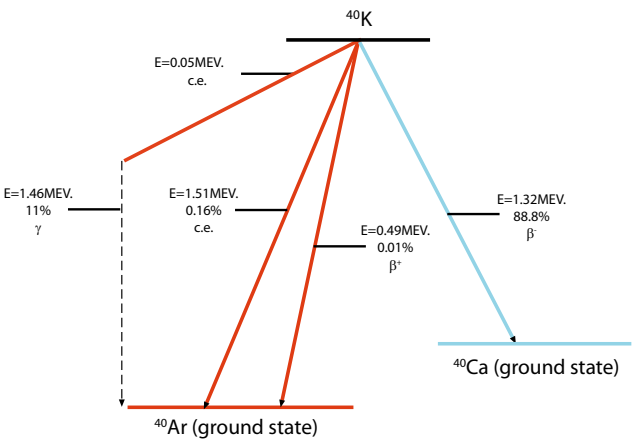

Fig. 5.1 Diagram of radioactive decay of ^{40}K

Table 5.1 Decay constants of ^{40}K and isotopic abundances of K and Ar. The values attributed to the constants were determined by Min et al. (2000), and for isotopic ratios by Garner et al. (1975) and Nier (1950)

Constant	Value
$\lambda_\varepsilon = \lambda^{40}Ar$	$(5.80 \pm 0.014) \times 10^{-11}$ a^{-1}
$\lambda_\beta = \lambda^{40}Ca$	$(4.884 \pm 0.099) \times 10^{-10}$ a^{-1}
$\lambda = \lambda_\varepsilon + \lambda_\beta$	$(5.464 \pm 0.107) \times 10^{-10}$ a^{-1}
^{39}K	93.2581%
^{40}K	0.01167%
^{41}K	6.7302%
^{40}Ar	99.600%
^{38}Ar	0.0632%
^{36}Ar	0.3364%

The half-life period ($N = N_0/2$) T is calculated from (5.1):

$$T = \frac{\ln 2}{\lambda} = 1.25 \times 10^9 \text{ years.}$$

Operation of the Potassium-Argon Clock

The radioactive clock $^{40}K/^{40}Ar$ is based on the process of accumulation. K is one of the components of magma. When this is in liquid form, the argon $^{40}Ar^*$ formed from the decay of ^{40}K escapes from the system. During a volcanic eruption, the magma that reaches the surface cools very quickly. Thus, argon $^{40}Ar^*$ is trapped in the solidified lava and accumulates in the crystalline lattice. The radiogenic argon ($^{40}Ar^*$) thus trapped can only escape if the rock or mineral are either melted or recrystallized, or heated to temperatures generally greater than or equal to 200 °C, in such a way that the argon can diffuse through the crystal lattice. Dalrymple and Lanphere (1969) illustrated the operation of the $^{40}K/^{40}Ar$ clock (Fig. 5.2) in a diagram, taking the crystallization of magma as an example. Ideally, there are three distinct stages. During the first stage, at high temperatures, the phenomenon of diffusion prevails. $^{40}Ar^*$ is not retained in the lattice. The second stage corresponds to a start of cooling and partial accumulation of the argon $^{40}Ar^*$. The last step corresponds to the rapid cooling of the surface of the silicate or magmatic melt. At this point, $^{40}Ar^*$ is retained entirely within the crystal lattice.

From this evolution came the basic assumptions for the application of the K-Ar clock which are detailed below.

1. The parent isotope ^{40}K decays at a constant rate, independently of the physical conditions of the system (P and T). The constants used are those in Table 5.1.
2. The $^{40}K/K_{total}$ ratio is constant in natural materials. This condition is important because it is not ^{40}K that is directly measured, but the total K (K-Ar) or $^{39}Ar_K$ ($^{40}Ar/^{39}Ar$). ^{40}K is deduced from the isotopic composition of K. This ratio has changed over time due to radioactive decay, but this term is not included in the age equation. At a given t, this ratio is constant in all materials because these isotopes do not fractionate as a result of the geological processes.
3. We consider that at $t = 0$, the moment of formation of the sample, it is devoid of radiogenic argon ($^{40}Ar^* = 0$); otherwise, ages obtained would be marred by an error of excess argon. In geochronology, this is the same as assuming that at $t = 0$, the $^{40}Ar/^{36}Ar$ ratio of the sample, called the initial ratio, is considered to be equal to that of the atmosphere, or 298.56. There are some deviations from this principle. These are cases of excess argon or inherited argon, which cannot be directly detected by the K-Ar method, but can be detected more easily by the $^{40}Ar/^{39}Ar$ method. These excesses of argon show up as an overestimation of the calculated ages and are an important limitation of the K-Ar method.
4. It is also necessary that the formation time of the system be negligible compared to the age of the sample. Therefore, volcanic rocks that form by very rapid cooling provide the most suitable samples for this method of dating.
5. It is essential to assume that the sample evolved within a closed system with regard to K and Ar ever since the geological event to be dated. This condition involves rigorously selecting unaltered samples, in order to avoid any disruption (re-opening subsequent to formation) in the isotopic system.

Datable Materials and Age Ranges

The main materials suitable for testing by the K-Ar and $^{39}Ar/^{40}Ar$ methods as well as the age ranges are listed below in Fig. 5.3:

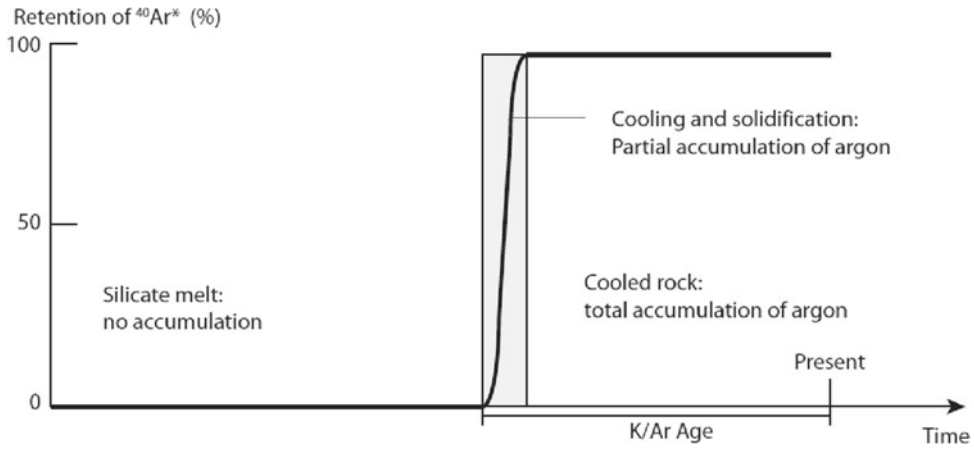

Fig. 5.2 Principle of the $^{40}K/^{40}Ar$ clock in the case of a simple-story magmatic rock (from Dalrymple and Lanphere 1969)

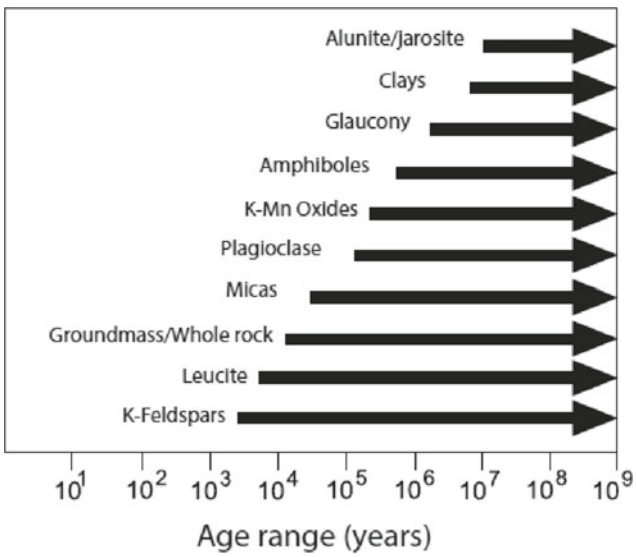

Fig. 5.3 Applicable age range of K-Ar and $^{40}Ar/^{39}Ar$ dating for various materials (from Renne 2000)

- volcanic rocks (calibration of time scales, stratigraphic studies); minerals: sanidine ($\geq$2 ka) anorthoclase ($\geq$5 ka), plagioclase ($\geq$200 ka), amphibole ($\geq$1 Ma), leucite, nepheline;
- rocks (lava and tephra): mesostasis (groundmass) of all types of unaltered rock ($\geq$3 4 ka), non-hydrated glass ($\geq$300 ka);
- plutonic rocks, metamorphic minerals; potassic feldspar, plagioclase, biotite, amphibole, muscovite, phengite, alunite, adularia;
- sediments; neoformed clays, glauconite, evaporites, detrital minerals rich in K, alunite/jarosite.

The Unspiked K-Ar Method

Selection and Preparation of the Samples

The stratigraphic and geographic location of the sample needs to be noted and established precisely in the field. This will enable external limits to be placed on the ages obtained. Only unaltered samples are retained, mainly to comply with the condition of evolution within a closed system, as discussed above. Freshness is controlled by macroscopic and microscopic observations, and by chemical analysis which measures the loss on ignition (L.O.I. almost equivalent to the water content), a reliable marker of the degree of alteration of the sample. For example, a basalt is considered unaltered if its L.O.I. value is less than 1%. The phase of the sample (mineral, glass, etc.) must be representative of the event to be dated. In the case of volcanic rocks, the selected phase for lava is the microcrystalline groundmass because it is formed by rapid cooling when the magma arrives at the surface; for tephra, phenocrystals (feldspar, mica and amphibole) synchronous with the eruption are selected. After sampling in the field, the rocks are cut, ground and sieved to a 0.250–0.125 mm size. The granulate obtained is washed in an ultrasonic bath of acetic acid (1 N) at 50 °C. The sample is then rinsed thoroughly with deionized water. Then, the separation of the mineralogical phases is done in the laboratory, by magnetic sorting and densitometry or picking under microscope. In the case of tephra, the preparatory procedure is identical. However, given the nature of the deposit, the grinding phase is bypassed.

Determining $^{40}Ar^{*}$

To calculate an age from Eq. (5.4), only the measurement of two variables is required: the content of radiogenic argon 40 ($^{40}Ar^{*}$) and of potassium 40 (^{40}K). The K-Ar method of dating used by the LSCE is the unspiked (with no tracer) K-Ar technique developed by Cassignol et al. (1978), Cassignol and Gillot (1982).

A schematic representation of the ultra-high vacuum line connected to the K-Ar mass spectrometer is given in Fig. 5.4. Prior to the dosing of argon, several stages, such as extraction and purification of the argon are required. Groundmass splits (0.5–2.0 g) of samples are wrapped into 99.5% copper foil packets, loaded in the sample holder, which has been turbo-molecular pumped for about 20 h (Fig. 5.4). During the last two hours of that stage, the molybdemium (Mo) crucible is degassed at about 1500 °C until the pressure decreases to 10^{-9} Torr. The sample is then dropped into the Mo crucible and becomes molten at full power of the induction furnace. During the melting stage (i.e. 20 min), the extracted gas is adsorbed by the first active charcoal finger at liquid nitrogen temperature.

After the melting, the gas is released by heating the charcoal to 110 °C and purified via the mutual action of a titanium sublimation pump and a SAES 10 GP-MK3 Zr-Al getter operated at 400 °C. This first step of gas clean-up (i.e. elimination of active gases) generally lasts 30 min (Fig. 5.5) and is followed by three consecutive exposures of five minutes each of the gas to SAES 10 GP-MK3 Zr-Al getters also operated at 400 °C. The remaining gas, mostly argon, is then adsorbed 5 min by a second active charcoal maintained at liquid nitrogen temperature.

The argon is then freed from the active charcoal finger n° 2 by bringing it to room temperature. After a rapid cryo-pumping of the spectrometer, the argon is introduced into the mass spectrometer. The argon, an inert gas, is ionised in the mass spectrometer, under the effect of an electronic source. ^{40}Ar becomes $^{40}Ar^{+}$ and ^{36}Ar becomes $^{36}Ar^{+}$. The atoms thus charged are accelerated under the influence of a difference in potential (about 620 volts). They then pass through a magnetic field. At this point, their trajectory becomes circular. In a chamber with a high vacuum, these ions with a mass of 40 and 36 and charged e, animated at speed due to a difference in potential (620 V), trace a trajectory of radius R, as they pass through a magnetic field H (3600 Gauss), according to the equation:

$$R = \frac{1439}{H}\left[\frac{m}{e}V\right]^{\frac{1}{2}}$$

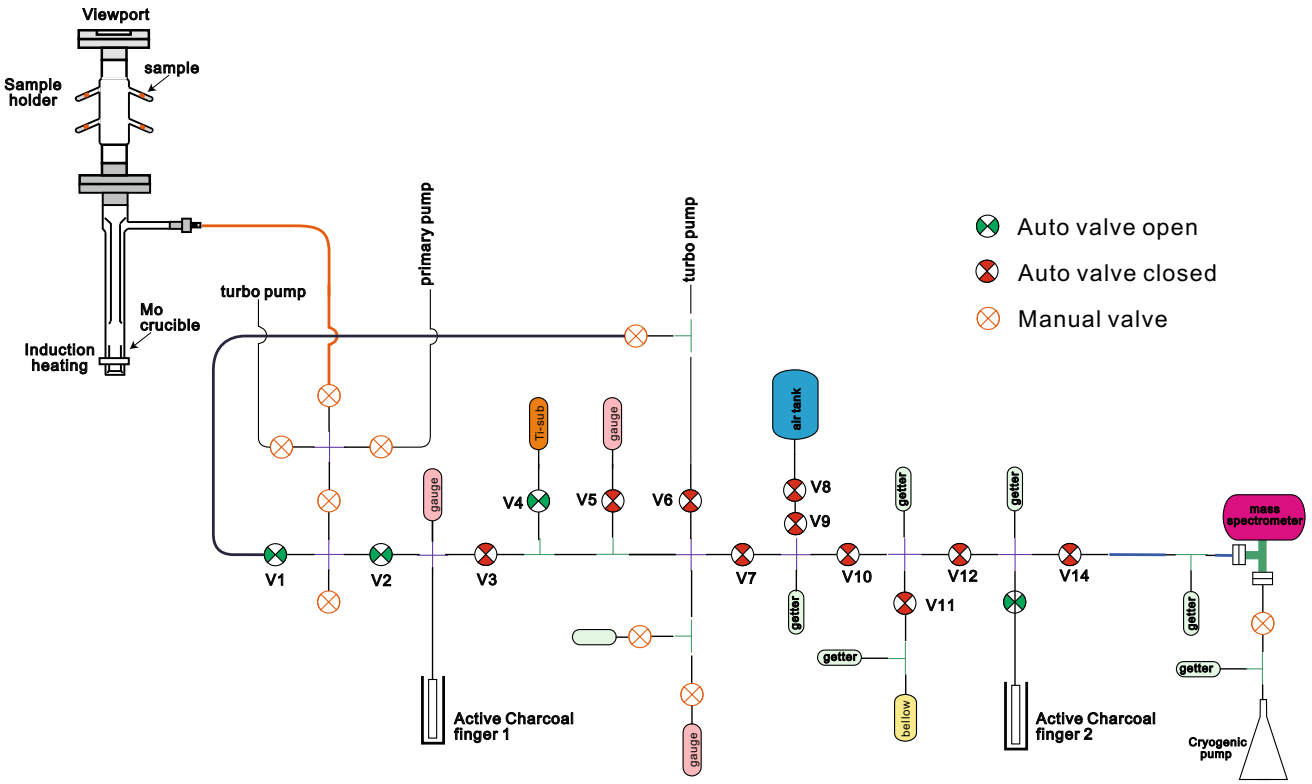

Fig. 5.4 Schematic representation of the ultra-high vacuum line connected to the K-Ar mass spectrometer. Ti-Sub: Titanium sublimation pump, V1-14: Ultra-high vacuum all metal valves. NB: the diagram is at a different scale between the preparation line and the sample holder

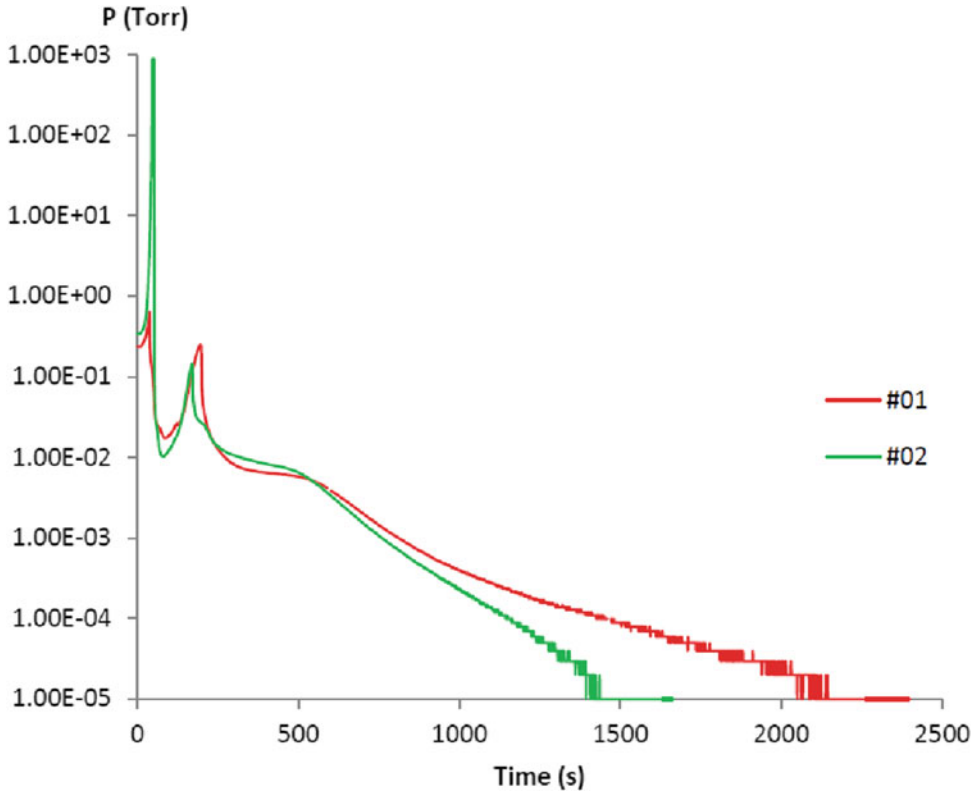

Fig. 5.5 Evolution of pressure versus time during the gas clean-up by means of a Titanium sublimation pump and a SAES 10 GP-MK3 Zr-Al getter. #01 and #02 are the reference numbers for the experiment

with *R*: radius in mm, *H*: magnetic field measured in Gauss, *m*: atomic mass of the ion, e: number of elemental charges carried by the ion, *V*: difference in potential in volts.

Thus, for a spectrometer configured with $H = 3600$ Gauss and $V = 620$ volts, the following is obtained: $R_{40} = 62.9$ mm and $R_{36} = 59.7$ mm.

The ^{40}Ar and ^{36}Ar isotopes of the sample are measured simultaneously on a dual manifold comprised of two Faraday cups, set at $m/e = 40$ and $m/e = 36$. The signals are integrated over a period of 100 s. Once the analysis of the gas is made, the sample is removed from the mass spectrometer by cryo-pumping. The reference atmospheric argon (at.) is taken by means of a double valve from a cylinder containing air from the laboratory (designed as Ref.Atm.). It is then introduced into the mass spectrometer and measured at the same pressure conditions as the sample. It allows the direct comparison of the two aliquots of gas (the sample and atmospheric reference) and the determination of the relative content of radiogenic argon (Fig. 5.6). This is done by varying the analysis volume via a variable volume (VV) connected to the mass-spectrometer cell.

The content of $^{40}Ar^*$ is given by the equation:

$$^{40}\mathrm{Ar}^* = \frac{\frac{^{40}Ar_s}{^{36}Ar_s} - \frac{^{40}Ar_{at}}{^{36}A_{at}}}{\frac{^{40}Ar_s}{^{36}Ar_s}}$$

The third measurement of an aliquot of gas is performed for calibration, in other words, the conversion of an electrical signal into a number of atoms. A known number of argon ^{40}Ar is fed from a calibrated cylinder into the mass spectrometer. The number of atoms is deduced from the measurement of standard minerals of a known age. The procedure for establishing the equation of the calibration curve (Fig. 5.7) is described in Charbit et al., (1998). The three previous steps are shown in the diagram in Fig. 5.6.

The characteristics of the standard minerals commonly used in K-Ar for calibration are shown in Table 5.2.

Potassium analysis is done by flame spectrometry (atomic absorption and emission), on several selections taken independently to ensure sample homogeneity. As this method is a conventional one, we will not enter into the details here.

Example of a Calculation of Age

Calibration of the Mass Spectrometer

Calibration requires an analysis of mineral standards of a known age. First, the ^{40}Ar and ^{36}Ar content of the standard is measured by mass spectrometry. The mineral standard studied here is LP-6. Its K content is 8.37% and that of $^{40}Ar^*$ is 1.158×10^{15} at./g. In the following example, 0.04442 g of this standard was molten. Then, three aliquots of air were

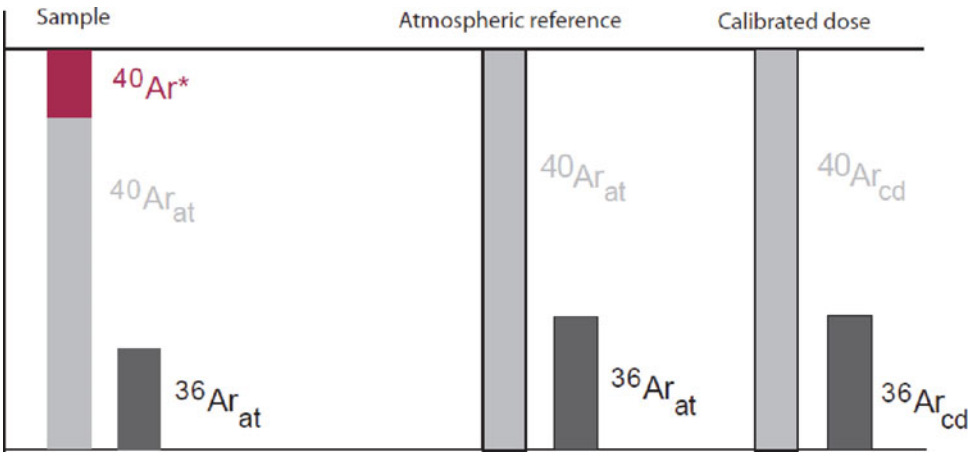

Fig. 5.6 Principle of the K-Ar method with no tracer. Two isotopes of argon (^{40}Ar and ^{36}Ar) are measured by mass spectrometer. The sample gas is composed of atmospheric argon $^{40}Ar_{at}$ and $^{36}Ar_{at}$, as well as radiogenic argon $^{40}Ar^{*}$, resulting from the decay of ^{40}K. s = sample; at = atmospheric, cd = calibrated dose

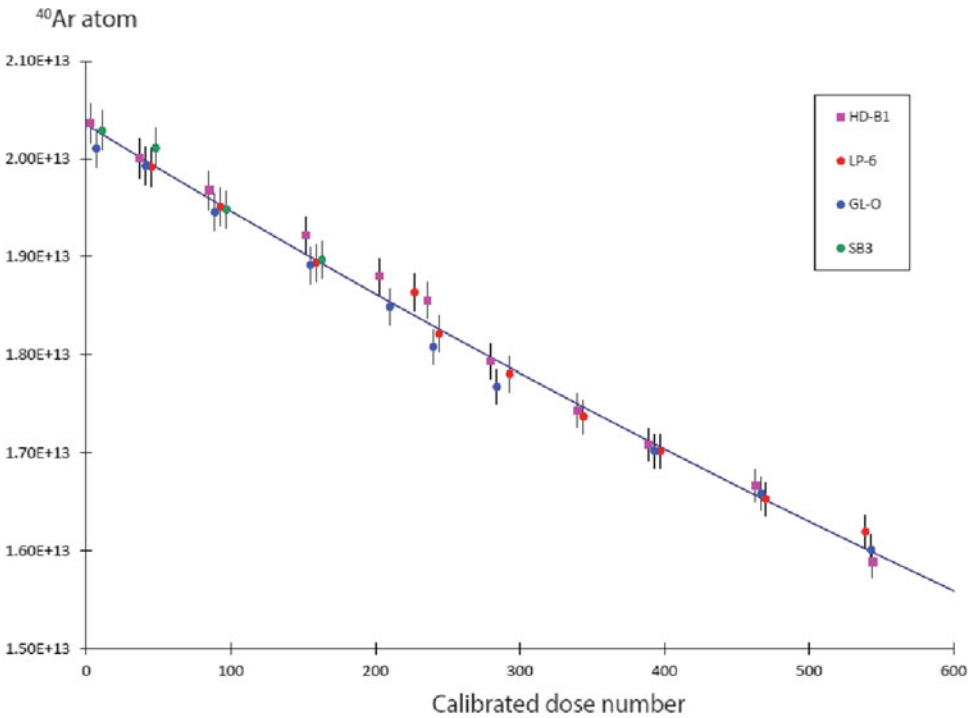

Fig. 5.7 Calibration curve of the mass-spectrometer on the 19th of November 2001

Table 5.2 Values of mineral standards

Standard	K (%)	$^{40}Ar^{*}$ (10^{-9} mol/g)	Age (Ma)	References
HD-B1	7.987	0.335	24.03 ± 0.41	Fuhrmann et al. (1987)
GL-O	6.56	1.093	93.60 ± 0.90	Charbit et al. (1998)
LP-6	8.37	1.923	127.8 ± 1.4	Odin (1982)
SB-3	7.483	2.213	162.9 ± 0.9	Lanphere and Dalrymple (2000)

taken up using a double valve system (pipette) from a calibration canister, and the ^{40}Ar and ^{36}Ar contents are measured.

The results of the analysis by mass spectrometry are shown in the following table.

	^{40}Ar in volts	^{36}Ar in millivolts
Sample (LP-6)	8.921	3.110
Atmospheric reference	7.637	28.252
Calibrated dose (3 doses)	7.637	

From these values, the equivalent $^{40}Ar/^{36}Ar$ ratios can be calculated as follows: $(^{40}Ar/^{36}Ar)_{sample} = R.I._s = 2\ 868.49$; $(^{40}Ar/^{36}Ar)_{tam} = R.I._{atm} = 270.32$; and the concentration of $^{40}Ar^*$ as: $^{40}Ar^*$, hence: $(R.I._s - R.I._{atm})/(R.I._s) = 90.58\%$.

We know the content of $^{40}Ar^*$ (1.158×10^{15} at/g) and the melted weight (0.04442 g) of the standard. We can calculate the number of argon $^{40}Ar^*$ atoms introduced in the mass spectrometer: $N_{at} = 1.158 \times 10^{15} \times 0.044\,42 = 5.144 \times 10^{13}$ at.

Out of the ^{40}Ar signal of the sample (8.921 V), 90.58% corresponds to $^{40}Ar^*$ that is to say 8080 V. From this, we deduce that 8080 V corresponds to 5.144×10^{13} at. of $^{40}Ar^*$.

Three aliquots of air produce a signal of 7.637 V, this therefore corresponds to $(7.637 \times 5.144 \times 10^{13})/8.080 = 4.862 \times 10^{13}$ at. of argon $^{40}Ar^*$.

An aliquot of air taken from the calibration canister is therefore equivalent to $4.862 \times 10^{13}/3 = 1.621 \times 10^{13}$ at. of ^{40}Ar. This canister can then be used to calibrate the mass spectrometer for the measurement of ordinary samples. Obviously, for each calibration measurement, the content of ^{40}Ar decreases in the cylinder. This change is monitored by a regular measurement of the mineral standard. This is the curve shown in Fig. 5.7.

Measuring a Sample of Unknown Age

Experimental data: melted weight: 1.0669 g; potassium content of the analyzed rock K % = 0.643; 1 calibrated dose = $1.608\ 2 \times 10^{13}$ atoms.

	Sample	Atmospheric reference	Calibrated dose
^{40}Ar (V)	1.196	1.323	3.912
^{36}Ar (mV)	4.225	4.884	14.474

The calculation of *R.I.* isotope ratios ($^{40}Ar/^{36}Ar$) gives: $R.I._s = 283.08$; $R.I._{atm} = 270.88$; $R.I._{cd} = 270.28$.

The level of radiogenic argon is calculated by:

$$^{40}Ar^*\% = \frac{R.I._s - R.I._{atm}}{R.I._s} = 4.31\%$$

The number of argon ^{40}Ar atoms in the sample is calculated using the calibration data. We know from the calibration curve that 3.912 volts correspond to $1.608\ 2 \times 10^{13}$ atoms. Therefore, 1.196 V (^{40}Ar sample) is equivalent to 0.492×10^{13} atoms. The concentration of atoms per gram is this value divided by the weight of the melted sample (1.0669 g) so 0.461×10^{13} at./g. 4.31% of the measured ^{40}Ar is radiogenic. This gives $^{40}Ar^*$ at./g = $0.461 \times 10^{13} \times 0.0431 \times 1.987 = 10^{13}$.

The number of ^{40}K atoms is calculated using:

$$^{40}K = \left(\frac{K \times 0.01}{39.098304} \times 0.0001167\right) \times 6.023 \times 10^{23} = 1.156 \times 10^{16}$$

The age is obtained from the equation:

$$t = \frac{1}{\lambda} \times \ln\left[\frac{^{40}Ar^*}{^{40}K}\left(\frac{\lambda}{\lambda\varepsilon}\right) + 1\right] = 296000 \text{ years}$$

($\lambda = 5.543 \times 10^{-10}$ and $\lambda_\varepsilon = 0.581 \times 10^{-10}$).

The $^{40}Ar/^{39}Ar$ Method: General Principles

The Age Equation

This method is a variant of the K-Ar method. Firstly, the samples undergo neutron activation. This activation under fast neutron flux within a nuclear reactor is intended to transform the isotope ^{39}K to ^{39}Ar. The amount of argon ^{39}Ar thus generated is proportional to the number of ^{39}K atoms and therefore of ^{40}K (parent atoms) present in the sample, the $^{40}K/^{39}K$ ratio being (supposedly) constant in nature. To do this, the samples are placed with samples of known age (standards) in aluminum discs themselves stacked in an aluminum tube (shuttle). This shuttle is then subjected to a fast neutron flux, for a period of between a few minutes and 24 h depending on the age and nature of the samples.

The irradiation causes the formation of an artificial argon isotope, ^{39}Ar, according to the reaction $^{39}_{18}K(n,p)^{39}_{18}Ar$ (capture band of 80 to 100 mbarn, Mitchell 1968; Roddick 1983). ^{39}Ar is radioactive. Its disintegration period is 265 years. As the analysis by spectrometer is performed less than one year after irradiation, the error margin on its estimation is negligible. The advantage of producing argon ^{39}Ar in proportion to the parent element (^{40}K) is that this transformation replaces the measurement of the $^{40}K/^{40}Ar$ ratio by two different methods (atomic absorption for ^{40}K and mass spectrometry for ^{40}Ar) with the direct measurement of the $^{40}Ar/^{39}Ar$ ratio (by mass spectrometry).

The precise knowledge of ^{39}Ar production yield is obtained by referring to known age standards. These standards are irradiated in the same shuttles as the samples. The radiation yield is calculated according to the equation established by Mitchell (1968).

$$^{39}Ar_s = {}^{39}K\Delta T \int \Phi_E \sigma_E d_E = {}^{39}K\Delta T I \qquad (5.5)$$

$$I = \int_0^\infty \Phi_E \sigma_E d_E$$

with: ^{39}K being the number of atoms of ^{39}K in the standard sample; $^{39}Ar_s$ the number of atoms of ^{39}Ar produced in the standard sample; Φ_E, the energy flux; σ_E, zone of efficient

capture of the reaction $^{39}K \rightarrow {}^{39}Ar$ at energy E; ΔT, the irradiation duration.

The amount of $^{40}Ar^{*}$ produced by the disintegration of ^{40}K follows the equation:

$$^{40}Ar^{*} = \frac{\lambda\varepsilon}{\lambda}{}^{40}K\left(e^{\lambda t_s} - 1\right) \tag{5.6}$$

with t_s, known age of the standard.

Combining (5.5) and (5.6), we obtain:

$$\frac{^{40}Ar^{*}}{^{39}Ar^{*}} = \frac{^{40}K}{^{39}K}\frac{\lambda\varepsilon}{\lambda}\frac{1}{\Delta T}\frac{\left(e^{\lambda t_s} - 1\right)}{I} \tag{5.7}$$

Equation (5.7) is simplified by defining the J parameter which is the radiation flux actually received by the sample:

$$J = \frac{^{39}K}{^{40}K}\frac{\lambda}{\lambda\varepsilon}\Delta T I \tag{5.8}$$

From (5.7), J becomes,

$$J = \frac{e^{\lambda t_s} - 1}{^{40}Ar^{*}/^{39}Ar} \tag{5.9}$$

It is then possible to resolve the age equation:

$$t_e = \frac{1}{\lambda}\ln\left[1 + \frac{\left(^{40}Ar^{*}/^{39}Ar\right)_e}{\left(^{40}Ar^{*}/^{39}Ar\right)_s}\left(e^{\lambda t_s} - 1\right)\right] \tag{5.10}$$

with s = standard and e = sample.

The following table shows the age of the main standard (or flux) minerals for $^{40}K/^{40}Ar$ and $^{40}Ar/^{39}Ar$ methods.

Name	Mineral	Age (Ma)	References
Hb-3gr	Hornblende	1072 ± 11	Turner et al. (1971)
MMhb-1	Hornblende	520.4 ± 1.7	Samson and Alexander (1987)
LP-6	Biotite	127.9 ± 1.1	Odin (1982)
SB-2	Biotite	162.1 ± 2.0	Dalrymple et al. (1981)
GA-1550	Biotite	97.9 ± 0.9	McDougall and Roksandic (1974)
B4M	Muscovite	18.6 ± 0.4	Flish (1982)
B4B	Biotite	17.3 ± 0.2	Flish (1982)
FCTs	Sanidine	28.187 ± 0.019	Phillips et al. (2017)
ACRs	Sanidine	1.18404 ± 0.00068	Phillips et al. (2017)

The age assigned to the standards may vary depending on the authors. With regard to FCTs and ACRs, the following references may be consulted among others: Kuiper et al. (2008), Renne et al. (2010), Jicha et al. (2016), Niespolo et al. (2017).

Corrections for Atmospheric Argon and Interference of Mass

As for the $^{40}K/^{40}Ar$ method, the correction for atmospheric argon is essential in order to determine the proportion of $^{40}Ar^{*}$. This adjustment is done by repeated mass spectrometric measurements of aliquots of air. This defines the instrumental $^{40}Ar/^{36}Ar$ atmospheric ratio. Most mass spectrometers give values slightly different from 298.56. It is therefore through the repeated measurements of aliquots of air that the bias in the measuring apparatus can be calculated. As a first approximation and for samples without calcium, the determination of the percentage of radiogenic argon can be done by simply comparing the $^{40}Ar/^{36}Ar$ ratio of the sample and the instrumental $^{40}Ar/^{36}Ar$ ratio of the atmosphere.

However, during irradiation, secondary reactions occur from Ca, K and Cl isotopes which also produce artificial isotopes of argon (Fig. 5.8):

- $^{40}Ca(n, n\alpha)\ ^{36}Ar$
- $^{42}Ca(n, \alpha)\ ^{39}Ar$
- $^{40}K(n, p)\ ^{40}Ar$
- $^{35}Cl(n, \gamma)\ ^{36}Cl - \beta^{-} \rightarrow {}^{36}Ar\ t_{1/2} = 300 \times 10^{3}$ years
- $^{37}Cl(n,\gamma)\ ^{38}Cl - \beta^{-} \rightarrow {}^{38}Ar\ t_{1/2} = 37.3$ min

The correction for interference of the masses 40, 39 and 36 due to Ca is possible because of an additional reaction:

- $^{40}Ca(n, \alpha)\ ^{37}Ar\ t_{1/2} = 35.1$ days

To know the $^{39}Ar_{Ca}$ and $^{36}Ar_{Ca}$ contents, it is necessary to irradiate a pure calcium salt, such as CaF_2, and measure its 39/37 and 40/37 ratios with the mass spectrometer. The initial value of argon ^{37}Ar of the irradiated sample, when it is taken from the reactor, also needs to be calculated. This is done by applying the law of radioactive decay:

$$^{37}Ar_0 = {}^{37}Ar_m e^{\lambda_{37} t_i}\lambda_{37} t_i / \left(1 - e^{\lambda_{37} t_i}\right)$$

with $^{37}Ar_0$ = amount of the isotope 37 produced at the end of the irradiation; $^{37}Ar_m$ = amount of the isotope 37 measured on the day of analysis; t = duration of the irradiation; t_i = time interval between irradiation and analysis; $\lambda_{37} = 0.0197\ 4\ j^{-1}$.

The correction factors $(^{39}Ar/^{37}Ar)_{Ca}$ and $(^{36}Ar/^{37}Ar)_{Ca}$, which depend on the yield from the irradiation on the salts, are thus well defined.

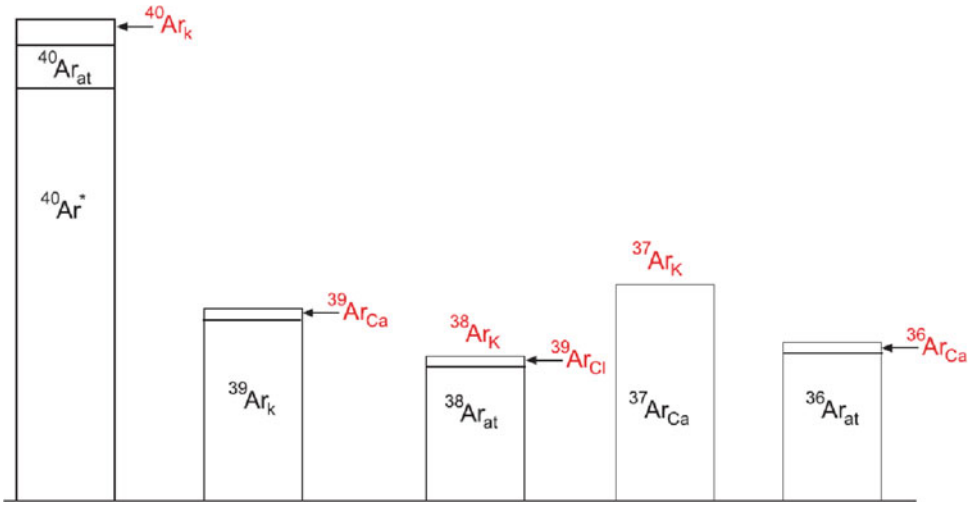

Fig. 5.8 Mass spectrum of an irradiated sample, deciphering the origin of the different isotopes (in red) generated from the neutronic activation

In order to know the correction factor associated with the production of ^{40}Ar from ^{40}K, a pure salt of K (K_2SO_4 or KF) is also irradiated. This allows the ratio $(^{40}Ar/^{39}Ar)_K$ to be defined, which is then used to calculate the share of argon ^{40}Ar resulting from irradiation of ^{40}K, which will be cut back from the total argon ^{40}Ar.

In summary, the masses corrected for interferences related to radiation and to the atmospheric component can be written:

$$^{40}Ar^{*} = {}^{40}Ar_m - \left({}^{40}Ar_{at} + {}^{40}Ar_K\right)$$
$$^{39}Ar = {}^{39}Ar_m - {}^{39}Ar_{Ca}$$
$$^{36}Ar = {}^{36}Ar_{at} - {}^{36}Ar_{Ca}$$

The Age Spectra

The $^{40}Ar/^{39}Ar$ method allows for the collection of more comprehensive information on the behavior of the radioisotopic clock than the $^{40}K/^{40}Ar$ method. In the experimental approach known as 'step-heating' (Turner et al. 1966), the sample is gradually heated in steps of increasing temperature (for example, by steps of 60°C). At each step, the isotopic composition of argon in the extracted and purified gas is measured by mass spectrometry. An apparent age can thus be calculated for each step. In the end, this results in an age spectrum. The general appearance of these spectra shows whether the sample and, consequently, the $^{40}K/^{40}Ar$ clock, were disrupted or not.

In the case of an undisturbed sample (Fig. 5.9), which evolved in a closed system, the K is homogeneously distributed in the crystal lattice. This is also true for $^{40}Ar^{*}$ and ^{39}Ar. When a sample is subjected to degassing in increasing temperature steps, the $^{40}Ar^{*}$ and ^{39}Ar isotopes will be extracted at a constant ratio. As a consequence, a similar apparent age, within error margins, will be obtained for all

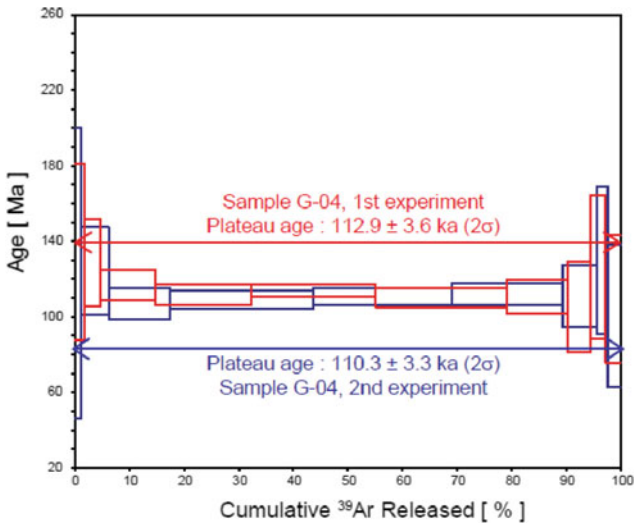

Fig. 5.9 Age spectra depicting $^{40}Ar/^{39}Ar$ experimental results from duplicated measurements of sample G-04, a lava from the Gelso section of Vulcano (Aeolian Islands, Italy). Uncertainties are ±2σ. In red, the first step-heating experiment; in blue, the second step-heating experiment

steps. The result of such experiments will be a consistent 'age spectrum' in horizontal form which defines the plateau age. Several definitions have been proposed for a plateau age (Dalrymple and Lanphere 1974; Berger and York 1981; McDougall and Harrison 1988). It is generally considered that a plateau is composed of at least three successive steps with at least 60% of the $^{39}Ar_k$ released and whose apparent ages are consistent within ±2 sigma (i.e. within the respective analytical error bars at 95.6% confidence interval).

Cases of inconsistent age spectra are relatively common and the reasons for this discrepancy are varied. One of the most frequently cited reasons is related to the 'recoil effect'. The transformation of ^{39}K into ^{39}Ar by the reaction $^{39}K(n, p)^{39}Ar$ can be accompanied by a loss of ^{39}Ar. In other words, the ^{39}Ar

atom can be founder-distributed, due to this reaction, in a different crystallographic site than that occupied by its parent, ^{39}K. The distance of this backwards movement is proportional, firstly, to the energy employed during the neutron activation, and secondly, to the sample density. Thus, this recoil effect can lead to a redistribution of $^{39}Ar_K$ in the samples with grains of a size less than 5–10 μm. This redistribution of $^{39}Ar_K$ can cause an over or underestimation of apparent ages at different temperature steps. The loss of $^{39}Ar_K$, related to the recoil effect, is seen in an overestimation of the ages obtained.

Other natural phenomena are also the cause of inconsistent age spectra. Alteration, metamorphism, hydrothermalism are all processes that might disrupt the K/Ar clock. These processes are the source of migration, loss or gain of argon and potassium isotopes.

The Single Grain Method

Technological developments of recent decades (increasing sensitivity of mass spectrometers, laser fusion system) make it possible to work on samples of smaller and smaller size. It is thus possible to get down to the level of the crystal. This approach is used in particular for dating tephra. Within a given tephra layer, several crystals of the same mineral type are selected. After irradiation, each crystal is individually melted by laser, the gas is extracted and it is then analyzed by mass spectrometer. An age is obtained for each constituent crystal at the tephra level. It is thus possible to establish spectra of age probability for a given tephra (Deino and Potts 1992). The analysis of these spectra allows homogeneity at the stratigraphic level to be estimated and the most statistically probable age to be defined (Fig. 5.10).

The Isochrones

The $^{40}Ar/^{39}Ar$ method is particularly suited to data processing by isochrones. In the inverse isochron diagram $^{40}Ar/^{36}Ar$ versus $^{39}Ar/^{36}Ar$ (Fig. 5.11), the slope is equivalent to the $^{40}Ar^*/^{39}Ar_K$ ratio which is itself proportional to the age, and the *intercept* on the y axis corresponds to the $(^{40}Ar/^{36}Ar)_I$ ratio. This last ratio indicates the proportion of ^{40}Ar and of ^{36}Ar at $t = 0$, in other words, at the moment the system closed. This value is directly comparable to the $^{40}Ar/^{36}Ar$ atmospheric ratio. It is thus possible, from the inverse isochron diagram, to highlight the presence or absence of excess argon. This information is particularly important because it allows one of the basic assumptions for application of the clock to be checked, namely that an age is considered correct if, at t = 0, $^{40}Ar^* = 0$ and $(^{40}Ar/^{36}Ar)_{initial} = (^{40}Ar/^{36}Ar)_{atmospheric}$.

This analysis by isochron is particularly useful for the dating of tephra. Indeed, ideally, all the minerals from the same layer of a tephra should be on the same isochron, as they have, in principle, the same age. Furthermore, the value $(^{40}Ar/^{36}Ar)_i$ must be equivalent to the atmospheric value. If some experimental points are not on this isochron, we can deduce that the corresponding crystals are xenocrysts i.e. older crystals remobilized during the eruptive event at the origin of the tephra (Fig. 5.11).

Selection and Preparation of Samples

The procedure is the same as that followed for the K/Ar method.

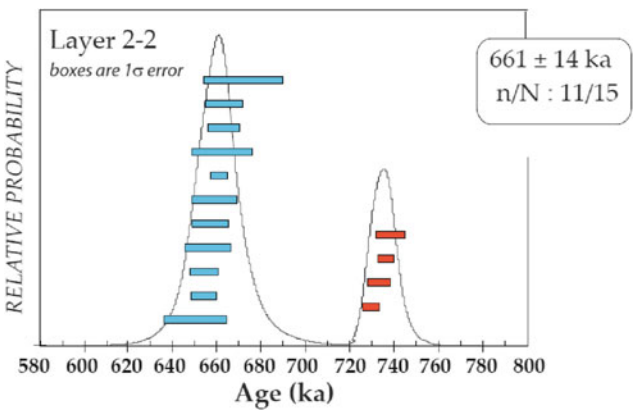

Fig. 5.10 Probability diagram obtained for the stratigraphic level N° 2-2 (Notarchirico archaeological site, Basilicata, Italy). 15 crystals were analyzed. Experiments in blue (11 crystals) define an age of 661 ± 14 ka. Red boxes are xenocrysts (4 crystals out of the 15 analyzed) and as a consequence, eliminated from the age calculation. Data are from Pereira et al. (2017)

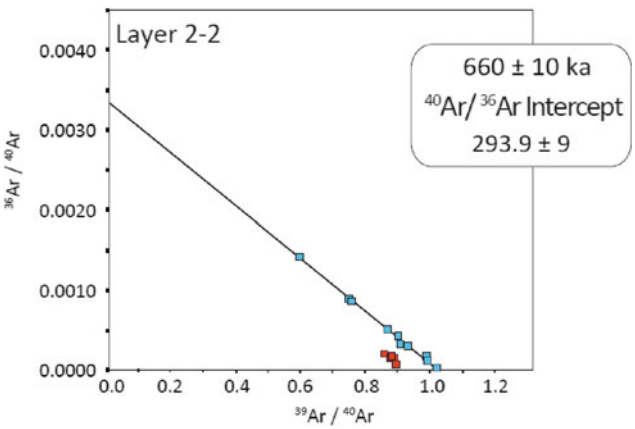

Fig. 5.11 Inverse isochron diagram obtained for the stratigraphic level N° 2-2 (Notarchirico archaeological site, Basilicata, Italy). 15 crystals were analyzed. Experiments in blue define an age of 660 ± 10 ka. Red boxes are xenocrysts, eliminated from the age calculation. Data are from Pereira et al. (2017)

Mass-Spectrometric Analysis

- **Stage 1: pumping—pre-degassing**. The sample (crystal or microcrystalline groundmass) is placed in a vacuum chamber including a crucible in the case of fusion in a furnace, and a viewport in the case of fusion by Laser CO_2), then placed under secondary high vacuum by means of turbo-molecular pumps. The sample is then heated to about 500 °C. This first gas extracted is eliminated by pumping.
- **Stage 2: fusion**. The sample is melted either by a CO_2 laser or in a double vacuum resistance furnace. In the case of fusion by laser, it applies essentially to the analysis of single crystals and to small groups of crystals (about 5–15 grains). The furnace is used for the analysis of microcrystalline groundmass. As seen before, this allows a step by step fusion, and hence a gradual degassing of the sample required for the 'step-heating' method.
- **Stage 3: purification**. The gas extracted from the sample is purified by the combined effect of Getters pumps and a titanium sublimation pump.
- **Stage 4: measurement by mass spectrometer**. After purification, the gas is introduced into the mass spectrometer. The purified gas is measured using a high-sensitivity noble gas GV5400 instrument operated in ion-counting mode. One analytical run consists of 20 peak scans of each argon isotope with integration times of 1 s (^{40}Ar, ^{39}Ar) or 10 s (^{36}Ar, ^{37}Ar, ^{38}Ar, baseline), first preceded by a peak centering routine on the five Ar isotopes, upon admission of the sample into the mass-spectrometer. The precision and accuracy of the mass discrimination correction is monitored by periodical measurements of air argon. This monitoring is performed using a dedicated air-calibration system featuring a 6 L tank filled with purified atmospheric argon. This tank is connected to the mass spectrometer vacuum line via two pneumatically- actuated air pipettes of approximately 0.1 and 1.0 cc. This system allows for a 1 cc (e.g. 600,000 counts s^{-1} (cps on ^{40}Ar)) and a 0.1 cc (e.g. 70 000 cps on ^{40}Ar) atmospheric aliquots to be delivered into the mass spectrometer and permits a careful monitoring of the mass discrimination over a wide dynamic range. The mineral standards used to calculate the flux are analyzed in the same way as the ordinary samples.

Calculation of Age

Determination of the *J* factor (Neutron flux received during irradiation)

J is determined for each sample. See the following analysis of a ACR-2 standard grain (1.194 Ma) subjected to a fast neutron flux for 30 min (Osiris reactor, CEA Saclay):

	^{40}Ar	^{39}Ar	^{38}Ar	^{37}Ar	^{36}Ar
Measured (mV)	9.246×10^{-3}	2.321×10^{-3}	3.576×10^{-5}	1.188×10^{-6}	1.375×10^{-6}
Blank (mV)	2.351×10^{-5}	2.586×10^{-7}	2.238×10^{-8}	6.672×10^{-7}	2.383×10^{-7}
Corrected measurement	2.312×10^{-3}	7.967×10^{-4}	1.234×10^{-5}	3.161×10^{-7}	2.981×10^{-6}

Using Eq. (5.9), J can be calculated by setting the $^{40}Ar^{*}/^{39}Ar_K$ ratio or R_e as follows:

$$R_e = \frac{[^{40}Ar/^{39}Ar]_m - [^{40}Ar/^{36}Ar]_A [^{36}Ar/^{39}Ar]_m + [^{40}Ar/^{36}Ar]_A [^{36}Ar/^{37}Ar]_{Ca} [^{37}Ar/^{39}Ar]_m}{1 - [^{39}Ar/^{37}Ar]_{Ca} [^{37}Ar/^{39}Ar]_m} - \left[\frac{^{40}Ar}{^{39}Ar}\right]_K$$

with *m:* measured ratios (see table above).

$[^{40}Ar/^{36}Ar]_A$ = atmospheric reference ratio = 292.8 (for this sample);

$[^{36}Ar/^{37}Ar]_{Ca}$ = (given by calcium salt) 5.60×10^{-4};

$[^{39}Ar/^{37}Ar]_{Ca}$ = (given by calcium salt) $6.95\ 10^{-4}$;

$[^{40}Ar/^{39}Ar]_K$ = (given by potassium salt) $3.52\ 10^{-3}$;

$$R_e = \frac{3.974 - 292.8 \times 4.898 \times 10^{-4} + 292.8 \times 5.60 \times 10^{-4} \times 5.09 \times 10^{-2}}{1 - 6.95 \times 10^{-4} \times 5.09 \times 10^{-2}} - 3.52 \times 10^{-3} = \underline{3.8355}$$

If t_s = 1.194 Ma and $\lambda = 5.543 \times 10^{-10}$; J is then calculated as follows:

$$J = \left(e^{1.194 \times 0.0000000005543} - 1\right)/3.8355 = \underline{1.726 \times 10^{-4}}$$

The measurement is repeated on at least three grains to quantify any possible external errors originating from the heterogeneity of the age standard ($\sim$1%). A weighted

average is then calculated from these measurements and used to calculate the sample value.

Age Calculation of a Sample

Here are the measurements obtained for 1 sanidine crystal irradiated for 90 min in the Osiris reactor (CEA Saclay):

	^{40}Ar	^{39}Ar	^{38}Ar	^{37}Ar	^{36}Ar
Measured (mV)	2.491×10^{-03}	7.969×10^{-04}	1.241×10^{-05}	4.612×10^{-07}	3.136×10^{-06}
Blank (mV)	1.791×10^{-04}	1.515×10^{-07}	7.158×10^{-08}	1.451×10^{-07}	1.554×10^{-07}
Corrected measurement	2.312×10^{-03}	7.967×10^{-04}	1.234×10^{-05}	3.161×10^{-07}	2.981×10^{-06}

By combining the expression of J (Eq. 5.9) with Eq. 5.10, the age calculation gives:

$$t_e = \frac{1}{\lambda}\ln\left[1 + J\frac{^{40}Ar^*}{^{39}Ar_K}\right]$$

with $J = 6.530 \times 10^{-4}$ (calculated for this sample);

$\lambda = 5.543 \times 10^{-10}$ (constant for total decay of ^{40}K);

$R_e = 1.790\ 8$ (see calculation of R_e above with $[^{40}Ar/^{36}Ar]_A = 296.1$);

$t_e = 1/(5.543 \times 10^{-10}) \times \ln(1 + 6.530 \times 10^{-4} \times 1.790\ 8) = \underline{2.108\ Ma}$.

Advantages and Limitations of the $^{40}K/^{40}Ar$ and $^{40}Ar/^{39}Ar$ Methods

The table below summarizes the advantages and limitations of both methods.

Method	$^{40}K/^{40}Ar$	$^{40}Ar/^{39}Ar$
Advantages	• Rapid implementation • No need for prior irradiation of samples • Precise measurement of low amounts of $^{40}Ar^*$ (well-suited to young basalts of mid-oceanic ridges)	• Basic assumptions can be verified (age spectrum, isochrons) • Dating possible on very small sample sizes (grain by grain dating well suited to tephra)
Limitations	• The basic assumptions (initial $^{40}Ar/^{36}Ar = 298.56$, evolution in a closed system) for application of the clock are not verified • Large weight (>1 g) of sample required These two points prohibit the dating of tephra by the K-Ar method	• Pre-irradiation leads to corrections (interference of masses) • The recoil effect makes dating of very fine-grained samples or ones with a glassy texture complicated

Application: Example of the Dating of the Laschamp Event

In the chapter on magnetic stratigraphy (Chap. 7), the importance of the dating of geomagnetic events is discussed. Here, we will show how the Laschamp excursion could be correctly dated with a high degree of precision.

The dating of this excursion was obtained by a geochronological study combining the $^{40}K/^{40}Ar$ and $^{40}Ar/^{39}Ar$ methods applied to two lavas from the Massif Central (Guillou et al. 2004). Prior to this study, estimates of ages were imprecise and inconsistent with the ages deduced from other means of dating, such as astronomical calibration.

Two lava flows have been subjected to paleomagnetic and geochronological study. One of these comes from the 'Puy de Laschamp' part of the *Chaine des Puys*, located in the French Massif Central. The second, called 'the Olby flow' comes from the 'Puy de Barme' also part of the Chaine des Puys.

For each sample, the K-Ar ages (unspiked method) are calculated from two independent measures of potassium and three, also independent, measures of argon. The ages obtained for the Laschamps lava flow (41.5 ± 1.9 ka) and that of Olby (41.4 ± 1.9 ka) are identical at the two sigma level. The weighted average of these two values gives an age of 41.4 ± 1.4 ka. As for $^{40}Ar/^{39}Ar$ ages (Fig. 5.12), seven experiments out of thirteen give consistent age spectra, for which 100% of the extracted gas could be used to define a plateau age. For the other six experiments, between 76 and 96% of the extracted gas was used to define a plateau age. Furthermore, the *intercept* values calculated from the inverse isochron diagrams are equivalent to the atmospheric ratio. This indicates that the age determinations are not marred by error due to either a loss or gain of argon. The weighted average for isochron ages for the two sampling sites for the Laschamps lava flow were 39.4 ± 2.6 ka and 38.3 ± 2.6 ka. The Olby lava flow has an age of 39.2 ± 4.9 ka. The combination of these three ages give a weighted average of 38.9 ± 1.7 ka.

The K-Ar and $^{40}Ar/^{39}Ar$ measurements are compatible at the two sigma level. As these two flows recorded the same paleomagnetic excursion, this is dated to 40.4 ± 1.1 ka. Note that if we take the uncertainty (2.4%) on the potassium decay constant into account, the error in age goes from 1.1 to 2.0 ka. Thus, the age retained for the excursion is 40.4 ± 2.0 ka. This age is comparable to that obtained by independent chronological methods (see Chap. 7). A new study (Laj et al. 2014), combining K-Ar and $^{40}Ar/^{39}Ar$ dating, associated with paleomagnetism, was applied to a larger number of volcanoes from the Chaine des Puys, and has since made it possible to narrow down the age of the Laschamps excursion to 41.2 ± 1.6 ka.

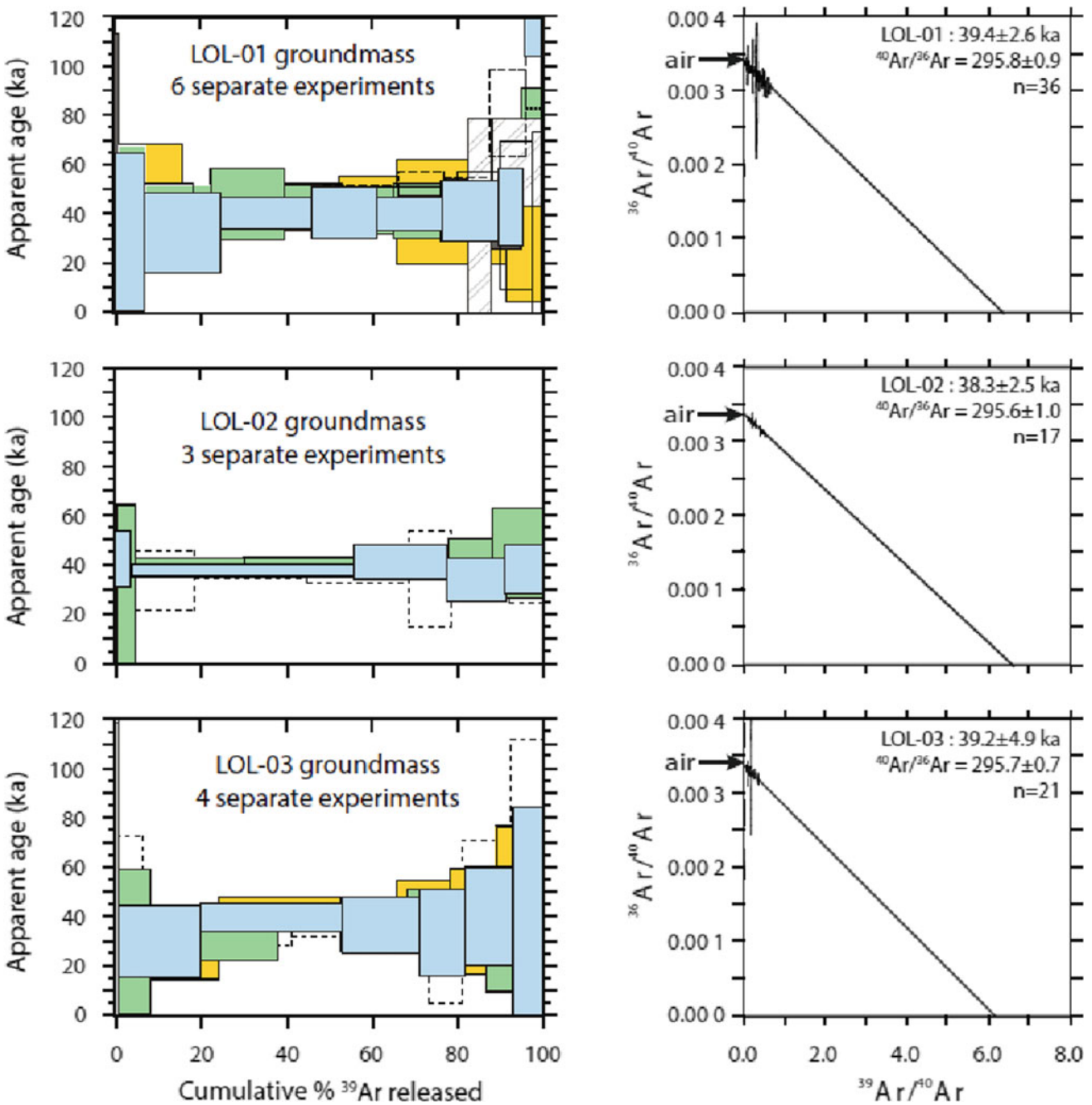

Fig. 5.12 Age spectra and isochron diagrams for samples from the Laschamp-1, Laschamp-2 and Olby sites. Isochron ages and statistics are weighted mean values from experiments on all the subsamples, (in Guillou et al. 2004). n = number of steps retained in the age calculation

This example highlights the potential of the K-Ar dating clock to date recent events of the Quaternary period. One of the applications of these chronological data to calibrate time scales, with various other useful applications in the earth sciences, archeology and paleoclimatology.

References

Berger, G. W., & York, D. (1981). Geothermometry from $^{40}Ar/^{39}Ar$ dating experiments. *Geochimica et Cosmochimica Acta, 45,* 795–811.

Cassignol, C., Cornette, Y., David, B., & Gillot, P. Y. (1978). Technologie potassium-argon. C.E.N., Saclay, Rapport CEA R-4802, 37 p.

Cassignol, C., & Gillot, P.-Y. (1982). Range and effectiveness of unspiked potassium-argon dating: Experimental groundwork and examples. In G. S. Odin (Ed.), *Numerical dating in stratigraphy* (pp. 159–179). Chichester: Wiley.

Charbit, S., Guillou, H., & Turpin, L. (1998). Cross calibration of K-Ar standard minerals using an unspiked Ar measurement technique. *Chemical Geology, 150,* 147–159.

Dalrymple, G. B., Alexander, E. C. Lanphere, M., & Kraker, G. P. (1981). Irradiation of samples for $^{40}Ar/^{39}Ar$ dating using the geological survey TRIGA reactor. U.S. Geological Survey Professional Paper, 1176.

Dalrymple, G. B., & Lanphere, M. A. (1969). In J. Gilluly & A. O. Woodford (Eds.), *Potassium-argon dating. Principles, techniques and applications to geochronology* (251 p.). San Francisco, CA: W. H. Freeman and Company.

Dalrymple, G. B., & Lanphere, M. A. (1974). $^{40}Ar/^{39}Ar$ age spectra of some undisturbed terrestrial samples. *Geochimica et Cosmochimica Acta, 38,* 715–738.

Deino, A. L., & Potts, R. (1992). Age-probability spectra for examination of single crystal $^{40}Ar/^{39}Ar$ dating results: Examples from Olorgesailie, Southern Kenya Rift. *Quaternary International, 13*(14), 47–53.

Flish, M. (1982). Potassium-argon analysis. In G. S. Odin (Ed.), *Numerical dating in stratigraphy* (pp. 151–158). New York: Wiley.

Fuhrmann, U., Lippolt, H., & Hess, C. J. (1987). HD-B1 biotite reference material for K-Ar Chronometry. *Chemical Geology, 66,* 41–51.

Garner, E. L., Murphy, T. J., Gramlich, J. W., Paulsen, P. J., & Barnes, I. L. (1975). Absolute isotopic abundance ratios and the atomic weight of a reference sample of potassium. *Journal of Research of the National Bureau of Standards, 79A,* 713–725.

Guillou, H., Singer, B. S., Laj, C., Kissel, C., Scaillet, S., & Jicha, B. R. (2004). On the age of the Laschamp geomagnetic excursion. *Earth and Planetary Science Letters*, *227*(3–4), 331–343.

Jicha, B. R., Singer, B. S., & Sobol, P. (2016). Re-evaluation of the ages of $^{40}Ar/^{39}Ar$ sanidine standards and super-eruptions in the western US using a Noblesse multi-collector mass spectrometer. *Chemical Geology, 431,* 54–66.

Kuiper, K. F., Deino, A., Hilgen, F. J., Krijgsman, W., Renne, P. R., & Wijbrans, J. R. (2008). Synchronizing rock clocks of Earth history. *Science, 320,* 500–505.

Laj, C., Guillou, H., & Kissel, C. (2014). Dynamics of the earth magnetic field in the 10-75 kyr period comprising the Laschamp and Mono Lake excursions: New results from the French Chaîne des Puys in a global perspective. *Earth and Planetary Science Letters, 387,* 184–197.

Lanphere, M. A., & Dalrymple, G. B. (2000). First principles calibration of ^{38}Ar Tracers. U.S. Geological Survey Professional Paper, 1621.

Lee, J. Y., Marti, K., Severinghaus, K., Kawamura, K., Yoo, H. S., Lee, J. B., et al. (2006). A redetermination of the isotopic abundances of atmospheric Ar. *Geochimica Cosmochimica Acta, 70,* 4507–4512.

McDougall, I., & Harrison, T. M. (1988). *Geochronology and thermochronology by the $^{40}Ar/^{39}Ar$ method* (p. 212). New York: Oxford University Press.

McDougall, I., & Roksandic, Z. (1974). Total fusion $^{40}Ar/^{39}Ar$ ages using HIFAR reactor. *Geological Society of Australia, 21*, 81–89.

Merrihue, C. (1965). Trace element determinations and potassium argon dating by mass spectroscopy of neutron irradiated samples. *Transactions American Geophysical Union, 46,* 125.

Merrihue, C., & Turner, G. (1966). Potassium-argon dating by activation with fast neutrons. *Journal of Geophysical Research, 71,* 2852–2857.

Min, K. W., Mundil, R., Renne, P. R., & Ludwig, K. R. (2000). A test for systematic errors in $^{40}Ar/^{39}Ar$ geochronology through comparison with U-Pb analysis of a 1.1 Ga rhyolite. *Geochimica Cosmochimica Acta, 64,* 73–98.

Mitchell, J. G. (1968). The Argon-40/Argon-39 dating in coesite-bearing and associated units of the Dora Maira Massif, Western Alps. *European Journal of Mineralogy, 3,* 239–262.

Nier, A. O. (1950). A redetermination of the relative abundances of the isotopes of carbon, nitrogen, oxygen, argon and potassium. *Physical Review, 77,* 789–793.

Niespolo, E. M., Rutte, D., Deino, A. L., & Renne, P. R. (2017). Intercalibration and age of the Alder Creek sanidine $^{40}Ar/^{39}Ar$ standard. *Quaternary Geochronology, 39,* 205–213.

Odin, G. S. (1982). Interlaboratory standards for dating purposes. In G. S. Odin (Ed.), *Numerical dating in stratigraphy* (pp. 123–158). New York: Wiley.

Pereira, A., Nomade, S., Bahain, J.-J., & Piperno, M. (2017). Datation par $^{40}Ar/^{39}Ar$ sur monocristaux de feldspaths potassiques: exemple d'application sur le site pléistocène moyen ancien de Notarchirico (Basilicate, Italie). *Quaternaire, 28*(2), 149–154.

Phillips, D., Matchan, E. L., Honda, M., & Kuiper, K. F. (2017). Astronomical calibration of $^{40}Ar/^{39}Ar$ reference minerals using high-precision, multi-collector (ARGUS VI) mass spectrometry. *Geochimica Cosmochimica Acta, 196,* 351–369.

Renne, P. R. (2000). In J. S. Noller, J. M. Sowers, & W. R. Lettis (Eds.), *K-Ar and $^{40}Ar/^{39}Ar$ dating, in quaternary geochronology: Methods and applications*. Washington, D.C.: American Geophysical Union. https://doi.org/10.1029/rf004p0077.

Renne, P. R., Mundil, R., Balco, G., Min, K., & Ludwig, K. R. (2010). Joint determination of 40 K decay constants and $^{40}Ar^*/^{40}K$ for the Fish Canyon sanidine standard and improved accuracy for $^{40}Ar/^{39}Ar$ geochronology. *Geochemica et Cosmochimica Acta, 74,* 5349–5367.

Roddick, J. C. (1983). High precision intercalibration of ^{40}Ar-^{39}Ar standards. *Geochemical and Cosmochimical Acta, 47,* 887–898.

Samson, S. D., & Alexander, E. C., Jr. (1987). Calibration of interlaboratory ^{40}Ar-^{39}Ar Dating Standard, MMhb-1. *Chemical Geology, 66,* 27–34.

Steiger, R. H., & Jäger, E. (1977). Subcommission on geochronology: Convention on the use of decay constants in geo- and cosmochronology. *Earth and Planetary Science Letters, 5,* 320–324.

Turner, G., Huneke, J. C., Podosek, F. A., & Wasserburg, G. J. (1971). ^{40}Ar-^{39}Ar ages and cosmic ray exposure rays of apollo 14 samples. *Earth and Planetary Science Letters, 12,* 19–35.

Turner, G., Miller, J. A., & Grasty, R. L. (1966). The thermal history of the bruderheim meteorite. *Earth and Planetary Science Letters, 1,* 155–157.

Wänke, H., & König, H. (1959). Eine neue Methode zür Kalium-Argon Alterbestimmung und ihre Anwendung auf Steinmeteorite. *Zeitschrift für Naturforschung A, 14a*, 860–866.

6 Dating of Corals and Other Geological Samples via the Radioactive Disequilibrium of Uranium and Thorium Isotopes

Norbert Frank and Freya Hemsing

Abstract

U/Th dating methods have become cornerstone tools for the determination of the age of climate change recorded in marine and continental carbonates. Here we describe the theoretical principles and analytical methods along the example of U/Th dating the aragonite skeletons of tropical corals. We demonstrate that a precision limiting factor is built in the dating principle, known as U-series open system behavior. Moreover, above all the quality of the samples is crucial for a successful and accurate age determination. When using well preserved fossil coral fragments ages provide measures of past sea level, contribute to the calibration of the radiocarbon time scale, and allow for the reconstruction of reef accumulation rates, tectonic subsidence, or uplift. We finally emphasize that U/Th dating also works for secondary carbonates such as stalagmites, calcareous tuff and travertine, but the boundary conditions regarding the U concentration, and the initial U and Th isotopic composition vary wildly and need careful consideration. When doing so, highest precision and accuracy can Is feasible.

Dating methods based on the radioactive disequilibrium in the uranium decay series were developed over the last fifty years. They can be applied to minerals that, at the time of their formation, incorporate uranium into their crystal lattice, but not thorium, whose isotope, ^{230}Th, is a daughter of ^{234}U (Fig. 6.1). This is the case for corals which form their aragonitic, calcareous skeletons from elements present in the seawater. They are used as an example throughout this chapter. The basic concept is that, in seawater, there is dissolved uranium but very little thorium, an insoluble element. Therefore, each crystal of aragonite formed by the coral incorporates only uranium and not its first-generation daughters which are all thorium isotopes. Uranium concentration in seawater is very stable and homogeneous with 3.3 μg of U per liter of water. The activity ratio (^{234}U/^{238}U) is also very stable in the ocean and is slightly above the radioactive equilibrium with a value of 1.1468 ± 0.0001 in the open ocean (Andersen et al. 2010). This slight excess of ^{234}U is due to preferential leaching of this isotope from rocks during weathering of the continental crust (Ivanovich and Harmon 1992). Henderson (2002) proposed that the seawater ratio (^{234}U/^{238}U) has remained constant for at least the past 800,000 years. However, moderate variations of ± 0.01 in this ratio are possible, due to changes in weathering of the continental crust, sea level changes, and variations in freshwater runoff from rivers resulting from climate changes (Esat and Yokoyama 2006). Very recently, it has been suggested that this ratio may also be dependent on the ocean circulation (Chen et al. 2016).

Let us go back to the coral. If the skeleton of a coral remains a chemically closed system after its formation (in other words, without any exchange of uranium or thorium with its sedimentary environment) the ^{230}Th from the decay of ^{234}U accumulates progressively over time, while the excess of ^{234}U decreases.

The state of this radioactive disequilibrium allows for a very precise determination of the coral age depending on the measurement technique used. When this dating method was developed, the isotopes of uranium and thorium were measured by their radioactivity, either directly by α spectrometry or indirectly by γ spectrometry, enabling age determination ranging from a few thousand years to about 300,000 years. Now, we are able to measure the abundance of these isotopes by characterizing them according to their masses, giving a much better accuracy. The age range measurable by thermal ionization mass spectrometry or even multi-collector inductively coupled plasma source mass spectrometry now

N. Frank
Laboratoire des Sciences du Climat et de L'Environnement, LSCE/IPSL, CEA-CNRS-UVSQ, Université Paris-Saclay, Gif-Sur-Yvette, 91190, France

N. Frank (✉) · F. Hemsing
Institute of Environmental Physics, Heidelberg University, Im Neuenheimer Feld 229, 69120 Heidelberg, Germany
e-mail: Norbert.Frank@iup.uni-heidelberg.de

G. Ramstein et al. (eds.), *Paleoclimatology*, Frontiers in Earth Sciences,
https://doi.org/10.1007/978-3-030-24982-3_6

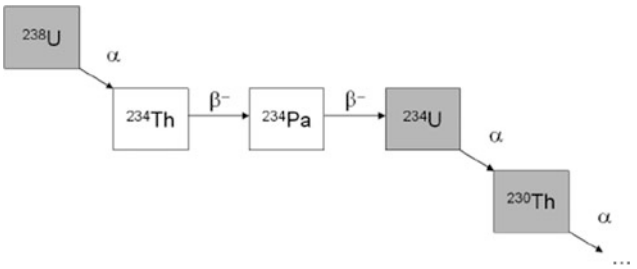

Fig. 6.1 Start of the radioactive decay chain ^{238}U

allows the dating range to be extended from a few years to a few hundred thousand years (>500,000 years). As a result, U/Th dating has now become an indispensable tool for precision geochronology and research on the environmental and climate changes in the late Quaternary.

Undoubtedly, one of the greatest successes of this chronometer is the precise reconstruction of sea levels throughout the climate cycles from growth series of corals (Thompson and Goldstein 2006). This geochronological technique also permits the determination of subsidence or elevation of reefs caused by tectonic movements over time (Frank et al. 2006). Significant progress has also been made on the calibration of ^{14}C ages by combined $^{230}Th/U$ and ^{14}C analysis (Reimer et al. 2013).

Over the past decade, it has become clear that the mineral system of a coral is not a completely closed system but sometimes uranium and thorium exchanges with its sedimentary environment occur. This conclusion was reached from the observation that uranium ^{234}U and ^{230}Th are often in excess of the theoretical levels of the activity ratios ($^{234}U/^{238}U$ and $^{230}Th/^{238}U$) that would be expected from radioactive decay. These inconsistencies are the result of recrystallization, early diagenesis, and radioactive decay of uranium. This makes the dating less precise than the analysis might indicate and makes it necessary to apply corrections to the estimated ages.

In light of these observations, correction models, categorized as 'open' system models were developed which take account of the influence of such disturbances on tropical corals. (Scholz et al. 2004, Szabo et al. 1994)

The focus of this chapter is to explore the dating of tropical corals and other carbonate climate archives using the U/Th method including open-system models, but excluding microstructure and biomineralization. We will examine the methodology in detail including the relevance of the open system and also some applications to geology and paleoclimatology.

This principle of dating by radioactive disequilibrium in the decay chain of uranium applies to many sources of climate records, such as deep-water corals, mollusk shells, and secondary carbonate precipitations on land (stalagmites and travertine). In each case, the formation process of these minerals favors the incorporation of uranium over its radioactive daughters. However, each mineral deposit has its own characteristics with regard to the incorporation of uranium and thorium and open system behavior Cheng et al. (2000a), Mallick and Frank (2002). Here, we will focus on one particular archive: tropical corals. At the end of the chapter, the possibility of dating other geological samples through uranium series disequilibrium will be analyzed briefly.

Methodology of $^{230}Th/^{238}U$ Dating

Principle of $^{230}Th/^{238}U$ Dating

This method is based on the radioactive decay chain of ^{238}U (Fig. 6.1).

The rates of decay in this radioactive chain are highly variable, ranging from a few billion years to hours. The radioactivity of ^{234}Th and ^{234}Pa decreases very rapidly with half-lives (also called periods) of 24.1 days and 6.7 h respectively. Therefore, these isotopes are insignificant relative to the periods of ^{234}U and ^{230}Th, key isotopes in $^{230}Th/^{238}U$ dating. During the formation of the skeleton, only the U isotopes are incorporated, hence ^{230}Th isotope is absent (^{230}Th concentration is zero at $t = 0$). It is therefore only by decay of ^{234}U that ^{230}Th accumulates over time in the coral structure.

To date a sample, it is essential to accurately measure the activities of ^{238}U, ^{234}U and ^{230}Th. Dating is performed by using the radioactive decay equations to define the activity ratios of $^{234}U/^{238}U$ and $^{230}Th/^{238}U$ so that the time elapsed since the formation of the coral skeleton can be calculated (Eqs. 6.1 and 2). The decay equation cannot be solved analytically but ages are estimated by iteration.

$$\left(\frac{^{230}Th}{^{238}U}\right) = 1 - e^{-\lambda_{230}t} + \frac{\delta^{234}U_m}{1000} \times \frac{\lambda_{230}}{\lambda_{230} - \lambda_{234}} \times \left(1 - e^{-(\lambda_{230} - \lambda_{234})t}\right) \tag{6.1}$$

$$\left(\frac{^{234}U}{^{238}U}\right) = \left(\frac{^{234}U}{^{238}U}\right)\text{initial} \times \left(1 - e^{-\lambda_{234}t}\right) \tag{6.2}$$

with λ_{230} and λ_{234}, the constants of decay of ^{230}Th and ^{234}U respectively (Table 6.1), and t the time elapsed since the system closed.

In Eq. (6.1), the activity ratio ($^{234}U/^{238}U$) is expressed as ‰ compared to the radioactive equilibrium:

$$\delta^{234}U = \left[\frac{\left(\frac{^{234}U}{^{238}U}\right)}{\left(\frac{^{234}U}{^{238}U}\right)} - 1\right] \times 1000 \tag{6.3}$$

Table 6.1 Decay of the daughters of ^{238}U by Cheng et al. (2000b) with $T_{1/2}$ the half-life and λ the decay constant

	$T_{1/2}$ (years)	λ
^{238}U	4,468,314,000	1.55125×10^{-10}
^{234}U	245,250	2.82629×10^{-06}
^{230}Th	75,690	9.15771×10^{-06}

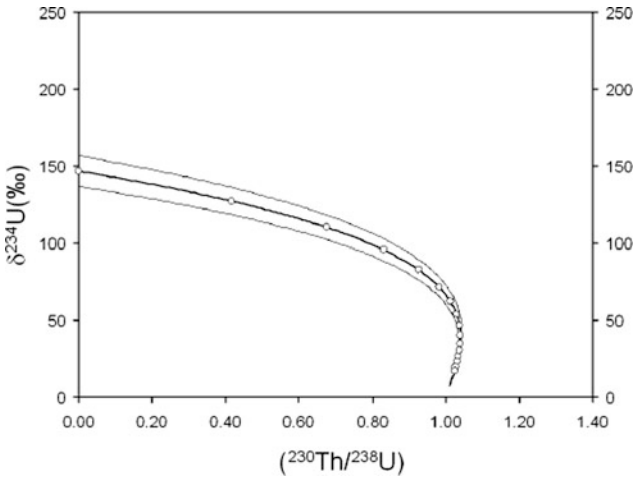

Fig. 6.2 Temporal evolution of the activity ratios ($^{230}Th/^{238}U$) and $\delta^{234}U$ in a closed system. The points (○) show the position of the coral every 50 thousand years

For the method to be applicable, two basic conditions need to hold:

1. During the formation of the aragonitic skeleton, only uranium is incorporated, and therefore ^{230}Th is absent.
2. The system remains closed to any exchange of uranium and thorium with the sedimentary environment after the aragonite is formed.

If a coral satisfies these essential conditions, the activity ratios of ($^{234}U/^{238}U$) and ($^{230}Th/^{238}U$) evolve over time (Fig. 6.2—assuming an activity ratio of ($^{234}U/^{238}U$) in seawater equal to 1.1468 ($\delta^{234}U$ = 146.8‰) at the moment of precipitation of the aragonite).

The accuracy of U/Th dating depends mainly on the accuracy with which the isotope ratios are measured, but the quality of the sample also plays a critical role because it determines whether the fundamental conditions for dating are met.

All of the radionuclides are alpha emitters. Historically, alpha spectrometry, i.e. the direct measurement of the alpha emission of each radionuclide, was the preferred method. However, in the late 1980s, the use of mass spectrometry, first with thermal-ionization, and nowadays with double-focusing inductively coupled plasma source mass spectrometry, became feasible leading to very high precision measurements of ^{238}U and its long-life daughters (^{234}U, ^{230}Th). The mass spectrometric methods have the advantage of directly measuring the number of atoms of an isotope, instead of measuring its radioactivity. This results in a very significant gain in accuracy because instead of measuring a few alpha emissions per minute, tens to millions of ions per second are detected. However, a very rigorous preliminary chemical treatment is essential as the presence of any other elements during ionization will decrease the quality of the measurement or even lead to isobaric interferences. From the number of atoms of each radionuclide measured by mass spectrometry, its activity A_i can be calculated according to the law of decay $A_i = \lambda \times N_i$; where N_i is the number of atoms measured by mass spectrometry and λ is the decay constant of the radionuclide. To calculate the activities of the daughters of ^{238}U from isotopic measurements, we use the decay rates shown in Table 6.1. These decay times have recently been updated Cheng et al. (2013), but we have opted to use the older values (Table 6.1) here because the re-evaluated values by Cheng et al. (2013) have still not been independently confirmed and are identical to the previous ones within a range of uncertainty.

In the following paragraphs, we will discuss the analytical aspect. However, we will firstly specify the sample selection criteria, before explaining the chemical process and finally the physical measurement (Fig. 6.3).

Selecting a Coral for $^{230}Th/^{238}U$ Dating

In order to get good accuracy on the age of the corals, it is crucial to select the best-preserved samples possible. The purpose of the analysis is to obtain ratios between ^{238}U, ^{234}U and ^{230}Th, produced exclusively by radioactive decay, and thus independent of any secondary addition or any depletion of uranium or thorium over the thousands of years the coral has spent as fossil in the reef environment. For this purpose, the selected coral fragments are physically and chemically cleaned of any metal oxide encrustations, traces of clay or organic residue identified beforehand by binocular microscope. This cleaning is carried out over several iterations of rinsing in an ultrasonic bath with ultrapure water, followed by diluted acid baths and oxidizing solutions. Finally, traces of potential bioerosion, caused for example by foraging mollusks, are sought out, and the contaminated parts eliminated.

To test the quality of the selection and cleaning processes, analysis by X-ray diffraction is conducted. This technique

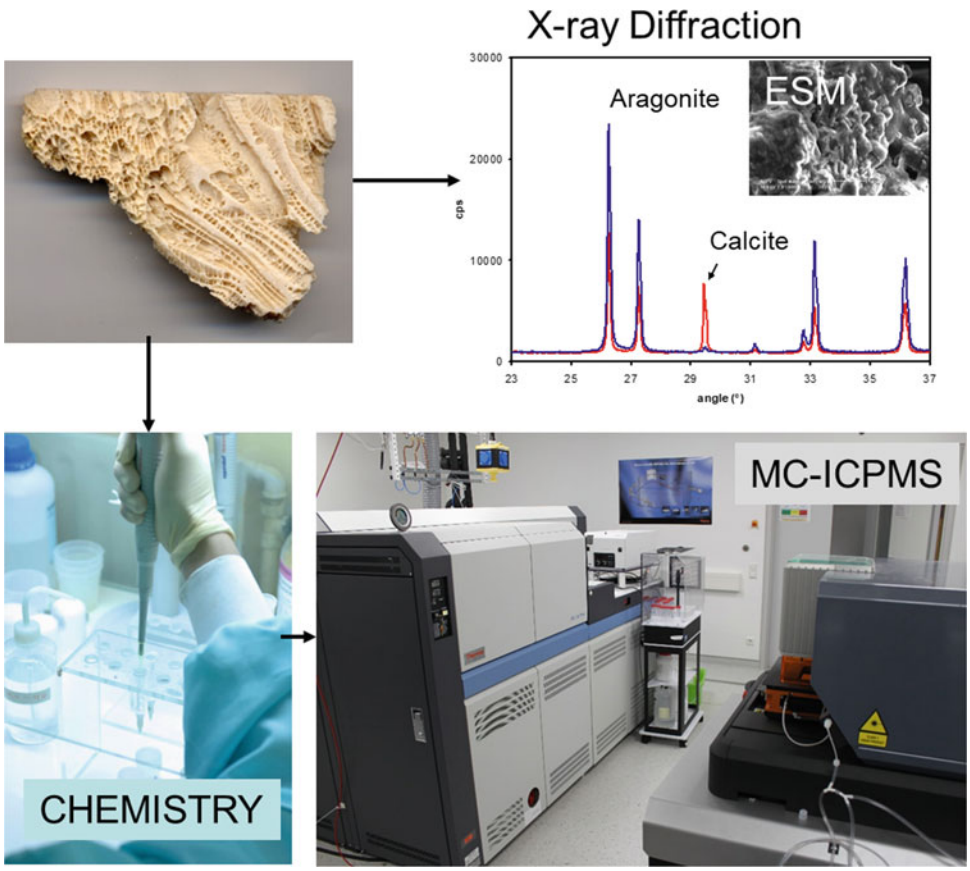

Fig. 6.3 Schematics of the U/Th disequilibrium methodology for fossil tropical coral. Subsamples of coral are taken from the skeleton in order to check that it is composed entirely of aragonite (analysis by X-ray diffraction). The scanning electron microscopy (ESM) identifies secondary aragonite fibers and signs of coral dissolution. Uranium and thorium are then extracted, chemically purified from the carbonate, and their isotopes are measured by inductively coupled plasma source mass spectrometry (MC-ICPMS)

identifies the abundance of various carbonate minerals in the sample, such as aragonite and calcite, the latter being either low or high in magnesium. Only samples identified with more than 98% of aragonite qualify for U/Th dating. More than 2% of calcite would indicate recrystallization and therefore poor preservation of the skeleton. In a less systematic approach, scanning electron microscopy may be carried out to determine the presence of micro traces of dissolution or precipitation of secondary aragonite fibers.

This selection process of the sample prior to dating is onerous, but often necessary, to ensure ages with the best accuracy and 'precision' possible. However, the samples are of macroscopic size, varying from a few tens to a few hundred milligrams, and a piece of coral is rarely perfectly preserved. The results of microanalysis on 1–5% aliquots of the sample, mean that the state of preservation was only tested on part of the sample later used for U/Th dating.

Chemical Procedure

The samples are placed in a strong acid solution (nitric acid or hydrochloric acid), and undergo a chemical treatment which involves several steps. Mass spectrometry measurements are of isotopic ratios, such as $^{234}U/^{238}U$ and $^{230}Th/^{232}Th$. The concentration or activity of the nuclides or the $^{230}Th/^{238}U$ ratio needed to calculate the age of the sample cannot be directly estimated. Consequently, a tracer, known as a 'spike', which contains isotopes of uranium and thorium that do not exist in the natural environment and have a well-established concentration, is added to the solution. These artificial isotopes allow the calculation of the concentration of natural nuclides. Generally, any U/Th dating by mass spectrometry depends on spikes containing ^{233}U, ^{236}U and ^{229}Th. Thus, measurements of the isotopic ratios $^{234}U/^{238}U$, $^{236}U/^{238}U$, $^{233}U/^{236}U$, $^{230}Th/^{229}Th$ and $^{232}Th/^{229}Th$ are needed to determine the concentration of ^{238}U, ^{230}Th and ^{232}Th in the sample, its isotopic ratios $^{234}U/^{238}U$, $^{230}Th/^{232}Th$ and $^{230}Th/^{238}U$, and the corresponding activity ratios.

Once chemical equilibrium between the spike and the sample in solution is reached, uranium and thorium are separated from the major, minor and trace elements by a column chemistry using an ion exchange resin. Several types of resins are used to purify the uranium and thorium from the sample. During the early days of Th/U dating most laboratories used successive series of anionic resin columns DOWEX 1X8. Nowadays, there are also separations for uranium and thorium using specifically designed resins such as the UTEVA resin, which allows for faster and highly effective purification. The sample dissolved in 3 N nitric acid is deposited on a column of UTEVA resin (0.5 ml), loaded in HNO_3 3 N. The column is rinsed several times in

3 N nitric acid (10 column volumes), then uranium and thorium are extracted with hydrochloric acid at different molarities (9–1 N) Douville et al (2010). This technique of chemical separation can be used to purify the uranium and thorium of any other component of the coral with an approximated yield of 100%. The entire chemical procedure can be done in approximately two days for about fifteen samples. For physical measurements, a similar time is required using the most effective tools, such as the MC-ICPMS described below. More recently it has become feasible to extract and purify uranium and thorium using automated extraction systems Wefing et al. (2017), but currently these tools remain the exception in the chemical preparation for U/Th dating. Lastly, the use of laser ablation systems has allowed for the direct extraction of material from samples, which are carried with a gas stream to the source of a mass spectrometer to detect the abundance of uranium and thorium isotopes. However, those techniques allow for rapid-age screening, but remain insufficiently precise for high precision age determination (Spooner et al. 2016).

Physical Measurement by Mass Spectrometry

After chemical purification, the fractions of uranium and thorium are deposited on a pure rhenium filament if analysis is performed on a mass spectrometer with a thermal source. For inductively coupled plasma mass spectrometry, the final solutions are diluted so that each sample has a similar concentration. The uranium and thorium atoms are ionized in the source of a mass spectrometer. Formerly thermal ionization of a solid sample from a heated filament was performed in thermal ionization mass spectrometry (TIMS) at temperatures of up to 1650 to 1800 °C. Most recent generations of mass spectrometers (MC-ICPMS) have substantially improved the ionization yield and hence the analytical accuracy due to their detection of the ions by simultaneous multi-collection and due to ionization temperatures in an Ar plasma of up to 8000 °C. Ions are accelerated by a high voltage and subsequently energy-filtered in an electrostatic filter and deflected by a magnet according to their mass to charge ratio. The ions are ultimately collected in a multi-collection system composed of several faraday cups and electron multipliers. With the advent of novel ultra-high resistances, faraday cups become available for low ion intensities otherwise typically measured on electron multipliers. The MC-ICPMS technology now makes it possible to determine isotopic ratios of uranium with an accuracy of less than 1‰, and of thorium with an accuracy of ± 1‰. This progress has resulted in a U/Th dating with a much higher analytical precision and accuracy than that obtained by TIMS.

Measurement routines using these complex instruments vary and require rigorous data processing. Data processing must, among other things, correct for the effects of mass fractionation related to the measurement, perform comparisons between standards and samples, and consider the impact of background noise from the instruments and from the chemical process (chemical blanks) on the measurements. Uranium standards, HU1 or NBL 112, with known isotopic ratios, are generally used to determine the reproducibility of physical measurements.

Overall, cutting edge mass spectrometry can achieve a dating with a higher precision than 100 years on corals of around 100,000 years. This possibility remains, however, theoretical due to the fact that the error on the final age not only depends on the quality of the physical measurement, but also, and above all, on the sample quality.

Once the isotopic ratios are measured, Eqs. 6.1 and 6.2 shown above are used to estimate the age of the coral and its initial $^{234}U/^{238}U$ ratio.

Limitations of the Method

Theoretically, the accuracy of U/Th dating is determined by the precision of the measurements by mass spectrometry of the isotopic ratios $^{230}Th/^{238}U$ and $^{234}U/^{238}U$. For this, it is assumed that the coral being studied was perfectly preserved and that the basic conditions mentioned above were respected. Therefore, the assumptions are that only uranium was incorporated into the aragonite skeleton at the time of its formation, that the system remained closed to any exchange of uranium and thorium with the sedimentary environment after the formation of aragonite, and finally, that the coral skeleton contained no ^{230}Th at the time of its formation. In

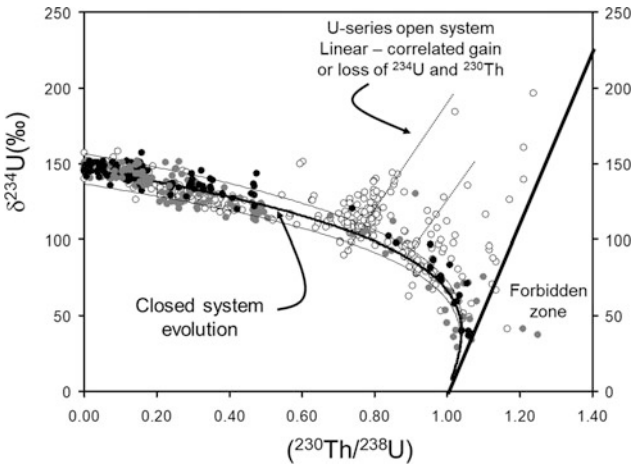

Fig. 6.4 Compilation of $\delta^{234}U$ activity ratios based on $^{230}Th/^{238}U$ ratios of fossil corals (black symbol: deep-water solitary corals; gray symbol: deep-water, reef-building corals; open symbol: tropical corals). The solid black line represents the variation in a closed system compared to the $\delta^{234}U$ ratio of present-day seawater. The dots on the right of the diagram in the 'forbidden' zone cannot be explained by the variation in a closed system. The straight dashed line indicates the distribution of isotopic ratios for co-genetic samples

addition, this dating method is based on the assumption that the activity ratio $^{234}U/^{238}U$ of sea water (equal to 1.1468) was constant over the last 500,000 years. For practical reasons, this ratio is commonly expressed as the relative deviation (in ‰) from radioactive equilibrium and is denoted $\delta^{234}U$ (Eq. 6.3).

Thus, today's $\delta^{234}U$ of seawater is 146.8 ± 0.1‰ (Andersen et al. 2010). Given the conditions mentioned above, using Eq. 6.2, we would expect to find an initial ratio of $^{234}U/^{238}U$ for the coral similar to that of seawater. However, it was observed that many corals more than 80,000 years old had a wide range of values for this ratio, and often values exceed the current value for seawater (Fig. 6.4). For example, a sample 125,000 years old, divided into several small pieces, can present age differences between its various fragments of more than 10,000 years, even though the measurement accuracy is ± 1000 years for each subsample. Variability of age within the same sample can be ten times larger than the measurement precision. In addition, the sub-samples of the same specimen can also show significant variability in their $^{234}U/^{238}U$ ratio over time. This highlights the crucial role of the $^{234}U/^{238}U$ ratio (or $\delta^{234}U$) in the U/Th dating method for tropical corals.

Henderson and Slowey (2000) and Gallup et al. (1994) were the first to realize that the increase of ^{234}U and of ^{230}Th in ancient marine carbonates are often correlated (Fig. 6.4). This proved to be a very important observation because diagenesis, such as the dissolution of the skeleton or precipitation of secondary aragonitic fibers, cannot explain this correlation. For example, the dissolution of the coral skeleton during diagenesis will return uranium to pore waters, but the thorium will be quickly re-precipitated because of its inability to remain in solution. Consequently, the $^{230}Th/^{238}U$ ratio of the coral will increase and the age calculated will be overstated. This process does not involve a significant change in the isotopes of uranium, so it is expected that sub-samples of the same coral will have variable $^{230}Th/^{238}U$ ratios but a constant $\delta^{234}U$. This equilibrium is reversed with the precipitation of secondary aragonitic fibers, as the fibers contain uranium but no thorium, leading to a reduction in the $^{230}Th/^{238}U$ ratio of a coral and an underestimate of age. Since these secondary fibers are younger than the skeleton and they supply uranium taken from seawater, the $\delta^{234}U$ of coral increases slightly but cannot exceed the $\delta^{234}U$ of seawater, i.e. 146.8‰ in total. It is clear that the disturbance in the dating system cannot be entirely attributed to these processes. In particular, this does not explain the observed depletion of ^{234}U and ^{230}Th.

With these points in mind, Henderson and Slowey (2000) and Gallup et al. (1994) proposed that the nuclear recoil effect resulting from the radioactive decay of ^{238}U and ^{234}U is responsible for the disturbance and developed a method to take this into account.

The Nuclear Recoil Effect and the 'Open' Dating System

During the radioactive decay of uranium isotopes, an α particle is ejected from the nucleus. The balance of kinetic energy requires that the nucleus produced (^{234}Th or ^{230}Th) recoils and therefore moves backward. In both cases, a thorium isotope is produced. The ^{234}Th in ^{234}U decays quickly ($T_{1/2}$ = 24.1 days) by emitting an electron. This process is not responsible for the movement of the nucleus, because the recoil energy is too low. Therefore, the backwards movement of the nucleus affects ^{234}U (which occupies the position of ^{234}Th) and ^{230}Th. The mobile nucleus can remain inside the crystal lattice but can also be ejected and pass through the pore fluids, or even into another neighboring crystal lattice (coral or sediment). This process, which occurs in both carbonates and sediments, or in organic matter present in a coral reef, is time-dependent: the more time has elapsed, the more the nuclei will have moved.

Obviously, this action is on a very small scale as displacement of the nucleus occurs over less than 20 nm. Therefore, it cannot be measured directly, but observed variations in concentration of the isotopes ^{234}U (^{234}Th) and ^{230}Th likely reflect the overall redistribution of radionuclides over the entire time elapsed since coral formation.

Thompson et al. (2003) and Villemant and Feuillet (2003) were the first to incorporate this process into the equation for dating (Eq. 6.1). Here, we restrict ourselves to the theoretical approach of Thompson and his colleagues, because, on the purely mathematical level, the two models of radionuclide redistribution are the same. The idea is simply to add a term to the laws of decay (Eqs. 6.1 and 6.2), that takes the recoil effect for ^{234}U and ^{230}Th into account. Equations 4 and 5 are essentially the same as Eqs. 6.1 and 6.2:

$$\left(\frac{^{230}\mathrm{Th}}{^{238}\mathrm{U}}\right) = \left(\frac{^{230}\mathrm{Th}}{^{238}\mathrm{U}}\right)\mathrm{initial} \times e^{(-\lambda_{230}t)} + f_{230}\, f_{234}\left(1 - e^{(-\lambda_{230}t)}\right) + f_{230}\,\frac{\lambda_{230}}{\lambda_{230} - \lambda_{234}}\left(e^{(-\lambda_{230}t)} - e^{(-\lambda_{234}t)}\right)(f_{234} - R_0) \tag{6.4}$$

$$\left(\frac{^{234}U}{^{238}U}\right) - f_{234} = \left(\left(\frac{^{234}U}{^{238}U}\right)\mathrm{initial} - f_{234}\right)e^{(-\lambda_{234}t)} \tag{6.5}$$

R_0 in Eq. 6.4 corresponds to the initial value of $^{234}U/^{238}U$ in seawater fixed at 1.148 ± 0.010 (current value ± 10‰ variability). f_{234} and f_{230} represent the proportions, expressed as activities, lost ($f < 1$) or gained ($f > 1$) following redistributions brought about by the nuclear recoil effect.

The redistribution factor f_{234} is estimated iteratively from the difference between the $^{234}U/^{238}U$ ratio resulting from the temporal evolution in a closed system and the corresponding evolution in an 'open' system.

The link between f_{230} and f_{234} (Eq. 6.6) is the difference of kinetic energy injected into the crystal lattice following the decay of ^{238}U and ^{234}U. The process of an α particle emission is the same with only the kinetic energy being different.

$$f_{234} = 1.157 \cdot (1 - f_{230}) \text{ (Villemant } \textit{and} \text{ Feuillet 2003)} \tag{6.6}$$

The definition of the redistribution factor f is purely mathematical, so gains and depletions in an open system for uranium are expressed as $f > 1$ and $f < 1$. Up to this point, the two calculations of Villemant and Feuillet (2003), and of Thompson et al. (2003) are identical. Assuming that the measured ratios can be used to determine f as defined above, it is possible to estimate the age of the coral in an open system (Eq. 6.4). This approach assumes that only the uranium and thorium in the coral are at the origin of the recoil process. However, this assumption is not always correct. In fact, the process of nuclear recoil, and thus the possible ejection of nuclei over time, does not allow a gain of either ^{234}U or ^{230}Th; the coral can only lose radionuclides. Therefore, a value of $f > 1$ is not expected. But the reality is quite different, because most of the corals show an increase ($f > 1$), and only very few corals show a depletion of radionuclides ($f < 1$).

Thompson and his colleagues considered this obstacle to be theoretical and therefore introduced further complexity in their approach. The gain of radionuclides can be explained, either by direct exchange of nuclei between corals very close to each other, or by fluids circulating in the reef, in other words, from an external source. Consequently, f is always < 1 and the gain in ^{234}U and ^{230}Th is the sum of the depletions over time and of the gain due to the retention of radionuclides ejected and/or transported in the reef. To account for this phenomenon, Thompson and his colleagues established the following equations derived for a simple exchange model:

Instead of estimating f directly from the activity ratios measured (Eq. 6.6), the values of f are fixed, but the excess of ^{234}U and redistribution slope m are estimated iteratively taking an external source into account (other corals or carbonates). Ultimately, we end up with equations that have the same form as those derived from Villemant and Feuillet's model (2003), because the source considered in this model is crucial and must have a composition similar to that of the corals. However, here it is possible to vary the parameters in the model and to find the slope m with the best fits for a set of samples of the same age.

These equations are used to correct for the nuclear recoil phenomenon and to place the values of the activity ratios measured, (^{230}Th/^{238}U) and (^{234}U/^{238}U), on a graph of variations in these ratios within a closed system to calculate the age of the corals.

For example, Fig. 6.5 shows the activity ratios (^{230}Th/^{238}U) and (^{234}U/^{238}U) measured in several corals of a coral reef on the Amedee Island, off the coast of New Caledonia (Frank et al. 2006). Ages calculated using Eqs. 6.1 and 6.2 and the measured activity ratios show a wide dispersion, from 123,600 to 146,000 years. These samples also show a high variability in the initial δ^{234}U, ranging from 119.2 to 211‰. A linear correlation between the ratios (^{230}Th/^{238}U) and (^{234}U/^{238}U) is obvious. This part of the reef very likely developed during the last interglacial period (isotopic stage 5), corresponding to the last sea level maximum and dating back to about 125,000 years. The results therefore demonstrate that this is an 'open system'. Two of the samples were in deficit and twelve had an excess of ^{230}Th and ^{234}U. None of the measured values thus reflect an evolution within a closed system. However, all samples were selected in a rigorous way and have 99% aragonite with minor traces of dissolution and secondary aragonite precipitation. Therefore, early diagenesis of carbonate cannot explain these observations. By applying the models of

$$\left(\frac{^{230}Th}{^{238}U}\right)\text{measured} = 1 - e^{-\lambda_{230}t} + \frac{\lambda_{230}}{\lambda_{230} - \lambda_{234}}\left(\left(\frac{^{234}U}{^{238}U}\right)\text{initial} - 1\right)\left(e^{-\lambda_{234}t} - e^{-\lambda_{230}t}\right)$$
$$+ \frac{1}{m}\left\{\left(\frac{^{234}U}{^{238}U}\right)\text{measured} - \left(\left[\left(\frac{^{234}U}{^{238}U}\right)\text{initial} - 1\right]e^{-\lambda_{234}t} + 1\right)\right\} \tag{6.7}$$

$$m = \frac{(1 - f_{234})\left(1 - e^{-\lambda_{234}t}\right)}{\left((1 - f_{234}f_{230})\left(1 - \frac{\lambda_{230}}{\lambda_{230}-\lambda_{234}}e^{-\lambda_{234}t} + \frac{\lambda_{234}}{\lambda_{230}-\lambda_{234}}e^{-\lambda_{230}t}\right) + (1 - f_{230})\frac{\lambda_{230}}{\lambda_{230}-\lambda_{234}}\left(\frac{^{234}U}{^{238}U}\right)\text{initial}\left(e^{-\lambda_{234}t} - e^{-\lambda_{230}t}\right)\right)} \tag{6.8}$$

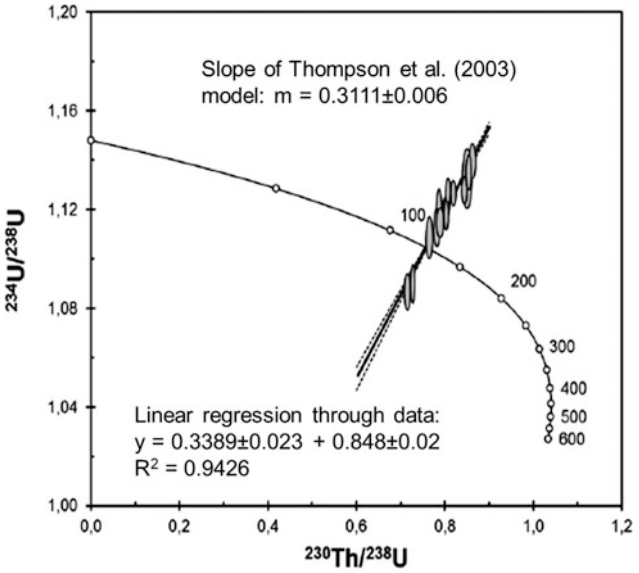

Fig. 6.5 Activity ratios measured in corals from the Amedee Island in New Caledonia. These corals came from a drilling site located between two zones of alteration, and show growth during the last stage of the interglacial (MIS 5.5), 125,000 years ago

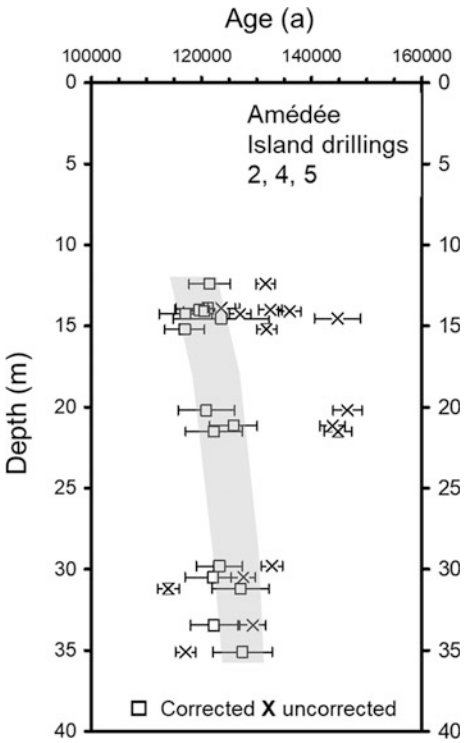

Fig. 6.6 'Raw' results from dating of the coral shown in Fig. 6.5 (× points) and adjusted by an open system model for the redistribution of U, subsequent to the recoil effect (□ points)

Thompson et al. and Villemant and Feuillet, ages are calculated which are consistent with the evolution of the reef during the last interglacial period.

Figure 6.6 shows the ages of the different samples taken from the reef according to depth. After correction using an open system model, it is obvious that the points are now organized in a linear trend, with older samples being located deeper in the core than the corals sampled above. The consistency in the linear relationship is such that it allows the aggregation rate of the reef to be assessed. We can therefore assume here that the process of nuclear recoil is the only mechanism disrupting the dating system. In this example, we applied the Thompson et al. model, with a value f_{234} of 0.975 ± 0.005 and an initial $\delta^{234}U$ of 148 ± 2‰, values determined by Thompson and his colleagues for corals from Barbados.

The Open System: Empirical Model

When dating a single coral, one option is to cut it into several sub-samples and to take them as independent samples to which corrections for an open system could be applied. If the corrected values show a linear correlation between the $^{230}Th/^{238}U$ and $^{234}U/^{238}U$ ratios indicating an excess or depletion of ^{234}U and ^{230}Th, it is possible to calculate the point where the regression line intersects the line of evolution in a closed system and to deduce the age of the coral.

In this way, a more accurate determination of age might be arrived at without having to apply a complicated theory. This idea was used by Scholz et al. (2004) to correct U/Th ages of corals from the Mediterranean. Scholz and his colleagues started with a result showing a variability of activity ratios ($^{230}Th/^{238}U$) and ($^{234}U/^{238}U$) between sub-samples of several corals that could not be explained by the Thompson model. The open system model, subsequent to the process of nuclear recoil, is logically limited to samples which have not undergone any physicochemical alteration. Once the coral skeleton is modified (dissolution, recrystallization, or other), uranium and thorium can be exchanged with the ambient environment. Hence, although still present, the recoil effect is no longer the only and predominant mechanism.

It is therefore obvious that theoretical models have strong limitations and coral selection becomes critical. Moreover, the open system models do not take small-scale variations in uranium concentration within the coral into account, even though these will also impact on the isotope redistribution process (Robinson et al. 2006).

Thus, it is essential to adapt the interpretation of results according to the quality of the selected samples to obtain the most accurate ages possible. It must be kept in mind that these ages, corrected by models, are approximations. In fact, models are created to bring the ages as close as possible to an unknown reality, and the researcher cannot know if the

model chosen takes account of the real phenomena sustained by the sample during its geological history.

In conclusion, the analytical equipment available to us at present provides high precision and potentially accurate measures of U/Th ages of marine carbonates, with precisions on the permil magnitude for ages ranging from current day to several hundreds of thousands of years old. The limits on dating are not technical but primarily imposed by the quality of the samples. For recent samples, up to 15,000 years in age, the U/Th dating system can be considered to be a closed system, since the physicochemical alteration of corals and the nuclear recoil effect have not yet had a significant impact altering the U-series age.

For older corals, however, the impact of physicochemical alteration and especially that of the nuclear recoil displacement result in a system partially open to exchange of ^{234}U and ^{230}Th, requiring subsequent correction to obtain reasonable and accurate ages. The use of correction models reduces precision in dating, as not only the analytical error must be taken into account, but also the parameters of the correction model used, such as the initial δ^{234}U and the exchange factors f_{234} and f_{230}. Selection of the best-preserved specimens possibly ensures the highest quality of dating results that we can expect. If, however, the sample shows signs of significant alteration, it is a prerequisite to measure several subsamples to better identify the extent to which the system may have behaved open for uranium.

Estimating the Change in Sea Level from Tropical Corals

Changes in sea level come from the growth and melting of polar ice caps when the climate of the Earth varies. Knowing the exact variations in sea level during climate cycles can help to reconstruct a precise chronology of climate changes and to connect them with other parameters such as temperature recorded in polar ice cores, the temperature and salinity of the surface waters of the ocean, or even climate variations recorded in continental archives. A chronological framework established in this way helps to better constrain the phase relationships between the various components of the climate system and to determine the teleconnections between the hemispheres. In addition, knowledge of sea level during climate cycles is essential to study the variations in the continental surfaces (expansion or reduction of the continental margins) and their erosion. We have seen that U/Th dating of corals is a powerful tool to determine the evolution of coral reefs over time. But how can the ages of coral reef terraces contribute to a reconstruction of changes in sea level?

Linking the age (its time of formation) and location of a coral taken in a particular part of the world to sea level is complex. In most cases, tropical corals are located in volcanic areas that can be very tectonically active (subsidence or uplift). The sampled coral needs to have grown in situ and not moved by erosion. Also, corals can live at different depths depending on the species. On the continental margins, the processes of eustasy (change in volume of ocean water) and isostasy (variation in altitude of the continent) are also important. With changes in the volume of ice caps during the climate cycles, the continent may well rise or fall depending on the weight it supports. Given all these variables, the reconstruction of sea level from tropical corals requires the selection of corals from a habitat whose characteristics are well known. Therefore, the tectonic processes, which may have had an impact on their original position compared to where they were collected, need to be identified. The parameters required can be defined as follows:

- chronological age t;
- the sampling height above present-day sea level h (+ or −);
- the rate of uplift or subsidence $\Delta h/\Delta t$;
- the average depth of the habitat of the species under study d;
- the variability in the ecological habitat Δd.

The sea level over time $m(t)$ can then be determined by the following equation:

$$m(t) = h + d + \Delta h/\Delta t \times t.$$

The associated uncertainty is:

$$\Delta m(t) = \delta h + \Delta d + t \times \delta(\Delta h/\Delta t) + \Delta h/\Delta t \times \delta t.$$

The reconstruction of sea level is highly dependent on time and the $\Delta h/\Delta t$ values. Moreover, it assumes that the rate of uplift or subsidence has remained constant over the time interval of the reconstruction.

The localization h and depth of habitat d can be well constrained and are not, or only very little, influenced by time. To minimize the impact of subsidence or uplift rates, the ideal is to collect corals in the most stable places possible, in terms of tectonics, for the sea level (m) to be almost completely a function of t. However, most studies are located in places with strong uplift rates because these coral terraces emerged and become easily accessible to sampling. This sampling approach means that there is uncertainty about the uplift rate and therefore about the reconstructed sea level. Figure 6.7 shows reconstructions of sea levels obtained from U/Th dating of tropical corals, as they have been published for various regions ranging from the Pacific (Tahiti, the Marquesas, Vanuatu, Australia, New Caledonia) to the Atlantic (Barbados) (Bard et al. 1990; Cabioch et al. 2003; Frank et al. 2006; Gallup et al. 1994; Hanebuth et al. 2000; Thompson and Goldstein 2005). The graph also

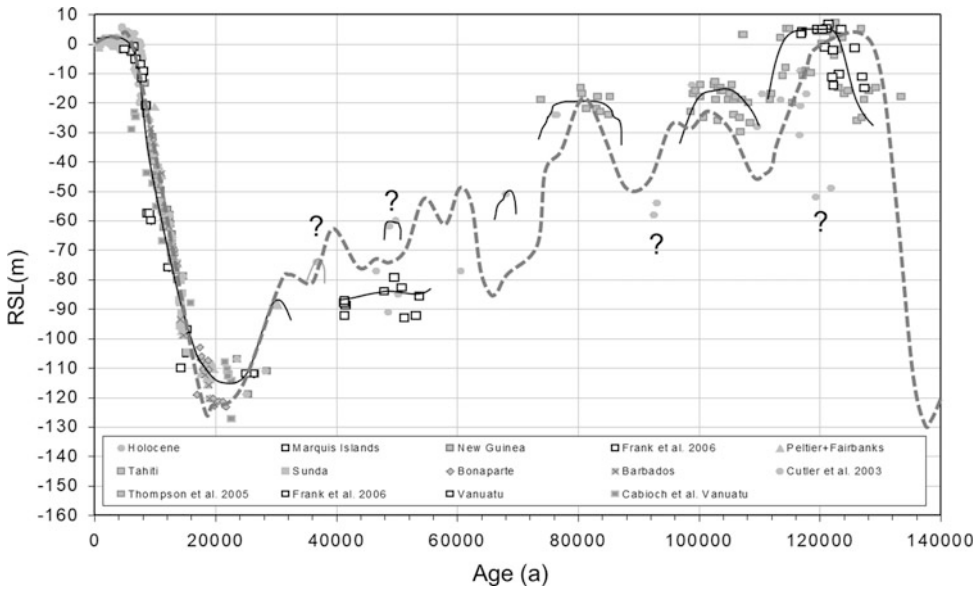

Fig. 6.7 Reconstruction of relative sea level (RSL) from U/Th dating of tropical corals (dots) and from oxygen isotopes in benthic foraminifera (black and gray lines)

shows a reconstruction of the variations in sea level and the associated uncertainty (black and gray lines) obtained from isotopic measurements of oxygen in marine sediments (Waelbroeck et al. 2002). This reconstruction is based on the assumption that the storage at the poles of a large quantity of freshwater depleted of ^{18}O causes an increase in the oceanic ^{18}O content. Therefore, the $^{18}O/^{16}O$ ratio recorded in 'deep water' foraminifera (less influenced by water temperature changes) can provide information on the size of ice sheets, and, by consequence the sea level during the lifetime of the foraminifera. With this approach, it is possible to reconstruct variations in sea level almost continuously. The various reconstructions show very similar variations in sea level, with a low level during cold climate periods and a high sea level during interglacial periods.

Over the past 140,000 years, the sea level has varied from +5 m (relative sea level, RSL) during the last interglacial maximum to about -120 m during the last and penultimate glacial maxima. A drop in sea level of this magnitude would correspond to a volume of ice of about 47 million km^3! By comparison, this is equivalent to an ice coverage over the entire North American continent with an average thickness of 2000 m. Knowing that an increase in sea level of one meter would have devastating impacts on much of the world population living today in coastal areas, it should be highlighted that natural changes in climate during the last transition (termination I) caused increases in sea level of 1.2 m every hundred years. It should further be noted that rapid changes in sea level are also evidenced during other climate transitions between glacial and interglacial periods. During the last interglacial, about 125,000 years ago, sea level was probably higher than the current level by about 5–9 m (Dutton and Lambeck 2012). Hence, in the context of the global warming observed since the early twentieth century, a rise in sea level of over one meter per century is quite conceivable if the ice sheets (Greenland, Antarctica) were to be destabilized.

The challenge for geochemists using U/Th dating of tropical corals is not to predict future changes in sea level. Rather, they hope to find new coral reefs to reconstruct past changes in sea level, and understand the pace and causes of these changes during climate transitions in more detail. Using corals has the great advantage that they can be dated more precisely than marine sediments. Hence, episodes of rapid climate change (Dansgaard-Oeschger cycle, Heinrich events, described in Volume 2) are the subject of special attention.

Other Geological Samples Datable by the U/Th Method

Other marine carbonates, such as deep-sea corals or shellfish shells can be dated by the U/Th method. In particular, deep-sea corals behave very similarly to their tropical counterparts, with a slightly higher concentration of uranium. However, there are two major differences that are very important for U/Th dating. First, the aragonite skeleton is often more robust in deep-water corals, especially for the species *Lophelia pertusa* and *Desmophyllum dianthus.* Secondly, the physicochemical alteration is less important because the skeleton remains underwater, from its formation to its removal. As a result, the openness of the uranium system due to the processes of nuclear recoil and physicochemical alteration seems less important for these species. However, in deep waters, an increase in ^{230}Th resulting from

decay of dissolved uranium is observed. Deep-water corals therefore incorporate small amounts of ^{230}Th during the formation of their skeleton, and a significant correction is required to achieve precision and accuracy in equivalent ages (Cheng et al. 2000a; Frank et al. 2004).

Shells of mollusks have another distinctive feature. The organism precludes incorporation of uranium during the formation of its aragonite shell through a still unknown biological process. A modern shell contains very little uranium (in the range of a few tens of ng/g), whereas an aragonite coral skeleton contains a few micrograms/g. This would not be problematic for U/Th dating if the shell remained in a closed system during its preservation in sediment. Unfortunately, it was observed that, after the death of the organism, the shell takes up uranium from its environment. The uranium concentration may increase by up to 10 mg/g, which is 100 times higher than at the time of its formation. As it is impossible to identify the source of the excess uranium and how it has accumulated over time, shells of mollusks are considered as open systems for uranium. Thus, one of the two basic conditions of dating mentioned above is violated (closed system), implying that based on our current knowledge, U/Th dating is not a suitable dating method for shells and mollusks (Kaufman et al. 1996).

For continental secondary carbonates, such as stalagmites, travertine or tuff, dating by U/Th follows the same 'analytical and theoretical' principles presuming the same two assumptions and using the same basic Eqs. (6.2) and (6.3) to determine the age. In groundwater a disequilibrium between ^{238}U, ^{234}U and ^{230}Th is created due to the fact that uranium is easily dissolved by the weathering of rocks, soils and sediments, while the less soluble thorium is essentially absent. In fact, the precipitation of calcite in the form of stalagmites, travertine or calcareous tuff leads to the co-precipitation of uranium in the carbonate without its radioactive daughter, ^{230}Th. Therefore, as in corals a radioactive disequilibrium is created during the formation of the carbonate. The concentration of uranium in these secondary carbonates is related to the uranium content of groundwater and the type of mineral formed. It can vary from a few ng/g to hundreds of µg/g. However, the application of the dating method is more complex than for marine organisms. The isotopic composition of uranium in groundwater can be highly variable depending on the weathering processes that come into play in an aquifer, leading to activity ratio values for (^{234}U/^{238}U) that vary between 0.8 and more than 5, or in delta notation between −200‰ and more than +5000‰ (Kaufman et al. 1996).

Another issue is that continental carbonates are often contaminated with clay or even organic particles. These may exhibit high uranium and thorium concentrations, without being in radioactive disequilibrium. Moreover, in porous carbonates, such as tuffs or travertines, several generations of crystals can be found in a single layer of carbonate, Mallick and Frank (2002). This means that U/Th dating of continental carbonates is far more difficult than for corals. The isotopy of uranium cannot be used to test if the system is open or closed, and the presence of an initial supply of thorium by groundwater or contaminants needs to be investigated. To estimate the importance of contaminants, the isotope—^{232}Th is used, Szabo et al. (1994). It is the most abundant isotope of natural thorium. It is at the origin of a decay chain called after ^{232}Th. As clay contains lots of thorium (>5 µg/g), the appearance of ^{232}Th in a carbonate sample is a sign of the presence of such contaminants (Ludwig and Titterington 1994).

Therefore, as for corals, sampling is a crucial stage of U/Th dating. It is essential to select a sample from a layer of carbonate containing a minimum of ^{232}Th, indicator of contaminants, and the sample must be representative of the original carbonate, i.e. the first generation deposited. Within these constraints, the U/Th dating of stalagmites, travertine and tuff can be accurate, and nowadays allows for precise determination of time frames for climate (Wang, et al. 2001), and archaeological (McDermott et al. 1993), studies.

Conclusions

Dating by U/Th methodologies has become a very powerful tool, widely used to obtain a fine chronology of the growth of coral reefs and many other carbonates. Although technical developments have been rapid in recent years, with precise isotopic measurements of radionuclides from the decay of uranium, the quality of the sample itself and the movement of radionuclides induced by their own radioactivity cause problems for dating. Today, we no longer refer to a dating system that is strictly closed, since the decay itself is partly the cause of exchanges of uranium and thorium with the coral environment. Correction models, known as 'open system age models' are emerging to incorporate this important issue. However, prior to being studied, the sampling process and characterization of the sample are crucial as dating samples significantly altered by diagenesis is doomed to failure.

A precise geochronological framework established under optimum analytical conditions and based on samples with as good a level of preservation as possible, provides exceptional opportunities to determine geological parameters such as the uplift or subsidence of a coral reef or variations in sea level. The U/Th dating method has now become a key element to place significant changes in major components of the climate system within a precise temporal context. This permits a direct comparison with astronomical forcings for the Quaternary.

References

Andersen, M. B., et al. (2010). Precise determination of the open ocean 234U/238U composition. *Geochemistry, Geophysics, Geosystems, 11*(12), n/a–n/a.

Bard, E., Hamelin, B., & Fairbanks, R. G. (1990). U-Th ages obtained by mass spectrometry in corals from Barbados: Sea level during the past 130,000 years. *Nature, 346,* 456–458.

Cabioch, G., Banks-Cutler, K. A., Beck, J. W., Burr, G. S., Corrège, T., Edwards, R. L. & Taylor, F. W. (2003). Continuous reef growth during the last 23 Kyr Cal BP in a Tectonically active zone (Vanuatu, South West Pacific). *Quaternary Science Reviews*, *22*, 1771–1786.

Chen, T. Y., et al. (2016). Ocean mixing and ice-sheet control of seawater U-234/U-238 during the last deglaciation. *Science, 354* (6312), 626–629.

Cheng, H., Adkins, J. F., Edwards, R. L. & Boyle, E. A. (2000a). U-Th dating of deep-Sea Corals. *Geochimica et Cosmochimica Acta*, *64*, 2401–2416.

Cheng, H., Edwards, R. L., Hoff, J., Gallup, C. D., Richards, D. A., & Asmeron, Y. (2000b). The half-lives of Uranium-234 and Thorium-230. *Chemical Geology, 169,* 17–33.

Cheng, H., et al. (2013). Improvements in 230Th dating, 230Th and 234U half-life values, and U-Th isotopic measurements by multi-collector inductively coupled plasma mass spectrometry. *Earth and Planetary Science Letters, 371–372,* 82–91.

Douville, E., Salle, E., Frank, N., Eisele, M., Pons-Branchu, E., & Ayrault, S. (2010). Rapid and precise ^{230}Th/U dating of Ancient Carbonates using inductively coupled plasma-quadrupole mass spectrometry. *Chemical Geology, 272,* 1–11.

Dutton, A., & Lambeck, K. (2012). Ice volume and sea level during the last interglacial. *Science, 337,* 216–219. https://doi.org/10.1126/science.1205749.

Esat, T. M. & Yokoyama, Y. (2006). Variability in the Uranium isotopic composition of the oceans over glacial-interglacial time-scales. *Geochimica Cosmochimica Acta*, *70*, 4140–4150.

Frank, N., Paterne, M., Ayliffe, L. K., Blamart, D., van Weering, T., & Henriet, J. P. (2004). Eastern North Atlantic Deep-Sea Corals: Tracing upper intermediate water D^{14}C during the Holocene. *Earth and Planetary Science Letters, 219,* 297–309.

Frank, N., Turpin, L., Cabioch, G., Blamart, D., Tressens-Fedou, M., Colin, C., et al. (2006). Open system U-series ages of corals from a subsiding reef in New Caledonia: Implications for sea level changes, and subsidence rate. *Earth and Planetary Science Letters, 249,* 274–289.

Gallup, C. D., Edwards, L., & Johnson, R. G. (1994). The timing of high sea levels over the past 200,000 years. *Science, 263,* 796–800.

Hanebuth, T., Stattegger, K., Grootes, P. (2000). Rapid flooding of the sunda shelf: A late glacial sea level record. *Science*, *288*, 1033–1035.

Henderson, G. M. (2002). Seawater (234U/238U) during the last 800 thousand years. *Earth and Planetary Science Letters, 199,* 97–110.

Henderson, G. M., & Slowey, N. C. (2000). Evidence from U-Th dating against northern hemisphere forcing of the penultimate deglaciation. *Nature, 404,* 61–68.

Ivanovich, M. & Harmon, R. S. (1992). *Uranium-series disequilibrium: Applications to earth, marine, and environmental sciences* (2nd ed., p. 910), Oxford: Clarendon Press.

Kaufman, A., Ghaleb, B., Wehmiller, J. F. & Hillaire-Marcel, C. (1996). Uranium concentration and isotope ratio profiles within Mercenaria Shells: Geochronological implications. *Geochimica et Cosmochimica Acta*, *60*(19), 3735–3746.

Ludwig, K. R. & Titterington, D. M. (1994). Calculation of ^{230}Th/U Isochrons, ages, and errors. *Geochimica et Cosmochimica Acta*, *58* (22), 5031–5042.

Mallick, R., & Frank, N. (2002). A new technique for precise uranium-series dating of travertine micro-samples. *Geochimica et Cosmochimica Acta, 66*(24), 4261–4272.

McDermott, F., Grün, R., Stringer, C. B., & Hawkesworth, C. J. (1993). Mass-spectrometric U-series dates for Israeli Neanderthal/early modern hominid sites. *Nature, 363,* 252–255.

Reimer, P. J., et al. (2013). Intcal13 and Marine13 radiocarbon age calibration curves 0–50,000 Years Cal Bp. *Radiocarbon, 55*(4), 1869–1887.

Robinson, L., Adkins, J., Fernandez, D. P., Burnett, D. S., Wang, S. L., Gagnon, A. C., et al. (2006). Primary U distribution in scleractinian corals and its implications for U series dating. *Geochemistry Geophysics Geosystem, 7,* 1–20.

Scholz, D., Mangini, A., & Felis, T. (2004). U-series dating of diagenetically altered fossil reef corals. *Earth and Planetary Science Letters, 218,* 163–178.

Spooner, P. T., Chen, T., Robinson, L. F., Coath, C. D. (2016). Rapid uranium-series age screening of carbonates by laser ablation mass spectrometry.*Quaternary Geochronology, 31*, 28–39.

Szabo, B. J., Ludwig, K. R., Muhs, D. R., & Simmons, K. R. (1994). Thorium-230 ages of corals and duration of the last interglacial sea-level high stand on Oahu, Hawaii. *Science, 266,* 93–96.

Thompson, W. G., & Goldstein, S. J. (2005). Open-system coral ages reveal persistent suborbital sea-level cycles. *Science, 308,* 401–404.

Thompson, W. G., Spiegelman, M. W., Goldstein, S. L., & Speed, R. C. (2003). An open-system model for U-series age determinations of fossil corals. *Earth and Planetary Science Letters, 210,* 365–381.

Thompson, W. G., & Goldstein, S. L. (2006). A radiometric calibration of the SPECMAP timescale. *Quaternary Science Reviews, 25*(23–24), 3207–3215.

Villemant, B., & Feuillet, N. (2003). Dating open systems by the ^{238}U-^{234}U-^{230}Th method: application to quaternary reef terraces. *Earth and Planetary Science Letters, 210,* 105–118.

Waelbroeck, C., Labeyrie, L., Michel, E., Duplessy, J. C., McManus, J. F., Lambeck, K., et al. (2002). Sea-level and deep water temperature changes derived from benthic foraminifera isotopic records. *Quaternary Science Reviews, 21,* 295–305.

Wang, Y. J., Cheng, H., Edwards, R. L., An, Z. S., Wu, J. Y. Shen, C.-C. & Dorale, J. A. (2001). A high-resolution absolute dated late pleistocene monsoon record from hulu cave, China. *Science*, *294*, 2345–2348.

Wefing, A. M., et al. (2017). High precision U-series dating of scleractinian cold-water corals using an automated chromatographic U and Th extraction. *Chemical Geology, 475,* 140–148.

Magnetostratigraphy: From a Million to a Thousand Years

7

Carlo Laj, James E. T. Channell, and Catherine Kissel

Since the publication in 1600 of the book *De Magnete* by William Gilbert, and the measurements by magnetic observatories progressively obtained from various parts of the globe, we know that the Earth's magnetic field is comparable to one that would be created by a bar-magnet placed at the center of the Earth and inclined by some 11° with respect to the axis of rotation (Fig. 7.1).

For each point on the Earth's surface, the intensity and direction of the Earth's magnetic field are defined in terms of two components: the declination, which is the angle on the horizontal plane between the magnetic north and the geographic North, and the inclination, which is the angle between the magnetic field vector and the horizontal plane. By convention, the declination is zero when the field vector points to the North (it is 180° if the field vector points to the South), and the inclination is positive when the field vector points downwards (which is the case today in the northern hemisphere).

Measurements by observatories, which began in 1576 in London and in 1617 in Paris, soon showed that declination and inclination were not stable throughout history: since measurements began, the inclination in Paris has changed by about 10° and the declination by about 30°.

The intensity has decreased by about 5% per century. This phenomenon is called the 'secular variation' of the geomagnetic field. Changes in declination are plotted on marine charts, essential tools for navigation by compass, before the development of GPS.

C. Laj (✉)
Department of Geosciences, Ecole Normale Supérieure, PSL Research University, 24 rue Lhomond, 75231 Paris Cédex, France
e-mail: carlo.laj@ens.fr

J. E. T. Channell
Department of Geological Sciences, University of Florida, 241 Williamson Hall, P.O. Box 112120 Gainesville, FL 32611, USA

C. Kissel
Laboratoire des Sciences du Climat et de l'Environnement, LSCE/IPSL, CEA-CNRS-UVSQ, Université Paris-Saclay, 91190 Gif-sur-Yvette, France

Secular variation was therefore identified as the first manifestation of the instability of the geomagnetic field. This was already surprising, but the biggest surprise was yet to come, when paleomagnetism methods were able to decipher the history of the geomagnetic field over prehistoric periods.

In 1906, Bernard Brunhes was the first to measure a direction of magnetization in rocks which was more or less opposite to that of the present geomagnetic field. Brunhes measured this magnetization both in a Miocene lava flow and in clays that had been baked when covered by this lava flow, which he called "natural brick". In doing so, Brunhes used for the first time a test in the field, now called the "baked contact test", which is based on the fact that, when a lava flow settles on a sedimentary layer, it re-magnetizes it, either partially or wholly, by heating it up.

If the direction of the magnetic field changed between the settling of the sediment and the arrival of the lava, the initial magnetic direction of the sediment will be replaced by the magnetic direction of the overlying lava. (To quote Bernard Brunhes "If, in the banks of natural clay, we have a well-defined magnetic direction and which differs from the direction of the current terrestrial field, it is reasonable to assume that the magnetic direction is that of the Earth's field at the time when the lava flow transformed the clays into "natural bricks"). Brunhes's conclusion that "at the time of the Miocene, around Saint-Flour, the North Pole was pointing upwards: it is the Earth's South Pole that was closest to Central France" is the first suggestion that the polarity of the magnetic field of the Earth could have reversed in the geological past.

Twenty years later, the Japanese scientist Motonori Matuyama was the first to attribute reverse magnetization of volcanic rocks in Japan and China to reversals of the Earth's geomagnetic field and to differentiate Pleistocene lava from Pliocene lava on the basis of the polarity of their magnetization. Matuyama was thus the first to use magnetic stratigraphy as a way to order sequences of rocks in time.

The modern era of magnetostratigraphy began in the 1950s in Iceland with the work of Hospers (1953). Hospers'

G. Ramstein et al. (eds.), *Paleoclimatology*, Frontiers in Earth Sciences,
https://doi.org/10.1007/978-3-030-24982-3_7

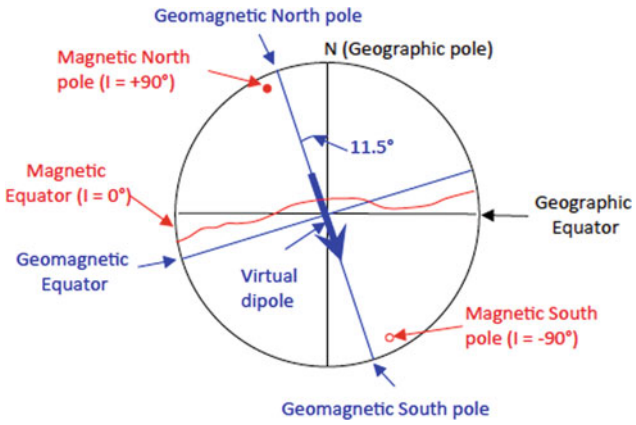

Fig. 7.1 Diagram of the geocentric, inclined dipole

work, followed by Wensink (1966), led to a subdivision of Icelandic Pliocene-Pleistocene lava in three polarity zones: normal-inverse-normal, from most recent to oldest. Afterwards, the joint use of paleomagnetic measures and potassium/argon dating (K-Ar, Chap. 5) by Cox et al. (1963) and McDougall and Tarling (1963a, b) marked the beginning of the development of the modern scale of magnetic polarities (Geomagnetic Polarity Time Scale, GPTS).

The first examples of magnetostratigraphic measures obtained from sedimentary sequences were those by Creer et al. (1954) and by Irving and Runcorn (1957), which demonstrated alternating positive and negative polarity in thirteen sites of Torridonian sandstone in Scotland, and in Devonian and Triassic rocks. In parallel, Khramov (1960) published magnetostratigraphic results from Pliocene-Pleistocene sediments in Turkmenistan, and proceeded to develop chromolithographic interpretations based on the assumption that the durations of the different polarity periods were identical. We now know that this assumption is unfounded. Other pioneering studies of magnetostratigraphy were carried out on red Triassic sandstone from the Chugwater Formation, on the European Triassic Bundsanstein and on the Moenkopi Formation from the Lower Triassic (see Opdyke and Channell 1996). All these studies were conducted on sandstone and silt mainly of continental origin, largely devoid of fauna, and therefore, the correlations based on the identification of polarity intervals were not supported by biostratigraphic correlations.

The first studies of marine sediments from the Pliocene-Pleistocene collected by coring in high southern latitudes (Opdyke et al. 1966) mark the beginning of modern magnetostratigraphy. These studies, combining magnetostratigraphy and biostratigraphy, improved and expanded the Geomagnetic Polarity Time-Scale (GPTS), which was obtained by the paleomagnetic study of basaltic outcrops and marine magnetic anomalies (MMA) (e.g. Heirtzler et al. 1968).

Over the past two decades, significant technical developments have enabled the dating of recent volcanic formations and sedimentary formations. In parallel, the development of corers like the Hydraulic Piston Corer from the Ocean Drilling Program (ODP) or the CALYPSO corer on board the research vessel *Marion Dufresne* of the French Polar Institute (IPEV) allowed the sampling of very long marine sedimentary sequences, with very high sedimentation rates. Thus, it was demonstrated that certain very brief changes in the magnetic polarity of the sediment, initially thought to be due to sampling artifacts, or to re-magnetization phenomena or to various sedimentary processes, were, in reality, reflecting coherent reversals in the polarity of the geomagnetic field, which are observed simultaneously at different locations on the surface of the globe. These "geomagnetic excursions", which occurred during periods previously considered "stable", such as the Brunhes or Matuyama periods, provide an exceptional tool for correlations over long distances. Provided that these excursions are well dated (on volcanic rocks with records of intermediary or reversed paleomagnetic directions), it is possible to establish a scale of geomagnetic instabilities (GITS = Geomagnetic Instabilities Time Scale), allowing a better temporal resolution than the scale of magnetic polarities.

Finally, over the last decade, a new method of magnetic correlation, based on the variations in intensity of the Earth's magnetic field, has been proposed. The records of geomagnetic paleointensity obtained from marine sediments contain a global signal, which is a global-scale correlation tool at an exceptional time resolution. Although this new method is more restrictive in its use (it requires a high level of homogeneity of the magnetic mineralogy of the sediments), it potentially allows cross-comparison with the stratigraphy of ice cores. As variations in geomagnetic paleointensity control the production of cosmogenic isotopes, like ^{10}Be and ^{36}Cl in the upper atmosphere, their flux, measured in ice cores from Greenland and Antarctica, is inversely correlated with these variations. This makes it possible to envisage a correlation between ice and marine sediments.

Below, we examine in turn the three major developments in magnetostratigraphy, first the polarity scale, then the scale of geomagnetic instabilities, and finally the development of the method of correlation by paleointensity. We adopt a "historical" approach, retracing the different stages and the main challenges encountered, and we will also attempt to highlight not only the advantages, but also the limitations of each method. We will illustrate, through examples, the unique role that magnetostratigraphy can play, especially in understanding the mechanisms of climate variability, by allowing the evaluation and possible quantification of temporal phase differences between various regions and between different records (ocean, cryosphere, land).

Establishing the Scale of Magnetic Polarities

First Coupled Measurements: Magnetization of Volcanic Rocks—K/Ar Dating; the McDougall and Tarling Scale and the Mankinen and Dalrymple Scale for the Plio-Pleistocene

In the 1960s, the first geomagnetic polarity time scales (GPTS) were developed using studies coupling magnetic polarity with radiometric dating (K/Ar, Chap. 5). These include the first studies conducted by Cox et al. (1963) in California and by McDougall and Tarling (1963a, b) on the Hawaiian Islands. Identification of the different zones of polarity of the Plio-Pleistocene was based solely on their radiometric age, as none of the volcanic sequences studied (apart from the Icelandic sequences studied by Watkins and Walker) had the continuity and duration to form a long, more or less continuous, stratigraphic sequence. The scale of polarities was therefore constructed by combining results from locations often very far from each other. So, there is no 'stratotype' (typical locality), as is the case for sedimentary outcrops.

The studies that marked this first phase of development of the scale were conducted from Jaramillo, the Cobb Mountain, in the Olduvai Gorge, Reunion, Mammoth, Cochiti and Nunivak (see Opdyke and Channell 1996). All these studies led to the gradual establishment of the magnetostratigraphic scale for the Plio-Pleistocene, shown in Fig. 7.2.

It was at this time that the custom of naming the long periods of polarity (polarity chrons) after the great geophysicists (Brunhes, Matuyama, Gilbert, Gauss) was introduced, while the shorter periods (polarity subchrons) were named after the place where they were discovered (Jaramillo, Mammoth, etc.).

The magnetic polarities scale by Mankinen and Dalrymple (1979) (Fig. 7.3), based on studies coupling magnetic polarity and K/Ar dating of volcanic rocks, is the last stage of this development phase of the magnetostratigraphic scale and remained the standard in the discipline covering the last five million years, for over ten years.

Further back than 5 million years, however, analytical uncertainties in radiometric dating become of the order of the duration of polarity periods, making their identification unreliable. Other methods are required to extend this scale to more ancient times.

Magnetic Stratigraphy in Pliocene-Pleistocene Sedimentary Series

It was the studies of magnetism of deep ocean sediments that first enabled this extension (Opdyke et al. 1974). The magnetic particles contained in the sediments were deposited with a preferred orientation along the lines of the geomagnetic field prevailing at the time of deposition. In many cases, this orientation was preserved over time: just as for lava, sediments have a "magnetic" memory. Although the precise mechanisms by which sediments acquire magnetism are still poorly understood and this may limit their use in some applications, sediments, on the other hand, have the enormous advantage of registering the direction of the geomagnetic field almost continuously unlike lava, where the continuity of the signal is conditioned by the sporadic nature of volcanic eruptions.

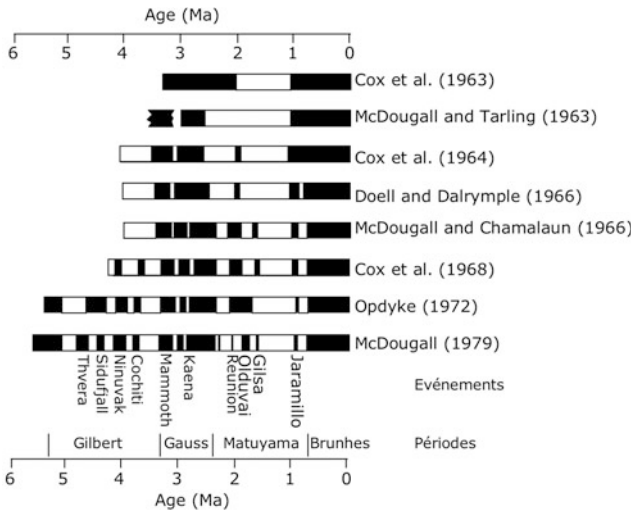

Fig. 7.2 The first scales of geomagnetic polarity for the Plio-Pleistocene period. After McDougall (1979). In black: normal periods, in white: inverse periods

Figure 7.4 shows an example of magnetic polarity recorded in the core RC12-65 collected by Opdyke et al. (1974), on the research vessel *R. Conrad* of the Lamont Doherty Earth Observatory, Columbia University, USA. While some details may differ, the sequence of polarity periods from the Mankinen and Dalrymple scale can be seen in the record (from the Brunhes to the Gilbert period).

However, the sediment core goes back further in time; the lowest level is from around 10 million years ago, based on paleontological estimates.

Magnetic Anomalies at Sea and the Heirtzler Scale of Magnetic Polarities

The study of magnetic anomalies at sea constituted the major step towards establishing the sequence of magnetic polarities, from the middle of the Mesozoic era through to recent times.

The hypothesis by Vine and Mathews (1963) of the spreading of the seafloor directly explains the formation of these magnetic anomalies on both sides of oceanic ridges (Fig. 7.5).

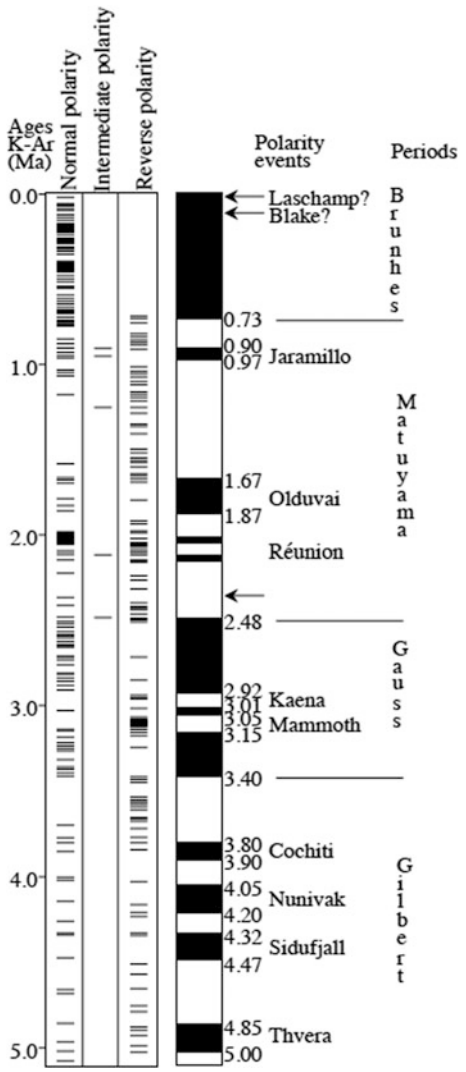

Fig. 7.3 Magnetostratigraphic scale established for the last five million years. After Mankinen and Dalrymple (1979)

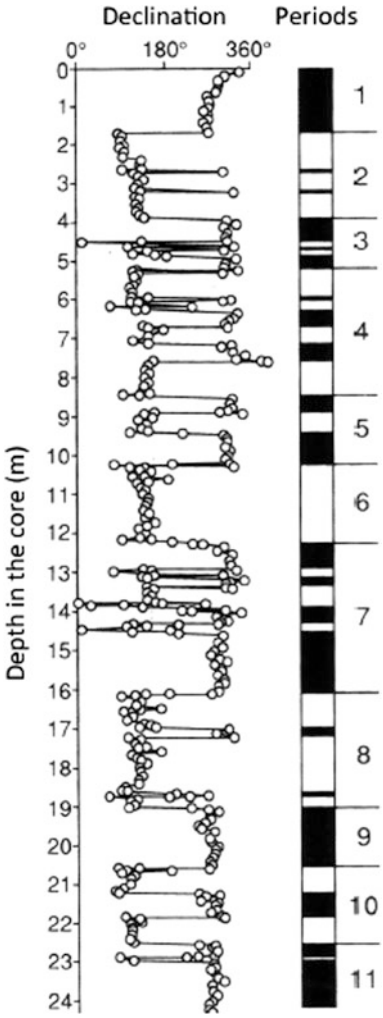

Fig. 7.4 Results obtained by Opdyke et al. (1974) on a marine sediment core showing changes in declination of natural magnetization illustrating the changes in magnetic polarity

During expansion, material from the upper mantle reaches the surface at the axis of the ocean ridges, solidifies, and is then pushed laterally in a symmetrical manner on either side of the ridge. The oceanic crust, composed of igneous rocks that contain magnetic minerals, acquires a thermoremanent magnetization during cooling and therefore registers the Earth's magnetic field at the time of cooling. Alternating normal and reverse polarities are recorded "continuously" in rocks at the ocean bottom, which gives the characteristic "pajama stripe" structure of the magnetic anomalies distribution at sea. This structure can be detected by trailing a magnetometer behind a research vessel.

This is exactly the type of work that was done by the Lamont Doherty Geological Observatory team led by Heirtzler, Pitman and Le Pichon. Their studies showed that magnetic anomalies, linear and symmetrical on both sides of the ridges, exist over large areas of the North and South Pacific and the Atlantic and South Indian oceans. In addition, assuming that the anomalies originate from a sequence of blocks magnetized in normal and reverse directions, they showed that these anomalies correspond to the same scale of magnetic polarities, the only difference being the rate of expansion of the various ocean basins. Heirtzler et al. (1968) also calculated the speed of expansion of the South Atlantic by using the date (known from another source) of 3.35 Ma for the Gauss/Gilbert boundary. Then, using various geophysical data and showing remarkable intuition, Heirtzler et al. (1968) considered that the rate of expansion of the South Atlantic remained constant for the last 80 million years. With this assumption, they proposed a scale of magnetic polarities going back to 80 Ma. With its new approach and results, this scale was a gigantic step forward. It extended the magnetostratigraphic scale from 5 Ma to 80 Ma and

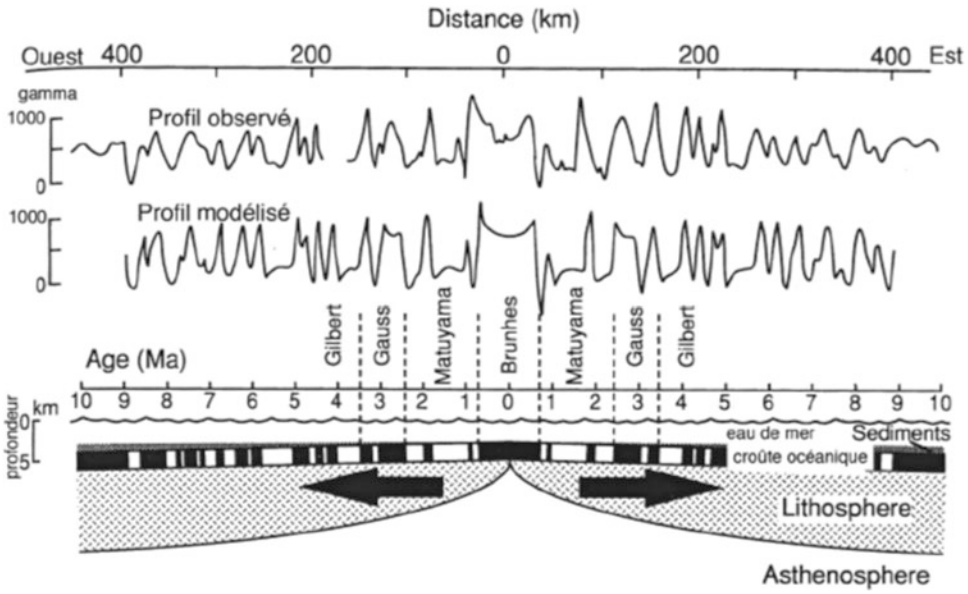

Fig. 7.5 Measurement of magnetic anomalies at sea on both sides of the mid-ocean ridge and comparison with the modeled profile proposed by Heirtzler et al. (1968)

proved to be very precise: in the thirty years since, studies have shown it to be out by only 5 Ma at 70 Ma!

In the scale of Heirtzler et al. (1968), the ages of the different polarity intervals were estimated solely assuming the rate of expansion of the seafloor. One of the objectives of the international program for ocean drilling (Deep Sea Drilling Project (DSDP), followed by ODP) was to link the scale of polarities inferred from the magnetic anomalies at sea to biostratigraphic ages. Sediments accumulate on the ocean crust as soon as this latter is created at the ridges. Therefore, the age of the crust is given by the sediment just above it.

Over the past forty years, hundreds of cores have been collected in the different oceans have allowed the Heirtzler scale to be extended to older ages, and to link it with biostratigraphic datings.

In parallel, the magnetostratigraphic scale has been improved by studies of emerged marine sediments, which allow specific intervals to be analyzed with a better temporal resolution than was achieved by studies at sea. These "segments" were then inserted in the magnetostratigraphic scale, thanks to the identification of specific characteristics.

The study by Lowrie and Alvarez, published in 1981, on the sediments of the Apennines in Umbria (Italy) is probably the most important of these. Not only has it led to a better understanding of the bio-magnetostratigraphic scale of the last 100 million years, but it also led to the discovery of a thin level of iridium-rich clay, from the Cretaceous-Tertiary boundary, which initiated the hypothesis of an extraterrestrial impact to explain the massive biological crisis that characterizes this boundary.

The Cande and Kent Polarity Scale

In a review of the Heirtzler scale, Cande and Kent (1992) also considered the magnetic profile of the South Atlantic as a starting point, in which they replaced some intervals with equivalent, more detailed intervals obtained from ridges in the Pacific and Indian oceans with a higher speed of expansion. However, they considered the rate of expansion of the South Atlantic to be continuous, but not constant as Heirtzler et al. (1968) had thought in their first approximation, and they adjusted the magnetic profile to match nine calibration points, whose ages had been estimated elsewhere (eight were high-precision $^{40}Ar/^{39}Ar$ ages, and the most recent age (2.60 Ma) was one proposed by Shackleton et al. (1990), at the Gauss/Matuyama boundary by astronomical calibration, see below).

In a more complete version of this work, Cande and Kent (1995) used astronomical calibration obtained by Shackleton et al. (1990), and Hilgen (1991a, b) for all the Pliocene/Pleistocene polarity reversals. They modified the Cretaceous-Tertiary boundary from 66 to 65 Ma. For a detailed description of this new scale (called CK95), which is the current benchmark for the Late Cretaceous and Cenozoic, we refer the reader to the original publication (Cande and Kent 1995).

The magnetostratigraphic scale available today is very reliable as far as the Late Jurassic. Traditionally, it is divided into two parts, the most recent corresponding to the Upper Cretaceous and Cenozoic eras, and the older corresponding to the Lower Cretaceous and Upper Jurassic eras. Polarity sequences for these two major periods are called C and M

sequences, respectively. On the ocean floor, they are separated by the normal, calm Cretaceous period, between 118 and 84 Ma, during which no geomagnetic reversal occurred and therefore no magnetic anomaly is observed.

Some important features of the geomagnetic field appear evident when looking at the scale of magnetic polarities. On the one hand, the total time for normal and reverse polarity intervals is essentially the same, with no tendency for the field to remain in one or the other of the polarities. On the other hand, during the Cenozoic, the rate of reversal increased: there was a reversal every million years or so at the beginning of this period, but this reached four reversals per million years during the last 5 million years. The current normal period which has lasted for about 780,000 years therefore seems abnormally long.

Before the Upper Jurassic, the entire ocean floor corresponding to the current tectonic phase was absorbed in ocean trenches. As a result, the polarity scale can only be extended in time through the study of continental rocks and is much less continuous and precise than for the Cenozoic and Mesozoic eras. The most obvious and probably most documented characteristic is the long period of reverse polarity during the Permo-Carboniferous which lasted about 70 million years, and which is called the Kiaman interval. This interval was preceded and followed by periods where the field reversed frequently.

Astronomical Calibration of the Polarity Scale

In a famous article published in 1976, Jim Hays, John Imbrie and Nicholas Shackleton were the first to show that some indicators (proxies) of paleoclimate, such as isotopic records of oxygen, evolved over time depending on the orbital cycles of the obliquity, eccentricity and precession. These cycles, initially calculated by Milutin Milankovitch, were established much more precisely by André Berger, and gave paleoclimatologists precise solutions for the last three million years. Hays et al. have "adjusted" their initial age model to "match" the obliquity cycle in the record to that given by astronomical calculation. In doing so, they established the first 'cyclostratigraphy'. This method was widely used in the 1980s to constrain the ages of isotopic records of oxygen during the Brunhes period with a precision of a few thousand years.

Subsequently, the development of a hydraulic corer in the DSDP program resulted in the acquisition of previously inaccessible, very deep sediments, allowing the study of continuous sequences in even older sediments. Applied to the Matuyama period, astronomical calibration based on obliquity cycles did not initially show significant age differences between the limits of "astronomical" polarity and those of the Mankinen and Dalrymple scale. But when an astro-timeline, based on precession, was obtained at Site ODP 677, it became clear that the polarity intervals of the Mankinen and Dalrymple scale were not accurately dated.

This study paved the way for a complete revision of the ages of the polarity intervals, especially during the Gauss and Gilbert periods (Hilgen 1991a, b). The realization of the "youth" of the ages obtained by the K/Ar method for the Plio-Pleistocene era compared to those obtained by cyclostratigraphy has led to the extensive use of the $^{40}Ar/^{39}Ar$ method (Chap. 5), which had recently been developed to test the validity of cyclostratigraphic ages of this period. The age of the Brunhes/Matuyama reversal (initially set at 0.73 Ma by K/Ar) has been re-evaluated to 0.78 Ma due to a large number of independent $^{40}Ar/^{39}Ar$ measurements. The latter value is consistent with the cyclostratigraphic age. Good agreement is also observed for the Plio-Pleistocene era, where the new $^{40}Ar/^{39}Ar$ estimations coincide with the ages given by Shackleton et al. (1990), and Hilgen (1991a, b).

Although these new estimations, in general, confirmed the astronomical ages, the ages of geomagnetic reversals given by Cande and Kent (1992), based on magnetic anomalies at sea, did not seem to be in agreement with astronomical dating. The authors had in fact adopted durations for the Plio-Pleistocene polarity intervals that have proven inaccurate. As mentioned above, it is precisely the astronomical ages for the Plio-Pleistocene that Cande and Kent (1995) adopted in their new version of the scale. The consistency they then obtained between $^{40}Ar/^{39}Ar$ estimates, magnetic anomalies at sea and astronomical calculations over the entire time period covered by the new scale can be considered as a validation of this method. With this method, the age of a geomagnetic reversal can be estimated within the duration of one precession cycle, in other words, less than two or three times the length of a polarity reversal. This very high resolution led Renne et al. (1994) to calibrate the age of one of the standards of the $^{40}Ar/^{39}Ar$ method (Fish Canyon Tuff, FCTs) with the astronomical method, which reduced the uncertainty to 0.6% for the calibrated ages compared with the standard.

Principle and Practice of Magnetostratigraphy

The magnetic polarities scale shows that polarity reversals are largely random in time, which means that sequences of four or five successive reversals do not repeat themselves identically in time; therefore, they constitute a kind of "fingerprint" of specific geological periods. Magnetostratigraphy is based on this characteristic: if a sequence characteristic of the magnetostratigraphic scale can be identified within a particular series, then a specific age can be assigned to this section.

Although simple in principle, matching of a particular sequence to a segment of the magnetostratigraphic scale is far from easy in practice. The ideal condition for a record of magnetic polarities to be perfectly continuous would be for the "rain" of sedimentary particles to accumulate continuously over time. But this is rarely the case. In general, the rate of accumulation of a sedimentary sequence is variable, with potential differences of an order of magnitude, depending, for instance, on the changing climatic/environmental conditions over time. Hiatuses can also occur. All these factors change the appearance of the sequence of polarities, making its identification in GPTS complicated. However, in marine sequences, close to ideal conditions can be found for periods of about a few million years.

It is certainly a major advantage for magnetostratigraphic studies to have thick sections (10^2–10^3 m). Indeed, the thicker a section is, the more likely it is that it will contain several polarity zones, and therefore can be more easily correlated with a defined segment of the reference magnetostratigraphic scale. Our colleague, Robert Butler, made an amusing analogy between identification of a particular sequence in the magnetic GPTS and fingerprinting in a police investigation. Usually, a full fingerprint can identify a person, half a fingerprint leaves identification open to discussion but a quarter fingerprint is unlikely to be accepted as irrefutable proof in a court of law.

In practice, even in favorable cases, the researcher is faced with a series of zones of normal and reverse polarity, which is often difficult to unambiguously correlate with the GPTS scale. The assumption made at the outset is that the rate of sedimentation of the sampled section is more or less constant. So, different ways of correlating the sequence to GPTS are tested. In most cases, however, it is necessary to have an independent marker in time (radiometric dating or biostratigraphic data already independently correlated to the GPTS) so that magnetostratigraphy can correlate the full section being studied to the GPTS, and thus, to specify its age, temporal thickness and rate of accumulation.

Cross-correlation has been used by some authors to assess the agreement between the sequence being studied and a particular segment of the GPTS, by calculating the correlation coefficient corresponding to the various, visually evaluated, solutions. A coefficient of maximum value indicates the most likely correlation, while a value close to zero allows rejection of that hypothesis. In practice, this method is only usable when the studied section contains a large number of polarity intervals.

Regardless of the method used to associate the studied sequence with a particular segment of the GPTS, the quality of a magnetostratigraphic study is primarily based on unambiguous identification of the magnetic polarity at each level of the studied sequence. This can sometimes be achieved if there is agreement between determination of polarity in two parallel and close sections. In general, however, this requires a complete paleomagnetic study (determination of the magnetic mineralogy, field test, progressive demagnetizations either by heating or by applying alternating fields) to establish the stability of the magnetization and its acquisition at the time of deposition. For this purpose, Opdyke and Channell (1996) established ten criteria to assess the quality of a study. The authors themselves recognize that it is very difficult to simultaneously comply with all ten for one section, but at least five should be present in a modern magnetostratigraphic study.

A High-Quality Magnetostratigraphic Study: The Siwalik Sequences in Pakistan

The deposits in the foothills of the Siwalik Basin in northern India and Pakistan are among the most studied fluvial sediments. Indeed, in them, many fossils of mammals, including primates, have been discovered. Their precise chronological study and the correlation of different outcropping sections is of crucial importance for understanding the evolution and migration of these hominids and their land use.

From a paleomagnetic point of view, the main problem with this study is that the deposits of Siwalik are "red beds" and magnetization is carried by hematite. The magnetization of this type of sediment is very complex, and it has been shown in some cases that magnetization was acquired as a result of chemical reactions in the sediment, considerably after deposition. It is therefore essential for a magnetostratigraphic study of Siwalik to establish that magnetization was acquired during deposition or immediately afterwards so as to prevent invalidating correlation with the magnetic polarity scale (GPTS).

The study of the magnetic mineralogy showed that the components of magnetization of these red beds fall under two different categories of hematite: a red pigmentation phase and a specular hematite phase. The red pigmentation phase acquired its magnetization well after deposition (at least one polarity interval later). However, the magnetization carried by specularite was acquired during deposition or immediately afterwards. These two components can be separated by thermal demagnetization, the magnetization of the specularite being isolated between 525 and 600 °C. This component can then be used to establish the magnetic polarity of the sampled sections (Fig. 7.6) which is then correlated with the scale of Mankinen and Dalrymple (1979) (Fig. 7.7).

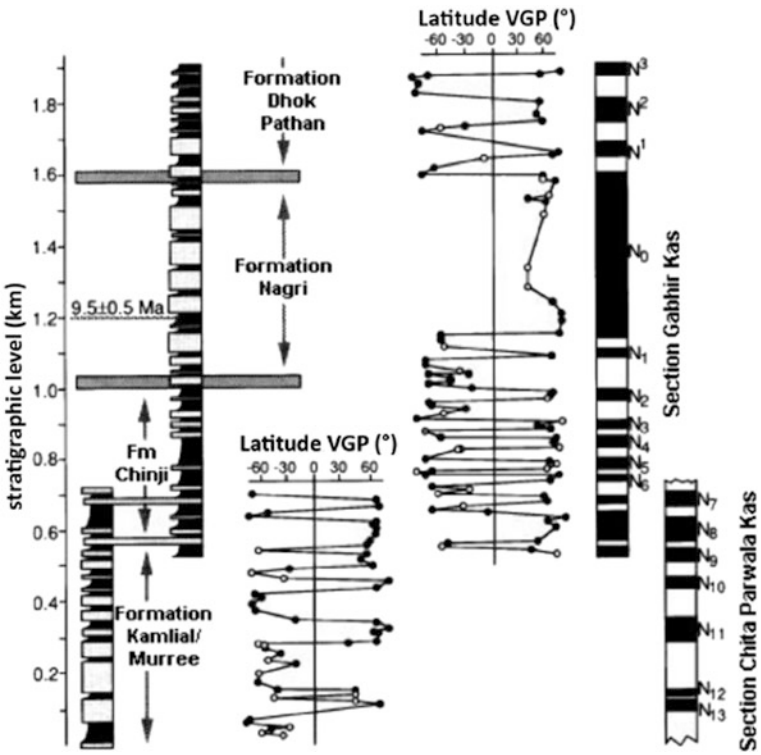

Fig. 7.6 Magnetostratigraphic results obtained by Johnson et al. (1985) on two sections from Chita Parwala and Gabhir Kas. Some levels of hard sandstone (represented in gray) clearly connect the two cuts. The magnetic data is shown as the virtual geomagnetic pole (VGP) latitude, which is located either in the southern hemisphere (reverse polarity) or in the northern hemisphere (normal polarity). The filled-in circles denote the most reliable estimates, the open circles represent the estimates of lower, but acceptable, "quality". The column on the right shows the sequence of polarities obtained along both cuts and their correlation

Geomagnetic Excursions and the Scale of Magnetic Instabilities (GITS)

Discovery of Geomagnetic Excursions

Throughout the process of establishing the scale of magnetic polarities, the presence of very short excursions of the field polarity was observed in lavas and sedimentary sequences. These excursions were often characterized by intermediate magnetization directions between direct and reverse polarities, and did not correlate to polarity intervals recognizable in the polarity scale well established on other sites. Therefore, these excursions were initially regarded with some skepticism by paleomagnetic researchers and were sometimes attributed to episodes of extreme amplitude of the secular variation or even to artifacts due to sampling, re-magnetization or sedimentological processes. The short duration of these excursions also meant that their registration in volcanic or sedimentary sequences was often random, and until very recently, no excursion was observed in more than one site.

A change of attitude in the community occurred about fifteen years ago, and can be largely attributed to a combination of two main factors: firstly, considerable progress in the dating methods of both volcanic rocks and sedimentary sequences allowed the unambiguous correlation of some of these excursions recorded in these two media, and, on the other hand, the discovery of rapid climate changes recorded in ice cores encouraged paleoceanographers to collect marine sedimentary sequences with a very high sedimentation rate, and with the longest possible series (IMAGES programs, ODP, IODP). This was made possible by the development of new corers as previously mentioned. These high rates of accumulation significantly increased the probability of recording rapid changes in magnetization, characteristic of an excursion.

Despite this progress, detailed records of excursions remain largely limited to the last two million years. The best documented excursions occur as double changes in polarity which define a very short polarity interval in the opposite direction to the initial and final polarities. The total duration of an excursion is very short: the most recent (and most accurate) estimates converge around a duration of around 1500–2000 years (Laj et al. 2000, 2004, 2014; Laj and Channell 2007). In addition, directional changes related to the best documented excursions like the Laschamp (LE) excursion or the Iceland Basin (IBE) excursion, seem to have occurred more or less simultaneously in the various places where they were recorded. Therefore, geomagnetic excursions, as well as being of fundamental interest as a probe into the phenomena of magnetic instability in the Earth's core, also provide very precise points of correlation with a global significance.

It is by now well established that excursions are accompanied by a decrease in the intensity of the geomagnetic

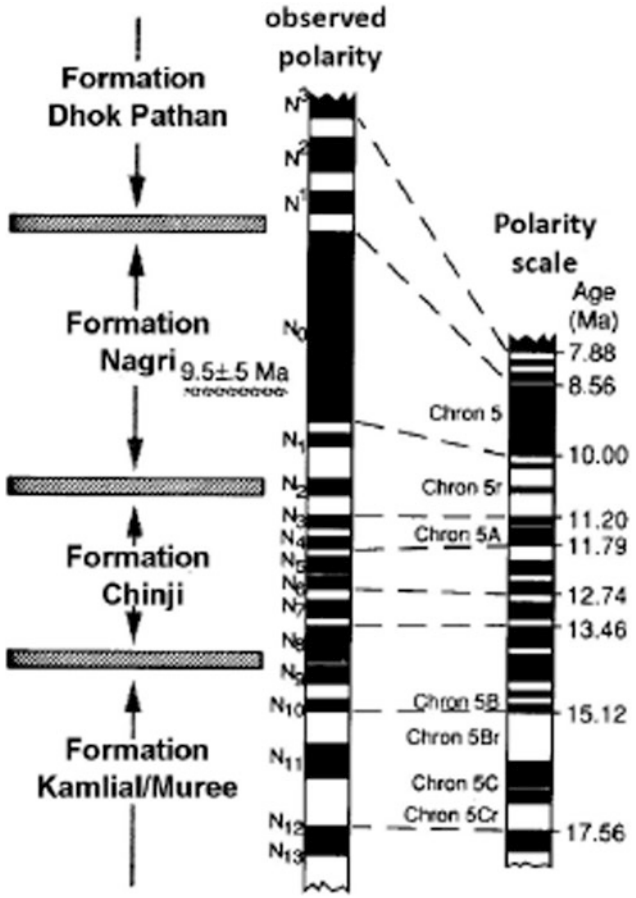

Fig. 7.7 Magnetic polarities observed in the Siwalik cut correlated with the Mankinen and Dalrymple (1979) polarities scale, the most complete and reliable at the time

field. The field acts as a screen for cosmic radiation (consisting essentially of charged particles), and this reduction causes a significant increase in the amount of cosmonuclides (^{14}C, ^{10}Be, ^{26}Al…) formed in the upper atmosphere through the impact of cosmic radiation on the various particles air. As ^{10}Be can be measured in polar ice cores, this opens up new opportunities for ice-sediment correlation.

A Scale of Geomagnetic Instabilities?

The use of geomagnetic excursions as precise temporal tie points could be particularly useful in at least two important areas of Earth sciences. This is especially useful to understand the operating mechanisms of the terrestrial dynamo which is the origin of the field itself. Recent models, theoretical and numerical, of the Earth's dynamo (Glatzmaier and Roberts 1995) indeed, give accurate assessments of time constants, frequencies and geometries of the transitional field during excursions. It is of prime importance to characterize the role of the solid inner core and the lower mantle in the mechanism of excursions and reversals. It is also important in paleoclimatology studies, where an independent chronology of climatic/environmental phenomena needs to be of higher resolution that the scale of polarities to allow evaluation of the synchronicity and phase shifts, either early or late, of climate events in different parts of the globe (examples are described below).

Currently, the major obstacle to the widespread use of this method is probably the difficulty of integrating sedimentary data and volcanic data into a single unified scale of geomagnetic instabilities. The brevity of the excursions is both an advantage (giving very precise temporal tie points), and paradoxically, it also represents an obstacle to the creation of this scale. In fact, a specific excursion is not systematically recorded in all sequences, including those with a medium to high sedimentation rate. Studies to develop a high-resolution chronology of geomagnetic instabilities, especially of excursions, are often based on accurate dating, using the K/Ar and ^{40}Ar/^{39}Ar methods, of as large a number as possible of lava flows recording either an abnormal direction, or a geomagnetic field with a very low intensity, or both characteristics together. It is important to keep in mind that ^{40}Ar/^{39}Ar datings are obtained by reference to standards whose ages were defined based on astro-chronological calibrations. So, several ages have been proposed for the same standard (e.g. Fish Canyon Sanidine, commonly used for dating in the Quaternary). It sometimes appears that none of them provides good agreement between the ^{40}Ar/^{39}Ar ages and the glaciological or astronomical scales. Further work is therefore necessary to "reconcile" these various approaches.

Today, at least seven geomagnetic excursions from the Brunhes period have been inventoried in detail: the excursions of Mono Lake (34 ka), Laschamp (41 ka), Blake (120 ka), Iceland Basin (188 ka) Pringle Falls (211 ka), Big Lost (560–580 ka) and Stage 17 (670 ka) (Laj and Channell 2007). Other excursions from the same period are being studied. Studies are also underway for earlier periods, such as the Matuyama period during which at least eleven excursions seem to have occurred. All of these excursions act as specific temporal tie points, that greatly increase the temporal resolution of the magnetostratigraphic scale.

Magnetostratigraphy Based on Variations in the Intensity of the Geomagnetic Field

Introduction

Over recent years, the stratigraphy of climate records has undergone a major change, particularly due to the discovery of rapid and precise markers, both lithostratigraphic (Heinrich events in marine sediments in the North Atlantic) and climatic (Dansgaard-Oeschger events in Greenland ice cores).

Sedimentary records from the North Atlantic can be correlated with a very good approximation to records obtained in ice cores, by using anchor points common to both types of records, such as levels of volcanic ash or melting events (Bond et al. 1993). However, the correlation of ice cores with sedimentary records or sedimentary records between themselves in very diverse parts of the world, is a far more complex problem: a direct correlation, based on the recognition of climate signals may not take into account the possibility of a time difference between the occurrence of a particular climatic event in two distant regions or by to different media. And yet an accurate calculation of these phase shifts (leads and lags) is of central concern to paleoclimatologists, since it is essential to understand the mechanisms of global climate change, and to the highlight of chains of causality and the spatio-temporal spread of a climate event.

At the scale of a basin, the magnetic susceptibility measured continuously in sediment cores, directly on-board research ocean vessels, usually allows the correlation of the different cores with a resolution of about one centimeter, which is sufficient for most studies. This physical measure allows splicing of records obtained from different cores, taken from the same site or in neighboring sites, to join together the different sections of cores obtained by the hydraulic piston corer, aboard the *Joides Resolution* within the ODP international program. Magnetic susceptibility reflects the ability of the sediment to acquire a magnetization induced by a weak magnetic field. Measurement of magnetic susceptibility is commonly used because it has the advantage of being non-destructive, as the induced magnetization measured disappears as soon as the imposed field is switched off. It varies depending on the magnetic content of the sediment, and particularly on the concentration of magnetic particles, their nature and size. As changes in these physical and chemical parameters are generally highly dependent on the paleo-environmental context, these are the same within the same basin or water mass, and so the magnetic susceptibility can be used as a local (or regional) correlation tool. Over long distances, oxygen isotopic ratios are the most commonly used stratigraphic tool. However, these ratios also include regional climate components, precisely those that researchers are trying to fix in time relative to each other. Correlating these ratios between distant locations could therefore mask the phase shifts which may really exist and that climatic studies attempt to quantify. Independent time constraints of climate variations with a global value are required for this exercise.

Initially proposed a decade ago, a new method, based on relative variations in the intensity of the geomagnetic field in the past recorded in sediments, is now being recognized as capable of revealing phase shifts over thousands of years at most, in climate records obtained from sites geographically very distant from each other. In this method, the relative changes in the paleointensity curve obtained from a specific sedimentary core is compared with a reference curve depicting the relative variations of the geomagnetic dipole field. The latter is, in fact, the only component of the field which varies synchronously across the globe. After synchronization of two magnetic profiles with the reference curve, the phase shifts and/or synchronicity of the two paleoclimate records from these two distant locations can be evaluated.

This method needs to be applied with some caution. Firstly, everywhere in the world, the local field is the superposition of the dipole field on multipolar components, which are much more variable in space and have shorter time constants. To plot the dipole field variations curve, the authors compiled records obtained from different parts of the world. These compilations eliminate the non-dipolar components which are averaged out in space. Compilations of relative paleointensity variations in the field for the last 800,000 years (Sint 800) (Guyodo and Valet 1999) and the last 1.5 Ma (PISO-1500) (Channell et al. 2009) show synchronization of characteristic events globally and the widespread attenuation of the non-dipolar field. However, only characteristics with time constants of the order of 10^4–10^5 years are apparent on these two compilations, as some of the individual records have been obtained from sediment with accumulation rates of a few centimeters per thousand years, insufficient to record short-term characteristics and rapid changes.

These rapid characteristics are, however, clear in other compilations characterized by a higher sediment accumulation rate. Initially proposed for the North Atlantic Ocean, the NAPIS-75 compilation (North Atlantic Paleointensity Stack for the last 75,000 years) (Laj et al. 2000), then SAPIS (South Atlantic Paleointensity Stack) (Stoner et al. 2002) and finally GLOPIS-75 (Global Paleointensity Stack) (Laj et al. 2004) have shown that rapid components of the variations in the intensity of the geomagnetic dipole field can be recognized globally in sedimentary records (Fig. 7.8). The outer limit of temporal resolution appears to be of the order of 400 years, which is the time constants of the dipolar field. GLOPIS-75 is currently the reference for the last 75,000 years because it is precisely placed on the accurate ice age model (Cf. Section "A Correlation Between Sediment and Polar Ice"). This new age scale for Greenland ice was developed by counting annual levels (Greenland Ice Core Chronology or GICC05) (Andersen et al. 2006; Svensson et al. 2006). For earlier periods, up to 1.5 Ma, PISO-1500 is used.

Although, in principle, the method is simple, its implementation is far from it. Firstly, a linear relationship between the intensity of the geomagnetic field existing at the time of deposition and the magnetization of the sediment only exists if a single magnetic mineral carries the magnetization and the

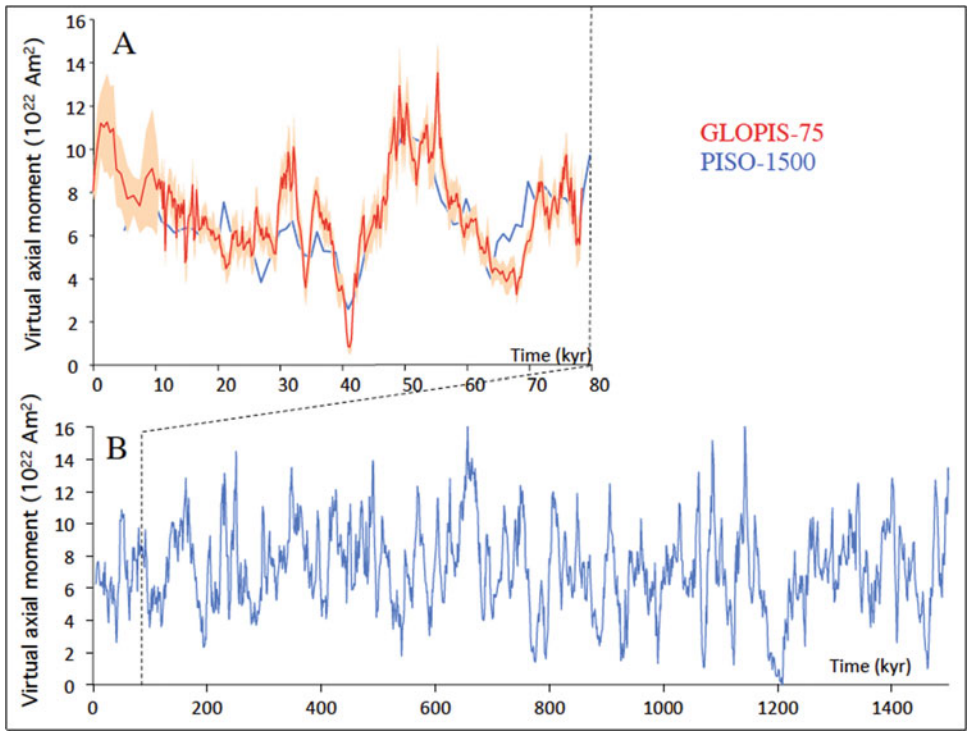

Fig. 7.8 Changes in the intensity of the geomagnetic dipole field. **a** Over the last 75 thousand years: global curve GLOPIS-75 (Laj et al. 2004) here placed on the most recent GICC05 ice age model (Laj et al. 2014) and compared to PISO-1500 on the same period of time; **b** Over the last 1.5 million years (PISO-1500) (Channell et al. 2009)

size of magnetic grains is constant along the sedimentary column, in other words, if the magnetic mineralogy of the sediment is uniform. All of these characteristics must be verified by a magneto-mineralogical study of the sediment (this verification can lead to the rejection of a significant proportion of cores, depending on the basin being studied), in order to obtain a reliable record of the relative variations of the field. This is obtained by dividing, at each stratigraphic level, the intensity of the measured natural remanent magnetization by a standardization parameter, which will take into account the variations in the concentration of magnetic grains. Of the three magnetic parameters related linearly to concentration: susceptibility; isothermal remanent magnetization (IRM) and anhysteretic remanent magnetization (ARM),[1] it is the latter that is most often used, since it depends primarily on the same magnetic grains as the ones carrying natural magnetization.

Three recent examples of long-distance, multi-archive correlations are described below showing the combined use of well-dated geomagnetic excursions and paleointensity records in paleoclimatology studies. The first one concerns a sediment-ice correlation. Of the other two, one is based on the propagation time of the North Atlantic deep-water mass from north to south, and the other on the anti-correlation between the intensities of the North Atlantic and Circum-Antarctic deep currents.

A Correlation Between Sediment and Polar Ice

The Laschamp geomagnetic excursion was the first to be discovered and is certainly the most studied excursion of the Brunhes period. Discovered in 1967 by Bonhommet and Babkine (1967), in lavas of the Puy de Laschamp, then in the Olby flow in the French Massif Central, it was originally dated between 20 and 8 ka. A series of studies conducted by different research groups demonstrated the difficulty of dating lavas as recent as these. Recently the combined use of K/Ar and $^{40}Ar/^{39}Ar$ methods (Chap. 5) on basalt samples collected at Laschamp and at Olby led to the establishment of a critical requisite for reliable dating of these recent samples: the absence of excess argon in the initial composition of the lava, or of any other potential disruption of the K/Ar system pre- or post eruption (Guillou et al. 2004).

Considering the uncertainty of 2.4% on the decay constant of ^{40}K, Guillou et al. (2004) proposed a date of 40.4 ± 2.0 ka, which was a considerable improvement, in terms of accuracy, over previous radiometric dating. Shown in Fig. 7.9 is a series of "snapshot data" obtained from lava flow from the Massif Central, the Canary Islands and New Zealand superimposed on the GLOPIS-75 curve. The

[1]Isothermal remanent magnetization (IRM) is the magnetization acquired by a sample at a given temperature (most often room temperature), after application of a constant magnetic field and subsequent cancellation. Anhysteretic remanent magnetization (ARM) is obtained at room temperature through the combined action of a stationary field at a similar level to the Earth's geomagnetic field and a strong alternative field in the same direction. The acquired magnetization is measured after cancellation of the two fields.

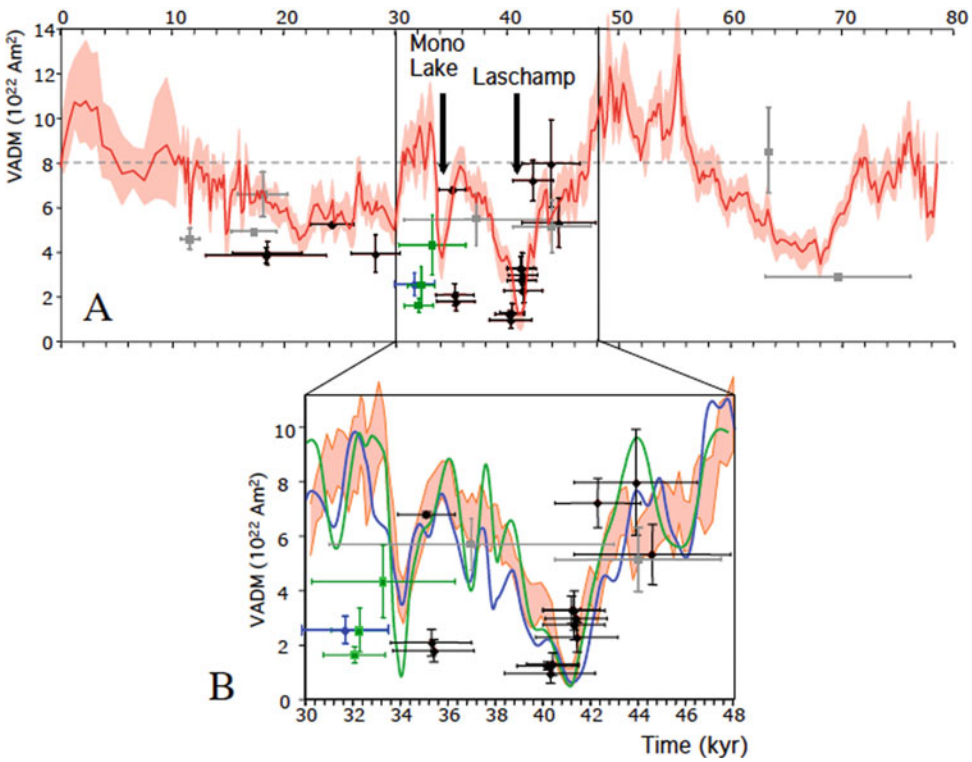

Fig. 7.9 **a** GLOPIS-75 curve (red) (Laj et al. 2004) together with Earth's magnetic field intensity data obtained from dated lava flows from the Massif central (black), the Canary Islands (green) and New Zealand (blue) (the grey dots are intensities reported on the age given by the geological map) (Laj et al. 2014). **b** Zoom on the 20–48 ka interval of the above diagram **a** with, in addition, the Earth's magnetic field intensity reconstructed from the ^{10}Be data (blue) and ^{36}Cl data (green) obtained from the Greenland ice core

absolute Earth's magnetic field intensity values obtained from the lava flows are precisely dated using the coupled K/Ar and ^{40}Ar/^{39}Ar methods. This figure also shows that the coupled volcanic intensity/dating is consistent with the one obtained by GLOPIS-75, placed on the GICC05 age model (Laj et al. 2014).

It also shows that geomagnetic variations observed in the sediments used to build NAPIS-75 and then GOPIS-75 are similar to those of the geomagnetic field, recalculated based on the concentrations of cosmogenic isotopes registered in Greenland ice (Wagner et al. 2000).

This results from the fact that the Earth's magnetic field shields our planet from cosmic and solar radiations and therefore modulates the production of cosmogenic isotopes (^{10}Be, ^{36}Cl, ^{14}C) in the upper atmosphere. Assuming a constant solar activity, a reduction (increase) in the intensity of the geomagnetic field leads to an increase (decrease) in this production. The concentration of these radionuclides, especially ^{36}Cl, recorded in Greenland ice, compared to the reference curve GLOPIS-75, has enabled a precise correlation, independent of climate, to be established between the ice and sedimentary records.

Transferred to the GICC05 age model, the maximum peak flow of ^{10}Be corresponding to the intensity minima of the Laschamp excursion, is dated at 41.25 ka, in perfect agreement with the radiometric dating (41.2 ± 1.6 ka; Laj et al. 2014). In addition, the width of this peak can be accurately estimated and thus gives a measure of the duration of the excursion as 1.5 ka, again in perfect agreement with sedimentary data.

If the Laschamp excursion (and also the more recent Mono Lake excursion) constitutes a critical tie point for all the stratigraphies (in ice and sediment), it is also observed that, even outside these instability periods, the intensity profile and that of ^{10}Be and ^{36}Cl are extremely similar in time and amplitude for the 20–50 ka interval.

These studies show that it is possible to accurately transfer the ice age model to sedimentary sequences, independently of climate variations. The magneto-stratigraphic tool based on variations in the intensity of the geomagnetic field is therefore a very powerful tool, within the limits of its application.

Paleo-Oceanographic Implications of High-Resolution Magnetic-Assisted Stratigraphy

The last glacial period was characterized by very rapid climate changes which have been observed in the upper and middle northern latitudes. Heinrich (H) and Dansgaard-Oeschger (DO) rapid climatic events, are associated with iceberg discharges into the ocean and large amplitude oscillations of air temperature over Greenland (Dansgaard

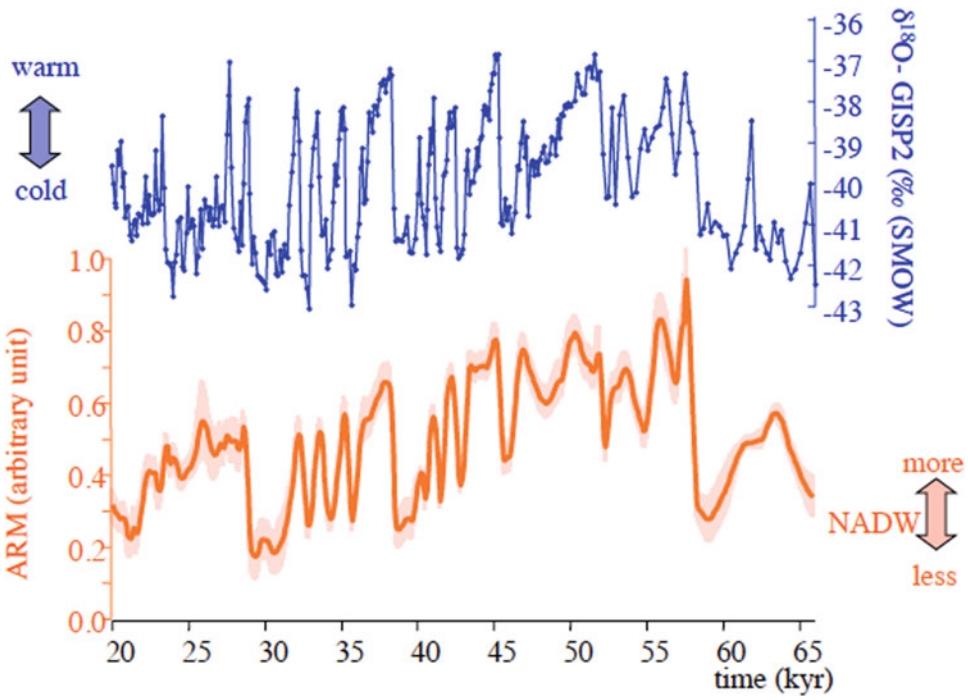

Fig. 7.10 Changes in the intensity of the North Atlantic Deep Water during the last glacial period (below) reconstructed from variations in the concentration of magnetic particles along the path of this deep-water mass. Top: curve showing air temperature changes over Greenland during the same period. From Kissel et al. (2008)

et al. 1993; Bond et al. 1993). The role of ocean circulation in these rapid climate changes remained to be defined. Consequently, the evolution of the deep North Atlantic water mass was investigated, in particular by the study of the magnetic properties of a number of sediment cores collected along the path of the Nort Atlantic Deep Water (NADW) (Kissel et al. 2008).

By this approach, changes in the strength of the North Atlantic deep current (NADW) in the North Atlantic have been shown to be completely synchronous with changes in atmospheric temperatures. This shows that the dynamics of deep ocean can change at a very high speed. This is shown in Fig. 7.10, which illustrates the amount of small magnetic grains, mobilized by the overflow water at the Faroe-Iceland and Iceland-Greenland sills and transported by the deep current, before being gradually deposited at each sampling site. Its oscillations therefore reflect the relative changes in the intensity of the convection in northern seas and of the deep current, as well as its ability to transport the magnetic particles from their basaltic source in the north (Iceland–Faroe) towards the south.

In the South Atlantic, during the same period, analysis of the carbon isotopic ratio of the benthic foraminifera shells (living on top of the sediment) and of the neodymium isotopic ratio showed that the NADW also varied in intensity, and was replaced by Antarctic deep water (AABW) as soon as it weakened (Charles et al. 1996; Piotrowski et al. 2005). These two water masses have indeed a different isotopic signature. These variations were supposed to match with the variations in air temperature over Greenland. The NADW activity in the Deep Cape basin was therefore correlated by the authors with warm events over Greenland.

However, this long-range correlation of climate parameters is entirely based on the assumption of synchronization between hemispheres. A new correlation between these paleoceanographic records from the north and south of the Atlantic was proposed, using global variations in the intensity of the Earth's magnetic field as a long-distance, climate-independent correlation tool, measured for each of the studied sedimentary sequences (Fig. 7.11). This showed, for each warm event over Greenland, that when the NADW becomes stronger in the north, it takes about 860 ± 220 years to spread to the depths in the south, "chasing out" and replacing the AABW (Kissel et al. 2008) (Fig. 7.11). This has been the only experimental attempt to quantify this time lag.

Compared with data obtained in the north from the Greenland ice sheet, those obtained from ice cores in central Antarctica appear to show a slightly different story, with less abrupt variations than in the north.

More important, after synchronization with the Greenland cores, using variations in the abundance of atmospheric methane trapped in the ice (Blunier and Brook 2001), gradual warming, called type A events, began around 1500 years before the main warm events (interstadials) in the northern hemisphere. A bipolar seesaw mechanism has been proposed, according to which the southern hemisphere warms up when the northern hemisphere cools (Broecker 1998). More recently, the EPICA community obtained a new record of the changes in air temperature from an ice core from the

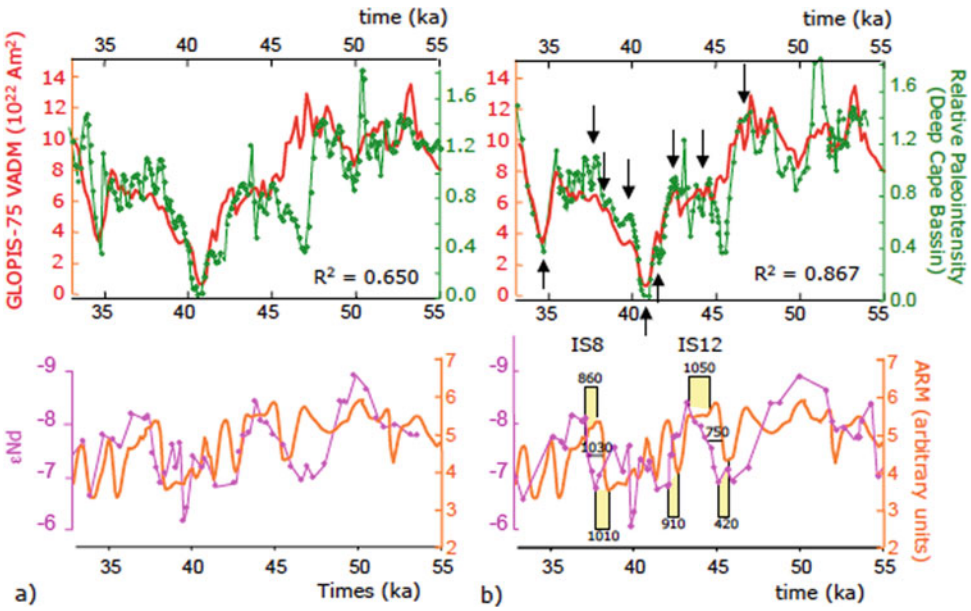

Fig. 7.11 **a** Top: Earth's magnetic field intensity of the core from the Deep Cape Basin (green) reported on its own age model and compared to GLOPIS-75 (red). Bottom: The age model of the core from the Deep Cape basin is based on the correlation between tracers of variations in relative intensity of deep waters of the North Atlantic based on the εNd in purple in the south, and variations in the quantity of magnetic grains (orange) in the north; **b** top: adjustment of the magnetic field intensity from the Cape Basin (green) onto the reference curve GLOPIS-75 (red). The R^2 is the correlation coefficient. Bottom: The lag between the two paleoceanographic curves after this adjustment is of the order of 880 years on average (underlined in yellow). From Kissel et al. (2008)

Antarctic Dronning Maud Land site (EDML). This core, because of its location, recorded the climate of the South Atlantic, with a resolution comparable to that of the Greenland ice cores. After synchronization, once again based on methane, it appears that all the warm events perfectly reflect the Dansgaard-Oeschger events in Greenland: the seesaw mechanism therefore also works on short time scales.

A study of marine cores from the South Indian ocean showed how the interhemispheric seesaw mechanism also concerns the Antarctic Circum Current (Mazaud et al. 2007). The record of relative paleointensity of core MD94-103 taken from the Kerguelen Plateau was precisely correlated with the reference curve GLOPIS-75, between 30 and 45 ka, thanks, in particular, to the identification of the minima of the Laschamp and Mono Lake excursions (Fig. 7.12). This correlation allowed all the paleoclimatic and paleoenvironmental records obtained from that core and other nearby cores to be transferred to the time scale defined for the Greenland ice cores (GISP2 at the time of the publication).

Similarly, to what is observed for cores located along the path of the NADW, the concentration of fine magnetic grains in the sediment shows, at these sites, located east of the volcanic islands of Kerguelen, the ability of the current to remobilize particles coming from erosion of basaltic series rich in magnetite and to transport them downstream, i.e. towards the east. This is the deep Antarctic Circumpolar Current (ACC). As in the north, the maxima of magnetic

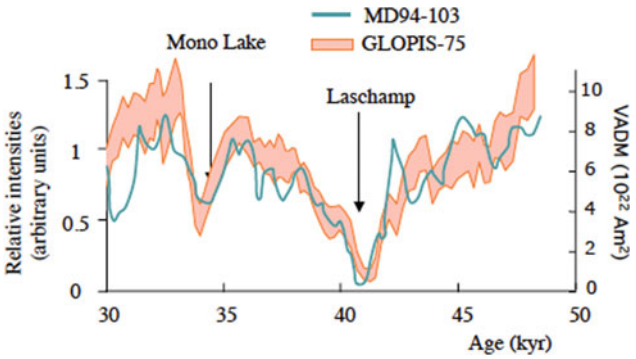

Fig. 7.12 Normalized relative intensity obtained from core MD94-103 (turquoise) compared and plotted on the same time scale as the reference curve GLOPIS-75 (Laj et al. 2004). Modified from Mazaud et al. (2007)

concentration observed during the study period and accurately fixed in time, correspond to increases in intensity of the ACC. These maxima are found to be in phase with periods of warming over Antarctica, events of type A, and in antiphase with those of Greenland. Similarly, these periods of intense activity of the ACC are in opposition to the periods of intense activity of the NADW (Fig. 7.13) demonstrating that the inter-hemispheric ocean seesaw mechanism, suggested by orbital scale models, was also functioning at the millennial scale at least during the last glacial period (Mazaud et al. 2007).

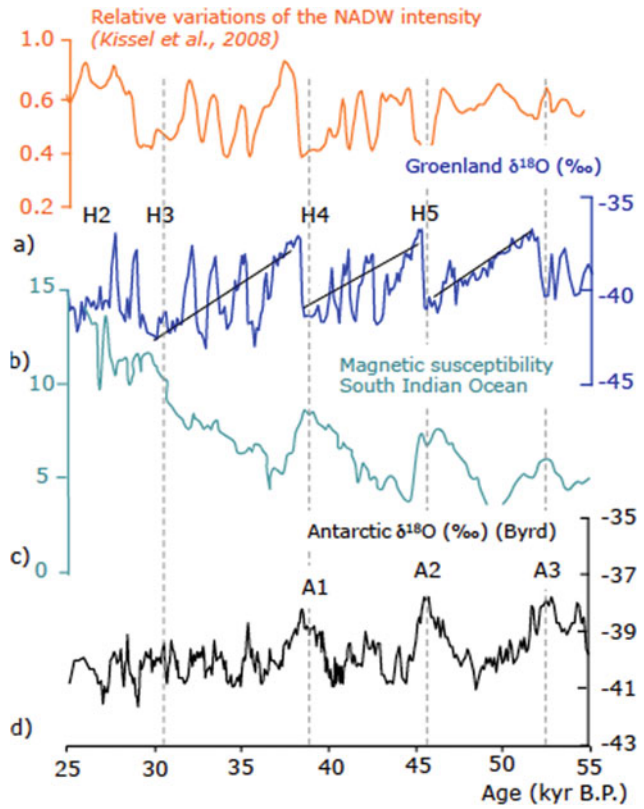

Fig. 7.13 **a** Past variations in the intensity of the NADW between 30 and 50 ka based on the magnetic concentration in North Atlantic sediments; **b** oxygen isotope record obtained from the GISP2 ice core in Greenland (H is for Heinrich events); **c** variations in the concentration of magnetic minerals observed east of the Kerguelen Plateau (compilation of three separate records); **d** oxygen Isotopic curve from Byrd ice (Antarctica) showing the A1 to A2 events. In this figure, all records are placed on the GISP2 age scale (following the correlation by Blunier and Brooks (2001) for Greenland and Antarctica and that shown in Fig. 7.12 for North Atlantic and Indian Ocean). From Mazaud et al. (2007)

Conclusions

During the years 1960–1980, the main objective of paleomagnetic studies of marine sediments and of the magnetization of the oceanic crust was to establish the sequence of magnetic polarities. The resultant magnetostratigraphic scale, whose basic features were well established by the late 1970s, constitutes a huge step forward in an impressive number of stratigraphic studies as well as tectonic studies focused in specific geographic areas or more globally at the scale of plate tectonics.

In its original form, magnetic stratigraphy, based on identifying polarity reversals of the geomagnetic field, typically had a million years as its unit of time.

The discovery, followed by the accurate documentation of geomagnetic excursions, was an important first development, by providing tie points of well-defined age and very short duration.

The scale of geomagnetic polarity reversals resolves the time intervals of the order of several hundreds of thousands of years and the short instabilities like excursions allow a resolution of a few hundreds of centuries to be achieved. Furthermore, the significant decrease in the intensity of the total geomagnetic field, documented in sediments during excursions, permitted a first connection with other natural archives such as ice cores from Greenland or Antarctica. The reduction in the field led to an increase in the production and therefore flux of cosmogenic isotopes such as ^{10}Be, ^{36}Cl and ^{14}C, arriving at the surface after their formation in the upper atmosphere, whose concentration is accurately measured in ice.

Finally, in recent years, identification of paleointensity profiles in sedimentary sequences provides an extremely accurate means of correlation. This opened up a new phase, still in development, of high-resolution magnetic stratigraphy. Since the understanding of mechanisms of climate change through the analysis of phase shifts between hemispheres and/or between low and high latitudes is of critical importance, it is clearly essential to dispose of a correlation tool independent of climate with a resolution of about a few hundred years.

By facilitating the unification of time scales for different types of records, both continental and oceanic, high resolution magnetic stratigraphy, based on changes in the relative intensity of the field contributes to a better understanding of the chronology and dynamics of mechanisms responsible for climate and geomagnetic variations at the scale of the recent Quaternary, between 0 and 500 ka.

References

Andersen, K. K., et al. (2006). The greenland ice core chronology 2005, 15–42 ka. Part 1: Constructing the time scale. *Quaternary Science Reviews, 25,* 3246–3257.

Blunier, T., & Brook, E. J. (2001). Timing of millennial-scale climate change in antarctica and greenland during the last glacial period. *Science, 291,* 109–112.

Bond, G., et al. (1993). Correlation between climate records from North Atlantic sediments and Greenland ice. *Nature, 365,* 143–147.

Bonhommet, N., & Babkine, J. (1967). Sur la présence d'aimantation inverse dans la Chaîne des Puys. *Comptes rendus des séances de l'Académie des sciences, série B, 264,* 92–94.

Broecker, W. S. (1998). Paleocean circulation during the last deglaciation: A bipolar see-saw? *Paleoceanography, 13,* 119–121.

Brunhes, B. (1906). Recherches sur la direction de l'aimantation des roches volcaniques. *Journal de physique, V*, 705–724.

Cande, S. C., & Kent, D. V. (1992). A new geomagnetic polarity timescale for the late cretaceous and cenozoic. *Journal of Geophysical Research, 97,* 13917–13951.

Cande, S. C., & Kent, D. V. (1995). Revised calibration of the geomagnetic polarity timescale for the late cretaceous and cenozoic. *Journal of Geophysical Research, 100,* 6093–6095.

Channell, J. E. T., et al. (2009). Stacking paleointensity and oxygen isotope data for the last 1.5 Myr (PISO-1500). *Earth and Planetary Science Letters, 283,* 14–23.

Charles, C. D., et al. (1996). Climate connections between the hemisphere revealed by deep sea sediment core/ice core correlations. *Earth and Planetary Science Letters, 142,* 19–27.

Cox, A., et al. (1963). Geomagnetic polarity epochs and pleistocene geochronometry. *Nature, 198*, 1049–1051.

Creer, K. M., et al. (1954). The direction of the geomagnetic field in remote epochs in Great Britain. *Journal of Geomagnetism and Geoelectricity, 6,* 164–168.

Dansgaard, W., et al. (1993). Evidence for general instability of past climate from a 250-kyr ice-core record. *Nature, 364,* 218–220.

Glatzmaier, G. A., & Roberts, P. H. (1995). A three-dimensional self-consistent computer simulation of a geomagnetic field reversal. *Nature, 377,* 203–209.

Guillou, H., et al. (2004). On the age of the laschamp geomagnetic event. *Earth and Planetary Science Letters, 227,* 331–343.

Guyodo, Y., & Valet, J.-P. (1999). Global changes in intensity of the Earth's magnetic field during the past 800 Kyr. *Nature, 399,* 249–252.

Hays, J. D., et al. (1976). Variations in the Earth's orbit: Pacemaker of the ice ages. *Science, 194,* 1121–1132.

Heirtzler, J. R., et al. (1968). Marine magnetic anomalies, geomagnetic field reversal and motions of the ocean floor and continents. *Journal of Geophysical Research, 73,* 2119–2136.

Hilgen, F. J. (1991a). Extension of the astronomically calibrated (polarity) time scale to the miocene/pliocene boundary. *Earth and Planetary Science Letters, 107,* 349–368.

Hilgen, F. J. (1991b). Astronomical calibration of Gauss to Matuyama sapropels in the Mediterranean and implications for the geomagnetic polarity time scale. *Earth and Planetary Science Letters, 104,* 226–244.

Hospers, J. (1953). Reversals of the main geomagnetic Field I, II, and III. *Proceedings of the Koninklijke Nederlandse Akademie van Wetenschappen B, 56,* 467–491.

Irving, E., & Runcorn, S. K. (1957). Analysis of the palaeomagnetism of the torridonian sandstone series of North-West Scotland. *Philosophical Transactions of Royal Society, London, A250,* 83–99.

Johnson, N. M., et al. (1985). Paleomagnetic chronology, fluvial processes, and tectonic implications of the Siwalik deposits near Chinji Village, Pakistan. *The Journal of Geology, 93,* 27–40.

Khramov, A. N. (1960). *Palaeomagnetism and stratigraphic correlation. Gostoptechjzdat* (218 p.), Leningrad. Geophys. Dept., A.N.U., Canberra.

Kissel, C., et al. (2008). Millennial-scale propagation of atlantic deep waters to the glacial southern ocean. *Paleocanography, 23*, PA2102. https://doi.org/10.1029/2008pa001624.

Laj, C., & Channell, J. E. T. (2007). Geomagnetic excursions. In M. Kono (Ed.), *Treatise on geophysics* (Vol. 5, pp. 373–416).

Laj, C., et al. (2000). North atlantic paleointensity stack since 75 ka (NAPIS-75) and the duration of the laschamp event. *Philosophical Transactions of the Royal Society of London. Series A: Mathematical, Physical and Engineering Sciences, 358,* 1009–1025.

Laj, C., et al. (2004). High-resolution global paleointensity stack since 75 kyrs (GLOPIS-75) calibrated to absolute values. *Timescales of the Geomagnetic Field (American Geophysical Union, Washington, C, 2004) Geophysical Monograph, 145,* 255–265.

Laj, C., et al. (2014). Dynamics of the earth magnetic field in the 10–75 kyr period comprising the Laschamp and Mono Lake excursions: New results from the French Chaîne des Puys in a global perspective. *Earth and Planetary Science Letters, 387,* 184–197.

Lowrie, W., & Alvarez, W. (1981). One hundred million years of geomagnetic polarity history. *Geology, 9,* 392–397.

Mankinen, E. A., & Dalrymple, G. B. (1979). Revised geomagnetic polarity time scale for the interval 0–5 m.y.b.p. *Journal of Geophysical Research, 84,* 615–626.

Mazaud, A., et al. (2007). Variations of the ACC-CDW during MIS3 traced by magnetic grain deposition in Midlatitude South Indian Ocean Cores: Connections with the Northern Hemisphere and with Central Antarctica. *Geochemistry, Geophysics, Geosystems, 8,* Q05012. https://doi.org/10.1029/2006GC001532.

McDougall, I. (1979). The present status of the geomagnetic polarity time scale. In M. W. McElhinny (Ed.), *The earth: its origin, structure and evolution* (pp. 543–566). London: Academic Press.

McDougall, I., & Tarling, D. H. (1963a). Dating of reversals of the Earth's magnetic field. *Nature, 198,* 1012–1013.

McDougall, I., & Tarling, D. H. (1963b). Dating of polarity zones in the Hawaiian Islands. *Nature, 200,* 54–56.

Opdyke, N. D., & Channell, J. E. T. (1996). *Magnetic stratigraphy* (346 p.). San Diego, CA: Academic Press.

Opdyke, N. D., et al. (1966). Paleomagnetic Study of Antarctic Deep-Sea Cores. *Science, 154,* 349–357.

Opdyke, N. D., et al. (1974). The extension of the magnetic time scale in sediments of the Central Pacific Ocean. *Earth and Planetary Science Letters, 22,* 300–306.

Piotrowski, A. M., et al. (2005). Temporal relationships of carbon cycling and ocean circulation at glacial boundaries. *Science, 307,* 1933–1938.

Renne, P. R., et al. (1994). Intercalibration of astronomical and radioisotopic time. *Geology, 22,* 783–786.

Shackleton, N. J., et al. (1990). An alternative astronomical calibration of the lower pleistocene timescale based on ODP Site 677. *Earth and Environmental Science Transactions of the Royal Society of Edinburgh, 81,* 251–261.

Stoner, J., et al. (2002). South Atlantic and North Atlantic geomagnetic paleointensity stacks (0–80 ka): Implications for inter-hemispheric correlation. *Quaternary Science Reviews, 21*, 1141–1151.

Svensson, A., et al. (2006). The Greenland ice core chronology 2005, 15–42 ka. Part 2: Comparison to other records. *Quaternary Science Reviews, 25,* 3258–3267.

Vine, F. J., & Mathews, D. H. (1963). Magnetic anomalies over oceanic ridges. *Nature, 199,* 947–949.

Wagner, G., et al. (2000). Chlorine-36 evidence for the mono lake event in the summit GRIP ice core. *Earth and Planetary Science Letters, 181,* 1–6.

Wensink, H. (1966). Paleomagnetic stratigraphy of younger basalts and intercalated Plio-Pleistocene tillites in Iceland. *Geologische Rundschau, 54,* 364–384.

Dendrochronology

8

Frédéric Guibal and Joël Guiot

Dendrochronology differs from other absolute dating methods in that the age assignment is not based on a simple, automatic count of annual deposits i.e. the rings, but on a set of intercomparisons of a large number of chronologies so as to ensure the annual status of each tree-ring (also known as growth rings), after eliminating the potential pitfall of anomalies in the anatomy of rings which may result, some years, in the absence of a ring or the formation of double rings (also known as false rings).

To understand the principle of this method, some fundamental aspects related to the formation of growth rings in trees in temperate regions should be recalled. Because of the marked climatic seasonal contrast of temperate regions an annual status can be assigned to each ring (with the exception of some accidents in growth).

A Bit of Botany and Ecology

The annual growth of woody plants is composed of an axial component which leads to the lengthening of branches (primary growth) and a radial component which leads to the formation of a ring (secondary growth). The radial growth of the trunk, branches and roots results from a layer of actively-dividing cells, the cambium, immediately beneath the bark. This gives rise to vascular tissues: wood, on the inside, responsible for, among other functions, the upward flow of the sap, and phloem, on the outside, responsible for the downward movement of the elaborated sap (Fig. 8.1). Year after year, the previously formed tissue is pushed inwards for wood and outwards for phloem.

In areas with a temperate climate, fluctuations in the physical aspects of the atmosphere (temperature, humidity, sunshine) mean that vegetation has a period of activity and a period of rest within the same calendar year. Cambial activity is discontinuous in time: in deciduous oaks on the plains in western France, cambial activity lasts from April to September; for larches which grow in the internal Alps above 1500 m, cambial activity extends from mid-June to mid-August.

A ring is made up of two parts: the earlywood which develops at the beginning of the growing season, and the final latewood which develops later in the growing season. These differ in terms of the cells that compose them, their dimensions, their disposition and the thickness of their walls. Variations in the thickness of the cell walls have consequences for the density of the wood, in the form of intra-annual and inter-annual variations more or less linked to changes in climate conditions. These conditions act according to the principle of limiting factors. Growth cannot proceed faster than is allowed by the most limiting factor. This limiting effect may be continuous, variable or sporadic depending on the case. The action of climatic factors is attenuated or amplified by other factors, both abiotic (soil, topography) and biotic (age, competition, pest attacks, phenology).

Crossdating

Aristotle, Buffon and Leonardo mentioned the existence of annual tree rings. Leonardo da Vinci, in particular, observed a relationship between ring widths and the weather conditions of the year. However, it is the American astronomer Andrew E. Douglass (1867–1962) who, in laying out the methodological foundations, is considered the father of

F. Guibal (✉)
Institut Méditerranéen de Biodiversité et d'Ecologie marine et continentale, UMR7 263 CNRS/Aix-Marseille Université/IRD/Univ Avignon, Europôle de l'Arbois, BP 80, 13545 Aix-en-Provence Cedex 04, France
e-mail: Frederic.guibal@imbe.fr

J. Guiot
European Centre for Research and Teaching in Environmental Geosciences CEREGE, Aix-Marseille University, CNRS, IRD, INRAE, Collège de France, BP 80, 13545 Aix-en-Provence Cedex 04, France

G. Ramstein et al. (eds.), *Paleoclimatology*, Frontiers in Earth Sciences,
https://doi.org/10.1007/978-3-030-24982-3_8

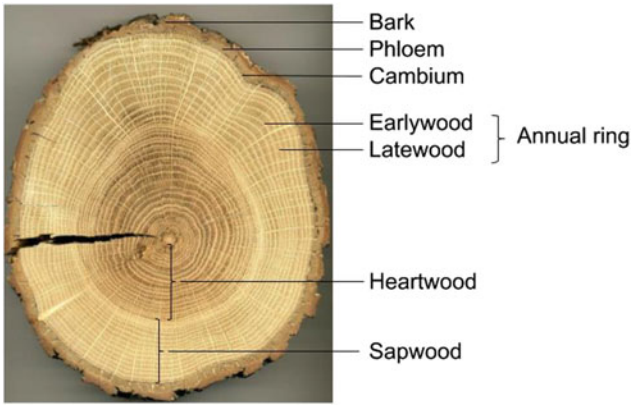

Fig. 8.1 Cross-section of deciduous oak

dendrochronology (*dendron*: tree, *chronos*: time, *logos*: study). Dendrochronology remained fairly discreet until it gained in notoriety about 1929, when Douglass succeeded for the first time in dating beams from ruins of Indian buildings in the US state of New Mexico, qualifying it as a dating method with an annual resolution (Robinson 1976). Despite this, it was not until the arrival of the computer in the 1960s, that dendrochronology truly took off, with a proliferation of research laboratories.

In the regions where the first dendrochronological studies were conducted (semi-arid regions of the southwestern USA and cold regions), the existence of a single limiting climate factor (rainfall in semi-arid regions, summer temperatures in cold regions) was instrumental in creating a series of rings whose width varied from one year to the next. However, in regions with a temperate climate, where growth depends on several factors, one factor can compensate for another, and the annual ring width series are less variable, making dendrochronological studies more complicated. In fact, if weather conditions are adequate, year after year, to meet the ecological requirements of the tree, the rings form a temporal series of constant width, and do not provide any chronological information, since it is extreme variations that serve as landmarks.

Dating with dendrochronology is based on a fundamental stage, called crossdating, which is relative dating assuring the proper placement in time of each ring. Crossdating is established by intercomparison of different pieces of wood on which sequences exhibiting similar ring patterns are identified. For this, similar sequences of coinciding narrow and wide rings, that is, separated by the same number of rings, need to be identified. This is possible only with two conditions. Firstly, the limiting factors for radial growth must vary in intensity from one year to another, with an unrepeatable series over time, so that the succession of ring widths are also variable in such a way as to be irreproducible. Secondly, the limiting factors must act in a similar way on trees with the same environmental requirements and over a wide enough geographical area to cause ring widths to vary the same way in many trees. This principle is important because ring widths can be crossdated only if one environmental factor becomes critically limiting.

Crossdating, or synchronization, is essential to check the accuracy of the ring count and the presence of any growth abnormalities. Abnormalities may appear as double rings (false rings) in the same calendar year or as missing rings. Indeed, some years, after a cold winter, possibly followed by a late spring or preceded by severe defoliation in the previous year, the ring may be partially or totally absent. In other years, as a result of the early onset of a summer drought (as in the Mediterranean region), the cambium may develop latewood elements and, then, thanks to improved weather conditions through the summer, may start producing earlywood elements again before producing latewood at the end of the normal growing season. In this case, the "first" ring is identified as supernumerary or false. Crossdating remains largely subjective and various methods have been developed to describe the observed similarities more objectively (McCarthy 2004).

In living trees of the same species, with a confirmed contemporaneity between the samples, synchronization is established by identifying sequences of similar rings over several series under a microscope (in cores or cross sections of trunk), firstly from the same tree, and then, between series from different trees. The operator compares the series from the bark inwards, records the rings and counts the sequences of narrow rings or ones with a distinguishing feature (color or width of the final wood, presence of any traumatic scars or ducts etc.). This stage allows the identification of each ring in terms of its vintage, after any anatomical abnormalities such as missing rings or double rings have been detected. After synchronization of the series has been established, ring width series are measured (1/100–1/1 000 mm).

On samples of unknown date, i.e. samples of wood from trees felled at an unknown date, the measurement of ring width series allows the establishment of digitized series from which graphs are drawn to compare the temporal variations in ring widths. The graphs are then compared in pairs and sequences of similar ring patterns are sought; maximum similarity between two curves is obtained when contemporary years are superimposed: maximum values, minimum values and the number of times two series show the same upward or downward trend in relation to the preceding year.

This analysis allows us to date the year of formation of each ring and identifies the felling date of the tree. The felling date of the tree is ensured when the outermost ring is still present; for species where the anatomical difference between sapwood (functional wood nearest the bark) and heartwood persists over time (oak, ash, elm, larch, etc.), the felling date of the tree is estimated based on the date assigned to the last ring.

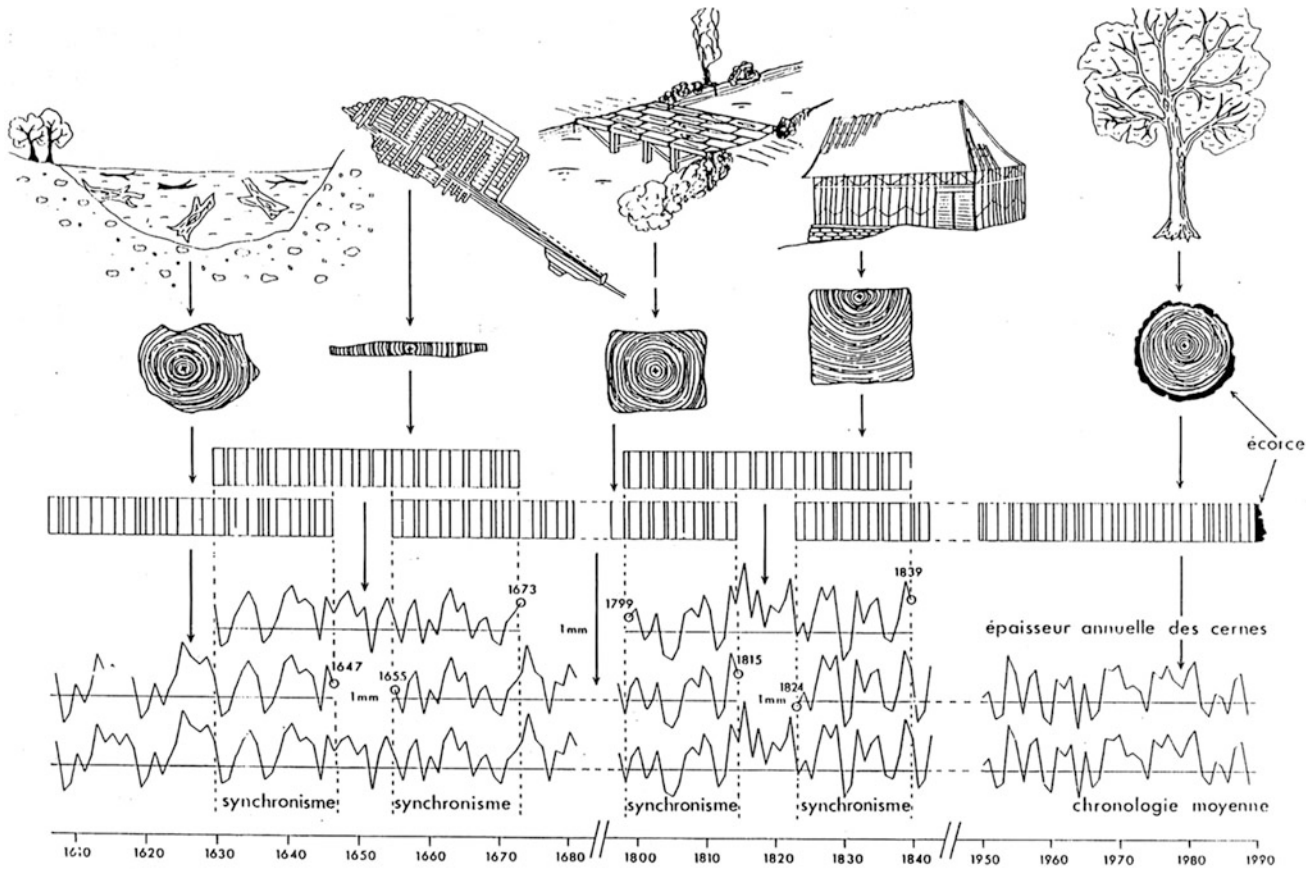

Fig. 8.2 Diagram of the theoretical construction of a master chronology

The dating of samples from trees which died at an unknown date requires synchronization between the analyzed series and a chronology of previously dated ring widths, called a master chronology. This master chronology must be composed of several series of rings from the same tree species as the one to be dated and from trees exposed to the same climatic factors, i.e. geographically close. Building a master chronology involves assembling several mean chronologies, homogeneous in their ecological and geographical origin, partially synchronous, based on the presence of ring patterns common to these timelines, and one of which is constructed from living trees for which the year of formation of the outermost ring is known. This permits each ring in the master to be assigned the year of its formation (Fig. 8.2). The representativity of a master chronology is related to its sample depth, i.e. the number of series included in the calculation of the mean ring width value. Even in climatically homogeneous regions, the geographic area covered inevitably leads to the inclusion of trees from forest stands subject to a variety of local climates, due to differences in altitude, exposure, continental character or even having grown in different site conditions (bedrock, exposure, phyto-ecological communities, degree of clearing of the site etc.) or having experienced more or less different stresses in the form of local disturbances. This summation results in a master chronology that is the average of annual wood layers over time of a given species in a region exposed to the same macro-climate, over a more or less extensive area.

Temporal and Spatial Extension

For the Holocene period, the longest chronologies, covering several thousand years, come from North America (Ferguson 1969; Ferguson and Graybill 1983), the British Isles (Pilcher et al. 1984; Baillie and Brown 1988), Central Europe (Leuschner 1992; Krapiec 1998; Schaub et al. 2008; Kaiser et al. 2011), North-West Europe (Eronen et al. 2002; Grudd et al. 2002) and Siberia (Naurzbaev and Vaganov 1999; Rashit et al. 2002). In the southern hemisphere, several groups have built thousand-year chronologies in Argentina and Tasmania (Barbetti et al. 1995; Roig et al. 1996; Cook et al. 2000).

In the same way that the representativeness of a master chronology is related to the quality of the climate signal evidenced by a high frequency of pointer years, the

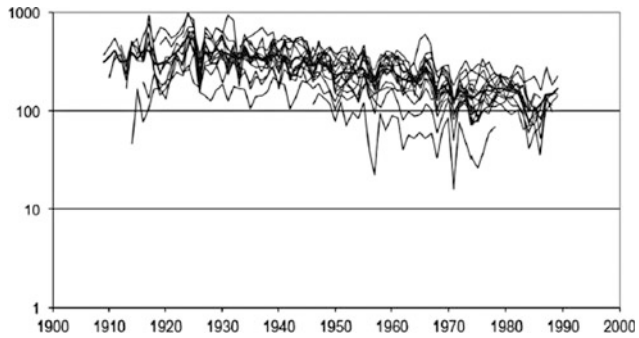

Fig. 8.3 Mean chronology (thick line) built up from multiple synchronous ring-width series of variable length (in line with the custom in dendrochronology, the y-axis is shown on a logarithmic scale to make the thinner rings more distinct)

chronological representativeness of the sample to be dated depends on the number of pointer years it contains. For this reason, trying to date a chronology composed of too few rings is usually an exercise doomed to failure. For a given site, a multiplicity of samples is essential to acquire a representative mean chronology for the site in which individual variances are minimized; in the field, this means sampling at least a dozen cases presumed to be contemporaneous, in order to achieve, whenever possible, a mean chronology of at least 80 years (Fig. 8.3). This methodological requirement explains the negative outcome of repeated attempts to date isolated pieces of wood, regardless of the context of their discovery, even if, in certain exceptional conditions (very long ring series, particularly well-documented period), statues and dugout canoes may have been dated by dendrochronology (Arnold 1996; Eckstein 2006)!

Synchronization between different tree species, called heteroconnexion, although discouraged because of differences in climate response and ecological requirements between species, is sometimes carried out between species with very similar ecological requirements. For example, comparisons are commonly made between oak and chestnut, oak and elm, larch and spruce.

Teleconnection or comparison of tree ring series over long distances, from areas subjected to different climate conditions, although theoretically just as frowned upon as the previous exercise is nevertheless, often done if the study is initiated in an area previously never investigated and for which there is no knowledge base.

In this way, the first master chronologies of oak representing the North East of France and Brittany were initiated. In a first example, master chronologies already in place for the South West of Germany were used to calibrate the first samples in Franche-Comté and Burgundy, which were analyzed by the Laboratory of Chrono-Ecology in Besançon, in the early 1980s. In a second example, master chronologies representative of the South West of England have allowed dating of sites located in the Loire valley, the Penthièvre and the Rennes basin by the City of London Polytechnic and Queen's University Belfast.

We should also mention that before starting to crossdate a piece of wood, it is often necessary to start with an approximate age of the piece, provided by ^{14}C dating which crossdating will then refine until accuracy to the year is achieved. It should also be noted that although dendrochronology is an absolute dating process accurate to a single year, this does not prevent occasional dating failures, especially when master chronologies for the species and/or region are lacking.

Contribution of ^{14}C to Calibration

Extremely valuable for its ability to date wood vestiges by establishing, under the conditions detailed above, the year of formation of each ring, even the year of death of the tree, dendrochronology has the undeniable advantage of contributing to the calibration of radiocarbon dates by converting ^{14}C age to the true calendar age.

In the 1950s, when the first radiocarbon datings were obtained on objects from past human societies, the match between the ^{14}C dates and the calendar dates was considered adequate. However, the archaeological material used was not very well dated or very old, and the ranges of uncertainty were so great that they masked potential minor deviations. According as the accuracy of ^{14}C dating improved and the body of datings grew, it quickly became obvious that the ^{14}C dates obtained were more recent than the dates obtained independently, in particular those obtained from remains from ancient Egypt. Given that any uncertainty inherent in relative dates obtained on such material could not be ruled out, and that in a living tree, only the outermost ring has a ^{14}C content in balance with that of the atmosphere, a program of ^{14}C dating of tree rings dated to the year by dendrochronology was initiated on long-living Methuselah pine (*Pinus aristata*) from the slopes of the White Mountains in California (Fig. 8.4). The results confirmed the disparity between ^{14}C dates and calendar dates (de Vries 1958). Irregular fluctuations were noted in the dates obtained, and led Suess (1965) to establish a calibration procedure for the ^{14}C dating of tree rings, in order to express the raw dates (conventional dates) in chronometrically calendar dates (calibrated dates). Measurements carried out on sequences of five or ten consecutive rings collected on the California pines have shown that the gap between the two calendars, ^{14}C years and actual years, remained low for the last 2500 years,

Fig. 8.4 View of a several thousand year old Methuselah pine (*Pinus aristata*) from the White Mountains (California)

but that from 500 BC, the gap increased sharply to almost 800 years at 5500 years BC.

A systematic study of this phenomenon was then carried out in the 1980s and 1990s by several laboratories on blocks of rings from American pines, oaks and European Scots pines. After publication in 1993, these curves, called radiocarbon calibration curves, established by thousands of measurements, constituted the basis on which corrections are now possible for the entire Holocene period, and currently, for the past 12,400 years (Stuiver et al. 1998). Extended into the past through the dating of tropical reef corals, varved sediments and speleothems (see Chap. 4), the calibration curves obtained from tree ring data are now being extended using series of dated tree rings series from Bølling Allerød and from Younger Dryas in Germany, the area around Zürich, Northwest Italy and watersheds of tributaries in the mid Durance valley (France).

The correction curve for ^{14}C dates in calendar years shows that the actual time seems compressed by about 15% before the sixth millennium BC, that there are plateaus along the curve (for example, around 500 BC. or during the ninth and tenth millennia BC.), and that multiple small fluctuations can, for some periods, affect the rectilinear shape of the curve. The practical consequences of these types of variations, showing that variations in concentration of atmospheric ^{14}C have been erratic, are very different: small fluctuations, after correction, can result in particularly inaccurate dates; but in some cases, very precise dates can be achieved for those periods particularly affected by fluctuations in the atmospheric content of ^{14}C.

Examined more closely, the radiocarbon calibration curve with its very twisted appearance reflects a stochastic process which constitutes, at certain times, a particularly valuable

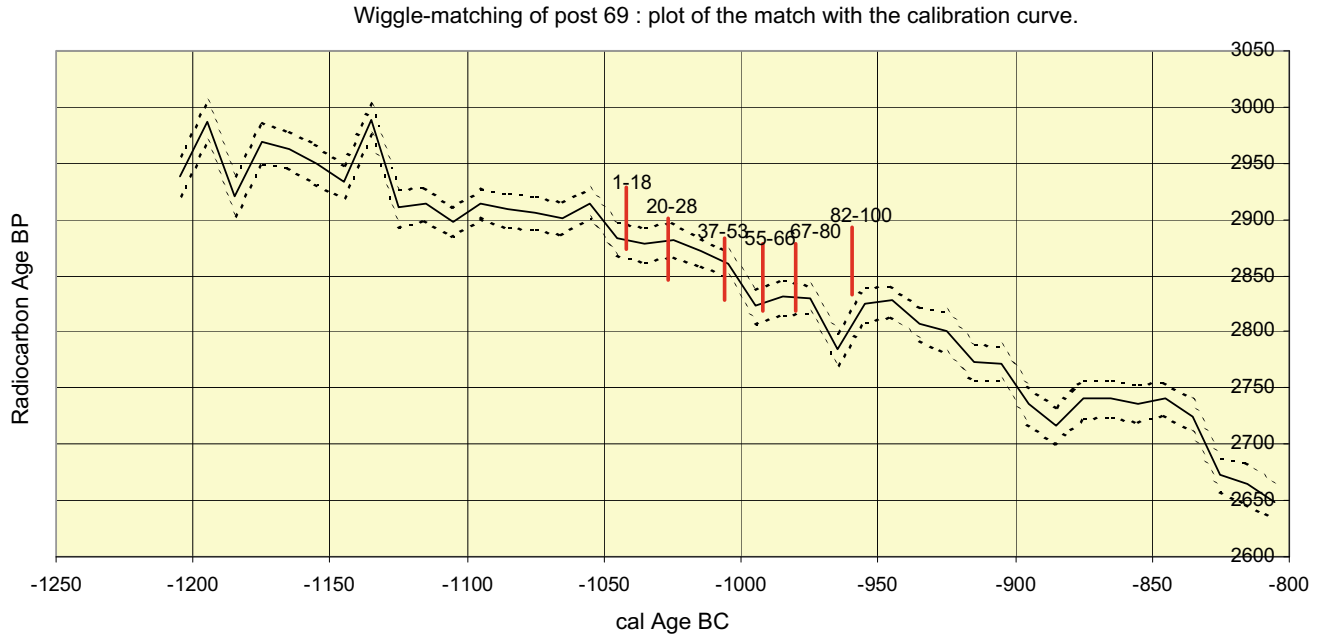

Fig. 8.5 Dating by wiggle-matching of the late Bronze age oak post n○ 69 from the submerged coastal habitat of Montpenèdre, Hérault (Oberlin et al. 2004). The x-axis corresponds to the calendar years; the y-axis corresponds to radiocarbon years. Vertical lines = standard deviation of the measure

chronological marker. Indeed, the matching of these kinks (known as wiggles), based on a multiplicity of ^{14}C dates obtained from blocks of tree rings, separated by a known number of calendar years, allows, by the method of "wiggle-matching" (Pearson 1986), a greatly improved accuracy of radiocarbon dating, as illustrated by the example of the post n° 69 (Fig. 8.5) from the submerged coastal habitat of Montpenèdre (Hérault, France).

References

Arnold, B. (1996). *Pirogues monoxyles d'Europe centrale. Construction, typologie, évolution* (Vol. 2). Coll. Archéologie aujourd'hui, Archéologie Neuchâteloise.

Baillie, M. G. L., & Brown, D. M. (1988). An overview of oak chronologies. In E. A. Slates & J. O. Tate (Eds.), *Science and archaeology* (196, pp. 543–548), Glasgow 1987, *Brit. Arch. Rep. Brit*.

Barbetti, M., Bird, T., Dolezal, G., Taylor, G., Francey, R. J., Cook, E., et al. (1995). Radiocarbon variations from tasmanian conifers: Results from three early Holocene logs. *Radiocarbon, 37*(2), 361–369.

Cook, E. R., Buckley, B. M., D'Arrigo, R. D., & Peterson, M. J. (2000). Warm-season temperatures since 1600 BC reconstructed from Tasmanian tree rings and their relationship to large scale sea-surface temperature anomalies. *Climate Dynamics, 16,* 79–91.

de Vries, H. (1958). Variation of the concentration of radiocarbon with time and location on Earth. *Proceedings of the Koninklijke Nederlandse Akademie van Wetenschappen: Proceedings Series B, 61,* 267–281.

Eckstein, D. (2006). Human time in tree-rings. *Dendrochronologia, 24* (2–3), 53–60.

Eronen, M., Zetterberg, P., Briffa, K. R., Lindholm, M., Meriläinen, J., & Timonen, M. (2002). The supra-long scots pine tree-ring record for Northern Finnish Lapland. Chronology construction and initial inferences. *The Holocene, 12*(6), 673–680.

Ferguson, C. W. (1969). A 7404-year annual tree-ring chronology for bristlecone pine, *pinus aristata*, from the White Mountains, California. *Tree-Ring Bull, 29*(3–4), 1–29.

Ferguson, C. W., & Graybill, D. A. (1983). Dendrochronology of bristlecone pine: A progress report. *Radiocarbon, 25*(2), 287–288.

Grudd, H., Briffa, K. R., Karlén, W., Bartholin, T. S., Jones, P. D., & Kromer, B. (2002). A 7 400-year tree-ring chronology in Northern Swedish Lapland: Natural climate variability expressed on annual to millennial time scales. *The Holocene, 12*(6), 657–665.

Kaiser, K. F., Friedrich, M., Miramont, C., Kromer, B., Sgier, M., Schaub, M., et al. (2011). Challenging process to make the late glacial tree-ring chronologies from Europe Absolute—An Inventory. *Quaternary Science Reviews,* 13 p. https://doi.org/10.1016/j.quascirev.2010.07.009.

Krapiec, M. (1998). Oak dendrochronology of the neoholocene in Poland. *Folia Quaternaria, 69,* 5–133.

Leuschner, H.-H. (1992). Subfossil trees. In T. S. dans Bartholin, B. E. Berglund, D. Eckstein, & F. H. Schweingruber (Eds.), *Tree rings and environment. Proceedings of the International Dendrochronological Symposium, Ystad, South Sweden, 3–9 September 1990* (pp. 193–197). Lund: Lund University, Department of Quaternary Geology.

McCarthy, B. C. (2004). *Introduction to dendrochronology*, Ohio University, World Wide Web homepage. http://www.plantbio.ohiou.edu/epb/instruct/ecology/dendro.htm.

Naurzbaev, M. M., & Vaganov, E. A. (1999). 1957-year chronology for Eastern Taimir. *Siberian Journal of Ecology, 6,* 67–78.

Oberlin, C., Leroy, F., & Guibal, F. (2004). High precision ^{14}C dating of a bronze age tree-ring chronology from the pile-dwelling settlement of Montpenèdre, Hérault, Southern France. In *Proceedings of the IVth Int. Symp. Radiocarbon and Archaeology*, Oxford, 9–14/04/2002, *Oxford University School of Archaeology Monograph* (Vol. 62, pp. 193–200).

Pearson, G. W. (1986). Precise calendrical dating of known growth-period samples using a 'curve fitting' technique. *Radiocarbon, 28*(2A), 292–299.

Pilcher, J. R., Baillie, M. G. L., Schmid, B., & Becker, B. (1984). A 7,272-year tree-ring chronology for Western Europe. *Nature, 312,* 150–152.

Rashit, M., Hantemirov, M., & Shiyatov, S. G. (2002). A continuous multimillenial ring-width chronology in Yamal, Northwestern Siberia. *The Holocene, 12*(6), 717–726.

Robinson, W. J. (1976). Tree-ring dating and archaeology in the American South-West. *Tree-Ring Bull, 36,* 9–20.

Roig, F., Jr., Roig, C., Rabassa, J., & Boninsegna, J. (1996). Fuegan floating tree-ring chronology from subfossil *Nothofagus* Wood. *The Holocene, 6*(4), 469–476.

Schaub, M., Kaiser, K. F., Frank, D. C., Buentgen, U., Kromer, B., & Talamo, T. (2008). Environmental change during the Allerød and Younger Dryas reconstructed from tree-ring data. *Boreas, 37,* 74–86.

Stuiver, M., Reimer, P. J., Bard, E., Beck, J. W., Burr, G. S., Hughen, K. A., et al. (1998). IntCal98 Radiocarbon Age Calibration, 24,000-0 cal BP. *Radiocarbon, 40*(3), 1041–1083.

Suess, H. E. (1965). Secular variations in the cosmic ray produced carbon-14 in the atmosphere and their interpretation. *Journal of Geophysical Research, 70*, 5937–5952.

The Dating of Ice-Core Archives

9

Frédéric Parrenin

The wealth of testimony about past variations in our climate and environment found in deep ice cores in Antarctica and Greenland is acknowledged well beyond the limits of glaciological research. Uniquely, both local climate variations and global atmospheric composition can be reconstructed from a single archive: the ice. Effective use of the information provided by the glacial archives requires dating as precisely as possible of these various records. To do this, the specific characteristics of ice need to be considered.

The first characteristic results from the compaction of snow layers under their own weight. At the surface, the snow is not very dense (0.3–0.4 g/cm^3): air circulates freely in the first meters of this porous milieu, the firn, and then with more difficulty as the density increases and the porosity decreases. When the density is greater than about 0.83 g/cm^3 (below about 100 meters in the center of Antarctica), air is trapped in bubbles in the ice and insulated from the atmosphere. In the depths, under the effect of pressure, the bubbles become compressed and are then transformed into clathrates, i.e. the gas molecules become incorporated into the crystalline structure of the ice. This means that the air is younger than the ice that imprisons it. Therefore, to date ice core archives, which have some signals recorded in the ice and others recorded in the air bubbles, two distinct chronologies are required. The evaluation of the age difference between gas and ice is discussed in Section "Ice-Air Age Difference".

Moreover, ice does not lend itself to the use of radioactive methods. Carbon-14 dating can only be used in exceptional cases, for example, on plant debris or when sufficient amounts of carbon dioxide are extracted. Although the quantities of ice necessary for carbon-14 dating have decreased since the advent of accelerator mass spectrometry, the dates obtained are only averages over a few meters of ice. In addition, this method is not applicable beyond a few tens of thousands of years because the period of radioactive decay of carbon-14 is 5730 years.

Datings developed by glaciologists are then based on complementary methods such as counting annual layers (Section "The Counting of Annual Layers"), comparison with other dated records (Section "Identification of dated horizons") and with variations in insolation (Section "Orbital Tuning and Indicators of Local Insolation"), and glaciological modeling (modeling of the accumulation of snow and the flow of ice, Section "Flow Modeling"). After these methods have been presented, we will describe, in Section "The Inverse Method: A Collective Approach", a statistical technique, known as the 'inverse method', which consists of collecting these different sources of chronological information to achieve an optimum date and to assess its confidence interval.

Ice-Air Age Difference

Introduction

The firn is the porous upper area of the ice caps. It marks the transition from snow on the surface to the ice below. Depending on its location, its thickness can vary from roughly 50 m (Greenland) to 120 m (central Antarctica). Its density varies from the surface density (typically 0.4 g/cm^3) to the density at the *close off* depth, i.e. the depth at which the pores close (typically 0.83 g/cm^3). At this depth, air is trapped in isolated bubbles and no longer circulates.

The study of transport of air in the firn has led to the development of a simple model (Sowers et al. 1992) from which we can distinguish four zones in the firn (Fig. 9.1).

- *The convective zone* is located just below the surface. Convection in this zone is caused partly by the thermal gradient and partly by surface winds. The depth of this zone varies from one site to another, and may reach 20 m

F. Parrenin (✉)
Institut des Géosciences de l'Environnement,
St Martin d'Hères, France
e-mail: frederic.parrenin@univ-grenoble-alpes.fr

G. Ramstein et al. (eds.), *Paleoclimatology*, Frontiers in Earth Sciences,
https://doi.org/10.1007/978-3-030-24982-3_9

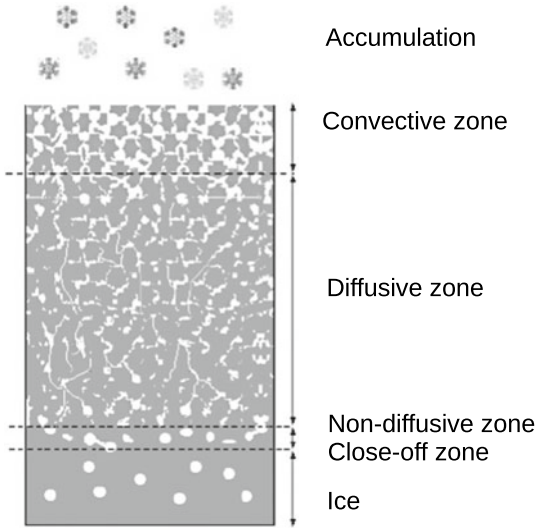

Fig. 9.1 Diagram showing the different parts of the firn. Adapted from Sowers (1992)

in sites with high winds and rugged relief (dunes) at the surface.

- The diffusive zone corresponds to an area where the air column is static (no convection). Movement happens at the molecular level (diffusion), and in this zone, elementary and isotopic fractionation is observed. For example, the heaviest molecules are located, in priority, in the cold deeper part, while the lighter molecules are more numerous in warmer, higher areas.
- *The non-diffusive zone* is the zone where the pores are almost closed and where molecular diffusion is negligible. From this point, the composition of the bubbles no longer changes, even though the total pressure can still evolve.
- *The close-off zone* is located at the base of the firn. The bubbles of air are closed off, and the air is trapped inside. This close off zone has a well-defined density of about 0.83 g/cm^3. This close-off depth will increase as the surface temperature decreases and will vary according to the rate of accumulation on the surface of the firn. As a result, the depth of the close-off zone will vary during glacial and interglacial periods.

The top of the non-diffusive zone is a depth of critical importance, above which the air contained in the pore space of the firn is still in contact with the surface atmosphere. Although the snow at this depth fell hundreds or even thousands of years earlier, the gas is still at age 'zero', i.e. at the age of the most recent snow. Consequently, at any depth of an ice core, the gas in the trapped air bubbles is younger than the ice surrounding it. The difference between the age of the ice and the age of the gas bubbles is denoted as Δage. In other words, the gas of the same age as the ice is found lower down, and this difference in depth is denoted Δdepth.

In reality, it is not possible to attribute an exact age to the gas at a given depth. As the air travels through the diffusive column, it mixes the gases from atmospheres of different periods, with a typical average time of a few decades. Moreover, as the close-off boundary is not attributed to a specific depth, but extends over several meters, gas trapped at the same depth may have become imprisoned at slightly different times. Therefore, the signal produced may be diffuse, all the more so if the accumulation of snow is low.

Modeling the Densification of the Firn

To evaluate the Δage, one must evaluate:

- *The density at the close-off* which is often calculated from the surface temperature, using observations carried out at different sites (Salamatin et al. 2009); it can also be deduced from the concentration of air in the ice;
- *The age of the gas at the close-off* which is often ignored in the case of Antarctic cores, as it is very tiny compared with the age of the ice; it can be assessed using a gas diffusion model for the firn in the case of Greenland cores, where the age of the ice at close-off is only a few hundred years (Schwander et al. 1997);
- *The density profile in the firn*, which is derived from a mechanical model; various mechanical models have been published (see, for example, Salamatin et al. 2009); they generally take into account the slippage of snow grains relative to each other, a dominant process at the surface, and the deformation of the grains which becomes dominant at greater depths.

As shown in Fig. 9.2, the calculated depth of the close-off increases when accumulation increases (vertical advection increases) or as the temperature decreases (densification happens more slowly). These models were validated using current data (especially density profiles) from sites with very varied average temperature and accumulation conditions, both in Antarctica and in Greenland (Fig. 9.2. See Salamatin et al. 2007). However, it is worth noting that no site included corresponds to the conditions of the last ice age in Antarctica, which had very cold temperatures and very low accumulation. Also, these validations only pertain to the present, with current orbital parameters and thus with very specific daily and seasonal insolation distributions.

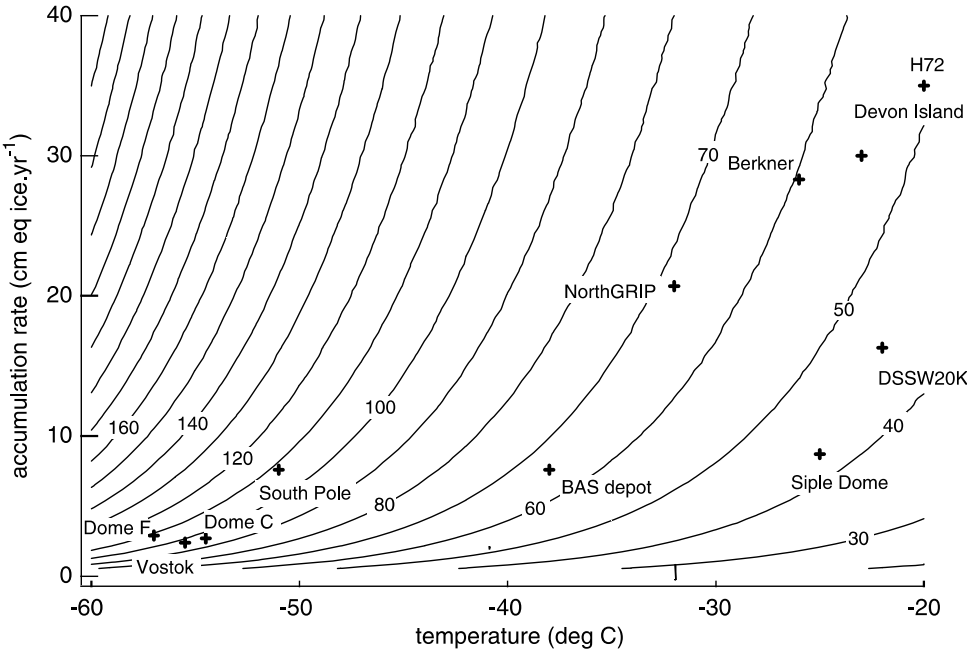

Fig. 9.2 Depth of the close-off of bubbles based on the rate of accumulation and the surface temperature, assumed to be at a steady state, as calculated by the model by Arnaud et al. (2000). The conditions in different polar sites are indicated by crosses. Adapted from Landais et al. (2006)

Application of the ^{15}N and ^{40}Ar Isotopes in the Bubbles

Nitrogen and argon have isotopic compositions (in ^{15}N and ^{40}Ar) in the atmosphere almost constant over the timescales studied in ice cores. But the isotopic composition of the air bubbles varies due to a process occurring in the firn.

Because of the mixing, no fractionation occurs in the convective zone. In the diffusive zone, two types of fractionation take place:

- *Gravitational fractionation*, under the influence of gravity, draws the heavy isotopes towards the bottom of the firn, according to the equation:

$$\delta_g = \left[\left(\frac{T}{T_0}\right)\right]\left[\exp\left(\frac{\Delta mgz}{RT}\right) - 1\right] \times 1000 \qquad (9.1)$$

where Δm is the difference in mass between the two isotopes, g is the gravitational acceleration, z is the height of the diffusive column, R is the constant of perfect gases and T is the temperature, expressed in Kelvin. This fractionation will therefore depend primarily on the height of the diffusive column, and to a lesser extent, on the temperature of the firn. All things being equal, the gravitational fractionation is proportional to the difference in mass between the two isotopes under consideration. So, it is four times higher for argon (^{40}Ar and ^{36}Ar) than it is for nitrogen (^{15}N and ^{14}N).

- *Thermal fractionation* draws the heaviest types towards the cold extremity. Thermal fractionation in equilibrium may be written as:

$$\delta_g = \left[\left(\frac{T}{T_0}\right)^{\alpha} - 1\right] \times 1000 \qquad (9.2)$$

where T and T_0 are the temperatures at either end of the diffusive column and α is the thermal diffusion coefficient, which depends in a complex way on the temperature.

Nitrogen-15 and argon-40 can thus be used in two different ways to constrain the age differences between ice and gas.

Firstly, abrupt changes in temperature can be identified in both the ice (where it is recorded in the variations in the isotopic composition of oxygen and of hydrogen in the H_2O molecule, see §11.3, Chap. 11), and in the air (in the isotopic composition anomaly due to thermal fractionation). Thus, an estimate of Δdepth may be deduced. This method was used to validate firn models in Greenland during major rapid changes in temperature, called Dansgaard-Oeschger events. In Antarctica, temperature variations are less abrupt, and so detection of the temperature anomaly remains ambiguous.

Secondly, assuming that the convective column is known and that no fractionation takes place during the pore closing process, we can calculate the thickness of the diffusive column. This technique also served to validate the firn models in Greenland. For sites on the Antarctic plateau, the situation is more complex, because nitrogen-15 and argon-40 suggest a decrease in the diffusive column during the glacial periods, although the firn models calculate an increase in the thickness of the firn (Landais et al. 2006). Three hypotheses may explain this discrepancy: (1) the height of the convective zone increased during glacial

periods; (2) firn models do not apply to glacial conditions of the Antarctic plateau; (3) another fractionation process occurs at the closure of the pores. This issue remains undecided at present.

Synchronization of Two Ice Cores

As explained above, the ice/gas differential in cores with a low rate of accumulation from the Eastern Antarctic shelf and during the ice ages is still poorly constrained. An alternative way to obtain an estimate, for both ice and gas recordings, is synchronization with a core with a higher rate of accumulation, wherein the ice/air differential is better constrained.

Loulergue et al. (2007) and Parrenin et al. (2012) have applied this method to constrain the Δage of the EDC (EPICA Dome C) from the EDML (EPICA Dronning Maud Land) and the TALDICE (Talos Dome Ice Core) cores. Gas synchronization is based on the rapid variations in methane, and ice synchronization uses volcanic signatures. So, this study shows that the firn model, forced with temperature and accumulation scenarios as for dating ice (Parrenin et al. 2007b), overestimates the Δage at EDC by 500–1000 years, during the last glacial period. Consequently, the densification mechanism during glacial periods at EDC is poorly understood and the models need to be improved.

The Δage, during glacial periods, for Antarctic plateau sites with low accumulation is therefore an open question. Further studies are needed to clarify this issue.

The Counting of Annual Layers

On the polar ice caps and glaciers, many of the properties of snow differ depending on whether it accumulates in summer or winter. For example, in summer, dust is more abundant in the snow, because during this season, the winds are more conducive to dust transport towards the poles. The annual layers can therefore be identified, either visually, or by chemical analysis or by isotopic analysis. Counting annual layers is a simple method of dating, provided that the accumulation of snow is sufficient, so that the stratigraphy is not destroyed by winds mixing the layers near the surface. For this reason, the counting of layers is impossible in the central regions of the Antarctic plateau where the deep drilling of Vostok, Dome C and Dome F are located, but it is possible over Greenland and the coastal regions of Antarctica.

A large project for systematic counting called Greenland Ice Core Chronology 2005 (GICC05) has been undertaken by a Danish team at the Niels Bohr Institute in Copenhagen. It is based on the cores of DYE-3, GRIP and NorthGRIP, and currently extends over the last 60,000 years (Svensson et al. 2008). More recently, the WAIS (West Antarctic Ice Sheet) Divide ice core has been counted back to 31,000 years (Sigl et al. 2016).

Glaciologists use various records to identify annual layers. Where possible, the isotopic variations in the ice ($\delta^{18}O$ and δD), which are dependent on the temperature at the moment of the precipitation, provide the most reliable recording of the changing of the seasons. However, water molecules diffuse in the form of vapor through the firn, then more slowly through the ice. This diffusion smooths out the seasonal isotopic signal until it disappears at a certain depth, even more rapidly when accumulation is low and the temperature is high. Thus, the seasonal cycle of isotopes is hardly recognizable on the NorthGRIP core, which has a low accumulation; it is quite muted in the GRIP core. The longest sequence on which the seasonal cycle oxygen-18 was used was obtained from the Dye-3 core in Greenland: 67,000 isotopic analyses allowed the dating of the core year by year over the last 7900 years. Beyond that, the thickness of annual layers is insufficient and the isotopic diffusion through the ice makes counting inaccurate.

Other data taken from the content of impurities in Continuous Flow Analysis (CFA), from the Electrical Conductivity Measurement (ECM), from the insoluble dust content, and from Visual Stratigraphy (VS) complete the isotopic information when this is available (Fig. 9.3). The CFA allows the various soluble compounds, such as Na^+, Ca^{2+}, H_2O_2, NH_4^+, NO_3^- and SO_4^{2-} to be separated. The ECM is a non-destructive measurement, conducted continuously in the field, but it only provides information on an amalgamation of these different soluble compounds. The VS uses the fact that impurities diffuse the light in the ice. However, this recording generally shows several peaks in a year and is therefore not easy to interpret. In Greenland and during the Holocene, a typical year is characterized by Na^+ (dominated mainly by marine inputs) showing a peak in late winter. Spring has a high dust content, high Ca^{2+} and low H_2O_2. Summer is characterized by high concentrations of NH_4^+, NO_3^-, and sometimes SO_4^{2-}. This method, based on data from CFA, ECM and VS from GRIP and NorthGRIP, was the one principally used to establish GICC05 in the period between 7900 and 14,800 years b2k (this notation means 'years before 2000') (Rasmussen et al. 2006). In the older part (14,800–60,000 Years b2k), the method is the same, but only NorthGRIP data were used (Svensson et al. 2008).

In summary, none of the individual indicators is perfect, but combined, they permit an annual dating, as long as the thickness of the layers, which thin out as they sink into the ice cap, remain sufficient. For GICC05, counting was carried out by different people and on different cores, and the independently obtained results were compared so as to

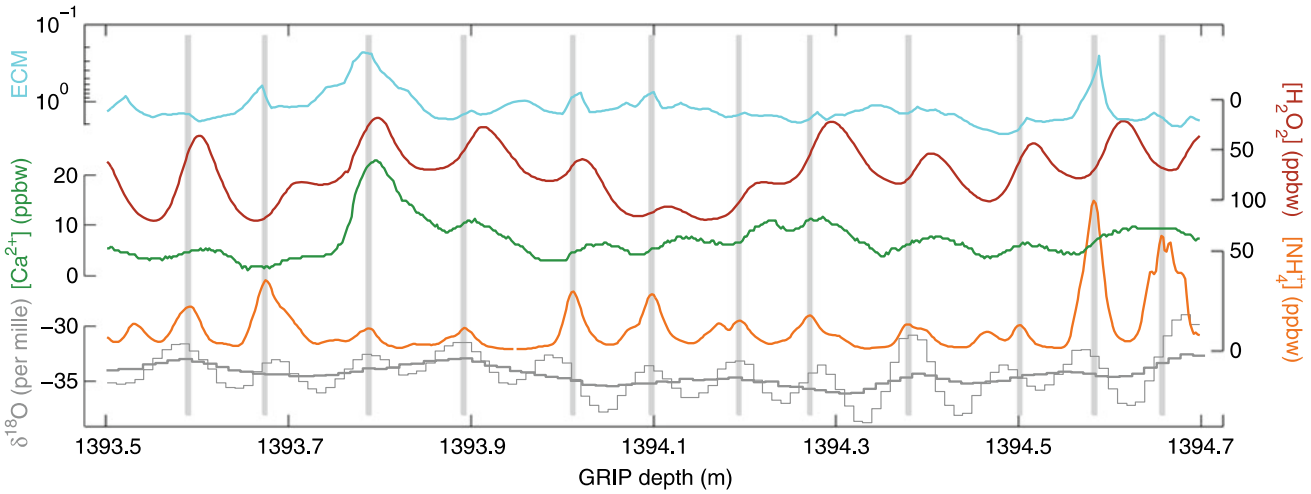

Fig. 9.3 Example of a 1.2 m section from the GRIP core of about 8.8 ka with the annual layers marked by the gray vertical bars. From top to bottom, the records used to identify annual layers are: ECM, H_2O_2, Ca^{2+}, NH_4^+ and $\delta^{18}O$. For this last indicator, the thick line represents the raw data and the fine line represents data after correction for the diffusion effect. Adapted from Rasmussen et al. (2006)

minimize subjective errors. Moreover, each uncertain layer was listed so as to obtain a confidence interval on the final chronology. The listed errors are few: under 2% as far back as the last deglaciation, and around 5% before for older ages (Fig. 9.4).

Identification of Dated Horizons

Even if ice cores cannot be dated directly by the conventional radiochronological methods, events that have been dated elsewhere can be identified in these cores: this is what we call the identification of dated horizons. In the following, we will detail the principal types of horizons used to date the polar cores.

Volcanic Horizons

Volcanic horizons can be identified in the cores, both in Antarctica and in Greenland. Some events are sufficiently intense or occur sufficiently close to the core to deposit volcanic dust (ash) visible to the naked eye. However, most events only deposit fine aerosols. These can then be identified with chemical analyses performed on the ice: sulfate, in particular, has several peaks corresponding to volcanic inputs that are easily identified because they far exceed the usual levels. These volcanic horizons also change the dielectric properties of the ice, which enables them to be identified by measuring its conductivity (this is a non-destructive measurement, generally carried out in the field, immediately after the cores have been brought to the surface).

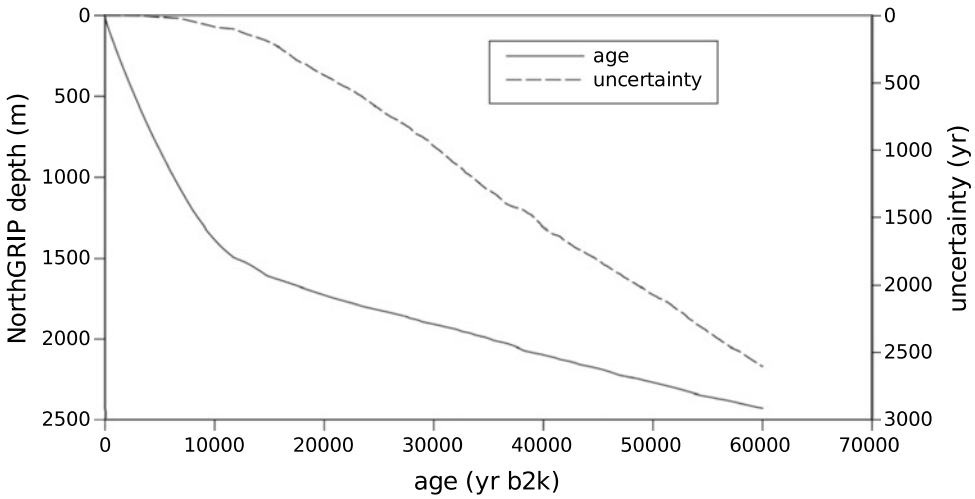

Fig. 9.4 Depth/age relationship on the NorthGRIP core according to the GICC05 scale (solid line) with associated uncertainty (dotted line). The notation 'b2k' means before 2000

For the last few thousand years, a large number of these volcanic events have been dated by different methods (Zielinski et al. 1994): either by counting the layers in sites with a sufficiently high accumulation or through historical writings, or by dating volcanic material near the volcano in question, especially by the carbon-14 method applied to biological debris (e.g., trees caught in the lava). Starting with an approximate glaciological dating, these events can generally be identified by their intensity in the cores. They can also allow two ice cores to be stratigraphically connected (see Fig. 9.5).

Before the Holocene, only a few layers of ash (Fig. 9.6) can be dated accurately. Chemical analysis of these ashes enables unambiguous identification of the relevant volcanic eruption. This signature can sometimes be connected to that of the volcanic material located close to a volcano. This volcanic material, in larger quantity, can be dated by conventional radiochronological methods.

In this way, a visible ash layer in the ice cores of Dome C and Dome Fuji could be dated by an American team using the argon/argon method (see Chap. 5) to date ash found near the volcano (Mt Berlin, Antarctica; Narcisi et al. 2006). For Greenland, notable volcanic horizons were identified that are referred as: Saksunarvatn, Vedde, Fugloyarbanki, '33 ka ^{14}C' and Z2. These horizons were dated by the carbon-14 method or by the argon/argon method (see Svensson et al. 2008 and included references for further detail).

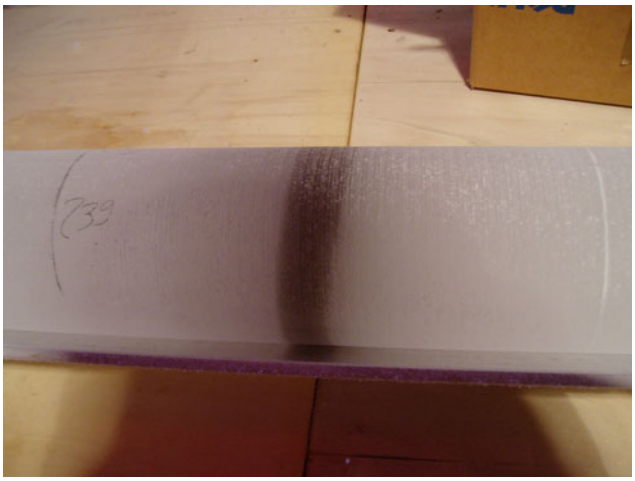

Fig. 9.6 Ash layer present at about 239 m in the core drilled at Talos Dome (East Antarctica). Copyright F. Parrenin (frederic.parrenin@univ-grenoble-alpes.fr)

Dansgaard-Oeschger Events

Dansgaard-Oeschger events (D-O) were identified for the first time in Greenland ice cores and correspond to abrupt changes in temperature during the last glacial period (see §3.2, Chap. 4). Synchronous variations (within a few decades) were also observed in the atmospheric content of methane (Severinghaus et al. 1998) measured in air bubbles from both Antarctic and Greenland ice. These events can therefore be dated by the Greenland cores which are relatively precisely dated through counting of the annual layers (See Section "The Counting of Annual Layers"). This dating can then be transferred to the Antarctic cores thanks to the methane records.

The changes in climate associated with the Dansgaard-Oeschger events, although their maximum impact was probably at the level of the North Atlantic, are visible in many locations on the planet, in other climate

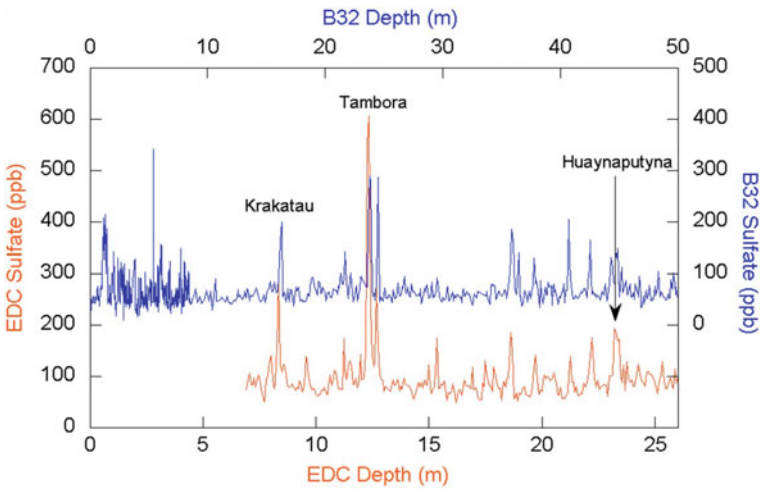

Fig. 9.5 Sulfate profiles for the first tens of meters in two ice cores from Eastern Antarctica: EDC (EPICA Dome C, bottom) and B32 (top), the latter located near the EDML site (EPICA Dronning Maud Land). Several well-known eruptions can be identified. Moreover, these volcanic profiles can be used to synchronize the ice cores between each other. Adapted from Severi et al. (2007)

archives. They are found in the isotopic composition of speleothems (stalactites and stalagmites found in caves) in Europe and Asia, in South America and the Indian Ocean. These speleothems can be dated with a precision of a few hundred years to one or two thousand years, using the uranium/thorium method, which provides a specific age for the marked transitions of the D-O events. Figures 9.7 and 9.8 summarize these recordings with their respective dating.

Variations in the Magnetic Field and in Solar Activity

Beryllium-10 and carbon-14 are both produced in the upper atmosphere by the flux of cosmic particles. This flux is modulated, partly by the magnetic field of the solar wind which deflects the charged particles, and partly by the terrestrial magnetic field. Unlike beryllium-10 whose deposition on the surface of the Earth is almost directly related to its production in the upper atmosphere, the composition of carbon-14 in the atmosphere is also influenced by the exchanges between the different carbon reservoirs on Earth. But the major changes in these two indicators (carbon-14 and beryllium-10) are simultaneous.

Beryllium-10 can be accurately measured in ice cores, both from Antarctica (see Raisbeck et al. 2007 and included references) and Greenland (see Beer et al. 2006 and included references). This allows the dating achieved by counting the annual layers in Greenland to be transferred to Antarctic cores for the Holocene (Ruth et al. 2007) and for the Laschamp anomaly in the geomagnetic field, which occurred about 41 ka ago (Raisbeck et al. 2007).

Carbon-14, meanwhile, is measured in tree rings, which are very accurately dated for the last 12.4 ka using dendrochronology (see Chap. 8). We can then import this dating to the ice cores when the variations in solar activity are significant enough so that beryllium-10 and carbon-14 can be synchronized. This method has been used to date the Holocene part of the Antarctic ice cores, where counting of the layers is not possible (Ruth et al. 2007).

Finally, significant anomalies in the geomagnetic field can be identified in other paleoenvironmental archives such as volcanic lava, which can be dated by the argon/argon or potassium/argon methods. The Laschamp anomaly is thus dated with a relatively good accuracy (Guillou et al. 2004), while the older Bruhnes-Matuyama transition is only very crudely dated (Raisbeck et al. 2006). Chap 7 provides more detail on magnetic stratigraphy.

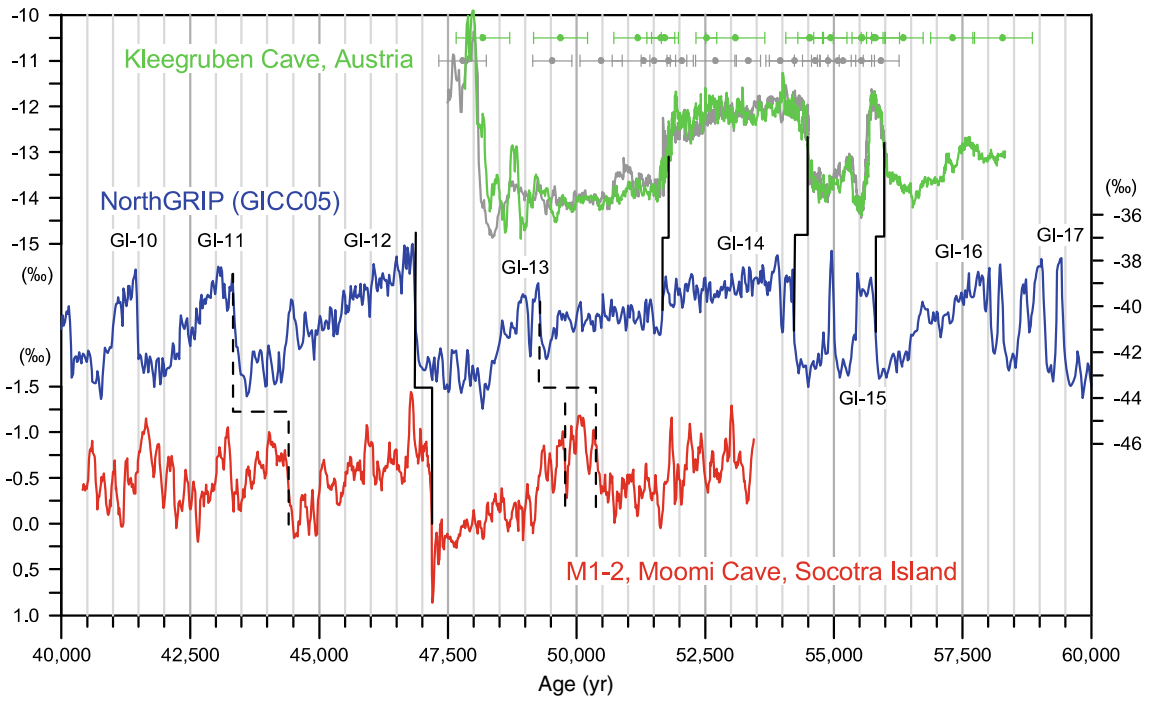

Fig. 9.7 The Dansgaard-Oeschger events identified in the North-GRIP core (GICC05 dating), and in records from the Kleegruben (Spötl et al. 2006) and Moomi (Burns et al. 2003) caves, the latter being dated by a uranium/thorium method. Adapted from Svensson et al. (2008)

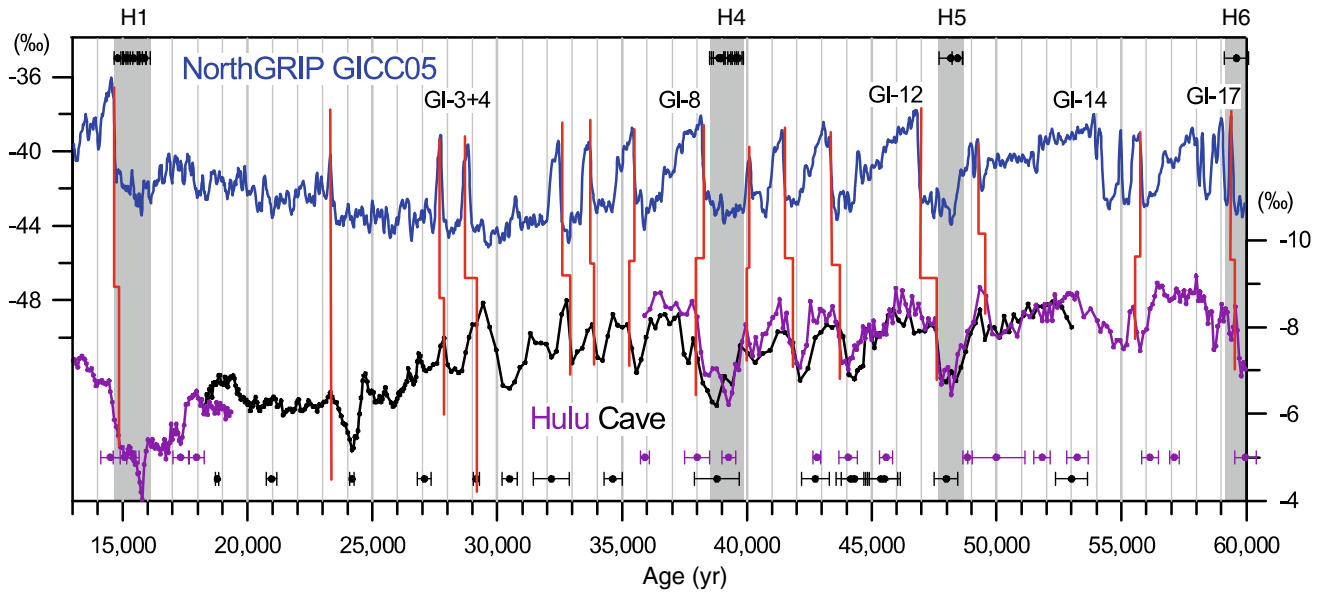

Fig. 9.8 The Dansgaard Oeschger events identified in the NorthGRIP core (GICC05 dating) and records from the Hulu cave (Wang et al. 2001). The points dated in the records from Hulu Cave by the uranium/thorium method are marked at the bottom of the figure (with their error bar). The shaded areas represent Heinrich events as identified in speleothems in Brazil (Wang et al. 2004). These points dated by the uranium/thorium method are also shown at the top of the figure. Adapted from Svensson et al. (2008)

Orbital Tuning and Indicators of Local Insolation

The evolution of orbital parameters of the Earth over the last million years is known with great precision (Laskar et al. 2004), and these variations leave a signature in most climate records. Therefore, the use of variations in insolation to date polar cores is a natural choice. Uncertainty in this dating is due, in part, to the assumption that there is a constant phase difference between orbital and climatic variations, and, secondly, to the evaluation of this phase difference. The advantage of this dating is that it has an almost constant uncertainty of a few thousand years along the length of the core, especially for the deeper parts, as long as we are able to recognize the orbital cycles.

Several parameters recorded in the ice cores show strong variations in the orbital frequencies. These were then used to align the ice cores with orbital cycles: these are the D/H ratio in the ice, an indicator of local temperature (for example, Parrenin et al. 2004) and the $^{18}O/^{16}O$ ($\delta^{18}O_{atm}$) ratio in the air bubbles (for example, Dreyfus et al. 2007). The variations in $\delta^{18}O_{atm}$ are a reflection of two aspects of the environment (Landais et al. 2010). The first one is that the variations in the $\delta^{18}O$ of the ocean, directly related to the volume of land ice, impact fully on the $\delta^{18}O$ of the atmospheric oxygen through the process of photosynthesis by seaweed. The second one is that a portion of the variations in $\delta^{18}O_{atm}$ is determined by the behavior of the terrestrial biosphere. This is the Dole effect which depends in a complex way on the reactions of photosynthesis and respiration. The $\delta^{18}O_{atm}$ signal shows variations mainly related to the precession, so it is very easy to use it to 'count' these cycles, at least for the periods during which they are sufficiently important variations in the insolation signal. However, there is no reason to assume that the phase difference between $\delta^{18}O_{atm}$ and insolation remained constant over time.

To avoid this limitation in the 'traditional' methods of orbital alignment, more direct indicators of local insolation have recently been proposed. Local insolation in summer alters the structure of the snow at the surface, and this signature remains present down to the close-off zone, regardless of the densification process. These structural parameters have an impact on the volume of the pores at close-off (and thus the air content), and also on the molecular fractionation processes between O_2 and N_2 when the pores close.

Bender (2002), was the first to suggest that the O_2/N_2 ratio in the air bubbles analyzed in the Vostok core was dependent on the local insolation at the summer solstice (Fig. 9.9). Recently, this link has been confirmed in the first core drilled at Dome Fuji (Kawamura et al. 2007) (Fig. 9.9) and recent measurements in the second core, with an improved analytical process, show an almost perfect correlation.

Raynaud et al. (2007) also studied in more detail the air content in the EDC core and suggested that it depended on local insolation averaged over a period centered on the

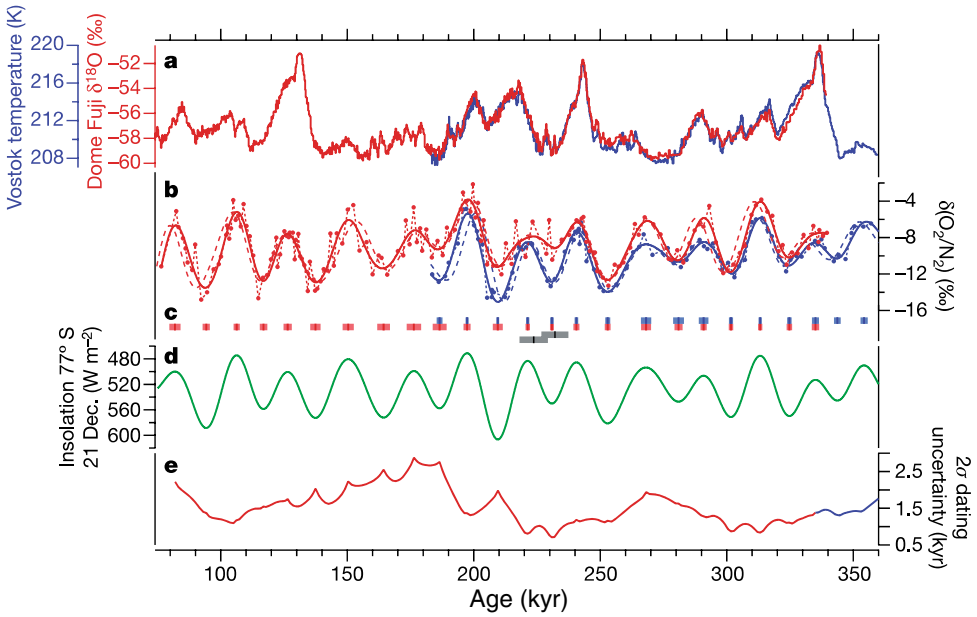

Fig. 9.9 **a** Isotopic composition of the ice and temperature at Vostok and Dome Fuji. **b** O_2/N_2 ratio measured in the air bubbles at Dome Fuji and Vostok. The dots are the raw data; the thick lines represent the filtered data. **c** Age markers deduced from the alignment with local insolation, with 2σ error bars. **d** Insolation at the summer solstice at 77° S used as an alignment target. **e** 2σ uncertainty of the O_2/N_2 dating. Adapted from Kawamura et al. (2007)

summer solstice. However, for this second indicator, it is important to correct for variations in the altitude at which the bubbles formed, as this will have an impact on atmospheric pressure and thus the air content of these bubbles.

Although the specific physical link between these indicators and insolation is still subject to debate and research, we can make two observations. Firstly, no signal with a 100 000 year periodicity is present in the O_2/N_2 record, so that the O_2/N_2 proxy does not seem to be dependent on climate. Secondly, although these indicators are measured in the gas bubbles, they are caused by modifications in the structure of the snow at the surface, and therefore provide a dating of the ice (and not of the bubbles!). This avoids uncertainty associated with Δage.

Flow Modeling

The ice has an enormous advantage over other archives in that it can be dated using physical models that take the variations in the rate of accumulation of snow and the flow of ice into account. The age in the ice core at an altitude of z can be written as:

$$\chi^{(z)} = \int \frac{d(z')}{T(z')a(z')} dz' \qquad (9.3)$$

where χ is the age of ice, d is the relative density of ice (compared with pure ice), a is the initial accumulation of snow (expressed in cm equivalent to pure ice per year, denoted as cm-i.e./year) and T is the thinning function, i.e. the thickness of an annual layer relative to its initial thickness at the time it fell. d can be measured from the ice core. The parameter a is generally calculated from indicators measured in the ice core, while the parameter T is obtained from a flow model. These two steps are detailed below.

Evaluation of Accumulation on the Surface

For the top few hundreds of meters, the thinning of the layers of snow and ice is minimal (T close to 1) and well-assessed by modelling. So, accumulation at the surface may be determined from well-dated horizons such as layers of volcanic ash (described in Section "Volcanic Horizons") using the formula (9.3). Below this depth, the isotopic composition of the ice (D/H or $^{18}O/^{16}O$) is generally used. As for the surface temperature, the field measurements in Antarctica and Greenland show a good correlation between isotopic composition and the surface accumulation of snow. In a review of measurements in Antarctica, Masson-Delmotte et al. (2008) derived a relationship as follows:

$$a = a_0 \exp(\beta(\delta D - \delta D_0)) \qquad (9.4)$$

where a and δD are respectively, a reference accumulation and a reference isotopic composition, and where $\beta = 0.0152$. This relationship is derived from the saturated vapor pressure of the ice and can be calculated from a simple model of precipitations of an air mass. Note, however, that it does not take into account the phenomenon of re-deposition of the snow by the wind, which modifies the accumulation without altering the isotopic composition of the snow. On the other hand, when we extrapolate this relationship to temporal variations in accumulation, it is important to consider the temperature variations and isotopic composition at the

source of the air masses which also alter the isotopic composition of the ice (Parrenin et al. 2007b).

Ice Flow Models

Ice has a solid exhibiting viscoplastic behavior where the relationship between stress and strain can be determined experimentally and theoretically. It is thus possible to simulate the trajectory followed by a particle of ice within the glacier over time in order to establish a chronology. Modeling of behavior of ice within an ice sheet requires not only a good knowledge of the viscoplastic properties of the material, but of the conditions at the boundaries of the cap. These boundary conditions are: (1) the temperature and surface accumulation over time; (2) basal conditions, such as the geothermal flow and the rate of friction on the bedrock; (3) the lateral conditions for the area under consideration, since local models are used for dating purposes. These lateral conditions generally result from global simulations of the polar cap over time (Ritz et al. 2001). In this way, the thinning function adapted to the ice core drilling site is obtained.

Below is a qualitative description of how this function varies. For a stationary dome, the thinning function can be written:

$$T = \frac{1 - \frac{m}{a}}{\omega + \frac{m}{a}} \tag{9.5}$$

with $\mu = m/a$ the ratio of basal fusion to surface accumulation and with ω the standard vertical profile of horizontal flow (see Parrenin et al. 2007b, for details). ω varies almost linearly from 0 at the ice base interface to 1 at the surface, because the deformation is concentrated at the base of glacier. For certain domes, the Raymond effect causes more deformation at the top of the ice and therefore a less linear ω profile.

In a non-stationary case, variations in the thickness of the ice (related to climatic variations) cause bumps in the thinning function (Fig. 9.10). Moreover, for ice core drilled along the flow line, like Vostok, the ice comes from upstream and more complex deformation effects exist. The parameter that most influences the thinning function is the thickness of ice at the place of origin of the ice: if this thickness is large compared to the thickness at the drill site, then the column of ice has become compressed overall, resulting in a strong thinning (that is, a low thinning function). And reciprocally.

The Limitations of Modeling

Unfortunately, dating using models becomes increasingly inaccurate as it approaches the base of the ice cap, for various reasons. Firstly, the mechanical properties of the ice are not perfectly understood. They depend not only on pressure and temperature conditions, but also on the size and orientation of the crystals that make up the ice. Secondly, the conditions at the base of the bedrock cannot be measured directly in situ. Finally, the lateral conditions throughout the past, the outcome of a large-scale model, may also be tainted by a significant error. These lateral conditions determine the position of the domes and dividing lines in the domain, and therefore the direction of the ice particles.

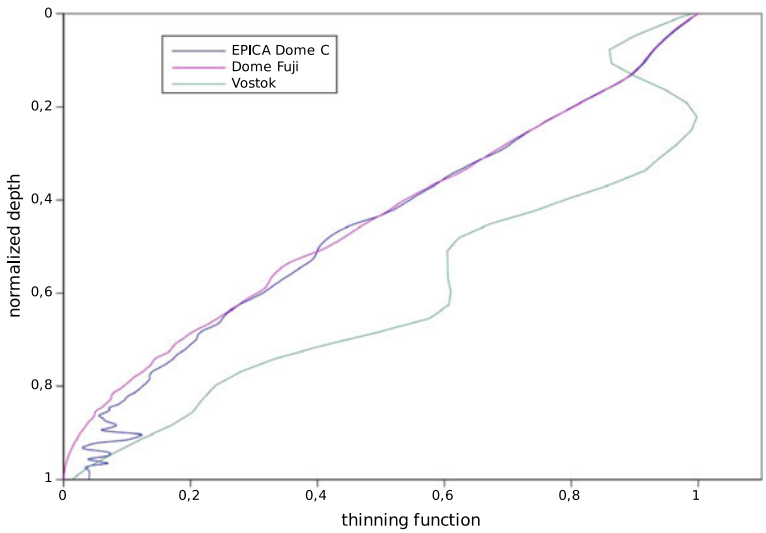

Fig. 9.10 Thinning functions for ice cores from Dome C (Parrenin et al. 2007b), Dome Fuji (Parrenin et al. 2007a) and Vostok (Parrenin et al. 2004)

The Inverse Method: A Collective Approach

All of absolute dating methods described in the preceding sections have advantages and disadvantages. The counting of layers and flow modeling are precise methods in terms of the duration of events (at least for relatively recent periods) because they are based on an assessment of the thickness of the annual layers. However, errors accumulate and inaccuracy in the absolute age increases rapidly with depth.

Orbital tuning is generally applicable over the entire length of a core, as long as the stratigraphy is maintained. In addition, accuracy does not diminish with depth, and so far, this is the most accurate method for dating the lower part of polar cores. Unfortunately, this method is not very accurate in terms of duration of events, and the accuracy in terms of absolute ages is limited by the assumption that there is a constant phase difference between the record being studied and the insolation (and obviously does not allow the variations in this phase to be reconstructed). Research into indicators of local insolation paves the way for a significant improvement in methods of orbital alignment, with a possibility of uncertainties below 1000 years. However, we still lack sufficient distance to assess the real accuracy of these methods. In addition, other methods will always be more accurate for very recent times.

Volcanic eruptions provide important dated horizons. This is particularly true for the last millennium, but beyond this, only a few have an absolute age that is sufficiently precise. Comparison with other dated records is particularly useful for the dating of Dansgaard-Oeschger events, which can be precisely localized using variations in the isotopic composition of ice (in Greenland cores only), or variations in the methane content in air bubbles. Most of these events have been dated accurately for the last ice age, especially from speleothems and the U/Th method (Chap. 6). Other studies are underway to improve this accuracy and to study previous ice ages. In any case, these dated horizons do not provide continuous dating and are mainly relevant to recent periods.

As these different sources of chronological information are complementary, it is clear that to obtain an optimum dating from the ice records, it is essential to combine them. This is what glaciologists have attempted to do with Antarctica ice cores. Initially, the poorly known parameters in flow models (such as melting and sliding at the base of the glacier) were adjusted by trial and error to obtain a good agreement with dated horizons. But this approach quickly becomes difficult when there are several free parameters and when the different error bars for the dated horizons must be taken into account.

In the early 2000s, an inverse method to formalize and systematize this optimization of dating in a probabilistic framework was developed (Parrenin et al. 2001). In the context of dated horizons with a certain error bar, it facilitates the determination of the probability density called *'a posteriori'* both for the uncertain parameters in the flow models and for the final dating. Concretely, this probability density not only provides an optimum dating, but also a confidence interval. This probabilistic method, based on the Metropolis-Hastings algorithm, was applied to the Vostok (Parrenin et al. 2004), Dome C (EDC3 dating, Parrenin et al 2007a, b) and Dome Fuji (Parrenin et al. 2007b) ice cores.

This inverse approach, however, has several limitations. Firstly, it only takes into account the errors related to the lack of understanding of poorly known parameters. In other words, the model is considered perfect once an optimal estimation of these parameters is achieved. This is the same as saying that the model is able to describe all the relevant flow mechanisms and is therefore, in agreement with all sets of markers whose age errors are correctly estimated. In reality, however, many physical phenomena influencing flow are not taken into account in the model, either because they are not properly understood, or because the level of complexity necessary to describe them is incompatible with inverse modeling (direct model is too costly in computing time with too many parameters to inverse). This limitation of the models appears clearly at the base of the EDC core where the model, even after optimization of its parameters, is unable to reproduce the age markers obtained by orbital alignment (Dreyfus et al. 2007). A second limitation of this inverse method is that it can be applied to only one core at a time, and the optimal dating obtained is different for each core, making it difficult to compare climate and environmental signals. In reality, these cores can be synchronized more accurately in the ice phase (for example, by volcanic horizons), as well as in the gas phase (for example, CH_4 and $\delta^{18}O_{atm}$).

As a result, a new method of optimization was developed (Lemieux-Dudon et al. 2010; Parrenin et al. 2015). This considers the information gleaned from modeling to be weakly constrained (the model is not deemed perfect) and applies to several cores simultaneously, taking into account the stratigraphic links between these cores, both in the ice and in the air. This method can thus provide an optimum dating common to the different cores from Antarctica and Greenland.

Conclusion

The dating of glacial archives is a complex problem which, in the absence of the radioactive methods, is based on several complementary techniques. For the Holocene and in high accumulation sites, dating by counting layers is

accurate to about 1%. This dating was confirmed by comparison with dendrochronology using beryllium-10, and with volcanic horizons dated by carbon-14. The last millennium can also be dated to within a few years through identification of known volcanic eruptions. For the rest of the Holocene, synchronization with the dendrochronological scale using beryllium-10 gives us dating accuracy to within a few decades.

For the last glacial period, the accuracy of counted time scales decreases to about 5% up to 60 ka. This dating provides ages for the Dansgaard-Oeschger events which are confirmed by uranium/thorium dating of speleothems in Europe and Asia. It is also compatible with some volcanic horizons dated by carbon-14 and argon/argon. The main methods of dating for the last 60 ka therefore now seem to be in agreement to within a few hundred years rather than a few thousand years as was the case until recently.

Further back than the last glacial period, counting of layers is no longer possible, and the chronologies are mainly based on speleothems, volcanic horizons and orbital alignment. Orbital tuning has a precision of about 5 ka. Local insolation indicators (O_2/N_2 ratio, air concentrations) could lead to an improved accuracy of 1–2 ka, but this must be confirmed by independent methods.

References

Arnaud, L., Barnola, J.-M., & Duval, P. (2000). Physical modeling of the densification of snow/firn and ice in the upper part of polar ice sheets. In T. Hondoh (Ed.), *Physics of Ice CoreRecords* (pp. 285–305). Japan.: Hokkaido University Press, Sapporo.

Beer, J., Vonmoos, M., & Muscheler, R. (2006). Solar variability over the past several millennia. *Space Science Reviews, 125*(1), 67–79.

Bender, M. L. (2002). Orbital tuning chronology for the Vostok climate record supported by trapped gas composition. *Science Letters, 204,* 275–289.

Burns, S. J., Fleitmann, D., Matter, A., Kramers, J., & Al-Subbary, A. (2003). Indian Ocean climate and absolute chronology over dansgaard/oeschger events 9–13. *Science*, *301,* 1365–1367.

Dreyfus, G. B., Parrenin, F., Lemieux-Dudon, B., Durand, G., Masson-Delmotte, V., Jouzel, J., et al. (2007). Anomalous flow below 2700 m in the EPICA Dome C ice core detected using δ18O of atmospheric oxygen measurements. *Climate of the Past Discussions*, *3*(2), 341–353. https://doi.org/10.5194/cp-3-341-2007.

Guillou, H., Singer, B. S., Laj, C., Kissel, C., Scaillet, S., & Jicha, B. R. (2004). On the age of the Laschamp geomagnetic excursion. *Earth and Planetary Science Letters, 227,* 331–343.

Kawamura, K., Parrenin, F., Uemura, R., Vimeux, F., Severinghaus, J. P., Matsumoto, K., et al. (2007). Northern hemisphere forcing of climatic cycles over the past 360,000 years implied by absolute dating of antarctic ice cores. *Nature, 448,* 912–917.

Landais, A., Barnola, J., Kawamura, K., Caillon, N., Delmotte, M., Ommen, T. V., et al. (2006). Firn-Air $\delta^{15}N$ in modern polar sites and glacial-interglacial ice: A model-data mismatch during glacial periods in antarctica? *Quaternary Science Reviews, 25*(1–2), 49–62.

Laskar, J., Robutel, P., Joutel, F., Gastineau, M., Correia, A. C. M., & Levrard, B. (2004). A Long-term numerical solution for the insolation quantities of the earth. *Astronomy & Astrophysics, 428,* 261–285.

Lemieux-Dudon, B., Blayo, Petit, J. R. E., Waelbroeck, C., Svensson, A., et al. (2010). Consistent dating for Antarctica and Greenland ice cores', *Quaternary Science Reviews,* 29(1–2), 8–20.

Masson-Delmotte, V., Hou, S., Ekaykin, A., Jouzel, J., Aristarain, A., Bernardo, R. T., et al. (2008). A review of Antarctic surface snow isotopic composition: Observations, atmospheric circulation, and isotopic modeling. *Journal of Climate*, *21*(13), 3359–3387.

Narcisi, B., Petit, J.-R. & Tiepolo, M. (2006). A volcanic marker (92 ka) for dating deep east Antarctic ice cores. *Quaternary Science Reviews, 25*, 2682–2687.

Parrenin, F., Barker, S., Blunier, T., Chappellaz, J., Jouzel, J., Landais, A., et al. (2012). On the gas-ice depth difference (Δdepth) along the EPICA Dome C ice core. *Climate of the Past, 8*(4), 1239–1255 https://doi.org/10.5194/cp-8-1239-2012.

Parrenin, F., Barnola, J.-M., Beer, J., Blunier, T., Castellano, E., Chappellaz, J., et al. (2007a). The EDC3 chronology for the EPICA dome C ice core. *Climate of the Past, 3,* 485–497.

Parrenin, F., Bazin, L., Capron, E., Landais, A., Lemieux-Dudon, B., & Masson-Delmotte, V. (2015). IceChrono1: A probabilistic model to compute a common and optimal chronology for several ice cores. *Geoscientific Model Development, 8*(5), 1473–1492. https://doi.org/10.5194/gmd-8-1473-2015.

Parrenin, F., Dreyfus, G., Durand, G., Fujita, S., Gagliardini, O., Gillet, F., et al. (2007b). Ice flow modelling at EPICA dome C and dome Fuji, East Antarctica. *Climate of the Past, 3,* 243–259.

Parrenin, F., Rémy, F., Ritz, C., Siegert, M., & Jouzel, J. (2004). New modelling of the Vostok ice flow line and implication for the glaciological chronology of the Vostok ice core. *Journal Geophysical Research, 109,* D20102.

Raisbeck, G. M., Yiou, F., Cattani, O., & Jouzel, J. (2006). ^{10}Be Evidence for the Matuyama-Brunhes geomagnetic reversal in the EPICA dome C ice core. *Nature, 444*(7115), 82–84.

Raisbeck, G. M., Yiou, F., Jouzel, J., & Stocker, T. F. (2007). Direct north-south synchronization of abrupt climate change record in ice cores using beryllium 10. *Climate of the Past, 3*(3), 541–547.

Rasmussen, S. O., Andersen, K. K., Svensson, A. M., Steffensen, J. P., Vinther, B. M., Clausen, H. B., et al. (2006). A new greenland ice core chronology for the last glacial termination. *Journal Geophysical Research, 111,* D06102.

Raynaud, D., Lipenkov, V., Lemieux-Dudon, B., Duval, P., Loutre, M.-F. & Lhomme, N. (2007). The local insolation signature of air content in Antarctic ice. A newstep toward an absolute dating of ice records. *Earth and Planetary Science Letters*, *261*(3–4), 337–349.

Ritz, C., Rommelaere, V., & Dumas, C. (2001). Modeling the evolution of antarctic ice sheet over the last 420,000 years: Implications for altitude changes in the Vostok Region. *Journal Geophysical Research, 106*(D23), 31943–31964.

Ruth, U., Barnola, J.-M., Beer, J., Bigler, M., Blunier, T., et al. 'EDML1: A chronology for the EDML ice core, Antarctica, over the last 150 000 Years. *Climate of the Past, 3*, 475–484 (2007).

Salamatin, A. N., Lipenkov, V. Y., Barnola, J. M., Hori, A., Duval, P., & Hondoh, T. (2009). Snow-Firn Densification in Polar Ice Sheets. In T. Hondoh (Ed.), *Physics of Ice Core Records-2*. Sapporo: Hokkaido University Press.

Schwander, J., Sowers, T., Barnola, J.-M., Blunier, T., Fuchs, A., & Malaizé, B. (1997). Age scale of the air in the summit ice: Implication for the glacial-interglacial temperature change. *Journal Geophysical Research, 102,* 19483–19493.

Severi, M., Castellano, E., Morganti, A., Udisti, R., Ruth, U., Fischer, H., et al. (2007). Synchronisation of the EDML1 and EDC3 timescales for the Last 52 Kyr by volcanic signature matching. *Climate of the Past, 3,* 367–374.

Severinghaus, J., Sowers, T., Brook, E., Alley, R., & Bender, M. (1998). Timing of abrupt climate change at the end of the Younger Dryas interval from thermally fractionated gases in polar ice. *Nature, 391,* 141–146.

Sigl, M., Fudge, T. J., Winstrup, M., Cole-Dai, J., Ferris, D., McConnell, J. R., et al. (2016). The WAIS Divide deep ice core WD2014 chronology—Part 2: Annual-layer counting (0–31 ka BP). *Climate of the Past, 12*(3), 769–786. https://doi.org/10.5194/cp-12-769-2016.

Sowers, T. A., Bender, M., Raynaud, D. & Korotkevich, Y. L. (1992). 'The $\delta^{15}N$ of O_2 in air trapped in Polar ice: A tracer of gas transport in the firn and a possible constraint on ice age-gas age differences. *Journal of Geophysical Research, 97*(15), 15683–15697.

Spötl, C., Mangini, A., & Richard, D. A. (2006). Chronology and Paleoenvironment of marine isotope stage 3 from two high-elevation speleothems, Austrian Alps. *Quaternary Science Reviews*, *25*(9–10), 1127–1136.

Svensson, A., Andersen, K. K., Bigler, M., Clausen, H. B., Dahl-Jensen, D., Davies, S. M., et al. (2008). A 60 000 year greenland stratigraphic ice core chronology. *Climate of the Past, 4* (1), 47–57.

Wang, X., Auler, A. S., Edwards, L., Cheng, H., Cristalli, P. S., Smart, P. L., et al. (2004). Wet periods in Northeastern Brazil over the past 210 Kyr linked to distant climate anomalies. *Nature, 432,* 740–743.

Wang, Y. J., Cheng, H., Edwards, R. L., An, Z. S., Wu, J. Y., Shen, C. C., & Dorale, J. A. (2001). A high-resolution absolute-dated late pleistocene monsoon record from Hulu Cave, China. *Science*, *294* (5550), 2345–2348.

Zielinski, G. A., Mayewski, P. A., Meeker, L. D., Whitlow, S., Twickler, M. S., Morrison, M., et al. (1994). Record of volcanism since 7000 B.C. from the GISP2 greenland ice core and implications for the volcano-climate system. *Science, 264*(5161), 948–952.

Parrenin, F., Jouzel, J., Waelbroeck, C., Ritz, C. and Barnola, J.-M (2001) Dating the Vostok ice core by an inverse method. *Journal of Geophysical Research: Atmospheres 106*, (D23), 31831–837851.

Reconstructing the Physics and Circulation of the Atmosphere

10

Valérie Masson-Delmotte and Joël Guiot

The variability and evolution of the physical parameters of atmospheric circulation are currently monitored in real time and on a global scale thanks to a dense network of weather stations (over 13,000 measurement sites on land and sea), and to satellite observations of the Earth. This 'instrumental' period, during which the physical parameters of the atmosphere were directly monitored, began in the mid seventeenth century following the invention and use of thermometers, barometers, rain gauges etc. However, standardization of measurement tools and their wide-scale use took a long time and was due to a continuous effort by the meteorological services. The outputs of ancient instruments from before 1950 must be homogenized to modern observation standards, and gaps exist in regional temperature information due to changes in the spatial monitoring network. The oldest meteorological series of data available are in Europe, where temperature series for the center of England start in 1659. Intensive work was carried out on the weather records of the Alpine region, providing access to accurate measurements, from 1780, of average monthly temperatures and cumulative monthly precipitations.

Work is underway to extend the use of these historical measurements to study monthly variability in temperature and precipitation, and to assess other parameters (pressure, sunshine etc.). Use of these old measurements involves working on documents of the time, computerizing the data, and statistical analysis of regional databases. With the exception of Europe, where instrumented measurements were conducted particularly early, weather information is generally only available from 1860, except for the most inaccessible areas, such as Antarctica, where systematic meteorological monitoring did not start until the International Geophysical Year 1957–1958. The 'instrumental period' is therefore very short compared to the time frame of the climate system and does not permit an understanding of the natural climate variability on a global scale for the period prior to when human activities affected the composition of the atmosphere.

In order to characterize natural climate evolution and to place the climate change of recent decades within a broader context, continental paleoclimatology has established methods of quantifying ancient climates by taking advantage of a large number of natural archives, in soils, lakes, vegetation, continental and polar ice. These archives have allowed qualitative or quantitative indices of the main parameters describing climate to be defined. These indices are often referred to as proxies. Below, we briefly review all the climate parameters reconstructed from these continental archives.

The atmospheric parameters most commonly determined from continental paleoclimate archives are surface air temperature (or surface lake water temperature) and parameters related to soil hydrology (e.g. precipitation, drought indices, etc.). In some cases, these parameters can be estimated over a season, when a resolution of less than a year can be detected in the archives (tree rings, ice cores in sites with a high level of snow accumulation) or when the archive is particularly sensitive to seasonal effects (temperature of the coldest month, temperature of the growing season for vegetation, etc.). Most continental proxies do not directly record the amount of precipitation, but reflect the local water balance (precipitation minus land-based evaporation, runoff into lakes, net accumulation of snow on the glaciers at the drilling sites). Quantification of these climate parameters from the records is often made difficult by the discontinuous nature of geological recording, for example, the process of sedimentation in lakes. Some records, such as tree rings, function as threshold systems and identify an atmospheric signal once the threshold is reached (low temperature, dry

V. Masson-Delmotte (✉)
Laboratoire des Sciences du Climat et de l'Environnement, LSCE/IPSL, CEA-CNRS-UVSQ, Université Paris-Saclay, 91190 Gif-sur-Yvette, France
e-mail: valerie.masson@lsce.ipsl.fr

J. Guiot
Centre for Research and Teaching in Environmental Geoscience CEREGE, Aix-Marseille University, CNRS, IRD, INRAE, Collège de France, BP 80 13545 Aix-en-Provence Cedex 04, France

G. Ramstein et al. (eds.), *Paleoclimatology*, Frontiers in Earth Sciences,
https://doi.org/10.1007/978-3-030-24982-3_10

season). Moreover, many proxies are not sensitive to a single atmospheric variable but to the combination of effects related to temperature and hydrology. The combined use of multiple markers within a single medium or multiple archives from the same site allows these effects to be separated out. Finally, comparison between proxies, paleoclimate reconstructions, modeling of climate and proxies all improve our understanding of how climate dynamics and proxies operate.

The dynamics of the atmosphere can also be estimated from the continental paleoclimate records. During the instrumental period, it is possible to determine how certain modes of atmospheric circulation such as the El Niño--Southern Oscillation (ENSO), the North Atlantic Oscillation (NAO), the Southern Annular Mode (SAM) or the Pacific-North American oscillation (PNA) modulate the spatial response of proxies, just as they affect the spatial distribution of temperature and rainfall. Provided that the spatial distribution of proxy records is sufficient in key areas, and depending on the stability of these tele-connections through time, this fingerprint can then be used to estimate past inter-annual variations in pressure indices characteristic of patterns of atmospheric circulation in recent centuries (PNA, NAO, ENSO, SAM).

Over large time scales, loess deposits and dunes reflect the prevailing wind direction. Similarly, concentrations of marine and continental aerosols, the size distribution of continental dust particles in polar ice, reflect changes in the aridity of the regions of origin as well as changes in the efficiency of transport of aerosols in the atmosphere. However, quantitative estimates of the intensity of surface winds remain a challenge. Past changes in other atmospheric parameters such as cloudiness are difficult to determine from proxy records in natural archives.

Continental paleoclimatology can also help to characterize the frequency and intensity of 'extreme' events. The intensity and amplitude of past droughts have been estimated using dendrochronological databases in North America and Europe. Sedimentary and geochemical markers from lake sediments are used to determine the intensity and occurrence of flooding by the great rivers. High-resolution analysis of lagoon sediments and the isotopic composition of tree rings or speleothems are currently being used in an attempt to characterize past variations in the activity (trajectories, intensity, frequency) of tropical cyclones and extratropical storms.

We have briefly presented the atmospheric variables that can be estimated from continental paleoclimate records. In the following chapters, we will explain the reconstruction methods used; the assumptions upon which they are based; their limitations and uncertainties; and finally, we will present several specific examples reflecting the diversity of continental archives (lakes, vegetation, ice) whose dating techniques were described in Part II. We will present some archives and some proxies particularly well suited to each of the interfaces under consideration. We have considered high latitudes and low latitudes separately. Several archives (lacustrine cores, speleothems) and proxies (pollen, diatoms) are present in both temperate and tropical regions, but their interpretation is specific to the particular geographical area.

In the high latitudes of both hemispheres, polar ice is of paramount importance in paleoclimatology because it records both climate forcings and some local and global climatic variations. Sedimentary archives (from lakes and bogs) with their pollen records have long been studied in paleoclimatology and cover almost all of the continents. They were initially understood to mostly reflect a local signal. However, the comparison with ice and marine records revealed the broad geographical spread of many events known to palynologists, such as the Younger Dryas cold episode which lasted for close to a millennium and was felt throughout the Atlantic area of the northern hemisphere. The loess covers a significant area of the continents; their sequences are excellent indicators of atmospheric circulation. On a shorter timescale, some archives provide information with annual or near annual resolution. Among these, tree rings provide a wealth of information on temperate regions. They are supplemented by multi-centennial archives from historical written documents, such as wine harvesting dates, in Europe, or cherry blossom dates, in Japan.

At low latitudes, sedimentological tracers collected in tropical lakes, complemented by biological proxies, such as the abundance of diatoms or pollen, contribute to a better understanding of the functioning of the major inter-tropical climate systems and give an insight into sometimes discontinuous records. Diatoms are good indicators of the characteristics of lake water and, complemented by adequate hydrological modeling, they allow an assessment of water resources in watersheds. At high altitudes, tropical glaciers are very sensitive to climate variations in the long and medium term.

Cave records, for instance from speleothems, offer well-dated, albeit discontinuous, records particularly sensitive to changes in the hydroclimate and vegetation cover above the caves, sometimes with very high temporal resolution.

Interpretation of Records, Limitations and Uncertainties

Paleoclimatology draws its information mainly from two types of approaches with their advantages and limitations. The first approach is the most basic and consists of using simple equations to interpret a climate signal from a univariate series. This is the preferred approach for geochemistry which often uses scaling to transform an isotopic signal

into a temperature curve (in the case of polar and tropical glaciers). This approach is also possible with data from historical documents, which, when they do not provide direct climatic information, recount events related to a climate variable (floods, droughts, freezing) that may be standardized semi-quantitatively (Pfister 1980).

Another approach is required for analysis of the living world. The climate signal recorded by microorganisms is complex and is a reaction to a combination of several climatic variables; temperature, salinity, and nutrients in the ocean; temperature and precipitation on land. It is therefore not possible to decode this signal with a simple equation and a multivariate approach is needed to interpret the changes in sets of pollen and diatoms in a continental environment, and of diatoms and foraminifera in a marine setting (Chap. 21). On a smaller timescale, the thickness or density of a tree ring, also influenced by a complex environment, can seldom be interpreted with a simple calibration equation. Several series from the same region need to be used to get a clear climate signal.

Uncertainties on the Temporal Scale

Before discussing the uncertainties and limitations associated with the interpretation of series of proxies, we will review the uncertainties related to their temporal resolution. Figure 10.1 shows the temporal characteristics of climate forcings (internal and external) and the different types of supports of commonly studied proxies. Many forcings and components of the climate system have characteristic times of less than a year, while most proxies have longer characteristic times. In addition, with the uncertainty of dating (see Part II), it is clear that time is an important factor of error in the study of the interactions between climate and proxy.

Among proxies providing a seasonal resolution, tree rings are prominent, but this is at the expense of the robustness of the long term signal. Although it is possible in theory to reach 10,000 years, trees have a much shorter lifespan and the long extended data series are achieved by splicing many short series together. The behavior of trees in the low frequency range is not exclusively due to climate, and this can lead to significant disturbances in reconstructions. Glaciers, another paleoclimate indicator, often have a high resolution for recent periods, due to compaction of the ice, but this reduces progressively as we go back in time. The same goes for marine and lake cores. In some cases, the deposition of their sediments may have an annual resolution (varved sediments), but bioturbation (disturbance of the sediment by small aquatic animals) often prevents this level being achieved in practice.

Historical records are often very accurate, but they have strong differences related to changes in instruments or observers. This provides series with a high resolution but over short periods. This review of climate records shows that no single proxy is perfect, and that without multi-proxy comparison, errors of interpretation could easily occur.

Uncertainties Associated with Geochemical Indicators: The Specific Case of the Isotopic Composition of Precipitations

Over the past forty years, quantitative reconstructions of temperature changes have been obtained from the estimation of past changes in the isotopic composition of precipitation. These are measured in various continental archives which hold ancient precipitation directly (glaciers, ice caps, groundwaters) or indirectly. Indeed, past changes in the isotopic composition of precipitation can leave a fingerprint in the isotopic composition of molecules formed using this water such as the calcite fossil skeletons of lake microorganisms, the calcite of speleothems, or the cellulose of tree rings.

Different stable isotopic forms of the water molecule are present on Earth. Their abundance is expressed by reference to the international standard SMOW (Standard Mean Ocean Water), which has 0.038% of $H_2^{17}O$, 0.310% of HDO, 0.2005% of $H_2^{18}O$ and 99.762% of the principal form, $H_2^{16}O$. The different isotopic molecules are characterized by a different number of neutrons, and therefore, different masses; different vapor saturation pressures; as well as differences in symmetry. During each change of phase (condensation, evaporation), the water molecules undergo isotopic fractionation, which includes processes at equilibrium (exchanges between infinite reservoirs) and kinetic processes: during evaporation on the surface of the ocean or re-evaporation of rain drops during their precipitation, or during the formation of ice crystals in the clouds, the processes are faster than the diffusion time of water molecules and cause kinetic effects associated with the molecular diffusivity of the different isotopic forms.

Since 1958, the International Atomic Energy Agency coordinates a network of observations and a database of the isotopic compositions of precipitations in modern times (Fig. 10.2a). Since the 1960s, the measurements have revealed a close relationship between the isotopic composition of precipitations and air temperature (the 'isotopic thermometer', Fig. 10.2b). This relationship at a local level has been used intensively to quantify the changes in past temperatures.

The use of natural archives to estimate variations in past climates from the isotopic composition of oxygen or of deuterium nevertheless poses many problems which are sources of uncertainty for the quantification of climate reconstructions:

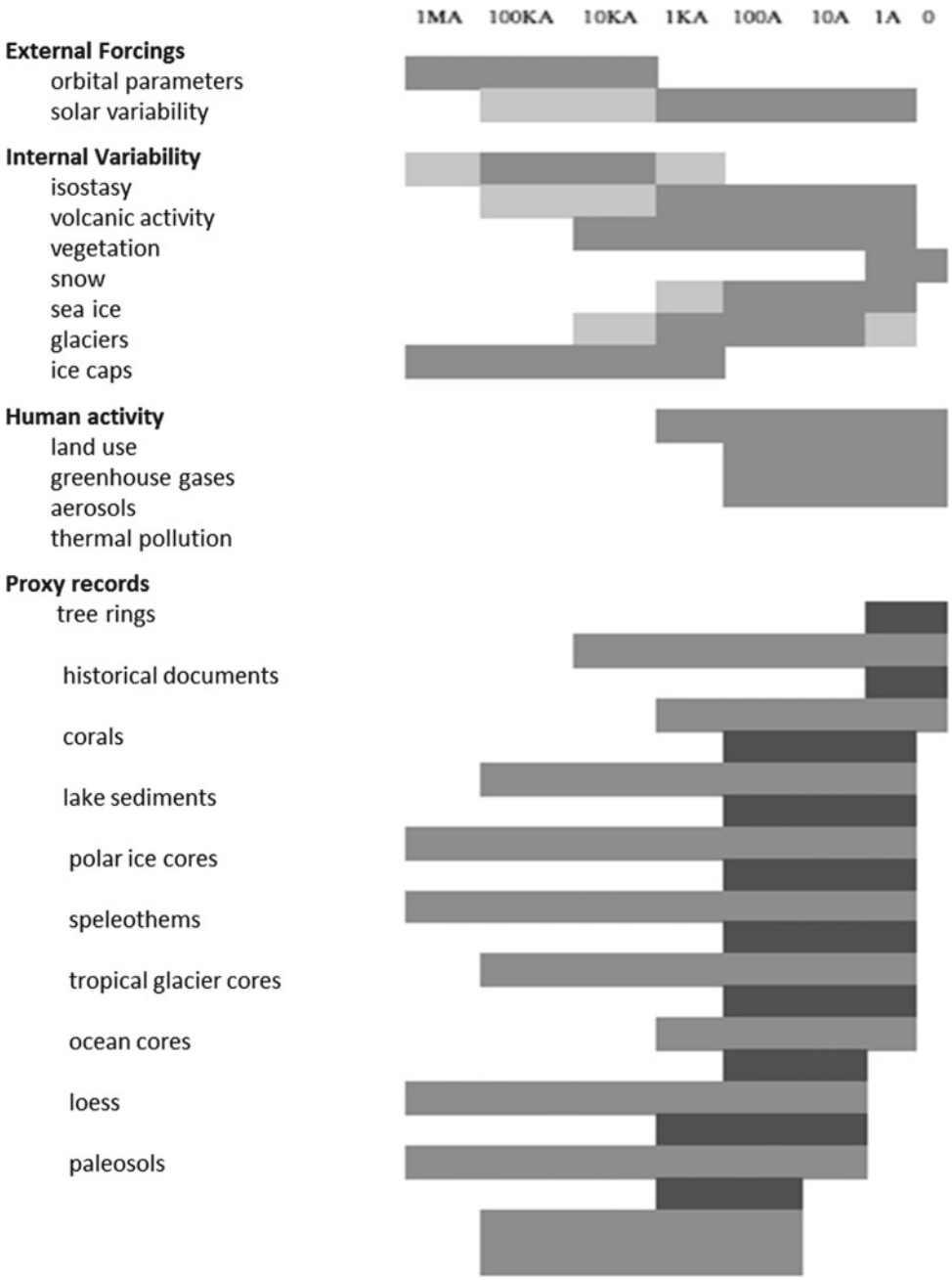

Fig. 10.1 Temporal characteristics of climate components and proxy supports used to reconstruct them. For climate components (above), the dark gray boxes represent the temporal range of the signal; these are extended by light gray boxes when the component becomes minor or occupies only part of the time slot. For proxies, black boxes indicate the maximum scope possible of the resolution, and gray boxes, the maximum range of time covered

- uncertainty in the measurement of the isotopic content; this is generally low, with an impact of around a tenth of degree on estimates of temperatures;
- uncertainty in the processes able to modify the relationship between the isotopic composition of precipitations and the isotopic composition of the archive (ice, calcite, cellulose…). The physicochemical and biological processes controlling the transfer of information between the precipitation and the archive must be understood and quantified in order to assess the uncertainty in the reconstruction of the initial isotopic composition of the precipitation. Each archive has specific biases described in the following sections, which are not necessarily constant over time: these uncertainties can only be estimated through proper understanding and modeling of transfer processes between the water from precipitation and that of the archive (hydro-isotopic models of the functioning of trees, and of lake systems). Recent work has, for instance, shown that the isotopic composition of Greenland or Antarctic surface snow can evolve between snowfall events, possibly due to the interplay of snow metamorphism with changes in surface water vapor

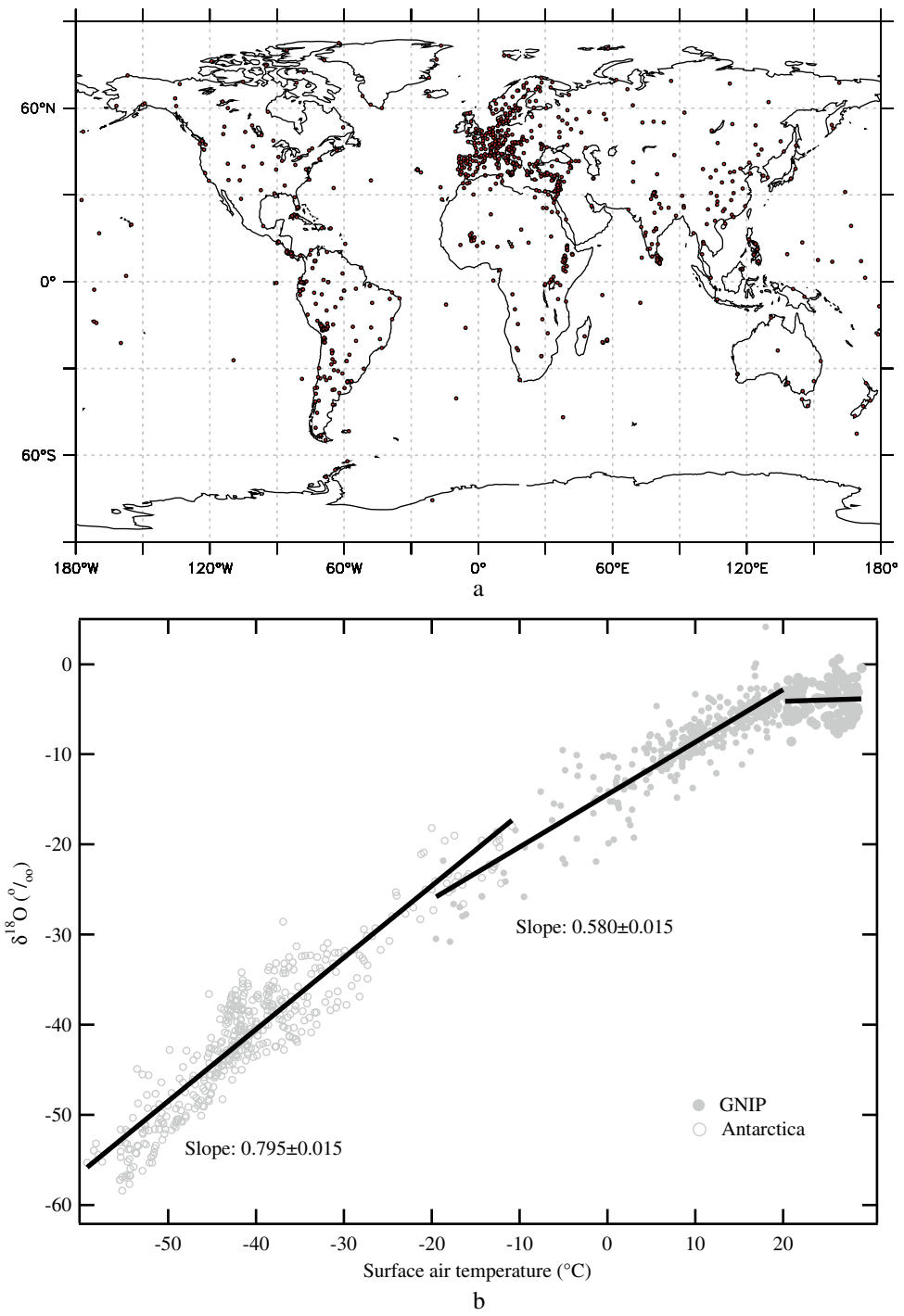

Fig. 10.2 **a** Global network monitoring the isotopic composition of precipitations, stations with several years of measurements (International Atomic Energy Agency, IAEA, www.iaea.org/water). **b** The relationship between the content of ^{18}O in precipitations and the air temperature at ground level, based on network measurements by IAEA (filled-in circles) and from a synthesis of surface snow measurements in Antarctica (open circles). The slope of the isotope-temperature relationship (in ‰ by °C) is presented for Antarctica, for IAEA data with annual temperatures below 20 °C, and IAEA data with annual temperatures above 20 °C

isotopic composition associated with different air mass trajectories. The exact effect of these uncertainties on temperature reconstructions remains difficult to quantify;

- uncertainty concerning the stability over time of the relationships between the isotopic abundances in precipitations and weather factors: even with an almost perfect archive of the isotopic composition of precipitations, how does this translate in terms of climate? Although condensation temperature is the key factor governing the isotopic distillation of an air mass, certain factors like the evaporation conditions, changes in the source of moisture or the vapor trajectory (including convective processes or not), continental recycling (precipitation/evaporation ratio), can affect the isotopic composition of the precipitations. Several critical aspects, such as the seasonality of the precipitations or the relationship between the

temperature of surface air and the temperature of condensation, can also affect the quality of reconstruction of paleoclimates. For Antarctica, for example, the uncertainty in the reconstruction of temperature is estimated to be of the order of 20–30% between glacial and interglacial periods, and recent work has produced evidence of spatio-temporal variations in this relationship over the last decades;

- Finally, it should be noted that in the tropics, it is not the temperature of surface air that determines the isotopic composition of rainfall. Indeed, both spatially and temporally (seasonal and inter-annual), the isotopic composition of rainfall is mainly related to its intensity ('mass effect'), because the intensity of the isotopic distillation depends on atmospheric convective activity, irrespective of the air temperature at the surface. The interpretation of isotopic signals of tropical glaciers is therefore fundamentally different from that of polar ice. Note that at time scales greater than a decade, it is still possible that tropical sea surface temperatures have a leading role on tropical precipitation isotopic composition through their impacts on atmospheric dynamics and convective activity (see Chap. 20).

Assessing the stability of the relationships between the isotopes of precipitation and meteorological parameters under different climate conditions requires the exploration of the processes associated with the three-dimensional atmospheric circulation and water cycle. This can be achieved using general or regional atmospheric circulation models implemented with the representation of the different isotopic forms of the water molecule and the associated fractionation processes. These modeling tools have been successfully used to explore the processes affecting the isotope-temperature relationship at glacial-interglacial scales. Current challenges are related to the ability to perform long (multi-centennial or longer) simulations using coupled ocean-atmosphere models equipped with water stable isotopes to quantify the climatic drivers of precipitation isotopic composition in different regions and over different time scales (seasonal, inter-annual, decennial, centennial etc.). Recently, new understanding has emerged from in situ and remote sensing monitoring of water vapor isotopic composition, which provides more continuous insights than the sampling of precipitation. These data are used to better understand the climatic drivers of water vapor isotopic composition, at the scale of weather events, but also to benchmark the ability of atmospheric models to correctly simulate the origin of atmospheric moisture.

Uncertainties Associated with Biological Indicators

The commonly used methods to reconstruct climate from biological assemblages are known under the term transfer function (Imbrie and Kipp 1971). Their principle is based on the expression of the relationship between the climate variable and the relative abundances of each taxon considered, as if the climate were dependent on the assemblage. This is an inverse approach, since the reality is that the assemblage depends on climatic conditions. The direct problem is called the response function. A few equations suffice to show the drawback of such an approach. Note X, the assemblage, C, all climate factors combined, D, all non-climatic factors that may also influence X (e.g. soil), and R, the response function of the assemblage to C and X = R(C,D). If climate dominates over non-climatic factors, the relationship can be approximated as follows: $X = R_c(C)$. The transfer function may be obtained by inversion: $\hat{C} = \hat{R}_c^{-1}(X)$. But in general, the number of variables included in the vector C is far fewer than the number of X variables, and in this case, only a least squares method can solve the system of equations by minimizing the deviation between C and its estimation which expresses C as a function of X: $\hat{C} = \hat{T}(X)$ where $\hat{T}$ denotes the transfer function.

The 'transfer function' (TF) approach is based on several assumptions which should be kept in mind:

1. climate conditions are the ultimate cause of any changes observed in the data; human action which often modifies the landscape is assumed to be negligible;
2. the ecological properties of the studied species have not changed between the period of analysis and the present: the relationships between species and climate are constant through time;
3. current observations contain all the information necessary to interpret fossil data: so, it is necessary that the vegetation of the past, for example, survived somewhere in the world and that we have the corresponding information. This third hypothesis, added to the second, may be translated as the principle of uniformitarianism (the present is the key to the past), which is implicit in any paleontological approach.

It is clear that these three assumptions are quite strong. The differences found between the various approaches often stem from the fact that these assumptions are not always entirely verifiable.

The analog method (AM) does not operate by calculating a statistical relationship between climate and assemblages, but it is nevertheless based on the same assumptions, making it subject to the same biases when these assumptions are not met. However, this approach has its own peculiarities, because it is not based on a statistical calibration but on a calculation of similarity. The fossil pollen spectrum (or any other assemblage of fossils) for which we would like to know the climatic conditions is compared to all current spectra, and a measurement of each fit ('distance') is performed (see Chap. 12). The few current spectra with the lowest distance from the fossil one are considered as the best analogs. The reconstructed climatic conditions arise from the climatic conditions corresponding to these analogs, weighted according to the inverse of the distance from each analog to the fossil assemblage.

Figure 10.3 illustrates three marginal cases where the two approaches (transfer function and analog) behave quite differently. In this figure, the horizontal axis represents the climate space (this space has several dimensions but here it is simplified into one). Similarly, the vertical axis represents the space of the assemblages (in reality one axis per taxon). The gray circles represent the current data and the empty circles represent the fossil data. The line represents the transfer function (TF). Once we know the abundance of each taxon, on the horizontal axis, then the ordinate can be found by projection along the line, and the climate conditions thereby deduced (see Example A whose climate is T_A). The three cases are represented by three different letters:

- The fossil assemblage A falls in an area without modern equivalent assemblage, but the TF allows the climate to be easily inferred by T_A even though this value does not exist in the current data. The closest analog of A is A_o whose climate is $C(A_o)$. This shows that the AM is unable to provide a climate different from that which exists in the data.
- The fossil assemblage B also falls in an area without current data. While the TF provides an estimate of T_B completely outside the realm of current data—which may not be realistic, the AM provides the climate $C(B_o)$ that may underestimate the reality, but which has the advantage of being realistic.
- The assemblage C has a very close analog (C_o) which is isolated from the other points. The AM will naturally take climate $C(C_o)$ as an estimate, but the TF will provide an estimate T_c which is very far from reality. The TF therefore follows the dominant gradient of the data and is unable to provide a reliable estimate for rare assemblages.

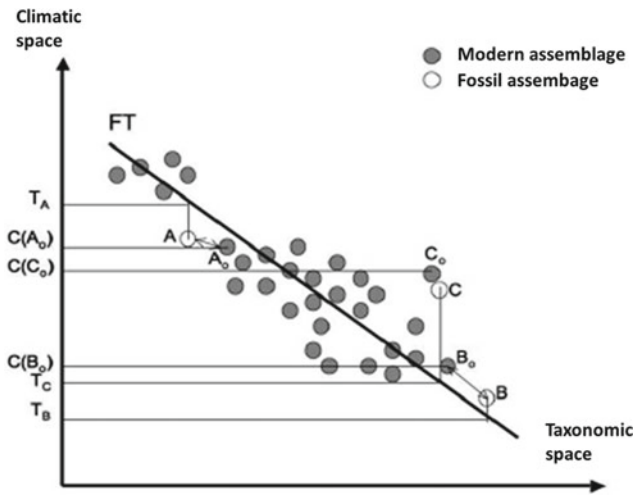

Fig. 10.3 Schematic representation of the main uncertainties related to transfer functions

This illustration shows that there is probably no perfect method and that the most effective way to validate the results (apart from comparing them to reconstructions from other proxies) is to try several methods, such as advocated by Kucera et al. (2005). About ten techniques can be identified in the literature, with the two TF and AM families (Guiot and de Vernal 2007). It is therefore possible to select a few of them and compare the reconstructions. Consistent results are a clear indication of their robustness.

Another problem arises from the fact that the climate variables to be reconstructed are often inter-correlated. If assemblages are available from only either wet and cold climates, or dry, hot climates, it would be impossible to reconstruct wet and warm, or dry and cold climates. If it is possible to collect some assemblages which differ from the dominant gradient, the analysis of point C in Fig. 10.3 shows that the AM was then more efficient than the TF.

A climate reconstruction is calibrated on current data and applied to fossil data. There is often a gap between the two situations. For example, in a continental environment, human activities act as a disruptive factor in the reference sample, and direct application of this to past data may cause biased reconstructions. This problem can only be minimized by selecting current data with limited anthropogenic influence.

Another problem inherent in any calibration is the risk of overestimation. In principle, if the number of parameters to be estimated (here, the weighting coefficients of each of the taxa in the TF) is high compared to the number of reference assemblies, it is possible to adjust a TF so that it passes through almost all the points (in Fig. 10.3, all the points are located on the line). Unfortunately, this line cannot provide a reliable forecast. Following principles of statistics, a good model is based on the lowest number possible of parameters to be estimated. An effective way to limit this problem is to

divide the current database into two parts, to calibrate the TF on the first part, to apply it to the second, called the validation sample, and to deduce the average validation error. If this error remains reasonable, being inevitably greater than the average calibration error, then the TF is considered to be applicable. The same procedure is repeated after exchanging the calibration and the validation subsets. If the two resulting TFs obtained are acceptable, the TF can then be calibrated on the full data set and used for fossil assemblies.

Other statistical techniques exist (bootstrap, jackknife, permutations, etc.), but the basic paradigm is always to verify the quality of the estimates on data independent from those used for the calibration. Another important point is to systematically provide confidence intervals associated with climate reconstructions. This can be achieved for both the TF and the AM. These confidence intervals mean that the tolerance of the biological assemblies for a more or less wide range of climatic conditions can be assessed and the imperfection of the model to adjust all the current reference points can be taken into account.

References

Guiot, J., & de Vernal, A. (2007). Transfer functions: Methods for quantitative paleoceanography based on microfossils. In C. Hillaire-Marcel & A. de Vernal (Eds.), *Developments in marine geology* (Vol. 1, pp. 548–588). Dordrecht: Elsevier.

Imbrie, J., & Kipp, N. G. (1971). A new micropaleontological method for quantitative paleoclimatology: Application to a Late Pleistocene Caribbean core. In K. K. Turekian (Ed.), *The Late Cenozoic glacial ages* (pp. 71–181). USA: Yale University Press.

Kucera, M., Weinelt, M., Kiefer, T., Pflaumann, U., Hayes, A., Weinelt, M., et al. (2005). Reconstruction of sea-surface temperatures from assemblages of planktonic foraminifera: Multi-technique approach based on geographically constrained calibration data sets and its application to glacial atlantic and Pacific Oceans. *Quaternary Science Reviews, 24,* 951–998.

Pfister, C. (1980). The climate of Switzerland in the last 450 years. *Geographica Helvetica* (numéro spécial), 15–20.

Air-Ice Interface: Polar Ice

11

Valérie Masson-Delmotte and Jean Jouzel

The deposition and preservation of layers of snow, year after year, enable many climate and environmental parameters to be recorded in the structure and composition of the ice, as well as in its gas inclusions and impurities. This section is devoted specifically to information on climate variables; the composition of the atmosphere and biogeochemical cycles are discussed in Chap. 1 of this volume and Chap. 1 of Volume 2.

Polar ice contains records of past changes in numerous climate variables, some specific to that particular site, such as temperature and accumulation with others relevant to a larger geographical scale, such as atmospheric circulation and the monsoon regimes. In a unique way, reconstructions of local variables, temperature and accumulation, are drawn from physical processes. Estimates of the accumulation of snow can be derived from the dating of ice (see volume 1, Chap. 9), for example, from the identification of seasonal cycles or reference horizons. Variations in accumulation throughout the ages are also estimated from changes in temperature in the past, through the dependent relationship between the saturation vapor pressure in the air and temperature. This chapter focuses on the various methods used to quantify temperature variations. We will discuss the exploitation of freeze-back layers caused by summer melt in some polar regions, the inversion of temperature profiles measured in the boreholes, the analysis and modeling of the stable isotope composition of the ice, and finally, the analysis of the isotopic composition of nitrogen and argon in the air trapped in the ice.

V. Masson-Delmotte · J. Jouzel (✉)
Laboratoire des Sciences du Climat et de l'Environnement, LSCE/IPSL, CEA-CNRS-UVSQ, Université Paris-Saclay, 91190 Gif-sur-Yvette, France
e-mail: jean.jouzel@lsce.ipsl.fr

G. Ramstein et al. (eds.), *Paleoclimatology*, Frontiers in Earth Sciences,
https://doi.org/10.1007/978-3-030-24982-3_11

Melt Index and Borehole Temperatures

Certain glaciers and ice caps from the Arctic coastal areas form a first collection of records where the structure of the ice allows the changes in summer temperatures to be estimated. Many of these locations are characterized by a summer temperature that can exceed 0 °C. In this case, the surface snow melts, percolates into the deeper colder layers and then refreezes. Identifying the freeze-back layers in the physical structure of the ice allows the indices of summer melting intensity to be reconstructed. This method was used to estimate changes in summer temperatures over time scales of a few centuries, such as in Spitsbergen (Svalbard) or in the Russian Arctic, and during the Holocene, in the Canadian Arctic (Koerner and Fisher 2002). In Greenland and Western Antarctica, some low-altitude sites (Siple Dome, Antarctica peninsula) are also characterized by the regular or occasional occurrence of summer melting. However, the vast majority of deep core samples taken from the Antarctica and Greenland ice are from sites where the temperature remains below 0 °C throughout the year and where there are no freeze-back layers in the ice. In these cases, several methods have been used to estimate past changes in the local temperature.

The diffusion of heat through the structure of the ice causes fluctuations in the vertical temperature profile, which, once drilling operations have been completed, can be measured with an accuracy of one thousandth of a degree in the liquid in the drill holes. The numerical inversion of the temperature profile allows, in principle, the large variations of past surface temperatures to be estimated. However, this problem is poorly constrained and requires general assumptions to be made about the shape of the function sought. There is a broad uncertainty associated with the temperature estimates both in terms of amplitude and chronology. Through this method, estimates of temperature variations over the last century, and even over the last millennia, have been made in some sites with high accumulation (Dahl-Jensen et al. 1999) as well as

estimates of the glacial-interglacial amplitude in the center of Greenland (Dahl-Jensen et al. 1998) and Antarctica (Salamatin et al. 1998).

Stable Isotopes of Water and Temperature

The most commonly used method to reconstruct variations in past temperatures at the center of Antarctica and Greenland is based on analyzing the isotopic composition of the ice. The study of the abundance of the isotopic forms of water molecules in precipitations, initiated in the 1950s (Dansgaard 1953), helped to highlight a spatial relationship between depletion in heavy isotopes and site temperature, a relationship on which the concept of the 'isotopic thermometer' is based. Natural waters, formed mainly of $H_2^{16}O$ molecules (99.7%), also present some rarer stable isotopic forms, including 0.2% of $H_2^{18}O$ and 0.03% of $HD^{16}O$ (D represents deuterium ^2H). The isotopic concentrations are expressed as the deviation in permil in δ notation (δD and $\delta^{18}O$) against an international standard, the V-SMOW. At temperate and polar latitudes, a linear relationship is observed between the isotopic ratios in precipitations today, δD or $\delta^{18}O$, and the temperature of the site. Figure 11.1 illustrates the 'isotopic thermometer' in Antarctica, where more than 900 sites were sampled. The spatial gradients observed are of the order of 6‰/ °C for δD and 0.8‰/ °C for $\delta^{18}O$.

Modeling the isotopic composition of precipitations has been developed using conceptual distillation models (Ciais and Jouzel 1994) and atmospheric general circulation models incorporating the representation of the cycles of the different isotopic forms of the water molecule (Joussaume et al. 1984). These digital tools take into account the effect of different fractionations related to the differences between the saturation vapor pressure (equilibrium effect) and the diffusivity in the air (kinetic effect) of the relevant molecules, and allow the distillation process behind this spatial relationship to be understood (Fig. 11.2).

The reconstruction of past temperatures is based on measuring the isotopic ratio of a thin strip of ice taken along the length of the cores. The isotope-temperature relationship is then applied to this isotopic measurement. The estimate of changes in past temperatures relies on the assumption that the current spatial relationship is applicable to an estimate of the difference in temperature between any two given periods at the drilling site; it assumes that this 'temporal' slope is equal to the spatial slope. For changes at the glacial-interglacial scale, a correction linked to variations in the isotopic composition of the ocean (Jouzel et al. 2003) needs to be taken into account. In the best of cases, the accuracy of measurements by mass spectrometry is ± 0.5‰ for δD and ± 0.05‰ for $\delta^{18}O$. Temporal resolution is very variable. In sites where the accumulation rate is high (more than 10 cm per year), it is possible to find a sub-annual (seasonal) resolution. However, the diffusion of water vapor in the upper layers of the firn quickly brings about a 'smoothing' of the isotopic composition and a loss of information with each snowfall. In low-accumulation sites, the redistribution of surface snow by the winds makes climate reconstruction on a time scale of less than twenty years impossible.

The uncertainty in the estimation of changes in past temperatures is not dependent on the accuracy of the measurements but rather on the different parameters that can influence the isotope-temperature relationship. Through the

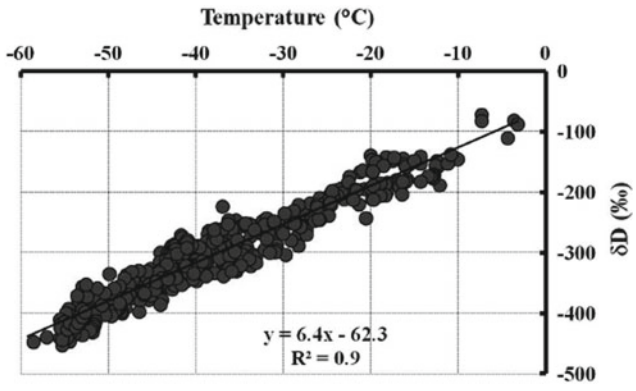

Fig. 11.1 Spatial relationship found between δD of surface snow and average annual temperature for 900 sites in Antarctica where both variables were measured (see Masson-Delmotte et al, 2008)

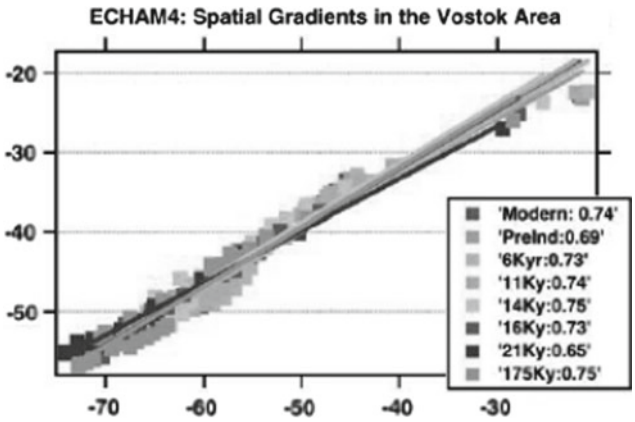

Fig. 11.2 Modeling of the isotopic composition of precipitations ($\delta^{18}O$) in the Vostok region (central plateau of Eastern Antarctica) using the ECHAM atmospheric general circulation model which includes explicit modeling of the cycle of the stable isotopes of water. This model was forced by boundary conditions (sunlight, ice caps, surface sea temperatures, sea ice, and atmospheric composition) estimated for different time intervals (current, pre-industrial, 6, 11, 14, 16, 21, 175 ky BP). The squares represent the results obtained for each simulation for the Vostok region: the temporal slope between $\delta^{18}O$ and temperature can then be estimated, and it can be seen that it is very close to the modern spatial slope

ages, changes in the seasonality of precipitation, in the altitude of condensation, in the trajectory and origin of precipitation, can all have significant effects on the relationship between isotopic composition and local surface temperature. Isotopic distillation models and atmospheric general circulation models, equipped with an explicit representation of stable water isotopes allow the impact of these factors to be estimated through sensitivity studies. A set of simulations conducted using the ECHAM-iso model, (Werner et al. 2001; Jouzel et al. 2007a; Werner et al. 2017) has helped to highlight the stability of the temperature-isotope relationship for the Antarctic central plateau, between the glacial and current climates, and to show that the temporal slope is very similar to the spatial slope. This supports the 'isotopic thermometer' approach for sites on the Antarctic plateau with an accuracy of between −10 and +30%, according to Jouzel et al. (2003).

However, this approach is debatable for climates warmer than the present. Sime et al. (2008) examined a scenario showing an increase in atmospheric concentration of CO_2 with the HadAM3-iso model. This simulation suggests a reduction in the isotope-temperature relationship in the Dome C region of Antarctica, in the context of a warmer global climate. This result remains difficult to apply to measurements from ice cores, because of a lack of analogy between climate changes caused by modifications in the Earth's orbit ('warm' interglacial periods) and those caused by an increase in the greenhouse effect.

Similarly, climate-isotope modeling and the comparison of isotopic analysis with other paleothermometry methods suggest that in central Greenland, the two slopes differ significantly, by up to a factor of 2 (Dahl-Jensen et al. 1998; Masson-Delmotte et al. 2005); the conventional approach underestimates variations in temperature by this amount.

Currently, the oldest isotopic composition profiles go back to 800,000 years in Antarctica on the Dome C site (Jouzel et al. 2007a) (Fig. 11.3); in Greenland, the deepest core, drilled at NorthGRIP, provides about 123,000 years of archives of the isotopic composition of ice (NorthGRIP-community-members 2004).

Cores from Summit, in Greenland, have revealed even older but discontinuous ice segments, identified by comparing the composition of the air to reference series obtained in Antarctica. The study of the isotopic composition of ice has thus allowed reconstructions of changes in local temperatures in the past to be proposed (see Masson-Delmotte et al. 2006), with a high level of consistency between cores from Eastern Antarctica, Vostok, Dome C (Watanabe et al. 2003) and Dome Fuji, where a new core now covers the last 720,000 years (Dome Fuji Ice Core Project Members 2017). The combined study of the different isotopic forms of water, also gave rise to a parameter of the second order, deuterium excess defined as $d = \delta D - 8\delta^{18}O$ (Dansgaard 1964). This parameter is strongly conditioned by the evaporation conditions of atmospheric water vapor masses, and it has been used to estimate the changes in the origin of polar precipitation over time (Jouzel et al. 2007b; Vimeux et al. 2001). Changes in 'source temperatures' calculated in this way, are difficult to compare with the reconstructions of surface temperature of the oceans (Chap. 10), because they

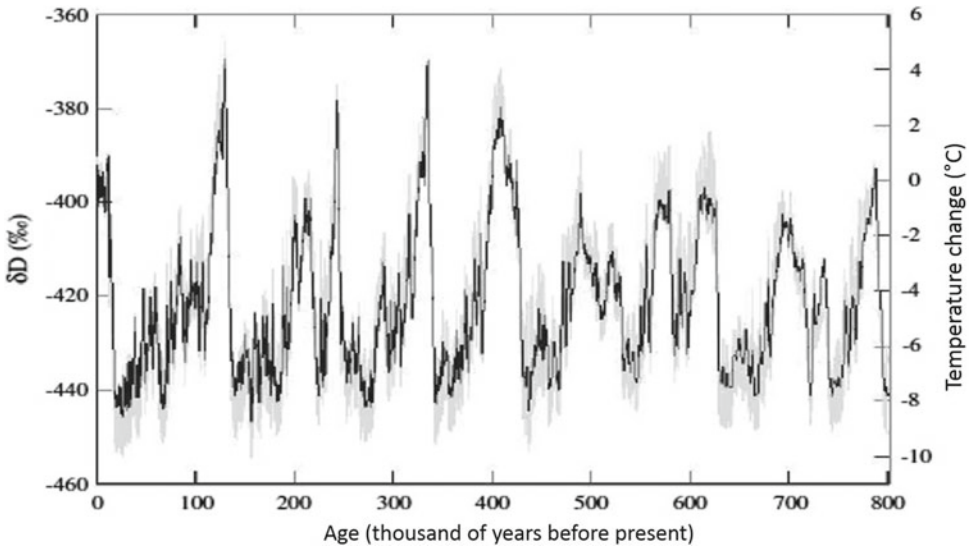

Fig. 11.3 Isotopic recordings of the EPICA Dome C drilling in Antarctica (Jouzel et al. 2007b). Data are shown as a function of time (x-axis, in thousands of years before the present, i.e. before the year 1950). The isotopic composition of the ice samples is indicated by the black line, on the left axis (δD, in ‰). The estimate of the corresponding temperature change (relative to the current temperature, in °C), calculated using the current spatial gradient (see Fig. 11.1), and adjusted for changes in isotopic composition of seawater, is indicated in gray (on the right axis)

correspond to a source of precipitations which may vary geographically over time. In addition, the isotopic composition of the ice may be affected by changes in altitude and run-off, bringing to a drill site on the side of a dome, old ice previously formed in a distant area, effects which need to be taken into consideration (Masson et al. 2000).

Stable Isotopes of Air and Temperature

New methods to quantify abrupt changes of temperature have been implemented, taking advantage of the thermal fractionation of nitrogen or argon (whose isotopic composition is stable in the atmosphere over these time scales) that occurs when air is trapped in the firn (Severinghaus et al. 1998). This approach reveals temperature change markers in the gas phase, and also allows a more detailed characterization of the phase shifts between changes in atmospheric composition (concentrations of greenhouse gases measured in the gas phase) and changes in polar temperature.

This method does not allow an accurate estimate of the temperature changes in the Antarctic, where gravitational fractionation effects dominate, because changes in temperature are slower and less intense. However, it was used to determine the phase shift between Antarctic warming and increasing atmospheric concentrations of carbon dioxide during deglaciations (Caillon et al. 2003).

In Greenland, study of the thermal fractionation of gases was conducted on a series of rapid events, recorded in the ice cores from GISP2, GRIP and NorthGRIP (Capron et al. 2010). Estimates of temperature changes through thermal fractionation of the air have led to an upward revision of the intensity of temperature changes during the warm Dansgaard-Oeschger events, reaching an amplitude of 8 to 16 $\pm$ 3 °C, and have called into question the presumed stability of the cold phases as they appear in the continuous recordings of the stable isotopes of water. The apparent discrepancy between the quantifications from the current spatial relationship between water isotopes and temperature and this alternative paleothermometry method can be explained by significant changes in the seasonality of the deposition of snow in Greenland over the ages, a process highlighted by the climate-isotope models between the Last Glacial Maximum and present times (Krinner 1997; Werner et al. 2001).

Conclusions

It is important to note that a number of methods may be applied to polar ice cores to quantify temperature changes. New avenues are being explored to improve quantifications of temperature change: isotopic measurements at very high resolution in order to quantify isotopic diffusion, a process which depends on the temperature; analysis of oxygen-17 in water to more accurately estimate the evaporation conditions (temperature, relative humidity) at the surface of the ocean; continuous analysis of the isotopic composition of argon, nitrogen and noble gases in order to characterize the thermal and gravitational fractionations of the firn. Much remains to be learned about the spatial and temporal variability of temperatures in Greenland and Antarctica, both over recent centuries and in the ancient climate cycles recorded in the polar ice.

References

Caillon, N., Severinghaus, J. P., Jouzel, J., Barnola, J. M., Kang, J. and Lipenkov, V. Y. (2003). Timing of atmospheric CO_2 and Antarctic temperature changes across termination III. *Science*, *299*, 1 728–1 731.

Capron, E., et al. (2010). Millennial and sub-millennial scale climatic variations recorded in polar ice cores over the last glacial period. *Climate of the Past, 6,* 345–365.

Ciais, P., Jouzel, J. (1994). Deuterium and Oxygen 18 in Precipitation: An isotopic model including mixed cloud processes. *Journal of Geophysics Research*, *99*, 16 793–16 803.

Dahl-Jensen, D., Morgan, V. I., & Elcheikh, A. (1999). Monte carlo inverse modeling of the law dome (Antarctica) temperature profile. *Annals of Glaciology, 29,* 145–150.

Dahl-Jensen, D., Mosegaard, K., Gundestrup, N., Clow, G. D., Johnsen, S. J., Hansen, A. W., et al. (1998). Past temperatures directly from the greenland ice sheet. *Science, 282,* 268–271.

Dansgaard, W. (1953). The abundance of ^{18}O in atmospheric water and water vapour. *Tellus, 5,* 461–469.

Dansgaard, W. (1964). Stable isotopes in precipitation. *Tellus, 16,* 436–468.

Dome Fuji Ice Core Project Members. (2017). State dependence of climatic instability over the past 720,000 years from Antarctic ice cores and and climate modeling. *Science Advances, 3*, e1600446.

Joussaume, S., Jouzel, J., & Sadourny, R. (1984). A general circulation model of water isotope cycles in the atmosphere. *Nature, 311,* 24–29.

Jouzel, J., Vimeux, F., Caillon, N., Delaygue, G., Hoffmann, G., Masson-Delmotte, V., & Parrenin, F. (2003). Magnitude of the isotope-temperature scaling for interpretation of central antarctic ice cores. *Journal of Geophysical Research, 108*, 1029–1046.

Jouzel, J., Masson-Delmotte, V., Cattani, O., Dreyfus, G., Falourd, S., Hoffmann, G., et al. (2007a). Orbital and millennial Antarctic climate variability over the past 800,000 years. *Science*, *317*, 793–797. https://doi.org/10.1126/science.1141038.

Jouzel, J., Stiévenard, M., Johnsen, S. J., Landais, A., Masson-Delmotte, V., Sveinbjornsdottir, A., et al. (2007b). The GRIP deuterium-excess record. *Quaternary Science Reviews, 26,* 1–17.

Koerner, R. M., & Fisher, D. A. (2002). Ice-Core evidence for widespread arctic glacier retreat in the last interglacial and the early Holocene. *Annals of Glaciology, 35,* 19–24.

Krinner, G., C. Genthon, and J. Jouzel (1997). GCM analysis of local influences on ice core δ signals. *Geophysical Research Letters, 24*, 2 825–2 828.

Masson, V., Vimeux, F., Jouzel, J., Morgan, V., Delmotte, M., Hammer, C., et al. (2000). Holocene Variability in Antarctica based on 11 ice core isotopic records. *Quaternary Research, 54,* 348–358.

Masson-Delmotte, V., Jouzel, J., Landais, A., Stievenard, M., Johnsen, S. J., White, A., et al. (2005). Deuterium excess reveals millennial and orbital scale fluctuations of greenland moisture origin. *Science, 309,* 118–121.

Masson-Delmotte, V., Braconnot, P., Dreyfus, G., Johnsen, S., Jouzel, J., Kageyama, M., et al. (2006). Past temperature reconstructions from deep ice cores: relevance for future climate change. *Climate of the Past, 2*(2), 145–165.

Masson-Delmotte, V., Hou, S., Ekaykin, A., Jouzel, J., Aristarain, A., Bernardo, R. T., Bromwhich, D., Cattani, O., Delmotte, M., Falourd, S., Frezzotti, M., Gallée, H., Genoni, L., Isaksson, E., Landais, A., Helsen, M., Hoffmann, G., Lopez, J., Morgan, V., Motoyama, H., Noone, D., Oerter, H., Petit, J. R., Royer, A., Uemura, R., Schmidt, G. A., Schlosser, E., Simões, J. C., Steig, E., Stenni, B., Stievenard, M., van den Broeke, M., van de Wal, R., van den Berg, W. J., Vimeux and F., White, J. W. C. (2008). A review of antarctic surface snow isotopic composition: observations, atmospheric circulation and isotopic modelling. *Journal of Climate*, *21*, 13, 3 359–3 387.

NorthGRIP-community-members. (2004). High resolution climate record of the northern hemisphere reaching into last interglacial period. *Nature, 431,* 147–151.

Salamatin, A. N., Lipenkov, V. Y., Barkov, N. I., Jouzel, J., Petit, J. R. & Raynaud, D. (1998). Ice-core age dating and paleothermometer calibration on the basis of isotope and temperature profiles from deep boreholes at Vostok station (East Antarctica). *Journal of Geophysical Research, 103*, 8 963–8 977.

Severinghaus, J., Sowers, T., Brook, E. J., Alley, R. B., & Bender, M. (1998). Timing of abrupt climate change at the end of the younger dryas interval from thermally fractionated gases in polar ice. *Nature, 391,* 141–146.

Sime, L. C., Tindall, J. C., Wolff, E. W., Connolly, W. M., & Valdes, P. J. (2008). Antarctic isotopic thermometer during a CO_2 forced warming event. *Journal Geophysical Research, 113,* D24119.

Vimeux, F., Masson, V., Delaygue, G., Jouzel, J., Petit, J.-R., &Stievenard, M. (2001). A 420,000 year deuterium excess record from East Antarctica: Information on Past Changes in the Origin of Precipitation at Vostok. *Journal of Geophysical Research*, *106*, 31 863–31 873.

Watanabe, O., Jouzel, J., Johnsen, S., Parrenin, F., Shoji, H., & Yoshida, N. (2003). Homogeneous climate variability across East Antarctica over the past three glacial cycles. *Nature, 422,* 509–512.

Werner, M., Heimann, M., & Hoffmann, G. (2001). Isotopic composition and origin of polar precipitation in present and glacial climate simulations. *Tellus, 53B,* 53–71.

Werner, M., Jouzel, J., Masson-Delmotte, V., & Lohmann, G. (2018). Reconciling glacial Antarctic water stable isotopes with ice sheet topography and the isotopic paleothermometer. *Nature Communications, 9,* 3537. https://doi.org/10.1038/s41467-018-05430-y

Air-Vegetation Interface: Pollen

12

Joël Guiot

From the Production of Pollen to Sediment

In order to persist in difficult conditions, most plants and terrestrial animals contain hard parts that are preserved in the sediments after death. For higher-level terrestrial plants, these parts consist mainly of pollen grains and spores which provide a widely-used tool in paleoclimatology, thanks to their abundance in wet sediments. These grains, which are dispersed over variable distances depending on their shape and size (from 5 to 100 microns), are an essential factor in the reproduction of higher-level plants. Their outer envelope (exine) is composed of sporopollenin, a highly resistant substance once it is protected from oxidation. Lakes and bogs are particularly good environments for the conservation of these plant remains. These grains are scattered by wind, insects, birds, water. In temperate regions, wind is the predominant vector, and because of its relative inefficiency, lots of pollen grains and spores are found not far from their source, in continental sediments and marine sediments near the coast. In rainforests, animals play a much more important role, so that many species are underrepresented in sediments.

After choosing a site representative of the surrounding vegetation, with good conservation of pollen and sufficient accumulation rates to permit studies over the desired time scale, cores are extracted, usually at the center of the lake or bog. These cores are studied stratigraphically and samples are dated in order to establish an absolute chronology of climate events. Samples are taken at regular intervals along the core. They are subjected to physical and chemical treatments to make the pollen grains clearly visible for examination under a microscope. The grains are then identified on the basis of their exine which have different morphologies depending on the plant type. The palynologist counts each pollen type to work out the relative abundance of the species of trees or grasses that produced the grains. It is not always possible to determine each species, and many plants can only be recognized at the level of the genus or even family. Because of this heterogeneity in the classification, the term 'pollen taxon' is used to characterize the type of plant that produced it. The total number of grains counted varies depending on the diversity of the vegetation: tropical vegetation is more diverse than temperate vegetation and therefore requires a much higher total number, sometimes more than a thousand grains compared with a few hundred in a temperate vegetation, and this ensures good statistical significance of the various fluctuations detected. The relative abundance of each taxon makes up a pollen assembly or spectrum. It provides information on the relative composition of the surrounding vegetation, but this signal is influenced by the abundance of pollen productivity, its mode and capacity of dispersion. Statistical methods are needed to reliably decode the pollen spectrum (Moore et al. 1991).

The Pollen Diagram

The set of pollen spectra along the core is presented graphically to provide a pollen diagram whose complexity depends on the number of taxa counted. It can be simplified either by grouping together similar taxa (i.e. taxa co-evolving in similar environments), or by representing only the most important ones. Figure 12.1 shows an example of a simplified diagram. The interpretation of the diagram is complex because of the large number of processes occurring between the pollen production by the vegetation and its record in the sediment. As in most paleontological disciplines, interpretation is done by comparison with modern data. This supposes that the principle of uniformity, that is, where the present is the key to the past, applies. This is generally the case for data from the Quaternary, and in

J. Guiot (✉)
European Centre for Research and Teaching in Environmental Geosciences CEREGE, Aix-Marseille University, CNRS, IRD, INRAE, Collège de France, BP 80, 13545, Aix-en-Provence, Cedex 04, France
e-mail: guiot@cerege.fr

G. Ramstein et al. (eds.), *Paleoclimatology*, Frontiers in Earth Sciences,
https://doi.org/10.1007/978-3-030-24982-3_12

particular for continuous sequences that have been correlated over 500 000 years (Tzedakis et al. 1997). To verify this assumption, pollen samples are taken from modern or recent moss and their pollen spectra are compared with current vegetation. From a qualitative point of view, we can already sketch the relationship between the abundances of pollen and the composition of the vegetation. For example, the study of an altitudinal transect provides an impression of what happened during a cooling climate. Many published articles are based on this approach. But if current pollen spectra are collected from vegetation as diverse as possible, the problem can be treated quantitatively and objective keys to interpretation can be established. We develop this perspective below.

Figure 12.1 shows that the vegetation around Lake Rotsee, Switzerland (Lotter and Zbinden 1989) was dominated by herbaceous vegetation before 11,000 years BP: sagebrush (*Artemisia*) and grasses (*Poaceae*), indicating an open environment with few trees. Around 11,500 years BP, birch (*Betula*) and, a century later, pine (*Pinus*) flourished until they occupied nearly 80% of the assemblage. This pioneer arboreal vegetation thrived due to a warmer climate. Around

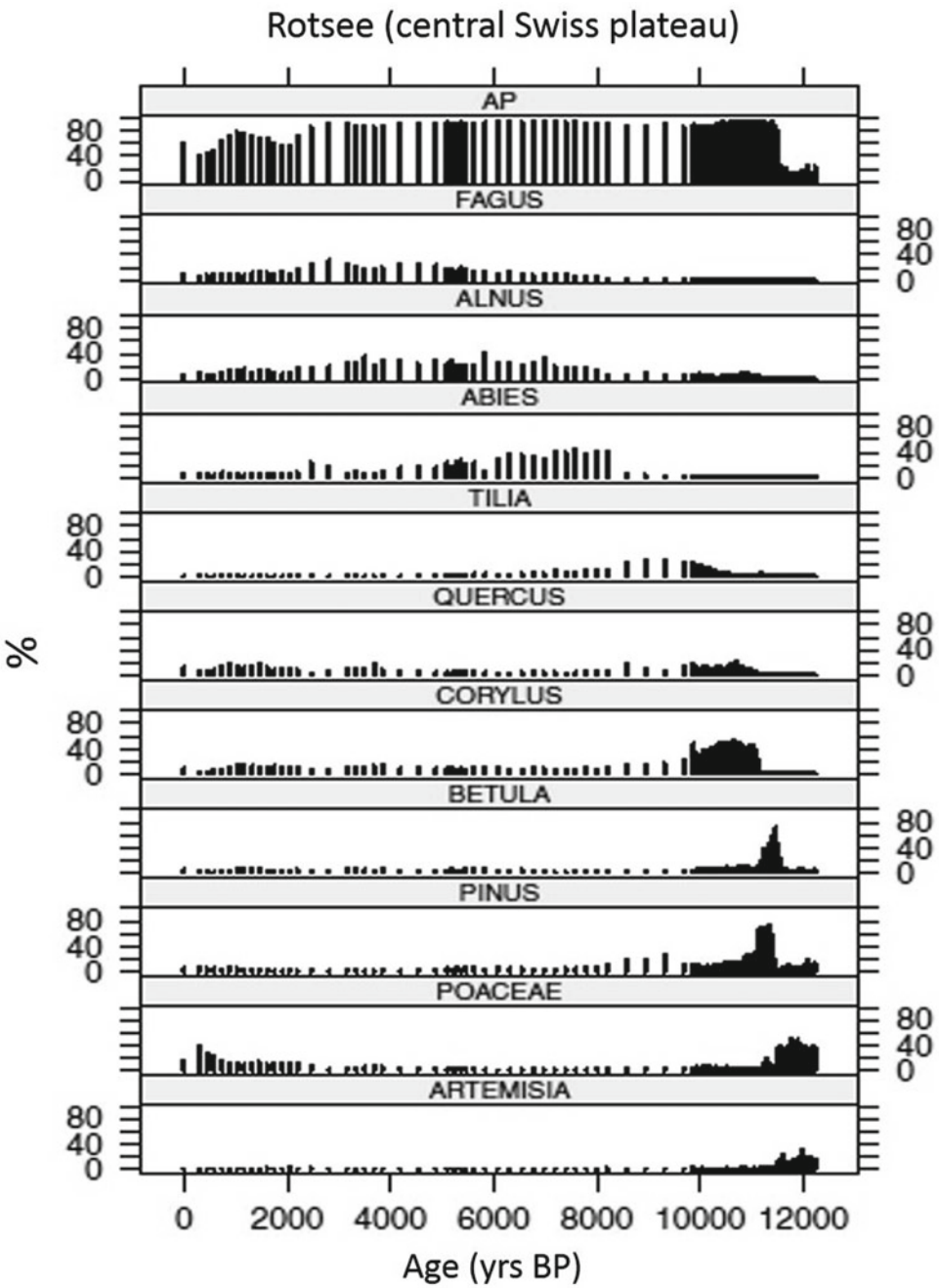

Fig. 12.1 Simplified pollen diagram of Lake Rotsee (8.33° E, 47.08° N, 419 m) in the Swiss Alps (Lotter and Zbinden 1989). The time period covered is from 12 000 years before now (BP) in calendar age to the present day. AP is the sum of all the arboreal pollen abundances

11,100 years BP, strong warming encouraged the proliferation of the hazel (*Corylus*), the oak (*Quercus*) three centuries later, and the lime tree (*Tilia*) five centuries later again, replacing these pioneers. This succession over less than a millennium is not necessarily exclusively due to climate: species expand geographically from refuges more or less distant from the studied area at a speed that is specific to them. Another, less dramatic change in climate (probably a wetter and cooler climate) around 8200 years BP enabled the fir (*Abies*) and alder (*Alnus*) to become established. Around 6300 years BP, it was the beech (*Fagus*) which progressed in the region. Around 2000 years BP, during the Roman period, the proportion of grasses increased and trees decreased (AP), a sign of anthropogenic deforestation.

Comparison of the different graphs in Fig. 12.1 shows that some taxa evolve together while others are diachronous. Taxa that are present at the same time on the same site will likely thrive in the same climatic conditions: they will be temperate or boreal, they will be resistant to drought or only survive in wet conditions. If, to this, we add characteristics related to the size of the plant (tree, shrub, grass), phenology (evergreen plant or deciduous), type of leaf (needles or broad leaves), a reasonable classification can be made. Prentice et al. (1996) have proposed one for Europe. This was then applied to other continents (Jolly 1998; Tarasov 1998). The types of plants defined in this way, known as plant functional types (PFTs), can be directly compared to simulations by vegetation models based on the same typology. These PFTs are used to define the vegetation of a site in the form of a biome: a bio-geographic area characterized by the species of plants (and animals) that live there. In Fig. 12.2 four such PFTs have been reproduced. The biome is determined by comparing them. Before 11,500 years BP, herbaceous plants dominated, as is currently the case in the arctic tundra and alpine grasslands. This period is called the Younger Dryas. Then, the presence of boreal deciduous trees, followed by conifers, indicated a warming sufficient for the taïga, as the forest in Northern Europe is called today, to develop. From 11,100 years BP, at the beginning of the Holocene, the temperate forest became established. The arrival of conifers around 8200 years BP, probably due to a well-known abrupt cooling (Tinner and Lotter 2006) transformed the landscape from a deciduous forest to a mixed forest which lasted until about 5000 years BP. The consequent growth of deciduous trees was disturbed around 4000 years BP and even more so around 2000 years BP, as a result of widespread deforestation by man. The reconstructed biome then became the steppe, although it was not exactly a proper one, being a mix of grasslands and forests.

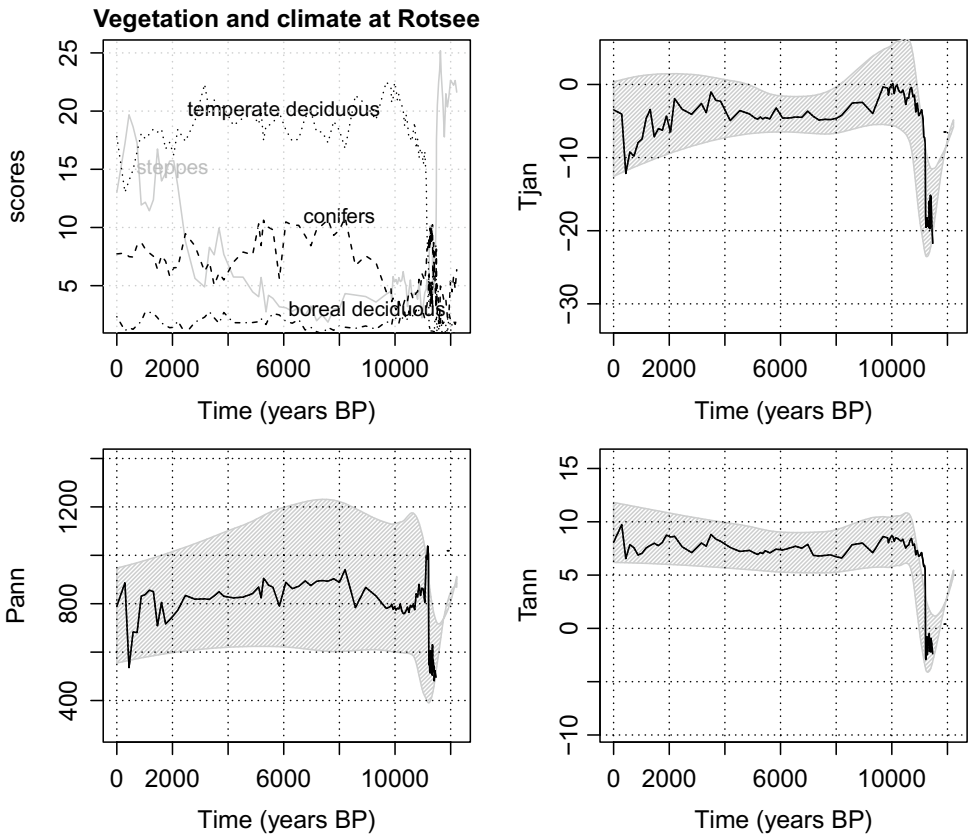

Fig. 12.2 Evolution of four functional plant types at Lake Rotsee. Continuous line gray: herbaceous steppe and tundra, dashed dotted line: boreal deciduous trees; dashed line: conifers; dotted line: temperate deciduous trees. On the same figure, the biomes that can be inferred from this are represented: steppe, temperate forest, mixed forest, taiga, tundra. The other three panels represent the three climate parameters reconstructed with their error bars: Pann (annual precipitation in mm/year), Tjan (January temperatures in °C), Tann (annual average temperature in °C). The error bar is given by the total variability between the analogs

Reconstruction of Climate

These interpretations are essentially qualitative. Transfer functions and the analog method (see Chap. 10, Sect. 10.1.3) provide quantitative information on climate. Here, we use the analog method, not on the percentages of taxa, but on the PFT scores (Fig. 12.2.), which has many advantages: it reduces the number of variables and groups together the taxa with similar behavior, making the approach more robust. Twelve analogs for each fossil spectrum were retained.

Figure 12.2 shows these reconstructions with the shaded area representing the range of variability between the analogs. The quality of the reconstructions is controlled by applying the same method to modern data: for each modern spectrum, the best analogs are determined (obviously excluding the spectrum itself) and the present climate is reconstructed so that it can be compared to direct observations. In this case, we find a coefficient of determination (r^2) of 0.64 for the annual precipitation (Pann), 0.89 for temperatures in January (Tjan) and 0.93 for annual average temperatures (Tann). The estimates obtained for precipitation will therefore contain larger errors than the other variables. This is confirmed by Fig. 12.2. In terms of climate, we see that the Younger Dryas was very cold (14 ± 7 °C colder than now) and dry (400 ± 400 mm/year less rainfall than now over the annual average), but that the uncertainties are large (in this method, this is the variability between analogs rather than an actual error bar). The temperature maximum (4 ± 2 °C more than now) occurred at around 10,000 years BP, when oak dominated, and the rainfall maximum (100 ± 250 mm more) occurred around 8200 years BP, with the arrival of the mixed forest. However, the 8200 BP event does not appear to have been short-lived since this forest continued for several millennia longer.

Several other methods have been proposed to reconstruct climate from pollen data (see Brewer et al. 2007; Birks 2011; Juggins 2013). They all have their strengths and weaknesses. It is not always easy to find the optimal method. It is recommended to try several and compare the results. The convergence of estimates is an indication of the robustness of the reconstruction, and their divergence is often a sign that the initial assumptions used for the reconstruction were not entirely valid. In particular, when the climate changes rapidly, vegetation adapts with a certain delay, which makes it difficult to find current analogs. Another problem is estimating the impact of non-climate constraints. For example, atmospheric CO_2 concentration during the Quaternary glaciations was lower than the current concentration (about 200 ppm instead of more than 280 ppm). We know that this level is an activator of photosynthesis and so it is unlikely that the principle of uniformity applies: vegetation will not respond to climate change in the same way when atmospheric CO_2 levels change. This problem was solved by the use of mechanistic models of vegetation (Guiot et al. 2000). Another avenue takes pollen dispersal and associated biases into account when reconstructing the landscape (Sugita 2007; Trondman et al. 2015). The relative abundance of pollen of a taxon depends on the height and distance of the productive plant, its pollen productivity, the weight and shape of the pollen grain, the dimensions of the lake into which it falls.

To improve climate reconstructions without resorting to overly complex models, the 'multiproxy' approach is recommended. This involves taking several simultaneous climate indicators into account: pollen, macro remains of plants or animals, carbon isotopes, lake levels, sedimentological parameters etc. as was done by Cheddadi et al. (1997). This multiproxy approach is also supported by mechanistic models (Rousseau et al. 2006. Guiot et al. 2009). These avenues of research are being explored both to reconstruct the climate of the past and to understand how it has influenced the vegetation.

References

Birks, H. J. B. (2011). Strengths and weaknesses of quantitative climate reconstructions based on late-quaternary biological proxies. *The Open Ecology Journal, 3,* 68–110. https://doi.org/10.2174/1874213001003020068.

Brewer, S., Guiot, J., Barboni, D. (2007). Pollen Data as Climate Proxies. In *Encyclopedia of Quaternary Sciences*, Elsevier.

Cheddadi, R., Yu, G., Guiot, J., Harrison, S. P., & Prentice, I. C. (1997). The Climate of Europe 6000 years ago. *Climate Dynamics, 13,* 1–9.

Guiot, J., Torre, F., Jolly, D., Peyron, O., Boreux, J. J., & Cheddadi, R. (2000). Inverse vegetation modeling by monte carlo sampling to reconstruct palaeoclimates under changed precipitation seasonality and CO_2 conditions: Application to glacial climate in mediterranean region. *Ecological Modelling, 127,* 119–140.

Guiot, J., Wu, H., Garreta, V., Hatti, L., & Magny, M. (2009). A few prospective ideas on climate reconstruction from a statistical single proxy approach towards a multi-proxy and dynamical approach. *Climate of the Past, 5,* 571–583.

Jolly, D. et al. (1998). Biome reconstruction from pollen and Plant Macrofossil data for Africa and the Arabian Peninsula at 0 and 6 ka. *Journal of Biogeography*, *25*, 1 007–1 028.

Juggins, S. (2013). Quantitative reconstructions in palaeolimnology: New paradigm or sick science? *Quaternary Science Review, 64*. https://doi.org/10.1016/j.quascirev.2012.12.014.

Lotter, A. F., & Zbinden, H. (1989). 'Late-glacial pollen analysis, Oxygen-Isotope and Radiocarbon stratigraphy from Rotsee (Lucerne), Central Swiss Plateau. *Ecologae Gologicae Helvetiae, 82,* 191–202.

Moore, P. D., Webb, J. A., & Collinson, M. E. (1991). *Pollen Analysis*. Oxford: Blackwell Scientific Publications.

Prentice, I. C., Guiot, J., Huntley, B., Jolly, D., & Cheddadi, R. (1996). Reconstructing biomes from Palaeoecological data: A general

method and its application to European pollen data at 0 and 6 ka. *Climate Dynamics, 12,* 185–194.

Rousseau, D., Hatté, C., Guiot, J., Duzer, D., Schevin, P. and Kukla, G. (2006). Reconstruction of the Grande Pile Eemian Using Inverse Modeling of Biomes and d13C. *Quaternary Science Reviews, 25*, 2 806–2 819.

Sugita, S. (2007). Theory of quantitative reconstruction of vegetation I: Pollen from Large Sites REVEALS regional vegetation composition. *The Holocene, 17,* 229–241.

Tarasov, P. E. et al. (1998). Present-Day and Mid-Holocene Biomes reconstructed from pollen and plant macrofossil data from the Former Soviet Union and Mongolia. *Journal of Biogeography*, *25*, 1 029–1 054.

Tinner, W., & Lotter, A. (2006). Holocene expansions of Fagus silvatica and Abies alba in Central Europe: where are we after eight decades of debate? *Quaternary Science Reviews*, *25*(5–6), 526–549. https://doi.org/10.1016/j.quascirev.2005.03.017.

Trondman, A. K., Gaillard, M. J., Mazier, F., Sugita, S., Fyfe, R., Nielsen, A. B., et al. (2015). Pollen-based quantitative reconstructions of Holocene regional vegetation cover (plant-functional types and land-cover types) in Europe suitable for climate modelling. Glob. Chang. Biol. 21. https://doi.org/10.1111/gcb.12737.

Tzedakis, P. C., Andrieu, V., de Beaulieu, J.-L., Crowhurst, S., Follieri, M., Hooghiemstra, H., et al. (1997). Comparison of terrestrial and marine record of changing climate of the last 500,000 years. *Earth and Planetary Science Letters, 50,* 171–176.

Ground-Air Interface: The Loess Sequences, Markers of Atmospheric Circulation

13

Denis-Didier Rousseau and Christine Hatté

Abstract

Atmospheric circulation is responsible for the rapid distribution of heat and moisture across the Earth and hence determines our weather and regional climate, today and in the past. During past climate cycles, the atmosphere has been much more dustier, except during the interglacials, inducing uncertainties about the impact of mineral aerosols on the past climate dynamics. There are abundant traces of the combination of past atmospheric dynamics and paleodust cycle such as eolian mineral material transported and deposited in terrestrial archives as loess. Records from loess deposits consistently suggest that atmospheric dynamics was highly variable, during the past climate cycles, much more than presently where the only sources of dust are the major deserts. In this chapter we explained the four main categories of parameters allowing to identify loess deposits as reliable markers for past air circulation.

Overview of Loess

Loess is an aeolian sediment which is relatively common in continental areas (Fig. 13.1). In Europe and North America, it is dispersed near former polar deserts or near the frontal moraines of the gigantic ice sheets that developed on these continents during the ice ages. In Asia, however, the situation is different, since the Loess Plateau is located south of the deserts of northern China and southern Mongolia. The loess sediments thus cover vast regions of the northern hemisphere, at latitudes where very few other records of the glacial paleoclimates are available, while in more southern latitudes, lakes, peat bogs, speleothems and marine sediments collected close to the coast provide continental records of a high quality. In Southern Hemisphere, loess is mostly associated with fluvial and piedmont deposits in the Pampean plains in South America, and fluvial abrasion and glacial grinding in New Zealand.

Loess is a fine sediment transported mainly by wind to various altitudes depending on the particle grain size, but also on the state of the substratum and on the environmental conditions in the region of origin of the material (Fig. 13.2). Dust emission is favored by a low rate of vegetation development and extension of river-emerged banks, source of fine mineral dust. Loess deposits are thus specific to glacial times with low sea-levels thus high river incision and weak vegetation development.

To simplify, coarse material is carried over distances of less than hundred kilometers and transport is mainly by saltation, that is to say, by a series of jumps. However, fine material (clay), which may be of local or remote origins, may equally have been transported over hundreds of kilometers to altitudes of several kilometers in the form of mineral dust and may have been redeposited through wet or dry deposition (depending on whether or not they are associated with precipitations). Loess is therefore usually a marker for air circulation in the past.

To illustrate our words and the research potential of loess sequences, most of our examples will be drawn from the extensively studied Nussloch loess sequence (Rhine Valley, Germany).

D.-D. Rousseau (✉)
École Normale Supérieure de Paris, Laboratoire de Météorologie Dynamique, UMR CNRS 8539, Université Paris Sciences et Lettres, 24 Rue Lhomond, 75231 Paris, France
e-mail: denis-didier.rousseau@lmd.ens.fr

Lamont-Doherty Earth Observatory of Columbia University, Palisades, NY 10964, USA

C. Hatté
Laboratoire des Sciences du Climat et de l'Environnement, LSCE/IPSL, Université Paris-Saclay, 91190 Gif-Sur-Yvette, France

G. Ramstein et al. (eds.), *Paleoclimatology*, Frontiers in Earth Sciences,
https://doi.org/10.1007/978-3-030-24982-3_13

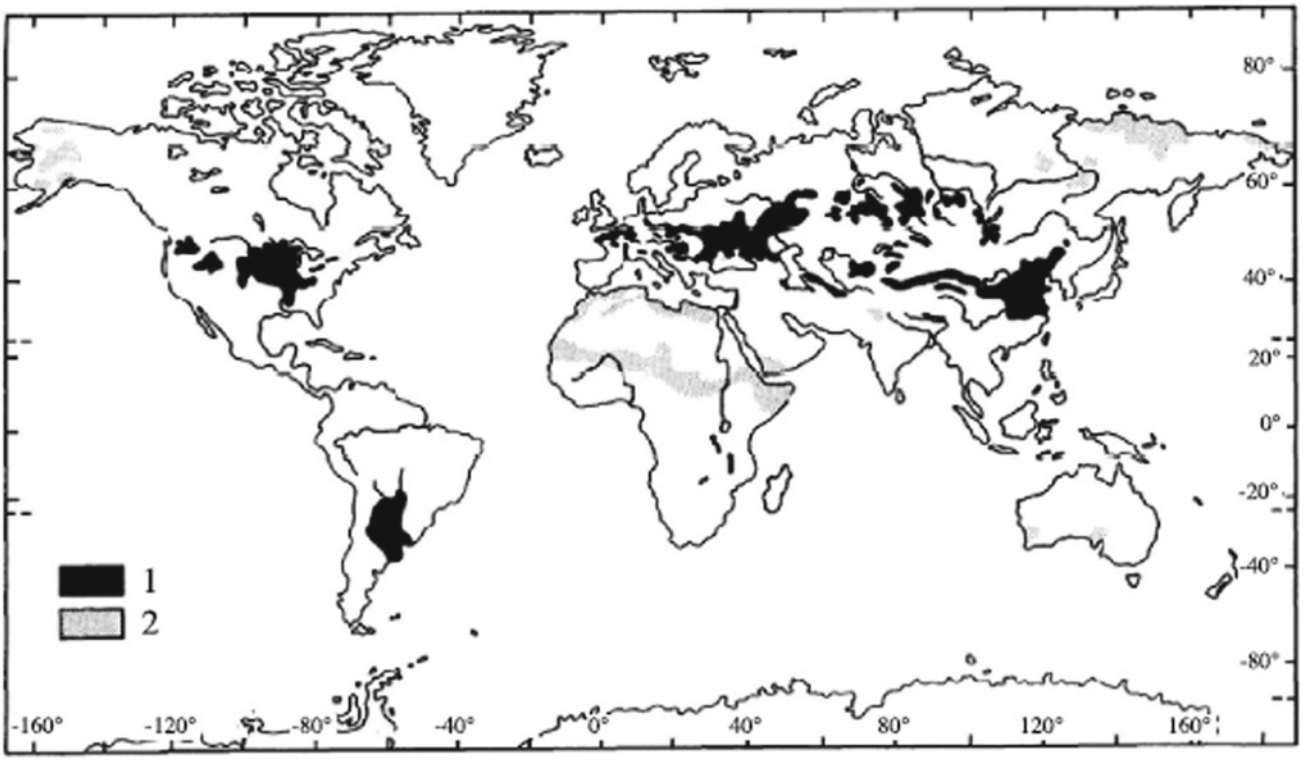

Fig. 13.1 Global distribution of loess sediments and equivalents. 1: loess sediments; 2: loess derivatives (according to Pécsi (1990))

Paleoclimate Indicators

Different paleoenvironmental indicators can be identified for this type of material, deposited at medium and high latitudes with climate conditions unfavorable for biological development (glacial periods). These parameters allow their interpretation in term of atmospheric circulation. Four major categories are presented below.

Sedimentological Indicators

The conceptual view

Even the observation of a loess sequence is instructive. Indeed, when a record is of one or more climate cycles, this is never made up of a single stratigraphic unit.

While loess sediment is characteristic of cold and quite arid periods, other warmer periods are marked by paleosols. Thus, if at low resolution, the loess-paleosol sequence corresponds to one or more climatic cycles; at higher resolution, the identification of more precise events is achieved by observing the sequence of soils or a particular hierarchy of pedo-sedimentary units. (Kukla and An (1989)). In Europe, a leached brown paleosol (Bt), at the base of a brown soil, indicates an interglacial level, while a humus-rich forest soil or a tundra gley (hydromorphic soil) are indicative of more temperate interstadial intervals (Antoine (2009)).

Since they present detailed records of past climate, reproducing the same pedostratigraphic and sedimentological units with the same succession of these units, the pedosedimentary record of loess sequences can be used as a powerful tool for chronostratigraphical correlation (Antoine, et al, (1999); Rousseau et al. (2007a, b)).

The grain size index

The study of the grain size, calculated through determination of the dominant classes, their mode distribution and relationships between them, can characterize the relative strengths of the winds that created the deposits (Rousseau et al. (2007a, b)). These wind dynamics are linked to changes in the general atmospheric circulation (Fig. 13.3). On a finer scale, Nussloch shows a progressive coarsening of the loess deposits between ca 30 and 22 ka (Rousseau et al. (2007b)). This coarsening trend ends with a short but major decrease in grain size, followed by an increase to a new maximum at 20 ± 2 ka ("W" shape). Correlation between the loess grain-size index and the Greenland ice-core dust records suggests a global connection between North Atlantic and Western European global atmospheric circulation and wind regimes (Antoine (2009); Rousseau et al. (2007b)).

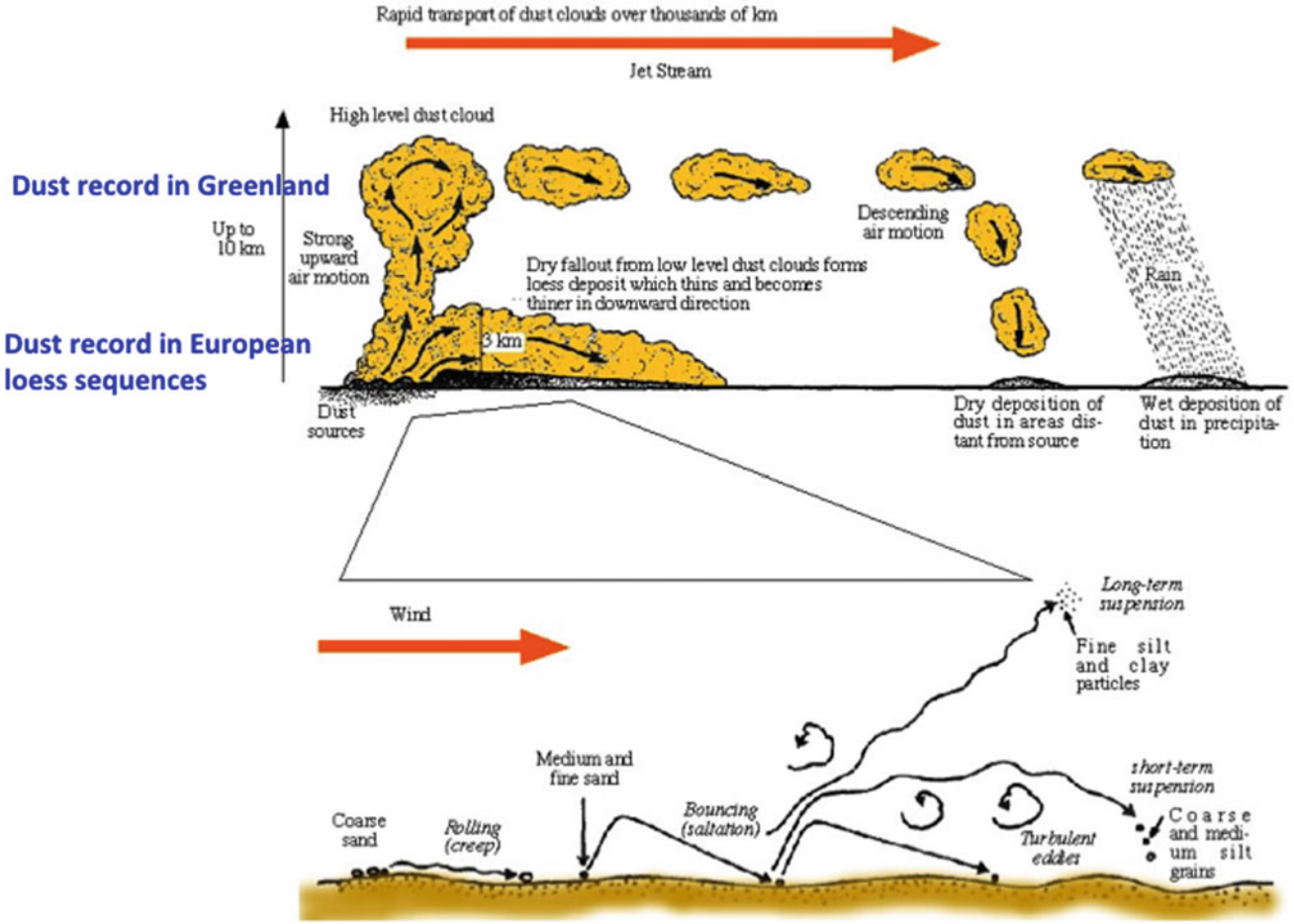

Fig. 13.2 Representation of the different types of dust transportation contributing to the formation of loess deposits. A—Two modes of transport and deposition of wind-blown dust from the northwestern deserts of China to the Loess Plateau and the North Pacific Ocean during the Quaternary (from Pye and Zhou (1989) modified). B—Diagram showing the various modes of transport of wind sediment particularly to the lower levels of the atmosphere (from Pye (1995) modified)

The loess deposit thickness

The thickness of the units is another characteristic which also allows the link with wind dynamics to be established. Indeed, monitoring a particular unit in a given territory allows the characterization of gradients which will be oriented according to the prevailing winds, the thickest part being upwind (Rousseau et al. (2007a)) (Figure 13.4).

Furthermore, the cyclic variation of the sedimentation rate has been shown to be a potential response to the North-Atlantic rapid climate changes, i.e. the Greenland stadial/interstadial cycles and the Heinrich events. This hypothesis has been tested by modeling the impact of North-Atlantic climate variations on dust emissions. This study clearly highlighted that, besides wind, precipitation, soil moisture and snow cover showing some differences in the dust emission intensity, vegetation cover is the main impacting parameter (Sima et al. (2009)). Dust fluxes for the cold climate states (Greenland stadial and Heinrich event) generally become more than twice as high as those for the relatively warmer Greenland interstadial, in agreement with the observed loess data (Sima et al. (2009)) (Fig. 13.4).

The mineralogy

The mineralogy, in particular its composition of heavy minerals, also helps to trace the origin of certain deposits and to deduce the prevailing winds responsible for their transport (Lautridou (1985)).

Biological Indicators

These are relatively diverse. Although the remains of micro-mammals: bones, teeth or skulls, or of larger mammals are identified quite sporadically, other fossils are more

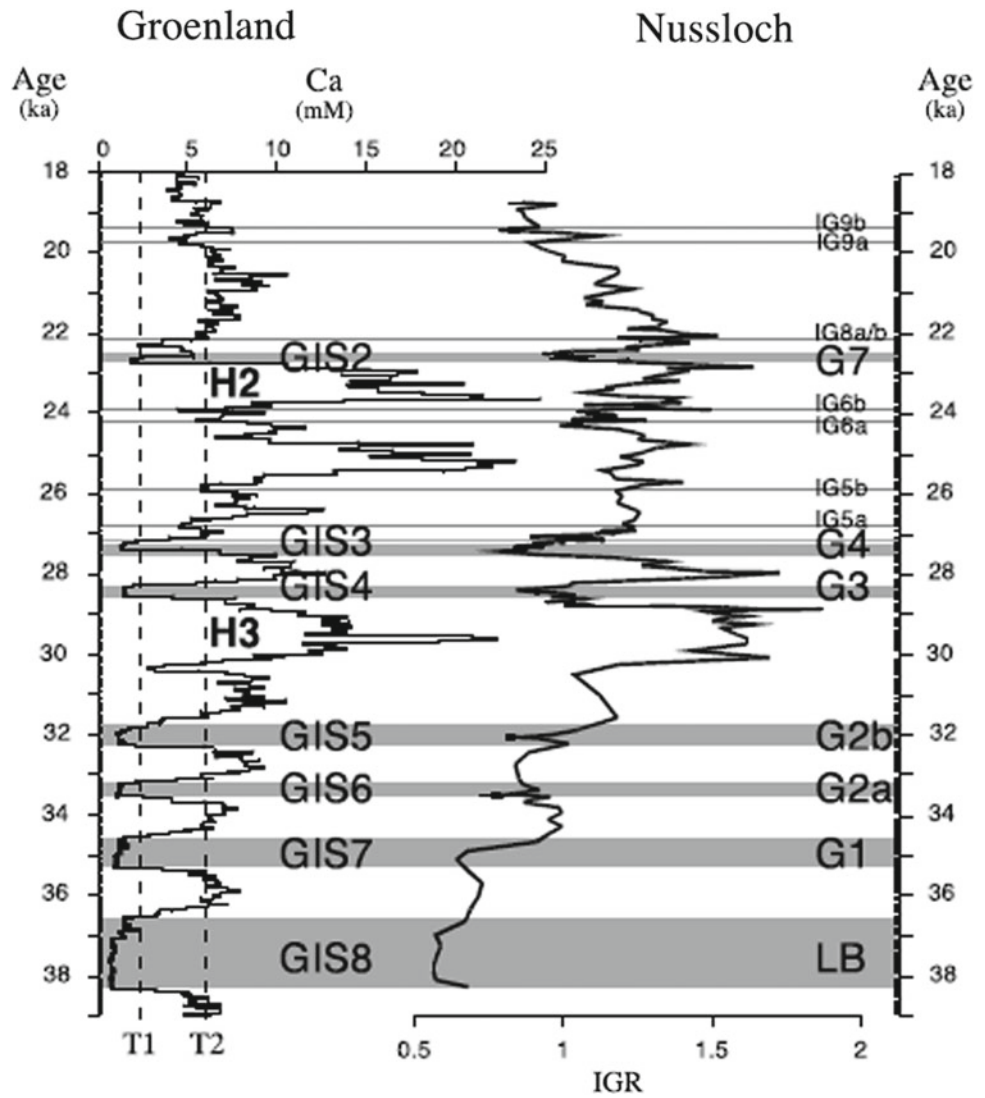

Fig. 13.3 Correlation of variations in particle size index (IGR) as defined at Nussloch with variations in calcium concentration (representing transported dust) from the GRIP survey. The T1 threshold applied to Greenland data highlights the main intervals with low dust concentration, which correspond to Dansgaard-Oeschger (DOI) interstadials 8 to 2. These are correlated to intervals where the IGR is low in Nussloch, corresponding to a brown boreal soil called Lohne Boden (LB) or to well-developed tundra gleys (G1, G2a, G2b, G3, G4 and G7). The T2 threshold defines intervals with very high dust concentration in Greenland, corresponding to the DO stadials, as well as some less significant peaks in dust (according to Rousseau et al. (2007b))

frequent. Among these, terrestrial mollusks form populations typical of diverse environments (Wu (2001); Rousseau (1987)).

Mollusk assemblages

Usually identified at the species level, these organisms have the advantage of persisting to the present day. In accordance with the principle of actualism, it is possible to apply modern requirements and ecological characteristics to individual fossils. Multivariate statistical analyses are used to reconstruct the environment in which a fossil community developed (Rousseau (1987)). Two examples follow: the first, in China, illustrates the long-term variations that can be correlated to terrestrial orbital frequencies and the second shows the short-term variation relating to the internal variability of the climate.

The long-term variability

Using the ecological requirements of taxa identified in the Chinese loess, it was possible to define environmental groups that have proven to be reliable indicators of the summer and winter monsoons through the ages (Fig. 13.5). Transfer

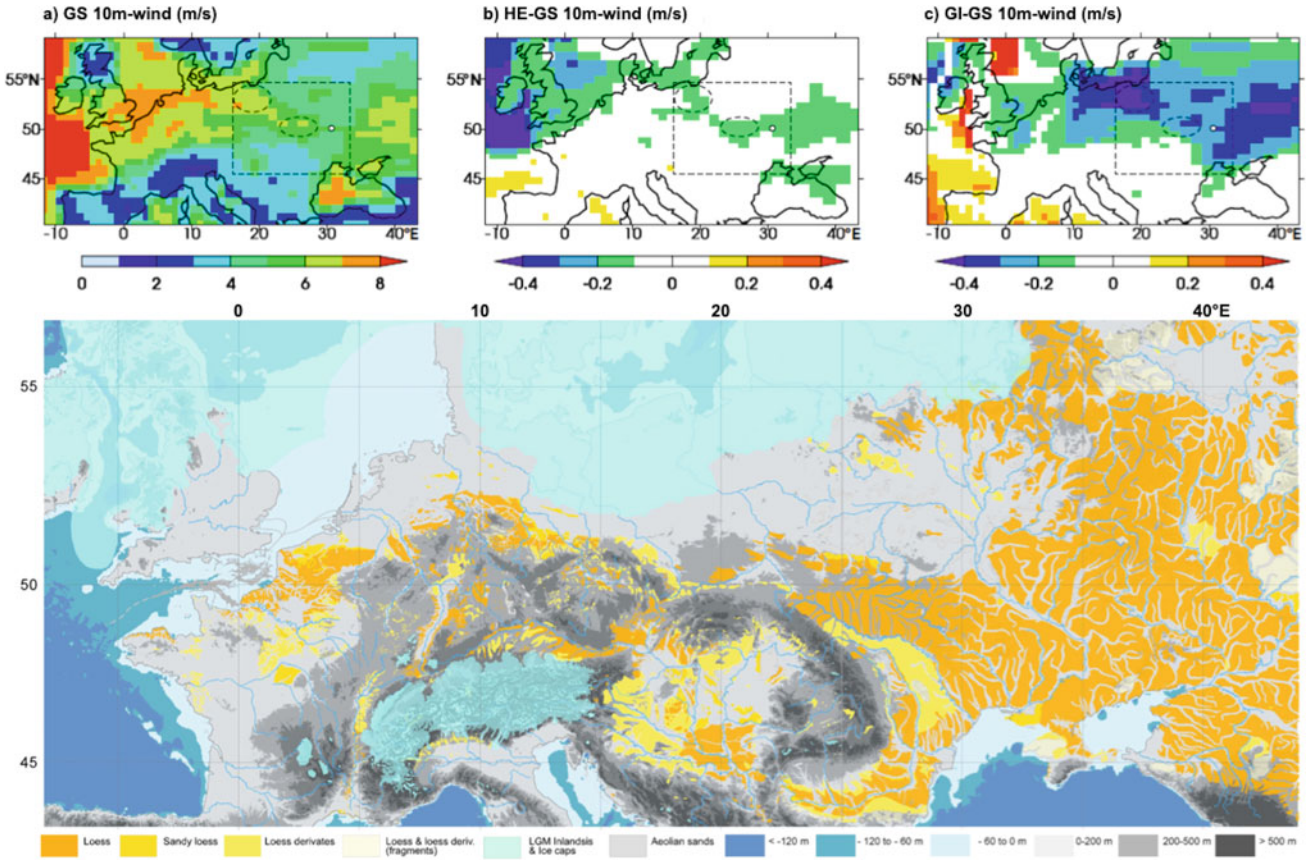

Fig. 13.4 Map of European loess deposits indicating the maximum expansion of the Fennoscandian and British ice sheets during the last glacial maximum (map by Antoine in [10] modified), with wind speed reconstructed for three climate conditions corresponding to northern oceanic influences: GS, HE-GS and GI-GS with GS = Greenland stadial, HE = Heinrich stadial, GI—Greenland interstadial (according to Sima et al. (2009) modified)

functions from terrestrial mollusks and using the principle of modern analogs, were developed to reconstruct the seasonal temperatures from the European loess sequences over three climate cycles (Rousseau (1991); Moine et al. (2002)).

The short-term variability

The high-resolution study (1 sample every 10 cm) of malacological assemblages from the Nussloch loess sequence allows vegetation change to be described along the 70 to 34 kyr cal BP period, recorded in 6 meters of sediment (Moine et al. (2005)). The mollusk changes reflect three short phases of vegetation development and climatic improvement related to soils of the interstadials. A steppe to herb/shrub tundra shift characterizes the Lower-Middle Pleniglacial transition and is followed by a decline in vegetation and humidity increase ending with a new increase in temperature and vegetation cover (Moine et al. (2005)).

Many other methods have been developed using micro-mammals or beetles, with the current distribution of species and the average ranges of associated climate acting as a reference (Liu et al. (1985)). Terrestrial mollusks have also been studied from their signature left in amino acids. This approach helps to distinguish important differences between one climate cycle and another (Oches and McCoy (1995)).

Another paleoclimate index also studied in loess sediments are phytoliths, siliceous concretions present in superficial plant tissue. In some cases, they are well preserved and identified, particularly in the Chinese loess sequences, where they helped in the reconstruction of the temperature and precipitation of the last climatic cycle (Lu et al. (2007)). Pollen, in contrast, are poorly preserved in loess sequences and are the subject of very few studies (Gerasimenko and Rousseau (2008); Rousseau et al. (2001)).

Recently, ***earthworm granules*** have been established as a new biological proxy (Prud'homme et al. (2015)). This proxy is not based on species recognition but is based on abundance. Counts of earthworm granules reveal a link between their abundance and the nature of the stratigraphic units and their associated climate conditions. They are in very high abundances in tundra gley and boreal brown soil horizons, i.e. during Greenland interstadial intervals and are

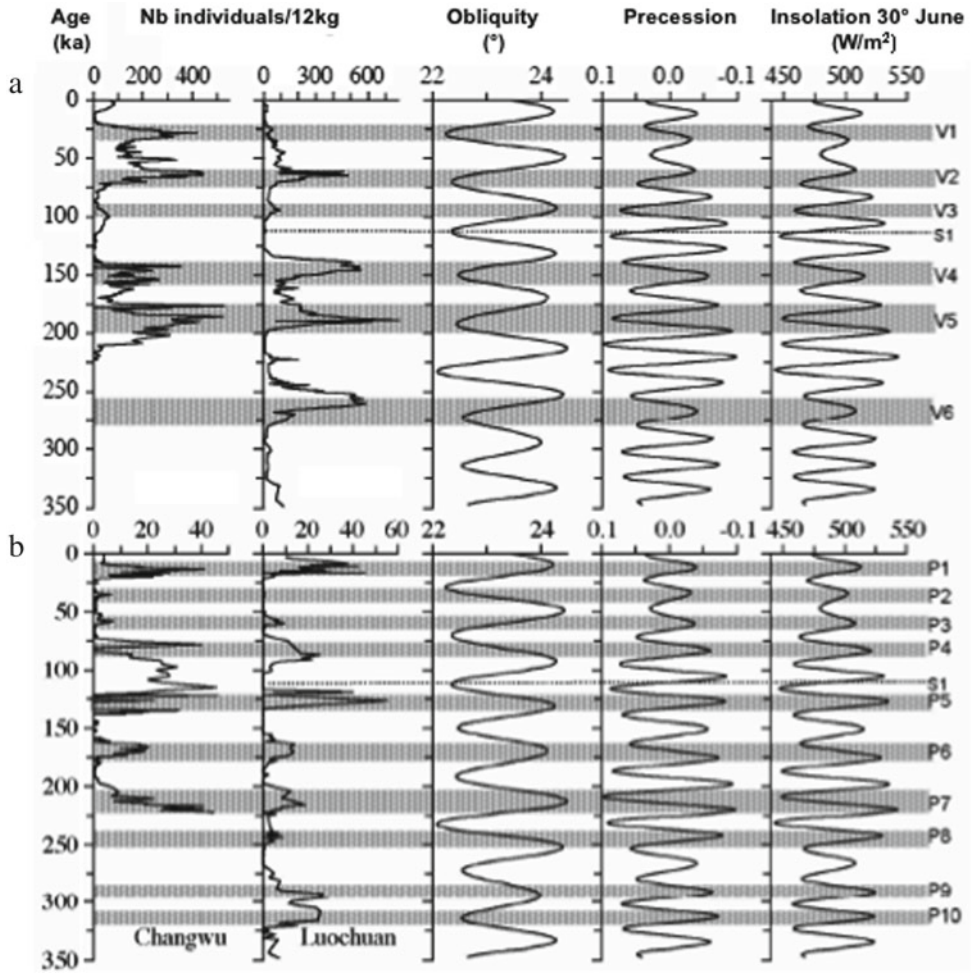

Fig. 13.5 Variations in the abundance of mollusks, characteristic of ancient summer and winter monsoons over the last three climate cycles in two sequences of the Chinese Loess Plateau (Changwu and Luochuan) and their relationship to astronomical parameters and insolation at 30° N. A—Variations in the abundance of *Vallonia tenera* and *Pupilla aeoli*, indicators of ancient winter monsoons. B—Variations in the abundance of *Punctum orphana*, indicator of ancient summer monsoons (according to Wu (2001))

almost absent in typical calcareous loess, associated with Greenland and Heinrich stadials (Prud'homme et al. (2015)).

Geophysical Indicators

This is mainly the magnetic sensitivity in low fields which allows, firstly, the different lithological units present in the same sequence to be characterized, and secondly, to identify the source of the matter through the magnetic particle size (Lagroix and Banerjee (2002)). In general, typical loess units have relatively low field magnetic susceptibility, unlike paleosols, which are characterized by significantly higher values. Widely used for the Chinese sequences, low-frequency magnetic sensitivity was interpreted by Kukla et al. (1990) as corresponding to a relatively constant supply of fine matter through the ages. According to this theory, the formation of soil in the various Chinese interglacial paleosols caused the magnetic grains to become concentrated. This led Kukla to propose a chronological model, independent of any astronomical calibration, while assuming continuous and complete sequences. However, the discovery in the paleosols of bacteria secreting magnetic grains called this debatable assumption into question (Zhou et al. (1990)). On the other hand, research on modern Chinese soils along gradients, reflecting the impact of the summer monsoon, has enabled the calibration of the sensitivity signal and the establishment of a transfer function for the region to reconstruct annual paleoprecipitation associated with the variations in the East Asian monsoon (Maher and Thompson (1995)). A new method of characterizing the origin of loess is to work directly taking a quartz grain and to study both the crystallinity index and the intensity of the spin resonance signal. This new technique makes it possible to differentiate between the origins of the grains and thus to follow the variations in the source of the transported material. Applied

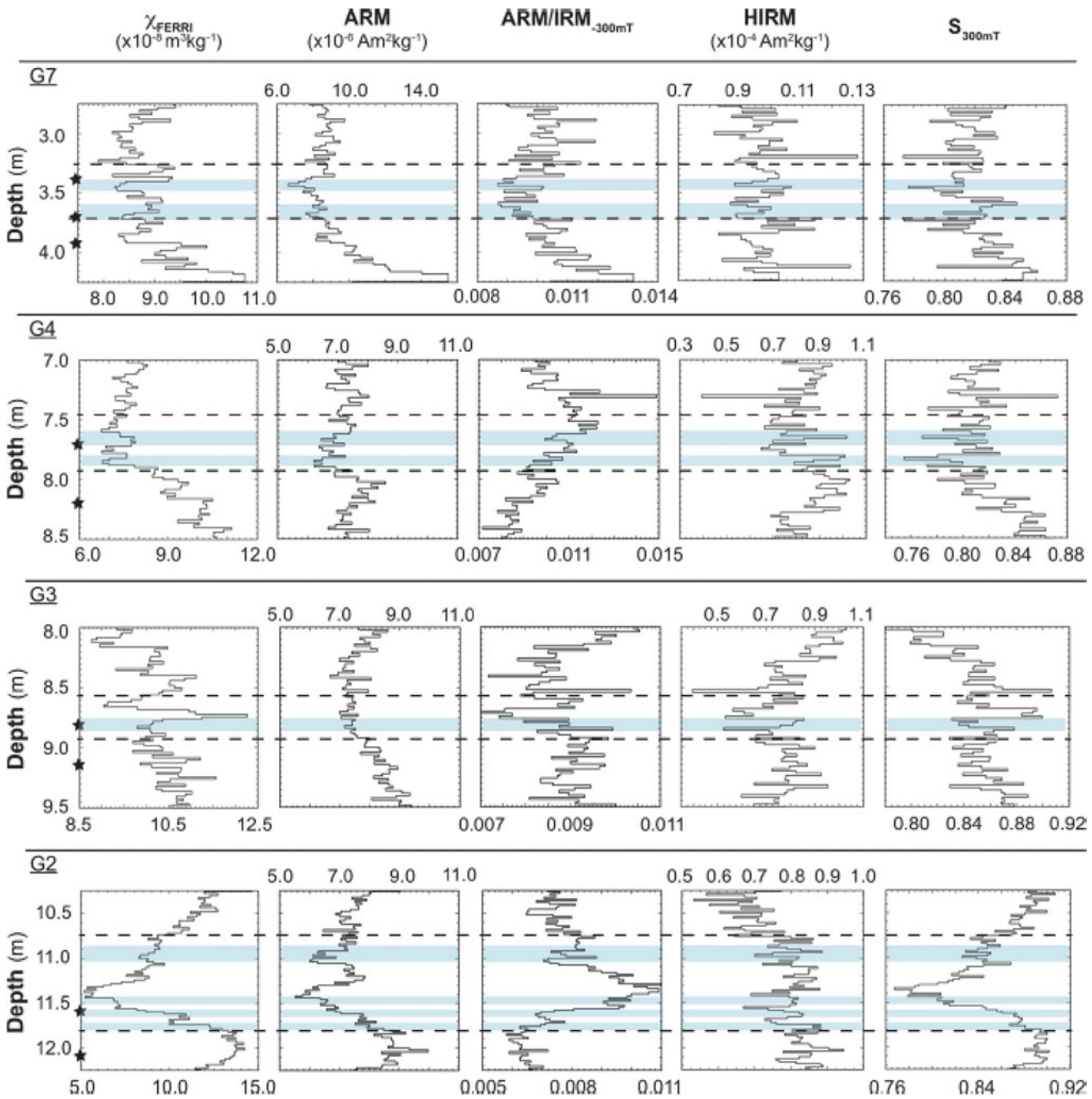

Fig. 13.6 Variation versus depth of rock magnetic parameters allowing the waterlogging in different tundra gleys from the Nussloch loess sequence to be characterized. From Taylor et al. (2014)

for the first time in the Chinese loess sequences, this method has helped to clarify the origin of the quartz grains transported to the Loess Plateau (the Gobi desert during stadial periods, deserts of northern China during the warmer periods) (Sun (2008)). More recently, the study of the mineral magnetic composition completed the classical interpretation of the magnetic susceptibility record by allowing waterlogging processes in tundra gley supporting the correlation of these paleosols with Greenland interstadials to be characterized (Taylor et al. (2014)) (Fig. 13.6).

Geochemical Indicators

The fourth category of indicators concerns geochemical indices and, in particular, isotopic parameters which constitute a powerful tool for interesting research perspectives.

Tracing paleodust sources

As representatives of the age of the geological formation, the dust particles derived from Sr and Pb isotopes are commonly

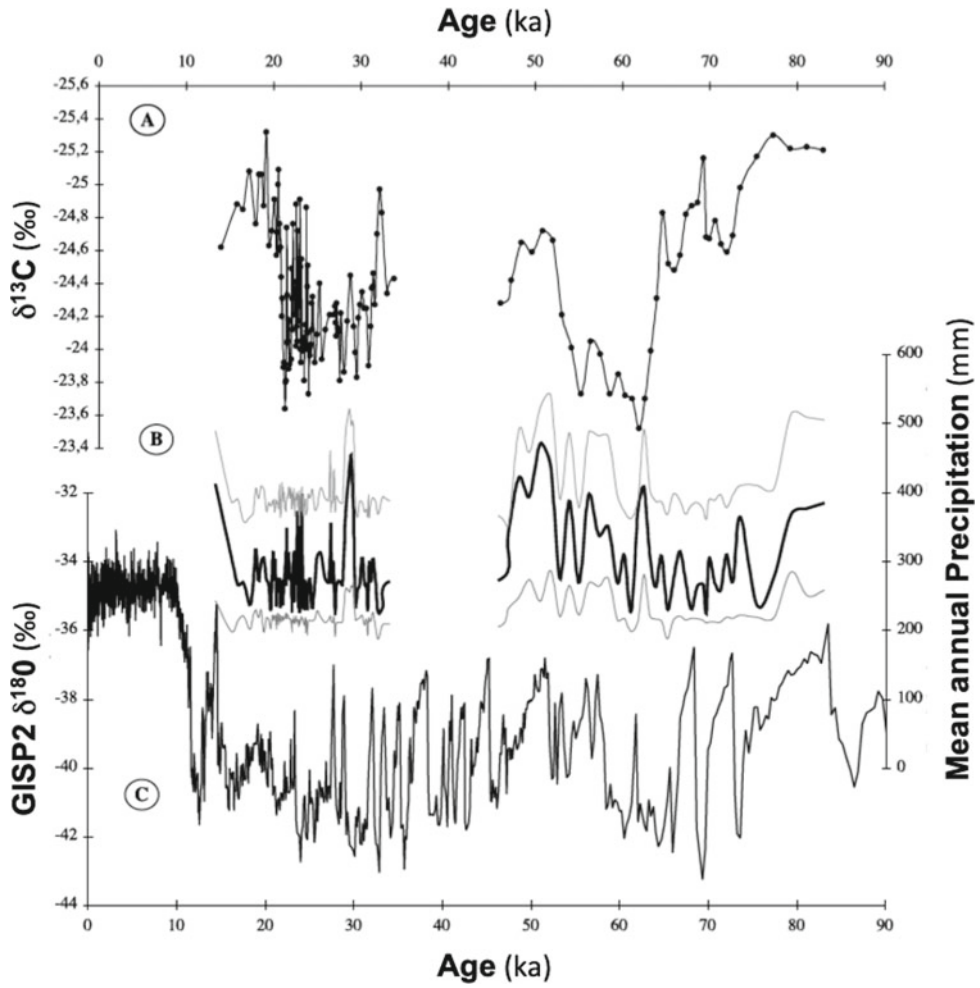

Fig. 13.7 Reconstructing the paleoprecipitation at Nussloch over the last 80 ka. A—$\delta^{13}C$ over time. The range of values obtained corresponds to plants of C3 photosynthetic type. B—Reconstruction of paleoprecipitation by inverse modeling of the isotopic signal (according to Hatté and Guiot (2005)). C—Comparison with $\delta^{18}O$ in Greenland ice (GISP2). During periods of high sea level, the warm phases of DO events result in a net increase in rainfall (+30 to 40%), while during periods of low sea level, the distance from the coastline insulates Nussloch from any climatic improvement that might result from a warm episode

regarded as source tracers. A recent study has been performed on loess samples, dated from the Last Glacial Maximum, located along a 50° N transect (from English Channel to Ukraine), chosen to represent the geographic and petrographic variability of the European loess belt. Geochemical results combined with dust emission simulations revealed that the dust was transported only over a few hundred kilometers. Moreover, the results highlighted that the sources were regional and that distinct sources prevailed within the European continent (Rousseau et al. (2014)).

Tracing past precipitation and seasonality

The analysis of $\delta^{13}C$ from organic matter preserved in very small quantities in the loess sediment indicates the presence of vegetation; this can also be observed through the presence of carbonated concretions developed around herbaceous rootlets (for example, Wang and Follmer (1998); Hatté et al. (2001a)). The values of this isotopic ratio also allow the characterization of the type of vegetation which trapped the dust during its deposition, and therefore the associated environmental and climatic conditions. Distinctions may be made at the level of the photosynthetic cycle (plants in C3 compared to those in C4) or within a similar photosynthetic type through the definition of seasonal variations in temperature or precipitation.

The inversion of vegetation models incorporating an isotopic fractionation module allows the reconstruction of fluctuations in the annual rainfall patterns occurring during the deposition of the sequence (Hatté and Guiot (2005)) (Fig. 13.7). Analysis of other chemical elements, such as rare earth elements, or other isotopes, contributes to the

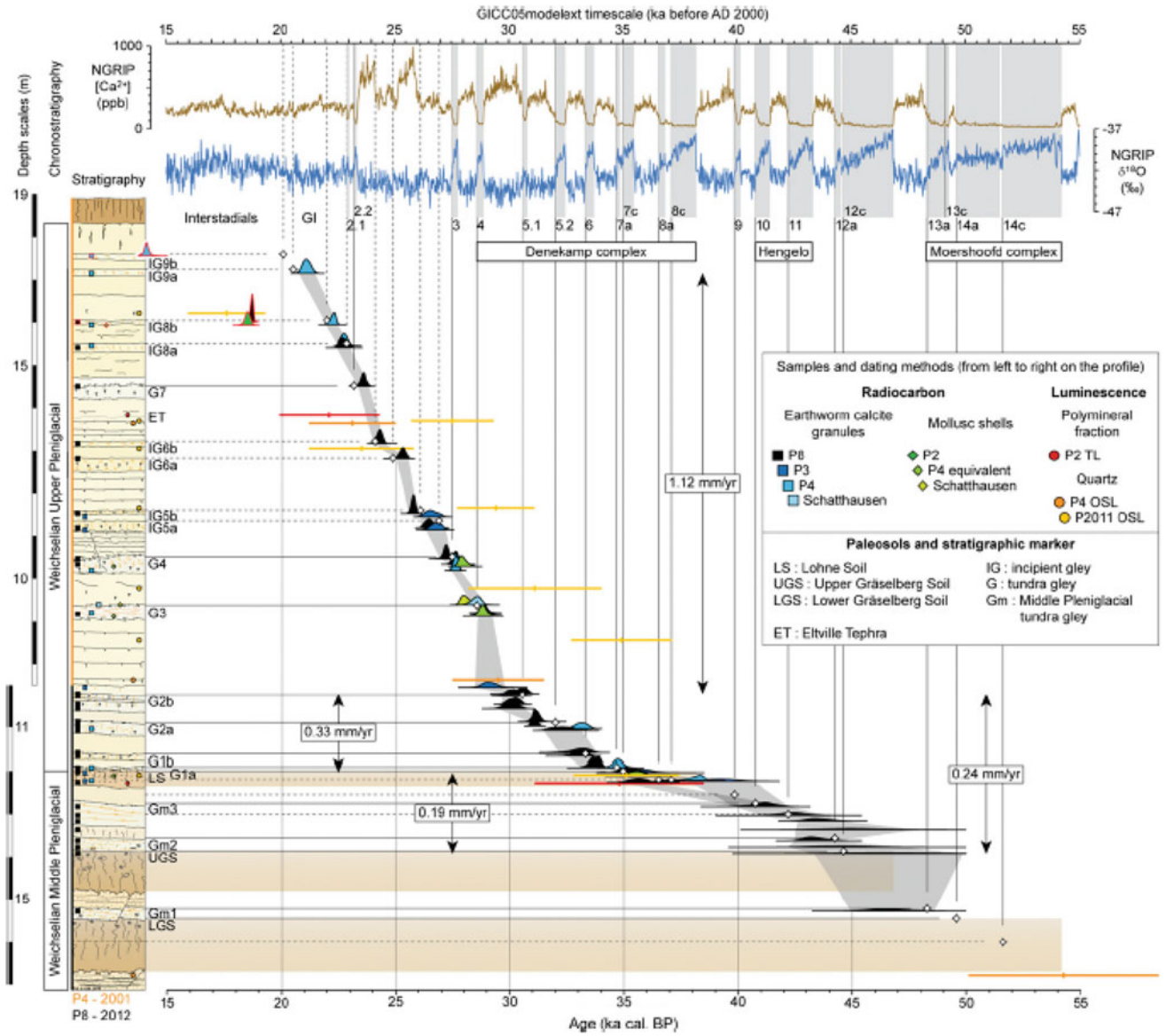

Fig. 13.8 ^{14}C dates obtained from earthworm granules collected in the different paleosols from the Nussloch sequence. Correlation with the NGRIP climate changes described by the dust and the $\delta^{18}O$ variations from Moine et al. (2017)

search for the origin of the transported matter, using samples taken from potential source areas, and thus, to estimate the transport-related mechanisms (Rousseau et al. (2014); Gallet et al. (1996); Guo et al. (2002)).

Tracing past precipitation and past temperature

At the same time as the abundance count of earthworm calcitic granules emerged as a paleoclimate proxy, study of their isotopic properties has also developed (Prud'homme et al. (2016), (2018)). The $\delta^{18}O$ granules and interlinked transfer functions between water cycle, air and soil temperatures allow the estimation of air temperatures. In Nussloch, the mean summer air temperature during Greenland interstadial has been estimated to have been 10–12 ± 4 °C (Prud'homme et al. (2016)). In line with loess organic $\delta^{13}C$ interpretation, $\delta^{13}C$ of earthworm granules has been interpreted as a proxy of paleoprecipitation. Thanks to transfer functions, the past precipitation in Nussloch during the Greenland interstadial has been estimated at about 159–574 mm/yr (Prud'homme et al. (2018)).

Loess Chronology

Loess chronology remains a major challenge since OSL returns a wide range of value depending on the choice of the mineral (type and grain size), the choice of light ray (IRSL,

OSL,), and the analytical choice to reconstruct the evolution through time of the ambient dose rate. Nevertheless, it provides a reliable frame allowing comparisons with speleothem or ice-core chronologies (Lang et al. (2003); Fuchs et al. (2013); Rousseau et al. (2013)).

^{14}C is limited by its 50–0 kyr range and by the fact that reliable supports such as charcoal or wood are rare in loess sequences. Trials on ubiquitous supports (loess OM bulk (Hatté et al. (2001b)) and alkane (Häggi (2014)) were not that conclusive, highly dependent on the status of the loess section studied and on the cleaning method of the outcrop. Even in the best conditions, they show poor reliability around (paleo) soil. However, the ^{14}C dates obtained from the calcitic earthworm granules allow perfect dating of the various paleosols (embryonic soils, tundra gleys and arctic brown paleosols) from which they are collected, as was recently demonstrated in the Nussloch sequence (Fig. 13.8) (Moine et al. (2017)). This new approach opens the door to precise and independent chronologies of loess sequences.

References

Antoine, P., et al. (1999). Last interglacial-glacial climatic cycle in loess-palaeosol successions of north-western France. *Boreas, 28,* 551–563.

Antoine, P., et al. (2009). Rapid and Cyclic Aeolian Deposition During the Last Glacial in European Loess: A High-Resolution Records from Nussloch, Germany. *Quaternary Science Reviews, 28*, 2 955–2 973.

Fuchs, M., et al. (2013). The loess sequence of Dolni Vestonice, Czech Republic: A new OSL based chronology of the Last Climatic Cycle. *Boreas, 42,* 664–677. https://doi.org/10.1111/j.1502-3885.2012.00299.x.

Gallet, S., et al. (1996). Geochemical characterization of the Luochuan Loess-Paleosol sequence, China, and Paleoclimatic Implications. *Chemical Geology, 133,* 67–88.

Gerasimenko, N., & Rousseau, D.-D. (2008). Stratigraphy and Paleoenvironments of the Last Pleniglacial in the Kyiv Loess Region (Ukraine). *Quaternaire, 19*(4), 293–307.

Guo, Z. T., et al. (2002). Onset of Asian desertification by 22 Myr ago inferred from loess deposits in China. *Nature, 416,* 159–163.

Häggi, C., et al. (2014). On the stratigraphic integrity of leaf-wax biomarkers in loess paleosols. *Biogeosciences, 11*, 2455–2463. Pécsi, M. (1990). Loess Is not just the accumulation of dust. *Quaternary International, 7/8*, 1–21.

Hatté, C., et al. (2001a). $\delta^{13}C$ Variation of loess organic matter as a potential proxy for paleoprecipitation. *Quaternary Research, 55,* 33–38.

Hatté, C., et al. (2001b). Development of an accurate and reliable ^{14}C chronology for loess sequences. Application to the loess sequence of Nußloch (Rhine valley, Germany). *Radiocarbon, 43,* 611–618.

Hatté, C., & Guiot, J. (2005). Palaeoprecipitation reconstruction by inverse modelling using the isotopic signal of loess organic matter: application to the Nussloch Loess Sequence (Rhine Valley, Germany). *Climate Dynamics, 25,* 315–327.

Kukla, G., et al. (1990). Magnetic susceptibility record of Chinese Loess. *Transactions of the Royal Society Edinburgh: Earth Sciences, 81,* 263–288.

Kukla, G. J., & An, Z. S. (1989). Loess stratigraphy in central China. *Palaeogeography, Palaeoclimatology, Palaeoecology, 72,* 203–225.

Lagroix, F., & Banerjee, S. K. (2002). Paleowind directions from the magnetic fabric of loess profiles in Central Alsaka. *Earth and Planetary Science Letters, 195,* 99–112.

Lang, A., et al. (2003). High-resolution chronologies for loess: Comparing AMS ^{14}C and optical dating results. *Quaternary Science Reviews, 22,* 953–959.

Lautridou, J. P. (1985). *Le Cycle Périglaciaire Pléistocène en Europe du Nord-Ouest et plus particulièrement en Normandie* (pp. 908). Centre Géomorphologie Caen: Thèse Etat, Université Caen, Caen.

Liu, T. S., et al. (1985). *Loess and the environment* (pp. 251). Beijing: China Ocean Press.

Lu, H. Y., et al. (2007). Phytoliths as quantitative indicators for the reconstruction of past environmental conditions in China II: Palaeoenvironmental reconstruction in the loess plateau. *Quaternary Science Reviews, 26,* 759–772.

Maher, B. A., & Thompson, R. (1995). Paleorainfall reconstructions from pedogenic magnetic susceptibility variations in the Chinese Loess and Paleosols. *Quaternary Research, 44,* 383–391.

Moine, O., et al. (2002). Paleoclimatic reconstruction using mutual climatic range on terrestrial mollusks. *Quaternary Research, 57,* 162–172.

Moine, O., et al. (2005). Terrestrial molluscan records of Weichselian Lower to Middle Pleniglacial climatic changes from the Nussloch loess series (Rhine Valley, Germany): the impact of local factors. *Boreas, 34,* 363–380.

Moine, O., et al. (2017). The impact of Last Glacial climate variability in west-European loess revealed by radiocarbon dating of fossil earthworm granules. *Proceedings of the National Academy of Sciences, 114,* 6209–6214.

Oches, E. A., & McCoy, W. (1995). Amino Acid geochronology applied to the correlation and dating of central European loess deposits. *Quaternary Science Review, 14,* 767–782.

Pécsi, M. (1990). Loess is not just the accumulation of dust. *Quaternary International, 7*(8), 1–21.

Prud'homme, C., et al. (2015). Earthworm calcite granules: a new tracker of millennial-timescale environmental changes in Last Glacial loess deposits. *Journal of Quaternary Science, 30,* 529–536.

Prud'homme, C., et al. (2016). Palaeotemperature reconstruction during the Last Glacial from $\delta^{18}O$ of earthworm calcite granules from Nussloch loess sequence, Germany. *Earth and Planetary Science Letters, 442,* 13–20.

Prud'homme, C., et al. (2018). $\delta^{13}C$ of earthworm calcite granules: a new proxy for palaeoprecipitation reconstructions during the Last Glacial in Western Europe. *Quaternary Science Reviews, 179,* 158–166.

Pye, K. (1995). The nature, origin and accumulation of loess. *Quaternary Science Reviews, 14,* 653–667.

Pye, K., & Zhou, L. P. (1989). Late Pleistocene and Holocene Aeolian Dust Deposition in North China and the Northwest Pacific-Ocean. *Palaeogeography, Palaeoclimatology, Palaeoecology, 73,* 11–23.

Rousseau, D.-D. (1987). Paleoclimatology of the Achenheim Series (Middle and Upper Pleistocene, Alsace, France). A Malacological Analysis. *Palaeogeography, Palaeoclimatology, Palaeoecology, 59,* 293–314.

Rousseau, D.-D. (1991). Climatic transfer function from quaternary mollusks in european loess deposits. *Quaternary Research, 36,* 195–209.

Rousseau, D.-D., et al. (2001). Late Pleistocene environments of the central Ukraine. *Quaternary Research, 56,* 349–356.

Rousseau, D.-D. et al. (2007a). Evidence of cyclic dust deposition in the US great plains during the last deglaciation from the high-resolution analysis of the peoria loess in the eustis sequence

(Nebraska, USA). *Earth and Planetary Science Letters, 262*, 159–174.

Rousseau, D.-D. et al. (2007b). Link Between European and North Atlantic Abrupt Climate Changes over the Last Glaciation. *Geophysical Research Letters, 34*, https://doi.org/10.1029/2007gl031716.

Rousseau, D. D., et al. (2013). Major dust events in Europe during marine isotope stage 5 (130–74 ka): A climatic interpretation of the 'markers. *Climate of the Past, 9,* 2213–2230.

Rousseau, D.-D., et al. (2014). European Glacial Dust Deposits: Geochemical Constraints on Atmospheric Dust Cycle Modeling. *Geophysical Research Lettters, 41,* 7666–7674. https://doi.org/10.1002/2014GL061382.

Sima, A., et al. (2009). Imprint of North-Atlantic millennial-timescale variability on Western European loess deposits as viewed in a dust emission model. *Quaternary Science Reviews, 28,* 2851–2866.

Sun, Y. et al. (2008). Tracing the provenance of fine-grained dust deposited on the central Chinese loess plateau. *Geophysical Research Letters, 35*. https://doi.org/10.1029/2007GL031672.

Taylor, S. N., et al. (2014). Mineral magnetic characterization of the Upper Pleniglacial Nussloch loess sequence (Germany): an insight into local environmental processes. *Geophysical Journal International, 199,* 1463–1480.

Wang, H., & Follmer, L. R. (1998). Proxy of monsoon seasonality in carbon isotopes from paleosols of the Southern Chinese loess plateau. *Geology, 26,* 987–990.

Wu, N. Q. et al., (2001). Orbital forcing of terrestrial mollusks and climatic changes from the loess plateau of China during the past 350 ka. *Journal of Geophysical Research—Atmospheres*, *106*, 20 045–20 054.

Zhou, L. P., et al. (1990). Partly Pedogenic Origin of Magnetic Variations in Chinese Loess. *Nature, 346,* 737–739.

Air-Ground Interface: Reconstruction of Paleoclimates Using Speleothems

14

Dominique Genty and Ana Moreno

Speleothems: Description, Distribution, Formation and Preservation

The term speleothem refers to carbonate deposits in caves: mainly stalactites, stalagmites and stalagmite floors. It is taken from the English (*speleothem*) which has its roots in Greek signifying 'subject' (*thema*) and 'cave' (*spelaion*). Composed of calcium carbonate, speleothems are most commonly made of calcite (ones in aragonite are rarer and less studied). Carbonate massifs which contain caves, within which speleothems are found, are widely scattered around the globe, and are found at all latitudes and in all continents, although less frequently in the southern hemisphere (Fig. 14.1).

Speleothems acquire their geochemical and structural characteristics as a result of the infiltration of rainwater through a limestone or dolomitic environment. The formation process is basically comprised of three steps: (1) at ground level, CO_2 (produced by the roots of plants and by microorganisms in the soil) is dissolved in rainwater; (2) the dissolution of the surrounding rock (limestone, dolomitic limestone, calcareous dolomites) either at ground level (known as dissolution in an open system – at the meeting of the three elements: air, water and rock), or at the level of the many tiny fissures in the surrounding carbonate (closed system); (3) once it arrives in the underground gallery, there is degassing of CO_2 and precipitation of $CaCO_3$.

Drops of water, emerging from micro-fissures, form stalactites at the ceiling of the gallery, and stalagmites on the ground. It is the latter which is most frequently studied because of its simple structure (resembling inverted interlocking calcite cups). The physical and chemical parameters that allow us to reconstruct paleoclimates from speleothems (stable isotopes, trace elements, growth rate) depend partly on the precipitation conditions of the calcite (the temperature in the cave, flow rate, moisture level) and, partly on the geochemical characteristics of the water supplying the speleothems (McDermott 2004; Fairchild and Baker 2012). Speleothems, once formed, seldom undergo subsequent changes (no erosion, no internal recirculation, some rare examples of diagenesis, such as, for example, the transformation of aragonite into calcite). The calcite in speleothems is a material that can be dated as far back as 500 ka using radiometric methods (U-Th series dating) or even as far back as several million years depending on their geochemical characteristics (U-Pb dating).

Growth and Chronology of Speleothems

The growth of speleothems is determined by the presence of infiltrating water. As a result, extremely dry or cold climates (water freezing above ground), causes a halt in growth (hiatus) except in certain exceptional circumstances found in the mountains (Luetscher et al. 2015). The speed of growth of a stalagmite depends not only on the amount of water infiltrating into the karst, but also on a number of environmental factors such as the Ca^{2+} concentration of the infiltrating water, the thickness of the film of water on the surface of the speleothem, the temperature and the partial pressure of CO_2 in the cave's atmosphere. Geochemical modeling of growth shows that the dominant factors are the flow rate and the Ca^{2+} content of the water (Dreybrodt

D. Genty (✉)
Laboratoire des Sciences du Climat et de l'Environnement, LSCE/IPSL, CEA-CNRS-UVSQ, Université Paris-Saclay, 91190 Gif-sur-Yvette, France
e-mail: dominique.genty@lsce.ipsl.fr; dominique.genty@u-bordeaux.fr

EPOC (Environnements et Paléoenvironnements Océaniques et Continentaux), Université de Bordeaux, bat. B18N, Allée Geoffroy Saint-Hilaire, 33615 Pessac Cedex, France

A. Moreno
Instituto Pirenaico de Ecología—CSIC, Avda. Montañana 1005, 50059 Saragossa, Spain

G. Ramstein et al. (eds.), *Paleoclimatology*, Frontiers in Earth Sciences,
https://doi.org/10.1007/978-3-030-24982-3_14

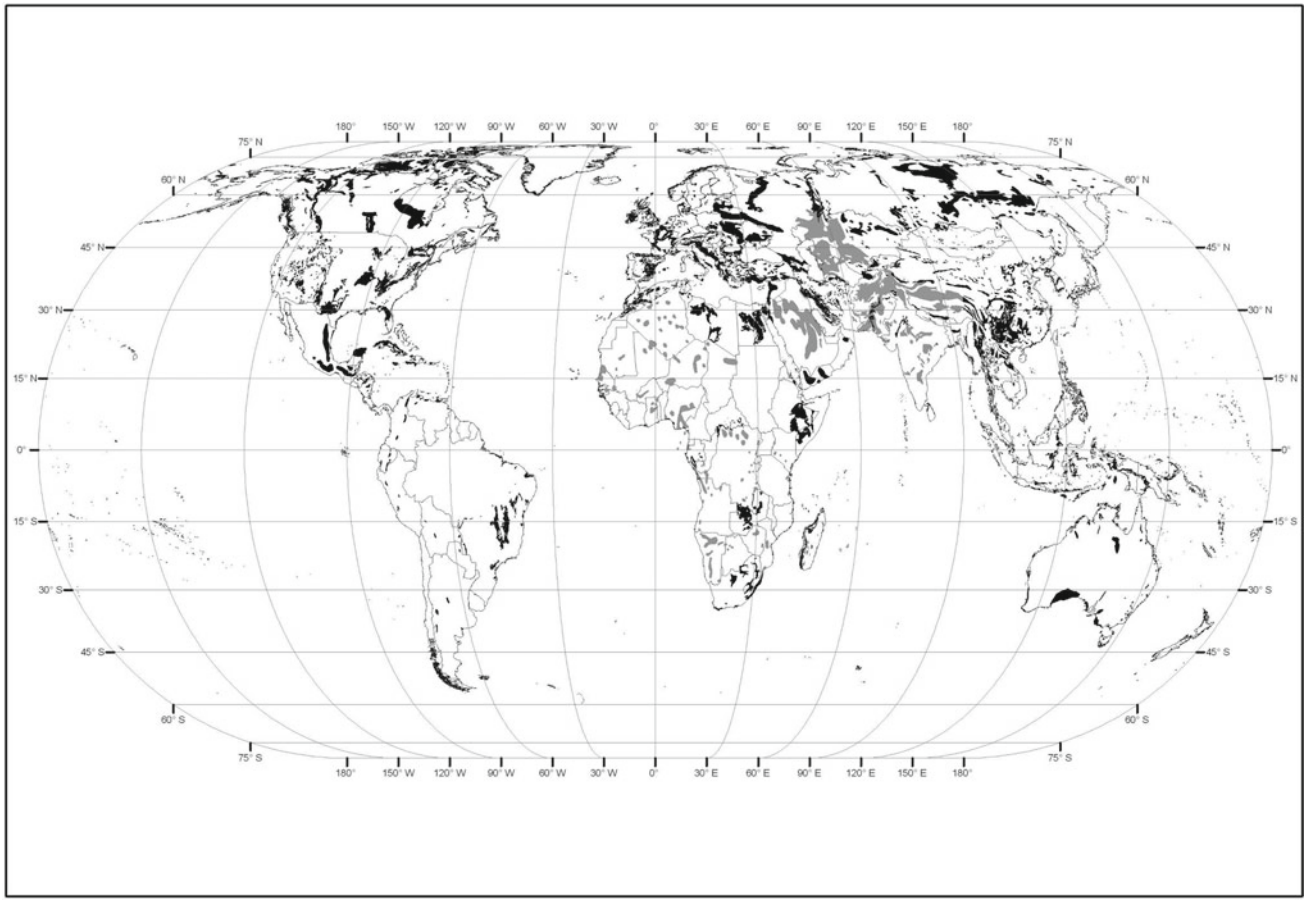

Fig. 14.1 Map showing the distribution of carbonate massifs (in black) where speleothems can be found (according to Ford and Williams (2007) and the University of Auckland http://web.env.auckland.ac.nz/our_research/Karst/)

1988). This model was verified by comparing the theoretical growth rates with the actual growth rates measured on modern calcite deposits at various latitudes. In a cold and humid climate (Scotland), the average vertical growth of a stalagmite is only 20 microns/year, while it can reach 1 mm/year in the caves of southern France (Baker et al. 1998). The sensitivity of the growth rate to environmental conditions provides an indicator of paleoclimatic conditions: more speleothems with a faster growth rate are produced in warm and humid periods than in cold, dry periods. It appears that below a certain rainfall threshold, the growth of speleothems may slow down due to under-saturation of the infiltration water.

The temperature of a cave is generally stable throughout the year and is close to the average annual exterior temperature. Depending on the depth of the cave, the exterior thermal wave which determines the cave temperature may take between several months and several years to travel through the thickness of the rock. However, there are marked seasonal variations in the water infiltration rate and in the concentrations of the different chemical elements (Ca, Sr, Mg, U, MO, etc.) even if the average infiltration time can be several years (Genty and Deflandre 1998; Genty et al. 2014). These have resulted in a seasonal variation in the growth rate and are probably responsible for the formation of visible or luminescent annual growth laminae (Genty and Quinif 1996). When such laminae are present, their identification (a clear and dark lamina is deposited each year) can provide a precise timeline and allows the study of the evolution of an isotopic or geochemical parameter to the nearest year. But annual lamination of stalagmites is not systematic and is often broken; examples rarely go back further than 1000 years (Baker et al. 2015).

The most common way to date speleothems is to measure the isotope series of uranium: ^{234}U, ^{238}U, ^{230}Th (See Chap. 6). Uranium, which is soluble, enters the karst system, while thorium, insoluble, remains above ground. The ^{230}Th measured in the stalagmites is therefore, theoretically, the result of the disintegration of ^{234}U. Sometimes, thorium is also brought by infiltrated water, often along with some detrital clay; a correction must then be made to take account of ^{232}Th (linked to detrital contamination) in the light of the initial $^{230}Th/^{232}Th$ ratio (Hellstrom 2006). Finally, uncertainty on the age of a calcite fragment is linked to the size of

the correction for detritus, and to the uranium concentration in the speleothem (varying from ~30 ppb to ~1 ppm). This is, on average, between less than 1% and 5% for the last three climate cycles, as far back as ~500 ka. The most common current technique to measure these isotopes is by MC-ICP-MS; this requires between a few milligrams to tens of milligrams of calcite to make a measurement. Moreover, thanks to the technical progress in ICP-MS equipment and an improved understanding of half-life constants of radioactive isotopes in recent years, the error in U-Th dates can be even lower (Cheng et al. 2013). Other methods are used incidentally, such as ^{14}C, whose concentration at the moment of deposition of the calcite depends on the proportions of atmospheric CO_2 and of CO_2 without ^{14}C, coming from the dissolution of limestone (Genty et al. 1999), ^{226}Ra for recent millennia (Ghaleb et al. 2004), and the U-Pb method which can trace back more than a million years (Woodhead et al. 2006).

Paleoclimate Reconstruction: A Qualitative Approach

The proxies used in speleothems to reconstruct past climates are isotopes of calcite ($\delta^{18}O_c$, $\delta^{13}C_c$), isotopes of fluid inclusions trapped in the calcite (δD, $\delta^{18}O$), trace elements (Sr, Ba, Mg, U), organic matter (lipids, amino acids), petrography and the growth rate.

The most common crystalline fabrics (layout and shape of the calcite crystals) in stalagmites is the palisading columnar one: large elongated crystals perpendicular to the growth laminae. However, the addition of detrital components, variations in humidity, in temperature or in pCO_2 over the course of climate variations can produce a variety of crystalline fabrics (dendritic, fibrous, microcrystalline, etc.). Even if we could establish links between crystal structures and environmental conditions through the study of modern calcite deposits (Frisia et al. 2000), this type of relationship is complex and should be examined with caution. Recently, a new approach to stalagmite characterization consists of precisely describing the petrography and categorizing the stalagmites and their bounding surfaces into six different classes (from individual crystallites to major nonconformities) (Martín-Chivelet et al. 2017).

Speleothem calcite contains, either in its crystalline defects, or by substitution of Ca in the crystal lattice, minor or trace elements, which provide information on the paleoenvironment (Fairchild et al. 2000). Interpretation of this is complex because it involves several factors: composition of the soil and of the surrounding limestone, the intensity of dissolution and the precipitation conditions of the calcite (temperature, supersaturation, growth rate, etc.). At the annual level, analysis of these trace elements contributes to an understanding of the dynamics of infiltration, especially when the elements measured are linked to the residence time of the infiltrating water. A new model called I-Stal was recently developed to investigate the factors involved in the interpretation of trace elements in speleothems (Stoll et al. 2012). To measure these elements, precise techniques are used to analyze points of a few micrometers in diameter on a polished section of stalagmite (LA-ICP-MS, XRF, X fluorescence by synchrotron, ionic microprobe). During the transfer of these trace elements, organic colloids play a major role. The sensitivity of each one to environmental conditions is different; for example, Ba, Na and Sr may be sensitive to the speleothem growth rate while Mg and U may reflect paleohydrology. Some, such as P, Zn and Cu, are related to the vegetation above ground. Trace elements are also chronological markers: when the annual laminae are not visible in the calcite structure, then the analysis of trace elements can reveal seasonal variations, thereby providing a relative or absolute chronology accurate to the nearest year. This type of analysis is used to determine the duration of a rapid climate event or of a transition (Bourdin et al. 2011).

The stable isotopes of calcite are the most commonly used to reconstruct climate variations, even though interpreting them into temperature and precipitation terms is not easy. The $\delta^{18}O_c$ of the calcite, when it precipitates at isotopic equilibrium (see below), depends on the temperature of the precipitation of calcite (temperature in the cave and therefore the average annual exterior temperature) and on the $\delta^{18}O_w$ of the infiltrating water. The latter is linked to the exterior temperature above the site, to the amount of water extracted from the cloud masses between the source of evaporation and the site and to the isotopic composition of the source, usually the ocean (isotope distillation process). During the precipitation of calcite, there is an inverse relationship between $\delta^{18}O_c$ and temperature (~−0.24‰/°C), whereas the relationship is direct between the rainfall $\delta^{18}O$ and outside temperature of (e.g. 0.3–0.7‰/°C). In summary:

$$\delta^{18}O_c = f\left(\delta^{18}O_w,\ T_{cave}, \text{isotopic equilibrium}\right)$$

with:

$$\delta^{18}O_w = f\left(\delta^{18}O_{rain}, \text{evapotranspiration in some cases}\right)$$

and

$$\delta^{18}O_{rain} = f\left(T_{ext.}, \text{quantity of rain, trajectory of cloud masses}, \delta^{18}O_{source}\right).$$

Consequently, depending on the location of the site relative to the main source of evaporation and on the prevailing conditions when the water masses were transported, the relationship between $\delta^{18}O_c$ and climate will be more or less marked. Thus, in the stalagmites of Southeast Asia the variations in intensity of the monsoon over the last two

climate cycles can be seen remarkably well: the $\delta^{18}O_c$ is systematically depleted by ~4‰ during periods of strong summer monsoon, mainly due to the effect of mass (the $\delta^{18}O$ of the rain is inversely proportional to the volume of rainfall) but also due to changes in the source (Wang et al. 2008). Thanks to the many U-Th datings carried out on several stalagmites in caves in Sanbao, Hulu and Dongge (25° N to 32° N, China), it has been shown that the $\delta^{18}O_c$ of the calcite had a periodicity of 23 ka and was directly correlated with changes in insolation at 65° N, demonstrating that variations in the monsoons were caused by orbital changes (Fig. 14.2) (Wang et al. 2008). Superimposed on these large climate variations, millennial climate events were also recorded and linked to Dansgaard-Oeschger events (D/O) detected in the Greenland ice, which shows the strong connection between the climate systems of South Asia and the North Atlantic. This interconnection between the monsoon regime and the North Atlantic region was confirmed by one of the longest and most precise paleoclimate recordings produced by the study of Chinese speleothems (Cheng et al. 2016). The variations in monsoon intensity were reconstructed for the past 640,000 years with an unmatched precision. The multiplicity of samples, precise U-Th dating and the very high resolution of isotopic analyses suggest new theories on the causes of the major glacial-interglacial climate cycles and millennial variability. One of these theories posits that the period between terminations (glacial-interglacial transitions) is equal to a multiple of the length of the precession cycles; moreover, a very strong teleconnection between the dynamics of the ice caps of the northern hemisphere, the circulation of the Atlantic Ocean and the Asian monsoon is implied. Similarly, the variation in monsoon intensity in South America was recorded in stalagmites from southern Brazil (24° S to 27° S), at the orbital and the millennial scale (Cruz et al. 2005). In this case, the latitudinal changes in the position of the ITCZ (intertropical convergence zone) seem to be the root cause of these variations.

At higher latitudes, in Europe for example, the $\delta^{18}O_c$ of calcite has a less pronounced response to changes in climate, probably because of the opposite effects controlling the $\delta^{18}O_c$ of calcite (e.g. external temperature impacts on the $\delta^{18}O$ of the rain while cave temperature impacts on $\delta^{18}O_c$ of calcite). However, the study of several European samples has revealed a certain logic within the paleoclimate chronicles of varying appearance: there is a variable gradient in the $\delta^{18}O_c$ speleothems during the Holocene along a west-east transect (McDermott et al. 2011). This is related to differences in warming during the Holocene depending on longitude and also on different atmospheric circulations. This logic shows that even if speleothems do not precipitate at isotopic equilibrium, they contain valuable information on atmospheric paleocirculation. As a result of the influence of these multiple climatic, hydrological and kinetic factors, the evolution of the $\delta^{18}O_c$ of the speleothem calcite is not uniform from one region to another: in general the $\delta^{18}O$ decreases when the climate becomes warm and humid (in temperate regions for example), while this trend may be reversed ($\delta^{18}O$ increases as the temperature increases) at certain altitudes as has been observed in the Alps (Boch et al. 2011; Moseley et al. 2014) and in eastern Europe on the coast of the Black Sea (Fleitmann et al. 2009).

The $\delta^{13}C_c$ of calcite may also react to climate changes, and sometimes in a more obvious way than $\delta^{18}O_c$. The carbon atoms of the calcite molecule, $CaCO_3$, which makes up the speleothems come from two main sources: CO_2 from the soil and $CaCO_3$ from the surrounding rock. Soil CO_2, produced by plant roots and microbial activity, has a $\delta^{13}C_c$ close to −24‰ (for C3 type plants, most frequently found in temperate areas), $CaCO_3$ from marine limestone has a $\delta^{13}C_c$ of between ~−2 and +2‰. It has been shown that the main source of carbon in speleothems is the CO_2 from the soil which can represent up to 90% of C contained in the $CaCO_3$ of speleothems (Genty et al. 1998). In several sites in the South of France, the carbon from the dissolution of limestone (also called dead carbon because it contains no ^{14}C) represents, in this particular case, only 15 ± 5% of the C in the speleothems. Consequently, any change in the vegetation above a cave brought about by climate change, such as proportion of type C3 to C4 or vegetation density, will have an impact on the $\delta^{13}C$ of the CO_2 in the soil and thus on the $\delta^{13}C_c$ of the speleothems. In summary:

$\delta^{13}C_c = f$ (type of vegetation, density of vegetation, hydrology, isotopic equilibrium).

The $\delta^{13}C_c$ in the stalagmites in the Villars cave (South-West France) shows abrupt changes from −2‰ to −5‰ over the last 80 ka. These have been linked to Dansgaard-Oeschger events recorded in Greenland ice cores and to temperature reconstructions using analyzes of pollen from lakes and marine cores (Genty et al. 2003).

The value of this comparison is, firstly, to test the chronology from other archives against the absolute chronology provided by speleothems, and if necessary, to adjust it. Refining the age of an abrupt climatic transition, such as the one which occurred at the beginning of D/O 12 (Fig. 14.3), is important in order to find out its cause by comparing a sequence of climate events with the external forcings and with archives from other latitudes. Comparison with pollen reconstructions shows the close link between changes in vegetation brought on by variations in temperature and humidity, and the $\delta^{13}C_c$ recorded in speleothems. Other examples show that the $\delta^{13}C_c$ recorded the last deglaciation, in New Zealand as well as in Europe (Genty et al. 2006; Moreno et al. 2010). Thus, a stalagmite from the Chauvet cave (Ardèche, France) records the climate events (e.g. Bølling-Allerød, Intra Allerød Cold Period, Younger-Dryas) that punctuated the last deglaciation with a

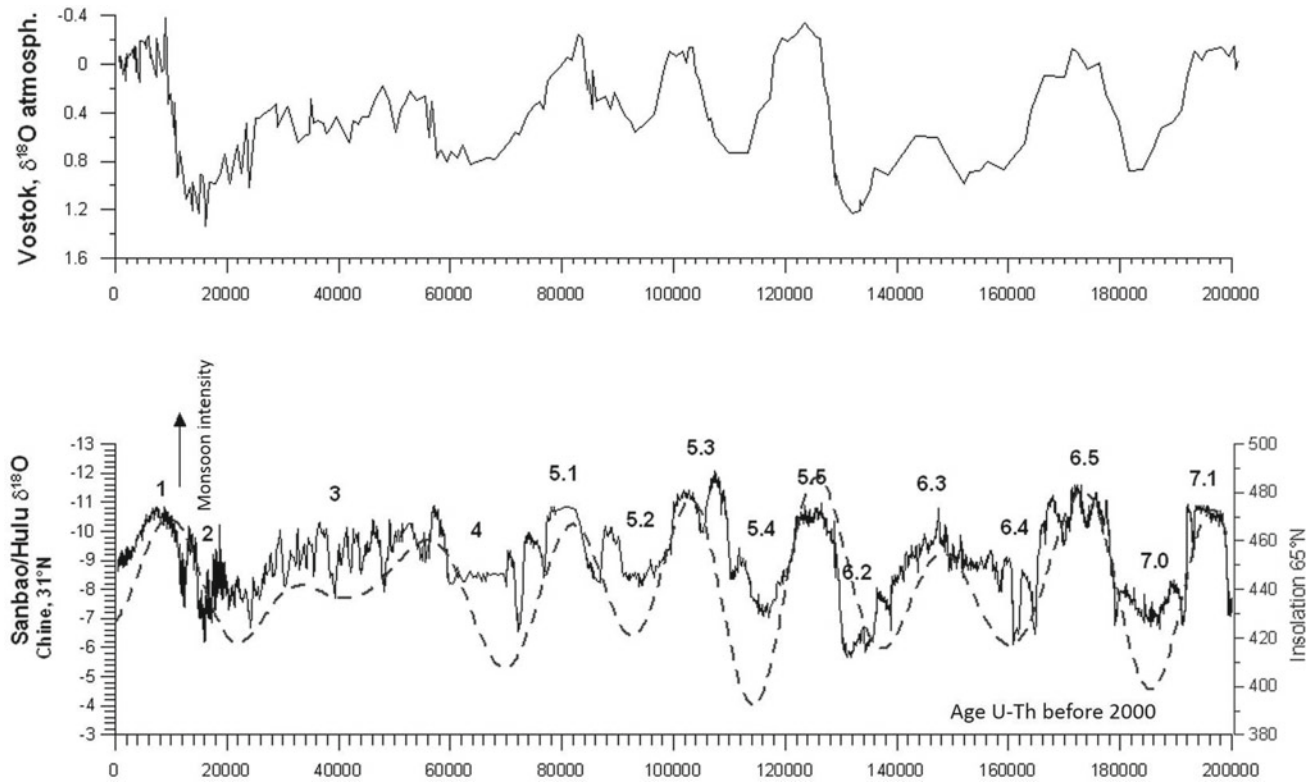

Fig. 14.2 After Wang et al, 2008—Example of a recording of the variations in intensity of the Asian monsoon using the $\delta^{18}O_c$ of Chinese stalagmites from Sanbao and Hulu caves (bottom graph). Comparison with July insolation at 65°N and the $\delta^{18}O_{atm}$ of Vostok ice core, Antarctica (dashed line). There is a good correlation between $\delta^{18}O_c$ and the insolation, dominated here by the precession (cycles of 23 ka). The $\delta^{18}O_{atm}$ from Vostok reflects the impact of the precession on low latitude water cycle and productivity of the biosphere (See Chap. 11 on polar ice)

resolution comparable to that obtained in ice cores from Greenland, with, however, some differences in the trends caused by different climate gradients.

Paleoclimate Reconstruction: A Quantitative Approach

During its growth, the speleothem calcite traps water in the form of microscopic fluid inclusions (1–10 microns large) or, more rarely, macroscopic ones (several mm). This water comes from the rainwater contemporaneous to the calcite deposition and can therefore be dated indirectly by dating the surrounding calcite. With an average composition of only a few nL of water per gram of calcite, the technical difficulties of extracting and analyzing this water have only recently been resolved (Verheyden et al. 2008; Vonhof et al. 2006; Affolter et al. 2014; Arienzo et al. 2013). There are many reasons for measuring the isotopic composition (δD, δ^{18}O) of the fluid inclusions of speleothems: (1) the value of the δ^{18}O of the inclusion water is close to that of the rainwater and so is a tracer of atmospheric circulation; (2) in conjunction with the $\delta^{18}O_c$ of the calcite, it is possible to calculate the temperature of calcite formation in the cave, which is equivalent to the average annual exterior temperature. For this second case, it is necessary for the calcite precipitation to have occurred at thermodynamic equilibrium (isotopic, by extension), in other words, that the exchanges between the different carbon species (e.g.HCO_3^-, CO_3^{2-}, CO_2 gas) have been completed.

Examples using this new technique are still rare, but are among the only ones, on land, to express the evolution of temperature (from direct measurements) over a precise absolute time scale. A stalagmite from Peru has thus shown that the isotopic composition of the rainwater followed the local winter insolation (6° S) due to changes in the intensity of convective rainfall during the Holocene, themselves linked to latitudinal variations in the ITCZ (Van Breukelen et al. 2008). The temperature, calculated using the above method, varied little (±2 °C) over the last 13.5 ka, unlike at higher latitudes, as is shown by another example from Vancouver Island (Canada 49° N), where the temperature has varied by more than 10°C between 6 ka and 10 ka (Zhang et al. 2008).

However, this method cannot be applied to all speleothems. Indeed, conditions of low humidity or low pCO_2

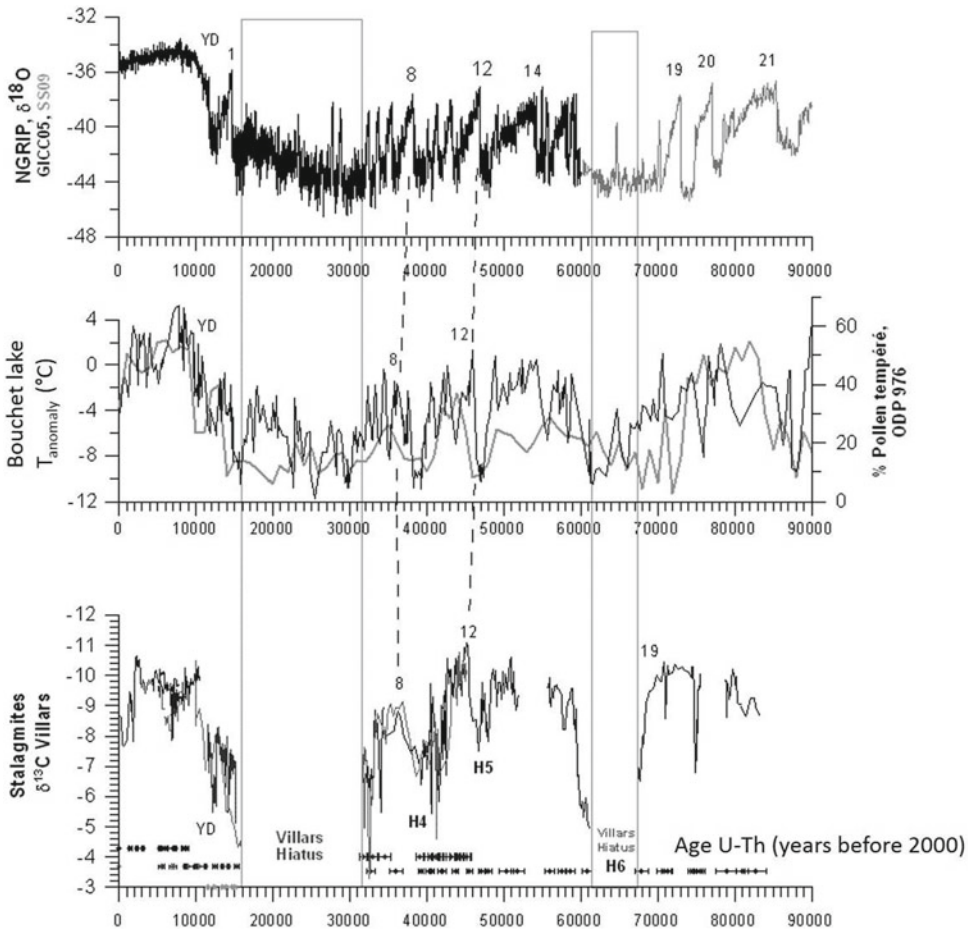

Fig. 14.3 Comparison between the $\delta^{13}C$ from Villars Cave stalagmites, the $\delta^{18}O$ from NGRIP (Greenland), the temperature reconstructions from Bouchet Lake (Massif Central) (Guiot et al. 1989) and marine core ODP976 from the south of Spain (Combourieu Nebout et al. 2002). The dots at the bottom of the graph show the U-Th datings with 2σ error bars

inside the cave can cause rapid degassing of CO_2, and thus lead to a kinetic effect causing a thermodynamic disequilibrium. There are several equations linking the isotopic compositions of calcite and of water with temperature, allowing this equilibrium to be checked (Kim and O'Neil 1997; Tremaine et al. 2011). However, the study of deposits of modern calcite shows that many of them are not deposited at isotopic equilibrium, but rather reflect a kinetic effect (Genty 2008; Mickler et al. 2006). In this case, calculation of the temperature is not valid (the $\delta^{18}O_c$ measured from calcite is generally too high, causing the calculated temperature to be too low).

There is a recent, promising method to reconstruct paleotemperatures using only isotopes from the mineral phase of the calcite, thus overcoming the difficulty of extracting water from the fluid inclusions (Daeron et al. 2008, 2011). It involves the clumped isotopes of the CO_3^{2-} molecules and is based on the thermo-dependence of the isotopic exchanges between these different molecules:

$$^{13}C^{16}O_3^{2-} + {}^{12}C^{18}O^{16}O_2^{2} < = > {}^{13}C^{18}O^{16}O_2^{2-} + {}^{12}C^{16} + {}^{12}C^{16}O_3^{2}$$

Called the Delta 47 method, this method reflects the statistical overabundance of mass 47 clumped isotopes in CO_2 ($^{13}C^{18}O^{16}O$) produced by acidc attack of carbonate minerals. When applied to speleothems which were deposited at thermodynamic equilibrium, precipitation temperatures can be reconstructed independently of the previous method which uses the $\delta^{18}O$ of the calcite and of the fluid inclusions. However, tests on modern deposits from caves in the South of France and in vitro experiments show the existence of a kinetic effect during precipitation (Daeron et al. 2011, 2008). In this case, the temperature can only be calculated by using both the Delta 47 measurement and the measurement of the $\delta^{18}O$ in calcite and fluid inclusions. The value of this is twofold: in addition to calculating the precipitation temperature, this method quantifies the state of thermodynamic disequilibrium, often difficult to detect, and which is also a reflection of the conditions of the paleoenvironment.

Another way of quantifying climate parameters is by calibrating proxies from the growth laminae of fast-growing modern stalagmites (Baker et al. 2007; Domínguez-Villar et al. 2018). The method consists of finding the best correlation between the signal measured on the stalagmite (e.g. the thickness of the annual growth laminae) and the climate signal from instrumental measurements outside

(e.g., rainfall). However, the water arriving at the end of a stalactite is, in fact, a mixture of water from a variety of networks of large and small micro-fissures which are more or less complex, with a variable transfer time from the exterior to the inner gallery (ranging from a few hours to few weeks, months or years). This mixture was modeled by A. Baker in a cave in Ethiopia, with components of different ages: a small proportion (10–30%) of water flowing quickly through the rock (from a few days to a few weeks) and a greater proportion (70–90%), of the water passing through slowly (months to a few years). The variation in the amount of water arriving at the particular stalagmite being studied (which largely determines the thickness of the annual laminae) is calculated by applying this mixture model to the rainfall provided by meteorological data. The proxy (the thicknesses, in this case) is then compared with the amount of water supplying the stalagmite (modeled using this simple mixture model). The timeframe is given by the annual growth laminae. This new method, applied to stalagmites in Ethiopia, has helped to reconstruct summer rainfall over the last 80 years (Baker et al. 2007). Other work is being developed around the modeling of the $\delta^{18}O$ of infiltration water involving reservoirs in the unsaturated zone (Fairchild and Baker 2012) or by empirical adjustment with modern climate data (Domínguez-Villar et al. 2018).

Conclusion

Speleothems constitute continental paleoclimate records that allow the reconstruction of climate changes on a precise and absolute chronological timescale over the last half-million years or more. They help to improve the accuracy of chronologies derived from other climate archives and, depending on the site, can be used to reconstruct variations in rain intensity, rain source and vegetation density on the continent. However, to correctly interpret the proxies measured in the speleothems, it is essential to know the present day environment of the studied site: climate, seasonality, hydrology, origin of the precipitations. Recent methods of analysis of fluid inclusions and of Delta 47 create opportunities to establish long series of continental temperature changes and of the isotopic composition of rainwater. The recent proliferation of studies of speleothems and the increasingly structured organization of the scientific community working on this archive (Karst Record symposiums for example) have led to the discovery of important results on climate change and their causes. Interactions between increasingly large datasets (INTIMATE-Moreno et al. 2014, SISAL database being constructed, Comas Bru et al. 2017) and climate models are multiplying so as to better understand the processes and causes of climate variations.

References

Affolter, S., Fleitmann, D., & Leuenberger, M. (2014). New online method for water isotope analysis of speleothem fluid inclusions using laser absorption spectroscopy (WS-CRDS). *Climate of the Past, 10,* 1291–1304. https://doi.org/10.5194/cp-10-1291-2014.

Arienzo, M. M., Swart, P. K., & Vonhof, H. B. (2013). Measurement of δ18O and δ2H values of fluid inclusion water in speleothems using cavity ring-down spectroscopy compared with isotope ratio mass spectrometry. *Rapid Communications in Mass Spectrometry, 27,* 2616–2624. https://doi.org/10.1002/rcm.6723.

Baker, A., Asrat, A., Fairchild, I. J., Leng, M. J., Wynn, P. M., Bryant, C., & Umer, M. (2007). Analysis of the climate signal contained within delta O-18 and growth rate parameters in two ethiopian stalagmites. *Geochimica et Cosmochimica Acta*, *71*, 2975–2988.

Baker, A., Genty, D., Dreybrodt, W., Barnes, W. L., Mockler, N. J., & Grapes, J. (1998). Testing theoretically predicted stalagmite growth rate with recent annually laminated samples: Implications for past stalagmite deposition. *Geochimica et Cosmochimica Acta, 62,* 393–404.

Baker, A., Hellstrom, J. C., Kelly, B. F. J., Mariethoz, G., & Trouet, V. (2015). A composite annual-resolution stalagmite record of North Atlantic climate over the last three millennia. *Scientific Reports, 5,* 10307. https://doi.org/10.1038/srep10307.

Boch, R., Cheng, H., Spötl, C., Edwards, R. L., Wang, X., & Häuselmann, P. (2011). NALPS: A precisely dated European climate record 120–60 ka. *Climate of the Past Discussions, 7,* 1049–1072. https://doi.org/10.5194/cpd-7-1049-2011.

Bourdin, C., Douville, E., & Genty, D. (2011). Alkaline-earth metal and rare-earth element incorporation control by ionic radius and growth rate on a stalagmite from the Chauvet Cave, Southeastern France. *Chemical Geology, 290,* 1–11.

Cheng, H., Edwards, R. L., Sinha, A., Spötl, C., Yi, L., Chen, S., et al. (2016). The Asian monsoon over the past 640,000 years and ice age terminations. *Nature, 534,* 640–646. https://doi.org/10.1038/nature18591.

Cheng, H., Lawrence Edwards, R., Shen, C.-C., Polyak, V. J., Asmerom, Y., Woodhead, J., et al. (2013). Improvements in 230Th dating, 230Th and 234U half-life values, and U-Th isotopic measurements by multi-collector inductively coupled plasma mass spectrometry. *Earth and Planetary Science Letters, 371–372,* 82–91. https://doi.org/10.1016/j.epsl.2013.04.006.

Comas Bru, L., Burstyn, Y., & Scroxton, N. (2017). From caves to climate: Creating the SISAL global speleothem database. *Past Global Change Magazine, 25*, 156–156. https://doi.org/10.22498/pages.25.3.156.

Combourieu Nebout, N., Turon, J. -L., Zahn, R., Capotondi, L., Londeix, L., & Pahnke, K. (2002). Enhanced aridity and atmospheric high-pressure stability over the western Mediterranean during the North Atlantic cold events of the past 50 ky. *Geology*, *30* (10), 863–866.

Cruz Jr, F. W., Burns, S. J., Karmann, I., Sharp, W. D., Vuille, M., Cardoso, et al. (2005). Insolation-driven changes in atmospheric circulation over the past 116,000 years in subtropical Brazil. *Nature, 434*, 63–66.

Daeron, M., Guo, W., Eiler, J., Genty, D., Blamart, D., Boch, R., et al. (2011). (13)C(18)O clumping in speleothems: Observations from natural caves and precipitation experiments. *Geochimica et Cosmochimica Acta, 75,* 3303–3317.

Daeron, M., et al. (2008). Absolute speleo-thermometry, using clumped isotope measurements to correct for kinetic isotope fractionations induced by CO2 degassing. *Geochimica et Cosmochimica Acta, 72,* A193–a193.

Domínguez-Villar, D., Lojen, S., Krklec, K., Kozdon, R., Edwards, R. L., & Cheng, H. (2018). Ion microprobe δ18O analyses to calibrate

slow growth rate speleothem records with regional δ18O records of precipitation. *Earth and Planetary Science Letters, 482,* 367–376. https://doi.org/10.1016/j.epsl.2017.11.012.

Dreybrodt, W. (1988). *Processes in karst systems*. Springer Verlag, 288p.

Fairchild, I. J., & Baker, A. (2012). *Speleothem science: From process to past environments*. Wiley.

Fairchild, I. J., Borsato, A., Tooth, A. F., Frisia, S., Hawkesworth, C. J., Huang, Y., et al. (2000). Controls on Trace Element (Sr-Mg) compositions of carbonate cave waters: Implications for speleothem climatic records. *Chemical Geology*, *166*, 255–269.

Fleitmann, D., Cheng, H., Badertscher, S., Edwards, R. L., Mudelsee, M., Gokturk, O. M., et al. (2009). Timing and climatic impact of Greenland interstadials recorded in stalagmites from northern Turkey. *Geophysical Research Letters, 36*.

Ford, D. C. & Williams, P. (2007). *Karst Geomorphology and Hydrology*, Wiley, 562p.

Frisia, S., Borsato, A., Fairchild, I. J. & McDermott, F. (2000). Calcite Fabrics, Growth Mechanisms, and Environments of formation in Speleothems from the Italian Alps and Southwestern Ireland. *Journal of Sedimentary Research*, *70*, 1183–1196.

Genty, D. (2008). Paleoclimate research in Villars Cave (Dordogne, SW-France). *International Journal of Speleology, 37,* 3.

Genty, D., Blamart, D., Ghaleb, B., Plagnes, V., Causse, C., Bakalowicz, M., et al. (2006). Timing and dynamics of the last deglaciation from European and North African δ13C stalagmite profiles—Comparison with Chinese and South Hemisphere stalagmites. *Quaternary Science Reviews, 25,* 2118–2142. https://doi.org/10.1016/j.quascirev.2006.01.030.

Genty, D., Blamart, D., Ouahdi, R., Gilmour, M., Baker, A., Jouzel, J., et al. (2003). Precise dating of Dansgaard-Oeschger climate oscillations in western Europe from stalagmite data. *Nature, 421,* 833–837.

Genty, D., & Deflandre, G. (1999). Drip flow variations under a stalactite of the Père Noël cave (Belgium). *Evidence of seasonal variations and air pressure constraints, Journal of Hydrology, 211,* 208–232.

Genty, D., Labuhn, I., Hoffmann, G., Danis, P. A., Mestre, O., Bourges, F., et al. (2014). Rainfall and cave water isotopic relationships in two South-France sites. *Geochimica et Cosmochimica Acta, 131,* 323–343. https://doi.org/10.1016/j.gca.2014.01.043.

Genty, D., Massault, M., Gilmour, M., Baker, A., Verheyden, S., & Kepens, E. (1998). Calculation of past dead carbon proportion and variability by the comparison of AMS ^{14}C and TIMS U/Th ages on two Holocene stalagmites. *Radiocarbon, 41,* 251–270.

Genty, D., & Quinif, Y. (1996). Annually laminated sequences in the internal structure of some Belgian stalagmites—Importance for paleoclimatology. *Journal of Sedimentary Research, 66,* 275–288.

Ghaleb, B., Pons-Branchu, E., & Deschamps, P. (2004). Improved method for radium extraction from environmental samples and its analysis by thermal ionization mass spectrometry. *Journal of Analytical Atomic Spectrometry, 19,* 906–910.

Guiot, J., Pons, A., de Beaulieu, J. L., & Reille, M. (1989). A 140,000-year continental climate reconstruction from two European pollen records. *Nature, 338,* 309–313.

Hellstrom, J. (2006). U-Th dating of speleothems with high initial Th-230 using stratigraphical constraint. *Quaternary Geochronology, 1,* 289–295.

Kim, S.-T., & O'Neil, J. R. (1997). Equilibrium and nonequilibrium oxygen isotope effects in synthetic carbonates. *Geochimica et Cosmochimica Acta, 61,* 3461–3475.

Luetscher, M., Boch, R., Sodemann, H., Spötl, C., Cheng, H., Edwards, R. L., et al. (2015). North Atlantic storm track changes during the Last Glacial Maximum recorded by Alpine speleothems. *Nature Communications, 6*, 7344. https://doi.org/10.1038/ncomms7344.

Martín-Chivelet, J., Muñoz-García, M. B., Cruz, J. A., Ortega, A. I., & Turrero, M. J. (2017). Speleothem Architectural Analysis: Integrated approach for stalagmite-based paleoclimate research. *Sedimentary Geology, 353,* 28–45. https://doi.org/10.1016/j.sedgeo.2017.03.003.

McDermott, F. (2004). Paleo-climate reconstruction from stable isotope variations in speleothems: A review. *Quaternary Science Reviews, 23,* 901–918.

McDermott, F., Atkinson, T. C., Fairchild, I. J., Baldini, L. M., & Mattey, D. P. (2011). A first evaluation of the spatial gradients in δ18O recorded by European Holocene speleothems. *Global and Planetary Change, 79,* 275–287. https://doi.org/10.1016/j.gloplacha.2011.01.005.

Mickler, P. J., Stern, L. A., & Banner, J. L. (2006). Large kinetic isotope effects in modern speleothems. *Geological Society of America Bulletin, 118,* 65–81.

Moreno, A., Stoll, H. M., Jiménez-Sánchez, M., Cacho, I., Valero-Garcés, B., Ito, E., & Edwards, L. R. (2010). A speleothem record of rapid climatic shifts during last glacial period from Northern Iberian Peninsula. *Global and Planetary Change, 71*, 218–231. https://doi.org/10.1016/j.gloplacha.2009.10.002.

Moreno, A., Svensson, A., Brooks, S. J., Connor, S., Engels, S., Fletcher, W., et al.(2014). A compilation of Western European terrestrial records 60–8 ka BP: towards an understanding of latitudinal climatic gradients. Quaternary Science Reviews, Dating, Synthesis, and Interpretation of Paleoclimatic Records and Model-data Integration: Advances of the INTIMATE project (INTegration of Ice core, Marine and Terrestrial records, COST Action ES0907) *106*, 167–185. https://doi.org/10.1016/j.quascirev.2014.06.030.

Moseley, G. E., Spötl, C., Svensson, A., Cheng, H., Brandstätter, S., & Edwards, R. L. (2014). Multi-speleothem record reveals tightly coupled climate between central Europe and Greenland during Marine Isotope Stage 3. *Geology, 42,* 1043–1046. https://doi.org/10.1130/G36063.1.

Stoll, H. M., Müller, W., & Prieto, M. (2012). I-STAL, a model for interpretation of Mg/Ca, Sr/Ca and Ba/Ca variations in speleothems and its forward and inverse application on seasonal to millennial scales: I-STAL SPELEOTHEM TRACE ELEMENT MODEL. Geochem. Geophys Geosystems 13, n/a-n/a. https://doi.org/10.1029/2012GC004183.

Tremaine, D. M., Froelich, P. N., & Wang, Y. (2011). Speleothem calcite farmed in situ: Modern calibration of δ18O and δ13C paleoclimate proxies in a continuously-monitored natural cave system. *Geochimica et Cosmochimica Acta, 75,* 4929–4950. https://doi.org/10.1016/j.gca.2011.06.005.

Van Breukelen, M. R., Vonhof, H. B., Hellstrom, J. C., Wester, W. C. G., & Kroon, D. (2008). Fossil dripwater in stalagmites reveals Holocene temperature and rainfall variation in Amazonia. *Earth and Planetary Science Letters, 275*(1–2), 54–60.

Verheyden, S., Genty, D., Cattani, O., & van Breukelen, M. R. (2008). Water release patterns of heated speleothem calcite and hydrogen isotope composition of fluid inclusions. *Chemical Geology, 247,* 266–281.

Vonhof, H. B., van Breukelen, M. R., Postma, O., Rowe, P. J., Atkinson, T. C., & Kroon, D. (2006). A continuous-flow crushing device for on-line delta H-2 analysis of fluid inclusion water in speleothems. *Rapid Communications in Mass Spectrometry, 20,* 2553–2558.

Wang, Y., Cheng, H., Edwards, R. L., Kong, X., Shao, X., Chen, S., & An, Z. (2008). Millennial- and orbital-scale changes in the East Asian monsoon over the past 224,000 years. *Nature, 451,* 1090–1093.

Woodhead, J., Hellstrom, J., Maas, R., Drysdale, R., Zanchetta, G., Devine, P., & Taylor, E. (2006). U-Pb geochronology of speleothems by MC-ICPMS. *Quaternary Geochronology, 1,* 208–221.

Zhang, R., Schwarcz, H. P., Ford, D. C., Schroeder, F. S., & Beddows, P. A. (2008). An absolute paleotemperature record from 10 to 6 Ka inferred from fluid inclusion D/H ratios of a stalagmite from Vancouver Island. *British Columbia, Canada, Geochimica Cosmochimica Acta, 72,* 1014–1026.

Air-Interface: $\delta^{18}O$ Records of Past Meteoric Water Using Benthic Ostracods from Deep Lakes

15

Ulrich von Grafenstein and Inga Labuhn

Introduction

Oxygen-isotope records offer an alternative way to quantitatively reconstruct paleoclimate, which, at first view, is independent of an ecosystem's reaction to climate change. The ice core records from high latitude inland ice, where the former precipitation and its isotopic composition ($\delta^{18}O_P$) are preserved in an almost original state, are widely accepted as valuable sources of paleoclimate information. Worldwide systematic observation of $\delta^{18}O_P$ (Rozanski et al. 1992), starting in the late sixties, together with the incorporation of the water isotopes in several generations of general circulation models (Hoffmann et al. 1998; Jouzel et al. 1987) and models of intermediate complexity have, not only increased the confidence in $\delta^{18}O_P$ as a powerful paleotemperature indicator in a number of key regions, but have also demonstrated its importance as a primary hydrometeorological parameter in regions where temperature dependence is less evident or absent.

In non-polar regions, investigations have been conducted on lake sediment (carbonate, bulk organic matter, cellulose, diatoms), speleothems, tree rings and soil carbonate. While all these terrestrial records respond to changes in the isotopic composition of past precipitation ($\delta^{18}O_P$), a number of secondary effects can alter the original atmospheric signal and thus limit or exclude a quantitative interpretation. Detecting past changes of $\delta^{18}O_P$ therefore not only provides a valuable paleoclimate proxy, but also largely facilitates the quantification of secondary effects in complex isotopic records. The problem is to find material, like polar ice, which contains quantitative information about the isotopic composition of past precipitation and from which secondary effects can either be excluded or quantified. Those include the alteration of the primary signal ($\delta^{18}O_P$) on its way to through the water cycle (hydrological effects) and during the formation of material in which it will be preserved (isotope fractionation effects).

Lake sediments very often cover reasonably long periods with relatively high accumulation rates, allowing sampling resolutions from individual years to decades. Ostracod valves preserved in those sediments can, with respect to their dominance and habitat, be considered as the lacustrine equivalent to benthic foraminifera in marine sediments (De Deckker 2002). As such, they are ideally suited for the geochemical characterization of former lake water, including stable isotope studies (Holmes and Chivas 2002). A major advantage they have compared to other materials, such as bulk carbonate or organic matter, is that ostracod valves can be relatively easily separated, cleaned (Danielopol et al. 2002), and assigned to different species for which biological and behavioural information is available from the study of modern materials (Horne et al. 2002). Moreover, the specific fractionation can be calibrated using the valves of individuals that grew and calcified under known conditions (Chivas et al. 2002; von Grafenstein et al. 1999a, b; Xia et al. 1997). The same applies to benthic molluscs belonging to the family of sphaeriides, which frequently can be found together with ostracods.

The focus of this chapter is on the special situation of ostracods and molluscs in the profundal sediments of deep lakes, where seasonal and long-term temperature changes are almost absent and where the $\delta^{18}O$ of the local water regularly approaches the average of the entire water column due to the cold season overturn. The fossil valves of these animals can be used to reconstruct precisely the isotopic composition of the lake water ($\delta^{18}O_L$) and, depending on the lake's hydrologic setting, the isotopic composition of former precipitation ($\delta^{18}O_P$). The first part of this chapter provides an overview of published deep-lake oxygen-isotope records. The following two parts more specifically address the processes implicated in the signal transfer from the atmospheric

U. von Grafenstein (✉) · I. Labuhn
Laboratoire des Sciences du Climat et de l'Environnement, LSCE/IPSL, CEA-CNRS-UVSQ, Université Paris-Saclay, 91190 Gif-sur-Yvette, France
e-mail: Ulrich.von-Grafensstein.fr@lsce.ipsl.fr

G. Ramstein et al. (eds.), *Paleoclimatology*, Frontiers in Earth Sciences,
https://doi.org/10.1007/978-3-030-24982-3_15

precipitation to the ostracod valve, i.e. (1) the major hydrological processes controlling the present and past links between $\delta^{18}O_L$ and $\delta^{18}O_P$, and (2) the effects related to the valve formation (temperature-dependent fractionation and vital effects). Most of the data used to illustrate those processes are from lakes situated within a small region of southern Germany and are the author's published or unpublished material. The data was collected to support and refine the quantitative interpretation of the $\delta^{18}O$ records from sub-recent and late Glacial to Holocene mainly from one of those lakes (Ammersee), which is presented in the fourth part of this chapter. The reason for this regional concentration is the lack of case studies as comprehensive from other regions, combining investigation of the modern isotope hydrology, the physical limnology, and the ostracod geochemistry within the settings of a fossil record. The last part of the chapter aims to show how $\delta^{18}O_P$ reconstruction from deep lake ostracods could be further developed and exploited to address secondary effects in more complex archives. This chapter is an update of a previously published book section (von Grafenstein 2002). It incorporates major advances concerning our understanding of the oxygen isotope signal preserved in ostracod valves and gives an overview of new and upcoming records in Europe.

Existing Deep-Lake Oxygen-Isotope Records

The first published ostracod stable isotope record was from Lake Erie (Fritz et al. 1975). This showed a 4‰ shift at the late Wisconsin to Holocene transition, which was interpreted as a temperature controlled change in $\delta^{18}O_P$. Later, deep-lake oxygen-isotope ostracod records from the Great Lakes demonstrated that the Late Wisconsin and Holocene re-arrangements of the hydrological pathways and episodic drainage from pro-glacial lakes largely controlled the isotopic composition of the lakes' water (Colman et al. 1994; Dettman et al. 1995; Forester et al. 1994; Lewis and Anderson 1992; Rea et al. 1994). Although it is almost impossible to extract information on $\delta^{18}O_P$ from those ostracod records, they are still excellent examples of successful and very useful reconstructions of relative $\delta^{18}O_L$ changes. Data for the isotopic composition of modern ostracod valves have been reported for Lake Huron (Dettman et al. 1995). However, whilst these data suggested that the most important taxa showed vital offsets, they were insufficient for these offsets to be quantified.

Lister et al. (1991) presented an oxygen-isotope record from Lake Qinghai (Qinghai-Tibetan Plateau) based on measurements of *Limnocythere inopinata* and *Eucypris inflata*, which alternately dominate the lake's benthic ostracod assemblage throughout the past 15,000 years. The record shows an overall increase of 6‰ from 8000 ^{14}C-years BP to 3000 ^{14}C-years BP, which the authors attribute to the slow accumulative evaporative concentration following a major reduction in humidity in the region. This hypothesis is strengthened by the fact that the reconstructed oxygen-isotope values of the lake water, prevailing for the last 3000 years, are close to the endpoint of isotopic enrichment under modern conditions. Short term excursions from this trend and a substantial variability before 8000 ^{14}C-years BP are interpreted as episodic changes in the lake's water balance and water level variations. However, it cannot be excluded that shifts of $^{18}O_P$ and/or $\delta^{18}O_A$ (which are documented in the $\delta^{18}O$ record from the Guliya ice cap (Thompson et al. 1997) or changes of the bottom water temperature (the lake today is only 23 m deep) might have contributed to both the long-term shifts and to the small-scale fluctuations of $\delta^{18}O_L$.

In Europe, early monospecific deep-lake records exist from Lake Zürich (Lister 1988) and Lake Lugano (Niessen and Kelts 1989), both have a strong glacial to interglacial shift but lack resolution of abrupt events during the transitions. Two moderately better-resolved $\delta^{18}O_L$ histories of two neighbouring lakes in the northern alpine foreland (Ammersee and Starnberger See, southern Germany) (von Grafenstein et al. 1992) provided evidence of climate-induced changes of $\delta^{18}O_P$ consistent with the pollen-inferred local climate history, including a strong negative excursion during the Younger Dryas. They also show systematic and constant offsets between the $\delta^{18}O$ values of different taxa from the same sediment layer, indicative of physiologically controlled fractionation in addition to temperature-dependent fractionation. $\delta^{18}O$ records of monospecific ostracod samples from a deep-lake core from Lac Neuchâtel (Switzerland), depicted similar millennial-scale, late-glacial variations, in addition to sudden changes in the lake's water balance and shifts of the mean isotopic composition of the input, due to the episodic connection to the Aare river system (Schwalb et al. 1994). Shallow-water, late-glacial records from the Ammersee (von Grafenstein et al. 1994), from southern Sweden (Hammarlund et al. 1999), and Switzerland (von Grafenstein et al. 2000, 2013) give evidence that the large shifts of $\delta^{18}O$, bracketing the Younger Dryas cold period, were accompanied by relative changes in summer water temperatures, consistent with air-temperature controlled shifts of $\delta^{18}O_P$. Quantitative reconstruction of $\delta^{18}O_P$ from those records remains biased by the temperature effects, by seasonal variation of shallow water $\delta^{18}O$, and often by unknown changes in the lakes' water balances. The best-resolved European oxygen-isotope record from deep-lake ostracod valves is from Ammersee (von Grafenstein et al. 1996, 1998, 1999a, b), and the accompanying hydrological and isotope-geochemical calibration (von Grafenstein et al. 1999a, b) will be used below as an example to discuss the possible effects in more detail.

A lower-resolved record from Lake Constance (Schwalb 2003) is in good agreement with the Ammersee record. A low-resolution record also exists from Lake Geneva covering the Holocene. More recently, the first results from a long-term project aiming to produce a new high-resolution record using a new sediment core from Mondsee (Austria) show a remarkable synchrony for the negative excursion during the 8.2 ky-event (Andersen et al. 2017) and over the entire glacial-interglacial transition (Lauterbach et al. 2011) Currently, a multidisciplinary team continues to work on the complete high-resolution $\delta^{18}O_P$ records from Ammersee (Germany), Mondsee (Austria) and Lac d'Annecy (France) for the last 15,000 years.

Hydro-Meteorological Effects

The Isotopic Composition of Atmospheric Precipitation

The isotopic composition of atmospheric precipitation at a given place and time is controlled by various fractionation effects, including (1) the moisture formation in the (mainly oceanic) source regions, (2) loss through precipitation along the moisture transport pathways, (3) re-evaporation and (4) the condensation and precipitation process at the sampling site. Thirty years of monthly observation at meteorological stations around the world show that, in high to mid latitudes, losses of the original moisture content along horizontal temperature gradients seem to prevail, leading to the existence of an overall positive correlation between $\delta^{18}O_P$ and local air temperatures on seasonal and inter-annual time scales as well as geographically (Dansgaard 1964; Rozanski et al. 1992). In low latitudes, a negative correlation between $\delta^{18}O_P$ and the amount of precipitation is observed and is explained by the vertical temperature gradients. These climate-$\delta^{18}O_P$ relations are, however, overlain by noise due to high short-term variability, reflecting the effects of the different condensation processes and the admixture of vapor from different marine or continental sources during a single precipitation event, and through spatial variability, due to relief effects. Evidently, the quantitative relation between $\delta^{18}O_P$ and climatic parameters, like temperature and precipitation, has to be checked for each basin before conclusions in terms of paleoclimate can be drawn from a record. However, even if such a relation is weak or absent, the reconstructed $\delta^{18}O_P$ itself remains a valuable information source for paleoclimate analyses and for the quantitative interpretation of isotopic records with strong secondary effects.

It is important to be aware of the seasonal variations of $\delta^{18}O_P$, which are large even with respect to the greater shifts recognised in paleo-records. In many cases, the retention times of water within the catchment and in the lake are long enough, so that the effective input into the lake carries an average isotope signal over several years. This average is often close to the average of $\delta^{18}O_P$, but might be offset by preferential losses of a part of the precipitation by evaporation and transpiration (see below). In the special case of short catchment retention times combined with a short residence time in the lake, the isotopic composition of the lake water ($\delta^{18}O_L$) can respond with oscillations either in or out of phase with the seasonal $\delta^{18}O_P$ cycle.

Catchment Effects

The term 'catchment effect' has been introduced and discussed in detail by Gat et al. (1995). It can be defined as the sum of effects from all hydrological processes occurring in the drainage basin that might alter the relation between long term $\delta^{18}O_P$ and $\delta^{18}O_L$. Besides the 'catchment effect' sensu stricto, which is the measurable difference between the isotopic compositions of the drainage basin runoff $\delta^{18}O_I$ and $\delta^{18}O_P$ (Δ_{P-I}), we also have to consider those processes that control the amount of runoff (I) and the spatial and temporal variability of both I and $\delta^{18}O_I$.

Potentially responsible for a significant Δ_{P-I} are losses via evaporation or sublimation, which can lead to an isotopic enrichment of the remaining water. The importance of these losses can be estimated by comparing the deuterium excess of the runoff with that of the mean precipitation. Usually they are small in humid climates and they depend on the proportion of open-water surfaces within a drainage basin. Alternatively, non-fractionating losses such as the uptake and consequent transpiration and evaporation of water by plants, or the recharge of deep groundwater, can be selective against a portion of the annual precipitation and thus can lead to a relative shift of $\delta^{18}O_P$. This effect theoretically could be greater than 1‰, if the evapotranspiration is restricted to the summer period and only summer precipitation is taken up. In practice, the largest part of water for evapotranspiration comes from the soils, which retain significant amounts of water over the year and where the seasonal variation of $\delta^{18}O_P$ and, in consequence, the effect on Δ_{P-I} is considerably reduced.

Stronger effects are to be expected in high-altitude drainage basins, including those in high alpine areas, where build-up of glaciers can retain significant amounts of isotopically-depleted winter precipitation and thus shift $\delta^{18}O_I$ to more positive values. Glacier growth is a relatively long-term process, which takes place over tens to hundreds of years during relatively cold periods, whereas ablation can be almost spontaneous with a consequent discharge of isotope-light water easily exceeding the amount of yearly retention during glacier growth. The isotopic composition of

runoff from partially glaciated areas may therefore be biased to more positive values compared to $\delta^{18}O_P$ during cold phases with glacier growth, and marked by strong negative spikes during subsequent warm periods.

Environmental changes including climate shifts can increase or decrease the runoff without significantly affecting Δ_{P-I}. The most evident is a change in precipitation, but evapotranspiration and groundwater recharge and discharge can also change either in concert with precipitation, or independently, as a response to climate change, vegetation change and human activity. Such variations of the runoff will alter the lake water balance and thus the link between $\delta^{18}O_P$ and the isotopic composition of lake water $\delta^{18}O_L$ by an amount dependent on the hydrological sensitivity of the lake (see below). Changes in the seasonal runoff characteristics can affect the link between $\delta^{18}O_P$ and $\delta^{18}O_L$. These may occur without any measurable changes in the annual runoff and mean annual $\delta^{18}O_I$, by moderation of the short-term reservoirs (soil, snow cover). Such effects are important in lakes with water residence times of close to or less than one year, but may also be visible in lakes with longer response times.

Probably the most efficient way to characterize the catchment effects in a given basin is through a survey of the isotopic composition of both the precipitation and the river runoff. Figure 15.1 gives an example for the Ammer River (southern Germany), the main contributor to Lake Ammersee. River water was sampled just upstream of the lake in two-weekly intervals for more than two years and on a daily base for the second of these two years (von Grafenstein et al. 1996). Atmospheric precipitation is collected routinely at one meteorological station (Hohenpeissenberg) within the drainage basin and at two additional stations (Neuherberg and Garmisch), about 50 km to the north and south, respectively, providing monthly values for $\delta^{18}O_P$ since 1970 AD. The oxygen isotope composition of the total two-years of runoff is −10.3‰, with a tendency to increase from −10.5‰ to −10.1‰ during this period. Interestingly, the two-year precipitation mean for the same period is −10.1‰, indicating that at least a part of the runoff is from longer term (groundwater) reservoirs. Indeed, the daily record of the second year allows the spontaneous, soil water and groundwater components to be separated out with a mean retention time of 9 months for the soil water component and of at least several years for the groundwater component. In the long term, the total contribution of soil water and spontaneous runoff is about 30%. It is therefore impossible to define an exact estimate of Δ_{P-I} without considering the history of $\delta^{18}O_P$ for the past few decades. The best explanation for the tendency of $\delta^{18}O_I$ over more than 4 years (including lower frequency measurements from 1989 on) is a mean age of three years for the groundwater component. However, even if we consider a much longer retention in the groundwater, Δ_{P-I} is less than +0.3‰ for the present-day conditions in the Ammersee drainage basin. A small decrease in the deuterium excess of the mean runoff (8‰) compared to that of the precipitation over the last decade (10‰) might indicate that this probable catchment effect in the case of the Ammer river is due to surface evaporation (from some smaller lakes in the basin).

In summary, catchment effects, even if they are seemingly small as in our example, have to be at least considered as a possible reason for changes of $\delta^{18}O_L$ in the past. Quantification is however rather complicated and has to be based on a proper description of the modern geomorphologic conditions and the vegetation cover of the drainage basin.

Lake Water Balance Effects

The isotopic composition of lake water is controlled by the amounts and the isotopic compositions of the inflowing water (I, $_I$) and loss via evaporation (E, $_E$). In steady state, i.e. if the environmental conditions are considered as stable for some time, δ_L approaches a constant value representing a mixture between δ_I (weighted by I) and δ^* (weighted by the evaporation and the atmospheric water vapor deficit):

$$\delta_L = (\delta_P I + \delta^* Eh/(1-h))/(I + Eh/(1-h)) \quad (1)$$

δ^* is the isotopic composition of water being in isotopic equilibrium with the atmospheric water vapor and thus the maximum that can be reached by evaporation:

$$\delta^* = (h\ \delta_A + \varepsilon)/(h - \varepsilon) \quad (2)$$

where h is the relative humidity, δ_A the isotopic composition of the atmospheric water vapour and ε the sum of the equilibrium and kinetic fractionation between water and vapour (Gat et al. 1994; Gibson et al. 1993) Several important facts with respect to the reconstruction of δ_P can be derived from these relations: (1) the isotopic enrichment due to evaporation is independent of the residence time of water (I/V), but depends, in addition to the atmospheric moisture conditions, on I (which is the product of P-ET, Precipitation-EvapoTranspiration, and the surface of the catchment basin) and E (which is the product of evaporation per surface unit and the lake's surface). Lakes with differing ratios between the lake surface A_L and drainage basin area A_C will therefore have significantly differing δ_L, even if the atmospheric conditions including δ_P, δ_A and the evaporative flux are equal. (2) Any change of P-ET or E will be weighted by this factor A_L/A_C, i.e. will induce a stronger reaction of δ_L for lakes with a larger A_L/A_C. The smaller the lake surface compared to the drainage basin, the smaller will be the influence of changing hydrology on the quantitative link between δ_I and δ_L (and consequently the link between δ_P and δ_L). (3) Comparison of

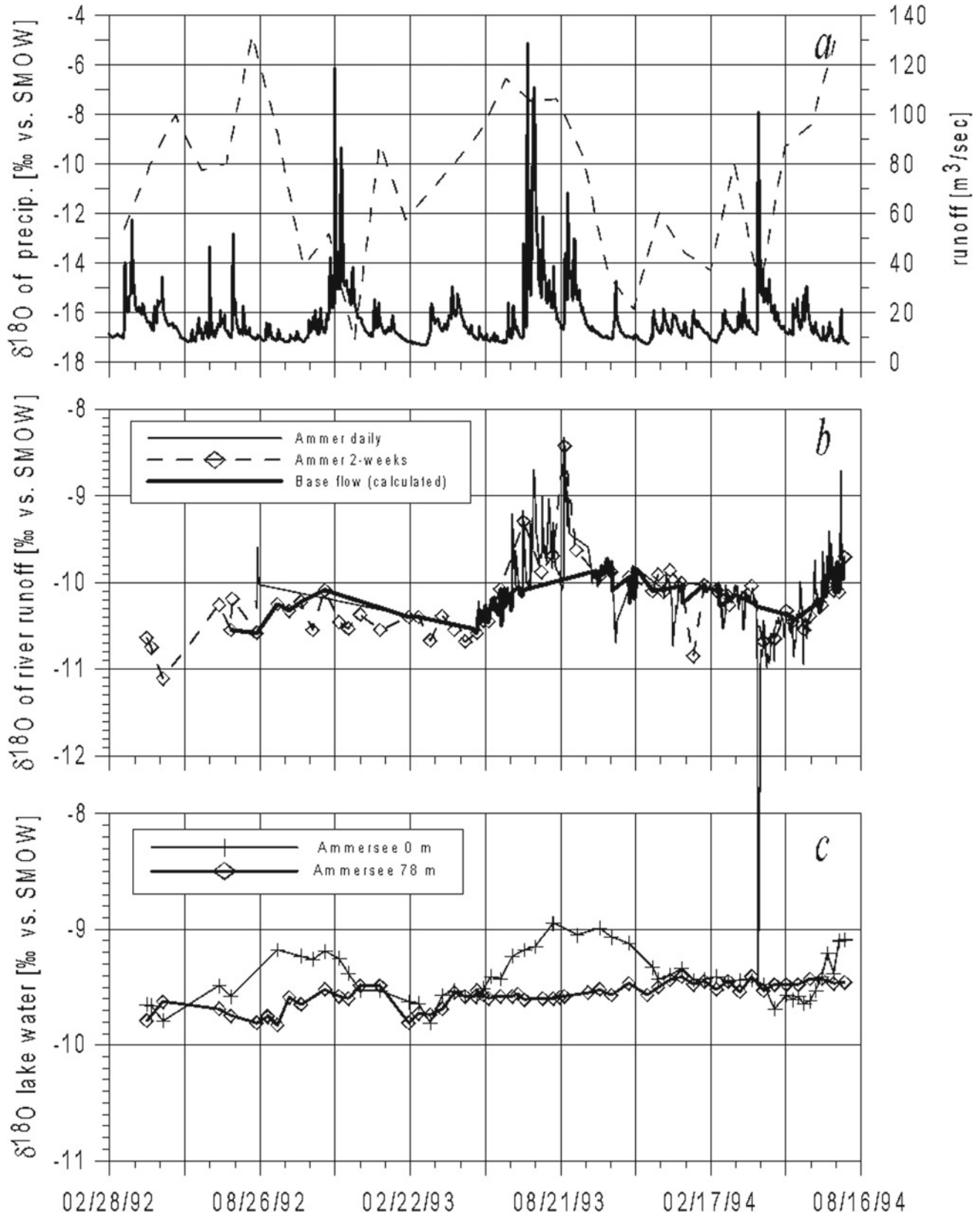

Fig. 15.1 **a** Daily runoff of the Ammer River (solid line) and the $\delta^{18}O$ of monthly precipitation at the meteorological station Hohenpeissenberg (stippled line); **b** $\delta^{18}O$ of the Ammer River sampled daily (continuous line) and in two-week intervals (diamonds and stippled line). $\delta^{18}O$ of days with runoff not exceeding 12 m^3/s are connected with the thick line and supposed to represent $\delta^{18}O$ of the base-flow; **c** $\delta^{18}O$ of surface and deep water in Ammersee (redrawn from von Grafenstein 2002)

δ_L from three neighbouring lakes with differing A_L/A_C should allow quantification of the evaporative enrichment and, in consequence, of Δ_{P-I}, P − ET, E, and h, if one stable water isotope is used ($\delta^{18}O$ or δD), and from two lakes if both $\delta^{18}O_L$ and δD_L are available.

Figure 15.2 gives an example of such a set of lakes (which in part are also used below for δ_P reconstruction). These four lakes are fed today by surface water of almost identical composition and are sufficiently close to assume that P − ET, h, δ_A, and evaporation from a surface unit are equal. Individual water samples, taken within the period from 1989 to 1994 in a δD–$\delta^{18}O$ diagram scatter around mean values from a lake, are clearly separated from the local meteoric precipitation and from lake to lake. Averages of the samples taken in the winter, when the lakes are well mixed, are plotted on a line with a slope of 4.9, indicating that the distance from the long-term average of the precipitation is due to the relative importance of evaporation from the individual lake surface. Using Eqs. 1 and 2, $\delta^{18}O_L$ measurements of the four lakes can be reproduced using mean climatic conditions for the region and assuming that the isotopic composition of atmospheric water vapor (δ_A) is in equilibrium with the long term mean of the isotopic composition of the precipitation ($\delta^{18}O_P$). Evaporation from a surface unit, as calculated from the isotope balances, is 535 mm, close to independent estimates from the water balances (ca. 600 mm) and from energy balance modelling (580 mm).

Figure 15.3 gives an example of a sensitivity test exploiting how the δ_L of the lakes in Fig. 15.2 will change if hydrologic conditions change (without a change of δ_P), such as a doubling of the input (I) or a doubling of the evaporation (E). Evidently, the lake with the lowest modern evaporative offset is also the least sensitive to changing hydrology, and therefore should give the most accurate estimate of δ_P from reconstructed δ_L.

Transient Changes and Dynamic Effects

The scatter of $\delta^{18}O_L$ of individual lake water samples in Fig. 15.2 is the result of temperature stratification, which leads to short-term deviations from the 'steady state.' In summer, the warm epilimnic water body, which is efficiently separated from the much larger hypolimnion, is both evaporatively enriched and fed by isotopically-enriched summer precipitation and river runoff. The first effect leads to systematic shifts parallel to the local evaporation line, whereas the second leads to less systematic scatter along lines connection the prevailing $_L$ with the respective isotopic composition of the precipitation and river water. Under present day conditions, these seasonal deviations of epilimnetic water in our examples can add up to at least 1.5‰ and are subject to significant inter-annual variability as shown in Fig. 15.1c. Hypolimnetic water, in consequence, is the better representation of the lake's reaction to the long-term development, being 'updated' once a year during the lake overturn in autumn, winter, and/or spring.

With respect to dynamic effects, the selection of the 'ideal' lake for δ_P reconstruction is a trade-off between a short residence time (I/V), which ensures an optimal response of δ_L to a change in δ_P, on the one hand, and a residence time that is long enough to efficiently suppress the seasonal variability of δ_I, on the other hand. A theoretical residence time of 2.7 years (as for the Ammersee) seems to be sufficiently long to suppress the present-day seasonal variability of δ_I. The reactivity of a lake to a change in $_P$ can be described by

$$\delta_{L(t)} = \delta_{L(0)} e^{-tI/V} + \delta_{L(\infty)} \left(1 - e^{-t/V}\right) \quad (3)$$

where $\delta_{L(0)}$ is the isotopic composition before a change, $\delta_{L(\infty)}$ is the new steady state after the change, and t is the elapsed time since the change. For example, after a change of 1‰ in $\delta^{18}O_P$, the isotopic composition of the lake will reach a value indistinguishable from the new equilibrium (±0.05‰) after $t = -\ln (0.05/\delta_{L(0)} - \delta_{L(\infty)}) * V/I$, which would be 8 years for the Ammersee against 63 years for the Starnberger See, the lake with the longest residence time in our selection. All variability of δ_P with higher frequency will have a response in δ_L with reduced amplitude.

In order to minimize the overall error of a $\delta^{18}O_P$ reconstruction from lake isotopic records, the 'ideal' lake should have a simple, well-defined drainage basin, which is large compared to the surface area of the lake to ensure a small evaporative isotopic enrichment of its water. The lake should be holomictic with a cold hypolimnion, i.e. a water depth exceeding 40 m, and should have a short residence time, but not much below 2 years. Most of these criteria can often be verified based on basic field observation and literature, but should be documented with isotopic determinations of river and lake water samples if a lake is considered to be a potential candidate for paleoclimatological or paleohydrological investigations. Such hydrological pre-site studies not only increase the significance of the interpretation of the isotopic records in terms of changing $\delta^{18}O_P$, but may also help to design studies on one or more distinct hydrological effects.

Isotope Geochemistry of Benthic Freshwater Ostracods

Theoretically, all benthic organisms living in the hypolimnion of lakes and producing identifiable fossil remains preserved in the sediments could be considered for the

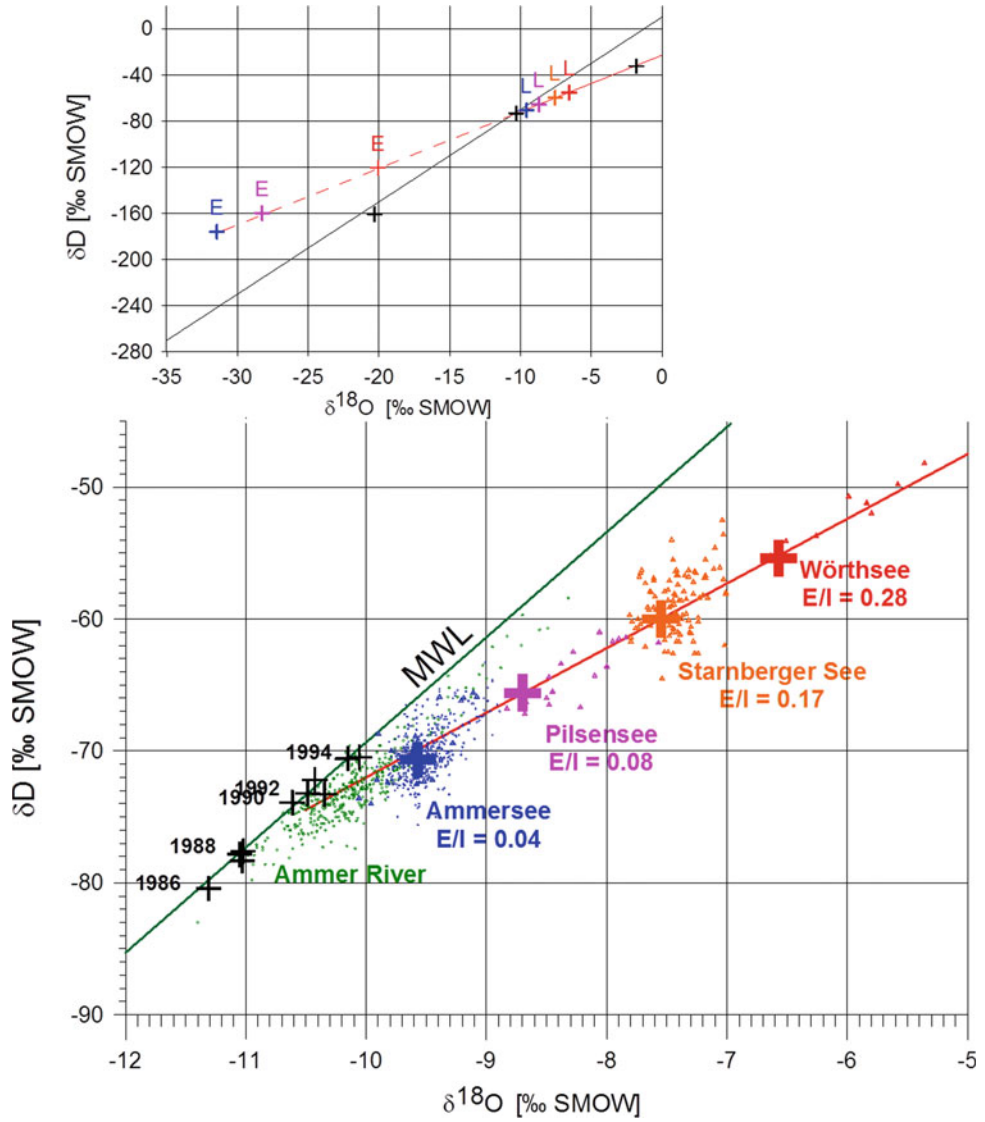

Fig. 15.2 Lower graph: water isotope ratios (δD versus $\delta^{18}O$) of lake water (Ammersee, blue; Pilsensee, magenta; Starnberger See, orange; Woerthsee, red), precipitation (IAEA-Station Hohenpeissenberg, large black crosses), and river water (Ammer, green) from the 'Fünf-Seen--Land' (Five Lakes District) close to Munich, Germany. Large symbols mark the average of the lake samples taken during the winter period, when the lakes are well mixed and effects from the thermal stratification are absent. Note the increasing distance of lake samples from the *Meteoric Water Line* (MWL) due to evaporative enrichment, proportional to the respective evaporation to input ratios (E/I). Scattering of the data from one lake is due to temporal variability of mean runoff (4 years of observation for Ammersee and Starnberger See) and to vertical differences in the water column in summer. All lakes have permanent outflow. The upper graph shows the calculated isotopic compositions of isotopically depleted water vapor produced from the lakes (δ_E, labelled as E), of lake water (δ_L, labelled as L), and of the limiting maximal enriched water (δ*, labelled as *) governed by the mean local climatic conditions, by the mean isotopic compositions of the atmospheric water vapor (δ_A, labelled as A) and precipitation (δ_P, labelled as P). Colours for the different lakes are the same as for the lower graph

reconstruction of the isotopic composition of former lake water. However, at present, studies have been restricted to valves of ostracods and small bivalve molluscs belonging to the genus *Pisidium*. One reason for this choice is that these organisms build protective shells or valves from $CaCO_3$, which are relatively easy to separate from the rest of the sediment. In addition, we now have the capacity to measure oxygen and carbon isotope ratios in quantities of carbonate as small as 10 μg (Chivas et al. 1993; von Grafenstein et al. 1992). Contamination by littoral fauna are also detectable through the occurrence of species typically restricted to shallow water. The existence of fossil fauna representing the former life assemblage (De Deckker 2002) is itself an excellent paleolimnological indicator of sufficient oxygen in the hypolimnion and thus for a regular winter overturn of the water column, which is needed for the transfer of the $\delta^{18}O_P$ signal into the hypolimnion.

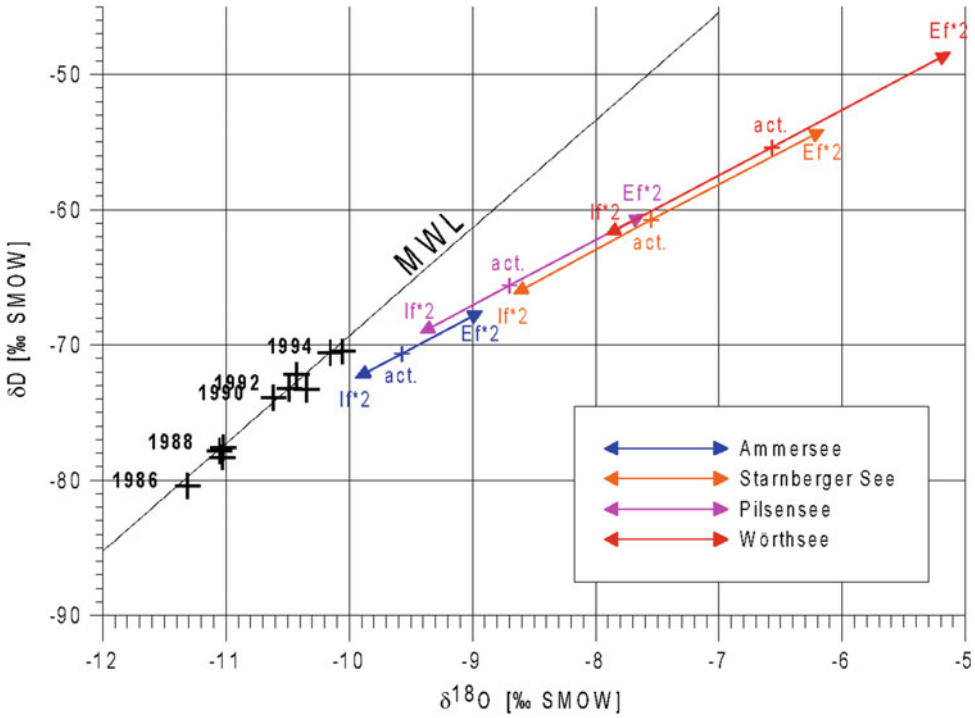

Fig. 15.3 Reaction of $\delta^{18}O_L$ to changes in the water balance (same colours as for Fig. 15.2). The modern isotopic compositions are labelled as 'act.', those resulting from to doubled input as 'I*2' and those from doubled evaporation as 'E*2'. Note that the $\delta^{18}O_L$ of Ammersee remains within a range of 1‰ for such hydrologic extremes, in contrast to the much stronger reaction of the $\delta^{18}O_L$ of Wörthsee (almost 3‰)

Vital Effects

However, the formation of the protective calcitic ostracod valves is a physiological process, which may affect the oxygen isotopic composition of the valves through systematic differences compared to an inorganic calcite formed in isotopic equilibrium. Indeed, such 'vital effects' have been postulated based on evidence from constant differences in valve $\delta^{18}O$ between different taxa in deep lake cores from Starnberger See and Ammersee (von Grafenstein et al. 1992). These effects have been quantified for some common European freshwater species by systematic field observation and collection (von Grafenstein et al. 1999a, b), and by laboratory cultivation for the North American species *Candona rawsoni (*Xia et al. 1997) and the Australian euryhaline nectic ostracod *Australocypris robusta* (Chivas et al. 2002). The result of the field observations in Ammersee and Starnberger See have been confirmed by a similar one-year observation in Lake Geneva (Decrouy et al. 2011). However, field and laboratory studies on ostracods from sites with variable salinity (Li and Liu 2010) and host water pH reporting (Chivas et al. 2002; Marco-Barba et al. 2012) indicate that the 'vital effect' might be influenced by host water conditions. Devriendt et al. (2017) therefore compiled all data from published 'calibration' studies (Chivas et al. 2002; Xia et al. 1997; von Grafenstein et al. 1999a, b; Decrouy et al. 2011; Li and Liu 2010; Didié and Bauch 2002; Keatings et al. 2002; Van der Meeren et al. 2011; Bornemann et al. 2012) and suggested that ostracod calcite reflects the oxygen isotopic composition of the sum of $[HCO_3^-]$ and $[CO_3^{2-}]$. For carbonate-dominated freshwater lakes with a pH of around 8.3 the contribution of $[CO_3^{2-}]$ to this sum is negligible. The isotopic composition of ostracods valves in these lakes therefore reflects almost exclusively the isotopic composition of $[HCO_3\text{-}]$ which in turn depends solely on $\delta^{18}O_L$ and the water temperatures, whereas, in waters with high and variable salinity, the variable contribution of $[CO_3^{2-}]$ leads to significant negative excursions in the $\delta^{18}O$ of the ostracod calcite, thus possibly influencing the reconstruction of the host water $\delta^{18}O$. This new calcification model nicely explains the apparent and up-to-now still enigmatic, positive offset of valve $\delta^{18}O$ with respect to an 'equilibrium calcite' in almost all freshwater settings. It could also be the key to understanding the significant differences of 'vital offsets' within taxonomic groups. For the deep freshwater lake situation, the correction for the empirical 'vital offset' and for the temperature-dependent fractionation between the $\delta^{18}O$ of ambient water and a calcite in isotopic equilibrium should still give an excellent measure of the $\delta^{18}O_L$, if the water temperature during the formation of the valve is known, or can be established.

Water Temperature Effects

Holomixis (the full overturn of the water column) of deep freshwater lakes occurs when the temperature of the entire water column approaches the density maximum of

freshwater at 4 °C. The exact temperature for the overturn might, however, deviate slightly from 4 °C, if the wind forcing during the holomixis is strong enough to overcome the density gradients. Nevertheless, the possible temperature range of 3–5 °C is relatively small. In regions where air temperatures of the coldest month are equal to, or below, 4 °C, positive deviations from 4 °C are restricted to a short period during the onset of the holomixis, and negative deviations are limited to the winter and to cases of a continuing wind-forced overturn. Most probably, the deep water is at 4 °C at the moment of stabilisation due to spring warming. During summer, the hypolimnion is efficiently insulated from irradiative warming. Small temperature increases up to 6 °C are, however, observed in lakes in regions with high geothermal gradients. Warmer bottom-water temperatures occur in meromictic lakes, in which the winter overturn only reaches down to a limited depth and in which a deeper and denser water body (monimolimnion) exists. However, as mentioned above, no benthic in situ ostracod and mollusc fauna will be found there due to the absence of oxygen in the monimolimnion. In order to further minimize any error in the reconstruction of $\delta^{18}O_L$ from benthic carbonate fossils, bottom-water temperatures of the respective lakes should be followed over several seasons and compared with those simulated by energy- and water-balance models driven by observed climate conditions for the same period. The models, validated in this way, can then be used to estimate bottom water temperatures and thus provide error estimates for $\delta^{18}O_L$ for a large range of climate conditions. For Ammersee and Lac d'Annecy, two of the few lakes which should be excellently suited for quantitative reconstruction of $\delta^{18}O_P$, this modelling approach was used, confirming deep water temperatures astonishingly constant at 4 °C for a very wide range of climate conditions, colder than today for Ammersee, but with the risk of meromixis in warmer climates, especially when winter mean daily temperatures remain significantly above 4 °C. In contrast, Lac d'Annecy continues to be episodically meromictic during modelled warmer periods, because of its higher transparency during the warmest summer month, allowing deep water to reach the warmer winter minimal air temperatures within a couple of years (Danis et al. 2003, 2004)

In our example from the Ammersee, the average temperature at 80 m over the last 20 years (1980–2000, data provided by Dr. B. Lenhardt, WWA Weilheim) was 4.15 °C, with a standard deviation of 0.45 °C, and extremes of 3.2 °C and 5.0 °C. With such a narrow range of water temperatures and the relatively constant $\delta^{18}O_L$ of the hypolimnion (see Fig. 15.1c), the preferred moulting and calcification period of the ostracods and their instars is almost irrelevant. This is in strong contrast to sites within the epilimnion, where differences of up to 3‰ between the $\delta^{18}O$ of summer and winter produced valves (after correction for vital offsets) are common (von Grafenstein et al. 1994; 1999a, b, 2013; Dettman et al. 1995). However, a problem with such deep-lake studies is the low abundance of ostracods compared to littoral sites; this is most probably related to the combination of low population densities of the different species with relatively elevated sediment accumulation rates (in average ~1 mm per year in core AS96-1 from Ammersee). High-resolution $\delta^{18}O$ records approaching the hydrologic resolution (ca. 8 years/sample) are therefore only possible if 10 to 20 valves of juveniles (instars A-5 to A-2) of the most abundant species *Fabaeformirscandona levanderi*, *F. tricicatricosa* or *Candona candida* are grouped together to produce samples of >10 µg calcite. This mixing of species and instars is not problematic, however, as the studied European *Candonidae* share identical vital offsets for $\delta^{18}O$.

The error of $\delta^{18}O_L$ reconstruction from Ammersee deep lake ostracod $\delta^{18}O$, is about ±0.2‰. The error of the $\delta^{18}O_P$ calculation, introduced by assuming that evaporative enrichment and catchment effects were as today, could, in times of extreme hydrological conditions, range from −0.3‰ to +0.6‰.

The Fossil Ostracod Record

Calibration Against the Instrumental Air Temperature Record

Despite the efforts to understand and quantify the transfer of an atmospheric $\delta^{18}O_P$ signal into a sedimentary archive, two points of significance with respect to paleoclimatic studies could not be addressed due to the short period of the relevant field observation. The first concerns the relationship between mean annual $\delta^{18}O_P$ and mean annual air temperature based on regional and European-wide inter-annual variability of the of the last three decades (Rozanski et al. 1992). This comparison had to be extended to at least the duration of existing instrumental records, to maximize the range of observed temperature changes and to meet the standards for the calibration of other paleotemperature proxies. The second open point was the overall reactivity of the coupled drainage basin-lake system to changes in $\delta^{18}O_P$, where, especially, the average retention time of the slowest runoff (groundwater) could only be roughly estimated to ~3 years from a tentative match between a four-year shift of $\delta^{18}O_L$ and long-term averages of $\delta^{18}O_P$.

Both concerns could be addressed by establishing a 300-year long ostracod-derived record of $\delta^{18}O_L$ from the uppermost 120 cm of sediment in 80 m water depth in Ammersee (von Grafenstein et al. 1996). The age-depth model of the core was based on clearly identifiable annual

lamination (Alefs et al. 1996; Czymzik et al. 2013) and the time represented by a sediment sample 1 cm thick was on average 2.5 years. A first, direct comparison of the youngest 200 years of the $\delta^{18}O_L$ with the adequately averaged mean annual air temperature (MAAT) record from Hohenpeissenberg (within the catchment of the lake) gave a reasonable correlation ($r^2 = 0.91$), but an apparent $\delta^{18}O_L$/MAAT sensitivity, which, with 0.38‰/°C, was significantly below the $\delta^{18}O_P$/MAAT sensitivity derived from three decades of observation in the region and for the rest of Europe (0.58‰/°C). In addition, all $\delta^{18}O_L$ values younger than 1920, while still showing the same temperature-dependence, were systematically displaced by −0.15‰ with respect to the older part of the record. The smaller-than-expected amplitude of $\delta^{18}O_L$ can clearly be attributed to oversampling of the record compared to the reactivity of the entire retention system and, in a next step, can be used to better quantify the catchment residence time. The abrupt relative shift of $\delta^{18}O_L$ is an indication of a change of the $\delta^{18}O_P$-$\delta^{18}O_L$ difference or of the catchment effect in its wider sense, related to the regulation of the Ammer River, which started in 1920 and ended in 1922. This regulation was designed to accelerate the runoff of storm-related flood events (which occur primarily in summer) and to allow cultivation of the extended river plains. Thus, after the regulation, a larger portion of isotopically-enriched summer water was transferred directly into the lake, was mixed into the epilimnion, and became partially lost via the outlet, whereas before regulation, those flood waters could infiltrate into the river plain aquifers and more efficiently change the longer term $\delta^{18}O_I$ and, in consequence, the $\delta^{18}O_L$.

After correction for this 'summer bypass effect', the entire $\delta^{18}O_L$ record was compared to the $\delta^{18}O_L$ calculated using a very basic lake model, by assuming a linear relation between $\delta^{18}O_P$ and the measured air temperature and by taking into account changes in the seasonal distribution of precipitation and the most obvious features of lake water mixing. Figure 15.4 shows the results of this modelling approach, which gives the best fit between calculated and observed $\delta^{18}O_L$, if the mean drainage basin retention time is set to 3 years and if the temperature dependence of $\delta^{18}O_P$ is assumed to be 0.58‰/°C, thus confirming the assumption that the correlation based on direct observation during the last decades was valid for the last two centuries.

The Record of $\delta^{18}O_P$ in Central Europe Over the Past 15,000 Years

The longer term history of $\delta^{18}O_P$ reconstructed from Ammersee deep-lake cores has been discussed in two publications, the first of which (von Grafenstein et al. 1998) concentrates on the synchrony of a cold event around 8200 years BP in Europe and Greenland and its probable forcing by the collapse of the Hudson Bay ice dome. The second (von Grafenstein et al. 1999a, b) makes a comparison between $\delta^{18}O_P$ in Europe and in Greenland over the period between 15,000 and 5500 years B.P. The most striking feature is probably the great similarity in the records, even at high frequencies, providing evidence that the climate of both regions (and most likely of the entire North Atlantic perimeter) experienced the same decadal variations, governed by the variability of the heat flux from the North Atlantic Ocean. Independent confirmation of the details of the $\delta^{18}O$ from ice in Central Greenland in a European record significantly increases confidence in the quantitative interpretation of changes of the regional air temperatures and helps to exclude alternative explanations such as significant changes in the prevailing water vapor sources for precipitation in both regions.

Like the 8.2-ka-event, the short, abrupt, cold oscillations during the relatively warm periods of the late Glacial and early Holocene were probably forced by cataclysmic fresh-water discharges into the Atlantic Ocean as a consequence of the disintegration of the continental ice sheets. Despite the high correlation at high frequencies, the quantitative comparison of both $\delta^{18}O_P$ records reveals periods of systematic change in the differences between Europe and Central Greenland around the Younger Dryas cold period. These might indicate slow systematic changes in the surface conditions and circulation in the Greenland-Norwegian Sea, governed by the persisting meltwater flux from the Scandinavian ice sheet during the relatively warm periods. The proposed mechanism (von Grafenstein et al. 1998) is also an attractive hypothesis for 'Dansgaard-Oeschger-events', occurring frequently during the period from ~80,000 to ~25,000 yr B.P.

Figure 15.5 shows an overview of the state of $\delta^{18}O_P$ reconstruction from Ammersee deep-lake ostracods. The lack of resolution for the last 5500 years is evident, even if the available data already show some similarity with the corresponding part of the $\delta^{18}O_P$ records from Greenland. The highest resolved parts of the record provide probably the best constrained and resolved $\delta^{18}O_P$ record existing in Europe. However, there is still uncertainty ranging between +0.6‰ and −0.3‰ from potential hydrological changes that have not been considered. In addition, the record might not be representative of the entire continent, at least during the late Glacial, when stronger and highly dynamic longitudinal climate gradients were very likely to have prevailed. Both the errors from hydrological change and those from regional European climatic gradients may partially explain the apparent cross North Atlantic differences. Another problem of the existing record from Ammersee is the quality of the age model which is based on the few radiocarbon measurements of macro plant and insect remains found in the

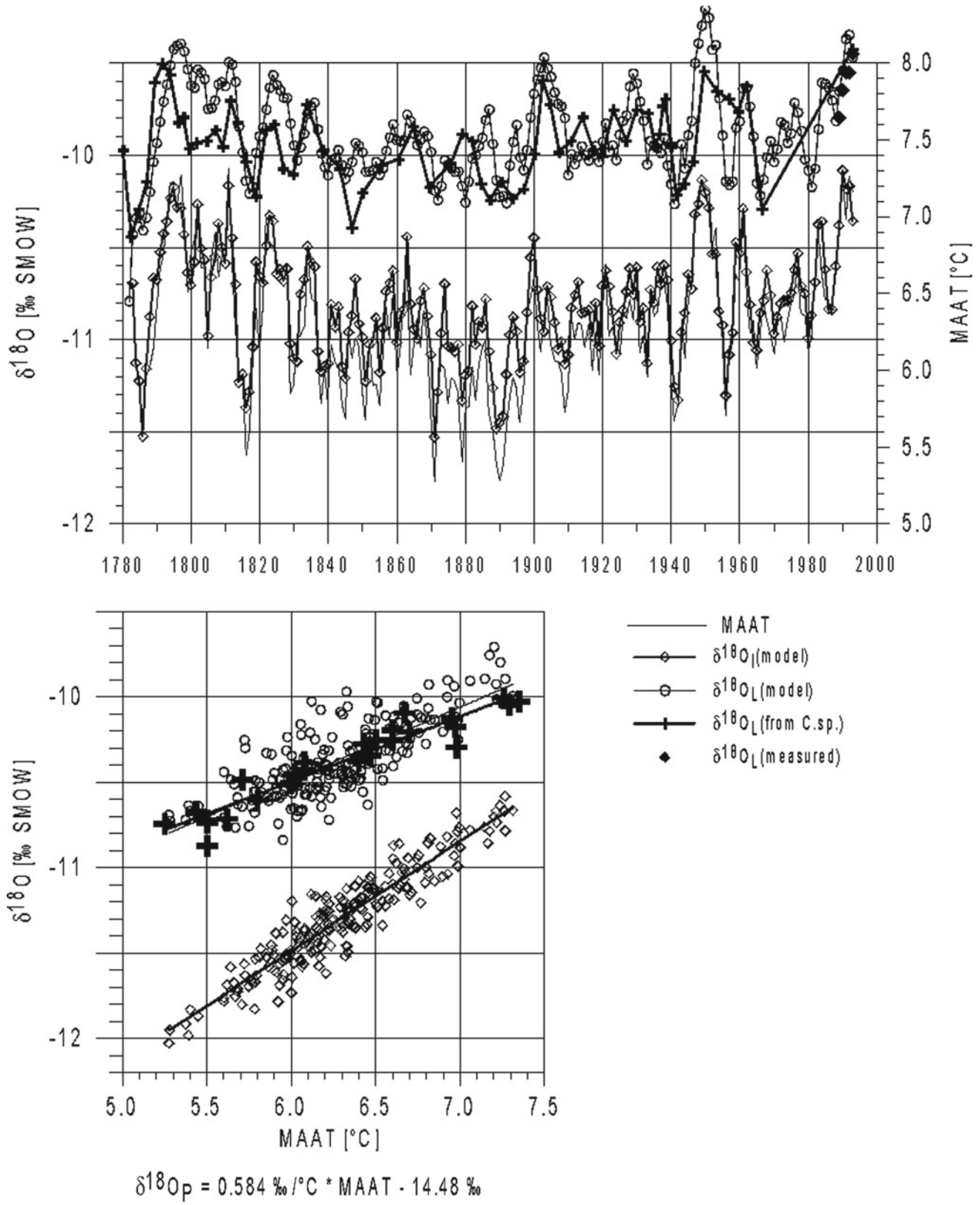

Fig. 15.4 Comparison of the $\delta^{18}O$ record of Lake Ammersee for the last two centuries derived from the $\delta^{18}O$ of juvenil Candona ($\delta^{18}O_L$(from C.sp), crosses) compared to the $\delta^{18}O_L$ as predicted by a two-box isotope hydrology model ($\delta^{18}O_L$ (model), open circles), if the lake was supplied with an inflow of river water with an isotopic composition ($\delta^{18}O_I$ (model), diamonds), controlled by the mean annual air temperature (MAAT) (using $\delta^{18}O_P$ = 0.58‰* MAAT—14.48‰ as $\delta^{18}O_P$–MAAT relation). The upper graph shows the development over time. The lower box compares the slope of the input relationship (diamonds) with the slopes of the modelled (open circles) and the ostracod-derived $\delta^{18}O_L$-MAAT relation. Air-temperature variations dominate both the modelled and observed lake responses. The slopes of the relationship of both the modelled and observed lake response to air temperatures are decreased compared to the $\delta^{18}O_P$—temperature relation, due to the incomplete reaction of $\delta^{18}O_L$ to the fast climate changes (von Grafenstein et al. 1996)

sediment core. We therefore decided to take a new sediment core at a position close to that of core AS96-1, using the latest generation of the UWITEC coring system available in 2010 which now provides excellent material to improve the age model by combining radiocarbon dating and varve counting for large parts of the Holocene (Czymzik et al. 2013) and through radiocarbon dating and tephrochronology for the Late Glacial period. Sample treatment and the selection of monospecific shell material from the last 5500 years are ongoing. More highly-resolved and well-dated records will come from Mondsee (Austria) and Lac d'Annecy (France). For both records, all necessary monospecific carbonate samples have been prepared and are currently being analysed. A new sediment core from Lago d'Iseo (Italy) will provide a $\delta^{18}O_P$ record for the southern central Alps. However, this record will be discontinuous due to the lack of preserved carbonate material in parts of the sequence.

Late Glacial and Early Holocene Shallow-Water Temperatures

As shown above, the $\delta^{18}O$ of ostracods and molluscs living in shallow water carries combined information on the $\delta^{18}O_L$ and the water temperature at the moment of calcification. Some of the species and their instars have a seasonal preference for calcification. Therefore, it should be possible to calculate the water temperature of this time interval from $\delta^{18}O$ of fossil valves, if $\delta^{18}O_L$ for the given deposition time is known. Figure 15.6 shows, for example, the $\delta^{18}O$ records of *Pisidium* from three cores taken in Ammersee at 6, 7 and 11 m modern water depth, compared with the deep-lake $\delta^{18}O$ measured on juvenile *Candona*, all corrected for the respective vital offsets. The difference between littoral and profundal $\delta^{18}O$ values should give the mean water temperature for the shell growth period of *Pisidium*, i.e. summer (t_s) at the littoral sites according to $t_s = 4\ °C - (\delta^{18}O_{Cs} - {}^{18}O_{Pi})/(0.23‰/°C)$ (von Grafenstein et al. 1999a, b). For the sites at 6 and 7 m, summer water temperatures are rather similar and range between 6 and 12 °C for the period from 14.8 to 12.7 ky B.P. (Bølling/Allerød), i.e. on average 4 °C colder than today's 13 °C at this water depth in Ammersee. During the Younger Dryas they are 6 °C, i.e. −7 °C with respect to modern values. Summer water temperatures reach present-day values immediately after the end of the Younger Dryas. For the core from 11 m water depth, the early Holocene summer water temperatures are also close to the respective observed modern equivalent (9 ± 3 °C), in contrast to the 6 ± 2 °C during the Younger Dryas. Together, these results indicate a strong reduction in the stability of the thermal summer stratification of the water column due to considerably colder air temperatures during the Younger Dryas.

The summer water temperatures calculated from the differences between valves from littoral and profundal benthic organisms are an independent confirmation of the climatic significance of the changes in $\delta^{18}O_P$. They provide one of the rare temperature reconstructions for the late Glacial in Central Europe, which is derived from a physicochemical process, such as the temperature-dependent oxygen isotope fractionation between water and calcite. Theoretically,

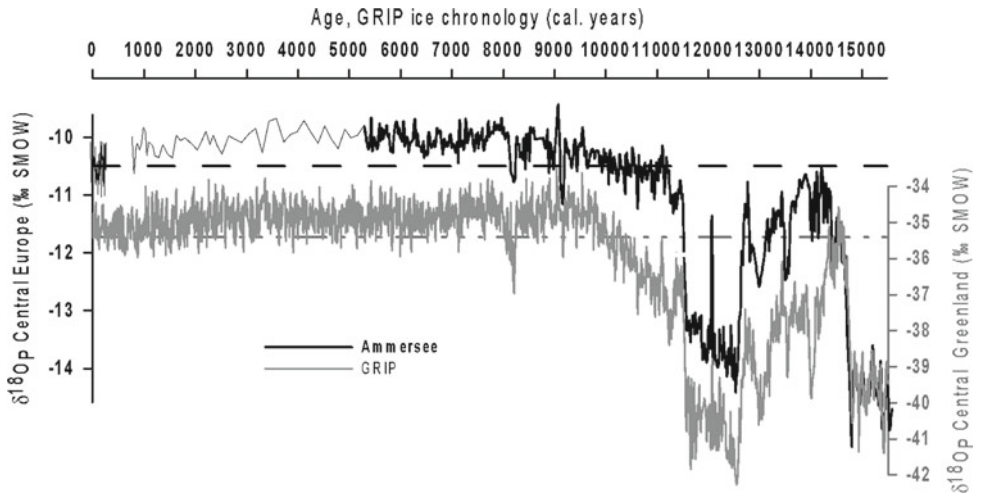

Fig. 15.5 Summary diagram showing the state of the $\delta^{18}O_P$ reconstruction from Ammersee deep-lake ostracods from AS Tmax (von Grafenstein 2002), AS 92-5 (von Grafenstein et al. 1998), and AS96-1 (von Grafenstein et al. 1998) cores. For sections sampled and measured with the optimal resolution (~10 years/sample), $\delta^{18}O_P$ is traced by the thicker black line. The thin black line indicates the interval (5500 B. P. to ~1700 AD) where further condensation is indicated. The high correlation with the $\delta^{18}O_P$ record from Central Greenland (grey line) that includes decadal events, provides strong evidence for a common control mechanism of the climate variability in both regions, probably via the North Atlantic thermohaline circulation

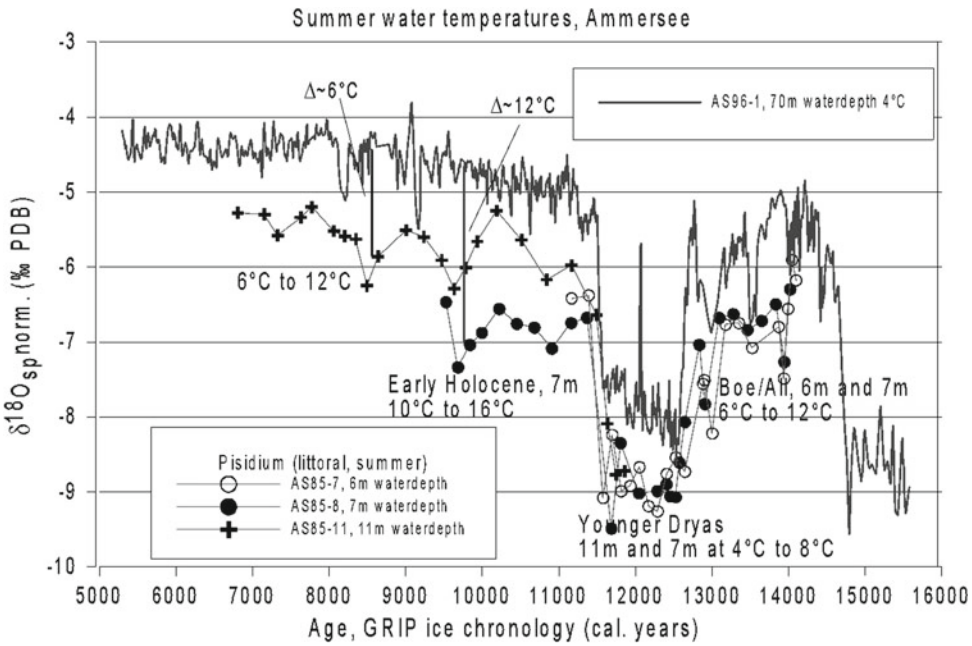

Fig. 15.6 Estimation of epilimnetic summer water temperatures in Ammersee by comparing the $\delta^{18}O$ of deep-lake ostracods (represented by $\delta^{18}O_L$, black line, data from (von Grafenstein et al. 1999a, b) with $\delta^{18}O$ of littoral *Pisidium* sp. in cores taken at water depths of 11 m (crosses), 7 m (filled circles), and 6 m (open circles) (von Grafenstein et al. 1994) The vital offsets and a systematic offset between epilimnetic summer $\delta^{18}O_L$ and hypolimnetic $\delta^{18}O_L$ (0.75‰) are taken into account

similar calculations could be made for all species and their instars present in shallow water cores and so provide water temperature information over the entire seasonal cycle and over a wide range of water depths. Because these temperature calculations are based on the differences alone, they are essentially independent of the respective $\delta^{18}O_L$ and therefore an attractive alternative among lake-based measurements, where the $\delta^{18}O_L$ itself is dominated by hydrological effects or in regions where the temperature-dependence of $\delta^{18}O_P$ is weak or absent (as for example in the north-American Great Lakes or in closed basins like Issyk-Kul).

Quantification of Hydrological Effects

Above, we have shown that the sensitivity of $\delta^{18}O_L$ to hydrological changes is dependent to a large extent on the ratio between the lake's surface and the drainage basin area (A_L/A_C), as this controls the relative importance of the evaporation (E/I). We also mentioned that the quantitative comparison of $\delta^{18}O_L$ records from neighbouring lakes with significantly differing A_L/A_C would allow detection of changes of the runoff (P-ET), the evaporation (E), and/or the relative humidity (h). These hydrological changes would lead, in contrast to a changing $\delta^{18}O_P$ and to deviations from the present day's $\delta^{18}O_L$ separation of the lakes.

Figure 15.7 shows an example of a comparison between the deep-lake records from Ammersee with a weak isotope-hydrological sensitivity (E/I = 0.04; $\Delta^{18}O_{L-P}$ = 0.75‰) and Starnberger See (E/I = 0.17; $\Delta^{18}O_{L-P}$ = 2.75‰). Similar to Ammersee, the core from Starnberger See comes from a water depth (88 m) sufficient to assume that calcification temperatures were very close to 4 °C. In addition, the species selected for isotope measurement are identical for both lakes, allowing direct comparison of their $\delta^{18}O$ values as representative of the $\delta^{18}O_L$ history of the lakes. The only restrictions for a direct comparison are the differences in the temporal resolution of the records and the much smaller reactivity of the Starnberger See to changes in $\delta^{18}O_P$. One sample from the Starnberger See record represents the average $\delta^{18}O_L$ over a period of several hundreds of years, compared to about ten years for an Ammersee sample. Similarly, the modern isotopic composition of Starnberger See water is integrated into the $\delta^{18}O_P$ history of at least the last 63 years, in contrast to about 8 years for the Ammersee. In order to get a meaningful 'modern' lake differential based on the same $\delta^{18}O_P$ reference, we calculated a longer term $\delta^{18}O_L$ average for the Ammersee since ~1930 from the ostracod record of the short gravity core TMAX and from the modelling of $\delta^{18}O_L$, which increase the reference lake offset to 2.5‰ compared to the apparent 2.0‰ offset in 1994. This is to a large extent due to the fact that Starnberger See water could not follow the rapid 0.5‰ increase of $\delta^{18}O_P$ between 1990 and 1994.

The 'modern' lake offset seems to be maintained or has slightly increased by up to 0.3‰ for the last 7000 years and for the Late Glacial (except for the Younger Dryas, which is not represented by ostracod valves in the core from Starnberger See). At the beginning of the Holocene, the difference was about 0.8‰ higher and approached the 'modern' offset between 9000 and 7000 years B.P. Lacking further evidence from another neighbouring lake or from δD_L records from both lakes, we can attribute the maximal increase of the difference to a reduction in the runoff (I = P − ET) of 50%,

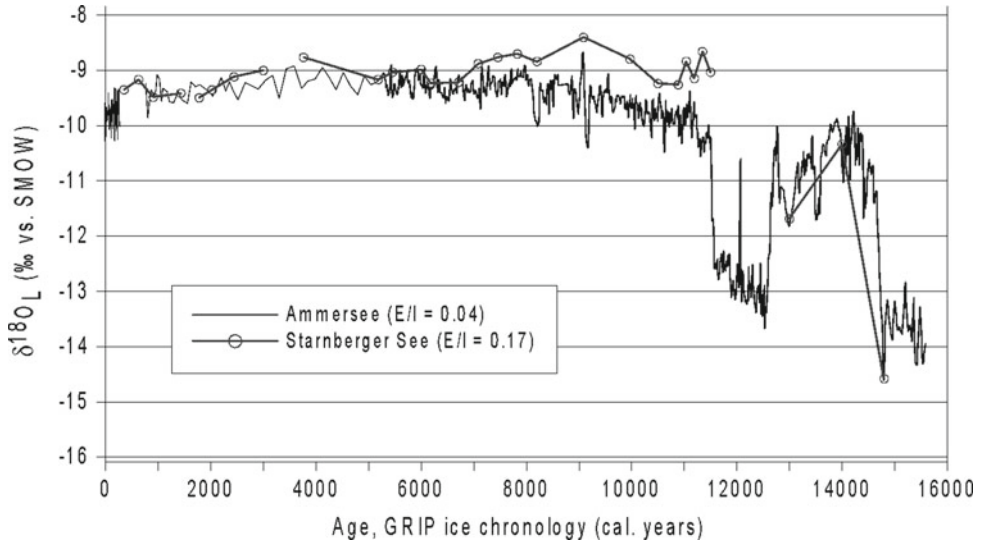

Fig. 15.7 Comparison of the deep-lake ostracod-derived $\delta^{18}O_L$ records of the Ammersee (black line) and the Starnberger See (open circles and line, corrected for the modern $\delta^{18}O_L$-difference between both lakes). The record from Starnberger See follows the low-frequency changes of $\delta^{18}O_L$ in Ammersee, with an offset very close to the modern difference for the last 7000 years and for the first warm period of the Late Glacial. The offset is increased by up to 0.8‰ during the Early Holocene (11,500 to 7000 years BP) indicating 'dryer than modern' conditions

an increase of the evaporation from the lakes' surfaces (E) of 100% or a reduction of the relative humidity from 0.74 to 0.5. Most probably, we need to distribute the overall effect to more moderate changes of all three parameters, which, in a natural world, are closely connected and often correlated. A reduction in I of 12%, together with an increase in E of 12%, and a relative humidity of 0.64, would, as would an infinitive number of other combinations, explain the increase in the lake offset of 0.8‰. However, all changes of these parameters had an effect not only on the difference of $\delta^{18}O_L$ jn the lakes but also on the evaporative enrichment and $\delta^{18}O_L$–$\delta^{18}O_P$ of the Ammersee, which we considered as constant for the $\delta^{18}O_P$ reconstruction. The resulting correction of the $\delta^{18}O_P$ estimate for the Early Holocene would be −0.6‰ in the case of highly improbable isolated changes of either E or I, against only −0.25‰ for our example of combined h, I, and E changes. Besides important paleohydrological information, the lake-to-lake comparison also allows us to exclude errors in the $\delta^{18}O_P$ reconstruction arising from water balance changes for last 7000 years. For the early Holocene, the $\delta^{18}O_P$-record from Ammersee is probably up to 0.25‰ too high. A correction can be proposed using all available data points from the Starnberger See, which would then largely reduce the hydrological-induced uncertainties of the Ammersee $\delta^{18}O_P$-record. In future, a condensation of the Starnberger See record should be considered to increase confidence in the quantitative reconstruction of $\delta^{18}O_P$ from its neighbour.

Conclusions

Oxygen isotope records from deep-lake ostracods can provide high-resolution quantitative records of $\delta^{18}O_P$, if those lakes that are selected have (1) a small relative contribution from evaporation to the lake water balance, (2) a well-defined drainage basin without evidence of major re-organisation of its associated fluvial system, (3) a theoretical residence time between 2 and 10 years, (4) a water depth in excess of 50 m, (5) an annual complete overturn, and (6) proven preservation of in situ ostracod fauna among its profundal sediments. The temporal resolution of $\delta^{18}O_P$ from benthic deep-lake ostracods is limited to roughly ten years, the ε-folding time of lakes with a buffering volume large enough to suppress eventual bias from the seasonal variability of $\delta^{18}O$ of precipitation and river water. It was shown, using the example from Ammersee that a maximal theoretical resolution can be practically obtained. Detailed hydrological, limnological, and isotopic investigations can provide the basis for a realistic quality control of the $\delta^{18}O_P$ reconstruction. For the $\delta^{18}O_P$ record of the last 15,500 years, the maximal error from water temperature effects is ±0.2‰, to which must be added uncertainty from possible hydrological changes of –0.3‰ to +0.6‰. Correction of the record using the quantification of the hydrological effects through comparison with the more strongly affected Starnberger See further reduces the overall error to a maximum of ±0.4‰ for the driest period in the Holocene.

$\delta^{18}O_P$ records provide quantitative hydro-meteorological information, which is largely independent of the biological response to climate change and thus can be used as a reference in multidisciplinary studies. For Central and Northwest Europe, those $\delta^{18}O_P$ records can be considered as a reasonable proxy for the mean air temperature. A calibration of the $\delta^{18}O$ record from Ammersee for the 200-year long period of instrumental climate observation confirmed the $\delta^{18}O_P$/temperature relationship derived from precipitation measurements (0.58‰/°C) for the last three decades in Europe. Independent qualitative evidence for colder air temperatures during the Younger Dryas could be extracted from water- and isotope-based shallow water temperature reconstruction, which further confirms the temperature-dependence of $\delta^{18}O_P$ in Europe. However, $\delta^{18}O_P$ records provide excellent quantitative paleoclimatic information even for regions where such a temperature-dependence is absent or weak. High quality $\delta^{18}O_P$ records are also very useful to increase the significance of $\delta^{18}O$ records from archives, which are more affected or dominated by secondary isotopic effects. Deep-lake ostracod valves from carefully selected lakes are, at the moment, the best material to obtain quantitative $\delta^{18}O_P$ records for significant time periods from temperate, non-glaciated areas. As such, they merit more consideration as a climate proxy in future research strategies.

Beside $\delta^{18}O_P$-reconstruction, deep-lake ostracod-based oxygen isotope records have been successfully used to unscramble the complex hydrological changes in the Great Lakes Basin, and, in combination with geomorphological lake level reconstruction, to provide information on the water balance development and humidity in hydrologically closed basins. In all cases, deep-lake ostracods provide very precise estimates for the isotopic composition of former lake water, which can be used as a reference to quantify the secondary effects on $\delta^{18}O$ of all other authigenic material produced in the same lake, such as water temperature-dependent fractionation in the case of littoral and sublittoral ostracods.

Perspectives

In future, archived and new core material from Ammersee, Mondsee, Lac d'Annecy, and Lago d'Iseo will be used to close the existing gaps and to provide optimally resolved $\delta^{18}O_P$ records for the entire period since the last glacial maximum. Besides their direct application as proxies for mean annual air temperatures, records of decadal $\delta^{18}O_P$ variations in Europe offer many possibilities for further hydrogeological and paleoclimatological studies. They could serve as 'marker input function' into groundwater and thus allow a better exploitation of stable isotope measurements of fossil groundwater for the last 15,500 years, which, for the moment, is considered as a simple, one-step function from cold, isotopically-depleted to present-day values. They will also facilitate quantification and climatic interpretation of records from less direct continental isotopic archives such as tree rings, shallow-water lake records, and stalagmites. Although lakes with the potential to provide a quantitative $\delta^{18}O_P$ record are characterized by a narrow range of hydrological and geomorphological settings, there are at least ten suitable candidates identified in Europe, for which a limited dataset of water isotopes exists. Those lakes could in future be exploited to provide a network of reasonably well distributed and highly resolved $\delta^{18}O_P$ records. It is likely that at least a similar number of such lakes can be found in the temperate regions of North and South America and within other formerly glaciated mountain ranges around the globe.

References

Alefs, J., Müller, J., & Wunsam, S. (1996). Die Rekonstruktion der epilimnischen Phosphorkonzentrationen im Ammersee seit 1958. *Gwf Wasser Abwasser, 137*(8), 443–448.

Andersen, N., Lauterbach, S., Erlenkeuser, H., Danielopol, D.L., Namiotko, T., Hüls, M., et al., (2017). Evidence for higher-than-average air temperatures after the 8.2 ka event provided by a Central European $\delta^{18}O$ record. *Quaternary Science Reviews, 172*, OP- 96.

Bornemann, A., Pirkenseer, C. M., De Deckker, P., & Speijer, R. P. (2012). Oxygen and carbon isotope fractionation of marine ostracod calcite from the eastern Mediterranean Sea. *Chemical Geology, 310–311,* 114–125.

Chivas, A. R., de Deckker, P., Cali, J. A., Chapman, A., Kiss, E., & Shelley, J. M. G. (1993). Coupled stable-isotope and trace-element measurements of lacustrine carbonates as paleoclimatic indicators. In P. K. Swart, K. C. Lohmann, J. Mckenzie & S. Savin (Eds.), *Climate change in continental isotopic records*. School of Marine and Atmospheric Science.

Chivas, A., De Deckker, P., Wang, S. X., & Cali, J.A. (2002) Oxygen-isotope systematics of the nektic ostracod *Australocypris robusta*. In J. A. Holmes, A. R. Chivas (Eds.), *Ostracoda, applications in quaternary research*. Geophysical Monograph Series (Vol. 131, pp. 301–313). American Geophysical Union (AGU).

Colman, S. M., Keigwin, L. D., & Forester, R. M. (1994). Two episodes of meltwater influx from Lake Agassiz into the Lake Michigan basin and their climatic contrasts. *Geology, 22,* 547–550.

Czymzik, M., Brauer, A., Dulski, P., Plessen, B., Naumann, R., von Grafenstein, U., et al. (2013). Orbital and solar forcing of shifts in Mid- to Late Holocene flood intensity from varved sediments of pre-alpine Lake Ammersee (southern Germany). *Quaternary Science Reviews, 61,* 96–110.

Danielopol, D. L., Ito, E., Wansard, G., Kamiya, T., Cronin, T.M., & Baltanas, A. (2002) Techniques for collection and study of ostracoda. In J. A. Holmes & A. R. Chivas (Eds.), *Ostracoda, Applications in quaternary research*, Geophysical Monograph Series (Vol. 131, pp. 65–97). American Geophysical Union (AGU).

Danis, P. A., von Grafenstein, U., & Masson-Delmotte, V. (2003) Sensitivity of deep lake temperature to past and future climatic changes: A modelling study for Lac d'Annecy, France, and Ammersee, Germany. *Journal of Geophysical Research-Atmospheres, 10*(D19).

Danis, P. A., von Grafenstein, U., Masson-Delmotte, V., Planton, S., Gerdeaux, D., & Moisselin, J. M. (2004) Vulnerability of two European lakes in response to future climatic changes. *Geophysical Research Letters, 31*(21).

Dansgaard, W. (1964). Stable isotopes in precipitation. *Tellus, 16,* 436–468.

De Deckker, P. (2002). Ostracod palaeoecology. In J. A. Holmes & A. R. Chivas (Eds.), *Ostracoda, applications in quaternary research*. Geophysical Monograph Series (Vol. 131, pp. 121–134). American Geophysical Union (AGU).

Decrouy, L., Vennemann, T. W., & Ariztegui, D. (2011) Controls on ostracod valve geochemistry: Part 2. Carbon and oxygen isotope compositions. *Geochimica et Cosmochimica Acta, 75*(22), 7380–7399.

Dettman, D. L., Smith, A. J., Rea, D. K., Moore, T. C., & Lohmann, K. C. (1995). Glacial meltwater in Lake Huron during Early Postglacial time as inferred from single-valve analysis of oxygen isotopes in ostracodes. *Quaternary Research, 43*(3), 297–310.

Devriendt, L. S., McGregor, H. V., & Chivas, A. R. (2017). Ostracod calcite records the18O/16O ratio of the bicarbonate and carbonate ions in water. *Geochimica et Cosmochimica Acta, 214,* 30–50.

Didié, C., & Bauch, H. A. (2002). *Implications of upper Quaternary stable isotope records of marine ostracods and benthic foraminifers for paleoecological and paleoceanographical Investigations* (pp. 279–299). American Geophysical Union (AGU).

Forester, R. M., Colman, S. M., Reynolds, R. L., & Keigwin, L. D. (1994). Lake Michigan's late Quaternary limnological and climate history from ostracod, oxygen isotope, and magnetic susceptibility. In: D. W. Folger, S. M. Colman, & P. W. Barnes (Eds.), *South. Lake Michigan Coast. Eros. Study* (pp. 93–107). Woods Hole, MA, USA: U. S. Geological Surve.

Fritz, P., Anderson, T. W., & Lewis, C. F. M. (1975). Late Quaternary climatic trends and history of Lake Erie from stable isotope studies. *Science, 160,* 267–269.

Gat, J. R., Lister, G. S., & Frenzel, B. (1995). The 'catchment effect' on the isotopic composition of lake waters; its importance in paleolimnological interpretations. In B. Frenzel, B. Stauffer, & M. M. Weiss (Eds.), *Problems of stable isotopes in tree-rings, lake sediments and peatbogs as climatic evidence for the Holocene*. Issue ESF Proj. 'European Palaeoclim. Man' 10 (pp. 1–16). Stuttgart/New York: Gustav Fischer Verlag.

Gibson, J. J., Edwards, T. W. D., Bursey, G. G., & Prowse, T. D. (1993). Estimating evaporation using stable isotopes: Quantitative results and sensitivity analysis for two catchments in Northern Canada. *Nordic Hydrology, 24,* 79–94.

Hammarlund, D., Edwards, T. W. D., Bjorck, S., Buchardt, B., & Wohlfarth, B. (1999). Climate and environment during the Younger Dryas (GS-1) as reflected by composite stable isotope records of lacustrine carbonates at Torreberga, Southern Sweden. *Journal of Quaternary Science, 14*(1), 17–28.

Hoffmann, G., Werner, M., & Heimann, M. (1998). The water Isotope module of the ECHAM atmospheric general circulation model—A study on time scales from days to several years. *Journal of Geophysical Research, 103*(16), 816–871, 896.

Holmes, J. A., & Chivas, A. R. (2002). Ostracod shell chemistry—overview. in: J.A. Holmes, A.R. Chivas (Eds.), *Ostracoda, applications in Quaternary research*, Geophysical Monograph Series (Vol. 131, pp. 1–4). American Geophysical Union (AGU).

Horne, D. J., Cohen, A., & Martens, K. (2002) Taxonomy, morphology and biology of Quaternary and living Ostracoda. In: J. A. Holmes & A. R. Chivas (Eds.), *Ostracoda, applications in Quaternary research*. Geophysical monograph series (Vol. 131, pp. 5–36). American Geophysical Union (AGU).

Jouzel, J., Russell, G. L., Suozzo, R. J., Koster, R. D., White, J. W. C., & Broecker, W. S. (1987). Simulations of the HDO and $H_2^{18}O$ atmospheric cycles using the NASA GISS general circulation model: The seasonal cycle for present-day conditions. *Journal of Geophysical Research, 92,* 14739–14760.

Keatings, K. W., Heaton, T. H. E., & Holmes, J. A. (2002). Carbon and oxygen isotope fractionation in non-marine ostracods: Results from a 'natural culture' environment. *Geochimica et Cosmochimica Acta, 66*(10), 1701–1711.

Lauterbach, S., Brauer, A., Andersen, N., Danielopol, D. L., Dulski, P., Hüls, M., et al. (2011). Environmental responses to Lateglacial climatic fluctuations recorded in the sediments of pre-Alpine Lake Mondsee (northeastern Alps). *Journal of Quaternary Science, 26* (3), 253–267.

Lewis, C. F. M., & Anderson, T. W. (1992). Stable isotope (O and C) and pollen trends in eastern Lake Erie, evidence for a locally induced climatic reversal of Younger Dryas age in the Great Lakes basin. *Climate Dynamics, 6,* 241–250.

Li, X., & Liu, W. (2010). Oxygen isotope fractionation in the ostracod *Eucypris mareotica*: Results from a culture experiment and implications for paleoclimate reconstruction. *Journal of Paleolimnology, 43*(1), 111–120.

Lister, G. S. (1988). A 15,000-year isotopic record from Lake Zürich of deglaciation and climatic change in Switzerland. *Quaternary Research, 29*(2), 129–141.

Lister, G. S., Kelts, K., Zao, C. K., Yu, J. Q., & Niessen, F. (1991). Lake Qinghai, China; closed-basin lake levels and the oxygen isotope record for Ostracoda since the latest Pleistocene. In A. R. Chivas & P. De Deckker (Eds.), *SLEADS conference*, Arkaroola, South Aust. (pp. 141–162), Aug. 8–16. 62 Refs.

Marco-Barba, J., Ito, E., Carbonell, E., & Mesquita-Joanes, F. (2012). Empirical calibration of shell chemistry of *Cyprideis torosa* (Jones, 1850) (Crustacea: Ostracoda). *Geochimica et Cosmochimica Acta, 93,* 143–163.

Niessen, F., & Kelts, K. (1989). The deglaciation and Holocene sedimentary evolution of southern perialpine Lake Lugano—Implications for Alpine paleoclimate. *Eclogae Geologicae Helveticae, 82*(1), 235–263.

Rea, D. K., Moore, T. C., Jr., Anderson, T. W., Lewis, C. F. M., Dobson, D. M., Dettman, D. L., et al. (1994). Great Lakes paleohydrology: Complex interplay of glacial meltwater, lake levels, and sill depths. *Geology, 22*(12), 1059.

Rozanski, K., Araguás-Araguás, L., & Gonfiantini, R. (1992). Relation between long-term trends of oxygen-18 isotope composition of precipitation and climate. *Science, 258,* 981–985.

Schwalb, A. (2003). Lacustrine ostracods as stable isotope recorders of late-glacial and Holocene environmental dynamics and climate. *Journal of Paleolimnology, 29*(3), 267–351.

Schwalb, A., Lister, G. S., & Kelts, K. (1994). Ostracode carbonate $d^{18}O$- and $d^{13}C$-signatures of hydrological and climatic changes affecting Lake Neuchâtel, Switzerland, since the latest Pleistocene. *Journal of Paleolimnology, 11,* 3–17.

Thompson, L. G., Yao, T., Davis, M. E., Henderson, K. A., Mosley-Thompson, E., Lin, P. N., et al. (1997). Tropical climate instability: The Last Glacial Cycle from a Qinghai-Tibetan Ice Core. *Science, 276,* 1821–1825.

Van der Meeren, T., Ito, E., Verschuren, D., Almendinger, J. E., & Martens, K. (2011). Valve chemistry of Limnocythere inopinata (Ostracoda) in a cold arid environment—Implications for paleolimnological interpretation. *Palaeogeography, Palaeoclimatology, Palaeoecology, 306*(3–4), 116–126.

von Grafenstein, U. (2002). Oxygen-isotope studies of ostracods from deep lakes. In J. A. Holmes & A. R. Chivas (Eds.), *Ostracoda, applications in quaternary research*. Geophysical Monograph Series (Vol. 131, pp. 249–265). American Geophysical Union (AGU).

von Grafenstein, U., Belmecheri, S., Eicher, U., van Raden, U.J., Erlenkeuser, H., Andersen, N., et al. (2013). The oxygen and carbon

isotopic signatures of biogenic carbonates in Gerzensee, Switzerland, during the rapid warming around 14,685 years BP and the following interstadial. *Palaeogeography, Palaeoclimatology, Palaeoecology, 391*(Part B OP-In Early Rapid Warning, Palaeogeography, Palaeoclimatology, Palaeoecology 1 December 2013 391 Part B: 25–32), 25.

von Grafenstein, U., Eicher, U., Erlenkeuser, H., Ruch, P., Schwander, J., & Ammann, B. (2000). Isotope signature of the Younger Dryas and two minor oscillations at Gerzensee (Switzerland): Palaeoclimatic and palaeolimnologic interpretation based on bulk and biogenic carbonates. *Palaeogeography, Palaeoclimatology, Palaeoecology, 159*(3–4), 215–229.

von Grafenstein, U., Erlenkeuser, H., Kleinmann, A., Müller, J., & Trimborn, P. (1994). High-frequency climatic oscillations as revealed by oxygen-isotope records of benthic organisms (Ammersee, Southern Germany). *Journal of Paleolimnology, 11,* 349–357.

von Grafenstein, U., Erlenkeuser, H., Müller, J., Jouzel, J., & Johnsen, S. (1998). The cold event 8200 years ago documented in oxygen isotope records of precipitation in Europe and Greenland. *Climate Dynamics, 14*(2), 73–81.

von Grafenstein, U., Erlenkeuser, H., Müller, J., & Kleinmann-Eisenmann, A. (1992). Oxygen isotope records of benthic ostracods in bavarian lake sediments—Reconstruction of late and postglacial air temperatures. *Naturwissenschaften, 79*(4), 145–152.

von Grafenstein, U., Erlenkeuser, H., Müller, J., Trimborn, P., & Alefs, J. (1996). A 200 year mid-European air temperature record preserved in lake sediments: An extension of the $d^{18}O_p$—Air temperature relation into the past. *Geochimica et Cosmochimica Acta, 60*(21), 4025–4036.

von Grafenstein, U., Erlernkeuser, H., & Trimborn, P. (1999a). Oxygen and carbon isotopes in modem freshwater ostracod valves: Assessing vital offsets and autecological effects of interest for palaeoclimate studies. *Palaeogeography, Palaeoclimatology, Palaeoecology, 148* (1–3), 133–152.

von Grafenstein, U., Erlenkeuser, H., Brauer, A., Jouzel, J., & Johnsen, S. (1999b). A mid-European decadal isotope-climate record from 15,500 to 5,000 years B.P. *Science, 284,* 1654–1657.

Xia, J., Ito, E., & Engstrom, D. R. (1997). Geochemistry of ostracod calcite: 1. An experimental determination of oxygen isotope fractionation. *Geochimica et Cosmochimica Acta, 61,* 377–382.

Vegetation-Atmosphere Interface: Tree Rings

16

Joël Guiot and Valérie Daux

A Dendrochonological Approach

In many parts of the world, there is a strong seasonality in the annual distribution of temperatures and rainfall. This seasonality is reflected in the growth of trees, which is the result of the interaction of the tree with its environment, via its leaves (for carbon and water exchanges) and its roots (for nutrients and water). In temperate latitudes, during the winter, the tree is dormant and woody cells are not produced. In spring, when the thermal conditions are met, the tree becomes active and starts to produce large, dispersed woody cells (early wood). Towards late spring and early summer, the cells produced are denser and smaller (late wood), then, at the end of the summer, cells are no longer produced along the trunk and the tree starts to store reserves for the following year. If a trunk is cut through, alternating light and dark bands can be observed, which, combined, constitute an annual growth ring. Comparison between rings shows a high level of variability. This variability is the direct consequence of the climate conditions (temperature, rainfall, sunlight) which prevailed during or before the formation of the cells (Fritts 1976).

These seasonal growths are produced by tissues in the cambium, a layer of cells between the wood and the bark which causes expansion in the diameter of the roots, trunk and branches of the tree. Besides climate, the thickness of the ring also depends on many other parameters including the species, the age of the ring, the availability of nutrients in the soil, the tree's ability to retain water, its exposure etc. Douglas (1920) was the first to recognize the potential of series of annual growth rings to provide information about past climates, and he established the fundamentals of what is now known as dendroclimatology. The main difficulty is to distinguish the impact of climate from other factors. The greater the climate stress the tree is subjected to, the easier this is to decode. Generally, there are two types of climate stress: heat stress and water stress. In arid or semi-arid regions, tree growth is limited by the availability of water. Therefore, this will be the main parameter recorded by the tree. Trees in the far north or at high altitudes are constrained by temperature. This makes them very good thermometers. The climate conditions in the months prior to the growing season also affect the ring. These may be the replenishment of groundwater reserves, or carbon reserves ready to be activated for the following year. This further complicates the decoding of climate information.

The dendroclimatic approach (Cook and Kairiukstis 1990; Trouet 2020) involves taking a number of cores from a given forest, at a rate of between two and four cores per tree from ten to twenty trees per stand. A core is a small tube taken from the bark to the middle of the tree, from which the sequence of rings can be read. The trees most likely to provide the best information on the climate parameter to be reconstructed are chosen. For example, when reconstructing a water parameter, trees growing in shallow soils which are unable to store much water will be selected. Each core is then dated by counting the rings from the bark to the heart of the tree. Each ring is supposed to be annual, but sometimes growth stops during the season because of a temporary drought and resumes if it starts to rain. This resulting growth arrest produces what is called a false ring. For this year, there are two rings. In other years, conditions are so unfavorable that the ring appears to be missing. These two types of phenomena will produce errors in the dating of rings. Cross dating, that is, the comparison of series between cores, helps eliminate these errors.

J. Guiot (✉)
European Centre for Research and Teaching in Environmental Geosciences CEREGE, Aix-Marseille University, CNRS, IRD, INRAE, Collège de France, BP 80, 13545 Aix-en-Provence Cedex 04, France
e-mail: guiot@cerege.fr

V. Daux
Laboratoire des Sciences du Climat et de l'Environnement, LSCE/IPSL, CEA-CNRS-UVSQ, Université Paris-Saclay, 91190 Gif-sur-Yvette, France

G. Ramstein et al. (eds.), *Paleoclimatology*, Frontiers in Earth Sciences,
https://doi.org/10.1007/978-3-030-24982-3_16

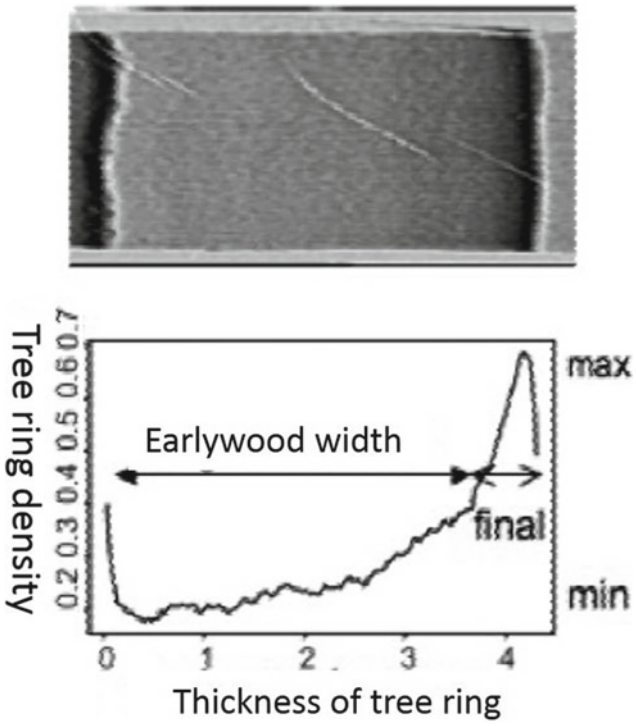

Fig. 16.1 Typical profile of a conifer ring (above) with the corresponding density curve (below) and the main parameters that can be deduced

Each ring is measured and a set of between twenty and forty time series is produced for each stand. As well as the thickness, the density may also be measured using a micro-densitometer (see typical profile in Fig. 16.1). One can thus obtain the thicknesses of the early wood and the summer wood as well as the average density of the early wood and the maximum density. These are the most frequently used parameters (Schweingruber et al. 1978).

The next step is to try to reconstruct the climate signal. Tree-ring series are often affected by trends associated with the age of the tree. Statistical methods are used to eliminate these. Various methods have been developed: polynomial curves, digital filters, exponential decay are removed from the raw data by division. This process is called indexing. The main problem with this is that often a part of the trend linked to climate is also removed. Figure 16.2 shows how one can get an indexed series from an untreated series of rings. The various indexed series from the same stand are averaged to produce a representative series for the stand, called the master timeline, in order to remove intra-site variability. This is done in an attempt to maximize the climate signal. Other indexing methods are increasingly used to try to best preserve climate variations over the long-term (Cook and Kairiukstis 1990).

A single average series (also called master series) of a stand is rarely able to provide a reliable climate reconstruction because the interactions between climate and growth are complex.

A network of master timelines for a given region needs to be established, including different species of trees, in order to better isolate the relevant climate variable. This is then followed by a statistical approach called transfer function (Cook and Kairiukstis 1990). On one side, a matrix of dendrochronological series, necessarily of variable length, is established, and on the other side, weather series for the same region are assembled. Over the time period common to both the meteorological and tree-ring series, a statistical relationship by regression methods can be calibrated.

The following example illustrates how it is possible to reconstruct summer temperatures in Europe from tree-ring series, supplemented by other proxies (Guiot et al. 2010). Among these proxies, we used series of harvest dates from several wine regions in France and Switzerland and the isotopic series for oxygen-18 in Greenland, which is considered to be related to the global climate. All these series are of variable length and resolution. They also represent different characteristics of the climate, but the climate parameter that best explains tree growth and the precociousness of the grape harvest is the temperature between April and September. Therefore, it is this summer temperature that was estimated using a statistical technique of similarities, called the analog method (Guiot et al. 2010).

The graph (Fig. 16.3) shows that the Little Ice Age (the defined span of which varies, but, here, is fixed at 1400–1900, and is marked by advancing glaciers in the Alps) was on average 0.35 °C colder than the 1961–1990 reference period, with a maximum cooling around 1600 (around −0.5 °C). The 1940–2007 period was 0.2 °C warmer than the reference period, and the last decade of the twentieth century topped this with a difference of 0.5 °C. Even taking into account that these averages are calculated over varying periods, the warming of the late twentieth century is significant. This is confirmed by the polynomial curve indicating a warming since the early nineteenth century of 0.6 °C for the century.

Dendro-isotopic Analysis

Tree rings are made up of organic material containing mainly carbon, oxygen and hydrogen. Each one of these elements has several isotopes. The isotopes of an element have chemical properties that are qualitatively identical. However, physical, chemical and biological processes can bring about a fractionation between light isotopes and heavy isotopes of the same element during physical or chemical reactions in which this element is involved. As a result, the isotopic ratios of oxygen ($\delta^{18}O$), carbon ($\delta^{13}C$) and hydrogen (δD) are a source of environmental information.

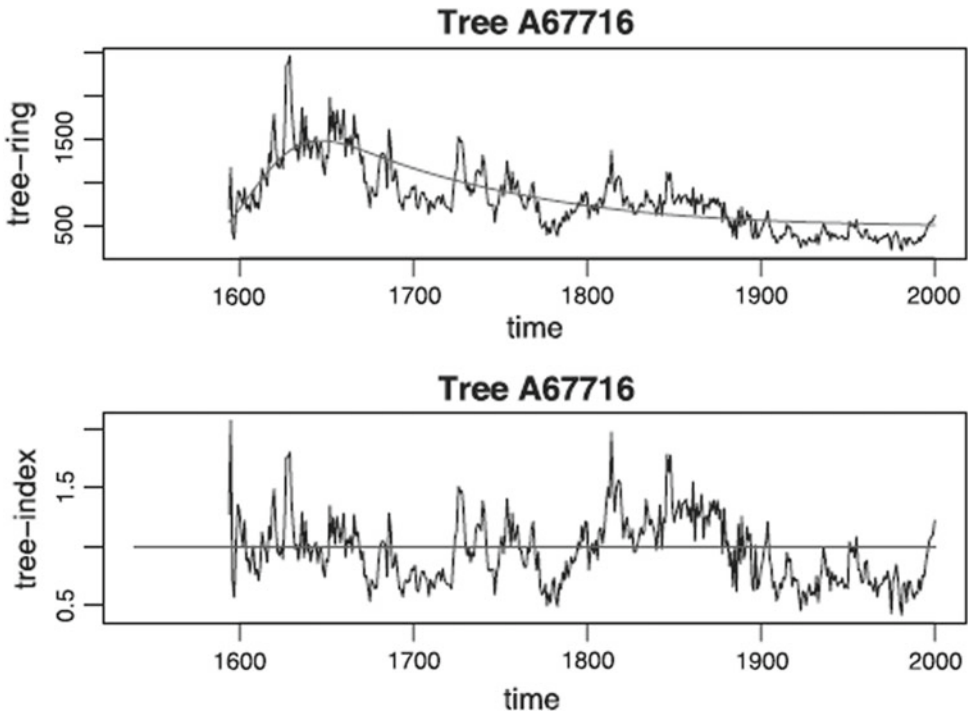

Fig. 16.2 Example of indexing of a tree-ring series: the top graph shows the raw data for the ring thicknesses with the trend line superimposed; the lower curve shows the indexed series, that is to say the raw series divided by the trend

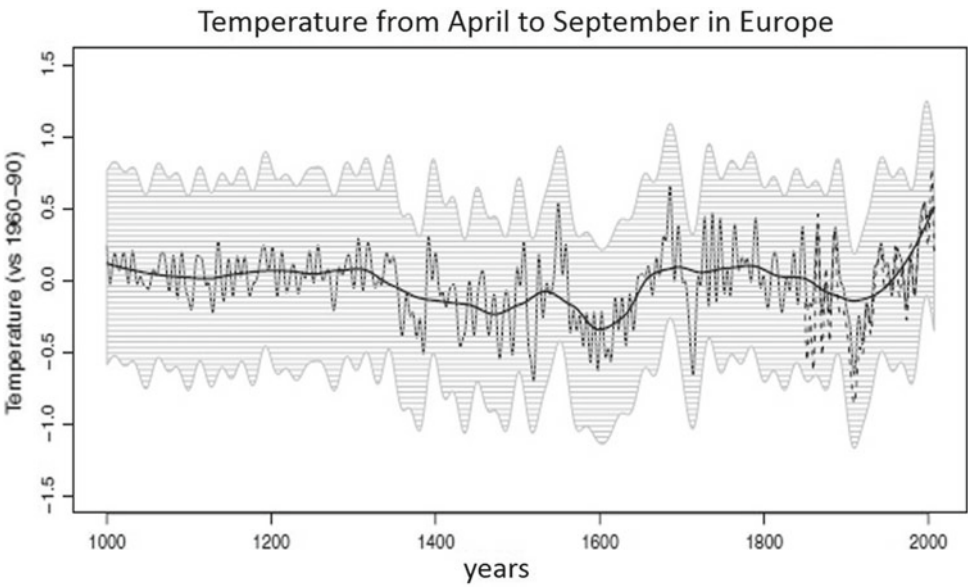

Fig. 16.3 Evolution of the summer temperatures reconstructed for Europe [10° O 60° E-and-30° N 85° N] taken from multiple proxies and smoothed. Shaded: the associated uncertainty (at 95%); dashed line: the corresponding observations (1850–2007); and, bold line: the trend line of the reconstruction (Guiot et al. 2010)

The isotopic composition of oxygen in precipitations is a function of temperature at high and middle latitudes. Water from precipitation infiltrates the soil. In the superficial levels, evaporation can result in oxygen enrichment of the infiltrated water compared to the original precipitation. Trees take most of their water from the superficial soil levels. Therefore, the water they draw can be enriched to some extent in heavy isotopes compared to the precipitation. Nevertheless, there is little or no enrichment in wooded areas where the soils are covered by thick litter that limits evaporation. The isotopic composition of the oxygen in the water of the xylem, through which water and mineral nutrients are transported, is the same as that of the soil water absorbed by the root system. Significant fractionation occurs before the water isotopes are fixed in the wood structure (for a summary of the isotopic composition of wood constituents see Gessler et al. 2014). The critical phase occurs in the leaves where evapotranspiration results in a loss of light isotopes. The extent to which the leaf is enriched with heavy isotopes depends on the difference between the isotopic compositions

of the water in the xylem and in the ambient vapor, as well as on the difference between the vapor pressure inside and outside the leaf. As a result of the evaporative fractionations, the isotopic composition of the glucose produced in the leaf is enriched by 27‰ compared to the water in the leaf. During synthesis of cellulose from glucose, about 40% of the oxygen atoms are exchanged with the xylem water. Consequently, the isotopic composition of the cellulose in tree rings reflects that of the source (soil water is more or less equivalent isotopically to precipitations) and the degree of enrichment by evaporation in the leaf. The link between the isotopic compositions of cellulose and rainfall is complex. Nevertheless, a growing number of studies have reported statistically significant correlations between the $\delta^{18}O$ of the cellulose in tree rings (oak, pine, larch, cedar) and that of the rainfall during the growing season, as well as certain other climate parameters (atmospheric temperature, relative humidity, water stress). Figure 16.4 shows examples of these correlations.

The $\delta^{13}C$ of atmospheric carbon is close to −8‰ (relative to the standard Pee Dee Belemnite). That of the leaves and the wood in the trees is in the region of −20‰ to −30‰. The isotopic fractionations which create the differences between the $\delta^{13}C$ of CO_2 in the air and the $\delta^{13}C$ of CO_2 in the plant, occur primarily in the leaf. Farquhar et al. (1982) has expressed this in the following equation:

$$\Delta^{13}C(‰) = a + (b - a)p_i/p_a,$$

where $\Delta^{13}C$ represents the discrimination of carbon between the $\delta^{13}C$ of glucose synthesized in the leaf and the CO_2 in the air, a is the fractionation due to diffusion through the stomata (4.4‰), b is the fractionation caused by carboxylation (27‰), p_i and p_a are the partial pressures of CO_2 in the substomatal cavity and the atmosphere respectively. The partial pressure of CO_2 within the substomatal cavity is conditioned by the opening of the stomata (resulting from a compromise between water loss and uptake of CO_2 from the ambient air). Additional isotopic fractionations, accentuating the depletion in ^{13}C, occur during the synthesis of cellulose and lignin. Plant-air exchanges are determined by the tree's environment (climate, water status of the soil). The outcome is that the $\delta^{13}C$ of the cellulose in tree rings is dependent on atmospheric temperature (Fig. 16.5).

The isotopic composition of hydrogen (δD) is linked to the atmospheric temperature, as is that of oxygen; it is not modified in the transfer from soil to tree, but it is affected by evapotranspiration, which causes isotopic enrichment of the water in the leaf and is subjected to fractionation during the process of photosynthesis. During photosynthesis, enzyme activity causes kinetic fractionations which may differ depending on the position of hydrogen in the glucose molecule (Augusti et al. 2006). During the transformation of glucose to cellulose in the trunk, the catalytic action of the enzymes generates isotopic exchanges between the sugars and water in the xylem which involve about 40% of the hydrogen atoms in the sugars (Waterhouse et al. 2002). As it is difficult to distinguish between the climate and physiological influences on the abundance of deuterium, the use of isotopic ratios of hydrogen in cellulose is complicated (Pendall 2000; Augusti et al. 2008).

As for the series of ring widths, the $\delta^{13}C$ cellulose of tree rings can show trends linked to age. This so-called 'juvenile' effect is characterized by low values of $\delta^{13}C$ in wood cellulose produced in the first decades of the tree (Francey and

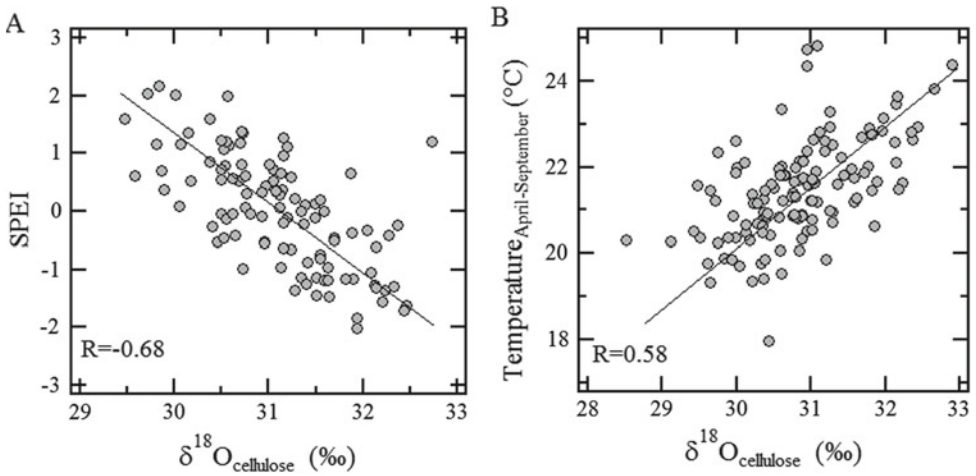

Fig. 16.4 Linear relationships between the isotopic composition of oxygen in the cellulose of oaks and **a** the Standardized Precipitation Evapotranspiration Index (SPEI) at Angoulême, France (SPEI; Labuhn et al. 2016), **b** the average maximum temperatures from April to September at Fontainebleau, France

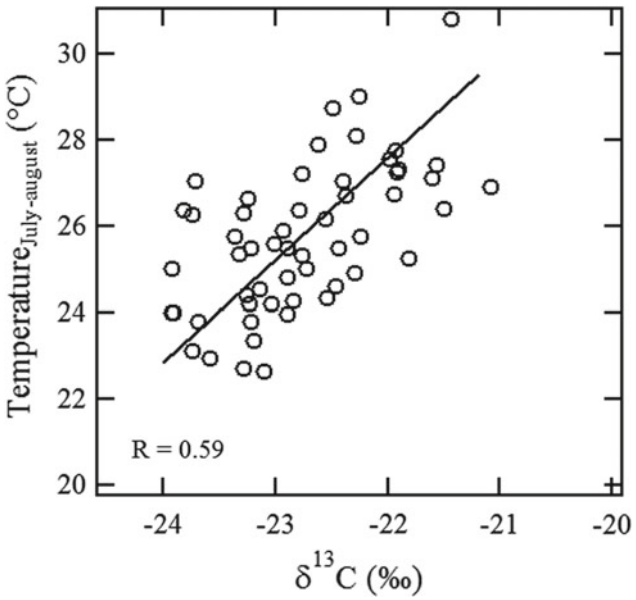

Fig. 16.5 Correlation between the isotopic composition of the carbon in the cellulose of larches in the Névache region (Alps, France) and the average maximum temperature in July–August (Daux et al. 2011)

Farquhar 1982). In most cases, the isotopic compositions of the oxygen and hydrogen in the cellulose are not affected by the juvenile effect, which makes these parameters particular interesting for the reconstruction of low-frequency climate variations.

Isotopic Reconstruction of the Variations in Climate Parameters Over Time

The variations in the isotopic compositions of the cellulose in rings are interpreted in different ways. Indeed, the reconstructed climate parameters are, depending on the case: temperature, relative humidity, sunshine, the amount of summer or winter rainfall, the average isotopic composition of this rainfall. The isotopic fractionations during the manufacture of cellulose are determined, as we have seen, by several factors. The conditions under which the growth takes place will determine which factor is dominant. For example, for trees in areas experiencing drought, stomatal conductance tends to dominate the carbon isotope fractionation processes. In this case, the environmental control factors are the relative humidity of the air and soil moisture; when, on the contrary, trees are growing in conditions where water is not limited, the fractionations are instead conditioned by the rate of photosynthesis which itself depends on the incident radiation and, to a lesser extent, by the temperature. The disparity in the reconstructions mentioned earlier, is a reflection of environmental disparities. The possibility of changes in the dominant factor over time must be contemplated when reconstructing temporal variations in the climate parameters.

Two reconstructions of atmospheric temperature are presented below, one from the δ^{13}C of the cellulose in *Fitzroya cupressoides* (Patagonia cypress, Argentina) cov-

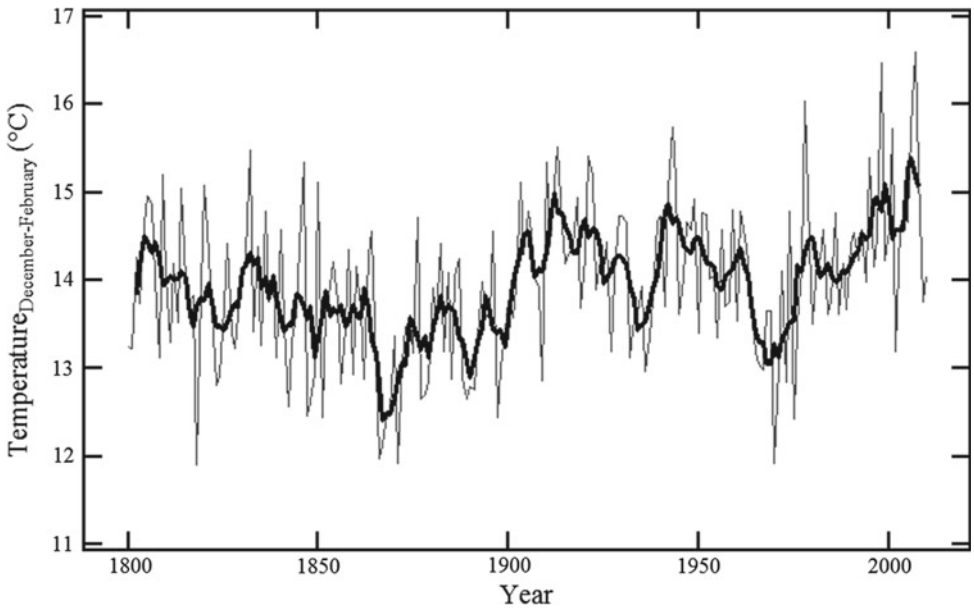

Fig. 16.6 Evolution of summer temperatures (December–February) over the last two centuries in northern Patagonia (Argentina), calculated from the isotopic composition of oxygen in the cellulose of Patagonian cypresses

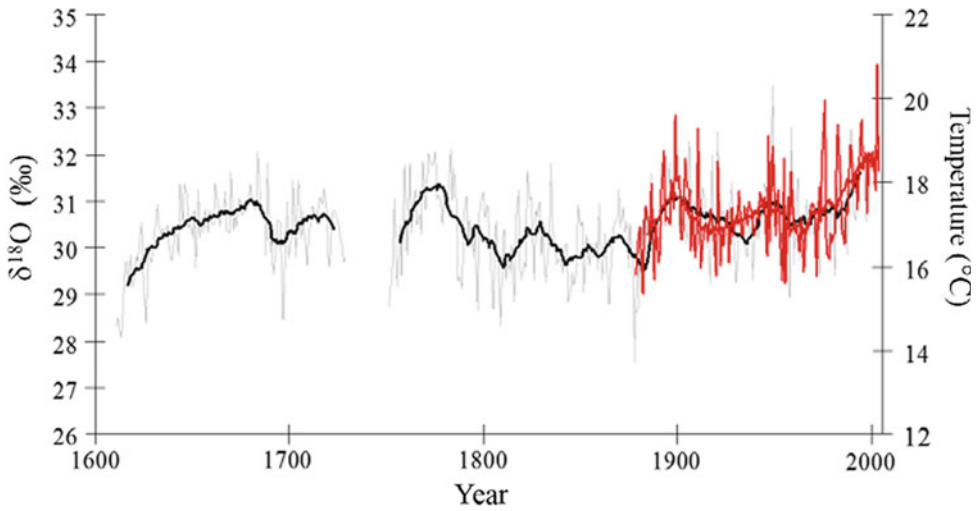

Fig. 16.7 Values for the $\delta^{13}C$ of cellulose taken from the summer wood of forest oaks (*Quercus robur*) and from buildings in Rennes (France) over the period 1610–1996 AD. The values of the reconstructed temperatures are indicated on the scale on the left. Instrumental temperatures, measured by Météo-France, from 1890 to 2003, are shown for comparison (Masson-Delmotte et al. 2005)

ering the period 1800–2011 (Lavergne et al. 2017) (Fig. 16.6) and the other from the $\delta^{18}O$ of the cellulose of *Quercus* (forest oaks and beams from old buildings in the Rennes region covering the last 400 years (Raffali-Delerce et al. 2004; Masson-Delmotte et al. 2005) (Fig. 16.7). The relationship between isotope data and temperature was established through calibrations carried out over the 1931–2011 period for the cypress from Patagonia, and over the 1951–1996 period for the oaks in Brittany. For Lavergne et al. (2018), the evolution of $\delta^{13}C$ in the cellulose of the cypresses implies that the summers (December to February) of the nineteenth century, particularly in the second half, were cool (an average temperature of 13.4 °C) and the summers of the twentieth and twenty-first centuries have higher temperatures (average temperature of 14.2 °C).

The reconstruction produced from the $\delta^{18}O$ of the cellulose of the oaks in Brittany also shows an increase in summer temperatures from the end of the nineteenth century onwards, in line with thermometer data. The similarity in the general shape of the graphs of the oak $\delta^{18}O$ and the instrumental temperatures shows that the dendro-isotopic parameter can be used with a high degree of confidence to reconstruct climate trends on a multi-year scale.

References

Augusti, A., Betson, T. R., & Schleucher, J. (2006). Hydrogen exchange during cellulose Synthesis Distinguishes climatic and biochemical Isotope fractionation in tree rings. *New Phytologist, 172,* 490–499.

Augusti, A., Betson, T. R., & Schleucher, J. (2008). Deriving correlated climate and physiological signals from deuterium isotopomers in tree rings. *Chemical Geology, 252,* 1–8.

Cook, E. R., & Kairiukstis, L. A. (Eds.). (1990). *Methods of dendrochronology: Applications in the environmental sciences*. Boston, MA: International Institute for Applied Systems Analysis, Kluwer Academic Publishers.

Daux, V., Edouard, J. L., Stievenard, M., Mestre, O., Guibal, F., Masson-Delmotte, V., & Thomas, A. (2011). Ring width, and carbon and oxygen Isotopic Composition of the cellulose in *Larix decidua* as climatic proxies: A case study in the French Alps. *Earth and Planetary Science Letters*.

Douglass, A. (1920). Evidence of climatic effects in the annual rings of Trees. *Ecology, 1*(1), 24–32.

Farquhar, G. D., O'Leavy, M. H., & Berry, J. A. (1982). On the relationship between carbon isotope discrimination and intercellular carbon dioxide concentration in leaves. *Australian Journal of Plant Physiology, 9,* 121–137.

Francey, R. J., & Farquhar, G. D. (1982). An explanation of $^{13}C/^{12}C$ variations in Tree rings. *Nature, 297,* 28–31.

Fritts, H. C. (1976). *Tree-rings and climate* (p. 567). New York: Academic Press.

Gessler, A., Ferrio, J. P., Hommel, R., Treydte, K., Werner, R. A., & Monson, R. K. (2014). Stable isotopes in tree rings: towards a mechanistic understanding of isotope fractionation and mixing processes from the leaves to the wood. *Tree Physiology, 34,* 796–818.

Guiot, J., Corona, C., & ESCARSEL Members. (2010). Growing season temperatures in Europe and climate forcings over the last 1400 years. *PLoS-one, 5*(4), e9972. https://doi.org/10.1371/journal.pone.0009972.

Labuhn, I., Daux, V., Girardclos, O., Stievenard, M., Pierre, M., & Masson-Delmotte, V. (2016). French summer droughts since 1326 CE: a reconstruction based on tree ring cellulose $\delta^{18}O$. *Climate of the Past, 12,* 1101–1117.

Lavergne, A., Daux, V., Villalba, R., Pierre, M., Stievenard, M., & Srur, A. M. (2017). Improvement of isotope-based climate reconstructions in Patagonia through a better understanding of climate influences on isotopic fractionation in tree rings. *Earth and Planetary Science Letters, 459,* 372–380.

Lavergne, A., Daux, V., Pierre, M., Stievenard, M., Srur, A. M., & Villalba, R. (2018). Past summer temperatures inferred from dendrochronological records of on the eastern slope of the northern patagonian andes. *Journal of Geophysical Research: Biogeosciences*, *123*(1), 32–45.

Masson-Delmotte, V., Raffali-Delerce, G., Danis, P., Yiou, P., Stievenard, M., Guibal, F., et al. (2005). Changes in European precipitation seasonality and in drought frequencies revealed by a four-century-long tree-ring isotopic record from Brittany, Western France. *Climate Dynamics, 24,* 57–69.

Pendall, E. (2000). Influence of precipitation seasonality on Piñon pine cellulose δD values. *Global Change Biology, 6,* 287–301.

Raffali-Delerce, G., Masson-Delmotte, V., Dupouey, J. L., Stievenard, M., Breda, N., & Moisselin, J. M. (2004). Reconstruction of SUMMER droughts using tree-ring cellulose isotopes: A calibration study with living Oaks from Brittany (Western France). *Tellus, 56,* 160–174.

Schweingruber, F. H., Fritts, H. C., Braeker, O. U., Drew, L. G., & Schaer, E. (1978). The X-ray technique as applied to dendroclimatology. *Tree-Ring Bulletin, 38,* 61–91.

Trouet, V. (2020). *Tree Story, the History of the World Written in Rings* (p. 256). Johns Hopkins University Press.

Waterhouse, J. S., Switsur, V. R., Barker, A. C., Carter, A. H. C., & Robertson, I. (2002). Oxygen and hydrogen isotope ratios in tree rings: How well do models predict observed values? *Earth and Planetary Science Letters, 201,* 421–430.

17 Air-Vegetation Interface: An Example of the Use of Historical Data on Grape Harvests

Valérie Daux

Historical data provide clues, often precise, of climate phenomena experienced by societies. The example below illustrates the scientific approach applied to records of grape harvest dates in order to quantitatively estimate the evolution of temperature in a region.

The vine is a hardy perennial Mediterranean plant, well adapted to hot dry weather conditions. Temperature is a key environmental factor which triggers its various phenological stages. Buds appear when daytime temperatures reach at least 10 °C for an extended period, usually in April. Flowering dates occur about two months later (usually June), when the daily temperatures cumulatively reach a certain threshold. The date of the onset of ripening, veraison (in August), is dependent on the date of flowering and the subsequent temperatures. Finally, the grape reaches maturity about thirty days after veraison, most often in September. Harvesting takes place when the grapes are perfectly ripe. The time between veraison and harvesting is fairly constant; it depends on the temperature, on the phytosanitary status of the vineyard and the amount of rainfall. The time periods given for the different phenological stages are approximate and vary according to grape varieties and regions.

Harvest dates, since they depend mainly on the temperatures during the growth and maturation of the vine, can be regarded as thermal indicators. Variations in harvest dates over the past centuries reflect historical variations in spring and summer temperatures.

Historical Series of Harvest Dates

In the Middle Ages, the official opening dates of harvest were set by informed feudal decision. After the Revolution, this tradition was theoretically abandoned; each owner could commence the harvest at will. However, the use of an official date was maintained in most parishes, for reasons of security and public order. After 1791, it was the mayor, advised by the vineyard owners, who fixed the date of the beginning of the harvest. The actual date of harvesting could take place some days after this date. The official and real dates of harvesting have been recorded in different registers depending on the place and time: these might be in monastic records, chapters of canons, hospital records (such as those from the *Hospices de Beaune, Burgundy, France*), municipal registers or private records (by the vineyards). During the 'Medieval Climate Optimum' (around 10th to thirteenth centuries), vineyards were planted at latitudes as far north as the shores of the Baltic or the south of England. Conversely, due to the cooling of the 'Little Ice Age' (from the 14th to the nineteenth centuries), most northern vineyards collapsed, and the vine growing season was shortened so much that the harvests were difficult even in some southern vineyards.

The series of published harvest dates are mostly composite series constructed from multiple sets of dates from different sites of the same vineyard. Ideally, the composite series should be established from local series of harvesting dates of the same grape variety, to avoid introducing bias related to a phenology which may vary by grape variety. The longest and most comprehensive series published to date is that of the vineyards of Burgundy (Fig. 17.1). This is a composite series constructed from data from multiple sites in the Côtes de Beaune and perhaps also from the Côtes de Dijon. The grapes harvested in that area since the fourteenth century are mostly pinot noir and chardonnay.

Reconstruction of Spring-Summer Temperatures Based on Grape Harvesting Dates

Grape harvesting data from the twentieth century, from different vineyards and varieties, were compared with regional meteorological data (Daux et al. 2007).

V. Daux (✉)
Laboratoire des Sciences du Climat et de l'Environnement, LSCE/IPSL, CEA-CNRS-UVSQ, Université Paris-Saclay, 91190 Gif-sur-Yvette, France
e-mail: valerie.daux@lsce.ipsl.fr

G. Ramstein et al. (eds.), *Paleoclimatology*, Frontiers in Earth Sciences,
https://doi.org/10.1007/978-3-030-24982-3_17

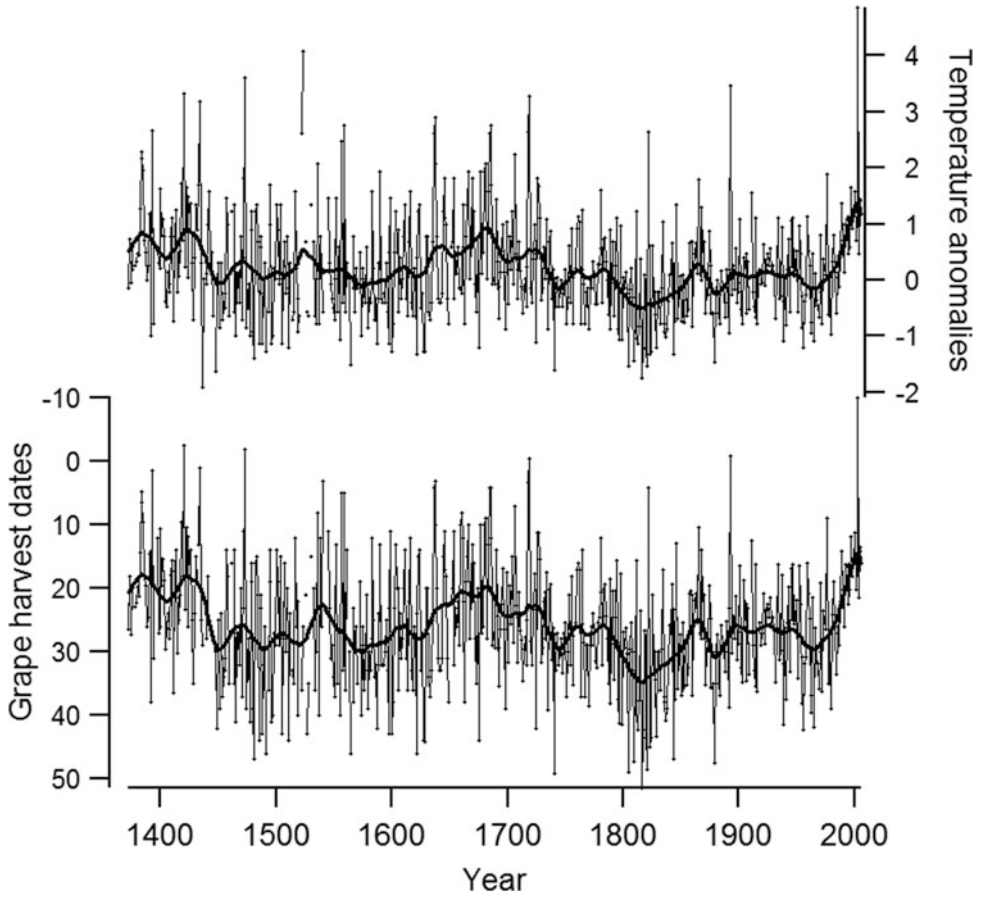

Fig. 17.1 Bottom: Harvest dates in Burgundy since 1370 (Daux et al. 2012). Dates are arbitrarily expressed in days after August 31st. Top: Anomalies in the corresponding temperatures, calculated using a phenological model. The anomalies are calculated compared to the reference period 1960–1989; according to Garcia de Cortazar et al. (2010). The bold lines are 29-year moving averages. The major climate events of the past seven centuries may be described as follows: warming in the 1380s, and from 1415 to 1435, a period that includes the wheat 'blast' that led to the famine of 1420; cooling during the second half of the '*Quattrocento*' particularly evident in the famine of 1481, arising from rain and cold conditions; hot spells during the 1520s, 1530s and 1550s; the strong cold surge of the Little Ice Age (LIA) from 1560. A cold seventeenth century'? This was the case from 1570 to 1630 (with a slight warming around 1600–1620), in 1675, during the 1690s and in the following century, from 1709 to 1715; heatwaves in summers of the 1630s, 1660s and 1680s; warming during the eighteenth century, particularly obvious in the years 1704–1707, 1718–1719, in the 1720s and 1730s, the years 1757–1765 and especially from 1778–1781 and during the 1780s; nevertheless, years of cool-cold-wet (1725, 1740, 1770); the Little Ice Age, which never quite ceased, became vigorous again from 1812 to 1860; added to this were the very cold snaps of 1812–1817; heatwave of 1846, affecting grain harvests; the definitive end of the Little Ice Age in 1860; warming during the twentieth century from around 1900 onwards with an acceleration since 1976 and the 1990s. After Le Roy Ladurie et al. (2006)

The harvest date series and temperatures present many similarities, at the annual, decadal and multi-decadal scale (see example in Fig. 17.2). The best correlations (statistically significant with a maximum R) between harvest dates and climate data are those with the average maximal temperatures from April to August. For these correlations, the slopes are around −6 to −10 days/°C for all the vineyards (Fig. 17.3). In other words, regardless of the earliness or lateness of the vines and regardless of the geographic location (including soil, orientation and meteorology), a variation of six to ten days on the date of the harvest reflects a difference of about 1 °C from the average maximum temperatures for the growing season (April in August; see also for example Cook and Wolkovich 2016).

The phenology of woody species can be simulated by models that express the relationship between the maturation process and daytime temperatures. A model is adapted to describe the phenology of a species, or a variety in the case of the vine. Chuine et al. (2004) have thus used recent observations of phenological development of the pinot noir variety, made between 1964 and 2001 in Colmar (France), by INRA, to model the phenology of this variety and to calculate the veraison and harvest dates from temperatures. The inverted model has been used here

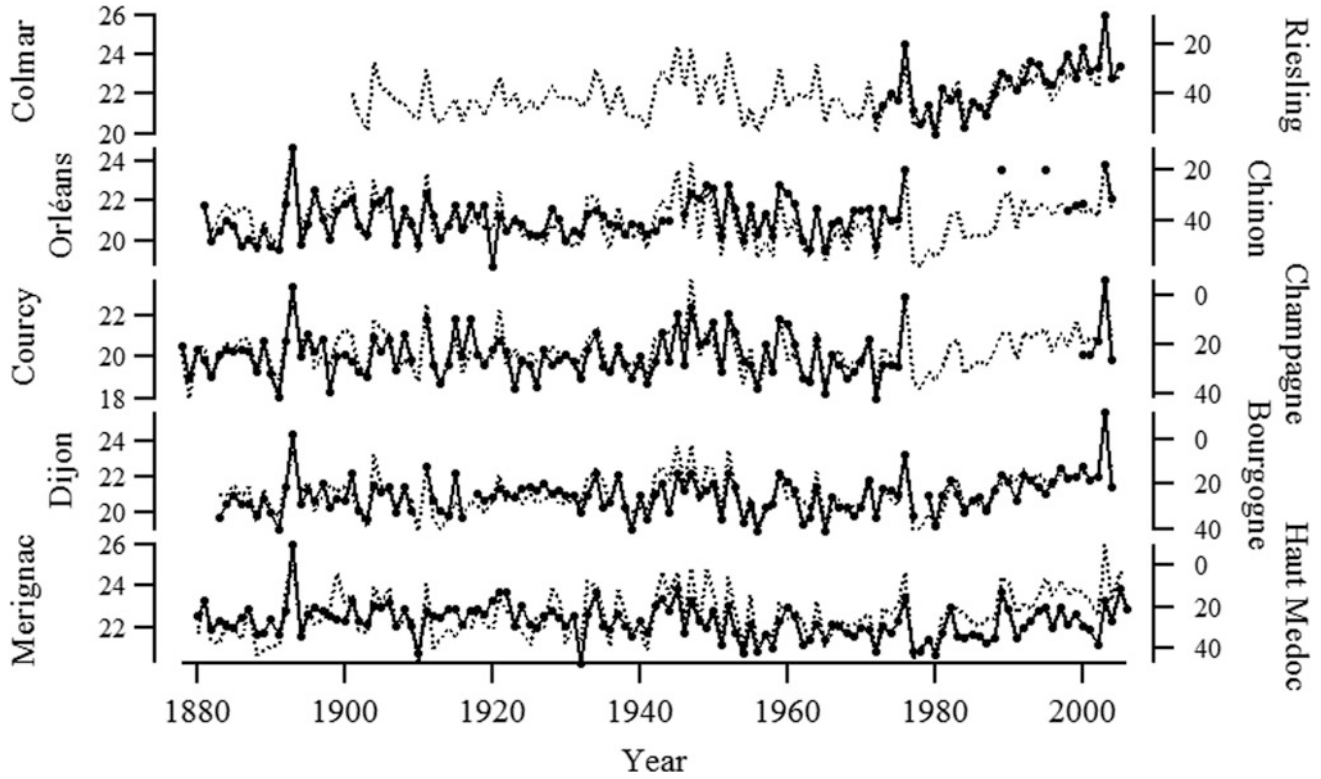

Fig. 17.2 Series of harvest dates (bold lines with symbols, scale on right; in days after August 31) and maximum daytime temperatures for the corresponding region (dotted lines, scales on left) versus time

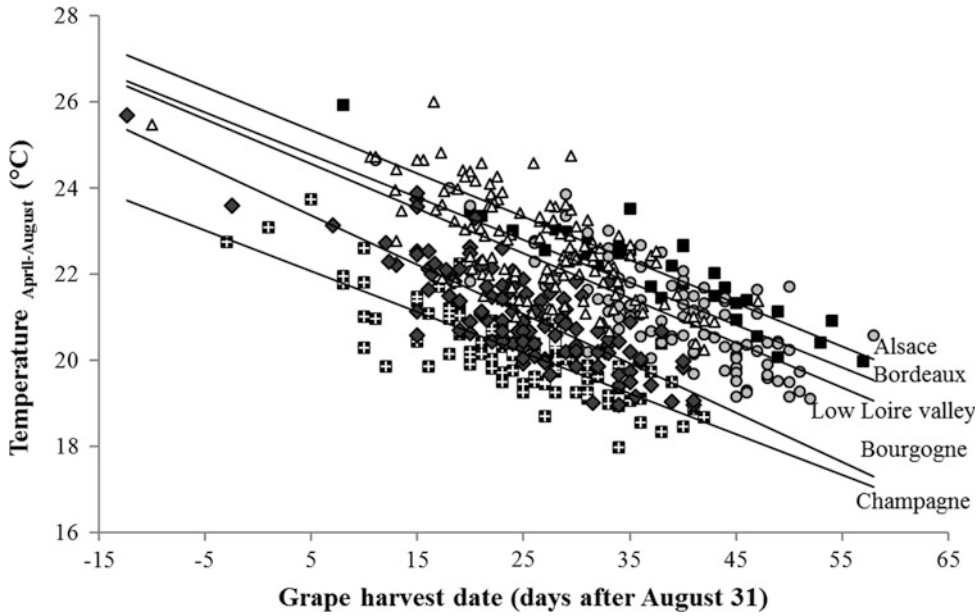

Fig. 17.3 Correlations among harvest dates (in days after August 31) and average monthly daytime temperatures from April to August (in °C) for the vineyards of the Champagne, Burgundy, Alsace, Bordeaux and Loire valley regions

to reconstruct variations in spring-summer temperatures in Burgundy since the fourteenth century from the series of dates shown in Fig. 17.1. This reconstruction highlights that the cooling of the climate in the period 1690–1800, the start of a long cool period that continued until 1970, was by a little more than one degree. The exceptionally hot summer of 2003 also shows up very clearly (Chuine et al. 2004).

Limitations of These Reconstructions: The Anthropic Effects

The decision to harvest is based on a simple principle: the grapes need to be harvested when they are ripe and not too long afterwards so as to avoid exposure to unfavorable weather conditions, such as hail or heavy rain. Judgment of the ideal state of ripeness may have evolved over time depending on the political and economic context, cultivation techniques, oenological practices and consumer tastes. Variations over time in these parameters can create trends and cause breaks in the data series. These variations caused by factors not related to the climate may not necessarily be detectable in a single series. To be as rigorous as possible, a climate reconstruction must be based on a collection of series (ideally of the same variety, from the same wine region), which is tested for disruptions and inter-correlations. Historical information of this type can provide insights and help to identify the proportion of variability attributable to anthropic effects.

References

Chuine, I., Yiou, P., Viovy, N., Seguin, B., Daux, V., & Le Roy Ladurie, E. (2004). Grape ripening as a past climate indicator. *Nature, 432,* 289–290.

Cook, B. I., & Wolkovich, E. M. (2016). Climate change decouples drought from early wine grape harvests in France. *Nature Climate Change, 6,* 715–719.

Daux, V., Garcia de Cortazar-Atauri, I., Yiou, P., Chuine, I., Garnier, E., Le Roy Ladurie, E., et al. (2012). An open-access database of grape harvest dates for climate research: data description and quality assessment. *Clim. Past, 8,* 1403–1418.

Daux, V., Yiou, P., Le Roy Ladurie, E., Mestre, O., Chevet, J.-M., & the OPHELIE team. (2007). Température et dates de vendanges en France', Articles du colloque 'Changement climatique, quels impacts probables sur le vignoble?', Dijon, 28–29 mars 2007, 10p.

Garcia de Cortazar-Atauri, I., Daux, V., Garnier, E., Yiou, P., Viovy, N., Seguin, B., et al. (2010). An assessment of error sources when using grape harvest date for past climate reconstruction. *Holocene, 20,* 599–608.

Le Roy Ladurie, E., Daux, V., & Luterbacher, J. (2006). Le climat de Bourgogne et d'ailleurs. *Histoire, Economie et Sociétés, 3,* 421–436.

Air-Ground Interface: Sediment Tracers in Tropical Lakes

18

David Williamson

The climate archives found at low latitudes are mostly sedimentary or geomorphological. Their formation and preservation depend fundamentally on favorable geomorphological and climatic conditions. Therefore, they differ according to the environment, the region and the climate and include moraines left behind by mountain glaciers, ancient shorelines of old lakes, dunes, flood levels, archeological sites occupied by animals or humans, continental carbonates (speleothems, travertine, stromatolites) and sedimentary sequences collected in cores from lakes and bogs. Additional archives consist of coastal deposits (e.g. corals) and marine hemipelagic sediments with a high deposition rate, especially near river deltas or coastal upwellings off Mauritania, Benguela and Somalia. The dating and study of aquifers, as well as of tree rings complete the range of climate records currently available and studied, particularly in semi-arid areas.

The physical, chemical and biological controls of the sedimentary records vary greatly according to the local or regional specificity of the areas of deposition. For example, the mixing or overturning of the water column of a lake is generally recorded by biological (diatoms) or organic proxies. It may be activated by an earthquake, outgassing from anoxic hypolimnion or by sediments, but also by the cooling of surface waters, the melting of ice, by wind intensity or by a drop in lakewater level. Hence, the climate or hydrological proxies (e.g. physicochemical properties or isotopic signatures of water and sediments, terrestrial or aquatic vegetation markers, erosional or atmospheric inputs) do not have the same fundamental meaning from one site to another.

To reduce the uncertainties in timing and interpretation, it is essential to undertake a detailed reconstruction of the deposition processes in several sites characteristic of the region and for a given climate. Among the non-destructive physical and chemical methods of measuring the variability of depositional environments, the measurement of magnetic sedimentary properties (low-magnetic field susceptibility, induced and remanent magnetizations) is a particularly appropriate one, because multiple measurements can be performed. The magnetic signature of sediments—and other surface materials—depends on changes in the concentration, grain size and mineralogy of iron minerals (mainly oxides, sulfides, carbonates). Iron mineral assemblages closely depend on the iron biogeochemical cycle, in particular on the weathering of primary minerals, pedogenetic processes, biomass fires, gravity deposition, redox changes, microbial activity, authigenesis and early diagenesis. Magnetic methods thus allow for the reconstruction of the dynamics of surface processes recorded along sedimentary sequences, and the identification of the main modes of environmental and climate variability (Thompson and Oldfield 1986).

Intertropical Hydrological Variability in Africa

Africa is characterized by a wide variety of climates, mainly defined by the amount and distribution of rainfall at the seasonal, annual, and year-to-year level (from less than 100 mm per year to more than 3000 mm per year) and temperature (especially at mid-latitudes and at altitude). From the humid equatorial climate of the Congo basin to the hyperarid or subtropical climates of the Sahel/Sahara and of the Kalahari/Namibia, regional climates respond to the annual and seasonal characteristics of global and tropical atmospheric circulation (in particular the activity of the Intertropical Convergence Zone, ITCZ). The temperatures and surface currents of the neighboring oceans and the regional orographies (e.g. East-African rift, great escarpment of Namibia) determine the regional rainfall patterns. Together with the local geomorphology, these regional climates have a determining influence on the presence, nature and historical continuity of most of the land-based climate archives.

D. Williamson (✉)
World Agroforestry Centre, Research Institute for Development, UMR LOCEAN, Université Pierre et Marie Curie, P.O. Box 30677-00100 Nairobi, Kenya
e-mail: david.williamson@ird.fr

G. Ramstein et al. (eds.), *Paleoclimatology*, Frontiers in Earth Sciences,
https://doi.org/10.1007/978-3-030-24982-3_18

Sahara, Kalahari and Arid Zones: Discontinuous Evidence of Hydrological Inversions

Since the 1950s and 1960s, the first robust evidence of major hydrological changes during the late Pleistocene and Holocene, have been found in the two African subtropical deserts in the form of proof of the existence of gigantic interdune lakes; flora and fauna assemblages; sites demonstrating a sedentary human presence and a positive water balance over centuries or millennia. A key outcome of this research is indications that, during the first half of the Holocene, there was an intensification of the African monsoon in the Sahara and a shift in the tropical summer rains (at the northern limit of the ITCZ) north of 20°N as well as a significant reduction in the Sahara as a biogeographical barrier during this period (Lézine et al. 1990; Petit-Maire and Riser 1981). Very similar evidence of major hydrological changes has been obtained for the Kalahari (Thomas et al. 2003). As shown in Fig. 18.1, these records show the asynchronism of the humidity 'optima' during the Holocene, north (from 11 to 6 ka BP) and south (after 6 ka BP) of the equator, illustrating the forcing of the changes in regional insolation on the monsoon circulation and summer tropical rainfall (from June to September in the Sahara and from December to March in the Kalahari). Furthermore, at the millennial scale, numerous sedimentary discontinuities suggest the occurrence of hydroclimatic thresholds, apparently linked with rapid changes in activity of the ITCZ from one latitude to another, corresponding to rapid climate fluctuations in the high latitudes (Mayewski et al. 2004). However, the difficulty with these archives remains in the discontinuity of the records and the lack of detailed chronological precision on dry periods. The preserved deposits contain the initial stages of wet periods, but the preservation of the signal, in particular for the phases of aridification, is hypothetical.

The depositional gaps and the differential removal of remaining deposits do not allow a continuous hydrological and climate dynamic to be reconstructed, particularly for the glacial period.

The dynamics of the African deserts must then be reconstructed from the proximate and hemipelagic marine field, especially at the mouths of the major rivers (Senegal, Niger, Orange River, Zambezi) and in upwelling zones (Mauritania, Benguela), where sedimentation rates permit a resolution at the millennial scale, coupled with isotopic stratigraphy for the last ice age(s). The data obtained confirm the important role of insolation in the low latitudes in monsoon circulation and the hydrology of the subtropical areas. They also confirm the instability of the edges of the Sahara and the Kalahari at the millennial scale (DeMenocal et al. 2000; Little et al. 1997), already highlighted for the

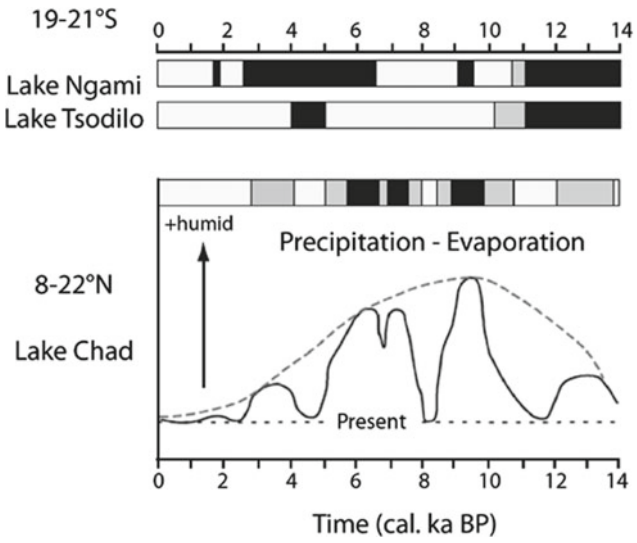

Fig. 18.1 Chronostratigraphy comparing lacustrine sequences from the Kalahari (Thomas et al. 2003) and Lake Chad (Servant and Servant-Vildary 1980). Black represents high water level; gray, the intermediate level; and white the low water level or drying out. Note the phase difference between the water balances of the southern tropical region (Kalahari) and the edge (Chad)

Holocene from Lake Chad (Servant and Servant-Vildary 1980). The coupling of the millennial climate variability in the high latitudes during the glacial period with the humidity of the Sahara is clearly demonstrated from marine sediments, in particular through erosion markers (Adegbie et al. 2003) and ecosystems (Schefuß et al. 2005). However, the information obtained often lacks spatial accuracy, and the critical contribution of transportation processes with regard to the interpretation of markers often remains hypothetical (Pichevin et al. 2005).

(Sub)Equatorial Zone: Changes in the Activity and Position of the ITCZ

The continental archives providing the most continuous recording of climate variability over the last 25 ka are located in sites that have remained relatively humid, located in equatorial regions or at altitude, and where the hydric balance [Precipitation—Evaporation, *P-E*) remained positive. These are cores taken either from large terminal lake reservoirs found in central Africa (Lake Victoria) or the East African Rift (e.g. Lakes Tanganyika and Malawi), or from small lake basins suitable for the reconstruction of regional conditions. As shown from the complete drying up of Lake Victoria at 18 and 16 ka BP (Stager et al. 2002), the drop by several hundred meters of the levels of lakes Tanganyika and Malawi during the last glacial period, or the rapid rise 18 (over a few decades) of great lakes that are today very

shallow or drying out (Rukwa, Victoria, Chad) (Williamson et al. 1993), the whole intertropical zone has recorded major and rapid changes in its water balance, linked mostly to changes in regional temperature. The changes affected the continental surfaces, the soils, the distribution and the biodiversity of terrestrial and aquatic ecosystems. For example, the iron mineralogy of soils was modified, and variations of several orders of magnitude of the concentration in magnetic minerals are evidenced (Williamson et al. 1993).

Owing to unrivaled chronological and spatial resolution, the data obtained from peat bogs or crater lakes, most especially the molecular markers of microbial origin (Coffinet et al. 2014), show that these rapid changes in atmospheric circulation and in the composition of the atmosphere (water, CO_2) were responsible for a fundamental reorganization of ecosystems, particularly with regard to the distribution of mountain ecosystems and most wetland areas.

These records confirm the dominant forcing of insolation and monsoon circulation over tropical hydrology. At the decennial to millennial scale, however, the depositional record clearly indicates the coupling of the tropical climate with the climate in the high latitudes, and with the activity of the thermohaline circulation, particularly during the glacial interval where the Dansgaard-Oeschger variability is identified in numerous hydrological records. New high resolution chronological records are required to identify the mechanisms and the potential phase-lags linked with such changes (Zhang et al. 2018).

Recent Anthropological Influence on Climate Archives: Both a Proof and a Tool to Assess the Impacts of Local and Regional Development

Superimposed on natural climate stress, the human impact on the hydrology and land-based environments of Africa remains poorly documented, and presents a challenge to a better understanding of the interactions between climate, environment and society in developing countries. The first large-scale human impacts on ecosystems (livestock domestication and pastoralism) are recorded as early as ca. 4000 yr B.P., especially during the last 2500 yr with deforestation and biomass burning (Thevenon et al. 2003) being associated with iron metallurgy, the expansion of farming activities and demography: rapid increases in the fluxes of microcharcoal, detrital inputs (especially magnetic) and pollen from ruderal vegetation (near habitations) and pioneer taxa (Zhang et al. 2018). In East Africa, the expansion of trade routes between the coast and the interior at least 1300 years ago increased the abundance of exotic plants, especially cultivated plants from Asia such as banana, taro, rice, and, more recently, plants from the new world such as maize, tobacco, tomatoes. However, it is only since the late nineteenth century and especially after the Second World War, that the archives show radical changes in the environment caused by man (Marchant et al. 2018): the organic components (on land and in water) and inorganic components, dissolved or suspended (notably magnetic), present in the environment are affected (Garcin et al. 2007).

In this context, just as changes in atmospheric composition have been reconstructed from ice cores, the land-based 'pre-industrial' archives recording changes in the climate and the tropical environment are now the local and regional references for environments relatively untouched by man, from the decadal to the millennial scale. Such references are required to establish a frame of reference so as to identify the various controls of climate and society on the structural changes in the landscape and in biodiversity, in vegetal production, in erosional processes, or in stored material (including pollutants), and thus to assess the extent and sustainability of the changes imposed by humans on the Earth's surface.

References

Adegbie, A. T., Schneider, R. R., Röhl, U., & Wefer, G. (2003). Glacial millennial-scale fluctuations in central African precipitation recorded in terrigenous sediment supply and freshwater signals offshore came.

Coffinet, S., Huguet, A., Williamson, D., Fosse, C., & Derenne, S. (2014). Potential of GDGTs as a temperature proxy along an altitudinal transect at Mount Rungwe (Tanzania). *Organic Geochemistry, 68,* 82–89.

DeMenocal, P., Ortiz, J., Guilderson, T., Adkins, J., Sarnthein, M., Baker, L., et al. (2000). Abrupt onset and termination of the African humid period: Rapid climate responses to gradual insolation forcing. *Quaternary Science Reviews, 19,* 347–361.

Garcin, Y., Williamson, D., Bergonzini, L., Radakovitch, O., Vincens, A., Buchet, G., et al. (2007). Solar and anthropogenic imprints on lake masoko (Southern Tanzania) during the last 500 years. *Journal of Paleolimnology, 37,* 475–490.

Lézine, A. M., Casanova, J., & Hillaire-Marcel, C. (1990). Across an early holocene humid phase in Western Sahara: Pollen and isotope stratigraphy. *Geology, 18,* 264–267.

Little, M. G., Schneider, R. R., Kroon, D., Price, B., Summerhayes, C. P., & Segl, M. (1997). Trade wind forcing of upwelling, seasonality, and heinrich events as a response to sub-milankovitch climate variability. *Paleoceanography, 12,* 568–576.

Marchant, R., Richer, S., Boles, O., Capitani, C., Courtney-Mustaphi, C. J., Lane, P., et al. (2018). Drivers and trajectories of land cover change in East Africa: Human and environmental interactions from 6000 years ago to present. *Earth-Science Reviews, 178,* 322–378.

Mayewski, P. A., Rohling, E. E., Stager, J. C., Karlén, W., Maasch, K. A., Meeker, L. D., et al. (2004). Holocene climate variability. *Quaternary Research, 62,* 243–255.

Petit-Maire, N., & Riser, J. (1981). Holocene lake deposits and palaeoenvironments in central Sahara, Northeastern Mali. *Palaeogeography Palaeoclimatology Palaeoecology, 35,* 45–61.

Pichevin, L., Cremer, M., Giraudeau, J., & Bertrand, P. (2005). A 190 Ky record of lithogenic grain-size on the namibian slope: Forging a tight link between past wind-strength and coastal upwelling dynamics. *Marine Geology, 218,* 81–96.

Servant, M., & Servant-Vildary, S. (1980). L'Environnement quaternaire du bassin du Tchad. The Sahara and the Nile. In M. A. J. Williams, & H. Faure (Ed.), (pp. 133–162). Leiden: Balkema.

Schefuß, E., Schouten, S., & et Schneider, R. R. (2005). Climatic controls on central African hydrology during the Past 20,000 Years. *Nature*, *437*, 1003–1006.

Stager, J. C., Mayewski, P. A., & Meeker, L. D. (2002). Cooling cycles, heinrich event 1, and the desiccation of lake victoria. *Paleogeography, Paleoclimatology, Paleoecology, 183,* 169–178.

Thevenon, F., Williamson, D., Vincens, A., Taieb, M., Merdaci, O., Decobert, M., et al. (2003). A late holocene charcoal record from Lake Masoko, SW Tanzania: Climatic and anthropologic implications. *The Holocene, 15,* 785–792.

Thomas, D. S. G., Brook, G., Shaw, P., Bateman, M., Appleton, C., Nash, D., et al. (2003). Late pleistocene wetting and drying in the NW Kalahari: an integrated study from the Tsodilo Hills, Botswana. *Quaternary International, 104,* 53–67.

Thompson, R., & Oldfield, F. (1986). *Environmental magnetism*. London: Allen and Unwin.

Williamson, D., Taieb, M., Damnati, B., Icole, M., & Thouveny, N. (1993). Equatorial extension of the younger dryas event: Rock-magnetic evidence from lake Magadi. *Global and Planetary Change, 7,* 235–242.

Williamson, D., Jelinowska, A., Kissel, C., Tucholka, P., Gibert, E., Gasse, F., et al. (1998). Mineral-magnetic proxies of erosion/oxidation cycles in tropical maar-lake sediments (Lake Tritrivakely, Madagascar): Paleoenvironmental implications. *Earth and Planetary Science Letters, 155,* 205–219.

Zhang, Y. C., Chiessi, C. M., Mulitza, S., Sawakuchi, A. O., Haggi, C., Zabel, M., et al. (2018). Different precipitation patterns across tropical South America during Heinrich and Dansgaard-Oeschger stadials. *Quaternary Science Reviews, 177,* 1–9.

Air-water Interface: Tropical Lake Diatoms and Isotope Hydrology Modeling

19

Florence Sylvestre, Françoise Gasse, Françoise Vimeux, and Benjamin Quesada

Regardless of the timescale, a distinctive characteristic of the tropics is a high variability in the water cycle, in particular in the *P-E* water balance [precipitation minus (evaporation + evapotranspiration)]. This variability has more impact on life in the tropics than the variability in temperature which only has a moderate influence compared to the high and middle latitudes. The time frame, speed and magnitude of hydrological events need to be established so that their causes and mechanisms can be understood. These events are recorded in terrestrial sediments (lacustrine deposits, deposits in caves), in fossil waters in deep aquifers, and imprinted in the landscape by geomorphological features (dried-up river channels, ancient lake shorelines).

Lacustrine archives are particularly interesting because they contain the imprint of hydrological variations recorded in lakes. They preserve a wide range of complementary indicators (or proxies), providing access to different environmental and climate parameters if they can be calibrated.

Lakes are today numerous in the humid tropics, and evidence of ancient lakes (i.e. paleolakes) are plentiful in certain regions that are now arid. They react to changes in climate with often dramatic fluctuations, accompanied by profound changes in chemistry, biology, water-mass dynamics and water-atmosphere heat transfers. Indeed, one way which is often forgotten that lakes can have a significant interaction on the continental hydrological cycle is through the source of water vapor they represent (Vallet-Coulomb et al. 2008). In this chapter, we will examine specifically the example of a hydro-isotopic reconstruction established from sedimentary records from a paleolake located in the tropical Andes (Fig. 19.1) and its impact on the local hydrological cycle during the last glacial-interglacial transition (18–12 ka) (Quesada et al. 2015). Over this period, this paleolake, called 'Tauca' (from the name of a village where the eponymous outcrops were discovered, Servant and Fontes 1978) underwent a transgression phase due to an increase in rainfall in the tropical Andes (Sylvestre et al. 1999; Blard et al. 2011), before disappearing abruptly around 14.3 ka. Here, we propose a reconstruction of the isotopic composition of the lake water and we explore how its disappearance might have disturbed the local atmospheric water cycle. In particular, we explore the possible link between a sudden evaporation of the Tauca paleolake and an abrupt event found in the isotopic composition (oxygen 18) of the glacier covering Mount Sajama overlooking the former lake (Thompson et al. 1998).

Site Selection and Collection of Samples

A fundamental criterion for the selection of study sites is the sensitivity of the lake system (the lake and its watershed) to variations in *P-E*. The change in volume of a lake during the time interval Δt is represented by the equation:

$$\Delta V_L/\Delta t = S_L(P_L - E_L) + A - D. \qquad (19.1)$$

where V_L is the volume of the lake (m^3) and S_L is the surface area (m^2). V_L and S_L are functions of the level of the lake (H_L). P_L and E_L are, respectively, the rates of precipitation

F. Gasse—Deceased.

F. Sylvestre (✉) · F. Gasse · B. Quesada
Aix-Marseille Université, CNRS, IRD, Collège de France, INRAE, CEREGE, Europôle Méditerranéen de l'Arbois, 13545 Aix-en-Provence cedex 4, France
e-mail: sylvestre@cerege.fr

F. Vimeux
Institut de Recherche pour le Développement (IRD), Laboratoire HydroSciences Montpellier (HSM), UMR 5569 (CNRS, IRD, UM), 34090 Montpellier, France

F. Vimeux · B. Quesada
Institut Pierre Simon Laplace (IPSL), Laboratoire des Sciences du Climat et de l'Environnement, LSCE/IPSL, CEA-CNRS-UVSQ, Université Paris-Saclay, 91190 Gif-sur-Yvette, France

G. Ramstein et al. (eds.), *Paleoclimatology*, Frontiers in Earth Sciences,
https://doi.org/10.1007/978-3-030-24982-3_19

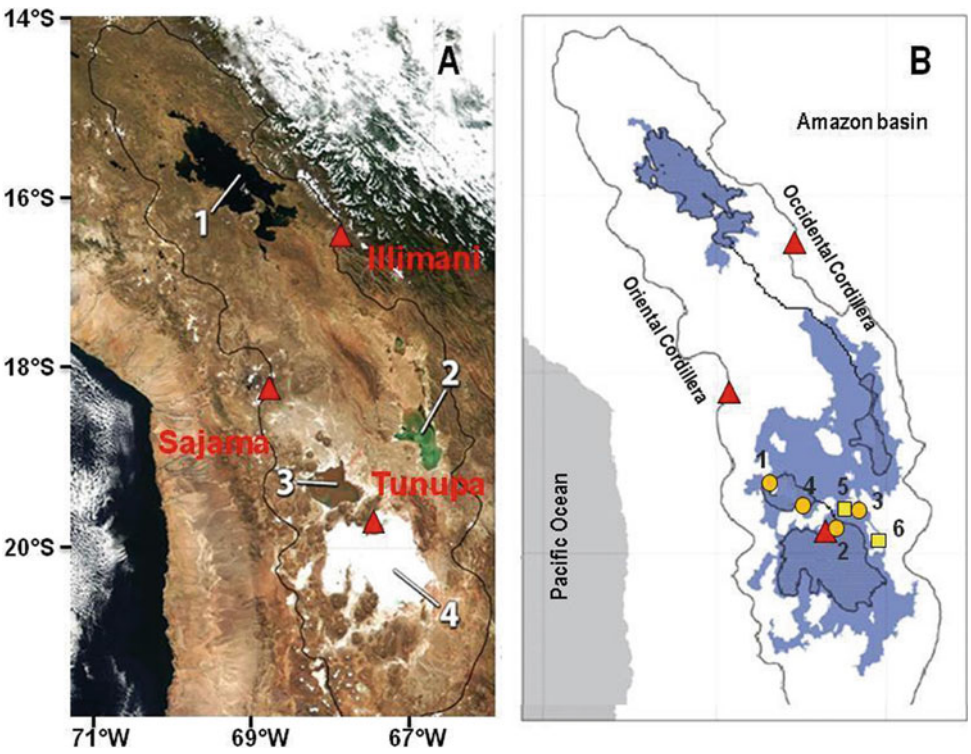

Fig. 19.1 **a** The Bolivian Altiplano (MODIS image modified from http://www.nssl.noaa.gov/projects/pacs/web/ALTIPLANO/) with 1. Lake Titicaca, 2. Lake Poopó, 3. The Salar de Coipasa, 4. The Salar of Uyuni. The red triangles indicate the position of the ice cores taken from the glaciers of Illimani, Mount Sajama and Tunupa. **b** Diagram of the Bolivian Altiplano indicating the contemporary lakes, the outline of the watershed (black line) and the extent of the Tauca paleolake shown in blue. The study sites are indicated by orange dots and yellow squares

and evaporation at the surface of the lake (m), A (m^3) is the sum of the surface and subterranean inflows. A is dependent on the P-E balance of the watershed ($P_B - E_B$) and its surface S_B. D (m^3) is the sum of the losses from the surface and from infiltration at the bottom of the lake. Equation (19.1) shows that closed lakes ($D = 0$), common in semi-arid or arid areas, are the most sensitive because they cumulate variations in the P-E of the lake and of its watershed. Thus, they amplify the responses to climate change.

The Bolivian Altiplano is located in the central tropical Andes between 15°S and 22°S latitude and 65°W and 69°W longitude at an average altitude of 3800 m. Today, it is occupied by a chain of four lakes of decreasing altitude and increasing salinity from north to south: Lake Titicaca, a deep lake of fresh water at 3810 m; Lake Poopó, a very shallow, hypersaline lake at 3686 m; and the Coipasa and Uyuni lakes at 3657 m and 3653 m which are now covered by two large salt crusts of 2,500 km^2 and 11,000 km^2 respectively, the remaining legacy following evaporation of the Tauca paleolake (Fig. 19.1a). This hydrological system is endorheic, and Lake Titicaca can flow into Lake Poopó, which itself, in very rainy seasons, can feed the Salars of Coipasa and Uyuni (Fig. 19.1a). The Bolivian Altiplano receives most of its precipitation during the rainy season which occurs from November to March. Today, precipitation comes mainly from the Atlantic, transported to the Altiplano by the easterly winds (Garreaud et al. 2003).

In a paleohydrological study of lacustrine archives, the maximum morphological, geological, meteorological, hydrological and hydrochemical information on the lake watershed is collected by satellite imagery, aerial photographs, field observations, and instrumental data. The spatial distribution of exposed lake deposits and former perched shorelines (beach deposits, notches eroded in the cliffs by waves, etc.) is measured by GPS and localized using a digital terrain model (DTM). Contemporary samples of water and silts are collected as references for the interpretation of past tracers. Sediments are taken at the outcrop and by coring. The sites are chosen according to the bathymetry and the continuity of the identified sediments. On the Bolivian Altiplano, the samples were selected from outcrops according to their altitude around the lake, making it possible to quantify the depth of the lake during its evolution through time (Fig. 19.1b) (Sylvestre et al. 1999).

Reconstruction of Paleohydrological Conditions

The study commences with a lithological description of the samples, a prerequisite to understanding the organization of the sedimentary deposits, before selecting the levels to establish their absolute chronology using radiometric methods such as radiocarbon. In stratigraphy, we find the strata

with remarkable sedimentary facies that allow the different profiles to be correlated. Indicators of a small sliver of water or of a drought located in the profile (mollusk shells, coarse sand beds, or paleosols) as well as former perched shorelines provide direct data on lake level fluctuations. The mineralogical composition of the sediments, their grain size, the geochemical properties of the various fractions (mineral or organic, detrital or authigenic), and the assemblages of fossilized organisms are indirect indicators of past environmental conditions.

In the outcrops of the Bolivian Altiplano, we focused our investigations on the diatoms. These are microscopic unicellular algae (3–100 μm), which are very sensitive to variations in environmental parameters, such as the depth or salinity of water, and each cell produces an easily fossilized bivalve siliceous outer skeleton. This external skeleton, called a frustule, consists of an inner layer of silica tetrahedra (Si_2O, nH_2O) bonded to each other, and of a hydrated outer layer made of organic material, mainly proteins and polysaccharides. Diatom valves are extracted from sediments by physicochemical treatment. In optical microscopy, the species are identified by the structure of their valves: their absolute (number of valves/g) and relative (percentage) abundance can then be estimated. Knowing the self-ecology of each species identified makes it possible to characterize the aquatic environment in which they developed.

The presence of oxygen in the inner layer of the frustule allows the isotopic composition in oxygen 18 to be measured. Preliminary dehydration is necessary because of the hydrated nature of the silica so that only the isotopes in the oxygen of the internal structure are measured. After extraction of oxygen and purification in a preparation line, the O_2 molecule is analyzed by mass spectrometry (Crespin et al. 2008, Crespin et al. 2010).

Quantification of the Oxygen Isotopic Composition of Lakes

In lacustrine environments, the isotopic oxygen composition of diatoms ($\delta^{18}O_{diatoms}$) varies with the temperature and isotopic composition of the lake water ($\delta^{18}O_{lake\ water}$). Diatomaceous silica precipitates in isotopic equilibrium with the lake water, and calibration studies have established the thermo-dependent relationship $[([\delta^{18}O_{diatoms} - \delta^{18}O_{lake\ water}]\ (‰\ vs.\ VSMOW) = a*T\ lake\ water\ (°C) + b)]$ to express the variation in the isotopic composition of diatoms as a function of temperature (Brandriss et al. 1998; Moschen et al. 2005; Crespin et al. 2010; Dodd and Sharp 2010; Dodd et al. 2012; Alexandre et al. 2012). These relationships between the oxygen isotopic composition of the diatoms and the water during formation have been experimentally established for lacustrine diatoms under contemporary environmental conditions, taking the seasonal to multi-annual variations into account (Fig. 19.2).

These relationships all show a low dependence on temperature, of around −0.20‰/°C. On the other hand, the fractionation factors are very different, which may be due either to sampling problems or to different methodological approaches when carrying out these calibrations (Crespin et al. 2010; Alexandre et al. 2012). Nevertheless, applied in different contexts, this method proved relevant to the reconstruction of the isotopic composition of lakes in the past (Leng and Barker 2006). In addition, the application of these different calibrations enables sensitivity tests to be conducted depending on the potential temperature range applicable during the period considered.

So that the thermo-dependence of the isotopic fractionation between the diatoms and the formation water is taken into account, the temperature of the lake water in which they develop must also be known. Diatoms are photosynthetic organisms which grow in the epilimnion and reflect the surface temperatures of the lake. For current periods, field observations are essential; for past periods, assumptions based on simulated atmospheric temperature data from climate models and data obtained from other proxies in the same region are used.

Hydro-Isotopic Modeling and Paleoclimatic Interpretation

A quantified estimate of the hydrological balance of lakes or of the *P-E* is obtained by hydrological modeling. The more or less sophisticated models used all rely on the balance equation for lake water (Eq. 1). The first step is to derive the contemporary water balance from the available instrumental data and the relationships between H_L, V_L and S_L constructed from a digital terrain model (DTM). Estimating evaporation, a function of temperature, solar radiation, humidity, wind and vegetation cover, is always complex. It involves the use of different hydrological and climatic concepts and methods. It is better constrained by connecting the water balance to the salt balance (Vallet-Coulomb et al. 2001) with a watershed runoff model (Legesse et al. 2004) or with an energy balance model (Kutzbach 1980). Application of the model to the past is usually done for a time interval where the lake is considered to have been in equilibrium ($\Delta V_L = 0$). We know S_B, H_L (from which we calculate V_L and S_L), the solar radiation provided by astronomical calculations, paleotemperatures and paleo- vegetation on the watershed can be deduced from data e.g. from palynology.

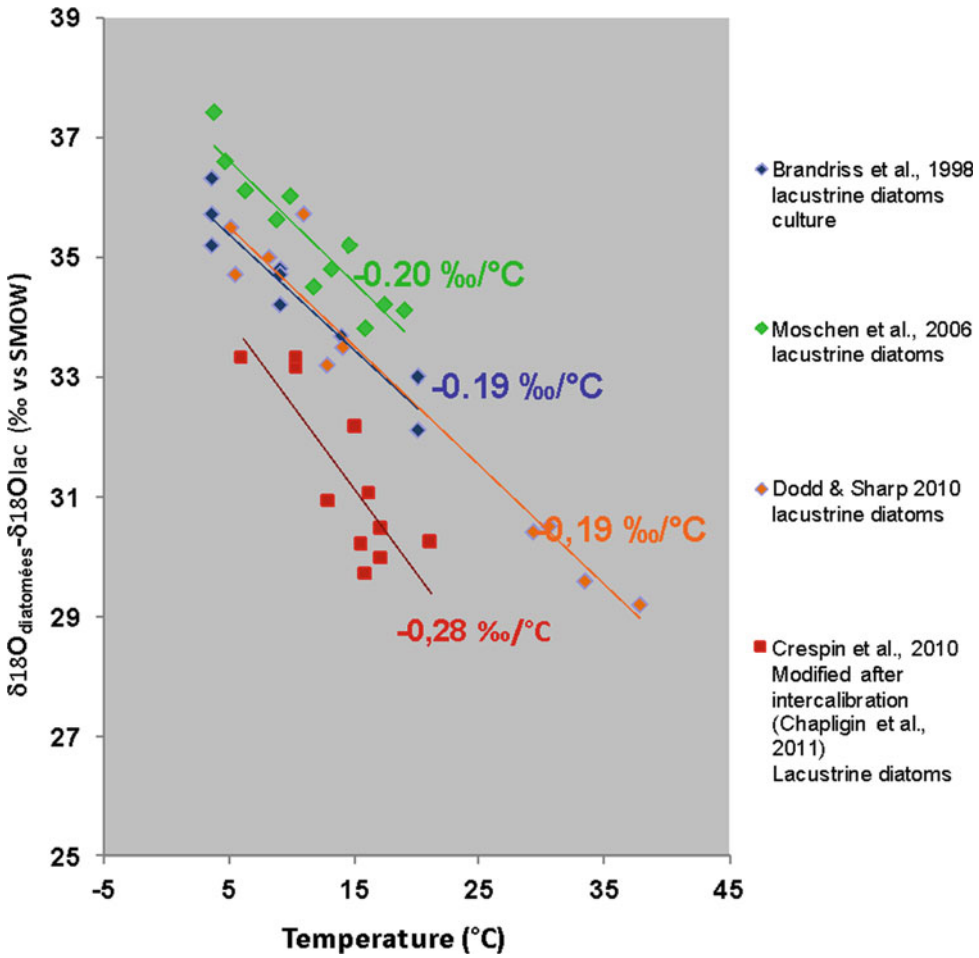

Fig. 19.2 Calibration of the thermo-dependent relationship between $\delta^{18}O_{diatoms}$ and $\delta^{18}O_{lake\ water}$ based on different calibrations of freshwater diatoms Modified from Crespin et al. (2010), Alexandre et al. (2012)

On the Bolivian Altiplano, paleohydrological data (Fig. 19.3) show that the Bolivian Altiplano experienced a first lacustrine transgression at 18,500 BP, interrupted between 18,100 BP and 15,800 BP by a phase of stagnation of the lake level, followed by a subsequent phase of maximum extension up to 15,000 BP years. After this date, this lake dried up. A second lacustrine transgression of lesser magnitude, named 'Coipasa', took place between 12,500 BP and 11,900 BP.

The reconstruction of the isotopic composition of the lake produces a very interesting result showing a spectacular decrease in its isotopic composition during the transgression phases (increase of the lake level) in response to rainfall inputs, followed by phases of isotopic enrichment during the phases when its level stabilizes (Fig. 19.3).

Simple hydro-isotopic modeling has shown that the increase in precipitation during the establishment of the lake is quantitatively consistent with the decrease recorded in the reconstruction of $\delta^{18}O_{lake\ water}$ (Quesada et al. 2015). It also partly explains the increase in the isotopic composition of the lake during its stability phases. This isotopic enrichment of lake waters is caused by interplay between lake evaporation and precipitation processes, both of which alter the isotopic composition of the lake differently. This confirms the establishment of the Tauca paleolake, probably caused by a massive influx of precipitation (significant decrease in $\delta^{18}O$ of the water of the paleolake) from the tropical Atlantic in the Altiplano watershed. The abrupt disappearance of the paleolake is contemporaneous with an isotopic excursion of +7‰ recorded in the ice of Mount Sajama (Thompson et al. 1998). Calculation of the isotopic composition of the vapor flux produced by evaporation of the paleolake, with its volume and surface taken into account, shows that this isotopic excursion could have been caused by an evaporation of 5–60% of the total volume of the lake. If this hypothesis is proven correct, it shows that the Tauca paleolake has certainly influenced the local, or even regional, hydrological cycle.

In conclusion, this example shows the potential impact of a lake on the local hydrological conditions, especially during

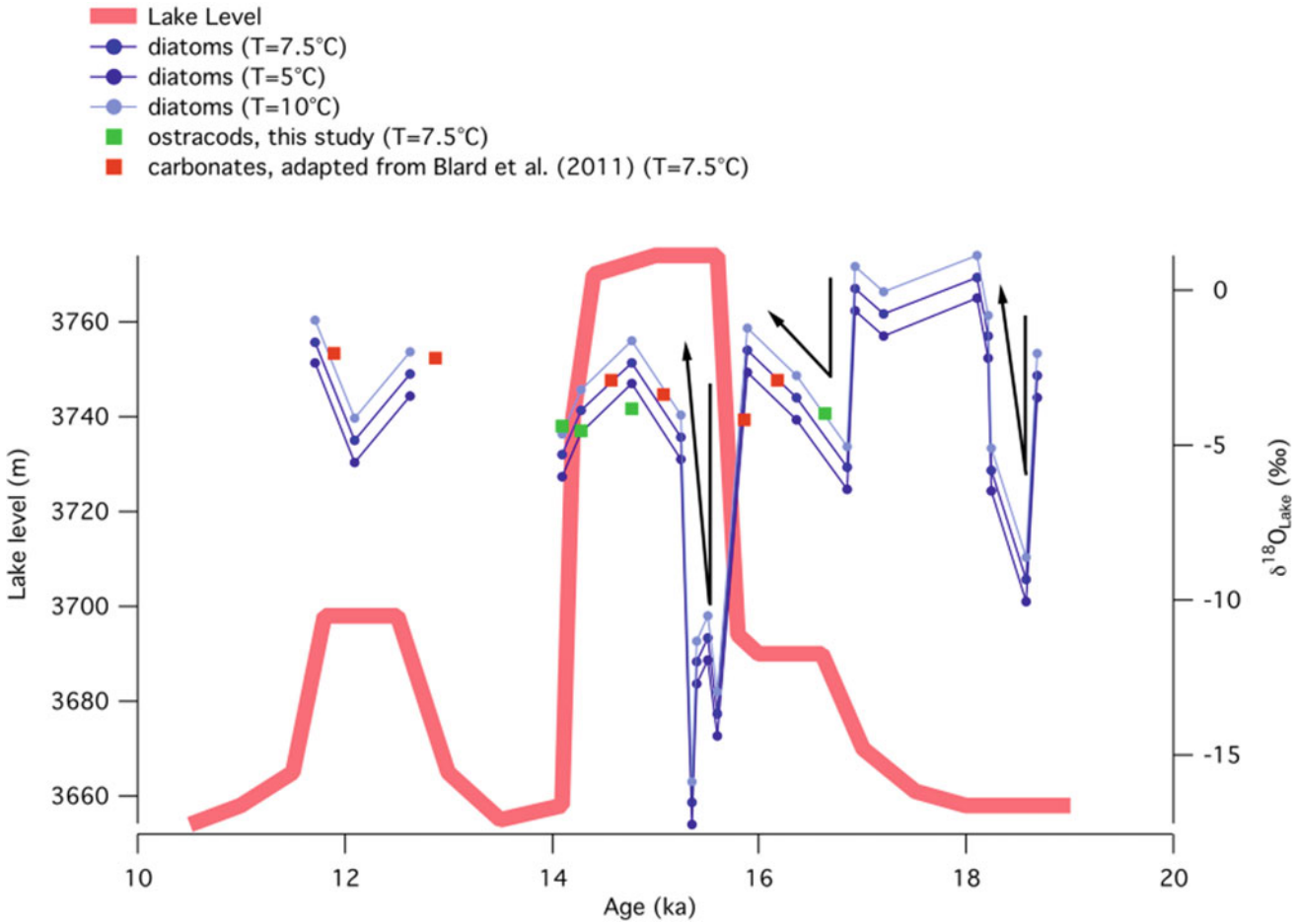

Fig. 19.3 Reconstruction of lake levels (m) and the isotopic oxygen composition $\delta^{18}O_{lake\ water}$ (‰ vs. V-SMOW) from (1) the isotopic oxygen composition of diatoms (blue lines) using the thermo-dependent relationship established by Dodd and Sharp (2010) for T = 5 °C, T = 7.5 °C and T = 10 °C, and (2) the isotopic oxygen composition of ostracods (green squares) and carbonates (red squares; Blard et al. 2011) for T = 7.5 °C

strong fluctuations in its level. Sites where several climate archives co-exist, allowing the large-scale climate signal to be differentiated from local conditions are relatively rare. The example discussed here shows the benefits to be gained from the co-location of a glacier archive and a lacustrine archive.

References

Alexandre, A., Crespin, J., Sylvestre, F., Sonzogni, C., & Hilbert, D. W. (2012). The oxygen isotopic composition of phytolith assemblages from tropical rainforest soil tops (Queensland, Australia): Validation of a new paleoenvironmental tool. *Climate of the Past, 8,* 307–324.

Blard, P.-H., Sylvestre, F., Tripati, A. K., Claude, C., Causse, C., Coudrain, A., et al. (2011). Lake highstands on the altiplano (Tropical Andes) contemporaneous with Heinrich 1 and the Younger Dryas: New insights from 14C, U-Th dating and δ18O of carbonates. *Quaternary Sciences Review, 30,* 3973–3989.

Brandriss, M. E., O'Neil, J. R., Edlund, M. B., & Stoermer, E. F. (1998). Oxygen isotope fractionation between diatomaceous silica and water. *Geochimica Cosmochimca Acta, 62,* 1119–1125.

Crespin, J., Alexandre, A., Sylvestre, F., Sonzogni, C., Paillès, C., Garreta, V. (2008). IR-laser-extraction technique applied to oxygen isotopes analysis of small biogenic silica samples. *Analytical Chemistry, 80,* 2372–2378.

Crespin, J., Sylvestre, F., Alexandre, A., Sonzogni, C., Paillès, C., & Perga, M.-E. (2010). Re-examination of the temperature-dependent relationship between $\delta^{18}O_{diatoms}$ and $\delta^{18}O_{lake\ water}$ and implications for paleoclimate inferences. *Journal of Paleolimnology, 44,* 547–557.

Dodd, J. P., & Sharp, Z. D. (2010). A laser fluorination method for oxygen isotope analysis of biogenic silica and a new oxygen isotope calibration of modern diatoms in freshwater environments. *Geochimica Cosmochimica Acta, 74,* 1381–1390.

Dodd, J. P., Sharp, Z. D., Fawcett, P. J., Brearley A. J., & McCubbin F. M. (2012). Rapid post-mortem maturation of diatom silica oxygen isotope values. Geochemistry, Geophysics, Geosystems, *13*. https://doi.org/10.1029/2011gc004019.

Garreaud, R. D., Vuille, M., & Clement, A. C. (2003). The climate of the Altiplano: Observed current conditions and mechanisms of past changes. *Palaeogeography, Palaeoclimatology, Palaeoecology, 194,* 5–22.

Kutzbach, J. E. (1980). Estimate of past climate at paleolake Chad, North Africa, based on a hydrological and energy balance model. *Quaternary Research, 14,* 210–223.

Legesse, D., Vallet-Coulomb, C., & Gasse, F. (2004). Analysis of the hydrological response of a tropical terminal lake, lake Abiyata (Main Ethiopian Rift Valley) to changes in climate and human activities. *Journal of Hydrological Processes, 18,* 487–504.

Leng, M. J., & Barker, P. A. (2006). A review of the oxygen isotope composition of lacustrine diatom silica for palaeoclimate reconstruction. *Earth-Science Review, 75,* 5–27.

Moschen, R., Lücke, A., & Schleser, G. (2005). Sensitivity of biogenic silica oxygen isotopes to changes in surface water temperature and palaeoclimatology. *Geophysical Research Letters, 32,* L07708. https://doi.org/10.1029/2004GL022167.

Quesada, B., Sylvestre, F., Vimeux, F., Black, J., Paillès, C., Sonzogni, C. et al. (2015). Impact of Bolivian paleolake evaporation on the $\delta^{18}O$ of the Andean glaciers during the last deglaciation (18.5–11.7 ka): Diatom-inferred $\delta^{18}O$ values and hydro-isotopic modeling. *Quaternary Science Review, 120,* 93–106.

Servant, M., & Fontes, J. C. (1978). Les lacs quaternaires des hauts plateaux des Andes boliviennes: Premières interprétations paléoclimatiques. *Cahiers ORSTOM. Série Géologie, 10,* 9–23.

Sylvestre, F., Servant, M., Servant-Vildary, S., Causse, C., Fournier, M., & Ybert, J.-P. (1999). Lake-level chronology on the Southern Bolivian Altiplano (18–23°S) during late-glacial time and the early holocene. *Quaternary Research, 51,* 54–66.

Thompson, L. G., Davis, M. E., Mosley-Thompson, E., & Sowers, T. A. (1998). A 25,000-Year tropical climate history from bolivian ice cores. *Science, 282,* 1858–1864.

Vallet-Coulomb, C., Legesse, D., Gasse, F., Travi, Y., & Chernet, T. (2001). Lake evaporation estimates in tropical Africa (Lake Ziway, Ethiopia). *Journal of Hydrology, 245,* 1–18.

Vallet-Coulomb, C., Gasse, F., & Sonzogni, C. (2008). Seasonal evolution of the isotopic composition of atmospheric water vapour above a tropical lake: Deuterium excess and implication for water recycling. *Geochimica Cosmochimica Acta, 72,* 4661–4674.

Air-Ice Interface: Tropical Glaciers

20

Françoise Vimeux

Just as the polar caps are excellent archives of information on past climates, so too are the high-altitude tropical glaciers. Indeed, the prevailing temperature and humidity conditions there usually ensure very good preservation of chemical and isotopic tracers. These archives have therefore been used for the past 25 years to study the variability of the tropical climate over past centuries and millennia. They are mostly found in the Andes in South America between 0° and 20° S (Vimeux 2009; Vimeux et al. 2009), although drilling has been conducted on Kilimanjaro (Thompson et al. 2002) and the southern Himalayas (Thompson et al. 2000, 2006). The focus of this chapter is on climate information taken from the Andean glaciers.

The rapid dynamic of these glaciers, the high level of snow accumulation per year (0.5–1 m) and reduced ice thickness (100–150 m) mean that it is not possible to access climate periods as old as those possible in polar cores. The oldest cores date back to the last glacial maximum, about 20 000 years ago, with the Sajama core (Bolivia, 6542 m, Western Cordillera, 18° 06′ S, 68° 53′ W) dating back to ~ 25,000 years (Thompson et al. 1998). On the other hand, the tropical ice allows our climate to be studied with a very good temporal resolution, at the seasonal level for recent centuries.

Paleoclimate Markers

Several types of quantifiable climate variables can be extracted from tropical glaciers: the net accumulation, the temperature in the borehole and regional precipitation. We propose to review these and to present the main results in terms of climate variability. Although complementary, we will not discuss here the qualitative results from the chemical analysis of ice, which essentially informs us about changes in the environmental, atmospheric transport processes and air pollution.

Over recent centuries, the seasonal cycles of the chemical elements and stable isotopes in precipitation allow us to date the annual layers with a relatively good degree of accuracy (±5 to 10 years around 1900). It is thus possible to calculate the annual net accumulation. To correct for the effects of snow compaction in the depths, an ice flow model is applied, or alternatively, the thinning of the layers is corrected by directly observing the relationship between the annual thickness and the depth, along the core. The latter method cannot however be used to discuss climate trends which are, in principle, corrected using the same method. The question that then arises is: what does the net accumulation represent given that it is actually the combination of the total accumulation (controlled by the precipitation and wind) minus removal (sublimation, erosion by wind), and that the latter processes can have different seasonalities? If one considers sites where accumulation is low (0.31 m of water/year) with a high level of sublimation throughout a long dry season, such as at Cerro Tapado (Chile, arid diagonal, 5550 m, 30° 08′ S, 69° 55′ W), it is difficult to use this parameter as a marker of the amount of deposited precipitation. This is less the case for sites such as the one at Illimani (Bolivia, eastern cordillera, 6350 m, 16° 37′ S, 67° 46′ W) where the rainfall season is longer, the annual snow accumulation heavier (0.58 m of water/year) and the sublimation is concentrated over a shorter time of the year which is different to the accumulation season (Ginot et al. 2006). Only the end of the rainy season which represents about 10% of the annual accumulation may be truncated in the records. In that case, we can we assume that large variations in the net accumulation are representative of the amount of precipitation. The accumulation estimates made on the Quelccaya core (Peru, 5670 m, 13° 56′ S, 70° 50′ W, the only core with dating by

F. Vimeux (✉)
Laboratoire HydroSciences Montpellier (HSM), Institut de Recherche pour le Développement (IRD), Montpellier, 34095, France
e-mail: Francoise.Vimeux@lsce.ipsl.fr

Laboratoire des Sciences du Climat et de l'Environnement (LSCE), Institut Pierre Simon Laplace (IPSL), 91191 Gif-sur-Yvette, France

G. Ramstein et al. (eds.), *Paleoclimatology*, Frontiers in Earth Sciences,
https://doi.org/10.1007/978-3-030-24982-3_20

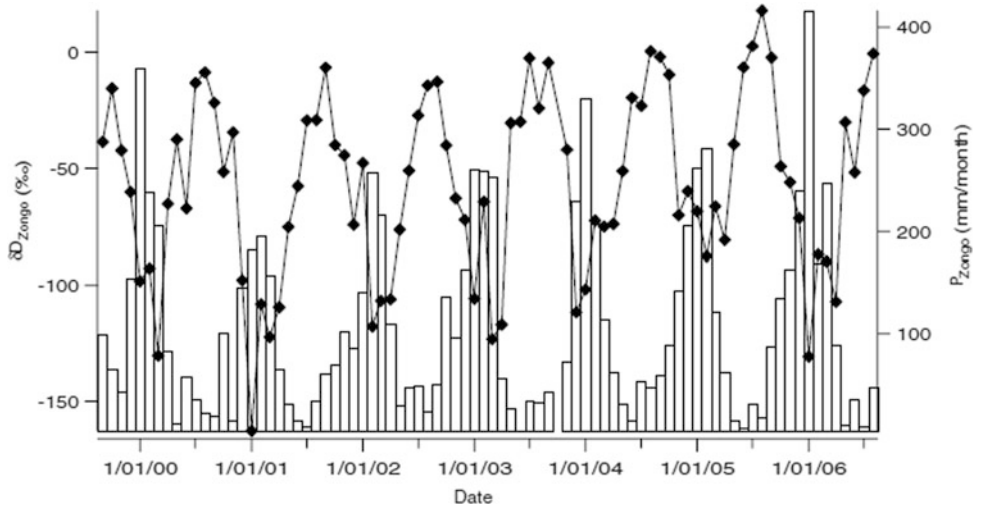

Fig. 20.1 Example of relationship between the isotopic composition of deuterium (‰) in rainfall collected in the Zongo Valley at multiple sites (Bolivia, 16° S, a valley linking the Andean peaks to the Amazon) (connected points) and the quantity of precipitation (mm/month) (bars), on a monthly scale over several years. During the rainy season, the isotopic composition is strongly depleted of heavy isotopes, while during the dry season, it is enriched. The correlation with local precipitation explains only 50% of the isotopic signal. The remainder of the variance can be explained by precipitation at the regional level. This figure is adapted from Vimeux et al. 2005

seasons over the past 1500 years) show sequences of high (the seventeenth and eighteenth centuries and in the twentieth century) and low (the nineteenth century) accumulations (Thompson et al. 2006).

As in polar ice, it is possible to measure the temperature in the borehole. This method does not allow past temperature changes to be reconstructed with a high temporal resolution, but it does offer the possibility of measuring slow fluctuations. In high altitude glaciers, this profile depends on the energy balance at the surface and on the flow of geothermal heat in the depths. The proximity of the ice to the bedrock does not allow these profiles to be applied to the second half of the cores although the surface profiles can be interpreted. In the cores where these profiles are available, an increase in temperature is observed for recent decades (Vimeux et al. 2009), reaching 1.1 °C in the twentieth century.

The measurement of the isotopic composition ($\delta^{18}O$ and δD) of tropical ice provides information on rainfall patterns caused by the air mass along its trajectory. The linear relationship between the isotopic composition of snow and surface air temperature, well established for the polar regions, does not hold true in the tropics. This relationship is mainly due to the fact that, in the middle and high latitudes, the amount of precipitation formed and air temperature are closely linked as per the Clausius-Clapeyron law. This is not the case in the tropics, where the majority of precipitation is convective and where the water cycle is complex (recycling of water vapor from the surface). The coupling of observations, through rainfall collection network systems, and modeling of atmospheric cycling of stable isotopes of water with a hierarchy of models (general circulation atmospheric model, mesoscale model correctly representing the topography and one dimension convection model) has shown that at the seasonal and interannual scale, the isotopic composition of Andean snow is strongly related to precipitation upstream from the drilling sites along the trajectories, in the Amazon and over the tropical Atlantic regions where the most intense convection phenomena are located (Vimeux et al. 2005; Vuille and Werner 2005; Vimeux et al. 2011) (Fig. 20.1). It was shown that the relationship between water isotopes in the Andes and precipitation is strongly dependent on convection conditions (re-evaporation of water droplets and recycling of the resulting vapor in the convective column) (Risi et al. 2008).

Some Important Results from the Interpretation of Andean Isotopic Records

Recent studies have sought to link the changes in precipitation in tropical South America to larger scale processes over the last century. Most of the interannual variability in rainfall for this region is linked to variations in intensity and geographical extension of the ascending and convective branch of the Hadley-Walker cell, affecting the South

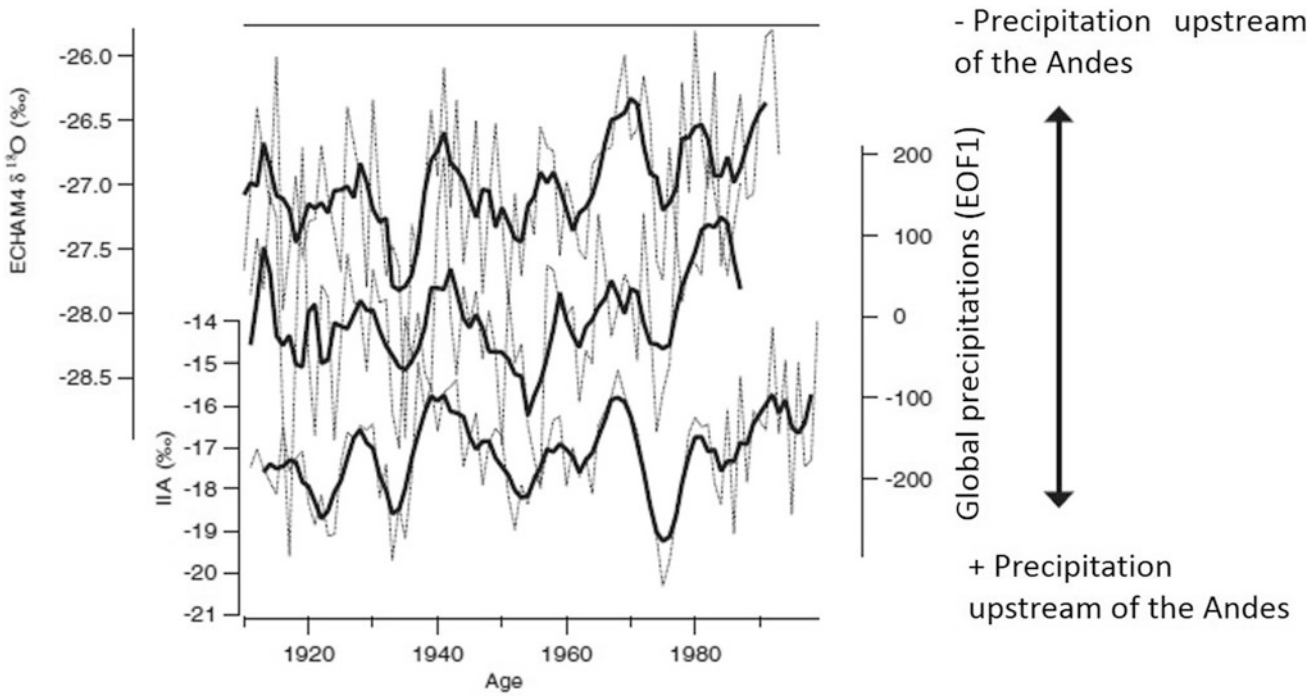

Fig. 20.2 The Andean Isotopic Index (AII) is built from the isotopic composition of four Andean ice cores having similar interannual variations and a sufficiently precise dating over the last century (in Bolivia: Illimani (16° S, 6300 m) and Sajama (18° S, 6542 m) in Peru: Huascaran (9° S, 6048 m) and Quelccaya (14° S, 5670 m)). It is compared here to: a) the first component of an analysis of the principal components of global precipitation (EOF1) which reflects the first mode of interannual climate variation that is ENSO; b) the isotopic composition of the oxygen-18 in Amazonian water vapor, simulated by the atmospheric model ECHAM-4. The lines in bold represent a moving average over 5 years. This figure is adapted from Hoffman et al. (2003)

American monsoon pattern. This cell is strongly disrupted by anomalies in the temperature of surface waters in the tropical Pacific.

We therefore think that ENSO events are likely to mark the isotopic composition of Andean ice (Bradley et al. 2003; Hoffmann et al. 2003). The isotopic composition recorded in several Andean cores over the last century effectively shows a common decadal signal, called Isotopic Andean Index strongly linked to rainfall variations in the Amazon, caused by the ENSO phenomenon (Fig. 20.2). However, variations in temperature of the surface waters of the tropical Atlantic also have a strong impact on the South American monsoon system (and so on regional precipitation), and it becomes difficult to untangle the different causes in the isotopic signal (Hoffmann 2003).

The Illimani and Quelccaya ice cores with their precise dating back to about 1700 show a significant loss of about 1.5‰ of $\delta^{18}O$ between the late seventeenth and early nineteenth century. This period also corresponds to the maximum spread of glacial moraines in Bolivia, Peru and Ecuador, dated by lichenometry (Jomelli et al. 2009). This comparison between the spread of glaciers and the $\delta^{18}O$ of ice suggests that during the Little Ice Age, the tropical Andes were wetter (depletion of isotopes and higher accumulation on the glaciers to increase the mass at their base) and colder (maximum spread of the glaciers).

At the glacial-interglacial scale, isotope profiles obtained on three Bolivian and Peruvian cores (Illimani; Huascaran, Peru, 6050 m, 9° 06′ S, 77° 30′ W and Sajama) show a common isotope signal in terms of variability and amplitude (Fig. 20.3). This signal, very similar to that recorded by the isotopic composition in the polar cores, highlights highly depleted values during the last glacial maximum and a gradual enrichment during deglaciation, with a return to depleted conditions before reaching an optimum around 11,000 years. This structure is similar to that described in polar ice, where known climate periods are recorded (glacial maximum, Younger Dryas and the Holocene optimum), although the interpretation of the isotopes in Andean ice (moisture) is different from that of polar ice (temperature). The translation of this glacial-interglacial variation in terms of humidity shows that 20,000 years ago, the air masses sustained a more major drain along their trajectories, corresponding to a precipitation increase of about 10% (Vimeux et al. 2005).

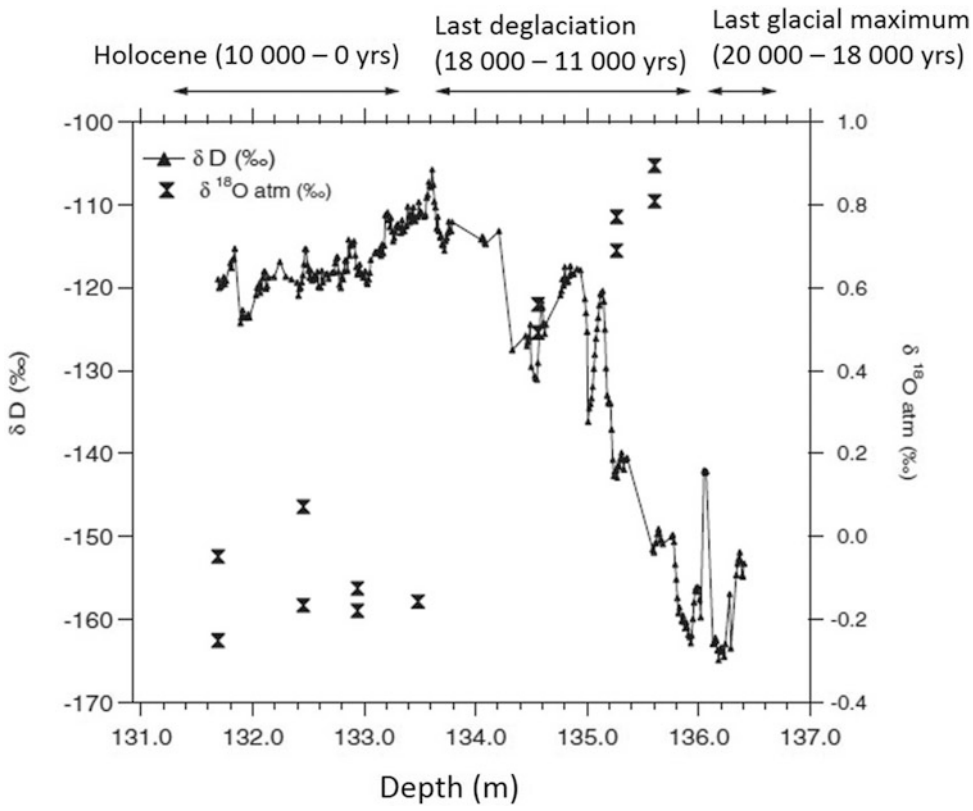

Fig. 20.3 Isotopic composition in deuterium (‰) over the last meters of the Illimani core and isotopic composition of oxygen (‰) of air trapped in the bubbles

A study using coupled ocean-atmosphere climate models for this glacial period shows that rainfall was indeed more intense 20,000 years ago in Northeast Brazil and the tropical South Atlantic, the cradle of Andean precipitation (Khodri 2009).

References

Bradley, R. S., Vuille, M. Hardy, D., & Thompson, L. G. (2003). Low latitude ice cores record Pacific sea surface temperatures. *Geophysical Research Letters*, *30*. https://doi.org/10.1029/2002gl016546.

Gilbert, A., Wagnon, P., Vincent, C., Ginot, P., & Funk, M. (2010). Atmospheric warming at a high-elevation tropical site revealed by englacial temperatures at Illimani, Bolivia (6340 m above sea level, 16° S, 67° W). *Journal Geophysical Research, 115,* D10109. https://doi.org/10.1029/2009JD012961.

Ginot, P., Kull, C., Schotterer, U., Schwikowski, M., & Gäggeler, H. W. (2006). Glacier mass balance reconstruction by sublimation induced enrichment of chemical species on Cerro Tapado (Chilean Andes). *Climate of the Past, 2,* 21–30.

Hoffmann, G., Ramirez, E., Taupin, J. D., Francou, B., Ribstein, P., Delmas, R., Dürr, H., Gallaire, R., Simoes, J., Schotterer, U., Stievenard, M., & Werner, M. (2003). Coherent isotope history of Andean ice cores over the last century. Geophysical Research Letters, *30*, 1179–1184.

Hoffmann, G. (2003). Taking the pulse of the tropical water cycle. *Science, 301,* 776–777.

Jomelli, V., Favier, V., Rabatel, A., Brunstein, D., Hoffmann, G., & Francou, B. (2009). Fluctuations of glaciers in the tropical andes over the last millennium and palaeoclimatic implications: A review. *Palaeogeography, Palaeoclimatology, Palaeoecology, 281,* 269–282. https://doi.org/10.1016/j.palaeo.2008.10.033.

Khodri, M. (2009). Sensitivity of South American tropical climate to last glacial maximum boundary conditions: Focus on teleconnections with tropics and extratropics. In F. Vimeux, F. Sylvestre, & M. Khodri (Eds.), *Developments in paleoenvironmental research series (DPER)* (Vol. 14, XVII, 418 p. 106 illus., 61 in color). Springer. ISBN 978-90-481-2671-2.

Risi, C., Bony, S., & Vimeux, F. (2008). Influence of convective processes on the isotopic composition (δ^{18}O and δD) of precipitation and water vapor in the tropics, part 2: Physical interpretation of the amount effect. *Journal of Geophysical Research, 113,* D19306. https://doi.org/10.1029/2008JD009943.

Thompson, L. G., Davis, M. E., Mosley-Thompson, E., Sowers, T.A., Henderson, K. A, Zagorodnov, V. S., Lin, P.-N., Mikhalenko, V. N., Campen, R. K., Bolzan, J. F., Cole-Dai, J., & Francou, B. (1998). A 25,000-Year tropical climate history from bolivian ice cores. *Science*, *282*, 1858–1864.

Thompson, L. G., Yao, T., Mosley-Thompson, E., Davis, M. E, Henderson, K. A., & Lin, P. -N. (2000). A high-resolution millennial record of the South Asian monsoon from himalayan ice cores. *Science*, *289*, 1916–1919.

Thompson, L. G., Mosley Thompson, E., Davis, M. E., Henderson, K. A., Brecher, H. H., Zagorodnov, V. S., et al. (2002). Kilimanjaro ice core records: Evidence of Holocene climate change in tropical Africa. *Science, 298,* 589–593.

Thompson, L. G., Mosley Thompson, E., Brecher, H., Davis,M., Leon, B., Les, D., Lin, P.-N., Mashiotta, T., & Mountain, K. (2006). Abrupt tropical climate change: Past and present. *Proceedings of the National Academy of Sciences*, *103*, 10536–10543.

Vimeux, F., Gallaire, R., Bony, S., Hoffmann, G., Chiang, J., & Fuertes, R. (2005). What are the climate controls on isotopic

composition (δD) of precipitation in Zongo Valley (Bolivia)? Implications for the Illimani ice core interpretation. *Earth and Planetary Science Letters, 240,* 205–220.

Vimeux, F., Ginot, P., Schwikowski, M., Vuille, M., Hoffmann, G., Thompson, L. G., et al. (2009). Climate variability during the last 1000 years inferred from Andean ice cores: A review of methodology and recent results. *Palaeogeography, Palaeoclimatology, Palaeoecology, 281,* 229–241. https://doi.org/10.1016/j.palaeo.2008.03.054.

Vimeux, F. (2009). Similarities and discrepancies between polar and andean ice cores over the last deglaciation in past climate variability from the last glacial maximum to the holocene in South America and surrounding regions. In F. Vimeux, F. Sylvestre, M. et Khodri (Eds.), *Developments in paleoenvironmental research series* (DPER) (Vol. 14, XVII, 418 p., 106 illus., 61 in color.). Springer. ISBN 978-90-481-2671-2.

Vimeux, F., Tremoy, G., Risi, C., & Gallaire, R. (2011). A strong control of the South American see-saw on the intra-seasonal variability of the isotopic composition of precipitation in the Bolivian Andes. *Earth and Planetary Sciences Letters, 307,* 47–58.

Vuille, M., & Werner, M. (2005). Stable isotopes in precipitation recording South American summer monsoon and ENSO variability: Observations and model results. *Climate Dynamics*, *25*. https://doi.org/10.1007/s00382-005-0049-9.

Climate and the Evolution of the Ocean: The Paleoceanographic Data

21

Thibaut Caley, Natalia Vázquez Riveiros, Laurent Labeyrie, Elsa Cortijo, and Jean-Claude Duplessy

Introduction: The Development of Tools and Concepts

The idea of reconstructing the history of oceans and climates in the past using marine sediment cores arrived quite late after the beginnings of oceanography. It was initiated in the twentieth century, well after the first attempts to measure variations in seawater temperature down the water column, which date back to the eighteenth century with the great circumnavigation expeditions. Land geologists were the first to propose paleoceanographic reconstructions from exposed marine series, limiting the collected information to former coastal waters. The first reconstructions of past seawater temperatures were made possible by the piston corer developed by the Swedish oceanographer Kullenberg, capable of collecting continuous sedimentary deposits without layer disruption. Geologists were therefore able to collect uninterrupted sedimentary series, sometimes over 20 m in length, for laboratory analysis, and thus study long records of the environmental conditions from the time the sediments were deposited. With this type of corer, the Swedish expedition of 1947–1948 collected over 300 different cores from various deep ocean basins that became the basis of the first studies on the geological history of the oceans. In parallel, during the 1950s, Maurice Ewing, the founder of the Lamont-Doherty Geological Observatory (USA), and one of the developers of seismic sediment mapping of the ocean floor, initiated the first systematic collection of marine sediment cores. The first descriptions of the main sedimentary systems, changes in fossil faunas and the timeframe for the first biostratigraphic age scales were proposed based on these cores. One of the main results of these studies was the continuous reconstruction of the alternating warm and cold phases that took place during the Pleistocene.

Unquestionably, the honor for the initiation of quantitative paleoceanography belongs to Cesare Emiliani. After the discovery of isotopic fractionation and the development of an accurate method to measure isotopic ratios, Harold Urey and his group in Chicago refined the use of the isotopic ratio $^{18}O/^{16}O$ in fossil carbonates as a paleothermometer. They realized that the $^{18}O/^{16}O$ ratio of foraminiferal shells and other carbonates depended on two variables: the temperature and the $^{18}O/^{16}O$ ratio of the water where the carbonate was formed. Changes in water temperature are reflected in variations in the isotopic fractionation between the carbonate and the water during the formation of the shell: for water with a given isotopic composition, the higher the temperature, the lower the $^{18}O/^{16}O$ ratio (Epstein et al. 1951, 1953). Emiliani (1955) applied this tool to foraminifera shells sampled along a sediment core from the Caribbean Sea to propose the first reconstruction of the variations in sea surface temperature (SST) over the past 400 ka (Fig. 21.1). He also established the major methodological guidelines for this type of study: use of continuous records, precise dating, and interpretation of parameters quantitatively linked to key variables of the climate system.

To extract a temperature signal from the $^{18}O/^{16}O$ ratio of planktonic foraminifera, Emiliani had to constrain the changes in the isotopic composition of the ocean water in which the foraminifera developed. The $^{18}O/^{16}O$ ratio of

Thibaut Caley, Natalia Vázquez Riveiros and Laurent Labeyrie—These authors have contributed equally to this chapter.

T. Caley (✉)
EPOC, UMR 5805, CNRS, University of Bordeaux, Pessac, France
e-mail: thibaut.caley@u-bordeaux.fr

N. V. Riveiros · L. Labeyrie · E. Cortijo · J.-C. Duplessy
Laboratoire des Sciences du Climat et de l'Environnement, LSCE/IPSL, CEA-CNRS-UVSQ, Université Paris-Saclay, 91190 Gif-sur-Yvette, France

N. V. Riveiros
Institut Français de Recherche pour l'Exploitation de la Mer (Ifremer), Unité de Geosciences Marines, Pointe du Diable, 29280 Plouzané, France

L. Labeyrie
LGO Université Bretagne Sud, 56000 Vannes, France

G. Ramstein et al. (eds.), *Paleoclimatology*, Frontiers in Earth Sciences,
https://doi.org/10.1007/978-3-030-24982-3_21

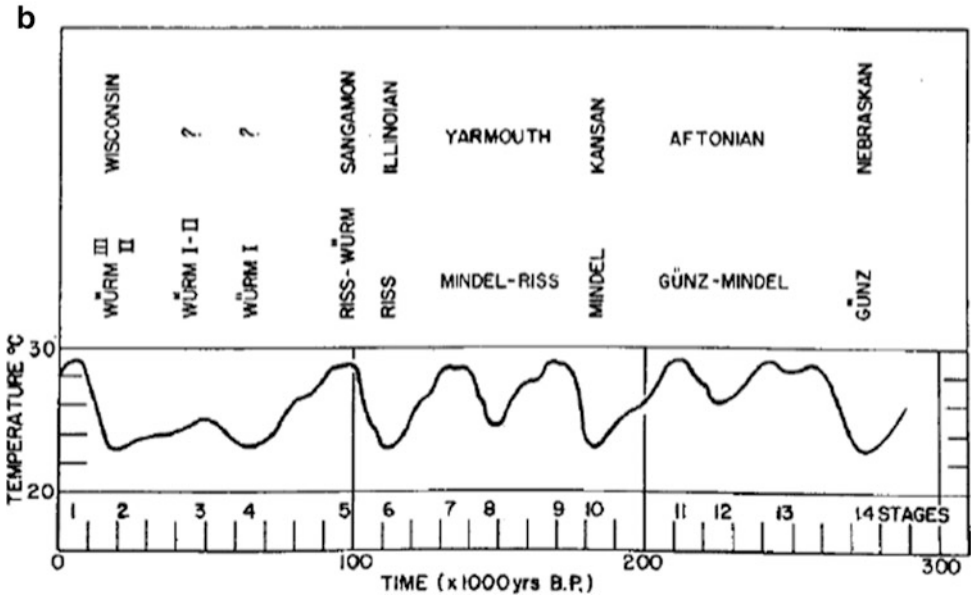

Fig. 21.1 **a** Cesare Emiliani, founder of isotopic marine paleoclimatology, in the early 1950s at the University of Chicago. (Photo from the archives of the Rosenstiel School of Marine and Atmospheric Science, University of Miami). **b** First attempt to evaluate surface water temperature changes in the Caribbean Sea, Emiliani (1955). Subsequent studies have shown that the timescale was underestimated by about 25% (the last interglacial, called Sangamon in American literature, is dated at about 125,000 years and not 100,000 years), and that the amplitude of temperature variations, calculated from a simple model (see below), was overestimated

seawater is affected by evaporation and precipitation: the vapor phase is depleted in the heavy ^{18}O isotopes relative to the liquid phase. Conversely, when the water vapor in clouds condenses, the precipitation is richer in ^{18}O than the vapor. Thus, the transport of air masses from low to high latitudes is accompanied by a large-scale isotopic distillation process in the water vapor that results in the gradual decline of the $^{18}O/^{16}O$ ratio in precipitation. For this reason, the $^{18}O/^{16}O$ ratio of snowfall feeding the high-latitude ice caps is depleted by more than 30‰ compared to that of the tropical ocean.

The growth and melting of ice caps, which involves considerable volumes of water (several million cubic kilometers), directly affect the salinity and the average $^{18}O/^{16}O$ ratio of the ocean, and therefore that of the foraminifera that develop there. Regional climate changes are also accompanied by local variations in evaporation and precipitation, which induce further regional variations in the salinity of surface seawater and its $^{18}O/^{16}O$ ratio.

From the data available at the time, Emiliani (1955) estimated that the development of large ice sheets covering Canada (the Laurentide ice sheet) and northern Europe (the

Fennoscandian ice sheet) at the maximum of the glaciation caused an enrichment in ^{18}O of the global ocean of +0.4‰. We now know that the enrichment in ^{18}O in the glacial ocean was in fact close to +1.0‰ (Schrag et al. 2002). Despite these inaccuracies, the work of Emiliani was the first to demonstrate from paleoclimate observations that glacial—interglacial periods indeed oscillated with cyclicities predicted by the Milankovitch theory several decades earlier (see Chap. 28). Emiliani also proposed the 'Marine Isotopic Stage' (MIS) nomenclature, now universally adopted, to characterize the alternation of warm and cold Pleistocene phases, with odd numbers for interglacial periods and even numbers for glacial ones (1 for the Holocene, 2 for the last glacial period, and so on). He also discovered that the last interglacial, or MIS 5 (Fig. 21.1), was interrupted by two colder periods, which led him to divide it into three warm subperiods (designated 5a, 5c and 5e from the most recent to the oldest) and two cold ones (5b and 5d). The term '5e' is still frequently used, as it has been incorporated into the European continental reconstructions as the equivalent to the Eemian warm period. The isotopic stratigraphy formalism has since been generalized, with subdivisions either numbered as decimals between alternating warmer (e.g., 5.1 for 5a, 5.3 for 5c and 5.5 for 5e) and colder (5.2 and 5.4) periods (Pisias et al. 1984) or as letters (Railsback et al. 2015).

With the assumption that past variations in foraminiferal $^{18}O/^{16}O$ ratios in cores from different ocean basins had to be approximately synchronous across global climate changes, Emiliani paved the way for a global marine isotopic stratigraphy. The demonstration that the volume of ice caps was indeed the dominant component of the isotopic signal recorded in marine cores reinforced the stratigraphic value of the marine isotopic stage age scale, which became a major reference tool for past climate change studies. The routine use of drilling ships as part of the International Ocean Drilling Program has allowed the recovery of sediment cores that cover the last tens of millions of years, extending the isotopic sequences not only to the Quaternary (Fig. 21.2), but as far back as the Paleocene, 60 Ma ago.

By 1970–1980, the paleoclimate community had arrived at the conclusion that variations in the oxygen isotopic composition provided a remarkable stratigraphic tool to establish long-term correlations. However, new tools still needed to be developed to precisely reconstruct past SST, as well as variations in other oceanic features such as salinity, or the direction and intensity of deep-water currents.

This chapter will focus on the development of classic and new paleoceanographic tracers over the last decades. We will mainly, but not exclusively, focus on tracers that are based on foraminifera, since these abundant microfossils have been extensively used because of their ubiquity in the oceans and their great preservation potential. Their faunal associations and isotopic composition have been widely used as paleoclimate indicators for decades, and the advent of relatively new indicators implies an undiminished interest. Other indicators such as corals will be briefly discussed in association with some of the tracers.

Sea Surface Temperature

The surface temperature of the ocean is an essential climate parameter that governs heat exchange with the atmosphere. SST also modulates the solubility of gases, oxygen and CO_2 in particular, and their exchange rates with the atmosphere. The amplitude of the spatial variability of SST is well known: it ranges between −1.96 °C, freezing point for seawater at 35 psu, and 30–35 °C, maximum temperature recorded for the open ocean. However, its temporal variability is more difficult to constrain because it not only varies on a daily basis, but also seasonally and annually. In situ measurement sensors are precise to ±0.001 °C at a given location, water depth and time. Satellite data provide global coverage and allow long-term monitoring of the evolution of SST, but their accuracy is, at best, close to 0.1 °C, and surface values are averaged over tens or hundreds of square kilometers. Paleoceanographers cannot aim to reconstruct SST variations with this level of precision. Nonetheless, given the magnitude of changes in the past, relevant information may be acquired when SST changes are estimated to the nearest degree. Paleoceanographers also aim to estimate, whenever possible, the amplitude of the seasonal cycle, and the temperature distribution of the upper water column.

For these studies, two major types of paleotemperature indicators are used: (i) changes in the distribution of fossil planktonic flora or fauna (foraminifera, diatoms, dinoflagellates, radiolarians), and (ii) geochemical tracers produced by these organisms or recorded in their fossil skeletons.

The Distribution of Marine Fauna and Flora

The distribution of the various groups that make up the marine planktonic ecosystem was extensively studied during the major exploration campaigns that marked the nineteenth and early twentieth centuries. Foraminifera, single-celled protozoans that secrete a calcareous shell, were the most generally recorded group. They are very diverse and inhabit all the oceans, from the coldest to the warmest. However, each individual species has a limited tolerance to environmental changes, particularly temperature, which allowed biologists at the end of the nineteenth century to highlight the zonal distribution of many species. They also established existing relationships between climate and the abundance of certain

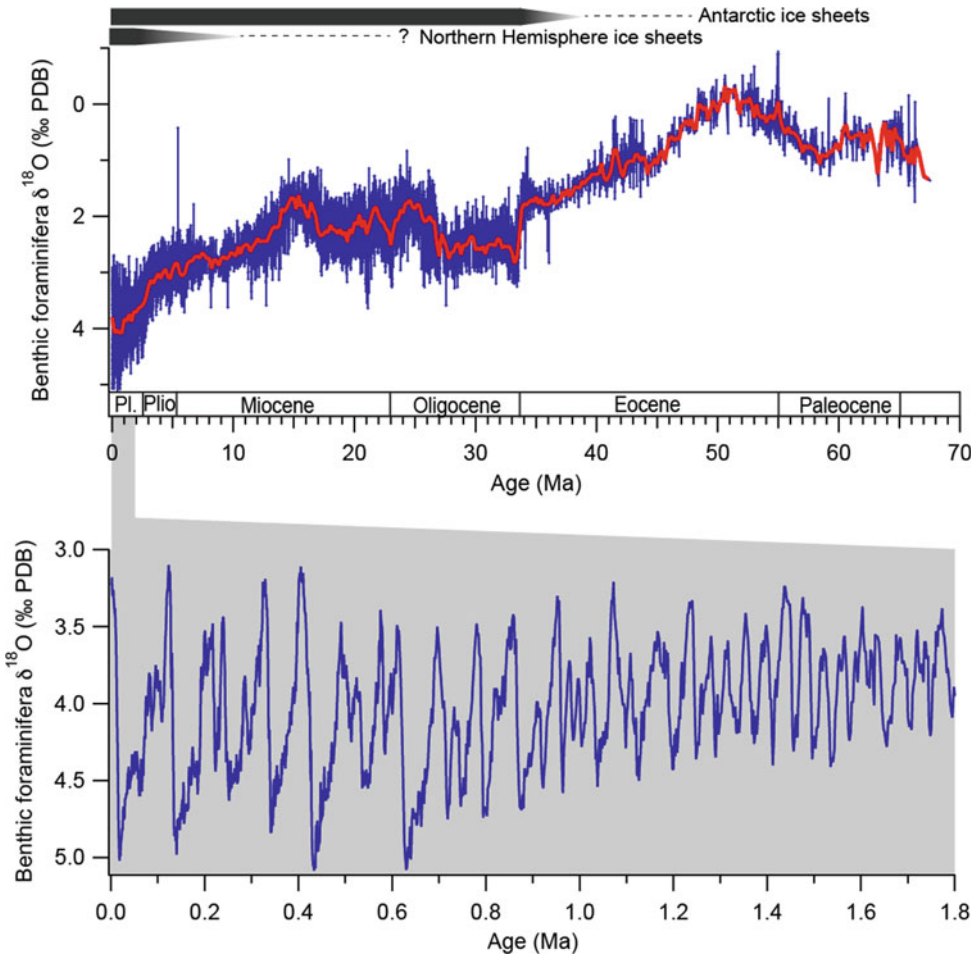

Fig. 21.2 Variations in the isotopic composition of the oxygen in benthic foraminifera from 70 million years ago (Zachos et al. 2008) with a detail of the last 1.8 Ma showing periodicities predicted by the astronomical theory of paleoclimate (Lisiecki and Raymo 2005). Presence of Northern Hemisphere and Antarctic ice sheets are from Zachos et al. (2008). Geological epochs (Pl. = Pleistocene, Plio = Pliocene) are indicated at the bottom of the top panel

species. These observations, along with the statistical method of 'transfer functions' developed by Imbrie and Kipp, served as a basis for the quantitative reconstruction of surface temperatures from fossil fauna found in marine sediments. Transfer functions allow the estimation of seawater temperature during both the cold and warm seasons, when adequate data is available. The basic principle for the reconstruction of SST changes in the past is to assume that the ecological requirements of the species present nowadays have not changed since the past period under consideration. The specific abundance of planktonic foraminifera samples from recent core tops may be expressed as a matrix (x species relative distributions within each of n sampling stations) from which the vectors corresponding to the main factors that describe the specific faunal (or floral) variance can be extracted. The method proposed by Imbrie and Kipp (1971) provides the best correlation between changes in these factors and the associated changes within the modern environmental parameters, systematically selected for the n stations (such as summer and winter temperatures, or other parameters, provided they are statistically independent). A similar factor analysis, when applied to fossil assemblages down sediment cores, allows the paleotemperature to be estimated using the ecological equations calculated from the modern core tops. This work led to the great success of the CLIMAP group (Climate Long-range Investigation, Mapping And Prediction), which reconstructed the first global map of summer and winter SST distribution during the Last Glacial Maximum (LGM) period, about 21 ka ago (Fig. 21.3).

One of the main problems with this paleo-reconstruction method is that it is based on the a priori stable statistical correlation between changes in the specific factors defined by the species distributions and the arbitrarily chosen environmental parameter, temperature, in this case. However, other environmental factors, such as the availability of food supply, may also be involved and change the sensitivity of foraminifera to temperature from one region to another.

There is also another potential problem with the transfer function approach: it will provide accurate estimates only if modern conditions are good analogs of the past hydrological conditions. This is not always necessarily the case. For example, the fossil fauna of the eastern Mediterranean Sea during the LGM period has no modern analogs. Indeed, this basin experienced hydrological and climate conditions very

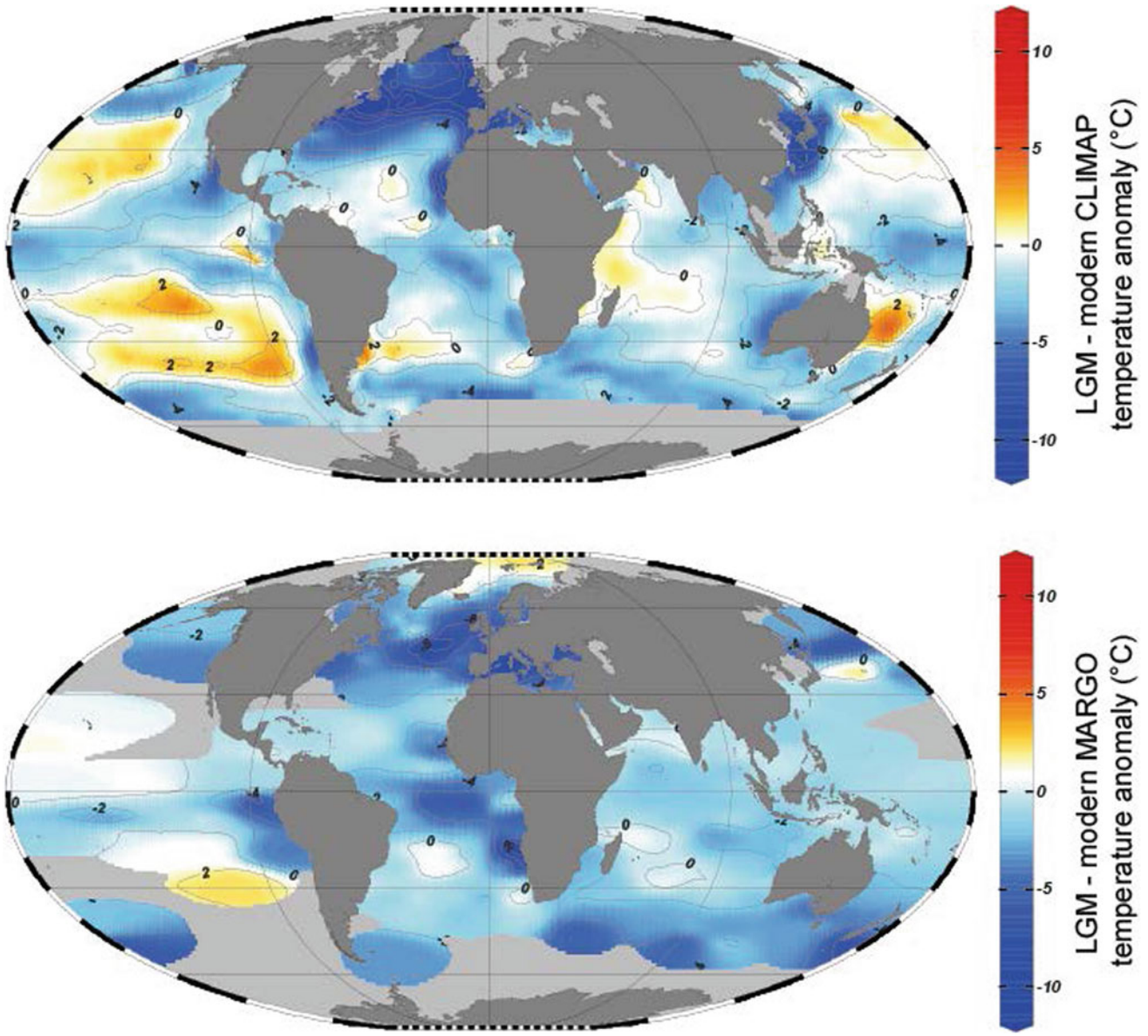

Fig. 21.3 Reconstructions of temperature anomalies (°C) between the Last Glacial Maximum (LGM) and modern surface waters as obtained by the CLIMAP (1981) (August temperatures, top figure) and MARGO (2009) programs (July–August–September temperatures, bottom figure). While the two reconstructions have many features in common, the cores studied under the MARGO program revealed the presence of larger longitudinal gradients in SST in all ocean basins than the estimates of CLIMAP (1981)

different from the modern ones, due to the development of large ice sheets over Northern Europe and to a very different hydrological cycle. In fact, the absence of direct analogs becomes the rule rather than the exception for the distant past: most fossil species from periods earlier than the Quaternary are not found in recently deposited sediments.

This is why the method used by Imbrie and Kipp (1971) was gradually replaced by the *best analogs* method. Its principle is simple: to compare the changes in fossil assemblages to modern references, without a preconceived idea of the origin of the observed changes. The closest analogs are defined using a mathematical distance calculation. The method is based on the assumption that the closer a fossil assemblage is to one or more modern references, the more similar their optimal growth conditions are (temperature and nutrient supply, in particular). The distance to the best analogs and the dispersion of associated environmental conditions provide an estimate of the reconstruction uncertainties (Waelbroeck et al. 1998).

In parallel with these statistical developments, recent advances in the field of artificial intelligence and neural networks have helped to improve paleoceanographic

reconstructions without fundamentally changing the principle. Still based on the comparison between fossil fauna and modern reference fauna, they do not require the establishment of specific mathematical relationships, but establish their own learning from available databases through minimization of the uncertainties (Malmgren et al. 2001).

These various methods, applied here to foraminifera, have also been used for diatom flora, coccoliths, dinoflagellate cysts and radiolarians. Diatoms, dominant in cold waters rich in silica, have been used in particular to reconstruct variations in sea ice cover in polar regions. The latest LGM SST global distribution, as reconstructed within the MARGO program, used several types of indicators and is presented in Fig. 21.3.

Statistical methods have many limitations: (i) they can only be used if the faunal assemblages are close to modern assemblages; (ii) the genetic diversity of species among different ocean regions may induce variations in their faunal responses to temperature and the corresponding statistical links; (iii) temperature reconstructions based on variations in the abundance of fossil fauna or flora assume that other factors, such as productivity for example, have no significant influence on the relative abundances of the different species; (iv) due to the activity of burrowing animals (bioturbation), marine sediments are usually mixed over several centimeters, so that the same stratigraphic level of a sediment core represents a mix of fauna that lived in different centuries (or even several thousand years apart if the sedimentation rate is low); (v) transfer function calibration is based on the assumption that sediment core top assemblages reflect modern hydrological conditions. This latest assumption ignores in particular ocean and climate changes which occurred over the last millennia, and that could have been significant enough to bias calibrations. These limitations have encouraged the development of new reconstruction methods based on either biological or geochemical mechanisms.

The biological approach is still in its infancy, and it is derived from ecological studies of the requirements of the different species in the modern ocean. A first approach directly calibrates the proxies (foraminifera or others) from controlled laboratory cultures with varying physiological and geochemical constraints that duplicate those observed in the marine environment. A more theoretical approach complements these calibrations by modeling the growth conditions within the natural environment, using the experimentally calibrated variables. Using such methods, it may be possible to obtain a reliable reconstruction of the hydrology corresponding to the specific habitat of the different species of planktonic foraminifera (e.g., Lombard et al. 2009).

Geochemical Methods

Organic Tracers

The organic geochemistry of marine sediments provides a different set of tracers. The most common so-called 'biomarker' is based on the changes in the abundance ratio of di- and tri-unsaturated alkenones (molecules with 37 carbon atoms containing two or three double bonds). This ratio is a function of the growth temperature of the synthesizing organisms, a group of algae called coccolithophorids, and in particular of the species *Emiliania huxleyi* for the modern ocean. The number of double bonds is inversely related to the temperature: the lower the temperature, the higher the number of double bonds (Prahl and Wakeham 1987). The abundance ratio of di- and tri-unsaturated alkenones is conventionally expressed by the index $U^{k'}_{37}$:

$$U^{k'}_{37} = [C_{37:2}]/[C_{37:2} + C_{37:3}]$$

The initial calibration of the $U^{k'}_{37}$ index is based on *E. huxleyi* cultures in controlled conditions (Prahl and Wakeham 1987) (Fig. 21.4), and has been subsequently verified using samples collected from ocean water or from the sediment surface (Müller et al. 1998; Conte et al. 2006; Tierney and Tingley 2018).

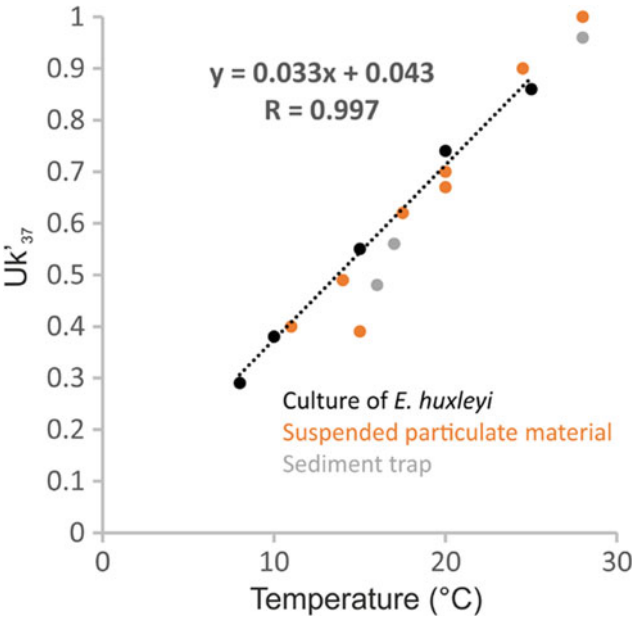

Fig. 21.4 Relationship between the unsaturation index $U^{k'}_{37}$ and SST. The line represents the temperature calibration curve based on cultures of *E. huxleyi* grown under laboratory conditions (Prahl and Wakeham 1987). Natural particulate samples collected are indicated (Prahl and Wakeham 1987)

However, like all paleoclimate indicators, the $U^{k'}_{37}$ index also presents various biases that limit its use in specific oceanographic contexts. A few of the most significant ones are as follows:

- The temporal evolution of the alkenone-producing species. *E. huxleyi*, which is currently the main producer of alkenones, was not present prior to MIS 8 (Thierstein et al. 1977). Alkenones are also produced by other species such as *Gephyrocapsa oceanica*, but with different temperature—$U^{k'}_{37}$ index relationships. Care must therefore be taken when applying the $U^{k'}_{37}$ method to ancient sediments.
- The tiny coccolithophorids are easily transported by sea currents, so these algae can travel long distances between their place of production and place of sedimentation. A significant portion of the residual input to sediments may thus originate from remote areas with very different hydrological conditions. This problem is particularly significant in areas of low productivity or in frontal zones that separate two distinctly different water masses (Sicre et al. 2005).
- Reconstructions could be biased toward a specific season (Rosell-Melé and Prahl 2013) and a degree of nonlinearity may exist in the relation between alkenones and SST at the higher and lower ends of the temperature range (Conte et al. 2006).

Another organic tracer to reconstruct past SST is based on the quantification of the average number of cyclopentane rings found in glycerol dialkyl glycerol tetraethers (GDGTs) of archaea membrane lipids. An index, called TEX_{86}, was deduced after analyzing the GDGTs distribution in marine surface sediments in comparison to annual mean SSTs (Schouten et al. 2002).

Recently, a number of different TEX_{86} calibrations have been developed (Kim et al. 2010; Tierney and Tingley 2014; Ho and Laepple 2016), in response to possible differences in membrane adaptation of the resident archaea communities at different temperatures, and to the differences found between the TEX_{86} ratio and other SST reconstruction proxies. A number of pre- and post-depositional processes can influence the TEX_{86} ratio. For some processes, this influence can be constrained. For example, the BIT index is used to track the amount of terrestrial GDGT input, using a ratio of branched versus isoprenoid GDGTs (Weijers et al. 2006; Schouten et al. 2013). Nonetheless, the scientific understanding of TEX_{86} remains imperfect, particularly since the effects of environmental factors such as salinity, nutrient concentrations, and water column structure may modulate the TEX_{86}–SST relationship (Tierney and Tingley 2014).

Chemical Tracers

The chemical composition of the carbonate from foraminiferal tests and coral skeletons may also provide paleotemperature or paleoenvironment indicators. For example, the concentration of magnesium incorporated in the calcium carbonate of foraminifera is an empirical function of the temperature at which that foraminifer crystallized its test. On time scales where the Mg/Ca of the oceans has remained constant, the sensitivity of Mg/Ca to temperature has been determined using either a culture-based, sediment trap or core top calibrations (see for example, Lea et al. 1999; Elderfield and Ganssen 2000; Anand et al. 2003; Mashiotta et al. 1999) (Fig. 21.5), and it takes the form:

$$\mathrm{Mg/Ca} = \mathrm{B}\exp(\mathrm{A} * \mathrm{T})$$

where A and B are the exponential and pre-exponential constants, respectively, and T is the temperature in °C.

Magnesium replaces calcium more easily at high than low temperatures, so the Mg/Ca ratio from carbonates increases with temperature at the time of calcite formation. Thermodynamic considerations suggested an exponential temperature dependence of Mg uptake into calcite (Rosenthal et al. 1997).

However, the growth temperature is not the only factor to be considered. Seawater salinity and alkalinity have also been shown to significantly alter the Mg/Ca ratio in

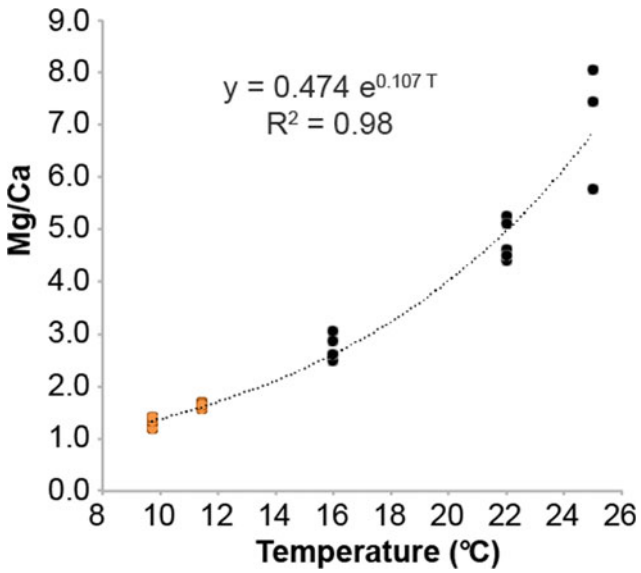

Fig. 21.5 Mg-temperature calibration results from culturing experiments with one species of planktonic foraminifera (*Globigerina bulloides*) (black dots) and core top samples (orange dots). Mg/Ca results are plotted versus calibration temperature (black dots) or World Ocean Atlas mean annual SST (orange dots) (modified from Mashiotta et al. 1999)

foraminiferal tests (Elderfield et al. 2006; Mathien-Blard and Bassinot 2009; Hönisch et al. 2013). Another issue is the observed offsets in both culture and field studies between Mg/Ca ratios among individual species, that indicate the need for single-species calibrations. In addition, the geographical extension of genotypes must be assessed when choosing to develop calibrations (Vázquez Riveiros et al. 2016). Recent studies try to simultaneously assess the relationship between foraminiferal Mg/Ca, and temperature, salinity, and the carbonate system using statistical approaches (Khider et al. 2015; Gray et al. 2018).

Mg/Ca in foraminifera has been cited here as a main example of a geochemical temperature tracer. Other ratios, such as Sr/Ca or Li/Mg in corals, are also used as tracers of temperature (Corrège 2006; Montagna et al. 2014).

Isotopic Tracers

As presented in this chapter's introduction, the first isotopic approach developed was the relationship between temperature, the isotopic composition of seawater and the isotopic composition of the biocarbonate that developed within that water. Traditionally, isotopic compositions are expressed using the notation δ, which is the relative difference (expressed in parts per thousand) between the isotope ratio R of the sample and that of a reference standard:

$$\delta = \left[\left(R_{\text{sample}}/R_{\text{st}}\right) - 1\right] \times 1000$$

The $\delta^{18}O$ of the water is denoted δ_w, that of a carbonate, δ_c, and the relationship between temperature T, δ_w and δ_c is known as the 'paleotemperature equation'. This relationship was experimentally determined by Urey's group in the 1950s and improved by Shackleton (1974) in the form below:

$$T = 16.9 - 4.38 \times (\delta_c - \delta_w) + 0.10 \times (\delta_c - \delta_w)^2 \quad (21.1)$$

In this empirical formula, δ_c represents the $\delta^{18}O$ of the CO_2 extracted from the carbonate through dissolution with phosphoric acid, and δ_w is the $\delta^{18}O$ of the CO_2 obtained by equilibration with the seawater to be analyzed. δ_c and δ_w are measured by mass spectrometry using the same CO_2 laboratory standard. Other $\delta^{18}O$—temperature relationships defined in the last decades (Bemis et al. 1998; Mulitza et al. 2003; Marchitto et al. 2014) use the same terminology.

Box 1. Practical Application of the Paleotemperature Formula

Nowadays, isotopic geochemistry laboratories have adopted the convention of expressing the δ_c isotopic compositions against the PDB (Pee-Dee Belemnite) international standard and δ_w against the SMOW (Standard Mean Ocean Water) international standard. These standards are distributed by international agencies for laboratory calibration. To properly apply the paleotemperature formula, which presumes that all isotopic compositions are expressed relative to the same standard, it is necessary to compare the isotopic ratio of the CO_2 extracted from the PDB standard by controlled phosphoric acid attack with the isotopic ratio of the CO_2 isotopically equilibrated with the SMOW standard. The latter is lower in ^{18}O content by 0.27‰ than the CO_2 extracted from PDB, so that for every water sample:

$$\delta_w(\text{vs.PDB} - CO_2) = \delta_w(\text{vs.SMOW} - CO_2) - 0.27. \quad (21.2)$$

If, as in the paleotemperature formula, PDB is used as the standard for carbonates and SMOW as the standard for waters, then Shackleton's equation becomes:

$$T = 16.9 - 4.38 \times (\delta_c - \delta_w + 0.27) + 0.10 \times (\delta_c - \delta_w + 0.27)^2.$$

One major disadvantage of the paleotemperature formula is that temperatures can only be determined if the isotopic composition of the water is known, which is almost never the case for geological samples.

A more recent isotopic method, still under development, is expected to overcome this constraint (Ghosh et al. 2006; Schauble et al. 2006). The crystal lattice of a carbonate consists of CO_3^{2-} groups and of cations (Ca^{2+}, for example). Among the CO_3^{2-} ions in a sample, the heavy isotopes ^{13}C and ^{18}O do not spread out randomly. Their relative abundance will depend on the isotopic equilibrium reaction:

$$^{13}C^{16}O_3^{(2-)} + {}^{12}C^{18}O^{16}O_2^{(2-)} \Leftrightarrow {}^{13}C^{18}O^{16}O_2^{(2-)} + {}^{12}C^{16}O_3^{(2-)}$$

so that the distribution of these four isotopic species depends on their own binding energy, itself a function of temperature.

The abundance of the various isotopic species is assessed by dissolving the carbonate with phosphoric acid and measuring the abundance of $^{13}C^{18}O^{16}O$ molecules (with a mass of 47) in the extracted CO_2, and comparing this to the abundances of other isotopic species with masses 45 and 46. The 'stochastic' state is taken as a reference and is defined by a random distribution of the isotopes of C and O within the molecules.

The thermodynamic variable, denoted as $\Delta 47$, which describes the state of the carbon dioxide and from which we deduce a paleotemperature, is defined by the relationship:

$$\Delta 47 = [(\mathrm{R47/R47*} - 1) - (\mathrm{R46/R46*} - 1) - (\mathrm{R45/R45*} - 1)] \times 1000$$

where *R*45, *R*46 and *R*47 are the abundance ratios of masses 45/44, 46/44 and 47/44, respectively, in the CO_2, and where *R* 45*, *R* 46* and *R* 47* denote these ratios for a gas with the same overall composition but in 'stochastic' state (Ghosh et al. 2006).

The main advantage of this method (called the Δ47 method) is that the thermodynamic-measured value reflects an internal balance of the crystal lattice and requires no knowledge of the composition of the original water. This method is based on properties obeying thermodynamical principles, so it can be applied to a variety of environments without changes (Fig. 21.6).

However, as it is the case for the paleotemperature formula, the calibration performed by Ghosh et al. (2006) only applies to carbonates precipitated at thermodynamic equilibrium. Therefore, testing for the possible existence of effects of parasitic isotopic fractionation of kinetic, biological or diagenetic origin should be carried out (Eiler et al. 2014; Saenger et al. 2012).

The temperature sensitivity of the Δ47 proxy is low (~0.003‰/°C) (Kele et al. 2015). It requires high measurement precision, which is commonly achieved by increasing counting times and/or the number of replicates analyzed per sample, a challenge for foraminifer-based reconstructions that use low carbonate samples. Recent studies have focused on the development of precise standardized calibrations that are applicable to paleoceanographic studies (Peral et al. 2018).

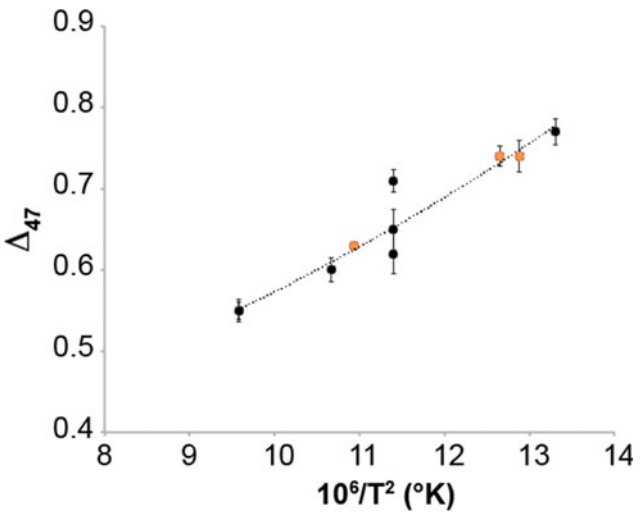

Fig. 21.6 Δ_{47} of CO_2 extracted from calcites grown from aqueous solution and of deep-sea corals (in orange) and surface corals (in black), plotted against $10^6/T^2$, where T is the known growth temperature in Kelvin (modified from Ghosh et al. 2006)

Sea Surface Salinity

While the temperature of seawater varies over a range of more than 30 °C in the open ocean, salinity changes much less (between 33 and 38 g of salt per liter (psu)). Salinity is highest in tropical areas, where evaporation exceeds precipitation (Fig. 21.7), and it decreases where precipitation dominates, in the equatorial belt and at high latitudes. As the hydrological cycle is greatly affected by the glaciations, significant variations in the salinity of the ocean during the Quaternary are to be expected.

Temperature and salinity jointly determine the density of seawater, the driver of deep ocean circulation. Dense waters sink at high latitudes and are progressively redistributed by deep currents through the various basins of the world's oceans. The reconstruction of the distribution of surface water salinity in the past would thus contribute to the understanding of why and how ocean circulation changed when climate conditions were different from today. It will also provide modelers with quantitative estimates to use as a forcing of numerical climate models.

Estimating the surface water salinity distribution of past oceans is difficult, partly due to the close correlation of temperature and salinity. Because of this correlation, changes in plankton distribution and transfer functions do not differentiate between changes in SST and changes in salinity. Moreover, the dominant signal recorded by most indicators is often temperature.

Nonetheless, reconstructions of past sea surface salinity (SSS) using transfer functions of dinoflagellate or diatom assemblages have been proposed in specific marine environments (DeSève 1999; De Vernal et al. 2001) with an accuracy of ±1.8 psu for the present day (De Vernal et al. 2001). However, these methods are difficult to extrapolate unambiguously to a global scale due to non-analogue situations in the past.

The most common method presently used to reconstruct past SSS is the calibration of salinity against stable oxygen isotope ratios measured on foraminifera (Duplessy et al. 1991; Malaizé and Caley 2009). Geochemical methods based on the analysis of trace metals have recently been developed; we will briefly discuss these two approaches in the sections that follow.

Isotopic Methods

Paleosalinities from Stable Oxygen Isotopes ($\delta^{18}O$)

In the open ocean, the isotopic composition of seawater is closely correlated to salinity (Figs. 21.7 and 21.8): the vapor pressure of $H_2^{18}O$ being lower than that of $H_2^{16}O$, isotopic ratio of vapor in the atmosphere is systematically lower than

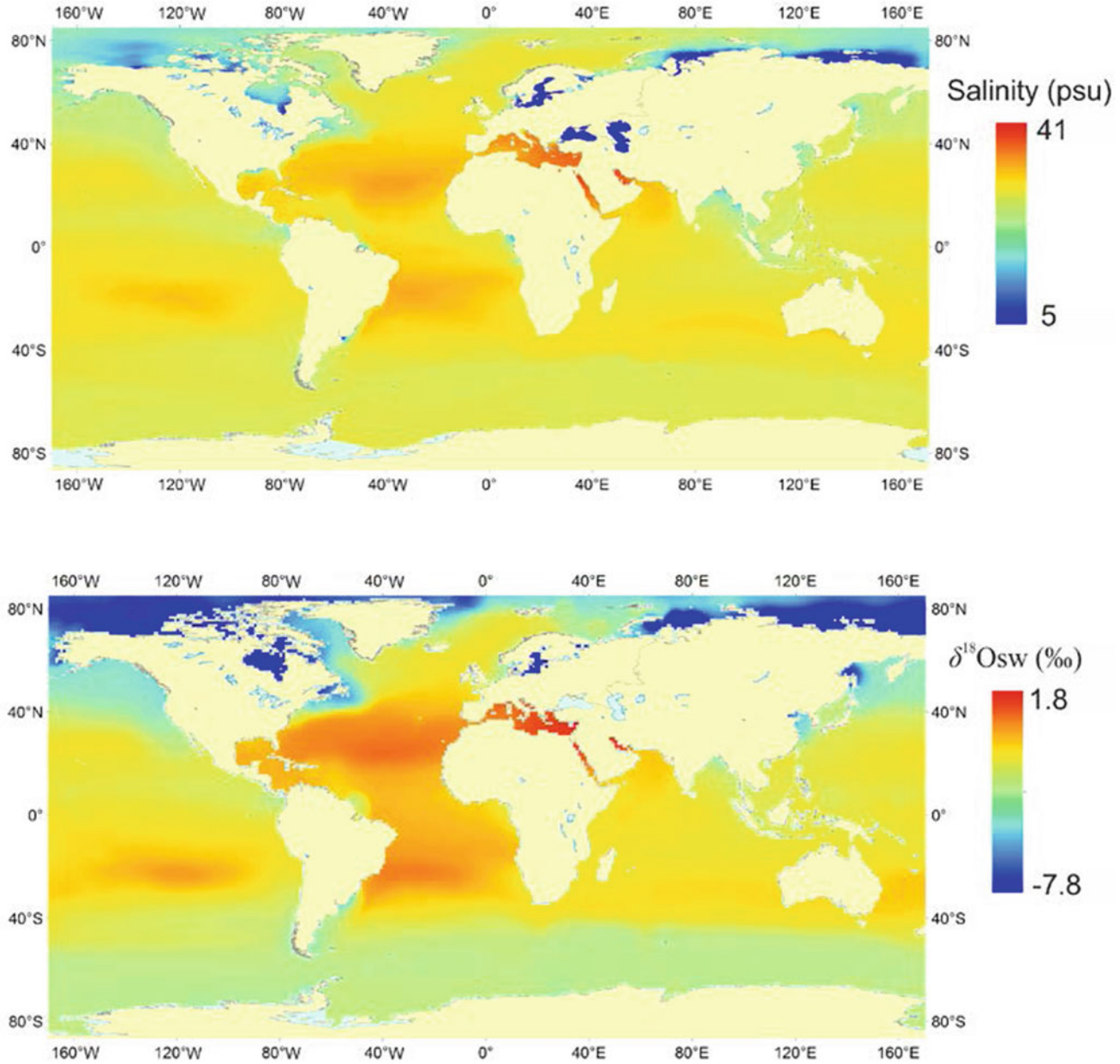

Fig. 21.7 Surface salinity of the modern oceans (WOA 2013: Zweng et al. 2013) and gridded data set of surface $\delta^{18}O$ of seawater (δ_w) (Legrande and Schmidt 2006)

in the condensed phase (ocean and rain). The more evaporation exceeds precipitation, the higher the surface water isotopic ratio. At local to regional scale, there is a linear relationship between salinity and δ_w (Fig. 21.8). This is the relationship which allows the estimation of past seawater salinities.

The major uncertainty in the 'paleotemperature formula' now becomes an advantage. δ_w can be determined when δ_c is measured if the foraminiferal habitat temperature T is estimated independently (by Mg/Ca ratios analysis of the same shells for example).

In the past, δ_w has been seen to vary globally. When the ice caps grew on land, they trapped snow poor in ^{18}O, and so the δ_w of the ocean increased. Thus, we observe a simultaneous drop in sea level and an increase in δ_w. Conversely, when the ice caps melt, sea level rises and δ_w decreases. The most recent studies (see Chap. 24) estimate that sea level dropped by about 120 m during the LGM, and that the average isotopic composition of the ocean was then at +1.0‰ SMOW (while the current value is 0‰ SMOW by definition). Various approaches aim to reconstruct changes in sea level linked with changes in continental ice volume.

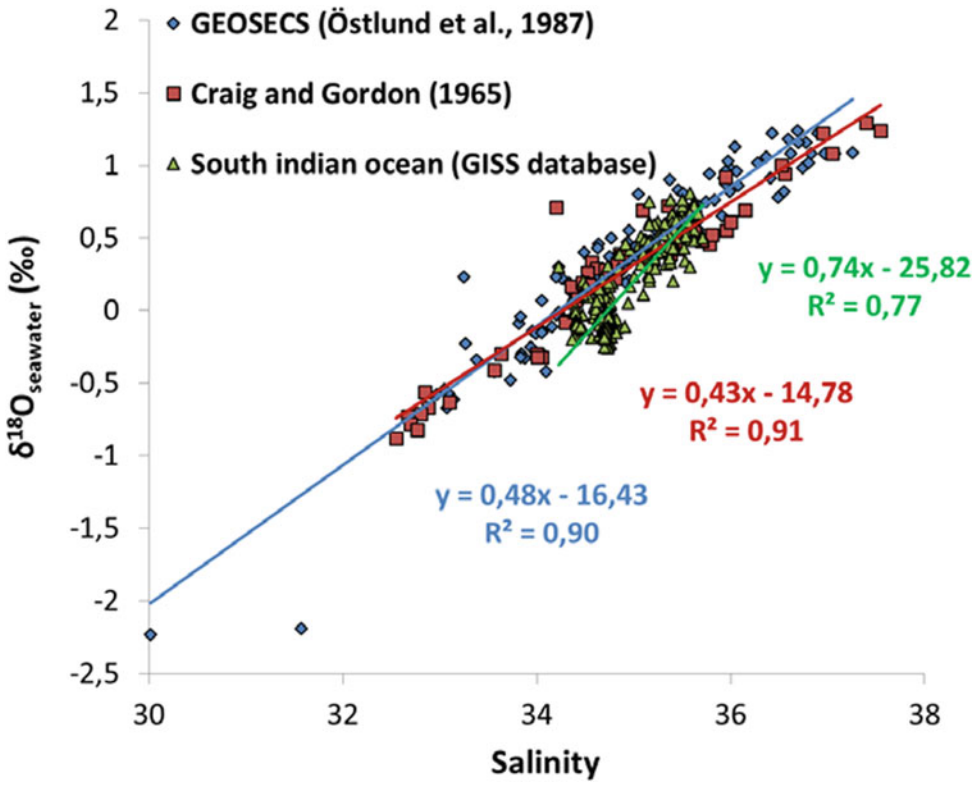

Fig. 21.8 The relationship between surface δ_w and salinity for the global ocean as measured within the international GEOSECS program (Ostlund 1987), by Craig and Gordon (1965), and for the South Indian Ocean with the GISS database (Schmidt et al. 1999)

It is then feasible to estimate the change in mean ocean δ_w related to variations in continental ice volume and sea level.

Locally, changes in the hydrological cycle (evaporation, precipitation, water mass movements, melting events) can cause additional variations in δ_w, of both climatic and hydrological origin.

Reconstructing the evolution of the isotopic composition of seawater in the past is in itself an interesting task because δ_w tracks changes in the hydrologic cycle. However, we can try to qualitatively interpret a record of paleo δ_w in terms of paleosalinities (see Box 2).

Box 2. Practical Calculation of Paleosalinities

Estimating paleosalinity changes along a sediment core requires the following steps:

- Measure δ_c and T at each level so as to derive a recording of paleo δ_w over the time period covered by the core, using the paleotemperature equation (Eq. 21.1).
- Estimate global δ_w changes $\left(\delta_w^{ice}\right)$ related to continental ice volume variations over the study period using known records of changes in sea level. A drop of 120 m in sea level is accompanied by an increase in δ_w^{ice} of +1.0‰. Given an average depth of the modern ocean of ~3900 m and an average salinity of 34.7 psu, and since the amount of salt in the ocean remains constant, a drop in sea level of 120 m is also accompanied by an increase in salinity. The average ocean salinity becomes:

$$(34.7 \times 3900)/3780 = 35.8\,\text{psu}.$$

  Salinity has thus increased by about 1.1 psu and δ_w^{ice} by +1.0‰. Coupled models of the Northern Hemisphere ice sheets allow the ice-sheet contribution to the variability in oxygen isotope composition and sea level changes to be determined (Bintanja et al. 2005).
- Estimate the variation in local isotopic composition δ_w^{local} due to hydrological changes by subtracting δ_w^{ice} changes from the δ_w value reconstructed for each core level. The corresponding change in salinity can be estimated from current observations (Fig. 21.7).

The statistical error associated with this approach is high and rarely permits meaningful quantitative salinity reconstructions because of the associated large uncertainties (Rohling and Bigg 1998; Schmidt 1999; Rohling 2000; Legrande and Schmidt 2011; Caley and Roche 2015). The structural/analytical error is in the

range of 0.8–1.8 psu (Schmidt 1999). In addition, the spatial and temporal evolution of the slope of the δ_w-salinity relationship, tested in isotope-enabled numerical climate models, can lead to very large errors (Legrande and Schmidt 2011), up to 25 psu in certain regions for the LGM (Caley and Roche 2015).

To reduce these very large errors on past SSS reconstructions, model-derived temporal slopes of the δ_w-salinity relationship can be used directly in the calculation. This approach has been tested with success for the LGM on a marine sediment record located in Gulf of Guinea and influenced by West African monsoon hydrology (Caley and Roche 2015). However, allowing model-derived regional δ_w-salinity relationships to vary through time can lead to significant uncertainties related to the shortcomings of the models, so complementary approaches should also be developed.

Paleosalinities from Stable Hydrogen Isotopes (δ^2H)

Another method uses hydrogen isotope changes to reconstruct paleosalinities. Culture experiments have found a constant offset between the hydrogen isotopic composition of water and the hydrogen isotopic composition of alkenones synthesized in that water (Paul 2002; Englebrecht and Sachs 2005). Schouten et al. (2006) demonstrated that this offset was dependent on salinity via biological fractionation processes. Reconstructing salinity by using the biological fractionation factor that is linked to it requires information on the past hydrogen isotope ratio of seawater (δ^2H_w).

Isotope-enabled climate model results indicate a rather stable dependence between δ^2H and surface δ_w in the past (Caley and Roche 2015). As δ_w can be reconstructed (see Sect. "Chemical Methods") this suggest that δ^2H_w can also be obtained. An estimation of paleosalinities based on δ^2H measurements in alkenones might therefore be possible if the slope and the intercept of the regression between the biological fractionation factor and salinity can be sufficiently constrained. The impact of species composition and growth phase on the use of alkenone δ^2H to reconstruct paleosalinity currently requires further investigations (Wolhowe et al. 2009; Chivall et al. 2014; M'Boule et al. 2014).

Pairing information from water isotopes, $\delta^{18}O$ and δ^2H (isotopologues), could yield better estimates for paleosalinity (Rohling 2007; Leduc et al. 2013). Numerical modeling experiments for the Holocene and the LGM periods have demonstrated that this combination of water isotopologues may indeed allow for a better estimation of paleosalinity variability (Legrande and Schmidt 2011; Caley and Roche 2015). Nonetheless, ecological biases introduced by combining proxies based on two different organisms (foraminifera are zooplankton and coccoliths are phytoplankton) could emerge, together with differences in dissolution and bioturbation in a sediment core.

Chemical Methods

Calibrations established using the modern Ba/Ca-salinity relationship (Carroll et al. 1993; Weldeab et al. 2007) (Fig. 21.9) have suggested that the Ba/Ca ratio of foraminiferal $CaCO_3$ can be used as a proxy for river runoff. This approach is limited to coastal regions affected by river runoff (i.e. prone to relatively large salinity changes) and assumes that (1) the Ba/Ca ratio in planktonic foraminifera shells is dominated by the Ba/Ca concentration of seawater (Hönisch et al. 2011) and not by other factors and (2) that the present-day calibration is applicable to the past.

Another recent study has established the potential of the Na/Ca ratio of foraminiferal calcite as a quantitative proxy for past salinities. In culture experiments, Wit et al. (2013) studied sodium incorporation in the benthic foraminifera *Ammonia tepida* at a range of salinities and suggested that foraminiferal Na/Ca could serve as a robust and independent proxy for salinity. More recently, the field study of Mezger et al. (2016) on planktonic foraminifera also suggested that salinity controls foraminiferal Na/Ca. Incorporation of Na in foraminiferal calcite could therefore constitute a potential proxy for salinity, although species-specific calibrations are still required and more research on the effect of temperature is needed.

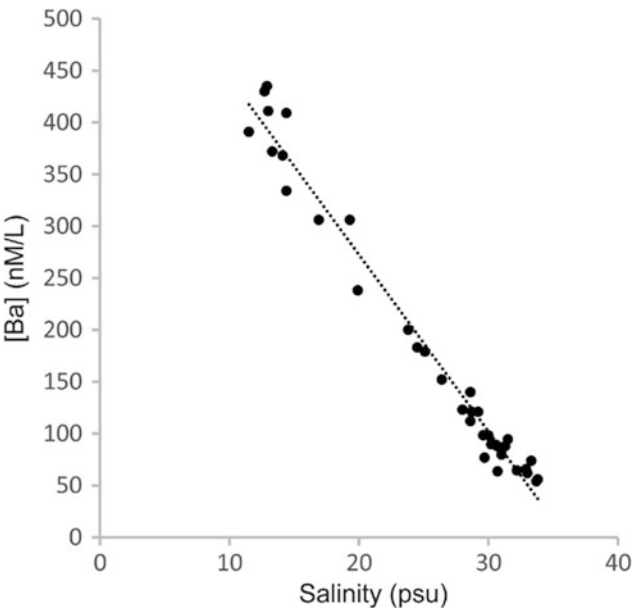

Fig. 21.9 Relationship between Ba in seawater and salinity in the Bay of Bengal (Carroll et al. 1993)

Reconstruction of the Hydrology of the Deep Ocean

Main Features of Modern Circulation

On a rotating planet like the Earth, surface ocean circulation is governed by the winds and the position of the continents that define the shape of the ocean basins. Deep circulation, on the other hand, is governed by the small variations in the density of the water masses. Since density depends on temperature and salinity, the term 'thermohaline circulation' is used. Reconstructing past changes in temperature, salinity and density in the intermediate and deep ocean is thus needed to understand the temporal variations of the circulation and distribution of water masses; it also provides a benchmark for simulations provided by general circulation models.

As we saw in Chap. 1, deep waters are currently formed in winter in highly localized areas of the high latitudes: the Norwegian Sea and the Labrador Sea in the northern hemisphere and the Weddell Sea and the Ross Sea near Antarctica. During winter, surface waters here become denser as they cool down but also because the formation of sea ice is accompanied by a release of salt. When surface waters become as dense as deep waters, large-scale convection movements are initiated and the waters sink into the abyssal depths. Once at depth, very small changes in density of the various deepwater masses govern their circulation through the different basins. Surface waters sinking in the Norwegian Sea cross the sills separating it from the Atlantic Ocean to form North Atlantic Deep Water (often referred to by the acronym NADW). This water mass then follows the American coast to join the Southern Ocean and is caught up in the Antarctic divergence, a large upwelling zone, where it mixes with the surface waters of southern high latitudes. Here, these very cold surface waters increase their density through winter sea ice formation, and sink along the Antarctic continental shelf forming the densest waters in the world. This water mass is called Antarctic Bottom Water (or AABW), and it lines the bottom of all ocean basins. At present, abyssal waters are not formed from the surface waters of the Indian and Pacific Oceans. The Antarctic waters that rush into these basins create the Pacific and Indian Deep Waters (PDW and IDW, respectively) by mixing with the waters of the main thermocline, and then return to the Southern Ocean at around 3 km depth. We can devise a simplified view of the global ocean circulation, where the Norwegian Sea is the main source of deep waters, and the Southern Ocean acts as a recirculation pump returning to the depths the surface waters surrounding Antarctica that have received upwelled NADW via the Antarctic divergence. This circulation pattern is critically dependent on the climate of the high latitudes of the Northern Hemisphere (North Atlantic Ocean, Norwegian and Labrador Seas) and of the Southern Ocean in the Southern Hemisphere.

Reconstructing the Temperature and Salinity of Deep Waters

The past evolution of the deep ocean has been the subject of extensive research. However, the reconstruction of the basic properties of bottom waters has been hindered by the lack of transfer functions linking the abundance of benthic species to the temperature of seawater in the vicinity of the sediment. In many environments, these abundances are essentially governed by the availability of food and by the proportion of dissolved oxygen. However, paleoceanographers have attempted to apply other approaches to the reconstruction of bottom water temperature.

Searching for a Reference Zone with Constant Temperature

As early as 1967, Shackleton (1967) suggested that the $\delta^{18}O$ of benthic foraminifera must closely resemble the $\delta^{18}O$ of deep waters, because these waters are formed close to freezing conditions and their temperature cannot drop much further during a glacial period. Labeyrie et al. (1987) further elaborated on this concept by analyzing the $\delta^{18}O$ of benthic foraminifera from a core in the Norwegian Sea where temperature, well below 0 °C in the deep basins, is constrained by exchanges with the ice. By comparing the isotopic record from this core with others from the Pacific and Indian Oceans, the authors were able to demonstrate, contrary to the assumptions of Shackleton, that deep water temperature in the major ocean basins did change significantly at the beginning of the last glaciation, with a cooling in all deep oceans to a temperature close to the freezing point (~ -1 °C) during the LGM. This result has been confirmed since by other tracers such as the Mg/Ca ratio of benthic foraminifera (see Sect. "Estimating the Temperature Independently of the Paleotemperature Formula"). Unfortunately, the isotopic benthic record of the Norwegian Sea is far from continuous and this method could not be successfully applied to reconstruct the evolution of the abyssal water temperature over the whole of the Quaternary.

It should be emphasized, however, that very low deep-water temperatures during glacial periods are to be expected. Indeed, under current conditions, NADW is formed from very cold water (close to the freezing point) that overflows from the Norwegian Sea through the sills located between Scotland, the Faroe Islands, Iceland and Greenland. However, the water that crosses these shallow

sills (with a depth of less than one kilometer) mixes with the much warmer waters of the North Atlantic, so that the newly formed NADW is characterized by a temperature of +3 °C and a salinity of 34.95 psu. Its density remains high, close to but slightly less than that of AABW (temperature of −1 to 0 °C, salinity of 34.6 psu). It is therefore AABW that lines the great ocean depths, and, in the Atlantic Ocean, is topped by NADW. During the last glaciation, the sinking of very cold water directly into the North Atlantic (and not into the Norwegian Sea anymore) explains why the deep waters of the world are all found to be at temperatures close to the freezing point.

Estimating the Temperature Independently of the Paleotemperature Formula

The simplest way to determine the temperature of the water close to the sediment is to use the concentration of trace metals (Mg/Ca) contained in the carbonate shells of benthic foraminifera. This independent estimate of bottom water temperature allows the calculation of the δ_w of deep water using the paleotemperature formula.

However, the temperature dependence of Mg incorporation in benthic foraminiferal tests is species-specific, and may depend on different hydrological factors such as salinity or carbonate ion saturation (Elderfield et al. 2006). In addition, the expected bottom water temperature variations during glacial-interglacial cycles are small compared to surface temperature changes, implying relatively small Mg/Ca variations. The recently discovered Δ47 method is only starting to be applied to this problem (Peral et al. 2018), although more precise measurements in benthic foraminifera are needed to confirm the utility of this technique.

Searching for the Geochemical Signature of Ancient Waters in Pore Waters

Adkins et al. (2002) found that in long cores extracted by drilling ships, pore water trapped within the sediments shows measurable differences in salinity and in δ_w. These differences increase initially with core depth, then reach a maximum after which they decrease slowly. They interpreted this maximum as the signature of highly saline water from the LGM that had diffused into the sedimentary column. Using a simple diffusion model, the authors estimated the values for the salinity and the δ_w of the bottom waters 20 ka ago. Using this estimate of the δ_w of bottom waters, and combining it with $\delta^{18}O$ measurements on the calcite of benthic foraminifera, the paleotemperature formula confirmed that the deep waters of the glacial ocean were actually at a temperature near freezing point and hypersaline. The sediment cores that have been measured for δ_w are too few to give a complete picture of the ocean during the last glaciation. However, they show a significant disparity in the salinities from one basin to another, with the Southern Ocean being the saltiest, in contrast with the modern situation.

Reconstructing Changes in Water Mass Distribution

Lynch-Stieglitz et al. (1999) and (2014) showed that an approximate direct relationship could be established between the $\delta^{18}O$ of benthic foraminifera and the density of seawater, within the temperature range where the temperature-salinity-density relationship is roughly linear (T greater than 2 °C). In this way, the authors were able to study the geostrophic deformations of the deep thermocline in the Straits of Florida and propose estimates of the changes in the meridian flow linked to the Atlantic thermohaline circulation between the LGM and the present.

Reconstructions using benthic foraminiferal $\delta^{18}O$ have also shown marked changes in the distribution of deep and intermediate water masses during the LGM compared to the present day. In the Atlantic Ocean, the temperature gradient currently observed at the base of NADW at around 3000 m was to be found at around 2000 m, and was much more pronounced than the one that currently separates NADW and AABW (Labeyrie et al. 1992). In the Indian Ocean, a strong gradient separated two water masses with distinctly different characteristics at a depth of around 2000 m (Kallel et al. 1988). More recent research even suggests the presence of a third deep water mass in the deepest North Atlantic at the LGM, formed by brine rejection and not by heat loss to the atmosphere (Keigwin and Swift 2017).

Reconstructing the Circulation of Deep Waters

Searching for Lines of Current from the $\delta^{13}C$ of Benthic Foraminifera

An original approach, independent of temperature and salinity, tries to characterize the main features of deep water circulation without trying to a priori understand the underlying physical mechanisms governing it. It is based on the carbon cycle and its tracer, the $^{13}C/^{12}C$ ratio usually denoted as $\delta^{13}C$. At the ocean surface, waters easily exchange their gas content with the atmosphere; they contain carbon dioxide and are rich in dissolved oxygen. During photosynthesis, phytoplankton preferentially absorbs $^{12}CO_2$ over $^{13}CO_2$. The organic material thus produced has a $\delta^{13}C$ close to −20‰, while the $\delta^{13}C$ of dissolved CO_2 in surface waters varies between +1 and +2‰. This surface organic matter forms the base of the ocean's food chain, and eventually falls to the depths carried in fecal pellets of zooplankton and higher animals. In the water column, settling organic matter undergoes a slow remineralization, which consumes any dissolved oxygen that may remain and produces CO_2

depleted in ^{13}C. Consumption of dissolved oxygen and production of CO_2, accompanied by a decrease in $\delta^{13}C$, take place in the deep waters (Fig. 21.10). The $\delta^{13}C$ of dissolved CO_2 in deep waters is thus lower than that of the surface waters.

The remineralization of organic matter is a slow process. This is why deep waters are characterized by a high $\delta^{13}C$ in regions close to their formation area (this is the case for the North Atlantic Ocean). Gradually, as they move away and circulate at depth, without the opportunity to exchange with the atmosphere, they become increasingly deprived of dissolved oxygen, while their $\delta^{13}C$ decreases through the mechanism described above. To give an order of magnitude, we can consider that the $\delta^{13}C$ of deep water decreases by about 1‰ per thousand years.

It is therefore the waters of the deep basins of the Pacific and Indian Oceans, at the end of the circulation scheme described in Sect. "Main Features of Modern Circulation", which have the lowest $\delta^{13}C$. The evolution of $\delta^{13}C$ in the deep ocean can thus be used as a tracer to characterize the lines of current and the exchanges between the various deep water masses. Epibenthic foraminifera, such as the species *Cibicides wuellerstorfi*, reflect this evolution of the water in which they grew, and variations in their $\delta^{13}C$ in cores extracted from different ocean basins are used to reconstruct changes in ocean circulation through time (Duplessy et al. 1984; Schmittner et al. 2017). For example, this proxy has been used to reconstruct ocean circulation during the LGM, when well ventilated (with a high $\delta^{13}C$) waters of the Atlantic Ocean formed Glacial North Atlantic Intermediate Waters (GNAIW), at a shallower depth than today's NADW, while deep waters (AABW) were even more poorly ventilated than today (Fig. 21.11). The understanding of this variability in the thermohaline circulation, which is a major regulatory mechanism of climate, is the subject of substantial research, both analytical and in modeling.

Using Trace Elements Measured in Benthic Foraminifera

In the modern ocean, geochemists have showed that cadmium (Cd) is included in organic matter, so that its cycle follows that of phosphate. The concentration of dissolved Cd in ocean waters shows therefore very similar variations to that of dissolved phosphate, a nutrient with a well-known cycle. It is assimilated by phytoplankton to ensure growth, so, as for all organic matter formed by photosynthesis, it falls into the water column with organic debris and is gradually released in the deep waters as bacteria oxidize it. Consequently, in the deep waters of the ocean, the consumption of dissolved oxygen and production of carbon dioxide (depleted in ^{13}C as we have seen) occur in parallel with increases in phosphate and cadmium.

The Cd ion has a charge and an ionic radius similar to that of Ca. It is therefore easily incorporated in trace amounts into the carbonate shells of benthic foraminifera, so that their Cd/Ca ratio reflects the concentration of Cd in the seawater

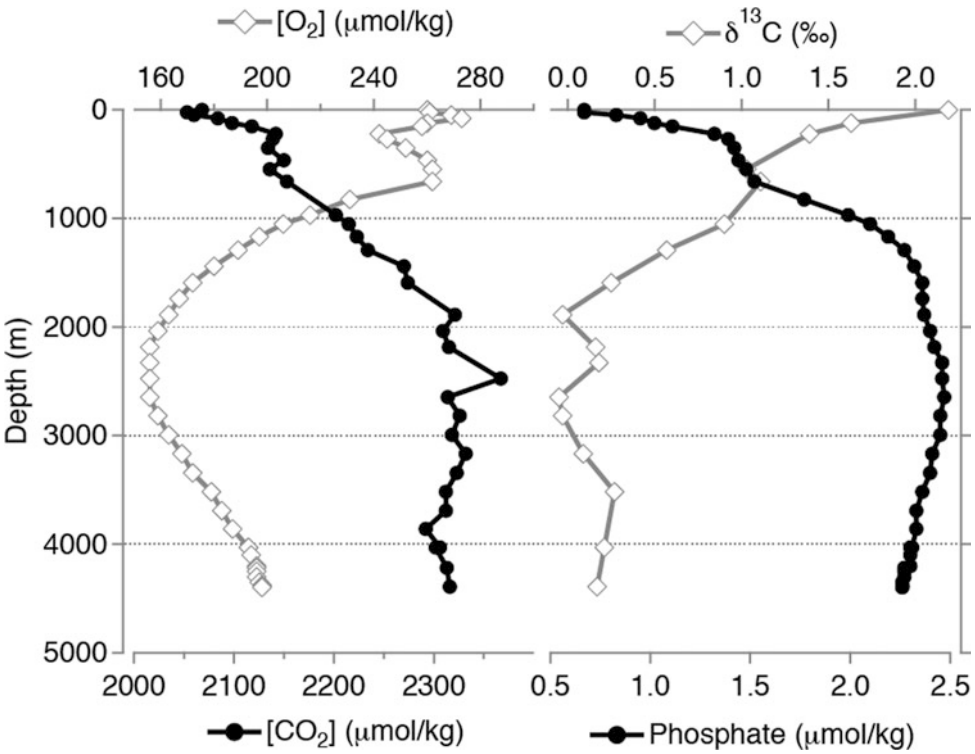

Fig. 21.10 Variations in the concentration of dissolved oxygen, the concentration of total dissolved CO_2, the $^{13}C/^{12}C$ ratio of the total dissolved CO_2 and phosphate with respect to depth at GEOSECS station 322 in the Pacific Ocean (43.0 °S/129.9 °W). The oxygen minimum at depth indicates consumption by marine bacteria. The resulting CO_2 production is characterized by a maximum of dissolved inorganic carbon concentrations and by a minimum of $\delta^{13}C$ (since carbon in organic matter is depleted by about 20‰ relative to dissolved inorganic carbon)

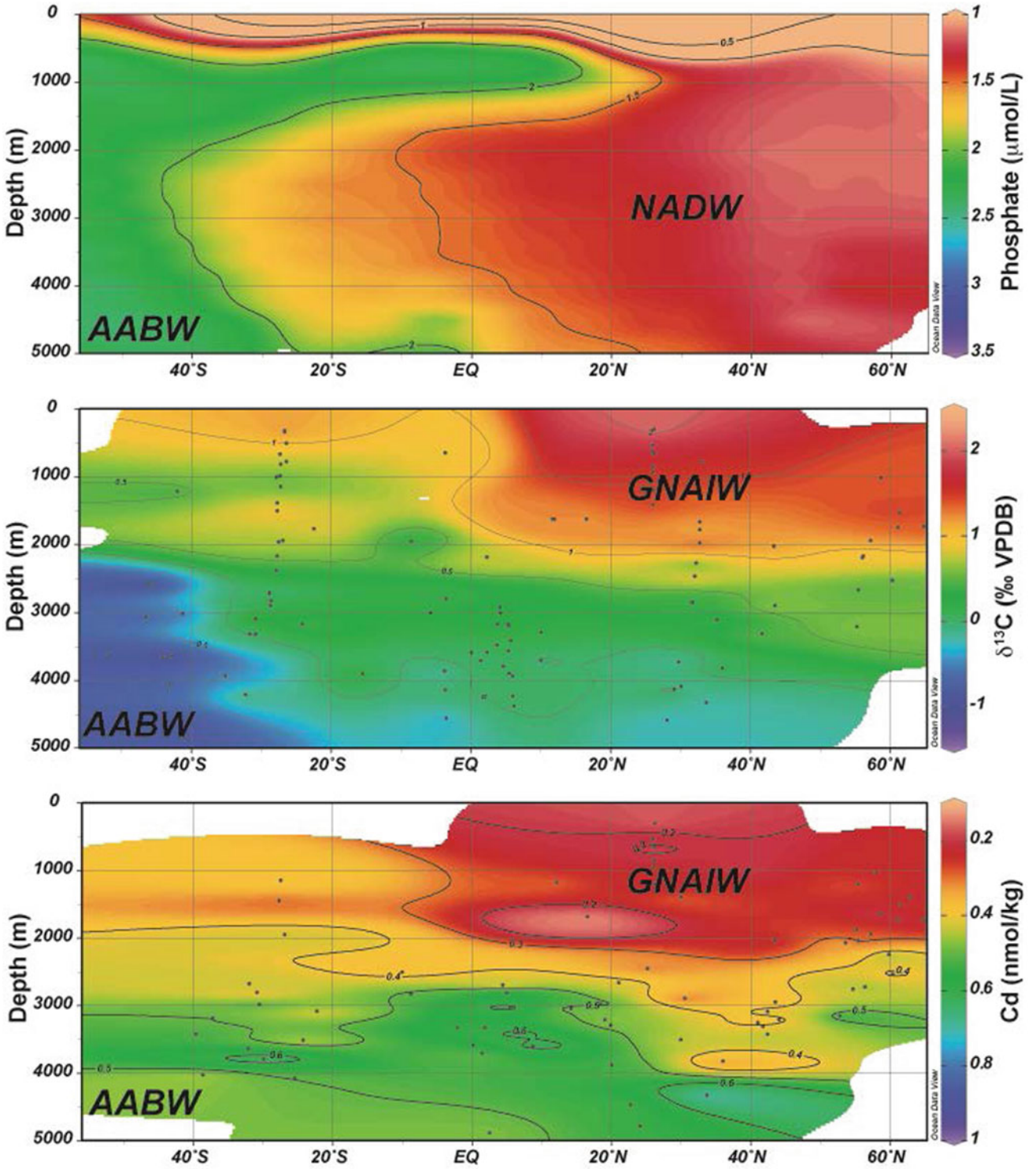

Fig. 21.11 (Top) Modern distribution of dissolved phosphate (µmol/liter) in the western Atlantic; (middle) reconstructed benthic $\delta^{13}C$ in the western and central Atlantic during the LGM; (bottom) estimates of the Cd concentration (nmol/kg) during the LGM based on the ratio of Cd/Ca in the shells of benthic foraminifera (figure modified from Lynch-Stieglitz et al. 2007)

in which the foraminifera developed. The Cd/Ca ratio is therefore a tracer for nutrient concentration of the water masses, present and past (Marchitto and Broecker 2006; Fig. 21.11).

Cd and ^{13}C have similar geochemical behaviors, with the essential difference that surface waters can exchange their dissolved carbon dioxide with the atmosphere, while Cd is not involved in ocean-atmosphere exchanges. In general, there is an excellent anti-correlation between the variations in the Cd/Ca ratio and the $^{13}C/^{12}C$ of benthic foraminifera measured in sediment cores. One notable exception is the Southern Ocean, where the benthic foraminifera that lived during the last ice age have very negative $\delta^{13}C$, while their concentrations in Cd are very similar to those of recent sediments from the Holocene. Despite inter-specific differences that may have affected $\delta^{13}C$ reconstructions based on benthic foraminifera (Gottschalk et al. 2016), or diagenetic and metabolic effects influencing the incorporation of trace metals into biogenic calcite (Marchitto and Broecker 2006; McCorkle et al. 1995), this discrepancy between the two indicators remains still to be explained.

Reconstructing the Dynamics of Water Masses

The tracers we have described so far allow the reconstruction of specific physical or chemical characteristics of water masses, but they do not convey information on their dynamics. In this section, we do not discuss in detail tracers related to particle transport at the ocean floor (particle size distribution, magnetic grain size, sortable silt). However, we will discuss two unstable radioactive tracers in the ocean: the concentration in ^{14}C of benthic foraminifera and the excess $^{231}Pa/^{230}Th$ ratio in sediments.

When surface waters exchange carbon dioxide with the atmosphere, they absorb ^{14}C. Currently, the ^{14}C concentration in the surface ocean is 95% of that of the atmosphere. When surface waters sink, they bring with them the dissolved carbon dioxide as well as the ^{14}C they contain. Once they reach the bottom of the ocean, these waters are isolated from the atmosphere, and ^{14}C decreases due to its own radioactive decay, with its period of 5720 years. The oldest waters in the northern Pacific and Indian Oceans have an apparent age of around 800 years (see Chap. 4). The planktonic foraminifera (that live in surface waters) and the benthic foraminifera (that live on the ocean floor) incorporate the ^{14}C of the waters around them into their shells. By comparing, at the same level of sediment, the ^{14}C ages of planktonic and benthic foraminifera, we can estimate the apparent age of the deep waters over the last ~40,000 years. This apparently simple method presents in fact many difficulties. Firstly, despite recent analytical developments, benthic foraminifera are not always sufficiently abundant, and it may be difficult to obtain the amount of carbonate required for analysis from a normal-size sample, even using the most sensitive technique, accelerator mass spectrometry. Second, the ^{14}C ages of foraminifera, once in the sediment, are very sensitive to bioturbation: the abundance of one species shows considerable variation over time, and shells that are found at one level may have been displaced by the activity of burrowing animals and therefore come from a significantly different age level than the selected one. Finally, the atmospheric ^{14}C concentration has undergone large scale changes, so much so that the difference in ^{14}C age between planktonic and benthic foraminifera does not directly reflect the residence time of the waters at depth.

Another approach to reconstruct the dynamics of deep-water masses makes use of the geochemical behavior of the decay chain of uranium in seawater. The isotopic composition of dissolved uranium is constant throughout the ocean. Two of the isotopes of uranium, ^{235}U and ^{234}U, decay producing ^{231}Pa and ^{230}Th respectively, with an output ratio that is constant and equal to 0.093. ^{231}Pa and ^{230}Th are very reactive to particles sinking in the water column: they are adsorbed on their surface and settle as sediment along with them. However, ^{231}Pa is less reactive than ^{230}Th, so that the residence time in seawater of dissolved ^{231}Pa is close to 200 years, while that of dissolved ^{230}Th is only thirty years (Yu et al. 1996). The residence time of ^{231}Pa is close to that of NADW in the Atlantic. Because of this, a fraction of the dissolved ^{231}Pa is advected out of the North Atlantic Ocean by NADW (about 50% in the modern ocean), while ^{230}Th is unaffected and settles completely with the particles. The net loss of ^{231}Pa in the water column at depths greater than or equal to the level at which NADW flows, leads to a deficit of ^{231}Pa in the sediments and therefore in the $^{231}Pa/^{230}Th$ ratios below the production ratio (0.093). If the circulation of NADW becomes slower, less ^{231}Pa is advected out of the basin, and the $^{231}Pa/^{230}Th$ ratio of the particles settling to the sediment increases to values closer to the production ratio.

It should be noted that sediments also contain ^{231}Pa and ^{230}Th, present as daughter isotopes of the uranium in clays that have reached secular equilibrium with their relevant parents. The addition of ^{231}Pa and ^{230}Th from settling particles thus produces an excess of these two radioisotopes in the sediment. Measuring the ratio of excess $^{231}Pa/^{230}Th$ in the sediments therefore allows the variations in the circulation of deep waters from the North Atlantic towards the Southern Ocean to be traced, and so to detect the variability associated with major changes in climate (McManus et al. 2004; Gherardi et al. 2009; Lippold et al. 2016). This technique has been used with success to reconstruct the 'strength' of the thermohaline circulation back to ~140 ky ago (Guihou et al. 2010, 2011; Böhm et al. 2015).

Major Fields of Paleoceanography

A prerequisite to reconstruct ocean circulation in the past is that marine sediments have not been buried in the mantle at subduction zones. Due to the renewal of the ocean floor by plate tectonics, the oldest sediments date back to the Triassic, about 200 million years ago. These very old sediments are rare, and found only in the Pacific Ocean. In practice, we can hope to obtain global reconstructions for the whole Tertiary era, but they become increasingly scarce as we go back to the Secondary era. Here, we will restrict ourselves to the analysis of some of the major aspects of the evolution of climate and paleoceanography over the last 25 million years, which correspond to the progressive establishment of glacial conditions in the high latitudes of both hemispheres.

From 'The Greenhouse Effect Era' to the 'Ice Ages'

The Quaternary period, which covers the last 2.6 million years of the history of our planet, is characterized by persistent major ice sheets in the high latitudes of both hemispheres. The volume of these caps and their geographical expansion fluctuate over timescales of 10^4 to 10^5 years, in response to changes in insolation controlled by the orbital parameters of the Earth (see Chap. 28).

The origin of these major glacial phases is discussed in several chapters that present the point of view of geophysicists, geochemists and modelers (see Chaps. 22, 26 and 27). At time scales exceeding a million years, the major causes of the development of glaciations are feedbacks related to plate tectonics. Among these feedbacks, the following may be highlighted:

- the varying shapes and positions of landmasses and ocean basins,
- the existence of passages between basins,
- the location and altitude of mountain ranges, both in the ocean and on land, affecting oceanic and atmospheric circulation and heat transfer,
- volcanism and erosion, and their impact on atmospheric chemistry and on the pCO_2 of the atmosphere.

The record describing the evolution of the $\delta^{18}O$ of benthic foraminifera over time shown in Fig. 21.2 is the result of a compilation of analyses made in more than forty ocean-drilling sites. This global compilation registers both the changes in δ_w and temperature, in accordance with the paleotemperature formula (Eq. 21.1). It shows that the current climate is the result of a long decline that started at the end of the climate optimum of the early Eocene (52–50 Ma ago). This decline is characterized by an increase in $\delta^{18}O$ over time that reflects the drop in ocean temperatures at higher latitudes (where deep waters are formed) in a world without major glaciers, followed by the growth of ice caps. The $\delta^{18}O$ of benthic foraminifera therefore dropped from an average of $\sim$0.2‰ during the climate optimum of the early Eocene, to an average of $\sim$4‰ at the end of the Quaternary.

This slow climate decline is generally attributed to two main factors: a gradual reduction in atmospheric CO_2 concentration, and the growing thermal isolation of the Antarctic continent due to the widening of the ocean passages that surround it.

Relatively abrupt incidents (that is, events happening over a much shorter time scale than the general trend), of large amplitude, are superimposed onto this slow drift, indicating that other climate drivers such as thresholds or rapid feedbacks are also involved. The first of these changes occurred at the very end of the Paleogene, at the boundary of the Eocene/Oligocene, about 33.5 Ma ago. It resulted in a rapid increase in benthic foraminiferal $\delta^{18}O$ from +1.6 to +2.8‰ over only 100–200 ka (Fig. 21.2). This change in $\delta^{18}O$ is attributed to the development of the Antarctic ice cap. The northward drift of the Australian continent allowed the opening of the Strait of Tasmania and the establishment of the Antarctic Circumpolar Current (Zachos et al. 2001). The isolation of this large land mass resulted in a drop in temperatures and the establishment of a permanent ice cap on East Antarctica, with an ice volume that may have reached about 50% of its current size. After a period of ten million years when the climate changed little, two warming phases, one at the end of the Oligocene and the other during the Middle Miocene, caused a significant reduction of the Antarctic ice sheet. The increase in temperature and the decrease in ice volume were reflected in a 1.2‰ decrease in the benthic $\delta^{18}O$ signal. The causes of these climatic changes are not clear yet.

The final phase of the climatic decline leading to the major glaciations of the Quaternary began from the Middle Miocene, between 14.2 and 12.2 Ma, and was marked by an increase in benthic foraminiferal $\delta^{18}O$ of 1.0‰ over two million years. Paleotemperature reconstructions based on Mg/Ca ratios in benthic foraminifera suggest that deep water temperature varied little, and that the growth of the Antarctic ice cap was the main contributor to the benthic $\delta^{18}O$ change (around $\sim$0.8‰). If these estimates were correct, the ice cap located on the eastern part of Antarctica would have reached 85% of its current volume. As for the West Antarctic ice cap, it seems to have only developed from 6 Ma on, as evidenced by the first coarse sediment deposits in the Weddell Sea, coming from melting icebergs emitted at the edge of this cap. These sediments transported by drifting ice result from land erosion caused by the friction of glaciers, and are often referred to by their acronym IRD (*ice rafted debris*).

Although the development of a permanent ice cap on Antarctica started early, during the early Neogene, the development of perennial continental ice caps in the high latitudes of the northern hemisphere did not occur until the end of the Neogene. The first deposits of IRD in the Norwegian Sea, proof of the early development of an ice cap (although perhaps not a permanent one) on Greenland are not observed before 5.5 Ma (Jansen and Sjoholm 1991). The rapid increase in $\delta^{18}O$ from ~3.2 Ma onwards may be interpreted as the beginning of permanent glaciation in high latitudes of the northern hemisphere. This glaciation intensified rapidly around 2.1–2.6 Ma, as evidenced by the massive IRD deposits in the Norwegian Sea.

Many studies have focused on the hypothesis of the 'closure of the Panama isthmus' as a potential trigger for the development of northern hemisphere ice sheets. The mechanism would involve warm intertropical waters no longer being able to cross from the Atlantic to the Pacific. They would therefore deviate into the North Atlantic, increasing oceanic evaporation in this basin and thus snow accumulation in the high latitudes. However, recent studies suggest that the closure of the Panama isthmus could have occurred during the Miocene, well before the intensification of glaciations (Montes et al. 2015). The recent work of Rohling et al. (2014) also observes a large temporal offset during the onset of the Plio-Pleistocene ice ages, between a marked cooling step at 2.73 My ago and the first major glaciation starting 2.15 My ago. Other theories indicate that a decrease in atmospheric CO_2 may have been responsible for a cooling, an increase of deep water formation in the North Atlantic and a change of circulation that together induced the start of the glaciations.

The 'Middle Pleistocene Transition' and the Establishment of 100-Ka Cycles

The trend towards the climatic decline (seen as an increase in benthic $\delta^{18}O$) discussed in Sect. "From 'The Greenhouse Effect Era' to the 'Ice Ages'" continued over the last two million years, as is shown in detail in Fig. 21.2. Superimposed on this trend are quasi-periodic oscillations. They reflect the alternating glacial periods—corresponding to a cooling of deep waters and an increase in ice volume at high latitudes—and interglacial periods, with warming and relative melting of the ice caps. It should be emphasized here that the use of the terms 'interglacial' and 'glacial' does not imply a *total* melting of ice sheets. During interglacial periods, ice sheets do not disappear, even if they are greatly reduced in the northern hemisphere. For example, during the LGM, the ice sheets in the northern hemisphere covered a large portion of North America and Europe. During the Holocene, the interglacial period we currently live in, these caps were largely diminished; the meltwater derived from them has caused sea level to rise by 120 m since the LGM. However, an ice cap of 2.8 million km^3 continues to exist on Greenland that would cause a further sea level rise of about 7 meters, if it were to completely melt.

The amplitude of the glacial-interglacial oscillations increased sharply between 1.2 and 0.6 Ma (Fig. 21.2). During this period, called 'the Middle Pleistocene Transition' (Clark et al. 2006; McClymont et al. 2013), a threshold response to longer-term atmospheric CO_2 decline has been proposed (Raymo et al. 1997). However, recent atmospheric partial pressure CO_2 reconstructions have failed to show this long-term decrease during the Pleistocene (Hönisch et al. 2009). The gradual increase in glacial-interglacial amplitude is mainly due to increasingly high values of $\delta^{18}O$ during glacial periods. The few available reconstructions of deep-water temperature during this period indicate near-freezing temperatures at every glacial maximum instead of a gradual cooling (Elderfield et al. 2012), which suggests that an increase in Antarctic ice volume would be responsible for the rapid and steep increase in seawater $\delta^{18}O$ at 0.9 Ma.

This change in amplitude of glacial-interglacial oscillations is accompanied by a disruption in the frequency content of the global $\delta^{18}O$ signal. While benthic foraminifera $\delta^{18}O$ oscillations show mainly a cycle of ~41 ka over most of the Neogene and early Quaternary, the last 600,000 years are dominated by oscillations with a cyclicity of ~100 ka (Fig. 21.2). Some authors have agreed on the progressive nature of the 'Middle Pleistocene Transition', with the amplification of the 100 ka cycles occurring over hundreds of thousands of years. However, in some ocean regions, the records fail to demonstrate this progressive nature. This is the case, for example, in the equatorial Atlantic, where the dynamics of the thermocline, reconstructed from micropaleontological tracers, suddenly change its variability around ~930 ka. The mechanisms responsible for this transition are still unclear, although it appears that an important role can be attributed to the enormous Laurentide ice sheet, which may have favored the frequency of 100 ka through its inertia (Clark and Pollard 1998) (see Chap. 28).

The Last Glacial Maximum (LGM)

The LGM has long been, and still remains, a major area of interest in paleoclimatology, in particular because it presents another extreme on the climate spectrum on which Earth System models can be validated (Kageyama et al. 2018). Early studies defined this period as the time encompassing

the last great cold maximum (as recorded by micropaleontology and pollen) as well as the maximum spread of the ice sheets (marked by the position of moraines on land masses). Radiocarbon dating has placed the maximum at around 16-20 ka ^{14}C (equivalent to 18–23 ka in calendar age). This period was the first to be the subject of a global paleoclimate study, thanks to the CLIMAP group. The isotopic maximum in $\delta^{18}O$ of planktonic and benthic foraminifera, interpreted as reflecting the cumulative effects of the cold and ice volume maxima, was used as a stratigraphic marker, and summer and winter sea surface temperatures were determined from micropaleontological transfer functions. This established the CLIMAP maps (CLIMAP 1981) (Fig. 21.3) that served as boundary conditions for the first comprehensive paleoclimate modeling experiments. The CLIMAP results have had a profound impact. For the first time, the magnitude of the temperature change between an ice age (LGM) and an interglacial period (modern times) could be quantified: the average global temperature dropped by 6 °C. However, this cooling was far from uniform: it exceeded 10 °C at high northern latitudes, while it was only a few degrees in the intertropical region. This intense cooling was associated with the development of large ice sheets over the landmasses of the northern hemisphere, which, with about 50 million cubic kilometers of ice, was the most glaciated hemisphere. In addition, analyses of Antarctic ice showed that atmospheric CO_2 concentration was about 100 ppmv below pre-industrial values (Petit et al. 1999).

It quickly became necessary to expand these early studies. Continental tracers in tropical regions, such as pollen series or concentration of noble gases in aquifers (which are dependent on the temperature of the rains feeding these aquifers), indicated a cooling of 3–6 °C during the LGM. In the nearby ocean, sea surface temperature alkenone reconstructions indicated a cooling of only about 2 °C, and micropaleontological transfer functions showed little or no change. Detailed studies were therefore conducted in later decades to explain the observed differences. It appeared that many cores taken from the tropical Pacific Ocean and used for the CLIMAP reconstruction had very low sedimentation rates, so that bioturbation caused the contrasts in fauna over time to disappear. In addition, the fauna from warm waters exhibited variability that did not solely respond to temperature changes, with the result that micropaleontological transfer functions became insensitive at the temperatures above 25 °C common in tropical regions. At the same time, high-resolution studies started to indicate strong climatic variability between 17 ka and 25 ka. In the North Atlantic, for example, the LGM does not correspond to the coldest conditions, which are instead associated with two periods framing the LGM: Heinrich Stadial (HS) 2 at around 24–22 ka and HS1 at around 19–17 ka.

It therefore became essential to reconsider the reconstruction of the surface ocean during the LGM. The latest and most comprehensive synthesis was carried out in the MARGO program (MARGO Project Members 2009), which focused on the period 19–23 ka corresponding to the LGM sensu stricto. This period corresponds to the maximum expansion of ice sheets, as opposed to the coldest conditions of Heinrich Stadials. The LGM MARGO reconstructions (Fig. 21.3) agree relatively well with CLIMAP, but they also revealed some important differences:

- the northern seas were ice-free during the summer;
- latitudinal and longitudinal thermal gradients were strong; the mid-latitudes of the North Atlantic Ocean experienced the strongest cooling (~ -10 °C);
- the decrease in temperature was generally larger on the eastern side than on the western side of the oceans; this was particularly marked along the African margin, especially in coastal upwelling zones of Namibia and South Africa;
- the cooling of tropical waters was close to 2 °C, although some localized waters of the Pacific and Indian Oceans experienced moderated warming;
- in the Southern Ocean, a cooling of 2–6 °C marked a northward displacement of the polar front.

Other studies have focused on the deep ocean during the LGM. We have mentioned several of them in the description of the various methodological techniques that have been developed over the last forty years. Significant differences between the LGM and the present day include:

- the downwelling of surface waters in the North Atlantic happened in open ocean, leading to the formation of very cold deep water that found its density equilibrium at 2000 m depth;
- the very cold and dense bottom waters formed in the southern hemisphere spread throughout the deep ocean, occupying a much larger volume than today;
- the boundary between deep and bottom waters was characterized by a much stronger gradient of physical (T, S, density) and geochemical ($\delta^{18}O$, $\delta^{13}C$) properties than today;
- the ventilation and renewal rates of deep waters are still poorly constrained because of conflicting information from different tracers with a complex geochemical behavior (^{14}C, $^{231}Pa/^{230}Th$); this uncertainty is also reflected in the simulations from general circulation models of the ocean and coupled ocean-atmosphere models. Most proxies do indicate, however, lower ventilation of the deep ocean and a resulting large accumulation of carbon dioxide in the deeper waters.

The Last Deglaciation

Several decades ago, continental paleoclimatologists described the warming by steps that occurred during the last disappearance of the large northern ice caps, a period extending from 20 to 8 ka. This 'last deglaciation' was also identified by paleoceanographers in marine sediment cores with high sedimentation rates (Fig. 21.12). The terminology for this succession of warming and relative cooling comes directly from the first descriptions made in the continental records based on pollen assemblages: Older Dryas, Middle Dryas, Bølling-Allerød and Younger Dryas all take their names from plant pollens (in the case of Dryas, it is associated with the reappearance of the cold flower *Dryas octopetala*), or from locations from which the samples were taken (the proglacial lake of Bølling and the city of Allerød in Denmark).

The drivers and feedbacks that led to this specific sequence of events are still being actively studied. The start of the deglaciation is linked to the evolution of the astronomical parameters, with a strong increase in summer insolation in the northern hemisphere between 20 and 10 ka (Milankovitch's theory), and aided by pulses of increases in atmospheric CO_2 likely released from the CO_2-rich deep waters of the Southern Ocean (Marcott et al. 2014). However, the mechanisms that explain the phase differences between the two hemispheres (Fig. 21.12) during the deglaciation are still unclear. A distinct warming trend appeared in Antarctica around 19 ka, while simultaneously, the northern hemisphere, after a brief warming trend, cooled

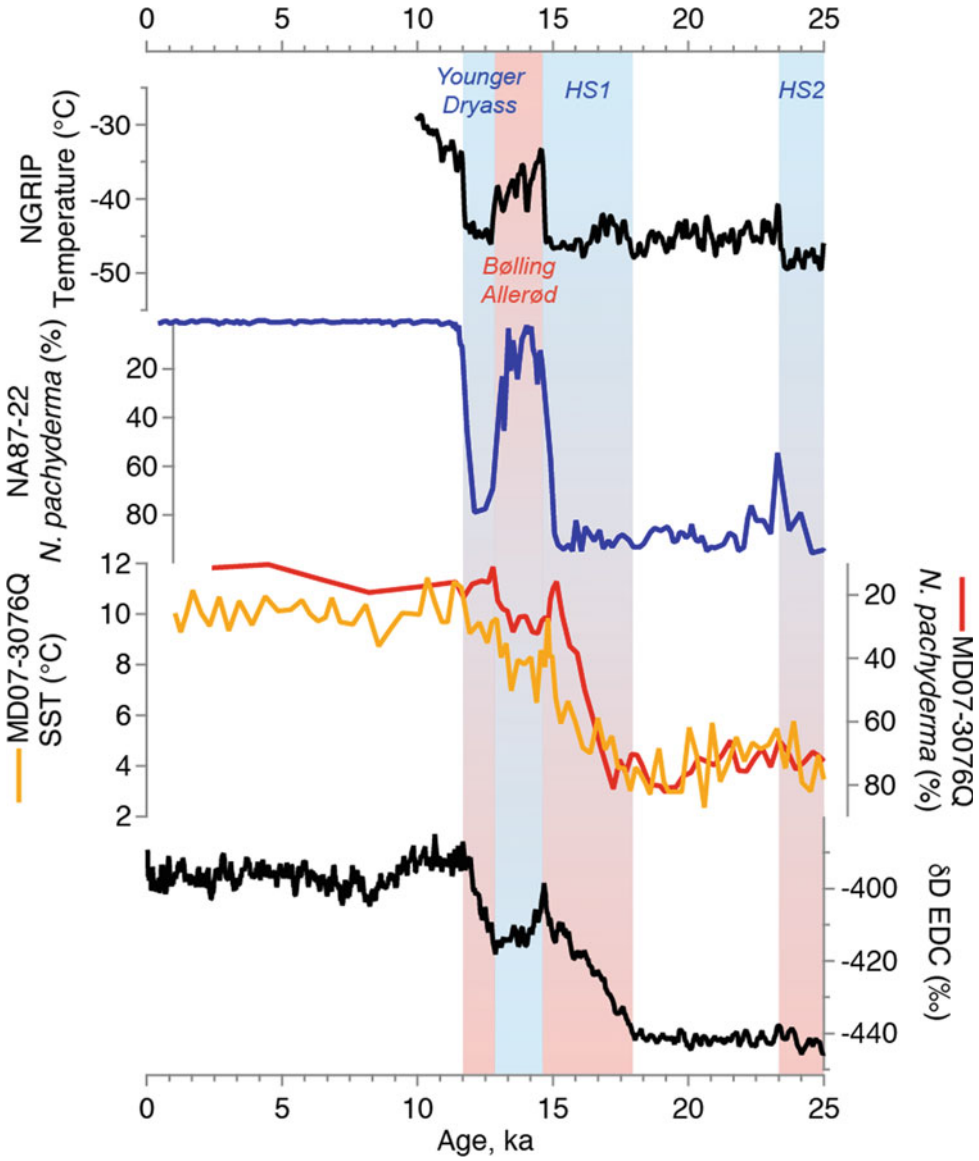

Fig. 21.12 Records of the last deglaciation in the high latitudes of both hemispheres. (Top) Variations in $\delta^{18}O$ in the ice from the NorthGRIP site (Greenland), a proxy for the local variations in atmospheric temperature (Rasmussen et al. 2014); (middle-top) variations in the percentage of the cold species *Neogloboquadrina pachyderma* in core NA87-22 from the North Atlantic (55 °30 ′N, 14 °42 ′W, 2161 m deep) (Waelbroeck et al. 2001; Vázquez Riveiros et al. 2013); (middle-bottom) variations in the isotopic composition of hydrogen δD of ice from Dome C (Antarctica), a proxy for local variations in atmospheric temperature (EPICA 2004); (bottom) variations in the percentage of the cold species *Neogloboquadrina pachyderma* and SST estimated by the Mg/Ca method in core MD07-3076Q from the Southern Ocean (44 ° 09 ′S, 14 °13 ′W, 3770 m deep) (modified from Vázquez Riveiros et al. 2010)

and presented armadas of icebergs linked to the HS1 event (see Chap. 29). Following this event, around 14 ka, northern hemisphere warming was strongly amplified with a culmination during the Bølling-Allerød, while temperatures in the southern hemisphere stabilized and even dropped in Antarctica during the so-called Antarctic Cold Reversal (Fig. 21.12). During this early phase of the deglaciation, the North-South antiphase is similar to what is observed during abrupt events of the last ice age, with the exception of the general deglacial warming trend. Recent studies point to CO_2 as a key mechanism of global warming during the last deglaciation. An anti-phased hemispheric temperature response to ocean circulation changes, superimposed on globally in-phase warming driven by increased CO_2 concentrations, is an explanation for much of the temperature change at the end of the most recent ice age (Barker et al. 2009; Shakun et al. 2012).

However, at the end of the Bølling-Allerød warm event, at about 12.5 ka, the ice caps stopped melting, the sea level stabilized and the deglaciation stopped: this was the Younger Dryas period (Fig. 21.12), characterized by a return to very cold conditions for about 1.5 kyr, despite insolation reaching maximum values. This return to almost ice age conditions still raises many questions. The most commonly accepted explanation is a sudden change in the path taken by meltwater from the Laurentide ice sheet (Leydet et al. 2018). Until about 12.5 ka, this huge flow of water was transported by the Mississippi River. Released into the Gulf of Mexico, the fresh water was drawn in by the circulation of the surface currents of the Atlantic (Gulf Stream followed by the North Atlantic Drift) and was very gradually diluted by the salty tropical waters without any major climate impact. During the Younger Dryas, however, the flow rate of the Mississippi River dropped considerably, which led to the hypothesis that the watershed of the meltwater plume changed and flowed instead through the St. Lawrence River to the northwest of the Atlantic Ocean. The salinity in this higher latitude area was reduced, interrupting deep water formation and thus the thermohaline circulation, and causing cooling and the growth of some glaciers. This hypothesis has been supported by simple ocean circulation models, although marine sediment cores recovered from the likely North Atlantic zone of evacuation of meltwater have, as of yet, failed to yield traces of this event. Recent study suggests multiple causes of the Younger Dryas cold period: a weakened Atlantic Meridional Overturning Circulation, moderate negative radioactive forcing and an altered atmospheric circulation (Renssen et al. 2015). The detailed study of this event could help us to better understand the interactions between ocean, ice and atmosphere under conditions of strong insolation.

Interglacial Periods, the Holocene and the Last Two Millennia

In order to explain the succession of glacial and interglacials periods over the last million years, Milankovitch developed the astronomical theory of paleoclimate. Since then, conceptual models have been able to describe the general trends, as well as the dominant periodicities centered around 100, 40 and 20 kyr fairly accurately (see Chap. 28). Although changes in ice cap volume during glacial periods and the time constants of their response to changes in insolation are relatively well understood, the same cannot be said for the evolution of climate during interglacial periods. In particular, the mechanisms causing the differences in duration, in temperature of the atmosphere and ocean, and in ocean circulation are not well understood, even though differences in forcing are precisely calculated (Past InterGlacialS Working Group of PAGES 2016). This lack of understanding is derived in part from the small ocean temperature differences between past interglacial periods and the present day, with temperature changes that remain close to the error of temperature reconstructions with the usual tracers (Sect. "Sea Surface Temperature"). A further complication arises because the internal mechanisms in the climate system must be investigated through its various components (atmosphere, ocean, continent), which involves the construction of time scales common to the various archives used to reconstruct each of them, and makes the study of the interglacial periods prior to the Holocene particularly difficult.

In this section, we limit ourselves to the analysis of the last two interglacial periods: the Last Interglacial (also called the Eemian), about 125 ka ago, and the Holocene, period in which we now live. Eemian and Holocene, the terms used in this chapter, are names borrowed from palynologists to identify these two interglacial periods. A short subsection will finally be devoted to results recently obtained for the last two millennia, which has the advantage of presenting a wide range of continental and marine records that can, in some cases, be compared with recorded meteorological data.

The Last Interglacial Period

Before presenting our understanding of this period of time, it is important to define what an interglacial is. It may in fact be defined in a number of ways depending on whether one considers, for example, variability in flora, ocean circulation, atmospheric temperature or ocean temperature (Past InterGlacialS Working Group of PAGES 2016). If we take ice volume as a marker, an interglacial period sensu stricto is the time interval during which the ice volume is at its minimum and remains constant for several millennia.

Strictly speaking, the interglacial comparable to the period we live in, and defined by an ice volume minimum is called the Last Interglacial, and runs from about 129–116 ka (Govin et al. 2015; Dutton et al. 2015). From 115 ka, the midpoint of the transition marking the entry into MIS 5d, ice volume had already increased significantly, so much so that sea level dropped by as much as −40 m at the height of MIS 5d at about 110 ka.

During the Last Interglacial, the insolation forcing was characterized by a relatively high eccentricity, the combination of a strong inclination and a perihelion close to the summer solstice. This orbital configuration triggered an increase in summer insolation in the northern hemisphere of more than 30 W/m^2 compared to the present day. Despite these differences in forcing, the general evolution of the Last Interglacial climate is to a first degree quite similar to that of the Holocene: high temperatures at higher northern latitudes until about 123 ka (in line with higher insolation and higher elevation of the sun on the horizon), followed by a gradual cooling linked to the decline in boreal summer insolation in parallel with the progressive growth of glacial conditions (Cortijo et al. 1999). However, the Last Interglacial temperature peak was reached at about 126 ka in the North Atlantic against 129 ka in the southern high latitudes. This hemispheric asynchrony is related to the disruption of the Atlantic overturning circulation due to freshwater discharges into the North Atlantic (in response to ice sheet melting) that led to the persistence of cold conditions in the northern high latitudes and the early warming of southern high latitudes during the early phase of the Last Interglacial (Capron et al. 2014, 2017) (Fig. 21.13).

Nevertheless, despite greenhouse gas concentrations that were similar to pre-industrial times, the larger increase in summer insolation in the northern hemisphere with respect to the current situation did have an impact on the climate of the Last Interglacial optimum. Surface water temperatures were 1–2 °C warmer in the North Atlantic, the Nordic Seas and the Southern Ocean than during the Holocene (Capron et al. 2014, 2017; Hoffman et al. 2017). Such warmer high latitudes during the Last Interglacial had a double impact:

- the warming by about 0.4 °C of the temperatures of the deep Atlantic waters, which was then carried into Antarctic circumpolar deep waters (Duplessy et al. 2007);
- the partial melting of Greenland and West Antarctica (Dutton et al. 2015).

These two combined actions brought about a rise in sea level of 6–9 m (Dutton et al. 2009) compared to current levels.

The Last Interglacial is a good case study to test our mechanistic understanding of the effect of warmer-than-present polar climate on sensitive components of the Earth system (e.g. ice sheets, sea level). It has recently sparked

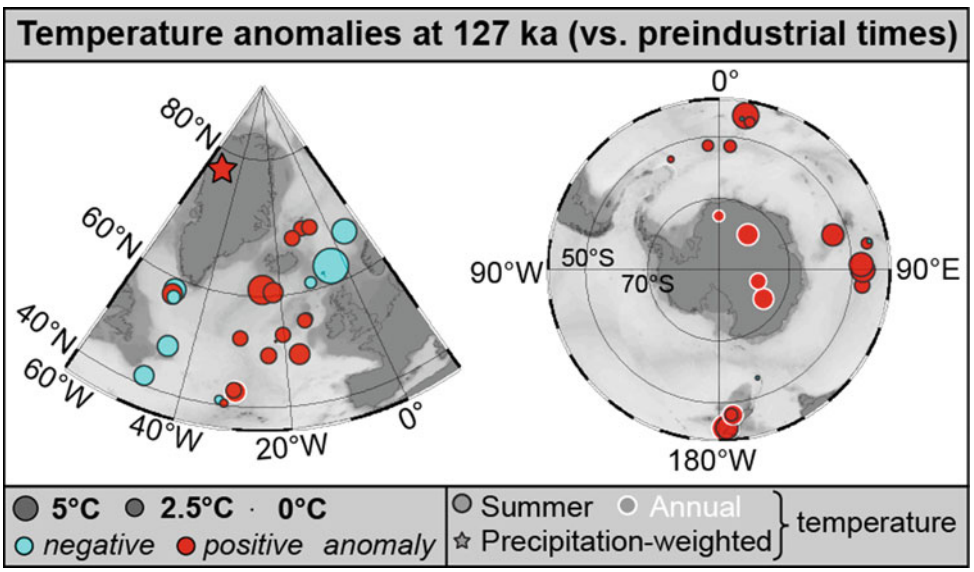

Fig. 21.13 Temperature anomalies at 127 ka compared to preindustrial times (1870–1899 CE) in the northern and southern high latitudes (modified after Capron et al. 2017). Negative (positive) temperature anomalies are shown in blue (red). The bigger the dot, the stronger the temperature anomaly. Most records indicate warmer conditions at 127 ka compared to preindustrial, in response to the high boreal summer insolation. The few cold anomalies suggest remnants of freshwater discharge into the North Atlantic, Nordic Seas and Labrador Seas

interest in the community, as shown by multiple paleo-data compilations and model-data comparison exercises (Otto-Bliesner et al. 2017).

The Holocene

The Holocene period started about 11 ka ago. The last major ice sheets had not completely disappeared, but major changes had occurred since the early deglaciation, both in terms of sea level and continental and oceanic temperatures. At first look, the climate over these past 11 ka seems stable, but this apparent stability hides very pronounced regional variations in the hydrological cycle, in the circulation of surface waters (especially during the final stage of melting of the residual ice caps), and in the general circulation of the Mediterranean Sea, a basin surrounded by land and with limited connections to the open ocean and thus very strongly affected by changes in rainfall intensity over its watershed.

The Holocene is a period of major movement and development of populations. However, for the most part of this period, human activities still had a negligible impact on the global environment, so the study of climate changes over recent millennia provide a benchmark against which disturbances caused by industrial and agricultural activities can be detected. The reconstruction of Holocene climate changes is facilitated by the precise chronology offered by carbon-14 analysis.

The forcing of summer insolation at 65°N at the beginning of the Holocene reached more than 390 W/m^2 and caused a global warming that would last until about 6 ka. The temperature optimum affected the high latitudes of the North Atlantic basin, including Iceland, the Norwegian Sea and the Scandinavian coast (Koç et al. 1993). In the Barents Sea, the temperature maximum was limited to the period from 7.9 to 6.9 ka due to the dissipation of the heat brought by the North Atlantic Drift by the melting of the surrounding ice. At lower latitudes, the temperature increase was accompanied by a northward shift of the Intertropical Convergence Zone (ITCZ) and a major change in monsoon dynamics, and therefore in the atmospheric water cycle. The increase in the thermal contrast between ocean and continent, for example, accentuated the African monsoon as far as the center of the continent.

The study of sediment cores from both the Mediterranean Sea and African lakes indicates the existence of major climate reorganizations. For example, before 6 ka, the Sahara was not the wide-ranging desert that it is today, but grassland dotted with lakes conducive to farming settlement. This period is called the African Humid Period (AHP). Around 6 ka, this wet period ended and conditions degraded at a rate that is still debated (Collins et al. 2017; Shanahan et al. 2016; Tierney and deMenocal (2013). The tropical vegetation of canopy forests along the rivers declined, and the Sahelian vegetation in turn disappeared about 2.7 ka ago to make way for the desert conditions present today. This major change could be related to the gradual decrease in insolation over the past 10 ka aided by the albedo feedback induced by the gradual disappearance of vegetation. Alternatively, a rapid termination of the AHP could have been triggered by northern-latitude cooling combined with biogeophysical feedbacks (Collins et al. 2017).

During this wet period, the Mediterranean Sea received more fresh water, especially in the eastern basin (Kallel et al. 1997). The sinking of well-ventilated, shallow water masses in winter became impossible in the Levantine basin, and bottom waters there became completely anoxic, leading to the disappearance of benthic fauna below 800 m depth. A layer of black sediment rich in organic matter, called a sapropel, marks this event (Rossignol-Strick et al. 1982; Rohling et al. 2015). Although ventilation of the eastern waters of the Mediterranean resumed at 6 ka, the deep fauna of this basin, whose colonization rate is slow, is still very poor.

In addition to these long-term reorganizations, the Holocene also recorded an abrupt event of short duration 8.2 ka ago. Without reaching the amplitude of the rapid and sudden climate changes of the last ice age, this event still left a significant imprint on northern hemisphere temperatures. Like its glacial counterparts, the '8.2 ka event' is associated with a freshwater discharge, in this case due to the rupture of a proglacial reservoir, Lake Agassiz, formed by the retreat of the Laurentide ice sheet (Barber et al. 1999; Wiersma and Renssen 2006; Hoffman et al. 2012). The sudden release of tens of thousands of km^3 of water (estimates vary from 50,000 to 120,000 km^3) over just 1–5 yrs had strong consequences, such as a reduction in the SST (about 1 °C) and salinity of the North Atlantic, a reduction of 2–6 °C in the atmospheric temperature above Greenland, a decrease in the temperature of air and water in the lakes of western Europe, and a decrease in the intensity of ocean circulation for a period of about 100 yrs after the freshwater discharge.

The study of the 8.2 event has shown that interglacial ocean circulation, such as the one of the early Holocene, may also be sensitive to an intense, although brief, freshwater discharge. Recent studies have pointed out that this may also have been the case during earlier interglacial periods (Galaasen et al. 2014).

The climate of the last two millennia has also been the subject of much focus, since it provides a relatively long-term perspective for recent observations from the World Meteorological Organization (WMO) network (restricted to the last 150 years) and from satellites dedicated to the observation of the Earth (limited to a few decades). The reconstructions of air temperature in the northern hemisphere, used as projections for the whole planet, have primarily been based on continental data (Mann et al. 1998).

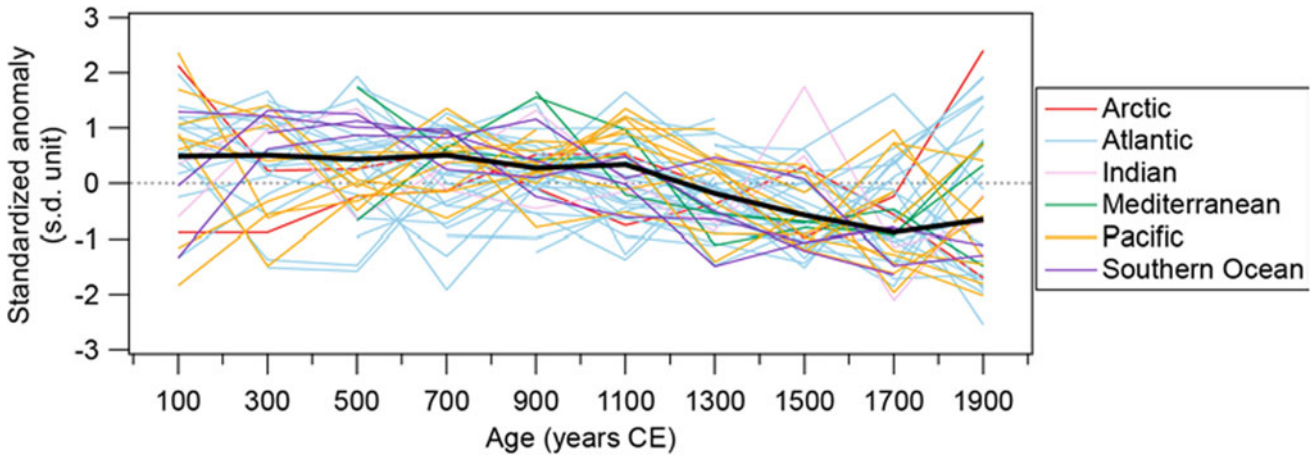

Fig. 21.14 Standardized SST anomalies over the last 2000 years (modified after McGregor et al. 2015). Thin colored lines represent individual SST reconstructions from different ocean basins, which have been averaged into 200-year long bins (e.g. 1–200 CE). The thick black line is the area-weighted median SST value

Reconstructing and understanding changes in the ocean over the last two millennia is particularly difficult, since oceanographic observations are only available for the last century at most, and for paleoceanographers this period is recorded in the uppermost portion of the sediment which is often poorly consolidated or lost.

Recently, much effort has been put on the gathering of the best time-series of the last two millennia as part of the Past Global Changes (PAGES) 2 k network (PAGES 2k Consortium 2013, 2017). Continental-scale temperature reconstructions provide evidence of twentieth century warming over all reconstructed regions except Antarctica (PAGES 2k Consortium 2013). A global SST compilation shows a 1800-year long cooling of the surface ocean over the pre-industrial past 2000 years (Fig. 21.14), and that the cooling from 801 to 1800 CE was likely caused by volcanic eruptions (McGregor et al. 2015). A more recent synthesis of paleoclimate records since 1500 CE has identified that sustained industrial-era warming of the tropical oceans first developed during the mid-nineteenth century and was nearly synchronous with Northern Hemisphere continental warming (Abram et al. 2016).

If we look at the deep ocean, the relative strength of the meridional overturning circulation has also been recently assessed for the last 1.6 ka (Thornalley et al. 2018). The authors suggest that, while it was relatively stable between 400 and 1850 CE, it has declined in strength by ~15% at the beginning of the industrial era. In addition, the comparison of SST patterns in the North Atlantic with model simulations points to an additional weakening over the last 150 yrs (Caesar et al. 2018).

Compilation studies like the ones presented above highlight the need for paleoclimate reconstructions, which can be compared to instrumental records that at present are too short to comprehensively assess anthropogenic climate change.

References

Abram, N. J., McGregor, H. V., Tierney, J. E., Evans, M. N., McKay, N. P., Kaufman, D. S., & The Pages 2 k Consortium. (2016). Early onset of industrial-era warming across the oceans and continents. *Nature, 536*, 411. https://doi.org/10.1038/nature19082.

Adkins, J. F., McIntyre, K., & Schrag, D. P. (2002). The salinity, temperature and $\delta^{18}O$ of the glacial deep ocean. *Science, 298,* 1769–1773.

Anand, P., Elderfield, H., & Conte, M. H. (2003). Calibration of Mg/Ca thermometry in planktonic foraminifera from a sediment trap time series. *Paleoceanography, 18*(2).

Barker, S., Diz, P., Vautravers, M. J., Pike, J., Knorr, G., Hall, I. R., et al. (2009). Interhemispheric Atlantic seesaw response during the last deglaciation. *Nature, 457*(7233), 1097.

Barber, D. C., Dyke, A., Hillaire-Marcel, C., Jennings, A. E., Andrews, J. T., Kerwin, M. W., et al. (1999). Forcing of the cold event of 8200 years ago by catastrophic drainage of Laurentide lakes. *Nature, 400,* 344. https://doi.org/10.1038/22504.

Bemis, B. E., Spero, H. J., Bijma, J., & Lea, D. W. (1998). Reevaluation of the oxygen isotopic composition of planktonic foraminifera: Experimental results and revised paleotemperature equations. *Paleoceanography, 13,* 150–160.

Bintanja, R., van de Wal, R. S., & Oerlemans, J. (2005). Modelled atmospheric temperatures and global sea levels over the past million years. *Nature, 437,* 125–128.

Böhm, E., Lippold, J., Gutjahr, M., Frank, M., Blaser, P., Antz, B., et al. (2015). Strong and deep Atlantic meridional overturning circulation during the last glacial cycle. *Nature, 517,* 73–76.

Caley, T., & Roche, D. M. (2015). Modeling water isotopologues during the last glacial: Implications for quantitative paleosalinity reconstruction. *Paleoceanography and Paleoclimatology, 30*(6), 739–750.

Capron, E., Govin, A., Stone, E. J., Masson-Delmotte, V., Mulitza, S., Otto-Bliesner, B., et al. (2014). Temporal and spatial structure of multi-millennial temperature changes at high latitudes during the Last Interglacial. *Quaternary Science Reviews, 103,* 116–133.

Capron, E., Govin, A., Feng, R., Otto-Bliesner, B., & Wolff, E. W. (2017). Critical evaluation of climate syntheses to benchmark CMIP6/PMIP4 127 ka Last Interglacial simulations in the high latitude regions. *Quaternary Science Reviews, 168,* 137–150.

Carroll, J., Brown, E. T., & Moore, W. S. (1993). The role of the Ganges-Brahmaputra mixing zone in supplying barium and ^{226}Ra to the Bay of Bengal. *Geochimica et Cosmochimica Acta, 57,* 2981–2990.

Caesar, L., Rahmstorf, S., Robinson, A., Feulner, G., & Saba, V. (2018). Observed fingerprint of a weakening Atlantic Ocean overturning circulation. *Nature, 556,* 191–198.

Chivall, D., M'Boule, D., Sinke-Schoen, D., Sinninghe Damsté, J. S., Schouten, S., & van der Meer, M. T. (2014). The effects of growth phase and salinity on the hydrogen isotopic composition of alkenones produced by coastal haptophyte algae. *Geochimica et Cosmochimica Acta, 140,* 381–390.

Clark, P. U., & Pollard, D. (1998). Origin of the middle Pleistocene transition by ice sheet erosion of regolith. *Paleoceanography and Paleoclimatology, 13*(1), 1–9.

Clark, P. U., Archer, D., Pollard, D., Blum, J. D., Rial, J. A., Brovkin, V., et al. (2006). The middle Pleistocene transition: Characteristics, mechanisms, and implications for long-term changes in atmospheric pCO_2. *Quaternary Science Reviews, 25,* 3150–3184.

CLIMAP. (1981). Seasonal reconstructions of the Earth's surface at the last glacial maximum. *Geological Society of America, Map and Chart Series, 36*.

Collins, J. A., Prange, M., Caley, T., Gimeno, L., Beckmann, B., Mulitza, S., et al. (2017). Rapid termination of the African Humid Period triggered by northern high-latitude cooling. *Nature Communications, 8,* 1372.

Conte, M. H., Sicre, M. A., Rühlemann, C., Weber, J. C., Schulte, S., Schulz-Bull, D., & Blanz, T. (2006). Global temperature calibration of the alkenone unsaturation index (UK′37) in surface waters and comparison with surface sediments. *Geochemistry, Geophysics, Geosystems, 7*(2).

Corrège, T. (2006). Sea surface temperature and salinity reconstruction from coral geochemical tracers. *Palaeogeography, Palaeoclimatology, Palaeoecology, 232*(2–4), 408–428.

Cortijo, E., Lehman, S., Keigwin, L., Chapman, M., Paillard, D., & Labeyrie, L. (1999). Changes in meridional temperature and salinity gradients in the North Atlantic Ocean (30–72 N) during the last interglacial period. *Paleoceanography, 14,* 23–33. https://doi.org/10.1029/1998PA900004.

Craig, H., & Gordon, L. I. (1965). Deuterium and oxygen-18 variations in the ocean and marine atmosphere. In E. Tongiorgi (Ed.), *Stable isotopes in oceanographic studies and paleotemperatures* (pp. 9–130). Pisa, Italy: Laboratory of Geology and Nuclear Science.

DeSève, A. M. (1999). Transfer function between surface sediment diatom assemblages and sea-surface temperature and salinity of the Labrador Sea. *Marine Micropaleontology, 36,* 249–267.

De Vernal, A., et al. (2001). Dinoflagellate cyst assemblages as tracers of sea-surface conditions in the Northern Atlantic, Arctic and sub-Arctic seas: The new n = 677 data base and its application for quantitative paleoceanographic reconstruction. *Journal of Quaternary Science, 16,* 681–698.

Duplessy, J. C., Shackleton, N. J., Matthews, R. K., Prell, W. L., Ruddiman, W. F., Caralp, M., et al. (1984). ^{13}C record of benthic foraminifera in the Last Interglacial Ocean: Implications for the carbon cycle and the global deep water circulation. *Quaternary Research, 21,* 225–243.

Duplessy, J. C., Labeyrie, L., Juillet-Leclerc, A., Maitre, F., Duprat, J., & Sarnthein, M. (1991). Surface salinity reconstruction of the North Atlantic Ocean during the last glacial maximum. *Oceanologica Acta, 14,* 311–324.

Duplessy, J. C., Roche, D. M., & Kageyama, M. (2007). The deep ocean during the last interglacial period. *Science, 316,* 89–91.

Dutton, A., Bard, E., Antonioli, F., Esat, T. M., Lambeck, K., & McCulloch, M. T. (2009). Phasing and amplitude of sea-level and climate change during the penultimate interglacial. *Nature Geoscience, 2,* 355–359.

Dutton, A., Carlson, A. E., Long, A. J., Milne, G. A., Clark, P. U., DeConto, R., Horton, B. P., Rahmstorf, S., & Raymo, M. E. (2015). Sea-level rise due to polar ice-sheet mass loss during past warm periods. *Science, 349*. https://doi.org/10.1126/science.aaa4019.

Eiler, J. M., Bergquist, B., Bourg, I., Cartigny, P., Farquhar, J., Gagnon, A., et al. (2014). Frontiers of stable isotope geoscience. *Chemical Geology, 372,* 119–143. https://doi.org/10.1016/j.chemgeo.2014.02.006.

Elderfield, H., Yu, J., Anand, P., Kiefer, T., & Nyland, B. (2006). Calibrations for benthic foraminiferal Mg/Ca paleothermometry and the carbonate ion hypothesis. *Earth and Planetary Science Letters, 250,* 633–649.

Elderfield, H., & Ganssen, G. (2000). Past temperature and d18O of surface ocean waters inferred from foraminiferal Mg/Ca ratios. *Nature, 405,* 442–445.

Elderfield, H., Ferretti, P., Greaves, M., Crowhurst, S., McCave, I. N., Hodell, D. A., et al. (2012). Evolution of ocean temperature and ice volume through the mid-Pleistocene climate transition. *Science, 337* (6095), 704–709.

Englebrecht, A. C., & Sachs, J. P. (2005). Determination of sediment provenance at drift sites using hydrogen isotopes and unsaturation ratios in alkenones. *Geochimica et Cosmochimica Acta, 69,* 4253–4265.

EPICA. (2004). Eight glacial cycles from an Antarctic ice core. *Nature, 429,* 623–628.

Epstein, S., Buchsbaum, R., Lowenstam, H., & Urey, H. C. (1951). Carbonate-water isotopic temperature scale. *Geological Society of America Bulletin, 62*(4), 417–426.

Epstein, S., Buchsbaum, R., Lowenstam, H. A., & Urey, H. C. (1953). Revised carbonate-water isotopic temperature scale. *Geological Society of America Bulletin, 64*(11), 1315–1326.

Emiliani, C. (1955). Pleistocene temperatures. *Journal of Geology, 63,* 538–578.

Galaasen, E. V., Ninnemann, U. S., Irvalı, N., Kleiven, H. K. F., Rosenthal, Y., Kissel, C., et al. (2014). Rapid reductions in North Atlantic deep water during the peak of the last interglacial period. *Science, 343*(6175), 1129–1132.

Gherardi, J. M., Labeyrie, L., Nave, S., Francois, R., McManus, J. F., & Cortijo, E. (2009). Glacial-interglacial circulation changes inferred from 231 Pa/230Th sedimentary record in the North Atlantic Region. *Paleoceanography, 24*, PA2204. https://doi.org/10.1029/2008pa001696.

Ghosh, P., Adkins, J., Affek, H., Balta, B., Guo, W., Schauble, E. A., Schrag, D. P., & Eiler, J. M. (2006). ^{13}C-^{18}O bonds in carbonate minerals: A new kind of paleothermometer. *Geochimica et Cosmochimica Acta, 70*, 1 439–1 456.

Gottschalk, J., Vázquez Riveiros, N., Waelbroeck, C., Skinner, L. C., Michel, E., Duplessy, J. C., et al. (2016). Carbon isotope offsets between benthic foraminifer species of the genus *Cibicides* (*Cibicidoides*) in the glacial sub-Antarctic Atlantic. *Paleoceanography, 31,* 1–20.

Govin, A., Capron, E., Tzedakis, P. C., Verheyden, S., Ghaleb, B., Hillaire-Marcel, C., et al. (2015). Sequence of events from the onset to the demise of the Last Interglacial: Evaluating strengths and limitations of chronologies used in climatic archives. *Quaternary Science Reviews, 129,* 1–36. https://doi.org/10.1016/j.quascirev.2015.09.018.

Gray, W. R., Weldeab, S., Lea, D. W., Rosenthal, Y., Gruber, N., Donner, B., et al. (2018). The effects of temperature, salinity, and the carbonate system on Mg/Ca in *Globigerinoides ruber* (white): A global sediment trap calibration. *Earth and Planetary Science Letters, 482,* 607–620. https://doi.org/10.1016/j.epsl.2017.11.026.

Guihou, A., Pichat, S., Nave, S., Govin, A., Labeyrie, L., Michel, E., et al. (2010). Late slowdown of the Atlantic Meridional overturning circulation during the last glacial inception: New constraint from sedimentary (231 Pa/230Th). *Earth and Planetary Science Letters, 289,* 520–529.

Guihou, A., Pichat, S., Govin, A., Nave, S., Michel, E., Duplessy, J.-C., et al. (2011). Enhanced Atlantic Meridional overturning circulation supports the last glacial inception. *Quaternary Science Reviews, 30,* 1576–1582. https://doi.org/10.1016/j.quascirev.2011.03.017.

Ho, S. L., & Laepple, T. (2016). Flat meridional temperature gradient in the early Eocene in the subsurface rather than surface ocean. *Nature Geoscience, 9*(8), 606.

Hoffman, J. S., Carlson, A. E., Winsor, K., Klinkhammer, G. P., LeGrande, A. N., Andrews, J. T., & Strasser, J. C. (2012). Linking the 8.2 ka event and its freshwater forcing in the Labrador Sea. *Geophysical Research Letters, 39*(18).

Hoffman, J. S., Clark, P. U., Parnell, A. C., & He, F. (2017). Regional and global sea-surface temperatures during the last interglaciation. *Science, 355*(6322), 276–279.

Hönisch, B., Hemming, N. G., Archer, D., Siddall, M., & McManus, J. F. (2009). Atmospheric carbon dioxide concentration across the Mid-Pleistocene transition. *Science, 324,* 1551–1556.

Hönisch, B., Allen, K. A., Russell, A. D., Eggins, S. M., Bijma, J., Spero, H. J., et al. (2011). Planktic foraminifers as recorders of seawater Ba/Ca. *Marine Micropaleontology, 79,* 52–57. https://doi.org/10.1016/j.marmicro.2011.01.003.

Hönisch, B., Allen, K. A., Lea, D. W., Spero, H. J., Eggins, S. M., Arbuszewski, J., et al. (2013). The influence of salinity on Mg/Ca in planktic foraminifers—Evidence from cultures, core-top sediments and complementary δ18O. *Geochimica et Cosmochimica Acta, 121,* 196–213. https://doi.org/10.1016/j.gca.2013.07.028.

Imbrie, J., & Kipp, N. G. (1971). A new micropaleontological method for quantitative paleoclimatology: Application to a late Pleistocene Caribbean Core. In K. K. Turekian (Ed.), *The late Cenozoic glacial ages* (pp. 71–181). Yale University Press.

Jansen, E., & Sjoholm, J. (1991). Reconstruction of glaciation over the 6 Myr from ice-borne deposits in the Norwegian Sea. *Nature, 349,* 600–603.

Kageyama, M., Braconnot, P., Harrison, S. P., Haywood, A. M., Jungclaus, J. H., Otto-Bliesner, B. L., et al. (2018). The PMIP4 contribution to CMIP6—Part 1: Overview and over-arching analysis plan. *Geoscientific Model Development, 11,* 1033–1057. https://doi.org/10.5194/gmd-11-1033-2018.

Kallel, N., Labeyrie, L. D., Juillet-Leclerc, A., & Duplessy, J. C. (1988). A deep hydrological front between intermediate and deep-water masses in the glacial Indian Ocean. *Nature, 333,* 651–655.

Kallel, N., Paterne, M., Duplessy, J. C., Vergnaud-Grazzini, C., Pujol, C., Labeyrie, L., et al. (1997). Enhanced rainfall in the Mediterranean Region during the last sapropel event. *Oceanologica Acta, 20,* 697–712.

Keigwin, L. D., & Swift, S. A. (2017). Carbon isotope evidence for a northern source of deep water in the glacial western North Atlantic. *Proceedings of the National Academy of Sciences, 114*(11), 2831–2835.

Kele, S., Breitenbach, S. F. M., Capezzuoli, E., Meckler, A. N., Ziegler, M., Millan, I. M., et al. (2015). Temperature dependence of oxygen- and clumped isotope fractionation in carbonates: A study of travertines and tufas in the 6–95 °C temperature range. *Geochimica et Cosmochimica Acta, 168,* 172–192. https://doi.org/10.1016/j.gca.2015.06.032.

Khider, D., Huerta, G., Jackson, C., Stott, L. D., & Emile-Geay, J. (2015). A Bayesian, multivariate calibration for *Globigerinoides ruber* Mg/Ca. *Geochemistry, Geophysics, Geosystems, 16,* 2916–2932. https://doi.org/10.1002/2015GC005844.

Kim, J.-H., van der Meer, J., Schouten, S., Helmke, P., Willmott, V., Sangiorgi, F., et al. (2010). New indices and calibrations derived from the distribution of crenarchaeal isoprenoid tetraether lipids: Implications for past sea surface temperature reconstructions. *Geochimica et Cosmochimica Acta, 74,* 4639–4654. https://doi.org/10.1016/j.gca.2010.05.027.

Koç, N., Jansen, E., & Haflidason, H. (1993). Paleoceanographic Reconstructions of surface Ocean conditions in the Greenland, Iceland and Norwegian Seas through the Last 14 Ka based on diatoms. *Quaternary Science Reviews, 12,* 115–140.

Labeyrie, L. D., Duplessy, J. C., & Blanc, P. L. (1987). Variations in mode of formation and temperature of oceanic deep waters over the past 125,000 years. *Nature, 327.*

Labeyrie, L., Duplessy, J. C., Duprat, J., Juillet-Leclerc, A., Moyes, J., Michel, E., et al. (1992). Changes in vertical structure of the North Atlantic Ocean between glacial and modern times. *Quaternary Science Reviews, 11,* 401–413.

Lea, D. W., Mashiotta, T. A., & Spero, H. J. (1999). Controls on magnesium and strontium uptake in planktonic foraminifera determined by live culturing. *Geochimica et Cosmochimica Acta, 63*(16), 2369–2379.

Leduc, G., Sachs, J. P., Kawka, O. E., & Schneider, R. R. (2013). Holocene changes in eastern equatorial Atlantic salinity as estimated by water isotopologues, Earth Planet. *Sci. Lett., 362,* 151–162.

LeGrande, A. N., & Schmidt, G. A. (2006). Global gridded data set of the oxygen isotopic composition in seawater. *Geophysical research letters, 33*(12).

LeGrande, A. N., & Schmidt, G. A. (2011). Water isotopologues as a quantitative paleosalinity proxy. *Paleoceanography, 26*, PA3225. https://doi.org/10.1029/2010pa002043.

Leydet, D. J., Carlson, A. E., Teller, J. T., Breckenridge, A., J. E., Barth, A. M., Ullman, D. J., Sinclair, G., Milne, G. A., Cuzzone, J. K., Caffee, M. W. (2018). Opening of glacial Lake Agassiz's eastern outlets by the start of the Younger Dryas cold period. *Geology, 46*, 155–158. https://doi.org/10.1130/G39501.1.

Lippold, J., Gutjahr, M., Blaser, P., Christner, E., de Carvalho Ferreira, M. L., Mulitza, S., et al. (2016). Deep water provenance and dynamics of the (de) glacial Atlantic meridional overturning circulation. *Earth and Planetary Science Letters, 445*, 68–78.

Lisiecki, L. E. & Raymo, M. E. (2005). A Pleiocene-Pleistocene stack of 57 globally distributed d^{18}O records. *Paleoceanography, 20*. https://doi.org/10.1029/2004PA001071.

Lombard, F., Labeyrie, L., Michel, E., Spero, H. J., & Lea, D. W. (2009). Modelling the temperature dependent growth rates of planktic foraminifera. *Marine Micropaleontology, 70,* 1–7.

Lynch-Stieglitz, J., Curry, W. B., & Slowey, N. (1999). A geostrophic transport estimate for the Florida current from the oxygen isotope composition of benthic foraminifera. *Paleoceanography, 14,* 360–373.

Lynch-Stieglitz, J., Adkins, J. F., Curry, W. B., Dokken, T., Hall, I. R., Herguera, J. C., Hirschi, J.l.J.M., Ivanova, E. V., Kissel, C., Marchal, O., Marchitto, T. M., McCave, I. N., McManus, J. F., Mulitza, S., Ninnemann, U., Peeters, F., Yu, E.-F., & Zahn, R. (2007). Atlantic Meridional overturning circulation during the last glacial maximum. *Science, 316*, 66–69. https://doi.org/10.1126/science.1137127.

Lynch-Stieglitz, J., Schmidt, M. W., Gene Henry, L., Curry, W. B., Skinner, L. C., Mulitza, S., et al. (2014). Muted change in Atlantic overturning circulation over some glacial-aged Heinrich events. *Nature Geoscience, 7,* 144–150. https://doi.org/10.1038/ngeo2045.

Malaizé, B., & Caley, T. (2009). Sea surface salinity reconstruction as seen with foraminifera shells: Methods and cases studies. *The European Physical Journal Conferences, 1*, 177–188. https://doi.org/10.1140/epjconf/e2009-00919-6.

Malmgren, B. A., Kucera, M., Nyberg, J., & Waelbroeck, C. (2001). Comparison of statistical and artificial neuronal network techniques for estimating past sea surface temperatures from planktonic foraminifera census data. *Paleoceanography, 16,* 520–530.

Mann, M. E., Bradley, R. S., & Hughes, M. K. (1998). Global-scale temperature patterns and climate forcing over the past six centuries. *Nature, 392*(6678), 779.

Marchitto, T. M., & Broecker, W. S. (2006). Deep water mass geometry in the glacial Atlantic Ocean: A review of constraints from the paleonutrient proxy Cd/Ca. *Geochemistry, Geophysics, Geosystems, 7,* Q12003.

Marchitto, T. M., Curry, W. B., Lynch-Stieglitz, J., Bryan, S. P., Cobb, K. M., & Lund, D. C. (2014). Improved oxygen isotope temperature calibrations for cosmopolitan benthic foraminifera. *Geochimica et Cosmochimica Acta, 130,* 1–11.

Marcott, S. A., Bauska, T. K., Buizert, C., Steig, E. J., Rosen, J. L., Cuffey, K. M., et al. (2014). Centennial-scale changes in the global carbon cycle during the last deglaciation. *Nature, 514,* 616–619.

MARGO Project Members. (2009). Constraints on the magnitude and patterns of ocean cooling at the last glacial maximum. *Nature Geoscience*. https://doi.org/10.1038/NGEO411.

Mashiotta, T. A., Lea, D. W., & Spero, H. J. (1999). Glacial–interglacial changes in Subantarctic sea surface temperature and δ^{18}O-water using foraminiferal Mg. *Earth and Planetary Science Letters, 170*(4), 417–432.

Mathien-Blard, E., & Bassinot, F. (2009). Salinity bias on the foraminifera Mg/Ca thermometry: Correction procedure and implications for past ocean hydrographic reconstructions. *Geochemistry, Geophysics, Geosystems, 10,* Q12011. https://doi.org/10.1029/2008gc002353.

M'boule, D., Chivall, D., Sinke-Schoen, D., Sinninghe Damsté, J. S., Schouten, S., & van der Meer, M. T. (2014). Salinity dependent hydrogen isotope fractionation in alkenones produced by coastal and open ocean haptophyte algae. *Geochimica et Cosmochimica Acta, 130*, 126–135.

McClymont, E. L., Sosdian, S. M., Rosell-Melé, A., & Rosenthal, Y. (2013). Pleistocene sea-surface temperature evolution: Early cooling, delayed glacial intensification, and implications for the mid-Pleistocene climate transition. *Earth-Science Reviews, 123,* 173–193.

McCorkle, D. C., Martin, P., Lea, D. W., & Klinkhammer, G. (1995). Evidence of a dissolution effect on benthic foraminiferal shell chemistry: δ^{13}C, Cd/Ca, Ba/Ca, and Sr/Ca results from the Ontong Java Plateau. *Paleoceanography, 10,* 699–714.

McGregor, H. V., Evans, M. N., Goosse, H., Leduc, G., Martrat, B., Addison, J. A., et al. (2015). Robust global ocean cooling trend for the pre-industrial Common Era. *Nature Geoscience, 8,* 671–677. https://doi.org/10.1038/ngeo2510.

McManus, J. F., Francois, R., Gherardi, J.-M., Keigwin, L. D., & Brown-Leger, S. (2004). Collapse and rapid resumption of Atlantic meridional circulation linked to deglacial climate changes. *Nature, 428,* 834–837.

Mezger, E. M., Nooijer, L. J., Boer, W., Brummer, G. J. A., & Reichart, G. J. (2016). Salinity controls on Na incorporation in Red Sea planktonic foraminifera. *Paleoceanography and Paleoclimatology, 31*(12), 1562–1582.

Montagna, P., McCulloch, M., Douville, E., López Correa, M., Trotter, J., Rodolfo-Metalpa, R., et al. (2014). Li/Mg systematics in scleractinian corals: Calibration of the thermometer. *Geochimica et Cosmochimica Acta, 132,* 288–310. https://doi.org/10.1016/j.gca.2014.02.005.

Montes, C., Cardona, A., Jaramillo, C., Pardo, A., Silva, J. C., Valencia, V., et al. (2015). Middle Miocene closure of the Central American seaway. *Science, 348,* 226–229.

Mulitza, S., Boltovskoy, D., Donner, B., Meggers, H., Paul, A., & Wefer, G. (2003). Temperature: [delta]18O relationships of planktonic foraminifera collected from surface waters. *Palaeogeography, Palaeoclimatology, Palaeoecology, 202,* 143–152. https://doi.org/10.1016/S0031-0182(03)00633-3.

Müller, P. J., Kirst, G., Ruhland, G., Von Storch, I., & Rosell-Melé, A. (1998). Calibration of the alkenone paleotemperature index U 37 K′ based on core-tops from the eastern South Atlantic and the global ocean (60 N-60 S). *Geochimica et Cosmochimica Acta, 62*(10), 1757–1772.

Otto-Bliesner, B. L., Braconnot, P., Harrison, S. P., Lunt, D. J., Abe-Ouchi, A., Albani, S., et al. (2017). The PMIP4 contribution to CMIP6—Part 2: Two interglacials, scientific objective and experimental design for Holocene and Last Interglacial simulations. *Geoscientific Model Development, 10,* 3979–4003. https://doi.org/10.5194/gmd-10-3979-2017.

Ostlund, H. G. (1987). *GEOSECS Atlantic, Pacific, and Indian Ocean Expeditions* (Vol. 7).

PAGES 2 k Consortium. (2013). Continental-scale temperature variability during the past two millennia. *Nature Geoscience, 6,* 339. https://doi.org/10.1038/ngeo1797.

PAGES 2 k Consortium. (2017). A global multiproxy database for temperature reconstructions of the common era. *Scientific Data, 4,* 170088. https://doi.org/10.1038/sdata.2017.88.

Past InterGlacialS Working Group of PAGES. (2016). Interglacials of the last 800,000 years. *Reviews of Geophysics, 54*.

Paul, H. (2002). *Application of novel stable isotope methods to reconstruct paleoenvironments: Compound specific hydrogen isotopes and pore-water oxygen isotopes*. Ph.D. thesis, 149 pp., Swiss Federal Institute of Technology.

Peral, M., Daëron, M., Blamart, D., Bassinot, F., Dewilde, F., Smialkowski, N., et al. (2018). Updated calibration of the clumped isotope thermometer in planktonic and benthic foraminifera. *Geochimica et Cosmochimica Acta, 239,* 1–16. https://doi.org/10.1016/j.gca.2018.07.016.

Petit, J. R., Jouzel, J., Raynaud, D., Barkov, N. I., Barnola, J. M., Basile, I., et al. (1999). Climate and atmospheric history of the past 420,000 years from the Vostok ice core, Antarctica. *Nature, 399,* 429–436.

Prahl, F. G., & Wakeham, S. G. (1987). Calibration of unsaturation patterns in long-chain ketone compositions for paleotemperature assessment. *Nature, 330,* 367–369.

Pisias, N. G., Martinson, D. G., Moore, T. C., Shackleton, N. J., Prell, W. L., Hays, J. D., et al. (1984). High resolution stratigraphic correlation of benthic oxygen isotopic records spanning the last 300,000 years. *Marine Geology, 56,* 119–136.

Railsback, L. B., Gibbard, P. L., Head, M. J., Voarintsoa, N. R. G., & Toucanne, S. (2015). An optimized scheme of lettered marine isotope substages for the last 1.0 million years, and the climatostratigraphic nature of isotope stages and substages. *Quaternary Science Reviews, 111,* 94–106.

Rasmussen, S. O., Bigler, M., Blockley, S. P., Blunier, T., Buchardt, S. L., Clausen, H. B., et al. (2014). A stratigraphic framework for abrupt climatic changes during the last glacial period based on three synchronized Greenland ice-core records: Refining and extending the INTIMATE event stratigraphy. *Quaternary Science Reviews, 106,* 14–28.

Raymo, M. E., Oppo, D. W., & Curry, W. (1997). The mid-Pleistocene climate transition: A deep sea carbon isotopic perspective. *Paleoceanography, 12*(4), 546–559.

Renssen, H., Mairesse, A., Goosse, H., Mathiot, P., Heiri, O., Roche, D. M., et al. (2015). Multiple causes of the Younger Dryas cold period. *Nature Geoscience, 8*(12), 946–949.

Rohling, E., & Bigg, G. (1998). Paleosalinity and $\delta^{18}O$: A critical assessment. *Journal Geophysical Research, 103,* 1307–1318. https://doi.org/10.1029/97JC01047.

Rohling, E. J. (2000). Paleosalinity: Confidence limits and future applications. *Marine Geology, 163,* 1–11.

Rohling, E. J. (2007). Progress in paleosalinity: Overview and presentation of a new approach. *Paleoceanography, 22*, PA3215. https://doi.org/10.1029/2007pa001437.

Rohling, E. J., Foster, G. L., Grant, K., Marino, G., Roberts, A. P., Tamisiea, M. E., et al. (2014). Sea-level and deep-sea-temperature variability over the past 5.3 million years. *Nature, 508,* 477–482.

Rohling, E. J., Marino, G., & Grant, K. M. (2015). Mediterranean climate and oceanography, and the periodic development of anoxic events (sapropels). *Earth-Science Reviews, 143,* 62–97.

Rosell-Melé, A., & Prahl, F. G. (2013). Seasonality of UK′ 37 temperature estimates as inferred from sediment trap data. *Quaternary Science Reviews, 72,* 128–136.

Rosenthal, Y., Boyle, E. A., & Slowey, N. (1997). Temperature control on the incorporation of magnesium, strontium, fluorine, and cadmium into benthic foraminiferal shells from Little Bahama Bank: Prospects for thermocline paleoceanography. *Geochimica et Cosmochimica Acta, 61*(17), 3633–3643.

Rossignol-Strick, M., Nesteroff, W., Olive, P., & Vergnaud-Grazzini, C. (1982). After the deluge: Mediterranean stagnation and sapropel formation. *Nature, 295*(5845), 105.

Saenger, C., Affek, H. P., Felis, T., Thiagarajan, N., Lough, J. M., & Holcomb, M. (2012). Carbonate clumped isotope variability in shallow water corals: Temperature dependence and growth-related vital effects. *Geochimica et Cosmochimica Acta, 99,* 224–242.

Schmidt, G. A., Bigg, G. R., & Rohling, E. J. (1999). Global Seawater oxygen-18 database—v1.21. Available at http://data.giss.nasa.gov/o18data/.

Schmidt, G. A. (1999). Error analysis of paleosalinity calculations. *Paleoceanography, 14,* 422–429.

Schmittner, A., Bostock, H. C., Cartapanis, O., Curry, W. B., Filipsson, H. L., Galbraith, E. D., et al. (2017). Calibration of the carbon isotope composition ($\delta^{13}C$) of benthic foraminifera. *Paleoceanography, 32,* 512–530.

Schauble, E. A., Ghosh, P., & Eiler, J. M. (2006). Preferential formation of 13C–18O bonds in carbonate minerals, estimated using first-principles lattice dynamics. *Geochimica et Cosmochimica Acta, 70*(10), 2510–2529.

Schouten, S., Hopmans, E. C., Schefuß, E., & Damste, J. S. S. (2002). Distributional variations in marine crenarchaeotal membrane lipids: A new tool for reconstructing ancient sea water temperatures? *Earth and Planetary Science Letters, 204*(1–2), 265–274.

Schouten, S., Ossebaar, J., Schreiber, K., Kienhuis, M. V. M., Langer, G., Benthien, A., et al. (2006). The effect of temperature, salinity and growth rate on the stable hydrogen isotopic composition of long chain alkenones produced by Emiliania huxleyi and Gephyrocapsa oceanica. *Biogeosciences, 3,* 113–119.

Schouten, S., Hopmans, E. C., & Damsté, J. S. S. (2013). The organic geochemistry of glycerol dialkyl glycerol tetraether lipids: A review. *Organic Geochemistry, 54,* 19–61.

Schrag, D. P., Adkins, J. F., McIntyre, K., Alexander, J. L., Hodell, D. A., Charles, C. D., et al. (2002). The oxygen isotopic composition of seawater during the last glacial maximum. *Quaternary Science Reviews, 21*(1–3), 331–342.

Shackleton, N. J. (1967). Oxygen isotope analysis and Pleistocene temperature reassessed. *Nature, 2151,* 15–17.

Shackleton, N. J. (1974). Attainment of isotopic equilibrium between ocean water and benthonic foraminifera genus Uvigerina: Isotopic changes in the ocean during the last glacial. dans Les méthodes quantitatives d'étude des variations du climat au cours du Pleistocène CNRS, Gif-sur-Yvette, pp. 203–209.

Shakun, J. D., Clark, P. U., He, F., Marcott, S. A., Mix, A. C., Liu, Z., et al. (2012). Global warming preceded by increasing carbon dioxide concentrations during the last deglaciation. *Nature, 484,* 49–54.

Shanahan, T. M., Hughen, K., McKay, N. P., Overpeck, J., Scholz, C. A., Gosling, W. D., et al. (2016). CO_2 and fire influence tropical ecosystem stability in response to climate change. *Scientific Reports, 6,* 29587.

Sicre, M. A., et al. (2005). Mid-latitude southern Indian ocean response to northern hemisphere Heinrich events. *Earth and Planetary Science Letters, 240*(3–4), 724–731.

Thierstein, H. R., Geitzenauer, K. R., Molfino, B., & Shackleton, N. J. (1977). Global synchroneity of late Quaternary coccolith datum levels validation by oxygen isotopes. *Geology, 5*(7), 400–404.

Thornalley, D. J. R., Oppo, D. W., Ortega, P., Robson, J. I., Brierley, C., Davis, R., et al. (2018). Anomalously weak Labrador Sea convection and Atlantic overturning during the past 150 years. *Nature, 556,* 227–232.

Tierney, J. E., & deMenocal, P. B. (2013). Abrupt shifts in Horn of Africa hydroclimate since the Last Glacial Maximum. *Science, 342* (6160), 843–846.

Tierney, J. E., & Tingley, M. P. (2018). BAYSPLINE: A new calibration for the alkenone paleothermometer. *Paleoceanography and Paleoclimatology, 33,* 281–301. https://doi.org/10.1002/2017PA003201.

Tierney, J. E., & Tingley, M. P. (2014). A Bayesian, spatially-varying calibration model for the TEX_{86} proxy. *Geochimica et Cosmochimica Acta, 127,* 83–106.

Vázquez Riveiros, N., Govin, A., Waelbroeck, C., Mackensen, A., Michel, E., Moreira, S., et al. (2016). Mg/Ca thermometry in planktic foraminifera: Improving paleotemperature estimations for *G. bulloides* and *N. pachyderma* left. *Geochemistry, Geophysics, Geosystems, 17,* 1249–1264.

Vázquez Riveiros, N., Waelbroeck, C., Skinner, L. C., Duplessy, J. C., McManus, J. F., Kandiano, E. S., et al. (2013). The 'MIS11 paradox' and ocean circulation: Role of millennial scale events. *Earth and Planetary Science Letters, 371–372,* 258–268.

Vázquez Riveiros, N., Waelbroeck, C., Skinner, L. C., Roche, D. M., Duplessy, J. C., & Michel, E. (2010). Response of South Atlantic deep waters to deglacial warming during terminations V and I. *Earth and Planetary Science Letters, 298,* 323–333.

Waelbroeck, C., Labeyrie, L., Duplessy, J. C., Guiot, J., Labracherie, M., Leclaire, H., et al. (1998). Improving past sea surface temperature estimates based on planktonic fossil faunas. *Paleoceanography, 13,* 272–283.

Waelbroeck, C., Duplessy, J. C., Michel, E., Labeyrie, L., Paillard, D., & Duprat, J. (2001). The timing of the last deglaciation in North Atlantic climate records. *Nature, 412,* 724–727.

Weijers, J. W., Schouten, S., Spaargaren, O. C., & Damsté, J. S. S. (2006). Occurrence and distribution of tetraether membrane lipids in soils: Implications for the use of the TEX86 proxy and the BIT index. *Organic Geochemistry, 37*(12), 1680–1693.

Weldeab, S., Lea, D. W., Schneider, R. R., & Andersen, N. (2007). 155,000 years of West African monsoon and ocean thermal evolution. *Science, 316,* 1303–1307.

Wiersma, A. P., & Renssen, H. (2006). Model–data comparison for the 8.2 ka BP event: Confirmation of a forcing mechanism by catastrophic drainage of Laurentide Lakes. *Quaternary Science Reviews, 25*(1–2), 63–88.

Wit, J. C., De Nooijer, L. J., Wolthers, M., & Reichart, G. J. (2013). A novel salinity proxy based on Na incorporation into foraminiferal calcite. *Biogeosciences, 10*(10), 6375–6387.

Wolhowe, M. D., Prahl, F. G., Probert, I., & Maldonado, M. (2009). Growth phase dependent hydrogen isotopic fractionation in alkenone-producing haptophytes. *Biogeosciences, 6,* 1681–1694.

Yu, E.-F., Francois, R., & Bacon, M. (1996). Similar rates of modern and last-glacial ocean thermohaline circulation inferred from radiochemical data. *Nature, 379,* 689–694.

Zachos, J. C., Shackleton, N. J., Revenaugh, J. S., Pälike, H., & Flower, B. P. (2001). Climate response to orbital forcing across the oligocene-miocene boundary. *Science, 292,* 274–278.

Zachos, J. C., Dickens, G. R., & Zeebe, R. E. (2008). An early Cenozoic perspective on greenhouse warming and carbon-cycle dynamics. *Nature, 451,* 279–283. https://doi.org/10.1038/nature06588.

Zweng, M. M., Reagan, J. R., Antonov, J. J., Locarnini, R. A., Mishonov, A. V., Boyer, T. P., Garcia, H. E., Baranova, O. K., Johnson, D. R., Seidov, D., & Biddle, M. M. (2013). *World Ocean Atlas 2013, Volume 2: Salinity*. In S. Levitus & A. V. Mishonov (Eds.), NOAA Atlas NESDIS 74, p. 39.

Climate Evolution on the Geological Timescale and the Role of Paleogeographic Changes

22

Frédéric Fluteau and Pierre Sepulchre

Throughout geological time, major climate changes have marked the history of the Earth (Fig. 22.1). Although paleoclimate markers provide us with the broad outlines of these changes, their causes could be manifold as feedback mechanisms occur between the different compartments of the climate system. In a system where the solid and fluid envelopes are closely linked, understanding the evolution of Earth's climates at the scale of geologic time involves knowing its paleogeographic history. Within this context, climate modelling is presented as a well-adapted tool to help to understand the factors causing climate change over geological time. However, modelling a continuous climate evolution over million-year timescales is out of reach, as it would require a detailed and reliable knowledge of the model boundary conditions, e.g. the location of the continents, the topography, the bathymetry as well as the chemical composition of the atmosphere. Prior to the recent Quaternary period, uncertainties generally tend to increase regarding these conditions, and our knowledge becomes increasingly fragmentary the further into the past we go. Moreover, even with a perfect knowledge of these conditions, several million years simulations are beyond the computing capabilities of the supercomputers and the codes used today to simulate climate. This methodological dilemma is routinely overcome by means of steady-state simulations, called "snapshot experiments", which simulate the response of the climate system to particular boundary conditions, and which require only a few thousand years of simulation, corresponding to the time needed to achieve equilibrium for all compartments of the climate system. The first step is to establish the boundary conditions so as to perform a "contextual" simulation of a large geologic time interval (for example, the late Miocene). One can then study the impact of paleogeographic or geochemical changes within this interval via sensitivity experiments in which, for example, a mountain range is uplifted or lowered, an ocean passage is opened or closed, the chemical composition of the atmosphere is changed or the orbital parameters of the Earth are altered in line with information provided by the geological, geophysical and geochemical data.

In the first part of this chapter, we present the broad outlines of the climate history of the earth and in the second part, we provide examples of how the direct and indirect couplings between the different envelopes, solid, liquid and gaseous, can be studied through modelling and show how they contribute to the explanation of the climate history of the Earth over long time scales.

The Evolution of Climate Over the Past 4.54 Billion Years

Although the Precambrian (4.54–0.54 Ga) represents 88% of the Earth's history we only have a very fragmentary knowledge of the climate during this period. There are very few records of the first 900 million years of the Earth's history (4.5–3.6 Ga). The oldest geological formations discovered in northwestern Canada (Acasta Gneiss) and in Greenland (Isua Greenstone Belt) are dated at 4 Ga and 3.8 Ga respectively (Valley 2006) but do not provide any climate constraints. However, the discovery of zircons in Australia in the Archean metaconglomerates of Mount Narryer and Jack Hills, dated at 4.4 Ga, is evidence of the existence of the first granitic proto-continents (sensu lato). The oxygen isotopic signature ($\delta^{18}O$) of these zircons (5–7‰) confirms the presence of liquid water, and certainly of oceans, 150 million years after the formation of the Earth. Between 4.3 and 2.8 Ga (Archean), the Earth's atmosphere consisted of a mixture of nitrogen and greenhouse gases, notably carbon dioxide and methane. There was no oxygen.

F. Fluteau (✉)
Université de Paris, Institut de Physique du Globe de Paris, CNRS, 75005 Paris, France
e-mail: fluteau@ipgp.fr

P. Sepulchre
Laboratoire des Sciences du Climat et de l'Environnement, CNRS-CEA-Université de Versailles Saint Quentin en Yvelines-Université Paris-Saclay, Gif-sur-Yvette, France

G. Ramstein et al. (eds.), *Paleoclimatology*, Frontiers in Earth Sciences,
https://doi.org/10.1007/978-3-030-24982-3_22

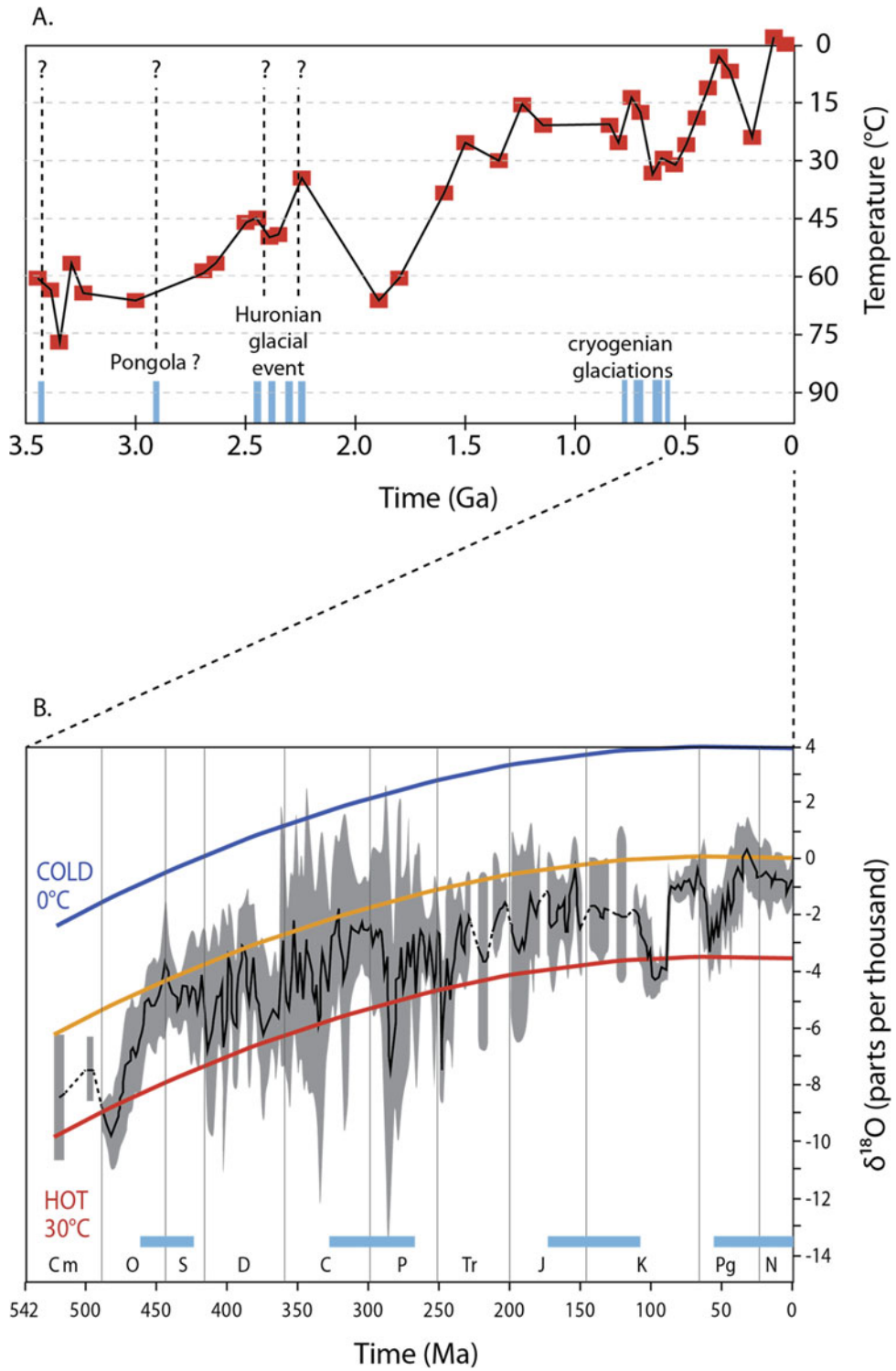

Fig. 22.1 **a** Estimates of water temperature calculated using maximum $\delta^{18}O$ chert value per 50 Ma age intervals, adapted from Tartèse et al. (2017). The secular trend shows an overall cooling of Earth through geological time. Blue bars indicate episods of widespread glaciation. Dashed lines, and question marks show the apparent contradiction between poorly dated warm temperature estimates and the relatively short glacial events. **b** Evolution of $\delta^{18}O$ data for low-latitude planktonic foraminifera younger than 118 Ma and brachiopods older than 117 Ma. The temperature curves were calculated using a baseline value for Phanerozoic seawater which mimics the present day 0‰ SMOW. Grey shading indicate 2-sigma intervals. Blue bars indicate the presence of ice caps. Adapted from Veizer and Prokoph (2015)

There are big uncertainties regarding Earth's surface temperature during the Archean, as deduced from isotopic measurements of oxygen in carbonate rocks, with values ranging from 26 to 85 °C (Knauth and Lowe 2003; Robert and Chaussidon 2006; De Wit and Furnes 2016). However, these values may be inaccurate due to our lack of understanding of the average $\delta^{18}O$ of the seawater at that time. Indeed, the average ^{18}O concentration in the oceans is determined by ^{18}O exchanges with oceanic crustal basalts during the circulation of seawater in the hydrothermal systems of the ocean ridges. There is no evidence to indicate that it was within the range of values observed much more recently. Measurements of the isotopic ratio of oxygen and silicon in cherts (siliceous rocks) suggest a paleotemperature of 60–80 °C (Fig. 22.1a). However, these values may be distorted by the contributions of the hydrothermal systems lining the oceanic crust at that time. To overcome these difficulties, new isotopic tools, called the clumped isotopes, have been developed. A promising paleothermometer, based not on the relative abundance of one single isotope to another, but on the abundance ratio of isotopologues with multiple rare isotopes relative to the expected quantity for a stochastic distribution of isotopes within a $(^{13}C^{18}O^{16}O_2)^{2-}$ group (Eiler 2007; Bonifacie et al. 2017). The thermodynamic variable measured and noted Δ_{47} is therefore based on the substitution of carbon and oxygen isotopes within the carbonate ions, which is a function of the temperature at which these carbonates formed. Although uncertainties remain (Daëron et al. 2019), this method does not require knowledge of the average isotopic composition of the ocean and can therefore be applied to the oceans of the Archean. Although the evolution of temperature during the Archean is up for debate, it remained within a range of values able to sustain liquid water on the Earth's surface. This is an essential condition for the development of life which could have started as early as 3.77 Ga (Dodd et al. 2017).

Maintaining a temperature conducive to the development of life on Earth was by no means guaranteed within the context of the "young Sun". In fact, the radiation emitted by a young star is weak, gradually increasing throughout its life. In the case of the Sun, the solar radiation is estimated to have been 30% lower 4 Ga ago than it is today, and 20% lower 3 Ga ago. In these radiation conditions, maintaining a temperature that would support the presence of liquid water on the surface of the globe during the Archean would have been impossible without a powerful greenhouse effect.

Let's examine the data to determine the constraints on the chemical composition of the atmosphere. Precipitation of sodium bicarbonate in the Archean oceans around 3.3 Ga argues in favour of a partial CO_2 pressure of between 1.4 and 15% of the atmospheric pressure of the time (Lowe and Tice 2004), and so lower than the estimates by the models. However, the chemical composition of the Precambrian atmosphere is the subject of intense debate because a high partial pressure of CO_2, necessary to counter the "young sun" effect, would have strongly acidified precipitations, causing the pH to fall to about 3.7, and cause a particularly intense chemical weathering of the rocks, which does not seem to be the case for the 3.5–3 Ga period (Kasting and Howard 2006). Another gas, methane, may therefore have played an important role. In the modern atmosphere, the residence time of methane is around eight years because it is quickly oxidized. However, in an atmosphere devoid of oxygen or at very low partial pressures ($<10^{-5}$ bar) as in the Archean, this residence time is considerably longer. Methane can thus accumulate in the atmosphere and significantly increase the greenhouse effect. We know of two sources of methane at that time: methanogenic organisms and the serpentinization of ultramafic rocks on the ocean floor. Taking the results of the work of Haqq-Mishra et al. (2008), with 1% methane in the atmosphere, the CO_2 partial pressure required to maintain the Earth at 30 °C drops to about 10^{-3} bar. The contribution of methane to the greenhouse effect is therefore extremely effective. Even if atmospheric concentrations remain poorly constrained, a CH_4 to CO_2 ratio greater than 0.2 is impossible (Zerkle et al. 2012).

Traces of several glacial periods, dated between 3.5 and 2.2 Ga, have been discovered in South Africa, Europe, North America and Australia. The oldest glaciation was discovered in South Africa within the Barberton Greenstone Belt. It was dated at about 3.4–3.5 Ga (De Wit and Furnes 2016) and in a latitude band between 20° and 40° (Biggin et al. 2011). It was followed by another glacial episode at 2.9 Ga discovered in units of the Mozaan geological group in South Africa (Young et al. 1998). The end of the Archean and the beginning of the Proterozoic produced the Huron glaciation, originally discovered in the province of Ontario in Canada, but identified in South Africa and Australia. It is actually a succession of three or four glacial events, dated between 2.45 and 2.2 Ga (Caquineau et al. 2018). One of these glacial episodes is demonstrated by the presence of glacial sediment at low latitudes and at low altitude suggesting that the Earth could have been completely frozen at this time. These glaciations are associated with a major event in the history of the Earth: the oxygenation of the atmosphere and of the shallow oceans.

The next billion years (between 1.85 and 0.85 Ga) is often referred to as the 'boring billion' due to the apparent climatic and environmental stability. Indeed, isotopic measurements of carbon ($\delta^{13}C$) show no major disturbance of the carbon cycle and the absence of any known glacial traces during this period suggest (but do not prove) that the Earth's climate had stabilized into a hot configuration. This climate stability ended with the Neoproterozoic. During this time, the Earth experienced three periods of glaciation: the Sturtian glaciation from 717 to 659 Ma, the Marinoan glaciation

from 645 to 636 Ma and finally the Gaskiers glaciation around 582 Ma. Marine glacial sedimentary formations at low latitudes indicate that during the Sturtian and Marinoan glaciations, the Earth was completely glaciated: these are the famous episodes of Snowball Earth (Hoffman et al. 2017). Directly on top of these glacial sedimentary formations we find carbonate formations (currently, carbonate production is mainly located in warm tropical seas). The rapidity of this transition between glacial and carbonate formations (on the scale of geological time) is a peculiarity in the climate history of the Earth. Numerous studies have been undertaken in recent years to understand the entry and exit modalities of these glacial phases (Hoffman et al. 2017; and Chap. 5).

The Precambrian/Cambrian boundary (542 Ma) marked a new turning point in the Earth's climate history. According to oxygen isotopic ratio measurements, the mean global temperatures of the Phanerozoic climate became stable within a range comparable to that of the modern day (Fig. 22.1b). This period was punctuated by three major glaciations: one at the end of the Ordovician (around 443 Ma), during the Permo-Carboniferous (between 335 and 260 Ma) and at the end of the Cenozoic (the last 40 Myr). Traces of the Ordovician glaciation are found in Africa, particularly in the Sahara and South Africa but also on the Arabian peninsula. This glaciation is estimated to have lasted a little more than one million years, and is marked by at least three glacial cycles alternating with interglacial periods (Ghienne et al. 2013). The glaciation is associated with a major disruption in the carbon cycle but also with one of the five mass extinctions of the Phanerozoic when close to 86% of the marine benthic and planktonic species died out. During the Silurian and Devonian periods, the Earth experienced a warmer global climate. Carbonate platforms, which develop in warm seas, stretched from 45° S to 60° N. An expansion of this scale would never be seen again (Copper and Scotese 2003). The strong latitudinal expansion of these carbonate platforms suggests weak latitudinal thermal gradients. The widespread evaporite facies suggest a semi-arid to arid climate at subtropical latitudes.

The Devonian period is also marked by the colonization of land surfaces by life. The first forests, made up of *Archeopteris,* appeared at the end of the Devonian at around 370 Ma (Meyer-Berthaud et al. 1999). During the Silurian, some plants, including bryophites, were the pioneers of this land colonization that, until then, had been deserted and barren. The emergence of the continental biosphere affected the carbon cycle and probably influenced the climate of the Earth (Le Hir et al. 2011). The end of the Devonian and the beginning of the Carboniferous mark the return of glacial periods and a more contrasted climate latitudinal gradient. The Earth then underwent a glacial period which started in the Carboniferous (~335 Ma) and which ended with the Permian around 260 Ma (Montañez and Poulsen 2013). This glaciation, which lasted 70 Ma, was punctuated by several phases of advance and withdrawal of the ice sheets. This is the longest and most important glacial episode of the entire Phanerozoic. Sedimentary formations, striated floors and 'dropstones' (pieces of rock deposited onto unconsolidated marine sediments by icebergs when they melted) are proof of the presence of ice in South America, southern and eastern Africa, on the Arabian peninsula, the Indian subcontinent and Australia, that is, the whole southern part of the Gondwana continent then located in the mid and high latitudes of the southern hemisphere.

At the end of the Carboniferous, while a cold climate developed at the high and mid latitudes of the southern hemisphere, paleoclimatic indicators indicate that there was a tropical and humid climate over a part of Europe and North America, then located close to the equator. At this time, there was a strong contrast between the climates of low and high latitudes.

These conditions disappeared in favor of a warmer and dryer climate during the Late Permian. Wet climates were limited to narrow bands around the equator and in the mid-latitudes. The Paleozoic era ended with two mass extinctions, the first at the end of the "Guadalupian" (~258 Ma) and the second at the Permo-Trias boundary (~251 Ma) (Bond et al. 2010; Bond and Wignall 2014). This last crisis is the most important mass extinction of the Phanerozoic with the disappearance of 90% of the fauna and flora (Erwin 1994). During this crisis, climate indicators show significant warming, a disruption of the carbon cycle as well as oceanic anoxia. An exceptionally high level of volcanic activity leading to the contemporaneous formation of the Siberian large igneous province is considered to be the main cause of the extinction. Although the relationship between volcanic activity and this crisis is not fully understood, it should be noted that every ecological crisis of the Phanerozoic, whatever its magnitude, occurred simultaneously with the establishment of a large basaltic province through particularly intense volcanic activity. After the Permo-Trias mass extinction, a warm global climate became established during the Triassic. During the Late Triassic, sedimentary facies in North America suggest a strong seasonal precipitation caused by "mega-monsoon" patterns (Dubiel et al. 1991; Bahr et al. 2020). Subsequently, the Earth experienced a colder global climate during the Jurassic. The presence of ice caps at high latitudes has been suggested, but this hypothesis is based on assumptions that have still to be confirmed (Dromart et al. 2003).

Until the mid-1990s, the Cretaceous (145–65 Ma) was described as a period with a uniformly warm global climate, but the accumulation of data from different climate indicators has completely changed our notions of the climate of this period. The beginning of the Cretaceous period was cold, probably with ice sheets, but experienced a particularly warm period towards the middle of the Cretaceous, before cooling towards the end of the period. On top of this long-term trend,

rapid climate variability was superimposed. The isotopic measurements of the oxygen in carbonate tests of planktonic foraminifera and fish teeth provide an estimate of the paleotemperature of the surface waters of the oceans. These data, as well as studies carried out in continental areas, on palynomorphs, for example, reflect the climate variability of this period (Ladant and Donnadieu 2016). Thus, $\delta^{18}O$ measurements show that the Turonian had a particularly hot climate, with sea surface temperatures of between 34 and 37 °C. However, the $\delta^{18}O$ measurements also show the existence of a glaciation event lasting less than 200,000 years (Bornemann et al. 2008). The Cretaceous ended with a rapid cooling just before the major mass extinction of the Cretaceous-Tertiary boundary at 66 Ma, during which nearly 60% of the species on Earth died out. As for the other crises of the Phanerozoic, this crisis is synchronous with the establishment of a large basaltic province, the Deccan traps in India, but also, with another event, the fall of an extraterrestrial body into the Gulf of Mexico.

After this crisis, the Earth entered a warm period during which signs of glaciation disappeared. This period was punctuated by the thermal maximum at the Palaeocene-Eocene boundary (55 Ma) (Zachos et al. 2001). This was a rapid transient event (at the geological time scale), lasting about 300 ka, marked by an abrupt increase in temperatures (considered as the best analogue to current global warming). Tropical flora, but also turtles, crocodiles, and many mammals were discovered on the Ellesmere and Axel Heiberg islands in northern Canada.

As early as the Late Eocene (~50 Ma), the Earth experienced gradual cooling with the onset of a new glacial period around 40 Ma marked by a first stage of development of the Antarctic ice cap, corresponding probably to the appearance of glaciers in the Trans-Antarctic chain. This ice cap grew quickly and reached the coast, as evidenced by glacial sediments found off the Antarctic continent, dating from the Eocene-Oligocene boundary (~34 Ma). Numerous measurements of the isotopic composition of oxygen in the carbonate tests of benthic foraminifera in sediments collected at different points around the globe confirm a consistent cooling during the Eocene. At the Eocene-Oligocene boundary, a significant and rapid cooling of the ocean bottom waters occurred, estimated at about 6 °C (Hren et al. 2013). Henceforth, the isotopic ratio of strontium increased significantly in response to intensified continental erosion.

During the Lower Miocene (23–15 Ma), the global trend was a slight warming interspersed with brief cooling episodes. Around 14 Ma, rapid cooling led to a new phase of development of the Antarctic ice sheet. This climate trend accelerated during the Upper Miocene and the Pliocene. The development of an ice cap on Greenland probably dates from the Upper Miocene or the Pliocene, but a high probability of sea ice on the Arctic Ocean starting from the climate transition of the Middle Miocene is suggested by the sedimentary facies observed in the Arctic Ocean. This cold climate impacts on the high latitudes of both hemispheres and provides the necessary conditions for the rapid glacial/interglacial fluctuations during the Pleistocene (but does not trigger them).

Paleoclimate indicators can be used to trace the evolution of the Earth's climate, so as to gradually refine its contours and to observe rapid fluctuations superimposed on longer-term trends. However, there are areas of uncertainty (as will probably always be the case), especially for the oldest periods. The causes and mechanisms of these climate changes at the scale of geological time are manifold. Data collected in the field allow us to document this evolution with increasing accuracy, but it is impossible to isolate with certainty the specific cause or causes of these climate disruptions. Since the 1970s, numerical modeling of climates has been used, in addition to data, to test the sensitivity of the climate to different forcings and to try to reproduce numerically the climate changes observed in the field. Over long time scales, paleogeographic changes brought about by plate tectonics have shaped the face of the Earth (Volume 1, Chap. 2) and are a major forcing of the Earth's climate history through their direct effects on atmospheric and oceanic circulation. We will also see the indirect effects of paleogeographic changes induced by feedback mechanisms, in particular on the regulation of the partial pressure of CO_2, another major contributor to the climate system.

Some Consequences of Paleogeographic Changes on the Earth's Climate

Continental Drift

Continental drift leads to changes in the latitudinal and longitudinal distribution of emerged lands with various consequences for climate. The main ones are: changes in the distribution of solar radiation received by the continents; changes in the atmospheric dynamics by the uplift or collapse of mountain ranges or during the formation or break-up of supercontinents; changes in ocean dynamics during the opening or closing of basins or ocean passages (also called seaways), and also indirect effects such as changes in weathering fluxes that impact on the carbon cycle (Donnadieu et al. 2004). In the Upper Permian (~260 Ma), paleoclimate indicators suggest that a warm, dry climate developed over a large part of Gondwana (southern hemisphere) located between the narrow rainy equatorial band and the narrow temperate mid-latitude band, below the theoretical subsidence zone of the Hadley cell. Several numerical climate simulations made it possible to develop

hypotheses to explain the various mechanisms involved. Fluteau et al. (2001) suggested that high seasonality in Gondwana was typical at mid and high latitudes due to the low heat capacity of the continents, and that monsoon-type atmospheric circulation marked the eastern side of the supercontinent. Other modeling studies (Kiehl and Shields 2005; Shields and Kiehl 2018) have confirmed these results, even suggesting that these characteristics continued despite a high atmospheric concentration of carbon dioxide (3550 ppm). Climate modeling has also looked at the consequences of supercontinent break-up. By simulating the climate response to paleogeographic changes between the Triassic and Cretaceous, it was suggested, for example, that the break-up of Gondwana and Laurasia annihilated the continental effect, preventing the development of large desert bands in the subtropics (Fig. 22.2), and favoring the establishment of wet conditions contemporaneous to the diversification of flowering plants (Angiosperms) (Fluteau et al. 2007; Chaboureau et al. 2014).

Paleogeographic Changes and Ocean Circulation

The oceans are a major component of the climate system. They ensure, in part, the transport of heat from the low to the high latitudes, particularly in modern times, via the Atlantic Meridional Overturning Circulation (AMOC). At the geological time scale, large changes in ocean basin geometry have controlled the dynamics of water bodies and the associated heat and salt fluxes by opening or closing interoceanic connections. This is, for example, the case of the opening of the South Atlantic Ocean which began 135 million years ago. Exchanges between the South Atlantic and Central Atlantic oceans have only happened since 100 Ma (Murphy and Thomas 2013; Granot and Dyment 2015) and led to changes in the global ocean circulation as shown by the isotopic data of neodymium and oxygen (e.g. Donnadieu et al. 2016). Although there is no consensus on the exact evolution of Cretaceous ocean circulation, taking these paleogeographic changes into account in numerical simulations suggests that the establishment of a sea passage between the South Atlantic and Central Atlantic played an important role in the formation and oxygenation of deep waters on a global scale (Poulsen et al. 2003).

The Cenozoic is also characterized by large-scale climate change, including global cooling and reorganization of ocean circulation. Apart from India and Australia, the drift in latitude of most of the continents is small over the last 60 million years, and cannot by itself explain the temperature changes implicit in the data. However, several openings and closings of ocean passages have altered the exchanges between water bodies and the associated heat flows. At the beginning of the Cenozoic, the distribution of the continents meant that the Pacific, Atlantic and Indian basins were connected in the tropical band via three open ocean passages: The Central American seaway (CAS), the east-Tethys seaway, and the Indonesian passage. Numerical simulations suggest that this interoceanic connection operated from east to west at the surface, with the formation of the circum-equatorial current (CEC). Conversely, in the southern hemisphere, the Drake and Tasmanian passages separating South America and Australia from Antarctica, respectively, were closed, preventing the formation of a strong Antarctic Circumpolar Current (ACC). At the Eocene-Oligocene transition, the circumpolar Antarctic maritime passages gradually opened, widened and deepened. This episode would be followed by the gradual closure of tropical passages in the Middle Miocene (15 Ma).

Numerical simulations show that both events contributed to the establishment of deep water formation in the northern hemisphere and to the cooling of the southern hemisphere (see Sijp et al. 2014 for an overview). Since the late 1970s, the establishment of the ACC in response to the opening of the marine passages of the southern hemisphere has been advanced as a cause of the freeze-up of the Antarctic (Kennett 1977). Indeed, the opening of the Tasman Sea and the oceanic exchanges through the Drake Passage in southern South America fostered the thermal isolation of Antarctica. Recent studies show that the paleogeographic configuration,

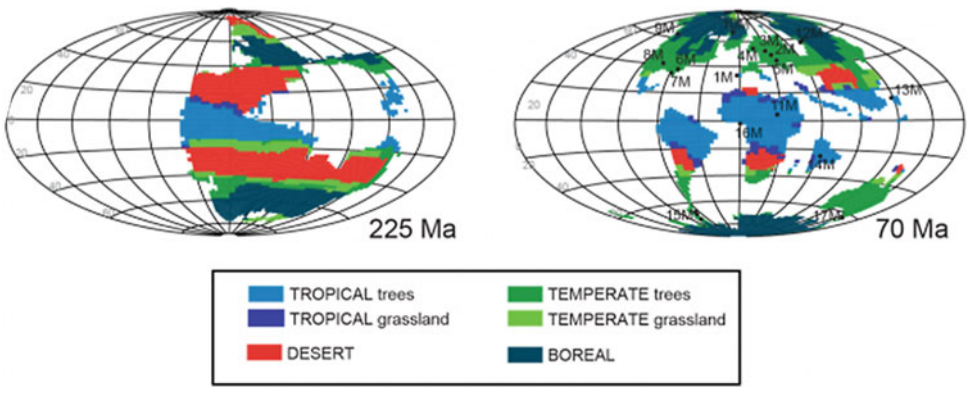

Fig. 22.2 Simulated Jurassic and Cretaceous bioclimatic zones. The numbered points indicate the localisation of angiosperm fossils. Adapted from Chaboureau et al. (2014)

in particular the bathymetry, is decisive to correctly quantify the cooling related to the change of configuration of the seaways, but also that the freeze-up of the Antarctic requires, in addition to paleogeographic changes, a significant decrease of the atmospheric partial pressure of carbon dioxide from 1160 to 560 ppm (Lefebvre et al. 2012).

Numerous modelling studies have also focused on the impact of the central American seaway (CAS) on climate. Early works by Haug and Tiedemann (1998) had suggested that the closure of the isthmus during the early Pliocene led to a reorganization of the Atlantic thermohaline circulation. Specifically, the authors inferred that the shallowing and closure of the CAS intensified the Gulf stream and strengthened deep water formation in the northern Atlantic. More importantly these authors suggested that warmer SST induced by this strengthening of the Gulf stream increased atmospheric moisture content, and ultimately favored the Greenland ice sheet growth. Later, numerous model experiments with open CAS with various depth and width have been carried out (see Zhang et al. 2012; Sepulchre et al. 2014 for reviews). Most of the model indeed showed intensified AMOC with the seaway closure, but models run with explicit ice sheet modelling failed to demonstrate that the closure had a significant impact on the Greenland icecap onset (Lunt et al. 2008; Tan et al. 2017). Our knowledge of the timing of CAS closure also evolved during the last 20 years. Although still very debated (O'Dea et al. 2016), authors have suggested that CAS constriction happened much earlier than previously thought (Montes et al. 2015; Bacon et al. 2015; Jaramillo 2018), with a very restricted seaway by the late Miocene (ca. 10 Ma, Fig. 23.3). This different chronology has many consequences on our understanding of CAS influence on climate, as it involves that its constriction has occurred during other major tectonics events, such as the uplift of the south American cordilleras (Andes).

Other maritime passages have seen their configuration change during the Cenozoic. The drift of Australia towards Indochina has progressively restricted the maritime exchanges between the Pacific Ocean and Indian Ocean through the Indonesian Passage. Numerical simulations show that before closure around 4 Ma, a warm ocean current flowed between the tropical Pacific Ocean and the Indian Ocean (Cane and Molnar 2001; Brierley and Fedorov 2016). After closure, this warm ocean current was blocked and was replaced by a colder current from the north Pacific. Simulated consequences involve a cooling of the surface waters of the Indian Ocean and a marked drying in East Africa, causing tree cover to decrease in favor of savanna vegetation. Although this drying has been confirmed by paleoclimate indicators (Bonnefille 2010), more proximal tectonics changes, namely the uplift of the east African dome might have played a role in this aridification (Sepulchre et al. 2006).

The Influence of Shelf and Epicontinental Seas

Variations in sea level have marked the history of the Earth. Reconstructions by Haq et al. (1987) of eustatic variations show that a high underlying sea level during the Upper Cretaceous (~95 Ma) is responsible for the formation of numerous shelf seas. The functioning and role of these shelf seas is still poorly understood as there is no modern equivalent of these water bodies. From the climate perspective, the answer seems simple: the higher the sea level, the less land surface is exposed, the smoother the seasonal cycle and the more homogeneous the climate becomes. Simulations conducted using a general atmospheric circulation model indicate that the climate response to the formation of shelf seas is

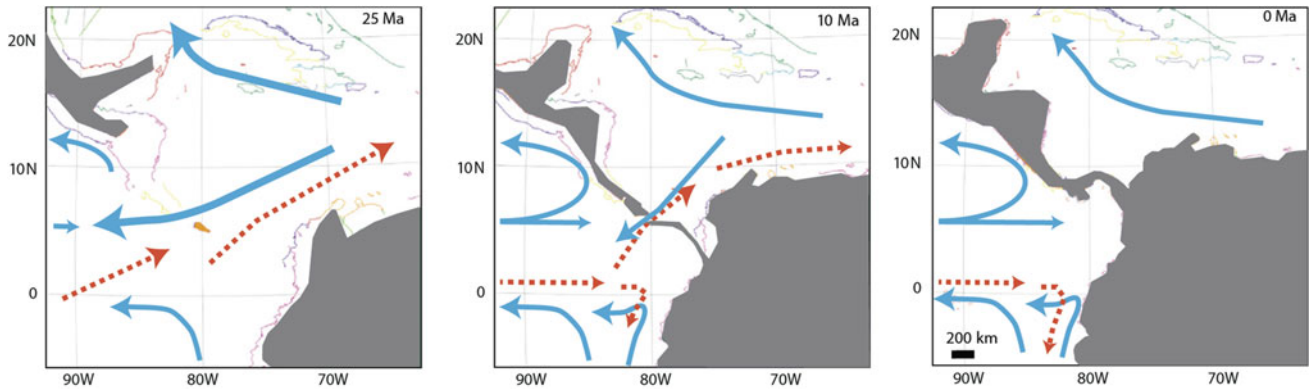

Fig. 22.3 Sketches of putative ocean currents in different paleogeographic configurations for Central America between 25 Ma and present. Reconstructions of continental areas are from Jaramillo (2018). Blues arrows show surface currents, and doted-red arrows show subsurface to mid-depth currents. In these reconstructions, a wide ocean gateway is open between the American continents at 25 Ma, whereas only a very narrow passage allows water exchange during the late Miocene. With this latter configuration, climate models suggest that surface currents flow westward, while undercurrents can bring fresher Pacific waters into the tropical Atlantic ocean

more complex than it might appear (Fluteau et al. 2006). A massive epicontinental sea in North America, the Western Interior Seaway (WIS), stretched across the North American continent from the Arctic ocean to the Gulf of Mexico, due to the sea incursion during the Middle Cretaceous, and to the dynamic topography caused by the subduction of the Farallon Plate under North America. During the Aptian (~20 Ma), this arm of the sea had not yet formed. Simulated atmospheric circulation in winter over North America is driven by a high pressure zone over the northeast of the continent. In summer, the opposite is the case; a zone of low pressure develops over the southwest of North America east of the mountains bordering the Pacific Ocean. The onset of the WIS completely disrupts the atmospheric circulation in summer across the continent (Fig. 22.4). The presence of this sea pushes the low-pressure zone to the east, while in winter temperatures increased by about 4 °C close to the WIS and precipitations, sometimes of snow, intensified along the Arctic Ocean. The warm temperate zones were shifted northward by up to 1000 km along the WIS following its establishment. Although, these results cannot be generalized since they depend on the location of the shelf seas relative to the high and low pressure areas that develop over the continent, they seem to have greatest impact on temperatures in the mid-latitudes and to induce significant increases in precipitation at low latitudes, as the shelf seas act as important reservoirs of water for the atmosphere.

The Impact of Mountains on Climate

As described in Volume 1, Chap. 2, much of the modern topography was formed during the Cenozoic. The paleoaltimetry proxies described earlier and the sedimentological record suggest that the Andes, the East-African dome, as well as the Himalayas and the Tibetan plateau rose mostly over the last twenty million years. These different reliefs form obstacles that alter climate through many mechanisms,

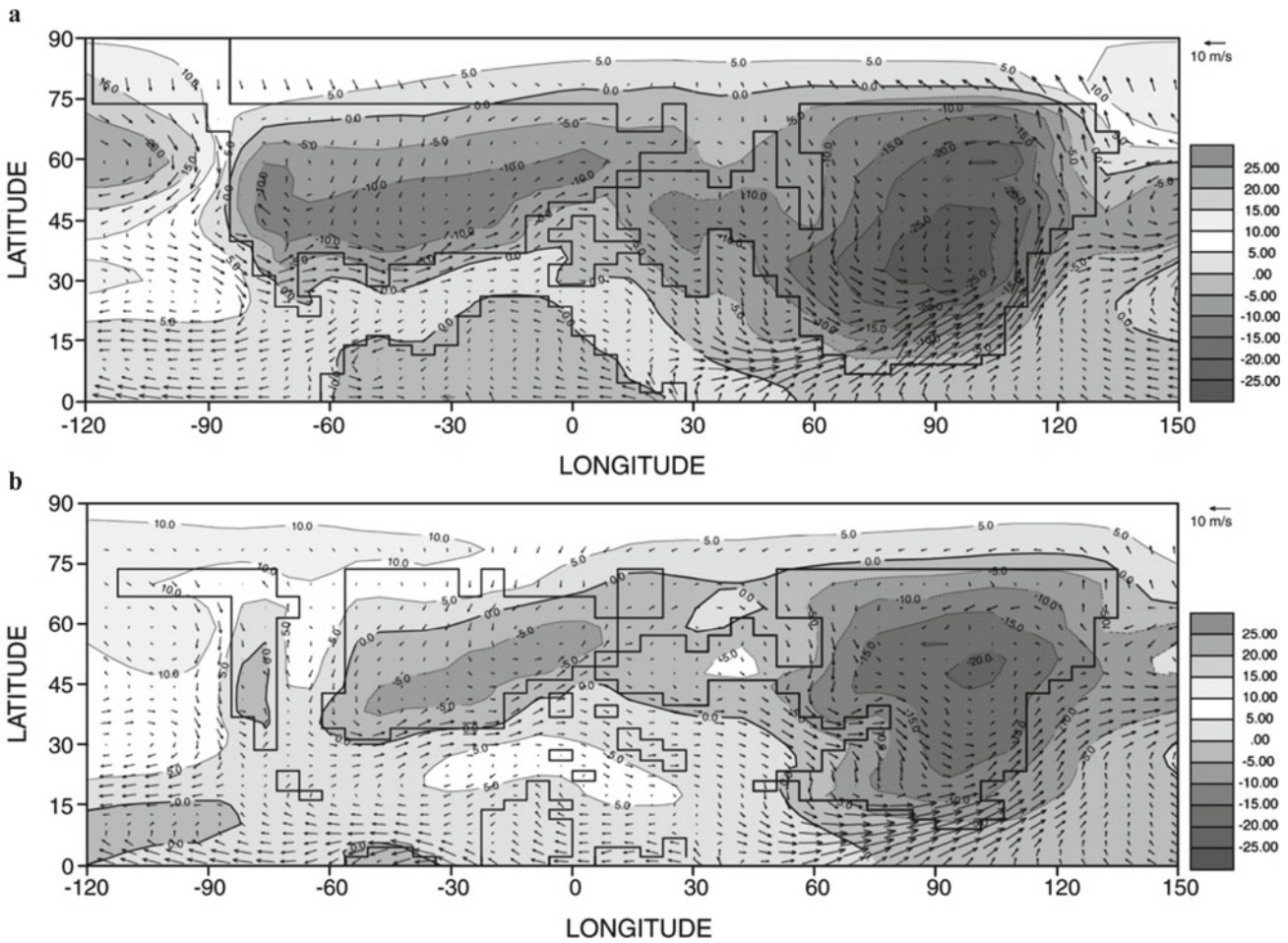

Fig. 22.4 Consequences of the establishment of the Western Interior Seaway (according to Fluteau et al. 2006). **a** Atmospheric circulation in summer during the Aptian (120 Ma). **b** Idem during the Cenomanian (95 Ma). Pressure fields are represented by isobars (P—1000 hPa) (HP = high pressure and BP = low pressure) and by winds (arrows) at 850 hPa (about 1500 m). Shaded areas: exposed land surfaces

at many spatial scales. Here we provide only a short overview of the main interactions between mountain uplift and climate dynamics to understand how the topographic changes of the Cenozoic have changed climate.

First, depending on its velocity, its angle with the mountain range and the size of the obstacle, air arriving towards a mountain range can undergo an orographic ascent that leads to adiabatic cooling until water condensate and precipitate on the windward slope, leading to a rainfall gradient between both sides of the orographic barrier. At the continental scale, this "rainshadow" produces strong heterogeneities in rainfall patterns and associated biomes, such as the ones observed today in Patagonia, for example. The varying temperature lapse rates, i.e. temperature decrease with elevation, that depends on air masses characteristics, also produce thermal heterogeneity in elevated regions. High mountains can also alter the surface radiative balance through snow-induced changes in albedo, creating thermal and pressure gradients that alter air circulation. Lastly, mountain ranges have long been shown to create different kinds of waves that propagate on the lee side and vertically, ultimately disturbing winds and the spatial distribution of precipitation (Warner 2004).

The impact of mountains on climate was considered as early as the middle of the nineteenth century, but it was not until the 1950s that studies quantified this relief-climate relationship. The meteorologists, Charney and Eliassen (1949), followed by Bolin (1950), assessed the impact of mountain ranges on the mid-latitude westerlies, while Flohn (1950) suggested that the Tibetan plateau was a source of sensible heat significant enough to explain the establishment of the Asian monsoon. Between the 1970s and 1990s, many studies benefited from the advances in atmospheric general circulation models to quantify the impact of mountain ranges on the distribution of arid zones globally and the establishment of the Asian monsoon. Broccoli and Manabe (1992) suggested that the aridity of Central Asia and the Great Plains of North America was partly due to the generation of stationary waves downwind of adjacent mountain ranges.

One specific geological event has captured the attention of scientists: the uplift of the Tibetan plateau and the Himalayan range in the context of the India-Asia collision, which occurred at the beginning of the Eocene (Molnar et al. 2010). The first assessment studies on the impact of the uplift of the Tibetan Plateau using climate models were based on sensitivity experiments with varying elevations of the plateau without differentiating between the Himalayan and Tibetan uplifts and without taking other paleogeographic changes into account (e.g. Kutzbach et al. 1993; Ruddiman et al. 1997). These studies suggested that the rise of the Tibetan plateau played a crucial role for atmospheric circulation in general, and for the Asian monsoon in particular. However, the physical mechanisms involved, which use the temperature gradients induced by a large continental area at high altitude, are still in question. Other studies have shown (i) that the thermal contrast between a flat continent and the Indian Ocean was enough to initiate a lower intensity monsoon than the modern monsoon pattern and (ii) that a prerequisite for this was the removal of the Paratethys Sea which enhanced the heating of Central Asia, and therefore the thermal contrast between the Indian Ocean and continental Asia (Ramstein et al. 1997; Fluteau et al. 1999). More recently, the separation of air masses on either side of a mountain range has been mentioned as a major factor in the initiation of convection and associated precipitation (see Boos 2015 for a review) and many modeling studies using various boundary conditions have been undertaken to try to understand the exact role of altitude (e.g., latitudinal position (Zhang et al. 2015, 2018), geographic extension (Chen et al. 2014) and of vegetation cover of the plateau (Hu and Boos 2017) in the establishment and intensification of the Asian monsoon.

Furthermore, the implications of the Himalayan-Tibetan relief for the climate are not limited to the atmosphere. Rind et al. (1997) used a general circulation model coupled with an ocean-atmosphere model (AOGCM) to show that these uplifts caused a rise in sea surface temperatures ($\sim$2 °C) in the North Atlantic (Norwegian Sea), an increase in heat transport at high latitudes (a crucial parameter for understanding climate change at high latitudes and possibly the freezing-over of Greenland) as well as a reduction of about 10% in deep water production in the Norwegian Sea (linked to the decrease in density of the water mass, due to the warming of the North Atlantic Ocean). More recently, Su et al. (2018) suggested that plateau uplift may have contributed to the establishment of the AMOC by changing the intensity and latitude of the zonal winds, thereby altering sea-ice formation and deep-water formation.

The impact of the reliefs on ocean-atmosphere dynamics are not limited to the Late Cenozoic orogenesis, because the Earth's history is dotted with uplifts creating mountain ranges with different locations, extensions, heights, and orientations. By comparing climate simulations for a world with its current topography and a "flat earth" world, Maffre et al. (2018) showed that the orographic barriers of the Andes and the Rockies constrain the transport of freshwater between the Pacific and the Atlantic, and thus contribute to the high salinity of the latter, favoring the formation of deep water. The Andean uplift is also believed to be responsible for the establishment of convective precipitation in tropical South America (Poulsen et al. 2010) and the strengthening of the Humboldt Current (Sepulchre et al. 2009). The establishment of reliefs in south and east Africa during the Mio-Pliocene probably led to the aridification of East Africa (Sepulchre et al. 2006), to the strengthening of the coastal upwellings of the Benguela current (Jung et al. 2014) and a change in position of the ITCZ in the Atlantic (Potter et al. 2017).

The Indirect Effects of Paleogeographic Changes

The atmospheric partial pressure of carbon dioxide (pCO_2) is driven by the carbon cycle. On the scale of geological time, pCO_2 reflects the balance between the CO_2 emission fluxes from volcanic systems (ocean ridges and aerial volcanism), the degree of magmatic activity from the mantle (plumes), decarbonation in subduction zones, and the CO_2 fluxes consumed by the weathering of the rock silicates on the surface of the Earth and in the oceanic crust, through the burial of the organic matter. Fluctuations in pCO_2 reflect the evolution of one or both of these flows. CO_2 emissions are proportional to the annual rate of production of oceanic crust. We have seen that the variability in this rate of production does not exceed 30% over the last 170 million years (Cogné and Humler 2006). To these rates should be added CO_2 emissions from plumes of mantle volcanism and from decarbonation in subduction zones. Significant magmatic events dating from the late Early Cretaceous and associated with the establishment of some large submarine basalt provinces, such as the Ontong-Java Plateau, increase the production rate of oceanic crust by about 25% (Cogné and Humler 2006) and about the same increase in CO_2 is injected into the ocean-atmosphere system. Contributions from the subduction zones are less constrained. Currently, this process is limited to a few subduction zones in the Pacific or around the Indonesian archipelago, while the main deposition zones are in the Atlantic and Indian Ocean. In the past, the subduction of the Tethysian Ocean could have emitted a significant CO_2 flux (Hoareau et al. 2015).

The intensity of the chemical weathering is a function of climate parameters such as surface temperature and runoff. Moreover, most geochemical models considered runoff as a function of surface temperature: the higher the temperature, the greater the runoff, and consequently, the chemical weathering. The chemical weathering of silicates acts as a climate regulator. We know now that this proportional relationship between temperature and runoff is based on current data and is not transferable to past periods. This is easily understood by analyzing the upper Permian climate. Simulation of chemical weathering is effective only in some areas experiencing a tropical and humid climate. This weak chemical weathering of silicates in the paleogeographic context implies a relatively high pCO_2 equilibrium of about 2500 ppm, and a high global average temperature of about 21 °C (considering that the rate of CO_2 emissions from the ridges is comparable to the current rate). Paleoclimate data confirm the hot and dry climate simulated over a large part of Pangea. The paleogeography of the Triassic maintained the Earth in a relatively stable climate dominated by a high simulated pCO_2 of around 3000 ppm and a high simulated global average temperature (between 21.5 and 23 °C). During the Jurassic, the drift of the Pangea to the north and its break-up brought about an increase in continental surfaces exposed to the hot and humid climate of the equatorial band. This resulted in intensified chemical weathering of silicates thus causing an increase in the consumption of CO_2. The simulated pCO_2 is lower at about 700 ppm as is the average temperature of the globe at a little over 18 °C. The end of the Mesozoic is marked by the final break-up of Gondwana. The arid areas reduced in size, reinforcing global chemical weathering. This resulted in a fairly low simulated pCO_2 of between 300 and 500 ppm for the Cretaceous. The effect of paleogeography on climate (through the regulation of chemical weathering of silicates) is therefore an effective process that can be seen in long-term trends, even if it does not explain every climate variations.

The conditions necessary for the high latitudes to freeze-up were not present at the end of the Permian, but they were in place for a long period from the Lower Carboniferous (340 Ma) to the Lower Permian (280 Ma), already in a supercontinent paleogeographic context. During this glacial period, the Earth experienced a succession of advances and retreats of continental ice over southern Gondwana. What mechanisms would push the Earth into a different climatic state? Although the geographical configuration of Pangea had not changed drastically between the Carboniferous and the Upper Permian, it had been drifting northwards during this period. Indeed, paleomagnetic data show that southern Gondwana was located at the pole during the Carboniferous, favoring a cooler summer in this region, but not yet cold enough for ice to remain outside some high reliefs. Another more effective mechanism was needed. The decrease in pCO_2 was therefore necessary to explain this glacial period. One suggestion was that colonization of emerged lands by plants during the Devonian increased the chemical weathering of silicates leading to a decrease in pCO_2 (Berner 2001). However, this vegetal colonization of continents took place tens of millions of years before the beginning of the glaciation. Goddéris et al. (2017) have shown that the Hercynian orogenesis could have played a major role. This orogenesis, resulting from the collision of Laurussia and Gondwana around 350 Ma, was at the origin of the uplift of a vast chain of mountains, the Hercynian chain, stretching for several thousands of kilometers in the equatorial band. With no mountains, the hot and humid climate of the lower latitudes causes a thick saprolite to form, considerably limiting the weathering of the underlying bedrock. With orogenesis, the presence of relief produces strong mechanical erosion due to the slopes which considerably limit the development of thick saprolites, thus the weathering of silicate rocks is increased, leading to a

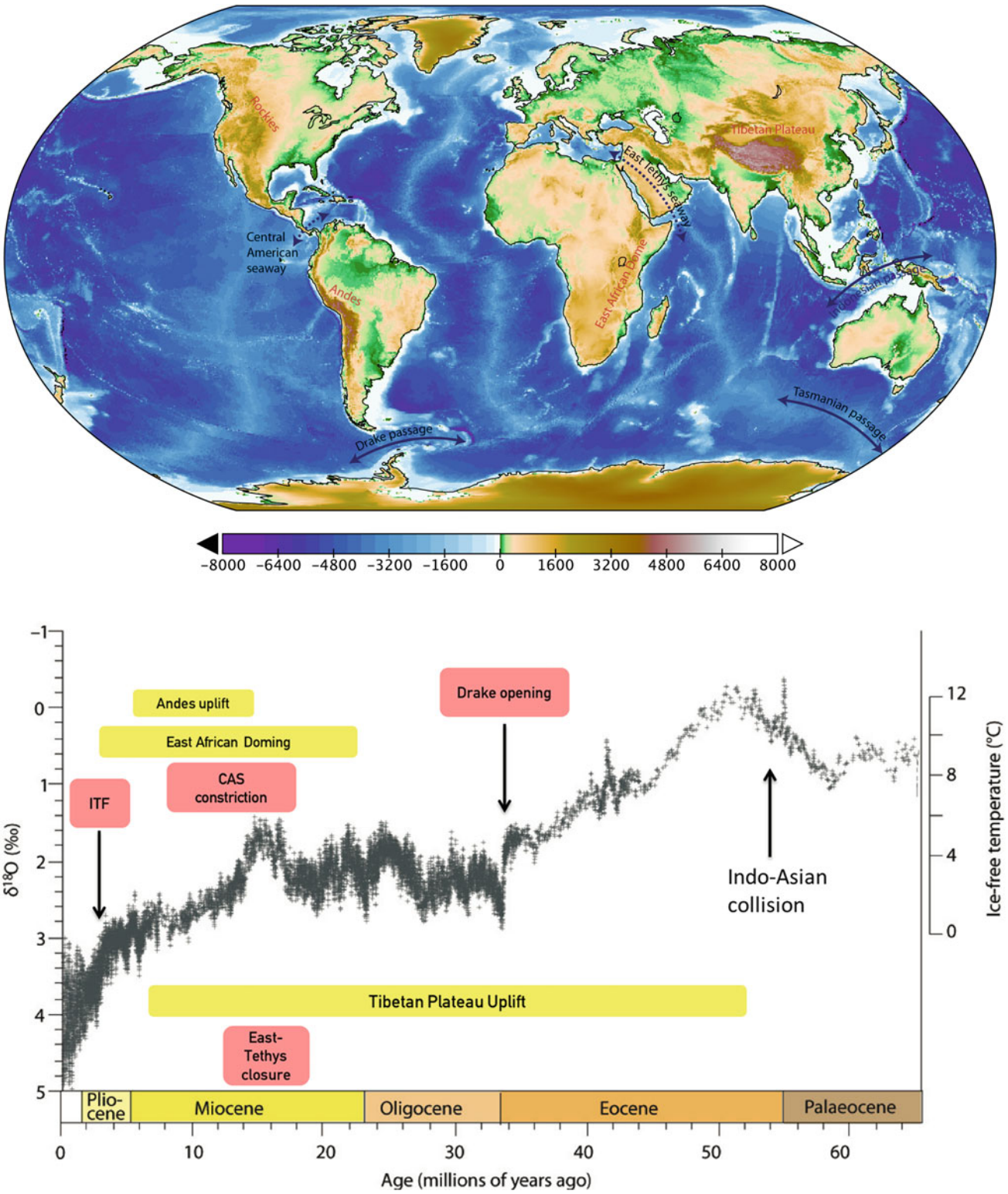

Fig. 22.5 Spatial positions (upper panel) and timing (lower panel) of the modification of the principal mountain ranges and seaways discussed in the text. Bathymetry and topographic are from NOAA. The stable isotope curve in the bottom panel can be interpreted as ice-free temperatures. Adapted from Zachos et al. (2001)

decrease in the pCO_2. This decline in pCO_2 is further reinforced by the increased transport of organic carbon and its burial in sedimentary basins at the foot of the reliefs (Goddéris et al. 2017). The threshold for freezing is defined by the level of atmospheric CO_2 concentration below which freezing occurs. This threshold was reduced during the Carboniferous because of the slow, inexorable increase in insolation produced by the Sun. Estimates, based on the analysis of fossil leaves and pedogenic carbonates, found that in basins at low latitudes pCO_2 fluctuated periodically from about 200 to 300 ppmv during the Upper Carboniferous with a minimum concentration of 160–300 ppmv (Montañez et al. 2016). The periodicity of these fluctuations seems to be dominated by an eccentricity signal of 405 ka. The vegetation cover of these equatorial basins also varies between dry vegetation during interglacials and humid tropical vegetation during interglacials (Montañez et al. 2016) which influence the organic carbon cycle, possibly causing fluctuations in the volume of continental ice on Gondwana and is superimposed on the long-term trend driven by geodynamics.

Conclusion

The impact of paleogeographic changes on climate and its evolution is fundamental. The presence of a supercontinent produces climates characterized by strong contrasts (continental climate at high latitudes, wide arid zone in the subtropics, as in the Permian), while a fragmented continent, combined with vast shelf seas produced as a consequence of a high sea level, as in the early Upper Cretaceous, will be conducive to a climate with relatively low contrasts. The dispersion of landmasses therefore represents an important climate forcing, which does not, however, offer a complete explanation for the climate history of the Earth. Orogenesis is another major forcing of the climate at geological timescales. It is therefore essential to delineate the spatio-temporal evolution of all the orogens as accurately as possible (Fig. 22.5), even if the reconstructed paleoaltitudes remain, for the time being, subject to considerable uncertainty. While the impact of paleogeography on atmospheric circulation has been widely studied through numerical modeling, the impact of paleogeographic changes on ocean circulation is far from well understood. Studies have quantified the impact of the opening of seaways (Panama or Indonesian) or large-scale ocean connections (South Atlantic—Central Atlantic) on the climate through the redistribution of heat carried by ocean currents. The chronology of the openings and closures of the ocean passages, in addition to that of the orogens, is thus essential to a good understanding of the climate system at the scale of geological time. In this framework, the development of new isotopic tools, the improvements of traditional proxies calibration and the rise of paleoclimate modelling should allow a better quantification of the links between paleogeography and climate in the next decades.

References

Bacon, C. D., Silvestro, D., Jaramillo, C., Smith, B. T., Chakrabarty, P., & Antonelli, A. (2015). Biological evidence supports an early and complex emergence of the Isthmus of Panama. *Proceedings of the National Academy of Sciences, 112,* 6110–6115.

Bahr, A., Kolber, G., Kaboth-Bahr, S., Reinhardt, L., Friedrich, O., Pross, J. (2020). Mega-monsoon variability during the late Triassic: Re-assessing the role of orbital forcing in the deposition of playa sediments in the Germanic Basin. *Sedimentology, 67*, 951–970. https://doi.org/10.1111/sed.12668.

Berner, R. A. (2001). GEOCARB III: A revised model of atmospheric CO_2 over Phanerozoic time. *American Journal of Science, 301*(2), 182–204. https://doi.org/10.2475/ajs.301.2.182.

Biggin, A. J., de Wit, M. J., Langereis, C. G., Zegers, T. E.,Voûte, S., Dekkers, M. J., & Drost, K. (2011). Palaeomagnetism of Archaean rocks of the Onverwacht Group, Barberton Greenstone Belt (southern Africa): Evidence for a stable and potentially reversing geomagnetic field at ca. 3.5 Ga. *Earth and Planetary Science Letters, 302*, 314–328.

Bolin, B. (1950). On the influence of the Earth's orography on the general character of the westerlies. *Tellus, 2*(3). http://www.tellusa.net/index.php/tellusa/article/download/8547/9993.

Bond, D. P. G., Hilton, J., Wignall, P. B., Ali, J. R., Stevens, L. G., Sun, Y., and Lai, X. (2010). The Middle Permian (Capitanian) mass extinction on land and in the oceans. *Earth-Science Reviews, 102*, 100–116, https://doi.org/10.1016/j.earscirev.2010.07.004.

Bond, D. P. G. & Wignall, P. B. (2014). Large igneous provinces and mass extinctions: An update. In G. Keller, & A. C. Kerr (Eds.), *Volcanism, impacts, and mass extinctions: Causes and effects: Geological society of America special paper, 505* (p. 29). https://doi.org/10.1130/2014.2505(02).

Bonifacie, M., et al. (2017). Calibration of the dolomite clumped isotope thermometer from 25 to 350 °C, and implications for a universal calibration for all (Ca, Mg, Fe) CO3 carbonates. *Geochimica et Cosmochimica Acta, 200*(1), 255–279.

Bonnefille, R. (2010). Cenozoic vegetation, climate changes and hominid evolution in tropical Africa. *Global and Planetary Change, 72,* 390–411.

Boos, W. R. (2015). A review of recent progress on Tibet's role in the South Asian monsoon. *CLIVAR Exchanges, 19*(23), 27.

Bornemann, A., Norris, R. D., Friedrich, O., Beckmann, B., Schouten, S., et al. (2008). Isotopic evidence for glaciation during the Cretaceous supergreenhouse. *Science, 319*, 189–192.

Brierley, C. M., & Fedorov, A. V. (2016). Comparing the impacts of Miocene–Pliocene changes in Inter-Ocean gateways on climate: Central American Seaway, Bering Strait, and Indonesia. *Earth and Planetary Science Letters, 444*(juin), 116–130. https://doi.org/10.1016/j.epsl.2016.03.010.

Broccoli, A. J., & Manabe, S. (1992). The effects of orography on Mid-latitude Northern Hemisphere Dry Climates. *Journal of Climate, 5*(11), 1181–1201. https://doi.org/10.1175/1520-0442(1992)005.

Cane, M. A., & Molnar, P. (2001). Closing of the Indonesian Seaway as a Precursor to East African aridification around 3–4 million years ago. *Nature, 411,* 157–162.

Caquineau, T., Paquette, J.-L., & Philippot, P. (2018). U-Pb detrital zircon geochronology of the Turee Creek Group, Hamersley Basin, Western Australia: Timing and correlation of the Paleoproterozoic glaciations. *Precambrian Research, 307,* 34–50. https://doi.org/10.1016/j.precamres.2018.01.003.

Chaboureau, A. C., Sepulchre, P., Donnadieu, Y., & Franc, A. (2014). Tectonic-driven climate change and the diversification of angiosperms. *Proceedings of the National Academy of Sciences, 111*(39), 14066–14070. https://doi.org/10.1073/pnas.1324002111.

Charney, J. G., & Eliassen, A. (1949). A numerical method for predicting the perturbations of the Middle Latitude Westerlies. *Tellus, 1*(2): 38–54. https://doi.org/10.1111/j.2153-3490.1949.tb01258.x.

Chen, G.-S., Liu, Z., & Kutzbach, J. E. (2014). Reexamining the barrier effect of the Tibetan Plateau on the South Asian Summer Monsoon. *Climate of the Past, 10*(3),1269–1275. https://doi.org/10.5194/cp-10-1269-2014.

Cogné, J. P., & Humler, E. (2006). Trends and rhythms in global seafloor generation rate. *Geochemistry, Geophysics, Geosystems, 7*, Q03011. https://doi.org/10.1029/2005GC001148.

Copper, P., & Scotese, C. R. (2003). Megareefs in Middle Devonain super greenhouse climates. *Special Publications - Geological Society of America, 370*, 209–230.

Daëron, M., Drysdale, R. N., Peral, M., Huyghe, D., Blamart, D., Coplen, T. B., et al. (2019). Most Earth-surface calcites precipitate out of isotopic equilibrium. *Nature Communications, 10*(1), 429. https://doi.org/10.1038/s41467-019-08336-5.

De Wit, M. J., & Furnes, H. (2016). 3.5-Ga hydrothermal fields and diamictites in the Barberton Greenstone Belt—Paleoarchean crust in cold environments. Science Advances, *2*, e1500368. https://doi.org/10.1126/sciadv.1500368.

Dodd, M. S., Papineau, D., Grenne, T., Slack, J. F., Rittner, M., Pirajno, F., et al. (2017). Evidence for early life in Earth's oldest hydrothermal vent precipitates. *Nature, 543*(7643), 60–64. https://doi.org/10.1038/nature21377.

Donnadieu, Y., Goddéris, Y., Ramstein, G., Nédélec, A., Meert, J. (2004). A 'snowball Earth'climate triggered by continental break-up through changes in runoff.*Nature, 428*(6980), 303–306.

Donnadieu, Y., Pucéat, E., Moiroud, M., Guillocheau, F., & Deconinc,. J. F. (2016). A better-ventilated ocean triggered by late Cretaceous changes in continental configuration. *Nature Communications, 7* (janvier), 10316. https://doi.org/10.1038/ncomms10316.

Dromart, G., Garcia, J.-P., Picard, S., Atrops, F., Lécuyer, C., & Sheppard, S. M. F. (2003). Ice Age at the Middle–Late Jurassic Transition? *Earth and Planetary Science Letters, 213*(3–4), 205–220. https://doi.org/10.1016/S0012-821X(03)00287-5.

Dubiel, R. F., Parrish, J. T., Parrish, J. M., & Good, S. C. (1991). The Pangaean megamonsoon: Evidence from the Upper Triassic Chinle Formation, Colorado Plateau. *Palaios, 6*, 347–370.

Eiler, J. M. (2007). "Clumped-isotope" geochemistry—the study of naturally-occurring, multiply-substituted isotopologues. *Earth and Planetary Science Letters, 262*, 309–327.

Erwin, D. H. (1994). The Permo-Triassic extinction. *Nature, 367*, 231–236. *https://doi.org/10.1038/367231a0*.

Flohn, H. (1950). Neue Anschauungen über die allgemeine Zirkulation der Atmosphäre und ihre klimatische Bedeutung. *Erdkunde, 4*(3/4), 141–162.

Fluteau, F., Besse, J., Broutin, J., Ramstein, G. (2001). The Late Permian climate. What can be inferred from climate modelling concerning Pangea scenarios and Hercynian range altitude? *Palaeogeography, Palaeoclimatology, Palaeoecology, 167*, 39–71.

Fluteau, F., Ramstein, G., Besse J. (1999). Simulating the evolution of the Asian and African Monsoons during the past 30 Myr using an atmospheric general circulation model. *Journal of Geophysical Research, 104*(D10), 11995–12018.

Fluteau, F., et al. (2006). The impacts of the Paleogeography and sea level changes on the Mid Cretaceous climate. *Palaeogeography, Palaeoclimatology, Palaeoecology, 247*(3–4), 357–381. https://doi.org/10.1016/j.palaeo.2006.11.016

Fluteau, F., Ramstein, G., Besse, J., Guiraud, R., & Masse. J. P. (2007). Impacts of Palaeogeography and sea level changes on the Mid Cretaceous climate. *Palaeogeography, Palaeoclimatology, Palaeoecology, 247*, 357–381.

Ghienne, J-F., Moreau, J., Degermann, L. et al. (2013). Lower Palaeozoic unconformities in an intracratonic platform setting: Glacial erosion versus tectonics in the eastern Murzuq Basin (southern Libya). *International Journal of Earth Sciences, 102*(2), 455–482.

Goddéris, Y., Donnadieu, Y., Carretier, S., Aretz, M., Dera, G., Macouin, M., & Regard, V. (2017). Onset and ending of the late Palaeozoic ice age triggered by tectonically paced rock weathering. *Nature Geoscience, 10*(5): 382–386. https://doi.org/10.1038/ngeo2931.

Granot, R., & Dyment, J. (2015). The Cretaceous opening of the South Atlantic Ocean. *Earth and Planetary Science Letters, 414*(mars), 156–163. https://doi.org/10.1016/j.epsl.2015.01.015.

Haq, B. U., et al. (1987). Chronology of fluctuating sea levels since the Triassic (250 million years ago to present). *Science, 235*, 1156–1166.

Haqq-Misra, J. D., et al. (2008). A revised, Hazy methane greenhouse for the Archean Earth. *Astrobiology, 8*, 1127–1137.

Haug, G. H., & Tiedemann, R. (1998). Effect of the formation of the Isthmus of Panama on Atlantic Ocean Thermohaline circulation. *Nature, 393,* 673–676.

Hoareau, G., Bomou, B., van Hinsbergen, D. J. J., Carry, N., Marquer, D. et al. (2015). Did high Neo-Tethys subduction rates contribute to early Cenozoic warming? *Climate of the Past, 11*(12), 1751–1767.

Hoffman, et al. (2017). Snowball Earth climate dynamics and Cryogenian geology-geobiology. *Science Advances, 3,* e1600983.

Hren, M. T., Sheldon, N. D., Grimes, S. T., Collinson, M. E, Hooker, J. J., Bugler, M., Lohmann, K. C. (2013). Terrestrial cooling in Northern Europe during the Eocene–Oligocene transition, *PNAS, 110*, 7562–7567.

Hu, S., & Boos, W. R. (2017). Competing effects of surface Albedo and Orographic elevated heating on regional climate: Albedo-Elevation compensation. *Geophysical Research Letters, 4*(13), 6966–6973. https://doi.org/10.1002/2016GL072441.

Jaramillo, C. (2018). Evolution of the Isthmus of Panama: Biological, Paleoceanographic and Paleoclimatological implications. In C. Hoorn, A. Perrigo, & A. Antonelli (Eds.), *Mountains, climate and biodiversity* (1st ed.). Wiley.

Jung, G., Prange, M., & Schulz, M. (2014). Uplift of Africa as a potential cause for Neogene Intensification of the Benguela upwelling system. *Nature Geoscience, 7*(10), 741–747. https://doi.org/10.1038/ngeo2249.

Kasting, J., & Howard, M. T. (2006). Atmospheric composition and climate on the early Earth. *Philosophical Transactions of the Royal Society B, 361*, 1733–1742.

Kennett, J. P. (1977). Cenozoic evolution of Antarctic Glaciation, the Circum-Antarctic Ocean, and their impact on global Paleoceanography. *Journal of Geophysical Research, 82*(27), 3843–3860. https://doi.org/10.1029/JC082i027p03843.

Kiehl, J. T., & Shields, C. A. (2005). Climate simulation of the latest Permian: Implications for mass extinction. *Geology, 33*(9), 757–760. https://doi.org/10.1130/G21654.1.

Kutzbach, J. E., Prell, W. L., & Ruddiman, W. F. (1993). Sensitivity of Eurasian climate to surface uplift of the Tibetan Plateau. *The Journal of Geology, 101*(2), 177–190. https://doi.org/10.1086/648215.

Knauth, L. P., & Lowe, D. R. (2003). High Archean climatic temperature inferred from oxygen isotope geochemistry of cherts in the 3.5 Ga Swaziland Supergroup, South Africa. *Geological Society of America Bulletin, 115*, 566–580 (2003).

Ladant, J. B., Donnadieu, Y. (2016). Palaeogeographic regulation of glacial events during the Cretaceous supergreenhous. *Nature communications, 7*, Article number: 12771.

Lefebvre, V., Donnadieu, Y., Sepulchre, P., Swingedouw, D., & Zhang, Z.-S. (2012). Deciphering the role of Southern Gateways and carbon dioxide on the onset of the Antarctic circumpolar current. *Paleoceanography, 27*(4), n/a–n/a. https://doi.org/10.1029/2012PA002345.

Le Hir, G., Donnadieu, Y., Goddéris, Y., Meyer-Berthaud, B., Ramstein, G., & Blakey, R. C. (2011). The climate change caused by the land plant invasion in the Devonian. *Earth and Planetary Science Letters, 310*(3), 203–212. https://doi.org/10.1016/j.epsl.2011.08.042.

Lowe, D. R., & Tice, M. M. (2004). Geologic evidence for Archean atmospheric and climatic evolution: Fluctuating levels of CO_2, CH_4, and O_2 with an overriding tectonic control. *Geology, 32,* 493–496.

Lunt, D. J., et al. (2008). Closure of the Panama Seaway during the Pliocene: Implications for climate and Northern Hemisphere Glaciation. *Climate Dynamics, 3,* 1–18.

Maffre, P., Ladant, J. B., Donnadieu, Y., Sepulchre, P., & Goddéris, Y. (2018). The influence of Orography on modern ocean circulation. *Climate Dynamics, 50*(3–4), 1277–1289. https://doi.org/10.1007/s00382-017-3683-0.

Matte, P. (1986). Tectonics and plate Tectonics model for the Variscan Belt of Europe. *Tectonophysics, 126,* 329–374.

Meyer-Berthaud, B., Scheckler, S., Wendt, J. (1999). Archaeopteris is the earliest known modern tree. *Nature, 398*, 700–701.

Molnar, P., Boos, W. R., & Battisti, D. S. (2010). Orographic controls on climate and Paleoclimate of Asia: Thermal and mechanical roles for the Tibetan Plateau. *Annual Review of Earth and Planetary Sciences, 38* (1), 77–102. https://doi.org/10.1146/annurev-earth-040809-152456.

Montañez, I., & Poulsen, C. (2013). The late Paleozoic ice age: An evolving paradigm. *Annual Review of Earth and Planetary Sciences, 41*, 24.1–24.28.

Montañez, I. P., McElwain, J. C., Poulsen, C. J., White, J. D., DiMichele, W. A., Wilson, J. P., Griggs, G., & Hren, M. T. (2016). Climate, pCO_2 and terrestrial carbon cycle linkages during late Palaeozoic glacial–interglacial cycles. *Nature Geoscience, 9*(11), 824–828. https://doi.org/10.1038/ngeo2822.

Montes, C., Cardona, A., Jaramillo, C., Pardo, A., Silva, J. C., Valencia, V., et al. (2015). Middle Miocene closure of the Central American Seaway. *Science, 348*(6231), 226–229. https://doi.org/10.1126/science.aaa2815.

Murphy, D. P., & Thomas, D. J. (2013). The evolution of late Cretaceous deep-ocean circulation in the Atlantic Basins: Neodymium isotope evidence from South Atlantic Drill Sites for Tectonic controls: Cretaceous Atlantic deep circulation. *Geochemistry, Geophysics, Geosystems, 14*(12), 5323–5340. https://doi.org/10.1002/2013GC004889.

O'Dea, A., Lessios, H. A., Coates, A. G., Eytan, R. I., Restrepo-Moreno, S. A., Cione, A. L., et al. (2016). Formation of the Isthmus of Panama. *Science Advances, 2*(8), e1600883. https://doi.org/10.1126/sciadv.1600883.

Potter, S. F., Dawson, E. J., & Frierson, D. M. W. (2017). Southern African Orography impacts on low clouds and the Atlantic ITCZ in a coupled model: African Orography impacts on the ITCZ. *Geophysical Research Letters, 44*(7), 3283–389. https://doi.org/10.1002/2017GL073098.

Poulsen, C. J., Ehlers, T. A., & Insel, N. (2010). Onset of convective rainfall during gradual late Miocene rise of the Central Andes. *Science, 328*(5977): 490–493. https://doi.org/10.1126/science.1185078.

Poulsen, C. J., Gendaszek, A. S., & Jacob, R. L. (2003). Did the rifting of the Atlantic Ocean Cause the Cretaceous thermal maximum? *Geology, 31*(2), 115–118. https://doi.org/10.1130/0091-7613(2003)031%3c0115:DTROTA%3e2.0.CO;2.

Ramstein, G., Fluteau, F., Besse, J., Joussaume, S. (1997). Effects of orogeny, sea-level change and tectonic drift on the monsoon over the past 30 millions years. *Nature, 386*, 788–795.

Rind, D. G., Russell, G., & Ruddiman, W. F. (1997). The effects of uplift on ocean-atmosphere circulation. In W. F. Ruddiman (Ed.), *Tectonic uplift and climate change* (pp. 123–147). New York: Plenum.

Robert, F., & Chaussidon, M. (2006). A palaeotemperature curve for the Precambrian oceans based on silicon isotopes in cherts. *Nature, 443,* 969–972.

Ruddiman, W. F., et al. (1997). The uplift-climate connection: A synthesis. In W. F. Ruddiman (Ed.), *Tectonic uplift and climate change* (pp. 471–515). New York: Plenum.

Sepulchre, P., Arsouze, T., Donnadieu, Y., Dutay, J-C., et al. (2014). Consequences of shoaling of the Central American Seaway determined from modeling Nd isotopes. *Paleoceanography, 29*(3), 176–189.

Sepulchre, P., Ramstein, G., Fluteau, F., Schuster, M., Tiercelin, J. J., & Brunet, M. (2006). Tectonic Uplift and Eastern Africa Aridification. *Science, 313*(5792), 1419–1423. https://doi.org/10.1126/science.1129158.

Sepulchre, P., Sloan, L. C., Snyder, M., & Fiechter, J. (2009). Impacts of Andean Uplift on the Humboldt current system: A climate model sensitivity study. *Paleoceanography, 24*(4). https://doi.org/10.1029/2008PA001668.

Shields, C. A., & Kiehl, J. T. (2018). Monsoonal precipitation in the Paleo-Tethys warm pool during the latest Permian. *Palaeogeography, Palaeoclimatology, Palaeoecology, 491*(février), 123–136. https://doi.org/10.1016/j.palaeo.2017.12.001.

Sijp, W. P., von der Heydt, A. S. Dijkstra, H. A. Flögel, S., Douglas, P. M. J., & Bijl. P. K. (2014). The role of ocean gateways on cooling climate on long time scales. *Global and Planetary Change, 119*(août), 1–22. https://doi.org/10.1016/j.gloplacha.2014.04.004.

Su, B., Jiang, D., Zhang, R., Sepulchre, P., & Ramstein, G. (2018). Difference between the North Atlantic and Pacific Meridional overturning circulation in response to the uplift of the Tibetan Plateau. *Climate of the Past, 14*(6), 751–762. https://doi.org/10.5194/cp-14-751-2018.

Tan, N., Ramstein, G., Dumas, C., Contoux, C., Ladant, J. B., Sepulchre, P., Zhang, Z., & De Schepper, S. (2017). Exploring the MIS M2 glaciation occurring during a warm and high atmospheric CO_2 Pliocene background climate. *Earth and Planetary Science Letters, 472*, 266–276.

Tartèse, R., Chaussidon, M., Gurenko, A., Delarue, F., & Robert, F. (2017). Warm Archaean Oceans reconstructed from oxygen isotope composition of early-life Remnants. *Geochemical Perspectives Letters*, 55–65. https://doi.org/10.7185/geochemlet.1706.

Valley, J. W. (2006). Early Earth. *Elements 2*(4), 201–204. https://doi-org.insu.bib.cnrs.fr/10.2113/gselements.2.4.201.

Veizer, J., & Prokoph, (2015). Temperatures and oxygen isotopic composition of Phanerozoic oceans. *Earth-Science Reviews, 146*, 92–104. https://doi.org/10.1016/j.earscirev.2015.03.008.

Warner, T. (2004). Desert Meteorology. Cambridge: Cambridge University Press. https://doi.org/10.1017/CBO9780511535789.

Young, G. M., Von Brunn, V., Gold, D. J. C., & Minter, W. E. L. (1998). Earth's oldest reported Glaciation: Physical and chemical evidence from the Archean Mozaan Group (2.9 Ga) of South Africa. *Journal of Geology, 106,* 523–538.

Zachos, J., et al. (2001). Trends, rhythms, and aberrations in global climate 65 Ma to present. *Science, 292,* 686–693.

Zerkle, A. L., Claire, M. W., Domagal-Goldman, S. D., Farquhar J., & Poulton, S. W. (2012). A bistable organic-rich atmosphere on the

Neoarchaean Earth. *Nature Geoscience, 5*, 359–363. https://doi.org/10.1038/ngeo1425.

Zhang, R., Jiang, D., Ramstein, G., Zhang, Z., Lippert, P. C. & Yu, E. (2018). Changes in Tibetan Plateau Latitude as an Important factor for understanding East Asian climate since the Eocene: A modeling study. *Earth and Planetary Science Letters, 484*(février), 295–308. https://doi.org/10.1016/j.epsl.2017.12.034.

Zhang, R., Jiang, D., Zhang, Z., & Yu, E. (2015). The impact of regional uplift of the Tibetan Plateau on the Asian Monsoon climate. *Palaeogeography, Palaeoclimatology, Palaeoecology, 417* (janvier), 137–150. https://doi.org/10.1016/j.palaeo.2014.10.030.

Zhang, X., Prange, M., Steph, S., Butzin, M., Krebs, U., Lunt, D. J., et al. (2012). Changes in equatorial Pacific thermocline depth in response to Panamanian seaway closure: Insights from a multi-model study. *Earth and Planetary Science Letters, 317–318,* 76–84.

Biogeochemical Cycles and Aerosols Over the Last Million Years

23

Nathaelle Bouttes, Laurent Bopp, Samuel Albani, Gilles Ramstein, Tristan Vadsaria, and Emilie Capron

Introduction

The biogeochemical cycles encompass the exchange of chemical elements between reservoirs such as the atmosphere, ocean, land and lithosphere. Those exchanges involve biological, geological and chemical processes, hence the term "biogeochemical cycles". A widely known cycle (which is not a biogeochemical cycle) is the water cycle, whose impact on climate is of major importance and which has been described in Volume 1, Chap. 1. Similarly, chemical elements such as carbon, nitrogen, oxygen and sulphur are also exchanged during cycles. Some of these elements can significantly impact climate through their effect on the atmospheric energy budget when they are in gaseous form (CO_2, CH_4, N_2O). The biogeochemical cycles are also affected by changes in climate, constituting a feedback in the Earth system. Other chemical compounds present in the atmosphere also influence the amount of energy available at the surface and therefore the dynamics of the climate: these are aerosols, small liquid or solid particles in suspension in the air. Because of the effect of climate on these chemical elements and particles, they sometimes record the changes that modified their cycle. It is possible to measure many of these tracers, which provide a valuable insight into past climate changes.

The link between the composition of the atmosphere and climate was discovered in the nineteenth century through the work of Jean-Baptiste Fourier, a French mathematician. He showed that the Earth would be much colder than it currently is, if it was heated by incoming solar radiation alone. To explain the additional heating, he proposed, among other possibilities, that the Earth is insulated by gases present in the atmosphere. This effect of atmospheric gases blocking some of the infrared radiation emitted by the planet is now known as the greenhouse effect. Later, in 1860, John Tyndall, an English chemist, demonstrated that the two main constituents of our atmosphere, dinitrogen and dioxygen, are transparent to infrared radiation and therefore do not contribute to the greenhouse effect. On the other hand, he identified water vapour (H_2O) and carbon dioxide (CO_2) as the two main greenhouse gases in our atmosphere. This led the way for another chemist, Svante Arrhenius, who, in 1896, was the first to estimate the change in the average temperature of the Earth's surface triggered by a change in the concentration of CO_2 in the atmosphere. Lastly, it was only in the second half of the twentieth century that advances in measurement techniques made it possible to measure the impacts of other gases such as methane (CH_4), nitrous oxide (N_2O), ozone (O_3), and chlorofluorocarbons (CFCs), on the greenhouse effect.

The direct effect of aerosols on climate was first suggested by Benjamin Franklin in the eighteenth century to explain the cold winter of 1783–84. Benjamin Franklin noted there was a "constant fog over all Europe, and a great part of North America" which resulted in colder conditions. He suggested volcanic eruptions in Iceland as a possible explanation for this fog. Since then, the big volcanic eruptions that have occurred in the nineteenth and twentieth centuries, such as the Krakatoa (1883), Santa Maria (1902),

N. Bouttes (✉) · L. Bopp · S. Albani · G. Ramstein · T. Vadsaria
Laboratoire des Sciences du Climat et de l'Environnement, LSCE/IPSL, CEA-CNRS-UVSQ, Université Paris-Saclay, 91191 Gif-sur-Yvette, France
e-mail: Nathaelle.bouttes@lsce.ipsl.fr

S. Albani
Department of Environmental and Earth Sciences, University of Milano-Bicocca, Milano, Italy

T. Vadsaria
Atmosphere and Ocean Research Institute, The University of Tokyo, Kashiwa, Chiba, Japan

E. Capron
British Antarctic Survey, High Cross, Madingley Road, Cambridge, CB3 OET, UK

E. Capron
Physics of Ice, Climate and Earth, Niels Bohr Institute, University of Copenhagen, Juliannes Maries Vej 30, 2100 Copenhagen Ø, Denmark

G. Ramstein et al. (eds.), *Paleoclimatology*, Frontiers in Earth Sciences,
https://doi.org/10.1007/978-3-030-24982-3_23

Katmai (1912), Agung (1963), El Chichon (1982) and Pinatubo (1991) have provided material to better understand the effects of aerosols that have recently been incorporated into climate models. The indirect effects of aerosols by modifying clouds were discovered more recently. The presence of aerosols can modify cloud characteristics by making them more reflective, or by extending their lifetime before precipitation, for example.

These chemical elements and aerosols are closely linked to climate and climate changes. Their concentration in the atmosphere impacts the Earth's energy budget, either directly or indirectly, while changes in climate modify the exchanges between reservoirs of these compounds and, in fine, their concentration in the atmosphere. Some atmospheric gases have the ability to modify the energy budget of the Earth (Volume 1, Chap. 1). The Earth receives shortwave radiation (ultraviolet, visible, and near-infrared) from the sun. Part of this radiation is reflected back by the surface, clouds and the atmosphere, part of it is absorbed by the atmosphere and clouds, and the last part is absorbed by the surface of the Earth. The Earth's surface emits longwave radiation (infrared) because it is colder than the sun, and also transfers energy to the atmosphere by latent and sensible heat. The longwave radiation from the Earth's surface is partly absorbed by the atmospheric greenhouse gases, which then re-emit radiation in all directions, including towards the surface of the Earth. The latter is then heated, resulting in a higher temperature than on an Earth without greenhouse gases. The radiation absorbed by the gases depends on their properties and in which zones they absorb radiation. Among the gases present in the atmosphere, the main greenhouse gases are, in decreasing order (excluding water vapor) carbon dioxide (CO_2), methane (CH_4) and nitrous oxide (N_2O).

Aerosols have two effects on the energy budget in the atmosphere: direct and indirect. Aerosols are tiny particles—such as sea salt, dust from deserts and fires—in suspension in the atmosphere, either in liquid or solid form. They can absorb and disperse solar radiation, as well as absorb and emit thermal radiation. This is the direct effect. Aerosols also form cloud condensation nuclei and ice nuclei: raindrops and ice develop around these nuclei. This is the indirect effect because it modifies the energy budget through the modification of the microphysics of clouds. Depending on the size of the drops, which is dependent on the type and size of nuclei, the clouds will reflect or absorb radiation. In addition, aerosols deposited back to the surface will alter the amount of solar radiation reflected back to space, and will disperse chemical elements that can influence various biogeochemical cycles.

Some of the changes impacting on the biogeochemical cycles and aerosols are recorded and preserved for thousands of years. The main natural archives that have been used to track such changes are sediment cores extracted from oceans or lakes, and ice cores, drilled from polar ice sheets (Fig. 23.1).

Marine sediment cores, collected from the bottom of the ocean, include various organic and inorganic elements, which can be used to get direct information. For example, examining the type of plankton that lived in a region at a given time can tell us how cold it was. A succession of species that thrive in warm or cold environments will indicate a succession of warm and cold periods. An analysis of the pollen present in sediment will yield information on the proportion of the major plants that lived on the nearby continent. In addition, the material is measured to obtain the ratio of chemical elements such as Pa/Th, and the ratio of isotopes such as oxygen and carbon isotopes ($\delta^{18}O$, $\delta^{13}C$, $\Delta^{14}C$), which can be used as indicators of specific processes such as ocean circulation changes, temperature changes, terrestrial biosphere changes, etc. (see Volume 1, Chap. 21).

The idea that ice from ice sheets could be used to provide information on past changes originated in the 1950s with the work of Willi Dansgaard and others, who hypothesized that the link between temperature and the number of heavy oxygen isotopes in precipitation could be applied to old ice to reconstruct past temperature changes. Ice core drilling began in Antarctica, Alaska and Greenland in the 1950s, but these cores were around 100 m deep and the recovery quality was low. Drilling to extract ice cores was spurred by the International Geophysical Year (1957–1958) and longer ice cores were drilled in Greenland at Site 2 (1956–1957) and in Antarctica at Byrd station (1957–1958) and at Little America V (1958–1959). Many more ice cores have been drilled since then, mainly in Greenland and Antarctica. Past climate and environmental changes are recorded both in the ice and in air bubbles trapped within the ice of the ice cores. For instance, the proportion of hydrogen and oxygen isotopes in the ice provide information on past surface temperatures, while the concentration of greenhouse gases can be directly measured in the air bubbles.

To understand the changes recorded in climate archives and to test various hypotheses on feedback mechanisms, more and more climate models now include biogeochemical cycles, and sometimes isotopes (see Volume 2, Chaps. 25 and 29). Additional mechanisms and elements are added progressively so that simulations and measured data can be compared directly. This continuous comparison helps to increase our knowledge of the climate system resulting in improved models that can be used to evaluate possible future changes. These coupled carbon-climate models are valuable tools to help understand past changes and increase our confidence in future climate projections.

In this chapter we describe the main biogeochemical cycles interacting with the climate: carbon (CO_2 and CH_4),

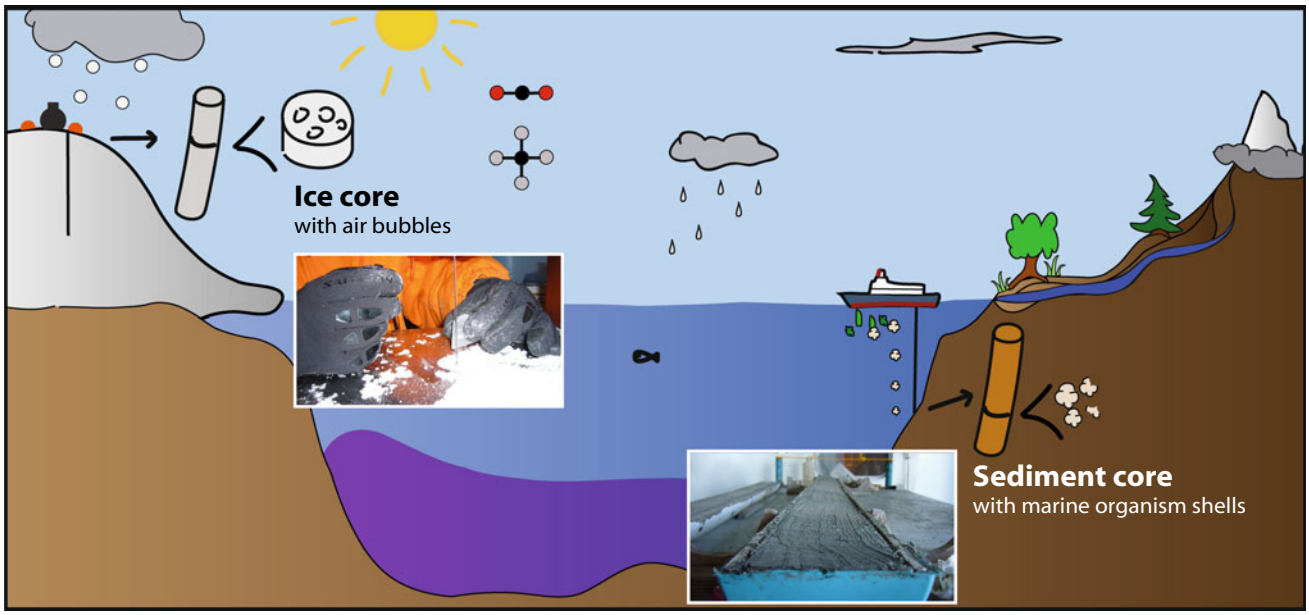

Fig. 23.1 Diagram of the Earth system and schemes showing ice cores and sediment cores extraction

nitrogen, oxygen, sulphur, as well as aerosols. We review existing records from marine sediment cores and ice cores and highlight the current knowns and unknowns.

Carbon Cycle

Two atmospheric gases containing carbon play a major role in the interactions between climate and biogeochemistry: carbon dioxide (CO_2) and methane (CH_4). While CO_2 is the most famous and most studied element, CH_4 is far from negligible and has a rather different cycle. We will first focus on CO_2, then on CH_4, before reviewing past changes.

Carbon Dioxide (CO_2)

On the timescale of a few hundred to a few tens of thousands of years, the main carbon reservoirs are the ocean (including sediments), atmosphere and land (including terrestrial biosphere and permafrost) (Fig. 23.2). On the longer timescale of a few million years the lithosphere (rocks) starts to play a major role (see Volume 1, Chap. 2, Volume 2, Chaps. 22 and 26). Exchanges between these reservoirs involve biotic processes, due to biological activity such as photosynthesis by plants, and abiotic processes.

In the atmosphere, CO_2 is the main form of carbon and is relatively well mixed over a year. Its concentration is currently increasing due to anthropogenic activity and, at the beginning of 2018, the atmospheric CO_2 concentration was over 400 ppm (408 in March 2018, NOAA, https://www.esrl.noaa.gov/gmd/ccgg/trends/monthly.html). At the beginning of the pre-industrial era, it was around 280 ppm, corresponding to a carbon stock of around 600 GtC.

On land, atmospheric CO_2 is taken up by plants during photosynthesis, turning CO_2 into organic carbon. The living biomass is then converted into dead organic carbon matter in litter and soils. Organic carbon is progressively returned to the atmosphere by autotrophic and heterotrophic respiration. Currently, carbon storage in the terrestrial biosphere is around 2500 GtC. If the conditions become cold enough, the soil freezes, locking the carbon into permafrost, i.e. frozen soil. During warming, the permafrost thaws, and carbon is returned to the atmosphere. The current estimate of carbon stored in permafrost is ~1700 GtC (Tarnocai et al. 2009), making it the single largest component of the terrestrial carbon pool. The fluxes of carbon between the atmosphere and land are around 120 GtC/year.

The ocean is the largest carbon reservoir (excluding the lithosphere) with around 38,000 GtC both in organic and inorganic forms. Carbon fluxes to the ocean come from the atmosphere through surface exchanges and from the continent from riverine inputs. In the ocean, dissolved carbon ($CO_{2(aq)}$) gets hydrated into H_2CO_3 (carbonic acid), which then gives bicarbonate ion (or hydrogen carbonate ion, HCO_3^-) and carbonate ion CO_3^{2-}. All these dissolved species are summed up in the term "dissolved inorganic carbon" (DIC). Because the concentration of H_2CO_3 is very small, it is included in $CO_{2(aq)}$. $CO_{2(aq)}$, HCO_3^- and CO_3^{2-} are in equilibrium following the chemical equations:

$$CO_{2(aq)} + H_2O \rightleftarrows HCO_3^- + H^+$$

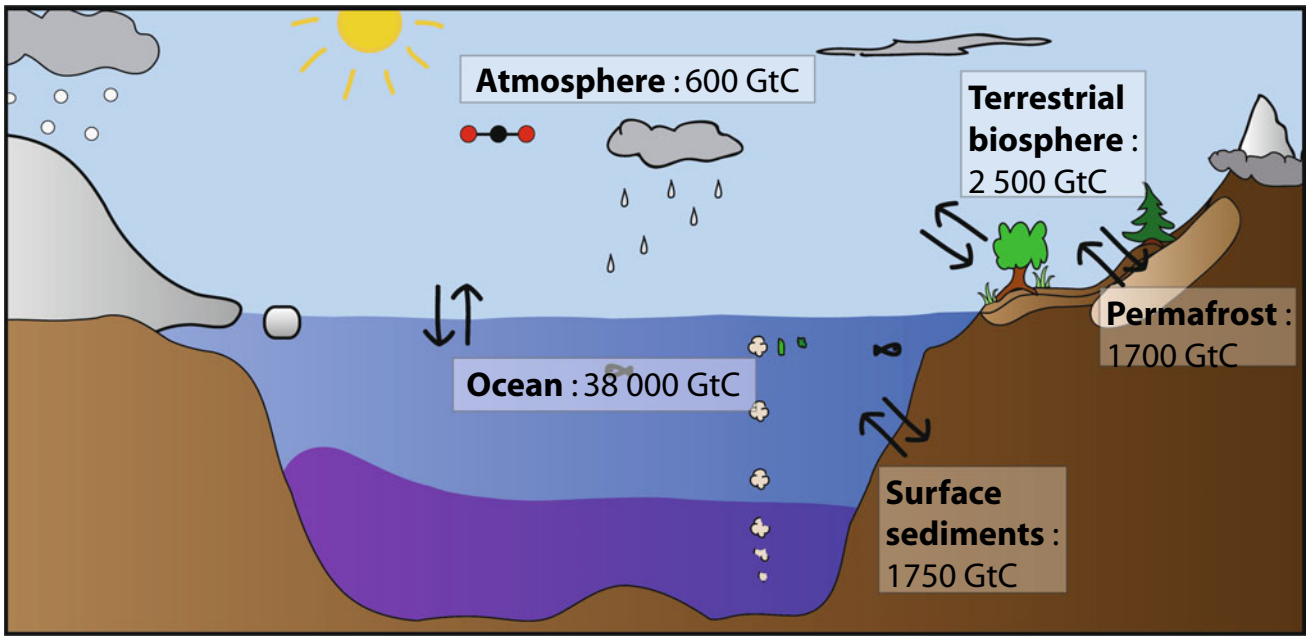

Fig. 23.2 Diagram of the short term carbon cycle (up to a few tens of thousands years)

$$HCO_3^- \rightleftarrows CO_3^{2-} + H^+$$

CO_2 is exchanged between the atmosphere and the surface ocean depending on the difference in partial pressure of CO_2 (pCO_2) between the atmosphere and ocean, on sea ice coverage and on wind. The pCO_2 in the ocean is governed by temperature and salinity. The flux of carbon between atmosphere and dissolved inorganic carbon is around 70 GtC/year in both directions.

In polar regions, CO_2 is more soluble in water because of the colder conditions, resulting in more dissolved inorganic carbon in the surface ocean. These regions are also major sites of deep convection, where surface water becomes denser due to colder and more saline conditions, and can sink to the ocean's depths. The carbon from the surface is thus transported to the deeper ocean. This uptake of carbon from the atmosphere to the ocean is called the solubility pump.

Marine phytoplankton uses dissolved CO_2 during photosynthesis, using nutrients and solar energy, following the simplified equation:

$$106\ CO_2 + 16\ NO_3^- + H_2PO_4^- + 17\ H_3O^+ + 105\ H_2O + \textit{solar energy} \rightarrow (CH_2O)_{106}(NH_3)_{16}(H_3PO_4) + 138\ O_2$$

The ratios C: N: P: O_2 are the Redfield ratios, and the inorganic carbon assimilated by biology constitutes the gross primary production. The difference between gross primary production and the carbon respired by phytoplankton is the net primary production. The phytoplankton that has synthetized organic carbon is then grazed by zooplankton. The depth to which sufficient light penetrates to sustain life is called the euphotic zone and extends to around 100–200 m deep. When plankton dies, it is partially remineralized at the surface, and the remainder sinks to the deeper ocean where it will be progressively remineralized. Carbon can then be found in two forms: particulate organic carbon or dissolved organic carbon. During remineralisation, carbon and nutrients are returned to the solution in dissolved form and can be used again in the euphotic zone for photosynthesis when it is brought back to the surface. Hence, biology also transfers carbon from the surface to the deep ocean leading to carbon being taken up from the atmosphere by the ocean: this is the biological pump. The flux of carbon between dissolved inorganic carbon and marine biology is around 50 GtC/year.

Marine biology not only produces organic carbon, but some organisms also create a shell made of calcium carbonate ($CaCO_3$). Most shells are made of calcite (coccolithophores and foraminifera) or aragonite (pteropods), two forms of calcium carbonate. The equation for calcium carbonate production is:

$$Ca^{2+} + CO_3^{2-} \rightarrow CaCO_3$$

In deep areas in the ocean where water is undersaturated with respect to calcium carbonate, the inverse equation takes place and the shells are progressively dissolved. If they reach the bottom of the ocean, they are buried in sediments. At the ocean surface, the production of calcium carbonate shells leads to a decrease in CO_3^{2-}, which increases CO_2 due to the following equation:

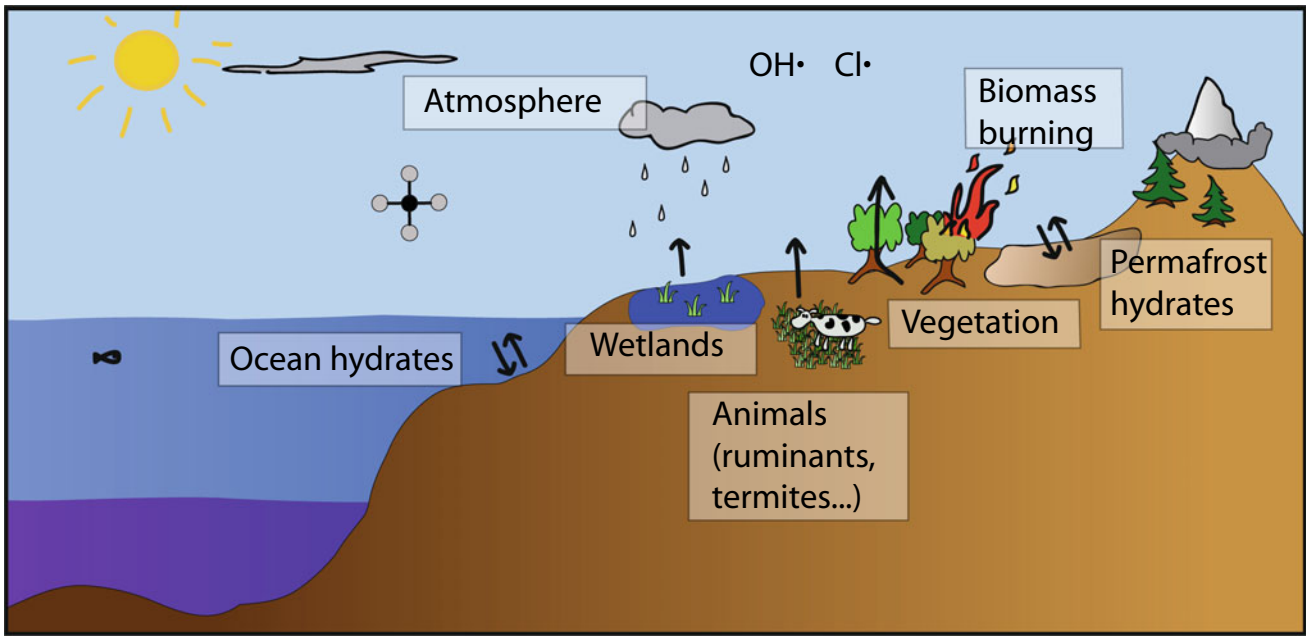

Fig. 23.3 Diagram of the methane cycle

$$CO_2 + CO_3^{2-} + H_2O \rightleftarrows 2HCO_3^-$$

Hence this process, called the carbonate pump, counteracts the two carbon pumps described above.

Finally, ocean circulation impacts on the carbon cycle in the ocean by modifying the distribution of carbon and nutrients, the latter modifying primary production and thus the carbon distribution. Primary production is limited by several nutrients such as nitrate (N), phosphorus (P) and iron (Fe). The concentration of these nutrients mainly depends on transport from the nutrient-rich deeper ocean layers to the surface which is nutrient-depleted due to nutrient absorption by marine biology. Hence, in upwelling zones where lots of nutrients are brought to the surface primary production is high. When deep convection is active, it also provides important nutrient transport to the surface favouring production. In the opposite, in low latitude gyres nutrients are lacking and primary production is low. Some regions in the North Pacific and in the Southern Ocean display low productivity despite high nitrate concentrations (HNLC regions for high nitrate low chlorophyll). This is due to the lack of iron which limits production.

Methane (CH_4)

Methane is the second most important greenhouse gas after CO_2. Discovered in 1976 by Wang et al., its capacity to absorb infrared radiation is around 28 times more efficient than CO_2, over a time period of 100 years. Hence, although the concentration of CH_4 is 20 times lower than CO_2, it still plays a crucial role as a greenhouse gas, with a radiative forcing of around one third that of CO_2. The natural sinks and sources of CH_4 are different from those of CO_2, yielding a distinctly different—although often with some common features—evolution over time as described in Sect. "Glacial-Interglacial Cycles".

In the atmosphere, CH_4, like CO_2, is well mixed over a year. However, while CO_2 stays around 100 years in the atmosphere, CH_4 has a shorter lifetime of around 9 years. This is because the main sink of CH_4 is in the atmosphere: CH_4 is oxidized by the hydroxyl radical, OH. Oxidation by OH, which is photochemically produced in the atmosphere, takes place mainly in the troposphere, but also, to a lesser extent, in the stratosphere, and depends on several parameters. First, it depends on the speed of the reaction with OH, hence on temperature. Second, it depends on the quantity of free OH, which itself, depends on other compounds reacting with OH such as volatile organic compounds (VOCs) and ozone. In addition, the reaction of CH_4 with OH produces the CH_4 feedback effect: if CH_4 decreases, OH increases, which in turn reduces even more the concentration of CH_4 (Prather 2007). Another smaller sink of CH_4 in the atmosphere is the reaction of CH_4 with chlorine gas.

Contrary to CO_2, the main natural sources of CH_4 are from the continents (Fig. 23.3). The main contributors are wetlands, areas saturated with water such as marshes and swamps. CH_4 is produced by microbes (methanogenic archaea) in anoxic conditions in wetlands. Locally, CH_4 production strongly depends on oxygen availability,

temperature and the composition of the soil. Currently, around three quarters of CH_4 production takes place in tropical regions and a quarter in boreal regions. Animals also produce CH_4, in particular termites and ruminant animals. In addition, vegetation is also involved in CH_4 emission. Vegetation as a CH_4 producer is still debated, but it can impact on the transport of CH_4 from the soil to the atmosphere. Permafrost can also be a source of CH_4 but related uncertainties are high. Finally, CH_4 is also emitted by biomass burning. There is also a small continental sink of atmospheric CH_4: the oxidation by methanotrophic bacteria in soils.

A smaller CH_4 source is from the ocean, with CH_4 coming mainly from coastal regions. However, the ocean could contain large CH_4 quantities trapped as methane clathrate in sediments, mainly on continental shelves. Methane clathrate, or methane hydrate, is a compound in which methane is trapped in a crystal of water. Clathrates are stable at low temperature and high pressure. The size of this reservoir is poorly constrained and could contain 500–2500 GtC, a smaller amount than the very high quantities suggested in the 1970s (Milkov 2004).

While the atmospheric CH_4 mixing ratio impacts on climate by modifying the atmospheric radiative balance, climate impacts on the sources and sinks of methane. In particular, wetlands are very dependent on the hydrological cycle and microbial activity, and thus the emission of methane, is strongly dependent on temperature. In addition, in the atmosphere, methane oxidation by OH radicals is one of the most temperature-sensitive reactions.

Glacial-Interglacial Cycles

The main archives used to infer past changes in the carbon cycle are ice cores and marine sediment cores (see Volume 1). While ice cores provide an invaluable direct way of assessing past changes in atmospheric CO_2 and CH_4, there is no direct record of past ocean and land carbon storage. Fortunately, the carbon element has three isotopes: ^{12}C, ^{13}C and ^{14}C, and their ratios, which can be measured from foraminifera shells in the sediments, as well as in the air in ice cores, provide clues to understand changes in past carbon reservoirs.

Ice Cores

Ice cores recording glacial-interglacial changes are extracted from the Greenland ice sheet in the Northern Hemisphere, and the Antarctic ice sheet in the Southern Hemisphere (Volume 1, Chap. 9). The oldest ice obtained from Greenland is ~130,000 years old (NEEM Community Members 2013), much younger than the oldest ice from Antarctica which is ~800,000 years old (EPICA Community Members 2004). This age could be extended further and future expeditions are planned to find and drill Antarctic ice older than a million years (Dahl-Jensen 2018).

Ice cores provide a direct record of past atmospheric gas concentrations, such as CO_2 and CH_4, thanks to air bubbles trapped in ice (Fig. 23.4). The air is trapped only at the bottom of the firn, a 60–120 m permeable layer below the surface where snow progressively densifies into ice (see Volume 1, Chap. 9). It results in an age difference between

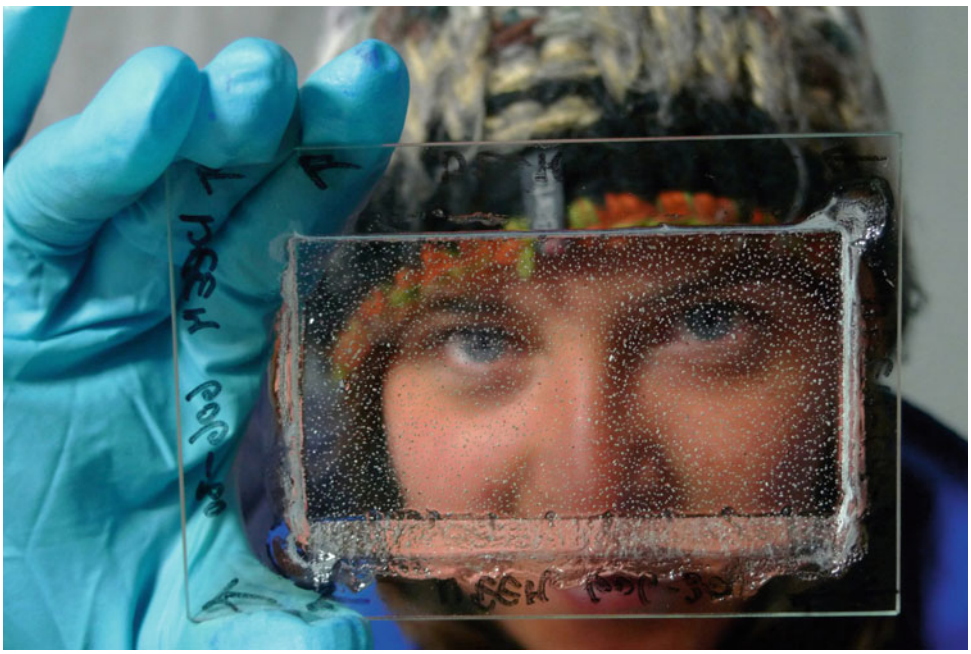

Fig. 23.4 Air bubbles trapped in ice taken from an ice core. *Credit* Sepp Kipfstuhl (Alfred Wegener Institute)

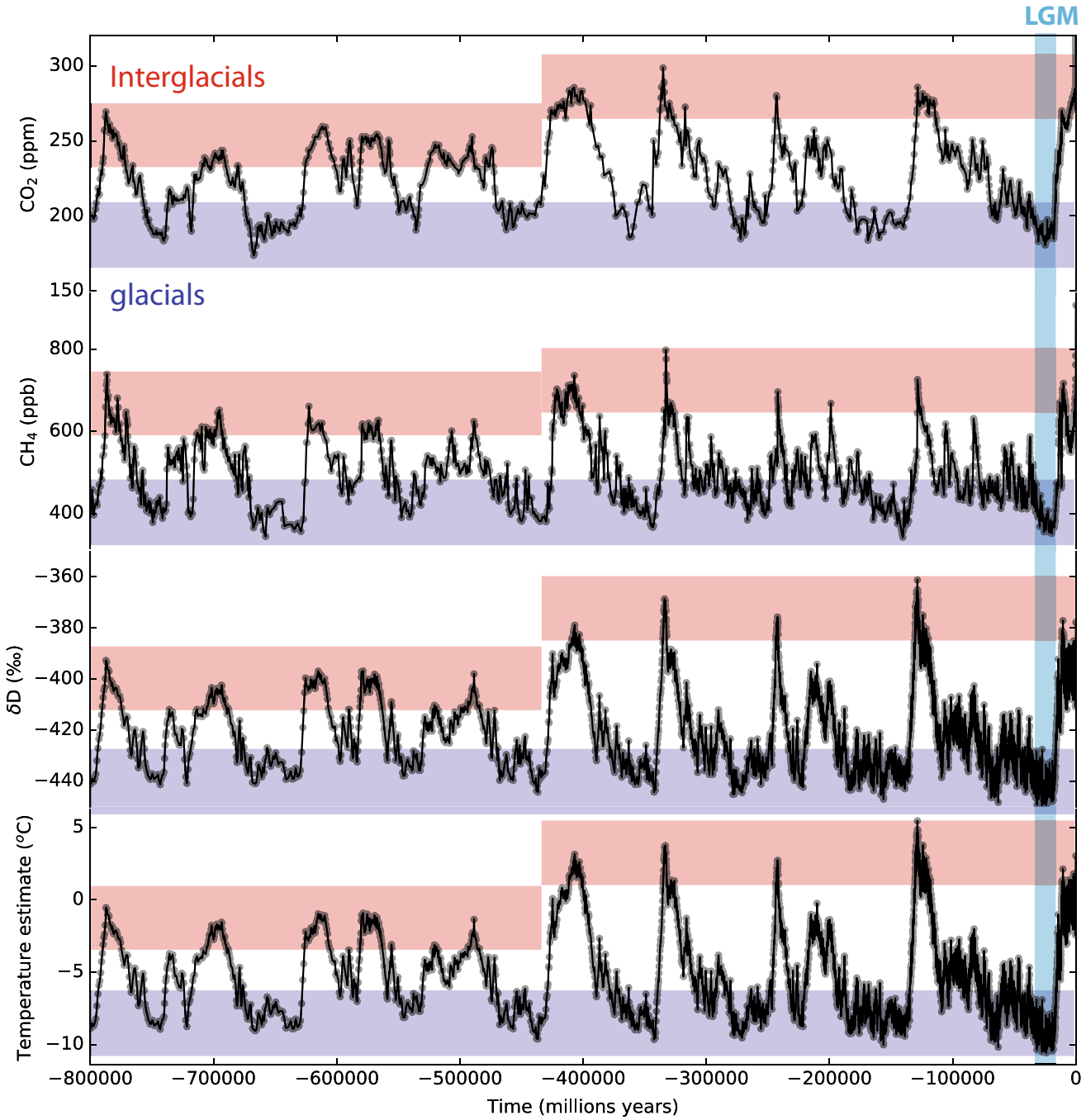

Fig. 23.5 Evolution of CO_2 (ppm), CH_4 (ppb), deuterium (‰) and temperature (°C) over the last 800,000 years. The Last Glacial Maximum (LGM) is indicated by the blue bar. Data from EPICA Community Members (2004), Jouzel et al. (2007), Loulergue et al. (2008), Bereiter et al. (2015)

the ice and the trapped air at a given depth level. This age difference that may be as much as several hundred years and even up to several thousands of years in the case of central Antarctic sites (Schwander and Stauffer 1984). Estimates of the age difference between the ice and the entrapped air are possible but there are associated uncertainties which are detailed in Volume 1, Chap. 8. The first reliable measurements of past CO_2 changes recorded in Antarctic ice were published in the 1980s, initially covering the last 30,000 years (Delmas et al. 1980), then the last 160,000 years (Barnola et al. 1987), and now as much as the last 800,000 years (Lüthi et al. 2008; Bereiter et al. 2015, Fig. 23.5). Note that only past atmospheric CO_2 concentrations determined from Antarctic ice cores are reliable, as

Greenland ice is prone to in situ production of CO_2, which alters the atmospheric CO_2 concentration already within the ice (Tschumi and Stauffer 2000). Measurements of past CH_4 concentrations extracted from both Greenland and Antarctic ice cores are reliable. While the first CH_4 records covered the last 160,000 years (Chappellaz et al. 1990), they also now date back to 800,000 years (Loulergue et al. 2008). In addition to greenhouse gas concentrations, measurements of the air from ice cores now also involve $\delta^{13}C$ from CO_2, termed $\delta^{13}CO_2$ (Schneider et al. 2013; Schmitt et al. 2012; Lourantou et al. 2010). Ice cores offer a unique possibility to quantify the sequence of events occurring between greenhouse gas variations and changes in ice core tracers inform on other parts of the climate system such as local surface temperature using ice $\delta^{18}O$ (see Volume 1, Chap. 11).

Sediment Cores

At the bottom of oceans and lakes, sediments progressively accumulate as various particles and debris are deposited. They include both organic material, such as shells, and inorganic material, such as clay. The invention of the first piston corer in 1947 by Kullenberg allowed marine sediment cores to be extracted from the ocean bottom, yielding a wealth of information on past ocean changes (Volume 1, Chap. 21). In particular, sediments provide information on past marine productivity, for example by measuring the fraction of organic material, calcite or opal (biogenic silica). The proportion of organic material measured in upwelling zones is large, because productivity is high. In regions where organic material is not well preserved, silicate can be used as another proxy for biological productivity. Other proxies are also used, such as ^{10}Be, authigenic U, $^{231}Pa/^{230}Th$). They rely on the fact that some elements preferentially fix to particles (Th) while others remain in solution (U, Pa). Their ratio gives an indication of past particle flux in the water column, hence biological productivity.

As detailed in Volume 1, Chap. 21, carbon isotopes are measured in foraminifera shells providing constraints on the carbon cycle. Whenever carbon is exchanged at an interface, fractionation takes place, which modifies $\delta^{13}C$ defined as:

$$\delta^{13}C = \left(\frac{\left(\frac{^{13}C}{^{12}C}\right)_{sample}}{\left(\frac{^{13}C}{^{12}C}\right)_{standard}} - 1 \right) \times 1000$$

The standard is the PDB (Peedee belemnite) carbon isotope standard, which corresponds approximately to average limestone (Craig 1957).

For example, biological activity preferentially uses the light ^{12}C over ^{13}C, so that plants or plankton are enriched in ^{12}C, and the environment (atmosphere for terrestrial biosphere, surface ocean for plankton) has higher $\delta^{13}C$ values

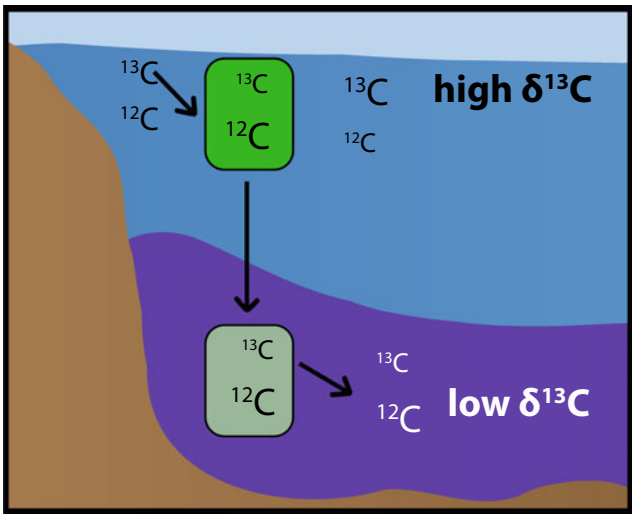

Fig. 23.6 Diagram of $\delta^{13}C$ in the surface and deep ocean. In the surface waters, the value of oceanic $\delta^{13}C$ is high because of photosynthetic activity, which preferentially uses light ^{12}C, thus enriching the environment with heavy ^{13}C. In the deep ocean, remineralisation releases carbon with more ^{12}C, therefore lowering $\delta^{13}C$

(Fig. 23.6). A more active biological productivity will thus increase the $\delta^{13}C$ in the surrounding environment.

Sediments on continents can also be extracted and studied, but continental sediment cores are scarcer than their marine counterpart. Pollen in these sediments, for example in loess, give information on past local plant types and help to reconstruct past vegetation changes.

Past Changes

Ice core data show large changes in concentrations of CO_2 and CH_4 between warm interglacials and cold glacials (Fig. 23.5). Concentrations of both CO_2 and CH_4 are higher during interglacials: around 280 ppm for CO_2 and 780 ppbv for CH_4, and lower during glacials: around 190 ppm for CO_2 and 320 ppbv for CH_4 (Lüthi et al. 2008; Bereiter et al. 2015; Loulergue et al. 2008). While values are relatively similar during all glacials, the interglacial CO_2 values are around 20 ppm lower for the older interglacials (before 430 ka) compared to the more recent ones. The concomitant records of climate and air composition demonstrate the strong link between climate and greenhouse gases, both for CO_2 (Barnola et al. 1987; Petit et al. 1999; Siegenthaler et al. 2005; Lüthi et al. 2008) and CH_4 (Chappellaz et al. 1990; Petit et al. 1999; Spahni et al. 2005; Loulergue et al. 2008). Recent research has shown that CO_2 and Antarctic temperature changed synchronously at the start of the two last deglaciations (within 200 years; Parrenin et al. 2013; Landais et al. 2013).

Several explanations have been put forward to explain the atmospheric CO_2 waxing and waning during

glacial-interglacial cycles. Atmospheric CO_2 changes are driven by changes in carbon storage in other reservoirs, particularly on land and in the ocean.

On land, the lower sea level, by 120 m, during glacial time increased the surface area where plants could develop, although the larger ice sheets covering part of North America and Eurasia reduced the available area. Overall, due to the colder and drier climate, as well as reduced atmospheric CO_2 concentration, photosynthesis by land vegetation is reduced and the terrestrial biosphere tends to represent a smaller carbon reservoir during glacial period, which would increase atmospheric CO_2, not lower it. This is indicated by ocean $\delta^{13}C$ which decreased by around 0.03–0.04‰ during the Last Glacial Maximum compared to the pre-industrial level. This is explained by the transfer of continental carbon with low $\delta^{13}C$ values (due to fractionation during photosynthesis) to the ocean (Shackleton 1977; Bird et al. 1994), causing a reduction in continental carbon of around 270–720 GtC. An understanding of the changes in the terrestrial biosphere can also be obtained from paleo-biomes, using pollen from sediment cores (Adams et al. 1990; Crowley 1995; Maslin et al. 1995) which show a carbon loss of around 750–1350 GtC. Pollen data have also been used to reconstruct maps of vegetation types during the LGM (Fig. 23.7).

However, frozen soils, i.e. permafrost, may have increased in glacial times, potentially storing more carbon, which could partly explain the lower CO_2 (Ciais et al. 2012) and help resolve the $\delta^{13}CO_2$ signal recorded in ice cores, which strongly depends on land carbon changes (Crichton et al. 2016).

Although permafrost probably played a role, most of the change is likely to have come from the ocean, which is a much bigger carbon reservoir. In addition, $\delta^{13}C$ measurements from sediment cores indicate large changes in the ocean (Curry and Oppo 2005; Marchal and Curry 2008; Hesse et al. 2011). In the ocean, the carbon cycle changes could originate from modifications of biological activity and physical or chemical changes. Known processes include temperature change as colder temperatures lead to more carbon being stored in the ocean. The sea level drop of $\sim$120 m during glacial maxima results in higher concentrations of salinity, which causes a reduction in the storage capacity of carbon in the ocean, and an increase in nutrients, which increases biological activity and thus increases ocean carbon storage. However, these processes are not sufficient to fully explain the decrease in CO_2 decrease (see review by Sigman and Boyle 2000; Archer et al. 2000), and additional mechanisms are needed.

Four main hypotheses have been proposed to explain the CO_2 lowering by increased ocean carbon storage: increased biological pump, isolation of the ocean from the atmosphere due to sea ice coverage, changes in ocean dynamics, and carbonate compensation.

The biological pump causes more carbon to be stored when it is stimulated, for example when more nutrients are delivered to the ocean (Broecker and Peng 1982). In regions of high nutrients low chlorophyll (HNLC), biological activity is limited due to the lack of iron. An influx of iron to these zones during glacial periods would increase biological activity. Alternatively, the biological pump could also store more carbon if it becomes more efficient, for example with a greater carbon to nutrient ratio (Broecker and Peng 1982) or a switch of plankton species with higher productivity (Archer and Maier-Reimer 1994). However, both data and model simulations have shown that changes in biological activity are not sufficient to sufficiently account for the decrease in atmospheric CO_2 (Kohfeld et al. 2005; Bopp et al. 2003a; Tagliabue et al. 2009; Lambert et al. 2015).

Increased sea ice coverage has also been proposed, as this could isolate the ocean, preventing carbon from getting to the atmosphere, hence lowering atmospheric CO_2 (Stephens and Keeling 2000). But such an impact has only been simulated in very simple models, more complex models do not show such an effect on CO_2 (Archer et al. 2003).

Most current theories involve changes in ocean dynamics, and point to the Southern Ocean (Fischer et al. 2010). A larger ocean volume occupied by AABW, or slower overturning, could result in more carbon stored in the deep ocean, reducing atmospheric CO_2. Ocean circulation changes are supported by data generally indicating a reduced NADW and a more stratified Southern Ocean (Adkins 2013). In particular, $\delta^{13}C$ measurements show lower $\delta^{13}C$ values in the deep glacial ocean, especially around Antarctica, and higher values near the surface (Curry and Oppo 2005; Marchal and Curry 2008; Hesse et al. 2011). In addition, very salty water has been measured in the deep Southern Ocean (Adkins et al. 2002). Complementary data, such as from neodymium isotopes (Basak et al. 2018), B/Ca ratio (Yu et al. 2016) and $\Delta^{14}C$ (Skinner et al. 2010), also point towards changes in the circulation in the Southern Ocean.

Comparison of model simulations over the last decade have shown that models simulate a large range of ocean circulation changes, which are generally opposite to those deduced from data. In PMIP3, most models simulate a strengthening and deepening of the NADW with LGM boundary conditions (Muglia and Schmittner 2015). Yet simulations have shown that better agreement with $\delta^{13}C$ and CO_2 data requires lower NADW intensity and/or shoaling of NADW (Tagliabue et al. 2009; Tschumi et al. 2011; Menviel et al. 2017). This is also seen in terms of water mass volume with a smaller volume of NADW and a larger volume of AABW filling the ocean. The latter has a larger DIC content,

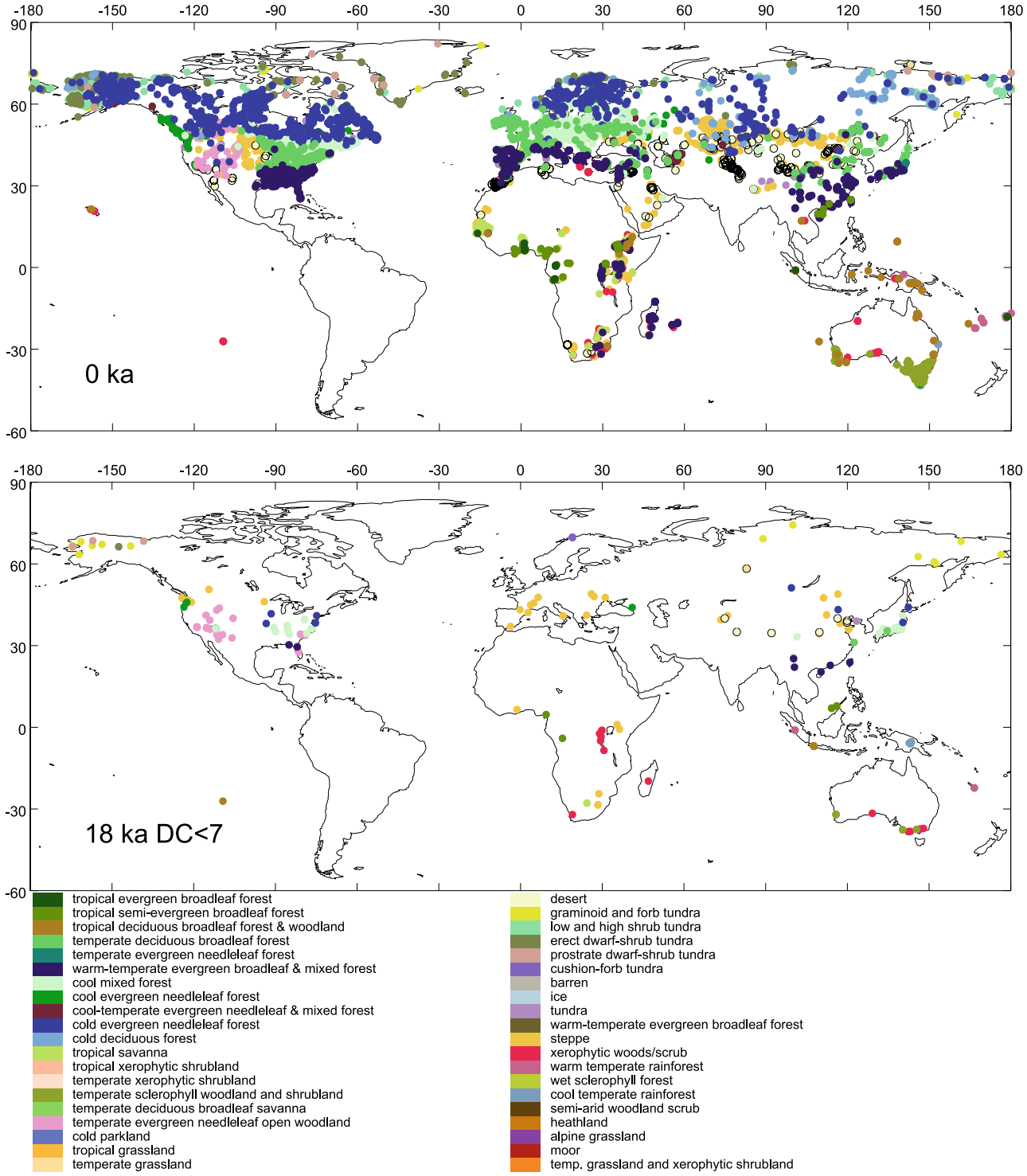

Fig. 23.7 Land vegetation maps for the modern era and the LGM, data from Prentice et al. (2000), Harrison et al. (2001), Bigelow et al. (2003) and Pickett et al. (2004). This figure with homogenised nomenclature has been downloaded from http://www.bridge.bris.ac.uk/resources/Databases/BIOMES_data

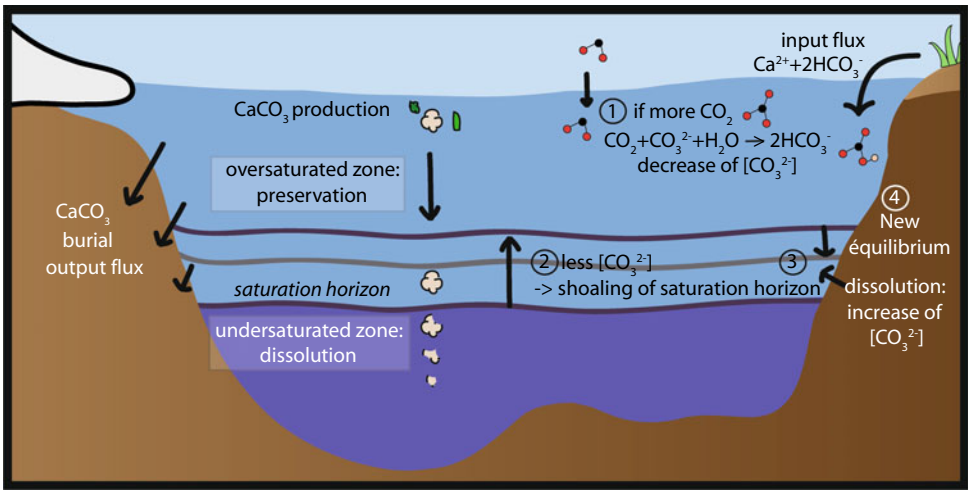

Fig. 23.8 Diagram of the carbonate compensation mechanism

resulting in more carbon in the ocean when the AABW occupies relatively more volume than the NADW (Brovkin et al. 2012). This is referred to as the "standing volume effect" (Skinner 2009).

Changes of ocean circulation could be due to changes of winds (Anderson et al. 2009; Toggweiler et al. 2006). But data show no clear evidence of large wind changes (Kohfeld et al. 2013) and model simulations have shown that this is unlikely to have had a strong effect on the carbon cycle (Menviel et al. 2008a). It could also be linked to ocean diffusion (Bouttes et al. 2009, 2011) and particularly to bottom topography induced diffusion (De Boer and Hogg 2014). Alternatively, it could be linked to sea ice changes and modifications in bottom water formation (Ferrari et al. 2014; Bouttes et al. 2010). Indeed, sea ice formation around Antarctica was probably enhanced, especially during winter (Gersonde et al. 2005). Yet models usually fail to represent glacial sea ice extent (Roche et al. 2012; Goosse et al. 2013; Marzocchi and Jansen 2017). Improving sea ice formation in models during the LGM and the sinking of dense water around Antarctica should help towards explaining the glacial atmospheric CO_2 concentration.

Finally, on longer timescales of a few thousand years, carbonate compensation amplifies the increase of oceanic carbon storage, by maintaining a balance between inputs and outputs of alkalinity fluxes (Fig. 23.8). For example, (1) if $[CO_{2(aq)}]$ increases (for example due to the solubility pump), the equation below is displaced towards more $[HCO_3^-]$, reducing $[CO_3^{2-}]$.

$$CO_2 + CO_3^{2-} + H_2O \rightleftarrows 2HCO_3^-$$

(2) When $[CO_3^{2-}]$ is reduced, the saturation horizon, the limit between oversaturated and undersaturated water, is shifted upwards and a larger volume of water is undersaturated. (3) The larger undersaturated zone results in more $CaCO_3$ dissolution, which increases $[CO_3^{2-}]$, counteracting the initial reduction and leading to a lowering of $[CO_2]$ as the previous equation is shifted to the right, allowing the ocean to take up more CO_2 from the atmosphere. (4) When $[CO_3^{2-}]$ is increased, the oversaturated zone increases and the saturation horizon is shifted down until a new equilibrium is reached. Overall, the ocean takes up more carbon with this mechanism through dissolution of $CaCO_3$.

The concomitant lowering of CH_4 during the glacial period could be due to either a decrease in CH_4 sources, mainly wetlands, or an increase in sinks, mainly more oxidation by increased OH.

During the LGM, the colder climate, larger ice sheets and reduced hydrological cycle all led to a reduction of wetlands and reduced emissions. The first hypothesis to explain the lower CH_4 concentration during the LGM has thus focused on reduced emissions, possibly from low latitude wetlands (Chappellaz et al. 1993). Later, process-based models were developed and used to evaluate emissions (Valdes et al. 2005; Kaplan et al. 2006; Weber et al. 2010). But the resulting reduction of emissions was not enough to account for the low CH_4 concentration detected in ice cores. It was then hypothesized that the oxidizing atmospheric capacity had changed, for instance through a reduction of emissions of volatile organic compounds (VOCs) from forests (Valdes et al. 2005). The VOCs react with OH in the same way as CH_4, thus constituting an OH sink, which increases the lifetime of CH_4. If more VOCs are produced, OH concentration is reduced and the concentration of CH_4 is increased. However, more complex chemical models show that certain processes compensate for the reduced atmospheric oxidizing capacity, such as temperature, humidity, lightening (Levine et al. 2011; Murray et al. 2014). In conclusion, it now appears that the atmospheric oxidizing capacity is probably of secondary importance, as process-based models and the

methane retroaction (less CH_4 leads to more OH, hence less CH_4) estimate emissions that explain almost entirely the low CH_4 value at LGM (Quiquet et al. 2015).

Beyond the problem of the large changes in glacial-interglacial GHG concentrations, another issue was raised in the 2000s when data became available for periods older than ~430,000 years BP. As shown on Fig. 23.5, older interglacials before ~430,000 ka BP (before the "Mid Brunhes Event") are characterized by a colder climate than more recent interglacials, associated to lower GHG concentrations. The colder interglacial climate can be attributed to different orbital configurations and lower CO_2 (Yin and Berger 2010, 2012) but the reason for the lower GHG concentrations still remains to be explained (Bouttes et al. 2018).

Abrupt Changes

At the centennial to millennial scale, climate variability is superimposed onto the orbital-scale glacial-interglacial cycles and is recorded by specific expressions at different latitudes and in different climate archives (Clement and Peterson 2008; see Volume 2, Chap. 29). Indeed, Greenland ice cores unveiled a succession of events called Dansgaard-Oeschger (D-O) events during the last glacial period (Dansgaard et al. 1993; North Greenland Ice Core Project Members 2004). Typically, a DO event is depicted as an abrupt warming of 5–16 °C of the mean annual surface temperature within a few decades toward a relatively mild phase. This phase is then usually characterised by a gradual cooling over several centuries and its end is marked by a rapid cooling leading to a relatively stable cold phase persisting over several centuries or even up to a thousand years. The signature of DO events is recorded in continental and marine records in the Northern Hemisphere. In the Southern Hemisphere, there are counterparts to these DO events. Ice cores indicate more gradual (millennial-scale) warming in Antarctica during the Greenland cold phases (EPICA Community Members 2006; Barker et al. 2009; WAIS Divide Project Members 2015). The antiphase relationship between the two hemispheres is attributed to the thermal bipolar seesaw, a mechanism whereby heat is redistributed in the Atlantic Ocean (Stocker and Johnsen 2003).

In addition to the succession of Dansgaard-Oeschger events, another prominent feature identified in marine sediments from the North Atlantic is the occurrence of the Heinrich events. Heinrich events are identified by the presence of debris in sediments, and were first discovered by Ruddiman in 1977. These debris are too big to be transported by oceanic currents, and in 1988 Heinrich proposed that they could have been brought by icebergs which melted above the zone where these ice rafted debris (IRD) were found in sediments (Hemming 2004).

Antarctic ice core records show a rapid rise in atmospheric CO_2 of around 15 ppm over 2000–4000 years (Fig. 23.9), generally synchronous with the millennial-scale Antarctic warming, followed by a more gradual decrease than the Antarctic temperature drop (Ahn and Brook 2008; Bereiter et al. 2012). Measurements have shown that the CO_2 rise was not steady, but punctuated by events with a rapid increase (Ahn et al. 2012). Other data measurements have resulted in several carbon sources being suggested to explain these increases in atmospheric CO_2, such as the Southern Ocean (Gottschalk et al. 2016) or the North Atlantic (Ezat et al. 2017).

These rapid changes of atmospheric CO_2 have been studied only relatively recently as previously, the temporal resolution in the records was not sufficient. Temperature changes have been studied for longer since more high resolution data were available. To replicate these rapid climate changes in simulations, modellers have found that artificially adding freshwater to the North Atlantic, for example theoretically due to the melting of numerous icebergs, could slow down or even stop the Atlantic meridional overturning circulation. This then generally leads to warming in the North Hemisphere and cooling in the South Hemisphere, in line with changes observed in the data (see Volume 2, Chap. 29).

More recently, the impact of such hosing experiments on the carbon cycle and atmospheric CO_2 evolution has also been tested in carbon-climate models, to evaluate the role of the terrestrial biosphere and the ocean, in particular, in coupled ocean-atmosphere-terrestrial biosphere models. The model response to the freshwater input appears to be very dependent on the type, duration and amplitude of the freshwater input, on the background climate (glacial vs pre-industrial) and the model. For example, the LOVECLIM model simulates a 15 ppmv increase in the context of a pre-industrial climate, but a 10 ppm CO_2 decrease in a glacial climate in response to a decrease in the AMOC driven by the same freshwater input (Menviel et al. 2008b). In both cases, the ocean takes up more carbon and the terrestrial biosphere loses carbon, but the balance between the two outcomes results in opposite effects on the atmospheric CO_2. This balance also depends on the different time reactions of the carbon reservoirs: vegetation reacts more rapidly than the ocean.

In general, most models simulate an overall increase in atmospheric CO_2 ranging from a few ppm up to more than 20 ppm, depending on the model and the size of the freshwater flux (Obata 2007; Schmittner and Galbraith 2008; Menviel et al. 2008b; Bozbiyik et al. 2011; Bouttes et al. 2012; Matsumoto and Yokoyama 2013), but the causes are different: in some models the ocean gains carbon and the

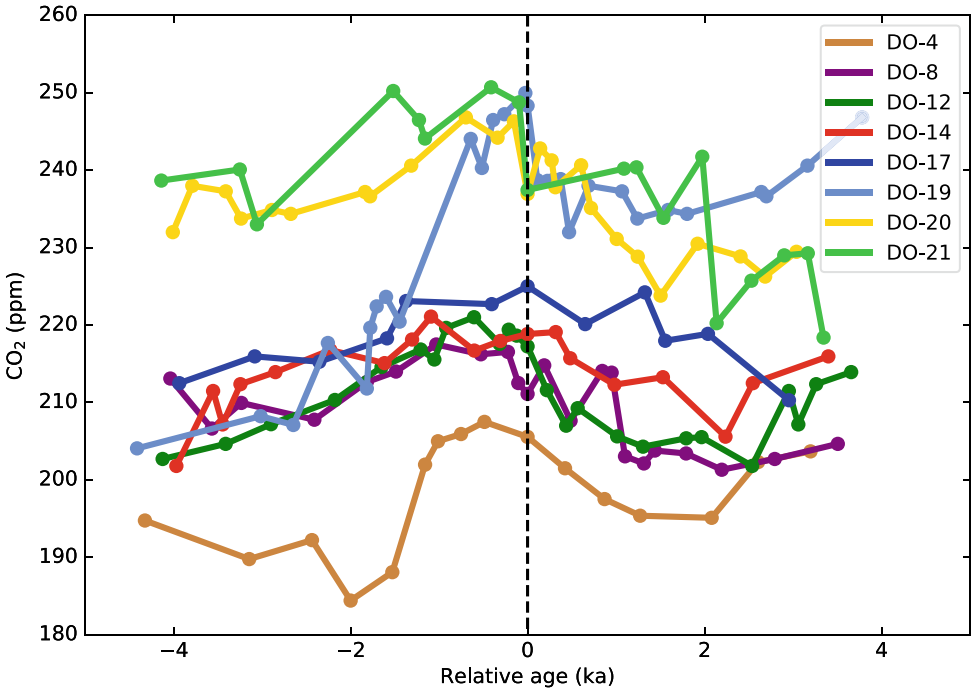

Fig. 23.9 CO_2 variations relative to abrupt warming in Greenland as presented in Ahn and Brook (2008)

terrestrial biosphere loses carbon (Obata 2007; Menviel et al. 2008b; Bozbiyik et al. 2011) while in others it is the opposite with the ocean losing carbon and terrestrial biosphere gaining carbon (Schmittner and Galbraith 2008; Bouttes et al. 2012; Matsumoto and Yokoyama 2013). Alternatively, simulations with artificially increased salinity in the Southern Ocean have been tested, resulting in a strengthening of the AABW and a loss of ocean carbon, yielding an overall CO_2 increase of around 20 ppm (Menviel et al. 2015). In general, simulations with atmosphere-ocean-terrestrial biosphere models in glacial background climate produce a large range of CO_2 changes due to the different processes, which are summed up in Fig. 23.10.

In addition, rapid CO_2 changes during the last deglaciation have been recently highlighted, such as the rapid CO_2 rise concomitant to the warming in the Northern Hemisphere at the Bølling Allerød around 14,600 years ago (Marcott et al. 2014). On top of changes in the Atlantic meridional overturning circulation, permafrost thawing, releasing large quantities of CO_2 trapped in frozen soil, has been suggested as a potential driver of the CO_2 rise (Köhler et al. 2014).

Changes in atmospheric methane (CH_4) concentration measured in ice cores are linked closely to the rapid surface temperature variations in Greenland during the last glacial period. In particular, CH_4 increases of 100–200 ppbv are associated with the abrupt DO warming events. CH_4 concentration is a global signal that reflects the response of the terrestrial biosphere, mainly wetlands, to hydroclimate changes (Brook et al. 2000) and its close link with Greenland temperature is classically interpreted as reflecting changing CH_4 emissions from tropical and boreal wetlands in phase with Greenland temperature (Chappellaz et al. 1993). A detailed study of the abrupt Bølling warming, the penultimate warming in the series of abrupt climate changes during the last glacial, suggests that changes in Greenland temperatures and atmospheric CH_4 emissions occurred essentially synchronously (within 20 yr; Rosen et al. 2014). CH_4 concentrations measured in Greenland ice cores are higher than those measured in Antarctic ice cores primarily because of enhanced CH_4 emissions in the Northern Hemisphere due to its larger land area (Chappellaz et al. 1997). However, rapid CH_4 changes are seen in both hemispheres and this feature is commonly used to synchronise Antarctic and Greenland ice core chronologies (Blunier et al. 1998; Buizert et al. 2015).

Nitrogen Cycle

Natural Nitrogen Cycle

Nitrogen (N) interacts with climate in two ways. First, like carbon dioxide and methane, nitrous oxide N_2O is a greenhouse gas. It is in fact more powerful than CO_2 or CH_4, but its atmospheric concentration is less, currently 325 ppb (NOAA, http://esrl.noaa.gov/gmd/). Second, nitrogen is also

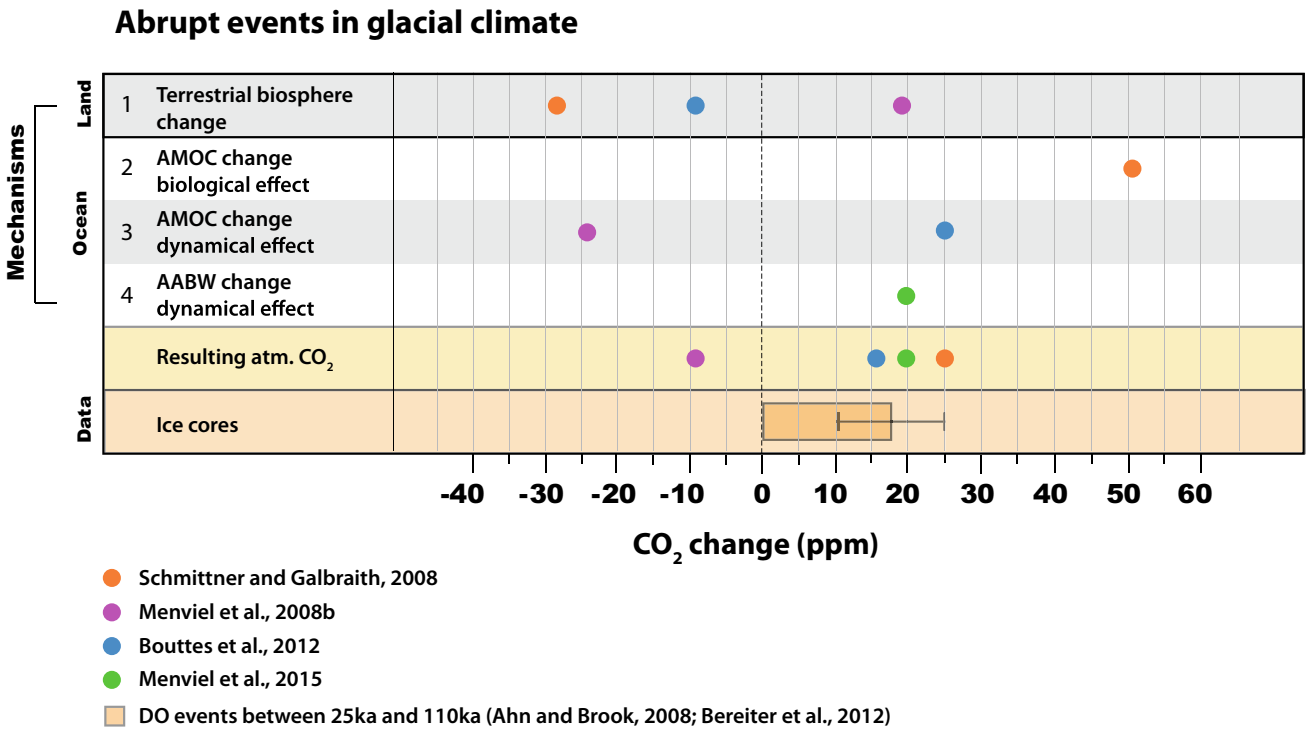

Fig. 23.10 Changes of atmospheric CO_2 due to different processes in atmosphere-ocean-terrestrial biosphere model simulations with glacial background climate. Figure modified from Mariotti (2013). Model data are taken from the simulations with maximum CO_2 change and at the time when atmospheric CO_2 for ocean and land carbon changes is at a peak

a limiting nutrient for the growth of vegetation on land and in the ocean, along with other nutrients such as phosphate. Nitrogen is essential for photosynthesis, which produces organic carbon. This connects the nitrogen cycle to the carbon cycle and atmospheric CO_2 concentration, and ultimately connects the nitrogen cycle to climate.

The nitrogen cycle is governed by biochemical reactions oxidising and reducing nitrogen which can be divided into three main processes: N_2-fixation, nitrification and denitrification (Fig. 23.11). These processes take place both in the ocean and on land.

Although N_2 is very abundant in the atmosphere it cannot be used in this form by most organisms. N_2 has to be transformed to a bioavailable—or reactive—form (ammonia NH_3 or ammonium NH_4^+) in order to be usable, a conversion, which requires a lot of energy to break the strong triple bond of the N_2 molecule. Most N_2 fixation is done by bacteria called diazotrophs, which have a specific enzyme called nitrogenase which combines gaseous nitrogen with hydrogen to produce ammonia. In the ocean, the main source of bioavailable nitrogen comes from N_2-fixation by marine diazotrophs (cyanobacteria and proteobacteria) which are mainly present in warm waters in the low latitudes. The efficiency of N_2-fixation depends on the environment, in particular, radiation, temperature, the presence of other nutrients (such as phosphate and iron), and O_2 concentration. Smaller marine inputs of bioavailable nitrogen include atmospheric nitrogen deposition and riverine inputs.

Nitrification by soil or marine bacteria is the oxidation of ammonia (NH_3) into nitrate (NO_3^-). This oxidation is done in two separate steps: first the oxidation from NH_3 to nitrite (NO_2^-) by ammonia-oxidizing bacteria and archaea. Then the oxidation of NO_2^- into NO_3^- by nitrite-oxidizing bacteria. Nitrification in the ocean takes place at the lower boundary of the euphotic zone where photosynthesis is limited by the low penetration of light, preventing the assimilation of nitrate by phytoplankton, and where remineralisation of organic matter increases nitrate concentration. In addition to this aerobic oxidation of ammonia into nitrate, anaerobic nitrification can also take place, called anammox (anaerobic ammonia oxidation).

Denitrification is the process that reduces NO_3^- to N_2 gas, releasing it back to the atmosphere. It happens during respiration by anaerobic bacteria in low O_2 conditions, and removes bioavailable nitrogen from the environment. In the process, intermediate gases are produced such as N_2O,

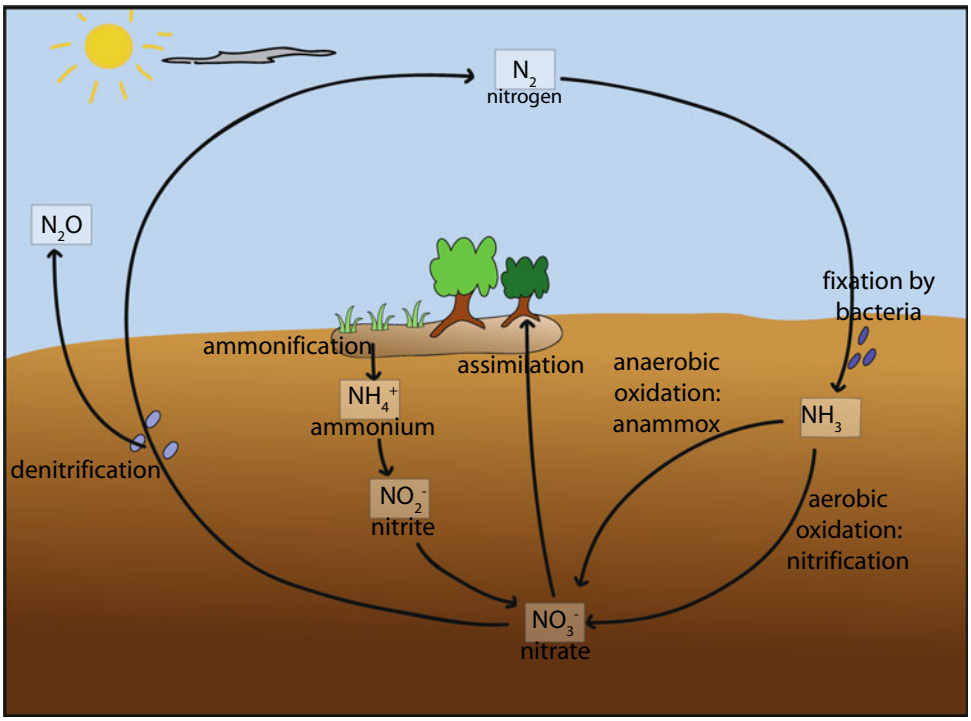

Fig. 23.11 Diagram of the nitrogen cycle

which is a powerful GHG. In conditions where O_2 is completely depleted, N_2O instead of NO_3^- is respired into N_2.

Ammonification is the production of NH_4^+ by bacteria and fungi from organic nitrogen originating from dead plants or animals, or animal waste.

During nitrification and denitrification, N_2O, a greenhouse gas, is also produced. The sources of N_2O come from both ocean and land. The sink of N_2O is due to photochemical reaction with ozone in the stratosphere.

Changes in the Nitrogen Cycle During Glacial Interglacial Cycles

Atmospheric nitrous oxide (N_2O) has a large glacial-interglacial amplitude (Fig. 23.12), with values of ~200 ppbv during glacial maxima and ~270 ppbv during interglacials including the Holocene and up to 280 ppb during the interglacial ~400,000 years ago (MIS 11) (Schilt et al. 2010). Unlike CO_2 and CH_4, the concentration of N_2O

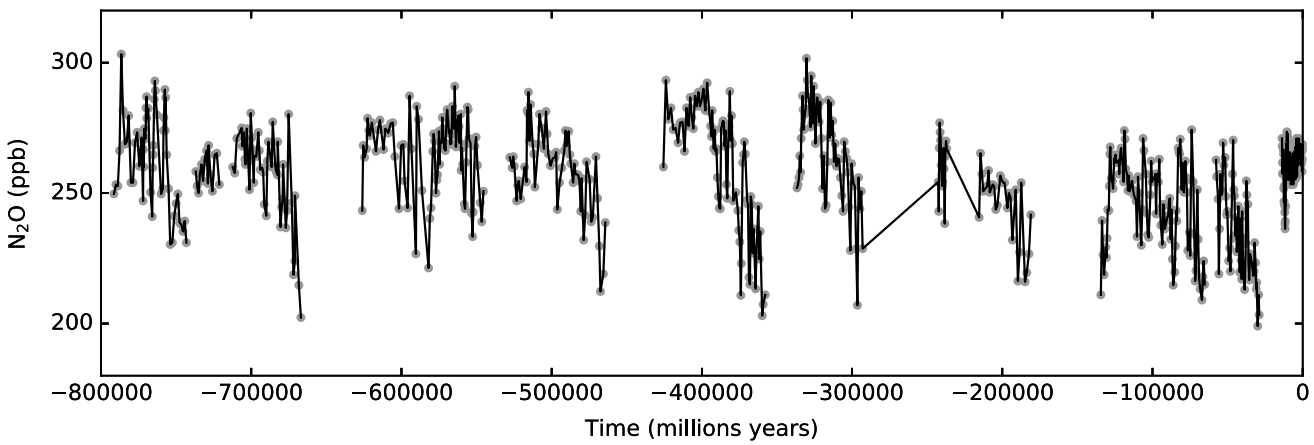

Fig. 23.12 Evolution of N_2O (ppb), over the last 800,000 years. Data from Schilt et al. (2010)

during the interglacial periods before 400 ka is not lower than the concentration during the more recent interglacial. In addition, N_2O shows a millennial variability similar to that of methane, with an amplitude very close to that of glacial-interglacial transitions (Schilt et al. 2013).

There is little information available to explain the glacial-interglacial and millennial variations in N_2O. The natural cycle of N_2O over these time scales is governed by two sources of approximately equal importance currently, an ocean source (estimated at 4 ± 2 TgN/year) and a terrestrial source (the natural part estimated at 7 TgN/year), and by an atmospheric sink mainly linked to the photolysis of the N_2O molecule in the stratosphere (12 Tg/yr). Modeling studies simulating atmospheric chemistry over the last few thousand years suggest that the N_2O sink during the LGM was similar to now (Crutzen and Brühl 1993), resulting in a lifetime of $\sim$120 years for N_2O in the atmosphere. Therefore, it appears that variations in the sources are responsible for the changes in its atmospheric concentration during the Quaternary.

Isotopic data, in particular measurements of the ^{15}N of N_2O, are used to separate the ocean source from the terrestrial source, as the former generally shows enriched isotopic signatures compared to the latter (probably due to a relatively stronger denitrification process in N_2O production in an ocean environment). These data suggest that the ratio of ocean to land sources did not change over the last 33,000 years (Sowers et al. 2003). These two sources appear to vary in phase with each other, with an increase of nearly 40% during warm periods compared to cold periods.

The mechanisms for explaining these variations are still largely hypothetical. The production of N_2O in the ocean is generally linked to the presence of suboxic zones, low in oxygen, which are found directly below some of the major productive regions (east of the tropical Pacific, the Arabian Sea). In these zones deficient in dissolved oxygen, nitrates are used by the microorganisms as a source of oxygen during the denitrification reactions leading to the remineralization of the organic matter; nitrous oxide (N_2O) is a by-product of these reactions. A decrease in the source of N_2O during the glacial period could be the consequence of a shrinking of these zones, which would itself be a result of changes in ocean dynamics or local marine productivity leading to an increase in dissolved oxygen at the sub-surface. However, this hypothesis is only partially supported by reconstructions of paleoproductivity.

Another theory concerning the ocean source is related to the expansion of flooded surfaces on the continental shelves. Recent estimates suggest that a significant portion (between 0.6 and 2.7 TgN/year) of marine N_2O production comes from the continental shelves. The significant drop in sea level (−120 m) during cold periods would have greatly reduced the flooded areas at the continental edges and thus the associated source of N_2O.

Several authors (Sowers et al. 2003; Flückiger et al. 2004; Schilt et al. 2013) also highlighted variations of around 40 ppbv in the N_2O concentration in the atmosphere in phase with Dansgaard-Oeschger events. These variations in N_2O are substantially different in amplitude from variations in CH_4. While methane recordings show a fairly strong correlation with insolation in the low and mid latitudes of the Northern Hemisphere, this is not the case for N_2O.

The concentration of N_2O begins to increase before methane (during the warming phase in the Southern Hemisphere), and then the concentrations of the two gases reach their maximum at the peak of the hot phase of the D-O event. This information is compatible with the idea that both marine and terrestrial sources play an important part in the evolution of N_2O: the marine source is stronger in the Southern Hemisphere, in phase with the warming period in the south, and the terrestrial source is stronger in the northern hemisphere, in phase with the warming period in the north.

So far, very little modelling work has focused on changes in the concentration of N_2O in the atmosphere over the last hundreds of thousands of years. A simulation for the Younger Dryas episode suggests a combination of changes in the marine and terrestrial sources of N_2O to explain the variations measured during this event. Simulations run by Schmittner and Galbraith (2008) show that changes in ocean circulation play a major role N_2O variations. A reduction of the AMOC leads to decreased productivity and better ventilation resulting in increased subsurface oxygen concentrations, which explains the decrease in N_2O production.

Oxygen Cycle

The Oxygen Cycle and Its Ocean Component

Atmospheric free oxygen does not directly impact climate since it does not absorb infrared radiations. Despite this fact, the cycle of oxygen has gained lots of attention primarily because of its tight relationship with life on Earth. Indeed, the main source of free oxygen comes as a waste product of photosynthesis by plants on land and phytoplankton in the ocean. The main oxygen sink is due to respiration and/or remineralization of organic matter by almost all living organisms, which consume di-oxygen and release carbon dioxide. Other minor sources include the photolosyis of N_2O and H_2O in the atmosphere, whereas oxygen sinks are numerous and include a number of oxidation and chemical weathering pathways (see Walker 1980, for a review of the global oxygen cycle).

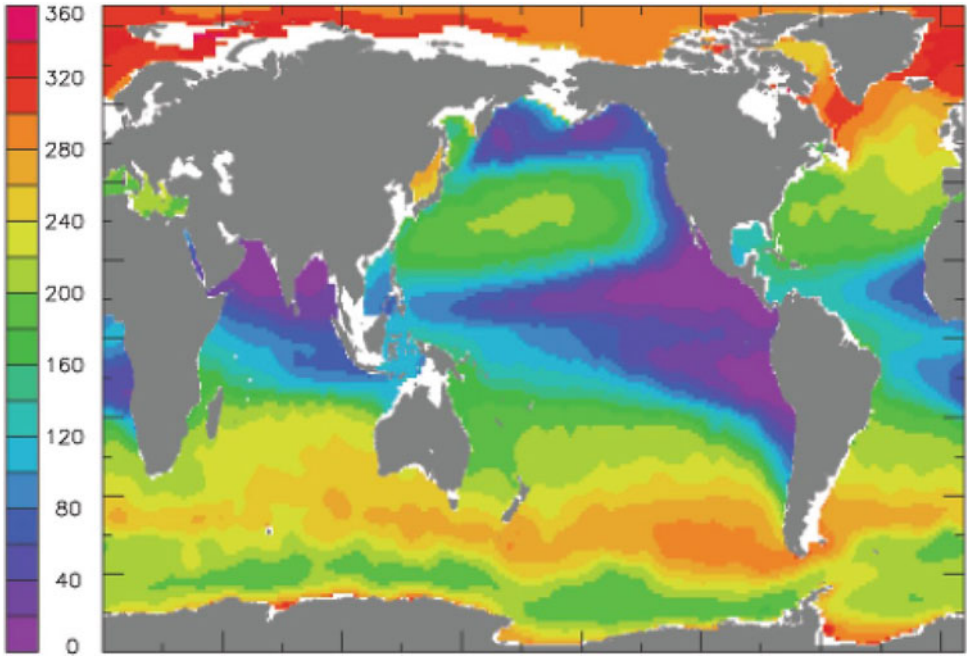

Fig. 23.13 O_2 concentrations at mid ocean depth (averaged over 200–600 m, in micromole/L) from the World Ocean Atlas (2009) (Garcia et al. 2010)

Many studies have examined the oxygenation of the Earth's atmosphere over geological time scales, focusing for example on the Great Oxidation Event 2.45 billion years ago (e.g., Holland 1994) or on the variations of atmospheric O_2 over the Phanerozoic (Berner et al. 2003). Over the last million years, the consensus is that the atmospheric concentration of O_2 has been very stable due to the very long residence time of O_2 in the atmosphere-ocean system (on the order of two million years, Catling and Claire 2005).

The oceanic component of the oxygen cycle has been however much more variable over glacial-interglacial cycles (Jaccard and Galbraith 2012). This is due to the fact that the oceanic reservoir of oxygen is much smaller than the atmospheric one (225 Tmol O_2 in the ocean vs. 3.8×10^7 Tmol of O_2 in the atmosphere), and that dissolved oxygen concentrations in the ocean are very heterogeneous, with O_2 concentrations ranging from 0 to almost 400 micromol/L. A map of O_2 concentrations at mid ocean depth illustrates this heterogeneity (Fig. 23.13), with O_2-enriched waters at high latitudes and O_2-depleted waters in the Eastern Tropical Pacific and in the Northern Indian Basin (depicting the so-called Oxygen Minimum Zones).

The oxygen content of the ocean results from a fine balance between the consumption of oxygen by respiring organisms feeding on organic matter sinking from the surface, and the supply of O_2-rich waters coming from the surface of the ocean through ocean ventilation.

Because oxygen is a fundamental resource for aerobic organisms, the distribution of oxygen in the ocean has a large imprint on marine life, shaping for example the habitat of large fish such as tunas or billfishes (Stramma et al. 2012).

Over the past decades, observations have shown that oxygen concentrations have decreased in the open ocean in many ocean regions and that the tropical oxygen minimum zones (OMZs) have likely expanded (Rhein et al. 2013). The mechanisms involved are a decrease in the oxygen solubility due to ocean warming and the combination of reduced ocean ventilation and increased stratification that prevents the penetration of oxygen into the interior of the ocean. These mechanisms are very consistent with the recent global warming trend, suggesting that deoxygenation will continue with future anthropogenic climate change. Indeed, climate models do simulate a clear deoxygenation trend with global warming, with an oceanic loss of oxygen of a few percent at the end of the twenty-first century (Bopp et al. 2013). At the regional scale however, there is yet no consensus on the evolution of subsurface oxygen levels, with very large model uncertainties.

Ocean Oxygenation at the Last Glacial Maximum

The past record of ocean oxygenation during glacial-interglacial cycles provides a complementary perspective on how the oceanic oxygen content may respond to climate change or climate variability. The reconstruction of past ocean oxygenation relies on sedimentary proxies of bottom water oxygenation. The most common proxies for ocean oxygenation are based on the presence of sediment laminations (that testify very low levels of bottom water oxygen levels), on redox sensitive trace metals (such as uranium and molybdenum) and on benthic foraminifera assemblages.

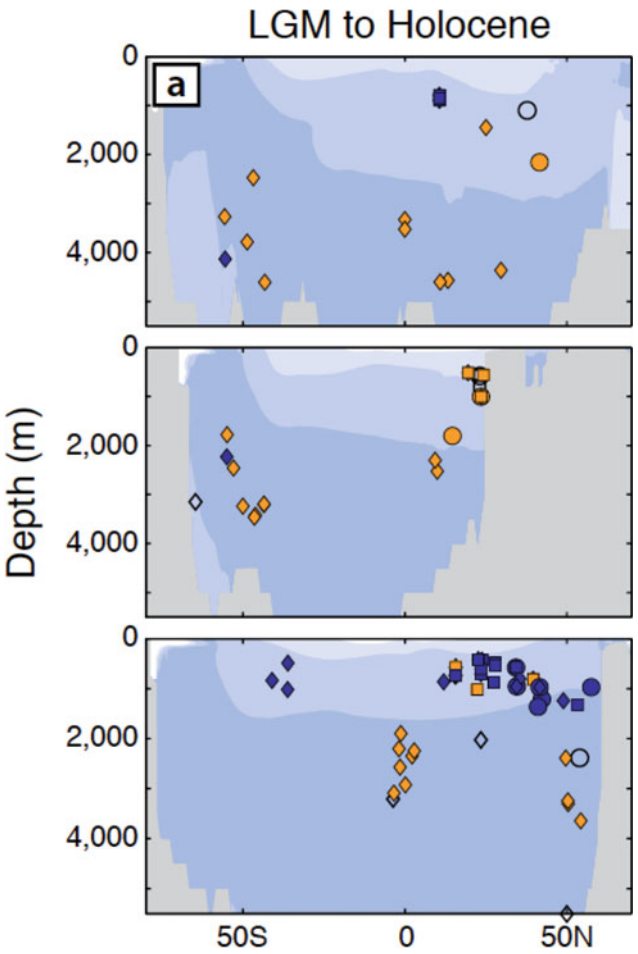

Fig. 23.14 Changes in ocean oxygenation between the Last Glacial Maximum and the Early Holocene for the Atlantic (top), Indian (middle) and Pacific (bottom) basins. The symbols refer to the different proxies used to infer past oxygenation (squares corresponding to laminations, circles to foraminifera species assemblages, and diamonds to redox-sensitive trace metals). Blue shadings indicate a relative decrease in oxygenation and orange shadings a relative increase in oxygenation from the LGM to the early Holocene. From Jaccard et al. (2014)

Despite recent progress on the developments of new proxies and the multiplication of the application of such methods to a growing number of sediment cores, the indications of past ocean oxygenation over the last glacial-interglacial cycles portrayed by these records stay very qualitative and mostly apply to the last deglaciation (Jaccard and Galbraith 2011). Overall, marine sediments indicate an oxygenation of the deep ocean throughout the last deglaciation and an expansion of low-oxygen waters in the upper ocean. These changes seem quite consistent across all ocean basins (Fig. 23.14).

The mechanisms responsible for such changes are still debated (Jaccard et al. 2014; Bopp et al. 2017). In the sub-surface ocean for example, the decreasing trend in oxygen levels during the deglaciation could be due to an increase in carbon export from the surface layers that would have increased oxygen consumption in the subsurface ocean (Jaccard and Galbraith 2012), but also to a decreased ventilation of sub-surface layers in response to changes in oceanic circulation (Bopp et al. 2017).

Ocean Oxygenation in the Mediterranean Sea: The Case of Sapropels

Definition and overview

Sapropel events are clearly identified in marine sediments. They are characterized by an organic rich layer sedimentation, mainly found in the eastern basin (Fig. 23.15). The peculiarity of this sedimentation suggests an anoxic environment allowing the organic matter preservation-due to the shutdown of the thermohaline ventilation (Möbius et al. 2010) and/or an enhanced biological productivity leading to an increased oxygen consumption (Martinez-Ruiz et al. 2000).

Sapropel events have been largely described and investigated since they have been identified in the middle of the twentieth century (Kullenberg 1952). Since the closure of East Tethys seaway 14 million years ago (Hamon et al. 2013), the only connection between the Mediterranean basin and the global ocean has been the Gibraltar straight. This semi-enclosed configuration favored sapropel events that occurred with a frequency of 21,000 years (Emeis et al. 2003).

Large variability in contexts, developments and processes associated with sapropels occurrences

There is a large variability in the imprints (strength, extension, duration) of these sapropels (see Rohling et al. (2015) for a review). For example the carbon organic content levels in sapropels typically range between 1 and 10% with a large variability, for instance sapropel S5 occurring during the last interglacial reached values from 7–15% (Grant et al. 2012) and Pliocene sapropel may reach 30% (Nijenhuis and De Lange 2000).

Whereas pacing of sapropel is strongly correlated to precessional cycles, there are major differences in preconditioning water masses that favor the occurrence of sapropels. Superimposed to this variability, the triggering of sapropel has been shown to be several thousand years after the maximum summer insolation in the northern hemisphere. Ziegler et al. (2010) inferred a recurrent lag between the northern hemisphere insolation maximum and sapropel deposition.

Sapropels typically lasted between ~3 and ~8 kyrs. For instance, durations of ~4.4, ~4.0, ~6.2, and ~7.4 kyr for S1, S3, S4, and S5, respectively has been attributed by different methods (Grant et al. 2012) Despite a large

Fig. 23.15 Left, sapropels within a sediment core recovered in 2001 during *RV Meteor* cruise M51-3 (Hemleben et al. 2003) (photograph by Eelco. J. Rohling and Kristian.C. Emeis). Right, late Pliocene sapropel layers outcropping at Punta Piccola (Plancq et al. 2015)

variability in time and space of benthic recolonization at the end of a sapropel. The end of enhance monsoon seems to mark a sharp and widespread (basinwide) onset of deep water oxygenation due to resumption of strong convective deep-water formation.

Sapropels are more common in the eastern Mediterranean (east of the Strait of Sicily) than in the western Mediterranean, where they are also known as Organic Rich Layers (ORLs) (Rogerson et al. 2008).

As suggested by Rohling et al. (2015), the eastern Mediterranean is more sensitive to development of deep-sea anoxia than the western Mediterranean, because of differences in the efficiency of deep-water renewal.

For a long time, the relationship between insolation changes associated with precession cycles and impacts on hydrological changes through fresh water inputs has been invoked as causal link to explain sapropel occurrences (Rossignol-Strick et al. 1982). Nevertheless, there are many different contexts in, which sapropels have occurred since the Miocene (Rohling et al. 2015). For instance, the role of the cryosphere was certainly different during Pliocene and Pleistocene. For Quaternary, it has been shown that, superimposed to the major effect of African monsoon and enhancement of freshwater from the Nile river, other forcing factors have to be accounted for. The imprint of glacial-interglacial cycle and associated sea level changes has been shown to contribute strongly for sapropel occurring during deglaciation as S1 (Rohling et al. 2015; Grimm et al. 2015).

Most recent advance on S1 sapropel modeling

Modeling represents also a unique tool to investigate the responses of the Mediterranean basin to different external forcing factors from insolation changes to associated hydrological perturbations that may produce sapropel events.

Two important developments have been down recently concerning sapropel modeling: much longer simulation and much higher spatial resolution.

Superimposed to precession cycles, since one million years the 100 ky glacial-interglacial cycle has also affected sapropel occurrence (Köng et al. 2017). Recent modeling studies (Grimm et al. 2015) aimed to simulate the S1 from its onset. A more specific scenario, involving a preconditioning of cold and poorly salted water coming from the last Heinrich event, was suggested as a possible cause for the S1 formation.

Another important issue is to reach high resolution to capture convection patterns in the Mediterranean basin. Using a coupled AOGCM (Atmospheric-Ocean Global Circulation Model) including a regional Mediterranean Sea model (1/8° much higher than previously used), Vadsaria et al. (2019) have revisited the impact of Nile hosing fresh water increase on triggering sapropel S1. This improvement allows for better simulating the intermediate and deep convection occurring in winter (Adloff et al. 2015).

Moreover, the simulation of oceanic tracer as Nd allows one to validate changes in ocean dynamics (Ayache et al. 2016).

Sulphur

The sulfur cycle is of interest to climatologists because it leads to the formation of sulfuric acid (H_2SO_4), a submicronic aerosol that reflects solar radiation efficiently (direct effect) and which, due to its highly hygroscopic nature, has a physical influence on clouds (indirect effect). It is formed in the atmosphere by the oxidation of SO_2 whose emission level through the combustion of fossil reserves is 35–45 Tg per year. The IPCC estimates that due to the increase in sulfate aerosols in the atmosphere, anthropogenic emissions of SO_2 could be responsible for a radiative forcing of -0.4 W/m^2, an opposite forcing but equivalent to about one third of the radiative forcing linked to the increase of CO_2 in the atmosphere ($+1.2$ W/m^2). However, as noted above, the comparison between these two values is of limited

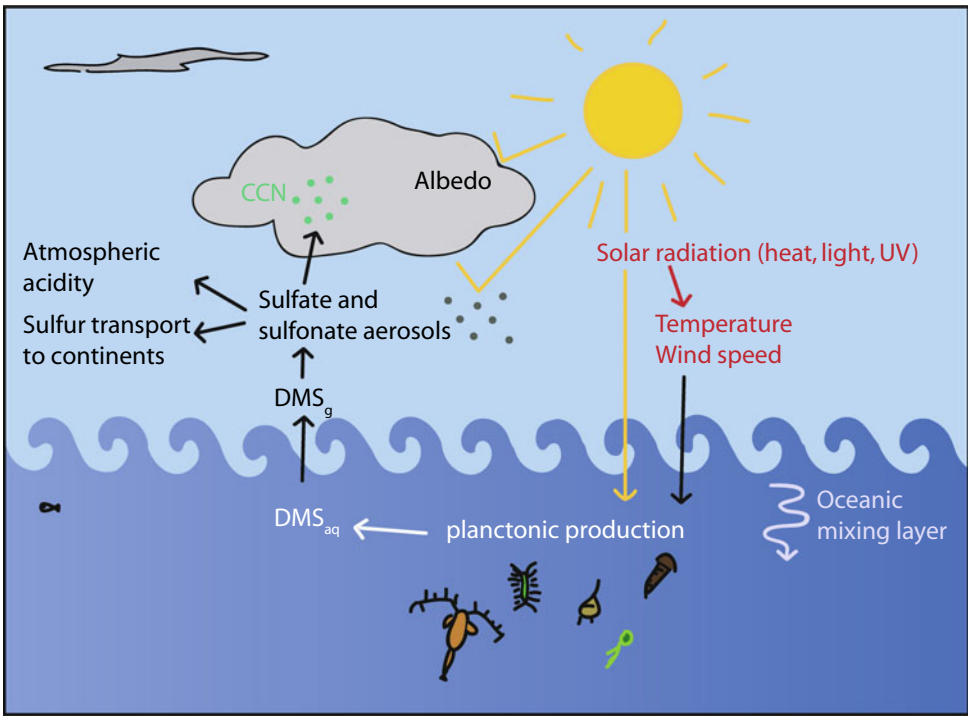

Fig. 23.16 Feedback mechanisms linking our planet's climate to DMS emissions from the ocean (adapted from Charlson et al. 1987)

significance since the forcing of the aerosol may, for example, be much greater over heavily anthropized regions of the northern hemisphere. Moreover, the temporal evolution of anthropogenic SO_2 emissions varies greatly from one continent to another: emissions reached a peak in the 1980s in Western Europe and the USA, while an acceleration of their emissions is underway in India, for example. The sulfur cycle in the atmosphere also involves two major natural sources, volcanic activity and marine DMS biogenic emissions. An important dimension of the latter source is its potential response to climate conditions, a hypothesis proposed by Charlson, Lovelock, Andreae and Warren, four authors of a well-known article in Nature in 1987, proposing that DMS emissions produced by plankton may act as a climate regulator (Fig. 23.16). Responses by the marine biosphere (changes in primary productivity, phytoplankton speciation, stratification of surface ocean layers, wind patterns, etc.) to the current climate change are thus possible. Its direction and magnitude remain uncertain, but some ocean-atmosphere models incorporating an ocean biology module, coupling sulfur and carbon, suggest that a 40% increase in DMS emissions could occur in the 40 °S zone in response to a doubling of CO_2 content and to the associated climate change (Bopp et al. 2003b).

The idea of examining the relationship between marine biogenic sulfur emissions and past climate is the motivation behind many ice core studies. Given that sulphate in the atmosphere has several origins, the first attempt at reconstituting marine biogenic emissions was made by examining the MSA content of ice (Saigne and Legrand 1987). This study of the last climate cycle in the Vostok ice core indicated an increase in MSA deposition fluxes by a factor of almost three between an interglacial period and the final stage of an ice age, despite the fact mentioned previously that sulphate flux has shown little variation in the past (Legrand et al. 1991). Since isotopic studies of sulfur undertaken on sulphate have subsequently clearly established that DMS emissions are the major source of sulphate in Antarctica, a contradiction therefore appeared between the two proxies of DMS emissions, with the MSA suggesting an increase in DMS emissions, but not in sulphate. The hypothesis of an increase in DMS emissions during the glacial period seemed reasonable given that the phytoplankton species that emits a lot of DMS (Phaeocystis) has a particular affinity with sea ice.

The difference between the sulphate and MSA records remains unclear to date. The atmospheric studies carried out over the last few years in Antarctica demonstrate the complexity of the problem. Although the atmospheric levels of the three sulfur species coincide well over time with the DMS concentrations in the Southern Ocean, the interannual variability observed in the Southern Ocean does not show any straightforward connection with annual sea ice cover (Preunkert et al. 2007). These measurements also reveal intricate processes involving photochemistry and atmospheric dynamics which makes the link between the two sulfur species and DMS very complex. These studies continue to be pursued actively due to the fact that, to date, only

from ice can past variability in marine biogenic emissions potentially be reconstructed, since organisms like Phaeocystis do not leave any traces in marine sediments. The issue is important because it contributes to our understanding of the feedback taking place in high latitudes (regions highly sensitive to global changes in climate), involving complex processes between marine biology, sea ice, and climate.

Aerosols and Dust

Aerosols are small liquid or solid particles, ranging from a few nm to 100 μm, in suspension in the atmosphere. Natural aerosols include desert dust, sea salt, carbonaceous, sulphur and nitrogen species, largely emitted from dry and vegetated landscapes, the oceans, and volcanoes (Carslaw et al. 2010). Primary aerosols are emitted directly from the surface of the Earth, whereas secondary aerosols are formed from gaseous precursors in the atmospheric environment. Aerosols are washed out by precipitation, or removed by gravitational settling and dry deposition, so that their lifetime in the atmosphere is short, a few days only—except when they reach the stratosphere, where they can stay for a few years, as can happen during giant volcanic eruptions. Therefore, unlike well-mixed GHGs, aerosols are considered to be short-lived climate forcing agents, and their impacts are characterized by a strong regional component (Boucher et al. 2013). Aerosol emissions vary depending on surface climate conditions; on the other hand, aerosols impact the climate system themselves, though direct and indirect (cloud-mediated) interactions with the atmospheric radiation budget, by changing the surface albedo, as well as by means of indirect impacts on global biogeochemical cycles (Mahowald et al. 2017).

Size, shape and composition define the specific interactions of aerosols with radiation, including absorption and scattering of shortwave (solar) and longwave (terrestrial) radiation. The scattering of shortwave radiation results in cooling, but absorption can lead to warming when it is above a highly reflective surface. Through their absorption of outgoing longwave radiation, aerosols also behave like GHGs. For some aerosol species, one particular effect is dominant, in other cases, opposing effects coexist. Considering the variability of aerosol spatial distribution, the coexistence and mixing of different aerosol species, and the diversity of aerosol-radiation interactions, it is clear that direct impacts of aerosols on climate constitute a complex problem (Boucher et al. 2013).

Aerosols also interact with clouds. Changes in relative humidity linked to the vertical stability of the atmospheric column and the surface evapotranspiration balance, occurring as a rapid adjustment to direct aerosol forcing, can influence cloud formation. This is called the semi-direct effect. The indirect effects, on the other hand, involve aerosols acting as cloud condensation (CCN) or ice nuclei (IN), which means that water or ice aggregates around them. This modifies the type, extent and lifetime of clouds. For example, the presence of aerosols leads to smaller but more numerous droplets, which yields a more reflective cloud than it would be without aerosols. This also means that clouds formed with aerosols will have a longer lifetime since the droplets are smaller and won't reach the critical size for precipitation. The indirect effect can result in warming or cooling depending on the altitude where clouds are formed. Because the effect of aerosols on radiation and on clouds is complex and depends on many parameters, it remains one of the main sources of uncertainties in models (Boucher et al. 2013).

In addition, aerosols depositing back to the surface can also modify the albedo. This is the case of dust, and especially black carbon; they can cause snow and ice to darken, which reduces the albedo and leads to warming.

In virtue of their composition, aerosols also act as carriers of specific elements, such as nitrogen, phosphorus, sulphur, and iron, which are linked to important biogeochemical cycles, including the carbon cycle (Mahowald et al. 2017). In particular, phosphorus and iron are linked to the dust cycle, and the peculiarity is that windblown inputs can be fundamental to the mass budgets of those elements in remote regions, far from the dust sources. For instance, dust-borne phosphorus from North Africa replenishes the pool of this element in the Amazon, where the loss by fluvial erosion would otherwise deplete it, with implications for the rainforest. Iron, on the other hand, is a micronutrient for marine ecosystems. Because its sources are the continents, remote marine areas are depleted in this element. Where the abundance of macronutrients such as nitrogen and phosphorus is accompanied by a relative scarcity of iron, which limits the primary production at the ecosystem level, i.e. in High-Nutrient Low-Chlorophyll (HNLC) areas, dust-borne inputs of iron become of great importance in sustaining algal blooms—this is notably the case of the Southern Ocean (Jickells et al. 2005).

Natural Aerosols: Overview

In this section we will briefly describe the main natural aerosol types. Note that mineral dust and sea salt are still the most abundant primary aerosol species by mass in the present day atmosphere.

Mineral (desert) dust (Fig. 23.17) is emitted into the atmosphere in response to wind erosion of the surface, in dry and semi-dry areas, with low vegetation cover. Far-travelled dust particles are mostly clays and fine silts below 10 μm in diameter, and are composed mainly of silicates, along with carbonates, gypsum, and metal oxides. Dust aerosols interact

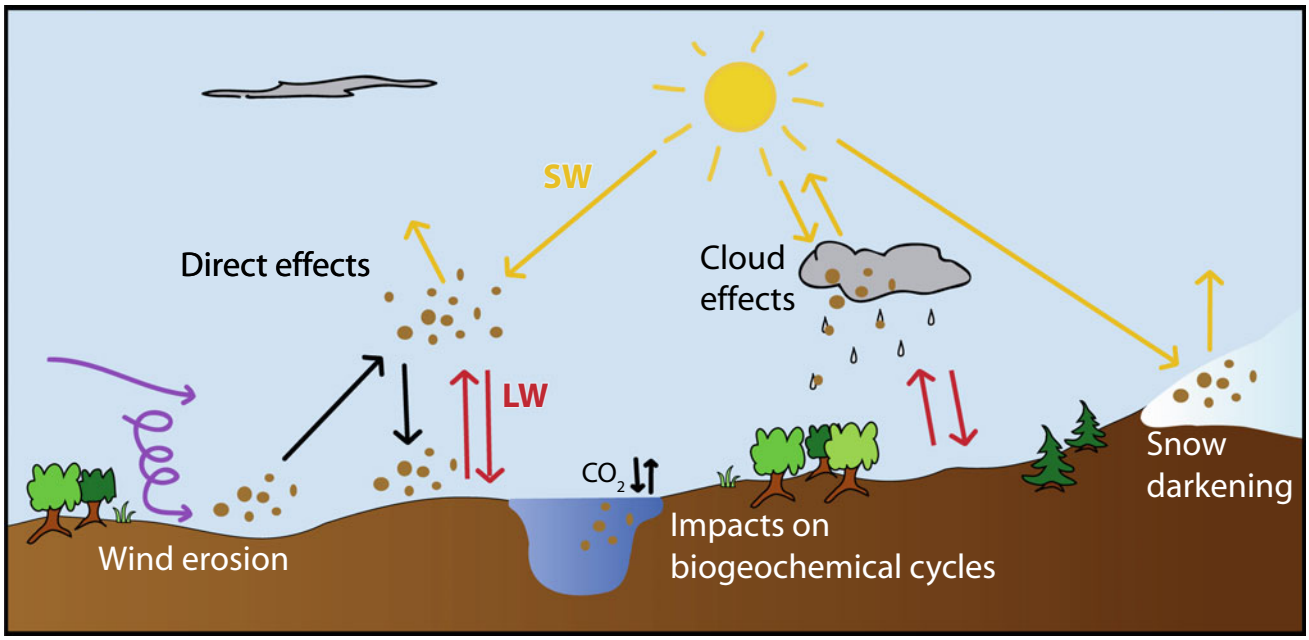

Fig. 23.17 Overview of the dust cycle and its interactions with the climate system

with both solar and terrestrial radiation, and act as ice nuclei in mixed phase clouds. As already mentioned, dust deposition on the surface can reduce snow albedo and impact on the carbon cycle through phosphorus and iron mediated interactions with global biogeochemical cycles.

Land vegetation is a source of primary biogenic aerosol particles (PBAP), in the form of fungal spores, viruses, bacteria, pollens and plant debris, as well as aerosol precursors such as isoprene and other volatile organic compounds (VOC), which result in the formation of secondary organic aerosols (SOA). Wildfires are responsible for the emissions of particulate organic matter and black carbon. Particulate carbonaceous aerosols have a slight net cooling effect in the atmosphere, and play a role as cloud condensation and ice nuclei. Black carbon is a strongly absorbing aerosol, associated with snow darkening and has a warming effect on the atmosphere.

Wetlands emissions of ammonia, and NO_x produced by biomass burning, biogenic soil emissions, stratospheric injection and by the interaction of lightning with atmospheric N_2, are the main precursors to nitrogen aerosol species, which overall have a moderate net cooling effect in the atmosphere, and may impact on biogeochemical cycles.

Volcanic emissions of SO_2 are one of the primary sources of precursors for the formation of natural sulphate aerosols, which are characterized by a strong cooling impact on the atmospheric radiation, and they are very efficient CCN. Volcanic eruptions can also eject glass shards and ash, which can leave a mark by depositing as tephra layers—very useful stratigraphic markers.

Wind stress on the surface of the oceans drives aerosol emissions at the sea-air interface, where bubbles bursting within breaking waves eject sea sprays composed mostly of sea salt (dominating the super-micron fraction), along with organic particles (concentrated in the sub-micron fraction). Sea salt and some organic particles are also emitted from the surface of sea ice, where these form frost flowers during the process of brine rejection that accompanies the freezing of seawater. Sea salts tend to cool the atmosphere, and because of their high hydroscopicity, they act as CCN (O'Dowd and de Leeuw 2007). Oceans are also a major source of precursors of sulphate aerosols, in the form of biogenic emissions of dimethylsulfide (DMS) that is then oxidised to sulphuric acid and methane sulfonic acid (MSA) in the atmospheric environment (Legrand and Mayewski 1997).

Dust Variability and Impacts on Past Climates

The past history of the dust cycle is imprinted in natural archives such as ice, marine sediments, loess/paleosol sequences, and peat bogs. Dust has the greatest preservation potential among all aerosol species, because it is essentially insoluble, and traces of it are present in a variety of environments all around the globe. In general, we can obtain a paleodust record from natural archives when the following conditions are met: there is preservation of the deposition signal; we can establish a chronology; and we are able to separate eolian contributions from the sedimentary matrix.

The fifty-meter thick loess deposits of China and North America are probably the most spectacular evidence of how the dust cycle is capable of shaping immense landscapes—loess deposits cover 10% of the emerged landmasses. Loess accumulation in China has been an ongoing process for over 20 million years, since the uplift of the Tibetan plateau caused widespread aridification of central-eastern Asia. Beyond that, little is known, although isolated information on deep paleoclimate conditions at least dating back to the Paleozoic (~500 million years ago) can be derived, based on the analysis of geologic formations whose origin can be ultimately linked to eolian sedimentation.

We have a better picture of the global dust cycle on Quaternary time scales, especially since the late Pleistocene. From polar ice core records we know that a strong dust-climate coupling was a persistent feature at least over the last eight glacial-interglacial cycles; colder climate states are characterized by increased dustiness, as shown by the milestone paleoclimate records from the Vostok and EPICA Dome C (EPICA Community Members 2004) ice cores from Antarctica (Fig. 23.18). Preservation of stratigraphy and chronologies based on numerical (absolute) dating methods allow for a more detailed reconstruction of the last glacial-interglacial cycle. In particular, global compilations of paleodust records based on dust mass accumulation rates provide a quantitative metric to compare paleodust records from different natural archives, and constitute a benchmarking tool for models (Kohfeld and Harrison 2001).

During the LGM, global dust emissions were enhanced by a factor of 2–4, and the increase in dust deposition in high latitudes was even by a factor of 10 or more. A combination of changes in dust source areas and transport patterns, driven

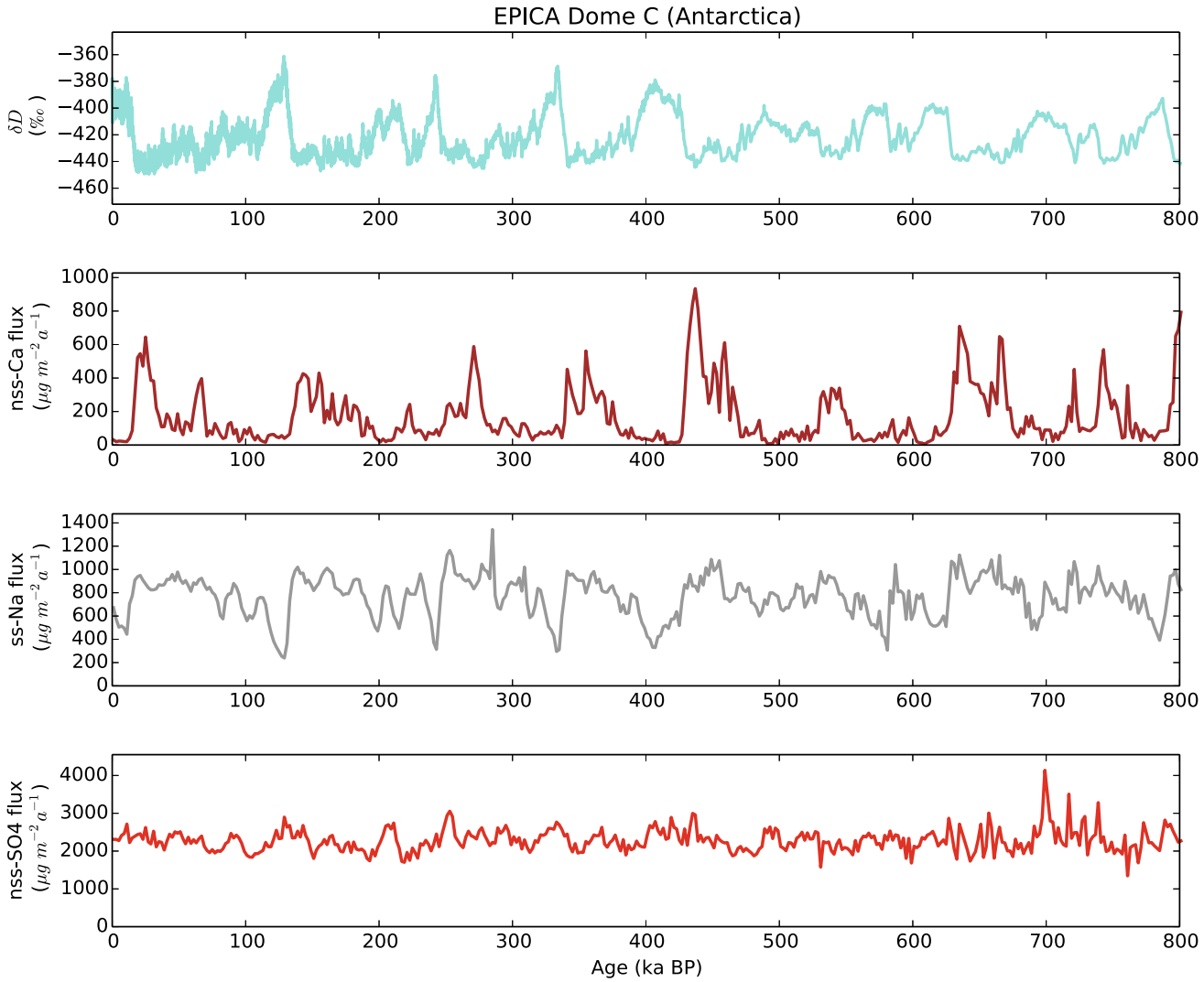

Fig. 23.18 Overview of aerosol (nss-SO_4^{2-} as a proxy for sulfate aerosols, ss-Na for sea salt, and nss-Ca for dust) deposition fluxes from the EPICA Dome C ice core (Wolff et al. 2006), Antarctica, along with indicators of global climate, i.e. deuterium excess (Jouzel et al. 2007)

by the large-scale atmospheric circulation, shaped the geographical variability in dust cycle dynamics. The sharp decline in dust deposition to Antarctica paralleling the rise in atmospheric CO_2 levels, led oceanographer John Martin ("Give me a tanker of iron, and I will give you an ice age"), in the late eighties, to formulate the famous iron hypothesis: the glacial increase in dust-borne iron inputs to the Southern Ocean may have stimulated the ocean biological pump, resulting in an increased productivity in HNLC areas and subsequent carbon sequestration in the deep ocean (Jickells et al. 2005). State of the art ESMs suggest that this mechanism may have been responsible for a decrease of ~20 ppmv of atmospheric CO_2, out of 80/100 ppmv—the overall decrease in CO_2 concentrations during the LGM measured in ice cores. On the other hand, the impact of the increased dust burden on atmospheric radiation is estimated by models to be at least −1 W/m^2 globally, compared to −6 W/m^2 forcing by reduced GHGs atmospheric concentrations and changes in surface albedo from decreased sea levels and the growth of ice sheets in the Northern Hemisphere. Nonetheless, this figure might hide much larger dust impacts of the opposite sign, with strong cooling downwind of the major dust sources, and warming over the bright, glaciated Arctic regions (Albani et al. 2018).

During the course of the entire glacial period, millennial scale variability expressed by Dansgaard-Oeschger and Heinrich events in the $\delta^{18}O$ record in Greenland ice cores, is almost paralleled by variations in dust deposition rates, with colder phases associated to dustier conditions (Rasmussen et al. 2014). The same picture emerges from the corresponding alternation of stadial/interstadial periods in Antarctica (EPICA Community Members 2006).

The deglaciation followed, characterized by a non-monotonic increase in global temperatures and CO_2, mirrored by decreasing dust levels in both hemispheres. While the Holocene was initially described as a relatively flat period in terms of dust, based on polar records, in the last three decades, a few studies of North Atlantic sediment cores highlighted the large variability in North African dust emissions; a reduction by a factor 2–5 corresponded to the "Green Sahara" phase of the Early and mid-Holocene, characterized by an enhanced summer monsoon, compared to the drier late Holocene after ~5 ka BP. The possible (positive or negative) feedbacks between the monsoon system and variations in the North African dust cycle are a subject of study by the modelling community (Albani et al. 2015).

Ironically, we know relatively less about the more recent past. Marine sediments and loess profiles generally can't achieve a temporal resolution fine enough to resolve the last millennia, and often surface layers of loess/paleosol deposits are disturbed by agricultural practices, as they tend to be very fertile soils. Ice cores do provide this kind of temporal resolution, but we still have very little data. The top meters of polar cores, corresponding to this time frame, are actually made of firn, which complicates the analysis because of the risk of contamination of the samples. Alpine ice cores, on other hand, allow the analysis of dust concentration and can have good chronologies for the last few decades, but reliable, quantitative estimates of dust mass accumulation rates are hampered by the extreme spatial variability of snow accumulation and post-depositional processes. Therefore, we do not have a clear pre-industrial reference state for dust (Carslaw et al. 2010). A few studies trying to address dust trends during the twentieth century yield contrasting results; a generally increasing trend over parts of the last century suggested by some authors may have "masked" a fraction of global temperature increase, due to the net cooling effect of dust.

Other Aerosol Species in Past Climates

There is much less information about other aerosol species in the past; unlike dust, solubility and volatility limit the preservation of most species in many environmental settings, and pose additional analytical challenges. Most of the information we have is from ice cores (Wolff et al. 2006; Preunkert and Legrand 2013).

Na^+ is a stable proxy for sea salts. Yet, we do not really have information from lower latitudes; sea salt records from polar ice cores (Fig. 23.18) show, similar to dust, increased deposition rates in glacial climates, by a factor 3–5 in Antarctica and 1.5–3 in Greenland. It is not fully clear to what extent this was due to an increase in emissions or transport from open waters, rather than to the expanded sea ice source, although the latter seems to be the dominant factor. Increases in sea salts could have had a negative forcing, via direct and indirect effects, on the atmospheric radiation budget.

Sulphur and nitrogen aerosol species present more important issues with preservation, and are more difficult to interpret. The baseline sulphate records from polar ice cores (Fig. 23.18), mainly derived from DMS emissions, show a flat signal in Antarctica and some variability in Greenland. This has dampened some early enthusiasm for the idea that DMS could be a dominant feedback in driving glacial-interglacial variability, given the strong cooling effects associated with sulphate aerosols. Sulphate concentration spikes are associated with inputs from large volcanic eruptions, and are sometimes associated with the presence of tephra. In certain cases, a lag of one or two years was observed in the peaking of the two signals, suggesting a longer stratospheric residence time of sulphates. There are

no clear trends in volcanic activity on late Quaternary time scales, although several volcanic spikes marked the deglaciation.

There is very little direct information on carbonaceous aerosols from ice cores on late Quaternary time scales. Some data is available on paleofire proxies, such as ammonium or levoglucosan, which can be combined with information from charcoal, preserved in paleosols, peat bogs, and lakes—on the other hand, an indicator of the source of the aerosols and precursors, rather than the sink. Finally, the variation of pollen assemblages archived in lakes and peat can provide information on the state of past vegetation, which is a source of many aerosols and precursors. The general picture is that land biogenic and fire emissions during the last glacial period were lower than today, at least at high latitudes, which is consistent with a drier and colder climate, and the reduction of vegetated areas linked to the growth of the large ice sheets in North America and Eurasia. More data on the recent past can be found in snow and ice, showing the influence of anthropic activities on carbonaceous, sulphate and nitrogen aerosols (Preunkert and Legrand 2013).

Conclusion

In this chapter, we have looked at the major biogeochemical cycles that interact with climate: carbon (CO_2 and CH_4), nitrogen (N_2O), sulphur (SO_2) as well as dust. These biogeochemical cycles are crucial for climate mainly because of their role in the atmospheric radiative budget. In turn, climate evolution impacts these cycles by changing their sources and sinks. Past changes are documented in archives such as sediment and ice cores, which have been described in more details in Volume 1. To better understand past changes of the carbon, nitrogen, sulphur and dust cycles and evaluate their impact on climate, they have been included in numerical climate models. Going back and forth between data and model simulations is crucial to unravel the causes of past changes, and in the future, both more data and improved modelling should help to better understand the changes in the biogeochemical cycles over the last million years.

References

Adams, J. M., Faure, H., Faure-Denard, L., McGlade, J. M., & Woodward, F. I. (1990). Increases in terrestrial carbon storage from the Last Glacial Maximum to the present. *Nature, 348,* 711–714.

Adkins, J. F., McIntyre, K., & Schrag, D. P. (2002). The salinity, temperature, and $\delta^{18}O$ of the glacial deep ocean. *Science, 298,* 1769–1773. https://doi.org/10.1126/science.1076252.

Adkins, J. F. (2013). The role of deep ocean circulation in setting glacial climates. *Paleoceanography, 28,* 539–561. https://doi.org/10.1002/palo.20046.

Adloff, F., Somot, S., Sevault, F., Jordà, G., Aznar, R., Déqué, M., et al. (2015). Mediterranean Sea response to climate change in an ensemble of twenty-first century scenarios. *Climate Dynamics, 45* (9–10), 2775–2802. https://doi.org/10.1007/s00382-015-2507-3.

Ahn, J., & Brook, E. J. (2008). Atmospheric CO_2 and climate on millennial time scales during the last glacial period. *Science, 322,* 83. https://doi.org/10.1126/science.1160832.

Ahn, J., Brook, E. J., Schmittner, A., & Kreutz, K. (2012). Abrupt change in atmospheric CO_2 during the last ice age. *Geophysical Reseach Letters, 39,* L18711. https://doi.org/10.1029/2012GL053018.

Albani, S., Mahowald, N. M., Winckler, G., Anderson, R. F., Bradtmiller, L. I., Delmonte, B., et al. (2015). Twelve thousand years of dust: The Holocene global dust cycle constrained by natural archives. *Climate of the Past, 11,* 869–903. https://doi.org/10.5194/cp-11-869-2015.

Albani, S., Balkanski, Y., Mahowald, N., Winckler, G., Maggi, V., & Delmonte, B. (2018). Aerosol-climate interactions during the Last Glacial Maximum. *Current Climate Change Reports, 4,* 99–114. https://doi.org/10.1007/s40641-018-0100-7.

Anderson, R. F., Ali, S., Bradtmiller, L. I., Nielsen, S. H. H., Fleisher, M. Q., Anderson, B. E., et al. (2009). Wind-driven upwelling in the Southern Ocean and the deglacial rise in atmospheric CO_2. *Science, 323,* 1443. https://doi.org/10.1126/science.1167441.

Archer, D., & Maier-Reimer, E. (1994). Effect of deep-sea sedimentary calcite preservation on atmospheric CO_2 concentration. *Nature, 367,* 260–263.

Archer, D., Winguth, A., Lea, D., & Mahowald, N. (2000). What caused the glacial/interglacial pCO_2 cycles? *Reviews of Geophysics, 38,* 159–189.

Archer, D. E., Martin, P. A., Milovich, J., Brovkin, V., Plattner, G.-K., & Ashendel, C. (2003). Model sensitivity in the effect of Antarctic sea ice and stratification on atmospheric pCO_2. *Paleoceanography, 18*(1), 1012.

Ayache, M., Dutay, J.-C., Arsouze, T., Révillon, S., Beuvier, J., & Jeandel, C. (2016), High resolution neodymium characterization along the Mediterranean margins and modeling of εNd distribution in the Mediterranean basins. Biogeosciences, (April), 1–31. http://doi.org/10.5194/bg-2016–109.

Barker, S., Diz, P., Vautravers, M. J., Pike, J., Knorr, G., Hall, I. R., et al. (2009). Interhemispheric Atlantic seesaw response during the last deglaciation. *Nature, 457,* 1097–1102. https://doi.org/10.1038/nature07770.

Barnola, J. M., Raynaud, D., Korotkevich, Y. S., & Lorius, C. (1987). Vostok ice core provides 160,000-year record of atmospheric CO_2. *Nature, 329,* 408–414.

Basak, C., Fröllje, H., Lamy, F., Gersonde, R., Benz, V., Anderson, R. F., et al. (2018). Breakup of last glacial deep stratification in the South Pacific. *Science, 359*(6378), 900–904. https://doi.org/10.1126/science.aao2473.

Bereiter, B., Lüthi, D., Siegrist, M., Schüpbach, S., Stocker, T. F., & Fischer H. (2012). Mode change of millennial CO_2 variability during the last glacial cycle associated with a bipolar marine carbon seesaw. *Proceedings of the National Academy of Sciences, 109*(25), 9755–9760. https://doi.org/10.1073/pnas.1204069109.

Bereiter, B., Eggleston, S., Schmitt, J., Nehrbass-Ahles, C., Stocker, T. F., Fischer, H., et al. (2015). Revision of the EPICA Dome C CO_2 record from 800 to 600 kyr before present. *Geophysical Reseach Letters, 42,* 542–549. https://doi.org/10.1002/2014GL061957.

Berner, R. A., Beerling, D. J., Dudley, R., Robinson, J. M., & Wildman, R. A. (2003). Phanerozoic atmospheric oxygen. *Annual Review of Earth and Planetary Sciences, 31,* 105–134.

Bigelow, N. H., Brubaker, L. B., Edwards, M. E., Harrison, S. P., Prentice, I. C., Anderson, P. M., Andreev, A. A., Bartlein, P. J., Christensen, T. R., Cramer, W., Kaplan, J. O., Lozhkin, A. V.,

Matveyeva, N. V., Murray, D. V., McGuire, A. D., Razzhivin, V. Y., Ritchie, J. C., Smith, B., Walker, D. A., Gajewski, K., Wolf, V., Holmqvist, B. H., Igarashi, Y., Kremenetskii, K., Paus, A., Pisaric, M. F. J., & Vokova, V. S. (2003). Climate change and Arctic ecosystems I. Vegetation changes north of 55 °N between the Last Glacial Maximum, mid-Holocene and present. *Journal of Geophysical Research, 108*(D19), 8170.

Bird, M. I., Lloyd, J., & Farquhar, G. D. (1994). Terrestrial carbon storage at the LGM. *Nature, 371,* 566.

Blunier, T., Chappellaz, J., Schwander, J., Dällenbach, A., Stauffer, B., Stocker, T. F., et al. (1998). Asynchrony of Antarctic and Greenland climate change during the last glacial period. *Nature, 394,* 739–743.

Buizert, C., Cuffey, K. M., Severinghaus, J. P., Baggenstos, D., Fudge, T. J., Steig, E. J., et al. (2015). The WAIS Divide deep ice core WD2014 chronology—Part 1: Methane synchronization (68–31 ka BP) and the gas age–ice age difference. *Climate of the Past, 11,* 153–173. https://doi.org/10.5194/cp-11-153-2015.

Bopp, L., Kohfeld, K. E., Quéré, C. L., & Aumont, O. (2003a). Dust impact on marinebiota and atmospheric CO_2 during glacial periods. *Paleoceanography, 18*(2), 1046.

Bopp, L. O., Aumont, S. Belviso, & Monfray, P. (2003b). Potential impact of climate change on marine dimethyl sulfide emissions. *Tellus B: Chemical and Physical Meteorology, 55*(1), 11–22. https://doi.org/10.3402/tellusb.v55i1.16359.

Bopp, L., et al. (2013). Multiple stressors of ocean ecosystems in the 21st century: Projections with CMIP5 models. *Biogeosciences, 10,* 6225–6245. https://doi.org/10.5194/bg-10-6225-2013.

Bopp, L., Resplandy, L., Untersee, A., Mezo, P. L., & Kageyama, M. (2017). Ocean (de)oxygenation from the Last Glacial Maximum to the twenty-first century: insights from Earth system models. *Philosophical Transactions of the Royal Society A, 375,* 20160323.

Boucher, O., Randall, D., Artaxo, P., Bretherton, C., Feingold, G., Forster, P., Kerminen, V.-M., Kondo, Y., Liao, H., Lohmann, U., Rasch, P., Satheesh, S. K., Sherwood, S., Stevens, B., & Zhang, X. Y. (2013). Clouds and aerosols. In T. F. Stocker, D. Qin, G.-K. Plattner, M. Tignor, S. K. Allen, J. Boschung, A. Nauels, Y. Xia, V. Bex, & P. M. Midgley (Eds.), *Climate Change 2013: The Physical Science Basis. Contribution of Working Group I to the Fifth Assessment Report of the Intergovernmental Panel on Climate Change*. Cambridge, UK and New York, NY, USA: Cambridge University Press.

Bouttes, N., Roche, D. M., & Paillard, D. (2009). Impact of strong deep ocean stratification on the glacial carbon cycle. *Paleoceanography, 24*, PA3203. https://doi.org/10.1029/2008pa001707.

Bouttes, N., Paillard, D., & Roche, D. M. (2010). Impact of brine-induced stratification on the glacial carbon cycle. *Climate of the Past, 6,* 575–589. https://doi.org/10.5194/cp-6-575-2010.

Bouttes, N., Paillard, D., Roche, D. M., Brovkin, V., & Bopp, L. (2011). Last Glacial Maximum CO_2 and $\delta^{13}C$ successfully reconciled. *Geophysical Reseach Letters, 38,* L02705. https://doi.org/10.1029/2010GL044499.

Bouttes, N., Roche, D., & Paillard, D. (2012). Systematic study of the impact of fresh water fluxes on the glacial carbon cycle. *Climate of the Past, 8,* 589–607.

Bouttes, N., Swingedouw, D., Roche, D. M., Sanchez-Goni, M. F., & Crosta, X. (2018). Response of the carbon cycle in an intermediate complexity model to the different climate configurations of the last nine interglacials. *Climate of the Past, 14,* 239–253. https://doi.org/10.5194/cp-14-239-2018.

Bozbiyik, A., Steinacher, M., Joos, F., Stocker, T. F., & Menviel, L. (2011). Fingerprints of changes in the terrestrial carbon cycle in response to large reorganizations in ocean circulation. *Climate of the Past, 7,* 319–338.

Broecker, W. S., & Peng, T.-H. (Eds.). (1982). *Tracers in the Sea*. Palisades, New York: Lamont-Doherty Geological Observatory of Columbia University.

Brook, E. J., Harder, S., Severinghaus, J., Steig, E. J., & Sucher, C. M. (2000). On the origin and timing of rapid changes in atmospheric methane during the last glacial period. *Global Biogeochemical Cycles, 14*(2), 559–572. https://doi.org/10.1029/1999GB001182.

Brovkin, V., Ganopolski, A., Archer, D., & Munhoven, G. (2012). Glacial CO_2 cycle as a succession of key physical and biogeochemical processes. *Climate of the Past, 8,* 251–264. https://doi.org/10.5194/cp-8-251-2012.

Carslaw, K. S., Boucher, O., Spracklen, D. V., Mann, G. W., Rae, J. G. L., Woodward, S., et al. (2010). A review of natural aerosol interactions and feedbacks within the Earth system. *Atmospheric Chemistry and Physics, 10*(4), 1701–1737.

Catling, D. C., & Claire, M. W. (2005). How Earth's atmosphere evolved to an oxic state: A status report. *Earth and Planetary Science Letters, 237,* 1–20.

Chappellaz, J., Barnola, J. M., Raynaud, D., Korotkevich, Y. S., & Lorius, C. (1990). Ice-Core Record of Atmospheric Methane over the Past 160,000 Years. *Nature, 345,* 127–131.

Chappellaz, J. A., Fung, I. Y., & Thompson, A. M. (1993). The atmospheric CH_4 increase since the Last Glacial Maximum. *Tellus, 45B,* 228–241. 1. Source Estimates.

Chappellaz, J., Brook, E., Blunier, T., & Malaizé, B. (1997). CH_4 and $\delta^{18}O$ of O_2 records from Antarctic and Greenland ice: A clue for stratigraphic disturbance in the bottom part of the Greenland Ice Core Project and the Greenland Ice Sheet Project 2 ice cores. *Journal Geophysical Research, 102,* 26547–26557.

Charlson, R. J., Lovelock, J. E., Andreae, M. O., & Warren, S. G. (1987). Oceanic phytoplankton, atmospheric sulphur, cloud albedo and climate. *Nature, 326,* 655–661.

Ciais, P., Tagliabue, A., Cuntz, M., Bopp, L., Scholze, M., Hoffmann, G., et al. (2012). Large inert carbon pool in the terrestrial biosphere during the Last Glacial Maximum. *Nature Geoscience, 5,* 74–79. https://doi.org/10.1038/ngeo1324.

Clement, A. C., & Peterson, L. C. (2008). Mechanisms of abrupt climate change of the last glacial period. *Reviews of Geophysics, 46*, RG4002. https://doi.org/10.1029/2006rg000204.

Craig, H. (1957). Isotopic standards for carbon and oxygen and correction factors for massspectrometric analysis of carbon dioxide. *Geochimica et Cosmochimica Acta, 12,* 133–149.

Crichton, K. A., Bouttes, N., Roche, D. R., Chappellaz, J., & Krinner, G. (2016). Permafrost carbon as a missing link to explain CO_2 changes during the last deglaciation. *Nature Geoscience, 9,* 683–686. https://doi.org/10.1038/ngeo2793.

Crowley, T. (1995). Ice age terrestrial carbon changes revisited. *Global Biogeochemical Cycles, 9*(3), 377–389.

Crutzen, P. J., & Brühl, C. (1993). A model study of atmospheric temperatures and the concentrations of ozone, hydroxyl, and some other photochemically active gases during the glacial, the pre-industrial Holocene and the present. *Geophysical Reseach Letters, 20*(11), 1047–1050.

Curry, W. B., & Oppo, D. W. (2005). Glacial water mass geometry and the distribution of $\delta^{13}C$ of ΣCO_2 in the western Atlantic Ocean. *Paleoceanography, 20*, PA1017. https://doi.org/10.1029/2004pa001021.

Dahl-Jensen, D. (2018). Drilling for the oldest ice. *Nature Geoscience, 11,* 703–704.

Dansgaard, W., Johnsen, S. J., Clausen, H. B., Dahl-Jensen, D., Gundestrup, N. S., Hammer, C. U., et al. (1993). Evidence for general instability of past climate from a 250-kyr ice-core record. *Nature, 364,* 218–220.

De Boer, A. M., & Hogg, A. M. C. (2014). Control of the glacial carbon budget by topographically induced mixing. *Geophysical Research Letters, 41*. doi:10.1002/2014GL059963.

Delmas, R., Ascencio, J. M., & Legrand, M. (1980). Polar ice evidence that atmospheric CO_2 20,000 year BP was 50% of present. *Nature, 284,* 155–157.

Emeis, K.-C., Schulz, H., Struck, U., Rossignol-Strick, M., Erlenkeuser, H., Howell, M. W., Kroon, D., Mackensen, A., Ishizuka, S., Oba, T., Sakamoto, T., & Koizumi, I. (2003). Eastern Mediterranean surface water temperatures and 18 O composition during deposition of sapropels in the late Quaternary. *Paleoceanography, 18*(1), n/a–n/a. https://doi.org/10.1029/2000pa000617.

EPICA Community Members. (2004). Eight glacial cycles from an Antarctic ice core. *Nature, 429,* 623–628. https://doi.org/10.1038/nature02599.

EPICA Community Members. (2006). One-to-one coupling of glacial climate variability in Greenland and Antarctica. *Nature, 444*(7116), 195–198. https://doi.org/10.1038/nature05301.

Ezat, M. M., Rasmussen, T. L., Hönisch, B., Groeneveld, J., & deMenocal, P. (2017). Episodic release of CO_2 from the high-latitude North Atlantic Ocean during the last 135 kyr. *Nature Communications, 8,* 14498.

Ferrari, R., Jansen, M. F., Adkins, J. F., Burke, A., Stewart, A. L., & Thompson, A. F. (2014). Antarctic sea ice control on ocean circulation in present and glacial climates. *PNAS, 111*(24), 8753–8758. https://doi.org/10.1073/pnas.1323922111.

Fischer, H., Schmitt, J., Lüthi, D., Stocker, T. F., Tschumi, T., Parekh, P., et al. (2010). The role of Southern Ocean processes on orbital and millennial CO_2 variations—A synthesis. *Quaternary Science Reviews, 29*(1–2), 193–205. https://doi.org/10.1016/j.quascirev.2009.06.007.

Flückiger, J., Blunier, T., Stauffer, B., Chappellaz, J., Spahni, R., Kawamura, K., Schwander, J., Stocker, T. F., & Dahl-Jensen D. (2004). N_2O and CH_4 variations during the last glacial epoch: Insight into global processes. *Global Biogeochemical Cycles, 18*, GB1020. https://doi.org/10.1029/2003gb002122.

Garcia, H. E., Locarnini, R. A., Boyer, T. P., Antonov, J. I., Baranova, O. K., Zweng, M. M., & Johnson, D. R. (2010). World Ocean Atlas 2009, Volume 3: Dissolved oxygen, apparent oxygen utilization, and oxygen saturation. In: S. Levitus (Ed.), NOAA Atlas NESDIS 70, Washington, D.C.: U.S. Government Printing Office, 344 pp.

Gersonde, R., Crosta, X., Abelmann, A., & Armand, L. (2005). Sea-surface temperature and sea ice distribution of the Southern Ocean at the EPILOG Last Glacial Maximum—A circum-Antarctic view based on siliceous microfossil records. *Quat. Sci. Rev., 24,* 869–896.

Goosse, H., Roche, D. M., Mairesse, A., & Berger, M. (2013). Modeling past sea ice changes. *Quaternary Science Reviews, 79,* 191–206. https://doi.org/10.1016/j.quascirev.2013.03.011.

Gottschalk, J., Skinner, L. C., Lippold, J., Vogel, H., Frank, N., Jaccard, S. L., et al. (2016). Biological and physical controls in the Southern Ocean on past millennial-scale atmospheric CO_2 changes. *Nature Communications, 7,* 11539.

Grant, K. M., Rohling, E. J., Bar-Matthews, M., Ayalon, A., Medina-Elizalde, M., Bronk Ramsey, C., et al. (2012). Rapid coupling between ice volume and polar temperature over the past 150 kyr. *Nature, 491,* 744–747.

Grimm, R., Maier-Reimer, E., Mikolajewicz, U., Schmiedl, G., Müller-Navarra, K., Adloff, F., Grant, K. M., Ziegler, M., Lourens, L. J., & Emeis, K.-C. (2015). Late glacial initiation of Holocene eastern Mediterranean sapropel formation. *Nature Communications, 6*(7099), 12 pp. https://doi.org/10.1038/ncomms8099.

Hamon, N., Sepulchre, P., Lefebvre, V., & Ramstein, G. (2013). The role of eastern Tethys seaway closure in the Middle Miocene Climatic Transition (ca. 14 Ma). *Climate of the Past, 9*(6), 2687–2702. https://doi.org/10.5194/cp-9-2687-2013.

Harrison, S. P., Yu, G., Takahara, H., & Prentice, I. C. (2001). Palaeovegetation—Diversity of temperate plants in east Asia. *Nature, 413,* 129–130.

Hemleben, C., Hoernle, K., Jørgensen, B. B., & Roether, W. (2003). Ostatlantik-Mittelmeer- Schwarzes Meer, Cruise 51, 12 September–28 December 2001. Meteor Ber. 03-1, 213 pp.

Hemming, S. R. (2004). Heinrich events: Massive late Pleistocene detritus layers of the North Atlantic and their global climate imprint. *Reviews of Geophysics, 42*, RG1005. https://doi.org/10.1029/2003rg000128.

Heinrich, H. (1988). Origin and consequences of cyclic ice rafting in the Northeast Atlantic Ocean during the past 130,000 years. *Quaternary Research, 29*(2), 142–152. https://doi.org/10.1016/0033-5894(88)90057-9.

Hesse, T., Butzin, M., Bickert, T., & Lohmann, G. (2011). A model-data comparison of $\delta^{13}C$ in the glacial Atlantic Ocean. *Paleoceanography, 26*, PA3220. https://doi.org/10.1029/2010pa002085.

Holland, H. D. (1994). *Early Life on Earth*. In S. Bengston (Ed.) (pp. 237–244). New York: Columbia University Press.

Jaccard, S. L., & Galbraith, E. D. (2011). Large climate-driven changes of oceanic oxygen concentrations during the last deglaciation. *Nature Geoscience, 5,* 151–156.

Jaccard, S. L., & Galbraith, E. D. (2012). Large climate-driven changes of oceanic oxygen concentrations during the last deglaciation. *Nature Geoscience, 5,* 151–156.

Jaccard, S., Galbraith, E., Frölicher, T., & Gruber, N. (2014). Ocean (de)oxygenation across the last deglaciation: Insights for the future. *Oceanography, 27,* 26–35.

Jickells, T. D., An, Z. S., Andersen, K. K., Baker, A. R., Bergametti, G., Brooks, N., et al. (2005). Global iron connections between desert dust, ocean biogeochemistry, and climate. *Science, 308,* 67. https://doi.org/10.1126/science.1105959.

Jouzel, J., Masson-Delmotte, V., Cattani, O., Dreyfus, G., Falourd, S., Hoffmann, G., et al. (2007). Orbital and Millennial Antarctic climate variability over the past 800,000 years. *Science, 317*(5839), 793–797.

Kaplan, J. O., Folberth, G., & Hauglustaine, D. A. (2006). Role of methane and biogenic volatile organic compound sources in late glacial and Holocene fluctuations of atmospheric methane concentrations. *Global Biogeochemical Cycles, 20*, GB2016. https://doi.org/10.1029/2005gb002590.

Kohfeld, K. E., & Harrison, S. P. (2001). DIRTMAP: The geological record of dust. *Earth-Science Reviews, 54,* 81–114. https://doi.org/10.1016/S0012-8252(01)00042-3.

Kohfeld, K. E., Quéré, C. L., Harrison, S. P., & Anderson, R. F. (2005). Role of marine biology in glacial-interglacial CO_2 cycles. *Science, 308,* 74–78.

Kohfeld, K. E., Graham, R. M., de Boer, A. M., Sime, L. C., Wolff, E. W., Le Quéré, C., et al. (2013). Southern Hemisphere westerly wind changes during the Last Glacial Maximum: Paleo-data synthesis. *Quaternary Science Reviews, 68,* 76–95. https://doi.org/10.1016/j.quascirev.2013.01.017.

Köhler, P., Knorr, G., & Bard, E. (2014). Permafrost thawing as a possible source of abrupt carbon release at the onset of the Bølling/Allerød. *Nature Communications*. https://doi.org/10.1038/ncomms6520.

Köng, E., Zaragosi, S., Schneider, J. L., Garlan, T., Bachèlery, P., Sabine, M., et al. (2017). Gravity-driven deposits in an active margin (Ionian Sea) over the last 330,000 years. *Geochemistry, Geophysics, Geosystems, 18*(11), 4186–4210. https://doi.org/10.1002/2017GC006950.

Kullenberg, B. (1952). On the salinity of the water contained in marine sediments. *Meddelanden från Oceanografiska institutet i Göteborg, 21,* 1–38.

Lambert, F., Tagliabue, A., Shaffer, G., Lamy, F., Winckler, G., Farias, L., et al. (2015). Dust fluxes and iron fertilization in Holocene and Last Glacial Maximum climates. *Geophysical Research Letters, 42,* 6014–6023. https://doi.org/10.1002/2015GL064250.

Landais, A., Dreyfus, G., Capron, E., Jouzel, J., Masson-Delmotte, V., Roche, D. M., et al. (2013). Two-phase change in CO_2, Antarctic temperature and global climate during termination II. *Nature Geoscience, 6,* 1062–1065. https://doi.org/10.1038/NGEO1985.

Legrand, M., Feniet-Saigne, C., Sattzman, E. S., Germain, C., Barkov, N. I., & Petrov, V. N. (1991). Ice-core record of oceanic emissions of dimethylsulphide during the last climate cycle. *Nature, 350,* 144–146.

Legrand, M., & Mayewski, P. (1997). Glaciochemistry of polar ice cores: A review. *Reviews of Geophysics, 35*(3), 219–243.

Levine, J. G., Wolff, E. W., Jones, A. E., Sime, L. C., Valdes, P. J., Archibald, A. T., et al. (2011). Reconciling the changes in atmospheric methane sources and sinks between the Last Glacial Maximum and the pre-industrial era. *Geophys. Res. Lett., 38,* L23804. https://doi.org/10.1029/2011GL049545.

Loulergue, L., Schilt, A., Spahni, R., Masson-Delmotte, V., Blunier, T., Lemieux, B., et al. (2008). Orbital and millennial-scale features of atmospheric CH_4 over the past 800,000 years. *Nature, 453,* 383–386. https://doi.org/10.1038/nature06950.

Lüthi, D., Le Floch, M., Bereiter, B., Blunier, T., Barnola, J.-M., Siegenthaler, U., et al. (2008). High-resolution carbon dioxide concentration record 650,000–800,000 years before present. *Nature, 453,* 379–382. https://doi.org/10.1038/nature06949.

Lourantou, A., Lavrič, J. V., Köhler, P., Barnola, J.-M., Paillard, D., Michel, E., Raynaud, D., & Chappellaz, J. (2010). Constraint of the CO_2 rise by new atmospheric carbon isotopic measurements during the last deglaciation. *Global Biogeochemical Cycles, 24*, GB2015. https://doi.org/10.1029/2009gb003545.

Mahowald, N. M., Scanza, R., Brahney, J., Goodale, C. L., Hess, P. G., Moore, J. K., et al. (2017). Aerosol deposition impacts on land and ocean carbon cycles. *Current Climate Change Reports, 3*(1), 16–31.

Marcott, S. A., Bauska, T. K., Buizert, C., Steig, E. J., Rosen, J. L., Cuffey, K. M., et al. (2014). Centennial-scale changes in the global carbon cycle during the last deglaciation. *Nature, 514,* 616–619. https://doi.org/10.1038/nature13799.

Mariotti, V. (2013). *Le cycle du carbone en climat glaciaire: état moyen et variabilité*, Ph.D. thesis. 252 p.

Marchal, O., & Curry, W. B. (2008). On the Abyssal circulation in the Glacial Atlantic. *Journal of Physical Oceanography, 38,* 2014–2037. https://doi.org/10.1175/2008JPO3895.1.

Martinez-Ruiz, F., Kastner, M., Paytan, A., Ortega-Huertas, M., & Bernasconi, S. (2000). Geochemical evidence for enhanced productivity during S1 sapropel deposition in the eastern Mediterranean. *Paleoceanography, 15*(2), 200–209. https://doi.org/10.1029/1999PA000419.

Marzocchi, A., & Jansen, M. F. (2017). Connecting Antarctic sea ice to deep-ocean circulation in modern and glacial climate simulations. *Geophysical Research Letters, 44,* 6286–6295. https://doi.org/10.1002/2017GL073936.

Maslin, M., Adams, J., Thomas, E., Faure, H., & Haines-Young, R. (1995). Estimating the carbon transfer between the ocean, atmosphere and the terrestrial biosphere since the Last Glacial Maximum. *Terra Nova, 7*(3), 358–366.

Matsumoto, K., & Yokoyama, Y. (2013). Atmospheric $\Delta^{14}C$ reduction in simulations of Atlantic overturning circulation shutdown, *Global Biogeochemical Cycles, 27*. https://doi.org/10.1002/gbc.20035.

Menviel, L., Timmermann, A., Mouchet, A., & Timm, O. (2008a). Climate and marine carbon cycle response to changes in the strength of the Southern Hemispheric westerlies. *Paleoceanography, 23*, PA4201.

Menviel, L., Timmermann, A., Mouchet, A., & Timm, O. (2008b). Meridional reorganizations of marine and terrestrial productivity during Heinrich events. *Paleoceanography, 23*, PA1203. https://doi.org/10.1029/2007pa001445.

Menviel, L., Spence, P., & England, M. H. (2015). Contribution of enhanced Antarctic bottom water formation to Antarctic warm events and millennial-scale atmospheric CO_2 increase. *Earth and Planetary Science Letters, 413,* 37–50. https://doi.org/10.1016/j.epsl.2014.12.050.

Menviel, L., Yu, J., Joos, F., Mouchet, A., Meissner, K. J., & England, M. H. (2017). Poorly ventilated deep ocean at the Last Glacial Maximum inferred from carbon isotopes: A data-model comparison study. *Paleoceanography, 32,* 2–17. https://doi.org/10.1002/2016PA003024.

Milkov, A. V. (2004). Global estimates of hydrate-bound gas in marine sediments: How much is really out there? *Earth-Science Reviews, 66*(3–4), 183–197. https://doi.org/10.1016/j.earscirev.2003.11.002.

Möbius, J., Lahajnar, N., & Emeis, K. C. (2010). Diagenetic control of nitrogen isotope ratios in Holocene sapropels and recent sediments from the Eastern Mediterranean Sea. *Biogeosciences, 7*(11), 3901–3914. https://doi.org/10.5194/bg-7-3901-2010.

Muglia, J., & Schmittner, A. (2015), Glacial Atlantic overturning increased by wind stress in climate models. *Geophysical Research Letters, 42*. https://doi.org/10.1002/2015GL064583.

Murray, L. T., Mickley, L. J., Kaplan, J. O., Sofen, E. D., Pfeiffer, M., & Alexander, B. (2014). Factors controlling variability in the oxidative capacity of the troposphere since the Last Glacial Maximum. *Atmospheric Chemistry and Physics, 14,* 3589–3622. https://doi.org/10.5194/acp-14-3589-2014.

NEEM Community Members. (2013). Eemian interglacial reconstructed from a Greenland folded ice core. *Nature, 493,* 489–494. https://doi.org/10.1038/nature11789.

Nijenhuis, I. A., & De Lange, G. J. (2000). Geochemical constraints on Pliocene sapropel formation in the eastern Mediterranean. *Mar. Geol., 163,* 41–63.

North Greenland Ice Core Project Members. (2004). High-resolution record of Northern Hemisphere climate extending into the last interglacial period. *Nature, 431,* 147–151.

Obata, A. (2007). Climate–carbon cycle model response to freshwater discharge into the North Atlantic. *Journal of Climate, 20,* 5962–5976. https://doi.org/10.1175/2007JCLI1808.1.

O'Dowd, C. D., & de Leeuw, G. (2007). Marine aerosol production: A review of the current knowledge. *Philosophical Transactions of the Royal Society A, 365*(1856), 1753–1774.

Parrenin, F., Masson-Delmotte, V., Köhler, P., Raynaud, D., Paillard, D., Schwander, J., Barbante, C., Landais, A., Wegner, A., & Jouzel, J. (2013). Synchronous change of atmospheric CO_2 and Antarctic temperature during the last deglacial warming. *Science, 339*, 1060. https://doi.org/10.1126/science.1226368.

Petit, J. R., Jouzel, J., Raynaud, D., Barkov, N. I., Barnola, J. M., Basile, I., et al. (1999). Climate and atmospheric history of the past 420,000 years from the Vostok Ice Core, Antarctica. *Nature, 399,* 429–436.

Pickett, E. J., Harrison, S. P., Hope, G., Harle, K., Dodson, J. R., Peter Kershaw, A., et al. (2004). Pollen-based reconstructions of biome distributions for Australia, Southeast Asia and the Pacific (SEAPAC region) at 0, 6000 and 18,000 14C yr BP. *Journal of Biogeography, 31,* 1381–1444. https://doi.org/10.1111/j.1365-2699.2004.01001.x.

Plancq, J., Grossi, V., Pittet, B., Huguet, C., Rosell-Melé, A., & Mattioli, E. (2015). Multi-proxy constraints on sapropel formation during the late Pliocene of central Mediterranean (southwest Sicily). *Earth and Planetary Science Letters, 420,* 30–44.

Prather, M. J. (2007). Lifetimes and time scales in atmospheric chemistry. *Philosophical Transactions of the Royal Society A: Mathematical, Physical and Engineering Sciences, 365*. http://doi.org/10.1098/rsta.2007.2040.

Prentice, I. C., Jolly, D., & BIOME 6000 Participants. (2000). Mid-Holocene and glacial-maximum vegetation geography of the northern continents and Africa. *Journal of Biogeography 27*, 507–519.

Preunkert, S., Legrand, M., Jourdain, B., Moulin, C., Belviso, S., Kasamatsu, N., et al. (2007). Interannual variability of dimethylsulfide in air and seawater and its atmospheric oxidation by-products (methanesulfonate and sulfate) at Dumont d'Urville, coastal Antarctica (1999–2003). *Journal of Geophysical Research, 112,* D06306. https://doi.org/10.1029/2006JD007585.

Preunkert, S., & Legrand, M. (2013). Towards a quasi-complete reconstruction of past atmospheric aerosol load and composition (organic and inorganic) over Europe since 1920 inferred from Alpine ice cores. *Climate of the Past, 9*(4), 1403–1416.

Quiquet, A., Archibald, A. T., Friend, A. D., Chappellaz, J., Levine, J. G., Stone, E. J., et al. (2015). The relative importance of methane sources and sinks over the Last Interglacial period and into the last glaciation. *Quaternary Science Reviews, 112,* 1–16. https://doi.org/10.1016/j.quascirev.2015.01.004.

Rasmussen, S. O., Bigler, M., Blockley, S. P., Blunier, T., Buchardt, S. L., Clausen, H. B., et al. (2014). A stratigraphic framework for abrupt climatic changes during the last glacial period based on three synchronized Greenland ice-core records: Refining and extending the INTIMATE event stratigraphy. *Quaternary Science Reviews, 106,* 14–28.

Rhein, M., et al. (2013). Observations: Ocean. In T. F. Stocker et al. (Eds.), *Climate Change 2013: The Physical Science Basis. Contribution of Working Group I to the Fifth Assessment Report of the Intergovernmental Panel on Climate Change* (pp. 255–310). Cambridge, UK: Cambridge University Press.

Roche, D. M., Crosta, X., & Renssen, H. (2012). Evaluating Southern Ocean sea ice for the Last Glacial Maximum and pre-industrial climates: PMIP-2 models and data evidences. *Quaternary Science Reviews, 56,* 99–106. https://doi.org/10.1016/j.quascirev.2012.09.020.

Rogerson, M., Cacho, I., Jimenez-Espejo, F., Reguera, M. I., Sierro, F. J., Martinez-Ruiz, F., Frigola, J., & Canals, M. (2008). A dynamic explanation for the origin of the western Mediterranean organic rich layers. *Geochemistry, Geophysics, Geosystems, 9*, Q07U01. https://doi.org/10.1029/2007gc001936.

Rohling, E. J., Marino, G., & Grant, K. M. (2015). Mediterranean climate and oceanography, and the periodic development of anoxic events (sapropels). *Earth-Science Reviews, 143*(2015), 62–97.

Rosen, J. L., Brook, E. J., Severinghaus, J. P., Blunier, T., Mitchell, L. E., Lee, J. E., et al. (2014). An ice core record of near-synchronous global climate changes at the Bølling transition. *Nature Geoscience, 7,* 459–463.

Rossignol-Strick, M., Nesteroff, V., Olive, P., & Vergnaud-Grazzini, C. (1982). After the deluge; Mediterranean stagnation and sapropel formation. *Nature, 295,* 105–110.

Saigne, C., & Legrand, M. (1987). Measurements of methanesulphonic acid in Antarctic ice. *Nature, 330,* 240–242.

Schilt, A., Baumgartner, M., Blunier, T., Schwander, J., Spahni, R., Fischer, H., et al. (2010). Glacial–interglacial and millennial-scale variations in the atmospheric nitrous oxide concentration during the last 800,000 years. *Quaternary Science Reviews, 29,* 182–192.

Schilt, A., Baumgartner, M., Eicher, O., Chappellaz, J., Schwander, J., Fischer, H., et al. (2013). The response of atmospheric nitrous oxide to climate variations during the last glacial period. *Geophysical Research Letters, 40,* 1888–1893. https://doi.org/10.1002/grl.50380.

Schmitt, J., Schneider, R., Elsig, J., Leuenberger, D., Lourantou, A., Chappellaz, J., Köhler, P., Joos, F., Stocker, T. F., Leuenberger, M., & Fischer, H. (2012). Carbon isotope constraints on the deglacial CO_2 rise from ice cores. *Science, 336*, 711. https://doi.org/10.1126/science.1217161.

Schmittner, A., & Galbraith, E. D. (2008). Glacial greenhouse-gas fluctuations controlled by ocean circulation changes. *Nature, 456* (7220), 373–376. https://doi.org/10.1038/nature07531.

Schneider, R., Schmitt, J., Köhler, P., Joos, F., & Fischer, H. (2013). A reconstruction of atmospheric carbon dioxide and its stable carbon isotopic composition from the penultimate glacial maximum to the last glacial inception. *Climate of the Past, 9,* 2507–2523. https://doi.org/10.5194/cp-9-2507-2013.

Schwander, J., & Stauffer, B. (1984). Age difference between polar ice and the air trapped in its bubbles. *Nature, 311,* 45–47.

Shackleton, N. J. (1977). Carbon-13 in Uvegerina: Tropical rainforest history and the equatorial Pacific carbonate dissolution cycles. In N. R. Andersen & A. Malako (Eds.), *The fate of fossil fuel CO_2 in the oceans* (pp. 401–428). New York: Plenum.

Siegenthaler, U., Stocker, T. F., Monnin, E., Lüthi, D., Schwander, J., Stauffer, B., et al. (2005). Stable carbon cycle-climate relationship during the Late Pleistocene. *Science, 310*(5752), 1313–1317. https://doi.org/10.1126/science.1120130.

Sigman, D. M., & Boyle, E. A. (2000). Glacial/interglacial variations in atmospheric carbon dioxide. *Nature, 407,* 859–869.

Skinner, L. C., Fallon, S., Waelbroeck, C., Michel, E., & Barker, S. (2010). Ventilation of the deep Southern Ocean and deglacial CO_2 rise. *Science, 328*(5982), 1147–1151. https://doi.org/10.1126/science.1183627.

Skinner, L. C. (2009). Glacial-interglacial atmospheric CO_2 change: A possible "standing volume" effect on deep-ocean carbon sequestration. *Climate of the Past, 5,* 537–550. https://doi.org/10.5194/cp-5-537-2009.

Sowers, T., Alley, R. B., & Jubenville, J. (2003). Ice core records of atmospheric N_2O covering the last 106,000 years. *Science, 301*, 945–948.

Stephens, B. B., & Keeling, R. F. (2000). The influence of Antarctic sea ice on glacial-interglacial CO_2 variations. *Nature, 404,* 171–174.

Stramma, L., Prince, E. D., Schmidtko, S., Luo, J., Hoolihan, J. P., Visbeck, M., et al. (2012). Expansion of oxygen minimum zones may reduce available habitat for tropical pelagic fishes. *Nature Climate Change, 2,* 33–37.

Spahni, R., Chappellaz, J., Stocker, T. F., Loulergue, L., Hausammann, G., Kawamura, K., et al. (2005). Atmospheric methane and nitrous oxide of the late Pleistocene from Antarctic ice cores. *Science, 310,* 1317–1321.

Stocker, T. F., & Johnsen, S. J. (2003). A minimum thermodynamic model for the bipolar seesaw. *Paleoceanography, 18*(4), 1087. https://doi.org/10.1029/2003PA000920.

Tagliabue, A., Bopp, L., Roche, D. M., Bouttes, N., Dutay, J.-C., Alkama, R., et al. (2009). Quantifying the roles of ocean circulation and biogeochemistry in governing ocean carbon-13 and atmospheric carbon dioxide at the Last Glacial Maximum. *Climate of the Past, 5,* 695–706.

Tarnocai, C., Canadell, J. G., Schuur, E. A. G., Kuhry, P., Mazhitova, G., & Zimov, S. (2009). Soil organic carbon pools in the northern circumpolar permafrost region. *Global Biogeochemical Cycles, 23*, GB2023. https://doi.org/10.1029/2008gb003327.

Toggweiler, J. R., Russell, J. L., & Carson, S. R. (2006). Midlatitude westerlies, atmospheric CO_2, and climate change during the ice ages. *Paleoceanography, 21*, PA2005.

Tschumi, J., & Stauffer, B. (2000). Reconstructing past atmospheric CO_2 concentration based on ice-core analyses: Open questions due to in situ production of CO_2 in the ice. *Journal of Glaciology, 46* (152), 45–53. https://doi.org/10.3189/172756500781833359.

Tschumi, T., Joos, F., Gehlen, M., & Heinze, C. (2011). Deep ocean ventilation, carbon isotopes, marine sedimentation and the deglacial CO_2 rise. *Climate of the Past, 7,* 771–800. https://doi.org/10.5194/cp-7-771-2011.

Vadsaria, T., Ramstein, G., Dutay, J. C., Li, L., Ayache, M., & Richon, C. (2019). Simulating the occurrence of the last sapropel event (S1): Mediterranean basin ocean dynamics simulations using Nd isotopic composition modeling. *Paleoceanography and Paleoclimatology*. http://doi.org/10.1029/2019PA003566.

Valdes, P. J., Beerling, D. J., & Johnson, C. E. (2005). The ice age methane budget. *Geophysical Research Letters, 32,* L02704. https://doi.org/10.1029/2004GL021004.

WAIS Divide Project Members. (2015). Precise interpolar phasing of abrupt climate change during the last ice age. *Nature, 520,* 661–668. https://doi.org/10.1038/nature14401.

Walker, J. C. G. (1980). The oxygen cycle. In O. Hutzinger (Ed.), *The natural environment and the biogeochemical cycles* (pp. 87–104). Berlin, Heidelberg: Springer.

Wang, W., Yung, Y., Lacis, A., Mo, T., & Hansen, J. (1976). Greenhouse effects due to man made perturbations of trace gases. *Science, 194*(4266), 685–690.

Weber, S. L., Drury, A. J., Toonen, W. H. J., & van Weele, M. (2010). Wetland methane emissions during the Last Glacial Maximum estimated from PMIP2 simulations: Climate, vegetation, and geographic controls. *Journal Geophysical Research, 115,* D06111. https://doi.org/10.1029/2009JD012110.

Wolff, E. W., Fischer, H., Fundel, F., Ruth, U., Twarloh, B., Littot, G. C., Mulvaney, R., Röthlisberger, R., de Angelis, M., Boutron, C. F., Hansson, M., Jonsell, U., Hutterli, M. A., Lambert, F., Kaufmann, P., Stauffer, B., Stocker, T. F., Steffensen, J. P., Bigler, M., Siggaard-Andersen, M. L., Udisti, R., Becagli, S., Castellano, E., Severi, M., Wagenbach, D., Barbante, C., Gabrielli P., & Gaspari V. (2006). Southern Ocean sea-ice extent, productivity and iron flux over the past eight glacial cycles. *Nature 440*, 23. https://doi.org/10.1038/nature04614.

Yin, Q. Z., & Berger, A. (2010). Insolation and CO_2 contribution to the interglacial climate before and after the Mid-Brunhes Event. *Nature Geoscience, 3,* 243–246. https://doi.org/10.1038/ngeo771.

Yin, Q. Z., & Berger, A. (2012). Individual contribution of insolation and CO_2 to the interglacial climates of the past 800,000 years. *Climate Dynamics, 38*(3–4), 709–724.

Yu, J., Menviel, L., Jin, Z. D., Thornalley, D. J. R., Barker, S., Marino, G., Rohling, E. J., Cai, Y., Zhang, F., Wang, X., Dai, Y., Chen P., & Broecker W. S. (2016). Sequestration of carbon in the deep Atlantic during the last glaciation. *Nature Geoscience, 9*, 319–324.

Ziegler, M., Tuenter, E., & Lourens, L. J. (2010). The precession phase of the boreal summer monsoon as viewed from the eastern Mediterranean (ODP Site 968). *Quaternary Science Reviews, 29,* 1481–1490.

The Cryosphere and Sea Level

24

Catherine Ritz, Vincent Peyaud, Claire Waelbroeck, and Florence Colleoni

Introduction

Several times during the history of the Earth extensive ice sheets covered part of the continents. As a result, a significant proportion of freshwater was stored in solid form, which caused a drop in sea level.

Because of their impact on other components of the Earth system (atmosphere, ocean, land), the dynamics of these ice masses must be taken into account in order to understand the evolution of the climate over the time scale of the last glacial-interglacial cycles. This topic can be addressed in different ways, depending to the various scientific disciplines and tools. One approach is to characterize these ice sheets according to the traces they have left behind, whether on land or in marine records. Marine sediments contain a record of changes in the overall volume of ice over time through changes in the oxygen isotopic composition of calcareous fossils. Due to isotopic fractionation that takes place during the evaporation of water, the drop in sea level during cold periods has been accompanied by an enrichment of seawater, not only in salt, but also in heavy isotopes of water (water molecules containing the ^{18}O isotope of oxygen rather than the most widespread isotope, ^{16}O. See Chap. 20, Volume 1). This enrichment leads to variations in the isotopic composition of the calcareous shells of the foraminifera preserved in the sediments. However, the isotopic composition of foraminifera also depends on the temperature at which the calcite was formed, so the benthic signal must be corrected in order to deduce the variations in sea level.

Another approach is to try to understand the physical mechanisms governing the formation and evolution of these ice masses. In both cases, observations of the two large remaining ice sheets, Antarctica and Greenland are pertinent. Finally, numeric simulation uses all of the information gathered (mechanisms, data) to develop models to calculate the evolution of the polar ice caps as they interact with the climate. These tools (referred to later as 'ice sheet models') allow us to study, for example, the role of the ice sheets in the climate system, in particular the non-linear effects that can amplify the forcings caused by variations in the Earth's orbital parameters. These models are also indispensable tools to assess the rise of sea levels in the context of global warming.

What Is an Ice Sheet?

Some definitions of glaciological terms

An ice cap is a mass of freshwater ice which rests on the ground. A notable difference between an ice cap and a mountain glacier is that the highest point of an ice cap, usually centered on a massif, is made of ice and called a dome, while a glacier flows down from a mountain (or from an ice cap). Ice caps can be of different sizes such as mountain peaks completely covered in ice in almost all the great mountain ranges of the world as well as significantly larger ice caps on the Arctic archipelagos (Fig. 24.1), in Iceland, on the Antarctic Peninsula and on some islands in the Southern Ocean. Finally, when an ice mass covers the land on a continental scale it is called an ice sheet. Two large ice sheets, in Greenland and Antarctica, cover virtually the whole continent on which they lie. North America and Northern Eurasia were partially covered by such ice sheets during glacial periods (Fig. 24.1). Although ice caps and ice sheets are driven by the same processes, the discussion below focuses on ice sheets that are large enough to significantly modify sea level.

C. Ritz (✉) · V. Peyaud
Institute of Engineering, Univ. Grenoble Alpes, CNRS, IRD, Grenoble INP, IGE, 38000 Grenoble, France
e-mail: catherine.ritz@univ-grenoble-alpes.fr

C. Waelbroeck
Laboratoire d'Océanographie et du Climat : Expérimentation et Approches Numériques, LOCEAN/IPSL, Sorbonne Université-CNRS-IRD-MNHN, UMR7159, Paris, France

F. Colleoni
OGS (National Institute of Oceanography and Applied Geophysics), Borgo Grotta Gigante 42/c, Viale Aldo Moro 44, 34010 Sgonico (TS), Italy

G. Ramstein et al. (eds.), *Paleoclimatology*, Frontiers in Earth Sciences,
https://doi.org/10.1007/978-3-030-24982-3_24

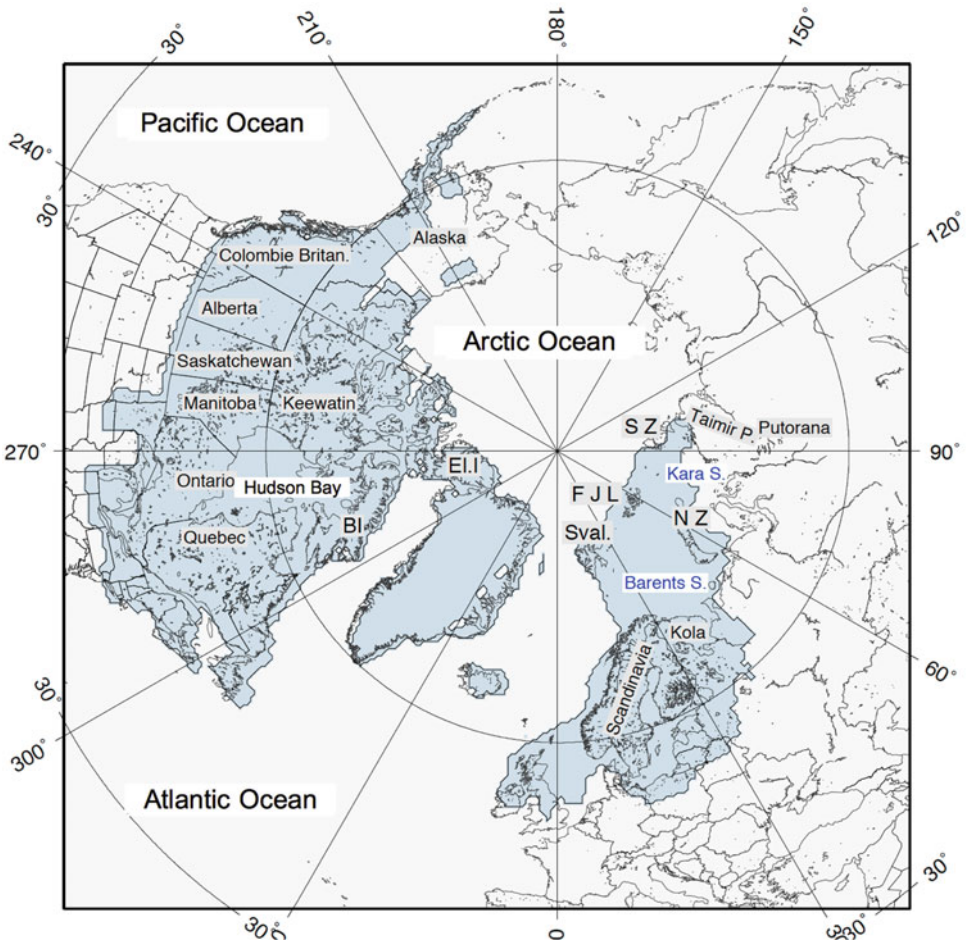

Fig. 24.1 Map of the northern hemisphere during the last glacial maximum. Ice caps and ice sheets are in blue (Peltier Ice4G). The ice sheet over North America is called Laurentide ice sheet. Sometimes, the ice cap over the Rocky Mountains is referred to as the Cordilleran ice cap. The Greenland ice sheet was not much larger than at present, but was probably connected to Ellesmere Island. The ice sheet over Eurasia was called the Fennoscandian ice sheet. The existence of a connection with the ice cap over the British islands is still disputed. It can be seen that a good part of the Fennoscandian ice sheet extended as far as Svalbard, occupying what is currently the sea of Barents. *Abbreviations* Sval—Svalbard; FJL—François Joseph Land; SZ—Severnaia Zembla; El.I.—Ellesmere Island; BI—Baffin Island. From the thesis of Peyaud (2007)

When the ice from an ice sheet flows to the coast, it begins to float on the sea, forming either tongues of ice or ice-shelves. Currently, the largest of these are the Ross and Ronne-Filchner ice shelves in Antarctica (see map on Fig. 24.2). The line where the ice begins to float is called the grounding line, and we will return to this point as it is important for the evolution of an ice sheet.

The thickness of the ice shelves can reach 2000 m at the grounding line, but they generally thin off rapidly as they reach the ocean and are about 200 m thick at the front. At the front, the ice shelves crack and break off, producing icebergs (calving phenomenon). Ice-shelves and sea ice should not be confused. The latter is made of seawater and, although some of the salt is expelled during the freezing process, they are still not composed of freshwater. Moreover, sea ice is only about a few meters thick.

Finally, the edge of a sheet (terrestrial or marine) is generally not uniform, but rather an alternation of fast-moving glaciers and relatively immobile zones. These fast-moving glaciers are called outlet glaciers. Their location depends on the topography of the bedrock (their flow is channeled into sub-glacial valleys) and on its geological properties with zones with relatively rapid flow (several hundred meters a year) being observed in the midst of relatively stagnant ice (a few meters per year). In Antarctica, some of these glaciers begin several hundred kilometers inside the ice sheet. When they are particularly wide ($\sim$40 km), they are also called ice streams.

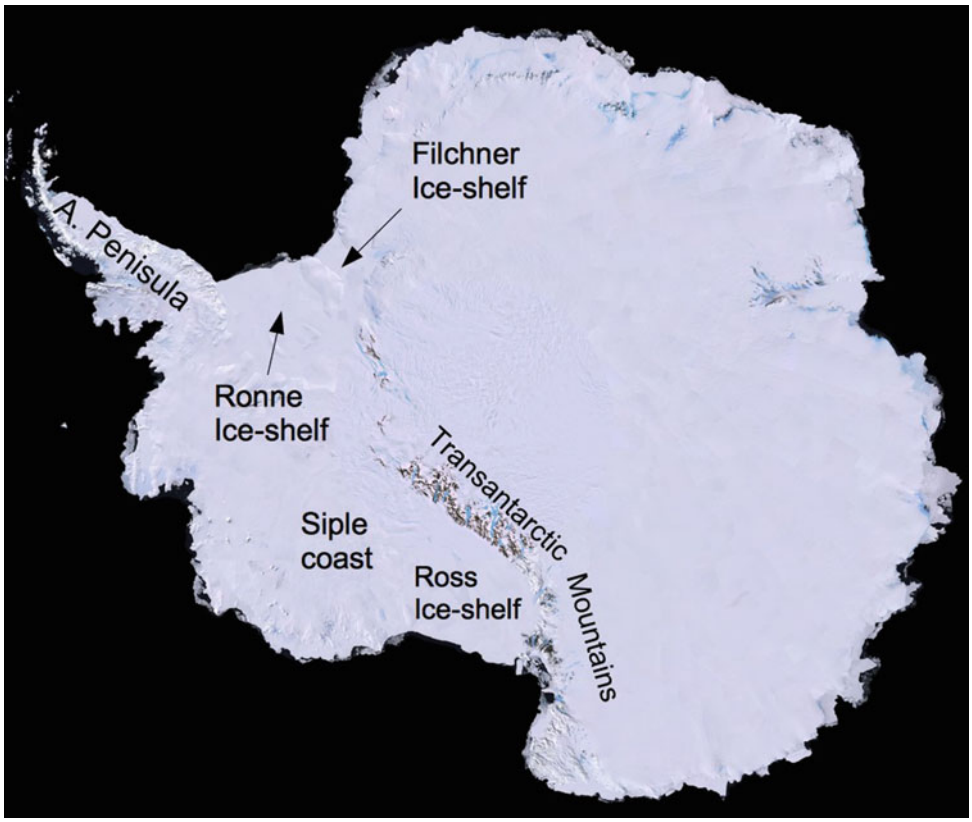

Fig. 24.2 Satellite image of Antarctica (Blue Marble, NASA) with localization of the main ice shelves i.e. floating ice platforms. Siple coast is a region characterized by very large ice streams. Ice covers the whole of the emerged continent, with the exception of mountains arising above the ice, for example, in the peninsula and the trans-Antarctic Mountains

What Determines Sea Level?

It may seem easy to determine how sea level varied over time, but it is in fact a difficult characteristic to estimate. Distinct mechanisms intervene in these variations, involving important regional specificities. Since many observations are local, the representativeness of each measurement must be estimated according to the place, the time and the nature of the observation. Here, we identify the various processes that cause sea level to vary and assess how they impact on the interpretation of observations. Since we are interested in large time scales, we focus only on the level averaged over several years and so exclude the effect of tides and currents.

Sea level depends first of all on the mass of liquid water available, a quantity that changes over time due to its storage as ice on the continents during cold periods. This information is for the whole globe and it can be evaluated through reconstructions of the average isotopic composition of the ocean. Records of the isotopic composition of seawater are indirect and are essentially of two types:

(1) The isotopic composition of deep water during the Last Glacial Maximum (LGM) can be estimated by inversion of the isotopic composition diffusion profile of the interstitial water in the sedimentary column from the water-sediment interface (Schrag et al. 1996). In this way, in cores taken from the Pacific Ocean (the world's largest ocean basin), it was possible to establish that the average enrichment of the ocean during the LGM was $1.0 \pm 0.1‰$ compared to today.

(2) The changes in the isotopic composition of deep water can be reconstructed from isotopic analyses carried out on the shells of benthic foraminifera after subtracting the influence on these values of the variations in temperature of the deep waters as well as the local variations in the deep water isotopic composition (Waelbroeck et al. EPILOG 2002).

Variations in the average isotopic composition of the ocean can be translated into variations in the eustatic level of the seas. Current knowledge indicates that the relationship between these two quantities can be approximated initially using a constant multiplicative factor, so that an enrichment of 1‰ during the LGM corresponds to a decrease in the eustatic sea level of about 130 m (Fig. 24.3). Sea level changes have also been reconstructed from isotopic analyses

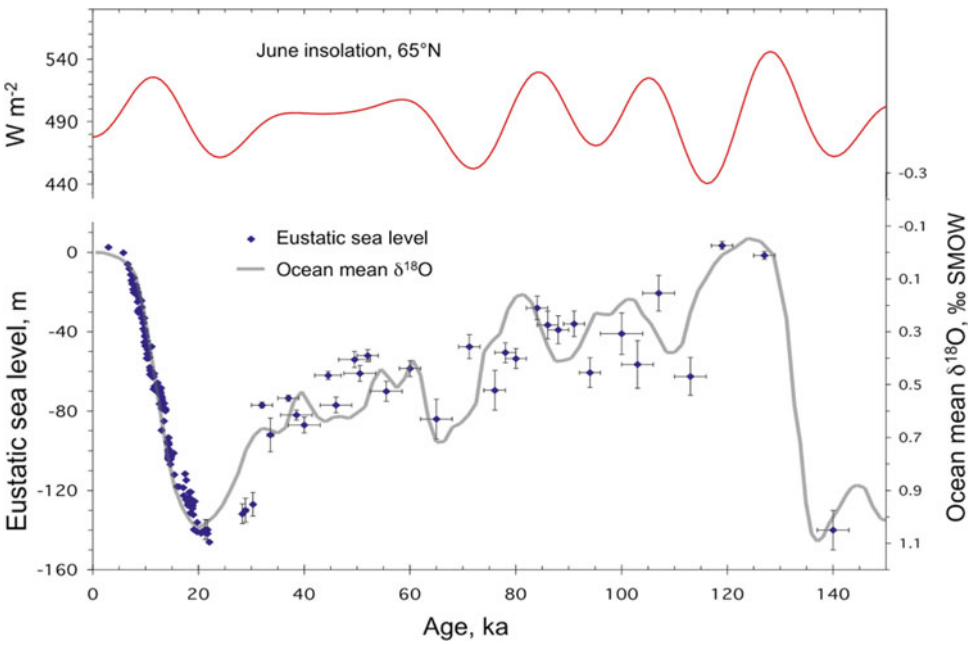

Fig. 24.3 Variations in summer sunshine levels at 65 °N and in the eustatic level of the sea during the last climate cycle. Eustatic levels calculated by Lambeck and Chappell (2001), based on measurements of the relative sea level. Reconstruction of $\delta^{18}O$ changes in the mean ocean from $\delta^{18}O$ of benthic foraminifera (Waelbroeck et al. EPILOG 2002)

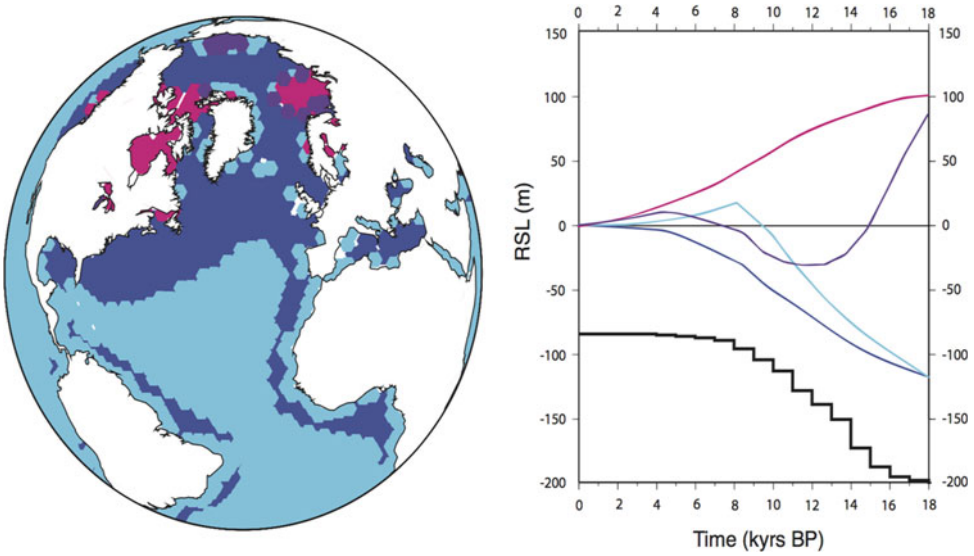

Fig. 24.4 Glacial isostasy

of the shells of planktonic foraminifera from the Red Sea, which record the large variations in salinity resulting from the closing and opening of the Bab el Mandab Straits caused by decreases and increases in sea level (Siddall et al. 2003).

At the glacial-interglacial scale, the changes in global ice volume constitutes the most important mechanism, and can cause variations in sea level of around one hundred meters ($\sim$130 m between the LGM and the present). These variations are called changes in the 'eustatic' level of the seas, and this corresponds roughly to the variations in the average level over the globe (see later for the concept of implicit ice). Alternatively, for the same mass of water, the volume changes with the temperature of the water because of thermal expansion (density depends on temperature). The impact of thermal expansion on the sea level is purely local, but its overall global average is sometimes added to the eustatic level of the seas.

In addition to the eustatic sea level, it is also important to take into account the isostatic variations which modify the shape of the ocean basins. Isostasy is the phenomenon of depression of the Earth's crust beneath the weight of the ice sheet (on land) and of water (under the oceans) (see Fig. 24.4). This means that both the changing quantity of liquid water and the changing shape of the basin need to be considered when attempting to measure the level of the water at the edges, which themselves can be affected by a vertical movement. Although it is now possible to observe the average level over the whole

globe by satellite, for past periods, the vast majority of observations are taken at the coasts. Variations in relative sea level (RSL) is tracked at particular coastal points. It is important to emphasize that isostasy has a reaction time of several thousand years and that Scandinavia, for example, is still rising (at the rate of about one meter per century) following the disappearance of the ice sheet that covered northern Europe during the last glacial maximum. At each point, the relative sea level is therefore a combination of eustatic (global), isostatic, and possibly tectonic (local) variations. There are several ways to estimate this relative sea level, using traces of ancient beaches, coral analysis, speleothems etc.

Box 1. Glacial Isostasy

Post-glacial rebound: The relative changes in sea level are the result of tectonic processes and climate changes. These latter involve the accretion or melting of the ice sheets on the continents (more than 5 km thick). During ice ages, the pressure exerted by the accumulated weight of the ice sheets on the continents modified the shape of the surface creating large depressions in the lithosphere. These changes in shape brought about disturbances of the geoid (equipotential surface of the Earth's gravity field corresponding to the theoretical surface of the oceans) as well as vertical and horizontal displacements of the lithosphere and the mantle. When the shape of the Earth or the volume of the oceans changes, the geoid is thus modified as is the sea level. When the continental ice sheets melt, the lithosphere is released from the weight of the ice and the deflection is reabsorbed at a speed which depends on the viscosity of the mantle. This return is called the post-glacial rebound, post-glacial describing the period from −6000 (ka BP) to today. (6 ka BP marks the end of the melting of the ice caps of the northern hemisphere: the Laurentide and the Eurasian ice sheets having completely melted). For the Last Glacial Maximum (LGM), the relaxation time of the lithosphere is estimated at about 3000 years.

Sea level: Variations in sea level are caused by changes in the geoid surface, in the Earth's topography and in ocean mass. Sea level can be broken down into three contributing factors: the ice load (S^{ICE}), the oceanic charge (S^{OCE}) and the glacio-eustatic level (S^{EUS}).

$$S = S^{ICE} + S^{EUS} + S^{OCE} \qquad (24.2.1)$$

Glacio-eustatic changes in sea level are controlled by the amount of ice stored on the continents. In glacial isostasy models, the glacio-eustatic sea level is defined for a totally rigid Earth without any disturbance of the gravity field. The glacial isostasy models allow us to estimate that the eustatic level during the Last Glacial Maximum was 130 ± 10 m below the current sea level (Lambeck, et al., EPILOG 2002). This estimate of the eustatic level is mainly based on the measurement of coral terraces in sites not affected by the postglacial rebound, such as the Seychelles, but also from calculations of the glacial isostasy models attempting to reproduce relative variations in sea level. The sea level at a given time and place in relation to the current sea level is defined as the relative sea level and can be described by the following equation:

$$\mathrm{RSL}\left(\omega, t^{BP}\right) = S(\omega, t^{BP}) - S\left(\omega, t^{P}\right) \qquad (24.2.2)$$

with ω being the geographical coordinates, t^{BP}, a time Before Present, et t^{P}, the present time. Equation (24.2.2) describes the relative level as the difference in sea level between the t^{BP} level and the current level. During the formation of ice sheets on the continents, the nearby regions and those further afield were affected differently depending on their distance from the ice masses and on the movements of the lithosphere and the mantle and therefore presented a sea level graph reflecting the trend of the regional ocean variations. These trends have been grouped into so-called 'Clark zones'. Figure 24.4 presents the result of modelled sea level changes due to postglacial rebound following the LGM according to the ICE-5G ice model (Peltier 2004). The graph shows changes in sea level for 18,000 years. The graphs are associated with their respective colors on the globe and each corresponds to a different regional trend of sea level variations. The pink and purple zones correspond to the regions that were either covered with ice during the LGM or were nearby, and so were very affected by the rebound of the lithosphere after the LGM. The dark blue zone represents regions showing subsidence of the lithosphere after the LGM. The light blue zone represents areas influenced by the late melting of ice from Antarctica after 9 ka BP (peak observed above the current sea level).

The level of the seas is an equipotential surface of the Earth's gravity field (the geoid) which is linked to the distribution of mass. This changes in the presence of an ice sheet or as a result of displacements of the asthenosphere (the ductile part of the Earth's mantle). This phenomenon must therefore also to be taken into account in the interpretation of relative sea levels. Although isostasy is a considerable complication for the interpretation of observations, this mechanism, on the other hand, it also provides

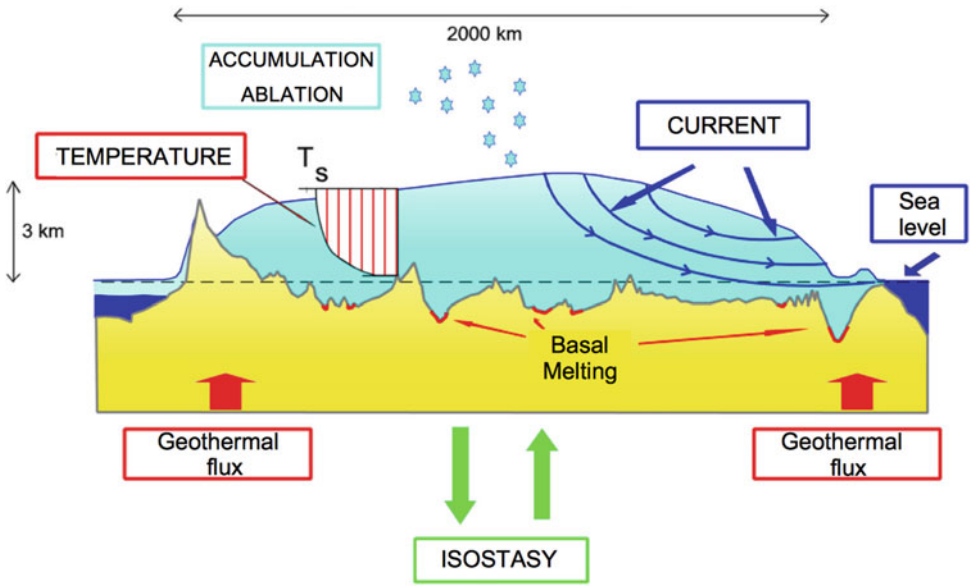

Fig. 24.5 Mechanisms involved in the evolution of polar ice sheets

information on the masses of the different ice sheets in the past. The extent of the ice sheet is generally estimated through geomorphological data. The inversion of relative sea level data using isostatic rebound models (including the geoid calculation) informs us about ice cap thicknesses in the past (Clark et al. 2002).

Finally, the ice sheets often lie on a bedrock that is below sea level. This is true for Western Antarctica currently. When the ice sheet melts, the sea replaces the volume of ice below the waterline and the impact on the sea level is thereby reduced. This volume of water is called 'implicit ice'.

Mechanisms Involved in the Evolution of an Ice Sheet

The evolution of an ice sheet obeys the law of conservation of mass. If the supply of snow is greater than the loss via melting or through the calving of icebergs, the sheet will grow or expand. In addition to this basic principle, there are many processes that interact with both external (atmosphere, ocean, solid Earth) and internal (for example, flow) interactions. In most cases, the geometry of the ice sheet is both a result of and a contributor to these feedbacks. The most important mechanisms are outlined in Fig. 24.5.

Box 2. Mechanisms Involved in the Evolution of Polar Ice Sheets

The geometry of an ice sheet depends on the supply of snow, the melting at the surface and the flow of ice to the edges where it may eventually drain into the ocean in the form of icebergs.

Surface mass balance is the difference between snowfall precipitation and ablation (fusion or sublimation). Redistribution by the wind can intervene as a positive or negative force, depending on the location. The accumulation zone is where the surface mass balance is positive (the central regions) and the ablation zone is where it is negative. We often refer to accumulation as the amount of snow accumulated before melting occurs. To take account of the density of snow, all these terms are generally expressed in water equivalent and the natural unit of time is the year (mass balance in m/year).

Flow: After snow is deposited, it becomes denser and transforms into firn and then into ice which flows due to the action of gravity depending on the slope of the surface. The displacement can therefore move across subglacial mountains or along with a rising bedrock. The flow can be broken down into two factors. One is the deformation of the ice which is linked to its mechanical properties. This means that it behaves like a highly viscous fluid, the viscosity of which depends on the temperature, the 'hotter' the ice, the more quickly it deforms. This deformation causes a variation in the velocity depending on depth and is generally concentrated in the underlying layers. The second is the ability of the ice to slide over the bedrock or, in the case of a sedimentary base, this base may deform. The two processes, the sliding and the sedimentary deformation, cause a horizontal velocity of the ice at the base. They can only act when the ice has reached melting point and their efficiency depends on the subglacial water pressure. We see that the ice flow

depends on the field temperature, through its effect on the viscosity and on the melting point threshold at the base.

The temperature of the ice varies from the surface where it takes the annual average temperature (down to −60 °C in Antarctica) to the melting point at the many points of interface with the bedrock. The temperature thus increases overall with depth and this is mainly due to the geothermal flux which brings continuous heat to the base of the ice (of around 50 mW/m^2). The flow affects temperature by transporting cold from the top to the bottom and from the center to the edges (advection). The heat produced by the deformation and by the sliding also has an impact and brings the base to melting point in active regions where speed of movement is high.

This interaction between velocity field and flow is called **thermo-mechanical coupling**.

Lastly, it is important to mention isostasy, which is the sinking of the bedrock under the weight of the ice (see Fig. 2.4).

Ice sheets have (and have had) different shapes and lifetimes, but they have followed a common pattern. An ice sheet begins to develop when, as a result of a cooling climate, snow becomes permanent in a region, i.e. when summer melting fails to eliminate all of the winter snow. It is usually in areas of high altitude where this process occurs first. In a mountain region, we see the emergence of glaciers in places where the slope is not too steep, that is to say, mainly in the high valleys. If the cooling continues, these glaciers will grow and descend until they fill up the lower valleys. When the region concerned is a high plateau, freezing is more abrupt with a threshold effect when the snow becomes perennial on the plateau. From this point on, the flow of ice plays a role by transporting ice to areas where snow is not permanent, whether by valley glaciers or by glaciers forming on the periphery of the plateau which bring ice to the surrounding plain.

From this moment on, two positive feedbacks supporting the ice expansion and cap formation are established. The first of these is the altitude-temperature feedback, which is based on the fact that atmospheric temperature drops with altitude. Areas where snow would normally not be permanent, freeze over due to the movement of ice, and this increases the altitude of their surface. As a result, the temperature at the surface of the ice drops and summer melting is reduced, so that eventually the snow becomes perennial. Over the years, this mechanism gradually causes the ice front to advance causing the accumulation zone (see Fig. 24.5) to extend further. The second feedback is the albedo. Because snow has a very high albedo (of around 0.9), the larger the accumulation zone, the greater the amount of solar energy reflected back to space instead of being used to heat the Earth's surface. The climate around an area of ice-cover will therefore change, facilitating the expansion of the permanent snow zone.

For a given climate, the expansion of an ice sheet will continue either until it reaches warm regions where melting prevails over the arriving flow of ice, or until it reaches the ocean and begins to float on the sea in the form of ice shelves, producing icebergs (see later the impact of geography).

It should be noted that we emphasize the impact of atmospheric temperature which governs the melting of snow and ice because this climate variable predominates. Precipitation, which governs the amount of snow accumulated, plays an important but lesser role and explains why, at the same temperature, certain regions become more easily covered in snow and ice than others. Among these regions are the glaciers in Norway today, but also the windward faces of reliefs (mountain or ice) where precipitation is increased by the orographic effect.

The same mechanisms apply to the retreat and disappearance of the ice caps (deglaciation) operating in the opposite direction within the context of global warming. The feedbacks mentioned are still active and they tend to amplify the retreat of the ice front. There are, however, two important differences. On the one hand, the growth rate of an ice sheet is limited by the supply of snow by precipitation, whereas the rate of decrease is limited by the amount of heat available to melt the ice. It is easy to understand that the latter limitation will not work well when the ice sheet reaches low latitudes and that deglaciation in this case can occur much faster than glaciation. This was the case for the two large ice sheets that existed during the Ice Age over America and Eurasia, and this had a strong impact on sea level. This explains the typical saw-tooth pattern of sea level rise and fall during a glacial period, with a slow drop followed by an abrupt rise (Fig. 24.3). On the other hand, the role of ice flow is not symmetrical between freezing and deglaciation. Although it helps the advance of the ice front as described, flow tends to thin the ice layer, so that its impact on the volume of ice is not uniform. In particular, it may happen that this flow 'runs away' and that the ice sheet then decreases abruptly (with the help of the altitude-temperature feedback), which can also lead to a rapid deglaciation phase.

Flow is a fundamental mechanism in the evolution of an ice sheet, and we explain below that it results from interaction between several processes which are themselves governed either by the major laws of physics or by laws (often empirical) describing the properties of the materials (ice of course but also the bedrock). We won't go into the detail of these equations which call upon continuum

mechanics, but we shall nevertheless indicate what these laws are, and what implications they have on the flow of the ice caps. In the following, we shall only deal with the case of ice assumed to be incompressible. This hypothesis does not hold true for snow, whose density increases from the surface down to a maximum depth of 100 m, but in most cases, the mechanical effect of this layer of snow and firn is the same as a layer of ice of the same weight would be, which amounts to removing about twenty meters from the total thickness of ice at the chosen spot (the thickness is of the order of a few kilometers).

If we consider the balance of forces applied to an ice particle, the only body force is gravity. The other forces are surface forces arising from contact with other ice particles, or with the base or water (when it is floating). The ice flows sufficiently slowly so that we can ignore accelerations and inertial forces (Coriolis), and the balance of forces applied to ice sheets is often referred to as a quasi-static equilibrium. In terms of mechanical behavior and at the scale of the strain rate occurring in ice sheets, ice is considered as a viscous fluid, i.e. the strain rate (deformation per unit of time, directly expressed as function of the spatial derivative of the velocities) is connected to the stress. Water, for example, is also a viscous fluid, but its viscosity (lower than that of ice) does not depend on the stress (nor on the strain rate). This is called linear viscosity (also known as Newtonian). Ice, on the other hand, is characterized by non-linear viscosity which decreases with stress according to a power law (with an exponent of approximately 2): the more the ice deforms, the easier it is to deform. This type of behavioral law is not exceptional, it is also found for lava, mud and even chocolate. As with most viscous materials (maintaining the analogy with chocolate), the viscosity of ice decreases as its temperature increases (in an exponential relationship). Depending on the location of the ice sheet, the temperature can vary from −50 °C at the surface to melting point at the base, and this can influence the viscosity by a factor of up to 500.

Combining the quasi-static equilibrium, the law of viscous behavior, incompressibility and the various boundary conditions, we arrive at a system of equations which rigorously takes into account the mechanical equations. This system (called ‘full stokes’) can be solved numerically, but the cost in terms of computation time is such that it is not conceivable at this time to apply this method to the entire ice sheet, especially when the aim is to also study its temporal evolution. This approach is therefore limited to localized research. Fortunately, an approximation exists which takes a ‘thin layer’ approach making it possible to treat the ice sheet overall. Indeed, a characteristic of ice sheets is their very small aspect ratio, i.e. the ratio of thickness to expanse. For Antarctica, for example, the thickness is around 3 km and the expanse is 3000 km (ratio of 1/1 000). If it were made into a scale model 3 m wide, it would only be 3 mm thick and would look like a thin sheet of ice. Capitalizing on this aspect ratio, two separate approximations have been proposed: one for the part of the ice sheet resting on land (Shallow Ice Approximation, SIA), the other for the floating part (Shallow Shelf Approximation, see later). These approximations are used in ice sheet models (Ritz 2001). Moreover, they allow a qualitative understanding of the interaction between the geometry of an ice sheet and its flow. For the resting part for example, the SIA shows that the velocity of the ice (averaged over its thickness) is proportional to the thickness to the power of four and to the slope of the surface to the power of three. Although the thickness shows little variation over the entire ice sheet, the slope varies from 10^{-3} in the central regions to nearly 10^{-2} at the edges, thus implying a speed 1000 times greater (the size of variation observed in reality). This also explains why the thickness of an ice sheets is strongly related to their expanse with the amount of snow accumulation being of only minor importance. When an ice sheet grows, its slope at the surface increases and its drainage increases greatly, creating a negative feedback which limits thickening. Another result of the SIA, used in the interpretation of ice cores, concerns the fact that most of the deformation is concentrated in the layers near the bottom, and that higher up, horizontal speed changes little with depth and in a first approximation, the thinning of the ice layers decreases linearly with depth.

The ice flows through deformation but its velocity at the interface with the bedrock (basal velocity) also contributes to the flow. Two processes intervene, the sliding over the bedrock and the deformation of the underlying sediment. Based on Antarctic observations, it appears that it is the latter mechanism which is the most effective, leading to speeds of several hundred meters per year. In both cases, the basal velocity is negligible as long as the temperature at the interface is below melting point. On the other hand, at the melting point, not only is sliding possible but water is produced. This brings about another mechanism, the higher the water pressure, the greater the basal velocity, due to both a lubrication effect (less friction) and the fact that the water-saturated sediment is easier to deform.

The temperature field in the ice thus affects the flow in at least three ways: through the viscosity, through the threshold (melting point) from which basal movement is possible and through the subglacial water pressure. The temperature in the ice can be estimated reasonably well by solving the heat equation and taking into account any changes in surface temperature over time. In general, temperature increases with depth. It is very cold at the surface. At around 10 m depth, where seasonal variations are mitigated, it has the value of the mean annual temperature. In Antarctica, for example, the temperature at 10 m varies from about −20 °C at the coast to −60 °C in the center. At the base of the ice, the temperature is often close to melting point because

geothermal energy (coming from the Earth) brings heat continuously to the base of the ice and the ice acts as an insulating material preventing this heat from escaping into the atmosphere. The thicker the ice, the higher the basal temperature. This temperature also depends on the amount of geothermal energy, which unfortunately is not well understood underneath the current ice sheets where it is difficult to measure directly. The variation in temperature with depth is not linear (this would be pure diffusion), because the flow transports cold from the top to the bottom and from upstream to downstream (advection). Moreover, the deformation of the ice produces heat (as it does with all materials). The same is true for the sliding on the bedrock and for the deformation of the sediment. Areas with rapid flow have a relatively warm base. If we ignore the phenomena related to flow (diffusive case), temperature would increase linearly with depth. Because of the flow, the ice is actually colder overall at the top and warmer at the base. Finally, if the base is at melting point, the additional heat is used for melting. It should be noted that the melting point drops with the ice pressure and therefore the depth. Below 3000 m of ice, the melting point is around −2.2 °C.

It can be seen that the temperature and velocity variables are connected by several terms. This interdependence is called 'thermomechanical coupling', and this coupling leads to a positive feedback which can have important effects on the evolution of the ice sheet. Suppose, for example, that an ice sheet is growing. Its basal temperature increases due to the insulating effect of the thickness of the ice, which reduces its viscosity and favors deformation. This produces heat which in turn increases the temperature. This positive feedback loop will quickly bring the base to the melting point where the water produced introduces a second feedback (the more water there is, the faster the basal velocity and the more heat is produced which in turn melts the ice). These feedbacks have been suggested as explanations for armadas of icebergs recorded as layers of ice rafted debris (IRD) in marine sediments during glacial periods (see Chap. 20). It is clear that this mechanism is involved in triggering a rapid flow. On the other hand, the most realistic numerical models have difficulties to simulate the return to a slow phase suggested by observations of rapid climate variability during glacial periods.

When the ice sheet ends with a marine edge, the ice streams enter the sea and form ice shelves. If the bay is sufficiently closed, these ice shelves limit the flow of the streams from which they originate or which flow into the same bay. This is called a buttressing effect. This effect occurs at all levels, from small bays of a few kilometers to large ice shelves such as the Ross and Ronne (see Fig. 24.2). The geometry and dynamics of ice streams are balanced by this buttress but if an ice shelf disintegrates (for example, through the effect of oceanic heat melting it from below), the drainage of all the tributary ice streams can be greatly increased. This phenomenon occurred a few years ago in the Antarctic Peninsula after the disintegration of the Larsen ice shelf. The question arises of how much it might have contributed to glacial variations in the past and whether or not it offers an alternative explanation to the IRD layers found in marine cores and which testify to the arrival of icebergs.

To mechanically model the floating part, we can use the shallow shelf approximation to determine a relationship between the extension rate (variations in speed along the length of the flow) and the thickness of the ice shelf (at a specific power determined by the authors). If the ice-shelf is not confined (if it does not encounter resistance from the coasts or an island), then its speed increases from the grounding line to the front where it can exceed one kilometer per year. Above all, this approximation makes it possible to demonstrate that the grounding line cannot be stable if the base is below sea level and with a reverse slope (if it goes upwards as one goes from the center to the edge of the ice sheet, Schoof 2007). This instability can be explained qualitatively as follows: if the ice flow at the grounding line increases strongly as the ice thickens, any retreat of the grounding line, caused, for example, by the disintegration of the corresponding ice shelf, will intensify drainage, leading to a further retreat of the grounding line. This result is particularly important because it indicates that some ice sheets are inherently unstable because the location of the grounding line determines the extent of the cap and its volume. This is especially the case for Western Antarctica, but also for some parts of East Antarctica. For ice sheets in previous ice ages, it is possible that this instability could have contributed to rapid deglaciation, a process which is not yet fully understood.

Finally, subglacial isostasy (see Fig. 24.4) is a mechanism which plays an important role because it modulates many of the others. For example, subsidence of the Earth's crust under the weight of the ice does not directly change its thickness but it alters the altitude of the surface allowing more intense melting since the surface is lower. Moreover, the slope of the surface is also decreased, which slows down the flow and tends to make the ice sheet larger. Since isostasy occurs with a lag, this also leads to highly non-linear effects. The position of the grounding line is another example of an element that is very sensitive to isostasy because it is defined by floating (on the marine side), and this is determined by the relative sea level, itself affected by isostasy.

Reconstruction of Sea Levels and Ice Sheets in the Past

Over the past several millions of years, the Earth has seen a succession of glacial periods during which huge ice sheets covered North America, Eurasia and many mountain ranges around the world (including the Alps). These long glacial periods were interspersed with interglacials, as is the case in the present day, when a warm climate prevailed, confining freezing to the polar regions and to the highest mountains.

These evolutions of the cryosphere have been studied since the nineteenth century, but a global understanding of these phenomena has only become possible in the past few decades, thanks to direct observation of the current ice sheets and to the discovery of the paleoclimatic information contained in numerous sedimentary deposits.

Data that Enable the Reconstruction of the Geography of Ancient Ice Sheets

Reconstruction of sea levels using the $^{18}O/^{16}O$ ratio of the ocean provides a representation of how the amount of ice evolved over time (Fig. 24.3), which acts as a good indicator of the overall volume of all of the ice sheets. However, to know where these ice sheets were located (America, Eurasia, etc.) and how far they extended, we must rely on geomorphological information which we shall briefly review. Figure 24.1 (Last Glacial Maximum in the northern hemisphere) and 2.2 (Antarctic) show the different regions mentioned.

The expanse and dynamics of ancient ice sheets can be estimated directly from the deposits and traces that they left behind on the ground. In general, pre-glacial bedrocks are preserved in areas where the base of the ice remained cold; while in regions where the base of the ice reached melting point (temperate base), the flow of ice and of basal water reshaped the bedrock. We can then distinguish between formations due to glacial erosion and those due to sediment deposition. Glacial erosion abrades (polishes) the rock outcrops and creates incisions (streaks caused by the scraping of transported debris). The drop in pressure downstream of the obstacles causes freezing of the basal water and the fracturing and plucking of rocks. This passage creates 'roches moutonnées' (or 'sheepback rocks'). On a larger scale, glacial erosion hollows out valleys into troughs (U-shaped), especially on coasts as fjords are formed. At sea, it is possible, using multi-frequency sonars, to observe underwater channels that have obviously been dug out by the flow of ice, highlighting the location of 'paleo ice streams' (Anderson et al. EPILOG 2002). Observations of this type have been detected around the Antarctic and the Arctic Ocean. All these marks indicate the direction and route of the ice flow locally. In some cases, a change in direction over time has been observed and this information makes it possible to infer variations in the geometry of the ice sheet, in particular the displacement of the domes.

The deposition of transported material leads to the formation of a wide variety of moraines. We note the frontal moraines which mark the maximum extent of each advance of a glacier. Ground moraines are not very thick (a few meters on average) and may be flat or irregular. Drumlins, often grouped in fields, are elongated ovoidal hills. All these deposits are structured by the flow of ice, and thus indicate its direction. During periods of retreat, a sub-glacial hydrological network is formed if the base is temperate. The deposits associated with these phases are formed when the materials transported are abandoned, e.g. eskers at the site of former sub-glacial canals. An esker occurs in the form of an elongated ridge sometimes over hundreds of meters in length. These ridges are formed by materials being deposited in the tunnels of the subglacial rivers located at the base of the glaciers. Their often winding shape follows that of the tunnels that created them. All these traces left behind on the ground have been observed and compiled since the nineteenth century. For about twenty years, satellites have helped to give a large scale view of these lineations. Traces sometimes indicate a multitude of contradictory directions that reflect changes in the flow of the ice over time. The traces must therefore be classified chronologically and then interpreted in large coherent sets. Based on this synthesis, it is possible to recreate the geometry of the caps at different times. A major difficulty arises from the fact that an advancing glacier moves the deposits of previous glaciers and, through erosion, can erase previous traces. Therefore, we can only reconstruct the glaciers from previous glaciations if their traces have not been erased, so only if another more extensive glaciation has not occurred since. This is the case for Fennoscandia, where the moraines of the penultimate glaciation (Saalien or MIS 6, ~180–140 ka BP) are still visible much further south than those of the Last Glacial Maximum (see Fig. 24.6). Another difficulty with formulating an overview comes from the dating of geomorphological traces. For recent periods, radiocarbon dating allows very precise estimates for the past 30,000 years approximately, although it is essential to use organic matter. Prior to this period, which only covers from the end of the last glaciation to the present, or when there is no organic material, other techniques are necessary. Optically stimulated luminescence (OSL) indicates how long a rock has been exposed to solar radiation and has been used, for example, to date quartz crystals in moraines throughout the last glaciation. More accurate datings have radically changed our notions of the history of Fennoscandia (Svendsen et al. 2004).

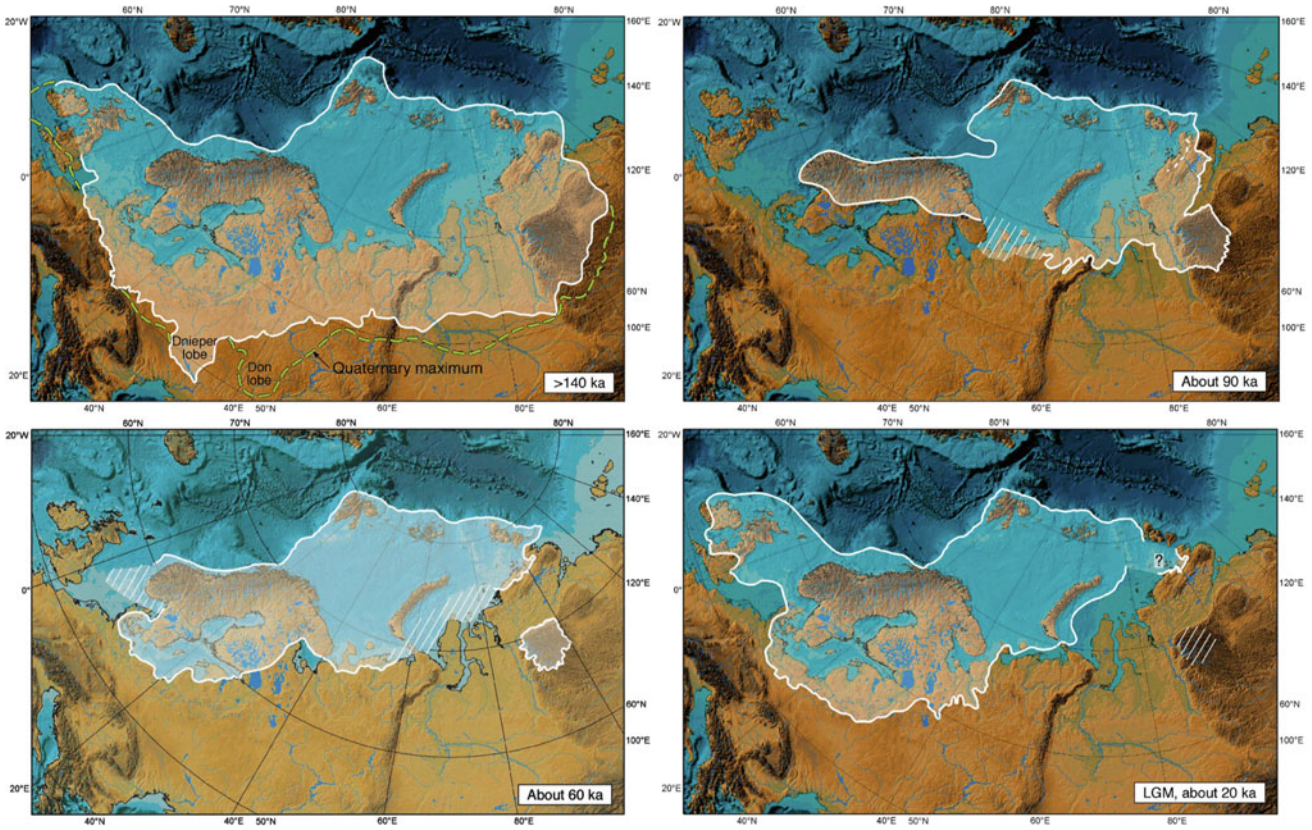

Fig. 24.6 The Eurasian ice sheet at various times in the past. Each map, centered on the Urals, represents the same region of northern Eurasia but at different times. The extent of the cap was determined from geomorphological data. During the Saalien (the penultimate glacial maximum, age >140 ka), the ice sheet extended particularly far towards the south reaching almost its maximum size during the Quaternary. The presence of lobes (the Dnieper during the Saalien and the Don for the maximum expansion) should be noted. These lobes may be the result of specific events called surges, during which the flow of glaciers or ice streams is particularly rapid. A tongue of ice then forms before disappearing, because its low altitude makes it prone to ablation. It can be seen that at the beginning of the Ice Age (90 ka), the ice sheet is prominent in the East but limited towards the West over Scandinavia. During the Last Glacial Maximum, the situation is reversed. Note that between each period represented here, there were periods when it was relatively clear of ice and snow, with the disappearance of the ice sheet located over the Sea of Barents and the separation into two sheets. Adapted from Svendsen et al. (2004)

The first major consolidated work to reconstruct the ice sheets at the end of the last glaciation was published by Denton and Hughes (1981). Their method of reconstruction involved the assumption that the profile of the ice sheets was parabolic (a hypothesis which is more or less valid for current ice sheets but which is based on the assumption of a stationary state) and the use of geomorphological data to constrain the extent. Since moraine dating was not as accurate at the time as it is now, in many areas it was assumed that the moraines were from the Last Glacial Maximum even though some had been formed during previous glaciations. Their reconstructions (even the 'minimal' one) are therefore considerably overestimated compared to the values acknowledged today. These reconstructions were also in contradiction with the global ice volume estimates from other sources (marine sediments, Mix and Ruddiman 1984).

Afterwards, understanding quickly evolved into a more dynamic view of ice sheets. For example, Boulton and Clark (1990) proposed a history of the Laurentide and in particular the migration and junction of the various domes (we will return to this in the section on the Laurentide). As for Fennoscandia, Lambeck et al. (2006) present its evolution throughout the last glaciation and Hughes et al. (2016) propose a chronology of the deglaciation. This type of overview often requires input from several groups of researchers and large-scale projects were established to estimate the extent and dynamics of ancient ice sheets (EPILOG 2002; QUEEN, Svendsen et al. 2004).

From the inversion of relative sea level data (RSL) and observations of the isostatic rebound which is still occurring, it is possible to estimate the ice load that produced these isostatic variations, and therefore the thickness of the ice sheets. This was the approach mainly used for the Last Glacial Maximum and for the last deglaciation (Peltier 2004; Clark et al. 2002; Lambeck et al. 2006).

Using all this information, it is possible to envisage a scenario representing the life of the ice sheets. This is the story outlined in the next section, with a focus on the last glacial-interglacial cycle for which there is more information available. It should be borne in mind, however, that although the main points are now well understood, there are still many regions and periods for which information is lacking.

The Last 50 Million Years

The Antarctic continent is located in the high latitudes since from the Late Cretaceous era (~240 Ma). However, it remained free of ice until the Eocene-Oligocene transition, 34 Ma ago (Chap. 6, Volume 2). Marine sediment recordings indicate an abrupt increase in benthic $\delta^{18}O$ at this date, suggesting that water depleted in ^{18}O was trapped in the form of ice. The appearance of the Antarctic ice sheet is attributed to the opening of an oceanic corridor between South America and the Antarctic Peninsula: the Drake Passage. The organization of the Antarctic circumpolar current would have led to the thermal isolation of Antarctica. However, more recently, based on modeling work, other authors believe that a reduction in CO_2 concentration was the cause of the cooling in Antarctica (De Conto and Pollard 2003).

In Chap. 6, a figure shows a new threshold around 15 Ma, to which the permanency of the East Antarctic ice sheet is attributed. There are indicators, however, that the ice may have retreated since 3 Ma, so that at 3 Ma the ice sheet could have been thicker than during the Last Glacial Maximum.

As for the northern hemisphere, scientists estimate that the first freeze-ups occurred 7 Ma ago on southern Greenland. Amplification of these glaciations then took place ~3 Ma ago. Several hypotheses have been proposed to explain this amplification: (i) the closure of the Panama Strait occurred at this time and modified the oceanic circulation, causing warm water to travel up to the high latitudes of the North Atlantic, providing a considerable source of water vapor and therefore precipitation; (ii) the reduction in CO_2 concentration leading to cooling; (iii) an uplift of the Rocky Mountains modifying the planetary waves. Ice appeared between 2.75 and 2.55 Ma in Eurasia, then in Alaska and Canada, as evidenced by debris transported by icebergs which then appeared in North Atlantic sediments (Shackleton et al. 1984).

The Last Three Million Years

For the past three million years, the Earth's climate has oscillated between glacial and interglacial periods and most of the variations are due to the formation and subsequent melting of ice sheets in the northern hemisphere. In Antarctica they only fluctuated, with significant variations in Western Antarctica and in the peninsula (Anderson et al., EPILOG 2002; Ritz et al. 2001).

Until ~1 Ma ago, the variations in the extent and volume of the ice sheets remained moderate, with variations of 60 m in sea level. The oscillations subsequently slowed down and gained amplitude. About 900 ka ago, the dominant periodicity of glaciations went from 40,000 to 100,000 years and the amplitude of the oscillations doubled, with variations of more than 100 m in the sea level. This event is known as the Mid-Pleistocene Revolution (MPR) (Raymo et al. 2006).

The freezing-up of the northern hemisphere has varied greatly over time: not all glaciations are alike, nor are all interglacials. The recent maximum expansion of the continental ice sheets is fairly well documented. However, many questions remain, in particular on the marine sides of the ice sheets. Below. we highlight some irregularities that are of interest.

The ice shelves in the Arctic Ocean

The Lomonosov Ridge is an underwater mountain range located at a depth of 1000 m. It stretches across the Arctic Ocean from Greenland to Siberia through the North Pole. Several striations aligned at the top of this ridge suggest the possibility of a gigantic ice-shelf that might have covered the center of the Arctic Ocean. These undated striations are unlikely to have been caused by icebergs which leave more random marks. They are also corroborated by marks in other parts of the Arctic Ocean (Jakobsson et al. 2008).

The Stage 11 Interglacial

During the Marine Isotope Stage 11, 400,000 years ago, the Earth experienced a long interglacial. Estimates (currently under discussion) of sea level vary between 20 m above and 8 m below the current level. If the high value is correct, it

would require not only a massive deglaciation of Greenland and Western Antarctica but also a moderate loss of ice in East Antarctica. Because the orbital parameters were close to those of today, this interglacial is often considered to be one of the best analogues of the present time.

Stage 6: Saale glaciation

The penultimate ice age, called Saale glaciation in Eurasia, reached its maximum about 140,000 years ago. The Eurasian ice sheet covered a large part of Eastern Europe, Russia and Siberia, practically equivalent to the maximum expansion during the Quaternary in these regions (Svendsen et al. 2004). The cooling causing the development of this cap must have been much greater than during the LGM. Its expansion towards the south is particularly impressive because one of its lobes (the Diepner lobe, probably a transitory phenomenon) came within 500 km of the Black Sea. It appears in the southeast, that signs of maximum extension are found even further south than for the Saale glaciation, but it is difficult to know if these correspond to the same ice sheet and what its age might be (see Fig. 24.6).

Scenario of the Last Glacial-Interglacial Cycle

The temporal pattern of the last glacial-interglacial cycle is shown in Fig. 24.3. The external forcing associated with variations in the Earth's orbit is represented by the evolution of summer insolation at 65 °N latitude. The sea level indicates the overall volume of ice.

It is clear that the volume of ice reacts systematically to variations in summer insolation. As it is mainly the summer climate that is responsible for the ablation, an orbital configuration with strong summer insolation is unfavorable to the ice sheets. In addition, the slow freeze-ups and the rapid deglaciations are not symmetrical. The volume over the whole cycle is a sawtooth trend because the retreats are not complete and each advance (around 120, 90, 80, 60 and 40 ka BP) resumes from a still glaciated situation, even more so as the Ice Age progresses.

However, the geographical distribution reveals great diversity (the geographical aspects are summarized in Fig. 24.6 for Fennoscandia and 2.7 for Laurentide).

During the Eemian (125 ka BP), the eustatic sea level was up to 6 m higher than currently, testifying to a strong retreat of the ice. The southern part of Greenland and Western Antarctica were probably much less ice-covered than they are at present. However, ice core drilling indicates that there was an ice cap in the central part of Greenland at an altitude comparable to the current altitude (NGRIP Members 2004).

The Laurentide Ice Sheet

The Laurentide ice sheet over North America was the first to form, with ice appearing on the heights in the form of two separate caps, one over Keewatin (itself derived from the junction of the Keewatin and Baffin caps) and the other on Labrador (Fig. 24.7). Throughout the ice age, it underwent fluctuations, with the two caps joining during the colder periods followed by growth (both in volume and area) of the resulting ice sheet, generally with two distinct domes.

Conversely, during interstadials (warmer intervals during the glaciation) it shrank and in some cases separated into two (or even three) ice sheets. Another ice cap also developed on the Rocky Mountains, the Cordilleran ice sheet, but it took at least 60 ka BP before there was a junction between the Laurentide sheet and the still undeveloped Cordilleran sheet. The Cordilleran ice sheet only became heavily glaciated at a late stage (after 30 ka BP). This phenomenon was attributed to the influence of the Laurentide on atmospheric circulation. The Laurentide needed to be high enough to affect the jet stream, which had the effect of increasing the transport of moisture to the Cordillera.

It should be noted that despite fluctuations, a significant amount of ice persisted over North America throughout the ice age.

During the Last Glacial Maximum (21 ka BP), the area covered is shown in Fig. 24.1. During the deglaciation, the retreat of the Laurentide accelerated from 15 ka BP. A proglacial lake (Lake Agassiz) was formed south of the ice sheet. It emptied around 8200 years by breaking its ice dam and rapidly injected a large quantity of fresh water into the North Atlantic, with repercussions on the thermohaline circulation. The deglaciation in North America continued up to 6 ka BP.

The Fennoscandian Ice Sheet

Ice appeared later on Eurasia and initially in a limited way on the Arctic archipelagos (Svalbard, François Joseph) and on the mountains of Scandinavia. It was only towards 90 ka BP that a major glaciation appeared in Western Siberia. Then, during each cold period a large sheet developed with a junction between the Svalbard archipelago, northern Scandinavia and New Zemble (Barents and Kara seas). During each interstadial, the Barents and Kara seas were free of ice and often ice only remained in arctic archipelagos and on high points in Scandinavia (Svendsen et al. 2004). This behavior, which suggests a strong sensitivity to the climate, can be explained by several positive feedbacks:

- the terrestrial part (lying on a bedrock above sea level) was more limited in area and thickness than the Laurentide. As a result, it is more subject to the

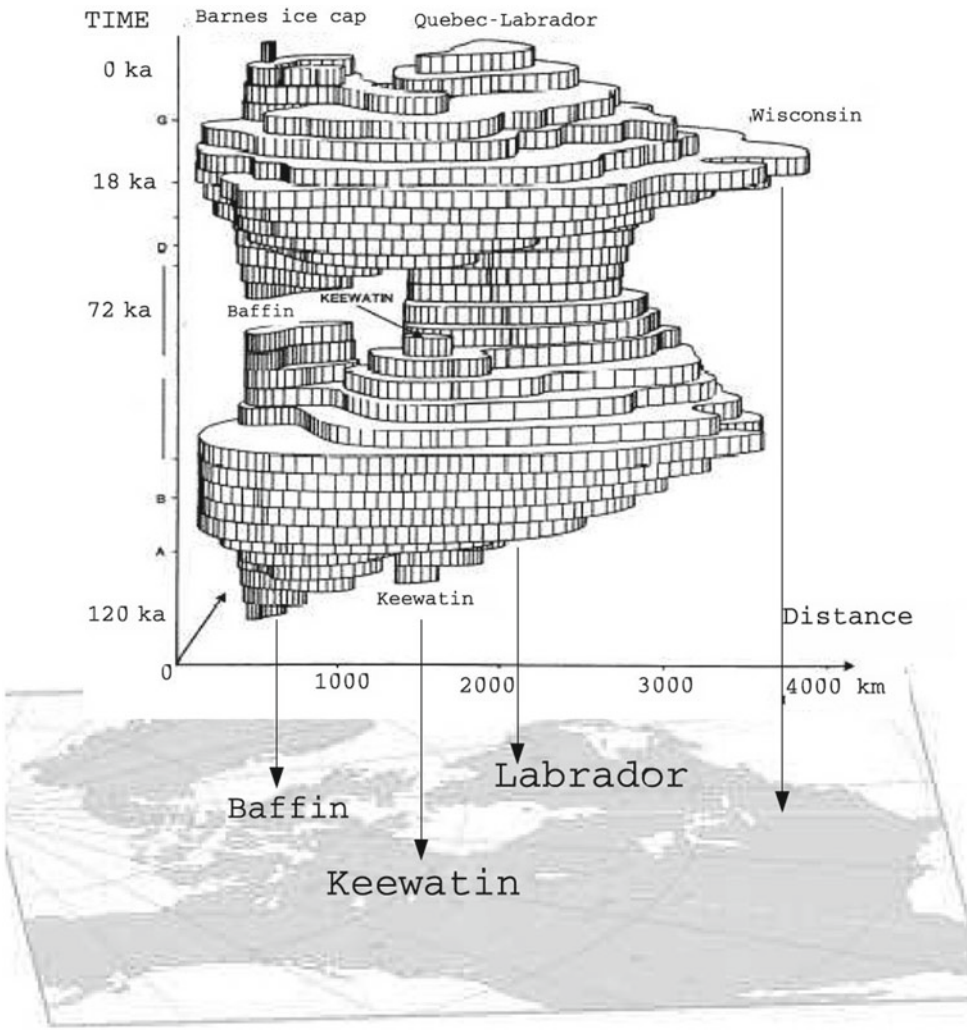

Fig. 24.7 Reconstruction of the Laurentide ice sheet during the glaciation. In general, there were three glacial centers: the first icecap developed on the Arctic archipelago (Baffin), followed quickly by another on Keewatin, and then these two caps grew together (then generally called the 'Keewatin cap'). At the same time, another cap developed on Labrador. Around 106 ka BP, the Labrador and Keewatin ice sheets were still independent, separated by the Hudson Bay. Later, they met to form a single mass of ice with two domes (Labrador and Keewatin/Baffin). This ice sheet again broke up into several small ones around 85–74 ka BP before finally reforming and growing until the LGM. Image adapted from Boulton and Clark (1990). According to Peyaud (2006)

altitude-surface temperature feedback. This instability is often referred to as the 'instability of small ice sheets';
– the Barents and Kara caps are ocean ice sheets whose base is below sea level (as is the case for West Antarctica) and this makes them sensitive to the instability of the marine ice sheets, which is linked to the dynamics of the ice flow. In addition, these ice sheets formed a glacial barrier which retained huge lakes. These lakes tempered the Siberian summers and reduced the melting of the glacial ice sheets, another positive feedback, but occurring during the cold period unlike the previous two.

Another interesting point concerns the location of the ice sheet during the glacial period. During the LGM, the Fennoscandian ice sheet was similar in size as it was at 90 ka BP, but located further to the west. This phenomenon is not explained but an interaction between the topography of the ice sheets and atmospheric circulation is suspected. For example, at the end of glaciation, the presence of the Scandinavian sheet prevented the transport of moisture towards the east.

The Fennoscandian ice sheet appears to have reached its maximum extent to the south between 20 and 18 ka BP. The deglaciation of the continental shelf began around 15 ka BP and from 13 ka BP onwards the ice retreated northward to the archipelagoes of the Arctic, while in the south, the Scandinavian cap receded to the Gulf of Bothnia and the Finnish border. After 10,000 years BP, the ice was confined to the Norwegian mountains and at the climate optimum of the Holocene, the ice cover was probably smaller than at present.

Antarctica

There is much less information available on the evolution of the Antarctic ice sheet partly because of the harsh conditions (logistics, climate), partly because the variations were smaller and partly because most traces of the Last Glacial Maximum are to be found at sea. Information comes from

ice core drilling (mostly located on the Antarctic plateau (see Chap. 10, Volume 1), marine drilling at the edges, multi-beam sonar data at sea and marks of glaciations on the rocks and mountains beyond the current cap (trimlines or the limit between the glacial erosion model and the model of erosion by atmospheric processes). Digital modeling of the ice cores helps to connect the various data to explain the mechanisms involved.

For the past 3 million years, Antarctica has oscillated between two (or even three) states, with the East Antarctic and West Antarctic ice sheets behaving differently (oppositely in terms of volume). Four processes govern this evolution: (i) the surface temperature has little immediate influence. Indeed, since the maximum temperature on the coasts is about −10 °C, ablation is not a significant mechanism except on ice shelves. In the long term, climate temperature variations propagate through the ice and eventually reach the base of the glacier, where deformation and sliding are concentrated. The flow is then intensified but it takes about ten thousand years before this process is felt; (ii) precipitation has an immediate effect: the more it snows, the more the ice sheet grows. In general, precipitation is deemed to be related to atmospheric temperature. Therefore, it snows more during warmer periods because the air can then hold more moisture and this is borne out (at least on the Antarctic plateau) by ice core analysis; (iii) flow brings the ice towards the coast, is sensitive to basal conditions and to the thermomechanical coupling mentioned above, but the main feature of Antarctica is the presence of ice shelves that act as a buttress limiting the speed of the ice streams. If these ice shelves disappear, the upstream glaciers will accelerate leading to thinning of the ice sheet; (iv) the movements of the grounding line govern the size of the ice sheet, and the larger the sheet, the thicker it becomes. The grounding line is sensitive to sea level (if this lowers, ice shelves are able to ground) by a purely geometric effect. In addition, the flow of ice streams and the shift in the grounding line are linked, as a retreat occurs in association with an acceleration. For example, a disintegration of the ice shelves through an acceleration of the flow may force a retreat of the grounding line. Conversely, a retreat of the grounding line reduces the basal friction of the ice stream (because it begins to float) and allows it to accelerate. It should be noted that the precipitation effect acts in opposition to the others and tends to produce a smaller ice sheet during the glacial period.

In the interglacial period, conditions are roughly similar to the current ones. Compared with the present, the glacial period has lower temperatures, less precipitation, a lower sea level, and a colder ocean which help to maintain the ice shelves. The grounding line then advances, now limited only by the continental slope as shown by the grounding line map proposed by Bentley et al. (RAISED 2014) (Fig. 24.8). It is the amplitude of the variation in the grounding line that makes the difference between the East and West ice sheets.

Recent modeling results (Pollard and DeConto 2009) indicate that a third state, even more free of ice than the current one, may occur during particularly long and warm interglacials. In this third state, West Antarctica virtually disappeared and this could explain the high sea level at some times in the past (Eemien, MIS11).

Around East Antarctica, the continental slope is located a few tens of kilometers from the current coast (see Fig. 24.8).

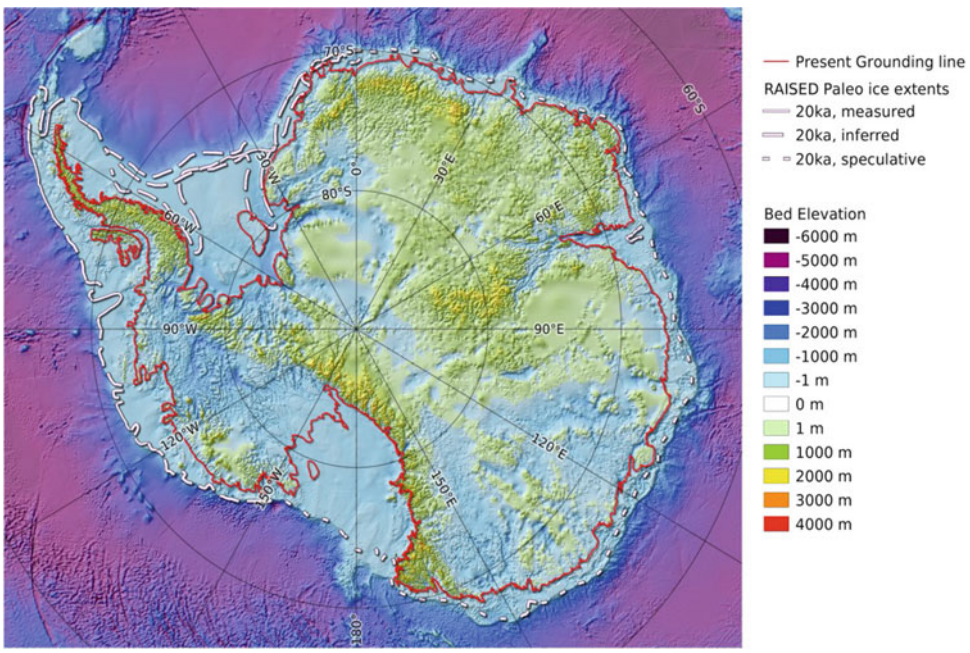

Fig. 24.8 Position of the grounding line in Antarctica. Current (red line) and during the last glacial (white lines). Note that during the glacial period this line is located near the continental slope and that the ice sheet has spread over most of the continental shelf (in light blue). Figure Quantarctica map, from Bentley et al. RAISED (2014)

This is the only margin of advance of the sheet. During glaciation, the East Antarctic ice sheet is therefore slightly thicker at the edges but this effect (confirmed by glaciation tracks on the mountains) remains confined to the edges. The central regions are thinner due to lower accumulation. It is estimated that the Antarctic shelf was about 100 m lower during the Last Glacial Maximum (Ritz et al. 2001). As for volume, the impact of the central regions is stronger and overall the volume of East Antarctica is less in glacial period than in interglacial.

West Antarctica has much more room to spread out (Fig. 24.8). Indeed, the two large embayments in which the ice shelves of Ross and Ronne-Filchner are located are shallow.

During glacial periods, these ice-shelves are grounded, advancing the grounding line by about one thousand kilometers. Here the effect of the grounding line far outweighs that of precipitation. This is why West Antarctica is more voluminous during glacial periods. However, there is still much debate about the exact volume. Estimates for the total contribution of the Antarctic to sea-level between the glacial maximum and now range from 7 m to over 20 m (sea level equivalent). These extremes correspond to two possible scenarios in West Antarctica during glaciation. For the same grounding line position, it is possible to have relatively stagnant ice streams and a very thick ice sheet at the edges, similar to the edges of East Antarctica currently. However, it could be that regions where there are ice shelves currently were very active, formed from huge ice streams comparable to the Sipple Coast in West Antarctica. These regions must have been relatively flat, which had repercussions as far as the center of West Antarctica. The first hypothesis was long supported by the trimlines which indicated altitudes at least 1000 m above the current level, but recent datings of these trimlines have in many places indicated that they are more than one million years old and therefore do not concern the Last Glacial Maximum (Bentley et al. 2010). Alternatively, the second hypothesis is supported by the ice core analysis from the Sipple Dome (the Ross ice-shelf slope) and Berkner Island (middle of the Ronne-Filchner ice-shelf).

For the time being, numerical modeling is the only tool to evaluate the evolution of Antarctic geometry during the recent glacial-interglacial cycles. Only a few polar cap models have tackled this problem because simulation of the movements of the grounding line remains a major difficulty. It should be noted that the mechanisms presented (which are included in the models) accurately reproduce the evolutions described above, that not all interglacials were similar (some were less frozen, like stage 11 or Eemian, others were intermediate between glacial and interglacial periods) and that the freezing-up process is slow, the volume increasing progressively throughout the glacial period. As for the last deglaciation, it appears to have occurred late (15 ka BP), but its speed depends on the model used (Huybrechts EPILOG 2002; Ritz et al. 2001), as well as on the volume of Antarctica ice during the glacial period. The speed of deglaciation depends on the model, but all agree that it has only just finished, which is in accordance with observations showing that the retreat of the grounding line in the Ross Sea continued until 3000 years BP (Conway et al. 1999).

Greenland

In terms of process, Greenland is an intermediate ice sheet. During the glacial periods, ablation was negligible there and its expanse was limited by the movement of the grounding line, in other words, it was limited by the continental slope. During interglacials, ablation plays an important role, as evidenced by the fact that its current edge is mostly terrestrial (there can be no coastline without ablation). This makes Greenland sensitive to warming climates and explains why it is assumed that this cap was significantly smaller during the Eemian. In terms of shape, Greenland changed from domed during interglacial (high and narrow) to flat and expanded during glacial periods.

Conclusions

The climate system is complex and the long-term component which includes sea level and the evolution of the polar ice sheets is no exception to this rule. In this chapter, we have seen that the mechanisms involved can be internal to the ice sheets such as thermomechanical coupling and feedbacks related to subglacial hydrology. However, most of the processes are related to interactions with other elements of the system:

- the atmosphere, due to the altitude-surface temperature link which causes the instability of small ice sheets. The influence of the ice sheets on the general circulation is also noted and we have seen that it could explain the interactions between the ice sheets;
- the ocean, since the ice sheets determine sea level, but also the oceanic general circulation. In the other direction, the movement of the grounding line, which is the key process of the Antarctic evolution, results from interaction between glacial dynamics and the local ocean;
- the solid Earth, through the mechanism of isostasy.

The data available for the past, in terms of sea level or through glacio-geomorphology reconstructions, indicate that all the mechanisms mentioned above are indeed active.

Moreover, numerical modeling makes it possible to simulate most of the recorded evolutions. However, the speed and amplitude of certain events remain hard to explain:

- During the deglaciation, there were periods of very rapid rise in sea level, of around 5 cm per year, for several centuries. This occurred in particular around 14,200 ka BP with an event called 'melt water pulse 1 A', the cause of which (Laurentide or Antarctica) is still controversial.
- The Heinrich events during which armadas of icebergs invaded the North Atlantic. Purely glacial mechanisms (thermo-mechanical coupling) have been suggested but this is difficult to reproduce correctly by the 3D ice sheet models. An interaction with the ocean that would melt an ice shelf at the mouth of the Hudson Strait has recently been suggested and would allow a better agreement with the ocean recordings than the previous hypothesis.

These two examples show that glacial dynamics may have played a more important role than was previously assumed, especially when the ice sheets are subjected to climate forcings (ocean or atmosphere), a hypothesis which is supported by the current observations of acceleration of outlet glaciers (in Greenland and Antarctica. For this reason, research in this area of glacial dynamics is being actively pursued in order to better assess the future behavior of the two remaining ice sheets, Greenland and Antarctica, in the context of climate change.

References

Bentley, M. J., Fogwill, C. J., Le Brocq, A. M., Hubbard, A. L., Sugden, D. E., Dunai, T. J., et al. (2010). Deglacial history of the West Antarctic ice sheet in the Weddell Sea embayment: Constraints on past ice volume change. *Geology, 38,* 411–414.

The RAISED Consortium, Bentley, M. J., et al. (2014). A community-based geological reconstruction of Antarctic ice sheet deglaciation since the Last Glacial Maximum. *Quaternary Science Reviews, 100*, 1–9.

Boulton, G. S., & Clark, C. D. (1990). A highly mobile Laurentide ice sheet revealed by satellite images of glacial lineations. *Nature, 346,* 813–817.

Clark, P. U., Mitrovica, J. X., Milne, G. A., & Tamisiea, M. E. (2002). Sea-level fingerprinting as a direct test for the source of global meltwater pulse I. *Science, 295,* 438–441.

Conway, H., Hall, B. L., Denton, G. H., Gades, A. M., & Waddington, E. D. (1999). Past and future grounding-line retreat of the West Antarctic ice sheet. *Science, 286,* 280–283.

De Conto, R. M., & Pollard, D. (2003). Rapid Cenozoic glaciation of Antarctica induced by a declining atmospheric CO_2. *Nature, 421,* 245–249.

Denton, G. H., & Hughes, T. J. (1981). *The last great ice sheets*. Wiley.

EPILOG. (2002). *Quaternary Science Reviews,* volume 21 (tous les articles dont Anderson, J. B. et al., pp. 49–70, Huybrechts, P., pp. 203–231, Lambeck, K. et al., pp. 343–360, Waelbroeck, C. et al., pp. 295–305).

Hughes, A. L. C., Gyllencreutz, R., Lohne, S., Mangerud, J., & Svendsen, J. I. (2016). The last Eurasian ice sheets—A chronological database and time-slice reconstruction, DATED-1. *Boreas, 45,* 1–45. https://doi.org/10.1111/bor.12142.

Jakobsson, M., Polyak, L., Edwards, M., Kleman, J., & Coakley, B. (2008). Glacial geomorphology of the Central Arctic Ocean: The chukchi borderland and the Lomorosov Ridge. *Earth Surface Processes and Landforms, 33,* 526–545.

Lambeck, K., & Chappell, J. (2001). Sea level change through the last glacial cycle. *Science, 292,* 679–686.

Lambeck, K., Purcell, A., Funder, S., Kjaer, K. H., Larsen, E., & Möller, P. (2006). Constraints on the Late Saalian to early Middle Weichselian ice sheet of Eurasia from field data and rebound modelling, *Boreas*, 35. https://doi.org/10.1080/03009480600781875.

Mix, A. C., & Ruddiman, W. F. (1984). Oxygen-Isotope Analyses and Pleistocene Ice Volume. *Quaternary Research, 21,* 1–20.

NGRIP Members. (2004). High resolution record of Northern Hemisphere climate extending into last interglacial period. *Nature, 431,* 147–151.

Pollard, P., & DeConto, R. M. (2009). Modelling West Antarctic ice sheet growth and collapse through the past five million years. *Nature, 458,* 329–332. https://doi.org/10.1038/nature07809.

Raymo, M. E., Lisiecki, L. E., & Nisancioglu, K. H. (2006). Plio-Pleistocene ice volume, Antarctic climate, and the global delta ^{18}O record. *Science, 313*(786), 492–495. https://doi.org/10.1126/science.1123296.

Peltier, W. (2004). Global glacial isostasy and the surface of the ice-age Earth: The ICE-5G(VM2) model and GRAC. *Annual Review of Earth and Planetary Sciences, 32,* 111–149.

Peyaud, V. (2006). *Rôle de la dynamique des calottes glaciaires dans les grands changements climatiques des périodes glaciaires-interglaciaires*. Thèse de doctorat, université Joseph Fourier, Grenoble 1.

Ritz, C., Rommeleare, V., & Dumas, C. (2001). Modeling the evolution of Antarctic ice sheet over the last 420,000 years: Implications for altitude changes in the Vostok Region. *Journal of Geophysical Research, 106*, 31, 943–31, 964.

Schoof, C. (2007). Ice sheet grounding line dynamics: Steady states, stability, and hysteresis. *Journal of Geophysical Research, 112*, F03S28, https://doi.org/10.1029/2006jf000664.

Schrag, D. P., Hampt, G., & Murray, D. W. (1996). Pore fluid constraints on the temperature and oxygen isotopic composition of the glacial ocean. *Science, 272*, 1930–1932.

Siddall, M., Rohling, E. J., Almogi-Labin, A., Hemleben, C., Meischner, D., Schmelzer, I., et al. (2003). Sea-level fluctuations during the last glacial cycle. *Nature, 423,* 853–858.

Shackleton, N. J., et al. (1984). Oxygen isotope calibration of the onset of ice-rafting and history of glaciation in the North Atlantic Region. *Nature, 307,* 620–623.

Svendsen, J. I., et al. (2004). Late quaternary ice sheet history of Northern Eurasia. *Quaternary Science Reviews, 23,* 1229–1271.

Modeling and Paleoclimatology

25

Masa Kageyama and Didier Paillard

Why Develop Paleoclimate Models?

Today, climate models are widely discussed because of the climate predictions they produce for the next century (see Chap. 31), particularly when the IPCC (Intergovernmental Panel on Climate Change) assessment reports are published. The models used for climate prediction are developed first and foremost based on the data from observations of recent decades. Before being applied to forecasting, these models are evaluated to assess their ability to reproduce the present climate and its recent variations over the last decades. They represent our understanding of the current climate and of the mechanisms that play important roles in recent variations, but also our ability to translate this understanding into digital codes which is necessarily limited by computing capabilities. Thus, even though the most powerful computers are currently used to produce simulations with the most complex climate models, they are limited by computing power in terms of resolution and system complexity. We will return later to this crucial question of finding the best compromise between the desired timespan for a climate simulation and the complexity of the climate model used, a question that is even more critical in paleoclimatology, where the time scales are much longer than for the IPCC predictions (which last a few centuries at most).

It is easy to understand why models are used for the forecasting of future climates: this approach, based on our understanding of the physics of the climate system, provides the only means of obtaining these forecasts. But modeling can also contribute a lot to our understanding of current and past climates which are characterized through observations and reconstructions. A first justification is the evaluation of the models used for future forecasts. During the development phase of a model, the first step in evaluation is to compare it to the available observations for the current climate and its short-term variability over time scales ranging from a few years to a few decades. In recent decades, anthropogenic disruption has created previously unknown levels of atmospheric greenhouse gas concentrations, so models need to be tested in climate configurations different to the current climate. There is no perfect paleoclimate equivalent for the forcing of anthropogenic disturbance, but paleoclimates, even if they are not recorded with the same precision as the present climate, offer examples of climates very different from the current one and of transitions of varying rapidity between states. If we have correctly understood the climate system and if we want to use this understanding to predict climate in the future, we must be able to reproduce the variations in past climates.

An example of an evaluation based on paleoclimates is one dealing with entry into the last glacial period, also called last glacial inception. This occurred about 115,000 years ago, and the major cause of this disturbance, external to the climate system, is the difference in insolation received by the Earth. In principle, a climate model, even if it does not include an ice sheet model, should be able to simulate perennial snow cover at the formation sites of the first ice caps located north of present-day Canada. Following various trials, it was found that very few atmospheric general circulation models were capable of simulating this perennial cover. Furthermore, those that did manage to do so were often ones that simulated a current climate that was much colder than observations. These trials were therefore far from satisfactory. However, as components (ocean, vegetation) were added one by one to the climate models, it was found that these components could play an important role in amplifying the initial insolation signal. Thus, over a longer period, the disappearance of forests or the appearance of sea ice, initiated by changes in insolation, support the development of perennial snow cover by modifying the albedo. It can therefore be concluded that it would be difficult to

M. Kageyama (✉) · D. Paillard
Laboratoire des Sciences du Climat et de l'Environnement, LSCE/IPSL, CEA-CNRS-UVSQ, Université Paris-Saclay, 91190 Gif-Sur-Yvette, France
e-mail: masa.kageyama@lsce.ipsl.fr

G. Ramstein et al. (eds.), *Paleoclimatology*, Frontiers in Earth Sciences,
https://doi.org/10.1007/978-3-030-24982-3_25

simulate permanent snow cover using only a simple atmospheric model because of the absence of positive feedback mechanisms. It can be seen here that while a simple evaluation can lead to a better understanding of the system, it is also only the start of an extensive exploration of increasingly complex models to find the one that best fits with the data.

Paleoclimate simulation is not only used to evaluate the models used for climate predictions over the next century. This would be an extremely narrow application, especially given the time scales that can be handled by these models. The starting point for the development of paleoclimate modeling is the assumptions applied when interpreting the data. A paleoclimate model seeks to formalize the assumptions based on the physical principles of the climate system and to test whether these principles can explain the observed climate variations. It is clear then that the models can be extremely varied depending on the data they are trying to interpret. Indeed, even though the components of the climate system are all interdependent, which is a defining feature of this system, it is not always necessary to represent them all in detail in order to reproduce an observed phenomenon. In fact, it is more interesting to isolate the processes or key components responsible for a phenomenon. This is one of the approaches to paleoclimate modeling which tries to build a 'minimal' model to explain a phenomenon. This is very different from the models used to predict the climate of the next century, but these approaches are important to provide a better understanding of the climate system and its evolution.

Modeling can also highlight the importance of a particular forcing or process. By comparing experiments which include a certain process or forcing with experiments which exclude it, it is possible to study its impact and identify which mechanisms explain this impact. These 'sensitivity experiments' are not necessarily very realistic but they complement the more realistic simulations of paleoclimates, by helping to better understand them. One example, in Section "General Circulation Models, Complex Models of the Earth System", an attempt is made to understand the impact of ice caps versus the impact of a lower atmospheric CO_2 concentration on the climate of the Last Glacial Maximum (LGM). In order to understand this, simulations are created where the ice caps of the LGM are placed in the context of the current CO_2 concentration, and also where the CO_2 concentration of the LGM is positioned with the current ice caps. Although these simulations do not correspond to real situations, they provide a better understanding of the simulated glacial climate by imposing both ice cap and CO_2 concentration forcings from the LGM.

This chapter starts by presenting the basic concepts of modeling, definitions essential to our understanding of models and the digital experiments used in climatology and paleoclimatology. We then focus on the three main families of paleoclimate models: the most complex general circulation models, climate models of intermediate complexity, and conceptual models. For each of these families of models, we give examples of their use in paleoclimatology.

Some Basic Modeling Concepts

Vocabulary

Before showing how climate modeling contributes to the study of past climates, it is useful to define the concept of a model. Indeed, this word has quite different meanings in the various scientific disciplines. In general, a 'model' is a representation of a set of scientific ideas, formulated within as rigorous a framework as possible, which explains a complete set of phenomena. The model is judged to be even more effective when it is simple and concise, and when it offers a maximum number of solutions. It becomes quantitative when it is based on mathematical relationships. When we talk about climate modeling, we mean 'physical' models of the climate system incorporating a set of mathematical equations that trace the evolution of the system from a starting position within boundary conditions. It is therefore a system of first-order differential equations, which can generally be written in the following form:

$$\frac{dX(t)}{dt} = f(X(t), t) \tag{25.1}$$

where $X(t)$ is a vector dimension N which provides an overall description of the state of the model at each instant t, and $f(X, t)$ is a function of X and of time t which describes the evolution of the system. The dimension N of the vector $X(t)$ thus represents the 'size' of the model, which is sometimes called the 'number of degrees of freedom' of the system, and the space of dimension N of all the vectors X is called 'the phase space'. If the state of the system is known at a given instant t_0, denoted by $X_0 = X(t_0)$ and called the 'initial condition', then Eq. (25.1) makes it possible to know the state of the system at all times.

When referring to a climate model, we may imagine a very 'complex' system, with a large number of degrees of freedom. This is often the case, but not always. Indeed, it is important to highlight two contradictory aspects of climate modeling. On the one hand, modeling aims to improve our understanding of how the system functions, and on the other hand, it is trying to provide the best possible representation of it. In order to explore and understand what is happening within a system of equations, it is preferable that the number of degrees of freedom N be small. Conversely, to achieve a good representation of a system as complex as the climate, the number of degrees of freedom N needs to be large and will be limited only by computing power. Although both of these qualify as modeling, the second case is more

accurately referred to as 'climate simulation' where the primary objective is to achieve a maximum of realism, at the expense of an in-depth understanding of how the system operates. In the most sophisticated climate models, there are several million degrees of freedom thus making it difficult to understand and analyze the detail of the sequence of processes involved in the simulations carried out by these models. A typical strategy is therefore to multiply the number of simulations, as described later, by carrying out sensitivity experiments. Conversely, much simpler models, which may produce less realistic results, can provide insight into the root causes of certain mechanisms that underlie the phenomena being represented. If the aim of modeling is summarized in the maxim 'understand so as to better simulate', it is obvious that a whole spectrum of models of varying complexities is necessary in order to tackle the different aspects of a problem.

Before further describing climate modeling in general and the problems encountered in paleoclimatology in particular, we will revisit Eq. (25.1) in more detail in order to explain some concepts that are widely used either implicitly or explicitly. The vector $X(t)$ which describes the whole system is also called the **prognostic variable set** of the model. This refers to all quantities $X_i(t)$ in the system (25.1) possessing an equation of evolution. Moreover, it is often useful to include additional variables to represent the physical quantities used in the equations, quantities which depend directly on the prognostic variables $X_i(t)$ without recourse to an associated evolution equation. For example, the quantity $y(t) = X_1(t) + X_2(t)$ is deduced from the quantities $X_i(t)$ and so the evolution equation for the derivative $dy(t)/dt$ is redundant in the system of Eq. (25.1). These additional variables are called the **diagnostic variables** of the model, because they are mainly used to provide a better understanding of the model in terms of the customary physical values. Thus, typically, in an atmospheric circulation model, the only prognostic variables at each point of the grid of the model are temperature, humidity, and wind velocity on the horizontal plane, with evolution equations representing the conservation of energy and water (transport equations) and the conservation of momentum (i.e. the Navier-Stokes equation) on the horizontal plane. All other values (vertical velocities, energy fluxes, precipitation, clouds etc.) are deduced more or less directly. These are merely diagnostic or secondary variables, but they are nevertheless very useful at all the stages of modeling, from the design of the model to the analysis of the results. These diagnostic variables, often more numerous than the prognostic variables, do not mean additional degrees of freedom.

Moreover, the notation of the system of Eq. (25.1) always involves values which are established at the outset, deeming these to be either physical values external to the model under consideration, or more or less well defined constants. These values are the **model parameters**. When these parameters are spatialized, i.e., dependent on their geographical location, they are then considered to be **boundary conditions**. When the parameters are time dependent, they may be referred to as model **forcings**. For example, for an atmospheric model, the surface temperature of the oceans is a boundary condition (and also a forcing, if it depends on time), and the atmospheric concentration of CO_2 is a parameter (and also a forcing, if it depends on time). For a coupled ocean-atmosphere model, this same sea surface temperature is a prognostic variable while pCO_2 remains a parameter. For a climate-carbon coupled model, pCO_2 is explicitly calculated and thus becomes a model variable as well. It is often interesting to explore how the model outcomes change when the values of certain parameters change. These are called **sensitivity experiments**, because the objective is not to perform realistic climate simulations, but to see how sensitive the model is to certain parameters (examples of experiments of this type are shown in Sections "General Circulation Models, Complex Models of the Earth System" and "Examples of Long-Term Simulations and Studies of Sensitivity to Forcings"). When this type of study systematically includes many parameter values and many parameters, this is called the **exploration of the parameter space** of the model, and is sometimes imprecisely referred to as the exploration of 'the phase space' (although, strictly speaking, it is the space of the prognostic variables and not of the parameters).

Dynamic Systems

It is also important to briefly outline the general results that can be obtained from an equation system such as system 25.1. First, the choice of functions $f(X, t)$ must be restricted to cases likely to have a physical meaning. Instead of starting from a single initial condition X_0, we start with a set of proximate initial conditions, which fill an initial volume V_0 in the phase space. For the 'physical' cases, the second principle of thermodynamics implies that, at time t, the corresponding states $X(t)$ fill a volume $V(t)$ which decreases with time (in the case of dissipative systems) or remains constant (in the case of conservative systems). While the conservative systems retain the memory of the initial condition, since the volume $V(t)$ remains constant, this information is gradually lost in dissipative systems. Indeed, in general, this volume tends towards zero as time t approaches infinity. Climate (like many other physical systems) is a dissipative system. Figure 25.1 gives examples of typical behaviors of a system for two different initial conditions.

As dissipative systems gradually forget their initial condition, this may turn out to be positive: because this initial information is in any case lost after a certain time, this information is not relevant to the long-term behavior of the

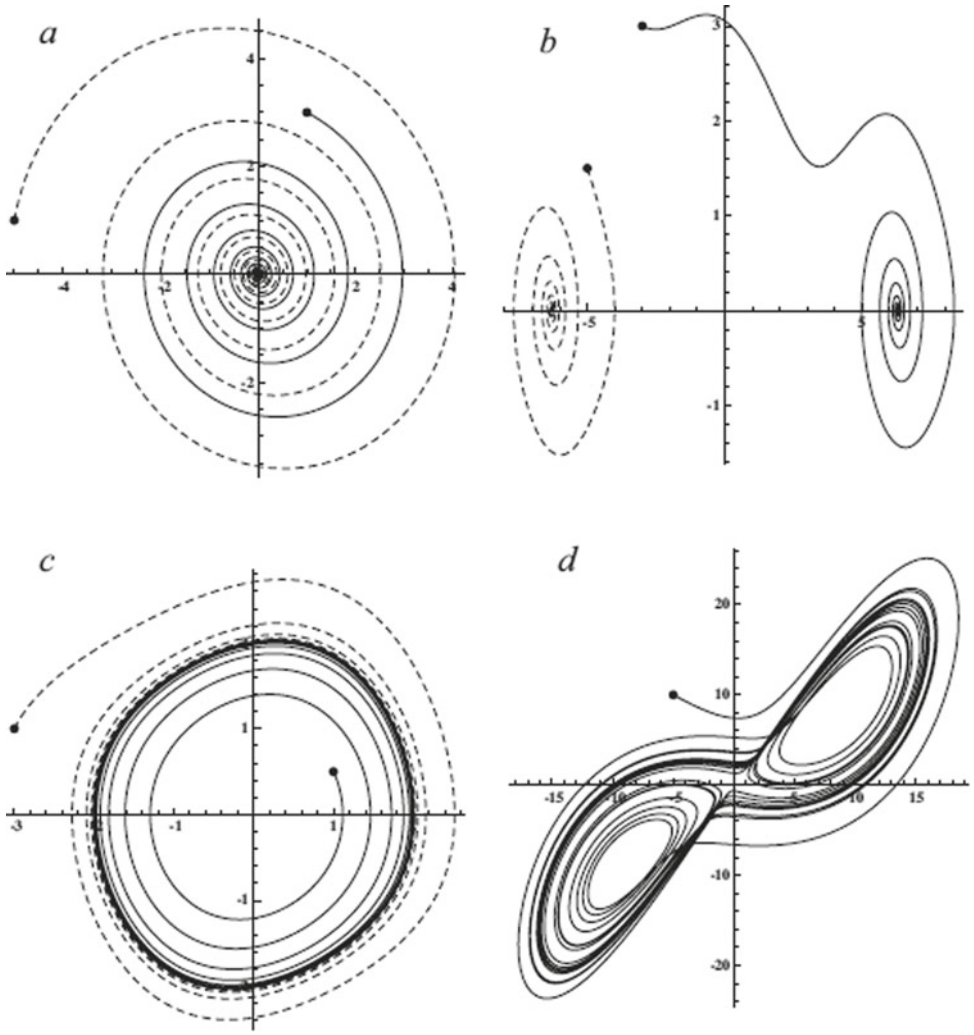

Fig. 25.1 Examples of behaviors of simple dissipative dynamic systems. The departure points are represented by the black dots. **a** Convergence of trajectories towards a single equilibrium point. **b** Convergence to a point of equilibrium dependent on the initial position. A 'catchment area' can thus be defined for each point of equilibrium. **c** Convergence towards a limit cycle. After a transitional phase, the system has a periodic oscillation. **d** Here, the trajectories converge towards a more complex object than a simple point or cycle. This object is called a 'strange attractor' (a well-known example of this case is the Lorenz system, 1963)

system. We can therefore focus on the asymptotic behavior alone in the model, that is to say its behavior from moment t_1 onwards, after this initial condition is forgotten. Conversely, the transitional phase between the beginning of the simulation at t_0 and time t_1, is highly dependent on the initial condition selected, and the results will only be relevant if this condition is correctly understood. Knowing that the duration $t_1 - t_0$ is a few weeks for atmospheric dynamics, we see here an essential difference between a climate model and a meteorological model. For the latter, this transitory phase is the most interesting. A major difficulty in weather forecasting is to provide, in real time, an initial condition that represents the state of the atmosphere 'now' in order to be able to anticipate its state in the hours and days to come. For the climatologist, the initial state of the atmosphere is of little importance, since it will be quickly forgotten. It should be noted, however, that this may not be the case for the initial state of other physical components of the system, such as the ocean, which have much longer time constants.

Nevertheless, this initial state of the atmosphere is not completely irrelevant. The discovery of chaotic systems in the 1970s demonstrated that the 'convergence' of the trajectories in a dissipative system does not necessarily mean that the model 'converges' towards a point of equilibrium (Fig. 25.1a), or even towards a simple trajectory such as a limit cycle (e.g. periodic oscillation, Fig. 25.1c). In fact, if the volume $V(t)$ tends to zero, this does not imply that it is a limit point, nor even a simple line (such as a closed curve, for an oscillator). The system can eventually 'converge' towards much more complex objects, known as 'strange attractors'.

A classic example is the Lorenz attractor, in the shape of butterfly wings, which has a fractal structure (Fig. 25.1d). This is the attractor of a very simple model, with only three degrees of freedom, which was formulated by Lorenz (1963), to illustrate the chaotic behavior of the atmosphere.

The result is that although the initial condition is effectively forgotten, it is nevertheless critical to the determination of the 'true trajectory' of the system. It is so critical that it makes it absurd for 'long-term' simulations, that it, beyond time t_1, to focus on a 'single real trajectory' for the model originating from a given initial state. Chaotic systems, like the atmosphere, are in fact characterized by a high dependence on the initial conditions: a tiny difference between two different starting points becomes exponentially greater. It can be shown that they are also highly dependent on the parameters used. For these systems, long-term deterministic predictions simply do not make sense. It is therefore necessary to focus on a set of trajectories, not to define a single result, but instead to assemble a set of possible results. Indeed, only the 'average' trajectory is significant as it represents a particular statistic of the attractor of the system.

In practice, it is therefore meaningless to try to calculate what the weather will be like on a given day at a given location, beyond a few weeks into the future. Only climate magnitudes (averages, differences, etc.) have some meaning. To calculate these climate averages, two solutions are possible. If we consider that the system is stationary, that is to say that its statistical features do not change over time (this would be the case, for example, in the absence of forcings), then it would simply be a matter of averaging the model results over several decades, as is done by geographers who use an average of weather variables over thirty years to define a 'climate'. We consider that the trajectory followed by the model represents the system that can be interpreted statistically, as is the case for the real climate. However, when the system is subjected to a forcing, such as the current anthropogenic disturbance, the system can no longer be considered 'stationary', and its statistical characteristics (i.e. climate values) will evolve over time. A temporal average is therefore no longer relevant and several simulations need to be carried out, differing only in their initial condition. This ensemble simulation establishes the range of different trajectories covering the range of possibilities.

Climate and Determinism

Before further describing (paleo)climate models, certain paradoxes surrounding the idea of climate should be highlighted. As we have seen above, climatology conveys a statistical approach, as opposed to meteorology, which has, above all, a deterministic perspective. The fundamental reason for this distinction stems mainly from the chaotic nature of the atmosphere, which becomes inherently unpredictable in a short period of time. If all the boundary conditions of the atmosphere (and all parameters) are considered to be either constant, or having a simple annual cyclical forcing, then the system will be stationary, in other words the statistical variables that define the climate will be stable over time. Although the terms of the system of Eq. (25.1) are never zero and the atmosphere changes endlessly, we refer to the climate model as being **in equilibrium**. Conversely, the climate will change only when the boundary conditions of the atmosphere, or some of its parameters, change over a time period of a decade or more, in other words, a timeframe compatible with the concept of climate. In a way, although a climate model aims to represent primarily atmospheric variables, it is only the slower physical components, other than the atmosphere, that cause the 'climate' of the model to evolve, i.e. to change the statistical distribution of the results. This is the case, for example, when there is a change in the ocean, carbon cycle, ice caps. The evolution of the climate is therefore only predictable if the 'non-atmospheric' components are predictable. The chaotic nature of the atmosphere does not imply that climate is unpredictable.

The Framework of a Climate Model

Selecting Components of the Climate System: Model and Boundary Conditions

In practice, it is not possible (or even desirable) to have a mathematical model that simulates all the phenomena that can interact with and modify the climate, including not only the atmosphere and the oceans, but also the terrestrial and marine biosphere, biogeochemical cycles, ice cap dynamics, hydrology and continental erosion. The first difficulty is to choose a relevant subsystem to define the variables of the model, and that can be the object of a temporal evolution given by a system of evolution equations, as above in (25.1). The other factors have to be imposed, in other words fixed as boundary conditions or forcings. For example, when coupled ocean-atmosphere models are used to simulate the past, the following will typically be imposed: (1) changes in coastlines, everything related to continental surfaces, particularly changes in topography, ice sheet extent and height, changes in ocean bathymetry; (2) everything related to atmospheric concentrations, in particular greenhouse gases, but also, in some cases, dust and other aerosols; (3) changes in the orbital parameters of the Earth. We then examine the response of the ocean-atmosphere system to these boundary conditions and forcings, either taken together in order to obtain a realistic simulation of the climate or taken separately to study the role of each of them individually. This is referred to as a sensitivity experiment.

Coupling of Several Components

In general, depending on the scientific question posed and the computing power available, the first step is to identify the part of the system which will be explicitly represented by the model. If, for example, the intention is to represent the evolution of the ice caps under the influence of the orbital parameters of the Earth, it is essential to concentrate on a model which explicitly represents the dynamic of the ice caps. However, when the focus is on fast-reacting components (ocean, atmosphere), it is acceptable to fix the slow-moving components by establishing these as boundary limits. The converse is not true. Thus, the evolution of the ice caps only makes sense when its interaction with a changing climate system is considered. Herein lies one of the main difficulties with modeling the climate over long periods of time (both past and future). How can the interactions (exchanges of energy and matter) between physical objects with very different time constants be calculated in a meaningful way? Several strategies are possible.

A—If only a state of equilibrium in the system is of interest, then the equilibrium of one of the systems (for example, the ice caps) can be found by fixing another (e.g. giving the atmosphere fixed boundary conditions), then by performing the inverse operation (the atmosphere is calculated while the ice caps are fixed), then reiterating the process until the results converge. This is called asynchronous coupling. In essence, the two physical components are coupled, but in a way that does not reflect (or very inexactly) the real flow of time. This makes it possible to achieve equilibrium of the coupled system over a relatively short period of time (for example, a few decades for the atmosphere), since the fast-reacting component (the atmosphere is the factor which demands the most computing time due to the fact that it has inherent small-scale variations) is always calculated by assuming an equilibrium with the slow component.

B—Although asynchronous coupling can be a good method of calculating climate equilibria, it is not a very rigorous way to calculate a meaningful evolution of the system. This may provide a useful approximation if the time constants of the physical systems are very different (e.g., atmosphere and ice caps), in which case it amounts to considering that the slow component is the sole driver of the evolution of the system with the fast component merely adapting to the slow component. If physical components with 'intermediate' times are included (such as the ocean, which reacts more slowly than the atmosphere but faster than the ice caps), this strategy may fail. Therefore, it is sometimes desirable to simplify the physics of fast-reacting components (especially the atmosphere) in an attempt to calculate only the long-term variations that can be used directly by the slower components. This has led to the development of models known as 'intermediate complexity' models (see Section "Earth system models of intermediate complexity (EMICS)").

Comparison with Paleoclimate Data

If our objective is to explain climate variations as reconstructed from paleoclimate records via modeling based as much as possible on the physics, it is important to set up the model and experimental design so that this comparison is easiest. This gives rise to a second major difficulty in paleoclimatology simulations: paleoclimate indicators (proxies) are never clear-cut in terms of the physical variables simulated by models. These indicators are dependent on particular climate parameters, but are these the ones being simulated? It is therefore risky to rely only on the same physical models as those specially developed for comparison with current observations, whose important parameters can be measured by oceanographers, glaciologists and meteorologists. The ideal situation is to be able to quantitatively compare paleoclimate simulations with paleoclimate indicators. The most promising strategy is to explicitly simulate these indicators in the models so that the multiple factors likely to influence them are taken into account. For example, it is useful to explicitly simulate the water isotopes (δ^{18}O and δD) in atmospheric and ocean models, and the carbon isotopes (δ^{13}C) in biogeochemical models, in order to have a more direct comparison between the output and the measurements. An example of the application of one of these models is given in Chap. 29.

Another important difficulty concerns the chronology of events. Climate models need boundary conditions and forcings (e.g. variations of insolation, concentrations of atmospheric CO_2, sea level) in order to produce results such as temperatures or precipitation. It is difficult to enter all of the forcing parameters at the same chronological scale into the model. It is also often problematic to compare the results of these simulations with paleoclimate data whose time scale is not clearly defined. This is especially true when using short-term simulations, such as the results of general circulation models (atmospheric or coupled ocean-atmosphere models). For example, to better understand how a glaciation starts, simulations of the atmosphere, or of the ocean-atmosphere system, are performed. But when is the start of a glaciation? If marine isotopes can be relied upon, the ice caps began to grow at around 120 or 122 ka BP. This moment could then be simulated by imposing to the model the insolation, greenhouse gas forcings etc. which best fit this time period. In the case of an 'equilibrium' simulation that numerically integrates the atmosphere over a few decades, or the ocean-atmosphere system over 1000–2000 years, with constant forcings, this strategy is likely to

be disappointing, since the forcing is 'barely' adequate to simulate the desired objective i.e. an accumulation of perennial snow on continents at high northern latitudes. The modeling strategy is then to start at 115 ka BP, when the astronomical forcing seems most favorable, to maximize the response of the system. Since it is difficult to modify all the boundary conditions of the model in a coherent way so that it aligns with the situation that existed 115 ka BP ago, the best approach is often to maintain conditions close to the control situation, the 'current' state, or rather the 'pre-industrial' state, such as sea level and greenhouse gases. Often, when modelers talk about experimenting with entry into glaciation using OAGCMs, this is in fact a simulation with the same boundary conditions and forcings as for the pre-industrial period except for the insolation, which is changed to correspond to the astronomical forcing of 115 ka BP ago. The objective is not to make an ice cap 'grow' (which would require a comprehensive ice cap model and thousands of years of integration) but simply to check that when insolation is modified, snow may accumulate in certain locations. There is only a very distant connection between this and the available paleoclimate observations, and therefore comparison with the data is not easy since the conditions imposed on the numerical experiment are idealized.

In general, models can only represent a small part of the global climate system with the other parts being imposed or ideally represented. Although their aim is to describe certain aspects of the problem in the most realistic way possible, they cannot claim to be exhaustive. Before embarking on any modeling exercise, it is essential to formulate a precise hypothesis corresponding to the selected configuration. Taking the example above of entry into glaciation, it is not possible to 'simulate the start of an ice age' in all of its aspects. However, some questions can be formulated and an attempt made to answer them. For example, for a general atmospheric circulation model: 'Taking a control situation i.e. a pre-industrial climate as a starting point, does simply changing the radiative forcing at the top of the atmosphere without changing ocean surface temperatures (which would require an ocean model), or vegetation (requiring a vegetation model), or the expansion of the ice sheet (requiring an ice sheet model), or anything else, bring about persistent snow cover in some northern regions?' Formulated in this way, it is easier to understand the gap between this and a broad-ranging simulation of a glacial inception. More comprehensive models can answer more general questions, but there is no 'all-encompassing' model. It is therefore important to correctly define the hypothesis to be tested, and to choose the relevant model configurations to do this.

The following sections describe the major families of climate models, from the most complex to the conceptual. Each section gives examples of the application of these models to paleoclimate questions.

General Circulation Models, Complex Models of the Earth System

Equations, Discretization and Parametrization: Example of Atmospheric General Circulation Models

A natural approach to simulate the characteristics of the Earth's climate is to look at the basic equations describing the behavior of the atmosphere and the ocean. First, we will describe how atmospheric general circulation models (AGCM) are constructed in order to represent the evolution of atmospheric characteristics (temperatures, winds, precipitation, etc.) on a global scale. We know (see Chap. 1) that at this scale, the atmospheric circulation is driven by the differential in insolation between the equator and the poles. The fundamental equations are therefore energy conservation, supplemented by mass conservation (of air and water), momentum conservation and the law of perfect gases.

Conservation of energy:

$$\mathrm{D}I/\mathrm{D}t = -\mathrm{p}\left(\mathrm{D}\rho^{-1}/\mathrm{D}t\right) + \mathrm{Q} \tag{25.2}$$

where

I is the internal energy per unit of mass ($I = c_pT$, c_p being the specific heat of air at constant pressure), p is the pressure,
ρ is the density of the atmosphere,
Q is the heating rate of the atmosphere per unit of mass,
D/Dt is the Lagrangian (Material) derivative: $\mathrm{D}/\mathrm{D}t = -\frac{\partial}{\partial t} + u\frac{\partial}{\partial x} + v\frac{\partial}{\partial y} + w\frac{\partial}{\partial z}$
u, v, w being the wind components with the dimensions x (longitude), y (latitude) and z (altitude).

Conservation of momentum:

$$\frac{\mathrm{D}\mathbf{v}}{\mathrm{D}t} = -2\Omega \times \mathbf{v} - \frac{1}{\rho}\mathrm{grad}(p) + g + F \tag{25.3}$$

where

$\mathbf{v} = (u, v, w)$ is the velocity of the wind relative to the surface of the Earth,
Ω is the rotational angular velocity of the Earth,
p is the atmospheric pressure,
g is the acceleration due to gravity,
F is the force exerted per unit of mass.

Conservation of mass (of air and water):

$$\frac{\mathrm{D}\rho}{\mathrm{D}t} = \rho - \mathrm{div}(\mathrm{v}) + \mathrm{C} - \mathrm{E} \tag{25.4}$$

where C is the creation rate of the species under consideration, and E is its destruction rate.

The law of perfect gases:

$$p = \rho r t \tag{25.5}$$

As described above, these equations are very general and are valid for both small and global spatial scales. The whole art of the modeler involves simplifying these equations for a given problem and expressing them in a form so that they can be solved numerically for this problem. It is the choice of the simplifications and of the expression of the equations that makes the differences between the models. These are always based on a set of assumptions deemed important for the problem being studied. Numerical simulations are then a test of our understanding of the system, expressed as a set of equations which define the numerical model.

A first simplification of Eqs. (25.2)–(25.5) is often done in current atmospheric general circulation models: the hydrostatic approximation. The objective of these models is to represent the characteristics of the troposphere, the lowest layer of the atmosphere which determines the climate on the Earth's surface. This layer, which reaches altitudes from 10 km (at the poles) to 20 km (at the equator), is extremely thin compared to the radius of the Earth ($\sim$6400 km) and is a fine layer in which particles of air travel much further and faster in a horizontal direction than a vertical one. From these considerations of scale, it can be deduced that when we consider atmospheric circulations with a horizontal scale much greater than the thickness of the troposphere, the atmosphere is close to the hydrostatic equilibrium, as described by the equation:

$$\Delta p_{atm} = -\rho g \, \Delta z \tag{25.6}$$

where Δp_{atm} is the difference in atmospheric pressure between two levels separated by altitude Δz, ρ is the density of air, g is the acceleration due to gravity.

This direct relationship between pressure and altitude leads atmospheric specialists to often present variations in vertical atmospheric properties as a function of pressure: for example, a pressure of 1000 hPa indicates a level close to the surface, a pressure of 500 hPa indicates the mid-troposphere and a pressure of 200 hPa indicates the altitude where the subtropical jet streams are most intense. It is just above this level of pressure that the transition between troposphere and stratosphere is found. The hydrostatic approximation considerably simplifies the solution of the system of Eqs. (25.2)–(25.5), because by judiciously choosing the vertical coordinate, the vertical speed is diagnostically deduced from the horizontal components of the wind (thanks to the continuity equation). The prognostic variables of the system of equations are therefore temperature and humidity, and the two components of the horizontal wind. All other characteristics of the atmosphere can be deduced from these four variables. It is therefore the evolution of these four variables that have to be calculated, using the fundamental equations, simplified by the hydrostatic approximation.

These equations are solved for the boundary conditions and forcings chosen by the modeler to answer the posited questions. For the atmosphere, these are greenhouse gas concentrations, insolation (the amount of energy entering the atmosphere at its summit) and surface conditions: distribution of the different surface types (oceans, land, ice caps, different types of vegetation), orography, ocean surface conditions (temperature and sea ice coverage). An initial state for all the prognostic variables of the model is also chosen. From this initial state, the evolution of the atmosphere is calculated over the time necessary for its characteristics (temperature, precipitation, wind etc.) to be in equilibrium with the imposed boundary conditions. It should be noted here that many climate models of the 'general circulation model' type have been developed from meteorological forecasting models, at least for their atmospheric part. However, this does not mean that these models can predict the weather (meteorology) on a specific date in the past or the future. Given the chaotic nature of the atmosphere, it is impossible to make weather predictions further out than ten days. What we are trying to establish is a statistical equilibrium for boundary conditions and for specific forcings, not the weather on a particular date.

How is this done in practice? It is not possible to solve the equations analytically, that is to say, it is not possible to obtain general formulae describing the temporal evolution of the prognostic variables of the system for a particular point of the troposphere. The equations are solved using numerical methods which involve discretizing them. The state of the atmosphere is described using a finite number of values which is nevertheless large for general circulation models (around 10^5–10^6). There are many methods of discretization and we will come back to this. One of the simplest ways is to describe the state of the atmosphere using the prognostic variables of the equations on a three-dimensional grid covering the globe. Let $X(t)$ be the set of these values describing the state of the atmosphere at time t. The basic unit of temporal discretization is called the '**time step**'. Starting from the initial state, describing the state of the atmosphere X_0 at time $t = t_0$, the equations enable the state of the atmosphere X to be calculated with the following $t = t_0 + \Delta t$ time step:

$$X(t_0 + \Delta t) = X_0 + \Delta X$$

ΔX can be obtained directly through the differential equations chosen to describe the evolution of the atmosphere, which allow us to calculate $\Delta X/\Delta t$ and then, once Δt is fixed, ΔX and $X(t_0 + \Delta t)$. Thus, progressing time step by time step, the evolution of the atmosphere can be calculated over a period long enough to obtain robust statistics, allowing a simulated climate to be defined based on the results of the model.

The time step Δt cannot be freely chosen. Obviously, the smaller the Δt, the longer it will take to get to the result. However, there is a maximum time step, equal to $c \times \Delta x$, where Δx is the chosen spatial resolution and c is the characteristic speed of propagation of the information from one point to another. This is called the Courant, Friedrichs and Lewy criterion (or CFL criterion), named after the mathematicians who formulated it. Thus, obtaining a simulation with a fine spatial resolution takes a long time because it requires not only calculations to be made on more points, but also a smaller time step. A compromise must therefore be made between spatial resolution and time taken to produce the simulation. Paleoclimate studies which require long simulations over several hundreds or even thousands of years often used models of coarser resolution rather than those used for climate forecasts into the next century. However, nowadays, there are specific projects in which the same models are used to compare the mechanisms of past and future climate changes.

Within the atmospheric general circulation models, two types of processes are often differentiated: **dynamic processes** and **physical processes**. The first type deals with the evolution of the circulation and can only be calculated from the three-dimensional spatial distribution of other variables, such as temperature. It is through the use of the dynamic laws [Eqs. (25.2)–(25.5)] that we can run the simulation forward, time step by time step. The second type are calculated for each vertical column separately for a given time step. These are mainly radiation, clouds, precipitation and surface exchanges. The distribution of the three-dimensional variables used at the dynamic stage of integration is obviously closely dependent on the evaluation of the physical processes for each vertical column. The dynamic and physical calculations are therefore carried out alternately, sometimes using different time steps. Taking the example of the atmospheric model included in the IPSL_CM6 model used in the Sixth IPCC Assessment Report (publication planned for 2021) the time steps are from 430 s (high-resolution version with 50 km and 79 vertical levels) to 2 min (low-resolution version with 300 km and 39 vertical levels) for the dynamic processes and 15 min for the physical ones.

In a general circulation model, we try to achieve the best representation of both types of processes. Circulation is calculated based on the basic laws of fluid mechanics, expressed for the particular case of a thin atmospheric layer surrounding a rotating planet. We have seen how these equations can be simplified for this specific context, based on the characteristic scales of global atmospheric circulation. However, there is a second type of simplification inherent to the construction of a model, and this is related to the physical processes defined above. The fine details of these processes are not always well understood. Moreover, their characteristic spatial scale is often much too small for them to be explicitly represented in current models, whose spatial resolution is of the order of a hundred kilometers. Therefore, the modeler will not attempt to represent the process in detail, but rather to represent its impact on the atmospheric characteristics at the resolution of the model. Thus, for example, each cloud is not represented individually; rather the impact of clouds on the radiative balance and on precipitations is formulated. This is called **parametrization** of a **subgrid process**. These parameterizations represent simplifications of reality in the sense that we have an incomplete knowledge of it and the process itself is not represented but rather its impact at the relevant scale. The parameterizations, as well as the methods of discretization of the equations used, along with the spatial and temporal resolutions, constitute the main characteristics of a model.

Returning to the methods of discretization of the equations governing the evolution of the state of the atmosphere, two approaches can be identified. The first is a description of the atmosphere in a finite number of points, generally organized into a three-dimensional grid. These are called '**grid-point models**' or 'grid-box models', with the 'box' referring to the smallest unit volumes of the grid. The resolution of the model is defined by the size of this box, or by the number of points used to describe the longitudes, latitudes, and the number of vertical levels. There are many examples of grids, among which grids whose points are regularly spaced in terms of longitude and latitude, and grids whose points are regularly spaced in terms of longitude and the cosine of latitude. In general, the vertical levels are not evenly distributed. In particular, they need to be closer together in the boundary layer of the atmosphere, the layer closest to the surface.

A second type of approach involves using spherical harmonics to describe the variations in the atmosphere on the horizontal plane. The grid point method is retained for the vertical dimension. These **'spectral' methods** are particularly suited to the atmosphere, which forms a continuum on the surface of a sphere. The calculations for this method are faster, in particular due to the fact that the first and second derivatives on the horizontal can be easily expressed for this type of decomposition. The spectral models are well suited for the representation of waves in the atmosphere with a smaller number of degrees of freedom than in the grid point models. The advantages of the spectral models are, however, less significant for fine resolutions, as there are many calculations, especially for physical processes, which still have to be carried out on a grid model. In general, the number of points in the grid exceeds the number of degrees of freedom in the spectral method so as to avoid problems with aliasing. These grids therefore give the impression of a finer resolution than the real number of degrees of freedom of the model. This is why the description of the resolution of these models refers to the number and type of harmonics chosen.

The oceanic general circulation models are also constructed based on fluid dynamics equations with the additional constraint of salt conservation. The discretization used is in grid point because of the geometry of the basins. The specificities of oceanic general circulation models are not detailed further here.

Towards an 'Integrated' Model of the Earth System

Historically, the first climate simulations carried out with general circulation models employed 'only' atmospheric models. Interactions with the surface, especially with the ocean, were very limited because the majority of the surface characteristics were imposed (surface temperature of the oceans, presence of sea ice, surface albedo, roughness of terrain etc.). As a result, the atmospheric circulation obtained was in equilibrium with these surface conditions and other forcings. In particular, it was then possible to evaluate the response of the atmosphere to changes in the ocean surface. It is clear, however, that the ocean, like vegetation and land surfaces, does not remain unaffected when faced with climate change. Modelers therefore quickly sought to estimate the impact of feedbacks from the other components of the climate system on the atmosphere, which in turn defines the climate at the surface. Figure 25.2 shows the evolution of climate models since their inception. It shows the coupling first with ocean surface models, then with complete ocean circulation models. In parallel, land surface models have progressed from simple hydrological models, with fixed albedo and surface terrain, to models including interactive vegetation, allowing the surface characteristics to be calculated according to changes in vegetation caused by changes in climate or by man. Finally, models increasingly include a representation of atmospheric chemistry and aerosols, which have a significant influence on radiation, as well as the biogeochemical cycles such as the carbon cycle. In this type of model, the atmospheric concentration of CO_2 is no longer imposed and is instead calculated from emissions.

Climate models developed in this way require enormous computing power. Simulations are generally carried out on supercomputers adapted to this type of coding. These computers are scarce, which explains the limited number of general circulation models in the world. The models, their resolution, as well as the components of the climate system and the processes to be included are chosen at the outset according to the issue to be addressed, but also in keeping with the current limits in computing power. The performance of the models will vary depending on the model and the computer used, but for example, the approximate computation times for the IPSL model are: run at very low resolution (IPSL-CM5A2: atmosphere 96 × 95 × 39, ocean 2°), about 70 years per day; at low resolution (IPSL-CM6-LR, atmosphere 144 × 133 × 79, ocean 1°) 16 years per day, and at medium resolution (IPSL-CM6-MR, atmosphere 280 × 280 × 79, ocean 1°) about 6 years per day.

Thanks to the improvements in supercomputers over recent decades, the development of coupled atmosphere-ocean models, followed by atmosphere-ocean-vegetation models has become possible. These models require a longer computing time, not because there are many additional calculations to be performed for a given duration, but because vegetation, and even more, the ocean, are components of the climate system whose response time is far greater that of the atmosphere. While we consider that simulations using an atmospheric model alone, forced by boundary conditions which repeat each year, must be integrated over a period of 20 to 50 years to obtain a response from the atmosphere in equilibrium with these boundary conditions, a coupled atmosphere-ocean model, in principle, needs to be integrated over one or even several thousand years. The biggest challenge then is to close-off the water and energy balances in the model to avoid a gradual drift related not to the imposed forcing but to the model itself.

'Realistic' Modelling of Paleoclimates

Boundary Conditions and Initial Conditions

Many paleoclimate simulations aim to 'recreate' past climates as accurately as possible. The models can then be evaluated in the context of climates documented by paleoclimate indicators which are different from the current climate. It also provides a better understanding of the possible connections between differences in climate between distant regions and supports reconstructions by providing better spatial and temporal coverage or by including a regional phenomenon not covered by the reconstructions, thereby improving our understanding of them. We will return to the comparison between models and data and the value of this exercise at the end of the section.

How can a 'realistic' simulation of a paleoclimate be achieved? First, depending on the question at stake, the part of the climate system being assessed needs to be defined. For example, if we want to study the continental climate in the context of given ocean conditions, it is best to use an atmospheric model, possibly coupled with a dynamic land surface model or vegetation model. Once the subsystem is selected, a paleoclimate simulation is carried out by imposing the most realistic forcings and boundary conditions possible on this subsystem for the simulation period. Thus, the more the subsystem is constrained, the more conditions there are to be imposed, conditions that need to be known for the study period. Continuing with the example of the simulation using only a general atmospheric

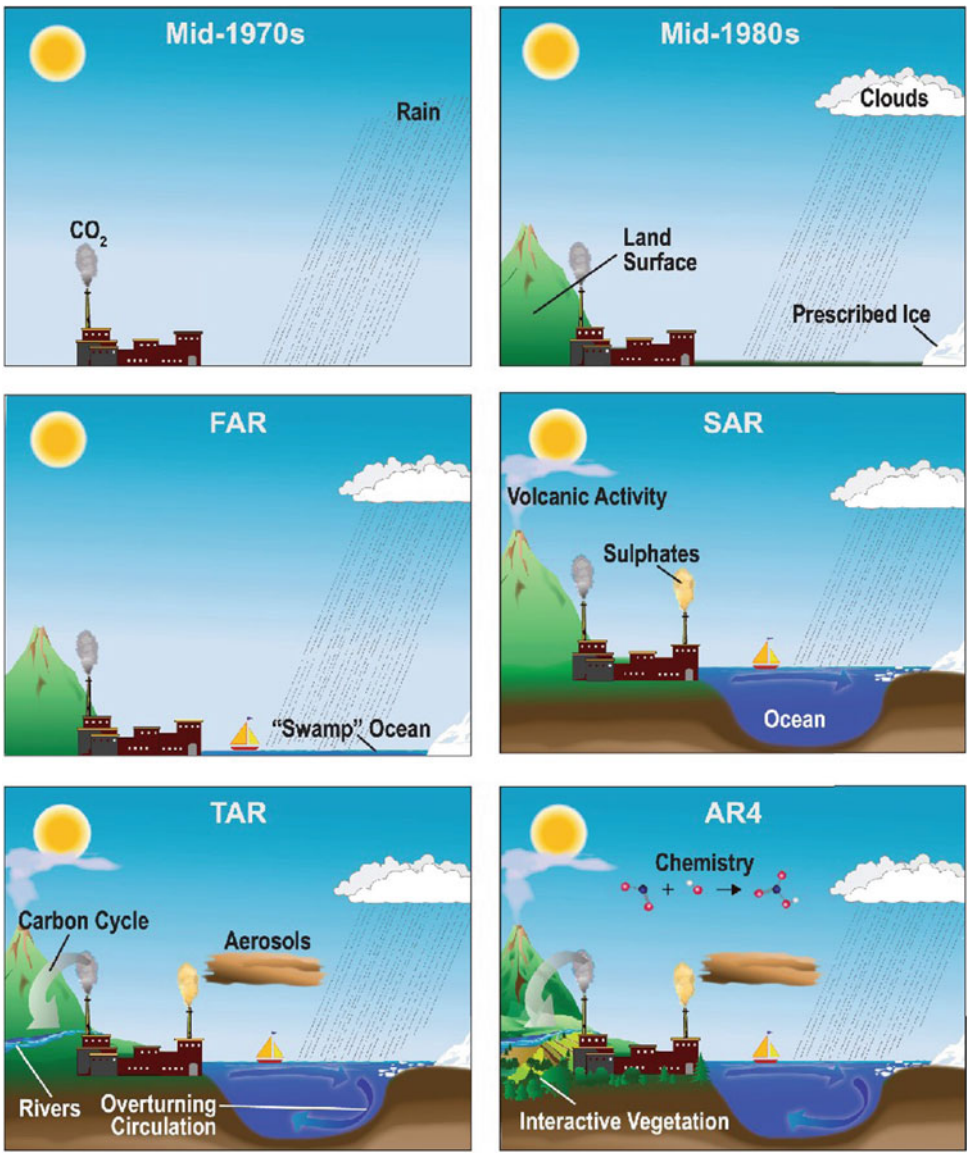

Fig. 25.2 History of climate models used in successive IPCC reports. From the 4th IPCC report (2007), Solomon et al. (Ed.), Cambridge University Press, http://www.ipcc.ch/publications_and_data/ar4/wg1/en/contents.html

circulation model, the ocean surface temperatures and the extent of sea ice have to be defined for all ocean-type points in the atmospheric model. In practice, this is extremely restrictive since at the very least, reconstructions of ocean surface conditions with a spatial resolution similar to the model for a typical seasonal cycle would be required. These numerical experiments are almost always based on strong assumptions as to the ocean surface conditions as well as the land-ocean distribution, topography, and extent and altitude of the ice sheets. The other forcings are better known, at least for the relatively recent periods of the Quaternary: insolation (Berger 1978; Laskar 2004) and atmospheric concentration of greenhouse gases, with measurements from Antarctic ice cores now dating as far back as 800,000 years.

Thus, a 'realistic' simulation of a paleoclimate is based on several series of assumptions: those related to the design of the model itself and those related to the fixing of boundary conditions for a specific experiment. So, this simulation summarizes both our knowledge of climate characterization (incorporated into the climate model), and our understanding of the forcings of this climate (expressed in the forcing and boundary conditions). It is also constrained by the limitations of computers and technology of its time.

Take the example of the climate simulations for the Last Glacial Maximum (LGM, about 21,000 years ago). The first simulations of the climate of this period (Gates 1976) were carried out shortly after the first reconstructions of the ocean surfaces (sea surface temperature, extent of sea ice) and of land (ice caps) were produced (CLIMAP 1976). At this time, the LGM atmospheric concentration of CO_2 was not known. It was only in the 1980s (Manabe and Broccoli 1985) that the first numerical simulation was carried out taking into

account the main forcings for the climate of the Last Glacial Maximum: the expanse and altitude of the ice sheets, ocean surface conditions and atmospheric concentration of CO_2. It was a simulation derived from one of the most sophisticated stand-alone atmospheric models of that time. The simulated duration was short (three months for the first simulation!) compared with current norms: theoretically, a few decades of simulations are required to obtain statistically robust results, depending on the region and the phenomenon in question. It must be recognized that at the time of the first paleoclimate simulations, the duration of the simulations carried out with general circulation models was greatly restricted by the cost of computing time. To save time, experiments were carried out under unchanging January or July sunshine conditions, producing significant results for relatively short durations of simulations (typically 90 days). These results, which were a technical feat at the time of their publication, would now probably be viewed very critically, mainly due to their short duration, even in conditions of fixed insolation. Models are evolving as our understanding of the climate system and computer capabilities improves. Simulations therefore need to be revised periodically in the light of these advances. The simulations of the first phase of the PMIP project (Paleoclimate Modeling Intercomparison Project, Joussaume and Taylor 1995) using general circulation models, ran for at least ten years after an adjustment for the boundary conditions of at least one year.

These first simulations of the climate of the Last Glacial Maximum used the ocean surface conditions reconstructed by the CLIMAP project (1976, 1981). These reconstructions were the result of a major work of data synthesis, but problems were quickly identified, particularly for the subtropical regions, where a higher temperature than is the case currently was reconstructed, and for the North Atlantic, where the winter sea ice cover was overestimated. These problems were partially amplified by the methods used to extrapolate the reconstructions for each site to cover the globe with an even grid. The CLIMAP project, at the specific request of modelers, provided reconstructions for the months of February and August. However, it is entirely possible that certain species used for reconstructing SSTs are not particularly sensitive to these specific months, but to other factors. Thus, manipulating data to construct boundary conditions for models, especially atmospheric ones, can prove to be extremely restrictive for the interpretation of data records. Furthermore, since they are used to establish the boundary conditions, they cannot also be used to validate the model. Therefore, as soon as they became available, it was very useful to use coupled ocean-atmosphere models to simulate paleoclimates. It is worth highlighting again the challenge represented by the first coupled simulations of the climate of the LGM. Again, in this case, the first published simulation was only about thirty years long, a very short time frame compared to the response time of the deep ocean! Within the international PMIP2 project, eight groups have carried out multi-centennial coupled ocean-atmosphere simulations, which shows how difficult this type of experiment is to perform. This was confirmed in the 3rd phase of the PMIP, contemporary with CMIP5, for which 9 models have finally yielded results for the LGM. For PMIP4, there are about fifteen modeling groups planning to undertake this simulation, the future will tell us how many succeed.

This example of modeling of the LGM climate shows that 'realistic' modeling of this climate has evolved in line with the forcings and tools available.

We have seen that the uncertainties in a 'realistic' simulation of a climate are due to two types of factors: those related to the formulation of the model and those inherent in the selection of boundary conditions. The next two sections show how to quantify these uncertainties, both through rigorous comparisons between the results of models forced by identical boundary conditions, and through sensitivity studies with respect to these boundary conditions.

Comparing results from different models: Modeling Intercomparison Projects

How can the results of different models be compared? These differences may be due to the models themselves, or to the boundary conditions and forcings imposed on these models. The results of several models can only be rigorously compared by assigning them the same boundary conditions/forcings. Such exercises have been proposed for the modeling of current climates using atmospheric general circulation models (AMIP project, Atmospheric Model Intercomparison Project, http://www-pcmdi.llnl.gov/projects/amip/), followed by coupled models, both for current and future climates (CMIP project, Coupled Model Intercomparison Project, http://www-pcmdi.llnl.gov/projects/cmip/). The CMIP5 exercise corresponds to the results produced for the 5th IPCC report and CMIP6, currently underway, will provide its first results for the 6th IPCC report, which will be published in 2022. In the same vein, PMIP (Paleoclimate Modeling Intercomparison Project), the project to compare paleoclimate models came into being in the 1990s (http://pmip.lsce.ipsl.fr). At first, this project involved atmospheric general circulation models (PMIP1 project, http://pmip1.lsce.ipsl.fr/) for the Middle Holocene (6000 years ago) and the Last Glacial Maximum (21,000 years ago). It was then extended to coupled atmosphere-ocean and atmosphere-ocean-vegetation models (PMIP2 project, Braconnot et al. (2007a, b), http://pmip2.lsce.ipsl.fr/). A new feature of PMIP3 was to use climate models strictly identical to those used for CMIP5. PMIP4 coordinates both CMIP6 simulations, which will therefore use the same models as those used for climate projections, and simulations based on other models, usually longer ones or for older climates. The PMIP4-CMIP6

simulations concern the following climates: the last millennium, the Middle Holocene, the Last Glacial Maximum, the last interglacial and the Middle Pliocene (Kageyama et al. 2018).

The PMIP project first focused on defining precise boundary conditions and forcings for the Middle Holocene and the Last Glacial Maximum. This made it possible to rigorously compare the results of the models participating in the project with the paleoclimate reconstructions. Below is an example of a comparison of PMIP2 model results for Europe during the Last Glacial Maximum. Figure 25.3 shows the temperature of the coldest month in an average seasonal cycle simulated for this period by the eight models whose results were available in the database in November 2009. The differences with the current climate are shown. The color of the diamonds indicates the average temperature reconstructed from pollen data by Wu et al, (2007), on the same color scale as for the one used for the model results. In this figure, it can be seen that the most noticeable cooling of at least 12 °C is simulated by the models in the northern part of the area under study, on the Fennoscandinavian cap and on the sea ice off the coast of Scandinavia. This cooling lessens towards the south, where it is about 3 °C. Even if the same boundary condition forcings are applied to the models, the climates obtained differ from one model to another. For example, the cooling simulated over the ice cap is between 12 and 18 °C for the ECBILTCLIO model, whereas it is greater than 30 °C in the HadCM3M2 model. Around the Mediterranean, the CCSM3 model simulates practically no temperature change for the coldest month, whereas the ECHAM5.3-MPIOM-127-LPJ model simulates a drop in temperature of between 3 and 6 °C.

This shows how models developed to first represent the current climate can diverge in their representation of climates different from the current one. This discrepancy is found in the forecasts of future climates, but only paleoclimate simulations allow climate simulations different from today's climate to be compared with the data.

Comparisons Against Paleoclimate Reconstructions

In Fig. 25.3, reconstructions of the temperature of the coldest month by Wu et al. (2007) are indicated by diamond shapes with the same color code as the output of the models. It should be noted that for Western Europe, all of the models simulated temperatures that are warmer than the reconstructed temperatures. However, it is important to take into account both the dispersion of the results of the models, which is done to a certain degree in Fig. 25.3 by including the results of all the models as well as the level of uncertainty of the reconstructions, which cannot be shown on the maps. Figure 25.4 compares the same model and reconstruction results from another perspective. Here, we have chosen to show the average temperature by longitude for Western (10° W–15° E) and Central Europe (15–50° E) and the reconstructions with their uncertainty range. This time we see that the temperatures simulated by the models are compatible with the reconstructions, if we take into account the uncertainty characterizing the reconstructions, including for Western Europe.

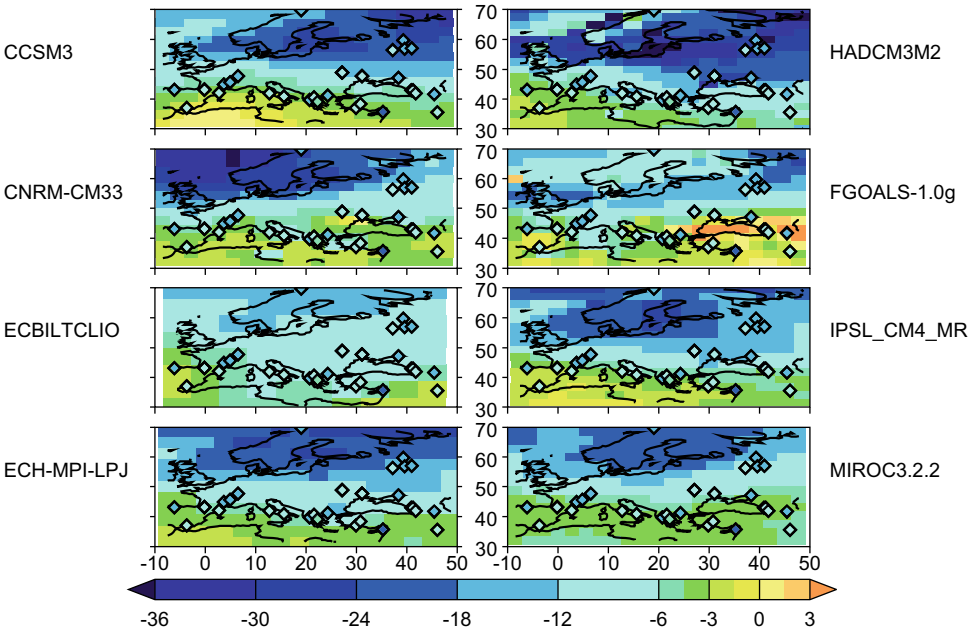

Fig. 25.3 Maps: temperature of the coldest month in an average seasonal cycle, as simulated by the coupled ocean-atmosphere models participating in the PMIP2 project (November 2009 PMIP2 database); Diamonds: same variable, as reconstructed by Wu et al. (2007)

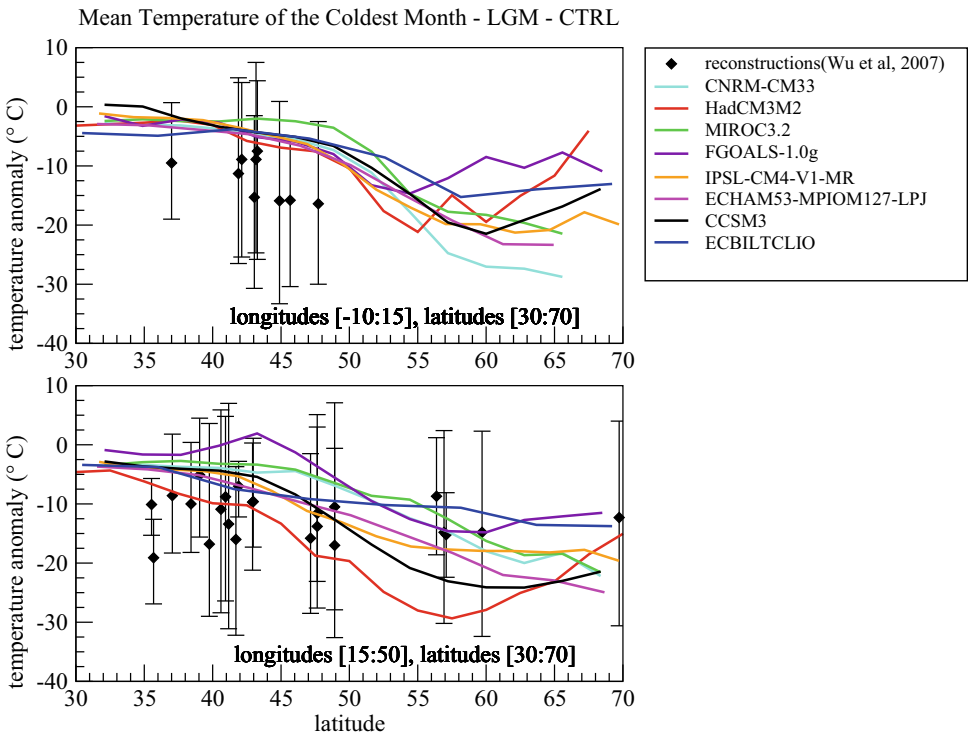

Fig. 25.4 Comparison between the simulated temperatures of the coldest month (during an average seasonal cycle) for the LGM in Europe (continuous lines, given for different models of the PMIP2 database), and reconstructed temperatures by Wu et al. (2007) (diamond shapes and the uncertainty bars associated with them) for the Atlantic (top) and Eastern (bottom) regions. The values shown are differences from the reference (pre-industrial) climate

Ramstein et al. (2007) summarized the efforts of the years 2000's to reach a congruent comparison between reconstructions and simulations for winter temperatures during the Last Glacial Maximum. The simulations of the PMIP1 project, using standalone atmospheric models forced by the CLIMAP (1981) ocean surface conditions, resulted in overly high winter temperatures compared to the initial pollen-based reconstructions of Peyron et al. (1998). By working on the boundary conditions (expansion of the ice caps), on the models (transition to coupled atmosphere-ocean models) and on reconstructions (new reconstructions by Wu et al. (2007), based on the same pollen records as used by Peyron et al. (1998), but taking into account the effect of low levels of CO_2 on vegetation) it became possible to reduce the large differences between simulated and reconstructed temperatures. It should be pointed out that for other variables (in particular the summer temperatures), the comparison between models and data was much more positive from the start. The example of the coldest month temperatures was taken specifically because it illustrated what can be learned from the models and the reconstructions through the sometimes tedious exercise of comparing models with data. This example shows that it is important to consider all the possible factors contributing to the differences between simulations and reconstructions in order to reduce these discrepancies: the models, boundary conditions, but also the reconstructions themselves. It is also important to have results from many models to overcome the uncertainty associated with the use of a single model.

Sensitivity Experiments

We have seen that the uncertainties in the results of numerical models stem from the formulation of the models themselves, since these models are built on assumptions considered relevant to the given problem, and on the conditions imposed on the model, which are themselves based on assumptions because we lack the necessary level of precision and spatial and temporal coverage. How can these uncertainties be calculated? One method, discussed above, is to increase the number of models used. Similarly, if we are unsure of the boundary conditions to be imposed on the model, or if there are several sets of boundary conditions possible, we can carry out several experiments with different sets of boundary conditions so that the climate responses to these conditions can be compared and we can determine whether these differences in boundary conditions cause differences in the simulated climate. For example, for climate simulations using an atmospheric general circulation model, the surface temperatures of the oceans are generally not known with great certainty for all months of a given period and for all the grid points of the model. Assumptions are then made so as to reconstruct the seasonal cycle of ocean surface temperatures based on the points that are available and about which there is also some uncertainty. It is possible for the model to perform several simulations based on different ocean surface temperature scenarios. We can then analyze the one that

produces the land temperatures/precipitation values most compatible with the reconstructed data. These are known as sensitivity experiments to sea surface temperatures.

In the case discussed above, we examined several scenarios with different ocean surface temperatures to find out which was most realistic for the period in question. More generally, it is also instructive to analyze the signature or influence of each forcing among several forcings and changes in boundary conditions. To continue with the example of the climate of the Last Glacial Maximum, if a coupled atmosphere-ocean model is used, the forcings applied to the model to obtain a simulation of the climate of this period are:

1. the insolation;
2. the greenhouse gas concentration (CO_2, CH_4, N_2O);
3. the altitude and extent of the ice caps and the change in land-ocean distribution caused by changes in sea level.

To better understand why the glacial period climate is different from the current climate, simulations can be carried out in which only one or two of these boundary conditions are imposed and the simulated climate is compared with a more 'realistic' simulation where all of the boundary conditions are applied. By carrying out these simulations where one or two boundary conditions or forcings are imposed with glaciation values, the aim is not to try to achieve a realistic simulation. Instead, the purpose is to gain a better understanding of the response to each type of forcing. These simulations are also called sensitivity experiments with 1, 2 or 3 forcings.

This approach is illustrated in Fig. 25.5 where the response of the IPSL climate model to LGM conditions is

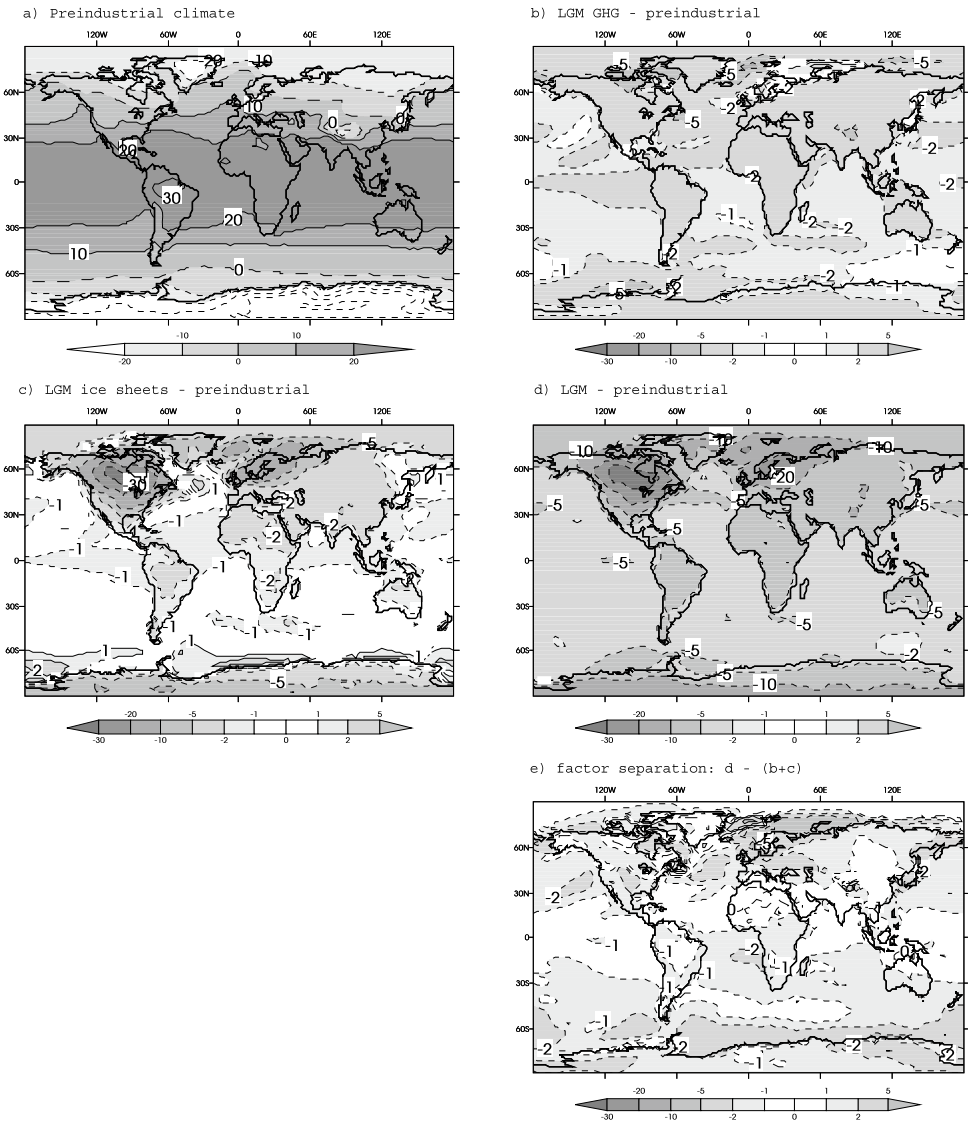

Fig. 25.5 Average annual air temperature at 2 m simulated by the coupled ocean-atmosphere IPSL model: **a** for pre-industrial conditions; **b**, **c** and **d** anomalies compared to this pre-industrial climate: **b** for a pre-industrial simulation, where the atmospheric greenhouse gas concentration has been replaced by ice age values; **c** same for ice caps, **d** simulation with all LGM conditions; **e** difference d − (b + c), allowing the quantification of the proportion of the difference between pre-industrial and the LGM related to the interactions between the impacts of the ice caps and the reduction in greenhouse gas concentrations. For figure (**a**), isolines every 10 °C, dashed lines for negative values, long dashes for 0 °C, and continuous lines for positive values

analyzed by separating the impact of the ice caps from the impact of the reduction of atmospheric greenhouse gas concentration. This figure refers to the annual average temperature of air 2 m above the surface. The values for this temperature in the pre-industrial climate simulation are shown in Fig. 25.5a and the differences between the simulated LGM and pre-industrial climates are shown in Fig. 25.5d. This map shows an overall global cooling, moderate (by a few degrees approximately) over the oceans but very strong (more than 30 °C) over the ice sheets of the northern hemisphere. Figure 25.5b shows that the contribution of greenhouse gases to this response is less extreme over the continents and a little weaker over the oceans than the response to all of the LGM conditions. Figure 25.5c shows the impact of the ice caps alone. It shows that these are responsible for a significant cooling over the continents of the northern hemisphere, but also for a cooling of between 0 and 2 °C over most of the oceans, with the notable exception of the Southern Ocean. It is worth noting that the sum of the anomalies shown in Fig. 25.5b and d is not equal to the difference between the LGM and pre-industrial climates shown in Fig. 25.5d. This difference is shown in Fig. 25.5e. This shows that in many regions the impact of the two factors taken together is greater than the sum of the impacts of each factor considered separately. This is referred to as the synergy between the various forcings. In other areas, such as north of the Nordic Seas, the impact of the two forcings together is lower than the sum of the impacts of the individual forcings. This shows that to quantify the impact of a specific forcing within a group of two forcings (as in this case, the impact of the ice caps and the reduction in greenhouse gases), four simulations must be carried out: a control simulation (in this case, the pre-industrial climate), one including all the forcings (in this case, the LGM) and simulations with each factor taken individually. This method is called the 'factor separation' method developed for the atmospheric sciences by Stein and Alpert (1993).

So far, we have studied sensitivity experiments on the forcings and boundary conditions imposed on models. Sensitivity experiments may also be applied to internal processes of the climate system. To examine the importance of this processes in the response by the climate system to a disturbance, its formulation in a model can be modified. For example, if deep convection at the equator is suspected to have an important influence on some aspect of the climate in the mid-latitudes, the formulation for deep convection in the model can be altered and a sensitivity experiment for this process can be performed with a modified model, under the same boundary conditions. This type of sensitivity experiment also makes it possible to evaluate the importance of a feedback by excluding or activating it.

Outlook

In this section, we mainly describe atmospheric general circulation models, including some coupled with oceanic general circulation models. These models, now complemented by vegetation models, carbon cycle models and atmospheric chemistry models, are becoming increasingly complex, with more components of the climate system, more processes and more associated feedbacks being included. The complex models of the Earth system have sometimes been described as the 'biggest' models that can run on the 'biggest' computers, a sort of 'maximum' model. These limit the number of numerical experiments that can be run for each given problem and the number of sensitivity experiments that can be conducted to better understand the influence of a particular process or mechanism. This situation is changing, as advances in computing now allow modelers to carry out more experiments for a given period. These experiments are essential to improve our understanding of the importance of forcings or processes within a change in climate. New developments in complex climate system models, the improvement in their resolution, the inclusion of new processes or new components must consider the necessary compromise between the computational time required for a simulation and the number of simulations that can be performed with the computer available. With increasing computing capabilities, it is possible to improve the resolution of the models and increase the number of processes included. The models used for the IPCC assessment exercises provide a good indication of the progress of climate modeling over the past two decades (Fig. 25.2). In the future, we will see new components of the climate system being integrated as for instance ice caps. The aim of these developments is mainly to provide a better prediction of the future climate, but they also contribute greatly to the study of paleoclimates, which in turn makes it possible to evaluate these models under climate conditions different to current ones.

Earth System Models of Intermediate Complexity (EMICS)

Basic Principles and History

We have seen that climate models developed from general circulation models were intended to be as comprehensive as possible in their representation of the climate system. This requires considerable computing power and calculation times, which in practice forces the modeler to limit the number of simulations performed. These simulations are also quite short

compared to the typical timeframe in climate evolution. Thus, in parallel with the development of general circulation models, simpler models, more adapted to the study of paleoclimates, have been developed. The aim was to represent from the outset the slow-moving components of the climate system, the ocean and the ice caps, in order to study long-term climate change (i.e. for time scales in excess of a thousand years). To develop these models, representation of the rapid components of the climate system, particularly of the atmosphere, has to be simplified. In fact, the term 'simple model' is misleading because it refers above all to models which are more efficient in their use of computing time. Developing a model of this type is not necessarily 'simple' because one cannot simply retain the basic equations of atmospheric dynamics. The saving of computation time is generally achieved by establishing parameters for the transport of heat and moisture by the stationary and/or transient waves (such as, for example, by the depressions of the mid-latitudes), in other words, by trying to represent the effect of these phenomena without explicitly calculating them. This makes it possible to extend the duration of a time step and to use a coarser spatial resolution. The number of degrees of freedom of these models lies between conceptual models (around ten) and general circulation models ($\sim 10^5$–10^6) and they are called 'EMICs', 'Earth system Models of Intermediate Complexity' (Claussen et al. 2002). In fact, the terminology was created long after the development of the first models in this category. It emerged at a time when the modelers who specialized in these models decided to join together to define the specificity of their models compared with others. These models are characterized by a more complete representation of the climate system than the 'simple' ocean-atmosphere models and by a relatively short computing time compared to the general circulation models, characteristics which allow the evolution of the climate system to be studied over long time scales and many different scenarios to be explored. There are many EMICs, corresponding to the many different ways the representation of the climate system can be 'simplified'. It should be noted that some models have been developed by 'downgrading' a general circulation model, i.e. by reducing its vertical and horizontal resolutions. These are the most complex models in the EMIC category.

As with general circulation models, climate models of intermediate complexity can be used to obtain realistic climate simulations or to study the sensitivity to certain forcings, processes or feedbacks of the represented system. In the following sections, we give examples of the use of EMICs, both for long-term simulations and for studies requiring numerous experiments. Experiments of this type could not have been carried out using general circulation models given current capacity of computing power. This shows the complementarity of the two types of models, one type being useful for its 'efficiency', the other for the spatial and temporal detail in its representation.

Examples of Long-Term Simulations and Studies of Sensitivity to Forcings

One of the first models of intermediate complexity of the climate system is the one developed by the Catholic University of Louvain-la-Neuve. This model includes simplified representations (by latitude and vertically, for the northern hemisphere) of the atmosphere, the ocean, sea ice and the polar ice sheet. It was developed specifically to study the glacial-interglacial cycles, as demonstrated by the first simulations of Gallée et al. (1992). Since then, Berger et al. (1998) and Loutre and Berger (2000) have taken up this model and carried out sensitivity experiments to identify the respective roles of orbital variations and greenhouse gases in the last glacial-interglacial cycle.

Figure 25.6 shows a selection of the results of these two articles in terms of volume of ice (top) and temperature in the northern hemisphere (bottom). The continuous lines represent the results of the model forced by both the variations in CO_2 recorded in the ice cores (Jouzel et al. 1993) and by the variations in the orbital parameters as calculated by Berger (1978). The initial state of the model is an interglacial state, with no ice sheet in the northern hemisphere. Over the last 200,000 years, the model simulates two major glaciations, with a complete freeze-up occurring in steps and a complete deglaciation following the glacial maximum. The coldest temperatures are of course simulated for these glacial maxima. During the last interglacial and the last glaciation (between 126,000 and 80,000 years), despite a high level of recorded variability, temperatures remain sufficiently high so that the frozen-over periods last no longer than 15,000 years.

The red lines correspond to a simulation where the insolation is constant and equal to the current insolation, and where CO_2 levels vary in a similar way to the previous simulation. It can be seen that the volume of ice increases to about 35×10^{15} m^3 and remains at around 30×10^{15} m^3 during the rest of the simulation. Although the average temperature of the northern hemisphere varies in line with the greenhouse gas forcing, it remains too cold to bring about deglaciation. The other curves are the result of simulations where CO_2 remains constant (fixed at 210 ppm for the alternating dash-dot line and at 250 ppm for the dashed curve) and where variations of the orbital parameters are taken into account. This time, alternation between glacial and interglacial periods is obtained, with maximum ice volumes reached for the same periods as in the reference simulation at values inversely related to the level of imposed

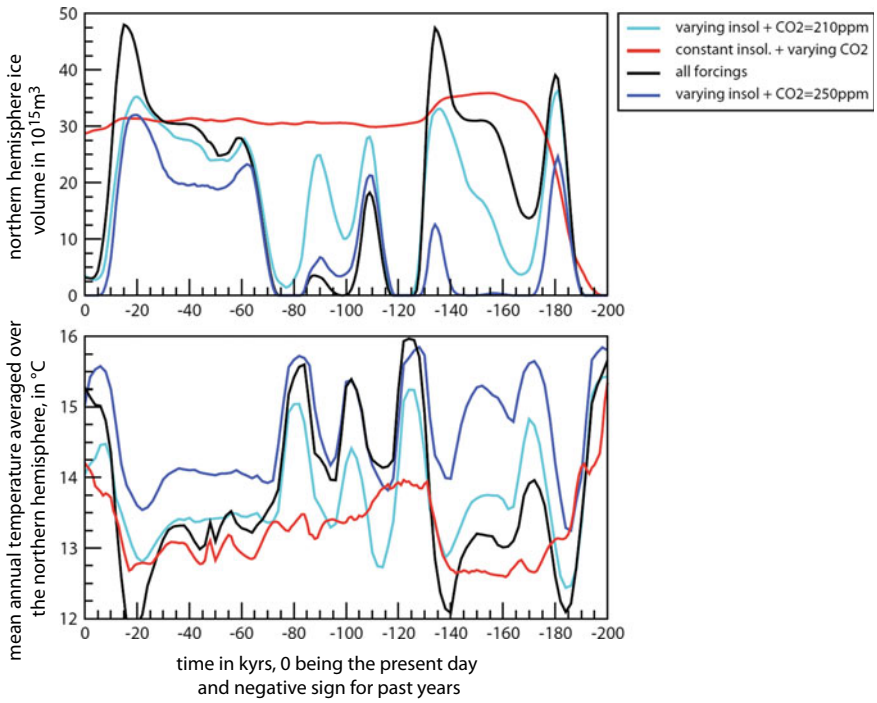

Fig. 25.6 Ice volume (top, in 10^{15} m^3) and average temperature of the northern hemisphere (bottom, °C), as a function of time in kyrs, simulated by the Louvain-la-Neuve coupled model ice sheet-northern hemisphere climate (Gallée et al. 1992) over the last 200,000 years. In black, the simulation where CO_2 and insolation vary in line with the Vostok data for CO_2 and according to the forcing by Berger (1978). The red line represents the results for constant insolation, equal to current levels, with variable CO_2. The light and dark blue lines represent the results for variable insolation and constant CO_2, at 210 and 250 ppm respectively. According to Berger et al. (1998), and Loutre and Berger (2000). The authors thank M.-F. Loutre for providing the results of the Louvain-la-Neuve model

CO_2. These sensitivity experiments show that variations in insolation are an essential forcing to explain glacial-interglacial cycles, because forcing the model with CO_2 variations alone does not produce these cycles. On the other hand, experiments with constant levels of CO_2 show that the extent of a glaciation is highly dependent on CO_2.

Examples of other long-range simulations are given in other chapters of this book. In Chap. 29, an example is given of modeling interactions between northern hemisphere ice sheets, the ocean and the atmosphere over a period of 50,000 years (Calov et al. 2002), as well as an example of modeling of ^{18}O variations in the glacial ocean in response to freshwater inputs from the North American ice cap (Roche and Paillard 2005).

Example of the Use of Intermediate Complexity Models to Explore a Multitude of Forcings or Parameters: Exploration of a 'Phase Space'

In the previous section, we showed that, thanks to its efficient use of computing time, a climate model of intermediate complexity allows us to perform long simulations over time scales able to reflect the variations in climate during the Quaternary (glacial-interglacial cycles, abrupt events from the last glacial period). This efficiency also means that it is possible to carry out numerous simulations to explore the sensitivity to the forcings used of a result or to choices made during the construction of the model. An example of this type of use of an intermediate complexity model is given in Chap. 29. The CLIMBER-2 model, incorporating a representation of oxygen isotopes in the ocean, is used to explore the response to freshwater discharges from the North American ice cap in multiple scenarios. The response is then compared to marine records to determine the most probable scenarios in terms of duration and amplitude of the freshwater input.

Another example is given by the work of Schneider von Deimling et al. (2006). This study analyzes ensembles of simulations for the climates of the present day, the future and the Last Glacial Maximum. These ensembles are formed by varying eleven parameters of the model within acceptable ranges, based on our current knowledge of the climate system. The main effect of changes in these parameters is to vary the amplitude of the feedbacks in the climate system and the climate sensitivity of the model (defined as the

difference in global temperature due to a doubling of CO_2, see Chap. 31). The current climate, as defined by the observations, makes it possible to make a first choice of parameters so that an acceptable simulated climate can be achieved. The authors show that reconstructions of tropical temperatures during the Last Glacial Maximum help to constrain even further the selection of values of these parameters and so reduce the uncertainties associated with future climate change. This study shows that modeling of past climates followed by comparison with reconstructions can help in the evaluation of climate models used to forecast future climate. This conclusion is also advanced by Hargreaves et al. (2007) using a general circulation model.

Outlook

It might be expected that with the advances in computing, climate models of intermediate complexity would no longer have any reason to exist. In fact, this is not the case because they will always be less time consuming than general circulation models, which incorporate more and more mechanisms and use an increasingly fine resolution. In some ways, general circulation models, such as those used for IPCC simulations, are defined by the capabilities of the most powerful computers. We need to be able to use these models to produce simulations of several hundred years within a reasonable time on available computers. Long simulations, necessary to understand past climate changes reconstructed using multiple indicators and the need to explore different scenarios and model parameters, require faster models. Today's general circulation models will no doubt become the intermediate complexity models of tomorrow, but this concept will continue to exist. In addition, it is important to retain this hierarchy of models because each type of model is established on different assumptions. By comparing the results of different models, it is possible to highlight the relative importance of a particular process which is included in one model but not in the other or which is represented differently in each model.

Conceptual Models

The main objective of the models described above is to try to reproduce the observations we have for the climate system and its variations in the past. As has been highlighted, modeling also aims to improve our understanding of these variations, and it is therefore useful to describe some aspects of the system using extremely simple models, which are intended to illustrate some key processes. These are called conceptual models. There are many varied examples. One example is the Lorenz model (Fig. 25.1d), which often serves as an archetype of the chaotic system. The meteorologist Edward Lorenz proposed a very simple model, based on an idealized thermal convection, which for the first time illustrated that the complexity of the behavior of a dynamic system was absolutely unrelated to the number of degrees of freedom of this system, as many previously imagined. He showed that a very simple system (in this case with only three degrees of freedom) can produce unpredictable behavior, called 'deterministic chaos'. This conceptual model still plays an important educational role, and its mathematical properties are still a subject of active research. Below, some examples directly relevant to the climate system are described in more detail. Other examples, shown in Chap. 28, aim to achieve a better understanding of the glacial-interglacial dynamics (Calder, Imbrie models etc.).

The Budyko/Sellers Model

The Earth's climate is determined above all by its radiative balance. By simulating simplified balances, it is possible to estimate the magnitude of a change in temperature caused by, for example, changes in the incident solar radiation (volcanic dust, changes in the solar constant, nuclear winter, etc.). In 1969, two publications (Budyko 1969, Sellers 1969) came to a somewhat surprising conclusion: if we take account of the feedback between temperature and albedo, a relatively small decrease in the solar constant (−1.5% or −2%) is enough for the Earth to completely freeze over. A similar result also occurs when the greenhouse effect is modified. This indicates that there is a critical threshold towards cooling which causes the climate system to move into a very different state. The meaning of these results has now become even more pertinent with the theory of Snowball Earth (Chap. 26).

In their original versions, Budyko's and Sellers' models are explicitly dependent on latitude and predict a temperature $T(y)$ where y is the latitude. A much simpler version can be formulated to represent the phenomenon of runaway albedo-temperature feedback, with a model with no geographical dimensions. Writing the radiative balance of the Earth as a global average:

$$(1-\alpha)\times\ S/4 = (1-\varepsilon)\sigma T^4 \qquad (25.7)$$

where α is the albedo of the Earth, S is the solar constant; ε is a corrective term to represent the greenhouse effect; σ is the Stefan-Bolztman constant; then the overall global temperature of the planet is easy to calculate.

The problem becomes more interesting with the albedo-temperature feedback. Indeed, if we assume that α is a decreasing function of T, with, for example a constant $\alpha(T)$ (~ 0.3) at high temperatures for a 'blue' planet, a constant $\alpha(T)$ (~ 0.7) at very cold temperatures for a 'white'

planet, and a linear $\alpha(T)$ in-between, then we obtain the diagram shown in Fig. 25.7.

The possibility of multiple equilibria leads to the existence of thresholds beyond which the climate system suddenly shifts to a new state of equilibrium. Moreover, this leads to a phenomenon of hysteresis, since it is not possible to easily return to the original state by reversing the disturbance. Thus, to return to the initial state, an inverse perturbation of much greater amplitude is necessary. This is one of the difficulties with the 'snowball' theory: although it is relatively 'easy' for the planet to freeze over completely, as was shown by Budyko and Sellers, it is much more difficult to get out of this cold state.

The Stommel Model (1961)

The existence of multiple equilibria concerns other components of the climate system and an important example in paleoclimatology is the Stommel model (Fig. 25.8).

The model is composed of two well-mixed boxes, of the same volume, representing a mass of cold water with low salinity for high latitudes (with temperature T_1 and salinity S_1) and a mass of warm water with high salinity for low latitudes (with temperature T_2 and of salinity S_2). The difference in density $\Delta\rho = \rho_2 - \rho_1$ between these two boxes is obtained as a function of the positive coefficients of thermal expansion α and saline contraction β assumed to be constant:

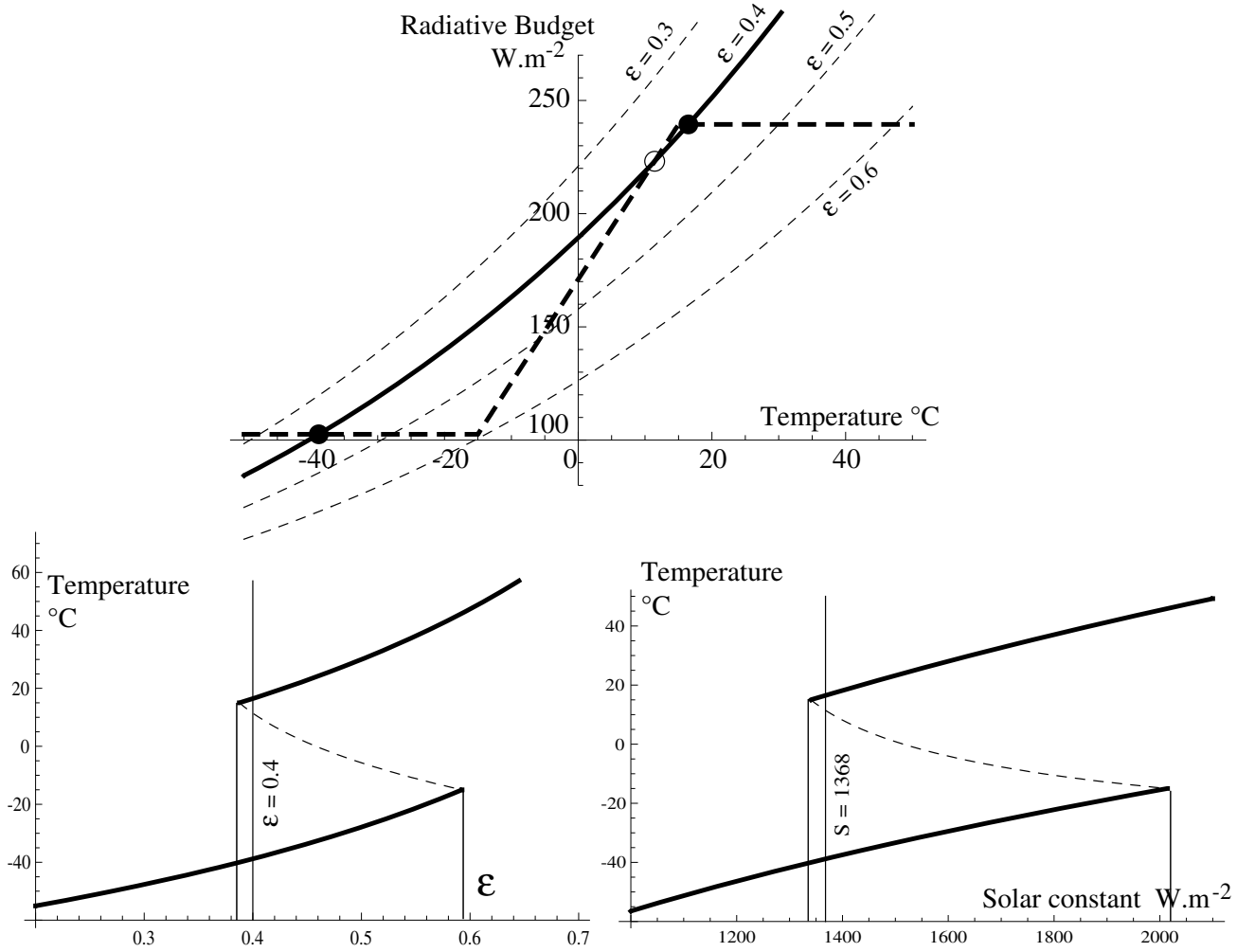

Fig. 25.7 Simplified Budyko and Sellers model. Top: dashed line, the solar term of the radiative balance, i.e. $(1 - \alpha(T)) \times S/4$, with $\alpha(T)$ linear between −15 and +15 °C, and constant beyond this range. Solid line, infrared term, for different values of the greenhouse effect. Balance is achieved when the curves intersect. Note that there are several points of equilibrium, especially for the current situation (ε = 0.4). Bottom: the corresponding points of radiative equilibrium as a function of the greenhouse effect ε (left), or as a function of the solar constant S (right). The equilibrium shown in dotted lines is unstable. For the current parameters, there are therefore two possible stable equilibria, corresponding either to our climate (temperature of around +15 °C) or to a completely frozen planet (temperature of around −40 °C)

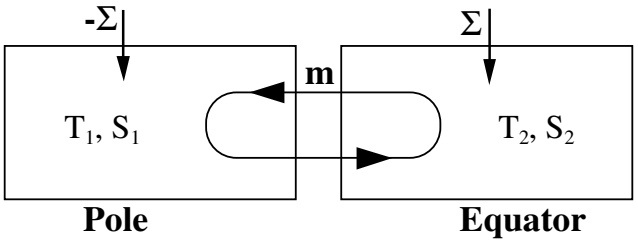

Fig. 25.8 Configuration of the Stommel model

$$\Delta\rho = -\alpha(T_2 - T_1) + \beta(S_2 - S_1) \tag{25.8}$$

A thermohaline circulation m, proportional to the difference in density between the two boxes, mixes the two corresponding bodies of water. This circulation will be positive (Fig. 25.8) when the cold water (box 1) is sufficiently dense to sink below the warm water (box 2), in other words when $\Delta\rho < 0$, and hence:

$$m = -\mu\Delta\rho = \mu[\alpha(T_2 - T_1) + \beta(S_2 - S_1)] \tag{25.9}$$

where μ is an arbitrary constant.

Conversely, if the saline water in box 2 is denser ($\Delta\rho > 0$), the thermohaline circulation m will be negative.

If we impose the temperature gradient $\Delta T = T_2 - T_1$ and force the salinities by applying a constant flow of salt Σ into box 2, and $-\Sigma$ into the box 1, we can infer the evolution in salinity, which are the only variables in the problem. For example, for box 1 (the strict opposite is in box 2):

$$\frac{dS_1}{dt} = -\Sigma + |m|(S_2 - S_1) = -\Sigma + \mu|\alpha\Delta T - \beta\Delta S|\Delta S. \tag{25.10}$$

The equilibrium (or equilibria) of the system is then easily obtained:

$$\Sigma = \mu|\alpha\Delta T - \beta\Delta S|\Delta S, \tag{25.11}$$

which gives a second-degree equation in ΔS, with an absolute value, which can be rewritten as:

$$F = x|1 - x| \text{ by setting: } x = \frac{\beta\Delta S}{\alpha\Delta T};\ F = \frac{\Sigma\beta}{\mu(\alpha\Delta T)^2} \tag{25.12}$$

The function $F(x)$ is plotted in Fig. 25.9.

The definition of x shows that x measures the intensity of the salinity gradient relative to the temperature gradient. The sign of m, and consequently, the direction of the thermohaline circulation is positive when x is less than one. The dominant effect is then that of the temperature gradient ΔT. This is a mode of 'thermal' circulation. This is the case for the unique solution x_T when F is negative. Conversely, if the imposed flux of salt Σ is sufficiently strong, and consequently, if F is large enough (greater than 0.25), the solution x_S of the problem is greater than 1, and the thermohaline circulation is reversed because the only equilibrium possible of the system is of the 'saline' type. On the other hand, for an intermediate value of the forcing F, the 'thermal' and 'saline' modes are both possible solutions of the problem.

A third equilibrium point also becomes possible with solution x_I. However, a rapid analysis of the stability of the equilibria obtained shows that this is an unstable equilibrium. In fact:

$$\frac{d\Delta S}{dt} = 2(\Sigma - |m|\Delta S) \tag{25.13}$$

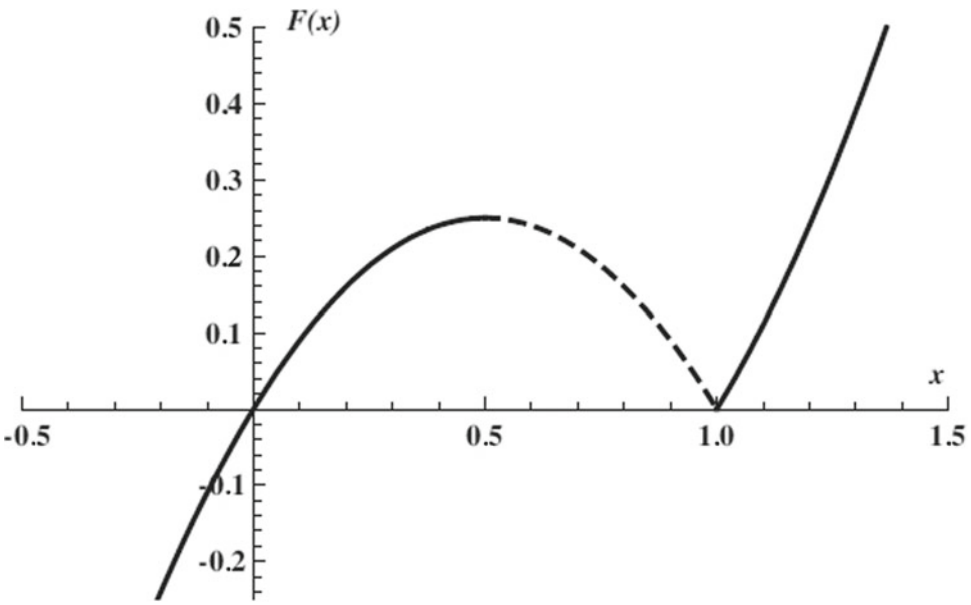

Fig. 25.9 Diagram of stability for the Stommel model (function $F(x)$ defined by Eq. (25.12)). The dotted section corresponds to an unstable equilibrium

The equilibrium is stable when any infinitesimal increase in the salinity gradient ΔS leads to an increase in the term $|m|\Delta S$, so that the derivative of ΔS relative to time becomes slightly negative. The direction of variation of $|m|\Delta S$ as a function of ΔS is in fact given directly by the figure representing $|1 - x|x$ as a function of x. The descending intermediate branch (dashed line in the figure) indicates a decrease in $|m|\Delta S$ when ΔS increases, leading to an unstable equilibrium. The 'thermal' and 'saline' branches, on the other hand, are perfectly stable. For the same value of the temperatures and the salt flux, there are therefore two stable equilibria possible in this system.

Interestingly, these multiple equilibria are found in much more complex models of the ocean, and even in some ocean-atmosphere coupled models (Rahmstorf 1996; Rahmstorf et al. 2005). It therefore seems that this very simple model captures an important aspect of thermohaline circulation, which explains the existence of sudden variations in the deep ocean circulation. These variations are most likely involved in the sudden climate changes observed during the ice ages (Heinrich events and Dansgaard-Oeschger events, see Chap. 29).

The Welander Model

The multiplicity of equilibria does not explain everything, and of course there are other types of possible behaviors. Another oceanographic example (Fig. 25.10), similar to the Stommel model, concerns convective-advective oscillations (Welander 1982). Although their relevance to climate variations is not established, some have suggested that these oscillations may play a role in the recurrence of Dansgaard-Oeschger events.

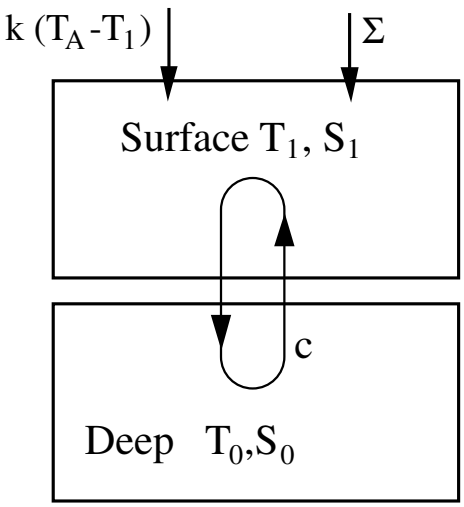

Fig. 25.10 Configuration of the Welander model (1982)

This model is composed of two superimposed boxes, one representing a mass of cold, low-salinity surface waters (temperature T_1 and salinity S_1), and the other a slightly warmer, saltier water mass for the depths (temperature T_0 and salinity S_0). The deep-water box is much larger than the surface water box, and we assume that T_0 and S_0 are constant. The difference in density $\Delta\rho = \rho_1 - \rho_0$ between these two boxes is obtained as a function of the positive coefficients of thermal expansion α and saline contraction β, assumed to be constant:

$$\Delta\rho = -\alpha(T_1 - T_0) + \beta(S_1 - S_0) \tag{25.14}$$

Vertical mixing (convection c) is very small if the column is well stratified (if $\Delta\rho < -\varepsilon < 0$). In the opposite case, it will be large:

$$c = c_0, \quad c_0 \text{ small if } \Delta\rho < -\varepsilon;$$
$$c = c_1, \quad c_1 \text{ large if } \Delta\rho > -\varepsilon.$$

The variables of the problem this time are the temperature and the salinity of the surface water box, and the equations for the corresponding evolution are formulated as follows:

$$\frac{dT_1}{dt} = k(T_A - T_1) + c(T_0 - T_1); \quad \frac{dS_1}{dt} = \Sigma + c(S_0 - S_1). \tag{25.15}$$

At equilibrium, the time derivatives in both equations are equal to zero, which yields:

$$T_1^e = \frac{kT_A + c^e T_O}{k + c^e}; \quad S_1^e = S_0 + \frac{\Sigma}{c^e} \tag{25.16}$$

where c^e is the value of the vertical mixing for a temperature T_1^e and a salinity S_1^e, that is, for a density difference of $\Delta\rho^e$ ($c^e = c_0$ if $\Delta\rho^e < -\varepsilon$; $c^e = c_1$ otherwise). This leads to a solution:

$$\Delta\rho^e = -\alpha\frac{k(T_A - T_O)}{k + c^e(\Delta\rho^e)} + \beta\frac{\Sigma}{c^e(\Delta\rho^e)}; \text{ i.e. } \Delta\rho^e = F(\Delta\rho^e) \tag{25.17}$$

where F is a constant depending on the sign of $\Delta\rho$ ($F = F_0$ if $\Delta\rho^e < -\varepsilon$; $F = F_1$ otherwise). So, there are zero, one or two solutions, depending on the parameter values, as shown in Fig. 25.11.

In general, if c is a continuous function of $\Delta\rho$ then $F(\Delta\rho)$ will also be a continuous function and there will be an odd number of solutions, alternately stable and unstable, as in the Stommel model. The case of 'zero solution' in Fig. 25.11 (discontinuous case) would in fact correspond to an 'unstable equilibrium' for a continuous model. There is then a boundary cycle (an oscillation): in the absence of intense convection ($c = c_0$), there is a tendency towards an equilibrium in the other domain (with a strong convection,

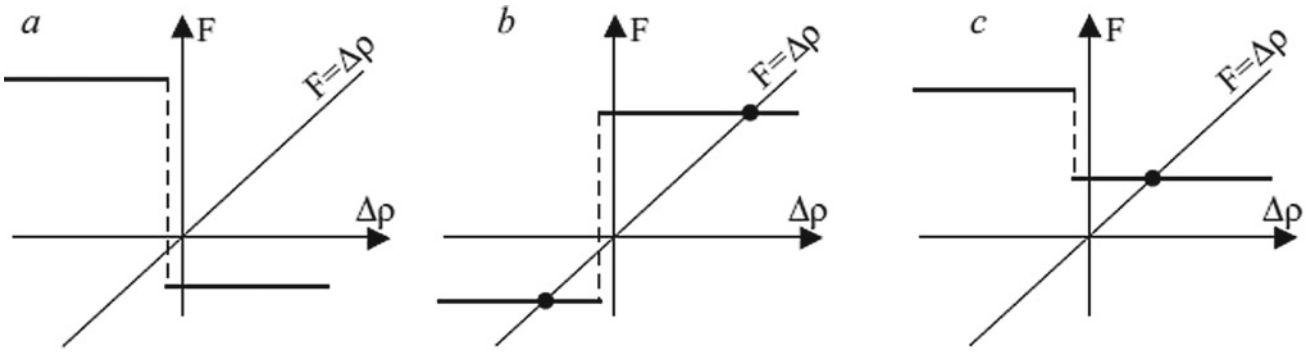

Fig. 25.11 Examples of equilibria given by $F = \Delta\rho$, where F is discontinuous and can only have two constant values. Depending on these values, there are three possible cases: **a** there is no solution (in fact, the system oscillates); **b** there are two equilibria which coexist, one convective and the other diffusive; **c** there is only one equilibrium (convective or diffusive)

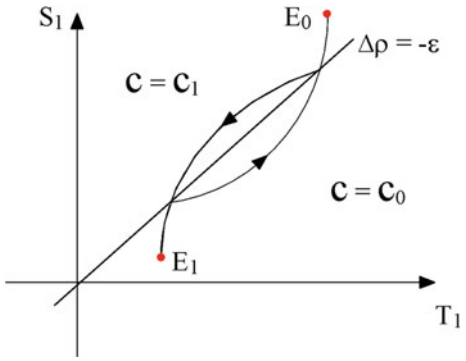

Fig. 25.12 Relaxed oscillation in the Welander model. On a *TS* diagram, a convective zone (when the density ρ_1 is large) and a diffusive zone, separated by an iso-density curve $\Delta\rho = -\varepsilon$, are defined. If the values T, S are located in the convective zone ($c = c_1$), the model tends to bring them back to the point of attraction E_1 (located in the diffusive zone). If they are in the diffusive domain ($c = c_0$), the model tends to bring them back to the point of attraction E_0 (located in the convective zone). The model will thus oscillate from one mode of operation to another, without ever reaching equilibrium

$c = c_1$), as indicated in Fig. 25.12. There is then an oscillation between a 'diffusive' state (c small = c_0) and a 'convective' state (c large = c_1). These type of oscillations have also been observed, under certain conditions, in three-dimensional ocean models.

Conclusions and Outlook

In this chapter, we explained the basic principles of climate modeling and illustrated their application through examples using models of different levels of complexity to show the strengths of each model type. This hierarchy of climate models is important not only for practical reasons related to the computing time required to study a particular scale of space or time, but above all, because it represents a range of grouped assumptions in each model type, which are necessary to understand the issue at hand. Using models based on different assumptions, it is possible to compare their importance and to better understand the role of a specific process. In principle then, one model is not more reliable than another. A model is always based on a set of assumptions and its relevance must be judged in relation to the question that the modeler has chosen to study. A model generally provides a result, without any uncertainty explicitly associated with this result. The uncertainty is concealed within the assumptions on which the model is based and in the imposed boundary conditions, which, although as realistic as possible, are never as well defined as we would ideally like. It is therefore interesting to compare the results of several models with the same boundary conditions, just as it is interesting to study the sensitivity of the results of a model to certain conditions with poorly constrained boundaries. This may help to determine if a better understanding of these conditions is required or if this is of little importance for the climate being studied.

Here, we mostly described the use of global models. We showed that the resolution of these models, even of the most complex ones, does not always allow comparison with reconstructions which are often representative of regions much smaller than the 'boxes' of a model. We saw that the modeling of paleoclimate indicators such as isotopes permits a more precise comparison and also an analysis of the recorded signal as a function of climate parameters. There are also models with a finer resolution that can be used on a regional scale. The use of this type of model for paleoclimates, still quite limited at the present time, is bound to develop in the future, in parallel with their increasing use for climate forecasts. An example of downscaling methods is given for the Last Glacial Maximum by Jost et al. (2005), which highlights the significant differences between the simulated climates at the European scale using these methods. There is still a lot of work to be done to generate these models. It should be noted that there

are also regional models which include a representation of climate indicators such as water isotopes (e.g., REMO-ISO, Sturm et al. 2007).

The evolution of climate models in the near future will involve not only an increasingly fine resolution as computing power increases and an explicit resolution of phenomena previously parametrized or ignored, but also the construction of increasingly comprehensive models of the climate system. Not only will the physical and dynamic aspects of the climate system be addressed, but also the biogeochemical cycles, in particular the carbon cycle. This trend is already emerging and is important not only to understand the evolution of past climates but also to forecast the climates of the future (see Chap. 31).

For Further Information

McGuffie, K., & Henderson-Sellers, A. (2005). *A climate modelling primer* (3rd ed., 280 p). Wiley.

References

Berger, A., (1978). Long-term variations of daily insolation and quaternary climatic changes. *Journal of the Atmospheric Sciences, 35*, 2362–2367.

Berger, A., et al. (1998). Sensitivity of the LLN Climate model to the astronomical and CO_2 forcings over the last 200 Ky. *Climate Dynamics, 14,* 615–629.

Braconnot, P., et al. (2007a). Results of PMIP2 coupled simulations of the Mid-Holocene and Last Glacial Maximum—Part 1: Experiments and large-scale features. *Climate of the Past, 3,* 261–277.

Braconnot, P., et al. (2007b). Results of PMIP2 coupled simulations of the Mid-Holocene and Last Glacial Maximum—Part 2: Feedbacks with emphasis on the location of the ITCZ and mid- and high latitudes heat budget. *Climate of the Past, 3,* 279–296.

Budyko, M. (1969). The effect of solar radiation variations on the climate of the earth. *Tellus, 21,* 611–619.

Calov, R., et al. (2002). Large-scale instabilities of the Laurentide ice sheet simulated in a fully coupled climate-system model. *Geophysical Research Letters, 29*, 2216.

Claussen, M., et al. (2002). Earth system models of Intermediate complexity: Closing the gap in the spectrum of climate system models. *Climate Dynamics, 18,* 579–586.

CLIMAP. (1976). The surface of the Ice-Age earth. *Science, 191*, 1138–1141.

CLIMAP. (1981). *Seasonal reconstructions of the earth's Surface at the Last Glacial Maximum*. Geological Society of America, Map Chart Series MC-36, Boulder, Colorado.

Gates, W. L. (1976). Modeling the Ice-Age climate. *Science, 191*, 1138–1144.

Gallée, H., van Ypersele, J.-P., Fichefet, T., Marsiat, I., Tricot, C., Berger, A. (1992). Simulation of the Last Glacial cycle by a coupled, sectorially averaged climate-ice sheet model. 2. Response to insolation and CO2 variations. *Journal of Geophysical Research, 971*, 15713–15740. https://doi.org/10.1029/92JD01256.

Hargreaves, J. C., et al. (2007). Linking Glacial and future Climates through an ensemble of GCM simulations. *Climate of the Past, 3,* 77–87.

IPCC. (2007). 4e rapport. http://www.ipcc.ch.

Jouzel, J., et al. (1993). Vostok ice cores: Extending the climatic records over the penultimate Glacial Period. *Nature, 364,* 407–412.

Joussaume, S. & Taylor, K. E. (1995). Status of the paleoclimate modeling intercomparison project (PMIP). In *Proceedings of the First International AMIP Scientific Conference*. WCRP Report, (pp. 425–430).

Jost, A., Lunt, D., Kageyama, M., Abe-Ouchi, A., Peyron, O., Valdes, P. J., Ramstein, G. (2005). High resolution simulations of the Last Glacial Maximum climate over Europe: A solution to discrepancies with continental paleoclimatic reconstructions? *Climate Dynamics, 24*, 577–590. https://doi.org/10.1007/s00382-005-0009-4.

Kageyama, M., Braconnot, P., Harrison, S. P., Haywood, A. M., Jungclaus, J. H., Otto-Bliesner, B. L., et al. (2018). The PMIP4 contribution to CMIP6—Part 1: Overview and over-arching analysis plan. *Geoscientific Model Development, 11,* 1033–1057. https://doi.org/10.5194/gmd-11-1033-2018.

Laskar, J., Robutel, P., Joutel, F., Gastineau, M., Correia, A., Levrard, B. A. (2004). A long-term numerical solution for the insolation quantities of the earth. *428*. https://doi.org/10.1051/0004-6361:20041335.

Lorenz, E. (1963). Deterministic nonperiodic flow. *Journal of the Atmospheric Sciences, 20,* 130–141.

Loutre, M.-F., & Berger, A. (2000). No Glacial-Interglacial cycle in the ice volume simulated under a constant astronomical forcing and a variable CO_2. *Geophysical Research Letters, 27,* 783–786.

Manabe, S., & Broccoli, A. J. (1985). A comparison of climate model Sensitivity with data from the Last Glacial Maximum. *Journal of the Atmospheric Sciences*, *42*, 2643–2651.

Peyron, O., et al. (1998). Climatic reconstruction in Europe for 18,000 YR B.P. from Pollen Data. *Quaternary Research, 49,* 183–196.

Rahmstorf, S. (1996). On the freshwater forcing and transport of the Atlantic Thermohaline circulation. *Climate Dynamics, 12,* 799–811.

Rahmstorf, S., et al. (2005). Thermohaline circulation hysteresis: A model intercomparison. *Geophysical Research Letters, 32,* L23605.

Ramstein, G., et al. (2007). How cold was Europe at the Last Glacial Maximum? A synthesis of the progress achieved since the first PMIP model-data comparison. *Climate of the Past, 3,* 331–339.

Roche, D., & Paillard, D. (2005). Modelling the oxygen-18 and rapid Glacial climatic events: A data–model comparison. *Comptes Rendus Geoscience, 337,* 928–934.

Schneider von Deimling, T., et al. (2006). Climate sensitivity estimated from ensemble simulations of Glacial Climate. *Climate Dynamics, 27,* 149–163.

Sellers, W. (1969). A global climatic model based on the energy balance of the earth-atmosphere system. *Journal of Applied Meteorology, 8,* 392–400.

Stein, U., & Alpert, P. (1993). Factor separation in numerical simulations. *Journal of the Atmospheric Sciences, 50*, 2107–2115.

Sturm, C. et al. (2007). Simulation of the stable water isotopes in precipitation over South America: Comparing regional to global circulation models. *Journal of Climate, 20*, 3730–3750.

Stommel, H. (1961). Thermohaline convection with two stable regimes of flow. *Tellus, 13,* 224–230.

Welander, P. (1982). A simple heat salt oscillator. *Dynamics of Atmosphere and Oceans, 6,* 233–242.

Wu, H., et al. (2007). Climatic changes in Eurasia and Africa at the Last Glacial Maximum and Mid-Holocene: Reconstruction from Pollen Data using inverse Vegetation modelling. *Climate Dynamics, 29,* 211–229.

The Precambrian Climate

26

Yves Goddéris, Gilles Ramstein, and Guillaume Le Hir

More than 88% of the history of the Earth occurred in the Precambrian. The Precambrian began with the formation of the Earth 4.6 billion years ago (Ga) and ended 542 million years ago (International Stratigraphic Chart, www.stratigraphy.org). It is subdivided into two large eons: the Archean (between 4 and 2.5 Ga) and the Proterozoic (from 2.5 to 0.542 Ga). The *International Commission on Stratigraphy* is proposing to add an extra eon, the Hadean, covering the first 600 million years of the history of our planet. Notwithstanding, this eon is described as having an *informal* status since no pre-Archean rock has been observed today. In fact, the oldest rocks date back to 4 billion years ago (U/Pb dating on zircon crystals). These are the Acasta gneisses in the Slave Province of Canada. The two formal eons of the Precambrian are subdivided into eras. In particular, the Proterozoic contains three eras: Paleoproterozoic (2.5–1.6 Ga), Mesoproterozoic (1.6–1.0 Ga) and Neoproterozoic (1.0–0.542 Ga).

Today, we find outcrops from the Archean on all the continents. Among the largest, two fragments of continents larger than 0.5×10^6 km^2 were identified: the craters of Kaapvaal (South Africa) and Pilbara (Australia). They are dated at about 3.6–2.9 Ga. Finally, the Precambrian has witnessed several major events in the history of the Earth. These include the onset of plate tectonics, the emergence of the biosphere at least 3.5 billion years ago, the rapid expansion of land surfaces between 3.2 and 2.6 billion years ago and the growth of the partial pressure of oxygen in the atmosphere around 2.3 Ga.

Climate Indicators

Little is known about the evolution of the Earth's climate during the Precambrian. The number of indicators available is very limited. Firstly, sedimentological data are difficult to interpret, given the age of these sediments which have generally been disarranged. Secondly, paleontological data are virtually unusable in terms of climate reconstruction. They are fragmentary and represent only a very simple monocellular biosphere, which is difficult to relate to any environmental evolution. Finally, the isotopic data measured on sediments generally have poorly preserved the original climate signal, having been very often subjected to post-deposit perturbations (diagenesis in particular). From a quantitative perspective, two isotopic signals have been used with varying degrees of success: $\delta^{18}O$ measured on siliceous (cherts) sediments since the 1970s (Knauth and Epstein 1976) and, more recently, the $\delta^{30}Si$ ratio measured on the same cherts (Robert and Chaussidon 2006).

Opal (SiO_2) was precipitated massively during the Archean. The reasons for this level of precipitation are unknown. It may have been caused by biological activity or directly abiotically from the silica-saturated ocean. Finally, this opal may have been produced during the stabilization of clay minerals on the seabed or may be derived from the weathering of volcanic glass. It was subsequently subjected to diagenesis and today appears as siliceous sedimentary rocks called cherts. The isotopic oxygen ($\delta^{18}O$) compositions of these cherts show them to be increasingly depleted in heavy isotopes as we go back in time, reaching a value of 16‰ compared to the international standard SMOW, 3 Ga ago (Fig. 26.1).

Y. Goddéris (✉)
Géoscience Environnement Toulouse, CNRS, Université de Toulouse III, UMR 5563, Toulouse, France
e-mail: yves.godderis@gmail.com

G. Ramstein
Laboratoire des Sciences du Climat et de l'Environnement, LSCE/IPSL, CEA-CNRS-UVSQ, Université Paris-Saclay, 91190 Gif-Sur-Yvette, France

G. Le Hir
Institut de Physique du Globe, CNRS, Université Pierre et Marie Curie, UMR 7154, Paris, France

G. Ramstein et al. (eds.), *Paleoclimatology*, Frontiers in Earth Sciences,
https://doi.org/10.1007/978-3-030-24982-3_26

Table 26.1 U-Pb and Re-Os geochronological constraints on Cryogenian glacial onsets and terminations

Paleocontinent	Age (Ma)	Method[a]	Reference
Marinoan deglaciation/cap carbonate: 636.0–634.7 Ma			
Laurentia	>632.3 ± 5.9	Re-Os	(63)
South China	635.2 ± 0.5	U-Pb ID-TIMS	(57)
Southern Australia	636.41 ± 0.45	U-Pb CA-ID-TIMS	(59)
Swakop	635.21 ± 0.59/0.61/0.92	U-Pb CA-ID-TIMS	(56, 83)
Marinoan glacial onset: 649.9–639.0 Ma			
Congo	>639.29 ± 0.26/0.31/0.75	U-Pb CA-ID-TIMS	(83)
Southern Australia	<645.1 ± 4.3	Re-Os	(137)
South China	<654.2 ± 2.7	U-Pb SIMS	(134)
South China	<654.5 ± 3.8	U-Pb SIMS	(58)
Sturtian deglaciation/cap carbonate: 659.3–658.5 Ma			
Southern Australia	>657.2 ± 2.4	Re-Os	(137)
Tuva-Mongol ia	659.0 ± 4.5	Re-Os	(63)
Southern Australia	<659.7 ± 5.3	U-Pb SIMS	(366)
Laurentia	662.4 ± 3.9	Re-Os	(60)
South China	>662.7 ± 6.2	U-Pb SIMS	(65)
Sturtian glacial onset: 717.5–716.3 Ma			
Oman	>713.7 ± 0.5	U-Pb ID-TIMS	(365)
South China	<714.6 ± 5.2	U-Pb SIMS	(64)
South China	<715.9 ± 2.3	U-Pb SIMS	(62)
South China	<716.1 ± 3.4	U-Pb SIMS	(62)
Laurentia	>716.5 ± 0.2	U-Pb CA-ID-TIMS	(32)
Laurentia	<717.4 ± 0.1	U-Pb CA-ID-TIMs	(32)
Laurentia	<719.47 ± 0.29	U-Pb CA-ID-TIMS	(61)

Re-Os isochron ages from sedimentary organic matter. Errors are quoted at the 2σ level of uncertainty. Where multiple uncertainties are given, they represent analytical/analytical + tracer solution/analytical + tracer solution + decay-constant uncertainties
Ca chemical abrasion; *ID6TIMS* isotope-dilution and termal-ionization mass spectrometry; *SIMS* secondary-ion mass spectrometry
Table from Hoffman et al., Sci. Adv. (2017)

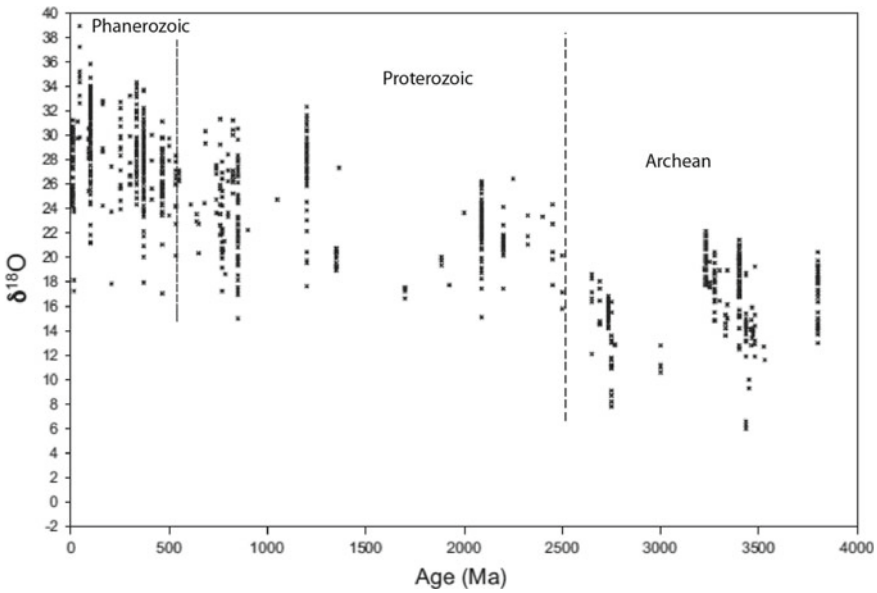

Fig. 26.1 The $\delta^{18}O$ of the Precambrian ocean measured in the cherts

As for carbonates, the $\delta^{18}O$ of silica is a function of the temperature and of the $\delta^{18}O$ of the water in which the silica precipitated:

$$1000 \ln \alpha = \left(3.09 \times \frac{10^6}{T(K)^2}\right) \quad (26.1)$$

where the fractionation factor

$$\alpha = \frac{1000 + \delta^{18}O_{chert}(SMOW)}{1000 + \delta^{18}O_{water}(SMOW)} \quad (26.2)$$

ln denotes its natural logarithm, and $\delta^{18}O_{water}$ is the $\delta^{18}O$ of the water from which the cherts precipitated.

Applied to the cherts, assuming that the isotopic composition of seawater was quite similar to that of today, this paleothermometer predicts the temperatures T of the water from which the cherts precipitated to be close to 85 °C 3 Ga ago, and 50 °C at the Precambrian-Cambrian boundary.

These temperatures are either the sign of very hot oceans or the consequence of an alteration of the cherts after deposition by meteoric or hydrothermal fluids, in which case they provide no information on climate. The question remains open because the $\delta^{18}O$ isotopic signal is particularly sensitive to diagenesis. A third hypothesis has been formulated more recently: it assumes that $\delta^{18}O$ of seawater was much lower than its present value, due to tectonic processes. Under these conditions, the temperature of the sea water could have been similar to the current one. Unfortunately, there is no constraint on the $\delta^{18}O$ of seawater during the Archean. Authors generally assume that this ratio remained constant over time at −1‰ in comparison with the SMOW, calculated from the level of the current ocean which would have received the melt water from all the ice caps on land. This value is the result of the equilibrium that is supposed to exist between the ^{18}O depletion of sea water resulting from the interactions between water and lithosphere at low temperatures and its ^{18}O enrichment during water/lithosphere interactions at high temperature in the hydrothermal systems. Recent work (Kasting et al. 2006) suggests that the $\delta^{18}O$ ratio may have been significantly lower (−9‰ compared to SMOW) during the Archean and Proterozoic periods. This argument is based on the fact that the Archean oceans were probably shallower than the oceans are currently. This results in a shallower water column over the oceanic ridges before 800 Ma, implying a reduction in hydrostatic pressure in the hydrothermal systems. This decrease in pressure limited the penetration of seawater into the ridges in the depths, thus reducing the gain in ^{18}O by sea water through alteration at high-temperature of the oceanic crust ($T > 350$ °C). This reduction in flux at high temperature results in an imbalance in the ^{18}O cycle in the ocean-atmosphere system and its stabilization at lower values than is currently the case. If this scenario proves to be correct, the temperature of the water as inferred from the $\delta^{18}O$ data on cherts, could be significantly lower. Kasting and Howard (2006) argue in favor of 'moderate' climates at the end of the Archean and during the Proterozoic.

An additional element was added to this debate by Robert and Chaussidon (2006), who measured the isotopic composition of silicon ($\delta^{30}Si$) in Precambrian cherts which is distinctly less sensitive to diagenesis than $\delta^{18}O$. These data, when translated into temperatures, (requiring the use of a silicon cycle model and therefore additional assumptions), suggest temperatures of around 70 °C, 3 Ga ago, and 20 °C, 800 million years ago, thus confirming very high temperatures in the distant past.

There remains a potentially major problem: the formation conditions of Precambrian cherts are unknown. Nevertheless, these results showing a gradual cooling of sea water from very high values seem to have been confirmed recently by a totally independent method, based on the resurrection of proteins of unicellular Archean organisms using phylogenetic and statistical methods of analysis (Gaucher et al. 2008).

Finally, irrespective of any debate on the terrestrial temperature during the Archean/Proterozoic, the $\delta^{18}O$ of the cherts show a significant increase at the end of the Archean, between 2.7 and 2.5 Ga (of about 10‰), suggesting a rapid cooling of the oceans of about 20 °C (Fig. 26.2).

The Theory of the Paleothermostat

In 1981, Walker, Hays and Kasting published a ground-breaking article explaining why the climate remained relatively stable (within a temperature range allowing water to remain in the liquid state) for between one million to one billion years (Walker et al. 1981). This study was carried out in order to solve the faint young sun paradox. The models of stellar evolution predict the evolution of the solar constant during the history of the Earth and make it possible to calculate that during the Archean, it would have been 20–30% weaker than today. Under these conditions, the Earth should have totally frozen over although this contradicts the isotopic data which provide an estimate of the temperature of the fluid envelopes of the Earth.

The residence time of the exosphere carbon content (i.e. all the carbon contained in the ocean, the biosphere and the atmosphere) is around 200,000 years which is very short compared to the geological processes of sedimentary carbon burial and continental weathering (François and Goddéris 1998). This measure gives an indication of the average time spent by a carbon atom entering the ocean-atmosphere system via volcanic degassing, for example, before exiting via sedimentary deposits. This response time is very short in the

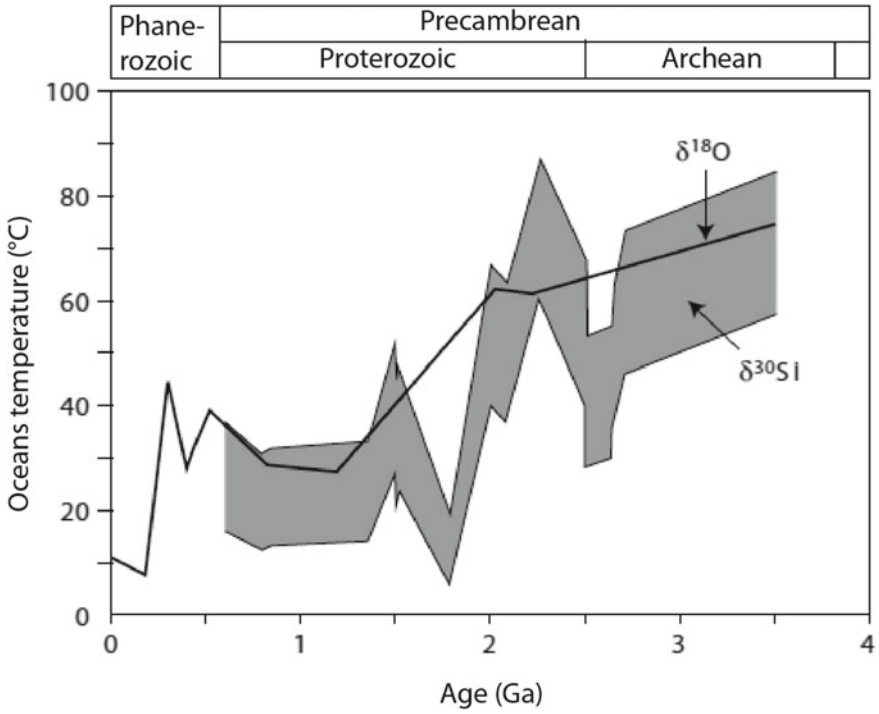

Fig. 26.2 Ocean temperatures reconstructed from δ^{30}Si and from δ^{18}O of Precambrian cherts

context of geological time. If the history of the Earth was condensed into one day, the entire carbon content of the ocean and atmosphere would be recycled about every 3 s. This short response time is obviously linked to the small size of the exosphere carbon reservoir (3×10^{18} mol) and to the fluxes in exchanges of matter (of around 10^{12}–10^{13} mol of carbon per year) between this reservoir and the geological reservoirs. The implications of this short residence time are important for the climate. Any imbalance between the carbon inflows (e.g. solid soil degassing) and outflows (e.g. CO_2 consumption due to silicate weathering) that would have occurred over several million years (a short timescale compared to the history of the Earth) would cause gigantic fluctuations (several orders of magnitude) of the carbon dioxide content in the atmosphere, with dramatic consequences for the climate. Fluctuations of this scale have not occurred in the history of the Earth, apart from some isolated episodes of global glaciations at the end of the Proterozoic. The carbon input and output flows must therefore be close to equilibrium over the geological time scale, from 10^6 to 10^9 years (see François and Goddéris (1998) for a complete mathematical assessment).

The carbon cycle at the million-year scale is described in Fig. 26.3. Only geological flows are taken into account, all rapid recycling (biosphere fluxes and ocean-atmosphere interface) are ignored.

The inflows to the ocean-atmosphere system are soil degassing from volcanoes, F_{vol} and from the oceanic ridges F_{MOR}; the dissolution of the continental carbonates which transfers carbon from the continental crust to the ocean in the dissolved form $HCO_3^- F_{cw}$; and the oxidation of old sedimentary organic compounds exposed to the atmosphere F_{ow} (black shales, for example, sediments rich in organic matter deposited during episodes of large-scale ocean anoxia and which are exposed to the atmosphere by tectonic activity):

$$CaCO_3 + CO_2 + H_2O \rightarrow Ca^{2+} + 2HCO_3^- \qquad (26.3)$$

dissolution of continental carbonates by carbonic acid:

$$CH_2O + O_2 \rightarrow 2HCO_3^- + H^+ \qquad (26.4)$$

oxidation of sedimentary organic carbon.

The sinks are represented by the precipitation of carbonate minerals F_{cd} on the ocean floor or on the continental shelves, through the mediation or not of biocalcification, and the burial of organic carbon within sediments F_{od}, both on land and in the ocean.

$$Ca^{2+} + 2HCO_3^- \rightarrow CaCO_3 + CO_2 + H_2O \qquad (26.5)$$

precipitation of carbonates

$$CO_2 + H_2O \rightarrow CH_2O + O_2 \qquad (26.6)$$

autotrophic productivity and burial of organic carbon.

The long-term equilibrium of the carbon cycle, mathematically required because of its low residence time in the

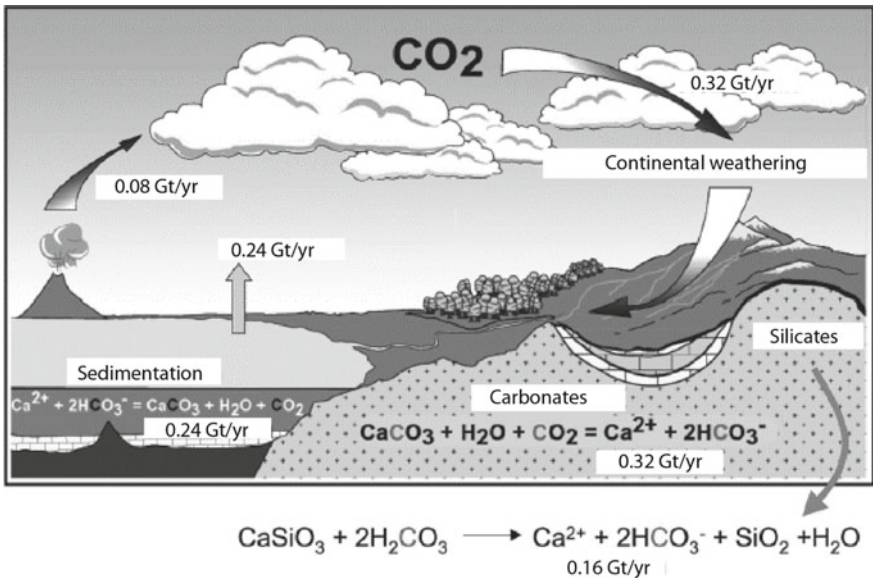

Fig. 26.3 The exosphere carbon cycle at the scale of a million years

exosphere system, results in the following proximate equation, which needs to be maintained on time scales of a million years to ensure relative stability of the climate:

$$F_{vol} + F_{MOR} + F_{cw} + F_{ow} \approx F_{cd} + F_{od} \tag{26.7}$$

Small deviations from this near equality are likely to explain the climate fluctuations, which may be as significant as the establishment of the Permo-Carboniferous glaciation or the climate optimum in the mid-Cretaceous. In general, under the effect of geological forcings, these imbalances are two orders of magnitude smaller than the fluxes themselves (François and Goddéris 1998). However, this quasi-equilibrium requires a physical basis, which the theory of the paleothermostat described below provides.

The flux of silicate weathering F_{sw} does not appear in the carbon balance because the silicates are not present in the continental crust in significant amounts. Yet, this flow actually consumes carbon from the exosphere:

$$CaSiO_3 + 2CO_2 + 2H_2O \rightarrow Ca^{2+} + 2HCO_3^- + SiO_2 \tag{26.8}$$

This reaction is a generic reaction, the silicate mineral (here the Wollastonite) is scarce on Earth, but it accounts for the alteration budget and therefore illustrates the point. The Ca^{2+} and HCO_3^- ions are carried to the ocean by the rivers. If the ocean is saturated with carbonate minerals, this increased alkalinity will cause the precipitation of calcium carbonates (Eq. 26.5), and thus the storage of exosphere carbon in the sedimentary envelope of the Earth. The contribution of alkalinity to the ocean is thus represented by silicate weathering and carbonates, whereas the loss of alkalinity is related to precipitation of the carbonates. The response time of the alkalinity cycle to any geological perturbation is around 3000 years, and is directly related to the ocean's mixing time which constrains the response time of the alkalinity of the world's oceans to any disturbance (François and Goddéris 1998). So, we again have the quasi-equality:

$$F_{sw} + F_{cw} \approx F_{cd} \tag{26.9}$$

The combination of the Eqs. (26.7) and (26.9) give the following proximate equation:

$$F_{vol} + F_{MOR} + F_{ow} \approx F_{sw} + F_{od} \tag{26.10}$$

If we ignore the existence of imbalances in the organic sub-cycle of carbon ($F_{ow} = F_{od}$, which is a strong assumption), we obtain:

$$F_{vol} + F_{MOR} \approx F_{sw} \tag{26.11}$$

The paleothermostat theory explains the physical reasons for this equality on the basis of two assumptions: firstly, that the weathering of continental silicate rocks depends on the climate and, in particular, on the temperature and the continental runoff. Secondly, excluding water vapor, atmospheric CO_2 is assumed to be the primary greenhouse gas whose variability controls the climate.

Concerning silicate weathering, the intuition of Walker et al. (1981), based on measurements of the dissolution rate of silicate minerals in the laboratory, has been largely verified in the natural environment. The consumption flux of atmospheric CO_2 by silicate weathering was measured on a

large number of monolithological silicate drainage basins, both granite $\left(F_{gra}\right)$ and basaltic (F_{bas}). It increases with temperature T and with continental runoff R according to the following laws:

$$\left(F_{gra}\right) = k_{gra} R \exp\left[-\frac{48200}{R}\left(\frac{1}{T}-\frac{1}{T_0}\right)\right] \tag{26.12}$$

$$(F_{bas}) = k_{bas} R \exp\left[-\frac{42300}{R}\left(\frac{1}{T}-\frac{1}{T_0}\right)\right] \tag{26.13}$$

where the fluxes are expressed in moles of CO_2 consumed per m^2 of land surface area and per year. The approximate Eq. (26.11) can thus be expressed as:

$$F_{vol} + F_{MAR} = A_{gra} k_{gra} R \exp\left[-\frac{48200}{R}\left(\frac{1}{T}-\frac{1}{T_0}\right)\right] + A_{bas} k_{bas} R \exp\left[-\frac{42300}{R}\left(\frac{1}{T}-\frac{1}{T_0}\right)\right] \tag{26.14}$$

where A_{gra} and A_{bas} are the land areas where granite and basalt areas touch. If, for some reason related to the internal geology, soil degassing increases, increases in temperature and runoff are required to maintain the carbon cycle balance. This increase occurs naturally due to the increase in the concentration of CO_2 in the atmosphere, in response to the degassing. Due to its dependence on climate, and because CO_2 is a greenhouse gas, the land silicate weathering on land will therefore track and compensate for the fluctuations in volcanic degassing of CO_2 over time and thus prevent massive fluctuations in the Earth's climate.

The paleothermostat theory is particularly useful to explain the absence of long-term global glaciations during the Archean, when the solar constant was 20–30% lower than it is currently. The colder climate resulting from the lower solar energy consumption led to a slowdown in the consumption of CO_2 by continental silicate weathering and therefore an increase in the CO_2 pressure in the air. The induced warming continued until the silicate weathering balanced out the soil degassing again. However, CO_2 is probably not the only greenhouse gas involved, which complicates the paleothermostat theory.

Methane, for example, is a less abundant but more efficient gas than CO_2 in terms of its greenhouse effect. Methane pressure results from the balance between its production time (methanogenesis) and its destruction time (oxidation by OH radials). In fact, any excess of methane over this balance is not very stable and connects with the CO_2 paleothermostat because a sudden injection of methane oxidizes quite quickly in CO_2.

Major Climate Events in the Precambrian

From 4.5 to 2.4 Ga

In the absence of indicators with the necessary level of resolution, the climate history of the Precambrian is essentially reconstructed through numerical modeling.

Three to four Ga ago, the solar constant was 30% lower than it is currently. In this context, extremely high levels of greenhouse gases would have been required to prevent prolonged global glaciation, which has not been observed in the bedrock from that time or in preserved sediments. NH_3 was suggested initially as a cause but this is not a likely candidate because it is rapidly destroyed by photolysis. This is not true for CO_2. At least 0.3 bar of CO_2 is required in the atmosphere to counteract the low solar constant (Pavlov et al. 2000). The reasons for the presence of very high levels of CO_2 are related to the paleothermostat theory involving the erosion of continental silicates (Walker et al. 1981). The weaker solar constant forces the climate towards colder conditions. This limits the consumption of CO_2 by silicate erosion and allows the CO_2 concentration in the air to grow until the climate becomes sufficiently hot and humid to stabilize the weathering of the silicates so that it reaches the point where it compensates for the soil degassing, leading to a balance in the exosphere cycle of carbon. Moreover, since this degassing is suspected to have been much more intense in this distant past, following the dissipation of the internal heat of the Earth, the CO_2 concentration in the air will be set at a high value, essential to ensure a high level of chemical erosion of the silicates.

However, the absence of siderite ($FeCO_3$) in Archean paleosols suggests an upper ceiling of 0.015 bar of CO_2 in the atmosphere (see references in Catling and Claire 2005). Another greenhouse gas was therefore necessary and methane may have played this role. Methanogenic bacteria are probably among the first organisms to have evolved on the surface of the Earth, and they must have constituted an important part of the primitive biosphere as early as 3.5 Ga. Before 3.5 Ga, probably more methane degassed from the ocean ridges into the prebiotic atmosphere than nowadays, given the lower mantle at this time (Kump et al. 2001). The virtual absence of oxygen in the atmosphere before 2.2 – 2.3 Ga allowed the methane to accumulate in it, probably with mixing ratios of close to 1.6 ppmv, a value one thousand times higher than at present. The residence time of methane in air was also probably a thousand times greater than at present, because, in this weakly oxidized atmosphere, the OH radicals produced by photolysis of water reacted with H_2. As a result, the surface temperature of the Earth could have been as high as 85 °C (Kasting and Howard 2006).

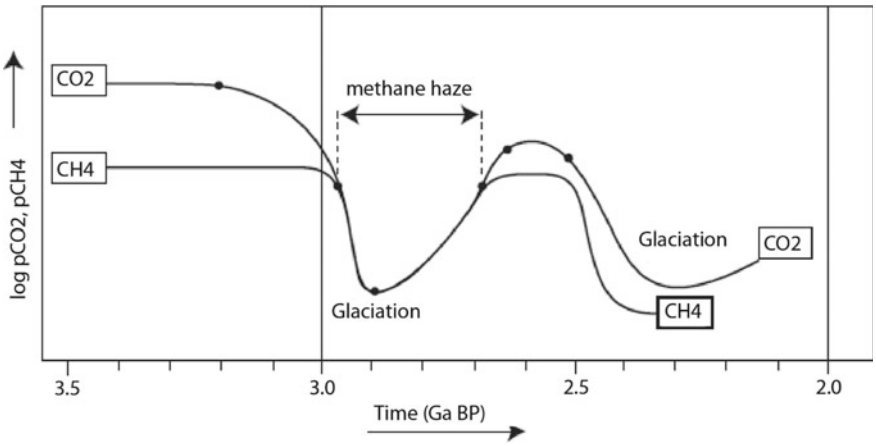

Fig. 26.4 Qualitative curve showing the evolution in the concentration of CO_2 and CH_4 in the atmosphere at the end of the Archean

The CH_4/CO_2 ratios probably remained well below 1 up to 3.0 Ga, preventing the formation of a haze of organic compounds in the atmosphere (Lowe and Tice 2004). However, in the 3.0–2.7 Ga range, the level of atmospheric CO_2 could have been considerably reduced, following the growth of the particularly active continental crust at that time. The continental crust had probably reached 60% of its present size, 3–2.9 Ga ago, whereas before 3.2 Ga it was only at 10%. In response to this growth in the surface area of the continents, silicate erosion increased, forcing the level of atmospheric CO_2 to decrease (Goddéris and Veizer 2000; Lowe and Tice 2004). The average global surface temperature dropped by 10 °C (Goddéris and Veizer 2000), at the same time as the CH_4/CO_2 ratio increased, allowing a haze of organic compounds to form around the Earth (Lowe and Tice 2004). This resulted in the cooling being reinforced before the paleothermostat slowly compensated. Traces of glaciations were indeed observed in the supergroups of Pongola and Witwatersrand in South Africa and in the green chists of Berlingue in Zimbabwe, all of these formations dating back to ~2.9 Ga (Fig. 26.4).

The Great Oxidation Event (GOE)

The geochemical and climatological event that marked the beginning of the Proterozoic is the oxygenation of the atmosphere. Biomarkers indicate that the first photosynthetic organisms appeared as early as 2.7 Ga. Atmospheric oxygen probably started to grow around 2.3 Ga. Over 100 or 200 million years, oxygen pressure increased from 10^{-5} bar to 2×10^{-2} bar (Catling and Claire 2005). The $\delta^{13}C$ of sedimentary carbonates (Fig. 26.5) shows a major surge of more than 10‰ at this time (see references in Catling and Claire 2005).

This increase in $\delta^{13}C$ is generally thought to result from the burial of a large amount of organic carbon; this burial caused an imbalance in the carbon cycle: organic matter, low in ^{13}C, was no longer depleted, while photosynthetic organisms continued to pump out carbon dioxide depleted in ^{13}C, causing an increase in the $\delta^{13}C$ of atmospheric CO_2 (reflected in the $\delta^{13}C$ of carbonates) and an increase in the O_2 content of the atmosphere (the oxygen created by photosynthesis not being fully consumed during the decay of

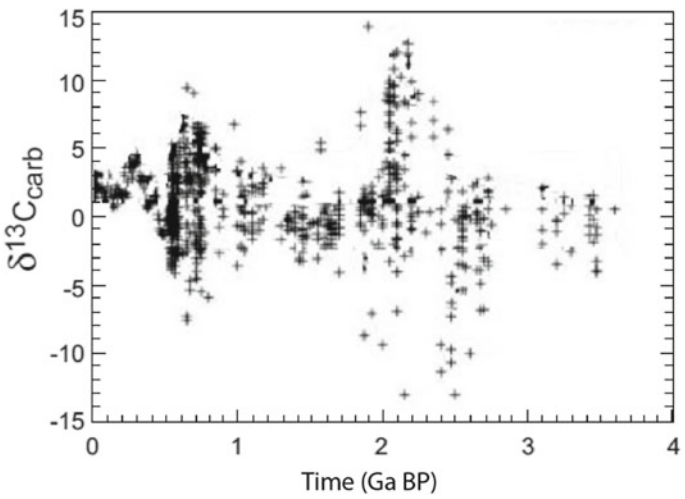

Fig. 26.5 The evolution of $\delta^{13}C$ in Precambrian carbonates

organic matter because of the increased level of conservation). The issue of the oxygen balance during the Paleoproterozoic is still debated to this day, and in particular, the possible role a decrease in the quantity of reduced gas degassed by the mantle is questioned (see references in Catling and Claire 2005). However, there is no doubt about the accumulation of O_2 between 2.3 and 2.1 Ga (Catling and Claire 2005). The GOE is also recorded in the variations in the isotopic composition of iron in sedimentary pyrites between 2.6 and 1.8 Ga, which is suspected to be related to the isotopic composition of seawater (Fig. 26.6). The δ^{56}Fe of these sediments shows widely dispersed values before 2.3 Ga, but this dispersion decreases considerably after 2.3 Ga. These changes are explained by the existence of an iron rich ocean, fed by hydrothermal springs (containing dissolved iron Fe^{2+}) before 2.3 Ga. This ocean periodically purges itself of a certain amount of its iron during the precipitation of iron oxides during upwelling episodes. Such purges brought water to more or less oxygenated zones. This precipitation extracts the isotope 56 preferentially from the iron; this process of fractional precipitation of iron is thus capable of modifying the δ^{56}Fe isotopic composition of the deep ocean so long as all the iron carried by the upwellings has not precipitated and a part of it returns to the deep ocean. After 2.3 Ga and the GOE, the Proterozoic ocean became stratified, characterized by a permanently and thoroughly oxygenated surface zone and an anoxic deep ocean. This configuration allows the precipitation of all of the hydrothermal Fe^{2+} brought by the upwellings (see references in Catling and Claire 2005). In this way, the isotopic composition of the deep ocean is no longer affected, since all the iron carried by upwellings precipitated, and stabilized at between 0 and 1‰. Finally, recent data using the independent fractionation of the mass of isotopes of sulfur Δ^{33}S confirm progressive oxidation of the surface layers from 2.4 to 2.3 Ga onwards (Papineau et al. 2007).

The consequences for the GOE climate were significant. The residence time of methane in the atmosphere decreased strongly and the concentration of CH_4 in the atmosphere probably fell to around 300–100 ppmv, a decrease by a factor of 5–16 compared to Archean values. This caused significant cooling, which could not be immediately compensated for by the low level of CO_2. This triggered the Huronian glaciations during the time it took for the paleothermostat to allow the partial pressure of CO_2 to rise. This major glacial phase may have included at least one episode of total glaciation, but paleomagnetic data on the position of the continental masses remain scanty and difficult to interpret. However, recent paleomagnetic studies show that the Huron glaciation was probably similar to the 'standard' glaciations of the Quaternary. However, the GOE context is completely different in terms of atmospheric composition, paleogeography, solar insolation… and therefore the rhythm of this glaciation is still an open question.

The Proterozoic

Following the Huronian glaciations, the Earth seems to have been subjected to a warm climate persisting over most of the Proterozoic, lasting for about 1 billion years. To date, no trace of glaciation has been found in the timespan 2–0.8 Ga. The measurement of δ^{13}C from acrytarches (microfossil remains of cysts of photosynthetic eukaryotic organisms) allows a rough estimation of the atmospheric CO_2 level. Indeed, the difference between these ratios and the mean ratio of oceanic carbonates (close to 0‰) defines, with some assumptions, the isotopic fractionation involved in photosynthesis that occurred during the Calvin cycle. This fractionation depends, among other things, on the CO_2 pressure of the water and can therefore be linked to atmospheric CO_2 pressure. At 1.4 Ga, the level of CO_2 was about 10–200

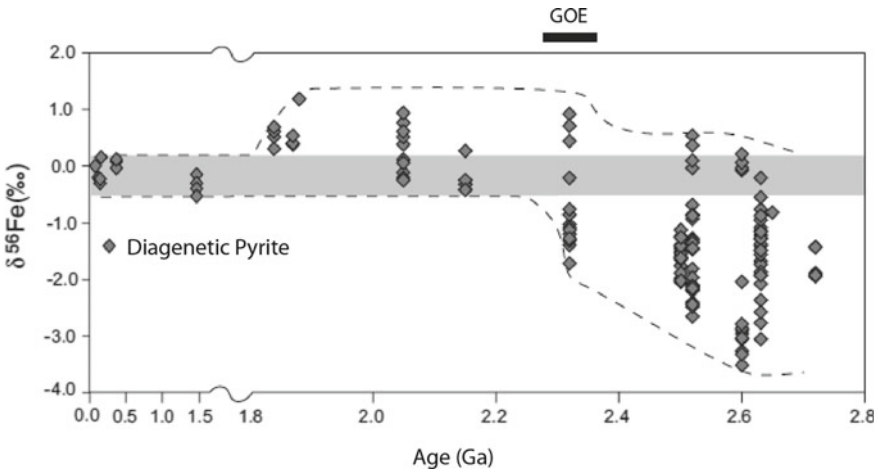

Fig. 26.6 The δ^{56}Fe of Precambrian sediments

times the pre-industrial level i.e. 2800–56,000 cm^3 of CO_2 per m^3 of air (Kaufman and Xiao 2003).

The level of Proterozoic methane is uncertain. The oxygen level (Fig. 26.7) is estimated to be about 5–18% of its current level, based on the low sulfate concentration of Proterozoic marine carbonates (Pavlov et al. 2003). Since these sulfates are produced by the oxidation of sulphides, their low abundance reflects a low partial pressure of oxygen. Based on these values, Pavlov et al. (2003) calculated a methane pressure in the range of 100–300 ppmv, assuming a CH_4 production in the deep anoxic ocean basins 20-fold higher than current levels. The surface temperature is unknown, the $\delta^{18}O$ of the cherts suggest 50 °C at the end of the Precambrian. As seen above, these high values remain questionable. In order to maintain an average global temperature of 15 °C on the Earth's surface, 300 PAL of CO_2 were needed at 2 Ga, and only 10 PAL at 0.6 Ga (1 PAL = present atmospheric level). Log_{10}.

The End of the Proterozoic: Global Glaciations

After more than a billion years of no glaciations, the end of the Proterozoic (the Neoproterozoic, from 900 to 543 Ma) was marked by the strongest glaciations in the history of the Earth. These are suspected to have been global, hence the name 'snowball' glaciations. Two events are acknowledged: the first between 723 and 667 Ma (the Sturtian glaciation) and the second between 667 and 634 million years (the Marinoan glaciation). They were followed by a glacial episode of lower intensity around 583 Ma, comparable to the glaciations of the Phanerozoic (the Gaskiers glaciation).

The Sturtian and Marinoan glaciations have a particular set of characteristics. (1) The paleolatitude of the glacial deposits was located mostly in the intertropical zone, which implies a major glaciation, since the ice reached the equator (Evans 2000). The histogram showing the presence of glacial deposits as a function of paleolatitude, is totally atypical for snowball glaciations. Although this histogram shows a peak at high latitudes for all of the Phanerozoic glaciations, this peak is displaced to the lower latitudes for snowball glaciations (Evans 2000). (2) Glacial deposits are directly overlaid with atypical carbonate deposits (cap carbonates) with no break, suggesting a transition of extraordinary rapidity on a geological scale from a very cold climate to a very hot climate (Hoffman et al. 1998). If the Earth was covered with ice, the hydrological cycle would have almost completely shut down, thereby allowing CO_2 to accumulate in the atmosphere as a result of volcanic degassing. When more than 0.29 bar of CO_2 has accumulated in the atmosphere (Pierrehumbert 2004), the greenhouse effect intensifies and deglaciation is suddenly initiated. A climate characterized by a strong greenhouse effect followed the very cold climate. Continental weathering recommenced and quickly reached a high level. The massive surge of alkalinity in the ocean became predominant over carbonates, which explains the presence of carbonate deposits directly on top of glacial deposits. (3) Banded iron formations (BIF) reappeared during and just after glaciation, although these had disappeared during the Proterozoic, around 1.8 Ga. The return of the BIFs is qualitatively compatible with the installation of sea ice over the whole of the oceans, greatly reducing the vertical mixing of the ocean and favoring the development of anoxic conditions in the deep ocean. The Fe^{2+} emitted at the ridges can therefore be transported by upwellings to the surface waters, where it precipitates as BIF in contact with oxygen. (4) The presence of an iridium peak in the basal cap carbonates suggests an accumulation of

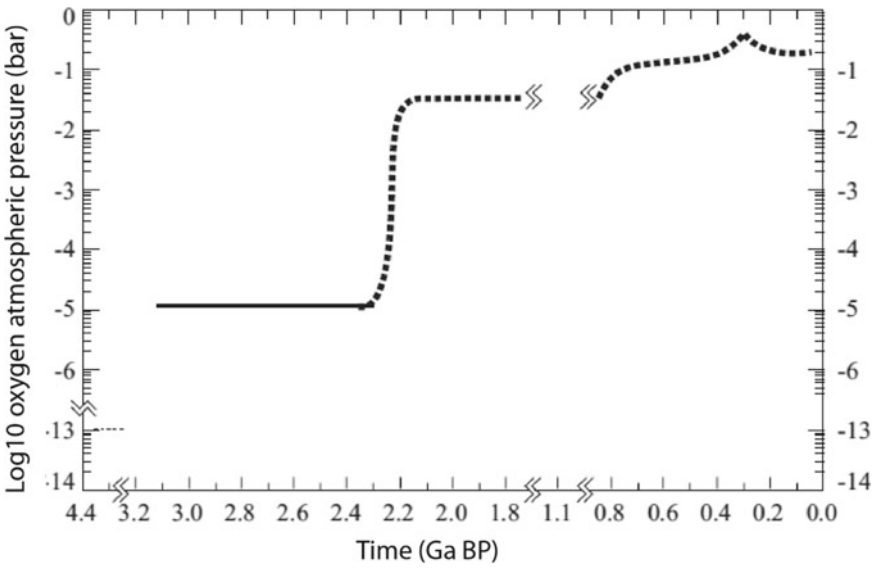

Fig. 26.7 History of the level of oxygen in the atmosphere

iridium (brought by cosmic materials falling to the ground) on pack ice for 3–12 million years and its inclusion in sediments at the time of an ice flood corresponding to the end of Marinoan glaciation (Bodiselitsch et al. 2005). These last decades the chronology of Neoproterozoic glaciations has been considerably improved. The chronology is now well established with two dissymmetric glaciations: a long lasting Sturtian episode for more that 50 Ma and a shorter Marinoan episode lasting around 15 Ma separated by a short interglacial period only lasting 10 Ma (Hoffman et al. 2017). (5) The $\delta^{13}C$ isotopic ratio of the cap carbonates is well documented, especially for the most recent snowball glaciation (Fig. 26.8). It is particularly low at around −3‰ towards the end of the glaciation, reaching very low values (−5‰) at the top of the cap carbonates (Halverson et al. 2005).

As early as 1998, Hoffman et al. interpreted this low value as a sign of shallow burial of organic carbon, in turn, an indicator of significantly slower biological productivity in the oceans. By taking the isotopic fractionation of carbon during photosynthesis at −20‰, the proportion of organic carbon buried relative to total carbon sedimentation increases from 10% at the base of the cap carbonates to 0% at the top (compared to 25% today). These low values suggest an oceanic biosphere very affected by the glacial episode, which is indicative of its magnitude. Nevertheless, there are still many uncertainties concerning the interpretation of the cap carbonates. They are largely related to the fact that cap carbonates are in fact dolomites and that the kinetics of their precipitation is still not fully understood although it appears to be associated with general conditions of anoxia and probably with a bacterial activity reducing the amount of sulphates at the water-sediment interface.

Glaciation Onset

Using models coupling climate and the carbon cycle, Donnadieu et al. (2004) showed that glacial triggering was closely linked to the configuration of the continents during the late Proterozoic. From 800 Ma onwards, the supercontinent Rodinia (Fig. 26.9), located at the equator, began to drift.

Numerous basaltic effusions mark the beginning of rifting. The formation of these highly weathered basaltic surfaces led to an increase in the consumption of atmospheric CO_2 (Goddéris et al. 2003). Moreover, the continental blocks began to drift, but remained between the latitudes 60° S and 60° N. The dislocation of Rodinia increased the supply of moisture to the continents, which favored continental weathering. This weathering occurred even more rapidly on large continental areas located in the hot and humid intertropical convergence zone. CO_2 consumption increased and atmospheric pressure of CO_2 plunged. The dislocation of Rodinia alone (Fig. 26.10) and the consequent increase in weathering (Fig. 26.11) explain a decrease in radiative forcing of 6.85 W/m^2 and an overall cooling of 8 °C. To this effect is added the intensified weathering of the fresh basaltic surfaces brought into the hot and humid climatic zones, conditions favoring their weathering (Goddéris et al. 2003).

This is particularly true of the magmatic Laurentian province (Donnadieu et al. 2004). The combined effects of lowering continental masses and weathered basaltic surfaces caused the system to tip into global glaciation, bringing sea ice as far south as 30°, at which point the positive feedback between albedo, ice cover and cooling accelerated. Atmospheric CO_2 increased from over 1800 ppmv, 800 Ma ago at the time of Rodinia, to a level below the threshold for global glaciation of 250 ppmv.

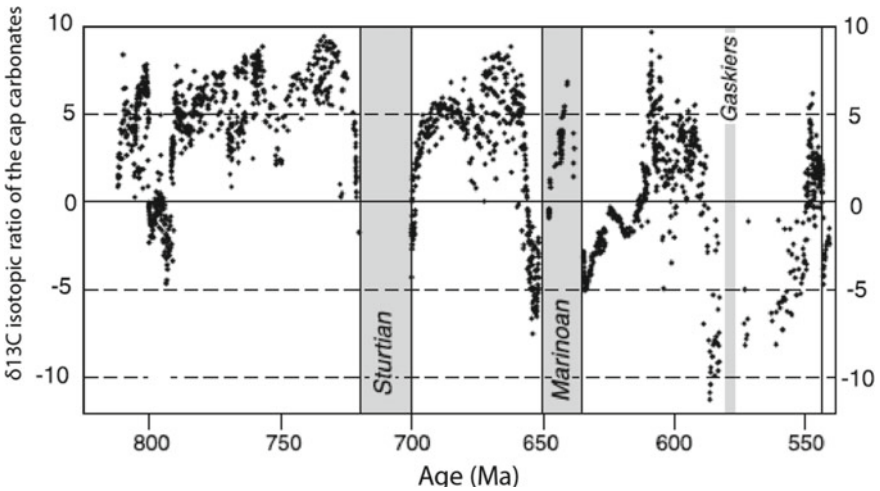

Fig. 26.8 Evolution of the $\delta^{13}C$ of sedimentary carbonates at the end of the Proterozoic. The two gray bands indicate the glaciations thought to be global

Fig. 26.9 The supercontinent Rodinia, about 800 million years ago

The tectonic theory for glacial inception has two advantages:

1. It explains the persistence of cold climates, even outside the episodes of 'snowball' glaciation for the duration of the Neoproterozoic, as long as the continents are dispersed along the equator. This configuration is observed in a window from 750 to 600 Ma (Torsvik et al. 2001) and thus includes the two extreme episodes.
2. It also explains why such global glaciations did not occur in more recent times. The equatorial configuration of the continents, the driver of global glaciation, never occurred during the Phanerozoic.

The possibility that clathrates (complexes formed from several molecules of methane and present today in certain marine sediments) played a destabilizing role has been proposed to explain the triggering of the Marinoan glaciation and the decrease of the $\delta^{13}C$ of the carbonate sediments just before glaciation (Fig. 26.8). This hypothesis suggests an ad hoc increase in CH_4 degassing from sediments just before glaciation. The result is a decrease of $\delta^{13}C$ in the sea water and an increase in the level of atmospheric CH_4. The resulting global warming disturbs the paleothermostat and CO_2 is consumed faster by the weathering of the silicates. The methane valve then closes for reasons that have still to be discovered and the remaining CO_2 level is no longer sufficient to prevent tipping into global glaciation. Finally, Pavlov et al. (2003) suggest that atmospheric methane levels remained high throughout the Proterozoic (100–300 ppmv) and that an additional episode of oxygenation of the surface layers created the conditions favorable to glaciation in the Neoproterozoic. This scenario is similar to the one elaborated to explain the Huronian glaciations. Rapid oxidation of methane to CO_2 considerably reduces the greenhouse effect in a time window too short for the paleothermostat to rebalance the temperature of the Earth's surface.

During Glaciation

During the main glacial period, the near absence of sedimentation does not allow data-based reconstruction. As a result, all theories are based on climate modeling. The average annual temperature over land during a complete glaciation is about −25 °C in the equatorial zone, with the coldest point being reached on the West African Craton with −110 °C (Donnadieu et al. 2003). The oceans become covered over with ice very quickly. The thickness of the sea ice is subject of debate. Model-based simulations suggest

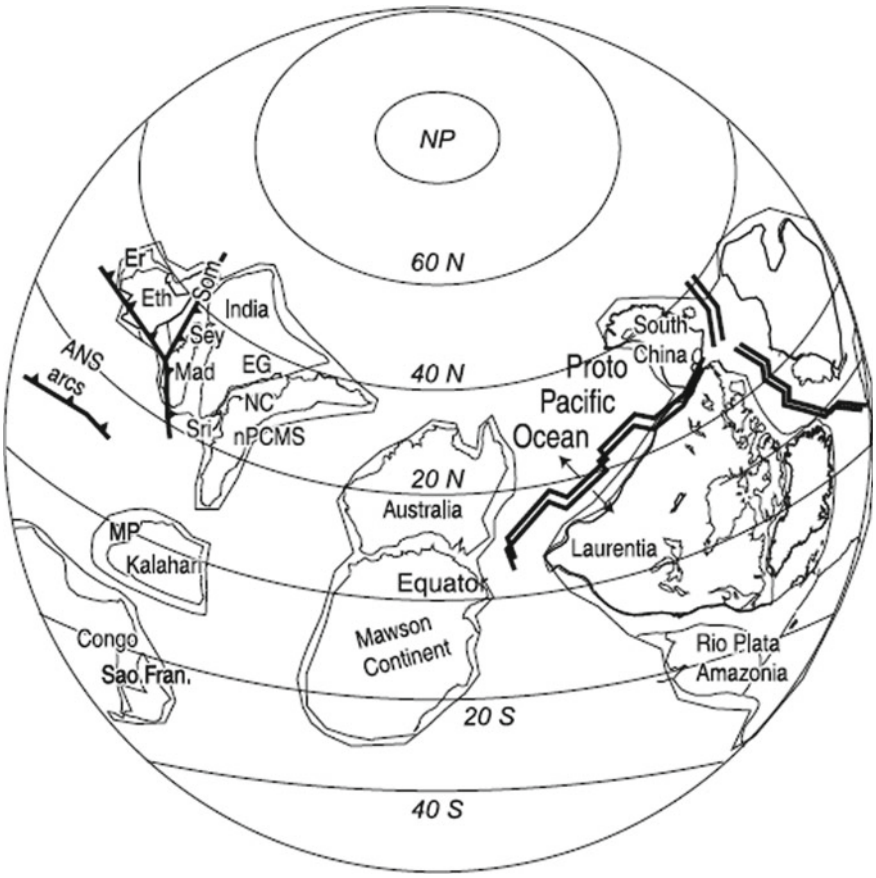

Fig. 26.10 The Rodinia dislocated about 750 million years ago

that this thickness must have rapidly exceeded a kilometer (Goodman 2006). However, for photosynthetic activity to persist during glaciation, the existence of thinner ice allowing light to filter through, at least in some areas, would be required. In contrast to the simulation suggesting thick ice everywhere, Hyde et al. (2000) presented a possibility where open water areas persisted in the tropical zone, while the rest of the ocean was completely covered with ice. This simulation was performed by coupling an energy balance model with an ice model. Nevertheless, simulations carried out with climate models taking into account the general circulation of the atmosphere and the ocean show that this solution is not stable. The ocean was probably entirely covered with ice with no real "oasis zones" where life could exist. By contrast, the presence of thin ice (of around 10 m thick) in the equatorial zone may have been possible. This was suggested by McKay (2000) and then modeled by Pollard and Kasting (2005). As for land masses, ice sheets became quickly established. Donnadieu et al. (2003) showed that by setting the CO_2 pressure at the pre-industrial value of 280 ppmv and by reducing the solar constant by 6%, the continental ice sheet would have taken 400,000 years to reach its equilibrium size of 190 million km^3 of ice covering 90% of continental surfaces (Fig. 26.12). Its maximum thickness would have been 5000 m. Even when the ice cover became total, light snowfall would have continued on the continents due to the sublimation of ice from the sea ice. In addition, the ice sheet would have remained dynamic as its base was wet. Ice flow rates of 5–10 m/year have been calculated for the most continental parts of the ice sheet and a rate of 50 m/year for coastal areas (Donnadieu et al. 2003). An active water cycle is therefore maintained during total glaciation, even if it is greatly reduced.

Exiting from Glaciation

In order to exit from glaciation, very high levels of CO_2 are required. Caldeira and Kasting (1992) calculated that a fully engulfed Earth would require 0.12 bar of CO_2 to initiate deglaciation. According to these authors, the greenhouse effect then becomes sufficiently powerful to counteract the high albedo of a totally frozen Earth. Unfortunately, the energy balance model used to produce this estimate was probably too simple for this particular environment but, even more importantly, the solar constant was fixed at its present value. Taking a solar constant of 6%, the deglaciation threshold becomes 0.29 bar. Pierrehumbert (2004) has also shown that the use of a GCM further pushes back this threshold for deglaciation and that 0.29 bar must be

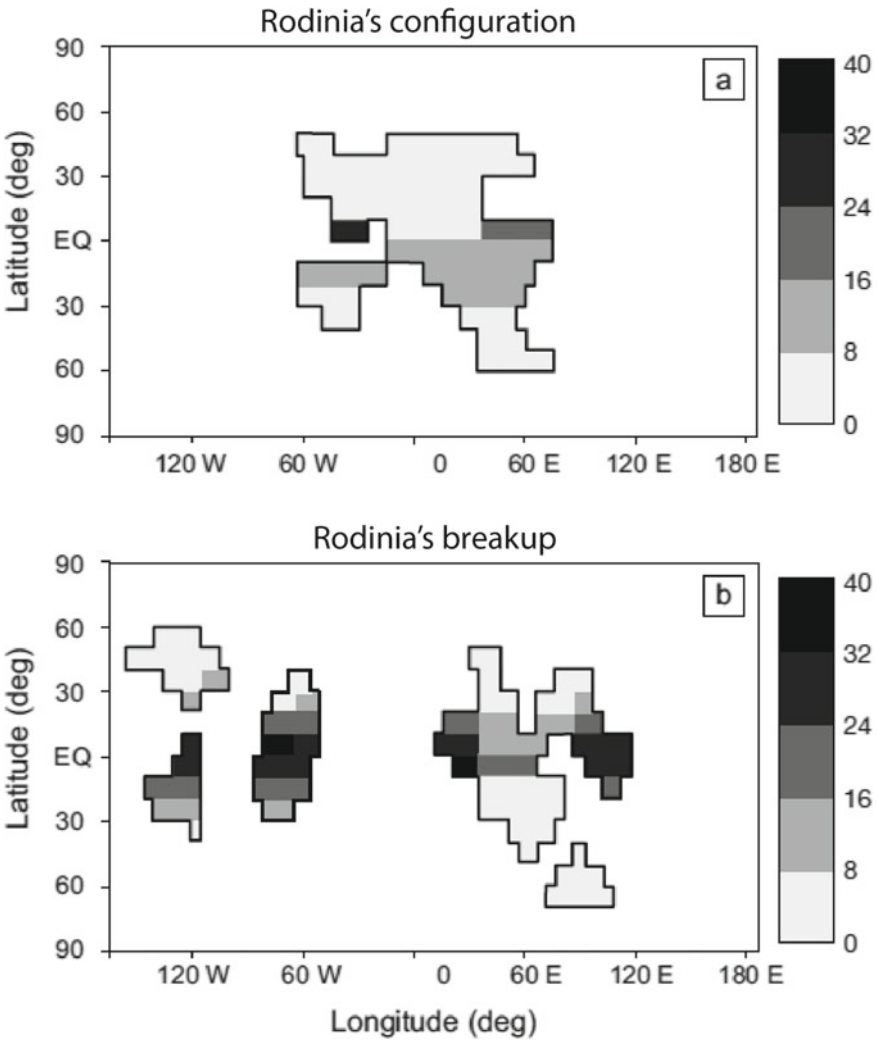

Fig. 26.11 Weathering rate of continental silicate rock (10^4 molCO_2/km^2/year) during the Neoproterozoic for the Rodinia configuration and for the dislocated configuration at 1800 ppmv of CO_2

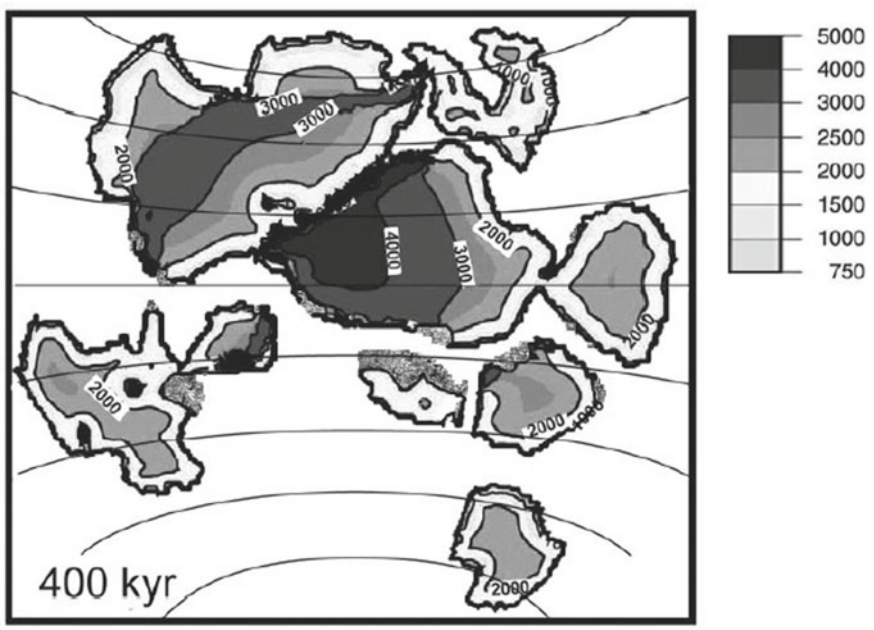

Fig. 26.12 Numerical simulation of the thickness of continental ice under Neoproterozoic conditions, at 280 ppmv of CO_2

considered to be a low limit. The reasons it is difficult to melt the 'snowball' Earth are multiple. One of these is that the dryness of the atmosphere resulting from the very low temperatures limits the formation of high-level clouds and thus the greenhouse effect. Similarly, the virtual absence of water vapor limits warming of the planet.

During the glaciation period, CO_2 accumulates in the atmosphere. Indeed, the virtual disappearance of the hydrological cycle means that atmospheric CO_2 is no longer absorbed by continental weathering (Hoffman et al. 1998). Carbon therefore accumulates in the atmosphere through volcanic degassing. By taking the current degassing rate of 6.8×10^{12} mol of CO_2 per year, it takes 8 million years for 0.29 bar of CO_2 to accumulate in the atmosphere. This timeframe is compatible with the estimates of the duration of 'Snowball' Earth (Bodiselitsch et al. 2005). However, this only applies if all of the carbon sinks are stopped during glaciation and this is not the case, since the existence of thin ice allows a fracture at the ocean-atmosphere interface. A surface area of 3000 km^2 of open water is sufficient to ensure a massive diffusion of CO_2 into the ocean, ensuring the balance between the ocean and the atmosphere (Le Hir et al. 2007). Under these conditions, the ocean undergoes major acidification (the pH drops to 6) and the weathering of the oceanic crust becomes an efficient carbon sink, prolonging glaciation by counteracting the growth of atmospheric CO_2. If this process is included, it appears that even over 30 million years, atmospheric CO_2 does not reach the threshold for deglaciation (Fig. 26.13)

The most recent studies show that an important problem with the hypothesis of 'Snowball' Earth is understanding the conditions under which it melts. Nevertheless, processes able to reduce the duration of the glaciation have never been tested. For example, prolonged volcanic activity during glaciation probably led to the accumulation of ash on the ice, decreasing its albedo, and therefore, the CO_2 threshold required to initiate deglaciation.

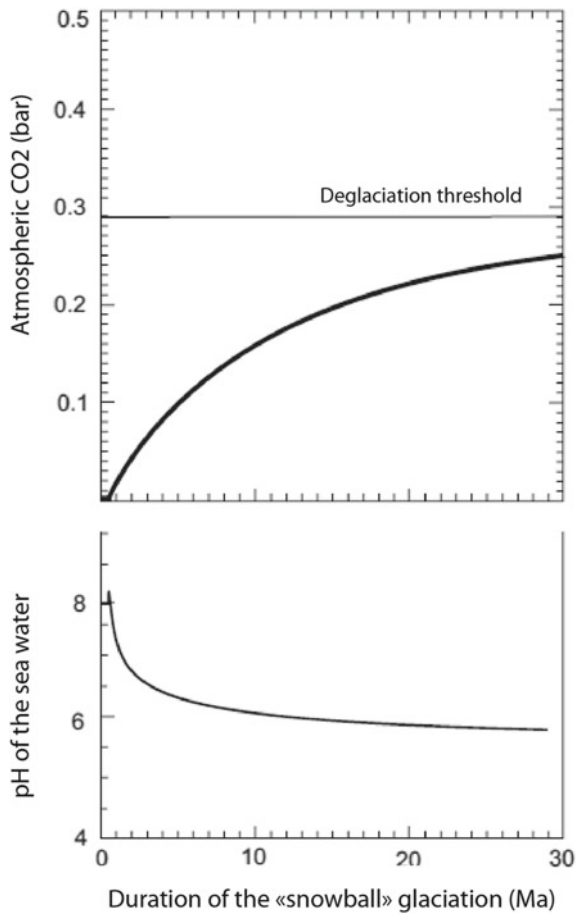

Fig. 26.13 Evolution of CO_2 concentration in the atmosphere and pH of the ocean during a global glaciation, assuming contact between the ocean and the atmosphere via fractures in sea ice

Conclusion

Twenty years ago, the Precambrian was a large unknown gap in our understanding of the geochemical and climate history of our planet. This period, lasting approximately 4 billion years, saw the emergence of the major regulatory processes in our environment (the emergence of the continents, the establishment of plate tectonics, the appearance of life and of the modern atmosphere). Our understanding gradually unfolded as the experimental techniques (in particular isotopic techniques) advanced and as modeling improved. This has been a major leap forward that has occurred in the past ten years. Very significant progress has been made in describing the evolution of the environment at the Archean-Proterozoic boundary. Today, thanks to the ever more refined study of the isotopic ratios of sedimentary rocks of this period ($\delta^{13}C$, $\delta^{56}Fe$, $\Delta^{33}S$), the Great Oxygenation Event is one of the best documented events of the Precambrian. Similarly, the description of the major, possibly global, glaciations that marked the end of this very long period has improved dramatically in recent years. We now know the number, age and probable extent of the glaciations that preceded the Cambrian explosion of life, and we have an increasingly coherent image of their modalities.

However, four billion years is a long time and many areas of uncertainty still remain. We have progressed to the point where certain key periods in the Precambrian have been clearly illuminated. For instance, the description of Neoproterozoic glaciation has improved on many issues. The most striking one of the new Cryogenian chronology is the grossly unequal duration of the cryochrons (Fig. 5.14a). The Sturtian lasted four time longer than the Marinoan. Another surprising caracteristic of the new chronology is the brevity of the nonglacial interlude between the cryochrons. When

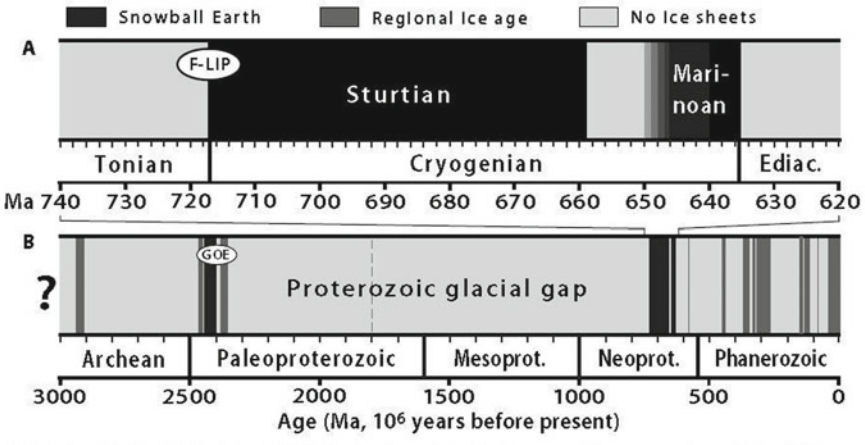

Fig. 26.14 Glacial epochs on Earth since 3.0 Ga. **a** Black bands indicate duration of the Sturtian and Marinoan cyrochrons (Table 26.1). The graded start to the Marinoan cryochron denotes chronometric uncertainty, not gradual onset. **B** Snowball Earth chrons (black), regional-scale ice ages (medium gray), and nonglacial intervals (light gray) since 3.0 Ga. Ellipse GOE is centered on the Great Oxidation Event, as recorded by the disappearance of mass-independent S isotope fractionations ≥ 0.3 per mil (‰) in sedimentary sulfide and sulfate mineral. The dashed gray line indicates questionable glaciation. Figure from Hoffman et al., Sci. Adv. 2017

the Marinoan began, a Snowball Earth had terminated less than 20 Ma earlier. When the Sturtian began, no low-latitude glaciation had occurred for 1.7 Ga (Fig. 5.14b). Nevertheless, more obscure periods, marked by slower, more progressive changes and yet which cover very long portions of the Precambrian, have still to be elucidated. In particular, the reasons why most of the Proterozoic did not experience any glaciation need to be explored. Is this truly the case or is there a bias in our observation of Precambrian formations? If this is true, then this would be the longest persistent hot period (1.2 billion years!) in the history of our planet. Why are the great quasi-periodic glacial advances observed since the emergence of multicellular life not active in the Paleo and Meso-Proterozoic? The climate history of the Precambrian that we have so far reconstructed concerns essentially that of its glacial crises (the GOE, the Neoproterozoic), but these represent only a small fraction of the immensely long Precambrian. Reconstructing a less disjointed image of this period is a major challenge for the coming decades.

References

Bodiselitsch, B., Koeberl, C., Master, S., & Reimold, W. U. (2005). Estimating duration and intensity of Neoproterozoic snowball Glaciations from Ir Anomalies. *Science, 308*(5719), 239–242.

Caldeira, K., & Kasting, J. F. (1992). Susceptibility of the early earth to irreversible Glaciation caused by carbon dioxide clouds. *Nature, 359,* 226–228.

Catling, D. C., & Claire, M. W. (2005). How Earth's atmosphere evolved to an oxic state: A status report. *Earth and Planetary Science Letters, 237,* 1–20.

Donnadieu, Y., Fluteau, F., Ramstein, G., Ritz, C., & Besse, J. (2003). Is there a conflict between the Neoproterozoic Glacial deposits and the Snowball Earth interpretation: An improved understanding with numerical modeling. *Earth and Planetary Science Letters, 08,* 101–112.

Donnadieu, Y., Goddéris, Y., Ramstein, G., Nédelec, A., & Meert, J. G. (2004). Snowball EARTH triggered by continental break-up through changes in runoff. *Nature, 428,* 303–306.

Evans, D. A. D. (2000). Stratigraphic, Geochronological, and paleomagnetic constraints upon the Neoproterozoic climatic paradox. *American Journal of Science, 300,* 347–433.

François, L. M., & Goddéris, Y. (1998). Isotopic constraints on the cenozoic evolution of the carbon cycle. *Chemical Geology, 145,* 177–212.

Gaucher, E. A., Govindarajan, S., & Ganesh, O. K. (2008). Paleotemperature trend for precambrian life inferred from resurrected proteins. *Nature, 451,* 704–708.

Goddéris, Y., et al. (2003). The Sturtian Glaciation: Fire and ice. *Earth and Planetary Science Letters, 211,* 1–12.

Goddéris, Y., & Veizer, J. (2000). Tectonic control of chemical and isotopic composition of ancient oceans: The impact of continental growth. *American Journal of Science, 300,* 434–461.

Goodman, J. C. (2006). Through thick and thin: Marine and meteoric ice in a 'Snowball Earth' climate. *Geophysical Research Letters, 33*. https://doi.org/10.1029/2006gl026840.

Halverson, G. P., Hoffman, P. F., Schrag, D. P., Maloof, A. C., & Rice, A. H. N. (2005). Towards a Neoproterozoic composite carbon isotope record. *Geological Society of America Bulletin, 117*, 1181–1207.

Hoffman, P. F., Abbot D. S., Ashkenazy, Y., Benn, D. I., Brocks, J. J., Cohen, P. A., et al. (2017). Snowball Earth climate dynamics and Cryogenian geology geobiology. *Science Advances.*

Hoffman, P. F., Kaufman, A. J., Halverson, G. P., & Schrag, D. P. (1998). A Neoproterozoic Snowball Earth. *Science, 281*, 1342–1346.

Hyde, W. T., Crowley, T. J., Baum, S. K., & Peltier, W. R. (2000). Neoproterozoic 'Snowball Earth' simulations with a coupled climate/ice sheet model. *Nature, 405,* 425–429.

Kasting, J. F., & Howard, M. T. (2006). Atmospheric composition and climate on the early earth. *Philosophical Transaction Royal Society London B, 361*, 1733–1742.

Kasting, J. F., et al. (2006). Paleoclimates, ocean depth, and the oxygen isotopic composition of seawater. *Earth and Planetary Science Letters, 252,* 82–93.

Kaufman, A. J., & Xiao, S. H. (2003). High CO_2 levels in the proterozoic atmosphere estimated from analyses of individual microfossils. *Nature, 425,* 279–282.

Knauth, L. P., & Epstein, S. (1976). Hydrogen and oxygen isotope ratios in nodular and bedded cherts. *Geochimica Cosmochimica Acta, 40*, 1095–1108.

Kump, L. R., Kasting, J. F., & Barley, M. E. (2001). Rise of atmospheric oxygen and the 'upside-down' Archean Mantle. *Geochemistry Geophysics Geosystems, 2*(1). https://doi.org/10.1029/2000gc000114.

Le Hir, G., Goddéris, Y., Ramstein, G., & Donnadieu, Y. (2007). A scenario for the evolution of the atmospheric pCO_2 during a Snowball Earth. *Geology* (in press).

Lowe, D. R., & Tice, M. M. (2004). Geologic evidence for Archean atmospheric and climatic evolution: Fluctuating levels of CO_2, CH_4, and O_2 with an overriding tectonic control. *Geology, 32*(6), 493–496.

McKay, C. P. (2000). Thickness of tropical ice and photosynthesis on a Snowball Earth. *Geophysical Research Letters, 27*, 2153–2156.

Papineau, D., Mojzsis, S. J., & Schmitt, A. K. (2007). Multiple sulfur isotopes from paleoproterozoic Huronian interglacial sediments and the rise of atmospheric oxygen. *Earth and Planetary Science Letters, 255,* 188–212.

Pavlov, A. A., Hurtgen, M. T., Kasting, J. F., & Arthur, M. A. (2003). Methane-rich proterozoic atmosphere. *Geology, 31,* 87–90.

Pavlov, A. A., Kasting, J. F., Brown, L. L., Rages, K. A., & Freedman, R. (2000). Greenhouse warming by CH_4 in the atmosphere of Early Earth. *Journal of Geophysical Research, 105*(E5), 11981–11990.

Pierrehumbert, R. T. (2004). High levels of atmospheric carbon dioxide necessary for the termination of global Glaciation. *Nature, 429,* 646–649.

Pollard, D., & Kasting, J. F. (2005). Snowball Earth: A thin-ice solution with flowing sea glaciers. *Journal of Geophysical Research, 111*.

Robert, F., & Chaussidon, M. (2006). A palaeotemperature curve for the precambrian oceans based on silicon isotopes in cherts. *Nature, 443,* 969–972.

Torsvik, T. H., et al. (2001). Rodinia refined or obscured: Paleomagnetism of the Malani igneous suite (NW India). *Precambrian Research, 108,* 319–333.

Walker, J. C. G., Hays, P. B., & Kasting, J. F. (1981). A negative feedback mechanism for the long-term stabilization of earth's surface temperature. *Journal of Geophysical Research, 86*, 9776–9782.

The Phanerozoic Climate

27

Yves Goddéris, Yannick Donnadieu, and Alexandre Pohl

The Phanerozoic period covers the last 542 million years of Earth's history, about 12% of the history of our planet. With regard to the evolution of life, the Phanerozoic experienced major events such as the rapid diversification of multicellular organisms which first appeared in the Cambrian (541–485 Ma), the colonization of continental surfaces by living organisms during the Ordovician (485–444 Ma) and the appearance of the first hominids about 8 million years ago. Over this same period, the appearance of the Earth's surface changed considerably: the continental drift during the Phanerozoic moved all of the continental masses situated in the southern hemisphere and along the equator since the Cambrian to join together around 280 million years ago to form a supercontinent: the Pangea. This would then disintegrate during the Jurassic around 180 million years ago with the emergence of the Atlantic Ocean.

Our understanding of the Phanerozoic climate, even if it is still incomplete, has been rapidly evolving in recent years. Data accumulated over the last few decades has improved consistently in quality and the numerical models used to reconstruct past climates have evolved considerably: they have a better spatial resolution and include an increasing number of processes. In general, it is true to say our conception of how and why the Earth's climate evolved during this key period in the history of life on Earth is now undergoing a true revolution.

Y. Goddéris (✉)
Géosciences Environnement Toulouse, CNRS-Université de Toulouse III, UMR 5563, Toulouse, France
e-mail: yves.godderis@gmail.com

Y. Donnadieu · A. Pohl
Aix-Marseille Université, CNRS, IRD, Coll France, CEREGE, Aix-en-Provence, France

G. Ramstein et al. (eds.), *Paleoclimatology*, Frontiers in Earth Sciences,
https://doi.org/10.1007/978-3-030-24982-3_27

The Proxies for the Phanerozoic Climate

There are no direct indicators of climate conditions in the geological past. However, qualitative reconstructions can be produced from sedimentological and paleontological data, and, in general, are more reliable than they are for the Precambrian. Geochemical data, in particular the isotopic indicators measured in marine sediments, provide some quantification, but interpretation of them is rarely straightforward. Below we provide a non-exhaustive list of examples of indicators. Finally, we will highlight the indicators that allow the reconstruction of CO_2 concentration in the atmosphere over geological time.

Sedimentological Indicators

A compilation of sedimentological data indicative of glacial climate was carried out in 1992 by Frakes et al. (1992). It consists of an inventory of tillite-type glacial deposits (clays formed from erosion products resulting from the friction of glaciers on their bedrock) and, on the other hand, a reconstruction of the minimum paleolatitude attained by rock debris carried by sea ice. The result shows a fluctuation of hot and cold modes over a period of approximately 135 Ma. The coldest climate mode was identified during the Permo-Carboniferous glaciation.

A more recent study provides results in agreement with those of Frakes et al. (1992). Boucot et al. (2004) compiled data on continental coal deposits, indicators of an arid climate, as a function of paleogeography and time. They constructed a qualitative curve of variations on the equator-pole climate gradient for the entire Phanerozoic. They interpret the existence of weak gradients as the sign of a warm climate.

Isotopic Indicators

The $\delta^{18}O$ of Carbonates

A detailed study of the isotopic composition of oxygen ($\delta^{18}O$) in carbonate sediments was carried out mainly on fossilized brachiopod shells (Veizer et al. 1999). It shows two trends (Fig. 27.1). The first is a slow, almost linear, increase of $\delta^{18}O$ from the Cambrian, from values of around −10‰ (relative to the standard Pee Dee Belemnite) up to current values close to 0‰. This increase is still difficult to interpret. If the $\delta^{18}O$ of the ocean has remained close to its present value and if the evolution of the $\delta^{18}O$ of the brachiopods is interpreted in terms of temperature over the last 540 million years, then the temperature of seawater must have reached 70 °C in the Cambrian, a level which is lethal to most marine organisms and therefore difficult to reconcile with the very large phase of diversification of marine organisms documented at this time (Zhuravlev and Riding 2001). Two possibilities have been proposed to solve this paradox: either the decrease of $\delta^{18}O$ in the past reflects a diagenetic alteration of the brachiopod shells, in which case the signal is irrelevant, or the $\delta^{18}O$ of seawater was lower in the past. Seawater is, in fact, influenced by the tectonic processes: as silicate rocks are transformed into $\delta^{18}O$-depleted clay sediments, continental and hydrothermal alteration at low temperatures tend to increase the $\delta^{18}O$ of the water in contact with the minerals. A fractionation of 20% is observed for the low-temperature alteration at the ridges, 12.5% for the continental alteration, while the high-temperature hydrothermal alteration decreases the $\delta^{18}O$ of seawater by enriching the alteration production with a fractionation of −18‰. The role of these geological processes on the $\delta^{18}O$ of seawater is not yet clearly understood. There is as yet no consensus on this issue especially since recent studies suggest that the value of the $\delta^{18}O$ of the ocean has remained constant since 760 Ma (Bergmann et al. 2018; Hodel et al. 2018).

The second trend highlighted in the long-term recordings of the $\delta^{18}O$ of the brachiopods is the periodic oscillations superimposed on the long-term linear trend described previously. If this is subtracted, the oscillations have an amplitude of 3–5‰ (Veizer et al. 2000). The most surprising aspect is that the period of these oscillations is in agreement with the periodicity of the hot and cold modes determined by Frakes et al. (1992), suggesting the presence of a true climate signal. The use of a paleothermometer, linking the isotopic fractionation between calcite and seawater to the precipitation temperature of the carbonate, makes it possible to reconstruct the temperature variations of the water in which the brachiopods lived, provided that the $\delta^{18}O$ of the seawater is known, a fact dependent on the volume of continental ice. It should be noted, however, that examples of diagenetic alteration have been identified in which isotopic exchange with runoff leads to values for $\delta^{18}O$ very different from the original values, but in which seasonal oscillations seem to be preserved. This is merely an artifact. Finding a pseudo-climatic periodicity in a diagenesis signal is not impossible and does not constitute proper evidence of the preservation and the consistency of the isotopic signal.

The fractionation α between calcite and water is expressed by the relationship:

$$T(\mathrm{K}) = \frac{18.03 \times 10^3}{1000 \ln \alpha + 32.42} \quad (1)$$

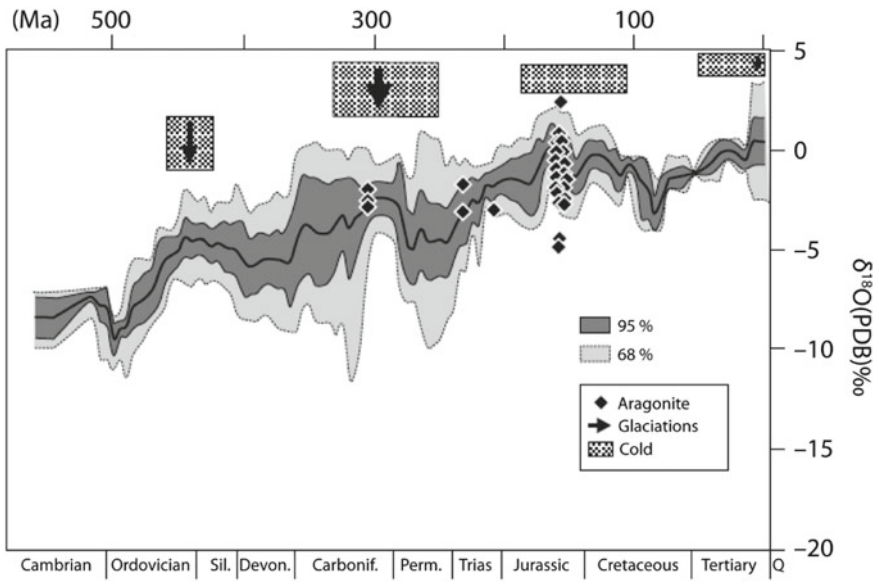

Fig. 27.1 $\delta^{18}O$ of carbonate sediments (calcite) measured over the whole Phanerozoic. The two light and dark shaded ranges contain 68% and 95% respectively of the data points. The lozenges represent measurements made on aragonitic fossils

where

$$\alpha = \frac{1000 + \sigma^{18}O^{PDB}_{sample}}{1000 + \sigma^{18}O^{PDB}_{solution}} \quad (2)$$

is the δ^{18}O (PDB) of the carbonate sample, and δ^{18}O is the δ^{18}O of the solution from which the carbonate precipitated. A δ^{18}O of seawater of 0‰ compared to SMOW is equivalent to −30‰ compared to PDB. A variation of −1‰ in the $\delta^{18}O_{sample}$ corresponds to an increase of +4 °C in the temperature at which precipitation occurred.

The volume of continental ice and the δ^{18}O of seawater are far from being well known through the geological past of the Earth. To simplify, Veizer et al. (2000) assumed the volume of continental ice to be twice the current volume at the glacial period peaks and to be zero during a warming period. An oscillation in the ice volume of this scale could account for a 2‰ change in the δ^{18}O of seawater, which presumes that the remaining 1–3‰ are attributable to temperature changes. Making these assumptions, Veizer et al. (2000) propose that seawater in the equatorial zone (where all fossil brachiopods have been found) was up to 3.5 °C colder during the Ordovician glacial maximum than now, 3 °C colder during the Permo-Carboniferous and 2 °C colder during the Jurassic, without taking into account rapid shifts which could reach amplitudes of 9 °C (Fig. 27.2).

It should be noted that the majority of the brachiopod fossils used are from the Paleozoic (Veizer et al. 1999) and that the resolution for the Mesozoic and Cenozoic ages is weak within this Phanerozoic database. The Mesozoic was covered more precisely by measurements of δ^{18}O from benthic and planktonic foraminiferal shells (e.g., Bice et Norris 2002) and on belemnite rostra (Dera et al. 2011). One of the most remarkable results is the estimation of the deep-water temperature during the Cretaceous. This temperature was approximately 10 °C at the end of the Cretaceous and could have reached 15 °C around 100 Ma (Friedrich et al. 2012). Measurements for the Mesozoic are also covered by δ^{18}O on phosphates (see next section).

Finally, the Cenozoic is covered by a high-resolution database (Zachos et al. 2008), which is the most significant step forward in terms of climate reconstruction (Fig. 27.3). The δ^{18}O measurements carried out in forty ODP and DSDP drill sites, were conducted on benthic foraminifera that once lived in the deep ocean. They are generally considered to be indicators of changes in surface water temperature at high latitudes (where dense surface waters sink to produce the deep waters of the global ocean) and of changes in the isotopic composition of the ocean on average, which are a function of the ice cap volume. They are particularly good at recording the phases of rapid growth of the Antarctic ice sheet.

The δ^{18}O of Phosphates

Another particularly promising approach is based on the study of δ^{18}O measured in phosphates, particularly in fish teeth or conodonts, small tooth-shaped structures of 0.25–2 mm, consisting of apatite and having belonged to vermiform animals that disappeared at the end of the Triassic. The paleothermometer is expressed as follows:

$$T(^{\circ}C) = 112.2 - 4.2\left(\sigma^{18}O^{SMOW}_{sample} - \sigma^{18}O^{SMOW}_{water}\right) \quad (3)$$

$\sigma^{18}O^{SMOW}_{sample}$ is the δ^{18}O (SMOW) of the phosphate sample, and $\sigma^{18}O^{SMOW}_{water}$ is the δ^{18}O of the solution from which the phosphate precipitated.

The advantage of phosphates, especially the enamel of fossil teeth and conodonts, is their greater resistance to diagenetic alteration than carbonates. In general, the δ^{18}O measured on phosphate does not appear to show significant

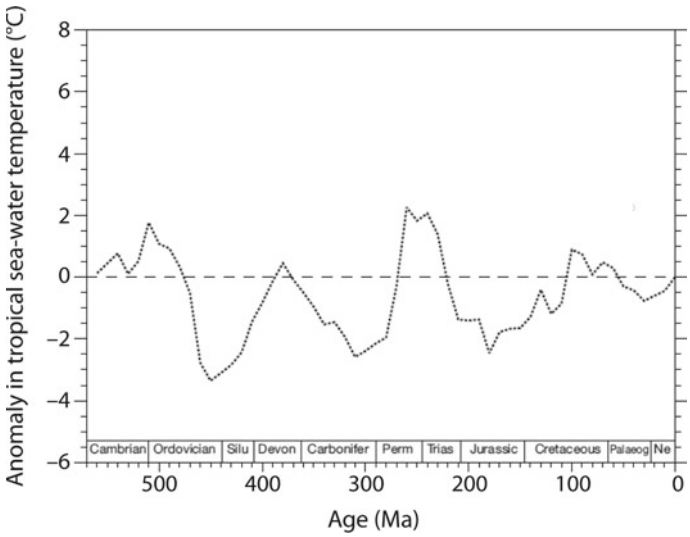

Fig. 27.2 Temperature anomalies of tropical waters reconstructed from δ^{18}O carbonate data

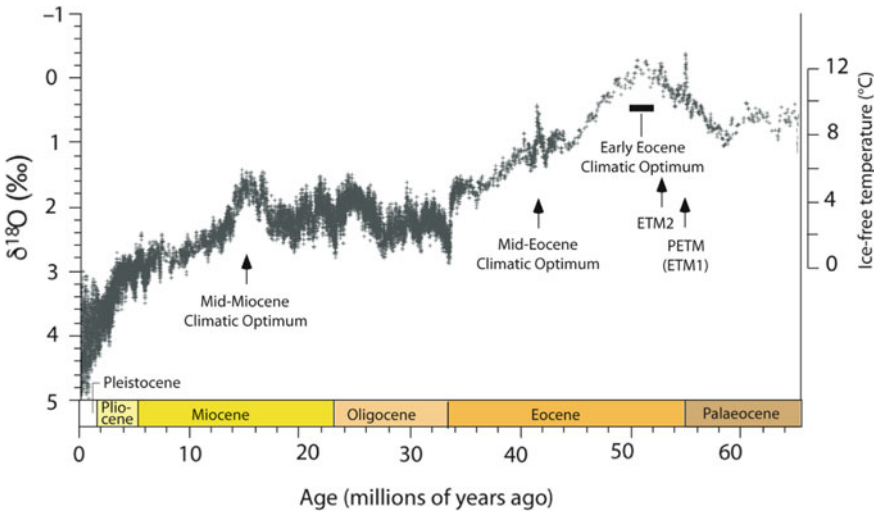

Fig. 27.3 $\delta^{18}O$ of benthic foraminifera during the Cenozoic

decay as one goes back in time, suggesting a lower sensitivity to diagenesis and therefore better reliability. This has been clearly demonstrated for the Devonian. The $\delta^{18}O$ measured on apatite from conodonts indicates a seawater temperature of about 25 °C for the end of Givetien and Frasnian (391–374 Ma), taking the $\delta^{18}O$ of the seawater to be −1‰ due to the probable absence of ice caps, as these only developed during the Famennian (Caputo et al. 2008). The $\delta^{18}O$ measured on the calcite of the brachiopod shells from the same period indicates significantly higher temperatures of between 30 and 40 °C (Veizer et al. 1999). Similar differences are observed in the amplitudes of the temperature changes between the two methods. For example, measurements of $\delta^{18}O$ on phosphates suggest a drop in tropical water temperature from 40 to 32 °C between 490 and 465 million years which seems to be correlated with a major acceleration in the expansion of biodiversity (Trotter et al. 2008). The $\delta^{18}O$ data from brachiopods suggest a temperature drop of only 4 °C over the same period. It appears that the isotopic composition of brachiopod shells depends largely on kinetic fractionation processes (typical of diagenesis) and, to a lesser extent, on the metabolism of these animals. Consequently, the $\delta^{18}O$ measured on the brachiopods could be a weak reflection of the environmental conditions that prevailed at the time of the formation of the shell. Nevertheless, the debate on the validity of the brachiopod data is still ongoing, especially since the recent publication of a new paleothermometer which revises upwards the temperatures reconstructed from phosphates (Pucéat et al. 2010).

The use of fish teeth from various parts of the world supports the reconstruction of latitudinal gradients of water temperatures, which provides essential clues to climates in the distant past. Finally, data from the teeth of fossil vertebrates offer immense opportunities in terms of the measurement of temperatures and their latitudinal gradients in continental environments.

The 'Clumped' Carbonate Isotope Method or the Δ_{47} Method

The major problem with using oxygen isotopes for the reconstruction of seawater temperatures in the past is the lack of knowledge of the $\delta^{18}O$ ratio of the seawater in which the carbonates and phosphates formed. A new technique has recently been proposed, which makes it possible to overcome this limitation. This involves essentially counting the number of bonds between rare isotopes in the $CaCO_3$ molecules, in particular, the ^{13}C–^{18}O bonds. The difference between the actual number of rare bonds and the number of bonds there would be if the bonds were stochastically distributed depends entirely on the temperature and not at all on the isotopic composition of the water in which the carbonate was formed. It is measured with the assistance of Δ_{47}:

$$\Delta_{47} = \left(\frac{R^{47}_{measured}}{R^{47}_{stochastic}} - 1\right) \times 1000 \qquad (4)$$

where $R^{47}_{measured}$ is the ratio of the mass of $^{18}O^{13}C^{16}O$ molecules to the mass of light $^{16}O^{12}C^{16}O$ molecules measured in the CO_2 emitted from the attack on carbonate by phosphoric acid. $R^{47}_{stochasitc}$ is the same as the ratio for a stochastic distribution of the molecules. The Δ_{47} depends on the temperature of the medium in which the carbonate formed (Ghosh et al. 2006) according to the formula:

$$\Delta_{47} = 0.0592(10^6 \times T^{-2}) - 0.02 \qquad (5)$$

This technique also has the advantage of being impervious to diagenesis within a temperature range of 0–200 °C. The first use of this technique was devoted to the study of samples from the Lower Silurian (around 435 million years) and from the Middle Pennsylvanian (Carboniferous, around 310 million years) (Came et al. 2007). It produces contradictory results: for the Carboniferous samples, they are, for example, in agreement with the $\delta^{18}O$ measurements on

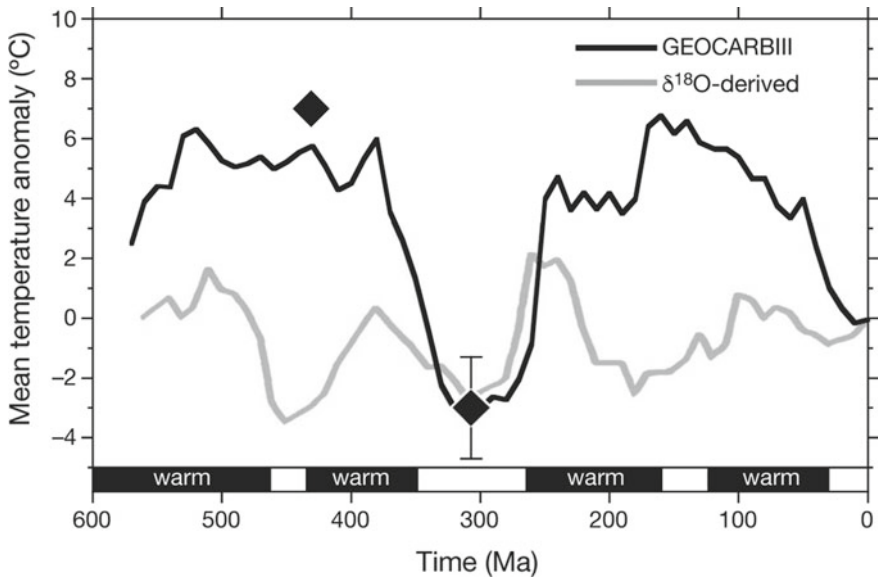

Fig. 27.4 Phanerozoic temperature anomalies. The black line tracks the output of a numerical model and represents the mean global temperature anomalies (Berner 1994). The gray line represents the $\delta^{18}O$ data on calcite (Veizer et al. 2000), and the two diamonds show the Δ_{47} data (Came et al. 2007)

brachiopods, but for the Silurien samples, they are completely opposite in that they indicate temperatures around 8 °C higher than the current ones, whereas the $\delta^{18}O$ data indicates temperatures around 2.5 °C lower than currently (Fig. 27.4).

By combining the $\delta^{18}O$ and Δ_{47} data from Ordovician sedimentary calcites, a recent study showed for the first time that it was possible to calculate the $\delta^{18}O$ ratio of seawater over this period of time and thus to trace back the volume of ice present on the continents during the glacial peak at the end of the Ordovician (Finnegan et al. 2011) the estimate of which is in agreement with the reconstruction of sea level variations for that time (Loi et al. 2010).

Indirect Isotopic Indicators

The $\delta^{13}C$ of Carbonate Sediments

The $^{13}C/^{12}C$ ratio ($\delta^{13}C$ expressed with respect to the PDB standard) of the carbonate sediments recorded the isotopic composition of the total carbon dissolved in seawater (in the form of dissolved CO_2, bicarbonate and carbonate ions, denoted by $\sum CO_2$ or by the acronym DIC—Dissolved Inorganic Carbon) at the time of deposition. The main trend of this isotopic indicator is a general increase during the Paleozoic, from −2‰ during the Cambrian to +4‰ at the end of the Carboniferous. Veizer et al. (2000) (Fig. 27.5).

This geological stage presents the highest value for this signal for the entire Phanerozoic. After a rapid decrease during the Permian, the $\delta^{13}C$ of carbonates registered minimal fluctuations around the present value of +1.5‰. This $\delta^{13}C$ is an indicator of the behavior of the carbon cycle, but unfortunately it is not very clear how exactly to interpret it.

The simplified budget of the $\delta^{13}C$ of the oceanic DIC δ_{oc} is written as:

$$C_{oc}\frac{d\delta_{oc}}{dt} = F_{cw}(\delta_{cw}-\delta_{oc}) + F_{ow}(\delta_{ow}-\delta_{oc}) + F_{cw}(\delta_{cw}-\delta_{oc}) + F_{MOR}(\delta_{MOR}-\delta_{oc}) - F_{cd}(\delta_{oc}-\varepsilon_{carb}-\delta_{oc}) - F_{od}(\delta_{oc}-\varepsilon_{MO}-\delta_{oc}) \quad (6)$$

where C_{oc} is the DIC content of the ocean and F_{cw}, F_{ow}, F_{vol} and F_{MOR} are the carbon fluxes transferred from the lithosphere to the ocean by dissolving continental carbonates, by the oxidation of sedimentary organic carbon, by degassing linked to the volcanic activity and by the oceanic ridges, respectively. F_{cd} and F_{od} are the fluxes of carbonate deposits from all environments, and the burial of organic carbon respectively. The δ are the $\delta^{13}C$ corresponding to each of these fluxes: δ_{cw} is close to 0‰, δ_{ow} to −25‰; δ_{MOR} is estimated at −5 or even −6‰. δ_{vol} is less well known, but its value is certainly located between the mantle value and that of the carbonates deposited on the abyssal sea floor, that is ±0‰ on average over a long-time scale. ε_{carb} is the isotopic fractionation between the DIC of seawater and the carbonate minerals. This fractionation is low (around 1.2‰) (Hayes et al. 1999), indicating that carbonate deposits cannot be responsible for the temporal evolution of δ_{oc}. However, the fractionation between the buried organic matter and the oceanic DIC ε_{MO} is very high (±20‰ today). The organic flows F_{ow} and F_{od} dominate the budget because this fractionation means that their combined flow is multiplied by $\delta^{13}C$ and so is an order of magnitude greater than the other terms. The flux variations most influencing the temporal evolution of the $\delta^{13}C$ of the ocean are therefore those that

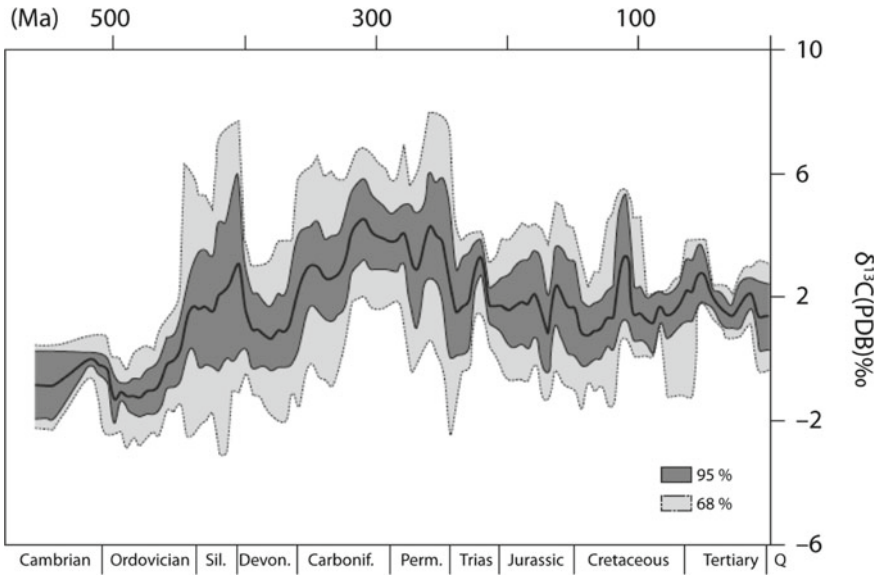

Fig. 27.5 $\delta^{13}C$ of calcite sediment from the Phanerozoic. % of data points

affect the processes with a $\delta^{13}C$ signature furthest away from the oceanic value, in other words, the oxidation of the organic sedimentary carbon exposed on land or the burial of organic carbon in sediment. However, it is impossible to discriminate between them using the $\delta^{13}C$ signal alone.

However, geochemical interpretation is possible for some major excursions. In particular, the positive and very large Carboniferous excursion (a positive excursion of 4‰ throughout the Carboniferous (Veizer et al. 1999) is interpreted as the recording of the burial of a very large amount of organic carbon (this was the time large coal beds were being deposited in Europe, Russia and North America), which extracted preferentially the ^{12}C from the ocean-atmosphere system. This resulted in a higher consumption of atmospheric CO_2 and a cooling of the climate which coincides reasonably well with the Permo-Carboniferous ice age. This observation encouraged the association of any positive excursion of $\delta^{13}C$ with a cooling of the climate, especially since many positive excursions coincide with episodes of extensive burial of organic matter (episodes of global anoxia and black shale formation), such as the end of the Devonian (Frasnian-Famennian episode, circa 375 Ma) or the global anoxic events of the Cretaceous (Aptian circa 120 Ma and Turonian circa 90 Ma). This interpretation, however, is not conclusive. To illustrate the difficulty of interpreting the $\delta^{13}C$ signal in geochemical and climate terms, it should be noted that certain anoxic episodes, during the formation of gray or black shales, are accompanied by negative excursions of the oceanic $\delta^{13}C$, such as the Toarcian anoxic episode. These events probably indicate favorable conditions (anoxic environment) for the preservation of organic matter, but the total amounts of organic matter ultimately buried are low. The Toarcian negative excursion can be interpreted as the result of a large CO_2 outgassing from the mantle when the Karoo-Ferrar traps were established in South Africa and could therefore be linked to a warming of the climate by the greenhouse effect. It should also be pointed out that, at shorter intervals during glacial-interglacial Quaternary oscillations, the $\delta^{13}C$ of the ocean decreased during glacial periods due to a reduction in the biosphere, a consequence of aridity on the continents (Part III, Chaps. 1 and 2).

Finally, some very rapid and pronounced negative excursions could be attributed to the destabilization of methane hydrates contained in marine sediments. The methane released by the sediments is characterized by a $\delta^{13}C$ of −60‰ and these negative values allow very pronounced excursions of $\delta^{13}C$. In general, it is assumed that the CH_4 contribution to the exosphere is short (10^4 to 10^5 years) and intense, resulting in rapid negative excursions (e.g. the thermal maximum of the Palaeocene-Eocene transition (McInerney and Wing 2011).

It is even possible to imagine a combination of effects: the Karoo traps were established in the coal-rich sediments of Gondwana 183 million years ago. As a result, a massive degassing of reduced carbon, low in ^{13}C, towards the atmosphere, causing the negative excursion in $\delta^{13}C$ observed during the Toarcian (McElwain et al. 2005).

Finally, a database of all the $\delta^{13}C$ values measured on benthic foraminifera from 40 ODP and DSDP drillings provides high-resolution coverage of the entire Cenozoic (Zachos et al. 2008). The dominant signal from this curve is the decrease in $\delta^{13}C$ of about 2‰ from mid-Miocene (15 Ma) onwards. The reasons for this reduction remain obscure. It could be a sign of a global decrease in the burial of organic carbon over the last 15 million years. However, over the same period, isotopic fractionation ε_{MO} decreased by approximately 8‰, whereas it remained relatively

constant over the rest of the Phanerozoic. This fractionation was reconstructed over the whole Phanerozoic by measuring the $\delta^{13}C$ of organic carbon in marine sediments over many different periods and comparing it to the $\delta^{13}C$ of sedimentary carbonates (Hayes et al. 1999). Since this fractionation is dependent on the concentration of H_2CO_3 in the waters, it can be inferred that its decline is linked to a drop in atmospheric CO_2 since the Miocene. Yet this simple interpretation is challenged by independent estimates of the CO_2 level suggesting pressures below 300 ppmv during the Miocene (see section on atmospheric CO_2). Nevertheless, the combination of the drop in ε_{MO} fractionation and the drop in oceanic $\delta^{13}C$ suggests an increase in CO_2 being buried in the form of organic carbon in sediments since 15 Ma, probably linked to the establishment of the Himalayan orogeny.

The $^{87}Sr/^{86}Sr$ Isotope Ratio of Carbonate Sediments

Marine carbonates record the strontium isotopic ratio, $^{87}Sr/^{86}Sr$, of seawater without fractionation. The residence time of Sr in seawater (2–5 million years) ensures an even value throughout the ocean and therefore low dispersion of the data. A high-resolution curve (1 million years) has been published by Veizer et al. (1999). This signal has been widely used to constrain the extent to which CO_2 is consumed by alteration of continental silicates during the Cenozoic, particularly in response to the Himalayan orogeny (Raymo 1991). Two main types of Sr intake to the ocean are identified: an exchange flux at the level of the ocean ridges, which doesn't affect the Sr concentration of the water but modifies its isotopic ratio. Today, the water enters the ocean ridges with a $^{87}Sr/^{86}Sr$ ratio of 0.709 and exits after contact with mantellic rocks with a typical value of 0.703. This process therefore tends to reduce the $^{87}Sr/^{86}Sr$ ratio of seawater and bring it closer to the mantle value. Conversely, the isotopic ratio of the rivers, inherited from the weathering of continental rocks is now equal to 0.712. There is some correlation between periods with high $^{87}Sr/^{86}Sr$ seawater ratios and glaciation episodes. This has been interpreted as a sign of greater weathering during cold climate periods, in response to intensified physical erosion, which in turn promotes chemical weathering. The signal is particularly clear for the last 40 million years, and the rapid increase in the $^{87}Sr/^{86}Sr$ ratio of seawater has been interpreted as the signature of increased continental weathering during the uplift of the Himalayas. It has been suggested that there is a correlation between this increase in the $^{87}Sr/^{86}Sr$ ratio and a decrease in the CO_2 concentration in the atmosphere. In this model, the Himalayas are considered to have triggered the cooling in the Cenozoic.

This hypothesis has been extensively developed. It is found again in the more recent literature, linking orogeny with global cooling of the climate in response to intensified weathering. Nevertheless, this hypothesis is in contradiction with the paleothermostat theory. In fact, weathering becomes a function of climate in a positive feedback loop. The colder it gets, the more erosion increases, forcing an uptake in CO_2 consumption by weathering, in turn forcing increased cooling. The silicate weathering and volcanic degassing are uncoupled, and the carbon content of the ocean and the atmosphere is consumed in less than a few million years (Goddéris and François 1996), which would lead to unregistered climate disasters during the Tertiary. It should be underlined, however, that it is possible that orogens pump CO_2 while respecting the paleothermostat theory. The consequences of the uplift of a mountain range are much more complex than a simple uplift causing increased weathering. We shall see later that they lead to a number of geological phenomena which ultimately link orogenesis to cooling.

Moreover, the evolution of the $^{87}Sr/^{86}Sr$ isotopic ratio of seawater cannot be interpreted solely in terms of changes in the relative importance of mantellic and continental flows. The isotopic ratio of the source rocks of the weathering may also have changed over time, and, particularly in the orogenic zones, which considerably complicates the interpretation of the isotopic sign of strontium. Nevertheless, the quality of the Phanerozoic signal should motivate further analysis of this indicator in the future.

Along with the $^{87}Sr/^{86}Sr$ isotopic signal, the $^{187}Os/^{188}Os$ osmium isotopic ratio of seawater measured from sediments taken during ocean drilling programs is also used to constrain the evolution of continental and hydrothermal weathering fluxes. The methodology is very similar to that of Sr, but the major advantage of osmium is its short residence time in the ocean, around 10–30 kyr, although it is sufficiently longer than the mixing time of the water masses to ensure values that are representative of the global ocean. River contributions are the dominant factor, with a $^{187}Os/^{188}Os$ ratio of 1.3 and a flux of 1800 mol per year^{-1}. Hydrothermal inputs have an isotopic signature of 0.13 and a flux of around 100 mol per year^{-1}. A flow linked to cosmic dust, with a ratio of 0.13 and a flux of 80 mol per year^{-1}, must also be added. The main sinks are ocean sediment deposits. The ratio can therefore be indirectly linked to the evolution of the Earth's climate and of greenhouse gases, through the characterization of the geological flows of the carbon cycle. Nevertheless, osmium is a very scarce element, which makes it difficult to measure. The mean concentration of Os is 10 fg/g (fentogram gram^{-1}, 1 fg = 10^{-15} g) in seawater and 9 fg g^{-1} in rivers.

The Level of Atmospheric CO_2

There is clearly no direct measurement of this level for the distant past beyond 900,000 years, the period covered by ice cores drilled in the Antarctic ice. All methods are therefore

indirect and depend on a number of assumptions. This inevitably produces significant uncertainties. In addition, the low residence time of carbon in the ocean-atmosphere system (200,000 years) is an inherent cause of scattering of data points. Temporal resolution for the geological past very rarely reaches this level of precision. It follows that two points, attributed to the same geological moment, may have very different values.

An excellent overview was carried out by Royer et al. (2001) using several reconstruction methods. For the very distant past, the counting of the stomata of the fossil leaves is commonly used. For modern species, there is a positive correlation between the number of stomata and the ambient CO_2 level. These correlations are applied to old geological samples. This is probably the least precise method, but it has the advantage of being able to go back very far in the past (as far back as the Devonian) and does not encounter the problems experienced by isotopic systems, such as diagenesis.

A second method allows measurements to be traced back to the Paleozoic. It involves measuring the $\delta^{13}C$ of pedogenic carbonates in paleosols and is based on the fact that the level of CO_2 in modern soils results from a mixing of the atmospheric CO_2 in the atmosphere and the CO_2 in the soil through respiration. The $\delta^{13}C$ of this C_2^{atm} mixture is registered in the pedogenic carbonates:

$$CO_2^{atm} = S(z)\frac{\delta_{sample} - 1.0044\delta_{resp} - 4.4}{\delta_{atm} - \delta_{sample}} \qquad (7)$$

where δ_{sample} is the $\delta^{13}C$ of the pedogenic carbonate. The method requires setting the $\delta^{13}C$ of the breathed CO_2, δ_{resp}, at typical values. It therefore depends on the proportion of C_4 plants to C_3 plants, for which the isotopic fractionations are very different. In practice, it is not applicable after the emergence of C_4 plants, 15 Ma ago. The method also requires knowledge of the $\delta^{13}C$ of the atmosphere δ_{atm} and $S(z)$, the amount of breathed CO_2 at the estimated depth z of the pedogenic carbonate in the paleosol. The $\delta^{13}C$ of the atmosphere is estimated by measuring the $\delta^{13}C$ of marine carbonates of the same age and by imposing the fractionation value between the carbonates and the atmospheric CO_2. As for the fraction of breathed CO_2, it is calculated by making major assumptions about soil temperature, porosity and biological productivity. In fact, if CO_2 production in soils is a function of productivity and temperature (which partially controls the degradation of organic matter by bacteria), its diffusion to the atmosphere depends largely on the physical structure of soils. The level of CO_2 at a given depth is therefore dependent on the relative importance of the production and loss by diffusion. This is by far the most uncertain method. A recent recalibration of the method has led to a considerable reduction in past reconstructed CO_2 pressures (Breecker et al. 2010; Foster et al. 2017). A similar method consists of studying the trace $\delta^{13}C$ of pedogenic carbonates contained in goethite, a mineral formed during soil alteration reactions (Royer et al. 2001).

A third approach uses the measurement of isotopic fractionation of carbon by phytoplankton and its relationship with the dissolved CO_2 content in seawater. Initially, the difference between the $\delta^{13}C$ of carbonates and that of total organic carbon was used. It was subsequently found to be error-prone, in particular due to the presence of organic matter of various origins in both continental and marine sediments. This fractionation is now measured by directly using biomarkers in the organic matter, such as alkenones (Pagani et al. 2005). The link between isotopic fractionation and the level of CO_2 dissolved in water is based on correlations established for the present. For example, this one is based on a compilation of GEOSECS campaign data:

$$\begin{aligned} &\varepsilon_P = 12.03\left[CO_{2aq}\right] - 3.56 \\ &10 \le \left[CO_{2aq}\right] \le 90\,\mu M \end{aligned} \qquad (8)$$

where ε_p is the photosynthetic fractionation of phytoplankton, and $\left[CO_{2aq}\right]$ is the concentration of gaseous CO_2 dissolved in water.

The use of correlations established for current conditions is the main weakness of this method, since they are extrapolated to CO_2 ranges that are significantly higher than the current level, using compounds made by organisms with an unknown metabolism. In addition, isotopic fractionation is also a function of the growth rate of these organisms, which complicates reconstruction.

A final method is based on the measurement of the ratio of boron isotopes $^{11}B/^{10}B$ ($\delta^{11}B$) in carbonate sediments (Royer et al. 2001). The relative abundance of the two dissolved borate species (H_4BO_4 and $H_3BO_4^-$) depends on the pH of the sea water. There is an isotopic fractionation of about 19‰ between the two species. The carbonates are mainly made up of the H_4BO_4 species and the isotopic $\delta^{11}B$ composition of the carbonates will therefore depend on the pH. Nevertheless, the link with atmospheric CO_2 is not clear. First, this requires assumptions that $\delta^{11}B$ of seawater remains constant over time, that the isotopes are shared between the two species and that the relative abundances of ^{11}B and ^{10}B remain the same. It was shown that this was probably not the case and that $\delta^{11}B$ of total borate probably changed in the past. Finally, we must make strong assumptions about the alkalinity of seawater, to bring the pH up to the pressure of atmospheric CO_2.

The compilation of all these reconstructions inevitably shows a large dispersion of points (Royer 2006; Foster et al. 2017) (Fig. 27.6). Nevertheless, some trends may emerge. The level of atmospheric CO_2 seems to have been high before the Devonian (with values generally in excess of 2000 ppmv). This period is followed by a time interval

covering the end of the Carboniferous and the beginning of the Permian, during which time atmospheric CO_2 remained between 200 and 500 ppmv. The data for the Mesozoic are more confusing and show no clear trend. For the same time period, it is common to have atmospheric CO_2 estimates varying by a factor of 5–10. Finally, the Cenozoic appears to be marked by a general decrease in atmospheric CO_2 pressure, reflected above all in a general reduction in the maximum reconstructed values. The most precise record (i.e., with the best temporal resolution and lowest dispersion) is the one obtained by reconstructing the isotopic fractionation in carbon of the oceanic biosphere based on the measurement of the $\delta^{13}C$ of the alkenones (Pagani et al. 2005). It shows a rapid decrease in atmospheric CO_2 from the beginning of the Eocene until the end of the Oligocene: around 50 million years ago, the CO_2 content is estimated to have been 1500 ppmv and fell to between 200 and 300 ppmv 23 million years ago. CO_2 levels then remained constant throughout the Miocene at values slightly below 250 ppmv. Finally, CO_2 levels during the Pliocene were explored using two methods: through isotopic fractionation in carbon and by the counting the stomata of fossil leaves. Both methods suggest that CO_2 levels have risen: between 350 and 450 ppmv from 2.9 to 3.3 million years for the first method, and between 370 and 250 ppmv from 5.3 to 2.6 million years for the second.

The Great Climate Modes of the Phanerozoic and Their Possible Causes

The climate reconstructions of the Phanerozoic show a succession of modes warmer than currently and of cold modes similar to currently, with the emergence of ice caps. This succession is observed in sedimentological records of glacial sedimentary deposits, including tillites, and in ice rafted debris (IRD), debris carried by sea ice (Frakes et al. 1992). However, these climate oscillations are also observed in isotopic data, such as in the $\delta^{18}O$ of carbonates deposited on the seabed, which reflect, at least partially, the $\delta^{18}O$ of seawater at the time of deposition (Veizer et al. 2000). These isotopic data remain difficult to interpret because they combine not only climate indicators (seawater temperature, continental ice volume), but also geochemical data such as salinity of the seawater, the speciation of carbonates, the $\delta^{18}O$ of seawater which is itself influenced by continental and hydrothermal alteration flows. Nevertheless, the $\delta^{18}O$ during the Phanerozoic shows oscillations with a periodicity of 135 million years, in line with sedimentological reconstructions, thereby reinforcing its validity as a good climate indicator. To date, this periodicity of 135 million years remains largely unexplained, but its length indicates that it might have to do with the tectonic processes that shaped the Earth's surface or with astronomical movements (Shaviv and Veizer 2003). The accumulation of recently obtained isotopic data on phosphates (including fossil fish teeth and conodonts) has greatly improved the resolution of the alternation of hot and cold modes, especially during the Mesozoic and Devonian periods (Dromart et al. 2003; Pucéat et al. 2003; Joachimski et al. 2004).

The cold climate modes of the Phanerozoic occur during the Ordovician (from about 470–440 Ma), the Permo-Carboniferous (from about 330–270 Ma), the Jurassic and the Cretaceous. This period is marked by a succession of short cold events: at the end of the Toarcian around 176 Ma, at the Callovian-Oxfordian boundary around 161 Ma, at the transition from the Lower Valanginian to the Middle Valanginian towards 140 Ma, at the beginning of the Aptian around 125 Ma and at the Cenomanian-Turonian boundary around 94 Ma. Finally, the end of the Cenozoic, when Antarctica first started to freeze over 34 million years ago up to the current period, was in cold mode with ice first appearing in the southern polar regions and later in the northern hemisphere.

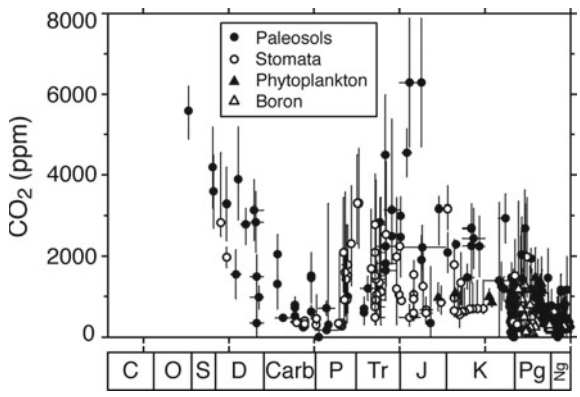

Fig. 27.6 Levels of phanerozoic CO_2 reconstructed by various methods based on proxies

The Causes of Cold Climate Modes

These are generally subjected to more study than the causes of warm modes. The following processes have been suggested:

1. Orogenesis
   The establishment of mountain chains causes an increase in physical weathering following the establishment of glaciers, steep slopes and alternating freeze-thaw regime (Raymo 1991). This results in a greater fracturation of the rock and thus greater sensitivity to chemical weathering which consumes CO_2. Therefore, locally, this process increases the vulnerability of the continental surfaces to

weathering. The result would be a drop in atmospheric CO_2 and an overall cooling. This theory is based on measurements of current weathering rates in mountain ranges, on the strong correlation between physical erosion and chemical weathering in modern watersheds, and on the $^{87}Sr/^{86}Sr$ isotopic ratio of the water run-off from the Himalayas. A second effect should also be taken into account: the very high sedimentation rates in the seas at the foot of the orogens lead to very efficient burial of organic carbon and thus to increased consumption of atmospheric CO_2 thanks to the action of the biological pump. This process is responsible for trapping two to three times more CO_2 than the silicate weathering in the Himalayan orogeny (Galy et al. 2007).

2. The development of vascular vegetation on land. Tall vegetation with a developed root system acts at three levels on weathering rates. The roots stabilize the soils and thus increase the contact time between inland waters and the silicate minerals. In addition, root and microbial respiration in soils increases the partial pressure of CO_2, and thus acidifies the water which percolates towards the bedrock. Finally, the plants secrete organic acids which also contribute to the acidification of the waters. As a result of these three effects, there is an increase in the consumption of atmospheric CO_2 through dissolution of the continental silicates. This hypothesis is based on studies carried out in particular in Iceland on lava flows on slopes covered and uncovered with stemmed vegetation. It appears that weathering rates are eight to ten times larger under dense vegetation cover (Berner 2004). A small-scale laboratory study suggests that non-vascular plants (lichens and mosses) could have a similarly accelerate chemical weathering of continental surfaces (Lenton et al. 2012).
3. Increased burial of organic carbon during the anoxic phase of the ocean. This hypothesis is often proposed to explain positive excursions in the $\delta^{13}C$ ratio of oceanic carbonates correlated with climate cooling. It requires particular environmental conditions: either conditions favorable to maintaining water stratification in large ocean basins and preventing the ventilation of the deep waters in these basins, or conditions of oceanic hyperproductivity leading to the absorption of oxygen in the deep waters through the recycling of organic matter produced in the euphotic zone. This burial may also occur on land-based environments, as has happened during the Carboniferous period.
4. The movement of the solar system into a galactic arm. This recent hypothesis attempts to explain the periodicity of 135 million years in cold modes. The galactic arm is an area of formation of intense stars and of emission of galactic cosmic rays. Reaching the atmosphere, these are thought to participate in the nucleation of low-level clouds, increasing the albedo of the atmosphere and cooling the climate (Shaviv and Veizer 2003). To date, there is no experimental evidence of the validity of this mechanism, which remains purely speculative.
5. The fragmentation of a supercontinent. The resulting increase in rainfall activates the consumption of CO_2 by silicate weathering and thus cools the climate. This effect is particularly important if the supercontinent breaks up along the equator, the site of intense rainfall (Goddéris et al. 2014).
6. The migration of continents towards the low latitudes, characterized by climatic conditions favoring the weathering of continental silicates and thus an increased consumption of atmospheric CO_2 (Nardin et al. 2011).
7. Any reduction in degassing of greenhouse gases from the mantle or sediments towards the atmosphere.
8. The establishment and subsequent weathering of basaltic provinces on the continents. Basalts weather much more efficiently than the average continental crust on which they spread (in equivalent conditions, basalt weathers eight times faster than granite). This finding was established from a study of weathering in basaltic watersheds (Dessert et al. 2001). The weathering of new basalt thus produces a long-term decrease in the partial pressure of atmospheric CO_2. The question remains as to the weathering of submarine basaltic plateaus. Do they contribute to the cooling of the climate system or not? The pH buffer imposed by carbonate speciation in seawater nevertheless suggests that weathering of oceanic basalts is a minor phenomenon, with basalt dissolution being minimal at around pH 8, a value for seawater which probably didn't change much over the course of the Phanerozoic.

The Causes of Warm Climate Modes

Curiously, cold modes have always been considered to be accidents in a prolonged warm state. This is probably the reason why the suggested causes of warm modes are fewer and less discussed in the literature, with the exception of the thermal event of the Palaeocene-Eocene transition.

The following mechanisms have been proposed:

1. Any increase in degassing of greenhouse gases from the mantle or sediments to the atmosphere. This could be due to increased volcanic activity releasing massive amounts of CO_2, basaltic effusion events over land (Dessert et al. 2001) or methane degassing from gas hydrates accumulated in sediments (McInerney and Wing 2011).
2. The creation of a supercontinent, reducing rainfall and thus weathering of the continental silicates, allowing an

increase in pressure of CO_2 in the air and a warming of the climate (Goddéris et al. 2014).

The Phanerozoic Terrestrial Paleothermostat

The short residence time (200,000 years) of carbon in the exosphere, as well as the reaction time of ocean alkalinity (3000 years) impose the following near-equal relationship between the fluxes of inorganic carbon, ignoring any possible imbalances in the organic carbon cycle (see Chap. 5):

$$F_{vol} + F_{MOR} \approx F_{sw} \tag{9}$$

where F_{vol} is volcanic degassing, F_{MOR} ocean ridge degassing and F_{sw} half the CO_2 consumption by silicate weathering. This factor of a half stems from the fact that two moles of atmospheric carbon are consumed for two equivalents of alkalinity produced by the dissolution reaction of the continental silicates. Only one of these two moles will finally be buried in the form of ocean carbonate. The other mole of carbon remains in the ocean-atmosphere system (see Chap. 5). The flux of CO_2 consumption by silicate weathering is a function of temperature and of continental runoff. Generally, it increases as the CO_2 content increases. But its response to an increase in CO_2 is also a function of the continental plant cover, the presence of orogens and of intense physical weathering, the configuration of the continents, the modification of the superficial lithology, following, for example, the establishment of basaltic surfaces on land during major magma events. F_{sw} can therefore be expressed in the following way:

$$\begin{aligned} F_{sw} \alpha f_1(T) \times f_2(R) \times f_3(\text{erosion}) \\ \times f_4(\text{vegetation}) \times f_5(\text{litho}) \end{aligned} \tag{10}$$

where T is the continental temperature, and R is the runoff. The functions f_1 and f_2 are known: the first is an exponential function of the temperature, the second a linear function of the runoff. f_1 and f_2 have been determined for granites and basalts. The function f_3 is unknown. The only indicator available is that there is a very strong positive correlation between physical erosion fluxes and chemical weathering fluxes for both large and small watersheds. We can deduce from this that f_3 is an increasing function of the rate of erosion, but its precise mathematical expression had yet to be defined. As for f_4, studies of lava flows in Iceland suggest that the rate of weathering increases by a factor of 8 when vascular vegetation develops (Berner 2004). f_4 increases with vegetation cover but also when mosses and lichens cede to vascular plants with a well-developed root system (see discussion on the Devonian in the following section). Finally, f_5 expresses the level of dependence on the lithological type. It can be expressed as a constant factor equal to 8 or 10 for new (rapidly deteriorating) basaltic surfaces and equal to 1 for granite surfaces (Dessert et al. 2001).

For example, this simple formalism shows that the establishment of an orogen leads to an increase in the consumption of atmospheric CO_2 through silicate weathering (f_3 increases), but that the conditions of the paleothermostat are always verified: the climate cools globally, and the decrease in the f_1 and f_2 factors compensates for the increase in f_3. It can then be said that the vulnerability of continental surfaces to weathering has changed. Indeed, if the degassing of the solid Earth does not change, Eq. (9) dictates that CO_2 consumption by silicate weathering remains virtually constant on the scale of several million years. However, Eq. (10) dictates a decrease in f_1 and f_2 to compensate for the increase in f_3. We can say that the weathering of continental surfaces has increased, whereas the total silicate weathering flux has remained unchanged. However, to allow f_1 and f_2 to adapt to the new conditions, the equilibrium level of CO_2 is lower, and the climate is colder and dryer. Similarly, the establishment of a basaltic province increases the factor f_5 and the climate will cool in compensation. The same applies to the colonization of the continental surfaces which are described below.

It should nevertheless be noted that the relation 10 is a simplification. The relationship between CO_2, temperature, and continental runoff is complex and is largely dependent on the paleogeographic configuration, which complicates the problem considerably.

Finally, if the possibility of imbalance in the organic carbon cycle is taken into account, the thermostat equation is written as:

$$F_{vol} + F_{MOR} + F_{ow} \approx F_{sw} + F_{od} \tag{12}$$

where F_{ow} is the oxidation of sedimentary organic carbon and F_{od} is the overall burial of organic carbon. If deposits were to increase, for example, due to the development of exceptional conditions for the preservation of organic matter (such as the appearance of large-scale anoxia), while the oxidation of exposed sedimentary organic carbon on land remained constant, this would give the following inequality:

$$(F_{vol} + F_{MOR}) - F_{sw} \approx F_{od} - F_{ow} \geq 0. \tag{13}$$

In this case, silicate weathering must be less than the total degassing of the solid Earth to maintain the paleothermostat balance. This condition will be verified because the increase in buried organic carbon reduces the CO_2 pressure in the air which, in the first order, causes a decrease in the f_1 and f_2 factors.

Finally, it should be noted that the paleothermostat constitutes a very powerful stabilizing force of the Earth's

climate. If causes external to the CO_2 cycle disturb the climate (cosmic rays and cloud nucleation, the passage of the Earth into a cloud of galactic dust, methane degassing), the resulting change in f_1 and f_2 factors would cause an imbalance in the carbon cycle, which would find a new balance over a few million years, by adjusting the pressure of atmospheric CO_2 to re-establish climate conditions verifying the paleothermostat.

The Paleozoic Climate: The Chronology of Major Trends and Their Causes

In general, the Paleozoic climate is described as warmer than the current one, except for two glacial events with very different characteristics.

The reasons for this warm climate state are not clearly understood, but several hypotheses have been put forward. On the one hand, the degassing of the solid Earth seems to have been generally greater by about 60% than it is at present. This assertion is based on the fact that the sea level was generally higher in the geological past than it is today, except for the Permo-Carboniferous transition. This high sea level can be explained firstly by the larger volume occupied by the ocean ridges and therefore a supposedly greater degassing of the solid Earth. This result has never been confirmed by other methods apart from sea level and remains questionable. On the other hand, the absence of abundant vascular vegetation until the end of the Devonian prevented the development of modern soils on land surfaces. This absence of soil reduced the contact time between the inland water and minerals, thus limiting their weathering. Similarly, the absence of a root system reduced the acidity of soil solutions and thus the consumption of atmospheric CO_2 by continental silicate weathering, which in turn promotes high CO_2 levels. Berner (2004) estimates that the average global temperature was ±6 °C higher than it is currently, based on a numerical modeling study. These very high values are confirmed by measurements using the paleothermometer made up of the number of rare molecules $Ca^{18}O^{13}C^{16}O_2$ in the carbonates of the Lower Silurian (Came et al. 2007).

Whatever the causes, this warm climate state was interrupted by several glacial events of very different durations and amplitudes. The Atlas Fig. chapter 3.9 shows the paleogeographic maps of the Earth during the main periods of the Phanerozoic.

The Ordovician Glaciation

The $\delta^{18}O$ data on apatite show a long-term cooling trend during the Lower and Middle Ordovician and a sudden drop in temperatures during the Hirnantian in the Late Ordovician (Trotter et al. 2008), which is independently confirmed by the $\Delta^{47}CO_2$ analysis (Finnegan et al. 2011, Fig. 27.7). Glacial sediments, which are the only direct evidence of Ordovician glaciation, are only documented during this very short cool interval, which has long suggested that glaciation is a short-term cold accident punctuating an otherwise very hot period of geological time. Geochemical studies reconstructing the composition of oceanic $\delta^{18}O$ (Finnegan et al. 2011) and glacio-eustatic variations (Loi et al. 2011) suggest that the ice cap at the South Pole would have reached a volume almost twice as large as during the Last Glacial Maximum. Indirect indices such as variations in sea level (Dabard et al. 2015) or $\delta^{18}O$ excursions (Rasmussen et al. 2016) today suggest that the first ice caps could have been in place since the Middle Darriwilien (about 470 Ma) in the Ordovician. In addition, it appears that glacial events also punctuated the Lower Silurian. The Ordovician glaciation is

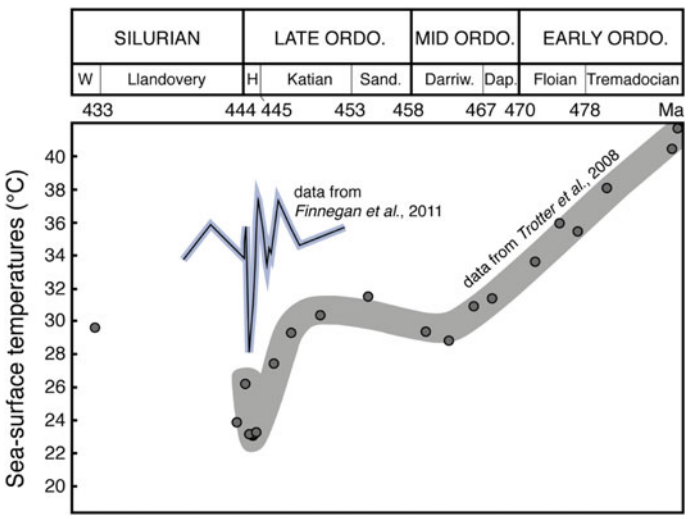

Fig. 27.7 Tropical sea-surface temperatures reconstructed based on $\delta^{18}O$ data measured on apatite (Trotter et al. 2008) and based on $\Delta^{47}CO_2$ proxy data (Finnegan et al. 2011)

therefore increasingly considered to have been a long cold period (about 470–425 Ma), sometimes referred to as 'Early Paleozoic Ice Age' (Page et al. 2007), and within which the Hirnantien only represents a glacial maximum. This vision is supported by the most recent climate models (Pohl et al. 2016).

The causes of this glaciation are still poorly understood. Nardin et al. (2011) showed that the long-term cooling of the climate can be explained by the paleogeographic evolution occurring throughout the Ordovician, and in particular the migration of continents in the intertropical zone conducive to weathering, which brings about a fall in the atmospheric concentration of CO_2. Regarding the Hirnantien glacial peak, the best explanations also suggest a fall in atmospheric CO_2, but the mechanisms to achieve this are subject to debate. Kump et al. (1999) proposed an interesting hypothesis: the fall in CO_2 level could have been a consequence of the establishment of New Caledonian and Appalachian orogens during the Middle and Upper Ordovician, which would have increased the vulnerability of the continental surfaces to weathering. Other mechanisms have also been proposed, including the establishment of the first plants on land (Lenton et al. 2012). The difficulty in explaining this event lies in the magnitude of the cooling, which is around −7 °C at tropical latitudes, whereas sea surface temperatures appear to have varied by only 1–2 °C at the same latitudes during the last glacial-interglacial cycle (CLIMAP Project 1981). However, numerical modeling of the ocean-atmosphere coupled system during the Ordovician revealed climatic instability associated with the sudden development of sea ice, which explains a sharp fall in temperatures in response to a moderate decrease in atmospheric CO_2 concentration, thus loosening the constraints that would be placed on CO_2 sinks to explain the geochemical data (Pohl et al. 2016). To explain the emergence from the Hirnantian glacial maximum, Kump et al. (1999) proposed the following mechanism: as the ice cover on the supercontinent Gondwana increased, the available surface of continental silicates exposed to weathering falls, thus causing an accumulation of CO_2 in the atmosphere. This persuasive scenario was tested with a simple climate model.

The Devonian Climate

The Devonian (419–359 Ma) is marked by numerous biological disturbances. Although the first traces of vegetation appeared during the Middle Ordovician (Rubinstein et al. 2010) and the existence of vegetation fires during the Silurian are suggested based on the presence of charcoal in the sedimentary record, the development of a long-stemmed biosphere begins in the Lower Devonian. Plants reaching heights of up to 2 to 3 meters were identified during the Eifelian (390 Ma; Stein et al. 2007). Trees, 8–10 m high, began to colonize the land towards the end of the Givetien (385 Ma), with, among others, giant ferns such as *Archeopteris* and *Cladoxyopsides* (Anderson et al. 1995). True large forests are likely to have become established towards the end of the Devonian (Frasnian; 380 Ma, Scott and Glaspool, 2006). As trees appeared and flourished, weathering of the continental silicates rapidly accelerated, while degassing from the solid Earth remained almost constant (Berner 2004). Soils developed along with root systems, increasing the acidification of the water in contact with the minerals as well as increasing the contact time between inland water and silicate rocks. This resulted in a rapid decrease in the partial pressure of atmospheric CO_2, from 2000 ppmv in the early Devonian to 1000 ppmv at the end (Foster et al. 2017). The extent to which the climate cooled as a result of this colonization is uncertain however because the change of the albedo of continental surfaces, following the replacement of bare soils by forests, compensates at least partially for the fall in atmospheric CO_2 (Le Hir et al. 2011). It is also interesting to note that the overall cooling of the climate may have been beneficial to the development of modern leaves, which are large in size and have many stomata, encouraging primary production on land to the detriment of more primitive plants. We can thus infer the establishment of a positive feedback between cooling and the colonization of land surfaces by ever more efficient plants.

Another mechanism that could explain the drop in CO_2 during the Devonian is an increase in the amount of CO_2 trapped in sediment, also as a result of colonization of land by continental plants. Indeed, the appearance of lignin in plant tissues from 410 Ma onwards increased the amount of organic carbon preserved in continental environments and on the margins. Lignin is indeed much more resistant to mineralization than marine organic matter. It was first thought that lignin appeared before the development of organisms capable of decomposing it, causing an increase in the burial of carbon and the reduction of CO_2, which could have contributed to the establishment of the glaciation of the Late Paleozoic (Nelsen et al. 2016). Nevertheless, recent studies have shown that decomposers evolved in parallel to lignin, which calls into question an 'organic' trigger for the Permo-Carboniferous glaciation (Nelsen et al. 2016).

Finally, the end of the Devonian is characterized by a mass extinction event, affecting tropical marine environments in particular. This event lasted approximately 1–3 million years, culminating at the Frasnian-Famennian boundary. It is accompanied by the deposition of anoxic sediments (black shales), accompanied by two positive excursions of the $\delta^{13}C$ of carbonate sediments. It has been proposed that these events are the consequence of the emergence of pulses as vascular plants colonized the land

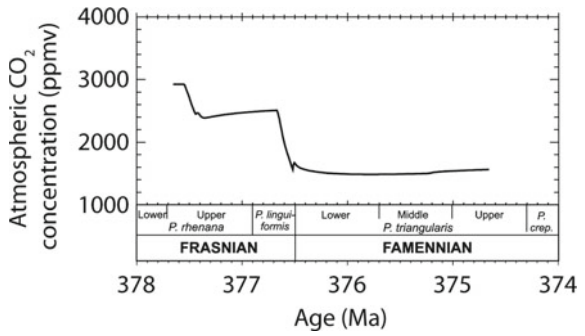

Fig. 27.8 Calculated levels of CO_2 in the atmosphere at the end of the Devonian

and of increased weathering bringing additional nutrients to the ocean and causing intense blooms in the oceanic biosphere. These would have led to increased oxygen consumption in the surface waters and the establishment of large-scale anoxia. Moreover, these anoxic events are correlated with second-order fluctuations of the sea level (a few tens of meters), thereby disturbing the weathering of carbonate platforms which alternate between being emerged and flooded. A numerical study, coupling a 1D energy balance climate model and a geochemical model of ocean and continental surfaces predicts a fall of 1500 ppmv across the Frasnian-Famennian boundary, over an interval of only 3 million years, as well as a cooling reaching more than 2 °C in the equatorial zones (Fig. 27.8; Goddéris et Joachimski 2004). These results are in agreement with the development of the first glaciers at the end of the Devonian.

The Permo-Carboniferous Glaciation

The cooling trend which started in the Devonian continued and reached its peak during the Permo-Carboniferous glaciation (330–270 Ma) also known as the '*Late Paleozoic Ice Age*' (Montañez and Poulsen 2013). It is the most important glacial event of the Phanerozoic. Debris carried by drifting icebergs reached the paleolatitude of 30° (Frakes et al. 1992). The temperature of the tropical waters was probably 2 °C below present values (Veizer et al. 2000). At the same time, the continents were covered with dense forests in low latitude areas (in the latitude band 15°N–15°S).

This major and prolonged cooling is traditionally considered to have been the final consequence of the colonization of continental surfaces by vascular plants, favoring continental weathering. A second major effect of this accelerated growth also occurred: the burial of organic carbon in continental environments reached a level during the Carboniferous never before attained during the whole Phanerozoic. Approximately 31×10^{15} mol Ma^{-1} of carbon were buried on the continents during the Carboniferous, while in the Devonian, this carbon sink was thirty times lower (Berner 2004). This is nearly double the estimated burial rate for the Cenozoic. The reason for the efficiency of this burial during the Carboniferous remains partly obscure, but it is probably linked to two interconnected factors: (i) the abundance of vegetation in certain zones, (ii) a low sea level during the Carboniferous (although it was high during the Devonian), creating low-lying coastal lands and extensive swamps. This efficient burial on the continents of reduced carbon depleted in ^{13}C, instigated the longest and most extensive positive excursion of the $\delta^{13}C$ in carbonate sediments (5‰, spread out over almost all of the Carboniferous and Permian).

Although this model of the forcing of the Carboniferous-Permian glaciation by biotic factors is commonly accepted, several elements today are causing us to question it. First, the colonization of the continents by vascular plants of large growth form was completed at the end of the Devonian, several tens of millions of years before the establishment of the Carboniferous-Permian glaciation (Davies and Gibling 2013). In addition, the increase in continental organic carbon burial seems relatively uncorrelated both with the $\delta^{13}C$ signal, which shows uniformly high values between 360 and 260 Ma (Fig. 27.5), and with the chronology of the colonization of continental surfaces by plants. A recent study coupling a climate model with a long-term carbon cycle model, highlighted the key role of tectonic changes in the entry into as well as the exit from the Carboniferous-Permian glaciation (Goddéris et al. 2017). The Hercynian orogen, by creating steep topographic slopes, would have allowed physical erosion to increase causing the destruction of the superficial soil formations, which had previously protected the bedrock from chemical weathering. The weathering of the newly exposed continental rocks would then have induced a drop in atmospheric CO_2 to levels allowing entry into glaciation (Fig. 27.9 carb). This scenario of tectonic forcing leading to glaciation is not in opposition to the biotic hypothesis, since the increased weathering of the continents would increase the nutrient flows to the ocean and thus necessarily favor an increase in primary productivity in the ocean.

The sequestration of organic carbon in continental sediments may have forced a decrease in CO_2 but it also led to a considerable increase in O_2 pressure in the atmosphere, from 15% at the end of the Devonian to 32% of the air content around 290 Ma (Berner 2004). This increase is also recorded in the $\delta^{13}C$ of fossil remains of continental vegetation. The fractionation of carbon isotopes reached 23‰ 290 Ma ago and was therefore about 5‰ higher than the average of the estimated values for the rest of the Paleozoic and Mesozoic. In modern plants, this fractionation is a function of the O_2/CO_2 ratio in the atmosphere. A value of 23‰ indicates a ratio of 1000. While the CO_2 pressure was around 300 ppmv

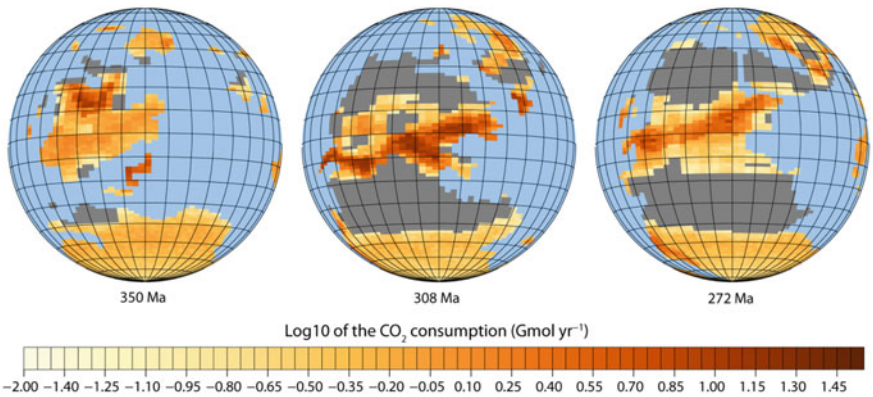

Fig. 27.9 carb—Paleogeographic pattern of CO_2 consumption by silicate weathering immediately before, during and after the Carboniferous-Permian glaciation. Weathering is inhibited by the development of a thick saprolith along the equator, except when steep slopes and high runoff maintain a high flow of erosion (308 Ma). The gray continental surfaces represent arid areas with no runoff and no weathering

(close to the current value), O_2 reached a pressure close to 30% of the total pressure of the atmosphere at ground level.

The End of the Paleozoic

The end of the Paleozoic is marked by the exit from the Permo-Carboniferous glaciation. The climate of the end of Permian is a much drier and warmer climate.

The transition from a cold mode to a warm mode is triggered during the final aggregation of the Pangea in the middle of the Permian. The formation of a supercontinent reduced the amount of precipitation on the continents, which partially inhibited the consumption of CO_2 by silicate weathering. In response to this imbalance between the volcanic source of CO_2 and the sinks through weathering and deposition of carbonates, atmospheric CO_2 accumulated, heating the system until the increased weathering due to increasing temperature compensated for the lack of precipitation, restoring the balance between sources and sinks of CO_2. This era is explored by much more powerful numerical models than the simple models used for the Paleozoic. The use of atmospheric general circulation models coupled with biogeochemical cycle models allows a more detailed investigation of the role of paleogeography.

Simulations carried out by atmospheric general circulation models coupled with biogeochemical cycle models calculate that 250 Ma ago, CO_2 pressure was only 2400 ppmv in response to the coming together of Pangea (Donnadieu et al. 2006) and that continental temperatures reached 19 °C on average. By comparison, today, a similar average, strongly influenced by the very cold Antarctic continent, would be only 6.7 °C. The end of the Permian is marked by a major negative excursion of the $\delta^{13}C$ of marine carbonates (−3‰ over about ten million years. See Fig. 27.5). This is interpreted as indicating a drastic reduction in the sequestration of continental organic carbon in response to the decline in productivity by the biosphere, due to a major reduction in precipitation (Berner 2004). Moreover, the end of the Permian is marked by intense volcanic activity, with the establishment of large fissural eruptions (traps) in Siberia. These three factors reinforced the global warming trend from the end of Permian onwards.

The Mesozoic

The three geological stages of the Mesozoic have long been considered to be typical examples of hot climates, especially the Cretaceous. Long-term carbon cycle models such as GEOCARB and all subsequent generations estimate very high values for atmospheric CO_2 pressure over the entire Mesoozoic, between 4 and 10 times the current value, supported by strong degassing of the solid Earth (Berner 2004). The only significant event was the appearance of flowering plants (angiosperms) in the Cretaceous, thought to further increase the efficiency of the consumption of atmospheric CO_2 through silicate weathering. This brought about a significant drop in CO_2 after 130 million years ago.

New perspectives on the climate trends of the Mesozoic have emerged recently and suggest other important long-term changes. The first notable feature (Fig. 27.10) is the steady increase in the $\delta^{13}C$ of carbonate sediments by about 1‰ from its lowest point in the Jurassic to the middle Miocene in the Cenozoic (Katz et al. 2005). This increase is typically explained by an increase in the ratio of organic carbon to total carbon buried in marine sediments, reaching ±20%, as the dislocation of Pangea increased the surface area available for the accumulation of organic carbon. Many sedimentological studies show a significant increase in

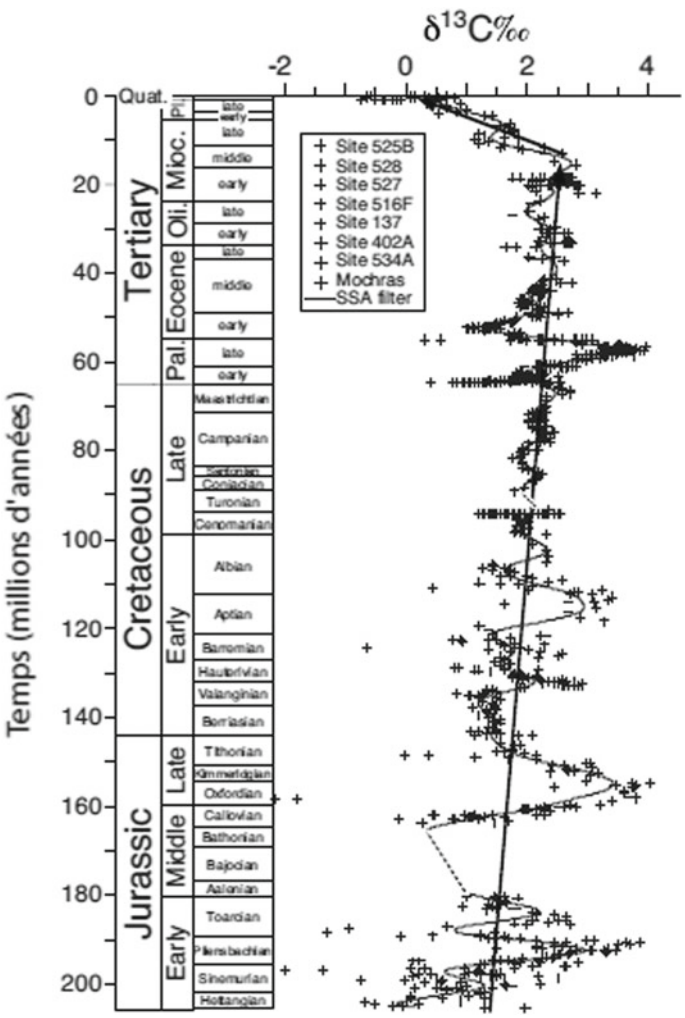

Fig. 27.10 $\delta^{13}C$ of carbonate sediments over the last 200 million years. (according to Katz et al. 2005)

the amount of organic carbon preserved on the shores of the Atlantic Ocean as it opened up during the Jurassic and Cretaceous periods.

This slow increase in the amount of buried organic carbon is also responsible for a net supply of oxygen to the ocean-atmosphere system (3×10^6 Gt O_2). This process should also consume atmospheric CO_2 by storing an increasing share of photosynthesized carbon in sediments. The paleothermostat (see Chap. 5, Volume 2) also allows the carbon cycle to be maintained close to equilibrium. Indeed, the cooling initiated by the increase in sequestration of organic carbon will be compensated for by a reduction in the consumption of CO_2 by the weathering of continental silicates. The response of CO_2 pressure in the atmosphere to this long-term evolution still needs to be quantified.

A second notable feature of the Mesozoic is the fragmentation of Pangea, which began as early as 250 Ma. An event of this magnitude has a major impact on the Earth's climate and the carbon cycle. Using a numerical model coupling an atmospheric general circulation model and a model of global biogeochemical cycles, Donnadieu et al. (2006) explored the climate and biogeochemical consequences of this dislocation. A configuration such as that of Pangea implies a weak continental runoff, due to its large continental nature. This causes a partial inhibition of continental silicate weathering. According to the theory of the paleothermostat, atmospheric CO_2 will increase, forcing the temperature to rise until the consumption of CO_2 by silicate weathering compensates once more for the degassing of the solid Earth. On the other hand, a configuration where the continents are dispersed leads to an increase in runoff and thus greater efficiency of silicate weathering. This results in increased CO_2 consumption due to weathering (Fig. 27.11), and the climate cools down until the paleothermostat is again balanced. At a constant rate of degassing of the Earth, the average annual temperature of the continents would have decreased from 19 °C at the beginning of the Triassic to 10 °C at the end of the Cretaceous (Donnadieu et al. 2006).

An interesting finding is that this simulated global cooling is not linear over the whole Mesozoic. The main episode of

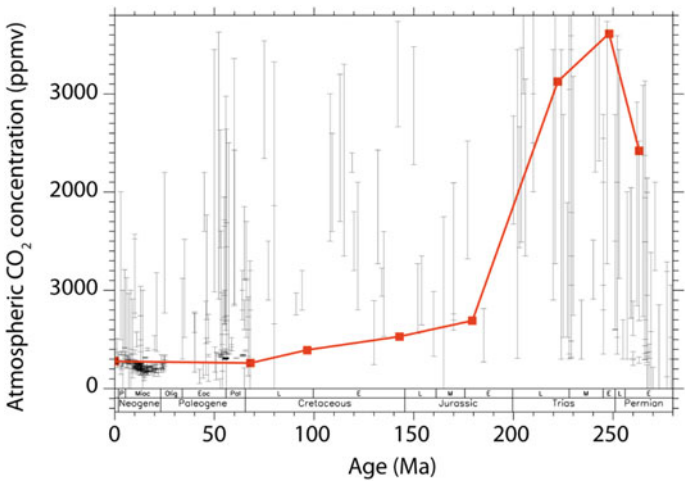

Fig. 27.11 Levels of atmospheric CO_2, calculated for the last 250 million years (red line), in response to continental drift. The vertical lines represent the available data

cooling and humidification of continental surfaces occurred during the Upper Triassic, between the Carnian and the Rhetian (237–201 Ma). The Lower and Middle Triassic are characterized by very high continental temperatures and extensive aridity (average annual continental runoff of only 23.5 cm/year), consistent with sedimentological data from the establishment of redbeds and massive deposits of evaporites. The corresponding atmospheric CO_2 pressures are close to 3000 ppmv, in agreement with the current reconstructions (Royer 2006), suggesting values between 2000 and 4000 ppmv for the same period.

An abrupt change occurred in the last stage of the Triassic (Rhetian 209–201 Ma), during which time 50% of the Mesozoic cooling occurred in the model. Goddéris et al. (2008) calculated CO_2 pressures of around 900 ppmv and global average temperatures lower by 4.6 °C. The CO_2 levels estimated based on the count of stomata on fossil leaves confirm these low levels of CO_2 between 500 and 1000 ppmv (Royer et al. 2004). The $\delta^{18}O$ measured on brachiopod shells show an increase of 0.8‰ between the Carnian and the Rhaetian, i.e. an overall cooling of more than 3 °C, (Korte et al. 2005) in line with modeling results. Similarly, sedimentological data clearly show an increase in moisture and a decrease in temperature during the Rhaetian (Fig. 27.12). Changes in clay mineralogy and in the conditions for pedogenesis are signs of the installation of cooler and wetter climate regimes around 209 Ma ago, during the Norian-Rhaetian transition (Ahlberg et al. 2002).

The causes of this rapid cooling may be found in the general drift of the Pangea towards the north. During the Middle Triassic, large continental areas were located in the southern zone of the inter-tropical divergence, a very arid area and therefore not conducive to weathering. The shift of the Pangea to the north brought these large areas into the humid equatorial zone, allowing increased atmospheric CO_2 consumption through increased runoff. Thus, the world became colder, but more humid, allowing the paleothermostat equilibrium to be maintained (equilibrium degassing of the solid Earth—silicate weathering), but at a lower level of CO_2 than in the middle of the Triassic. It is remarkable that these cooler conditions (but nevertheless up to 4 °C warmer than is currently the case on the continents) persisted after the Triassic, driven by the break-up of the Pangea rather than by its general latitudinal movement.

The Cenozoic

The overall climate evolution of the Cenozoic is better understood than that of the preceding epochs. Nevertheless, the causes of this evolution are still widely disputed. The climate history of the last 65 million years is that of a transition from the warmer Cretaceous climate, characterized by little or no polar ice caps, towards the current glacial climate.

The oldest stage of the Cenozoic, the Paleocene, is characterized by a climate similar to that of the late Cretaceous. The first break with the Mesozoic is at the Paleocene-Eocene transition (56 Ma, Fig. 27.3). This transition is marked by an extremely intense global warming. The deep waters of the ocean warmed up to about 5–7 °C in response to global warming and to a reorganization of ocean circulation. Similarly, the surface waters heated up by 8 °C (Thomas et al. 1999; Zachos et al. 2003; Sluijs et al. 2006). This warming, probably reinforced by the destabilization of methane hydrates in the sediments (McInerney and Wing 2011) was of short duration, spanning just 200,000 years.

This brief episode was followed by the Eocene climate, which lasted about 5 million years. (Fig. 27.3).

From the time of entry into the Middle Eocene, the climate began to cool down globally, leading to the appearance of small temporary ice sheets that developed on the Antarctic

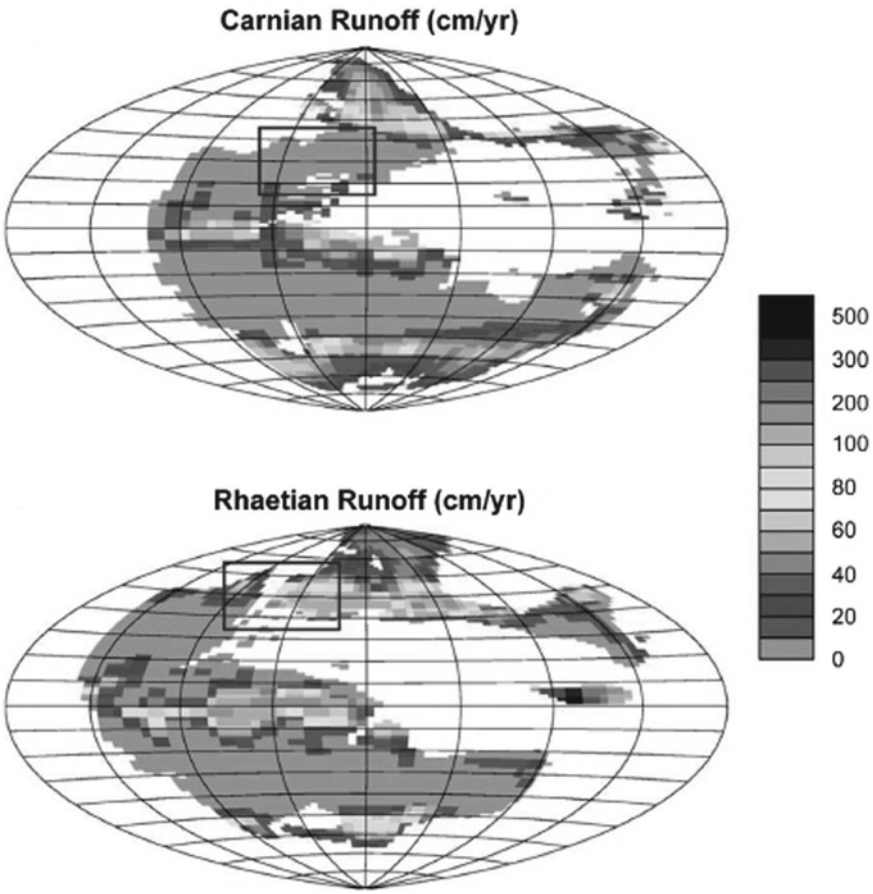

Fig. 27.12 Continental runoff calculated for the Carnian and Rhaetian, two stages of the Triassic, at 3122 ppmv of CO_2. The red rectangle shows the position of Europe and indicates increased humidification of the area between the Carnian and the Rhaetian

in the last phase of the Eocene (Zachos et al. 2008). At the Eocene-Oligocene transition (34 Ma) a distinct, cold climate pulse was experienced. The $\delta^{18}O$ data obtained from benthic foraminifera show a deep-water cooling of about 4 °C (Fig. 27.3). A permanent Antarctic cap began to emerge (Zachos et al. 2008).

The second step towards global cooling occurred at the Oligocene-Miocene boundary (23 Ma). But this cold episode is followed by the Miocene climate optimum between 23 and 15 Ma. The latter is particularly problematic because, according to the $\delta^{11}B$ and $\delta^{13}C$ data from alkenones, atmospheric CO_2 pressure should have been low, at around the present value, or even lower, between 200 and 300 ppmv (Pagani et al. 1999). The reasons for this climate optimum are still unknown.

From 15 Ma onwards, the climate cooled rapidly and the East Antarctic sheet developed. The last stage of cooling, 5 Ma ago, was marked by the establishment of the West Antarctic ice sheet (Fig. 27.3).

The reasons for this cooling are still in dispute. There are two opposing theories. According to one, the climate evolution of the Cenozoic was largely driven by the opening of key ocean passages and the closure of others. According to the other, it was the drop in CO_2 level that was responsible for this cooling. From 50 Ma onwards, ocean basins began to become established in the Drake Passage area, allowing shallow water exchanges between the Atlantic and Pacific Oceans. Isotopic analyses of neodymium in deep sediments indicate that around 41 Ma, the flow of exchanges between ocean basins intensified around Antarctica (Scher and Martin 2006). The intensification of the rate of expansion of the seabed in the Drake and the Tasmanian Passages 34 Ma ago, allowed the Antarctic circumpolar current to become established, definitively isolating the South Pole continent. This date coincides with a major development phase of the Antarctic ice cap.

The role of ocean passages in global climate change has been called into question by modeling studies, which tend to show that glaciation and the appearance of an ice cap over Antarctica are mainly associated with a decrease in the level of CO_2 Lefebvre et al. (2012), see also Chap. 3. It should be noted, however, that this premise is very poorly documented. Indeed, this is a period for which $\delta^{11}B$ data are non-existent. At best, we know that CO_2 levels were around 1000 ppmv 40 Ma ago, and about 300 ppmv 24 Ma ago. These data suggest decreasing levels of CO_2 although it is not possible to document the evolution precisely. Nevertheless, DeConto and Pollard (2003) have shown in a simulation that even

where the Drake Passage is kept artificially closed, the decrease in atmospheric CO_2 concentration causes glaciation to occur over the Antarctic. Glaciation is simply delayed by about 2 to 3 million years.

Changes in the climate caused by the opening or non-opening of the Drake Passage will also affect the global carbon cycle, potentially increasing the climate response of the system. One possible consequence of the opening of the Drake Passage is an upheaval of the thermohaline circulation facilitating the formation of deep waters in the Antarctic and triggering the plunging of waters in the North Atlantic (Huber and Nof 2006). The result is a warming of the northern hemisphere of approximately 3 °C and a severe cooling of the Antarctic. As most of the continental area is located in the northern hemisphere, an increase in global consumption of CO_2 by continental silicate weathering is to be expected and thus a reduction in the amount of CO_2 in the atmosphere, reinforcing the cold climate mode being established (Elsworth et al. 2017). In conclusion, although the overall climate effect of the opening of the Drake Passage remains weak, there may have been positive feedbacks in the carbon cycle which substantially amplified the response. These have yet to be documented with precision.

A second driver of the evolution of climate also took place during the Cenozoic: the Himalayan orogen.

How orogeny affects the carbon cycle is complex. We have identified two effects: one is the chemical weathering of exposed silicates in the mountain chains, the other is the sequestration of organic carbon at the foot of the mountains. Take first the increase in weathering of continental surfaces through increased erosion. The development of glaciers, the alternating freezing and thawing patterns at high altitudes and steep slopes all favor the break-up of rocks and increase the area of contact with solutions. This results in increased weathering and increased consumption of CO_2. This increased weathering is seen in an increase in the erosion factor f_3 in Eq. (10), and the level of CO_2 is lowered until the weathering of the silicates again compensates for the degassing of the solid Earth (Goddéris and François 1996). Currently, 4×10^{12} kg yr^{-1} of suspended solids are transported to the ocean from the Himalayan zone, representing 17% of the world's erosion flow, whereas the ratio of the Himalayan surface to the total continental area is only 4%. It is therefore to be expected that a major orogen would considerably increase the consumption of atmospheric CO_2 through chemical weathering of the exposed rocks (increase in factor f_3). However, this result is not confirmed by current data of fluxes of dissolved elements in the rivers from the Himalayas. They suggest a modest consumption of 0.7×10^{12} mol yr^{-1} of CO_2 by weathering of Himalayan silicates, only 6% of the world total of 11.7×10^{12} mol yr^{-1}. One of the reasons for this low rate of chemical weathering may be that the erosion motor is too efficient in the Himalayas and that the discharge of the debris produced by mechanical erosion is too fast to allow the progress of effective chemical weathering. This would produce a weathering system which would be very limited by the very slow kinetics of the dissolution of minerals. In addition, the lithology is such that calcium silicates are scarce in the Himalayas and the weathering fluxes are mostly of sodium and potassium silicates. Since these chemical reactions do not lead to precipitation of carbonates, their effect on the carbon cycle is minimal over the long term (France-Lanord and Derry 1997).

However, the rate of sedimentation, which is extremely high in the Bay of Bengal, is responsible for the preservation of very large quantities of organic matter, of both continental and marine origin. It is estimated that the sequestration of carbon at the foot of the orogen is two to three times higher than the consumption of CO_2 by weathering of the Himalayan silicates. A recent study shows that 100% of the organic carbon of continental origin transported by the Himalayan rivers is preserved in the sediments of the Gulf of Bengal (Galy et al. 2007). France-Lanord and Derry (1997) estimated that the sedimentary organic carbon reservoir grew to 0.6×10^{12} mol yr^{-1}. This value is of a similar order of magnitude to estimates from numerical simulations, carried out using a carbon cycle model reversing the records of $\delta^{13}C$ in carbonates during the Cenozoic period (Goddéris and François 1996). The Himalayas consume carbon (Fig. 27.13), but in organic form, and therefore, they are, at least partially, responsible for the cooling of the climate during the Cenozoic. The quantification of the impact of this mechanism on atmospheric CO_2 has yet to be completed.

Abrupt Climate Events During the Phanerozoic

As well as defining the major climate modes of the Phanerozoic, recent efforts have defined episodes of rapid climate change that have punctuated the history of the Earth at a $100{,}000^{-year}$ scale. We outline below three of these events, discussing their causes.

The Callovian-Oxfordian Transition (Middle Jurassic-Upper Jurassic)

This was a brief cooling episode during the Jurassic. Such events occurred several times during the Jurassic and Cretaceous periods.

The $\delta^{18}O$ values measured in fish teeth and belemnites suggest an abrupt drop in temperature of 8 °C starting in the Upper Callovian and remaining until the middle Oxfordian. At the same time, boreal ammonite fauna invaded the

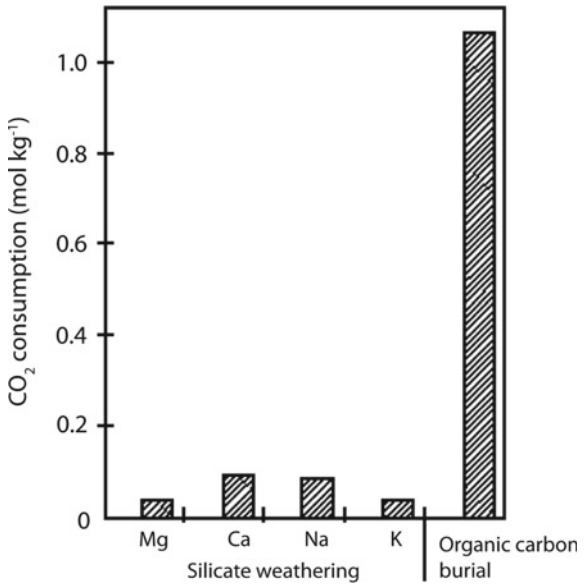

Fig. 27.13 Atmospheric CO_2 consumption by the Himalayas, per kg of sediment exported. On the left, the contribution of silicate weathering, reconstructed from the balance of each cation exported by the mountain range. On the right, the contribution associated with the sequestration of organic carbon in the Bay of Bengal (France-Lanord and Derry 1997)

Tethyan domain, suggesting widespread cooling at all latitudes (Dromart et al. 2003). The total duration of the event was about 3 million years. This episode is also marked by the reduction, by a factor of about 10, of carbonate deposits. The $\delta^{13}C$ values also suggest a positive excursion of about 0.5‰ over the same period. Finally, a drop in the sea level of several tens of meters is supported by evidence (Dromart et al. 2003), suggesting the establishment of temporary ice caps (Fig. 27.14).

The reasons for this cooling are not completely understood, nor, indeed are those of all the abrupt cooling episodes of the Jurassic and the Cretaceous. However, several avenues of enquiry have been opened. In particular, for this specific event, the amount of organic matter buried in marine sediments increased greatly during the middle Callovian just before the cooling. The percentage of organic matter increased from less than 1% during the early Callovian to 5%, and even 10% in the middle Callovian. This increased rate of burial of organic matter may have led to an increase in consumption of atmospheric CO_2 on a temporal scale sufficiently short, relative to the response time of the terrestrial paleothermostat so that it was unable to intervene as a stabilizer. This would have resulted in a reduction in CO_2 pressure which could have initiated the subsequent cooling. This cooling, accompanied by a drop in sea level caused by the development of glaciers on the coldest continents, was responsible for the near halting of carbonate sedimentation on the continental shelves.

Another hypothesis advanced recently connects the massive reduction in carbonate deposits on the continental shelves to the cooling episode. To date, it was assumed that the arrival of colder climate conditions resulted in a reduction in bioconstruction activity in the reef areas. Conversely, Donnadieu et al. (2011) suggest that the strong decrease in carbonate reef activity due to external causes (tectonic reasons for example) caused an accumulation of alkalinity in the oceans. In fact, this alkalinity continued to be supplied by rivers (continental weathering), whereas the alkalinity sink by deposition of carbonates was greatly reduced. The result was a massive dissolution of atmospheric CO_2 in the oceans. This caused CO_2 pressure to drop from 800 to 200 ppmv during crises in the carbonate production (lasting a few hundred thousand years), resulting in a global average cooling of 9 °C.

The Cretaceous-Tertiary Boundary, Meteorite and the Deccan Traps

The Cretaceous-Tertiary boundary (K–T), dating back to 66 Ma, has been studied in detail because it corresponds to a mass extinction event, which eliminated, among other species, the dinosaurs. Two major events occurred at the K–T boundary: the collision of a meteorite with the Earth and the establishment of the Deccan traps. This latter is a major magmatic event which may have had a major impact on the biosphere, but certainly had on the Earth's climate from 10^5 to 10^6 years.

Dessert et al. (2001) have simulated the impact of the Deccan Traps on the geochemistry and climate of the Earth. The total volume of lava put in place is 3×10^6 km^3, corresponding to the emission of 1.6×10^{18} mol of CO_2, or half the current carbon content of the exosphere. This emission could have occurred within a timeframe of about 10^5 years. This time scale is shorter than the response time of the geological carbon cycle. This is thus far beyond the capacity of the Earth's paleothermostat to respond. This produced a very rapid increase in the partial pressure of CO_2 which was increased to more than 3.5 times its initial level in 100 000 years (i.e. 1000 ppmv, assuming that the pre-disturbance CO_2 levels were at the pre-industrial level of 280 ppmv: Dessert et al. 2001) The global average temperature was thus increased by 4 °C a hundred thousand years after the establishment of the Traps.

Once the eruption ended and time passed, the Earth's paleothermostat could then take on its stabilizing role. The surplus CO_2 was slowly consumed by silicate weathering, which was itself accelerated by the increased greenhouse effect. Over 2 million years, the level of CO_2 returned to a stable level, one that was lower than the pre-disturbance level by 60 ppmv, corresponding to an overall cooling

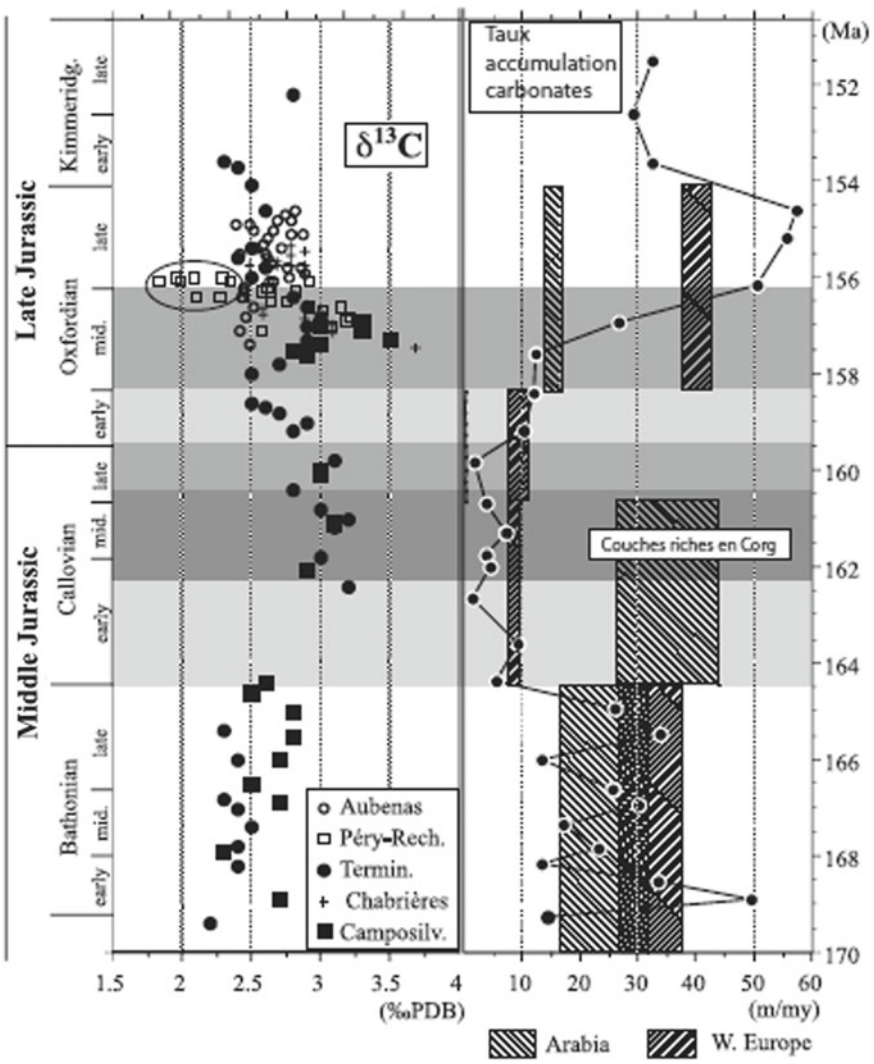

Fig. 27.14 Summary of events at the Middle Jurassic-Upper Jurassic transition. On the left, the $\delta^{13}C$ of the carbonates, measured at different locations. On the right, layers rich in organic carbon, and the accumulation rate of carbonates

of ±0.5 °C compared to the temperature prior to the establishment of the Deccan Traps (Fig. 27.15). This cooling was the result of continental surfaces (continental shelf) that were very resistant to weathering, being replaced by 500,000 km^2 of fresh basaltic surfaces, eight to ten times more prone to weathering. Mathematically, it is the factor f_5 (Eq. 10) of the paleothermostat which has increased globally (the whole of the continental surfaces being slightly more vulnerable to weathering) and, for a degassing which returned to its pre-disturbance level, the CO_2 must stabilize at a lower level in order to correct the imbalance due to continental weathering.

The result of a magma episode, such as the establishment of continental traps, is initially a short-lived warming episode (10^5 years), followed by a global cooling that persists for several million years, as long as the basaltic surfaces exposed to the atmosphere are not entirely destroyed by weathering. A similar study carried out on Siberian traps (Permo-Triassic boundary) shows that the atmospheric CO_2 level stabilized a few million years after the end of the event at 750 ppmv below its pre-disturbance level of 4500 ppmv, which caused a global cooling of more than 1 °C.

At the time of the K–T limit, another major phenomenon occurred: a large meteorite with a diameter estimated at about ten kilometers collided with the Earth and fell into the Yucatan Peninsula. The impact created a large crater, identified by geophysics, which is currently buried under a thousand meters of sediment (the Chicxulub crater). This event was catastrophic, much shorter than the great fissure eruptions of the Deccan, which date from the same period, but which have had a prolonged impact for several hundreds of thousands of years.

The impact of the meteorite is easily identified because sediments from the K–T boundary are composed of a thin layer, rich in iridium, a very rare metal on Earth, a sign of contribution of cosmic origin. This layer also contains minerals (spinels) whose chemical composition indicates that they could not have been formed on Earth. Analysis of

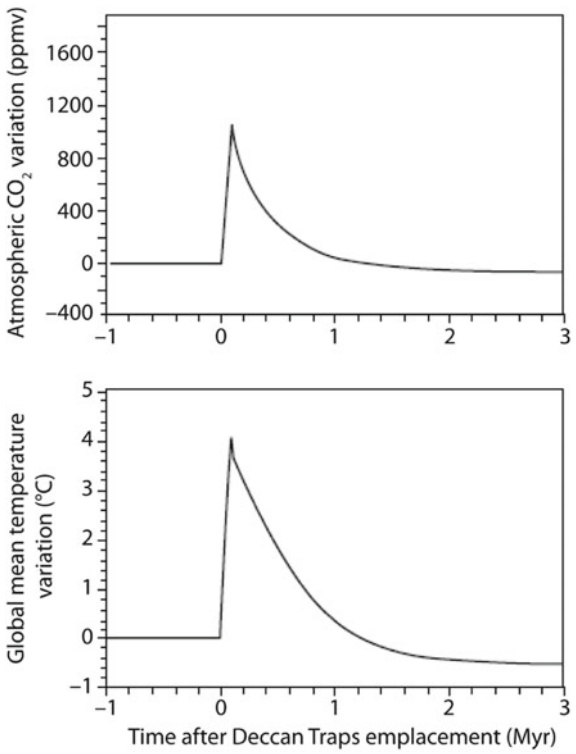

Fig. 27.15 Quantification of the impact of the establishment of the Deccan traps on the global average temperature and the level of atmospheric CO_2

the spinels showed that the meteorite had the chemical composition of carbon chondrites, with the particularity of being very rich in sulfur. The impact of such a collision was considerable. This impact, out of all proportion with current observations, is difficult to simulate because of the extent of the disturbance to the chemistry of the atmosphere. Thus, the simulations are based on assumptions made in the context of studies on a 'nuclear winter', where climatologists have calculated the impact on the global climate of a large-scale nuclear conflict. This can only be considered to be a very simplified approach.

The collision of a meteorite with the Earth has many consequences, although it is difficult to quantify them precisely:

- it releases an enormous quantity of aerosols (sulfates, nitrates) which reach the upper atmosphere where they can remain for several years;
- the aerosols cause an attenuation of about 50% of the solar radiation, resulting in a cooling of about ten degrees on the ground for a decade. Agronomists estimate that half the vegetation of the northern hemisphere could have been killed in the first years;
- the disruption is greatest if the impact occurs in the spring when the vegetation most needs solar radiation;
- an enormous quantity of water vapor is emitted into the atmosphere, which becomes charged with nitrates and sulfates, and falls back in the form of highly acid rain, toxic to plants;
- finally, chondrites contain many toxic heavy metals, particularly nickel, which inhibits chlorophyll activity.

We are obviously far from a full comprehension of all the events that marked the end of the Cretaceous, with the disappearance of many animal and vegetal species. Continental sediments testify to the appearance of widespread fires and to the pioneering return of the ferns, the most resistant of plants and the first to colonize the areas devastated by fire. In the ocean, sedimentological, biological and geochemical data show a considerable decrease in primary production by algae; this only returned to its former level after about five or six million years.

It is likely that the collision with the meteorite and fumes from the Deccan fissures both contributed to the major changes in the environment that marked the KT boundary, the first event through considerable sudden effects lasting several years and the second through geochemical effects that persisted over long periods relative to the time constants of the biosphere.

The Paleocene–Eocene Thermal Maximum (PETM)

The destabilization of methane hydrates (very active greenhouse gases) in sediments can cause climate fluctuations over short timescales (10^5 years). Several events of this type have been identified during the Phanerozoic, but the best documented is located at the Paleocene-Eocene transition. In the space of 20 000 years (Fig. 27.16), the $\delta^{13}C$ of the ocean decreased by 3‰, before returning to its initial value 240 000 years later (McInerney and Wing 2011). Over the same time, the temperature of the deep ocean waters increased from 5 to 7 °C. Similarly, a warming of 8 °C of surface waters was recorded. This warming is attributed to a sudden destabilization of methane hydrates in ocean sediments (Dickens 2003). The methane released by sediments is characterized by a $\delta^{13}C$ of −60‰. As a result, a flow of 2500 Gt of carbon spread over 20,000 years is sufficient to explain the observed isotopic excursion. This event caused a significant but temporary warming of the atmosphere. The $\delta^{13}C$ excursion is then reabsorbed over 200,000 years by the 'conventional' processes of the carbon cycle: continental weathering and sequestration in sediments.

The reason for the destabilization of the gas hydrates has yet to be explained. These can be released into the ocean and atmosphere if the water temperature rises or the pressure decreases. For example, regional eruptions occurred in the North Atlantic 55 Ma ago, shortly before the PETM

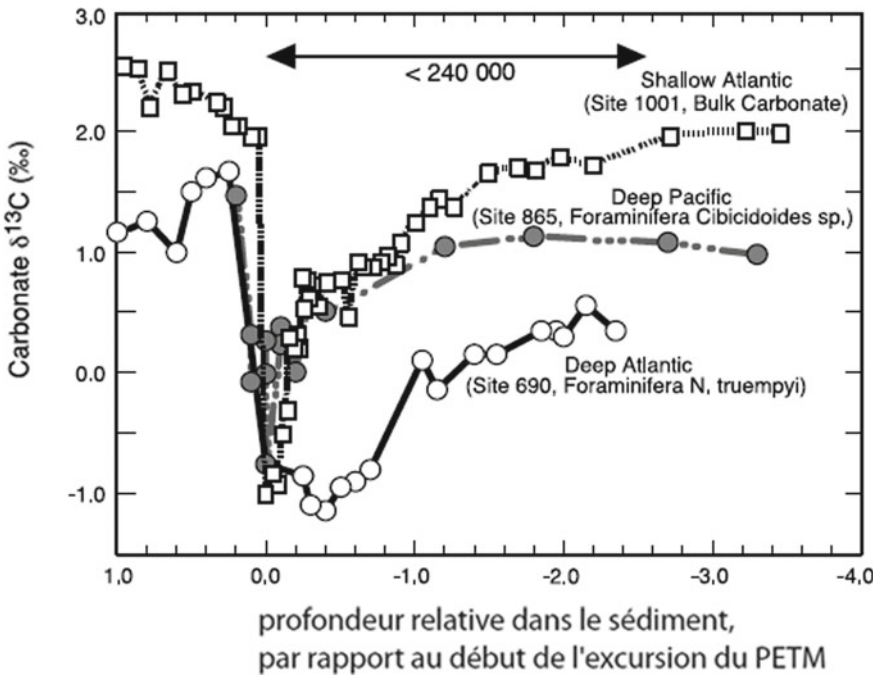

Fig. 27.16 Temporal evolution of $\delta^{13}C$ of benthic foraminifera at the Paleocene-Eocene transition at three distant oceanic sites. The arrow represents a period of 240,000 years

(McLennan and Jones 2006). The reduction in the height of the water column could have led to a drop in pressure and a destabilization of the methane hydrates in sediments. There may be a link between these regional eruptions and the PETM, although this assumption needs to be tested by more precise dating. Another hypothesis is that a significant change in ocean circulation could have significantly warmed the deep waters (by 4–5 °C), causing the destabilization of gas hydrates stored in sediments and initiating the PETM.

Conclusions

The reconstruction of climates on the scale of geological time is still open to discussion. The main difficulty lies in the fact that climate and biogeochemical cycles cannot be dissociated. There are numerous indicators of geochemical and climatic changes, but they are always difficult to interpret because of their indirect nature. The numerical models used are often very simple, taking a global average approach in most studies, which does not explicitly take into consideration the many parameters of the climate system. Yet ancient climates also represent an amazing testing-ground where new techniques can be developed and innovative ideas can be explored. In this field of study, climate models, initially developed to understand the evolution of current climate, are applied to extreme conditions, and the extent to which they are suitable is questionable. One limitation is the simplistic way the changing geographical configuration of the past is taken into account due to the lack of precise information. This is a climate factor of the highest importance and we are not sure that complex models, such as atmospheric general circulation models coupled with ocean-atmospheric models, react correctly when boundary conditions are changed in such a drastic manner.

Nevertheless, the refining of analytical techniques and models, the process of trial and error, the successes and the failures allow us to discover a general history of the Earth's climate at the same time as multicellular organisms evolved. One of the major debates of recent years has been around the link between the level of atmospheric CO_2 and the evolution of climate during the Phanerozoic, which appear to have been decoupled during certain major events. Given the enormous uncertainties that exist in the reconstruction of CO_2 levels using isotopic methods or based on paleontological data (Royer 2006) and taking into account the uncertainties around isotope-based climate reconstructions, it is not possible to claim the existence or non-existence of a decorrelation between CO_2 level on one side and climate on the other. However, the use of a new generation of models that closely couples the carbon cycle with climate by taking into account the spatial variability of the processes suggests a coherence in the joint history of CO_2 and climate, in line with the major climate trends of the Mesozoic (Donnadieu et al. 2006). Similarly, the emergence of isotopic techniques allowing the reconstruction of the climate with increasingly fine latitudinal resolution makes it possible to reconsider the commonly studied events in the climate history of our planet. New consolidated images appear, in which atmospheric CO_2 is a key driver of climate change but is modulated by first order factors, such as the paleogeographic configuration, largely ignored for a long time, or the more or less periodic

variations in the Earth's orbit, the role of which is explained in Chap. 7.

One of the major challenges for the near future is understanding the relationship between these climate and geochemical evolutions on the one hand and biological evolution on the other.

References

Ahlberg, A., Arndorff, L., & Guy-Ohlson, D. (2002). Onshore climate change during the Late Triassic marine inundation of the Central European Basin. *Terra Nova, 14*(4), 241–248.

Anderson, H. M., Hiller, N., & Gess, R. W. (1995). Archeopteris (progymnospermopsida) from the Devonian of Southern Africa. *Journal of the Linnean Society, 117*(4), 305–320.

Bergmann, K. D. et al. (2018). A 600-million-year carbonate clumped-isotope record from the Sultanate of Oman. *Journal of Sedimentary Research, 88*, 960–979

Berner, R. A. (2004). *The phanerozoic carbon cycle* (p. 150p). New York: Oxford University Press.

Bice, K. L., & Norris, R. D. (2002). Possible atmospheric CO_2 extremes of the Middle Cretaceous (late Albian-Turonian). *Paleoceanography, 17*, 1070.

Boucot, A. J., Xu, C., & Scotese, C. R. (2004). Phanerozoic climatic zones and paleogeography with a consideration of atmospheric CO_2 level. *Paleontological Journal, 38,* 115–122.

Breecker, D. O., Sharp, Z. D., & McFadden, L. D. (2010). Atmospheric CO_2 concentrations during ancient greenhouse climates were similar to those predicted for AD 2100. *Proceedings of the National Academy of Science, 107,* 576–580.

Came, R. E., et al. (2007). Coupling of surface temperatures and atmospheric CO_2 concentrations during the paleozoic era. *Nature, 449,* 198–201.

Caputo M. V. et al. (2008). Late devonian and early carboniferous glacial records of South America. In *Resolving the late Paleozoic ice age in time and space* (Vol. 441). Geological Society of America Special Papers, (pp. 161–173).

Dabard M. P. et al. (2015). Sea-level curve for the Middle to early Late Ordovician in the Armorican Massif (western France): icehouse third-order glacio-eustatic cycles.*Palaeogeography Palaeoclimatology Palaeoecology, 436,* 96–111.

Davies N. S., & Gibling, M. R. (2013). The sedimentary record of Carboniferous rivers: continuing influence of land plant evolution on alluvial processes and Palaeozoic ecosystems. *Earth-Science Reviews, 120*, 40–79.

DeConto, R. M., & Pollard, D. (2003). Rapid cenozoic glaciation of antarctica induced by declining atmospheric CO_2. *Nature, 412,* 245–248.

Dera, G. et al. (2011). Climatic ups and downs in a disturbed Jurassic world. *Geology, 39*(3), 215–218.

Dessert, C., et al. (2001). Erosion of deccan traps determined by river geochemistry: Impact on the global climate and the $^{87}Sr/^{86}Sr$ ratio of seawater. *Earth and Planetary Science Letters, 188*(3/4), 459–474.

Dickens, G. R. (2003). Rethinking the global carbon cycle with a large, dynamic and microbially mediated gas hydrate capacitor. *Earth and Planetary Science Letters, 213*(3–4), 169–183.

Donnadieu, Y., et al. (2011). A mechanism for brief glacial episodes in the mesozoic greenhouse. *Paleoceanography*, *26*. https://doi.org/10.1029/2010pa002100.

Donnadieu, Y., et al. (2006). A GEOCLIM simulation of climatic and biogeochemical consequences of Pangea breakup. *Geochemistry Geophysics Geosystems*, *7*(11). https://doi.org/10.1029/2006gc001278.

Dromart, G., et al. (2003). Ice age at the middle-late jurassic transition? *Earth and Planetary Science Letters, 213,* 205–220.

Elsworth, G. et al. (2017). Enhanced weathering and CO_2 drawdown caused by the latest Eocene strengthening of the Atlantic meridional overturning circulation. *Nature Geoscience, 10*(3), 213–216.

Finnegan, S., et al. (2011). The magnitude and duration of late ordovician-early silurian glaciation. *Science, 331,* 903–906.

Foster, G. L., Royer, D. L., Lunt, D. J. (2017) Future climate forcing potentially without precedent in the last 420 million years. *Nature Communications*. https://doi.org/10.1038/ncomms14845.

Frakes, L. A., Francis, J. E., & Syktus, J. I. (1992). *Climate modes of the phanerozoic*. Cambridge: Cambridge University Press.

France-Lanord, C., & Derry, L. A. (1997). Organic carbon burial forcing of the carbon cycle from Himalaya erosion. *Nature, 390,* 65–67.

Friedrich, O. et al. (2012). Evolution of middle to Late Cretaceous oceans - a 55 m.y. record of Earth's temperature and carbon cycle. *Geology, 40*(2), 107–110.

Galy, V., et al. (2007). Efficient organic carbon burial in the Bengal fan sustained by the Himalayan erosional system. *Nature, 450,* 407–410.

Ghosh, P., Garzione, C. N., & Eiler, J. M. (2006). Rapid uplift of the Altiplano revealed through C-13-O-18 bonds in paleosol carbonates. *Science, 311*(5760), 511–515.

Goddéris, Y., et al. (2008). Causal of casual link between the rise of nannoplankton calcification and a tectonically-driven massive decrease in the Late Triassic Atmospheric CO_2? *Earth and Planetary Science Letters, 267,* 247–255.

Goddéris, Y., & François, L. M. (1996). Balancing the cenozoic Carbon and Alkalinity Cycles: Constraints from isotopic records. *Geophysical research letters*, *23*(25), 3743–3746.

Goddéris, Y. et al. (2014). The role of palaeogeography in the Phanerozoic history of atmospheric CO_2 and climate. *Earth-Science Reviews, 128*, 122–138.

Goddéris, Y. et al. (2017). Onset and ending of the late Palaeozoic ice age triggered by tectonically paced rock weathering. *Nature Geoscience, 10*(5), 382–385.

Hayes, J. M., Strauss, H., & Kaufman, A. J. (1999). The abundance of ^{13}C in marine organic matter and isotopic fractionation in the global biogeochemical cycle of carbon during the past 800 Ma. *Chemical Geology, 161,* 103–125.

Hodel, F. et al. (2018). Fossil black smoker yields oxygen isotopic composition of Neoproterozoic seawater. *Nature Communications, 9*, Article Number: 1453.

Huber, M., & Nof, D. (2006). The ocean circulation in the Southern Hemisphere and its climatic impacts in the eocene. *Palaeogeography, Palaeoclimatology, Palaeoecology, 231,* 9–28.

Joachimski, M. M. et al. (2004). Oxygen isotope evolution of biogenic calcite and apatite during the Middle and Late Devonian. *International Journal of Earth Sciences,93*(4): 542–553.

Katz, M. E. et al. (2005). Biological overprint of the geological carbon cycle. *Marine Geology, 217*, 323–338.

Kump, L. R., et al. (1999). A weathering hypothesis for glaciation at high atmospheric pCO_2 during the late ordovician. *Palaeogeography, Palaeoclimatology, Palaeoecology, 152,* 173–187.

Le Hir, et al. (2011). The climate change caused by the land plant invasion in the Devonian. *Earth and Planetary Science Letters, 310* (3–4), 203–212.

Lefebvre, V. et al. (2013). Was the Antarctic glaciation delayed by a high degassing rate during the Early Cenozoic? *Earth and Planetary Science Letters, 371–372,* 203–211.

Lenton, T. M. et al. (2012). First plants cooled the Ordovician. *Nature Geoscience, 5*, 86–89.

Loi, A. et al. (2010). The Late Ordovician glacio-eustatic record from a high-latitude storm-dominated shelf succession: The Bou Ingarf section (Anti-Atlas, Southern Morocco). *Palaeogeography Palaeoclimatology Palaeoecology, 296*(3–4), 332–358.

McElwain, J. C., Wade-Murphy, J., Hesselbo, S. P. (2005). Changes in carbon dioxide during an oceanic anoxic event linked to intrusion into Gondwana coals. *Nature, 435*(7041), 479–482.

McInerney, F. A., & Wing, S. L. (2011). The paleocene-eocene thermal maximum: A perturbation of carbon cycle, climate, and biosphere with implications for the future. *Annual Review of Earth and Planetary Sciences, 39,* 489–516.

Mountanez, I. P., & Poulsen, C. J. (2013). The late paleozoic ice age: An evolving paradigm. *Annual Review of Earth and Planetary Sciences, 41*, 629–656.

Nardin, E., et al. (2011). Modeling the early paleozoic long-term climatic trend. *Geological Society of America Bulletin*, *123*, 1181–1192.

Nelsen, M. P. et al. (2016). Delayed fungal evolution did not cause the Paleozoic peak in coal production. *Proceedings of the National Academy of Science, 113*(9), 2442–2447.

Pagani, M., Zachos, J. C., Freeman, K. H., Tipple, B., & Bohaty, S. (2005). Marked decline in atmospheric carbon dioxide concentrations during the Paleogene. *Science, 309,* 600–603.

Page, A. A. et al. (2007). Were transgressive black shales a negative feedback modulating glacioeustasy in the Early Palaeozoic icehouse? In *Deep-time perspectives on climate change: marrying the signal from computer models and biological proxies*. pp. 123–156.

Pohl, A. et al. (2016). Glacial onset predated Late Ordovician climate cooling. *Paleoceanography, 31*(6), 800–821

Pucéat, E., et al. (2010). Revised phosphate-water fractionation equation reassessing paleotemperatures derived from biogenic apatite. *Earth and Planetary Science Letters, 298,* 135–142.

Pucéat, E. et al. (2003). Thermal evolution of Cretaceous Tethyan marine waters inferred from oxygen isotope composition of fish tooth enamels. *Paleoceanography, 18,*(2), Article Number: 1029.

Rasmussen, C. M. O. et al. (2016). Onset of main Phanerozoic marine radiation sparked by emerging Mid Ordovician icehouse. *Scientific Reports, 6,* Article Number: 18884.

Raymo, M. E. (1991). Geochemical evidence supporting T.C. chamberlin's theory of glaciation. *Geology, 19,* 344–347.

Royer, D. L. (2006). CO_2-forced climate thresholds during the phanerozoic. *Geochimica and Cosmochimica Acta*, *70*, 5665–5675.

Royer, D. L., Berner, R. A., & Beerling, D. J. (2001). Phanerozoic atmospheric CO_2 change: Evaluating geochemical and paleobiological approaches. *Earth-Science Reviews, 54,* 349–392.

Rubinstein, C. V. et al. (2010). Early middle ordovician evidence for land plants in Argentina (eastern Gondwana). *New Phytologist, 188* (2), 365–369.

Scher, H. D., & Martin, E. E. (2006). Timing and climatic consequences of the opening of drake passage. *Science, 312,* 428–431.

Scott, A. C., & Glasspool, J. (2006). The diversification of Paleozoic fire systems and fluctuations in atmospheric oxygen concentration. *Proceedings of the National Academy of Science, 103*(29), 10861–10865.

Shaviv, N. J., & Veizer, J. (2003). Celestial driver of phanerozoic climate? *GSA Today, 13*(7), 4–10.

Sluijs, H. et al. (2006). Subtropical arctic ocean temperatures during the Palaeocene/Eocene thermal maximum. *Nature, 441*(7093), 610–613.

Stein, W. E. et al. (2007). Giant cladoxylopsid trees resolve the enigma of the Earth's earliest forest stumps at Gilboa. *Nature, 446*(7138), 904–907.

Thomas, D. J. et al. (1999). New evidence for subtropical warming during the late Paleocene thermal maximum: stable isotopes from the Deep Sea Drilling Project Site 527, Walvis Ridge. *Paleoceanography, 14*, 561–570.

Trotter, J. A. et al. (2008). Did cooling oceans trigger Ordovician biodiversification? Evidence from conodont thermometry. *Science, 321*, 550–554

Veizer, J., et al. (1999). $^{87}Sr/^{86}Sr$, $\delta^{13}C$ and $\delta^{18}O$ evolution of phanerozoic seawater. *Chemical Geology, 161,* 59–88.

Veizer, J., Goddéris, Y., & François, L. M. (2000). Evidence for decoupling of atmospheric CO_2 and global climate during the phanerozoic eon. *Nature, 408,* 698–701.

Zachos, J. C. et al. (2003). A transient rise in tropical sea surface temperature during the Paleocene-Eocene Thermal Maximum. *Science, 302*(5650), 1551–1554.

Zachos, J. C., Dickens, G. R., & et Zeebe, R. E. (2008). An early Cenozoic perspective on greenhouse warming and carbon-cycle dynamics. *Nature*, *451*(17). https://doi.org/10.1038/nature.

Zhuravlev, A. Y., & Riding, R., (2001). The ecology of the Cambrian radiation - Introduction. Perspectives in paleobiology and Earth history series, pp. 1–7.

Climate and Astronomical Cycles

28

Didier Paillard

A Little History

From the Discovery of Ice Ages to the First Climate Theories

The scientific notion that climate could evolve over time first appeared along with the birth of paleoclimatology in the nineteenth century when the existence of ice ages was discovered. Although the scientists of the time were aware that the Earth had undergone many upheavals, notably through the successions of various animal and vegetable fossil species, it was only when evidence of previous glacial periods emerged that the idea of a changing climate really took shape. The traces left behind by the movement of glaciers during the last glacial period: moraines, erratic boulders, glacial striations and features, were clearly identified in many regions of Europe and North America and promoted the idea that the climate, at least in the northern hemisphere, may have been considerably colder in the past. The nineteenth-century scientists' point of view on glaciations was quite different from ours, deeply rooted as it was in a 'catastrophic' perspective on the evolution of the Earth, which was at that time imagined to have been punctuated by 'deluges' and other cataclysms, as highlighted in the excerpt below.

> The appearance of these large sheets of ice must have led to the annihilation of all organic life on the surface of the earth. The soil of Europe, formerly ornamented with tropical vegetation and inhabited by troops of great elephants, enormous hippopotamuses and gigantic predators, was suddenly buried under a vast mantle of ice covering the plains, lakes, seas and plateaus. The movement of a powerful creation was succeeded by the silence of death. The springs dried up, the rivers ceased to flow, and the rays of the sun, rising on this frozen beach (that's if they reached it), were only greeted by the whistles of the northern winds and the thunder of the crevasses that opened on the surface of this vast ocean of ice.
> (L. Agassiz, *Studies on glaciers*, 1840)

For geologists of that era, climate changes were primarily related to changes in topography. Although the continental drift was not yet well established, the scientists tried to explain their field observations by means of vertical movements of the continents: uplift of the mountains, erosion, change in sea level etc. Under the influence of Charles Lyell, these changes came to be seen as slow and progressive. The assumption of catastrophism faded away to be replaced with gradualism which presupposes that the modifications of the Earth's surface obey the physical laws that now apply but over immensely long durations. This new point of view was opposed to any external (especially heavenly) influence, which no doubt explains the reluctance of geologists when faced with the first astronomical theories of glaciations:

> But though I am inclined to profit by Croll's maximum eccentricity for the glacial period, I consider it quite subordinate to geographical causes or the relative position of land and sea and abnormal excess of land in polar regions.
> (C. Lyell to C. Darwin, 1866)

The idea that the climate stems above all from geography and topography has indeed merit. One need only look at the etymology of the word climate (κλιμα = inclination, i.e. the height of the Sun above the horizon, in other words, the latitude of the location) or look for 'climatology' in an academic organization chart to be convinced that this idea is still valid. The physical principles underlying the functioning of the climate system were also updated in the nineteenth century, notably by Joseph Fourier, who established the laws of heat diffusion, explaining how heat is redistributed by the surface fluids of the atmosphere and the ocean, and also discussed the essential role of the greenhouse effect:

D. Paillard (✉)
Laboratoire des Sciences du Climat et de l'Environnement, LSCE/IPSL, CEA-CNRS-UVSQ, Université Paris-Saclay, 91190 Gif-sur-Yvette, France
e-mail: Didier.Paillard@lsce.ipsl.fr

G. Ramstein et al. (eds.), *Paleoclimatology*, Frontiers in Earth Sciences,
https://doi.org/10.1007/978-3-030-24982-3_28

> The temperature can be increased by the interposition of the atmosphere, because the heat finds less obstacle to penetrate the air, being in the state of light, than it finds it to pass through the air when converted into dark heat.
> (J. Fourier, 1824)

It is in this context that the two main physical theories are presented, which are still relevant today, and which make it possible to explain the existence of glacial periods: the astronomical theory and the variations in the atmospheric concentration of CO_2.

From Adhémar to Milankovitch: The Role of Insolation

Although the notion that the climate is influenced by the stars has undoubtedly been around for a very long time, the first astronomical scientific theory of the ice ages was formulated by Joseph Adhemar in 1842. It was based simply on common sense: since ancient times, astronomers have highlighted the 'three movements of the Earth': the diurnal cycle, the annual cycle, and the precession of the equinoxes (Hipparchus, about 130 before J.-C.). While it is clear that the annual and diurnal cycles generate temperature variations, the same must be true of the third movement of the Earth. As will be explained a little later, the precession of equinoxes has the consequence of modifying the position of the perihelion (point of the Earth's orbit closest to the Sun) in relation to the seasons: today, the Earth is closest to the Sun around January 4 but this date changes slowly to cover the whole of the year over about 21,000 years. In contrast to today, 10,500 years ago, the Earth was far from the Sun in January and close to it in July. Adhemar suggested that this mechanism could modify the climate. More specifically, the winters of the northern hemisphere now occur when the Earth is close to the Sun and, conversely, those of the southern hemisphere when the Earth is far from the Sun. Adhemar proposed that this explains the absence of a large ice cap in the north, due to milder and shorter winters, and conversely, the presence of a large Antarctic cap. The situation would have been exactly the opposite 10,500 years ago, which allowed him to explain the periods of great glacial expansion that had just been revealed by geologists.

Adhemar's theory was criticized for many reasons, some largely unfounded, but it was on the very foundations of his theory that his detractors, Charles Lyell and Alexander von Humbolt, would find compelling arguments. In fact, the mechanism of precession works in an anti-symmetrical way between the poles, but also between the seasons. It can easily be shown that although, for example, less energy is received in winter, this is compensated for by an equivalent excess of energy received in summer. If the seasonal contrast varies with the precession, the full complement of energy received does not change. How then could this have any effect on climate? According to Adhemar, although the astronomical forcing is effectively anti-symmetric with respect to the seasons and zero for the annual average, the climate processes are probably not.

In 1864, James Croll clarified this concept. According to him, the accumulation of snow occurs chiefly in winter, with melting occurring in summer. Croll emphasized the role of the winter accumulation which essentially supports Adhemar's argument: longer or colder winters favor a greater accumulation of ice allows the initiation of a glaciation. In addition, aware of the progress that had been made in celestial mechanics notably by Pierre Simon de Laplace and Urbain le Verrier, Croll went on to introduce the effect of variations in the eccentricity of the Earth's orbit. These variations modulate the intensity of seasonal contrasts. Indeed, in the case of a circular orbit, the effect of the precession on climate is zero, since there would be neither a perihelion (nearest point) nor an aphelion (farthest point). The greater the eccentricity, the greater the climate effects of the precession. Croll therefore linked the great glaciations with eccentricity maxima. Hence, he pushed back the estimate of the last glaciation to 80,000 years ago, and suggested an even more intense glaciation 240,000 years ago. Although Croll proposed a much more solid and evolved astronomical theory, he did not succeed in convincing the scientific community of his time. However, the interglacial-glacial alternations discovered in some sediments argued in favor of a more or less periodic mechanism. Yet the first dating of elements available from that time, extrapolating the rates of erosion or counting lake varves, indicated a much more recent glaciation. Croll went on to introduce a third important astronomical parameter for the calculation of the variations of the solar energy received in a given place: the obliquity of the terrestrial axis, that is to say its inclination with respect to the plane of the Earth's orbit. However, obliquity has little effect on winter insolation, and therefore was of little importance in Croll's theory.

Milankovitch (1941) formulated the astronomical theory which still applies today. The main criticism that can be levelled at Croll's theory is that it considered winter to be the most pertinent season. This objection was already expressed by Joseph Murphy during Croll's time, as observations of the eternal snow and mountain glaciers showed that summer melting had much more impact on the ice mass balance than snow accumulation. However, the precession was often advanced to explain the current asymmetry of temperatures between the northern hemisphere and the southern hemisphere, and the presence of Antarctica, since today, the austral winter is longer and further from the Sun than the northern winter. Croll's theory was therefore probably based on this nineteenth century misconception of the current climate.

Milankovitch resolved this problem by deducing that the current north-south asymmetry was linked to geography and

not to astronomical forcing. The critical season for the evolution of ice caps is therefore summer, which completely reverses the reasoning of Adhemar and Croll. The obliquity of the Earth's axis, that is to say its inclination with respect to the plane of Earth's orbit, becomes the most important parameter for glacial-interglacial evolution. The foundations of modern astronomical theory were thus laid down.

From Tyndall to Arrhénius: The Role of Carbon Dioxide

The importance of the role of the greenhouse effect was well understood by the nineteenth century, notably through the work of Joseph Fourier. As early as 1845, Jacques Joseph Ebelmen, a French chemist, first suggested that changes in the atmospheric concentration of CO_2 might have consequences for the climate (Bard 2004). Indeed, by focusing on the chemistry of minerals, he established the bases of carbon geochemistry: a source primarily of volcanic origin and sinks related to the erosion of silicates and the burial of the organic material. Since all these processes appear to be disconnected, it seems unlikely that the atmospheric concentration of CO_2 would be constant over geological time. In 1861, John Tyndall further authenticated the theory of the greenhouse effect. By measuring the absorption and infrared emission of the various gases present in the air, he demonstrated that nitrogen or oxygen are essentially transparent to infrared rays and that the greenhouse effect of our planet is caused primarily by gases in very small quantities, in large part by water vapor, but also carbon dioxide, methane, nitrous oxide and ozone. Tyndall then suggested that all of the climate changes discovered by geologists, including ice ages, could be explained by changes in the levels of atmospheric greenhouse gases.

But it was the Swedish chemist Svante Arrhenius (1896) who managed to calculate the effect of carbon dioxide on the climate, in an attempt to explain the ice ages. Based on geological data on moraine positions during glacial periods, he estimated a cooling of 4 or 5 °C and calculated that this could be explained by a reduction of about 40% in the atmospheric concentration of CO_2. The measurement of pCO_2 from this glacial period, carried out on air bubbles from ice cores taken from Antarctica in the years 1980–1990, confirmed his calculations: the atmospheric concentration of CO_2 was indeed 30% lower during the ice age. This scientific prediction, nearly a century before it could be confirmed through observation, is a good illustration of the essential role of greenhouse gases in the deployment of the Quaternary cycles. Arrhenius also considered that future global warming would be linked to anthropogenic CO_2 emissions. He calculated an increase in global temperatures of about 5 °C for a doubling of CO_2, a figure surprisingly close to the most recent estimates of about 3.5 °C, another prediction likely to become true in the not too distant future.

All these arguments were underscored by the American geologist Chamberlin, who highlighted the succession of at least five glacial stages in the United States. According to Chamberlin, there was a sort of oscillation between the climate and the geochemistry of the Earth: a decrease in CO_2 leading to cooling, with the effect of reducing carbon sinks on Earth by reducing the burial of organic matter as well as the erosion of silicates. This would then lead to a gradual increase in atmospheric CO_2 until it switches over to the opposite situation. Chamberlin therefore attempted to formulate an 'internal oscillation' to explain the succession of ice ages, without calling on a '*Deus ex machina*' such as the astronomical forcing.

It is interesting to note that these two opposing theories of the glacial periods have existed since the middle of the nineteenth century and are still largely valid today: it remains to be understood how they relate and complement each other.

Astronomical Parameters and Insolation

Before proceeding further, it is useful to review the various astronomical parameters that influence the energy received at the top of the Earth's atmosphere, which we call 'insolation'.

Eccentricity

According to Kepler's first law, the Earth's orbit is an ellipse. This is characterized by a major parameter, the semi-major axis, often denoted *a,* by a shape or flattening parameter, the eccentricity, often denoted *e*, and also by three parameters defining the position of this ellipse in space, two of which define the orbital plane (the inclination *i* with respect to a reference plane and the longitude of the ascending node Ω defined by the intersection of these two planes), and another to define the absolute position of the perihelion (the longitude π). In fact, as soon as the system is made up of three material bodies (the Sun with two planets) or more, the movement is no longer strictly an ellipse, and there is no analytical solution to the problem of celestial mechanics at *N* bodies, for $N > 2$. It is therefore appropriate to calculate the perturbations or the approximate numerical resolutions. The notion of terrestrial orbit nevertheless still makes sense because the perturbations are secondary. It is therefore useful to reason in terms of elliptical orbit, which deforms and moves over time.

The perturbations induced by the other planets do not modify the semi-major axis of the ellipse *a*, only the terrestrial trajectory, i.e. the eccentricity *e* and the orientation

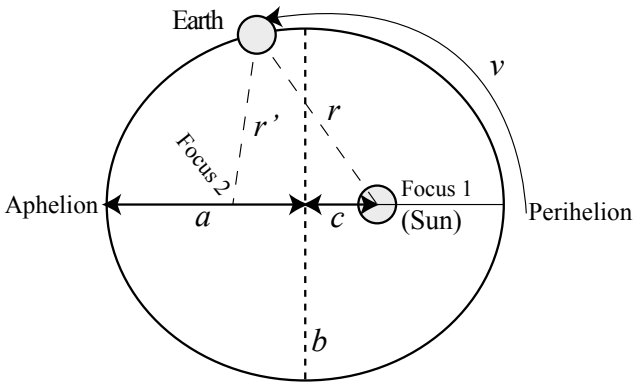

Fig. 28.1 An ellipse can be defined as the locus of the points whose sum of distances to the two foci is constant: $r + r = 2a$. The eccentricity is defined as the ratio $e = c/a$. The semi-minor axis b is therefore given by the theorem of Pythagoras: $b = a(1 - e^2)^{1/2}$

parameters of the ellipse (i, Ω, π). So a will be a constant (at least over hundreds of millions of years). Moreover, the orientation of the ellipse in space does not have a direct consequence on the solar radiation received by the Earth. The only orbital parameter which is liable to modify the insolation is therefore the eccentricity e.

The eccentricity e is defined by the ratio between the distance from the focus to the center of the ellipse c, and the semi-major axis a, as shown in Fig. 28.1. Although today it is 0.0167 (i.e. a flattening of 1.67%), it has varied between values of almost-zero and 0.06, with periodicities appearing to be around 100,000 and 400,000 years.

Eccentricity is the only parameter capable of modifying the average annual energy received by the Earth. As the semi-major axis is constant, the average distance between the Earth and the Sun depends on its eccentricity. The second law of Kepler (conservation of angular momentum) is written as:

$$r^2 \frac{dv}{dt} = \frac{2\pi a^2 \sqrt{1 - e^2}}{T}$$

The 'solar constant' S_0, defined as the average energy received by the Earth, is deduced by integrating it into a complete orbit:

$$S_0 = \frac{S}{T} \int_0^T \frac{a^2}{r^2} dt = S \int_0^{2\pi} \frac{dv}{2\pi\sqrt{1 - e^2}} = \frac{S}{\sqrt{1 - e^2}}$$

The average annual energy received by the Earth, S_0, depends on the energy S (assumed here to be truly constant) received at the distance a from the Sun and on the eccentricity e. A higher eccentricity leads to a more flattened orbit, on average closer to the Sun, and thus to greater overall solar energy being received by the Earth. However, the variations remain very small, since for $e = 0.06$, the maximum is calculated as $S_0 = 1.0018\ S$, i.e. an increase of only 0.18%. These tiny variations have almost no effect on the climate. They are of the same order of magnitude as the observed variations in solar flux S over the 11-year cycle, which generate temperature variations of the order of 0.1 °C. On the other hand, as we will see a little later, it is through the modulation of the effects of precession that eccentricity plays an essential role in climate.

It is relevant to note that the solar system is chaotic. This means that the calculation of the orbital parameters in general, and in particular that of eccentricity, is only possible for instants not too far from the current period. In fact, errors increase exponentially with time, and it is not possible to arrive at an estimation beyond a certain time. For the eccentricity, this timeframe is only around 20–30 million years, which is very short compared to the age of the Earth. Beyond that, although variations in eccentricity remain similar in nature (with identical periodicities of approximately 100,000 and 400,000 years), it becomes impossible to say whether the eccentricity was minimal (close to zero) or maximum (close to 0.06) 600 million years ago. In other words, the phase of the oscillations becomes theoretically unreliable over the long term (Laskar et al. 2004).

Obliquity

In addition to the parameters of the Earth's orbit, the position of the rotational axis of the Earth relative to the orbital and ecliptic planes must also be taken into account. This position is given by two axial parameters; the obliquity, denoted ε, representing the inclination of this axis relative to the ecliptic; and the precession of the equinoxes, which indicates its absolute position compared to the stars. The position of the Earth's axis is modified by the differential attraction of the Moon (and, to a lesser extent, the Sun) at the equatorial bulge. In fact, our planet is slightly flattened, because of the Earth's rotation, and the gravitational pull of the Moon towards the Earth is therefore not exactly symmetrical. The equatorial bulge, at an incline relative to the lunar orbit, is subject to attraction forces which create a torque on the Earth's axis and modify its orientation. Contrary to orbital parameters, such as eccentricity, which depend only on point mechanics, the axial parameters (obliquity and precession) depend on the shape of the Earth, which introduces new sources of error and uncertainty. The timeframe beyond which the calculation of the axial parameters becomes impossible is therefore probably shorter than for the eccentricity. The calculations become more complicated further back than a few million years if the shape of the Earth changes slightly under the influence of glaciations due to the enormous volumes of ice accumulating on the continents of the northern hemisphere at the glacial maxima. It has been suggested that this could have consequences for the

calculation of axial parameters further back than only a few million years. Similarly, internal convection in the Earth's mantle potentially induces changes in the distribution of masses which are difficult to take into account in these astronomical calculations. The phase of the obliquity, like that of the precession, is therefore subject to caution when extrapolating calculations for the distant past or future beyond about ten million years. Moreover, the periodicity of these axial parameters depends on the Earth-Moon distance, but the lunar recession is rather poorly constrained in the distant geological past, and the frequencies of the obliquity and precession also become uncertain.

The obliquity today is 23° 27′, which defines the latitude of the polar circles (67° 33′ north and south) and the tropics (23° 27′ north and south). This value oscillates between extremes of around 21.9° and 24.5°, with a periodicity of around 41,000 years. It is clear that any change in obliquity will have consequences for the climate by altering the size of the polar and tropical areas. Thus, on the island of Taiwan, in the county of Chiayi (Jia-Yi), for almost a century, there has been a monument marking the Tropic of Cancer. However, the current decline in obliquity, at a rate of 0.46 arc-seconds per year, means that there has been a displacement of the tropics of 14.4 m per year, i.e. 4 cm per day and thus more than 1 km since the monument was first erected. The Taiwanese have therefore regularly built new monuments to follow the southward movement of the Tropic of Cancer.

Although the average global incident radiation has not changed, its geographical distribution depends on the obliquity. To be precise, if one calculates the average annual solar incident radiation, it is found that this depends mainly on the obliquity and, to a lesser extent, on the eccentricity as mentioned above. An increase in obliquity ε results in an increase in insolation at high latitudes and a decrease in the tropics. At the poles (north and south) and at the equator, incident is calculated as follows:

$$W_{\mathrm{Year}}(\mathrm{pole}) = \frac{S}{\pi\sqrt{1-e^2}}\sin\varepsilon;$$
$$W_{\mathrm{Year}}(\mathrm{equator}) = \frac{2S}{\pi^2\sqrt{1-e^2}}E(\sin\varepsilon)$$

where $E(x) = E(\pi/2,\ x)$ is the secondary complete elliptic integral. For a eccentricity e of zero, when ε goes from 21.9° to 24.5°, changes of around 1%, i.e. 18 W/m^2 are obtained for W_{Year} (pole) and changes of around 0.4%, i.e. 5 W/m^2 are obtained for W_{Year} (equator). It should be noted that for very large obliquities (for $\pi \sin \varepsilon > 2\ E(\sin \varepsilon)$, in other words, for $\varepsilon > \varepsilon c = 53{,}896°$), the poles receive a higher annual energy average than the equator. This is currently the case on Uranus and Pluto.

Moreover, the phenomenon of the seasons is directly linked to the obliquity, and it is all the more marked when the obliquity is large. For example, for a circular orbit ($e = 0$), we obtain the following expression of daily insolation at the poles during solstices:

$$W_{\mathrm{summer}}(\mathrm{pole}) = S\sin\varepsilon;\ W_{\mathrm{winter}}(\mathrm{pole}) = 0.$$

If insolation at the winter solstice remains zero, the summer solstice will vary between $W_{\mathrm{summer}}(\mathrm{pole}) = 0.373\ S$ and $W_{\mathrm{summer}}(\mathrm{pole}) = 0.415\ S$, when the Quaternary ε goes from 21.9° to 24.5°, i.e. an increase of around 4%, that is to say more than 50 W/m^2. This is far from negligible.

In addition, it is essential to notice that, contrary to the precession which we detail below, the effect of the obliquity on the insolation is symmetrical relative to the equator. This is an important aspect of Milankovitch's theory: contrary to the theories of Croll and Adhemar, which involve winter insolation (mainly dependent on the precession), Milankovitch's theory is based on summer insolation. which strongly depends on the obliquity. On a planet with symmetrical topography, this would imply the presence of ice caps oscillating largely in phase in both hemispheres. Of course, the distribution of continents on Earth is not symmetrical and several other factors will also affect how climates are distributed on Earth.

Precession of the Equinoxes and Climate Precession

In addition to the alternation of day and night and the phenomenon of seasons which have been known since the dawn of time, astronomers have observed since ancient times a slow drift of the polar axis relative to the celestial sphere. This discovery is generally attributed to Hipparchus (130 B.C.) who estimated the drift at approximately 1° per century (that is to say, a periodicity of about 360 centuries). This estimate is remarkable since we now know that the precession does have a periodicity of 25,765 years (1.397° per century). It is also likely that the Egyptians and the Mesopotamian astronomers were already well aware of this phenomenon because, centuries earlier, they identified the position of the celestial pole as well as the constellations of the zodiac. changed the orientation of certain temples to 'follow' this movement. As Nicolas Copernic already noted, this is the 'third movement' of the Earth, the first two corresponding to the day and year. It was therefore logical for Adhémar to focus on the consequences for the climate of this 'third movement'.

Nevertheless, a distinction should be made between the precession of the equinoxes and the climate precession. Indeed, the 'absolute' position of the axis of the Earth,

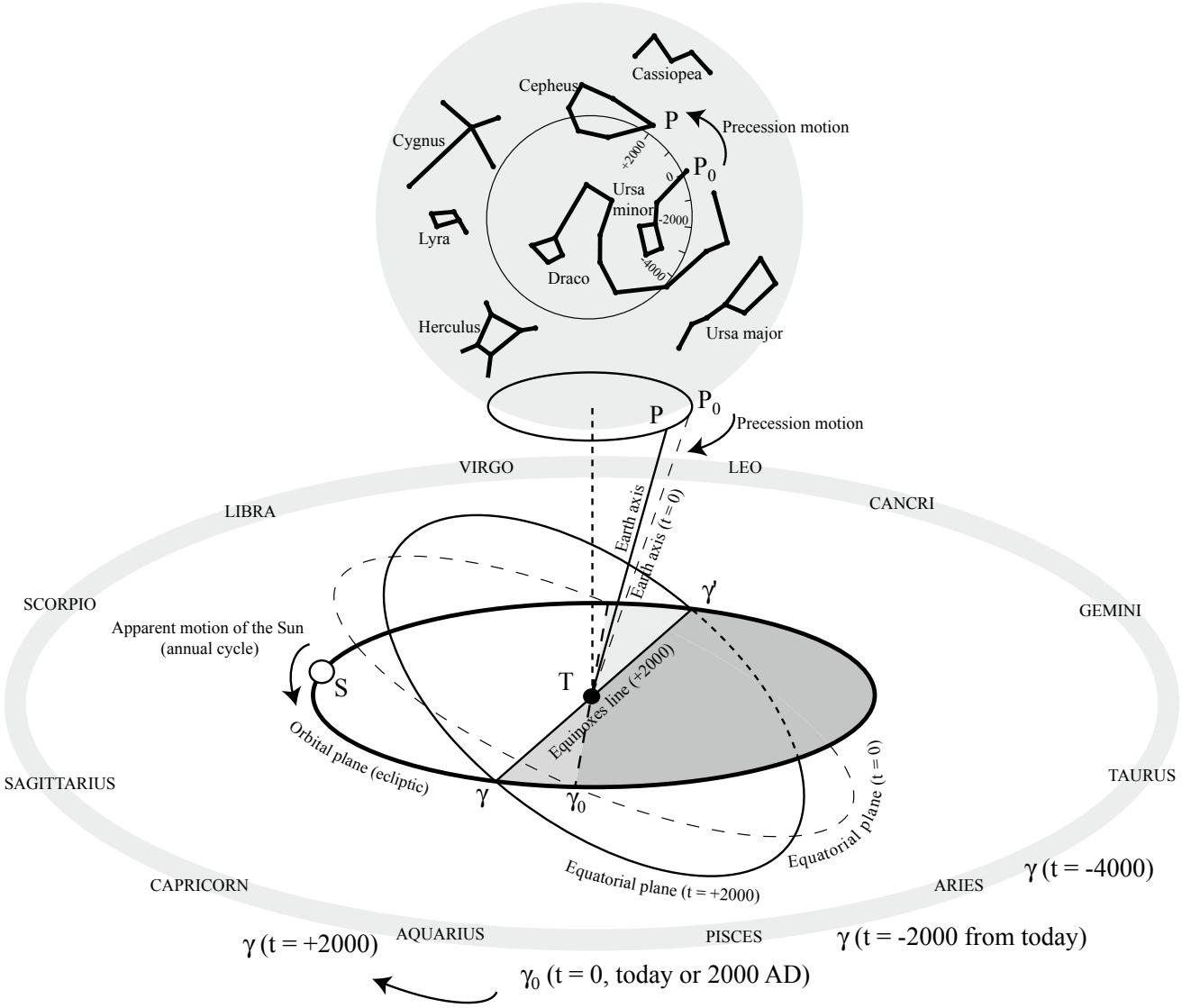

Fig. 28.2 The precession of the equinoxes corresponds to the rotational motion of the Earth's axis (T). The pole thus moves relative to the stars (from P_0 today, pointing towards the polar star, to P in the future in the constellation of Cepheus). The same applies to the equinox line $\gamma\gamma'$ (intersection of the orbital plane and the equatorial plane). The current point γ_0 is in the Pisces constellation and is drifting towards the constellation of Aquarius

relative to the stars, has, in itself, no effect on the climate. However, when this axis is oriented differently, so too is the equatorial plane of the Earth. The equinox line is defined as the intersection of the equatorial plane and the ecliptic (orbital) plane. The precession of the equinoxes (from which the origin of the name) corresponds to a drift of the equinoxes relative to the constellations, as shown in Fig. 28.2.

Thus, while the Sun is now in the constellation of Pisces on the day of the spring equinox (thus defining what astronomers call the vernal point γ), it was in Aries of the time of the Greeks and in Taurus at the time of the Egyptians. The symbol used (γ) since antiquity comes from the zodiacal symbol of the ram. This succession (Taurus, Aries, Pisces) certainly has close symbolic links, via astrology, with the history of religions (the pre-Hebraic bull, the ram or the lamb for the Jews, and the fish for the Christians). The vernal point, and therefore the position of the seasons on the Earth's orbit, moves with the precession of the equinoxes. Knowing that the orbit is elliptical makes it easy to understand that the seasons will be situated at different distances from the Sun, depending on whether the vernal point is closer or further from the perihelion or the aphelion. The effect of the precession on climate is therefore measured by the relative position of the vernal point and the perihelion. The latter also moves, as mentioned in the paragraph concerning eccentricity (this is the orbital parameter π)

according to a movement called 'precession of the perihelion'. The combination of the precession of the equinoxes and the precession of the perihelion thus makes it possible to define the relative position of the seasons and the principal axes of the ellipse. The climate precession, denoted by $\tilde{\omega}$ ('curvilinear pi'), is defined as the angle between the vernal point and the perihelion. If the vernal point carries out a complete cycle in approximately 25,700 years, the perihelion does the same in about 112,000 years. As these two movements occur in opposite directions, we can deduce an average periodicity of 21,000 years for climate precession (1/25.7 + 1/112 ∼ 1/21).

However, there is a small additional complication. When the orbit is circular ($e = 0$), there is no longer a perihelion. The angle $\tilde{\omega}$ is then not defined. Moreover, it is clear that the effect of changes in precession $\tilde{\omega}$ on the climate will be greater as the eccentricity increases, since the distance between the Earth and the Sun will be greater between its maximum $a(1 + e)$ (aphelion) and its minimum $a(1 - e)$ (perihelion).

This effect will be zero when $e = 0$. For all these reasons, it is appropriate to introduce the 'climate precession parameter' $e \sin \tilde{\omega}$, which cancels out when ϖ is not defined (for $e = 0$) and which increases with e. In fact, it is mathematically useful to replace the pair of parameters (e, $\tilde{\omega}$), defined only if e is not zero, with the pair ($e \cos \tilde{\omega}$, $e \sin \tilde{\omega}$), which is always well defined, in other words, a polar-Cartesian coordinate change. The effect of the precession is thus modulated by the eccentricity, as can be seen in the following insolation formula. This results in a duplication of frequencies (more precisely, a multiplication, since e has itself multiple periodicities). If e varies with a single periodicity of 100 000 years, as for example the function $|e0 \cos(t/200)|$, and $\tilde{\omega}$ has a cycle of 21 000 years, we can deduce:

$$e \sin \tilde{\omega} = |e_0 \cos(t/200)| \sin(t/21)$$

hence the periodicities of 19,000 and 23,000 years (1/21 + 1/200 ∼ 1/19 and 1/21 − 1/200 ∼ 1/23), which have been detected in oceanic paleoclimate records and form a strong argument in favor of Milankovitch's theory.

Calculations of Insolation, Calendar Problems

Knowing the three astronomical parameters e, ε, $\tilde{\omega}$, it is easy (with the application of some trigonometry) to determine the radiation received by the Earth, or insolation, for each location (latitude ϕ) and for each season. It is common practice to use the daily insolation, by giving an orbital position with respect to the spring equinox (i.e. the moment in the year) identified by a longitude λ (for example, $\lambda = 90°$ at the summer solstice, or $\lambda = 270°$ at the winter solstice), as shown in Fig. 28.3. It is then assumed that this longitude λ is 'fixed' during the day, as the astronomical parameters are. The only movement that is taken into account and which is averaged is therefore the rotation of the Earth on itself in a day.

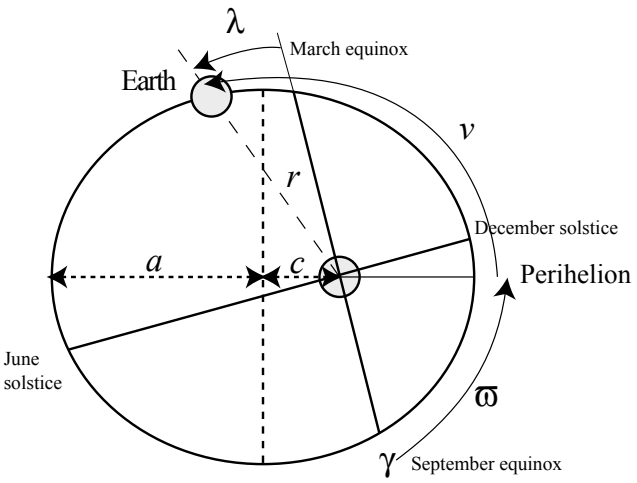

Fig. 28.3 Definitions of the longitude λ, of the climate precession $\tilde{\omega}$, and the anomaly ν, with respect to the seasons, the perihelion and the vernal point γ

By formulating:

$$s = \mathrm{Max}(0; 1 - \sin^2\phi - \sin^2\delta) = \mathrm{Max}(0\,; 1 - \sin^2\phi - \sin^2\varepsilon \sin^2\lambda)$$

$$p = \sin\phi \sin\delta = \sin\phi \sin\varepsilon \sin\lambda$$

The following expression of daily insolation can be used:

$$-\text{if } \; s = p = 0, \quad W_D = 0$$

$$-\text{ otherwise}\left(\sqrt{s + p^2} \neq 0\right),$$

$$W_D = S\left(\frac{1 - e\cos(\lambda - \tilde{\omega})}{1 - e^2}\right)^2 \left(\frac{p \arccos\left(\frac{-p}{\sqrt{s+p^2}}\right) + \sqrt{s}}{\pi}\right)$$

In this formulation, three factors can be identified:

1. The solar constant (S);
2. A term for the Earth-Sun distance that depends on the time of year (λ), climate precession ($\tilde{\omega}$) and eccentricity (e);
3. A geometric term that depends only on the time of year (λ), the obliquity (ε) and the latitude of the location (ϕ).

In particular, the geometrical term remains unchanged if ϕ is changed to $-\phi$ and λ is changed to $\lambda + \pi$ simultaneously (if the hemisphere and half-year are changed). Similarly, the distance term remains unchanged if $\tilde{\omega}$ is changed to

$\tilde{\omega} + x$ and λ is changed to $\lambda + x$ simultaneously (if the precession and the moment of the year are shifted by the same quantity). We note also that the integral over the year (between $\lambda = 0$ and 2π) of the insolation does not depend on the precession $\tilde{\omega}$.

In these formulas, it is important to note that the longitude λ is the angle that represents the position of the Earth in its seasonal cycle, but that λ is not quite proportional to the time that elapses during the year. In fact, when the Earth is close to the perihelion, its velocity is greater and λ changes more rapidly than when the Earth is at the aphelion.

To be precise, the equation of the ellipse (in polar coordinates, centered on the Sun) is:

$$\mathrm{r} = \frac{a(1-e^2)}{1+e\cos v}$$

where v is the position relative to the perihelion ($v = \lambda - \tilde{\omega} + \pi$).

The second Kepler equation $\left(r^2 \frac{dv}{dt} = \frac{2\pi a^2\sqrt{1-e^2}}{T}\right)$ can be written:

$$\mathrm{a}^2\left(1-e^2\right)^2 \int \frac{dv}{1+(e\cos v)^2} = \frac{2\pi a^2\sqrt{1-e^2}}{T} = \int dt$$

This fits into:

$$E - e\sin E = \frac{2\pi}{T}\,\mathrm{t} \quad \text{with} \quad \tan\frac{E}{2} = \sqrt{\frac{1-e}{1+e}}\tan\frac{v}{2}$$

which is called the 'Kepler equation', where the new angle E is called the eccentric anomaly. With these equations, the time $t_2 - t_1$ necessary to pass from orbital position λ_1 to λ_2 is deduced.

The duration of the seasons thus changes with the climate precession $\tilde{\omega}$. This poses a problem to define the calendar. In particular, our Gregorian calendar is partly adjusted for shorter winters and longer summers (CDD (Cooling Degree Days): 90.25 days, MAM: 92 days, JJA: 92 days, SON: 91 days), partially in line with the true duration of the seasons (winter: 89.0 days, spring: 92.8 days, summer: 93.6 days, autumn: 89.8 days). While it is important for paleoclimate data to be based on the astronomical calendar (and therefore on seasons defined by the solstices and equinoxes), models need above all a temporal seasonal axis and have to take into account variable durations for the seasons. Most often, these are defined by a fixed time interval (either a quarter of a year or based on the current schedule) using the March equinox as a reference point. This results in a significant lag with the astronomical seasons, up to about two weeks, especially in September, the month furthest from the reference point. The alternative is to rely on the real astronomical seasons which do not have the same number of days, leading to diagnoses more complicated to implement (Joussaume and Braconnot 1997).

Which Astronomical Forcing Should Be Applied to the Climate?

In addition to the definition of the seasons, another critical issue is the clarification of the concept of 'summer' insolation, which is used as a forcing term for Milankovitch's theory of the evolution of ice cover in the northern hemisphere. Should the value of this insolation be taken on a given day (for example, the summer solstice)? Or should an average for the whole season be taken? Or possibly over another orbital interval $[\lambda_1, \lambda_2]$? Or over a time interval? Or should every day of all the seasons be taken and applied to an explicit coupled climate-ice cap physical model? While this latter solution is the most relevant one, it is, in practice, difficult to implement and it is still useful to understand the bases behind the theory by formulating simpler versions.

Milankovitch calculated an average of the isolation for half the year, centered on the June solstice which he called 'calorific insolation'. The usual practice since the 1970s is to choose a given day, often the summer solstice. The typical forcing used is thus the daily insolation at 65°N on the June solstice. Nevertheless, insolations averaged over durations greater than one day may be useful.

For example, it was suggested (Huybers 2006) that a much more relevant astronomical forcing would be an integral of insolation above a critical threshold, since this forcing will melt or not, the ice or snow cover, and corresponding to temperatures above or below the zero degree Celsius threshold. An insolation integral above a threshold is a reasonably good fit with what glaciologists use as a climate forcing, i.e. a temperature integral called Positive Degree Days (PDD).

In practice, the longer the integration period chosen, the more important the role of obliquity in the result. If one integrates over the whole year, precession is eliminated, leaving only the obliquity. In any case, it is essential to be aware of the non-uniform motion of the Earth in its orbit. Indeed, the integration of insolation W_D must be done according to the time variable, even if the result concerns an orbital interval $[\lambda_1, \lambda_2]$. The calculation leads to elliptic integrals that can then easily be evaluated numerically.

The Successes and Difficulties of Milankovitch's Theory

From Hypothesis to Evidence

Milankovitch's theory was not accepted by the majority of geologists for a long time. In fact, stratigraphic studies by Penk and Brückner had made it possible to define only four successive glacial episodes in the Alps (Günz-Mindel--Riss-Würm), and not a succession of regular events. It was not until the middle of the twentieth century that thanks to studies on marine sediments that the number of glacial cycles identified increased considerably (see Chap. 20, volume 1). In particular, in the 1950s, C. Emiliani carried out the first isotopic measurements on marine carbonates, showing more than a dozen glacial-interglacial successions with a clear cyclicity, which put an end to the traditional denomination (Günz-Mindel-Riss-Würm). From then on, astronomical theory became accepted.

Emiliani thus defined the 'isotopic stages' which are still used today to designate glacial and interglacial periods, odd numbers for interglacial periods and even numbers for glacial periods. It is interesting to note that Stage 3 appears to be an exception, since it is now unanimously considered to be part of the last glacial period (which includes Stages 4, 3 and 2). This apparent inconsistency stems from the simple fact that astronomical theory predicts a dominant periodicity associated with variations in obliquity, i.e. cycles of 41,000 years.

The very rare chronological information available from this time suggests a stage 3 around 30–50 ka BP, preceded by many other older cycles of greater amplitude, but with uncertain dating. It was therefore logical to begin the numbering of past interglacials from stage 3, in accordance with the idea of a dominant cyclicity linked to the obliquity. It was not until the 1960s and 1970s, thanks to the Pa–Th datings, that the main cyclicity appeared to be around 100,000 years, an observation which seemed strange in the context of astronomical theory (Broecker and van Donk 1970). This famous 'problem of the 100,000 years' is still a major obstacle, as will be explained later.

Advances in dating techniques using radioisotopes have resulted in a gradual refinement of the chronology, in particular through the use of coral reefs and magnetic reversals that can be identified in both marine sediments and volcanic flows. This enabled a more precise time frame to be proposed and the paleoclimate periodicities to be precisely defined. The paper by Hays et al. (1976) identified cycles of 23,000 years, 41,000 years, and 100,000 years, which correspond well to astronomical frequencies (Berger 1978). This demonstrated unambiguously the astronomical imprint on the climate and the value of Milankovitch's theory that it is astronomy that drives the Quaternary climate cycles. Nevertheless, this paper also highlights the main problem. The 100,000 year cycle is the dominant cycle, but according to the theory, it should hardly appear. It seems that there is a link between the dominant cycle of 100,000 years and eccentricity, but the causes are unknown. In other words, this 'historical' paper demonstrates both that the astronomical theory is necessary, but that, alone, it does not explain the observations.

A Quasi-linear System for Precession and Obliquity

Although the astronomical periodicities are indeed present in paleoclimate records, a simple relation connecting the two has yet to be verified. Various analytical techniques have been used to this end. It is thus possible to assess the consistency, in other words, the correlation in the spectral domain (or frequency domain) between the astronomical forcing and the paleoclimatic, geochemical and micropaleontological data. The results are quite significant for the periodicities of 23,000 and 41,000 years, i.e. the variations of obliquity and precession. There is therefore a close link between astronomical changes and climate for these two frequencies, which can be interpreted in terms of a 'quasi-linear' model. Another way to be sure of this is to observe the amplitude modulation of the astronomical forcing and that of the climate for these periodicities. For example, for obliquity, we note that the greater the amplitude of the variation in the obliquity, the greater the climate response around the corresponding periodicities (i.e. 41,000 years), as illustrated in Fig. 28.4.

This close relationship between astronomical forcing and 'climate' thus seems sufficiently well established to be used

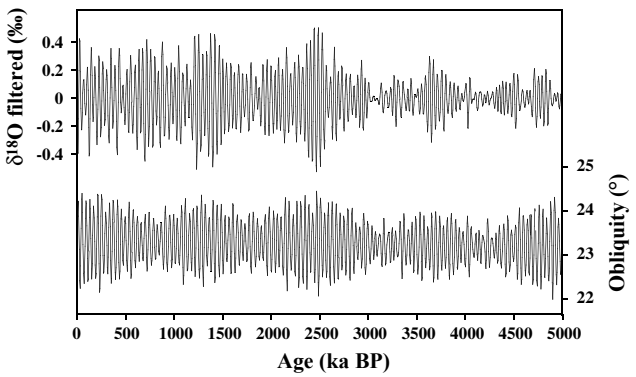

Fig. 28.4 Isotope recording (ODP 659, Tiedemann et al. 1994) filtered around 41 ka (above) and variations in obliquity (Laskar et al. 2004) (below). It is clear that when the obliquity variations increase, so too do the associated climate variations

to date past recordings. Indeed, a persistent difficulty in paleoclimate reconstructions is the establishment of a reliable chronology. As such, absolute dating obtained from the radioactive decay of certain isotopes (^{14}C, $^{40}K/^{39}Ar$, $^{40}Ar/^{39}Ar$, U/Th) is often rare and difficult to obtain. Moreover, they are imprecise. For example, a 1% error in the measured age translates to an error of 10,000 years for samples of one million years. The error only grows as one goes back in time. It is therefore extremely tempting to use astronomical theory to identify the cycles measured in a paleoclimate recording by referring to the cycles of the astronomical forcing. This link seems particularly relevant for precession or obliquity, at least for the Quaternary. In the case where correct identification of all the cycles is possible, which turns out to be quite frequently, this methodology has the enormous advantage of having an associated error which does not increase disproportionately with time. This is because if one does not 'skip' a cycle, then only the phase relationship between the forcing and climate is cast into doubt, which limits the error to a few thousand years, even if we go back tens of millions of years into the geological past. In this case, isotopic stratigraphy shows how extraordinarily efficient it is, and the establishment of an astronomical chronology for a substantial part of the Earth's history is currently underway. However, the chaotic nature of celestial mechanics mentioned above imposes limits on the calculation of certain astronomical parameters. Conversely, it is possible that we may be able to place geological constraints on the evolution of the parameters of the solar system (Pälike et al. 2004).

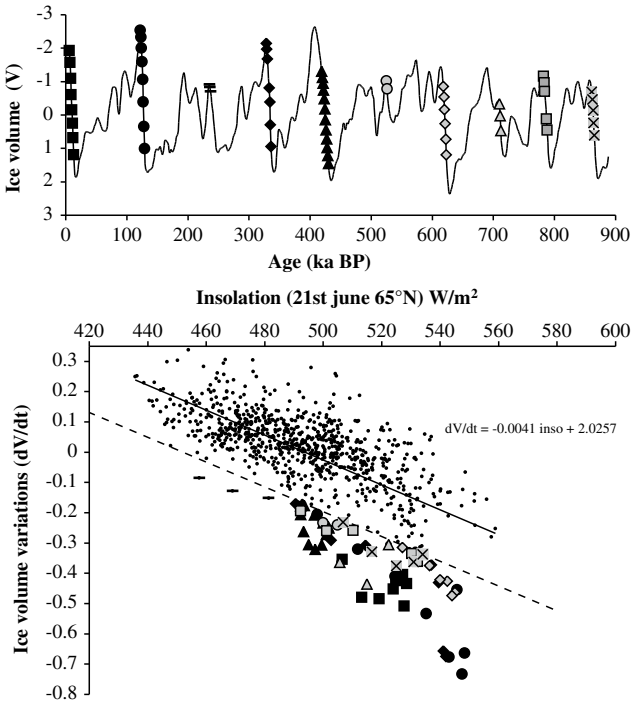

Fig. 28.5 On top: SPECMAP isotopic recording (Imbrie et al. 1984) (normalized) interpreted like a record of ice cap volume. Bottom, this volume of ice is derived according to the time (taking the difference between two successive points), then the derivative is represented as a function of summer insolation at 65°N. Good correlation between the two, for the majority of points, is interpreted as a proof of Milankovitch's theory. The points which deviate substantially from this correlation are marked by symbols which are also shown in the top figure. It is these specific points that are the terminations

The Difficulty of the 100,000-Year Cycles

What is true for the 23,000 and 41,000 year cycles is not true for the major climate cycles that occur more or less every 100,000 years. The first two are highly asymmetric a marked by a much shorter deglaciation phase than the 100,000-year cycle, and as was already noted in the 1970s, the latter did not fit very well into the framework of asronomical theory (Broecker and van Donk 1970). These deglaciations are consequently called 'terminations'. This is not only a visual impression, and it is possible to define these mathematically, by observing that they all correspond systematically to an accelerated decrease in the volume of the ice caps, as illustrated in Fig. 28.5. As such, the terminations are therefore, from the start, outside the scope of Milankovitch's theory.

Moreover, we can no longer observe any real link (in consistency or amplitude modulation) between the variations of eccentricity and the major climate cycles. The very notion of the 100,000-year cycle is problematic because during the Quaternary these have only existed for about a million years and so we only have about ten of these cycles. As a result, statistics have struggled to attribute a specific periodicity to them. It seems that the periodicity of 100,000 years is merely an average between cycles with each having significantly different durations (see Paillard 2001, Table 1). Some authors even suggest that these so-called '100,000-year cycles' are really a double or triple obliquity period (i.e. $2 \times 41 = 82$ ka, or $3 \times 41 = 123$ ka) (Huybers and Wunsch 2005).

To put it simply, as noted above, variations of eccentricity only have a negligible role on the energy received by the Earth, so, it is necessary in any case to imagine relatively complex processes to achieve a climate response in this frequency band where the forcing is almost non-existent.

The simplest way of doing this is to assume the existence of thresholds in the climate system. For example, the system would not function in exactly the same way during the large terminations as during the rest of the cycle. This strategy can be assessed by very simple conceptual models.

A Few Simple Models

Milankovitch's accomplishment was to calculate the orbital parameters of the Earth and the associated insolation occurring over hundreds of thousands of years. Neither a model of evolution of the ice caps nor a climate model was available at this time. He simply linked the minimums in the astronomical forcing with episodes of glaciation. He explained that due to a very high probably inertia in the caps, there would be a gap of several thousand years between the astronomical forcing and the evolution of the caps, even to the point of 'smoothing' the astronomical forcing if the caps do not have the time to react. Indeed, the volume of the caps is not directly related to the insolation, but rather it is the variation in the volume of ice which is a function of insolation. In other words, an extremely simple model of evolution of the caps consists of integrating the astronomical forcing over time. As the important physical object is the cap, it is essential to look at the dynamics of the cap, not only the forcing.

Surprisingly, no scientist seems to have focused on this task, following either in the footsteps of Adhémar or Croll, or those of Milankovitch. It was therefore a journalist (Calder 1974) who would publish a scientific article describing, for the first time, a model of ice cap evolution in the Quaternary, more than a century after the ice ages were observed. This model was both very simple and informative. It is based on a simple integration of the forcing [see Paillard (2001, 2010, 2015)]:

$$dV/dt = -k(i - i_0).$$

where V is the volume of the cap and $i(t)$ is the astronomical forcing, i.e. summer insolation at the high latitudes of the northern hemisphere. Above a fixed isolation value i_0, the volume of ice V decreases proportionally to i-i_0 and, below this value, V increases. This model works relatively well provided that an asymmetry between the melting and accumulation episodes is introduced, with a different k coefficient in the two cases, $k = k_F$ and k_A depending on whether $i > i_0$ (melting) or not. In addition, V is imposed as a positive value. Although this model fails to closely reproduce the observations, it nevertheless has some remarkable characteristics. In particular, it correctly predicts the position of the large terminations, where many other more sophisticated models fail, see Fig. 28.6. We will return to this point.

This model is quite unstable and small changes in the parameters (i_0 or k_A/k_F) lead to significantly different results. This is easily understood, since the volume of ice is, ultimately only the integral of the insolation. Small changes in the threshold or the coefficient quickly lead to very different volumes.

A much more robust model was formulated by Imbrie and Imbrie in 1980 (see Paillard 2001):

$$dV/dt = (-i - V)/\tau$$

where, in a way, the threshold i_0 has been replaced by the volume of ice V. This time, the insolation i is taken as normalized (by subtracting its average value and dividing it by the standard deviation) and so it is possible for the volume of ice to also be negative. As before, the coefficient, or time constant, τ, will have two different values depending on whether the cap melts ($-i$-$V < 0$) or grows ($-i$-$V > 0$). This model reproduces quite well the evolution of the cycles linked to precession and obliquity, but fails to reproduce the 100,000-year cycles. In particular, it produces a strong 400,000 year cycle, clearly present in the eccentricity, but not in the paleoclimate data on the volume of the ice caps, see Fig. 28.7. This model thus illustrates the 'Stage 11 problem'. About 430,000 years ago, the eccentricity was very low and therefore the variations in the precession parameter $e \sin \tilde{\omega}$ were minimal. This was reflected in very little variation in the Imbrie model. Conversely, the paleoclimate data show that this period corresponds to a major transition between a very intense glacial stage (stage 12) and a very marked interglacial

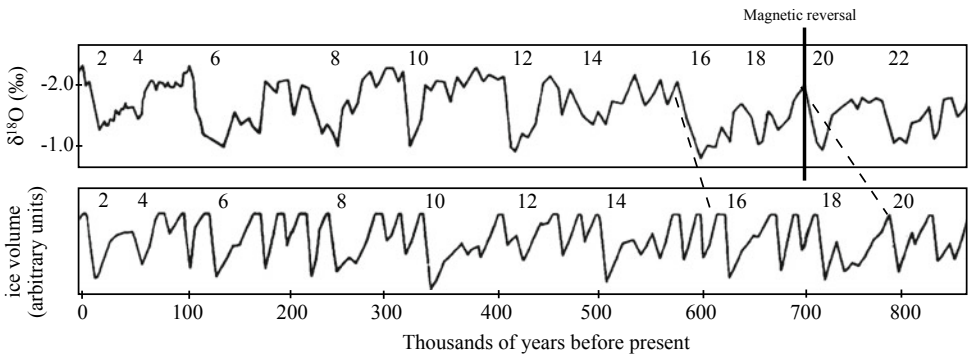

Fig. 28.6 Comparison between the Calder model (bottom) and the V28-238 core (top) (see Paillard 2015). The glacial-interglacial transitions are predicted for the correct dates by the model, while the isotopic data in 1974 were displaced in time, with a too-early date for the Brunhes-Matuyama magnetic reversal, now fixed at around 772 ka (good match between cycles indicated by the dotted lines). In hindsight, the prediction made by the Calder model was quite remarkable

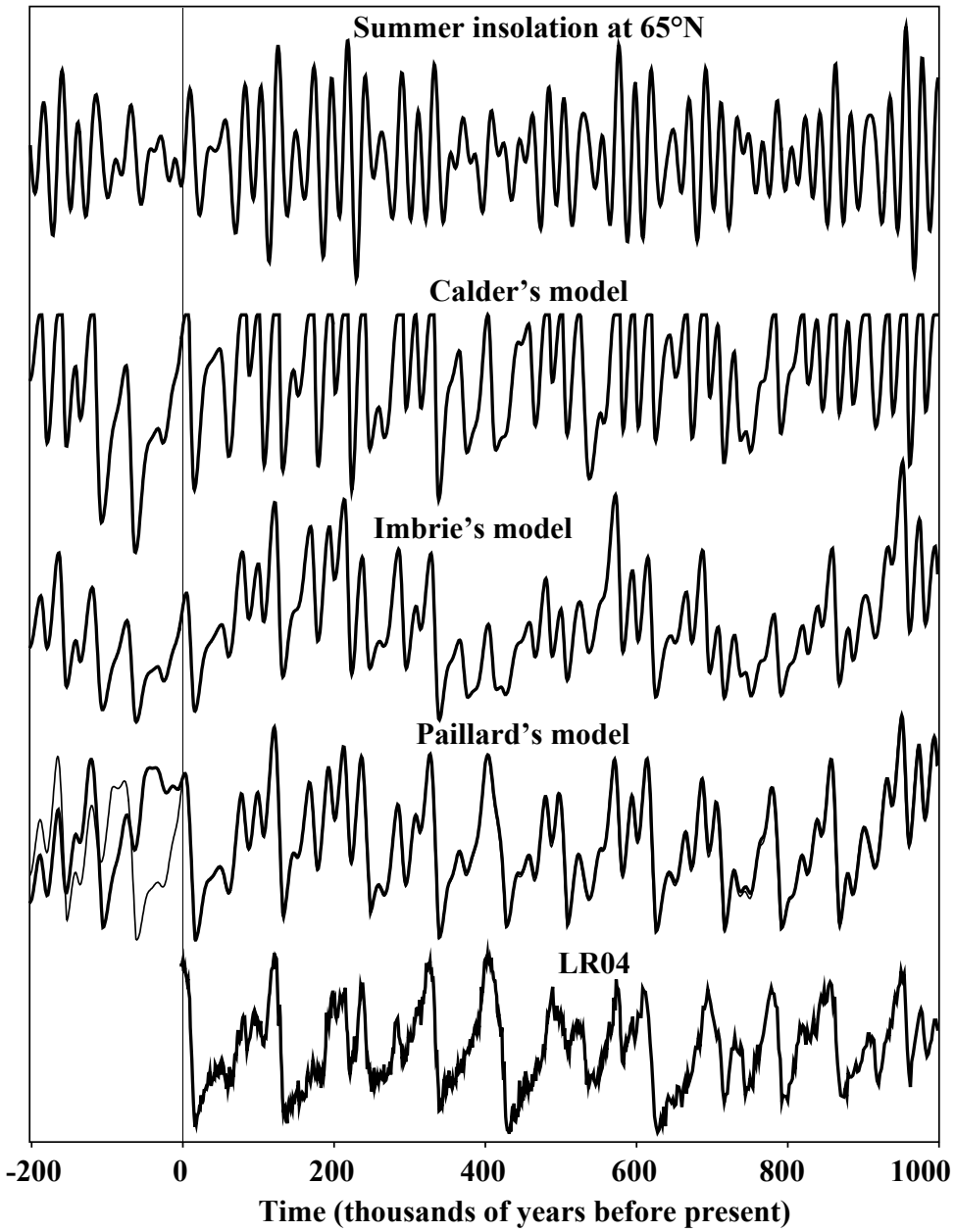

Fig. 28.7 Comparison between the various simple models discussed, over the last million years and the next 200,000 years. From top to bottom: daily summer insolation (65°N, June solstice) (Laskar et al. 2004), results from the Calder model; Imbrie model; Paillard model 1998 and marine isotopic data LR04 (Lisiecki and Raymo 2005). Note that in Paillard's threshold model, there are two possible solutions for the future climate cycles, depending on whether the threshold for entry into glaciation has already been crossed or not (see Paillard 2001)

(stage 11). How can small variations in insolation lead to the greatest of transitions? A natural solution is to view the great cycles at 100,000 years, not as a linear oscillation around an equilibrium point whose amplitude is inevitably linked to the amplitude of the forcing, but rather as a relaxation oscillation between two different climate modes between which the system can switch as soon as certain thresholds are crossed. This is what is proposed in the Paillard model (1998):

$$dV/dt = (V_R - V)/\tau_R - F/\tau_F$$

This time, the volume of ice is 'relaxed' towards different V_R values: the 'climate mode' R is changed as a function of certain threshold overruns on the astronomical forcing i and on the volume of ice V. In particular, an essential point emerging from the study of this model is that in order to predict deglaciations at the right position, they must be linked to the glacial maxima: the switch between

glacial-interglacial regimes needs to be triggered by a threshold overrun of the ice cap volume. This relationship is what allows Calder's model to finally work 'well', because Calder is more successful at predicting glacial maxima than transitions. In other words, for still unknown physical reasons, deglaciations are facilitated by the occurrence of a glacial maximum, which triggers a relaxation oscillation, propelling the system into the opposite state.

Although this astronomical forcing is at the root of the climate variations in the Quaternary, the understanding of the climate mechanisms in play is limited. In Milankovich's theory there is a very simple hypothesis which, in a way, equates the concept of 'climate' with the expansion of the ice caps in the northern hemisphere. Milankovitch's theory, strictly speaking, is not a climate theory, but rather, an ice cap theory, a point emphasized by the conceptual models above. The action of insolation on the ice caps of the northern hemisphere accounts for certain Quaternary phenomena, but does not explain all the observations, in particular the existence of the 100,000-year cycles, punctuated by exceptional deglaciations (or terminations). This theory therefore needs to be further completed to make it a true climate theory.

Recent Advances

The Vital Role of Atmospheric CO_2

Shortly after the discovery of the role of astronomical periodicities in the climate (Hays et al. 1976), analysis of air bubbles in Antarctic ice cores demonstrated that the last glacial period was also characterized by a significantly lower atmospheric concentration of CO_2, in line with the predictions of Arrhenius. Since the work on the Vostok ice cores (Petit et al. 1999) and Dôme C ice cores (Monnin et al. 2001), it is now well established that the glacial-interglacial cycles also correspond to cycles in atmospheric greenhouse gas composition, and in particular of CO_2, which varies between about 280 ppm (cm^3/m^3 of air) during the interglacial period and 180 ppm during the glacial period. These measurements make it possible to demonstrate that the two traditional theories, astronomical and geochemical, are not mutually exclusive, but that both are necessary. This was largely confirmed by numerous numerical experiments in the simulation of the glacial climate: in order to explain the paleoclimate observations, it is essential to take into account the 30% decrease in partial CO_2 pressure. In addition, during the terminations and in particular during the last deglaciation, it is well established that the concentration of CO_2 increased several thousand years before the rise of the sea level associated with the melting of the ice caps, or, in other words, the actual deglaciation, as illustrated in Fig. 28.8. Although it is relatively easy to apply Milankovitch's theory to most of the past cycles, considerable difficulties arise for the deglaciations as is highlighted in Fig. 28.5. It is therefore for these specific moments, when the astronomical theory alone is insufficient, that other mechanisms need to be explored.

In other words, glacial-interglacial changes are not limited to changes in the expansion of the ice caps that could subsequently influence the rest of the climate system. They are, on the contrary, a combination of changes for the caps, but also for the biogeochemical cycles and the climate as a whole. Milankovitch's theory only accounts for part of this reality, the other part most likely involves the carbon cycle coupled with climate variations.

Unfortunately, our understanding of the carbon cycle during the Last Glacial Maximum is very patchy. To make a first approximation, it is reasonable to consider the ocean + atmosphere + terrestrial biosphere system as isolated, i.e. with no significant exchanges of geological carbon (via volcanoes or rivers). The problem is therefore to reduce the atmospheric reservoir by about 200 GtC (billion tons of carbon) while increasing the others by the same amount. However, the terrestrial biosphere was considerably reduced during the glacial period (between 300 GtC and 700 GtC), making the problem all the more difficult, since all this atmospheric and biospheric carbon needs to be trapped in the ocean. Many hypotheses have been put forward to try to explain this low level of pCO_2 during the Last Glacial Maximum, but no consensus has yet emerged. A complex combination of multiple factors (physical and biogeochemical) is one possibility which would explain a glacial-interglacial difference of 100 ppm, but the high level of similarity between the climate recordings around the Antarctic and the pCO_2 records argue for a relatively simple mechanism which would link the Southern Ocean and its climate with the atmospheric concentration of CO_2.

Towards a Consolidation of Astronomical and Geochemical Theories?

Nevertheless, very recent progress makes a forthcoming solution possible. The conceptual models mentioned above suggest viewing the 'glacial' and 'interglacial' states as distinct states able to account for a relaxation oscillation between two (or more) different modes of operation. In this context, it is interesting to mention the hypothesis of a glacial ocean with very cold and above all salty bottom waters. This hypothesis is largely supported by measurements of interstitial fluids in marine sediment cores (Adkins et al. 2002), which directly estimate the salinity of the ocean floor in the past. The glacial ocean was therefore likely to have been profoundly different from the current ocean, with strong stratification between the upper and lower halves of

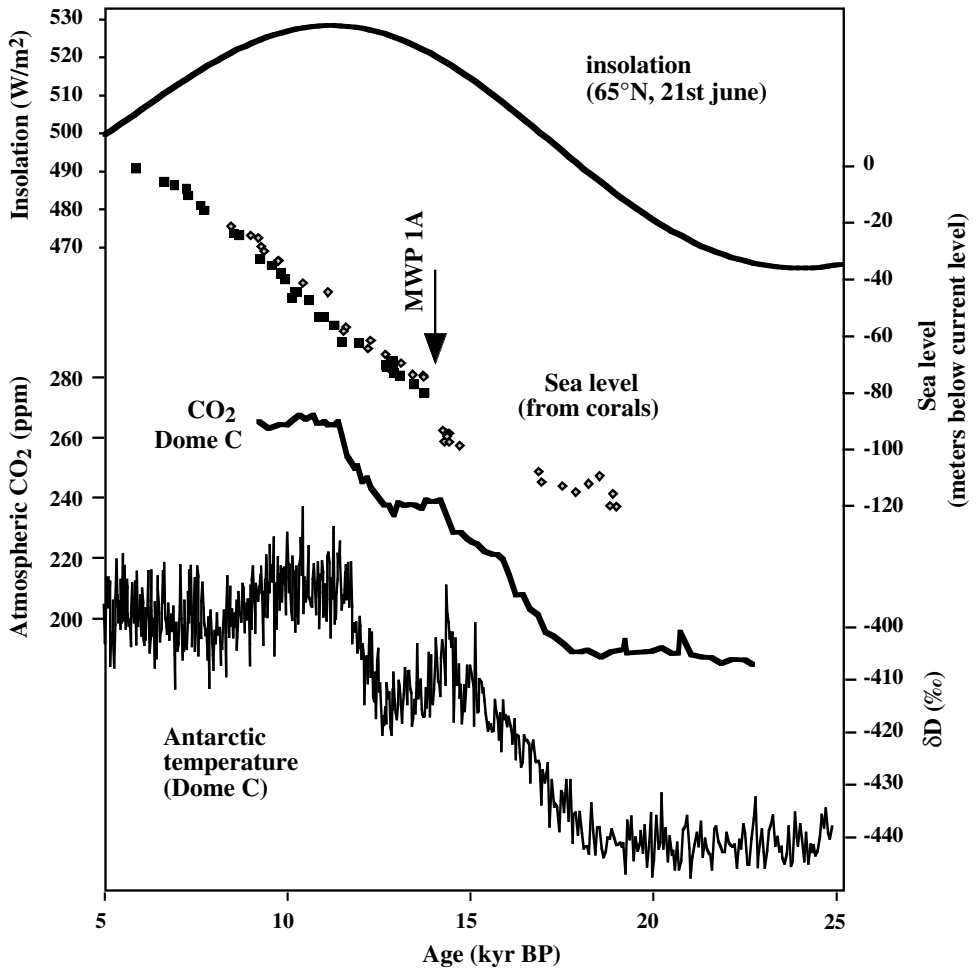

Fig. 28.8 The last deglaciation. From top to bottom: daily insolation (65°N summer solstice) (Laskar et al. 2004); sea level (Bard et al. 1996); atmospheric CO_2 and temperature at Dome C in Antarctica (Monnin et al. 2001). At about 15 kyr BP (15,000 years before the present day), while the sea level remains close to its ice age level (about −100 m), atmospheric CO_2 has already increased by about 60 ppm above its ice age value, more than half of the full transition

the water column. These highly saline bottom waters are likely to form around Antarctica, due to the salt deposits that occur during the formation of sea ice. Indeed, thanks to the continental shelf, these very salty waters are able to flow along the topography (Ohshima et al. 2013) and reach the abyss of the Southern Ocean. The consequences for the carbon cycle of this ocean configuration are considerable. With a mechanism of this type, it is possible to store a lot of carbon at the bottom of the ocean and to explain the low level of atmospheric CO_2. This mechanism was recently confirmed in a relatively simple model coupling climate and carbon cycle (Bouttes et al. 2011). This makes it possible to formulate a scenario that accounts for the glacial-interglacial cycles, both in terms of changes in the expanse of the ice sheets, but also in terms of atmospheric CO_2 and hence global climate (Paillard and Parrenin 2004), as shown in Fig. 28.9.

In this model, terminations are explicitly induced by an increase in atmospheric CO_2, itself caused by the previous glacial maximum, which destabilizes the stratification of the deep ocean. Since this model is based on a bi-modal system, it correctly reproduces certain characteristics already present in even simpler models (Paillard 1998), such as the possibility of switching between dominant periodicities, from 23,000-year cycles before the Quaternary glaciations became established, to 41,000-year cycles 3 million years ago, and then to 100,000-year cycles in the last million years.

Pre-quaternary Astronomical Cycles

Periodic variations of insolation have existed throughout the history of our planet. Although their effects on the climate have been particularly marked for about a million years

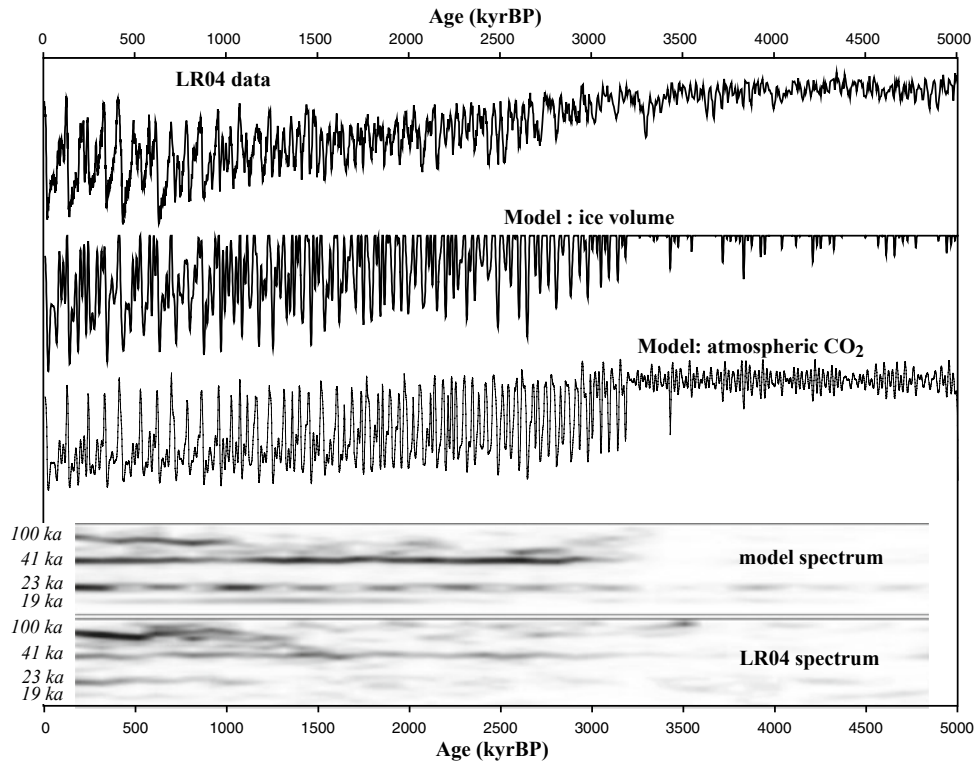

Fig. 28.9 Results of the Paillard and Parrenin model (2004) which includes a mechanism coupling the evolution of ice caps and changes in the carbon cycle, forced by summer insolation at 65°N. By adding a slow drift to the critical threshold parameter, it is possible to account for periodicity switches with the emergence of the 41,000-year cycles about 3 million years ago, and then the 100,000-year cycles for the last million years. From top to bottom: ice volume data (Lisiecki and Raymo 2005), the model results in terms of ice caps and CO_2, and then the decomposition into periodicities (spectrum) for the model and the data

through the glacial-interglacial alternations, it is normal to expect possibly more subtle types of changes in climate when the Earth was less ice-covered or even not at all. Climate variations of astronomical origin may well involve other components of the Earth system besides the ice caps, such as monsoons, biological productivity, or other aspects of our planet. These astronomical cycles are also often incorrectly called 'Milankovitch cycles', although, for the most part, they have nothing to do with changes in the expansion of the ice caps, which were, more often than not, non-existent throughout the history of the Earth. Milankovitch's theory is a theory of the evolution of the ice caps. It is not a climate theory and therefore does not apply to all of the changes in climate due to astronomical causes. Theoretically, there is no reason to select summer insolation in the northern hemisphere as a dominant forcing parameter for components of the system other than the ice caps in the northern hemisphere. According to measured indicators (sedimentology, isotopes of oxygen or carbon, color, etc.), depending on the sites and the geological periods under consideration, the cycles line up with different astronomical periodicities corresponding to variations in precession, obliquity or eccentricity. These alternating sedimentary layers may be from very different origins, and they are sometimes rather poorly understood. There are examples of this in more or less all the epochs of the history of the Earth.

A prime example concerns deposits of organic matter in the Mediterranean Sea, which occur regularly in the form of clearly identifiable layers of black silt called sapropeles. These layers rich in organic matter are explained either by an increase in biological production at the surface or by a change in the circulation of the deep waters of the Mediterranean, which would have been poorly oxygenated during these events, just as the Black Sea is today. In fact, these sapropel events correspond to rainfall episodes in Saharan Africa, or even over the Mediterranean basin as a whole, which brought significantly large supplies of freshwater via the Nile and the rains and disrupted the formation of deep waters and therefore the oxygenation levels of the Mediterranean. Whatever the mechanism, these sedimentary levels appear, with a few exceptions, to be governed by precessional variations since the Miocene, about 14 million years ago, until the last event designated S1, at the beginning of our interglacial period, about 7000 years ago. As shown in Fig. 28.10, this cyclicity is sufficiently well-marked to be used not only as a dating method but also to calibrate the

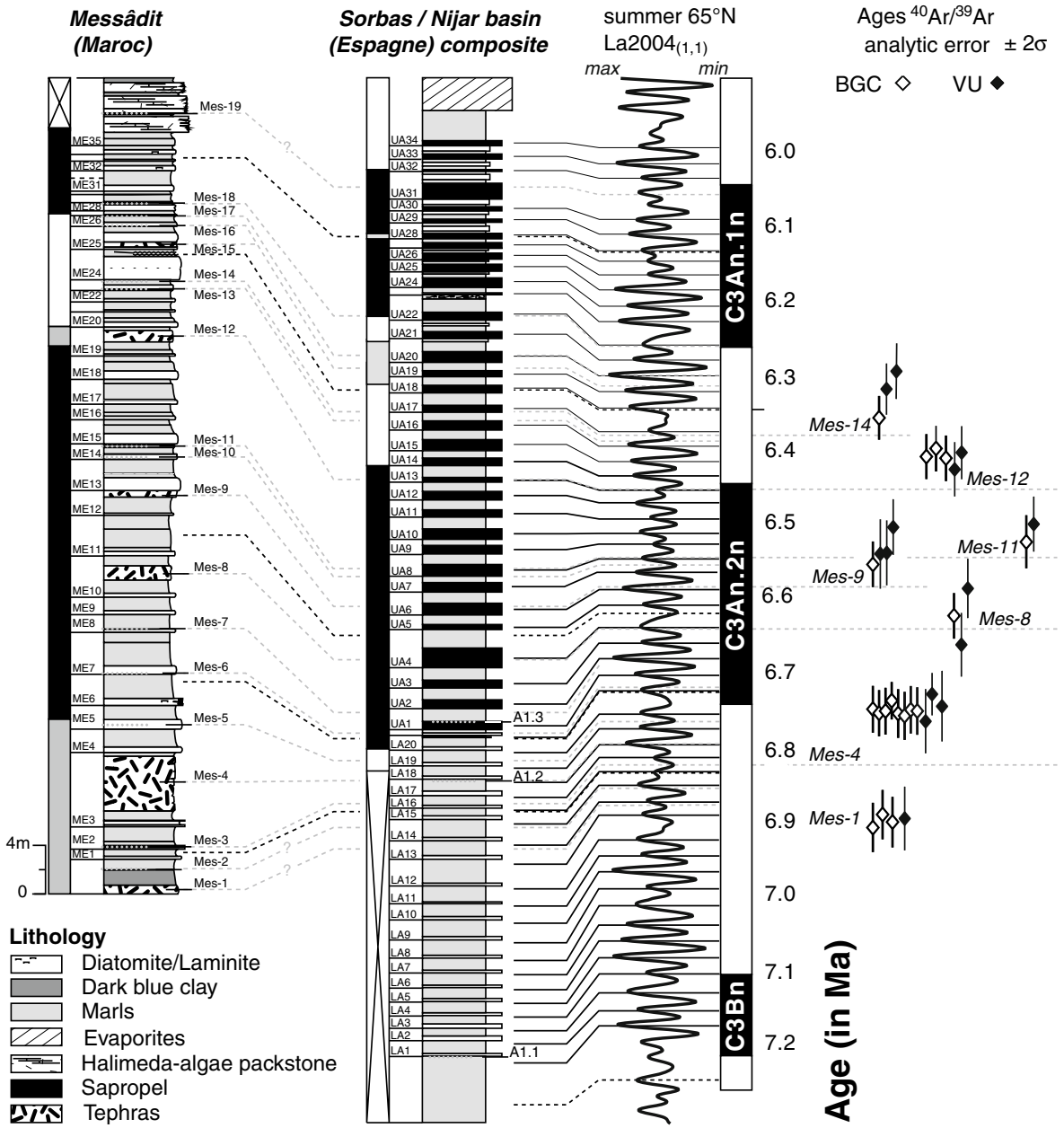

Fig. 28.10 According to Kuiper et al. 2008. Astronomical calibration of the Messinian (between 7.2 and 5.3 Ma) where the alternating marl/sapropel series can be correlated with the astronomical forcing (in agreement with many other stratigraphic markers). This astronomical calibration is then used to better constrain the $^{40}Ar/^{39}Ar$ method (measured here in tephras), since the disintegration constant of ^{40}K is only known with to an error of about 3 or 4% ($(5.463 \pm 0.214) \times 10^{-10}$ an^{-1})

$^{40}Ar/^{39}Ar$ radiometric method (Kuiper et al. 2008). As mentioned above, this way of establishing age scales, or cyclostratigraphy, makes it possible to achieve a level of precision far superior to the usual radiometric methods, the uncertainties of which increase as we go back in time.

The chronology is thus often the first point of interest when identifying astronomical cycles in old sedimentary series. The most famous example of cyclicity found in geological recordings concerns the alternating marl-limestone series. As early as the end of the nineteenth century, Gilbert suggested that these sedimentary successions from the Cretaceous, which he studied in the limestone formations of the Green River in Colorado, were probably caused by astronomical changes. Extrapolating from the limited outcrops that he had at his disposal, he assumed that they were linked to the precession cycles, which led him to

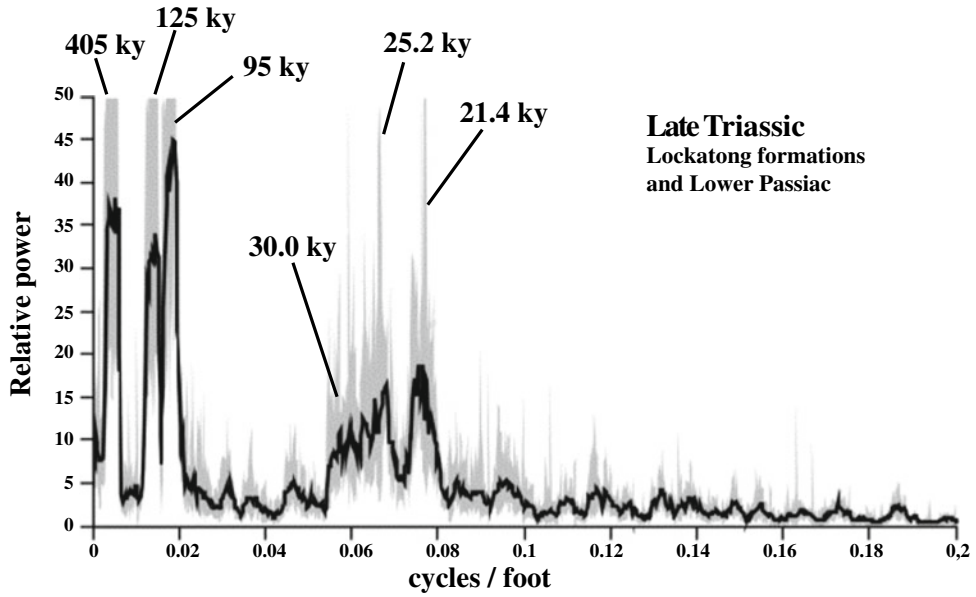

Fig. 28.11 Spectrum of the Triassic lake levels in New Jersey (Olsen and Kent 1996)

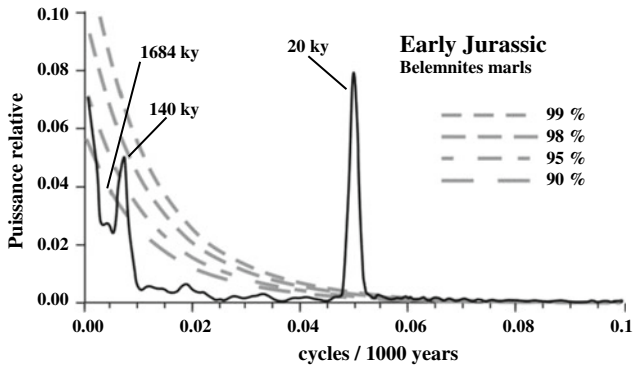

Fig. 28.12 Spectrum of the percentage of carbonate, Jurassic, England (Weedon et al. 1999)

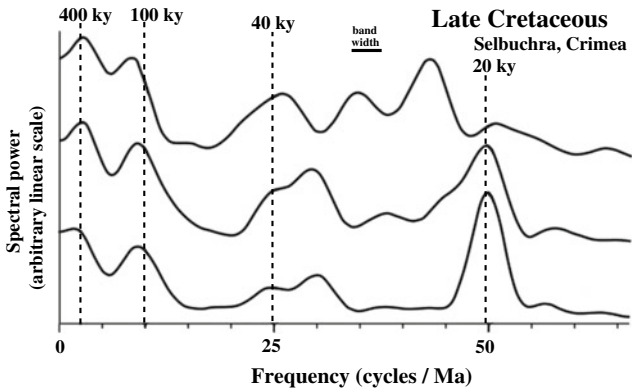

Fig. 28.13 Spectra of sedimentary reflectance, Cretaceous, Crimea (Gale et al. 1999) with various chronological hypotheses

suggest that the Upper Cretaceous lasted between 20 and 40 million years. This is in line with recent estimates (34 million years). Numerous studies have since confirmed the existence of these Triassic, Jurassic and Cretaceous cycles, as illustrated in the following Figs. 28.11, 28.12 and 28.13. In particular, it can be seen that although the precession is often dominant, the cycles linked to the obliquity or to the eccentricity also play very important roles.

The influence of astronomical cycles has also been demonstrated in the Paleozoic, although there are fewer studies on this subject. This is due to the difficulty in finding chronological benchmarks that are sufficiently precise and reliable to be able to unambiguously attribute the cyclicality found to astronomical parameters. For example, during the Carboniferous, alternating marine sediment and coalbed layers, called cyclothems, probably correspond to changes in sea level in the delta regions, where abundant vegetation during low sea levels (regressions) was followed by sedimentary deposits during high sea levels (transgressions). This is ultimately to be expected, as the Carboniferous, like the Quaternary, corresponds to a 'glacial' period with consequential ice caps which are likely to fluctuate in line with astronomical changes. Similarly in the Devonian, sedimentary cyclicities are observed and these are usually interpreted in terms of the evolution of the large ice caps present at that time. It is also possible to find much older cycles, such as the Archean, for example, more than 2 billion years ago (Hofmann et al. 2004).

The further back in time we go, the more important it is to take possible changes in astronomical periodicities into account. In particular, the movements of the Earth's axis (precession and obliquity) will be strongly affected by the Earth-Moon distance which increases over time due to tidal dissipation. Thus, the periodicity of the precession of the equinoxes, between 25,700 years ago and today, was noticeably faster before. The same applies to the cycles of climate precession and obliquity, which are directly related to it, and which are today 19, 23 and 41 ka. Considering the current rate of lunar recession, we obtain respective periodicities of 16, 18.7 and 29 ka for 500 million years ago. These values are too quick and are inconsistent with geological observations, which underscores the need for a slower lunar recession in the past, due to the current isostatic rebound but also to changes in sea level, in the topography of the ocean floors, and even ocean stratification. Generally speaking, even more than finding a given periodicity, the aim is to find a coherence between several periodicities which corresponds well to the astronomical forcing. For example, the presence of three periodicities in a 1:5:20 ratio is often interpreted as the precession (~20 ka) and the eccentricity (~100 ka and ~400 ka) periodicities, even though the frequencies have varied in the past, and even if the chronological information does not allow the recorded periodicities to be determined with confidence.

If one had to choose a particularly stable periodicity in the past, the 405 ka cycle associated with variations in eccentricity would probably be the best choice (Laskar et al. 2004). As stated in paragraph IIa, the solar system is chaotic and it is impossible to calculate precisely its evolution further back than a few tens of millions of years. However, if the perturbations associated with the internal planets (from Mercury to Mars) become quickly unpredictable, the outer planets (in particular, Jupiter and Saturn) have much more regular long-term movements. This produces high stability for the periodicity at 405 ka, which can therefore be used as a chronological reference over several hundred million years. According to Laskar et al. (2004), the spread of solutions over the last 250 million years for this periodicity is less than one cycle (<400 ka). This therefore, creates the opportunity to construct a very precise absolute chronology not only for the Cenozoic (since 65 Ma) but also for the whole of the Mesozoic (between 65 Ma and 250 Ma). These cycles can be systematically numbered from the present time to the distant past, thus offering a new way of stratigraphic tracking on the geological scale. For example, in Fig. 28.14, the clear presence of these cycles is observed during the Oligocene period. Moreover, the Eocene-Oligocene (Oi-1 event) or Oligocene-Miocene (Mi-1 event) transitions correspond to particularly 'cold' climate periods according to the oxygen isotopes. These extreme values can be related to the minima of the astronomical forcing linked to the obliquity (minima of the amplitude modulation).

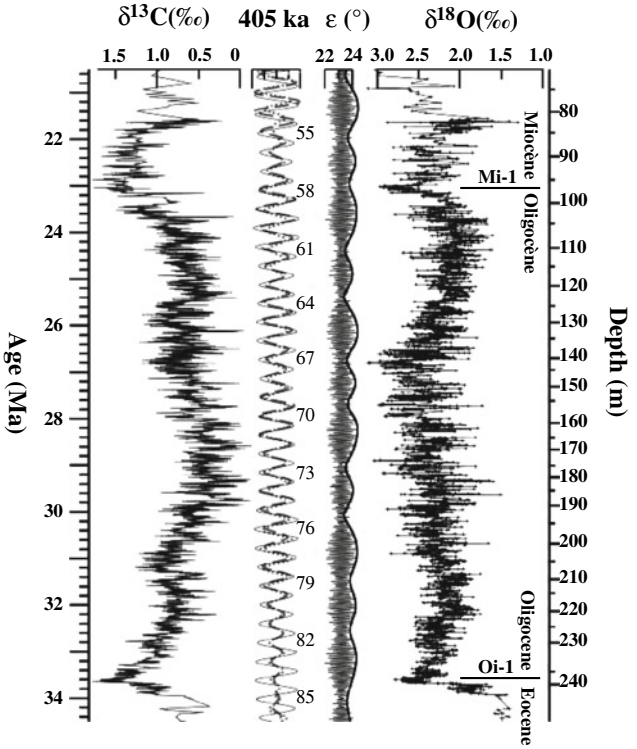

Fig. 28.14 According to Pälike et al. 2006. Stable ^{13}C and ^{18}O benthic isotopes of the ODP 1218 site, obliquity (ε) with its amplitude modulation, and filtering of the eccentricity and the isotopic signals at 405 ka. The 405 ka periodicity is clearly visible in the isotopic signals, particularly ^{13}C, which makes it possible to define an astronomical chronology (numbering the 405 ka cycles from the current one). The minimum amplitude in variation of the obliquity very often correspond to maxima for the ^{18}O

These 405 ka eccentricity cycles probably play an important role in the evolution of climate in the Quaternary. Although changes in ice cap volume are largely dominated by the 100 ka cycle, this is not necessarily the case for other indicators. In particular, we find a clear signature in this frequency band in the ^{13}C of benthic foraminifera with cycles between 400 and 500 ka (Wang et al. 2004). These changes in the global carbon cycle are probably the cause of the different climate phases of the last million years: the beginning of the glaciations (Pliocene-Pleistocene transition around 2.6 Ma), as well as the transition between the 41 ka cycles and the 100 ka cycles (Mid-Pleistocene transition around 0.7 Ma) corresponding to the amplitude modulation of this 400 ka eccentricity cycle (Paillard 2017).

Although cycles were probably present throughout the Earth's history, it is important to avoid systematically ascribing an astronomical origin to all periodicity observed in sedimentary records. Indeed, it is quite conceivable that certain components of the Earth system could generate more or less periodic internal oscillations at frequencies that have little to do with celestial dynamics. Thus, in the Quaternary,

there is a so-called 'sub-Milankovitch' variability corresponding to the Dansgaard-Oeschger and Heinrich events. It is likely that cyclicities of this type have also existed at other times in Earth's history. For example, the 470 m thick Triassic strata, observed in Latemar in the Italian Dolomites, have a well-marked periodic structure showing about 600 cycles. There is controversy between those who support the hypotheses of astronomical cycles, who see precession cycles and therefore a total recording time of around 10 million years, and the proponents of much quicker environmental variations, using radiometric dating to estimate a total duration of around a million years only, hence an order of magnitude faster. Although the debate is not yet settled, it highlights that it is not enough to identify the cycles in geological records to systematically find an astronomical signature. The dynamics of the Earth system are indeed likely to reveal many more surprises.

Conclusions

The dynamics of the glacial-interglacial cycles of the Quaternary are far from fully understood and this is even more true for the pre-Quaternary astronomical cycles. Moreover, the climate during glacial periods can sometimes change very abruptly during the Dansgaard-Oeschger or Heinrich events, for reasons unrelated to astronomical forcing or to atmospheric CO_2 variations. It is noteworthy that the last deglaciation was punctuated by such rapid events. It is therefore quite possible that they also play a decisive role in the dynamics of large cycles, and even more so if one considers that they are based on tipping points that allow a shift from a glacial state to an interglacial state.

The conceptual models presented here are far from sufficient to account for the physical and biogeochemical interactions involved in these climate changes. The most sophisticated climate models that are used to simulate the twenty-first century, or 'general circulation models', are unfortunately unable to simulate these changes because the time scales involved are far too long. In addition, the ice cap changes and the dynamics of the main biogeochemical cycles must also be taken into account, which these models are not yet able to do correctly. For all these reasons, simpler models of the 'Earth system' (or models of intermediate complexity) are used to address this type of question. Recent advances, both in terms of paleoclimate reconstructions but also in terms of modeling (Bouttes et al. 2011), provide hope that a new theory of the glacial-interglacial cycles of the Quaternary that takes into account the various aspects of terrestrial environmental changes (ice caps, carbon, vegetation, climate) can be developed in the years to come. An overview of this type would provide a much better understanding of the great climate changes experienced so far by *homo sapiens.*

References

Adkins, J., McIntyre, K., & Schrag, D. (2002). The salinity, temperature and $\delta^{18}O$ of the glacial deep Ocean. *Science, 298,* 1769–1773.

Arrhenius, S. (1896). On the influence of carbonic acid in the air upon the temperature of the ground. *Philosophical Magazine and Journal of Science, 41,* 237–276.

Bard, E. (2004). Greenhouse effect and ice ages: Historical perspective. *C. R. Geoscience, 336,* 603–638.

Bard, E., Hamelin, B., Arnold, M., Montaggioni, L., Cabioch, G., Faure, G., et al. (1996). Deglacial sea-level record from tahiti corals and the timing of global meltwater discharge. *Nature, 382,* 241–244.

Berger, A. (1978). Long-term variations of daily insolation and quaternary climatic change. *Journal of the Atmospheric Sciences, 35,* 2362–2367.

Bouttes, N., Paillard, D., Roche, D. M., Brovkin, V., & Bopp, L. (2011). Last glacial maximum CO_2 and $\delta^{13}C$ successfully reconciled. *Geophysical Reseach Letters, 38,* 1–5.

Broecker, W., & van Donk, J. (1970). insolation changes, ice volumes and the O^{18} record in deep-sea cores. *Reviews of Geophysics and Space Physics, 8,* 169–197.

Calder, N. (1974). Arithmetic of ice ages. *Nature*, *252*, 216–218.

Gale, A. S., Young, J. R., Shackleton, N. J., Crowhurst, S. J., & Wray, D. S. (1999). Orbital tuning of cenomanian marly chalk successions: Towards a milankovitch time-scale for the late cretaceous. *Philosophical Transactions of the Royal Society A*, *357*, 1815–1829.

Hays, J., Imbrie, J., & Shackleton, N. J. (1976). Variations in the earth's orbit: Pacemakers of the ice ages. *Science*, *194*, 1121–1132.

Hofmann, A., Dirks, P. H. G. M., & Jelsma, H. A. (2004). Shallowing-upward carbonate cycles in the belingwe greenstone belt, zimbabwe: A record of archean sea-level oscillations. *Journal of Sedimentary Research, 74,* 64–81.

Huybers, P. (2006). Early pleistocene glacial cycles and the integrated summer insolation forcing. *Science, 313,* 508–511.

Huybers, P., & Wunsch, C. (2005). Obliquity pacing of the late pleistocene glacial terminations. *Nature, 434,* 491–494.

Imbrie, J., Hays, J., Martinson, D., McIntyre, A., Mix, A., Morley, J. J., Pisias, N., Prell, W., Shackleton, N., Berger, A., Kukla, G., & Saltzman, B. (1984). The orbital theory of pleistocene climate: Support from a revised chronology of the marine d^{18}O record. In A. dans Berger (Ed.), *Milankovitch and climate* (pp. 269–305), Dordrecht: Kluwer Academic Publishers (Nato ASI Ser. C).

Joussaume, S., Braconnot, P. (1997). Sensitivity of paleoclimate simulation results to season definitions. *Journal of Geophysical Research D*, *102*, 1943–1956.

Kuiper, K., Deino, A., Hilgen, F. J., Krijgsman, W., Renne, P. R., & Wijbrans, J. R. (2008). Synchronizing rock clocks of earth history. *Science, 320,* 500–504.

Laskar, J., Robutel, P., Joutel, F., Gastineau, M., Correia, A. C. M., & Levrard, B. (2004). A long-term numerical solution for the insolation quantities of the earth. *Astronomy & Astrophysics, 428,* 261–285.

Lisiecki, L. E., & Raymo, M. E. (2005). A pliocene-pleistocene stack of 57 globally distributed benthic $\delta^{18}O$ records. *Paleoceanography*, *20*, PA1003. https://doi.org/10.1029/2004pa001071.

Milankovitch, M. (1941). *Kanon der Erdbestrahlung und seine Andwendung auf das Eiszeiten-problem*. (p. 633).

Monnin, E., Indermühle, A., Dällenbach, A., Flückiger, J., Stauffer, B., Stocker, T., et al. (2001). Atmospheric CO_2 concentrations over the last glacial termination. *Science, 291,* 112–114.

Ohshima, et al. (2013). Antarctic bottom water production by intense sea-ice formation in the Cape Darnley polynya. *Nature Geoscience, 6,* 235–240.

Olsen, P. E., & Kent, D. V. (1996). Milankovitch climate forcing in the tropics of pangaea during the late triassic. *Palaeogeography Palaeoclimatology Paleoecology, 122,* 1–26.

Paillard, D. (1998). The timing of pleistocene glaciations from a simple multiple-state climate model. *Nature, 391,* 378–381.

Paillard, D. (2001). Glacial cycles: Toward a new paradigm. *Reviews of Geophysics, 39,* 325–346.

Paillard, D., & Parrenin, F. (2004). The antarctic ice-sheet and the triggering of deglaciations. *Earth Planet Science Letters, 227,* 263–271.

Paillard, D. (2010). Climate and the orbital parameters of the earth. *C. R. Geoscience, 342,* 273–285.

Paillard, D. (2015). Quaternary glaciations: from observations to theories. *Quaternary Science Reviews*, *107*, 11–24.

Paillard, D. (2017). The plio-pleistocene climatic evolution as a consequence of orbital forcing on the carbon cycle. *Climate of the Past, 13,* 1259–1267.

Pälike, H., Laskar, J., & Shackleton, N. (2004). Geologic constraints on the chaotic diffusion of the solar system. *Geology, 32,* 929.

Pälike, H., Norris, R. D., Herrle, J. O., Wilson, P. A., Coxall, H. K., Lear, C. H., Shackleton, N. J., Tripati, A. K., & Wade, B. S. (2006). The Heartbeat of the oligocene climate system. *Science*, *314*, 1894–1898.

Petit, J.-R., Jouzel, J., Raynaud, D., Barkov, N., Barnola, J.-M., Basile, I., et al. (1999). Climate and atmospheric history of the past 420,000 years from the Vostok ice core, Antarctica. *Nature, 399,* 429–436.

Tiedemann, R., Sarnthein, M., & Shackleton, N. (1994). Astronomic timescale for the pliocene atlantic $\delta^{18}O$ and dust records of ocean drilling program site 659. *Paleoceanography, 9,* 619–638.

Wang, P., Tian, J., Cheng, X., Liu, C., & Xu, J. (2004). Major pleistocene stages in a carbon perspective: The South China sea record and its global comparison. *Paleoceanography*, *19*, PA4005. https://doi.org/10.1029/2003pa000991.

Weedon, G. P., Jenkyns, H. C., Coe, A. L., & Hesselbo, S. P. (1999). Astronomical calibration of the jurassic time-scale from cyclostratigraphy in British mudrock formations. *Philosophical Transactions of the Royal Society A*, *357*, 1787–1813.

Rapid Climate Variability: Description and Mechanisms

29

Masa Kageyama, Didier M. Roche, Nathalie Combourieu Nebout, and Jorge Alvarez-Solas

The previous chapters focused on climate variations stemming from factors external to the climate system: tectonics, orogeny, variations in insolation. Yet the study of glacial records and marine sediments over the past three decades has revealed major changes within the climate system over much shorter time scales than previously envisaged. These abrupt reorganisations of the climate system, which cannot be explained by forcings external to the system, are true climate 'surprises'. They have been the subject of many studies, both to describe the expression of these events on a global scale and to model these events and their impacts. This work is still going on to better characterize and understand this type of climate variability, called millennial variability, in contrast to the time scales associated with the Milankovitch forcings (see Chap. 7), or abrupt (rapid) variability, because the transitions between climate states take place on even shorter time scales, ranging from ten to one hundred years. This chapter presents a synthesis of current knowledge on rapid climate variability.

M. Kageyama (✉) · D. M. Roche
Laboratoire des Sciences du Climat et de l'Environnement, LSCE/IPSL, CEA-CNRS-UVSQ, Université Paris-Saclay, 91191 Gif-sur-Yvette, France
e-mail: masa.kageyama@lsce.ipsl.fr

N. C. Nebout
UMR 7194 CNRS/UPVD/MNHN, HNHP-Histoire Naturelle de l'Homme Préhistorique, Département Homme et Environnement, Muséum National d'Histoire naturelle, Paris, France

N. C. Nebout
Institut de Paléontologie Humaine, 1 rue René Panhard, 75013 Paris, France

J. Alvarez-Solas
Departamento de Física de la Tierra y Astrofísica, Facultad de Ciencias Físicas, Universidad Complutense de Madrid, 28040 Madrid, Spain

J. Alvarez-Solas
Instituto de Geociencias, Consejo Superior de Investigaciones Científicas-Universidad Complutense de Madrid, 28040 Madrid, Spain

Rapid Climate Changes During Glacial Periods: Heinrich and Dansgaard-Oeschger Events

The Discovery

Abrupt climate changes were first discovered in the context of the last glacial period (see the review by Hemming 2004). In 1977, Ruddiman showed that during Marine Isotopic Stages 4, 3 and 2, large quantities of coarse detrital material transported by icebergs detaching from the Northern Hemisphere ice sheets were deposited at the mid-latitudes of the North Atlantic between 40 and 65° N in a band now known as the Ruddiman Belt, while the main deposition area for Stage 5 is closer to Greenland and Newfoundland. The concentration of detrital material measured in marine sediments is thus linked with the size and expansion of continental ice sheets over the Milankovitch timescale. In 1988, H. Heinrich showed that six major events of coarse detrital material deposition occurred in the Ruddiman band during the last glacial period at intervals of about 10,000 years, and therefore at time scales shorter than those of Milankovitch. These six events are often accompanied by a major change in the composition of assemblages of planktonic foraminifera, with a predominance of the left-coiling *Neogloboquadrina pachyderma* polar species, an indicator of a particularly cold environment. Heinrich initially based his interpretation of these results on the fact that the period of 10,000 years is about half a precession cycle. He speculated that the coarse detrital material was transported either by icebergs (in orbital conditions favoring a 'cold' period) or by the melting of the ice sheets ('warm' situation). This hypothesis did not stand up to more precise dating and analyses of marine records in the North Atlantic but it shows that, at the time of this discovery, the variations in orbital insolation were considered the main contributors to the evolution of the climate system. At that time, sudden changes to the system were not envisaged. The discovery

G. Ramstein et al. (eds.), *Paleoclimatology*, Frontiers in Earth Sciences,
https://doi.org/10.1007/978-3-030-24982-3_29

however initiated much research on these major deposits of coarse detrital material, which were named Heinrich events (HE) by Broecker et al. in 1992. Heinrich events are defined by these authors in terms of both their characteristic low concentration of planktonic foraminifera and high concentration of detrital material. They further demonstrate that these events are related to armadas of icebergs that broke off from the ice sheets rather than to the melting of these ice sheets. The layers of detrital material may be several meters thick in the Labrador Sea. This thickness is less, although still significant, close to the European coasts. Subsequent studies of the composition and properties of this ice-rafted detrital material show that its origin is mostly from the Canadian shield and has therefore been transported by icebergs which detached from the North American ice sheet.

During the same period, the analysis of the $\delta^{18}O$ isotopic signal from ice cores taken from the summit of the Greenland ice cap (Dansgaard et al. 1993) shows the contrast between interglacial periods, and particularly between the remarkably stable Holocene, and the last glacial period, characterized by high amplitude oscillations. This amplitude can be as much as half of the glacial-interglacial difference in Greenland. The warming events were named 'Dansgaard-Oeschger events' (D/O), because these two authors had already detected rapid $\delta^{18}O$ fluctuations in the ice in a core from Camp Century. At the time, the record appeared dubious due to large simultaneous variations in the CO_2 content in the air bubbles trapped in the ice. We now know that the latter are artefacts caused by the presence of carbonate dust attacked by the sulfuric acid present in the ice. However, the rapid fluctuations of $\delta^{18}O$ are indeed significant.

D/O warming appears to have occurred particularly quickly, over a few decades, solely when ice sheets developed on the continents of the northern hemisphere. The relatively warm period following the D/O event is called the 'interstadial period' and is characterized by gradual cooling. It ends with a rapid return to the coldest levels recorded, known as 'stadial periods'. This return completes a D/O cycle, which lasts a total of about 1500 years. There are therefore more D/O events than Heinrich events.

The existence of abrupt variations in both the surface climate in Greenland and in the ocean conditions over time scales far shorter than the Milankovich cycles contributed to the emerging idea that the climate system could have multiple equilibrium points and that it could be abruptly reorganized as it transfers from one equilibrium to another. This idea was reinforced by the correlations between marine and glacial records, first demonstrated by Bond et al. (1993). These authors suggest a perspective of glacial variability that integrates the Heinrich and Dansgaard-Oeschger events. The glacial millennial variability is organized in cycles, later called "Bond cycles" (Fig. 29.1). Each cycle begins at the end of a Heinrich event, by the first Dansgaard-Oeschger event, which has a large amplitude. This is followed by a few other Dansgaard-Oeschger cycles, of diminishing amplitude. The last cycle ends with a massive discharge of icebergs from the Laurentide sheet, in other words, by a Heinrich event. Each cycle lasts approximately 7000–10,000 years.

Since these discoveries in the early 1990s, millennial variability has become a subject of intense research. Numerous records were analyzed with as fine a resolution as possible and they showed that variability at shorter time scales than those of Milankovitch was not limited to the North Atlantic and adjacent regions. The challenge is then to be able to synchronize these different records to better characterize this type of variability, as well as to better understand the connections between climate signals recorded all over the globe. In the following sections, we focus on the signature of the Heinrich and D/O events, on their impact on climate and on the efforts to understand these climate instabilities through modeling.

The Regional Impacts of the Heinrich and Dansgaard-Oeschger Events: North Atlantic and Adjacent Regions

Atlantic Ocean

The Heinrich Events

The melting of massive armadas of icebergs profoundly modified the ocean surface conditions in the North Atlantic. The changes are recorded in ocean sediment cores, particularly in $\delta^{18}O$ signals from planktonic foraminifera. Indeed, excursions towards lighter $\delta^{18}O$ are measured in the calcite of these foraminifera, indicating either less saline surface waters or warmer temperatures. The fauna of fossil foraminifera in sediments reveal very cold conditions during Heinrich events (see, for example, Hemming 2004; Cortijo et al. 2005). The melting of icebergs is responsible for a huge inflow of freshwater, desalinating the surface of the ocean and introducing a highly negative $\delta^{18}O$ signal, typical of ice contained in the ice sheets.

Other paleoceanographic records reveal significant reorganizations during the Heinrich events. In particular, the study of $\delta^{13}C$ in sediment cores proves that the bottom waters of the Atlantic Ocean were less well ventilated (Elliot 2002), demonstrating a reorganization of ocean circulation. These studies were corroborated by analyses of the magnetic properties of sediment cores collected in the North Atlantic (see Kissel 2005 for a compilation), which show that the melting of icebergs was accompanied by a slowing of deep currents and of the thermohaline circulation.

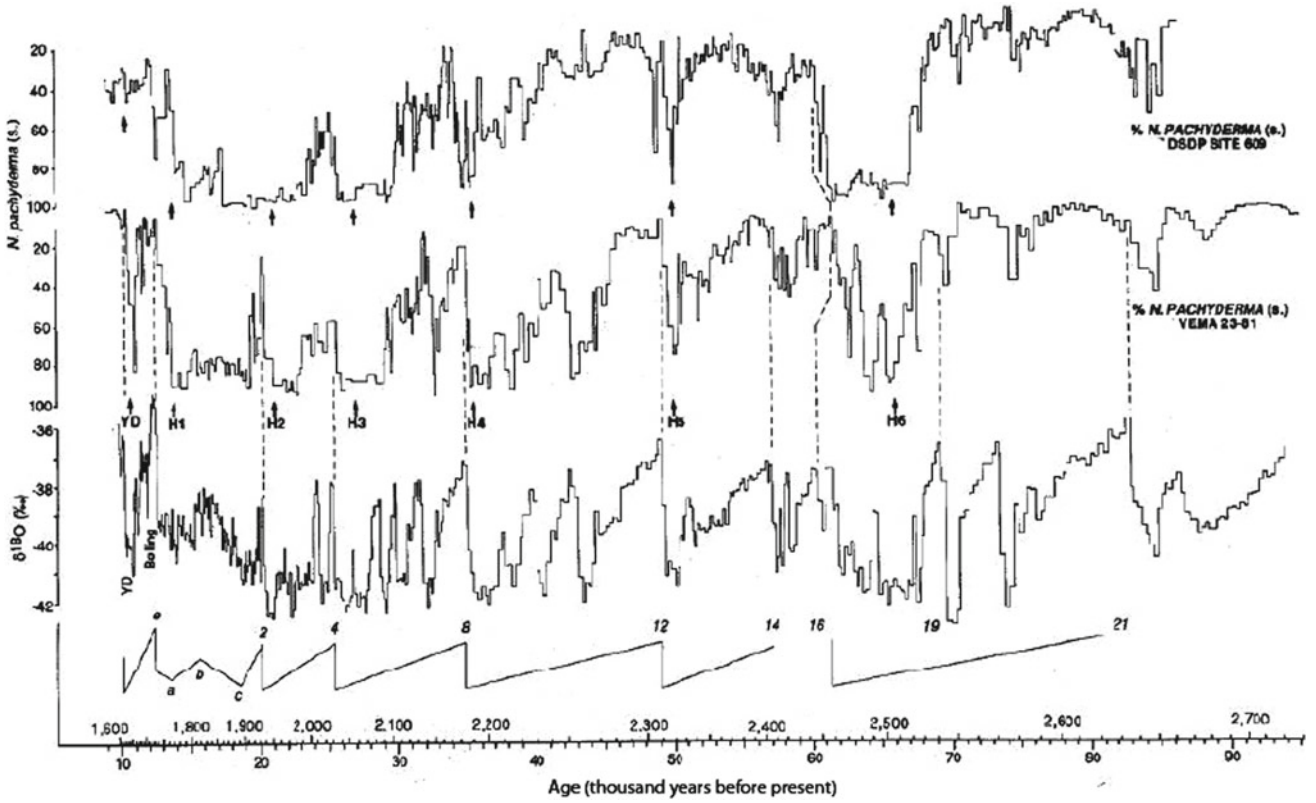

Fig. 29.1 Bond cycles (from Bond et al. 1993). The top two curves represent the abundance of *N. Pachyderma* (s.) in sediment records from the DSDP-609 and VEMA23-51 cores from the North Atlantic at 50 and 54° N, respectively. The Heinrich events and the Younger Dryas are indicated by arrows under the second curve. The third curve shows the $\delta^{18}O$ record in an ice core from the GRIP project in Greenland. These curves show how events recorded in marine cores and those recorded in ice cores correspond with each other. The fourth curve is a schematic representation of the Dansgaard-Oeschger and Heinrich events organized into cycles now called 'Bond cycles'. The figures over the age axis indicate the depth in the GRIP core

The isotopic study (Sr/Nd) of the grains brought by the icebergs to the North Atlantic during the Heinrich events made it possible to determine where these icebergs came from. Grousset et al. (1993) first demonstrated that within the Heinrich levels, although most of the detrital material brought to the Ruddiman belt came from the Laurentide ice sheet, there were some detrital elements from European and Icelandic ice sheets. Subsequent, more detailed studies of the Heinrich events complemented this panorama by showing that during each Heinrich event a level of detrital material from the European ice sheets preceded the level coming from the North American ice sheet. This almost systematic phase relationship led these authors to question the possibility of a causal relationship: could the icebergs from the European ice sheet be triggering the discharge of icebergs from the North American ice sheet? Another interpretation of these observations is to imagine that the European ice sheets were smaller and oscillated faster than the larger Laurentide ice sheet, causing them to precede it during the Heinrich events, with no obvious causality between the two.

The Heinrich events continue to attract a lot of attention from researchers, and many connections between these iceberg armada events and other records sensitive to temperature, precipitation and other climatic factors have been highlighted. This has led, in some publications, to a shortcut being made between the iceberg armada event and its supposed climate impact. It should be noted that, strictly speaking, a Heinrich event can only be defined by the presence of coarse detrital elements in sedimentary cores taken from the Ruddiman band. This implies in particular that the presence of detrital elements in an ocean core from the Fennoscandian ice sheet margin does not necessarily indicate a Heinrich event, but could be due to the melting of icebergs from European ice sheets. In addition, it is not generally possible to define Heinrich events from marine records outside the Ruddiman band and, even less so, from continental records. As a result, the term 'cold Heinrich event' is often inaccurately used because it applies only to the Ruddiman band, and is simplistic, because the drop in temperature is only one aspect of the climate changes associated with a Heinrich event. One exception is pollen records from marine cores containing detrital material. These provide simultaneous records from the adjacent continent (pollen) and from the iceberg armadas originating from the North

American ice sheet. They can therefore safely be used to reconstruct continental climate changes associated with Heinrich events (Sánchez-Goñi et al. 2002; Combourieu-Nebout et al. 2002).

Dansgaard-Oeschger Events

When the cores are studied at century-scale resolution, records of calcite $\delta^{18}O$ from foraminifera from the ocean surface indicate that abrupt changes also occurred during Dansgaard-Oeschger events. The variations recorded by marine indicators are very similar to those obtained from Greenland ice data. It is therefore tempting to directly link an observed variation in one set of records to one observed in the other and to assume that they are responses to a common cause. While this is certainly partially true (the $\delta^{18}O$ of polar ice is above all a response to temperature and the $\delta^{18}O$ of the foraminiferal calcite also contains a temperature signal), especially in the case of marine records close to the ice sheets, it should be borne in mind that it is paleoclimate indicators and not climate variables, such as temperature, that are being measured. Directly correlating every small variation in the two records is therefore hasty and inordinate. Despite these difficulties, marine records reveal that during Dansgaard-Oeschger events, the surface ocean and the deep ocean undergo changes of great amplitude in the surface temperature and/or the $\delta^{18}O$ of the sea water (see Rasmussen et al. 1996; Shackleton et al. 2000). The reconstruction of ocean surface temperatures from independent indicators shows that the temperature signals in Greenland cores are matched in the neighboring North Atlantic.

Associated with these changes in temperature and hydrological conditions are signals of relatively small amplitude in oceanic $\delta^{13}C$ records (Elliot 2002). Since $\delta^{13}C$ is an indicator of the ventilation of ocean water bodies, it would appear that at least for the North Atlantic and the Arctic, transitions between stadial and interstadial periods are not associated with large anomalies in ventilation, and therefore with any drastic change in thermohaline circulation in the Atlantic. This observation shows the different mechanisms operating during the Dansgaard-Oeschger events and Heinrich events, the latter having very marked anomalies in ocean $\delta^{13}C$ records.

Neighbouring Continents

The evolution of continental paleo-conditions is recorded in numerous environments, such as in caves (e.g. in concretions or speleothems), lakes (lake sediments), peat bogs, loess or marine cores. For continental regions adjacent to the Ruddiman belt, these records show a clear correlation between the evolution of the ocean and continent during periods of strong glacial variability. Pollen data, for example, show that during this period, rapid climate changes, whether D/O oscillations or Heinrich events, had repercussions on vegetation.

In Western Europe, D/O events resulted in periodic changes in forest cover (Fig. 29.2), with warm events corresponding to the expansion of oak forests, also implying wet conditions (e.g. Sánchez-Goñi et al. 2002; Combourieu-Nebout et al. 2002). On the other side of the Atlantic, in Florida, over the same periods, the oak is associated with large quantities of herbaceous plants (*Ambrosia, Poaceae*), indicating drier phases (Grimm et al. 2006). During the Heinrich events, the vegetation cover of western Europe became steppe-like, indicating a cold and very dry climate, especially in the Mediterranean region (Fig. 29.2). These cold conditions prevailing over Europe are associated with high $\delta^{13}C$ values recorded in several stalagmites in the south of France. They show up in a slowing down, or even a curtailment of growth as the cold conditions prevent the infiltration necessary for the formation of stalagmites (Genty et al. 2005).

At the same time, vegetation in Florida was characterized by an abundance of pine trees and the regression of herbaceous plants and oak trees which is interpreted as a consequence of a warmer and more humid climate (Grimm et al. 2006). The strong contrast between the responses by climate and vegetation to abrupt climate events on the two sides are examined with the cases of Europe and Florida. In Florida, this response may seem to be counter-intuitive, since the climate becomes warmer and more humid during the Heinrich events, although they are responsible for a major cooling in the North Atlantic. However, as records obtained for Florida have a relatively poor temporal resolution, it is possible that this contrasting response with the European one is due to problems of synchronization in the reconstructions. Another possibility is that the climates of Europe and Florida do not have the same sensitivity to freshwater incursions into the North Atlantic and the associated cooling. Europe, indeed, has a regime of prevailing westerly winds and is therefore under the direct influence of the cooling of the North Atlantic, unlike Florida on the other side of the Atlantic. It is thus crucial to be able to explain the complexity of these different signals. Modeling, as will be shown later in this chapter, can provide a coherent framework for reconstructions of climate changes in regions geographically distant from each other.

Millennial-Scale Variability in Other Regions of the World

After the discovery of abrupt climate changes in Greenland, the North Atlantic and adjacent regions, rapid changes in the characteristics of the climate system were discovered in

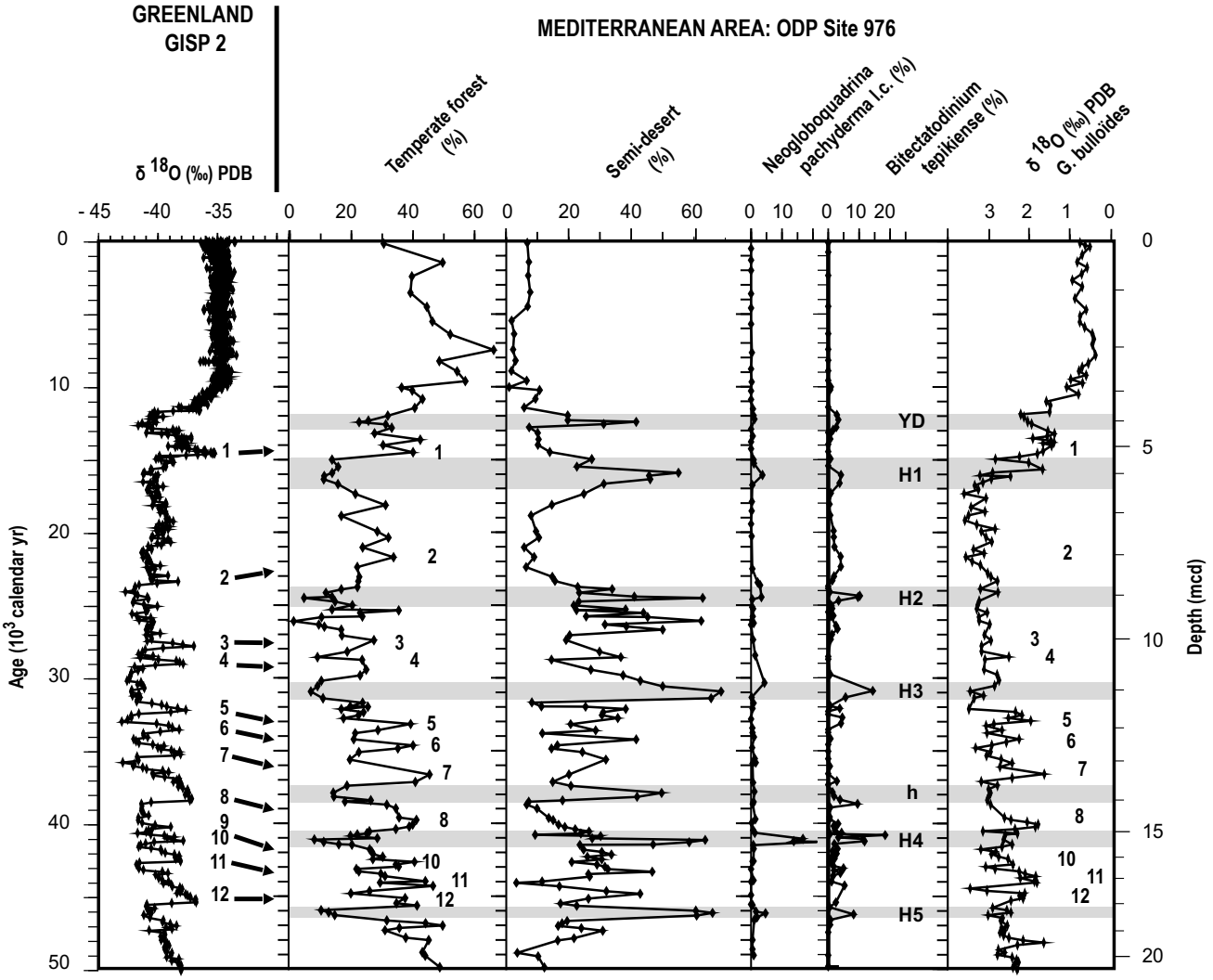

Fig. 29.2 Comparison of the $\delta^{18}O$ curves of the GISP2 ice core from Greenland with the paleoenvironmental reconstructions obtained for the ODP 976 (Alboran Sea) site. The curves are presented as a function of calendar age (on the left) and as a function of depth in the ODP 976 core, in m (on the right). D/O events are indicated by the numbers 1–12 on the GISP2 curve, with the corresponding numbers on the Mediterranean curves. The Heinrich events and the Younger Dryas are indicated by the gray bands. Adapted from Combourieu-Nebout et al. (2002)

other parts of the world, in some cases far from the North Atlantic. Abrupt changes in the δD of the ice at Vostok in Antarctica were reported as early as 1994 by the team of M. Bender, who established a correlation with the Greenland records, through the oxygen isotopes in the air preserved in the ice. In 1995, abrupt changes in ventilation were observed in the Santa Barbara Basin off California. In 1998, abrupt changes in biological productivity in the Arabian Sea, strongly related to monsoon intensity, were shown over time scales similar to Dansgaard-Oeschger cycles. In 2000, significant variations in the hydrological cycle in the low latitudes of the North Atlantic (Cariaco basin) were shown to correspond with events observed in the North Atlantic. Voelker et al. (2002) list 183 sites where variations of this type are recorded. Since this review, new records have been produced, confirming the global nature of these abrupt climate variations, and suggesting the involvement of a mechanism operating on a global scale.

Rapid climate variations of great amplitude have thus been found at many points on the globe. The most difficult part of interpreting these records is to synchronize them. The ideal would be to have an absolute dating for each record, on the same scale of the abrupt events, i.e., on a decadal scale. For most paleoclimate indicators, this is impossible to obtain. A dating method such as that based on ^{14}C does not offer sufficient precision over the glacial period to be able to link abrupt events recorded in two different places, in other words, to establish the phase differences between the various

records. In addition, knowing that the residence time of ^{14}C in the ocean (reservoir age variations) varies during abrupt events makes absolute dating based on this single variable even more difficult. However, these variations are interesting because they give us information on changes in ocean ventilation and ocean circulation (Chap. 21).

However, it is possible to synchronize the different records with each other using parameters known to be the same or to vary in a similar manner in different locations on the planet. This allows us to study the chronology of events recorded in different places and to propose hypotheses about the mechanisms behind glacial abrupt climate variability. Specific events, such as volcanic eruptions, whose falling ash appears in ice, marine and lake sediments, can help to synchronize records (Rasmussen et al. 2014). Other parameters can be used depending on the type of record.

One example is the use of variations in the atmospheric concentration of methane to place Greenland and Antarctic ice records on the same time scale. Methane is well mixed in the atmosphere and so variations in its concentration are the same everywhere on the globe. Members of the EPICA community (2006) used this method to compare the expression of abrupt events at the two poles. Comparisons show an anti-correlation between isotopic signals in Greenland and Antarctica. In addition, the strength of the warming in Antarctica is related to the length of the cooling in Greenland.

Another example is the use of magnetic properties to synchronize marine records (see Chap. 7). At the scale of the ocean basin (e.g., the North Atlantic, Elliot 2002), variations in rock magnetism can be used to put marine records on a common timescale. At the interhemispheric scale, paleomagnetic intensity can be used, especially for episodes of sudden and intense variation, such as around the Laschamp event.

Mechanisms

The climate reconstructions described above demonstrate the existence of rapid climate variability of great amplitude that involve all the components of the climate system. Understanding all aspects of this type of variability is still a challenge for the scientific community. An approach to test our understanding of these phenomena is to build models that include processes that are thought to contribute in a critical way to rapid variability. Well-informed choices from the possible forcings and processes can highlight the importance of each one for a particular type of event or for a level of variability (see Chap. 25, volume 2). Models have thus been constructed to explain the iceberg armadas (the Heinrich events themselves, strictly speaking) or to estimate the inflow of freshwater to the North Atlantic that could explain the observations or even to establish the connection between the inflow of freshwater to the North Atlantic and the climate consequences. Each study focuses on one aspect of the rapid climate variability. For the time being, no study has tried to include all of the factors of rapid climate variability in a single model, which would require a representation of the ice sheets, climate, ocean, chemical composition of the atmosphere, conditions of land surfaces, etc. constituting an almost complete model of the Earth system, which does not currently exist. The following sections present some of the suggested mechanisms behind Heinrich events and how they impact on global climate as well as on the Dansgaard-Oeschger cycles.

Heinrich Events

Ice-Sheet Instabilities

One of the first explanations of the cycles of spectacular armadas of icebergs discharged from the North American ice sheet was proposed by MacAyeal in 1993. He constructed a model of the part of the Laurentide ice sheet positioned on what is today the Hudson Bay, that is, on a sediment-covered bedrock. When the base of the ice sheet reaches its melting point, causing liquid water to be present there, the ice slides much more easily than it would if the base of the ice sheet and the sediments were frozen or if it was on a bedrock not covered with sediment. The ice basal layer can warm up through the input of geothermal energy when the ice sheet is thick enough, because the temperature at the base of an ice column is dependent on the pressure exerted by this column and because of the ice insulating its base from the cold conditions at its top. Based on these properties, MacAyeal proposes the following cycle: (1) the ice sheet grows due to the accumulation of snow on the surface (assumed to be constant over time in this model) and the base of the ice is frozen; (2) once the ice sheet is thick enough, its base melts and a layer of liquid water forms at the base-sediment-ice interface; (3) the ice sheet then quickly slides towards the ocean and its elevation decreases; (4) the elevation of the ice sheet decreases sufficiently so that the basal layer freezes again, thus slowing down the movement of the ice, and returning to step 1. MacAyeal calls this model ‘binge/purge’. In this model, the time between two “purge” events (i.e. between two episodes of iceberg break-up) is determined by the characteristic time necessaryfor the ice sheet to ticken and hence depends on the configuration of the ice sheet (size, distance to margins, characteristics of the underlying surface) and on its surface mass balance. It should be stressed that this mechanism works even for a constant climate. MacAyeal demonstrates an inherent oscillation in the ice sheets and shows that for the Laurentide

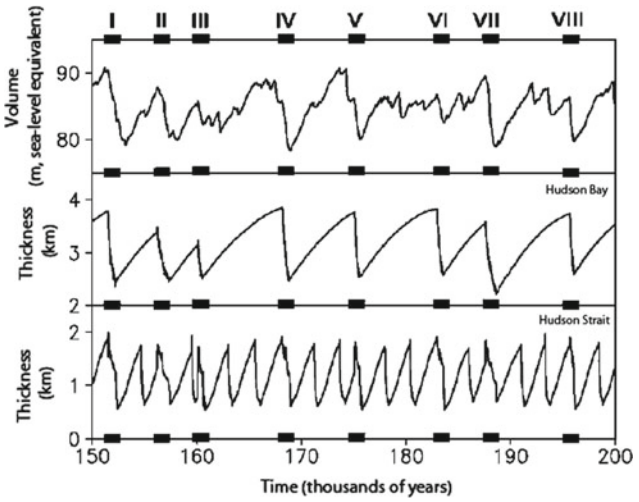

Fig. 29.3 Modeling of the instabilities of the atmosphere-ocean-North American ice sheet system in the context of a glaciation (Calov 2002). The climate model used is the CLIMBER-2 model, the model for the North American cap is the SICOPOLIS model in which the possibility of the ice cap sliding when the base is not frozen is incorporated. The model simulates a series of instabilities of the North American cap. **a** Ice volume of the ice cap. **b** Altitude of the ice cap above Hudson Bay (85.5° W, 61.5° N). **c** Altitude of the ice cap near the mouth of Hudson Bay (67° W, 60.75° N). The periods indicated in bold indicate periods when the ice cap releases armadas of icebergs, in other words, Heinrich events simulated by the model

ice sheet the length of the cycle is about 7000 years, which is of the same order of magnitude as the observed period. One criticism of this explanation is precisely that the ice sheets can oscillate independently, whereas a certain consistency between the break-up events in North America and Scandinavia has been observed (Grousset et al. 1993). However, the MacAyeal mechanism was reproduced in a more complex model (Calov 2002), which included the ocean, atmosphere, vegetation and ice sheets of the northern hemisphere, the characteristics of the bedrock at the base of the Laurentide ice sheet being imposed and spatially variable (Fig. 29.3). This latter study shows that although instabilities of the Laurentide ice sheet exist under constant forcing, the rest of the climate system can play a synchronization role for the events.

Hulbe et al. (2004), with MacAyeal as co-author, proposed an alternative to the "binge-purge" mechanism. Their explanation relies on the speculated presence of a massive ice shelf on the Labrador Sea. A break-up of this floating part of the Laurentide ice sheet would indeed be very efficient source of the icebergs defining the Heinrich events in the North Atlantic. A drawback of this theory, however, consists in the difficulty of identifying the ultimate reason of the ice-shelf break-up during cold surface conditions such as those observed during Heinrich events. Alvarez-Solas et al. (2013) postulated that such an ice-shelf break-up could be triggered by warmer subsurface waters. By using the hybrid ice-sheet/ice-shelf thermomechanical model GRISLI (Ritz et al. 2001), they simulated the effects that such an ice-shelf removal has on the inner part of the Laurentide ice sheet. Under this theory, not only the floating parts of the ice sheet contribute to the generation of the iceberg armadas but also the subsequent acceleration of the ice streams terminating in the ocean. For this mechanism to work, the ice shelves need to be destabilized from beneath and thus it assumes the existence of an external (to the ice sheet) forcing of Heinrich events. At the same time, Marcott et al. (2011) showed through the analysis of Mg/Ca in benthic foraminifera that the North Atlantic Ocean indeed experienced marked warmings of its subsurface waters during Heinrich events. Later on, in 2015, in a study entitled "Icebergs not the trigger for North Atlantic cold events", Barker et al. analysed several marine sediment records. They demonstrated that the melting of icebergs into the North Atlantic could not be the cause of the observed surface cooling because the icebergs simply arrive too late to these sites. They concluded that although the freshwater from icebergs could provide a positive feedback for lengthening stadial conditions, it does not trigger northern stadial events. Recently, Bassis et al. (2017) further expanded on the idea of the Heinrich events being triggered by the ocean by simulating the response of the Laurentide grounding line and the associated ice-streams acceleration.

Therefore, recent advances both in modelling and paleorecord analyses suggest that Heinrich events are a consequence of oceanic circulation changes rather than their primary cause. In this theory, a shift into a cold surface stadial condition in the Northern Hemisphere caused by a weakening of the Atlantic oceanic circulation would be accompanied by a warming of the subsurface waters of the Labrador Sea, facilitating the occurrence of a Heinrich event. An important fact here is that Heinrich events appear at the middle of the stadial phases. Subsequently, the massive presence of icebergs in the North Atlantic will amplify the decrease of the oceanic circulation intensity or even halt it, therefore enhancing stadial conditions. This interpretation of the chain of events involved in Heinrich events remains fully compatible with the observed excursions towards the lighter $\delta^{18}O$ observed in planktonic foraminifera. Nonetheless, this theory does not explicitly explain yet why Heinrich events do not appear for every stadial. The likeliness of this theory does not remove any value to the modeling exercises based on mimicking Heinrich events by means of freshwater flux injections into the North Atlantic. These have been very helpful in understanding the mechanisms by which a weakened or suppressed Atlantic circulation can have impacts on the rest of the climate system.

Evaluation of the Freshwater Influx Associated with a Heinrich Event: Example of a Joint Model-Data Approach

The thickness and location of the detritic levels found in the North Atlantic open the question of the volume of icebergs released in this region, especially as the records of sea level change during the deglaciation do not show the Heinrich 1 event having any impact. This would lead us to assume that the volume of icebergs is low (a maximum of 3–5 m of sea level). However, estimates achieved using other methods (Roche et al. 2004) have quite different results. Yet, in order to reproduce the evolution of these events in climate models, we must know the influx of freshwater represented by the corresponding armada of icebergs. It is therefore necessary to determine not only the volume of icebergs released into the ocean, but also the timeframe over which they were released. The classic ^{14}C dating method presents a major problem related to the reorganization of the ocean. Indeed, the postulated shutdown of the thermohaline circulation is causing a change in the distribution of carbon within the ocean reservoir, the largest in the Earth system. Basically, the stopping of the thermohaline circulation would make the surface waters appear younger, and the bottom waters appear older during the event, and it would make the surface waters appear older, and the bottom waters younger after the event, making it difficult to evaluate the duration of the event.

As the results from conventional methods assessing the duration and volume of icebergs emitted during these events have a very high degree of uncertainty, a more detailed estimation using different methods is necessary. An approach combining model and data was undertaken by Roche et al. (2004), based on the simulation of $\delta^{18}O$ of water in the ocean. In fact, there is a large number of $\delta^{18}O$ records of foraminiferal calcite from marine sedimentary cores from the North Atlantic, which constrain tightly the evolution of this indicator during the Heinrich 1 and 4 events. The basis of this new evaluation method is to consider that the geographical distribution of the $\delta^{18}O$ anomaly recorded in planktonic foraminifera provides information about the duration and volume of icebergs emitted. If the thermohaline circulation slows down, the slight anomaly in $\delta^{18}O$ created by the melting of the armadas of icebergs will tend to remain longer at the surface (and vice versa). The maximum recorded anomaly should also be related to the maximum of the iceberg flux. To assess this relationship, Roche et al. (2004) performed a large set of simulations by varying the duration and influx of additional freshwater for all of the feasible values (determined from the data). Then, the simulated $\delta^{18}O$ anomaly was compared with the anomaly measured in the marine sediment cores. The simulations that best represent the distribution described by the data were selected to provide a new estimate of the volume of icebergs discharged and the duration of these events: for the Heinrich 4 event (about 45 ka BP) the most likely duration is 300 ± 100 years and the volume of icebergs discharged is equivalent to about 3 m of sea level. These results were later confirmed by a method based on a sediment/iceberg model (Roberts et al. 2014).

Interpretation of the Isotopic Signal Measured in the North Atlantic

We have seen that the $\delta^{18}O$ records from Greenland cores and from ocean sediment cores appear to have very similar signals during periods of rapid climate variability. These similarities should not lead to the conclusion that both signals have the same climatic cause. Indeed, $\delta^{18}O$ records from foraminiferal calcite are complex, sensitive to both temperature and hydrological changes. Hydrological changes have a particularly strong impact. To separate out the influences of the different causes of $\delta^{18}O$ variations in calcite, one solution is to simulate this indicator within a climate model to analyze the importance of the various processes at work. Roche and Paillard (2005) performed this type of simulation for the series of Dansgaard-Oeschger events surrounding the Heinrich 4 event (about 40 ka BP). The result is shown in Fig. 29.4. The first outcome is the accuracy of the model in reproducing the variations measured in the ocean record. The advantage of using a climate model is that not only the $\delta^{18}O$ of calcite can be simulated but also temperature and salinity, prognostic variables for the climate model. The 'temperature' and 'hydrological cycle' components can then be extracted from the $\delta^{18}O$ signal of the calcite. The surprising result from Fig. 29.4 is that, in the model, the strongest changes in both temperature and $\delta^{18}O$ of the water over the entire simulated period are shown to be during the Heinrich 4 event. In the $\delta^{18}O$ record in calcite, the greatest variation is associated with the Dansgaard-Oeschger events. The reason for this difference is that since the variations in temperature and in the $\delta^{18}O$ of water have, from the point of view of the calcite $\delta^{18}O$, opposing signatures, their effects partially cancel each other out in the $\delta^{18}O$ of the calcite, hiding the strongest signal in the marine sedimentary data. This example shows how difficult it is to interpret isotopic paleoclimate indicators in terms of climate and how an integrated data-model approach can provide a better understanding of climate dynamics in the past.

Transmission of the Signal to the Continents

The pollen records extracted from the marine cores provide information on the evolution of the vegetation contemporaneous with the evolution of the oceanic conditions. The two

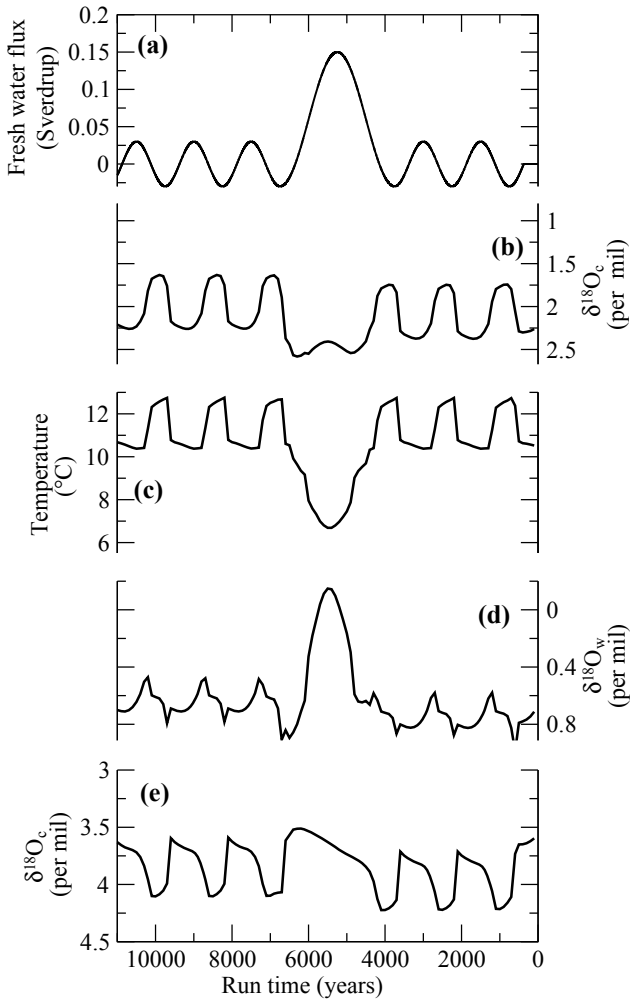

Fig. 29.4 Analysis of glacial variability (D/O and Heinrich events) in the North Atlantic Ocean, in the intermediate complexity model CLIMBER2-ISO, an atmosphere-ocean-vegetation coupled model including calculations of ^{18}O concentration, which allows direct comparison of the model results with measurements from marine sediments (foraminiferal calcite). Adapted from Roche and Paillard (2005). **a** Scenario of freshwater influx in Sverdrup (10^6 m^3/s). All model outputs are given at 41.25° N in the Atlantic for easy comparison with the MD95-2042 core. **b** $\delta^{18}O$ of the calcite in the ocean model's surface layer, i.e. the first 50 m (expressed in parts per thousand versus SMOW). **c** Evolution of the temperature at the surface simulated by the model (in °C). **d** Results of the simulation in $\delta^{18}O$ of the water (in parts per thousand versus SMOW). e) $\delta^{18}O$ of simulated calcite at a depth of 3000 m. The results for the temperature and the $\delta^{18}O$ of the water are not included for this depth because their variations are in the same direction and each contribute half of the $\delta^{18}O$ signal of the calcite

types of reconstructions, marine and continental, are synchronized because they come from the same sediment core. Thus, by looking for pollen associations that appeared at the same time as the levels of detritus, the vegetation present during Heinrich events can be reconstructed. More generally, it is possible to study the relationship between ocean conditions and vegetation, as has been done for the Eastern Atlantic, Mediterranean and the west coast of Europe (Sánchez-Goñi et al. 2002; Combourieu-Nebout et al. 2002, cf. Figure 29.2). The question is then to understand these relationships. The climate in a region such as Western Europe depends not only on the ocean surface conditions in the North-East Atlantic and the Mediterranean, but also on much more distant marine and continental conditions which impact on atmospheric and oceanic circulation.

To continue with the example of the impact a Heinrich event has on the climate and on the vegetation of Western Europe, we have seen that the signature of this event in terms of ocean surface temperature is firstly, a cold anomaly of several degrees Celsius at the mid-latitudes of the North Atlantic. We know, moreover, that at these latitudes the atmospheric circulation is dominated by westerly winds. A simple transmission mechanism of the oceanic signal would be its advection, i.e. its transport, by the prevailing atmospheric circulation, towards the 'leeward' continents, in this case, Western Europe. However, it is difficult to estimate how far the signal can travel and the atmospheric circulation itself can be modified by the changes in sea surface temperatures. The initial response may also be reinforced or negated by positive or negative feedbacks, such as, for example, snow cover or clouds (Chap. 1). Another question is: what can be said a priori about changes in precipitation associated with a cold event in the North Atlantic? Two processes need to be taken into account. A first constraint is that a colder atmosphere contains less water vapor (Clausius-Clapeyron relation) which makes it less conducive to the formation of precipitation. Second, in the mid-latitudes, over the oceans and the western side of the continents, most precipitation comes from weather systems that form over the oceans and pushed towards the western coasts of the continents by the prevailing winds. These perturbations are the result of atmospheric instabilities related to the meridional temperature gradient. A shift of the areas of higher gradient is important because it causes a displacement of the precipitation zones. A negative anomaly of ocean surface temperatures at the mid-latitudes of the North Atlantic implies a shift of the high meridional gradient zone of ocean surface temperatures towards the south. This should favor a southward migration of the prevailing wind belt and the precipitation associated with weather systems. If these weather systems are stronger, this can offset the direct influence of temperature on precipitation. This shows how important it is to have information from multiple locations in order to interpret a given record. For example, in order to interpret reconstructions of precipitations in Western Europe, it is important to know the temperatures in the region, which, in general, is relatively easy to infer from the same core, but it is also important to know the meridional temperature gradient over the North Atlantic and this requires having data from several cores located far from, but yet

synchronized with, the original core. This shows how important it is to synchronize the different cores. This can be complex. Given the application of the comparison of results from different cores, it is important to understand how this synchronization is done.

At this stage of interpretation, climate models (Chap. 25) can also be useful to better understand the possible links between changes in climate recorded at different locations. We now continue our analysis of the impact of a Heinrich event on climate and vegetation in Western Europe. In a first series of numerical experiments we hypothesized that for the climate of Western Europe, the main forcing linked to a Heinrich event is a cooling by 4 °C of the North Atlantic at the mid-latitudes. We used the LMDZ atmospheric general circulation model (developed at the Laboratoire de Météorologie Dynamique—Dynamic Meteorology Laboratory, Paris) to estimate the impact of such an anomaly in the context of glaciation, in this case, the Last Glacial Maximum. We therefore carried out two experiments by forcing the atmospheric model with glacial boundary conditions (see http://pmip1.lsce.ipsl.fr): ice sheets as reconstructed for the LGM, concentrations of greenhouse gases as measured for this period from ice cores, orbital parametres as they were 21,000 years ago. In the first experiment, we used the surface temperatures of the oceans as reconstructed by the CLIMAP project (Chap. 21). The only difference in the second experiment is the surface temperatures of the oceans in the North Atlantic. In this experiment, we decrease these temperatures by 4 °C between 40 and 50 °N. The second experiment is a sensitivity experiment to the ocean surface temperatures of the North Atlantic at the mid-latitudes.

Kageyama et al. (2005) show the results of this experiment for climate in France and the Iberian Peninsula. Figure 29.5 summarizes their results. The model does not simulate a propagation of the cooling imposed in the North Atlantic very far inland over the European continent. The place on the European continent where this cooling is most important in terms of temperature of the coldest month is in the northwest of the Iberian Peninsula. It brings about an increase of only 1 °C in this region, which is low compared to the 4 °C imposed in the North Atlantic. On the other hand, the precipitation anomaly simulated by the model in response to the cooling imposed in the North Atlantic is much greater: it reaches −200 mm/year (a shortfall of 200 mm/year, a drop of about 30%) over the Iberian Peninsula. Examining the results of the model for the North Atlantic and Europe, we see that the band of strong westerly winds is shifted southward, contributing to the decrease of precipitation over Europe. The slight precipitation increase over northwestern Africa can also be partly attributed to this atmospheric circulation change.

Kageyama et al. (2005) also show the impact of this change in climate on vegetation, as simulated by the dynamic ORCHIDEE vegetation model. The climate changes simulated by the climate model for a cold event in the North Atlantic, as weak as the impacts may seem on the land masses, result in a significant decrease in vegetation cover, of both trees and herbaceous plants. This result suggests that during glaciations vegetation in Europe and the Mediterranean is, as indicated by pollen records, extremely sensitive to changes in climate.

It may be noted that there is an area on the Mediterranean side of the Iberian peninsula where precipitation increases in the sensitivity experiment on colder ocean surface temperatures at the mid-latitudes of the North Atlantic. This anomaly, in opposition to the existing reconstructions for this zone (Combourieu-Nebout et al. 2002; Kageyama et al. 2005), shows the limitations of this experiment. The hypothesis that the factor responsible for the changes in climate in western Europe was the differences in surface temperatures of the North Atlantic Ocean at mid-latitudes is not sufficient to explain all the climate anomalies reconstructed around the Mediterranean region. A first explanation could be that the differences in surface temperature of the Mediterranean Sea were not taken into account. A second explanation could simply be that the model is not able to simulate the climate correctly for this region. A third explanation could be an error in the interpretation of the records. In a case like this, it is very instructive for both modelers and palynologists to compare their data. It is also for this reason that the results of the models should be analyzed not only from the point of view of surface climate variables but also from the point of view of the circulation and physics of the atmosphere, was this makes it possible to identify the mechanisms responsible for the simulated changes in climate and to improve the model and future experiments.

These experiments allow the influence of the various mechanisms suggested above to be quantified: propagation of the ocean temperature anomaly to the adjacent continents by the mean circulation, the shift of the prevailing winds following the migration of the zones with a strong meridian temperature gradient, the impact of atmospheric instabilities and average temperature on precipitation. In this way, a model can help interpret reconstructions and, in particular, can confirm or rebut scenarios established using several records located far away from each other.

It is important to be aware of the limitations of experiments of this type: regions where the anomaly is imposed, lack of vegetation or ocean feedback, assumptions in the model design and experimentation. These aspects can be evaluated by additional sensitivity experiments (see Chap. 25).

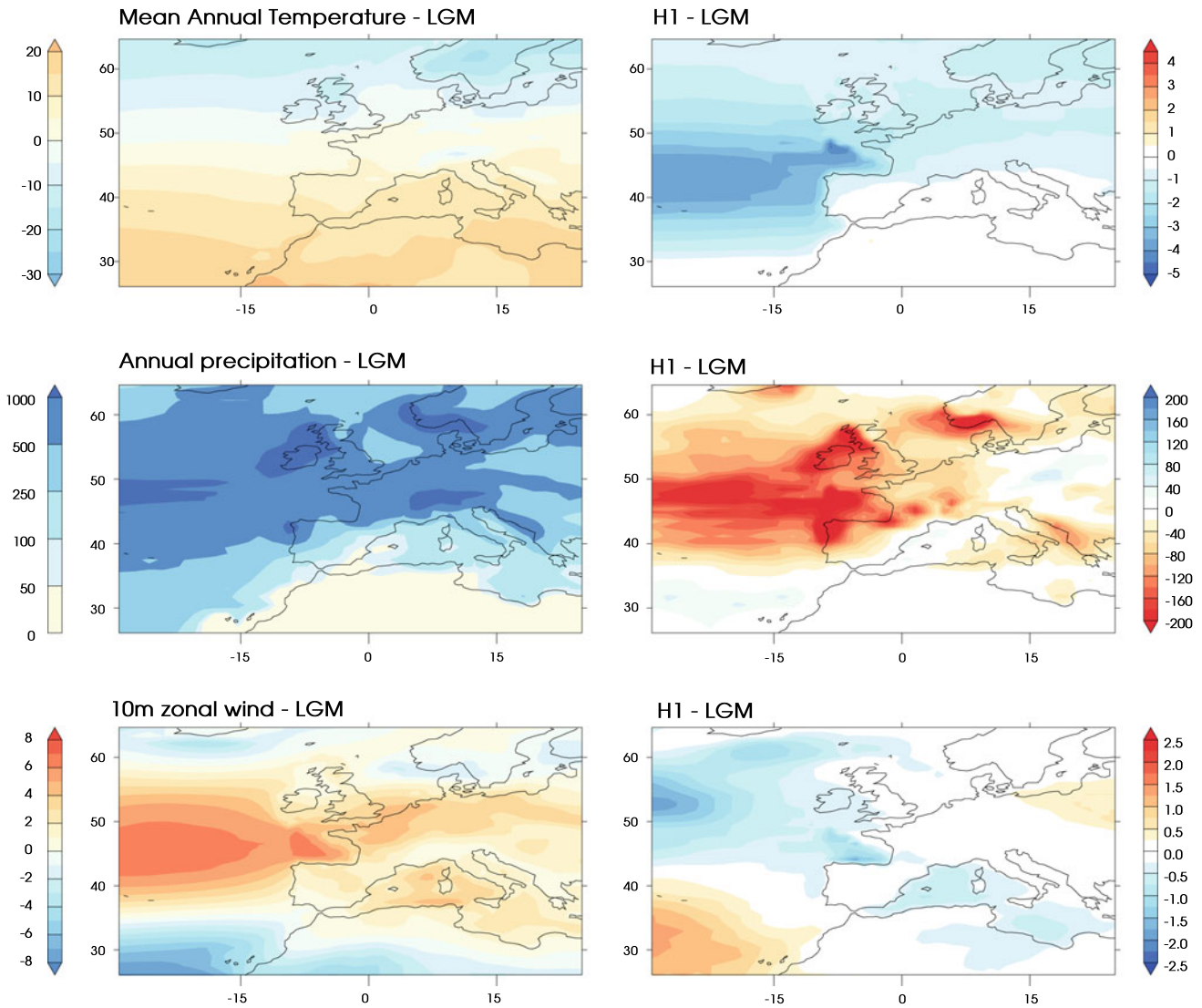

Fig. 29.5 Simulated climate variables for the LGM and the Heinrich 1 event (H1). Left column: LGM results: annual temperatures (°C), annual precipitation (mm/year), surface zonal wind (m/s). Right column: H1—LGM anomalies (simulations described in Kageyama et al. 2005)

Dansgaard-Oeschger Cycles

The Dansgaard-Oeschger cycles modify the climate on a global scale (see Voelker (2002) for a review). Therefore, the underlying mechanism must either have a global origin as well, or else must modify a major element of the climate system, which has a global impact. We will now consider three possible mechanisms that fulfil these requirements.

One of the simplest ways to obtain a global response is a variation in a forcing external to the climate system. It could be a mechanism operating on long time scales (Milankovitch forcing) or on short ones (volcanic changes, for example). It has therefore been proposed that variations in solar forcing may be responsible for Dansgaard-Oeschger events (Braun et al. 2005). However, the relationship between the small variations in the solar cycle at the relevant highlighted times and the observed climate variations remain questionable.

The component of the climate system most likely to be the cause of the Dansgaard-Oeschger events is undoubtedly the ocean, and more particularly ocean circulation. It has two main characteristics of interest here: it reacts on a global scale, on time scales compatible with the Dansgaard-Oeschger cycles, and it can respond to a relatively local forcing. Studies such as Ganopolski and Rahmstorf (2001) have shown that a semi-periodic freshwater forcing can, under certain conditions, reproduce oscillations that resemble the cycles observed in the paleoclimate data. However, this does not provide any indication of the origin of this freshwater forcing and therefore gives no new explanation as to the mechanism at work.

To compensate for this lack of a proven periodic climate forcing, some authors propose mechanisms with oscillations internal to the climate system. One of the most interesting

explanations today relies on an internal oscillation of oceanic circulation under given boundary conditions (Paillard 2004), without involving any external forcing. The big advantage of this hypothesis is that it accounts both for the frequency of cycles, compatible with what we know of the ocean, and for their global character. A coupled ocean-atmosphere internal oscillation has more recently been proposed as the reason for the occurence of Dansgaard-Oeschger events as well (Peltier and Vettoretti 2014). This study has the advantage of showing such an internal oscillation of the climate system in a more realistic General Circulation Model.

Nevertheless, opposing theories coexist nowadays when trying to explain the triggering mechanisms of Dansgaard-Oeschger events. Banderas et al. (2015) also relate their occurence to an internal climatic oscillation, but in their case, it is controlled by the effects of Southern-Ocean wind stress and CO_2 on the oceanic circulation. Similarly, Dima et al. (2018) proposed that the meridional overturning circulation changes are ultimately controlled by the Southern Ocean with links to gradual global climate changes. Besides, it has recently been proposed that Dansgaard-Oeschger events owe their existence to the interactions between the North Atlantic ice shelves, sea ice and oceanic circulation (Boers et al. 2018).

To conclude, there is no consensus today on the cause of the Dansgaard-Oeschger events, despite an increasing understanding of the effects that these events have had on global climate.

Sudden Events During Interglacial Periods

The Discovery

Although the climate oscillation called 'the 8200-year event' left traces in the Greenland cores, the first publications presenting the isotopic records from the ice in Greenland from GRIP cores (Dansgaard et al. 1993) described the climate of the Holocene as stable, as the weak oscillation occurring around 8200 years before today was considered to be background noise. Even the discovery of a second record with exactly the same oscillation did not allow the correct recognition of this climate event. It was not until four years later that the notion of 'the 8200-year event' was introduced in an article by a team led by R. Alley. Efforts to place this climate evolution event on a hemispheric scale have indicated that this event had in fact been identified since 1973 from other records.

The Observations

The 8200-year event has been recorded in numerous climate archives, including the Greenland polar ice cap, continental archives (lakes, vegetation, speleothems) and the ocean.

In Greenland cores, this event shows up as a decrease in $\delta^{18}O$ of about two permil over a period of about 100 years. This decrease is interpreted as a drop in local temperature in Greenland of 6 ± 2 °C (see Thomas et al. 2007). It was estimated at 7.4 °C using an independent method based on oxygen isotopes ($\delta^{15}N$) (Kobashi et al. 2007). This was a fairly dramatic event, at least over Greenland. This oscillation is found in all the cores of adequate resolution obtained from the Greenland ice sheet: GRIP, GISP2, NGRIP, Dye-3. This is therefore an event with a regional impact, at least, on the scale of Greenland.

The cold period equating to the 8200-year event in Greenland is also recorded in other paleoclimate indicators. Although this event was not recognized as such in polar ice records, it was well identified in records from Norwegian lakes and in the extended ice sheets reconstructed from the end moraines. Indeed, the cold and dry period 'Finse[1]' was identified (Dahl and Nesje 1994), and then connected to the 8200-year event in the ice cores. Simultaneously, this event was associated with a cold spell reconstructed from variations in planktonic foraminiferal fauna in a marine core from the south of Norway. This record proves that it is indeed a significant climate event on the scale of the North Atlantic, but also that the ocean was affected almost simultaneously. This interpretation is reinforced by other more distant records of the event. One of the first studies to show this was the study of the $\delta^{18}O$ of the ostracod shells from a Bavarian lake (Ammersee, Germany), which recorded changes in the $\delta^{18}O$ of the precipitations associated with cooling (Chap. 15, von Grafenstein 1998).

In the oceans, records marking the 8200-year event are rare, as identification requires a temporal resolution of much less than a century. Of these records, those from the northern seas show a decrease of about 3 °C in ocean surface temperature. This study proves that this event was the largest during the entire Holocene in this region. Finally, these authors show that the oceanic change affected not only the surface but also the deep ocean. These last changes have been confirmed recently in a core from southern Greenland, which shows changes in the formation of deep water bodies in the North Atlantic.

On the continent, the 8200-year event is expressed as a cooling especially evident in Europe. Studies of the changes

[1]Named after the Finsevatn, the Norwegian Hardanger Lake where the record originated.

in the level of European lakes indicate that during this event the climate was wetter between 50 and 43° N, while north and south of this zone, it was drier. Pollen records rarely show this event, perhaps because these climate variations were not significant enough to modify the vegetation in a major way, or because it did not affect the growing period of the main plants characteristic of these paleoenvironments, as was shown in Northern Europe and North America.

The Mechanisms

The scale of changes observed as well as the multiplicity of their impacts (precipitation, temperature, oceanic circulation), very quickly pointed to the Atlantic thermohaline circulation as a major actor in this abrupt change in climate. The experience of Heinrich events (see above) suggested that here too, a sudden influx of fresh water to the ocean could have altered the thermohaline circulation and the climate around the North Atlantic. However, 8200 years ago, only a small part of the Laurentide ice sheet could have been involved, with the disappearance at this time of the dome covering what is currently the Hudson Bay. Traces of paleo-shorelines of lakes also indicate the disappearance of two large pro-glacial lakes (the Ojibway and Agassiz lakes) around this period, which could have contributed an influx of fresh water to the ocean. However, the first ^{14}C datings did not enable a precise chronology of these events. More precise dating, as well as an evaluation of the volume released, make it possible to pinpoint the massive draining of Lake Agassiz as a cause of this cold event (Clarke et al. 2004). These data indicate a draining of about 100,000 km^3 of water in about a year, thus causing a massive influx to the ocean.

Modeling and the Global and Hemispheric Consequences

Nevertheless, can the consequences for the climate of this extremely abrupt but yet short-lived influx be replicated in coupled climate models? Although the impact of this huge influx to the ocean was quickly identified, the first simulation of the 8200-year event using boundary conditions consistent with the time period was achieved in the early 2000s (Renssen et al. 2001). These authors were able to show that by forcing an ocean general circulation model coupled with a simplified atmospheric model using an idealized water flux of 0.75 Sv for twenty years, they produced a slowing of the thermohaline circulation in the Atlantic for about three centuries, with a temperature drop of 1–5 °C on the continents bordering the North Atlantic. This result fits well with the data, although the freshwater forcing is relatively larger than is accepted today. Even more importantly, it revealed disparities in the seasonal climate response, with a greater anomaly in summer than in winter over northern Europe and a north-south bipolarity, with cooling in the north and warming at 60° S. Subsequent studies confirmed that a freshwater influx, even one lasting only one year, was sufficient to obtain a climate response consistent with the one obtained from the analysis of paleoclimate indicators. The climate impact was not immediate, as can be seen in Fig. 29.6. For example, in Greenland, the maximum point was reached after about thirty years.

Other authors have also highlighted the role of climate 'noise' in the duration of the ocean's response to the freshwater forcing. Indeed, they show that by adding noise (with an average value of zero) to the freshwater forcing, the duration of the response by the model can be changed from a few decades to two or three centuries. This highlights the importance of the initial climate state to the response to a given forcing, as the response can have a more or less global effect as was the case for the 8200-year event, or have a local impact on a decadal scale. The 8200-year event was also reproduced in a coupled general circulation model incorporating water isotopes (Legrande et al. 2006), demonstrating that the results were consistent not only with temperature estimates but also with the paleoclimate indicators themselves, directly simulated in the model.

These authors were able to correctly predict the variations in $\delta^{18}O$ associated with the 8200-year event from the calcite of marine sediments before the publication of the first data showing the 8200-year event in marine sediment cores.

It is important to note that although the 8200-year event is considered an abrupt event during the interglacial period, this classification is not quite accurate. In fact, it is a final manifestation of the glacial climate through the draining of a periglacial lake, the result of a melting ice sheet . To date, no abrupt temperature changes involving glacial ice sheet behavior have been observed during the Holocene.

Outlook

Global Connections

The work of the last thirty years has made it possible to demonstrate a variability in the climate system on millennial time scales, characterized by transitions occurring, in some cases, over only a few decades. This variability was first observed in North Atlantic marine sediment cores for Heinrich events, and in Greenland ice cores for Dansgaard-Oeschger events. Gradually, climate records have been analyzed at increasingly fine temporal resolutions and variations with temporal characteristics similar to those in the North Atlantic and Greenland have been discovered in areas

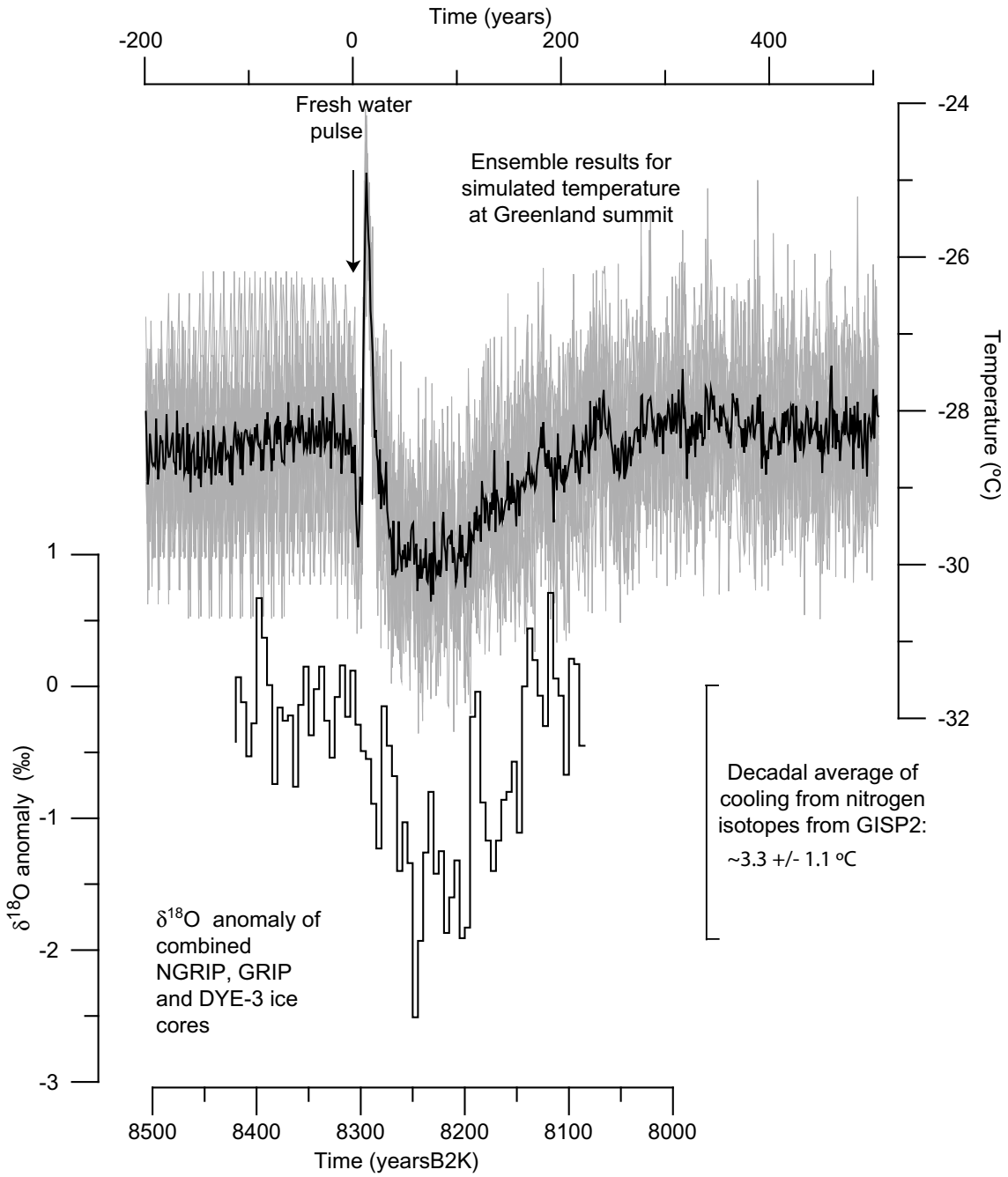

Fig. 29.6 Simulated surface air temperatures for the summit of Greenland for a set of ten simulations (gray). The average is drawn in black. These results are compared with the reconstructed $\delta^{18}O$ profile from measurements from Dye-3, GRIP and NGRIP ice cores. The same scale is used for the time axes, the $\delta^{18}O$ curve is positioned in relation to the model results, by aligning the first decrease in $\delta^{18}O$ with the first decrease in simulated temperature. The temperature axis is selected so that the decrease of 3.3 °C reconstructed from the nitrogen isotopes in the GISP2 core corresponds to the minimum anomaly in $\delta^{18}O$. Adapted from Wiersma et al. (2011)

very far from the original regions, as far away as the South Pacific and Antarctica, and including China and the northern Indian Ocean, influenced by monsoons. The interpretation of these data is based on the assumption that the time scales associated with each record can be accurately synchronized. This crucial synchronization is still a challenge despite advances made in methods of relative synchronization (such as methane concentration in ice cores or paleo-magnetic properties in marine cores) for the scientific community seeking to characterize rapid variability.

A comprehensive description on a global scale is very important for our understanding of the climate and of the

variations that may have been experienced contemporaneously in parts of the globe very distant from each other. Finding the explanation for these connections is also a challenge faced by modellers, because attempting to model these events means testing our knowledge of climate as it is interpreted in the models which are also used to predict future climates. In terms of modeling, the first experiments testing the sensitivity of the ocean-atmosphere system to freshwater discharges in the North Atlantic in a glacial context have been carried out in the years 2000.

These experiments, if they are to be carried out with a resolution sufficiently fine to enable comparison between model results and reconstructions, require a calculation time at the forefront of the capability of the most powerful modern computers. For example, Kageyama et al. (2009), using an ocean-atmosphere general circulation model, show that the link between the cooling in the North Atlantic and the decrease in the Indian monsoon can be explained by a decrease in the summer temperature gradient in the upper half of the troposphere between the Indian Ocean and the Tibetan plateau. However, these results are obtained for conditions corresponding to the LGM and not to Marine Isotopic Stage 3, and further experiments will be required to better understand the signal transmission mechanisms between the North Atlantic and Asia. Furthermore, although these experiments reproduce certain climate events contemporaneous with the Heinrich events (southward migration of the Intertropical Convergence Zone, reduction of the Indian monsoon, cooling and drying in Western Europe), they do not manage to reproduce others, such as variations in the Southeast Asian monsoon. The modeling and understanding of the millennial variability within the climate system thus remains in many respects a challenge for modellers.

We have, until now, attempted to describe climate variability on the millennial scale mainly in terms of the "physical" Earth system, that is, including the ocean, the atmosphere and the cryosphere. However, the records contain more information than this simple description. Take, for example, the case of methane concentrations. We have shown that they are useful to synchronize the records from Greenland and Antarctica but this important greenhouse gas emitted mainly from the wetlands in the tropics and high latitudes shows significant variations. The role of biogeochemical phenomena in millennial climate variability also needs to be better understood and modeled.

Abrupt Event Interactions—Large Climate Transitions

Although abrupt events are the result of internal variability in the climate system, they are nonetheless sensitive to its large longer term variations. In particular, these events are more numerous and of greater amplitude in glacial periods than in interglacial periods. This suggests a different expression of millennial variability depending on the size of the ice sheets in the northern hemisphere. The high-resolution records of the most recent climate transitions (the deglaciation between LGM and the Holocene as well as the entry into the last glaciation) may provide information on the conditions favoring events of larger amplitude. However, these transitions are punctuated by abrupt climate events. This raises the question of the role that these events might play in the transition itself, knowing that a rapid event can have, in the case of Dansgaard-Oeschger events in the Greenland cores, an amplitude equivalent to half the difference between glacial and interglacial states.

Let us consider the case of the last deglaciation (Fig. 29.7). A few thousand years after the LGM came the Heinrich H1 event. Climate conditions returned to an almost glacial level. This event was followed by a warm phase, with the transition between these two events showing up as abrupt in many records, particularly around the North Atlantic. This is the Bølling-Allerød phase, whose climate is almost interglacial. However, this period was followed by the cold period of the Younger Dryas, which is sometimes considered to be the most recent Heinrich event (H0), which is wrong because there is no corresponding layer of detritic elements in the Ruddiman belt. It is after this last cold phase that the climate of the current interglacial, the Holocene, became definitively established (apart from the 8200-year event).

This shows that the last deglaciation was not a smooth transition. On the contrary, it is a series of abrupt events, as if the climate system 'hesitated' between two equilibria, one glacial and the other interglacial. The role of abrupt events during this climate transition is therefore important, but they still need to be understood and modeled.

Entry into the last glaciation at the end of the Eemian is also characterized by the appearance of abrupt events, $\sim$110 ka before today, in a context where glacial ice sheets had already developed over Canada. One might think that these cold events would promote entry into glaciation, but this assumption ignores the fact that cooler air at high latitudes also contains less water and is therefore less able to supply the water needed to build the ice sheets up at a significant rate. These compensating factors need to be assessed. Here again, the influence of abrupt events on the evolution of the ice sheets has yet to be assessed, in comparison with other mechanisms and feedbacks, such as the slower changes in state of the ocean, cryosphere, vegetation, atmospheric concentrations of greenhouse gases, as well as external changes such as changes in insolation. Models of the Earth system can lead to a better understanding of the reconstructed signals by conducting sensitivity experiments for each of these factors.

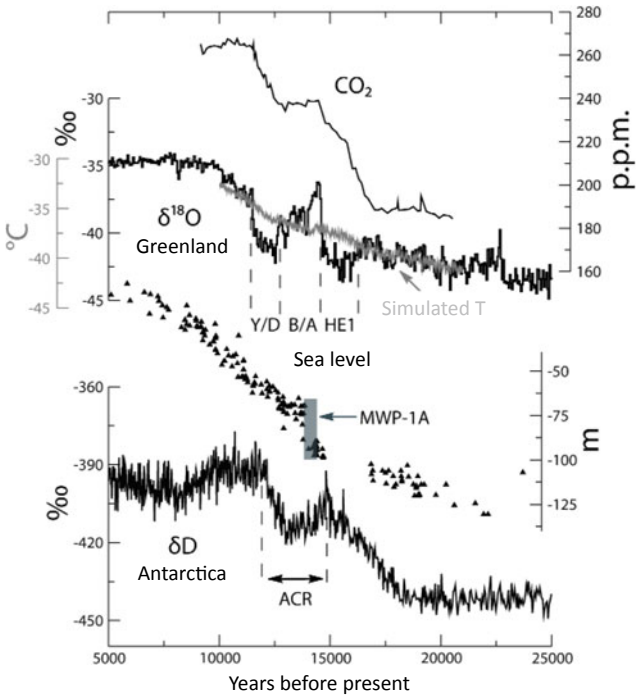

Fig. 29.7 An overview of the last deglaciation. From top to bottom: atmospheric CO_2 as measured in air bubbles from Antarctic ice cores; $\delta^{18}O$ measured in Greenland ice (GRIP members 1993) as a first-order indicator of local temperature, superimposed with the simulated average annual temperature in Greenland from the iLOVECLIM model; the scaling between model and data implies that the sudden increase of $\delta^{18}O$ at the HE1/B/A limit is 10 °C. The periods corresponding to the Heinrich 1 event (HE1), Bolling-Allerod (B/A) and the Younger Dryas (Y/D) are indicated below. It may be noted that there is no abrupt event in the temperature simulated by the climate model. Sea-level (Peltier and Fairbanks 2006) (black triangles) in meters relative to the current sea level, as reconstructed from corals with the abrupt event "Meltwater Pulse-1A" (MWP-1A) indicated, representing a rise of about 20 m in ~300 years. Isotopic abundance of deuterium in Antarctic ice (Peltier and Fairbanks 2006) as a first-order indicator of local temperature with the Antarctic Cold Reversal (ACR) indicated, a cold spell interrupting the warming of the deglaciation

References

Alvarez-Solas, J., Robinson, A., Montoya, M., & Ritz, C. (2013). Iceberg discharges of the last glacial period driven by oceanic circulation changes. *Proceedings of the National Academy of Sciences, 110*(41), 16350–16354.

Banderas, R., Alvarez-Solas, J., Robinson, A., & Montoya, M. (2015). An interhemispheric mechanism for glacial abrupt climate change. *Climate Dynamics, 44*(9–10), 2897–2908.

Barker, S., Chen, J., Gong, X., Jonkers, L., Knorr, G., & Thornalley, D. (2015). Icebergs not the trigger for North Atlantic cold events. *Nature, 520*(7547), 333.

Bassis, J. N., Petersen, S. V., & Mac Cathles, L. (2017). Heinrich events triggered by ocean forcing and modulated by isostatic adjustment. *Nature, 542*(7641), 332.

Boers, N., Ghil, M., & Rousseau, D. D. (2018). Ocean circulation, ice shelf, and sea ice interactions explain Dansgaard-Oeschger cycles. *Proceedings of the National Academy of Sciences, 115*(47), E11005–E11014.

Bond, G., et al. (1993). Correlations between climate records from North Atlantic sediments and greenland ice. *Nature, 365,* 143–147.

Braun, H., Christl, M., Rahmstorf, S., Ganopolski, A., Mangini, A., Kubatzki, C., et al. (2005). Possible solar origin of the 1470-year glacial climate cycle demonstrated in a coupled model. *Nature, 438* (7065), 208.

Broecker, W., et al. (1992). Origin of the northern Atlantic's Heinrich events. *Climate Dynamics, 6,* 265–273.

Calov, R., et al. (2002). Large-scale instabilities of the Laurentide Ice sheet simulated in a fully coupled climate-system model. *Geophysical Research Letters*, *29*, 2216. https://doi.org/10.1029/2002gl016078.

Clarke, G. K. C., et al. (2004). Paleohydraulics of the last outburst flood from glacial lake agassiz and the 8200 BP cold event. *Quaternary Science Reviews, 23,* 389–407. https://doi.org/10.1016/j.quascirev.2003.06.004.

Combourieu-Nebout, N., et al. (2002). Enhanced aridity and atmospheric high-pressure stability over the western mediterranean during the North Atlantic cold events of the past 50 k.y. *Geology, 30,* 863–866.

Cortijo, E., et al. (2005). Heinrich events: Hydrological impact. *Comptes Rendus Geoscience, 337,* 897–907. https://doi.org/10.1016/j.crte.2005.04.011.

Dahl, S. O., & Nesje, A. (1994). Holocene glacier fluctuations at hardangerjøkulen, Central-Southern Norway: A high-resolution composite chronology from lacustrine and terrestrial deposits. *The Holocene, 4,* 269–277.

Dansgaard, W., et al. (1993). Evidence for general instability of past climate from a 250-kyr ice-core record. *Nature, 364,* 218–220.

Dima, M., Lohman, G., & Knorr, G. (2018). North Atlantic versus global control on dansgaard-oeschger events. *Geophysical Research Letters*.

Elliot, M., et al. (2002). Changes in North Atlantic deep-water formation associated with the dansgaard-oeschger temperature oscillations (60–10 ka), *Quaternary Science Reviews*, *21*, 1153–1165.

EPICA community members. (2006). One-to-one coupling of glacial climate variability in Greenland and Antarctica. *Nature, 444,* 195–198.

Ganopolski, A., & Rahmstorf, S. (2001). Rapid changes of glacial climate simulated in a coupled climate model. *Nature, 409,* 153–158. https://doi.org/10.1038/35051500.

Genty, D., et al. (2005). Rapid climatic changes of the last 90 kyr recorded on the European Continent. *Comptes Rendus Geoscience, 337,* 970–982.

Greenland Ice-core Project (GRIP) Members. (1993). Climate instability during the last interglacial period recorded in the GRIP ice core. *Nature, 364,* 203–207. https://doi.org/10.1038/364203a0.

Grimm, E. C., et al. (2006). Evidence for warm wet heinrich events in Florida. *Quaternary Science Reviews, 25,* 2197–2211. https://doi.org/10.1016/j.quascirev.2006.04.008.

Grousset, F. E., et al. (1993). Patterns of ice-rafted detritus in the Glacial North Atlantic. *Paleoceanography, 8,* 175–192.

Heinrich, H. (1988). Origin and consequences of cyclic ice rafting in the Northeast Atlantic ocean during the past 130000 years. *Quaternary Research, 29,* 142–152.

Hemming, S. R. (2004). Heinrich events: Massive late pleistocene detritus layers of the North Atlantic and their global climate imprint. *Review of Geophysics*, *42*, RG1005.

Hulbe, C. L., MacAyeal, D. R., Denton, G. H., Kleman, J., & Lowell, T. V. (2004). Catastrophic ice shelf breakup as the source of Heinrich event icebergs. *Paleoceanography, 19*(1).

Kageyama, M., et al. (2005). Le Dernier Maximum glaciaire et l'événement de Heinrich 1 en termes de climat et de végétation autour de la mer d'Alboran: une comparaison préliminaire entre modèles et données. *Compte Rendus Geoscience, 337,* 983–992.

Kageyama, M., et al. (2009). Glacial climate sensitivity to different States of the Atlantic meridional overturning circulation: Results from the IPSL model. *Climate of the Past, 5,* 551–570.

Kissel, C. (2005). Magnetic signature of rapid climatic variations in Glacial North Atlantic, a review. *Comptes Rendus Geoscience, 337,* 908–918. https://doi.org/10.1016/j.crte.2005.04.009.

Kobashi, T., Severinghaus, J. P., Brook, E. J., Barnola, J. M., & Grachev, A. M. (2007). Precise timing and characterization of abrupt climate change 8200 years ago from air trapped in polar ice. *Quaternary Science Reviews, 26*(9–10), 1212–1222.

Legrande, A., et al. (2006). Consistent simulations of multiple proxy responses to an abrupt climate change event. *Proceedings of the National Academy of Sciences of the United States of America, 103,* 837–842. https://doi.org/10.1073/pnas.0510095103.

MacAyeal, D. R. (1993). Binge/purge oscillations of the Laurentide ice sheet as a cause of the North Atlantic's heinrich events. *Paleoceanography, 8,* 775–784.

Marcott, S. A., Clark, P. U., Padman, L., Klinkhammer, G. P., Springer, S. R., Liu, Z., et al. (2011). Ice-shelf collapse from subsurface warming as a trigger for Heinrich events. *Proceedings of the National Academy of Sciences, 108*(33), 13415–13419.

Paillard, D. (2004). Modelling rapid events within the climate system. *Comptes Rendus Geoscience, 336,* 733–740. https://doi.org/10.1016/j.crte.2003.12.019.

Peltier, W. R., & Fairbanks, R. G. (2006). Global glacial ice volume and Last Glacial Maximum duration from an extended Barbados sea level record. *Quaternary Science Reviews, 25,* 3322–3337.

Peltier, W. R., & Vettoretti, G. (2014). Dansgaard-Oeschger oscillations predicted in a comprehensive model of glacial climate: A "kicked" salt oscillator in the Atlantic. *Geophysical Research Letters, 41*(20), 7306–7313.

Rasmussen, T. L., et al. (1996). Rapid changes in surface and deep water conditions at the faeroe margin during the last 58,000 years. *Paleoceanography, 11,* 757–771. https://doi.org/10.1029/96PA02618.

Rasmussen, S. O., et al. (2014). A stratigraphic framework for abrupt climatic changes during the Last Glacial period based on three synchronized Greenland ice-core records: refining and extending the INTIMATE event stratigraphy. *Quaternary Science Reviews, 106,* 14–28. https://doi.org/10.1016/j.quascirev.2014.09.007.

Renssen, H., et al. (2001). The 8.2 Kyr BP event simulated by a global atmosphere-sea-ice-ocean model. *Geophysical Research Letters*, *28*, 1567–1570. https://doi.org/10.1029/2000gl012602.

Ritz, C., Rommelaere, V., & Dumas, C. (2001). Modeling the evolution of Antarctic ice sheet over the last 420,000 years: Implications for altitude changes in the Vostok region. *Journal of Geophysical Research: Atmospheres, 106*(D23), 31943–31964.

Roberts, W. H. G., et al. (2014). A new constraint on the size of Heinrich Events from an iceberg/sediment model. *Earth and Planetary Science Letters, 386,* 1–9.

Roche, D. M., & Paillard, D. (2005). Modelling the oxygen-18 and rapid glacial climatic events: A data-model comparison. *Comptes Rendus Geoscience, 337,* 928–934. https://doi.org/10.1016/j.crte.2005.03.019.

Roche, D. M., et al. (2004). Constraints on the duration and freshwater release of Heinrich event 4 through isotope modelling. *Nature, 432,* 379–382. https://doi.org/10.1038/nature03059.

Ruddiman, W. (1977). Late quaternary deposition of ice-rafted sand in the subpolar North Atlantic (lat 40° to 65° N), *GSA Bulletin,* 1813–1827.

Sánchez-Goñi, M. F., et al. (2002). Synchroneity between marine and terrestrial responses to millennial scale climatic variability during the last glacial period in the Mediterranean region. *Climate Dynamics, 19,* 95–105. https://doi.org/10.1007/s00382-001-0212-x.

Shackleton, N. J., et al. (2000). Phase relationships between millennial-scale events 64,000–24,000. *Paleoceanography, 15*(6), 565–569.

Thomas, E. R., et al. (2007). The 8.2 Ka event from greenland ice cores. *Quaternary Science Reviews, 26,* 70–81. https://doi.org/10.1016/j.quascirev.2006.07.017.

Voelker, A. H. L., et al. (2002). Global distribution of centennial-scale records for marine isotope stage (MIS) 3: A database, *Quaternary Science Reviews*, *21*, 1185–1212.

von Grafenstein, U., et al. (1998). A Mid-european decadal isotope-climate record from 15,500 to 5000 years BP, *Science*, *284*, 1654–1657.

Wiersma, A. P., et al. (2011). Fingerprinting the 8.2 Ka event climate response in a coupled climate model. *Journal of Quaternary Science, 26,* 118–127. https://doi.org/10.1002/jqs.1439.

An Introduction to the Holocene and Anthropic Disturbance

30

Pascale Braconnot and Pascal Yiou

The Major Trends of the Holocene

The Different Radiative Disturbances

The Holocene started about 10,000 years ago at the end of the last glaciation. The last thousand years of this period is marked by the growing impact of human activity (changes in land use and atmospheric composition). At first sight, the numerous data show us variations that are less spectacular than the great upheavals engendered by deglaciation. Nevertheless, the general natural trend, driven by changes in solar radiation at the top of the atmosphere, is characterized by radical changes in the monsoon and the El Niño phenomenon in the tropics. In the mid-latitudes of the northern hemisphere, the changes are seen in the characteristics of the main modes of variability. Several abrupt events also punctuate the unfolding of the process.

Slow variations in solar radiation at the top of the atmosphere, caused by variations in orbital parameters, are the driving force behind the evolution of the main climate characteristics on this 10,000-year scale. Variation in the obliquity, from 24.23° at the beginning of the Holocene to 23.44° at the present time, has brought about an increase in the average annual solar radiation at high latitudes of 1.5 W/m^2 over this period. During the same period, solar radiation in the low latitudes dropped by 1.10 W/m^2. Added to this effect of obliquity is the precession of the equinoxes. At the beginning of the Holocene, the summer solstice was located at the perihelion of the ecliptic. It is now at the aphelion. Thus, the solar radiation received at the top of the atmosphere (insolation) in June was 48 W/m^2 higher at 60° N at the beginning of the Holocene than it is today (Fig. 30.1), and 5 W/m^2 higher about 3000 years ago. Also, the amplitude of the seasonal cycle of insolation at the beginning of the Holocene was greater in the northern hemisphere but less in the southern hemisphere. This variation in amplitude is not symmetrical on either side of the equator, with greater variations in the northern hemisphere and in the tropics (Fig. 30.1). The precession also alters the length of the seasons. According to Kepler's laws, the boreal summer, defined as the time between the spring and autumn equinoxes, lasted 172 days 9500 years and 176 days 6000 years ago with 180 days currently. In the northern hemisphere, summer insolation was therefore more intense over a shorter period.

Greenhouse gases, volcanism and the solar constant are other factors that have influenced the climate of the Holocene through their impact on the radiative balance (Fig. 30.2). These are also the dominant factors of the last 2000 years, ever since insolation has reached approximate current values. Indeed, the combined effect of these greenhouse gases has resulted in a reduction in the radiative balance of the planet of around 0.5 W/m^2 from the beginning of the Holocene to the beginning of the industrial era. This slight perturbation of the radiative balance is due to a 7 ppm increase in atmospheric carbon content at the beginning of the Holocene, followed by a decrease of 20 ppm up to the beginning of the industrial era. Methane levels decreased from 730 ppb at the beginning of the Holocene to 580 ppb in the Middle Holocene (6000 years ago), and gradually returned to early Holocene levels in the pre-industrial era. Levels of atmospheric N_2O follow the variations of CO_2 and have varied between 2 and 10 ppb. In more recent times, the evolution of greenhouse gases is dominated by anthropic emissions. The combined effects of human activity correspond to an increase of 1.6 W/m^2 in the radiative balance. This estimate takes into account the dominant effect of the increase in greenhouse gases and the negative contribution of aerosols for the twentieth century (Solomon et al. 2007; IPCC 2013).

P. Braconnot (✉) · P. Yiou
Laboratoire des Sciences du Climat et de l'Environnement
LSCE/IPSL, CEA-CNRS-UVSQ, Université Paris-Saclay,
91191 Gif-sur-Yvette, France
e-mail: pascale.braconnot@lsce.ipsl.fr

G. Ramstein et al. (eds.), *Paleoclimatology*, Frontiers in Earth Sciences,
https://doi.org/10.1007/978-3-030-24982-3_30

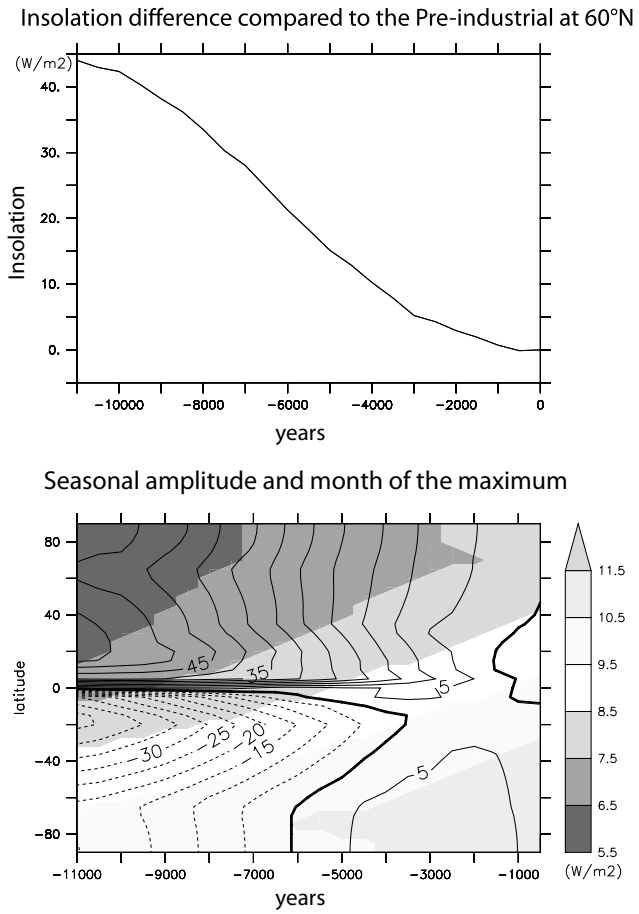

Fig. 30.1 **a** Difference in insolation at 60°N between the Holocene and the current period. **b** Change in the amplitude of the seasonal cycle during the Holocene, calculated as the difference between the month of maximum insolation and the month of minimum insolation (isolines, W/m^2), and months of maximum difference (shaded, number of the month)

Estimates of the forcings induced by changes in the solar constant and volcanism are more open to controversy because they are more difficult to measure directly. Estimates from satellite data suggest that the differences between periods of solar activity and inactivity are due to fluctuations of about 0.08% in solar irradiance (1 965 W/m^2) over the last twenty years. For older periods, cosmogenic isotopes, the number of sunspots and observations of the aurora borealis are all indicators of solar activity (see Chap. 1, Volume 1). The amplitude of solar variations over the last millennium has recently been revised downwards and current best estimates suggest an increase of between 0.05 and 1.2% in solar irradiance between the Maunder minimum (between 1650 and 1720) and the current period, which corresponds to a radiative disturbance of 0.1 to 0.3 W/m^2.

Very intense volcanic eruptions introduce sulfate aerosols into the stratosphere, which reflect back solar radiation and thus contribute to a cooling of the climate in the year following the eruption.

There are many proofs of volcanic activity during the Holocene, but there is no quantified series for the overall period. Data has become more accurate for the last century, although the eruption timing, geographic location and quantities of aerosols emitted are not known with precision. Thus, depending on the sources of information, the amplitude and the date of the Holocene eruptions vary greatly.

The Evolution of Temperature in the Various Records

The recorded variations in temperatures during the Holocene reflect the response of the climate system to the various radiative disturbances listed above, as well as other various feedbacks, such as water vapor and melting snow and ice caps. The climate optimum at the beginning of the Holocene did not occur simultaneously at all latitudes (Fig. 30.3), as insolation depends on latitude and the season and feedbacks produce a delay between the forcing and its maximum summer temperatures 10,000–8000 years ago. Reconstructions for the mid-latitudes of the northern hemisphere are characterized by slow decreases in sea-surface temperature (SST) during the Holocene. In North America, the hottest period was between 7000 and 5000 years ago. Pollen data and macrofossil remains (see Volume 1, Chap. 10 for methodologies) indicate that temperate forests were found further north than they are today and that glaciers had retreated. The early warming at high southern latitudes at the beginning of the Holocene cannot be explained simply as a response to local insolation conditions, and appears to be a manifestation of a large-scale reorganization of atmospheric and oceanic heat transport. Yet most tropical regions show a gradual warming during the Holocene, reflecting an increase in insolation in these regions.

The growing abundance of chronicles relating the impacts of climate extremes (due to the expansion of humanity) provides a description of the intra-annual climate variability over the last 2000 years. This can be superimposed on the secular fluctuations mentioned above. Figure 30.4 summarizes the current state of knowledge of temperature changes since the year 700 AD. Taking uncertainties into account, the temperature of the northern hemisphere is fairly stable between the year 700 and the end of the nineteenth century, and begins to increase continuously from the twentieth century onwards (Fig. 30.4c). The shape of this curve resembles a hockey stick, hence its iconic name. Excluding the twentieth century, for which there is an abundance of meteorological recordings, the value of the curve is that it shows a relatively warm phase between the year 1000 and 1300 (often called the 'Medieval Warm Period') and a relatively cold phase between 1350 and 1850 (called the 'Little Ice Age'). The causes of the inter-annual variations in

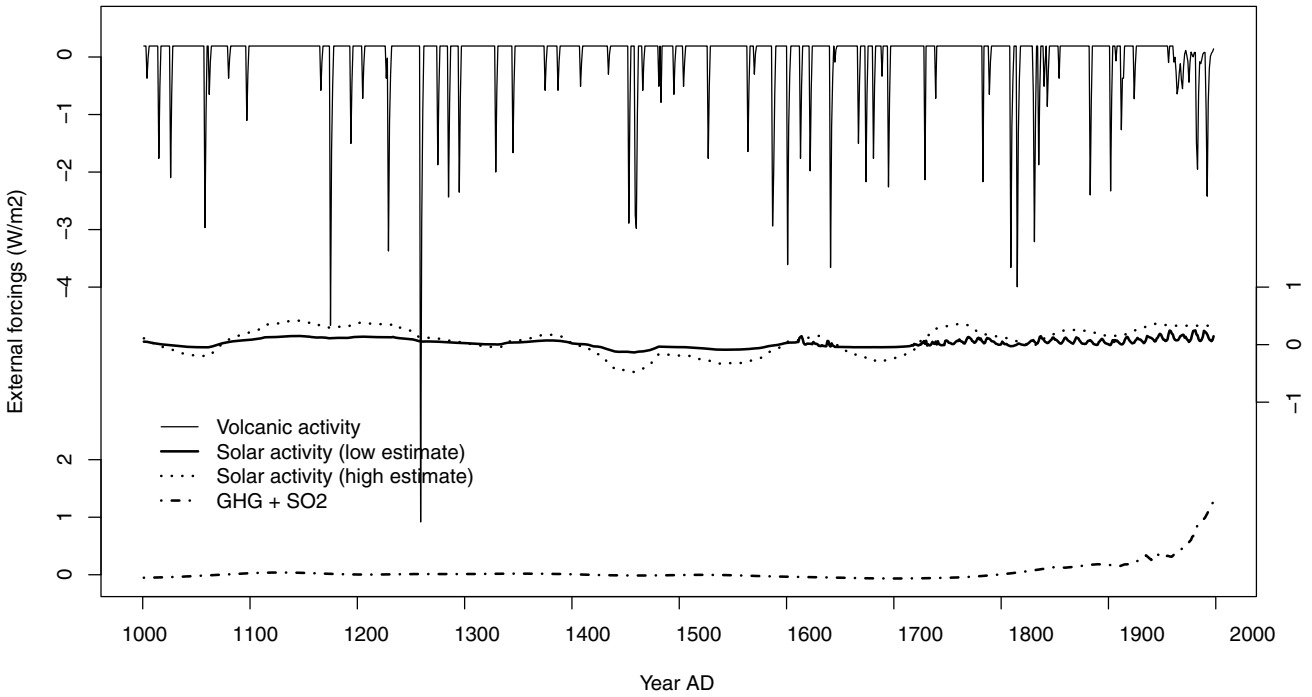

Fig. 30.2 Evolution of the estimates of radiative forcing (W/m^2) since the year 1000 AD. Top panel: volcanic activity; middle panel: solar activity (with low and high estimates from paleoclimate reconstructions); bottom panel: greenhouse gases (GHG) and sulfate (SO_2) aerosols (Jansen 2007)

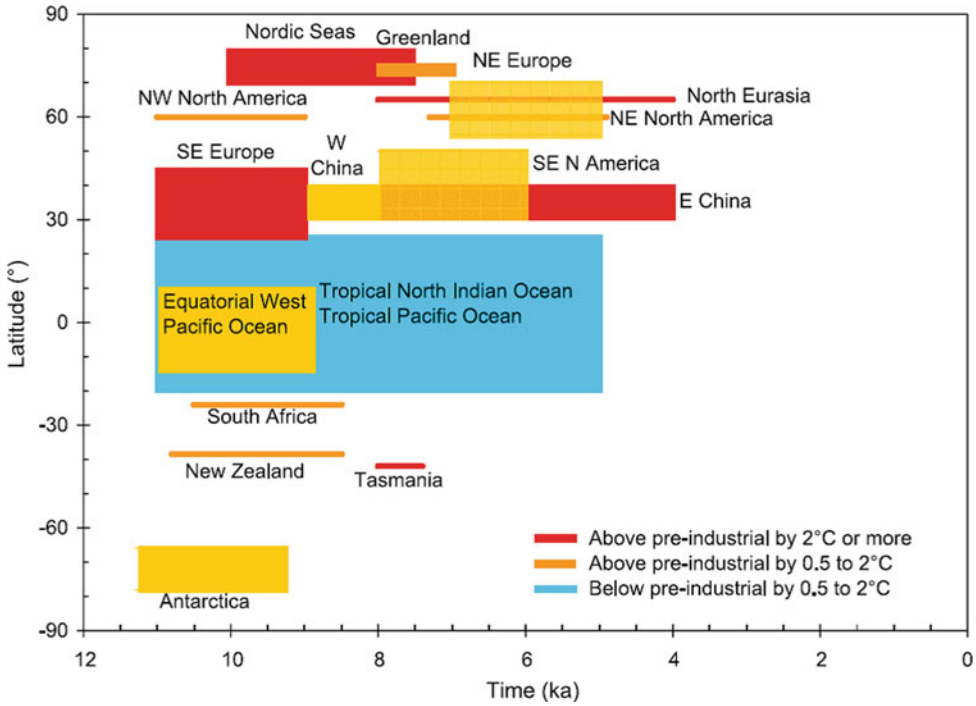

Fig. 30.3 Epochs (in thousands of years) and intensities of the maxima of temperature differences relative to the pre-industrial era, by latitude. The colors indicate the level of variance from pre-industrial levels (according to Jansen 2007)

temperature over the last two millennia are still not fully understood, especially since climate reconstructions are sometimes in disagreement for certain cold periods. Large-scale volcanic eruptions cool the atmosphere by one to two degrees, but these effects don't last longer than two years (Fig. 30.2). On the other hand, solar activity has a more modest effect on the radiative balance but one that is much more durable, as the phases of solar activity (Fig. 30.2) last several decades. In particular, the solar irradiance minimum, the 'Maunder Minimum' occurring in the middle of the seventeenth century corresponds to a marked cooling in the northern hemisphere.

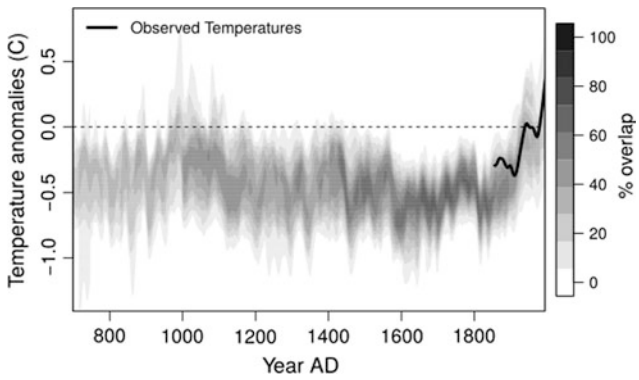

Fig. 30.4 Ensemble of reconstructions of the temperature anomalies of the northern hemisphere since the year 700 (shaded areas) (Jansen 2007) and average measured temperature anomalies (solid line). Anomalies of temperature are defined as differences with respect to a modern climatology (here 1960–1990). The shading accounts for the uncertainties of the reconstructions

Important Events of the Holocene

Several events punctuate the history of the Holocene. Here we will focus on the end of the humid period in Africa, about 4500 years ago, on the Medieval Warm Period, on the Little Ice Age and on the first lasting traces of human activity. The cooling observed about 8 200 years before now is discussed in Chap. 15 of volume 1 and not here because it is considered to be linked to the end of deglaciation.

The End of the Humid Period in Africa

About 4500 years ago, dry tropical Africa experienced variations in precipitation of much greater amplitude than it has for the last century. Lake levels fluctuated by several tens of meters and the surface area of Lake Chad reduced from 350,000 to 5000 km^2. Several 'climate crises', occurring over just a few years, punctuated this period and led to the complete drying up of lakes and the cessation of surface runoff (Gasse 2000). Wind-carried sediment recorded in a marine core off Mauritania suggests that a sharp change in atmospheric circulation occurred off the coast of dry tropical Africa between 5500 and 4000 years BP (deMenocal 2000). This period therefore corresponds with the end of the African Wet Period and the establishment of the current climate conditions. The resulting aridification of the Sahara conditioned the settlement of this area, where the activities of the populations were mainly farming and breeding of animals (Kropelin and Kuper 2006). However, rapid fluctuations do not seem to have impacted on the different regions of the Sahara-Sahel complex simultaneously, and signs of rapid events range are found from 4500 years to 2000 years BP depending on the latitude considered and the specific local conditions (Fig. 30.5). For example, the Dahomey dry interval was established about 4000 years ago in the middle of an area occupied by the Guineo-Congolese forest. The forest, fed by underground galleries, disappeared between 4500 and 3500 years ago in northern Nigeria but only 2000 years ago in the western Sahel. There are still many

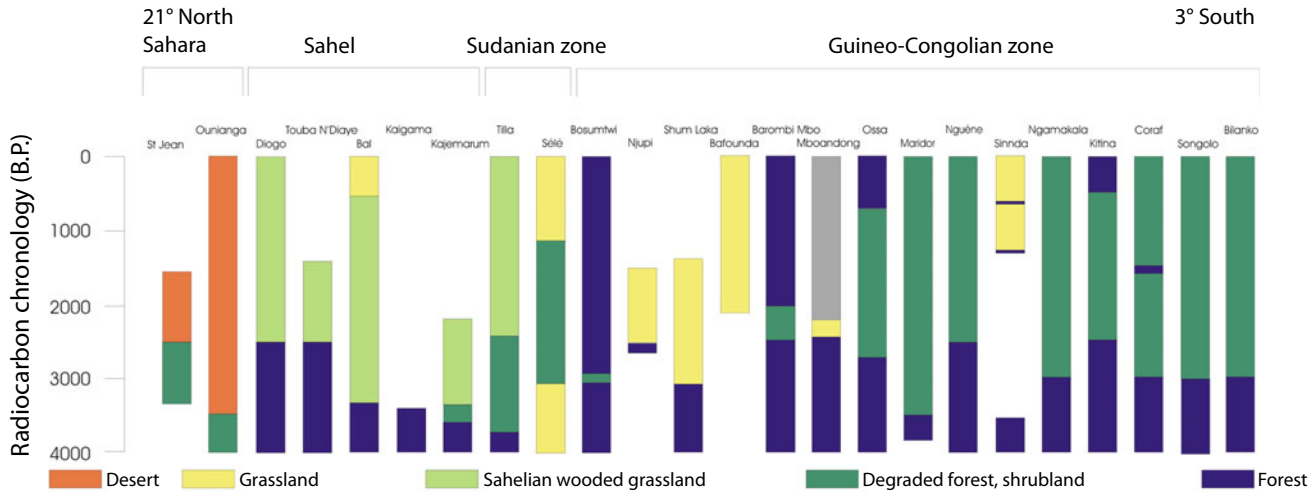

Fig. 30.5 Evolution of vegetation based on pollen data from different sites in Africa covering the transect between the Sahara at 21° N and the Guineo-Congolese zone in the south. This figure shows that the main transitions are not contemporaneous in the different locations (Courtesy of Anne-Marie Lézine)

grey areas concerning this period. Nevertheless, as insolation seasonality varied gradually, with reduced insolation during boreal summer, over the course of the Holocene, the rapid establishment of these dry conditions are the result of non-linear interactions between climates and ecosystems.

Medieval Warm Period

Through the study of historical archives, the British meteorologist Lamb reconstructed in the 1960s, the severity of the winters and the humidity of the summers since the year 1000 (Le Roy Ladurie 1967). He concluded that Europe experienced an escalation of dry summers during the period 1080–1200, unparalleled since then. He named this period the Medieval Warm Period. It is important to note that there are no direct temperature measurements for this time, since the thermometer did not yet exist. More recent studies (Jones and Mann 2004) suggest that Lamb's conclusions cannot be generalized to the entire planet.

From more extensive datasets, several studies have confirmed that many regions of the northern hemisphere experienced warmer conditions during the eleventh and twelfth centuries. However, several regions do not present signs of having experienced this optimum, or else did at a different time in history. For example, it appears that even though the summers were warmer at that time, winters were often very harsh in Western Europe until 1170. These apparent contradictions, probably due to a small number of observations, may be completed by new climate reconstruction programs in the future. Meanwhile, it should not be ruled out that this Medieval Warm Period was purely a regional phenomenon. It is also not a direct analogue to the current warming, as it was not associated with an increase in the atmospheric content of greenhouse gases.

The Little Ice Age

The Medieval Warm Period was interrupted at the beginning of the fifteenth century by the arrival of the Little Ice Age, which took hold until 1850. Again, there is no precise date for the beginning of this period: the Scandinavians felt a cooling at the end of the nineteenth century, whereas in France, the degradation of the weather was felt around 1430 (Bradley 1999; Le Roy Ladurie 1967). During this Little Ice Age in France there was a growth of alpine glaciers, very harsh winters and a succession of terrible summers. For example, the Bossons glacier, near Chamonix, descended 1000 m lower than presently. Though possibly influenced by the artistic trends of the time, the study of old engravings and paintings shows a striking difference with the present period. The strongest cooling was undoubtedly in northern Europe, with lakes being systematically frozen over in winter.

There are also signs of cooling in Equatorial America and New Zealand (Bradley 1999). This relatively cold period (on average, 1 °C cooler than currently in France) was responsible for the loss of crops and spikes in wheat prices, and often for insurrections, as well as an increase in the number of witches burned alive in public squares (Le Roy Ladurie 1967). After 1850, the glaciers began to retreat and the temperature to rise steadily, marking the end of the Little Ice Age.

The Little Ice Age is marked by a few particularly cold decades in Europe between 1650 and 1720. A decrease in the number of sunspots was observed at this time. These decades are called the Maunder Minimum, after the American astronomer Edward W. Maunder (1851–1928), who studied the relationship between sunspots and sun activity. It should be noted that it was the German astronomer Friederich W. G. Spörer (1822–1895) who first noticed the decrease in the number of sunspots between 1650 and 1720. History bestowed the Spörer Minimum between 1420 and 1570 on him. The variation in temperature caused by the direct influence of solar activity on the radiative balance at the Earth's surface (0.5 W/m^2) is less than 0.08 °C for the northern hemisphere (Jansen 2007) and is not sufficient to explain a cooling of between 0.2 and 0.5 °C in the northern hemisphere.

The Little Ice Age was also marked by intense volcanic eruptions that affected temperatures in a visible but not very durable manner (Fig. 30.4). Eruptions having a global effect generally took place in the tropics (Tambora, Krakatoa, Agung, Pinatubo etc.), and injected enough dust into the stratosphere to be homogeneously distributed globally (Robock 2000). Extratropical volcanoes (e.g., Laki in Iceland in 1783, St Helens in the United States in 1980) have had significant effects regionally in the northern hemisphere due to dust transport in the troposphere. However, their impact on a global scale was minor, because the volcanic dust they emitted did not reach the stratosphere.

The Anthropocene Era

The Anthropocene is a recently devised term that refers to the period when the climate and the environment became influenced by human activity. It is accepted that this period started at the beginning of the industrial era (in the middle of the nineteenth century), which also coincides with the first functioning weather service networks. It is possible, however, to argue that man began to impact on the climate from the middle of the Holocene. Land-clearing, the start of farming and slash-and-burn cultivation have emitted enough

greenhouse gases into the atmosphere to be detectable in the glacial and sedimentary archives (Ruddiman 2007).

Climate Reconstructions for the Holocene

The Different Archives

The reconstruction of climate conditions during the Holocene poses several major challenges for the scientific community. The low amplitude of the variations in mean temperature, compared to the amplitude observed during the glacial ages, makes it difficult to use the usual indicators to identify a signal. Moreover, the need to take sub-annual time scales into account to describe the significant events means pushing the interpretation of many climate indicators to the limit, or else finding new ones compared to the ones traditionally used in paleoclimatology.

The typology of paleoclimate indicators for the Holocene allows them to be divided into two main categories: natural archives and societal archives. The characteristics of these archival types are summarized in Table 30.1.

This section does not discuss the natural archives treated in volume 1 (ice cores, marine cores, corals, lake sediments etc.). The focus here is on societal archives, because their study requires an expertise not called on previously: that of historians.

Societal Archives

One big difference between the study of climate during the Quaternary and during recent centuries is that detailed and quantitative records made by direct witnesses of the climate events exist for recent times. Societal archives have been mined mainly by historians, most notably by Emmanuel Le Roy Ladurie, who pioneered the study of climate through history on a European scale (Le Roy Ladurie 1967).

The study of climate through history (or of historical climatology) relies on the study of old archives describing chronicles, empirical measures, events (Brazdil 2005). The most important aspect of this study is not necessarily the production of databases that can be used by climatologists, but the verification of sources and the demonstration of their relevance to our understanding of climate.

Indirect Indicators

The climate has an influence on the evolution of the maturation of certain fruits. This is especially the case for grapes (*vitis vinifera*). In France, the harvesting dates for grapes have been recorded in parish or municipal records for several centuries. These records provide valuable indicators of temperature variations, as explained in Chap. 17 of Volume 1.

Similarly, there are series of harvest dates for other crops in France dating back to the Middle Ages, series of the bloom dates of fruit trees (e.g. the Kyoto series in Japan, dating back to 800 AD). These historical phenological indicators are responses to climate variations and provide information on the temperature conditions during the months preceding the harvest. For example, making the reasonable assumption that wheat is harvested when the grain is mature (or shortly afterwards), an understanding of the vegetative cycle of wheat and a knowledge of the date of harvest (which usually takes place at the beginning of summer) gives an idea of the spring temperatures for the region. An important point for the climatologist is to identify the species of wheat grown at that time so as to make an accurate estimate of the phenological cycle.

Societal archives are comprised mainly of chronicles of extreme climate or meteorological events (droughts, heat waves, storms, intense rain etc.) which had destructive impacts on agriculture or buildings. These records tend to contain such records as rogations, i.e. religious processions carried out to ask for divine help when drought or persistent rain threaten crops. The invoked saints are usually thanked when the requested effect occurs. These registers provide indications of the length of these climate episodes (Brazdil 2005; Garnier 2009).

In farming accounts in newspapers and in journals kept by local scholars, we find chronicles describing more or less precisely the influence of certain climate events on society: freezing days, ice jams on rivers, storms etc. This climate information is obtained through accounts of the damage caused and the costs incurred.

One of the reasons for the name ‘Little Ice Age’ is linked to the progress of the Alpine glaciers into the valleys that contained them from the fifteenth century on. Using dated indicators, such as moraines displaced as the glaciers advanced, it is possible to have an idea of how the

Table 30.1 Types of climate archives used to reconstruct the climate of the Holocene

	Natural archives	Societal archives
Direct climate data	None	Narrative descriptions, instrumented measurements
Indirect organic data	Tree rings, pollens etc.	Vegetation growth
Indirect non-organic data	Ice cores, sediments, glaciers, corals	Precipitations, ice floes, frosts etc.

volume of these glaciers evolved over the centuries. To get a better idea, climatologists also use graphical representations by painters, and later by photographers. It is thus clear that after a spread to maximum size at the beginning of the nineteenth century, the majority of the Alpine glaciers retreated by several kilometers over a century and a half, with an acceleration of this retreat at the end of the twentieth century.

Direct Indicators

Historians classify direct observations of climate and meteorology since the year 1000 into several types of historical phases. These phases qualify the type, abundance and quality of the information.

Before 1300, these were isolated accounts of extreme anomalies and natural disasters (Brazdil 2005; Le Roy Ladurie 1967). These accounts describe in particular the ravages caused by natural disasters: destruction of crops, buildings, floods, increased mortality etc. A detailed study of them, by cross-referencing sources and checking them, makes it possible to track the chronology of extreme events.

From 1300 to 1500, more or less continuous descriptions of the character of summers and winters (and to a lesser extent those of spring and autumn) become available, containing indications of everyday conditions.

From 1500 to 1800, more or less regular descriptions of monthly or daily conditions start to become available. These descriptions can be corroborated by records of processions or rogations organized by the local parishes to end droughts or avert events that might endanger crops (Le Roy Ladurie 1967).

Between 1680 and 1860, the very first instrumental measurements appeared. The barometer was invented by Torricelli and the thermometer by Galileo. The first attempts to establish international meteorological networks were made during this time. In France, the first network of systematic observations dates from the reign of Louis XVI. In 1776, Félix Vicq d'Azyr, secretary of the Academy of Medicine, asked the doctors of the kingdom to record the temperature of the air three times a day, as well as to write a summary of the diseases treated during the month. This initiative was founded on the idea that variations in climate could have an impact on the health of the population. This work was maintained for a few decades, and many doctors in France contributed to the exercise, scrupulously noting temperatures and diseases. Unfortunately, this directive was discontinued, and it is not possible to have continuous data. In addition, the physicians of the day obviously had no knowledge of meteorology or instrumentation, and not all of their measurements were reliable.

From 1860 onwards, meteorology was developed within the framework of national and international networks. Urbain Le Verrier, who discovered the planet Neptune by calculation, was also an influential politician of the Second Empire. Like his astronomer predecessors of the Observatoire de Paris, Cassini, Maraldi and de la Hire, he was also interested in meteorology and, as a politician, in the strategic advantage that could be derived from weather forecasting. Following the disaster of Sevastopol in 1854, when the Allied fleet was destroyed by a storm, Le Verrier claimed that it was possible to predict this event through a network of ad hoc meteorological observations. This marked the birth of centralized meteorological networks via the telegraph, which would for a long time be under the control of the army in most countries in the world.

Statistical Methods for Climate Reconstruction

Methods for obtaining the temperature curves from Fig. 4 are based on statistical regressions between several categories of climate indicators. The general concept behind reconstructing a hemispheric temperature is to use a set of indicators (thickness of tree rings, isotopic concentrations, pollen concentrations, harvest dates etc.) evenly distributed over the hemisphere. This is called a 'multi-proxy' approach because it uses a mix of several types of climate indicators (referred to as proxies from now on).

The strategy of these reconstructions (Jones and Mann 2004) is generally in three steps and requires a temperature dataset with sufficiently good coverage of the globe, hemisphere or well-defined region (e.g., The North Atlantic or the Equatorial Pacific).

The first step is to determine a small number of general statistical characteristics (space or time) for recent observations. The best known temperature reconstructions (Mann et al. 1998) use statistical techniques of decomposition into *principal components* (von Storch and Zwiers 2001), however there are alternatives, depending on the distribution of the proxies and their properties. Thus, the temperature field T, which depends on time t and space x, can be written in the form:

$$T(x,t) \approx \sum_{i=1}^{5} a_k(t) E_k(x).$$

In this equation, the $E_k(t)$ are the spatial modes of the variability of T, and the $a_k(t)$ are the associated time coefficients (von Storch and Zwiers 2001), generally called principal components (denoted PC). In this equation, we only keep 5 modes.

The climate indicators (proxies) are then compared with the evolution of the statistical characteristics of observations over a calibration period, where proxies and observations are available. This calibration period may cover all or part of the twentieth century. There is a technical debate about the

selection of this learning period (Jansen 2007) and the number of statistical components to be used, but the result in the end is not very sensitive to this selection. During this period, a linear regression is performed between the proxies and the statistical characteristics observed. This regression attaches weights to proxies in order to maximize their correlation with temperatures. This analysis also makes it possible to eliminate the proxies which have a poor correlation with the temperature signal during the learning period.

A 'verification' period prior to the learning period for which instrumental temperature data are available is then used. This verification period identifies the errors incurred in the regression obtained for the calibration period. For this verification period, it is also possible to determine the error linked to the omission of proxies in the estimation of the temperature. This calculation is essential because it is obvious that the further back in time we go, the fewer climate series are available and the more uncertain the reconstruction of temperatures becomes.

Finally, temperatures can be reconstructed for the last millennium. It should be noted that this reconstruction has a spatial aspect. It is important to bear in mind that this type of method relies on basic assumptions about the temporal stability of the climate modes identified in the temperature data during the calibration period and the temporal stability of the relationship between proxies and temperatures. These two types of stability can be quantified over the verification period, but it is impossible to exclude the possibility of changes over a longer period. Another problem with this type of reconstruction comes from the statistical regression between proxies and main components over the calibration period. Since a regression is generally imperfect, it inevitably leads to an underestimation of the variance when this is used to reconstruct the climate, which can lead to a poor estimation of long-term climate variations. It is possible to partially solve this problem by using proxies that represent different time scales, and are thus sensitive to scales varying from inter-annual to centennial (Jansen 2007).

A major advance in the quality of climate reconstructions lies in the improved understanding of the mechanism linking the 'proxy' to the climate variation, which helps the statistical steps described above to be guided by knowledge of the physics. This research topic is particularly active at the moment.

Several research teams have proposed temperature reconstructions for the last millennium, based on different proxy datasets (Jansen 2007). These reconstructions often have common foundations (often, tree ring data) but the spatial distribution of the proxies used varies considerably from one reconstruction to another.

The evolution of the error bars of these reconstructions shown in Fig. 30.4 shows the discrepancies between the estimates of temperature changes, especially during cold periods. It should be noted in particular that the latter part of the twentieth century emerges significantly from the error bars of the temperature variations for the preceding millennium.

Climate Simulations

Climate simulations provide an understanding of how different forcings affect the climate and quantify the main feedbacks. Moreover, comparison between the model results and the data makes it possible to determine whether the models are capable of representing a climate different from the current one. The models used for Holocene simulations cover the spectrum of models presented in Chap. 4 of this volume which describes the different hypotheses and the protocols to run such simulations. In the case of the Holocene, it is mainly the characteristics of the seasonal cycle that have been analyzed, as changes in insolation, driven by precession, strongly modulate seasonality but have little impact on the annual average of the different climate variables. For the last 2000 years, the emphasis is on understanding the forcing associated with fluctuations in the solar constant and in volcanism, and the identification of associated feedbacks. This is a major step towards gaining perspective on recent centuries strongly disrupted by human activity. Increased understanding of interannual to centennial variability is necessary in order to detect climate change and, where appropriate, to attribute it to human activities.

Holocene Simulations

Major Trends

There are very few simulations that cover the entire Holocene. Those that exist were carried out using models of intermediate complexity (see Chap 4), because it is impossible to simulate a period of 10,000 years within an acceptable time frame using general circulation models, which need an average of one month to achieve 100 years of simulation on supercomputers.

The main objective of simulations of the whole Holocene period is to reproduce the major climate trends caused by variations in orbital parameters and by the concentration of greenhouse gases. They generally do not take into consideration the full set of forcings such as volcanism or the evolution of the solar constant, factors which are not well known for the whole period. The applied models of intermediate complexity take account of atmospheric and ocean circulation in a simplified way, as well as sea ice and vegetation (Crucifix et al. 2002; Renssen et al. 2005). They nevertheless have different levels of complexity.

The first model considers the ocean and the atmosphere in terms of latitudinal sectors, while the second takes a

three-dimensional ocean model coupled with a simplified atmospheric model. The simulated annual temperature changes are very low, in accordance with the low amplitude of the change in insolation. Between 60° N and 70° N, these studies show cooling during the Holocene in response to the reduction in summer insolation relatively in line with observations (Fig. 30.3). The increase in greenhouse gas concentrations since the Middle Holocene partly offsets the reduction in temperature by about 0.5 °C. The beginning of the Holocene is also a time when the ocean was still disturbed by the recent deglaciation and when there were larger ice caps than are currently present in North America and Greenland. Simulations (Renssen et al. 2005) indicate that the main effect of the Fennoscandian cap at the beginning of the Holocene was to delay the climate optimum in eastern Canada and Greenland (Fig. 30.3). These studies also suggest an increase in variability during the Holocene, mainly around the northern seas, resulting from feedbacks between atmospheric circulation, ocean and sea ice.

The simulations show no major changes in thermohaline circulation of the ocean during the Holocene, except perhaps a slight increase between 9000 and 8000 years before the present. It also appears that the initial conditions and the long-term variations of the intermediate and deep ocean have had little impact on the characteristics of the climate during the Holocene. Thus, it can be taken that the different periods are more or less in equilibrium with the forcings. Hence, equilibrium simulations for a particular period of the Holocene can be used to correctly identify the main characteristics of the climate. This result is important because the ignorance of oceanic conditions at the global scale at the beginning of the Holocene is a source of uncertainty for numerical simulations. Nevertheless, the equilibrium is not necessarily verified over the last 4000 years because of a 200-year lag between the forcing and the climate response of the reorganization of the boreal forest in the northern hemisphere (Crucifix et al. 2002).

Reference Periods and Analysis of Feedbacks

Simulations from intermediate complexity models describe the major trends and main feedbacks that have shaped the Holocene in the mid and high latitudes of the northern hemisphere but do not allow for a detailed analysis of feedbacks or changes in variability. Some periods, such as the beginning of the Holocene (9500 years ago) and the Middle Holocene (6000 years ago), have been the subject of numerous modeling studies and benefit from international coordination (Joussaume and Taylor 1995; Joussaume et al. 1999; Kutzbach 1988; Braconnot et al. 2007a).

In particular, there is an effort to compile data at the global scale for the Holocene (Prentice and Webb 1998), and this helps, along with simulations, to improve our understanding of the mechanisms and the different feedbacks involved and to assess the ability of climate models used for climate projections for the next century to represent a different climate than the current one (Cane et al. 2006; Braconnot et al. 2012).

Feedbacks from Snow, Vegetation and from Sea Ice in High Latitudes

Feedbacks from ocean, vegetation and snow and ice cover are the main factors that have conditioned the evolution of temperature in the different regions of the northern hemisphere during the Holocene. When forest is replaced by grass, the reflective power of the combination of snow and vegetation is more marked. This results in a positive loop of increasing snow, cooling and withdrawal of the forest. This mechanism in particular describes entry into the last glaciation (de Noblet 1996). The ocean response leads to a phase shift in the seasonal cycle due to its high thermal inertia and evaporation capacity, which limits surface heating. Thus, spring and autumn are more affected than summer and winter by oceanic feedbacks. These effects combine with the feedback from sea ice and snow to reduce seasonal contrasts at high latitudes and to amplify the cooling during the Holocene (Wohlfahrt et al. 2004).

The feedback from snow and sea ice is manifested in a modification of the surface albedo. It is therefore possible to quantify it in terms of energy (W/m^2), using a simple approach to climate sensitivity analysis (Taylor 2007). This allows us to define this effect as:

$$\text{Albedo effect} = (SWncs_{pal} - SWncs_{Ok}) - SWf$$

where $SWf = (1 - \alpha_{Ok})\Delta SWi$ represents the radiative forcing related to the change in insolation and *SWncs* represents the net solar radiation (SW: short wave) in a clear sky (*ncs*) for the paleoclimatological (*pal*) simulation and for the control simulation (*Ok*). The radiative forcing takes into account the model characteristics via the albedo of the control simulation. Indeed, although the same insolation disturbance *SWi* is applied to different models, the difference in net incident solar radiation depends on the selected model as a function of the surface characteristics, the representation of clouds etc. which characterize the planetary albedo in the model (Fig. 30.6).

As an example, Fig. 30.6 shows that between February and April, the estimated radiative forcing for two different models ranges from −12 to −4 W/m^2 between 20° N and 50° N. The cooling associated with this insolation deficit allows the snow to remain longer on land.

This snow introduces a local feedback of −4 to −16 W/m^2 on the continent which reinforces the insolation deficit and the cooling. Both simulations produce the same type of feedback, but with different amplitudes and geographical localization. On the other hand, in summer, the

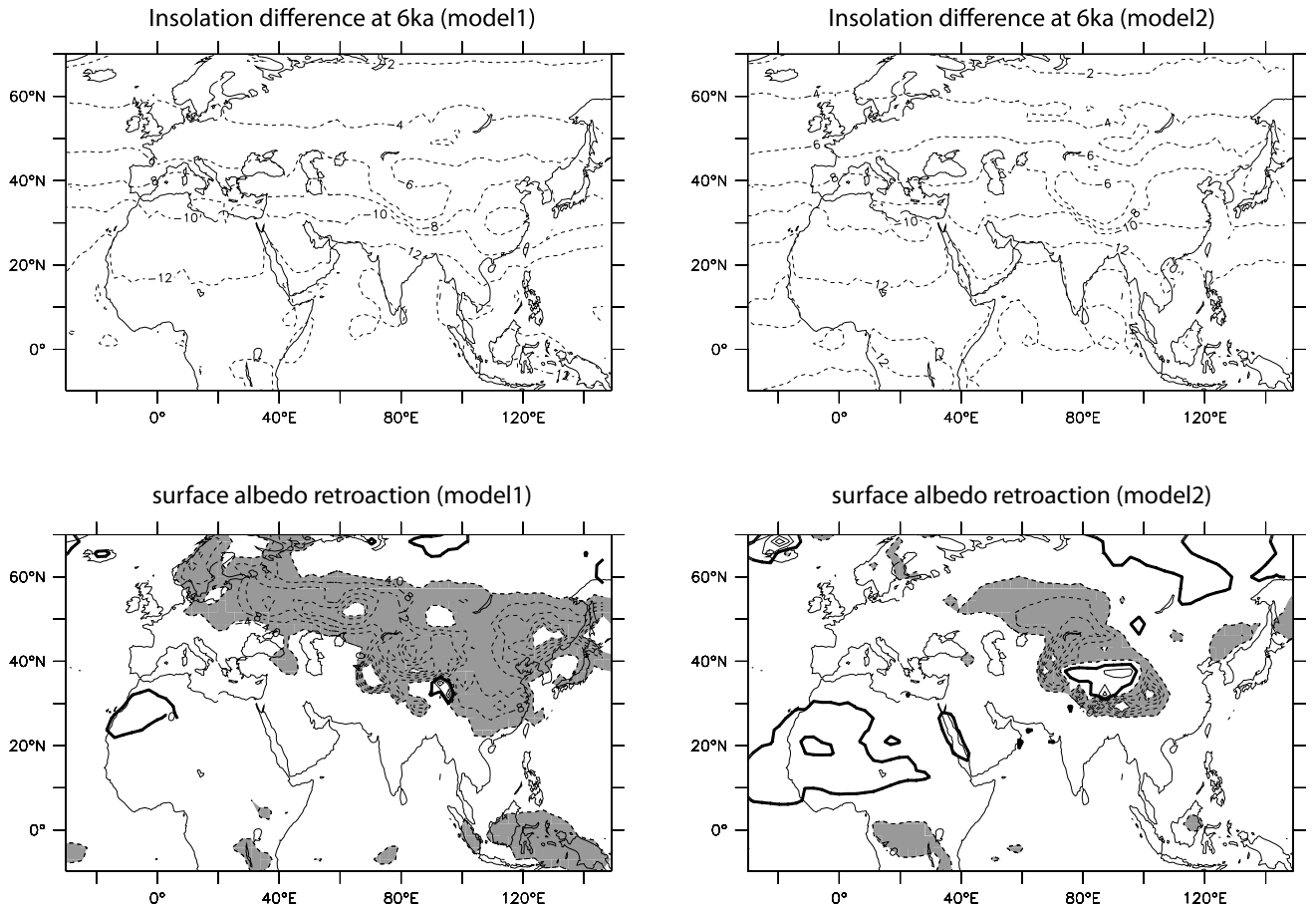

Fig. 30.6 Radiative forcing due to the change in incident radiation at the top of the atmosphere during the Mid Holocene (W/m^2) and feedback resulting from surface changes (mainly change in snow cover) for the months of February to April from two climate models. Adapted from Braconnot et al. (2007b)

lower coverage of sea ice and snow induces a heating surplus of 5 W/m^2 above 30° N. The water vapor feedback adds to this effect, contributing an additional 2.5 W/m^2 to summer warming in these regions. These different feedbacks amplify the direct effect of insolation. The way in which they are represented in the models is the source of the differences between simulations and of the uncertainty on their amplitude.

Monsoons and Ocean and Vegetation Feedbacks

The amplification of monsoon regimes in the northern hemisphere is the main climate characteristic in tropical regions during the first half of the Holocene. The wet belt extending from Africa to India and South Asia recorded strong changes in precipitation regimes, in line with the northward extension of the intertropical convergence zone.

These fluctuations are recorded in both continental and ocean data. Several factors explain the stronger monsoons between the beginning of the Holocene and the Mid Holocene. The first contributory factor is the amplification of the seasonal insolation cycle in the northern hemisphere. The monsoon is the result of differential heating between the hemispheres and between the continents and the oceans. Higher summer insolation increases the contrast in temperature between the land and the ocean. This contrast alone does not explain all the monsoon characteristics. The orography and the warming at high altitudes of the Tibetan plateau constitute a source of energy which contributes to the establishment of this planetary thermal current. As the monsoon becomes established, the release of latent heat at the time of condensation is an additional source of heat enhancing the convergence of moisture in areas of high convective activity.

For the climate of 6000 years ago, Fig. 30.7 shows the changes in temperature, precipitation and large scale circulation linked to the reinforcement of the monsoon in Africa and India in response to increased insolation of the northern hemisphere, as well as the uncertainties arising from differences between the models. Continental warming in July-August reaches about 2.5–3 °C. This heating is

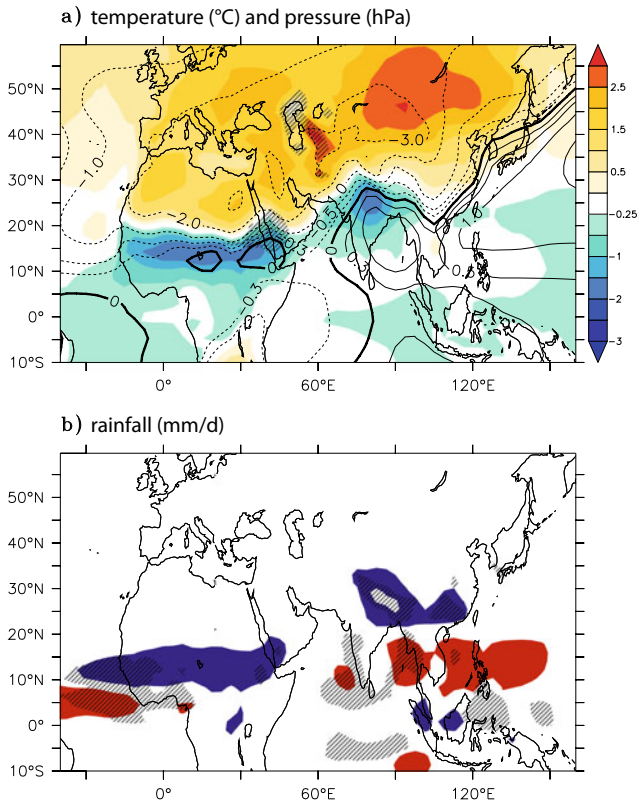

Fig. 30.7 **a** Temperature change (shaded, °C) and surface pressure (hPa) between the Mid Holocene 6000 years ago and the current period based on the average of the set of simulations from the international PMIP project. **b** As for a, but for ocean surface temperatures (isolines, °C) and precipitation (gray). In figures a and b, the hatching indicates the regions with the most variable results from one model to another

associated with a deepening of the thermal depression which is reinforced where warming is at a maximum. Large-scale circulation leads to increased convergence of ocean winds towards the interior of the continents. Large-scale moisture convergence follows this circulation in the lower layers of the atmosphere, explaining the increase in precipitation in Africa and northern India. These main features are reproduced by all of the models. However, there is great disparity in the magnitude of the simulated changes in many regions such as East Africa, Arabia and northern India.

Several factors amplify or offset the atmosphere's response to insolation. These have been described in several overview articles (e.g. Braconnot et al. 2012) of which the main points are summarized here. The method used to study the ocean and vegetation feedbacks consists mainly of removing the feedbacks one by one.

The Role of the Ocean

The ocean plays a major role in modulating the amplitude and phase of the seasonal cycle. Figure 30.8 summarizes the simulated SST (Sea Surface Temperature) changes for key regions of the different tropical ocean basins (Zhao et al. 2005). Coupled models capture the main features of the SST evolution for the current climate. It should be noted, however, that differences between the simulations range from 0.5 °C to more than 2 °C. The amplitude and phase of the seasonal cycle are relatively well reproduced in most of the models. The results show the greatest amount of disparity for the Indian Ocean as models do not correctly capture the semi-annual SST signal.

Despite the differences for the current climate, the response of the ocean to the change in insolation is very consistent from one model to another. All of the tropical regions are marked by a cooling in the first part of the year, a direct response to the change of insolation. Warming occurs one to two months after the change in insolation hits its peak, depending on the region. The shift in phase between the regions comes from the discrepancy in seasonal insolation between the northern hemisphere and the southern hemisphere and from localized changes in the thermal inertia of the ocean. Although the main changes are relatively similar between the models, dispersion between results can be up to a factor of 2. The phase differences between the models are greater in winter than in summer because the change in insolation is weaker and lasts longer. The tropical ocean is relatively cold in late spring, when the monsoon starts, and accentuates the contrast between land and ocean, promoting moisture advection on the continent. In the Atlantic Ocean, a dipole occurs on both sides of 5° N, with warmer temperatures in the north and colder in the south than is currently the case. It strengthens the low pressure zone between 10 and 20° N, the convergence of humidity in this region and the monsoon influx in West Africa. This differential between the two hemispheres originates in the heating differential linked to the insolation on either side of 5° N. The heating of the surface ocean is reinforced to the north of 5° N by a decrease in evaporation due to a weakening of the trade winds, part of which converges towards the African continent instead of crossing the Atlantic. In addition, enhancing the monsoon influx initiates an Ekman[1] transport in the surface layers of the ocean, contributing to a delay in the warming of the region south of 5° N (Zhao et al. 2005). The system relaxes in autumn when insolation on the equator is sufficient to smooth the temperature gradient. In India and South-East Asia, warming of the western part of the Indian Ocean and of the 'warm pool' promotes the convergence of surface circulation to these warm waters to the detriment of the continent. The Indian monsoon seems

[1]The current generated by the surface wind is rotated to the right of the wind in the northern hemisphere under the effect of the Coriolis force and reduces with depth under the effect of friction in the form of a spiral (Ekman's spiral). The transport generated (Ekman transport) over the entire Ekman layer (about 100 m) is perpendicular to the wind.

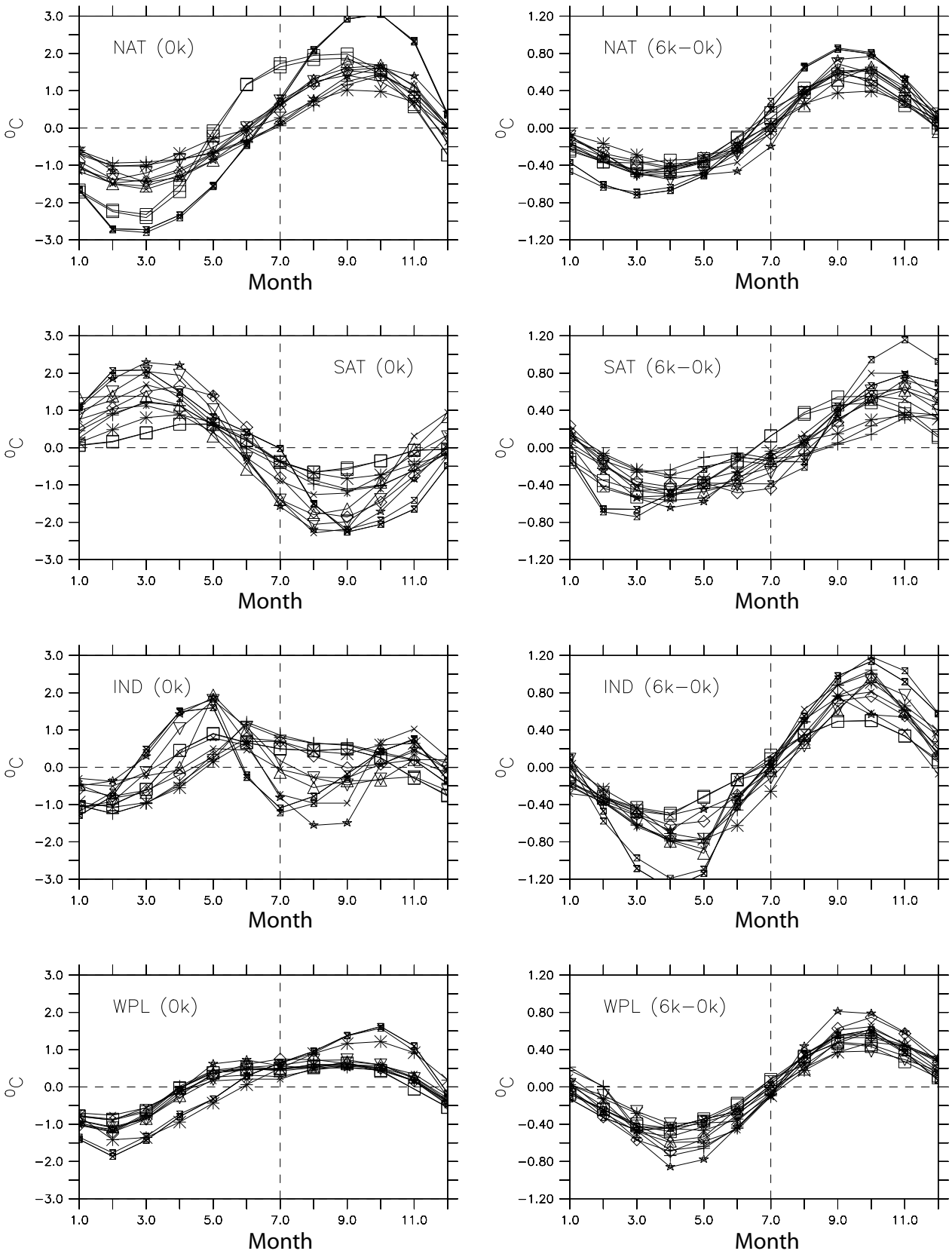

Fig. 30.8 Surface temperature simulated by different models of the PMIP project for the current period (left) and the difference between the Middle Holocene and the current period (right) and four key regions of the tropical ocean, NAT (60° W–20° W; 10° N–20° N), SAT (30° W–0° W; 10° S–0° S), IND (55° E–75° E; 5° N–15° N) et WPL (110° E–160° E; 0° N–20° N). Each curve and acronym represents a different model

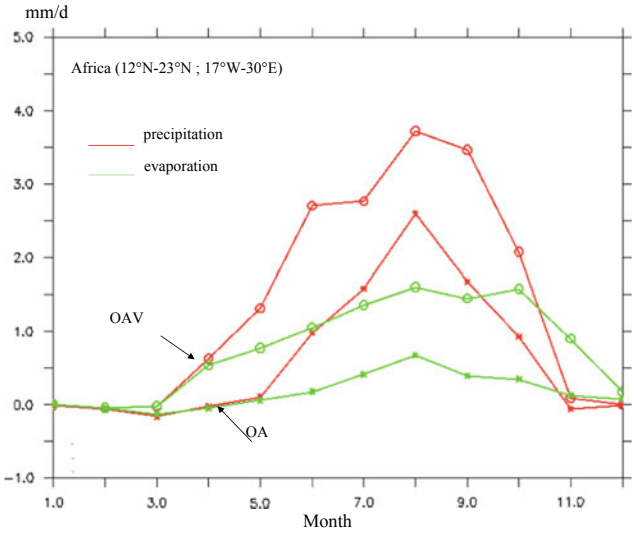

Fig. 30.9 Seasonal evolution of the change in evaporation (mm/d) and in precipitation (mm/d) between the Middle Holocene and the current time as simulated by the IPSL-CM1 model coupled (OAV) and uncoupled (OA) asynchronously with a vegetation model (from Braconnot et al. 1999)

less amplified in the case of an interactive ocean than in older simulations, carried out with atmospheric models forced by the current SST.

The Role of Vegetation

Another factor that affects the characteristics of the monsoon is changing vegetation. Vegetation modifies the surface albedo and the ways in which soil water is used. Depending on the type of vegetation, water losses through interception, evaporation from bare soil and transpiration are distributed differently. All climate models incorporate a more or less complex land surface model to determine the exchanges of heat and water between the surface and the atmosphere. The types of vegetation and the resulting surface characteristics (albedo, roughness, resistance to evaporation) are prescribed from current data. Simulations of the Middle Holocene tend to underestimate the hydrological changes in the Sahelian region (Joussaume et al. 1999). Vegetation characteristics are generally set in line with current ones although pollen data indicate changes in vegetation (Jolly 1998). Change in vegetation, not taken into account in these simulations, is a likely candidate to explain this underestimate.

The first coupled atmosphere-vegetation simulations involved an iterative coupling between climate and vegetation. For this, a vegetation model was used to simulate a vegetation in equilibrium with the climate produced by the atmospheric model and then was reintroduced as a boundary condition to the climate model (Claussen and Gayler 1997; de Noblet 1996). The process is reiterated until climate and vegetation are in equilibrium, i.e. with no major difference between two iterations. New versions of land surface models include the carbon cycle and vegetation dynamics (Krinner 2005), which allows for interactive representation of vegetation changes, taking into account both slow changes in vegetation (replacement of one vegetation type by another) and the interactions of these vegetation changes with the climate. There are still many uncertainties in how these couplings are represented, which results in marked differences in the amplitude of how vegetation reinforces precipitation in monsoon regions (Braconnot et al. 2007b). Nevertheless, some of the broad outlines appear robust.

When vegetation is interactive, the role of local recycling of water becomes more important. Figure 30.9 shows the contributions from advection and local recycling (evaporation) in the Sahelian region, estimated from coupled ocean-atmosphere-vegetation simulations. In this case, the vegetation was coupled asynchronously to the atmosphere model. Simulations with interactive vegetation indicate that the desert in the Sahelian region was replaced by steppe. The albedo was thus decreased in the region, reinforcing the local warming over land at the beginning of the monsoon season, and favoring the advection of humidity and precipitation. During the monsoon season, vegetation is more efficient than bare soil at recycling water, and this also increases precipitation. Finally, at the end of the monsoon season, vegetation absorbs the soil water, which contributes to a lengthening of the rainy season (Texier et al. 2000). All of these effects explain why simulations incorporating interactive vegetation are generally in better agreement with the data for the region of West Africa stretching from 15 to 20° N.

However, there are still great disparities between the results of the different models. These come from small-scale phenomena (clouds, boundary layer, turbulent flows etc.) which need to be better represented in climate models.

Vegetation and the End of the Wet Season in Africa

The role of vegetation and the changing variabilities are two factors that have also been suggested to explain the abrupt end of the wet period in Africa. Early studies using a model of intermediate complexity (Claussen 1999) showed sudden aridification around 5000 years BP in Africa, accompanied by a rapid reduction in precipitation, in line with the data (deMenocal 2000). Rapid vegetation feedback is the source of this abrupt variation, as vegetation can produce multiple equilibria in which green Sahara conditions and desert conditions can coexist.

In the early part of the Holocene, vegetation gradually decreased in response to the reduced summer insolation and the associated reduction in precipitation. When the system reached a threshold where 'green Sahara' conditions could no longer be maintained, the coupled system abruptly produced a desert state accompanied by a sudden drop in

precipitation. This sudden change in state is therefore associated with a strong positive feedback from the vegetation. Liu (2007) have another interpretation based on coupled ocean-atmosphere simulations in which the rapid disappearance of vegetation is not accompanied by sudden aridification implying no strong positive feedback induced by vegetation. The mechanism in this case is linked to the internal variability of precipitations. This variability can be considered to be a stochastic forcing that generates slow stochastic variability of soil moisture. This variability interacts with the nonlinearities of the plant system to generate a rapid decrease in vegetation. It is therefore the nonlinear response of the vegetation to the strong internal variability that is responsible for the sudden change of state of the vegetation when a bioclimate threshold is reached. All these studies provide insights into the interactions between long-term insolation variations, climate and vegetation. Nevertheless, we do not yet know the exact reasons and the dominant mechanisms in these African regions. Progress is essential to better represent the semi-arid zones and to obtain hydrological and ecological data at high temporal resolution.

The Recent Climate (Recent Centuries)

Simulating the climate variations of the last millennium is a major scientific challenge for the beginning of the twenty-first century. The first problem is a technological one: these simulations require several months of intensive calculations on the most powerful computers available. This explains why the number of available simulations have gradually increased from one IPCC report to the other (IPCC 2007, 2013). The second problem is how to define an initial state for the ocean and the atmosphere. This problem is avoided by using the output from an ocean model output using pre-industrial conditions and for which no drift is observed. The idea behind this approximation is that the climate will adjust sufficiently quickly to forcing conditions so that the initial conditions of the beginning of the last millennium are not critical. The third problem is purely physical and is the definition of the climate forcings over time. On this time scale, the main forcings are:

- Changes in solar activity. The role of solar activity is not yet clear. Fluctuations in the energy received in the troposphere are theoretically very low. Fluctuations in solar activity also affect the chemistry of the stratosphere. The modulation of reactions with ozone, in particular, can cause heating of the stratosphere and its expansion, thus favoring atmospheric circulation patterns in the troposphere (Shindell 2001). Variations in solar activity in numerical climate simulations can have a purely radiative effect. More sophisticated models include chemical reactions with stratospheric ozone (Shindell 2001) which can produce a warming. This option is more complicated to implement because most of the models used for this exercise do not include stratospheric chemistry, which is very demanding on computing time.
- Volcanic eruptions, particularly the most powerful, which emit sulfurous SO_2 and dust into the stratosphere. The solid particles are quickly pulverized but the sulfurous gas turns into sulfuric acid, which is only washed away after several months. Large volcanic eruptions (e.g. Pinatubo 1991) have the effect of cooling the planet for two to three years (Robock 2000). Volcanism is generally accounted for rather crudely in climate models (Jansen 2007) and is often done by decreasing the solar constant by a few W/m^2 for two years. This representation, although it saves calculation time, cannot account for the dispersion of the volcanic particles across latitude in the stratosphere and therefore for its impact on atmospheric circulation.
- Greenhouse gases added to those already present in the atmosphere. This additional greenhouse effect is noticeable from the twentieth century onwards. These are almost exclusively emissions related to human activity. Sulfate aerosols are also linked to human activity and have a cooling effect on the atmosphere locally.

Estimates of the radiative effects of these forcings during the last millennium are shown in Fig. 30.2.

The details of the atmospheric circulation responses vary widely from one model to another, particularly for GCMs. Simpler models such as EMICs, on the other hand, show similar behaviors because the atmospheric responses have few degrees of freedom, which constrains these models to behave in the same way.

Characteristics of Climate Variability

Extratropical Circulation

The North Atlantic Oscillation (NAO) is the climate regime of the atmospheric circulation dominating the North Atlantic region. This regime was first detected in temperature anomaly structures around the North Atlantic basin. A temperature anomaly, the term used by meteorologists, is the difference between the observed temperature and the average temperature. Sir Gilbert Walker, the British meteorologist, noticed opposing temperature anomalies between Labrador and North Africa on the one hand and the eastern United States and Western Europe on the other. Thus, when it is warmer than usual in the American East (a positive temperature anomaly), it is generally colder than usual in the south of France (a negative anomaly).

This temperature structure is related to fluctuations in the atmospheric circulation in the extra-tropics of the northern hemisphere. Theoretically, this circulation blows from west to east between 30° N and 70° N, and is diverted to the north by the Coriolis force (due to the rotation of the Earth). The North Atlantic has a characteristic zone of low pressure (depression) around Iceland and a zone of high pressure (anticyclone) around the Azores. It is the modulation of the respective influences of these two phenomena that is at the origin of the NAO.

At the level of the North Atlantic basin, the atmospheric flow (of density ρ) is governed by an equilibrium between the pressure forces (P) and the Coriolis force (f perpendicular to the movement). It is the geostrophic equilibrium which is valid on a large spatial scale and over a few weeks:

$$V = \frac{1}{\rho f}\vec{k} \times grad\ P.$$

In this equation, the velocity field V is related to the pressure gradient between low and high latitudes and $\vec{k}$ is a unit vector on the vertical. A strong gradient not only deflects the flow but also accelerates it. The pressure gradient term can be approximated by the pressure difference between two selected locations, for example the Azores and Iceland. This pressure difference is called the North Atlantic Oscillation Index (NAO). A reason for the choice of these locations is that pressure data is available for them since 1825.

So when the pressure gradient between the Azores and Iceland is pronounced (high NAO index), circulation becomes more active and flows towards northern Europe. In this way, moisture is transported to Scandinavia, and during this time, southern Europe is mild and dry. On the other hand, if this gradient is low, the atmospheric flow is towards Southern Europe, causing it to experience wet and cold climate conditions.

During the 1990s, the NAO index was consistently very positive, resulting in a rise in temperatures in Europe (while cold records were being broken in Canada). This consistent index has been interpreted by some as a link with global warming. However, a similar situation with a very strong NAO index was already encountered at the beginning of the twentieth century and is probably not exceptional. Moreover, the index has returned to negative values at the beginning of the 21st century, while the temperature of Western Europe continued to increase.

Thanks to the NAO signature on temperature and precipitations, it has been possible to use paleoclimate data (tree rings or glacial drilling) to extend this 'instrumental' NAO index to the last millennium. This application makes it possible to determine an index based on atmospheric pressure without having access to pressure itself. It is based on large-scale relationships between climate variables and pressure differences, for which the contemporary period can be used to verify. Of course, such reconstructions can yield ambiguities and may have diverged before the nineteenth century, depending on the indices used, because the relationship between the pressure gradient (the NAO index) and variables such as temperature or precipitation may have changed over time.

Looking at the daily weather charts, it can be seen that on some days in winter an anticyclone settles over Scandinavia, causing high pressures that prevents the western winds from reaching France. This kind of weather situation, often referred to as a 'Scandinavian blocking', can last several weeks resulting in generally dry weather. Another meteorological situation that can occur, this time with an abnormally high pressure zone in the middle of the Atlantic is the 'North Atlantic ridge'. The air crossing the Atlantic is diverted to the north of this zone and passes over Greenland, before returning to Europe, causing a cold snap. We can thus count several types of weather with longer or shorter lifetimes. The most common types of weather patterns are the two phases of the NAO, the Scandinavian blocking and the North Atlantic ridge. Figure 30.10 shows the four weather patterns that dominate the atmospheric circulation in winter around the North Atlantic. These four situations are obtained through statistical calculations on pressure data for the last fifty years. The isolines indicate the general direction of the wind.

As part of the heat is transported by atmospheric flow, each of these weather regimes has a different influence on temperature in Europe. In the case of winter in France, cold episodes are more linked to patterns such as the North Atlantic ridge or the negative phase of the NAO and mild spells are more related to the positive phase regimes of the NAO or the Scandinavian blocking. A change in the distribution of these patterns can affect the transport of heat, and thus have an impact on the surface temperature. The effect of this change in atmospheric circulation is comparable to the effect of external forcings (greenhouse gases, volcanism and solar activity) on the variability of temperatures. During the exceptionally hot summer of 2003, these high temperatures were shown to be partly due to the persistence of an anticyclone over Europe, which was in turn related to a precipitation anomaly over the Sahel, which dried up the atmospheric column. It is therefore essential to consider changes in the distribution of atmospheric circulation regimes in order to interpret climate change.

This representation facilitates the interpretation of relationships between meteorology (fluctuations on very short time scales, such as weather regimes) and climatology (centennial climate fluctuations). This concept was applied to a very different climate, such as that of the Last Glacial Maximum 21,000 years before the present. Using numerical simulations of the climate of this period, Kageyama et al. (1999) found that the notion of weather regimes was not

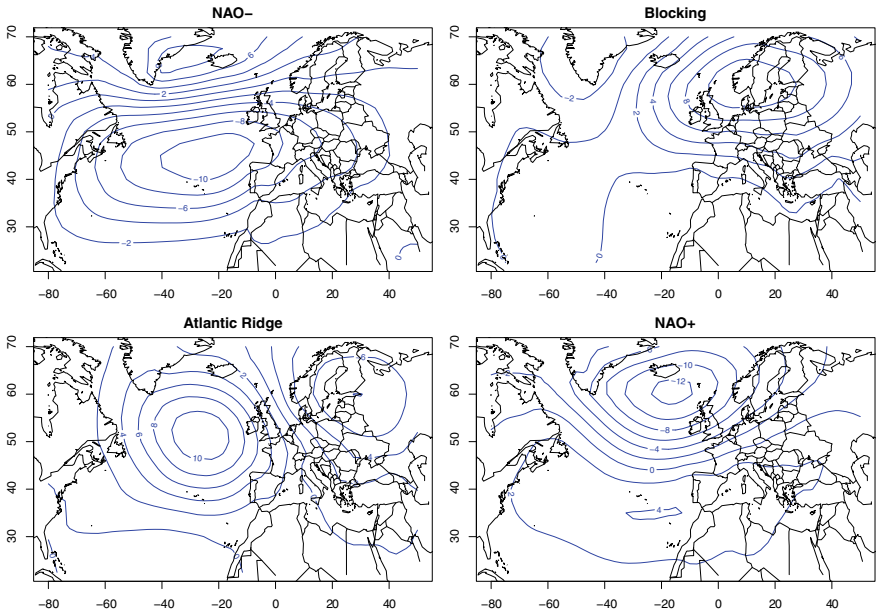

Fig. 30.10 Four common weather regimes around the North Atlantic. These regimes are calculated from sea-level pressure data from 1948 to 2009. General wind direction follows the isobars (iso-pressure lines) from west to east, turning in a clockwise direction around the high pressure zones. From top left clockwise, the weather regimes are: the negative phase of the North Atlantic Oscillation (NAO−), Scandinavian Blocking (Blocking), the positive phase of the North Atlantic Oscillation (NAO+) and the North Atlantic Ridge (Ridge)

applicable at that time, and that the types of stationary circulation observed today were not present then.

The Equatorial Pacific (ENSO)

El Niño events are a major manifestation of the coupled ocean-atmosphere variability of tropical regions originating in the Pacific Ocean (Philander 1990). The normal conditions of the Pacific Ocean are characterized by the 'warm pool' (using the language of climatologists) in the western part of the basin and by the development of an upwelling in the eastern part, brought about by the divergence of the southeast trade wind and, closer to the coast, by the meridian component of the northerly wind along the coast of South America, which favors the development of a coastal upwelling.

The El Niño years are characterized by abnormally warm waters between the date line and the South American coast, and are accompanied by a weakening of the temperature gradient across the Pacific basin (Fig. 30.11).

These oceanic structures are strongly linked to the atmosphere and to the southern oscillation and modulate the intensity of the trade winds, large-scale tropical circulation and precipitation. El Niño occurs every three to seven years and alternates with La Niña periods, which, on the contrary introduces cold conditions in the eastern equatorial Pacific. The impact of El Niño events is not limited to equatorial regions and spreads to mid-latitudes via an atmospheric wave train. Nevertheless, the intensity and frequency of these events, as well as the links between ENSO (El Niño-Southern Oscillation) variability and the average climate state, are still poorly understood.

The Holocene is a period of particular interest to understand these different aspects. Variations in the frequency and intensity of El Niño events for this period were recorded in corals, tropical glaciers and lake sediments. The different studies are in agreement that El Niño events were less intense during most of the Holocene and that the recent period is unusual in this context (Cobb et al. 2013; Carre et al. 2014; Emile-Geay et al. 2016). Although all modeling studies agree on this reduction in activity in the Mid

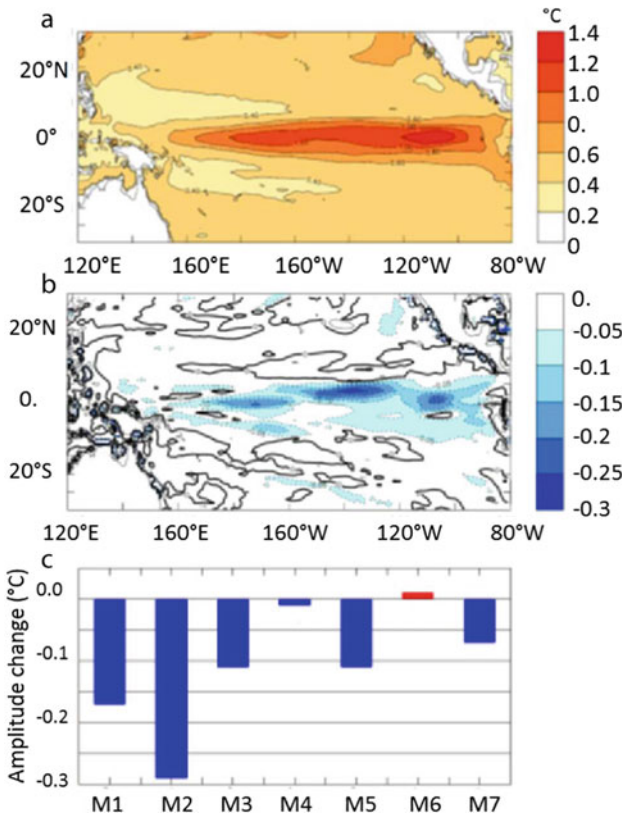

Fig. 30.11 **a** Interannual variability of simulated sea surface temperatures for the current period. **b** Changes in sea surface temperature variability for the Middle Holocene. **c** Changes in simulated variability by eight climate models for the Eastern Pacific. Figures (**a**) and (**b**) represent the median of the results of the various models shown in figure (**c**)

Holocene, they have come to slightly different conclusions about the origin of this evolution. All of the studies, however, attribute the main source of variation to solar radiation and a change in the seasonal cycle.

The first simulations were carried out with a model of intermediate complexity dedicated to the study of this phenomenon (Clement et al. 2000). The area covered by the model was limited to the tropical Pacific Ocean. The different equations are treated with regard to their difference from the mean state. These simulations do not therefore explicitly include changes in the seasonal cycle brought about by changes in insolation during the Holocene. Nevertheless, they have helped to improve our understanding of the response by the tropical ocean to changes in surface fluxes. The basic mechanism implies a behavioral difference between the western part of the basin, where warm waters accumulate, and the eastern part, where equatorial upwelling develops. During the northern polar summer, the increase in insolation warms the western part of the basin more than the east. It increases the temperature gradient across the basin and, strengthens the easterly trade winds and hence favors the development of equatorial upwelling and the temperature gradient. This feedback is called the Bjerknes mechanism (1969).

Although simulations from general circulation models also show wind intensification and a reduction in El Niño events, they do not show a coupling between winds and the temperature gradient across the basin at an annual scale. Rather, the results of these simulations indicate a link with large-scale changes in circulation. In particular, the intensification of the Asian monsoon promotes the intensification of the winds in the Pacific and their convergence towards the southeast of the Asian continent. These winds counteract the development of El Niño events (Zheng et al. 2008). Also the seasonal changes in insolation prevents the development of the upwelling Kelvin wave associated with El Ninõ (Luan et al. 2012).

This result is very different from that obtained for other climates, such as the climate of the future or the climate of the Last Glacial Maximum. It shows the strong constraint exerted by the changes in large-scale dynamics, which are dominant over the changes in local heat fluxes in tropical regions. For the Mid Holocene, this decrease in intensity of El Niño events is also accompanied by a reduction in the El Niño impact on other regions of the world, such as on the Sahelian region (Zhao et al. 2007). However, it is not yet possible to estimate whether these changes in teleconnection have played a role in the environmental modifications in Africa, nor to test this result against available data.

Fluctuations in El Niño events have also been reported for the last millennium, particularly in corals in the Pacific (Bradley 1999). The results indicate that the ENSO had characteristics in the mid-seventeenth century similar to those of the current period, with events that may have been as intense as the El Niño of 1997–1998. In the period from the twelfth to the fourteenth centuries, however, events appear to have been less intense. However, it is not possible to make the connection between the average conditions and the characteristics of the El Niño events. Other authors have found statistical links between the intensity of El Niño events and volcanic eruptions (Adams et al. 2003). ENSO variability is reduced in the years following a volcanic eruption, and this is confirmed by simulations conducted by Mann et al. (2005), but had not been identified in previous studies. These relatively contradictory results come from the difficulty in representing all of the facets of El Niño events in current models. Certain systematic biases in the models interfere with the representation of interannual variability, for example, the dual 'intertropical convergence zone' (ITCZ) which is overly pronounced in the eastern Pacific in coupled ocean-atmosphere simulations, or the fact that the structure of the equatorial upwelling is too confined along

the equator and extends too far into the western part of the basin [Chap. 8 of Solomon et al. (2007)].

Climate Extremes Relative to the Average

We have seen how it is possible to reconstruct average climate conditions from environmental indicators or simulate them with climate models of varying levels of complexity. By average we mean both in terms of space (hemispherically, globally or regionally) and time (seasonal, annual and decadal averages). Thus, most indicators show that the average temperature of the planet rose by $\sim$0.74 °C in the course of the last century. It is obvious that behind this average variation there are significant regional and temporal disparities: not all the places on the planet heat up at the same rate (high latitudes seem to be more affected than low ones), and gradual warming does not eliminate the possibility of local cold spells that can last several days. It is even statistically possible for local cold records to be beaten in a climate that is warming globally.

If we examine precipitation patterns, we can observe a trend towards aridification in southern Europe over the last few decades. This is reflected in a lower average seasonal water balance than during the first part of the twentieth century. On the other hand, observations show that extreme precipitation events (such as the flooding episodes that occur during the autumn in southern France or the wet winters in the UK) may become more frequent and more intense.

Typical extreme climate events can be classified into several categories:

- Heatwaves and cold snaps, i.e. when the temperature exceeds certain thresholds for a certain duration. The definition of a heatwave differs depending on the location: a heatwave in Paris is a typical summer in Seville!
- Intense precipitation and droughts. On a one-month scale, it is important to distinguish between long episodes of 'average' precipitation and those that last only a few hours. They are responses to distinctly different meteorological conditions.
- Storms, cyclones and other hurricanes.

These examples illustrate the use of statistics and probabilities to describe climate phenomena (von Storch and Zwiers 2001). These are particularly relevant when describing the interactions between normal climatological magnitudes (mean temperatures and precipitations) and the occurrence of extreme or rare events. A typical paradigm for describing temperatures is to represent them as an average and a standard deviation. These are the statistical parameters necessary to carry out reconstructions of average temperatures over recent millennia.

Let's assume that temperature can be represented by a Gaussian shape, a debatable assumption but one which simplifies the subject. If an event is defined as extreme when it is more than two standard deviations from the mean (which theoretically happens $\sim$2.5 times out of 100) then, at constant standard deviation, it is obvious that the probability of reaching a given higher temperature increases as the average temperature increases.

This hypothesis of Gaussian representation doesn't hold for daily precipitation, for which the standard deviation is ill-defined. One of the crucial parameters to describe precipitation is the one that describes the tail of the distribution, that is, the way rare values occur. A Gaussian possesses what is referred to as a 'light' tail, so that if big events are possible, they are exponentially rare.

However, the occurrence of rare major precipitations, for most locations on the planet, decreases much more slowly than in a Gaussian graph. The theory of extreme values makes it possible to statistically describe these phenomena (Coles 2001). Armed with this statistical theory, it is possible to model the different ways in which average precipitation and extreme precipitation behave which do not necessarily respond in the same way to climate change. This statistical characterization of climate variability makes it possible to predict the evolution of the probabilities of intense events, as well as the uncertainty associated with this prediction.

Outstanding Questions at the Beginning of the Twenty-First Century

Weather or Climate

Variations in the climate of the Holocene up to the present time have been punctuated by very short-lived meteorological events that have had a variety of consequences, but were often disastrous for societies. Since the end of the twentieth century, there appears to have been an upsurge in extreme events on the planet (the storms of 1999, record monsoons, deadly heat waves etc.). Assuming that this increase is not due to improved communication of information on the planet, the first question to be answered is whether this state of events has been 'observed' in the recent past (such as over the last millennium). To answer this question, it is essential to gather as much information as possible on extreme events (of all types) and put them into perspective. The gathering of this information is the subject of many national and international programs on historical research and the climate reconstruction of extreme events.

A parallel approach is the numerical simulation of climates at a resolution sufficiently high to enable the extremes to be adequately represented (over the current period). The most sophisticated models can be used to simulate the reported

weather over recent centuries, and thus to examine how meteorological statistics (regimes, extremes etc.) respond to forcings over the long-term. The confrontation of models with observations, within the context of extremes, becomes a crucial issue, involving complex statistical theories. These mathematical tools allow for the regionalization of the climate, with the aim of forecasting climate variables on a very small scale (e.g. precipitation at the scale of a city or a field) based on understanding of large-scale variables (such as atmospheric circulation on the scale of the North Atlantic basin).

Detection and Attribution of Climate Change

Understanding the role of human activity in climate change has become a major issue in recent years. The identification of this role is not limited to superimposing demographic, greenhouse gas and temperature curves on each other and highlighting their simultaneous growth. The difficulty in assessing this role is that there is no 'control' version of the Earth on which the climate with no human activity can be evaluated.

To attribute climate change to any one factor, it is necessary to evaluate the role of all other possible factors and to show that the characteristics of the change are compatible with this factor alone. This endeavor is usually done by researchers through climate model simulations, taking into account all of the physical factors minus one, and then comparing the simulations obtained with the observations. The key is to then identify the crucial factor(s) that best allows simulations to resemble observations. The difficulty with this evaluation is defining the statistical criteria for the comparisons and to obtain the necessary confidence intervals.

In order to make progress in this direction, improved models able to take the many interactions in the climate system into account are essential. This requires considering not only physical interactions involving energy and water cycles, but also the interactions between climate and the biogeochemical cycles. In particular, land use, deforestation, different types of aerosols (natural and anthropic) are often excluded from climate simulations. The distinction between meteorology and changes in average climate also necessitates improvement in the resolution of the models used, which goes hand in hand with better representation of small-scale processes. All of these elements combined with high-resolution data make it possible to better understand the risks associated with the profound changes in our environment linked to the ongoing global warming.

The attribution of extreme events is a rather recent field of research, that poses many scientific challenges (NAS 2016). Since 2012, the Bulletin of the American Meteorological Society (BAMS) publishes a summary of the analyses of past extreme events and their attribution to climate change. One of the teams has developed the weather@home system (Massey et al. 2015), which was devised to calculate tens of thousands of high resolution climate simulations. Those large ensembles are performed with present day greenhouse gas concentration and natural variability, and with natural variability only. They allow estimating the probability density function that a key climate variable (temperature, precipitation) exceeds a large threshold, with and without climate change. Other statistical methods have been devised since then to attribute extreme events to climate change (Stott et al. 2016; Jézéquel et al. 2018).

References

Adams, J., et al. (2003). Proxy Evidence for an El Niño-like Response to Volcanic Forcing. *Nature, 426*(6964), 274–278.

Bjerknes, J. (1969). Atmospheric teleconnections from equatorial pacific. *Monthly Weather Review, 97*(3), 163–172.

Braconnot, P., Harrison, S. P., Kageyama, M., Bartlein, P. J., Masson-Delmotte, V., Abe-Ouchi, A., et al. (2012). Evaluation of climate models using palaeoclimatic data. *Nature Climate Change, 2,* 417–424. https://doi.org/10.1038/nclimate1456.

Braconnot, P., Joussaume, S., Marti, O., & de Noblet, N. (1999). Synergistic feedbacks from ocean and vegetation on the African monsoon response to mid-Holocene insolation. *Geophysical Reseach Letters, 26,* 2481–2484.

Braconnot, P., et al. (2007a). Results of PMIP2 coupled simulations of the mid-holocene and last glacial maximum—Part 1: Experiments and large-scale features. *Climate of the Past, 3*(2), 261–277.

Braconnot, P., et al. (2007b). Results of PMIP2 coupled simulations of the mid-holocene and last glacial maximum—Part 2: Feedbacks with emphasis on the location of the ITCZ and mid- and high latitudes heat budget. *Climate of the Past, 3*(2), 279–296.

Bradley, R. S. (1999). *Paleoclimatology: Reconstructing climates of the quaternary*, 2nd edn. San Diego: Harcourt/Academic, 613p.

Brazdil, R., et al. (2005). Historical climatology in Europe—The state of the art. *Climatic Change, 70*(3), 363–430.

Cane, M., et al. (2006). Progress in paleoclimate modeling. *Journal of Climate, 19*(20), 5031–5057.

Carre, M., Sachs, J. P., Purca, S., Schauer, A. J., Braconnot, P., Falcon, R. A., et al. (2014). Holocene history of ENSO variance and asymmetry in the eastern tropical Pacific. *Science, 345,* 1045–1048.

Claussen, M., et al. (1999). Simulation of an Abrupt change in saharan vegetation in the mid-holocene. *Geophysical Research Letters, 26* (14), 2037–2040.

Claussen, M., & Gayler, V. (1997). The greening of the sahara during the mid-holocene: Results of an interactive atmosphere-biome model. *Global Ecology and Biogeography Letters, 6,* 369–377.

Clement, A. C., et al. (2000). Suppression of El Nino during the mid-holocene by changes in the earth's orbit. *Paleoceanography, 15*(6), 731–737.

Cobb, K. M., Westphal, N., Sayani, H. R., Watson, J. T., Di Lorenzo, E., Cheng, H., et al. (2013). Highly variable El Nino-southern oscillation throughout the holocene. *Science, 339,* 67–70.

Coles, S. (2001). *An introduction to statistical modeling of extreme values* (p. 208). London, New York: Springer.

Crucifix, M., et al. (2002). Climate evolution during the holocene: A study with an earth system model of intermediate complexity. *Climate Dynamics, 19*(1), 43–60.

de Noblet, N., et al. (1996). Possible role of atmosphere-biosphere interactions in triggering the last glaciation. *Nature, 23*(22), 3191–3194.

deMenocal, P., et al. (2000). Coherent high- and low-latitude climate variability during the holocene warm period, *Science*, *288*(5474), 2198–2202.

Emile-Geay, J., Cobb, K. M., Carre, M., Braconnot, P., Leloup, J., Zhou, Y., Harrison, S. P., Correge, T., McGregor, H. V., Collins, M., Driscoll, R., Elliot, M., Schneider, B., & Tudhope, A. (2016). Links between tropical Pacific seasonal, interannual and orbital variability during the Holocene. *Nature Geoscience, 9*, 168-+.

Garnier, E. (2009). *Les Dérangements du temps: 500 ans de chaud et de froid en Europe*. Paris: Plon.

Gasse, F. (2000). Hydrological changes in the African tropics since the last glacial maximum. *Quaternary Science Reviews, 19*(1–5), 189–211.

IPCC. (2007). Climate change 2007: The physical science basis. contribution of working group I to the fourth assessment report of the intergovernmental panel on climate change. In: S. Solomon, D. Qin, M. Manning, Z. Chen, M. Marquis, K.B. Averyt, M. Tignor & H.L. Miller (Eds.), Cambridge, United Kingdom and New York, NY, USA: Cambridge University Press, 996pp.

IPCC. (2013). Climate change 2013: The physical science basis. contribution of working group I to the fifth assessment report of the intergovernmental panel on climate change. In: T. F. Stocker, D. Qin, G.-K. Plattner, M. Tignor, S. K. Allen, J. Boschung, A. Nauels, Y. Xia, V. Bex, & P. M. Midgley (Eds.), Cambridge, United Kingdom and New York, NY, USA: Cambridge University Press, 1535pp.

Jansen, E., et al. (2007). Palaeoclimate, dans Solomon, In S. et al., (Ed.), *Climate change 2007: The physical science basis. contribution of working group I to the fourth assessment report of the intergovernmental panel on climate change*, Cambridge: Cambridge University Press.

Jézéquel, A., Dépoues, V., Guillemot, H., Trolliet, M., Vanderlinden, J.-P., & Yiou, P. (2018). Behind the veil of extreme event attribution, *Climatic Change*. https://doi-org.insu.bib.cnrs.fr/10.1007/s10584-018-2252-9.

Jolly, D., et al. (1998). Biome reconstruction from pollen and plant macrofossil data for Africa and the Arabian Peninsula at 0 and 6000 Years. *Journal of Biogeography*, *25*(6), 1007–1027.

Jones, P., & Mann, M. (2004). Climate over past millennia, *Reviews of Geophysics, 42*(2).

Joussaume, S. & Taylor, K. E. (1995). Status of the paleoclimate modeling intercomparison project, dans. In *Proceedings of the first international AMIP scientific conference, WCRP-92, Monterey,* USA, pp. 425–430.

Joussaume, S., et al. (1999). Monsoon changes for 6000 years ago: Results of 18 simulations from the paleoclimate modeling intercomparison project (PMIP). *Geophysical Reseach Letters, 26*(7), 859–862.

Kageyama, M., et al. (1999). Weather regimes in past climate atmospheric general circulation model simulations. *Climate Dynamics, 15*(10), 773–793.

Krinner, G., et al. (2005). A dynamic global vegetation model for studies of the coupled atmosphere-biosphere system, *Global Biogeochemical Cycles*, *19*(1).

Kropelin, S., & Kuper, R. (2006). Climate-controlled holocene occupation in the Sahara: Motor of Africa's evolution. *Science, 313*(5788), 803–807.

Kutzbach, J. E. (1988). Climatic changes of the last 18,000 years—observations and model simulations, *Science*, *241*(4869), 1043–1052.

Le Roy Ladurie, E. (1967). *Histoire du climat depuis l'an mil* (p. 381). Paris: Flammarion.

Liu, Z., et al. (2007). Simulating the Transient Evolution and Abrupt Change of Northern Africa Atmosphere-Ocean-Terrestrial Ecosystem in the Holocene, *Quaternary Science Reviews*, *26*(13–14), 1818–1837.

Luan, Y., Braconnot, P., Yu, Y., Zheng, W., & Marti, O. (2012). Early and mid-Holocene climate in the tropical Pacific: Seasonal cycle and interannual variability induced by insolation changes. *Climate of the Past, 8,* 1093–1108.

Mann, M., Bradley, R., & Hughes, M. (1998). Global-scale temperature patterns and climate forcing over the past six centuries. *Nature, 392,* 779–787.

Mann, M., et al. (2005). Volcanic and solar forcing of the tropical pacific over the past 1000 years. *Journal of Climate, 18*(3), 447–456.

Massey, N., Jones, R., Otto, F. E. L., Aina, T., Wilson, S., Murphy, J. M., et al. (2015). Weather@home—development and validation of a very large ensemble modelling system for probabilistic event attribution. *Quarterly Journal of the Royal Meteorological Society, 141*(690), 1528–1545. https://doi.org/10.1002/qj.2455.

National Academies of Sciences Engineering and Medicine. (2016). éd. *Attribution of extreme weather events in the context of climate change*. Washington, DC: The National Academies Press. https://doi.org/10.17226/21852.

Philander, S. G. H. (Ed.). (1990). *El Niño, La Niña, and the Southern Oscillation* (p. 312). San Diego: Academic Press.

Prentice, I. C., & Webb, T. (1998). BIOME 6000: Reconstructing Global Mid-Holocene Vegetation Patterns from Palaeoecological Records, *Journal of Biogeography*, *25*(6), 997–1005.

Renssen, H., et al. (2005). Simulating the holocene climate evolution at northern high latitudes using a coupled atmosphere-sea ice-ocean-vegetation model. *Climate Dynamics, 24*(1), 23–43.

Robock, A. (2000). Volcanic eruptions and climate. *Reviews of Geophysics, 38*(2), 191–219.

Ruddiman, W. (2007). The early anthropogenic hypothesis: challenges and responses, *Reviews Of Geophysics*, *45*(3).

Shindell, D., et al. (2001). Solar forcing of regional climate change during the maunder minimum, *Science, 294*(5549), 2149–2152.

Solomon, S., et al. (Eds.). (2007). *Climate change 2007: The physical science basis: Contribution of working group I to the fourth assessment report of the intergovernmental panel on climate change* (p. 996). Cambridge, New York: Cambridge University Press.

Stott, P. A., Christidis, N., Otto, F. E. Sun, Y., Vanderlinden, J.-P., van Oldenborgh, G. J., et al. (2016). Attribution of extreme weather and climate-related events, *Wiley Interdisciplinary Reviews, Climate Change, 7*(1), 23–41, https://doi.org/10.1002/wcc.380.

Taylor, K. E., et al. (2007). Estimating shortwave radiative forcing and response in climate models. *Journal of Climate*, *20*(11), 2530–2543.

Texier, D., et al. (2000). Sensitivity of the African and Asian monsoons to mid-holocene insolation and data-inferred surface changes. *Journal of Climate, 13*(1), 164–181.

von Storch, H., & Zwiers, F. W. (2001). *Statistical Analysis in Climate Research*. Cambridge: Cambridge University Press.

Wohlfahrt, J., et al. (2004). Synergistic feedbacks between ocean and vegetation on mid- and high-latitude climates during the mid-holocene. *Climate Dynamics, 22*(2–3), 223–238.

Zhao, Y., et al. (2005). A multi-model analysis of the role of the ocean on the African and Indian monsoon during the mid-holocene. *Climate Dynamics, 25*(7–8), 777–800.

Zhao, Y., et al. (2007). Simulated changes in the relationship between tropical ocean temperatures and the western african monsoon during the mid-holocene. *Climate Dynamics, 28*(5), 533–551.

Zheng, W., et al. (2008). ENSO at 6 Ka and 21 Ka from ocean-atmosphere coupled model simulations. *Climate Dynamics, 30*(7–8), 745–762.

From the Climates of the Past to the Climates of the Future

31

Sylvie Charbit, Nathaelle Bouttes, Aurélien Quiquet, Laurent Bopp, Gilles Ramstein, Jean-Louis Dufresne, and Julien Cattiaux

This chapter connects everything we have learned about past climates (both from the analysis of natural archives and from numerical simulations), and future climate projections. The models used to explore the future are similar to those used for past climates, except that the results are based on emission scenarios of greenhouse gas emissions whereas past climate simulations may be compared to reconstructions from the natural archives described in volume 1. The climate of the past 1000 years can be seen as the 'background noise' of the recent natural evolution of the climate system. On this basis, the current climate change can be analyzed. Over the longer term, analysis of ice cores allows us to trace back the history of atmospheric CO_2 concentration over the last 800,000 years, and shows that the anthropogenic disturbance (producing an atmospheric CO_2 concentration currently in excess of 410 ppm) is completely outside the documented glacial-interglacial variations over the last million years, ranging from 180 to 280 ppm. With this awareness you are well equipped to now explore the climate of the future.

Climate Observations in Recent Decades: The First Signs of Warming

The principles of the physical laws governing the temperature on the Earth's surface were formulated at the beginning of the nineteenth century by Joseph Fourier, who established that the energy balance at the surface of our planet is dominated by incoming solar radiation which is the primary source of energy, and infrared emission exchanges which control energy losses. He concluded that any change in surface conditions could lead to a change in climate and argued that *the development and progress of human societies can notably change the state of the ground surface over vast regions, as well as the distribution of waters and the great movements of the air* and that *such effects have the ability to cause the mean degree of heat to vary over the course of several centuries*. Joseph Fourier also identified the trapping of infrared radiation by the gases in the atmosphere (Fourier 1824).

This was the beginning of the greenhouse effect theory. Starting from this seminal work, numerous studies were conducted throughout the nineteenth and twentieth centuries. Within a scientific context where the understanding of the glacial-interglacial cycles was the matter of a very hot debate, the Swedish chemist Svante Arrhenius was the first one to quantify the effect of the atmospheric carbon dioxide concentration on the average surface temperature of the Earth and to suggest that substantial variations of the atmospheric CO_2 levels could explain the glacial advances and retreats. However, it is only since the late 1970s that we can calculate precisely the radiation exchanges using radiative transfer codes and spectral databases to break down energy by wavelength.

Long time refuted, or at least underestimated, global warming has now become an incontrovertible reality: in 2001, the scientific review by the Intergovernmental Panel on Climate Change (IPCC) concluded that there was a growing body of evidence confirming global warming as well as other changes in the climate system. Based on the results of numerical experiments with coupled atmosphere-ocean general circulation models (AOGCMs), the Fifth IPCC Assessment Report, published in September 2013 (IPCC 2013), established with a probability of more than 95%, that the global warming observed in recent decades is due to anthropogenic activities. This situation has no

S. Charbit (✉) · N. Bouttes · A. Quiquet · L. Bopp · G. Ramstein
Laboratoire des Sciences du Climat et de l'Environnement, LSCE/IPSL, CEA-CNRS-UVSQ, Université Paris-Saclay, 91190 Gif-sur-Yvette, France
e-mail: Sylvie.Charbit@lsce.ipsl.fr

J.-L. Dufresne
Laboratoire de Météorologie Dynamique/IPSL, Université Pierre et Marie Curie, BP 99, 4 Place Jussieu, Cedex 05, 75252 Paris, France

J. Cattiaux
Centre National de Recherches Météorologiques, Université de Toulouse, CNRS, Météo-France, 42 Avenue Gaspard Coriolis, 31057 Toulouse Cedex, France

G. Ramstein et al. (eds.), *Paleoclimatology*, Frontiers in Earth Sciences,
https://doi.org/10.1007/978-3-030-24982-3_31

direct equivalent in the past climates of the Earth. The last time we find a climate with the current level of atmospheric CO_2 is several million years ago. The climate at this period corresponds to a warm Earth, with a reduced cryosphere (no Greenland) and a smaller Antarctic ice sheet yielding a much higher sea level (15–30 m higher as reported by Haywood et al. 2011, 2016).

Evolution of Greenhouse Gases

We have seen in previous chapters that the greenhouse effect is above all a natural phenomenon, without which the surface temperature of the Earth would be about −18 °C, making life, as we know it today, impossible. The main greenhouse gases naturally present are water vapor (H_2O), carbon dioxide (CO_2) emitted by volcanic eruptions and forest fires, methane (CH_4) produced by wetlands and various fermentation processes, ozone (O_3), and the nitrous oxide (N_2O) emitted by soils. Industrialization has led societies to discharge massive amounts of these gases through the combustion of fossil fuels (oil, gas, coal), deforestation, agriculture, intensive livestock breeding and fertilizer production. An inhabitant of an industrialized country releases on average ten tons of carbon per year (or CO_2 equivalent) compared with only two tons per year for an inhabitant of most emerging countries. However, these estimates mask large disparities from one country to another, with differences ranging from 0.12 ton of CO_2 per year and per inhabitant for Ethiopia to 49.3 tons of CO_2 per year and per inhabitant for Qatar (from Global Carbon Atlas 2017). In addition, human activities produce fluorinated gases (CFCs, HFCs, PFCs, SF_6) used especially in refrigeration and air conditioning systems, as well as in aerosol cans. In total, more than forty of these gases have been identified by the IPCC. The greenhouse effect produced by human activities is called *additional greenhouse effec*t. The contribution of each gas to the additional greenhouse effect can be estimated by taking into account the increase in their concentration and their 'radiative efficiency'. Between 1750 and 2011, the variation in their concentration increased the greenhouse effect by about 2.83 W/m^2, with main contributions of 64% for CO_2, 17% for CH_4, 12% for O_3 and 6% for N_2O (Fig. 31.1). Since 1750, in other words, since the beginning of the industrial era, this anthropogenic phenomenon has produced an energy imbalance of the Earth and has caused a warming of the lower layers of the atmosphere. The additional radiative forcing corresponds to approximately 1% of the total radiation received.

Analysis of air bubbles trapped in the ice of the Antarctic ice sheet revealed that over the last 800,000 years, CO_2 levels have changed by no more than 100 ppm, going from 180 ppm during glacial periods to 280 ppm in interglacial periods. For periods prior to 1950, analysis of air bubbles in the ice is the only reliable way to track the chemical composition of the atmosphere. In recent times, the first direct measurements (i.e. in situ) were obtained in 1958 at the Mauna Loa site in Hawaii (Keeling et al. 1995). These measurements revealed for the first time that not only was CO_2 increasing in the atmosphere, but that this increase was modulated in line with seasonal variations due to photosynthesis of the terrestrial biosphere. This first measurement campaign was then supplemented by campaigns covering other sites in the northern and southern hemispheres. Currently, a wide range of direct and indirect measurements confirm that atmospheric CO_2 levels have increased since the beginning of the preindustrial era, rising from 275–285 ppm between the years 1000 and 1750, to about 380 ppm in 2005 (Fig. 31.1) and to more than 410 ppm in 2018, that is a difference of more than 100 ppm compared to the pre-industrial period. About 30% of the current atmospheric CO_2 has been emitted by anthropogenic sources. In addition, the amount of annual anthropogenic emissions has been continuously increasing throughout the industrial era. In 1990, 2000, 2010 and 2017, global CO_2 emissions from human activities (fossil fuel combustion, cement production, land-use change) reached 22, 25, 32 and 37 Gt CO_2/yr respectively. The increase in annual CO_2 emissions accelerated from 1.1% per year in the 1990s to 3.3% per year in the 2000s. This growth rate of atmospheric CO_2 is ten times faster than the highest rates recorded in ice cores, and is mainly due to the rapid growth of developing countries and a drop in the efficiency of fossil fuel use in the global economy. Between 65% and 80% of CO_2 released in the atmosphere is trapped and/or dissolved in the ocean and the terrestrial biosphere in 20–200 years, depending on the various estimations. The rest is removed by slower processes, including chemical weathering and rock formation that take several thousands of years, indicating that the effect of anthropogenic CO_2 will persist for hundreds to thousands of years into the future (Archer et al. 2009).

Atmospheric methane is the third most important greenhouse gas after H_2O and CO_2 in terms of atmospheric concentration. Averaged over 100 years, the radiative efficiency of methane is estimated to be 28–36 times greater than that of CO_2 but its lifetime in the atmosphere (i.e. the time it takes for a CH_4 molecule to be removed from the atmosphere by chemical reaction) is much less ($\sim$ 9–12 years) than that of CO_2. Ice core records indicate that CH_4 levels in the atmosphere also show variations from about 350 ppb (during glacial periods) to 700 ppb (during interglacial periods). In 2011, the level of methane in the atmosphere, established from a network of measurements covering both hemispheres, was at 1803 ppb, a level never attained, at least throughout the last 800,000 years. Since the pre-industrial era, CH_4 has increased by approximately 250%. Although the growth rate of methane was over 1%

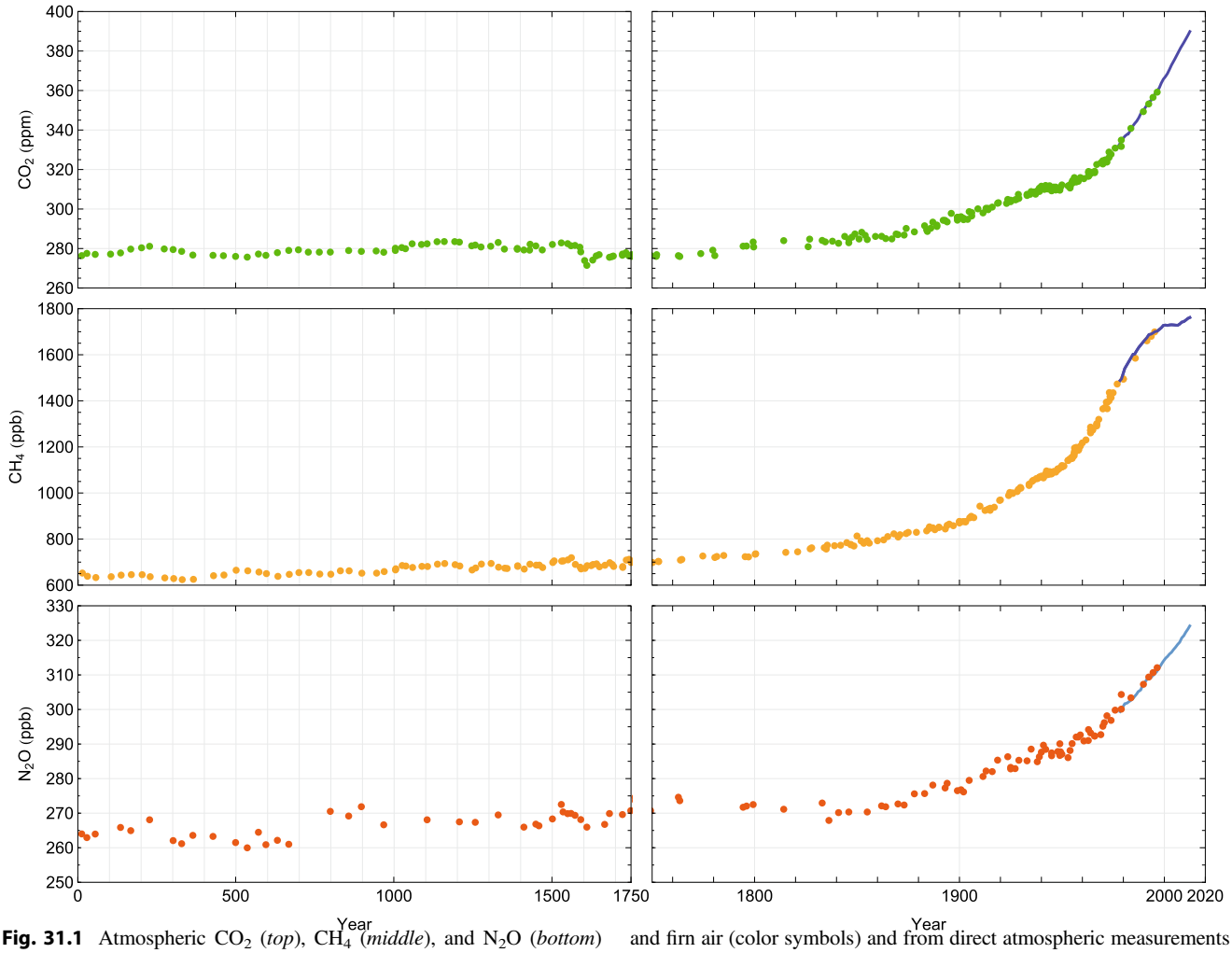

Fig. 31.1 Atmospheric CO_2 (*top*), CH_4 (*middle*), and N_2O (*bottom*) concentrations history since the beginning of the industrial era (right) and from years 0 to 1750 (left), determined from air trapped in ice cores and firn air (color symbols) and from direct atmospheric measurements (blue lines, measurements from the Cape Grim observatory) (*Source* IPCC 2013)

per year during the 1970s and early 1980s, the 1990s and early 2000s saw this rate stabilize, resulting in relatively stable concentrations. However, atmospheric CH_4 concentrations started growing again from 2007, although the true cause of this renewed increase is still unclear. CH_4 is emitted by many agricultural activities (ruminant farming, rice cultivation), by industrial activities (biomass combustion, the oil and gas industry), as well as by natural processes (wetlands, permafrost, peat bogs). There are no available data on annual CH_4 emissions from industrial activities as these are difficult to quantify. When the climate warms up, CH_4 emissions from natural processes can increase. This has been observed with permafrost thawing in Sweden, but no large-scale evidence is available to clearly relate this process to the recent increase in methane. If the observed increase is caused by the response of natural reservoirs to global warming, this could last for several decades, even centuries, and thus reinforce the enhanced greenhouse effect (positive feedback).

The greenhouse gas with the fourth contribution to radiative forcing is nitrous oxide (N_2O). Its level has steadily increased from 270 ppb in 1750 to 323 ppb in 2011. The main natural emissions of this gas come from soil microbial activity and ocean processes. As for anthropogenic emissions, they come mainly from the use of nitrogen fertilizers in agriculture, fossil fuel combustion and chemical industry.

Halocarbons (or halogenated hydrocarbons), responsible in particular for the destruction of stratospheric ozone, generate a lower radiative forcing (about 0.35 W/m^2 in 2011) than the three main greenhouse gases (CO_2, CH_4 and N_2O), whose total contribution is 2.30 W/m^2. The emissions of these gases are almost exclusively anthropogenic. To combat the destruction of stratospheric ozone, the Montreal Protocol regulated the production of halocarbons containing chlorine (chlorofluorocarbons or CFCs) and bromine. Substitute products adopted to replace CFCs, for example in refrigeration processes, do not affect the ozone layer but remain powerful greenhouse gases. Perfluorinated

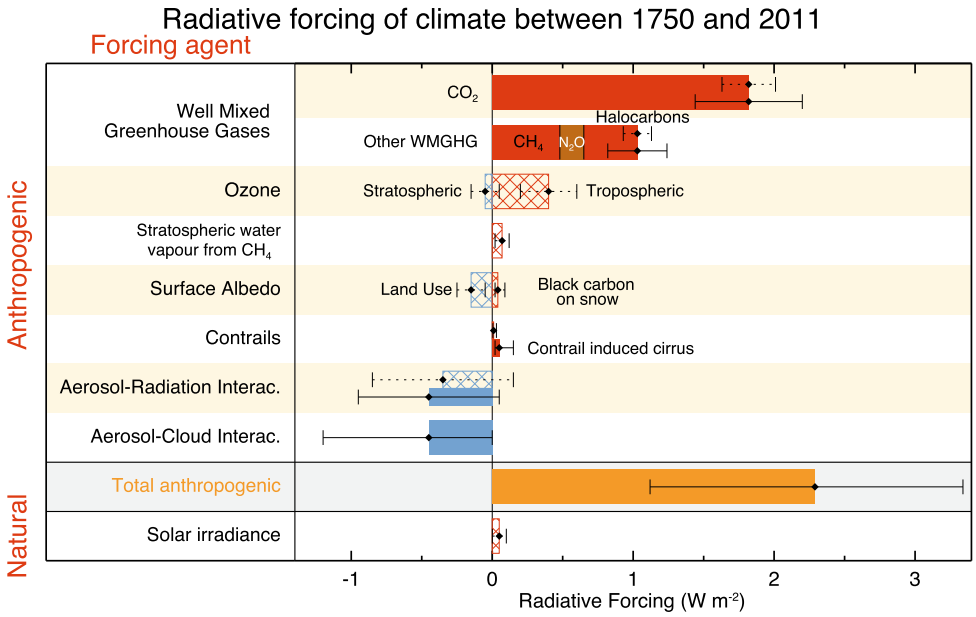

Fig. 31.2 Main components of radiative forcing involved in climate change coming from both natural processes and human activities. The values correspond to the estimated difference between 2011 and 1750. Anthropogenic contributions are responsible for most of the radiative forcing. Positive forcings cause global warming, while negative forcings lead to cooling. The black lines associated with each box show the associated uncertainties (*Source* IPCC 2013)

hydrocarbons (PFCs, such as CF_4 and C_2F_6) and sulfur hexafluoride have extremely long residence times in the atmosphere and are excellent absorbers of infrared radiation. Thus, even though these compounds are released in small quantities, their impact on the greenhouse effect and the climate is far from negligible.

Although ozone is also a greenhouse gas, it is not emitted directly, but is formed from photochemical reactions involving other precursor gases of natural and anthropogenic origin. Its impact on the radiative budget depends on the altitude at which the changes in its concentration occur, as these vary spatially. Moreover, once formed, its residence time in the atmosphere is very short, unlike the greenhouse gases mentioned previously. For this reason, it is difficult to establish precisely its role in the radiative budget.

In addition to the production of greenhouse gases, human activities also produce aerosols. These can have a direct impact on radiative forcing by absorbing or reflecting solar and infrared radiation. Some of them contribute negatively to radiative forcing, others positively. Finally, aerosols can have an indirect effect by modifying the reflective properties of clouds. Taking the totality of aerosols into account, the overall contribution is negative and therefore partially compensates the effect of greenhouse gases. In 2011, the estimated forcing of anthropogenic aerosols is about -0.9 W/m^2, albeit with large uncertainties (-1.9 to -0.1 W/m^2, IPCC 2013). Overall, taking into account both greenhouse gases and aerosols, anthropogenic activities are responsible for a positive radiative forcing since the beginning of the industrial era, estimated at 2.3 W/m^2 in 2011 (IPCC 2013). The main components involved in climate change are summarized in Fig. 31.2.

Evolution of Surface Temperatures

Instrumental observations documented for the past 150 years show an overall increase in temperature on the Earth's surface (Fig. 31.3). According to the synthesis presented in the Fifth IPCC Assessment Report (IPCC 2013), it has increased by an average of 0.89 ± 0.20 °C over the last century (1901–2012), that is an increase of about 0.08 ± 0.02 °C per decade. This multi-decadal signal (warming trend) emerges as significant from the noise of the internal climate variability – a global warming is thus detected. Furthermore, dedicated studies have shown that the observed warming cannot be explained solely by natural forcings (solar and volcanic activities), and that anthropogenic forcings necessarily contribute: global warming is thus *attributed* to both natural and anthropogenic causes. In particular, *"it is extremely likely that human activities caused more than half of the observed increase in global average surface temperature from 1951 to 2010"* (IPCC 2013). However, this increase has not been steady over time, due to decadal fluctuations in both the internal climate variability and the external natural and anthropogenic forcings. Indeed, the observations highlight two periods of accelerated warming: one from 1910 to about 1940, and the other, even more important, since 1970, while temperatures were relatively stable between 1940 and 1970 (Fig. 31.3). Trends computed over short time periods are highly uncertain. For instance, the warming rate over the 15-year period 1998–2012 is about 0.05 °C per decade, which is weaker than the 1901–2012 warming trend mentioned above (0.08 °C per decade). However, the associated confidence interval is large (± 0.10 °C per decade), so that there is no inconsistency between both values. More

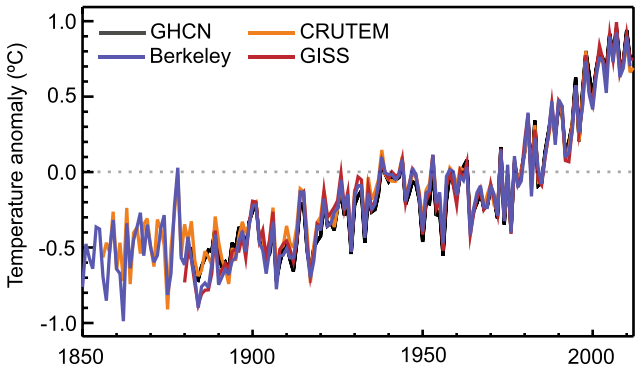

Fig. 31.3 Global annual average land-surface air temperature (LSAT) anomalies relative to the 1961–1990 climatology from the latest versions of four different data sets (Berkeley, CRUTEM, GHCN and GISS) (*Source* IPCC 2013)

generally, global warming is a long-term process that is superimposed on the internal climate variability, and it remains possible to have occasional short-term cooling trends in a warming world. Importantly, the decade of the 2000s appears to be the warmest compared to the entire period covered by instrumental data. The decade of the 2010s is likely to break this record, since the years 2014–2018 have been the five hottest years observed at global scale.

The values mentioned above are global mean annual values. There are, in fact, large disparities from one region to another, as well as large seasonal disparities. In general, warming is amplified in high latitude regions in summer, partly due to the albedo effect induced by the decrease in snow cover and/or in the sea-ice extent. In addition, warming over the continents is much faster than over the oceans because of their weaker thermal inertia but also due to changes in evaporation. Not all regions exhibit a statistically significant warming over the observational period (e.g. South Greenland and North-West Atlantic); but no region exhibits a statistically significant cooling. Climate change detection is a signal-to-noise ratio problem: the higher the temperature variability, the harder it is to detect long-term warming. In other words, internal variability can hide climate change over small spatial domains and/or short time periods; but this does not call into doubt the existence of a long-term global warming trend, nor the fact that it is attributable to the anthropogenic fingerprint.

Evolution of Temperature in the Troposphere

In response to an enhanced greenhouse effect (e.g. due to anthropogenic activities), the physical theory of radiative transfer indicates that not only the surface, but the entire lower atmospheric layer, namely the *troposphere* (altitude 0–10 km), should warm. Conversely, the atmospheric layer above, namely the *stratosphere* (altitude 10–50 km), should cool. Observations of the vertical temperature profile are more difficult to obtain than at the surface, but available data unanimously reveal a warming troposphere and a cooling stratosphere since the mid-twentieth century. This provides further evidence for the anthropogenic nature of the recent climate change. However, there has been a recent controversy about the amplitude of these changes. The IPCC's Fourth Assessment Report published in 2007 (IPCC 2007) indicated persistent uncertainty on temperature trends in the middle atmosphere since 1979. Indeed, most of the available data from radiosondes and satellite measurements indicated a lower warming in the tropical high troposphere (between 10 and 15 km altitude) than that recorded at the surface, whereas all of the climate models projected an amplified warming in this zone of the atmosphere, especially in the tropics. This apparent difference between data and numerical model outputs has been widely cited to emphasize the inconsistency between observational data and models. Some have used this example to call into question the impact of human activities on the climate, even going so far as to deny the existence of the current warming. But more in-depth analyzes have revealed that the observations on which this controversy was based were unreliable, particularly because the measurements did not take into account interannual climate variability. Since then, researchers have re-analyzed these measurements using more rigorous techniques (Allen and Sherwood 2008). New estimates of these observations show greater warming than previously reported, and this new larger set of estimates now falls within the model trends, thus removing any concerns expressed in the 2007 Fourth IPCC Assessment Report.

Precipitations and Water Balance

While the increase in mean surface temperatures is one of the most obvious manifestations of ongoing climate change, spatial and temporal changes in the hydrological cycle (e.g. precipitation, evaporation, runoff) appear to be just as important but are much more difficult to simulate. The term precipitation refers to all the meteoric waters that fall to Earth in the form of liquid (rain, mist, showers) or solid (snow, hail, sleet) water. The formation of precipitation requires the condensation of water vapor around what are called condensation nuclei, which allow the water molecules to aggregate together. This phenomenon is called coalescence. Condensation only occurs when the amount of water vapor per unit of volume exceeds a threshold value, called the saturation value. This is an increasing function of temperature. Warmer air can therefore hold more water vapor before condensation occurs: this physical law is called the Clausius-Clapeyron relationship. For the Earth's atmosphere, the additional humidity that can be held by warmer air is estimated at 7% per °C. Once the water vapor

condensates, the different precipitation episodes can be categorized according to their intensity, duration, frequency, and by type (stratiform, like those caused by depressions in the mid-latitudes, or convective, like heavy rains and tropical cyclones in the intertropical convergence zone). These characteristics depend to a large extent on local temperature and weather conditions (wind speed and direction, pressure, humidity, evaporation). It is thus clear that a change in any of these parameters will affect the hydrological cycle as a whole.

Throughout the twentieth century, for example, annual precipitation increased on the eastern side of the South and North American continents. In contrast, a significant rainfall deficit has been observed in south and west Africa, as well as in the Sahel. In northwestern India, an increase of about 20% was observed for the period 1901–2005, despite a sharp decrease between 1979 and 2005. However, changes in precipitation are hard to measure using the existing records, and there is only medium confidence that observed trends are due to the anthropogenic influence.

Observed trends in relative humidity (i.e. air humidity/saturation humidity) suggest that these have remained constant through the tropospheric column down to the surface. However, if the amount of water vapor at saturation increases and the relative humidity remains constant, then this means that the absolute humidity (and thus the amount of water vapor) has increased in the atmosphere. Observations indicate that tropospheric water vapor has increased by about 3.5% over the past 40 years, which is consistent with the observed temperature change of 0.5 °C over the same time period. Climate models confirm these empirical observations: a warmer climate leads to increased moisture content in the atmosphere and more intense precipitation events (although total precipitation over a full year is reduced) and therefore flooding is more likely to occur. Thus, in winter, it is observed that for most of the extratropical land surface areas of the northern hemisphere, the greatest precipitation is linked to higher temperatures. Conversely, in areas with low rainfall, such as the Mediterranean basin, rising temperatures are associated with a higher risk of drought. This general intensification of the hydrological cycle can be summarized by: wet gets wetter, dry gets drier.

Added to these complex phenomena is the variability in atmospheric circulation. In Sect. "Climate Variability", the modes of atmospheric variability will be examined in greater detail. However, we already know that fluctuations in atmospheric circulation over the North Atlantic brought heavy rainfall in the 1990s to northern Europe, and, in contrast, led to a drying-up of the Mediterranean basin. In addition, the severe Sahelian drought over more than 20 years (1970–1990) was linked to changes in both atmospheric circulation and surface ocean temperatures in all three of the Pacific, Indian and Atlantic basins. Although this trend towards drought still persists, it has become less pronounced since the early 1990s.

There are numerous uncertainties surrounding the determination of the hydrological cycle variables. This is due to a lack of data for some regions (for example, Canada, Greenland and Antarctica, some desert regions such as the Sahara, the Tibetan plateau and over the oceans), and to the fact that accurate measurements have only been available for a very short time. In addition, it is very difficult to measure precipitation rates and to accurately quantify their changes at the global and regional scales.

In situ measurements are affected by atmospheric conditions (e.g. the effect of strong winds especially on snowfall). Spatial observations, on the other hand, provide only instantaneous measurements and are affected by the uncertainties associated with the algorithms used to convert radiometric measurements into precipitation rates. Because of these difficulties, climatologists explore the coherence between the whole set of complementary variables associated with the hydrological cycle. One way to represent precipitation changes over the past century or over decades is to calculate the Palmer Drought Severity Index. This index is a measure of drought, in other words, the accumulated surface soil moisture deficit compared to average local conditions. It is based on recent rainfall and atmospheric humidity (determined from temperatures). In general, analyzes of the last century suggest a trend towards drying for much of Africa, southern Eurasia, Canada and Alaska. Other direct or indirect measurements (e.g. from river flow estimations or ocean salinity measurements) show that during the twentieth century precipitation has generally increased on land surfaces between 30°N and 85°N, but significant reductions have been observed over the last thirty or forty years between 10°S and 30°N.

At present, the main challenge is to determine the interannual variations and trends in precipitation changes over the oceans. Global averages are often unrepresentative and mask large regional disparities. However, particularly pronounced droughts in the last 30 years, as well as heavy rainfall events in many regions clearly illustrate an intensification of the hydrological cycle.

Extreme Weather Events

Extreme weather events result from exceptional fluctuations of a climate variable, and are generally associated with significant impacts on society and the environment. As illustrated by the frequent exposure by the media of the most impressive events, the statistical evolution of climate extreme characteristics (frequency, amplitude) is of major concern for current climate change, especially in the development of adaptation strategies. The term 'weather extreme'

covers a wide spectrum of events at spatio-temporal scales ranging from intense local precipitation lasting a few hours to exceptional hot years for the whole planet. In addition, because they are by definition rare, extreme events offer few case studies, and the detection of possible man-induced trends requires analysis over long periods of time and/or large spatial domains. The study of extreme events is thus often restricted by the availability of datasets of sufficient spatial and temporal resolution.

Temperature Extremes

Extreme temperature events typically affect large areas (usually several thousand kilometers), and are often accompanied by extremes in other climate variables (e.g. drought during a hot summer, snowstorms during a cold winter). Their impacts on ecosystems and human activities are thus particularly important.

One of the most striking recent examples is the European heat wave in summer 2003 which, with a temperature 2.5 °C higher than the seasonal mean, exceeded by three standard deviations the distribution of summer temperatures in Europe. It had dramatic socio-economic and environmental impacts: high mortality, loss of energy production, acute urban pollution, fires, accelerated melting of glaciers etc. The return period of this particular event was estimated at 250 years at the time it occurred (2003); it would have taken 4 times longer (1000 years) without human intervention (Stott et al. 2004).

This illustrates an expected feature of climate change: hot extremes become more frequent in a warmer world, and conversely, cold extremes become less common, but remain still possible. For instance, in the U.S., the ratio of the record of high maximum daily temperatures to the record of low minimum temperatures—which should be 1 to 1 in a stationary climate—is currently about 2 to 1 and is likely to reach about 50 to 1 by the end of the twenty-first century (Meehl et al. 2009).

At the global scale the geographical distribution of changes in the frequency and amplitude of temperature extremes is consistent with the distribution of average warming (IPCC 2013). This finding is nonetheless nuanced by the fact that changes in temperature distributions are often more complex than a uniform shift towards warmer values: spreading, tightening, and/or asymmetry of values may also show up in the statistical distribution. For instance, in Europe and Central U.S., the variability of summer temperatures is expected to increase in a warmer climate, due to the increase in evapotranspiration which leads to drier soils (Douville et al. 2016). This would result in a widening of the temperature distribution, and further amplify the increase in the frequency of hot extremes in these regions.

Precipitation Extremes, Tropical Cyclones and Extra-Tropical Storms

Changes in the frequency and intensity of droughts and floods, in response to global warming, are also of major concern, as our industrialized societies become increasingly vulnerable to rainfall extremes. Although the study of droughts is similar to that of heat waves, since they both have impacts over large areas, the analysis of extremes of intense precipitation is more difficult because it requires data with finer spatio-temporal resolution.

As illustrated by the record floods in summer 2002 in Europe, intense precipitation events have been on the increase since 1950 in the mid-latitudes of the northern hemisphere. Even in the Mediterranean Basin, where rainfall is decreasing on average, the episodes of heavy rainfall are more intense. A recent example is given by the intense precipitation that occurred in South of France in autumn 2018. This upward trend is noticeable on a global scale, although the increases are more moderate than those observed for temperature. Changes in precipitation extremes are consistent with the Clausius-Clapeyron relationship: warmer air can hold more humidity, so there is more water to be mobilized by condensation when rainfall events occur.

Paradoxically, the extent of regions affected by drought is also increasing, illustrating the fact that climate change not only affects the mean of statistical distributions, but also its variability. Africa, southern Eurasia and North America are, according to the Fifth IPCC Assessment Report, the regions most affected by these droughts in recent times, as illustrated by the dry conditions persisting from 2014 to 2018 over the west of the United States (California). The increase in the frequency and/or intensity of both intense rainfall episodes and droughts is consistent with the overall intensification of the hydrological cycle in a warmer world (wet gets wetter, dry gets drier).

Lastly, climate change may also affect meteorological systems like tropical cyclones or extra-tropical storms. In a warmer world, the former are expected to occur less frequently in general, due to less frequent atmospheric conditions favorable to the cyclogenesis (reduced temperature difference between the surface and the high-troposphere). However, once triggered, future cyclones should get more energy from a warmer ocean: the intensity of the strongest tropical cyclones is therefore expected to increase. Unfortunately, so far, trends are difficult to detect from the past due to the lack of homogeneous data. For extratropical storms, forecasting is even more difficult: projections performed with climate models do not unanimously agree on their frequency and/or intensity. The only robust future signal seems to be a poleward shift of the storm tracks, but again, available observations are insufficient to capture any past trend.

Evolution of the Cryosphere

The exact estimate of the influence of human activities on climate is still limited because it is critically dependent on our ability to distinguish the signal related to this additional radiative forcing from the natural variability of the climate. However, there is a growing number of tangible factors indicating that man has had a perceptible influence on the climate. In particular, the global warming observed over the past century has been accompanied by a rise in sea level (Clark et al. 2016), largely attributed to the thermal expansion of the oceans, but also to significant changes in the cryospheric components of the climate system over the whole planet. The cryosphere represents all the water in solid form on Earth and contains more than 70% of the Earth's freshwater reservoir. It is an excellent indicator of climate change. It includes ice sheets, floating ice-shelves, mountain glaciers, snow and sea ice, but also the water in rivers and lakes that freezes in winter, as well as the permafrost, that is to say the permanently frozen ground, covered by an 'active' soil layer which melts each summer and whose thickness is variable.

Each of these components interacts in various ways with the other components of the climate system over a wide range of time scales, from seasonal (snow, permafrost, rivers, lakes, sea ice) to a hundred thousand years for the glacial-interglacial cycles. While the cryosphere is particularly important in the polar regions, there are also many glaciers in the low and mid-latitude regions, which provide an overview of the relationship between climate change and changes in the cryosphere.

Snow Cover

Estimating the extent of snow cover and the physical properties of snow is of paramount importance for both hydrological applications, such as modeling or predicting runoff due to snowmelt, and for the understanding of local or regional weather patterns. Typical snow parameters, derived from radar data, include the extent of snow cover, the water equivalent of the snow layer, and the state of the snow (wet or dry).

The extent of snow cover has a direct influence on the energy balance on the Earth's surface, but also on the soil water content. Fresh snow reflects between 80 and 90% of incident solar radiation. The warming trend decreases the snow cover, which in turn decreases the fraction of solar energy reflected back to space, and increases the absorption of incoming radiation, thereby increasing warming, which in turn accelerates the snow melting. This amplifying mechanism is known as the 'temperature-albedo' effect. Thus, the surface temperature is strongly dependent on the presence or absence of snow. Another important aspect of snow cover is the role it plays in thermal insulation. In winter, snow covered grounds cool much less quickly than bare grounds, hence the importance of snow depth for plant and animal life. Finally, melting snow in spring and summer requires a high latent heat of fusion, so that snow cover represents a significant heat loss for the atmosphere during the melting season. As a result, seasonal snow produces thermal inertia within the climate system, as it involves significant energy exchanges, with little or no change in temperature.

In the northern hemisphere, snow cover varies seasonally with a maximum in winter and a minimum in summer, but with large inter-annual variations. Since the end of the nineteenth century, daily records of snowfall and snow depth have been kept by many countries. Nevertheless, these measurements were only fully developed after 1950, and in particular from 1966 onwards, with the arrival of satellites.

All of these data series reveal that snow cover has decreased in spring and summer since the 1920s, with an even more striking decrease since the end of the 1970s. According to the Fifth IPCC Assessment report, this decrease in March-April snow cover extent ranges from −0.8% per decade over the 1922–2012 period to −2.2% per decade between years 1979 and 2012. For the fall and winter seasons, the signal is less clear: some data sets suggest positive trends as a result of increased snowfall in a warming climate, while others suggest negative trends similar to what is observed in spring and summer. Nevertheless, there is a consensus that the mean annual snow cover has decreased with a shift from February to January of the maximum extent, an earlier onset of melting ($\sim$5.3 days since winter 1972–1973) and thus a reduction of snow cover duration. This drop in snow cover is mainly observed in the northern hemisphere. In the southern hemisphere, very few data exist outside of Antarctica, and these are often of much lower quality than in the northern hemisphere.

Evolution of Sea Ice

Sea ice is frozen seawater. When freezing occurs, salt is expelled from the ice crystals, thus raising the density of the surface ocean waters. The formation of sea ice can therefore have a direct impact on the intensity of the thermohaline circulation. Sea ice is a highly reflective surface with a high albedo of about 0.8. Conversely, when sea ice melts, the ice-free ocean surface absorbs about 90% of the radiation due to large albedo changes, causing the ocean to warm up, followed by a further increase in surface temperature. This phenomenon is a positive feedback between temperature and albedo. Thus, sea ice regulates heat exchanges between the atmosphere and the polar ocean. It isolates the relatively 'warm' ocean waters from the much colder atmosphere, except when there are winter 'leads' occurring as a result of sea-ice break-up. These leads allow the exchange of heat and

water vapor between the atmosphere and ocean which can affect local cloud cover and precipitation rate.

The extent (i.e. area of the sea covered by sea ice), and the thickness of sea ice are the two indicators of sea ice conditions. Typically, the average sea-ice extent ranges from 14 to 16 $\times$ 10^6 km^2 at the end of winter (7 to 9 $\times$ 10^6 km^2 at the end of summer) for the Arctic and from 17 to 20 $\times$ 10^6 km^2 (3 to 4 $\times$ 10^6 km^2 at the end of summer) for Antarctica. The first systematic monitoring of sea ice conditions began in 1972 with the first satellite observations. For older periods, only a few scattered data are available. Most of the analysis of the variability and trends in sea ice cover relates to the post-1978 period. The results from different types of satellites give very consistent results, and all highlight an asymmetry between the Arctic and the Austral Ocean, with a clear decreasing trend for the Arctic and a slight growth for Antarctica, although the latter trend is not statistically significant.

Before the satellite era, sea-ice data are relatively sparse and inconsistent. Nevertheless, although these data indicate significant regional variability, all confirm an increase in sea-ice cover during the nineteenth century and the first half of the twentieth century, and a sharp decline in sea ice from 1970 onwards. According to the assessment by the National Snow and Ice Data Center, sea ice coverage in September has decreased at a rate of ~12.8% per decade from 1979 to 2018 relative to the 1981–2010 average (Fig. 31.4). One striking result was the record reached in 2007 when the total area of sea ice fell to 4.1 $\times$ 10^6 km^2 in mid-September. In 2012, this record was broken with a minimum sea ice coverage of 3.4 $\times$ 10^6 km^2 (i.e. ~20% below the previous record) making 2012 the lowest minimum since the beginning of satellite era. Although measurements did not reach new records between 2012 and 2018, the recorded September minima for sea ice extent for the 2015–2018 period are all below 5.0 $\times$ 10^6 km^2. The persistence of these minima shows that the decrease in Arctic sea ice is accelerating. In the context of global warming, this observation is of growing concern for scientists, especially since the phenomenon is amplified by the temperature-albedo feedback. Moreover, in the past, a year marked by a very small sea-ice extent was generally followed the year after by a return to normal conditions. Observations made in recent years suggest that a progressive disappearance of the oldest ice could occur if the decrease in sea ice continues at the same rate as in the last two decades.

The decline in sea ice observed in recent years seems to be mainly driven by rising temperatures. However, atmospheric variability, and in particular the Arctic oscillation, may also favor the decreasing trend if the Arctic oscillation is in a positive mode. This has the effect of shifting the jet stream from the mid-latitudes to higher latitudes and causes the older, thicker sea ice to be pushed out of the Arctic. More

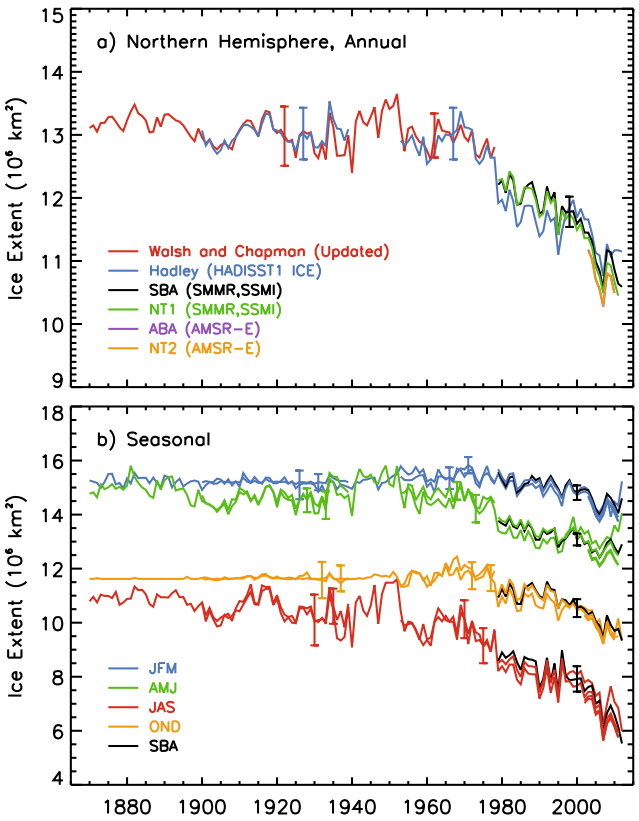

Fig. 31.4 Evolution of Arctic sea-ice extent from 1870 to 2011. **a** Annual sea-ice extent and **b** seasonal ice extent using averages of mid-month values derived from in situ measurements and remote sensing observations In (**b**), data from the different seasons are shown in different colors to illustrate variation between seasons (blue: January–February–March; green: April-May-June; red: July-August-September; orange: October–November–December). The black lines in **a** and **b** correspond to data coming from the Scanning Multichannel Microwave Radiometer and passive microwave data from the Special Sensor Microwave Imager (*Source* IPCC 2013)

recent thinner ice remains in the region and is more prone to disappear during the melt season (Rigor and Wallace 2004). Between 1989 and 1995 the Arctic Oscillation entered a very positive mode, thereby reducing the extent of sea ice. Since the mid-1990s, only a few years have seen a positive or a neutral mode. Meanwhile, the thickness of Arctic sea ice continues to drop due to increasing temperatures. In March 1985, the fraction of first-year ice was ~50% against 70% or more in 2015, and during the 1985–2015 period, the multi-year ice (4 years and older) dropped dramatically from 20% to only 3% (Tschudi et al. 2016).

The situation is different in Antarctica mainly because of its geographic location (surrounded by the Southern Ocean and centered on the South Pole). Atmospheric winds and the oceanic circumpolar currents act as barriers to warmer air and warmer waters coming from the north. Changes in sea-ice coverage are more tenuous, with an increase of 1.2–1.8% per decade between 1979 and 2012 (IPCC 2013). However,

changes in the distribution of Antarctic sea ice show major regional differences. For example, the Weddell and Ross seas are experiencing an increase in sea ice extent due to large-scale changes in atmospheric circulation, while in West Antarctica, the surface covered by sea ice is drastically decreasing, consistent with the observed warming in this region.

Permafrost

Permafrost is defined as soil that remains permanently frozen for at least two consecutive years. It is topped by a so-called 'active layer' that thaws each summer, and whose thickness can vary from a few centimeters to a few meters, depending on altitude and latitude. In areas where it has persisted for several glacial-interglacial cycles, the permafrost can be several hundred meters thick, and even exceeds 1000 m in some parts of Siberia and Canada. During the last glacial-interglacial cycle, there have been large variations in area and depth of permafrost over North America (Tarasov and Peltier 2007) or Europe (VandenBerghe 2011). Currently, permafrost covers 22.8×10^6 km^2 of the northern hemisphere, or about 24% of the continental areas. Permafrost occurs mainly in polar and circumpolar areas and in mountain regions at lower latitudes (e.g. Chile, the Alps, the Himalayas). It can also be found in the seabed of the Arctic Ocean in the continental shelf areas. When surface conditions are not spatially homogeneous (e.g. snow cover, vegetation) permafrost can occur in patches. Such permafrost areas are called 'discontinuous permafrost zones'. When temperatures drop at higher latitudes, gaps in permafrost are less frequent. When surface conditions become homogeneous, permafrost is referred to as 'continuous permafrost'.

The presence of permafrost is critically dependent on the soil temperature, which is itself controlled by the surface energy balance, and thus, by several climatic factors such as incoming solar radiation, cloudiness, snow cover, vegetation cover, surface and subsurface hydrology, and carbon exchanges between the soil and the atmosphere. One of the key factors affecting permafrost distribution is the insulating effect of snow. When snow is present, ground temperatures are generally warmer than those which would occur under smaller snow cover or snow-free conditions. In continuous permafrost areas, snow cover exerts a direct influence on the active layer thickness. For example, it has been shown that a doubling of snow cover from 25 to 50 cm may increase the mean annual surface soil temperature by several degrees (Fig. 31.5). On the other hand, if seasonal snow melting occurs in late spring or early summer, ground warming is delayed.

The permafrost thermal state is also influenced by rainfall. Firstly, ground temperatures can be increased through the energy flux released by liquid precipitation penetrating into the soil. Secondly, rain falling on a snow covered surface may alter the snow insulating effect causing

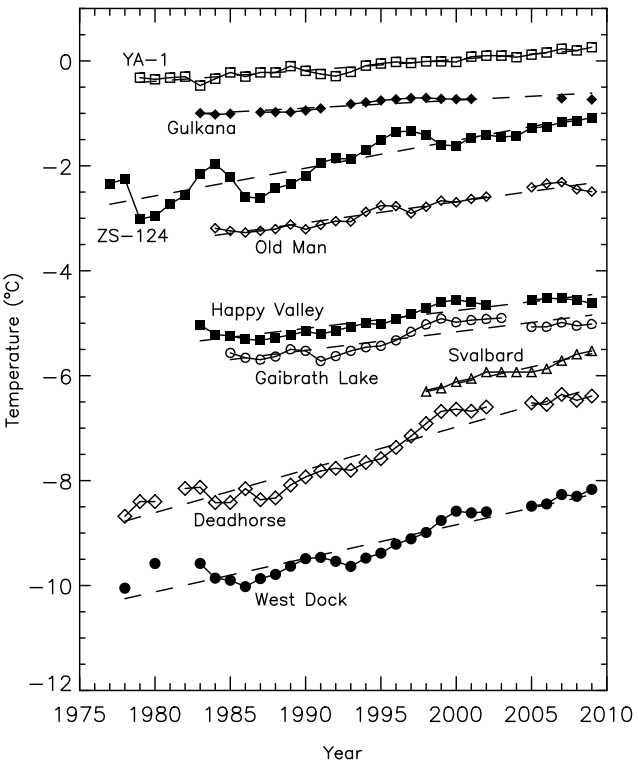

Fig. 31.5 Time series of mean annual ground temperatures at depths between 10 and 20 m for boreholes located throughout the circumpolar northern permafrost regions (Romanovsky et al. 2010a). Data sources are from Romanovsky et al. (2010b) and Christiansen et al. (2010). Measurement depth is 10 m for Russian boreholes, 15 m for Gulkana and Oldman, and 20 m for all other boreholes. Borehole locations are: ZS-124, 67.48°N 063.48°E; 85-8A, 61.68°N 121.18°W; Gulkana, 62.28°N 145.58°W; YA-1, 67.58°N 648°E; Oldman, 66.48°N 150.68° W; Happy Valley, 69.18°N 148.88°W; Svalbard, 78.28°N 016.58°E; Deadhorse, 70.28°N 148.58°W and West Dock, 70.48°N 148.58°W. The rate of change (degrees Celsius per decade) in permafrost temperature over the period of each site record is: ZS-124: 0.53 ± 0.07; YA-1: 0.21 ± 0.02; West Dock: 0.64 ± 0.08; Deadhorse: 0.82 ± 0.07; Happy Valley: 0.34 ± 0.05; Gaibrath Lake: 0.35 ± 0.07; Gulkana: 0.15 ± 0.03; Old Man: 0.40 ± 0.04 and Svalvard: 0.63 ± 0.09. The trends indicate the very likely range, 90% (*Source* IPCC 2013)

temperatures to lower. Interception of precipitation by vegetation also has an impact on ground temperatures through evaporation and transpiration and the associated turbulent heat exchanges between atmosphere and surface layers. However, the direct effect of vegetation on ground temperatures is less important than its role on snow cover. Interception of snow in boreal forests reduces snow cover on soils and acts to reduce ground temperatures. These examples show that the formation or degradation of permafrost is strongly influenced by climate. It is thus studied as an indicator of climate change by a global network of researchers (Romanovsky et al. 2010a, b) who rely on temperature measurements taken from boreholes and from

satellite tracking. In the framework of the International Polar Year (2007–2009), a large permafrost- monitoring network was developed and ground temperatures (which control the thermal state of the permafrost) have been measured in 575 sites located in arctic regions (North America, Nordic Eurasian regions and Russia). In most sites belonging to the network, permafrost temperatures have increased in recent decades. The observed rate of change of mean annual ground temperatures from mid-1970s to 2010 ranges from 0.15 ± 0.03 to 0.82 ± 0.07 °C per decade, depending on the site (Fig. 31.5). In cold permafrost regions (mostly in continuous permafrost zones), the mean annual ground temperatures have increased by up to 2 °C, compared to less than 1 °C in warm, forested permafrost areas (discontinuous permafrost). This can be explained by the fact that the amount of ice in warm permafrost is usually larger than for cold permafrost. Indeed, in case of ice melting, the overall warming trend is counteracted by the latent heat effect. Moreover, in forested areas, the snow insulating effect is limited due to the interception of snow by vegetation.

One of the main consequences of permafrost warming is increased thickness of the active layer, although some permafrost areas exhibit only modest thickening or even a thinning. Indeed, a study based on the analysis of 169 circumpolar and mid-latitude sites revealed that only 43.2% of them have experienced an increase of the active layer thickness since the 1990s (Luo et al. 2016). However, there is great spatio-temporal variability from one site to the other ranging from a few tenths of cm/yr to more than 10 cm/yr. Thickening of the active layer is a matter of great concern since it may have large consequences on the stability of the surface due to the melting of shallow ground ice. Potential impacts include thaw settlement, soil creeps, slope failures and ponding of surface water. All these features can cause severe damages to infrastructures, such as roads, dams or structural building foundations but also to vegetation. In forested areas, thaw modifies the hydrological conditions and can lead, for example, to the destruction of tree roots, causing drastic changes in the ecosystems. When permafrost thaws and the active layer thickens, more organic matter is likely to be decomposed by bacteria that produce either methane or carbon. In both cases, the bacterial action enhances greenhouse gas emissions and thus promotes global warming. However, the magnitude of this thaw-related feedback is a great unknown. The total amount of carbon stored in the permafrost has been estimated at 1672 Gt, of which 277 Gt is found in peat bogs. This is about twice the amount of carbon in the atmosphere.

We still do not know for sure if the increase in atmospheric methane concentration observed in recent years, after about ten years of relative stability, is due to the warming of the high northern latitudes. Another amplification reaction observed at high northern latitudes involves the microbial transformation of nitrogen trapped in soils into nitrous oxide, which could increase with increasing temperatures and thus, in turn, amplify global warming.

In any case, even if there are still many uncertainties, the Fifth IPCC assessment report emphasized on the positive feedback of permafrost melting on climate warming: "*the release of CO_2 or CH_4 to the atmosphere from thawing permafrost carbon stocks over the twenty-first century is assessed to be in the range of 50 to 250 GtC for RCP8.5*" (IPCC 2013). The RCP scenarios are defined in the section "Projecting the Future of the Climate System" of this chapter.

Glaciers

A glacier is a mass of ice formed by the successive accumulation of layers of snow year after year. Over the years, under the pressure of its own weight, the snow hardens and becomes granular (firn), then turns into ice and expels the air it contained. Under the action of gravity, the ice flows along the slope, thus supplying the lower parts of the glacier. A glacier is in constant movement and carries mass from high altitudes to lower altitudes. In winter, the glacier grows due to snow accumulation on its surface. During the following summer, the glacier loses all or part of the mass it gained during winter. The disappearance of ice through surface processes is called ablation. The difference between accumulation and ablation determines the surface mass balance of the glacier. This brings about a change in ice volume. A positive balance overall causes the glacier to grow while a negative balance leads to a loss of ice volume which can be accompanied by a retreat of the glacial front.

The mass balance of temperate glaciers in the mid-latitudes is mainly dependent on winter precipitation, summer temperature and summer snowfalls (temporally reducing the melt due to the increased albedo). In contrast, the glaciers in low latitudes, where ablation occurs throughout the year and multiple accumulation seasons exist, are strongly influenced by variations in the atmospheric moisture content which affects incoming solar radiation, atmospheric long-wave emission, albedo, precipitation and sublimation. In monsoon areas, such as the Himalayas, accumulation and ablation occur mainly in summer. Glaciers at high altitudes and in polar regions can experience accumulation in any season.

The retreat of mountain glaciers is one of the most visible examples of climate change. A compilation of observations made by the World Glacier Monitoring Service on 19 regions around the world, gathering more than 40,000 observations, shows that the retreat is an almost global phenomenon, despite some intermittent readvances related to dynamical instabilities (e.g. Island, Svalbard) or to specific climatic conditions (i.e. increased winter snowfall) observed on a few individual glaciers in Scandinavia or New Zealand in the 1990s. However, the periods of glacier front advances are short compared to the overall ice retreat. By compiling

the data obtained on 169 glaciers since 1700, Oerlemans (2005) shows that the retreat of glacier fronts began in the nineteenth century, and accelerated strongly from 1850 onwards, with a continuation throughout the twentieth century and early decades of the twenty-first century.

Regional analyses have shown that, until around 2000, the average mass balance cumulated over all European glaciers was close to zero, with significant mass losses for Alpine glaciers being compensated for by advances of glaciers in western Norway stemming from a sharp increase in precipitation in response to a positive phase of the North Atlantic Oscillation. From the year 2000 onwards, the Norwegian glaciers began to retreat in response to a decrease in precipitation. Over the period 2003–2009, the most negative mass balances occurred for glaciers in the northwestern United States and southwestern Canada, Central Europe, Southern Andes and low latitude areas. In the Alps, glaciers have been retreating since the mid-nineteenth century. In Switzerland, they currently cover only 60% of the area they occupied in 1850. Due to the heat wave, an exceptionally high loss of mass occurred in 2003, corresponding to a reduction of 2500 kg m^{-2} yr^{-1} for the nine glaciers studied. This value exceeds the previous record 1600 kg m^{-2} yr^{-1} in 1996 and is four times higher than the average measured between 1980 and 2001 (600 kg m^{-2} yr^{-1}). In Africa, the glacier area at the top of Kilimanjaro is now only 20% of what it was at the beginning of the twentieth century. In Patagonia, the 'icefields' have lost between 3 and 13 km^3/yr of ice since the 1970s. The retreat of the glaciers in Nepal and Himalayas seems to have accelerated over the past twenty years, and in Tibet, the number of glaciers in retreat has recently multiplied.

The Fifth IPCC Assessment Report estimated that the contribution of glaciers and small ice caps to sea level rise over the 1993–2010 period was about 0.76 mm/yr (IPCC 2013). Since then, new estimates based on new data indicate a higher contribution, demonstrating that mass loss from glaciers and small ice caps has accelerated significantly since the early 1990s, and currently contributes between 1.05 and 1.12 mm/yr to the rise of the global sea level.

Polar Ice Sheets

Polar ice sheets are huge masses of ice formed, like glaciers, by continual accumulation of snow in excess of ablation, which gradually turns into ice under the effect of compaction. As for glaciers, this transformation occurs in a transition zone about one hundred meters thick called firn. Currently, the ice sheets are located at high latitudes, one near the North Pole, Greenland, the other centered on the South Pole, Antarctica. The area of the Greenland ice sheet is about 1.8×10^6 km^2. In the center, the ice thickness is greater than 3000 m. The Greenland ice volume ($\sim 3.0 \times 10^6$ km^2) represents about 10% of the worldwide freshwater supplies. Antarctica is composed of two effectively distinct ice sheets in the east and west, separated by the Transantarctic Mountains. Its ice volume is close to 27×10^6 km^2 and its surface, almost 98% covered by ice, is about 14×10^6 km^2. A large part of the western ice sheet lies below sea level. The West Antarctic ice sheet extends locally over the sea to form floating ice shelves, mainly in the embayments of the coast, as in the Weddell and Ross Seas. In contrast, East Antarctica, which is larger, rests largely on bedrock. It forms a plateau with an area exceeding 10×10^6 km^2 covered by a large ice layer of more than 4000 m thick in the center.

The evolution of the part of an ice sheet grounded on the bedrock depends on its surface mass balance and its flow due to the deformation of the ice itself. When the temperature is high enough, the ice melts at the surface. As for glaciers, the surface mass balance is determined by the difference between accumulation and ablation. In addition, under the effect of its own weight, the ice flows by plastic deformation along the line of steeper slope, as well as by sliding on the bedrock when the local temperature is close to the melting point: this is called basal sliding. As ice is an insulating material, a temperature gradient is established between the colder surface and the warmer base. Furthermore, by changing the ice viscosity, the temperature also affects the flow velocities from the surface to the base of the ice sheet. Thus, the processes involved in the ice deformation are not the same at the surface and at the base of the ice sheet.

In the case of the Antarctic ice sheet, the surface temperature generally remains low enough so that ablation is negligible. The ice then drains into the ocean or feeds the floating ice shelves through ice streams which are characterized by a rapid outflow (i.e. low basal friction). The sources of these ice streams are found far upstream, and their contribution to the evacuation of grounded ice from the center of the ice sheet towards the edges is estimated at nearly 90%. The flow regime through the ice shelves is very different from that of grounded ice. In fact, whereas grounded ice is characterized by a shear regime in the vertical plane, the predominant constraints on the ice shelves are the horizontal shear and the pressure forces exerted by the sea. The destabilization of these glacial platforms is due to the increase in sea level, but also to the basal melting beneath the platforms. This melting is therefore related to the ocean temperatures under the ice shelves and to the energy released by ocean currents. The dislocation of these glacial plateaus leads to the formation of icebergs (i.e. ice calving). This is exactly what happened with the dislocation of the Larsen B ice shelf in 2002 which resulted in a surface loss of about 3250 km^2. This could also occur in the coming years with the break-up of the Larsen C ice shelf in July 2017 (6000 km^2 of surface loss) and the continuous acceleration of the Twaithes glacier reported by satellite observations

since 1992. Moreover, as the ice shelves exert a buttressing effect for the upstream grounded ice, their disintegration can cause the destabilization of a large part of the ice sheet.

There are different methods to measure the amount of ice stored in an ice sheet:

(a) **The measurement of inflow** (snow accumulation) **and outflow** (ablation, discharges to the ocean). Snow accumulation is often estimated from annual layers in ice cores and interpolated between different drilling sites. The use of high resolution atmospheric models is also becoming more common. Discharges of ice to the ocean are estimated from seismic or radar measurements of the ice thickness and from measurements of ice flow velocity. Ablation is usually determined from ice models forced with atmospheric reanalyses, climatology or outputs from global climate models calibrated with surface observations. The loss of mass beneath the ice shelves remains very difficult to quantify. In general, inflows and outflows cannot be estimated with a margin error of less than 5%, which implies uncertainties of 40 and 140 Gt/yr on the estimate of the mass balance of Greenland and Antarctica respectively.

(b) **Remote-sensing techniques**. These include altimetry measurements from radio-echo sounding, interferometry and gravimetry. Interferometry provides information on ice flow velocities. The altimetric measurements provide information on the spatial and temporal variations of the topography, which makes it possible to trace the ice volume variations, after correcting for the altitude of the bedrock and for variations in the thickness and density of the firn. These measurements are strongly dependent on the nature of the terrain (flat, sloping or hilly surfaces) and the snow surface conditions (density, viscosity, etc.) and this may, in some cases, make interpretation difficult. Finally, satellite measurements of the gravity field provide, for the first time, estimates of the ice mass changes. However, there are still significant uncertainties, especially regarding the cause of the change in mass, as this could come from the ice sheet itself, the air column, the evolution of the subglacial bedrock or even from masses near the ice sheet (i.e. ocean mass, masses of water or snow contained on nearby continents). These different effects are evaluated and then corrected, but a significant uncertainty remains, mainly on how to correct for the altitude of the underlying Antarctic bedrock. Other sources of uncertainty relating to satellite measurements come from the fact that they do not provide complete coverage of the ice sheets. Moreover, in Greenland, for example, remote sensing techniques may underestimate the extent of the ablation area and the increased rainfall over some parts of the ice sheet during rainfall events.

Past published estimates of Greenland and Antarctic ice sheets obtained with these methods have often diverged. This was due to the way in which the different sources of uncertainty were estimated and to the fact that the different measurements did not cover the same regions and the same time periods. Within the IMBIE framework (Ice-sheet Mass Balance Intercomparison Exercise), scientists made a huge effort to combine, over common survey periods and common regions, various observations from satellite geodetic techniques (altimetry, interferometry, radio-echo sounding and gravimetry) with simulated surface mass balance estimates inferred from regional atmospheric models. This allowed for a reconciliation of the apparent disparities between the different methods and for a consistent picture of ice-sheet mass balance to be created (Shepherd et al. 2012).

For Greenland, this compilation effort confirmed with a high confidence level that the ice sheet is continuously losing mass and that this process now affects all sectors of the ice sheet (Fig. 31.6a–c). However, after a record mass loss in summer 2012, Greenland has seen a slight decrease in the short-term mass loss trend. The mass loss is partitioned between surface melting and dynamic ice discharges. Shepherd et al. (2012) estimate that the ice mass loss is about -142 ± 49 Gt/yr over the IMBIE time period (1992–2011) with an acceleration of the mass loss rate as illustrated by the comparison between the estimations made for 1992–2000 (-51 ± 65 Gt/yr) and 2005–2010 (-263 ± 30 Gt/yr). Using gravimetry observations, Velicogna et al. (2014) provide a more recent estimate of the Greenland ice sheet mass loss for the 2003–2013 decade of 280 ± 58 Gt/yr with an acceleration of the loss rate bringing it to 25.4 ± 58 Gt/yr^2.

The case of the Antarctic ice sheet (Fig. 31.6b) is a bit different since recent observations have shown that mass loss was mainly driven by dynamic ice discharge resulting from enhanced ice flow of marine-terminating glaciers. The main region experiencing mass loss is the West Antarctic ice sheet (WAIS), especially in the Amundsen/Bellingshausen Sea sectors (e.g. Thwaites and Pine Island glaciers) and, to a lesser extent, in the Antarctic Peninsula. According to a recent update of the IMBIE estimates (IMBIE team, 2018), the mass loss from the Amundsen and Bellingshausen Sea sectors increased from 53 ± 29 Gt/yr to 159 ± 26 Gt/yr over the 1992–2017 period, and from 7 ± 13 Gt/yr to 33 ± 16 Gt/yr in the Antarctic Peninsula. It has long been considered that the East Antarctic ice sheet (EAIS) was gaining mass due to enhanced precipitation, despite no firm

consensus being established (Velicogna and Wahr 2006; Ramillien et al. 2006). However, recent estimates suggest that some sectors, such as the Wilkes Land region, are losing mass. As a result, the rate of change in ice-sheet mass is estimated to be +11 ± 58 Gt/yr in 1992 (mass gain) and −28 ± 30 Gt/yr (mass loss) in 2017 (IMBIE team, 2018). Using a different technique, Rignot et al. (2019) estimate an even larger mass loss from EAIS with a strongly reduced uncertainty.

Overall, taking the Antarctic and Greenland ice sheets together, it appears that mass losses have accelerated in recent years. This trend is correlated with an increase in surface ablation due to increasing temperatures, but also with an acceleration of ice flow and subsequent dynamic ice discharges.

Several processes are at the origin of ice mass loss. The increasing surface ablation, mainly observed in Greenland, is a direct response to increased atmospheric temperatures. However, the ocean warming also plays a key role. As oceanic temperatures rise, basal melting under the ice shelves is enhanced. Eventually, this may lead to the dislocation of ice shelves and to the removal of the buttressing effect mentioned above. This causes an inland retreat of the grounding line (i.e. the limit beyond which ice starts to float), and subsequently, an acceleration of the upstream grounded ice. Theoretically, this process is only valid for ice-shelves confined within their embayment. It is responsible for more than half of the ice mass loss at the margins of the Antarctic ice sheet. For unconfined ice shelves, another process, known as the Marine Ice Sheet Instability, may also apply. For a marine-based ice sheet, such as the WAIS, bedrock is often more depressed in the center of the ice sheet than it is at the margins. As ice flux increases with ice thickness, the position of the grounding line becomes highly unstable in areas of reverse bed slopes, and any change in ice thickness in the vicinity of the grounding line creates an irreversible retreat of the grounding line position. A second hypothesis is the lubrication of the subglacial substratum caused by meltwater produced at the surface that percolates to the base of the ice sheet. A third process that may be

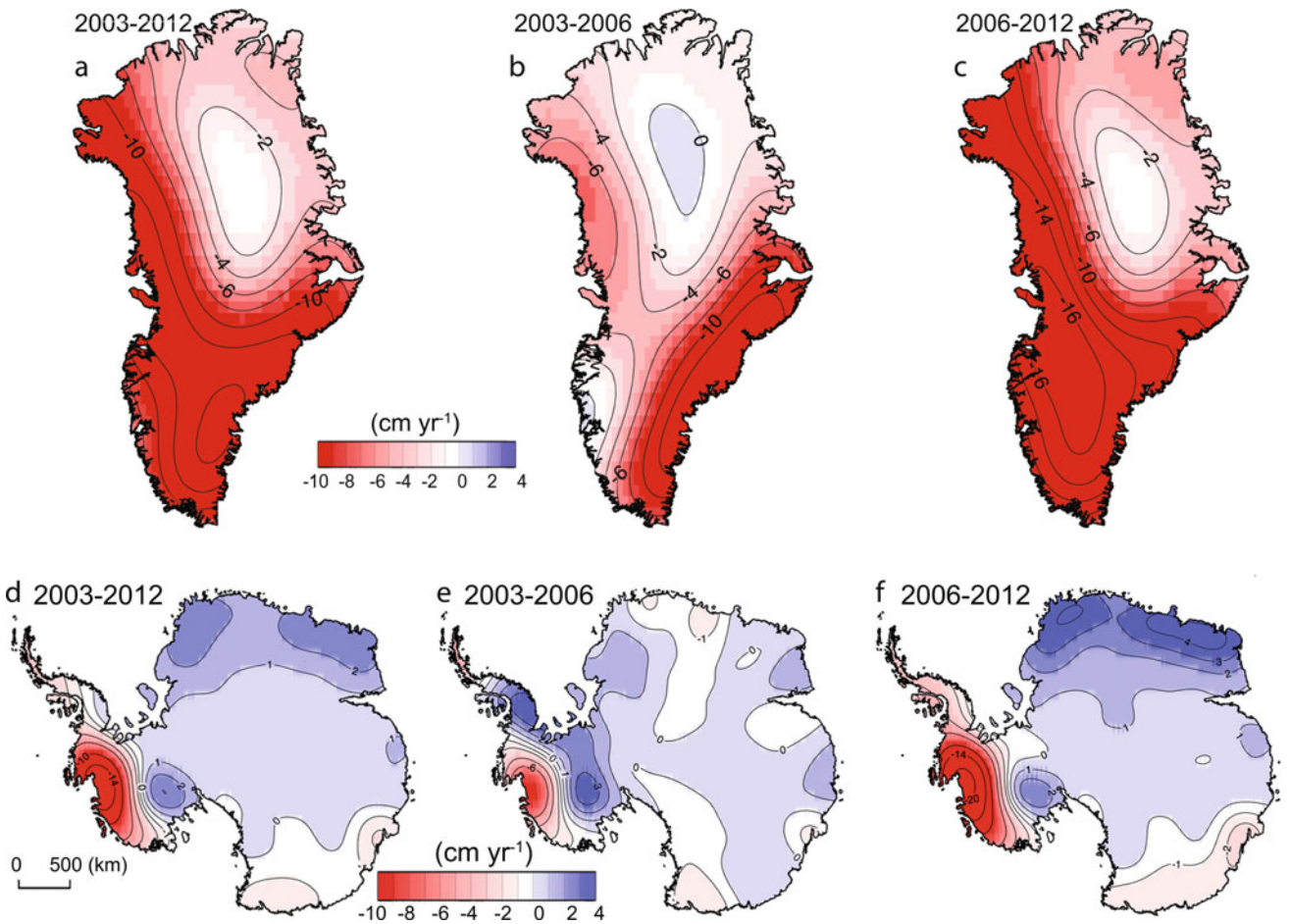

Fig. 31.6 Temporal evolution of ice loss in Greenland (top) and Antarctica (bottom) determined from time variable gravimetry observations from the GRACE satellite, shown in centimeters of water per year for the periods 2003–2012, 2003–2006 and 2006–2012, color coded red (loss) to blue (gain) (*Source* IPCC 2013)

responsible for ice flow acceleration is hydro-fracturing (DeConto and Pollard 2016). This mechanism is related to water coming from ice melting at the surface of the ice shelf that may percolate inside the ice-shelves. Crevasses can form and widen when the water pressure is high enough, thereby favoring iceberg calving. Ultimately, this process may lead to ice-shelf collapse. It may also favor the marine ice sheet instability. Indeed, once the ice shelves have collapsed, ice cliffs become unstable and fall down if their height is greater than ∼ 90 m. However, this process remains poorly constrained and is still a matter of debate.

A special attention is given to the evolution of ice sheets. Indeed, ice sheets strongly interact with the other components of the climate system. These interactions can lead to a highly non-linear climate response. This means that the effects of the radiative disturbance (caused by variations in insolation or in the amount of greenhouse gas in the atmosphere) can be amplified or mitigated by these feedback processes, as illustrated in Chap. 28 for abrupt events. Many studies on these interactions have been published over the past two decades. They would deserve a full chapter. Here, we only give some quick examples for time scales ranging from a few decades to a few centuries. Ice sheet melting is first of all accompanied by possible changes in albedo and therefore in the surface energy balance. This effect is almost instantaneous. In turn, a change in the energy balance can lead to changes in the mass balance of the ice sheets. Another consequence of the melting and/or mechanical destabilization of the ice sheets, widely discussed in the literature, concerns the freshwater flux released in the ocean. Locally, this release leads to a decrease in ocean surface temperatures, a change in sea ice cover and a reduction of ocean density in the vicinity of the ice sheets. Density changes also cause a disruption of large-scale ocean circulation by altering deep-water convection. For example, meltwater from Greenland has the potential to weaken the Atlantic Meridional Overturning Circulation. These changes can have effects in regions far from the polar zones. For example, the recent study by Defrance (2017) showed that for a substantial melting of Greenland under a climate change driven by the RCP8.5 scenario, Greenland meltwater could cause a massive alteration of the monsoon regime with a drastic decrease in West African rainfall, and subsequently with a significant reduction in cultivable areas. Therefore, in addition to the direct and obvious consequences on sea level, the future of polar ice sheets is of primary importance for the future of human societies, all the more so if they are already economically fragile.

Sea Level Changes

Sea level variations are the result of changes in both the volume of the oceans and ocean basins, as well as changes in the mass of water contained in the oceans. Depending on the time scale being considered, these types of variations have different origins. Over geological time scales, changes in the shape of ocean basins and in the continent/ocean distribution are the main factors affecting sea level. Over glacial-interglacial cycles, sea-level variations are mainly related to changes in continental ice volume and to the isostatic adjustment due to the vertical movements of the Earth's crust in response to changes in the mass of land ice. Following the last deglaciation initiated about 21,000 years ago, sea level rose by ∼ 120 m and then stabilized around 6000 years ago. Geological data indicate that sea level has not changed by more than 30 cm from that time until the end of the nineteenth century.

On time scales ranging from a few years to a few decades, variations in the mean sea level are the result of two factors, mainly related to climate change:

(a) Variation of the ocean volume caused by changes in sea temperature. As temperature increases, the volume of water expands. This process is called thermal expansion;
(b) Variations in the bodies of oceanic water resulting mainly from exchanges with continental reservoirs, such as rivers, lakes and inland seas, snowpack, ground water, but also mountain glaciers and polar ice sheets.

Other factors such as ocean circulation or atmospheric pressure can bring about local variations, without altering the mean global sea level. In addition, some human interventions have the effect of modifying regional hydrology by modifying the runoff of freshwater released to the ocean, and thus the sea level. This occurs in the case of dams, irrigation, urbanization, water extraction from aquifers and deforestation. Some of these processes have the effect of increasing runoff (urbanization, deforestation); others, such as dams and irrigation, contribute to the sequestration of freshwater on the continents. Current estimates of the net land water storage are based on observations and models, and vary between −0.33 and 0.23 mm/yr over the period 2002–2014/15 (WCRP Global Sea Level Budget Group 2018).

Measurements of current sea-level variations are based on two different techniques: tide gauges, which began to be installed in the nineteenth century, and altimetry data from satellite observations since 1992. The two main limitations of tide gauges are their inhomogeneous spatial and temporal coverage, and the inclusion of vertical land motion in their record, which needs to be corrected for to obtain relative sea-level changes. To limit the uncertainties related to these movements, which are difficult to quantify in current models, only a few tens of geologically stable sites, mainly located along the coasts of North America and Europe, are taken into account to inform us of the sea level evolution in the course of the twentieth century. Based on a compilation of the most recent estimates, the sea-level rise as indicated by tide gauge

data is estimated at 1.7 ± 0.2 mm/yr between 1901 and 2010 for a total sea level rise of 0.19 ± 0.02 m (IPCC 2013).

Since 1992 and the launch of the TOPEX/Poseidon satellite, altimetric data have provided a new way of estimating sea-level variations, based on the time required for the round trip of the radar wave and on the satellite altitude defined above a standard reference surface. These measurements are thus independent on the vertical land motion, in spite of a small correction (around 0.3 mm/year) to account for the change in the reference level at the ocean bottom due to the post-glacial rebound (Peltier et al., 2015). This results in an increase of about 3.2 ± 0.4 mm/yr between 1993 and 2012 (IPCC 2013, Fig. 31.7), now reevaluated at 3.1 ± 0.4 mm/yr between 1993 and 2017 (WCRP Global Sea Level Budget Group 2018). Satellite altimetry data now cover a time period of 25 years, long enough to identify an acceleration of the sea level rise estimated at around 0.084 ± 0.025 mm/yr^2 (Nerem et al. 2018).

These altimetry data show significant regional disparity, with some regions showing a sea-level rise well above the global mean and other regions showing a decrease in sea level. This regional variability partially explains the differences between tide gauge data and altimetry data, and is due to several factors including density variations, ocean circulation, atmospheric pressure, and variations within the solid Earth or the geoid. For example, the Scandinavian shield continues to rise at a faster rate than the mean and, so paradoxically, a decrease in local sea level is recorded there.

Tide gauges and altimetry data provide ways of quantifying the global mean sea level rise and its different components. Data on ocean temperature changes allow us to quantify the contribution from thermal expansion. Recent advances in temperature measurements have greatly improved our knowledge. Since 2000, the Argo project has deployed thousands of free-drifting profiling floats measuring temperature (and salinity) in the ocean at depths between 0 and 2000 m, providing a continuous record of heat penetrating in the ocean. In addition, ship-based data were collected during the World Ocean Circulation Experiment, providing the means to estimate the deeper ocean temperature change (Johnson et al. 2007; Purkey and Johnson 2010; Kouketsu et al. 2011). These data show that, globally, the ocean has warmed significantly over the last 50 years, and in particular, over the past two decades. By vertically integrating the temperature data along the water column at each oceanic point, sea-level changes due to oceanic thermal changes can be estimated over the past 50 years. Based on data gathered over a depth of 700 m, the contribution of thermal expansion to sea level rise was estimated at 0.60 ± 0.2 mm/yr for the period 1971–2010 (0.8 ± 0.3 mm/yr if the deep ocean contribution is included). For the more recent period 1993-2017, this contribution is 1.3 ± 0.4 mm/yr (Table 10.1). In recent decades, this has been the dominant contribution to global sea level rise.

The other factors contributing to the rise in sea level come from changes in the oceanic water mass (Table 31.1). One of the most important contributions is from mountain glaciers (excluding Greenland and Antarctica) which cause a global sea level increase of 0.62 ± 0.37 mm/year for the period 1971–2010 and 0.65 ± 0.15 mm/year for the period 1993–2017. Both polar ice sheets also contribute to the recent rise in global sea level with 0.48 ± 0.10 mm/yr for Greenland

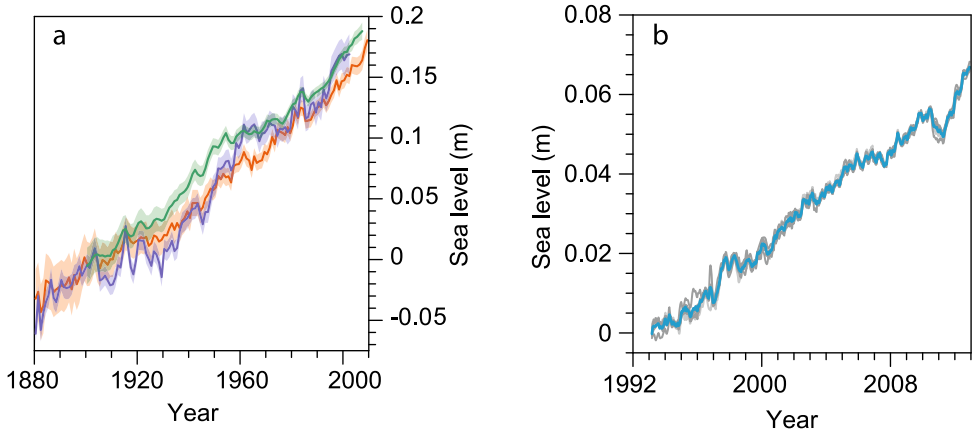

Fig. 31.7 **a** Yearly average global mean sea level (GMSL) reconstructed from tide gauges by three different approaches: orange from Church and White (2011), blue from Jevrejeva et al. (2008), green from Ray and Douglas (2011), **b** Changes in the mean global sea level from altimetry data sets from five groups (University of Colorado (CU), National Oceanic and Atmospheric Administration (NOAA), Goddard Space Flight Centre (GSFC), Archiving, Validation and Interpretation of Satellite Oceanographic (AVISO), Commonwealth Scientific and Industrial Research Organisation (CSIRO) with the mean of the five shown as a bright blue line (*Source* IPCC 2013)

Table 31.1 Sea level rise from different sources, adapted from IPCC (2013), Chapter 13, with additional data from WCRP Global Sea Level Budget Group (2018). The percentages are relative to the sum of contributions

Components	Sea level rise (mm/yr) 1993–2010 (IPCC, 2013)	Sea level rise (mm/yr) 1993–2017 (WCRP Global Sea Level Budget Group, 2018)	Sea level rise (mm/yr) 2005–2017 (WCRP Global Sea Level Budget Group, 2018)
1. Thermal expansion	1.1 ± 0.2	1.3 ± 0.4 (48%)	1.3 ± 0.4 (44%)
2. Glaciers (excluding Greenland and Antarctica)	0.76 ± 0.37	0.65 ± 0.15 (24%)	0.74 ± 0.1 (25%)
3. Greenland ice sheet	0.33 ± 0.08	0.48 ± 0.10 (18%)	0.76 ± 0.1 (26%)
4. Antarctic ice-sheet	0.27 ± 0.11	0.25 ± 0.10 (9%)	0.42 ± 0.1 (14%)
5. Land water storage	0.38 ± 0.11	/	−0.27 ± 0.15 (−9%)
Total of contributions (1 + 2 +3 + 4 + 5)	2.8 ± 0.5	2.7 ± 0.23	2.95 ± 0.21
Observed global mean sea level rise	3.2 ± 0.4	3.07 ± 0.37	3.5 ± 0.2
Thermal expansion + GRACE-based ocean mass			3.6 ± 0.4

and 0.25 ± 0.10 mm/yr for Antarctica for 1993–2017. The ice-sheet contribution to sea-level rise has been increasing from 27% of the total contributions for 1993–2017 to 40% for 2005–2017.

The sum of all contributions, including land water storage, amounts to 2.8 ± 0.5 mm/yr for the period 1993–2010, which is lower than the observed global mean sea level rise of 3.2 ± 0.4 mm/yr (Table 31.1). Similarly, for the most recent period 2005-2017, the sum of contributions is 2.95 ± 0.21 mm/yr, lower than 3.5 ± 0.2 mm/yr which is the observed global mean sea level rise. This discrepancy is due to uncertainties in the estimation of the different components of ocean mass contributions (glaciers, ice sheets and land water storage). Instead, if the ocean mass contribution is taken from gravity measurements using GRACE (Gravity Recovery And Climate Experiment), the sum of thermal expansion and GRACE-based ocean mass contributions is 3.6 ± 0.4 mm/yr, which is in the error bar of the observed global mean sea level rise for this period (3.5 ± 0.2 mm/yr).

Climate Modeling and Recent Changes

Simple Radiative Climate Models and Their Limitations

To estimate the changes in the mean Earth's temperature in response to different radiative forcings (solar irradiance, greenhouse gases, energy re-emitted by the surface etc.), a first approach is to use purely radiative models. With these models, one can easily and accurately calculate the temperature changes with some simplifications: it is assumed that only the temperatures change, and that this affects only the radiation emission law, without modifying any radiative property of the atmosphere or the surface. For example, with a doubling of atmospheric CO_2 concentration, a temperature increase of 1.2 ± 0.1 °C is obtained. However, these simplified assumptions are not reliable, because when the temperature changes, all the other climate variables (e.g. humidity, wind, clouds, rain, snow cover) also change. These changes can in turn modify the energy balance of the surface and the atmosphere and thus have an additional effect on temperatures. These are called *feedback processes*. They are said to be positive when they amplify the initial disturbances, and are said to be negative when the opposite is true, when they work towards the stabilization of the system.

The first studies which took these feedbacks into account were carried out using radiative-convective models, with only one vertical dimension. For example, Manabe and Wetherald (1967) showed with their model, that the surface warming due to a doubling of the atmospheric CO_2 concentration was 1.3 °C when the absolute humidity of the atmosphere remained constant, but reached 2.4 °C in case of constant relative humidity. Numerous other studies have confirmed the crucial importance of feedback mechanisms on the magnitude of global warming: they can amplify twice to four times the temperature variation compared to the situation where no feedback is taken into account. These studies have also shown that the magnitude of these feedbacks is strongly dependent on complex physical processes (less understood than radiative transfer), such as turbulence, convection, cloud formation and precipitation (Ramanathan and Coakley 1978). These processes, and in particular, the atmospheric circulation which determines how energy and

water vapor are redistributed within the atmosphere, cannot be represented in a useful way in the radiative-convective models. Thus, even rough estimates of the changes in the global mean temperature require the atmospheric dynamics to be taken into consideration and, for more precise calculations, three-dimensional models representing the general circulation of the global atmosphere of the Earth are needed.

General Circulation Models: Progress and Limitations

The Evolution of Climate Models

A general circulation climate model is a simplified representation of the climate system, but including as best as possible most processes that influence the climate. It is based on a preliminary physical analysis, in order to reduce the number of processes to be incorporated, as well as on appropriate mathematical and numerical formulations. Numerical modeling of the climate began in the 1970s and has since greatly progressed, thanks to the steady increase in the processing power of computers. The general philosophy behind this development, established by Charney and his collaborators in the 1950s, was to understand the problem on a global scale, even if this meant making very general approximations initially, with the aim of gradually improving the model by identifying its drawbacks and its limitations. The first models only described the atmosphere and the continental surfaces. In order to reduce model complexity, the oceanic surface temperature was imposed: even if the energy balance of the ocean surface is very different from the observed measurement, the surface temperature is maintained at its prescribed value. However, to investigate the variations in climate accounting for oceanic temperatures is required.

The first studies of the impact of a CO_2 doubling using this type of model were carried out in the 1970s at the GFDL (Geophysical Fluid Dynamics Laboratory, Princeton, USA) with a representation of the ocean with no circulation and zero heat capacity, so that equilibrium with the atmosphere could be achieved quickly. In this model, there was no diurnal or annual variation in insolation, and ad hoc corrections were applied to heat fluxes at the air-sea interface to keep the ocean surface temperature close to observations. The use of this type of model became widespread during the 1980s, with a gradual increase in sophistication and realism. For example, both annual and diurnal insolation variations were incorporated, modeling of cloud formation processes began, etc. At the same time, new satellites were being used to estimate global cloud cover and radiative fluxes at the top of the atmosphere, which contributed to the improvement and evaluation of atmospheric models.

In parallel, ocean general circulation models were developed to simulate heat transport and to study the role of the ocean in the Earth's energy balance. Progressively, they included sea-ice models and, from the 1990s onwards, they were coupled with atmospheric models to simulate the atmosphere-ocean-sea ice interactions. These early models did not simulate the heat and water fluxes at the air-sea interface, resulting in strong biases in the simulated oceanic surface temperatures. To fix these shortcomings, the fluxes at the air-sea interface were corrected in an ad hoc way, before these corrections were gradually removed after the end of the 1990s, thanks to continuous model improvement.

These coupled atmosphere-ocean models gradually became the basic tool for studying both past and future climate variations. For example, in preparation for the Fourth IPCC Assessment Report (IPCC 2007), some twenty of these coupled models performed a whole series of climate change simulations, and only six of them were based on flux correction at the air-sea interface. These models can simulate a natural climate variability that can then be compared to observations at different time scales: a few days, a few years (interannual variability, the best known of which is El Niño), or a few tens, or even several hundred years.

In a schematic way, climate models simulate the energy and water cycles. Progressively, representations of chemical reactions in the atmosphere, biogeochemical cycles and the transport of species were introduced into modeling so as to study new aspects of climate variations: the effect of aerosols, coupling between climate change and the chemical composition of the atmosphere, and between climate change and the carbon and methane cycles. This required advances in our understanding of each of the components of the system: atmosphere, ocean, vegetation, continental surface, sea ice. Numerical climate models progressively incorporate, in a coherent way, a wide range of physical processes governing the climate variations and the interactions between the different climate components. On the other hand, the inclusion of a growing number of physical processes has made the models more complex and more difficult to develop and evaluate.

As ice sheets interact with atmosphere, ocean and vegetation, the next key challenge for the climate modeling community is to incorporate ice-sheet models in general circulation climate models. This is a necessary step to obtain a comprehensive representation of the climate system for past, present and future time periods.

What Are the Uncertainties Inherent in Climate Models?

The climate is characterized by a very wide range of both spatial (from the micrometer to several thousand kilometers) and temporal (from the second to several thousand years or more) scales. The processes at these different scales interact

with one another, and in principle, it is never possible to know which scales should be considered and how to represent the neglected scales in a simplified way. A typical example is the formation of clouds and precipitation. Let's take the example of convective clouds (of the cumulonimbus type), whose core is a rising column of moist air in which the water vapor condenses as it rises. This ascending column mixes with the surrounding drier air, and this mixing depends on many factors (for example, the intensity of the upward thermal current and wind shear). In order to take these mixtures into account, it is first necessary to know precisely the vertical profile of the atmospheric variables in the vicinity of the column. The turbulent exchanges between the column and its environment must also be calculated, as well as the coupling between these turbulent exchanges and the formation or dissipation of rain drops, hail or snowflakes. This requires a modeling on a very small scale (a few hundred nanometers to a few meters), which is not possible with global models. Therefore, a simplified model must be developed based only on large scale variables which reproduce the effect of unresolved small scale processes. This type of modeling, called parameterization, is based on important simplifications that nevertheless require a thorough physical analysis and an in-depth understanding of the phenomena. The aim is to obtain a simplified model that is not only as accurate as possible, but also justified and well understood.

There are many parameterizations in a climate model which can be directly related with the atmospheric circulation (for example gravity waves and orographic effects), the calculation of radiative exchanges, deep convection, or boundary layer phenomena. Many of these parameterizations play a key role in the water cycle, the formation of clouds and their radiative properties, precipitation, heat and water fluxes on the surface of continents or oceans, among others. All these phenomena have an impact on the simulation of the current climate and as there are strong interactions between them, it is often very difficult to identify the precise role of each of the parameterizations on the simulation of these phenomena, and in particular to understand why some of them are poorly simulated.

Parameterizations also play a very important role in the climate response to different forcings, and in the simulation of past and future climate changes. One example is the simulation of clouds. Clouds exert two opposing effects on the terrestrial radiative balance: on the one hand, they reflect part of the solar radiation, and on the other, they absorb infrared radiation and thus contribute to the greenhouse effect. The relative importance of these two effects depends on many factors, in particular, cloud altitude. Over the past twenty years, we have learned that, on average, the first effect outweighs the second, and therefore that clouds have a cooling effect on the climate, especially low-lying clouds, because they have little impact on infrared radiation. However, this does not explain the role that clouds could play in global warming. Depending on how their properties change, clouds may attenuate or, on the contrary, amplify, global warming. The physical formation mechanisms involve so many processes and spatial scales (from a micrometer to a thousand kilometers), and their radiative properties depend on so many factors that it is impossible to conclude on the basis of theory, simple reasoning or analysis of available observations, how they will evolve in the future.

Simulation of the Current Climate and Recent Changes

Analysis of simulated climate combined to the comparison of model results with observations is an important step to establish the reliability of climate models. The aim is to evaluate not only the mean climate, but also the climate variability at different time scales (from a few days to a few decades) as well as recent climate changes. Unless otherwise indicated, this section presents the simulated climate characteristics from the twenty AOGCMs that contributed to the preparation of the Fifth IPCC Assessment Report (IPCC 2013).

Mean Climate

The difference in mean insolation is what causes the temperature difference between the equator and the poles. This difference is the main driver of atmospheric and oceanic circulations, which act to reduce the equator-pole temperature gradient. It is also influenced by the presence of clouds, reflective surfaces (snow, glaciers, sea ice), large mountain ranges and the topography of the ocean. Latitudinal temperature variations are thus a key criterion for evaluation of climate models. All the models simulate this strong equator-pole gradient: the simulated temperature is 25 °C at the equator, −20 °C at the North Pole and −40 °C at the South Pole, which agrees with observations. However, the models also show significant biases over Antarctica, Greenland, and over large mountain ranges in general, such as the Himalayas. These are due to an approximate representation of the topography (due to the limited spatial resolution of the models) and a poor representation of turbulent exchanges under conditions of strong thermal stability. Over the oceans, there is a warm bias on the eastern coasts caused by a poor representation of stratus clouds observed in these regions.

The annual variation in solar radiation is the strongest energy 'disruption', apart from the diurnal cycle, to which the surface of the Earth is subjected. The observed seasonal temperature cycle is generally well reproduced by the models: it is higher at high latitudes than at low ones (30 °C vs. 5 °C, essentially reflecting the seasonal amplitude of

incoming solar radiation), and is higher over continental areas than above the oceans, mainly because of the lower thermal inertia of the continents.

The formation of precipitation involves numerous processes, some of them on a small scale, and remains one of the phenomena that models have the largest difficulties in correctly simulating. Around the equator, the area of maximum precipitation corresponding to the intertropical convergence zone, is well simulated by the models (Fig. 31.8). In the Pacific Ocean, observations show that the maximum is at 10°N, indicating that this convergence zone is located mainly in the northern hemisphere. The models, on the contrary, generally have two maxima located on either side of the equator, the southern maximum extending almost to the coasts of Peru, although observations indicate that precipitation is almost absent in this region. In observations, the maximum rainfall ranges from northern New Guinea to southern South America. On the continents, one of the biggest flaws of the models is that the intensity of rainfall over the Amazon is too low.

The extent and characteristics of sea ice are relatively well simulated by current models, both in terms of mean value and seasonal cycle. However, in the Arctic basin, few models are able to successfully replicate the distribution of sea ice thickness, which should be less than 1 m north of Siberia, to more than 5 m north of Greenland and of the Canadian archipelago. This difference in ice thickness is mainly due to winds, which move ice from the Siberian coasts to Canadian shores and Greenland. These winds allowed FRAM, the F. Nansen's boat, to cross the Arctic Ocean at the end of the nineteenth century although it was trapped in the ice. The spatial distribution of ice thickness is generally poorly simulated by the models due mainly to poorly simulated surface winds.

Climate Variability

The mean climate state gives a very incomplete picture of the climate. Indeed, climate varies continuously over a very wide range of space and time scales with fluctuations having hourly, daily, interannual, decadal or even longer time scales.

One way to characterize these fluctuations is to select those having a large-scale spatial structure (typically, the scale of an ocean basin or a continent), whether fixed or spreading, and to characterize its temporal evolution (amplitude, phase). To describe these fluctuations, we refer to what we call *modes of variability*. Some of which are well known, such as the El Niño-Southern Oscillation (ENSO) in the tropical Pacific or the North Atlantic Oscillation (NAO), which dominates the weather and climate fluctuations over Europe.

ENSO is the dominant mode of tropical variability at the interannual to decadal time scale. The warm phase, or the El Niño event, is characterized by a warming of the eastern tropical Pacific (along the equatorial cold water tongue) and an easterly displacement of the zone of maximum precipitation, usually located above Indonesia. The cold phase, or La Niña, is characterized by negative sea surface temperature anomalies (i.e. temperatures below the climatological mean) and can be interpreted as an enhancement of the seasonal climatological cycle. This mode of variability is a coupled ocean-atmosphere oscillation that affects atmospheric circulation throughout the tropical belt and ocean circulation throughout the Indo-Pacific basin. Its periodicity is between three and seven years, and the characteristics of ENSO events observed in the twentieth century can vary considerably from one event to another. All current climate models simulate a mode of tropical variability with general

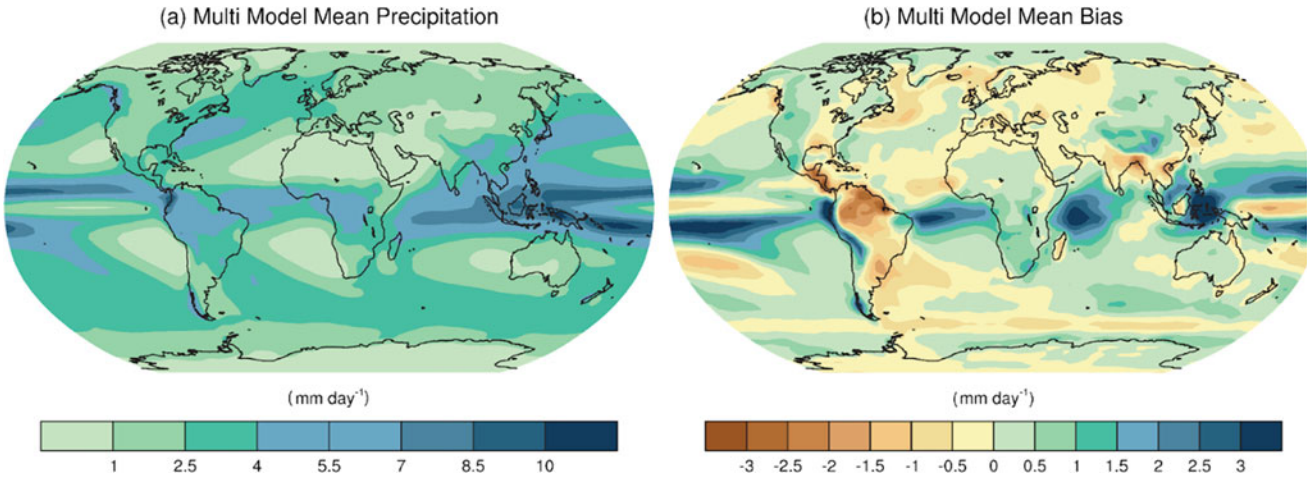

Fig. 31.8 Annual-mean precipitation rate (mm/day) for the 1980–2005 period. **a** Multi-model-mean constructed with one realization of all available AOGCMs used in the CMIP5 (Coupled Models Intercomparison Project, Phase 5) historical experiment. **b** Difference between multi-model mean and precipitation analyses from the Global Precipitation Climatology Project (Adler et al. 2003) (*Source* IPCC 2013)

characteristics resembling those of ENSO. This was not the case with the previous generation of climate models. Nevertheless, the spatial structure of these events is not generally well simulated, such as the asymmetry between the El Niño and La Niña episodes. In terms of the recurrence of these events, the periodicity simulated by the models is usually too short and too regular. In general, the strong diversity of observed spatial and temporal characteristics of ENSO is often poorly simulated. Research works are being done to identify the impact of the different atmospheric and oceanic processes on the characteristics of ENSO, and on the reasons for model errors.

The Madden and Julian—MJO—oscillation (Madden and Julian 1994) is the main mode of intra-seasonal variability in the tropical region, with a periodicity of between 30 and 90 days. Unlike ENSO, whose spatial structure is stationary, this oscillation is characterized by a wave that propagates from west to east, the intensity of the convection alternating between reinforced and reduced. An MJO- type signal is present in the results of most models, but several essential characteristics of this mode of variability (amplitude, phase, propagation) are not realistic. The roles of the different processes and their interactions in the characteristics of this mode of coupled atmosphere-ocean variability have not been well identified and several hypotheses have been proposed.

In the extratropical regions, an important mode of variability is the North Atlantic Oscillation (NAO). It is a pressure oscillation between the temperate and the subpolar latitudes, often defined as the difference in normalized pressure between the Icelandic low and the Azores anticyclone. It is associated with changes in prevailing westerly winds throughout the North Atlantic Basin, and affects the climate of Europe and its surroundings. For example, the positive phases of NAO (NAO+) are associated with a northward shift of low pressure systems with mild and rainy winters and droughts in southern Europe. Current models correctly simulate the spatial properties of the NAO, but are not as good at simulating its temporal properties. In particular, the current trend of the NAO (an increase in positive phases) is underestimated by the models. The reasons for this underestimation are diverse: poor representations of i/the interactions between the stratosphere and the troposphere, ii/the exchanges between stationary waves and transient activity (storms) and iii/the exchanges with the surface of the ocean.

Recent Evolution of the Climate

Over the last 150 years, the evolution of the global surface temperature is documented with a large set of observations. Simulating this evolution is therefore one way to test climate models. Between 1850 and 2000 the steady increase in the concentration of greenhouse gases has led to an increase in radiative forcing of about 2.5 W/m^2. The uncertainty in this forcing is estimated to be quite low at less than ±10%. Since fossil fuels contain sulfur, CO_2 emissions are accompanied by SO_2 emissions which lead to the formation of sulfate aerosols. In 2000, these aerosols produced a radiative forcing of about − 1 W/m^2, but, depending on how it is estimated, this value varies from − 0.5 to −2 W/m^2. In addition, other aerosols, such as soot or aerosols from biomass fires, may also play an important role, but their effects are even less well known. Thus, about a third of the positive radiative forcing (albeit with a high degree of uncertainty) from the increase in greenhouse gases is masked by the negative radiative forcing from aerosols. In addition to anthropogenic forcings, there are natural forcings. At the century time scale, aerosols are mainly injected into the stratosphere by variations in the intensity of incoming solar radiation, and by strong volcanic eruptions where they can remain for several months or even years. These aerosols reflect solar radiation, creating a negative forcing. At the end of the twentieth century, strong volcanic eruptions were more frequent than at the beginning, resulting in an enhanced radiative forcing. Therefore, regardless of the climate response, there is already an inherent uncertainty in the radiative forcing of about ± 50% (IPCC 2013).

When only natural forcings are considered, simulated warming is not in line with observations, especially since the 1980s (Fig. 31.9). However when all forcings are taken into account (natural + anthropogenic), all models are able to correctly simulate the increase in the mean Earth temperature over the past 150 years (Fig. 31.9). Models simulate a greater increase in temperature over the continents than over the ocean and a geographic distribution of warming in agreement with observations (IPCC 2013). Thus, temperature changes over the past 150 years make it possible to verify that the climate response simulated by the models is coherent with the observed temperature variations, although there is too much uncertainty in the forcings to be able to constrain precisely the climate sensitivity of the models.

The aerosols have two opposing effects: one warming the surface, the other cooling it. The first one, called the direct effect, is the diffusion of incoming solar radiation, where part of the solar radiation is returned to space. The second, the indirect effect, is the modification of the optical properties of clouds: the presence of a large number of aerosols increases the number of condensation nuclei. For the same amount of liquid water, more numerous drops forming the clouds tend to have a smaller radius and thus to diffuse more solar radiation. Aerosols are also likely to modify the formation of rain, and therefore the liquid water content of clouds. The complexity of the radiative properties of aerosols in the atmosphere make it more difficult to model the impact of cloud physics.

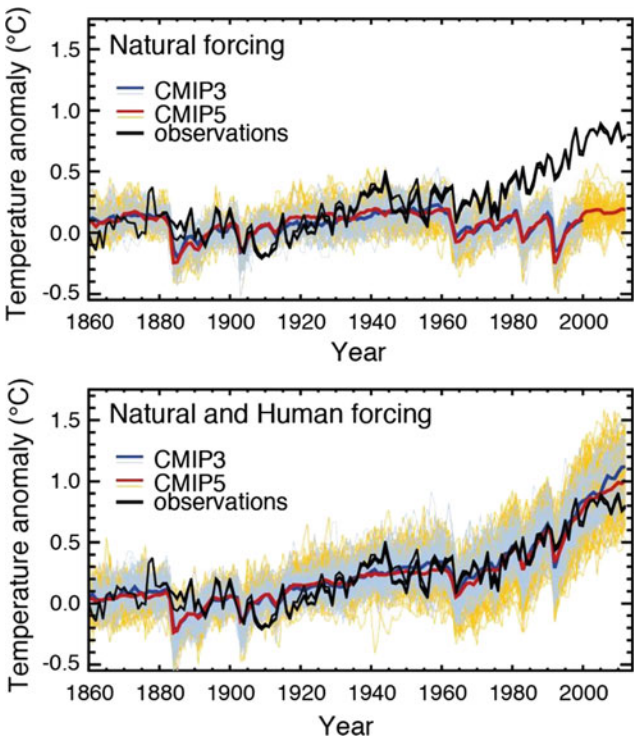

Fig. 31.9 Temporal evolution of the global surface air temperature of the Earth: observations (black line) model simulations taking only natural forcings into account (top), and taking both natural and anthropogenic forcings into account (bottom). The red and blue lines represent the multi-model average of the CMIP3 and CMIP5 (Coupled Models Intercomparison Project, Phases 3 and 5) models respectively (*Source* IPCC 2013)

Projecting the Future of the Climate System

Climate Response to a Doubling of CO_2: Forcings and Feedbacks

Perturbations that modify the energy balance of the climate system are quantified in terms of energy flux at the top of the atmosphere. Quantifying the forcing due to a variation in average insolation is immediate. For a change in the greenhouse gas concentration, a radiative model is used to calculate how these changes affect fluxes at the top of the atmosphere. Since the late 1980s, it is now possible to perform these calculations using radiative transfer codes and spectral databases, provided that all other atmospheric (e.g. clouds, aerosols) and surface (e.g. snow cover) characteristics are assumed to be fixed. For a doubling of the atmospheric CO_2 concentration, the global mean annual radiative forcing at the top of the atmosphere is 3.7 ± 0.2 W/m^2. As we focus on slow climate variations, the calculation of the radiative forcing takes into account the rapid adjustment of the stratospheric temperature.

In response to the radiative forcing ΔQ, the different climate models simulate a temperature change at equilibrium ΔT which is different from one model to another. These differences are difficult to analyze and interpret directly because of the high level of model complexity. A standard method to identify the origin of these differences is the feedback analysis (see, for example, Dufresne and Saint-Lu 2016). From the temperature change at equilibrium ΔT, a 'feedback parameter' λ is defined:

$$\lambda = -\Delta Q/\Delta T.$$

By writing this equation in the form $\lambda \times \Delta T + \Delta Q = 0$, we see that $\lambda \times \Delta T$ represents the variation in the average flux at the top of the atmosphere necessary to compensate for the radiative forcing ΔQ. We can therefore write $\lambda = -\mathrm{d}F/\mathrm{d}T$, with F being the net radiative flux at the top of the atmosphere, counted as positive when it is descending. This derivative can be decomposed, in the first order, as a sum of partial derivatives:

$$\lambda = -\Sigma \partial F/\partial X \times \partial X/\partial T$$

The sum over X is the sum of all the X variables affecting the radiative balance at the top of the atmosphere and that are modified when the surface temperature changes. These are mainly the three-dimensional fields of temperature, water vapor and clouds, and the two-dimensional fields of surface albedo. The change in the temperature field is generally broken down into two terms, one corresponding to a uniform temperature change, the other to the non-uniform part of the temperature change. Finally, the parameter λ can be decomposed as follows:

$$\lambda = \lambda_P + \lambda_L + \lambda_c + \lambda_w + \lambda_a$$

The terms of the right-hand side are the respective feedback parameters: Planck λ_P (uniform temperature change), the temperature gradient λ_L (non-uniform part of the temperature change), clouds λ_c, water vapor λ_w and surface albedo λ_a.

These parameters are often calculated as follows using the partial radiative perturbation method. For a given climate model, two simulations are carried out, a reference one and a perturbed one. The fluxes at the top of the atmosphere are calculated off-line from the outputs of the reference simulation using a radiative code. They are then recalculated by replacing the values of some variables (temperature, humidity, clouds, surface albedo) from the reference simulation with the corresponding values from the perturbed simulation. The difference between these two fluxes gives the sensitivity of the fluxes at the top of the atmosphere to a perturbation of each of the variables.

The particular Planck parameter λ_P corresponds to the response of the flux at the top of the atmosphere to a uniform

temperature change at the surface and within the whole atmosphere. Its value is approximately − 3.2 W/m^2 K. There is very little change in this value from one model to another, and the sign convention used corresponds to a decrease in the Earth's energy balance when the surface temperature increases. In response to a radiative forcing, ΔQ, the surface temperature response can be calculated if the Planck parameter λ_P is the only non-zero feedback parameter:

$$T_P = -\Delta Q/\lambda_P.$$

This so-called Planck response causes an increase of 1.2 °C for a forcing of 3.7 W/m^2, resulting from a doubling of the CO_2 concentration. It is the response of an idealized system in which only the atmospheric and surface temperatures can change uniformly and where only the radiation emission law is affected (see Sect. "Simple Radiative Climate Models and Their Limitations" of this chapter). It can be said that this is the response with no feedback from the climate system. By combining the above equations, the increase in temperature at equilibrium ΔT can be written as a function of the Planck response:

$$\Delta T = \Delta T_P/(1 - g)$$

where g is the feedback gain of the system:

$$g = -(\lambda_L + \lambda_c + \lambda_w + \lambda_a)/\lambda_P.$$

If the gain g is positive and less than 1, the feedbacks will amplify the temperature increase ΔT, relative to ΔT_P. Conversely, if the gain is negative, the ΔT increase will be attenuated. In the preparation of the Fifth IPCC Assessment Report (IPCC 2013), climate change simulations were conducted within the CMIP5 project by around forty climate models. In particular, for a doubling of the CO_2 concentration, the models simulate a global warming of 3 °C on average (between 2.0 and 4.6 °C depending on the model), until a new energy equilibrium is found. We have seen that in the absence of feedbacks, this warming would be 1.2 °C. This means that climate feedbacks amplify this warming by a factor of 2 to 4 depending on the model.

Other developments make it possible to use the feedback parameters to estimate the temperature increase due to the Planck response and to the various feedbacks (Dufresne and Bony 2008). They were applied to twelve CMIP3 (Coupled Models Intercomparison Project) models, and the results are shown in Fig. 31.10 illustrating both the average contribution of the models and the inter-model dispersion. These results were confirmed for the CMIP5 models (Vial et al. 2013).

Several of the mechanisms governing the feedback parameter values, and hence the gain, are now well identified (Bony 2006). For example, an increase in the temperature of the atmosphere increases the saturation vapor pressure of the water vapor. If there is little variation in the relative humidity, this results in an increase in the concentration of water vapor in the atmosphere, and therefore in the greenhouse effect, thus constituting a very powerful amplification mechanism of the warming: 1.7 °C on average for the models considered here.

For thermodynamic reasons (variation of the adiabatic temperature gradient as a function of humidity), it is also expected that, in the case of a humid tropical atmosphere, variations in water vapor will be accompanied by greater warming at high altitudes than close to the surface (except at high latitudes). This increases the emission of infrared radiation from the upper atmosphere and is the only negative feedback: it decreases warming (− 0.8 °C on average). As these two feedbacks are very strongly correlated for physical reasons, their combined effect is generally considered to contribute about 1 °C to the increase in mean temperature (Fig. 31.10a).

The mechanisms behind the surface albedo feedback are also well identified: an increase in temperature increases the melting of snow and ice. This decreases the area covered by surfaces that reflect solar radiation, and therefore increases the amount of energy absorbed by the Earth. This effect contributes about 0.2 °C to the temperature increase (Fig. 31.10a).

Finally, the increase in temperature is likely to impact cloud cover. As seen before, clouds exert two opposing effects on the terrestrial radiative balance: on the one hand, by reflecting solar radiation, they contribute to a cooling of the Earth, and on the other, by absorbing infrared radiation, they contribute to increase the greenhouse effect. The relative importance of these two effects depends on multiple factors. The average contribution of clouds estimated by the models considered here is equivalent to a warming of 0.7 °C (Fig. 31.10a). However, the dispersion between models is high (Fig. 31.10b): while some models predict a relatively neutral cloud response, most predict a decrease in cloud cover as temperature increases and an increase in global warming of up to 2 °C.

Recent studies indicate that this uncertainty stems mainly from the way different climate models predict the response of low clouds (stratus, stratocumulus or small cumulus clouds) to global warming. The way other clouds (including large cumulonimbus storm clouds) respond to climate change is also uncertain. This response contributes only poorly to the uncertainty on the magnitude of global warming, but contributes strongly to uncertainties in regional precipitation changes associated with global warming.

Other feedbacks exist in the climate system, for example, those potentially causing changes in the atmospheric carbon storage capabilities by the ocean and the biosphere. They will be discussed below (Sect. "The CO_2 Cycle").

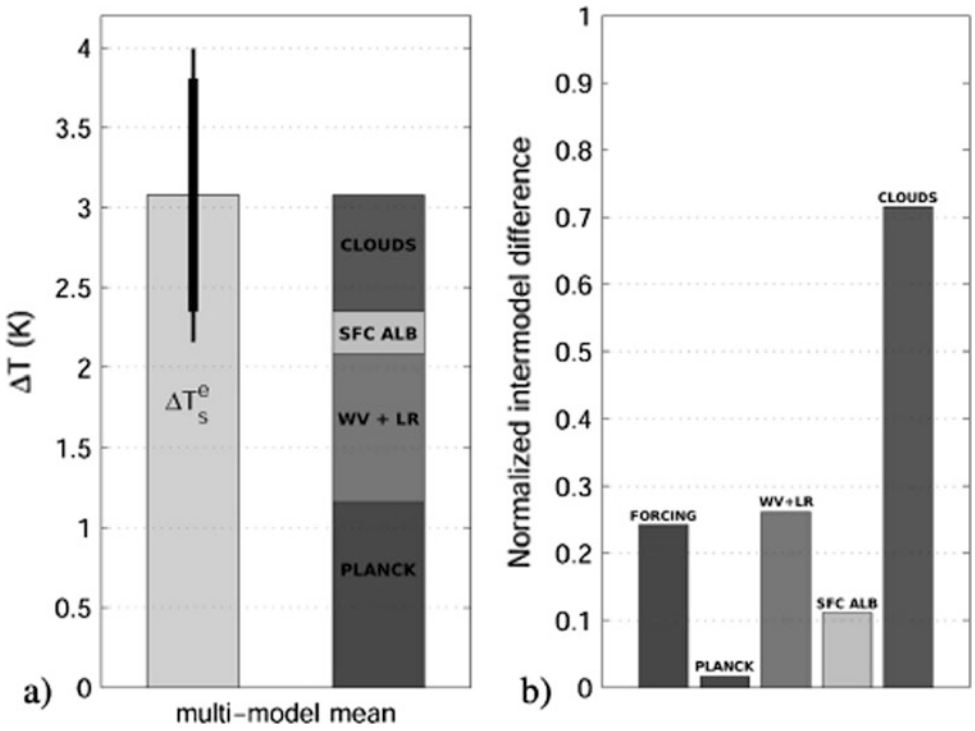

Fig. 31.10 For a doubling of atmospheric CO_2: **a** bar on the left, multi-model mean ± 1 standard deviation of increase in global temperature (ΔT_e, °C) and, bar on the right, part of this increase due to the Planck response and to the different feedbacks: combined effects of water vapor and temperature gradient (WV + LR), surface albedo and clouds. **b** Standard deviation of the inter-model difference in temperature increase attributable to radiative forcing, the Planck response, and various feedbacks, normalized by the standard deviation of the increase in global temperature. According to Dufresne and Bony (2008)

Future Scenarios

It is important to keep in mind that the future climate cannot be accurately predicted. This can be explained by several reasons including model uncertainties, uncertainties in scenarios of future greenhouse gas emissions and uncertainties in natural disturbances, such as volcanism, having a strong impact on radiative forcing. However, we can try to answer specific questions: independently of the natural forcings, how would the climate evolve if greenhouse gas emissions followed this or that emission pathway? To this end, various socio-economic scenarios for the evolution of human activities have been established. Four representative concentration pathways (RCP) scenarios have been selected, labeled by a value that corresponds approximatively to the radiative forcing in 2100: RCP2.6, RCP4.5, RCP6.0, RCP8.5 (top of Fig. 31.11). On one extreme, CO_2 emissions rapidly stabilize and then decrease down to zero before 2100 for scenario RCP2.6. On the other extreme, CO_2 emissions continue to grow until 2100 for scenario RCP8.5, which is for now the most realistic one. CO_2 emissions are mainly due to the use of fossil fuels (oil, coal, gas) and to the SO_2 emissions from the sulfur contained in these fuels. Mainly for health reasons, fuels are increasingly purified of sulfur before use, resulting in a slower increase in CO_2 emissions (or a faster reduction) than for CO_2 in almost all scenarios. For the last IPCC exercise (IPCC 2013), the concentrations of the different gases were calculated from their emissions by biogeochemical cycle models and by chemical-transport models for sulfate aerosols. The concentrations of each of these constituents can then be used to calculate the corresponding radiative forcing. For example, the evolution of the different forcings from 1860 to 2100 for the RCP8.5 scenarios is shown at the bottom of Fig. 31.11.

The CO_2 Cycle

As described in Chap. 23, the carbon cycle is strongly linked to the living world. Understanding the roles of the two main reservoirs, the ocean and the terrestrial biosphere, is therefore crucial to understanding how atmospheric CO_2 will evolve in the coming decades. The ocean is the largest carbon reservoir (holding 40 times the atmospheric content) and can regulate the atmospheric CO_2 concentration by exchanging CO_2 with the atmosphere. These exchanges depend largely on the vertical carbon gradient in the ocean: surface waters are depleted of inorganic carbon and mineral salts; conversely, the deep ocean is enriched in carbon and mineral salts. The existence of this vertical gradient is driven mainly by ocean biology, which establishes a biological pump and transfers carbon from the surface to the bottom. Any modification of this pump may ultimately influence the atmospheric reservoir.

What about anthropogenic disturbances and their impacts on the carbon cycle? These impacts are manifold: a direct chemical consequence of the increase in atmospheric CO_2 is the acidification of the oceans; a thermal consequence of the

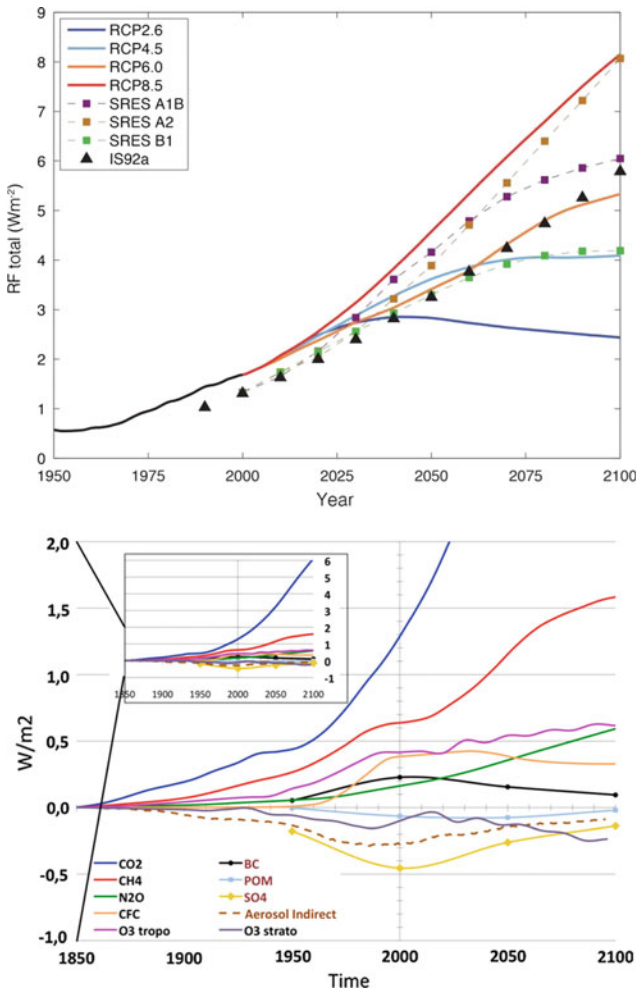

Fig. 31.11 Top: Time evolution of the total radiative forcing (in W/m^2) due to human activities for the three SRES emission scenarios used in IPCC-AR4 (IPCC 2007) and the four RCP scenarios used in IPCC-AR5 (IPCC 2013). Bottom: Temporal evolution of the radiative forcing (in W/m^2) due to the different chemical agents for the scenario RCP8.5 (Szopa et al. 2013)

warming of the water is a decrease in the capacity of the ocean to absorb CO_2, and a biological effect is a modification in the distribution of species due to environmental changes (salinity, temperature) which can cause transformations in the trophic chain and therefore in the biological pump. In terms of CO_2 sinks, it is now known that for two CO_2 molecules emitted, only one remains in the atmospheric reservoir while the other is stored either in the terrestrial biosphere or in the ocean. This ratio is the result of many processes involved in the regulation of the carbon cycle; therefore, due to the anthropogenic perturbation it is expected to vary. The capacity of continents to store carbon can change either gradually or abruptly. For example, permafrost thawing in Siberia would release the equivalent of an additional 100 ppm of CO_2 at least into the atmosphere. As for the biological pump, this will depend on how life functions and adapts in a warming world, which is not easy to predict.

Climate Projections for 2100: What the Models Say: Main Climate Characteristics

In this section, the results are derived, unless otherwise indicated, from simulations performed by the forty or so coupled atmosphere-ocean general circulation models (or climate models) that contributed to the CMIP5 exercise. The values given below are the average of the models ± 1 standard deviation.

The Amplitude of the Warming

In response to both anthropogenic (greenhouse gases and aerosols) and natural (volcanoes and solar intensity) forcings, the models simulate an average global increase in air temperature near the surface of about 0.8 °C between the beginning and the end of the twentieth century, consistent with observed measurements. Sensitivity studies, with different forcings, have shown that this warming is mainly due to anthropogenic forcings. Today, the climate system is out of balance; if the concentrations of greenhouse gases and aerosols were maintained at their 2000 values, the climate would continue to warm by around 0.4 °C through the twenty-first century. However, the simulated increase in temperature depends above all on the emission scenarios. Indeed over twenty models, when the concentration of greenhouse gases is prescribed, there is on average a variation of a little less than 1 °C for the RCP2.6 scenario and of 4 °C for the RCP8.5 scenario (Fig. 31.12). The dispersion of the simulated warming by the different models at the end of the century is ± 0.5 °C, the main reasons for which are outlined in Sect. "Climate Response to a Doubling of CO_2: Forcings and Feedbacks" of this chapter.

Geographical Distribution of Temperature Changes

The geographical distribution of the temperature increase is roughly similar for the different scenarios (although the amplitudes are very different). Figure 31.13 illustrates the RCP2.6 and RCP8.5 scenarios. It shows results that are now well established: the temperature increase is higher on land than on the oceans, and is particularly strong in the high latitudes of the northern hemisphere.

In the tropics, the greater increase in temperature over land than over ocean is partly explained by changes in

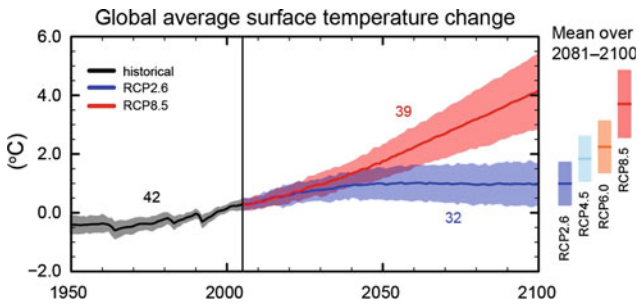

Fig. 31.12 Multi-model time series of air surface temperature anomaly (°C) (compared to the 1986–2005 average), for the twentieth and twenty-first centuries under two different scenarios with very contrasting emission scenarios: RCP2.6 (blue) and RCP8.5 (red). The mean and associated uncertainties averaged over 2081–2100 are given for all RCP scenarios as colored vertical bars. The line represents the average of the models and the light-colored regions, the spread

evaporation. Over the oceans, the amount of water available for evaporation is not limited, while on the continents it depends on the amount of water available in the soil, and thus, on the amount of precipitation. Due to latent heat exchanges, evaporation cools the surface and this cooling effect is larger over the oceans than over continental areas. For example, with the IPSL model, evaporative cooling is found to reduce the surface radiative balance by 9.8 W/m^2 over the ocean against only 0.2 W/m^2 over the continents. Other processes, such as changing cloud cover or changing atmospheric circulation, also play a role in the ocean-continent warming differential.

In the mid and high latitude regions, the smaller increase in ocean surface temperature is partly due to its thermal inertia. This is particularly true in the southern hemisphere, where very strong winds cause great mixing of the ocean, and where the ocean temperature remains homogeneous to a considerable depth. In order for the temperature of the ocean surface to increase, a large amount of water must be heated up.

The larger increase in temperature in the high latitudes of the northern hemisphere is partly due to the surface albedo feedback. The increase in temperature is accompanied by a decrease in snow cover and sea ice extent in spring and summer. This reduces the reflection of solar radiation at the surface, increases the amount of radiation absorbed and tends to amplify the initial increase in temperature. In regions where the sea ice thins, or even disappears, air temperature rises sharply as the temperature of the ocean surface is higher than that of sea ice. Finally, a change in atmospheric circulation (and in particular the increase in water vapor transported to the high latitudes) is another reason for the strong increase in temperature in these regions. In the south and east of Greenland, it is noted that the temperature of the air near the surface increases only slightly. This trend is more or less marked depending on the model, with some even simulating a slight local cooling. The reason for this is a change in the ocean circulation, and especially in the thermohaline circulation. In these areas, the density of sea water decreases at the surface because of increasing temperatures and/or precipitation. Surface waters are no longer dense enough to sink, reducing oceanic convection and the associated North Atlantic drift. The effect of this density reduction on temperature depends on the model, both in terms of amplitude and geographical extension. It modulates global warming locally and influences global warming slightly, but nevertheless this warming remains significant on all continents of the northern hemisphere, especially in Europe.

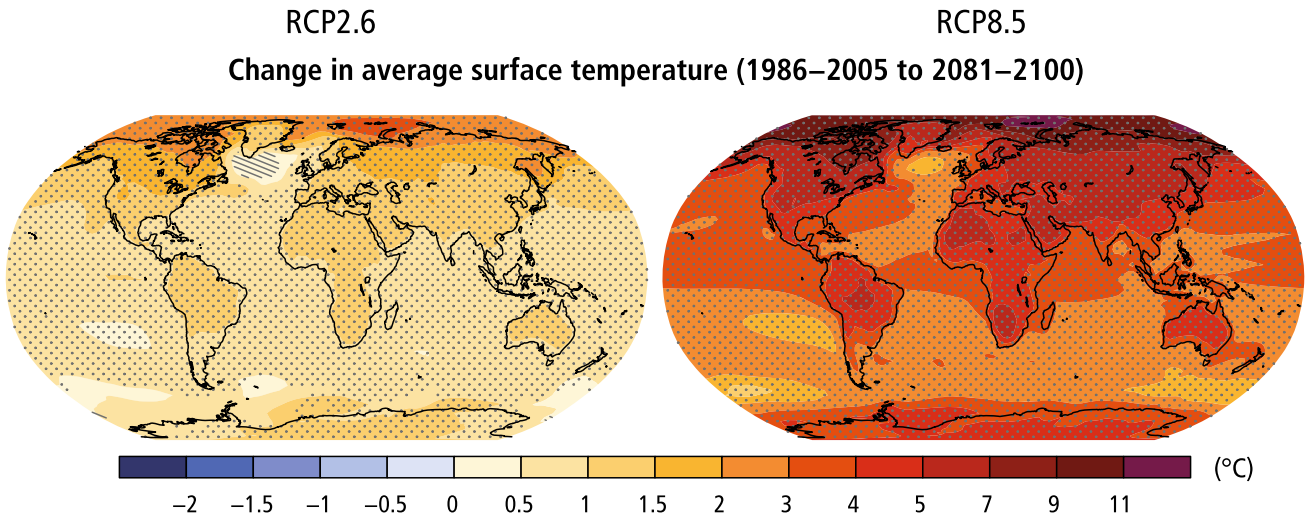

Fig. 31.13 Multi-model average of the difference in air surface temperature (°C), between the end of the twenty-first century (2081–2100) and the end of the twentieth century (1986–2005), for the RCP2.6 (left) and RCP8.5 (right) scenarios (*Source* IPCC 2013)

Changes in Precipitation

Although there is a large spread between climate models, on average, they project an increase in precipitation over the twenty-first century alongside increased temperatures (IPCC 2013). Projected precipitation changes exceed 0.05 mm/day and 0.15 mm/day with the RCP2.6 and RCP8.5 scenarios respectively. These changes are far from being spatially homogeneous and exhibit a strong seasonal variability (Fig. 31.14). However, if we consider the zonal means, there is a tendency towards increased precipitation everywhere, except in the subtropical regions (around 30°N and 30°S) and in the Mediterranean basin where they decrease. The general increase in precipitation is due to the increase in atmospheric water vapor content, while the decrease simulated in the subtropical regions is related to a change in atmospheric circulation.

It can be seen that the models consistently simulate a year-round increase in precipitation at high latitudes, and a winter increase in the mid-latitudes (Fig. 31.14). Similarly, they consistently simulate a decrease in precipitation in subtropical regions. In Europe, models simulate an increase in precipitation in the north and, on the contrary, a drying up around the Mediterranean Basin. On the other hand, changes in precipitation in the equatorial and tropical regions are not consistent from one model to the other, especially on the continents such as South America, West and Central Africa, India and South-East Asia. In these areas, some models simulate a decrease in precipitation, while others simulate an increase. These differences between models are particularly pronounced in the monsoon regions. In general, changes in precipitation on the continents remain very uncertain, even in terms of annual mean. This is due to major uncertainties in the representation of the different processes. Currently, there

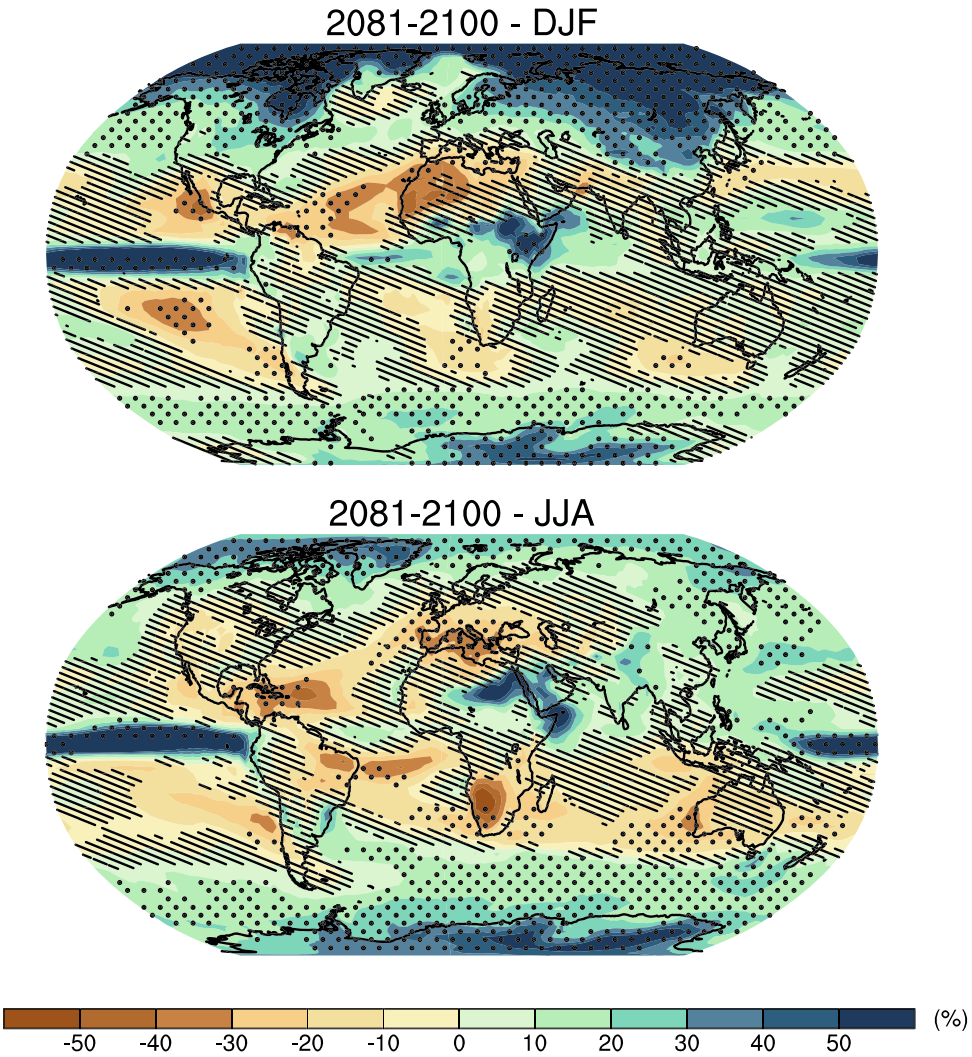

Fig. 31.14 Multi-model average of the precipitation difference (%) between the end of the twenty-first century (average between 2081 and 2100) and the end of the twentieth century (average between 1980 and 1999), for the RCP8.5 scenario for December–January–February (*top*) and (*bottom*) June–July–August. Hatching indicates regions where the multi-model mean change is less than one standard deviation of internal variability. Stippling indicates regions where the multi-model mean change is greater than two standard deviations of internal variability and where at least 90% of models agree on the sign of change

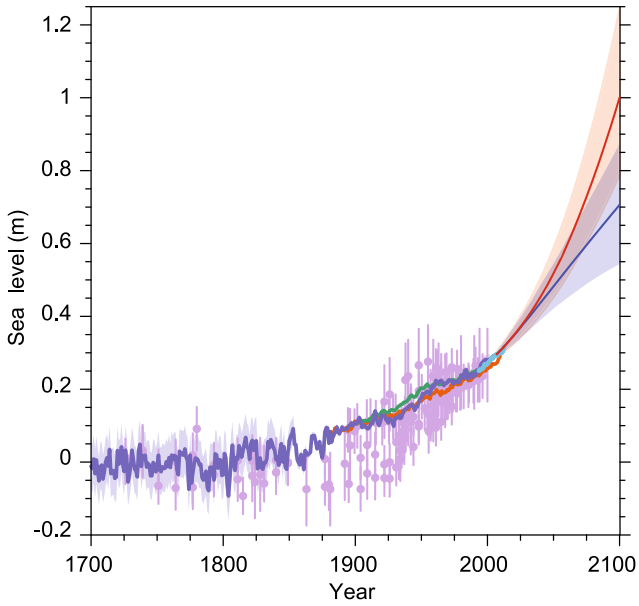

Fig. 31.15 Compilation of paleo sea level data, tide gauge data, altimeter data and central estimates and likely ranges for projections of global mean sea level rise for RCP2.6 (blue) and RCP8.5 (red) scenarios, all relative to pre-industrial values (*Source* IPCC 2013)

is no clear way of identifying which of the results are the most reliable (Fig. 31.15).

Changes in Storm Patterns

Under climate change, the characteristics of lows in the mid-latitudes (particularly those reaching the coast of Brittany) are likely to change for two reasons: the first is a change in the equator-pole temperature gradient, which tends to decrease near the surface but to increase with altitude. The second reason is an increase in the total amount of water vapor in the atmosphere, and in turn, in the amount of water vapor that can be condensed and thus release latent heat. In climate change simulations, we observe a poleward shift of low-pressure, a reduction in the total number of depressions, but an increase in the number of deeper and hence stronger troughs. For example, according to the diagnoses made by Lambert and Fyfe (2006), the models simulate, on average, in 2100 and for a moderate greenhouse gas scenario, a decrease in the total number of depressions of around 10% in the southern hemisphere and a little less in the northern hemisphere. They also simulate an increase of 20% of the number of intense depressions in the northern hemisphere and of 40% in the southern hemisphere.

Evolution of Sea Ice

The analysis of CMIP3 and CMIP5 models clearly highlights a sea-ice decline in the course of the twenty-first century, the dominant factor being the rising summer temperatures rather than the winter ones which are projected to remain negative. Though most of the CMIP5 models project a nearly ice-free Arctic Ocean by 2100 with a sea ice extent of less than 1×10^6 km^2 (for at least 5 consecutive years) at the end of summer in the RCP8.5 scenario, some show large changes occurring before 2050. However, these results are strongly dependent on the ability of models to reproduce the climatological mean state of the Arctic sea ice cover over 1979–2012. Based on the CMIP5 multi-model ensemble, projections of average reductions in Arctic sea ice extent for 2081–2100 compared to 1986–2005 range from 8% (RCP2.6) to 34% (RCP8.5) in February and from 43% (RCP2.6) to 94% (RCP8.5) in September. The evolution of sea ice around the Antarctic is more uncertain. The CMIP5 multi-model mean projects a decrease in sea ice extent ranging from 16% for RCP2.6 to 67% for RCP8.5 in February and from 8% for RCP2.6 to 30% for RCP8.5 in September for 2081–2100 compared to 1986–2005. There is, however, low confidence in those values because of the wide inter-model spread and the inability of almost all of the available models to reproduce the mean annual cycle, the interannual variability and the overall increase of the Antarctic sea ice coverage observed during the satellite era.

Evolution of Continental Ice

Retreat of the glaciers

Glaciers react quickly to climatic effects and are thus good indicators of climate change. For more than a century, and especially since the 1980s, the retreat of glaciers has been a phenomenon occurring almost everywhere on the globe. This phenomenon is likely to increase in the twenty-first century with the rising temperatures, and could even lead to the disappearance of certain glaciers in the coming decades. Projections of the future evolution of glaciers depend, on the one hand, on climate scenarios but also, on their sensitivity to global warming.

Glaciers located in dry and cold regions (such as the Canadian Arctic) have low sensitivity to global warming and are more prone to resist. On the contrary, glaciers located in coastal regions are subject to oceanic influence and have a greater sensitivity to global warming. This is the case of Norwegian glaciers, for example. In recent decades, these have tended to grow due to increased precipitation. But in

recent years, this trend seems to have been reversed. Alpine glaciers are in an intermediate situation. We will not review exhaustively the melting of glaciers, but we chose to illustrate this behavior through the study of two alpine glaciers.

At the Environment Geosciences Institute of Grenoble, two studies were carried out on alpine glaciers, one on the Saint-Sorlin, the other at the dome of Goûter, in the Mont-Blanc massif.

The first study simulated the future evolution of the mass balance of the Saint-Sorlin, located in the Grandes Rousses massif whose highest point is at 3400 m altitude. The results show that even with an optimistic greenhouse gas emission scenario (+1.8 °C in 2100), the equilibrium line (i.e. the lowest limit of eternal snow) is at a higher altitude than the highest point of the glacier. This means that over a full year, the glacier does not accumulate snow (or ice) and is therefore in a state of chronic ablation. In order to simulate the dynamic response of the glacier, these results were then used as inputs for a two-dimensional ice flow model. Despite a moderate global warming, the model suggests a complete disappearance of the glacier around 2070. The dynamic response of the glaciers is complex because it depends not only on their specific morphology, which is different from one glacier to another, but also on many physical processes, which are sometimes difficult to simulate, and which determine their temporal response, i.e. on what timescale the glacier will grow or, on the contrary, disappear. Nevertheless, this study suggests that alpine glaciers similar in size and located at an altitude close to that of the Saint-Sorlin, could undergo the same type of evolution in the twenty-first century under the influence of moderate global warming.

The second study is based on borehole temperature measurements (140 m deep) located at the Dome du Goûter at 4250 m altitude. These measurements showed a warming of 1 to 1.5 °C over the first 60 m of ice, between 1994 and 2005. A physical modeling of the process of heat diffusion in the ice made it possible to show that the observed warming results not only from atmospheric warming, but also from the heat produced by the refreezing of surface melt water that percolates at depth.

Moreover, simulations carried out for different global warming scenarios confirm the twenty-first century trend and show that, regardless of the scenario, the Alpine glaciers, currently classified as 'cold' and located between 3500 and 4250 m altitude with an internal temperature ranging from 0 to −11 °C, could become 'temperate', with an internal temperature close to the melting point.

Other modeling studies using different greenhouse gas scenarios lead to similar and equally disturbing conclusions. A study conducted in the Montana region in the Glacier National Park shows that, with a doubling of CO_2, some glaciers would disappear by 2030, despite an increase of 5–10% in average precipitation in the mid and high latitudes.

The future of ice sheets

There are different approaches to determine how polar ice sheets will evolve in the future. The first one is to determine their surface mass balance which is directly dependent on the climate. To simulate as precisely as possible the mass balance of the ice sheets, high-resolution climate models are necessary to properly represent the topography of the ice sheets, especially the steep slopes at the margins. These areas correspond to the ablation zones and are also the locations where most of the precipitation falls. However, AOGCMs usually tend to overestimate precipitation and underestimate ablation. In addition, snowpack models implemented in general circulation models are often too simplistic and do not account for key processes taking place in the snowpack. Among the missing processes are the refreezing of surface melt water that percolates at depth, the transport of snow by winds, the snow metamorphism and the transformation of snow into ice. These processes are crucial for the estimates of surface mass balance. For example, water refreezing modulates surface runoff and snow metamorphism strongly modifies the albedo and thus the surface energy balance.

Regional atmospheric models generally offer a better representation of the surface energy balance than AOGCMs because of their finer resolution and the inclusion of more sophisticated snow models. However, as they are forced at their lateral boundaries by outputs from global climate models, they may suffer from the global model deficiencies. As a result, the uncertainties associated with the GCM-based forcing represent about half of the uncertainty associated with changes in surface mass balance inferred from regional climate models (RCM). All RCM-based studies project an increase in precipitation over large parts of Greenland and Antarctic ice sheets in response to global warming, but there is great uncertainty as to the magnitude of this increase. Projections suggest that over Greenland, ablation will largely exceed the increase in snowfall. Conversely, in East Antarctica, precipitation is expected to exceed ablation throughout the twenty-first century, but the key question is whether the mass gain will be offset by dynamical ice losses from the West Antarctic ice sheet.

The surface mass balance is not the only important parameter in the determination of the evolution of polar ice sheets. As explained earlier, their dynamic response must also be considered. This can be achieved through the use of three-dimensional ice-sheet models which include most of the processes responsible for the ice-sheet evolution as a function of climate forcing (temperatures and precipitation or surface mass balance). For a more thorough description of ice-sheet models, we ask the reader to refer to Chap. 24 of this volume. However, several problems may arise when using such models. As previously mentioned, the surface

mass balance can be computed by a climate model (RCM or AOGCM), but frequently, ablation is still determined from an empirical formulation that relates the number of positive-degree-days (integral of positive temperatures) to the snow and ice melting rates. The main drawbacks of this approach is that it does not account for albedo changes and it has been validated on only a few Greenland sites for the present-day period. The mass balance derived from such methods is generally more uncertain than that obtained using regional models. Another difficulty is linked to the difference of resolution between climate and ice-sheet models. As temperature, precipitation and surface mass balance are highly dependent on topography, the development of appropriate downscaling techniques is required to account for the effect of altitude.

In addition, researchers still face many challenges in representing some processes related to rapid dynamics, such as those occurring at the base of the ice sheet or at the ice-ocean interface, where small disturbances seem capable of triggering strong instabilities, which can propagate up to a thousand kilometers upstream, and lead to a destabilization of the entire ice sheet. However, understanding the impact of small-scale processes on the large scale is still in its infancy. Over the last two decades, observations have shown an increase in the flow of outlet glaciers, suggesting that these could respond much more quickly than previously expected to variations in atmospheric and oceanic conditions, making possible a significant retreat of the ice sheet in the more or less distant future. The physical laws governing ice flow in these glaciers still remain poorly known. For example, although the marine ice-sheet instability is increasingly well represented in new generation ice-sheet models, there is no consensus on hydro-fracturing yet. Large uncertainties also exist on the physical laws governing iceberg calving and basal melting under the ice shelves. A last, but not least, problem is related to the initial state of the ice sheets. Indeed, starting future short-term (a few centuries) simulations from a realistic present-day state of the ice sheet is of primary importance to avoid as much as possible spurious biases in the results. Getting an accurate initial state is challenging however because of the scarcity of observations on vertical velocity and temperature profiles, and also on basal conditions (e.g. frozen or thawed bed areas, bedrock topography). Several approaches have been developed ranging from long free-evolving simulations over one or several glacial-interglacial cycles to more formal optimization approaches often based on inversion techniques, with various target criteria (either surface velocities or topography in agreement with observations, or internal properties accounting for the past history of ice sheets). Each of these techniques presents some advantages and drawbacks, but their efficiency should improve in the future as the number of observations grows. Recent remote sensing observations made over Greenland and Antarctica are expected to refine numerical simulations and thus to improve the relevance of future forecasting models. Finally, part of the uncertainty in the future ice-sheet responses comes from uncertainty in the climate forcing itself. This is due to our lack of knowledge in the future socio-economic pathways and to the biases of the climate models. Moreover, climate-ice sheet interactions are still very rarely taken into account in the models. Accounting for these interactions may have the potential to strongly modify not only the simulated climate and ice-sheet responses but also sea-level projections (Bronselaer et al. 2018; Golledge et al. 2019).

Sea Level Change

We have seen, in the first part of this chapter, that at the scale of a few decades, the main causes of sea-level variations are due, on the one hand, to the thermal expansion of the ocean (in the case of a warming climate), and on the other hand, to changes in the mass of water in the ocean due to exchanges with continental reservoirs. Based on the results from 21 AOGCMs, the sea-level projections reported in the Fifth IPCC report (IPCC 2013), all show an increase in sea-level by the end of the twenty-first century (2081-2100) compared to the 1986–2005 period, with an average global mean sea-level rise ranging from 0.28 to 0.61 m for RCP2.6 and from 0.52 to 0.98 m for RCP8.5. For the RCP8.5 scenario, the rate of sea-level rise increases throughout the twenty-first century, going from 3.2 ± 0.4 mm/yr (for the 1993–2010 period) to 11.2 mm/yr (2081–2100), whereas, in the RCP2.6 scenario, the rate increases up to 4.4 mm/yr around 2050 and slightly declines in the second half of the century.

According to the Fifth IPCC report (IPCC 2013), thermal expansion remains the main contributor (30 to 55%) to global mean sea-level rise over the twenty-first century with median rates of 0.14 ± 0.04 m (RCP2.6) and 0.27 ± 0.04 m (RCP8.5) in 2081–2100. These contributions can be estimated from changes in ocean heat uptake increasing roughly linearly with global mean surface air temperatures simulated by the AOGCMs. It should be noted that AOGCM simulations do not include volcanic forcing which may reduce the projected contribution of thermal expansion.

The AOGCM simulations forced by the different RCP scenarios highlight a spatial variability of sea level (Fig. 31.16). As they do not take into account the freshwater fluxes coming from ice sheets, this regional variability, previously observed in satellite measurements over the 1993–2010 period, is linked to a variability in the atmosphere-ocean-sea-ice system. More specifically, regional variability can be due not only to variations in temperature and salinity (i.e. precipitation/evaporation ratio) and therefore density, but also to variations in ocean and atmospheric circulations

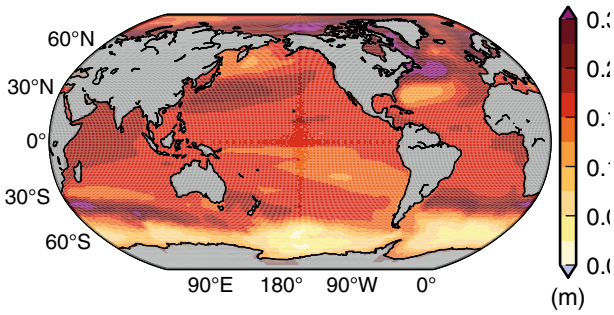

Fig. 31.16 Ensemble mean projection of the time-averaged dynamic and steric sea-level changes for the period 2081–2100 relative to the reference period 1986–2005, computed from 21 CMIP5 climate models (in meters), using the RCP4.5 experiment. The figure includes the globally-averaged steric sea level increase of 0.18 ± 0.05 m (*Source* IPCC 2013)

(variations in wind direction and intensity). From one model to another, the spatial distributions of sea level variations are not identical. However, some common features emerge in the projections for the end of the twenty-first century that are identified in Fig. 31.16. For example, the Southern Ocean is characterized by a lower-than-average sea-level rise, likely related to changes in wind stress and heat fluxes. These changes are also responsible for the greater sea-level rise in the Pacific (Bouttes and Gregory 2014). A dipole pattern with greater sea-level rise in the north and smaller sea-level rise in the south can also be seen in the North Atlantic and is attributed to changes in heat and freshwater fluxes.

While changes in sea level due to thermal expansion can easily be determined from climate models, we have seen in the previous section that there are significant uncertainties in the simulation of future continental ice. These uncertainties dominate the projections of sea-level rise resulting from ice-sheet surface melting, dynamic ice discharges or iceberg calving. As a result, these projections are not very different from one climate scenario to another. For example, in the last IPCC report (IPCC 2013), the contribution from the rapid dynamics of the ice sheets is estimated to be between 0.03 and 0.19 m for the RCP2.6 scenario and between 0.03 and 0.20 m for the RCP8.5 scenario.

To better represent the contribution of polar ice sheets to sea-level rise in the future, an accurate representation of rapid ice dynamics in ice-sheet models is of primary importance. The resolution (5–10 km) of the previous generation of three-dimensional large-scale ice-sheet models is not fine enough to properly capture the rapid ice streams whose characteristic spatial scale may be smaller than 1 km in some cases. Moreover, these models are based on approximations resulting in simplified equations of ice dynamics. While these approximations are crucial to investigate the ice-sheet behavior at the multi-millennial time scale, they may cause deficiencies in the representation of rapid ice dynamics as well as in the representation of grounding line migration, which plays a crucial role in ice-sheet evolution as mentioned earlier. However, significant progress has been made in the development of ice-sheet models, such as the Full Stokes models (e.g. Gillet-Chaulet et al. 2012). These models do not rely on simplifying assumptions and have an adaptive mesh that may be less than 1 km at the ice-sheet margins, thereby providing a more accurate representation of ice-sheet dynamics. However, these models are highly expensive in terms of computational time and have not yet been applied to the whole Antarctic ice sheet. A second limiting factor is related to the fact that some processes remain poorly constrained due to the scarcity of observations (e.g. basal conditions or hydro-fracturing), or poorly understood (e.g. basal melting under the ice shelves or iceberg calving). Finally, as mentioned in the previous section, there is a crucial need to develop Earth System Models which account for the feedbacks between climate and ice sheets so as to refine sea-level projections.

It is important to note that since the publication of the last IPCC report (IPCC 2013), many projections coming from individual studies have provided higher estimates of the projected sea-level rise compared to those reported by the IPCC (0.52 to 0.98 m for the highest emission scenario). The main reasons for this disagreement are related to the large uncertainties associated with the future ice-sheet evolution and to the fact that the IPCC only selected the most likely range of sea-level rise estimates and excluded the most extreme (considered as less likely) outcomes. All the projections together give a range of 0.16–2.54 m in 2100 (Garner et al. 2018) which reflects the large uncertainties in the maximum contribution of Greenland and Antarctica (DeConto and Pollard 2016) and suggests the possibility for these ice sheets to become the main contributor to global mean sea-level rise in the course of the twenty-first century.

The Climate of the Next Millennium: Towards Integrated Modeling of the Earth System

Climate Change: Anthropogenic Disturbance Versus Variations in Insolation

In Chap. 28, we analyzed in detail the climate variations induced by the orbital parameter variations over the scale of tens of thousands of years. We are interested here in much longer time scales ranging from 100,000 to millions of years. The amplitude of warming projected by climate models over the next decades and even the next century raises questions about the impact of this profound change in the climate system over several millennia, especially as the acceleration of CO_2 emissions suggests that the magnitude of the perturbation may be even greater than that predicted by the most pessimistic scenario.

Data from Vostok and EPICA ice cores in Antarctica, showed that atmospheric CO_2 varied by about 100 ppm during the transition from an ice age to an interglacial period, and that these variations were correlated with changes in air temperatures, suggesting a link between CO_2 and climate. Today, this link is commonly accepted and attention is focused on global warming due to the increase in greenhouse gases in the atmosphere. However almost forty years ago, in 1972, the climatological community met in the United States to discuss the imminence of the next ice age. This question arose because geological data showed that for about a million years, the Earth had alternated between cold episodes corresponding to the glaciation phases, and the warmer interglacial periods, with a pseudo-periodicity of 100,000 years.

Data available in 1972 showed that the previous two interglacial periods had lasted about 10,000 years. Yet, the Holocene, the interglacial period we are currently experiencing, has been going on for 10,000 years. It seemed therefore reasonable to think that this warm phase would soon end and give way to a new ice age. This reasoning was based on the assumption that all interglacial periods are of equal duration. However, although the first numerical experiments carried out with statistical models indicated that the cooling initiated 6000 years ago (after the Holocene climate optimum) would continue in the future, Oerlemans and Van der Veen (1984) of the University of Utrecht showed, with an ice-sheet model, that the transition to a new glacial phase would not occur before 50,000 years.

Based on data from marine sediments and ice cores, it is now well established that the duration of an interglacial period varies considerably from one climatic cycle to the next. The same models used to predict the future were used to simulate the last interglacial-glacial transition. Indeed, taking into account the atmosphere-ocean feedbacks, these models produce perennial snow in the Canadian archipelago (Khodri et al. 2001). It is also known that the Earth's orbital parameters (see Chap. 28) that govern the seasonal and latitudinal distribution of solar energy can vary considerably from one cycle to another. For example, geological data tell us that the interglacial period occurring 400,000 years ago (marine isotopic stage 11) was exceptionally long. This situation corresponds to a weak eccentricity where the seasonal and latitudinal distribution of solar energy varied very little. Celestial mechanics tell us that a similar situation should recur within 20,000 years, and for this reason the marine isotopic stage 11 is often considered to be one of the best analogues for the future climate. Many internal feedbacks generated by the different components of the climate system amplify or reduce the effect of the latitudinal and seasonal distribution of insolation. Thus, climate projections on the scale of a few hundreds of thousands of years require the variations of both insolation and atmospheric CO_2 (and other greenhouse gases) to be taken into account in models including representations of the atmosphere, ocean, cryosphere, lithosphere and vegetation.

One of the first models of this type was developed for the northern hemisphere at the University of Louvain-la-Neuve, Belgium (Gallée 1992). It successfully reproduced the main characteristics of the current climate, as well as the variations in ice volume during glacial-interglacial cycles. Since the model has been shown to provide reasonable simulations of the 100,000-year cycle, it has been applied as a second step to the simulation of future climates. Several tests have thus been carried out on the climate of the next 130,000 years, either by keeping the CO_2 constant at different levels (290 ppm, 200 ppm and 250 ppm), or by using the CO_2 variations of the last glacial-interglacial cycle (Loutre and Berger 2000). The results of these simulations suggest, on the one hand, that the climate of the next 50,000 years is particularly sensitive to the level of atmospheric CO_2 concentration and that our current interglacial period will be much longer than any other one in the past. It could last more than 55,000 years with CO_2 levels between 230 and 290 ppm: the first glacial stage would appear around 60,000 AD, and the next glacial maximum (in terms of ice volume) would be around 100,000 AD, followed by a deglaciation phase that would end around 120,000 AD. These results suggest that the marked differences between our interglacial period (present and future) and the previous Quaternary warm periods are due to the small insolation variations that characterize the former. Based on another scenario designed to reproduce the natural variations of CO_2 and not the anthropogenic contribution, other simulations have been carried out, either with a more elaborate version of the Loutre and Berger's model, or with a climate model of intermediate complexity coupled with a more sophisticated model of the evolution of polar ice sheets (Ganopolski et al. 2016). The results of these simulations are in agreement with those presented previously, and show that the next glacial inception will be postponed by at least 100,000 years.

Although, the variations in summer insolation at 65°N have long been considered as the pacemaker of glacial-interglacial transitions, the above results show that the level of atmospheric CO_2 will be a key parameter in the future. While the natural variations of CO_2 along with the insolation forcing exclude the possibility of a glacial episode in the future for at least 50,000 years, it is possible that the impact of the anthropogenic contribution will lead to a complete disappearance of polar ice sheets, and that a return to a glacial phase could occur only in 100,000 years. Coupled climate-ice sheet models, validated on the last glacial-interglacial cycle, will make it possible to explore the threshold values of CO_2 which could have long-term effects on the fate of ice sheets.

The Long-Term Future of the Polar Ice Sheets: Impact and Irreversibility

As seen earlier, the response times of the different components of the climate system are extremely variable, ranging from a few minutes to a few days for the atmosphere and from a few months to several hundreds of years for the ocean. While the ice sheets have long been considered as a slow component of the Earth system (with characteristic time scales ranging from thousands to hundreds of thousands of years), recent observations provide evidences that they can react to climate change far more quickly than previously thought. The last glacial-interglacial cycle demonstrates how deeply the climate is influenced by the slow development and rapid collapse of the ice sheets.

The ice core records retrieved from the Vostok and Dome C sites in Antarctica show that, for 800,000 years, the world has alternated between four ice sheets (during glacial periods) and only two ice sheets (during interglacial periods). In other words, Greenland and Antarctica withstood the warming that led to the disappearance of the Fennoscandian and North American ice sheets. There is no doubt that Greenland and West Antarctica have not always emerged unscathed from glacial-interglacial cycles. Indeed, during the last interglacial period (i.e. 130–115 ka ago), the sea level was 6 to 9 m higher (Kopp et al. 2009). It is therefore possible that anthropogenic activity could lead to the partial or total melting of Greenland (Charbit et al. 2008).

Recent observations of Greenland, and, more surprisingly, of Antarctica mass balances (Velicogna 2009) show that these ice sheets have become one of the main contributors to the increase in sea level (Cazenave et al. 2009). Their complete disappearance would lead to a sea-level rise of nearly 60 m: 6.6 m for Greenland and 52.8 m for Antarctica, of which 3.3 m would come from West Antarctica. These figures should be compared to the 120 m sea-level rise corresponding to the disappearance of the North American and Fennoscandian ice sheets in response to very small changes in insolation compared to the additional radiative forcing from anthropogenic activities. Also, the disappearance of past ice sheets was spread over 14,000 years (from the Last Glacial Maximum to the Mid-Holocene). The long-term effects (several hundred years) of anthropogenic forcing on ice sheets are not easy to model, partly because of uncertainties in the future socio-economic pathways over the twenty-first century and therefore in the evolution of the greenhouse gas concentrations in the atmosphere. It is therefore even more difficult to establish scenarios over several centuries (Charbit et al. 2008). However, several assumptions can be made about the long-term evolution of greenhouse gas emissions to explore the sensitivity of the present-day ice sheets with numerous scenarios. Performing simulations over several centuries or several millennia cannot be achieved through the use of general circulation models, which are too expensive in terms of computational time, and simplified climate models coupled with efficient ice-sheet models are required.

In fact, there are three different time frames relevant in the study of the evolution of ice sheets. The evolution over the twenty-first century, the basis of all IPCC analyzes, will very likely bring about a rise in sea level of several tens of centimeters (or even more), although there is a great deal of uncertainty linked to the emission scenarios, to climate model biases and to difficulties of ice-sheet models to capture the processes causing rapid dynamical change. The second horizon, beyond the twenty-first and the following centuries, is one where the CO_2 level may stabilize at three or four times that of the pre-industrial level, likely resulting in a massive retreat of Greenland and West Antarctica. These changes are also likely to modify the ocean circulation and the global climate. If this high level of CO_2 persists for a long time in the atmosphere, the ice-sheet melting could be irreversible, in the sense that there would no longer be any perennial snow in Greenland (Charbit et al. 2008). Finally, there is the much more distant third horizon, which raises the following question: for the last million years, our climate has oscillated between ice ages (long periods of about 100,000 years) and interglacial periods (short periods of about 10,000 years). Is it possible that the anthropogenic perturbation might cause a switch to another climate mode with strongly reduced ice sheets or even no ice sheet at all, similar to the hot climate mode of the pre-Quaternary era? In other words, is it possible that anthropogenic disturbance could induce modifications such that the next marked decline in summer insolation due in about 100,000 years (Loutre and Berger 2000) might not bring about an ice age?

Even if this question seems ‘futuristic’, we have good reasons to believe that the glacial-interglacial cycles of the last million years will no longer occur because the expected decline of insolation will not be large enough to compensate for the radiative forcing due to the high atmospheric CO_2 levels. This is what is suggested by the results of simulations carried out for periods such as the Pliocene around 3 Ma where the CO_2 level is estimated to have been around 405 ± 50 ppm.

In these scenarios, a key factor is the long time required to reach atmospheric CO_2 equilibrium which can be several tens to hundreds of thousands years (Archer et al. 1997). The anthropogenic disturbance is almost instantaneous, but its consequences will last for a very long time, and the

Milankovitch cycles that have so far allowed glacial-interglacial transitions through profoundly non-linear processes, can become inoperative in the future. Is it a bit presumptuous though to think that a couple of hundred years of 'energy profligacy' leading to a very large increase in atmospheric CO_2 could still be felt tens of thousands of years later? Maybe, but still, it is important to remember that studies of the Earth past climates show that the presence of ice sheets is associated with low CO_2 levels. It is therefore logical to think that, in a world that sustains high CO_2 concentrations, the behavior of present-day ice sheets will change in the short and medium term.

The world at the beginning of the Cenozoic (with 1120 ppm of CO_2 in the atmosphere) was much hotter than today. Antarctica was already in its polar position since the end of the Cretaceous (70 Ma ago), but far from forming an ice sheet, it was covered with forests. There was no sign of an ice sheet, until the CO_2 level dropped sufficiently to trigger the progressive freeze-up of Antarctica (DeConto and Pollard 2003). A planet with no ice sheet is not a figment of the imagination, rather their presence being the exception when viewed over geological times.

This book shows how the face of our planet changed over these time scales: from plate tectonics (millions of years) to the development of huge ice sheets at temperate latitudes (hundreds of thousands of years), with very strong variability in glacial climates at the scale of a few thousand years. Our own interglacial period, the Holocene, has been much more stable in terms of climate and has contributed to the extraordinary expansion of the human population. With an Earth inhabited by more than 9 billion men and women, it will be essential to manage climate change in order to protect societies and their environment. The past teaches us that our little blue planet has undergone many changes. It is not the planet that is in danger, it is rather the populations, especially as they do not have an equal standing in the face of climate change. And so, paradoxically, if man has become a major actor in climate change through industrial development and massive use of fossil fuels, he could also suffer at his own expense from upheavals and difficult situations that he has created himself.

References

Adler, R. F., et al. (2003). The Version 2 Global Precipitation Climatology Project (GPCP) monthly precipitation analysis (1979–Present). *Journal of Hydrometeorology, 4,* 1147–1167.

Allen, R. J., & Sherwood, S. C. (2008). Warming maximum in the tropical upper troposphere deduced from thermal winds. *Nature Geoscience, 1,* 399–403.

Archer, D., et al. (1997). Multiple timescales for neutralization of fossil fuel CO_2. *Geophysical Research Letters, 24,* 405–408.

Archer, D., et al. (2009). Atmospheric lifetime of fossil fuel carbon dioxide. *Annual Review of Earth and Planetary Sciences, 37,* 117–134. https://doi.org/10.1146/annurevearth031208.100296.

Bony, S., et al. (2006). How well do we understand and evaluate climate change feedback processes? *Journal of Climate, 19*(15), 3445–3482.

Bouttes, N., & Gregory, J. M. (2014). Attribution of the spatial pattern of CO_2-forced sea level change to ocean surface flux changes. *Environmental Research Letters, 9,* 034004. https://doi.org/10.1088/1748-9326/9/3/034004.

Bronselaer, B., et al. (2018). Change in future climate due to Antarctic meltwater. *Nature, 564,* 53–58. https://doi.org/10.1038/s41586-018-0712-z.

Cazenave, A., et al. (2009). Sea level budget over 2003-2008: A reevaluation from GRACE space gravimetry; Satellite altimetry and argo. *Global and Planetary Change, 65,* 83–88.

Charbit, S., et al. (2008). Amount of CO_2 emissions irreversibly leading to the total melting of Greenland. *Geophysical Research Letters, 35,* L12503. https://doi.org/10.1029/2008GLO33472.

Church, J. A., & White, N. J. (2011). Sea-level rise from the late 19th to the early 21st century. *Survey of Geophysics, 32,* 585–602.

Christiansen, H. H., et al. (2010). The thermal state of permafrost in the Nordic area during the International Polar Year 2007–2009. *Permafrost Periglacial Processes, 21,* 156–181.

Clark, P. U., et al. (2016). Consequences of twenty-first-century policy for multi-millennial climate and sea-level change. *Nature Climate Change, 6,* 360–369.

DeConto, R. M., & Pollard, D. (2003). Rapid cenozoic glaciation of Antarctica induced by declining atmospheric CO_2. *Nature, 421,* 245–249. https://doi.org/10.1038/nature01290.

DeConto, R. M., & Pollard, D. (2016). Contribution of Antarctica to past and future sea-level rise. *Nature, 531,* 591–597. https://doi.org/10.1038/nature17145.

Defrance, D., et al. (2017). Consequences of rapid ice-sheet melting on the Sahelian population vulnerability. In *Proceedings of the National Academy of Sciences* (Vol. 114, Issue 25). https://doi.org/10.1073/pnas.1619358114.

Dufresne, J.-L., & Bony, S. (2008). An assessment of the primary sources of spread of global warming estimates from coupled atmosphere-ocean models. *Journal of Climate, 21*(19), 5135–5144. https://doi.org/10.1175/2008jcli2239.1.

Dufresne, J.-L., & Saint-Lu, M. (2016). Positive feedback in climate: Stabilization or runaway, illustrated by a simple experiment. *Bulletin of American Meteorological. Society, 97*(5), 755–765. https://doi.org/10.1175/bams-d-14-00022.1.

Fourier, J.-B. (1824). Remarques générales sur les températures du globe terrestre et des espaces planétaires. *Annales de Chimie et de Physique,* 2e série, *XXVII*, 136–167.

Gallée, H., et al. (1992). Simulation of the last glacial cycle by a coupled, sectorially averaged climate-ice-sheet model 2. Response to insolation and CO_2 variations. *Journal of Geophysical Research, 97*(D14), 15713–15740.

Ganopolski, A., et al. (2016). Critical insolation-CO_2 relation for diagnosing past and future glacial inception. *Nature, 529,* 200–203. https://doi.org/10.1038/nature16494.

Garner, A. J., et al. (2018). Evolution of 21st century sea level rise projections. *Earth's Future, 6,* 1603–1615. https://doi.org/10.1029/2018EF000991.

Gillet-Chaulet, F., et al. (2012). Greenland ice sheet contribution to sea-level rise from a new-generation ice-sheet model. *The Cryosphere, 6,* 1561–1576. https://doi.org/10.5194/tc-6-1561-2012.

Golledge, N. R., et al. (2019). Global environmental consequences of twenty-first-century ice-sheet melt. *Nature, 566,* 65–72. https://doi.org/10.1038/s41586-019-0889-9.

Haywood, A. M., et al. (2011). Pliocene Model Intercomparison Project (PlioMIP): Experimental design and boundary conditions (experiment 2. *Geoscientific Model Development, 4,* 571–577. https://doi.org/10.5194/gmd-4-571-2011.

Haywood, A. M. et al. (2016). The Pliocene Model Intercomparison Project (PlioMIP) Phase 2: Scientific objectives and experimental design. *Climate of the Past, 12, 663–675*. https://doi.org/10.5194/cp-12-663-2016IMBIE team (2018). Mass balance of the Antarctic ice sheet from 1992–2017. *Nature*, 558, 219–222. https://doi.org/10.1038/s41586-018-0179.

IPCC. (Ed.). *Climate Change 2007: The Physical Science Basis; Contribution of Working Group I to the Fourth Assessment Report of the Intergovernmental Panel on Climate Change,* Cambridge, United Kingdom, and New-York, USA, Cambridge University Press.

IPCC. (Ed.). *Climate Change (2013): The Physical Science Basis; Contribution of Working Group I to the Fifth Assessment Report of the Intergovernmental Panel on Climate Change*, Cambridge, United Kingdom, and New-York, USA, Cambridge University Press.

Jevrejeva, S., Moore, J. C., Grinsted, A., & Woodworth, P. L. (2008). Recent global sea level acceleration started over 200 years ago? *Geophysical Research Letters, 35,* L08715.

Johnson, G. C., et al. (2007). Recent bottom water warming in the Pacific Ocean. *Journal of Climate, 20,* 5365–5375.

Keeling, C. D., et al. (1995). Interannual extremes in the rate of rise of atmospheric carbon dioxide since 1980. *Nature, 375,* 666–670.

Khodri, M., et al. (2001). Simulating the amplification of orbital forcing by ocean feedbacks in the last glaciation. *Nature, 410,* 570–574.

Kopp, R. E., et al. (2009). Probabilistic assessment of sea level during the last interglacial stage. *Nature, 462,* 863–867. https://doi.org/10.1038/nature08686.

Kouketsu, S., et al. (2011). Deep ocean heat content changes estimated from observation and reanalysis product and their influence on sea level change. *Journal of Geophysical Research (Ocean), 116,* C03012.

Lambert, S. J., & Fyfe, J. C. (2006). Changes in winter cyclone frequencies and strengths simulated in enhanced greenhouse warming experiments: results from the models participating in the IPCC diagnostic exercise. *Climate Dynamics, 26,* 713–728. https://doi.org/10.1007/s00382-006-0110-3.

Loutre, M.-F., & Berger, A. (2000). Are we entering an exceptionally long interglacial? *Climatic Change, 46,* 61–90.

Luo, D., et al. (2016). *Environmental Earth Science, 75,* 555. https://doi.org/10.1007/s12665-015-5229-2.

Madden, R. A., & Julian, P. R. (1994). Observations of the 40-50 day tropical oscillation: A review. *Monthly Weather Review, 122,* 814–837.

Manabe, S., & Wetherald, R. T. (1967). Thermal equilibrium of the atmosphere with a given distribution of relative humidity. *Journal of the Atmospheric Sciences, 24*(3), 241–259. https://doi.org/10.1175/1520-0469(1967)024%3c0241:TEOTAW%3e2.0.CO;2.

Meehl, G. A., Tebaldi, C., Walton, G., Easterling, D., & McDaniel, L. (2009). Relative increase of record high maximum temperatures compared to record low minimum temperatures in the U.S. *Geophysical Research Letters*, 36, L23701. https://doi.org/10.1029/2009gl040736.

Nerem, R. S., Beckley, B. D., Fasullo, J. T., Hamlington, B. D., Masters, D., & Mitchum G. T. (2018). Climate-change–driven accelerated sea-level rise. *Proceedings of the National Academy of Sciences*, 115(9), 2022–2025. https://doi.org/10.1073/pnas.1717312115.

Oerlemans, J., & Van der Veen, C. J. (1984). *Ice Sheets and Climate*, Reidel, 217 pp.

Oerlemans, J. (2005). Extracting a climate signal from 169 glacier records. *Science, 308*(5722), 675–677.

Peltier, D. F., et al. (2015). ICE-5G and ICE-6G models of postglacial relative sea-level history a Space geodesy constrains ice age terminal deglaciation: The global ICE-6G_C (VM5a) model. *Journal of Geophysical Research (Solid Earth), 120,* 450–487.

Purkey, S. G., & Johnson, G. C. (2010). Warming of global abyssal and deep southern ocean waters between the 1990s and 2000s: Contributions to global heat and sea level rise budgets. *Journal of Climate, 23,* 6336–6351.

Ramanathan, V., & Coakley, J. A., Jr. (1978). Climate modeling through radiative-convective models. *Reviews of Geophysics and Space Physics, 16*(4), 465.

Ramillien, G., et al. (2006). Interannual variations of the mass balance of the Antarctica and Greenland ice sheets from GRACE. *Global and Planetary Change, 53,* 198–208.

Ray, R. D., & Douglas, B. C. (2011). Experiments in reconstructing twentieth-century sea levels. *Progress in Oceanography, 91,* 495–515.

Rignot, E., et al. (2019). Four decades of Antarctic ice sheet mass balance from 1979–2017. *Proceedings of the National Academy of Sciences, 116*(4), 1095–1103. https://doi.org/10.1073/pnas.18128883116.

Rigor, I. G., & Wallace, J. M. (2004). Variations in the age of sea ice and summer sea ice extent. *Geophysical Research Letters, 31*. https://doi.org/10.1029/2004GL019492.

Romanovsky, V. E., Smith, S. L., & Christiansen, H. H. (2010a). Permafrost thermal state in the polar Northern Hemisphere during the International Polar Year 2007–2009: A synthesis. *Permafrost Periglacial Processes, 21,* 106–116.

Romanovsky, V. E., et al. (2010b). Thermal state of permafrost in Russia. *Permafrost Periglacial Processes, 21,* 136–155.

Shepherd, et al. (2012). A reconciled estimate of ice-sheet mass balance. *Science, 338,* 1183. https://doi.org/10.1126/science.1228102.

Stott, P. A., et al. (2004). Human contribution to the European heatwave of 2003. *Nature, 432,* 610–614.

Szopa, S., et al. (2013). Aerosol and ozone changes as forcing for climate evolution between 1850 and 2100. *Climate Dynamics, 40* (9–10), 2223–2250. https://doi.org/10.1007/s00382-012-1408-y.

Tarasov, L., & Peltier, W. R. (2007). Coevolution of continental ice cover and permafrost extent over the last glacial-interglacial cycle in North America. *Journal of Geophysical Research, 112*, F02S08. https://doi.org/10.1029/2006jf000661.

Tschudi, M. A., Stroeve, J. C., & Stewart, J. S. (2016). Relating the age of Arctic sea ice to its thickness, as measured during NASA's ICESat and IceBridge campaigns. *Remote Sensing*, *8*(6). https://doi.org/10.3390/rs8060457.

VandenBerghe, J. (2011). *Permafrost during the Pleistocene in North West and Central Europe*. Permafrost Response on Economic

Development, Environmental Security and Natural Resources (pp. 185–194).
Vial, J., et al. (2013). On the interpretation of inter-model spread in CMIP5 climate sensitivity estimates. *Climate Dynamics, 41*(11–12), 3339–3362. https://doi.org/10.1007/s00382-013-1725-9.
Velicogna, I., & Wahr, J. (2006). Measurements of time-variable gravity show mass loss in Antarctica. *Science, 311*, 1754–1756.
Velicogna, I. (2009). 'Increasing Rates of Ice Mass Loss from the Greenland and Antarctic Ice Sheets Revealed by GRACE'. *Geophysical Research Letters, 36*(L19503). https://doi.org/10.1029/2009glo4022.
Velicogna, I., et al. (2014). Regional acceleration in ice mass loss from Greenland and Antarctica using GRACE time-variable gravity data. *Geophysical Research Letters, 41,* 8130–8137. https://doi.org/10.1002/2014GL061052.
WCRP Global Sea Level Budget Group. (2018). Global sea-level budget 1993–present. *Earth Syst. Sci. Data, 10*, 1551–1590. https://doi-org.insu.bib.cnrs.fr/10.5194/essd-10-1551-2018.